

CRC Press
Taylor & Francis Group

HIGH VOLTAGE ENGINEERING

FAROUK A.M. RIZK • GIAO N. TRINH



HIGH VOLTAGE ENGINEERING

www.TechnicalBooksPdf.com

www.TechnicalBooksPdf.com

HIGH VOLTAGE ENGINEERING

FAROUK A.M. RIZK
Life Fellow IEEE
Lightning Electrotechnologies Inc

GIAO N. TRINH
Life Fellow IEEE
Consultant

CRC Press
Taylor & Francis Group
Boca Raton London New York

CRC Press is an imprint of the
Taylor & Francis Group, an **informa** business

www.TechnicalBooksPdf.com

CRC Press
Taylor & Francis Group
6000 Broken Sound Parkway NW, Suite 300
Boca Raton, FL 33487-2742

© 2014 by Taylor & Francis Group, LLC
CRC Press is an imprint of Taylor & Francis Group, an Informa business

No claim to original U.S. Government works
Version Date: 20140210

International Standard Book Number-13: 978-1-4665-1377-8 (eBook - PDF)

This book contains information obtained from authentic and highly regarded sources. Reasonable efforts have been made to publish reliable data and information, but the author and publisher cannot assume responsibility for the validity of all materials or the consequences of their use. The authors and publishers have attempted to trace the copyright holders of all material reproduced in this publication and apologize to copyright holders if permission to publish in this form has not been obtained. If any copyright material has not been acknowledged please write and let us know so we may rectify in any future reprint.

Except as permitted under U.S. Copyright Law, no part of this book may be reprinted, reproduced, transmitted, or utilized in any form by any electronic, mechanical, or other means, now known or hereafter invented, including photocopying, microfilming, and recording, or in any information storage or retrieval system, without written permission from the publishers.

For permission to photocopy or use material electronically from this work, please access www.copyright.com (http://www.copyright.com/) or contact the Copyright Clearance Center, Inc. (CCC), 222 Rosewood Drive, Danvers, MA 01923, 978-750-8400. CCC is a not-for-profit organization that provides licenses and registration for a variety of users. For organizations that have been granted a photocopy license by the CCC, a separate system of payment has been arranged.

Trademark Notice: Product or corporate names may be trademarks or registered trademarks, and are used only for identification and explanation without intent to infringe.

Visit the Taylor & Francis Web site at
http://www.taylorandfrancis.com

and the CRC Press Web site at
http://www.crcpress.com

www.TechnicalBooksPdf.com

Contents

Preface xix
Acknowledgments xxv
Authors xxvii

1. Power System Overvoltages 1
1.1 Introduction 1
1.2 Lumped Circuits 2
1.3 Distributed Parameter Circuits 4
1.3.1 Temporary Overvoltages 4
1.3.1.1 Ferranti Effect 4
1.3.1.2 Voltage Rise on Sound Phases 8
1.3.2 Transient Overvoltages on Transmission Lines 10
1.3.2.1 Wave Equations 10
1.3.2.2 Points of Discontinuity 11
1.3.2.3 Traveling Waves of General Form 14
1.3.2.4 Lattice Diagram 16
1.3.2.5 Energization of Open Line 17
1.3.2.6 Three-Phase Lines 17
1.3.3 Overvoltages due to Current Interruption 19
1.3.3.1 Interruption of Small Inductive Currents 19
1.3.3.2 Interruption of Capacitive Current 20
1.4 Electromagnetic Transient Program 21
References 23

2. Electrostatic Field Calculation 25
2.1 Electromagnetism: Maxwell Equations 25
2.1.1 Fundamental Laws 25
2.1.2 Boundary Conditions 26
2.2 Electrostatics: Laplace Equation 27
2.3 Analytical Solution of the Laplace Equation 28
2.3.1 Cartesian Coordinates 29
2.3.1.1 Uniform Field 29
2.3.1.2 Uniform Field Electrodes 30
2.3.1.3 Uniform Field in the Presence of Composite Dielectrics 35
2.3.2 Cylindrical Coordinates 36
2.3.2.1 Coaxial Cable 37
2.3.2.2 Cylindrical Field in the Presence of Composite Dielectrics 38
2.3.3 Spherical Coordinates 40
2.3.3.1 Spherical Field 40
2.3.4 Spheroidal Coordinates 42
2.3.4.1 Prolate Spheroidal Coordinates 42
2.3.4.2 Hyperboloidal Field 49
2.3.4.3 Oblate Spheroidal Metal Protrusion in a Uniform Field 50

www.TechnicalBooksPdf.com

2.4 Methods of Transformation 53
2.4.1 Method of Images 53
2.4.1.1 Images with Respect to a Ground Plane 53
2.4.1.2 Image with Respect to a Cylindrical Conductor 55
2.4.1.3 Sphere Gap 56
2.5 Numerical Solution Laplace Equation 60
2.5.1 Field and Potential around Elementary Charges 60
2.5.2 Method of Successive Images 62
2.5.2.1 Overhead Line 63
2.5.2.2 High-Voltage Cable 66
2.5.3 Method of Charge Simulation 69
2.5.3.1 Two-Dimensional Field 69
2.5.3.2 Field in the Presence of Composite Dielectrics 70
2.5.3.3 Three-Dimensional Field: Representation of the Surface Charge by Orthogonal Functions 70
2.5.3.4 Floating Electrode 72
2.5.4 Method of Global Solution 74
2.5.4.1 Method of Finite Differences 74
2.5.4.2 Method of Finite Elements 75
References 79

3. Application of Statistical Analysis in High Voltage Engineering 81
3.1 Introduction 81
3.2 Characterization of a Set of Data under Specific Conditions 81
3.2.1 Global Statistical Parameters 82
3.2.2 Experimental (Discrete) Distribution 82
3.2.2.1 Experimental Distribution with a Small Amount of Data 82
3.2.2.2 Experimental Distribution with a Large Amount of Data 84
3.2.2.3 Correspondence with the Global Parameters 85
3.2.2.4 Other Characteristic Parameters 85
3.2.3 Statistical Functions (Models) 85
3.2.3.1 Discrete Distributions 85
3.2.3.2 Continuous Distributions 88
3.3 Estimation of the Population Distribution 94
3.3.1 Randomness Test 94
3.3.2 Using the Sample's Statistic Parameters 94
3.3.2.1 Sample Means 95
3.3.2.2 Sample Variance 95
3.3.3 Confidence Interval 96
3.3.3.1 One-Sided Test 96
3.3.3.2 Two-Sided Test 97
3.3.4 Distribution Test 98
3.3.4.1 Chi-Square Test 98
3.3.4.2 Graphical Test 98
3.3.4.3 Linear Regression Analysis 103
3.3.5 Adequacy Representation of a Statistical Model 104
3.3.5.1 Extreme Value Distribution 107
3.3.5.2 Weibull Distribution 108
3.3.5.3 Discussion 109
3.3.6 Direct Extrapolation of Experimental Data 110
3.3.7 Verification of an Experimental Law 110
3.4 Weak Link Statistics 112

www.TechnicalBooksPdf.com

3.5 Optimization of Experimental Data 112
3.5.1 Determination of the Component Distributions 113
3.5.1.1 Audible Noise 113
3.5.1.2 Streamer Length 113
3.5.2 Improvement of Experimental Data 114
3.5.2.1 Breakdown Probability of Elementary Volume 116
3.6 Joint Probability 117
3.6.1 Risk of Failure 117
3.6.2 *V–t* Breakdown Characteristic 117
3.7 Verification of Characteristics or Behavior by Specific Tests 118
3.7.1 Optimization of the Number of Test Samples 118
3.7.1.1 Minimum Required Number of Tests 118
3.7.2 Statistical Significance of Test Procedures 118
3.7.2.1 Test with Impulse Voltage 119
3.7.2.2 Practical Test Procedures 120
3.7.2.3 Test with AC Voltage 122
3.7.3 Computer Simulation of Test Procedures 124
3.7.3.1 Hancox Test Procedures 125
3.7.3.2 Fryxell (or α–β) Test Procedures 126
3.7.3.3 Modified α–β Test Procedures 126
3.8 Conclusions 127
References 127

4. Electrical Breakdown in Gases 129
4.1 Introduction 129
4.2 Gases Composed Uniquely of Neutral Molecules 130
4.2.1 General Laws and Definitions 130
4.2.1.1 Conservation of Energy 130
4.2.1.2 Conservation of Momentum 130
4.2.1.3 Inelastic Collisions 131
4.2.1.4 Hypothesis of Avogadro 132
4.2.1.5 Law of Gay-Lussac 132
4.2.2 Distribution of Velocities of Gas Molecules 133
4.2.2.1 Distribution Function of the Velocities of Gas Molecules 134
4.2.2.2 Some Characteristic Values of the Velocity *c* of Gas Molecules in Air and SF_6 135
4.2.3 Equal Partition of Energy 136
4.2.4 Mean Free Path 137
4.2.4.1 Statistical Distribution of Free Paths 137
4.2.4.2 Evaluation of the Mean Free Path 138
4.2.5 Diffusion in a Gas 139
4.2.5.1 Number of Molecules Traversing a Unit Area per Second 139
4.2.5.2 General Equation of Diffusion 140
4.2.5.3 Diffusion of a Gas in Another Gas 141
4.3 Atomic Structure of the Elements 145
4.3.1 Bohr's Atomic Model 145
4.3.2 Energy States of an Electron in an Atom 150
4.3.3 Exclusion Principle of Pauli 150
4.3.4 Interpretation of the Periodic Table of Elements 150
4.4 Excitation and Ionization of Atoms 151
4.4.1 Ionization by Electronic Collisions 152
4.4.2 Ionization by Ionic Collisions 154

www.TechnicalBooksPdf.com

4.4.3 Photoionization 155
4.4.4 Thermal Ionization 156
4.4.5 Cumulative Ionization 157
4.5 Ion Movement in an Electric Field 157
4.5.1 Ion Mobility 157
4.5.2 Electron Mobility 161
4.5.3 Ions in a Gas Subjected to an Electric Field 162
4.5.4 Electric Current Produced by the Movement of a Charged Particle 163
4.6 Deionization and Deexcitation 164
4.6.1 Recombination 165
4.6.2 Attachment 166
4.6.3 Deionization by Diffusion 166
4.7 Sources of Free Electrons 167
4.8 Development of Electron Avalanches 170
4.8.1 Townsend Discharge 170
4.8.2 Ionization by Electron Collisions in the Gas Volume 171
4.8.2.1 Mechanism of Discharge by Electronic Collisions: Electron Avalanche 171
4.8.2.2 Townsend's First Coefficient of Ionization, α 173
4.8.2.3 Practical Expressions of Townsend's First Ionization Coefficient 174
4.8.3 Electronegative Gases 175
4.9 Classical Theory of Gaseous Discharges 176
4.9.1 Influence of Secondary Processes 176
4.9.2 Regimes of Sustained and Self-Sustained Discharges 178
4.9.3 Onset Conditions of Self-Sustained Discharge 179
4.9.3.1 Breakdown Voltage in Uniform Fields: Paschen's Law 179
4.9.3.2 Streamer Criterion: Onset Condition in Nonuniform Fields 180
4.10 Examples of Self-Sustained Discharges 181
4.10.1 Glow Discharges 182
4.10.1.1 Physical Mechanism of the Discharge 183
4.10.1.2 Electrical Characteristics 184
4.10.2 Electric Arc 185
4.10.2.1 Physical Mechanism 186
4.10.2.2 Arc Characteristics 186
4.11 Fundamentals of Corona Discharges in Atmospheric Air 187
4.11.1 Empirical Expressions of Onset and Breakdown of Practical Gap Configurations 188
4.11.2 Active Ionization Processes and Source of Free Electrons 188
4.11.3 Corona Discharges under Negative Polarity 189
4.11.3.1 Electron Avalanche and Space Charges 189
4.11.3.2 Negative Corona Modes 192
4.11.4 Corona Discharges under Positive Polarity 199
4.11.4.1 Electron Avalanche and Ion Space Charge 199
4.11.4.2 Modes of Positive Corona Discharges 201
4.11.5 Corona Discharges under Alternating Voltage 208
4.11.6 Impact of Corona Discharges 209
4.11.6.1 Main Effect of Corona Discharges on High-Voltage Testing 209
4.11.6.2 Main Effects of Corona Discharges on Overhead Lines 209
4.12 Electric Breakdown in Compressed Gases: Sulfur Hexafluoride 213
4.12.1 Sulfur Hexafluoride 213
4.12.2 Ionization Processes and Source of Free Electrons 214
4.12.3 Mixtures of SF_6 and Neutral Gases 215

www.TechnicalBooksPdf.com

4.12.4 Dielectric Withstand 217
4.12.4.1 Uniform and Quasiuniform Fields 217
4.12.4.2 Leader Breakdown in Nonuniform Fields 218
References 220

5. Breakdown Characteristics of Long Air Gaps 223
5.1 Introduction 223
5.2 Breakdown of Long Air Gaps with Fast Front Impulses 224
5.2.1 Breakdown Mechanism 224
5.2.2 Standard Lightning Impulse Breakdown Voltage 228
5.3 Air Gap Strength under Direct Voltage 228
5.4 Positive Switching Surge Strength of Long Gaps 230
5.4.1 System Overvoltages 230
5.4.2 Air Gap Strength Data 231
5.4.3 Modeling of Positive Critical Switching Impulse Breakdown 233
5.5 Air Gap Breakdown under Composite Stress 236
5.5.1 Experimental Results 236
5.5.2 Modeling of Air Gap Breakdown under Composite Voltages 238
5.6 AC Breakdown of Long Air Gaps 241
5.6.1 Breakdown Mechanism 241
5.6.2 AC Breakdown Test Procedures 241
5.6.3 AC Breakdown Test Data 243
5.7 Altitude Effect on Air Gap Breakdown 244
5.8 Humidity Effects on Air Gap Breakdown 246
5.8.1 Effect of Humidity with Special Reference to Streamer Breakdown 247
5.8.2 Effect of Humidity on Switching Impulse Breakdown 248
5.8.3 More Recent Approaches to Humidity Corrections 250
5.8.4 Modeling of Humidity Effects on Switching Impulse Breakdown 252
5.8.5 Comparison of Correction Factors 255
5.8.6 Further Application of Generalized Correction Approach 256
References 257

6. Electric Breakdown in Liquids 261
6.1 Chemical Composition of Mineral Oil 261
6.2 Interest in Synthetic Oils 262
6.2.1 Required Properties for Synthetic Oils 263
6.2.2 Principal Synthetic Oils Presently Available 263
6.2.2.1 Aliphatic Hydrocarbons 265
6.2.2.2 Silicone Oil 265
6.2.2.3 Perfluorocarbons 266
6.2.2.4 Synthetic Esters 266
6.3 Breakdown Mechanisms 266
6.3.1 Early Studies 266
6.3.1.1 Electrical Conduction and Strength of Pure Liquids 267
6.3.1.2 Conduction and Breakdown Processes 268
6.3.1.3 Breakdown of Commercial Liquids 269
6.3.1.4 Breakdown of Liquid–Solid Dielectrics 270
6.3.2 Breakdown in Short Gaps 271
6.3.2.1 Streamer Discharges in Oil 271
6.3.2.2 Formation of a Gaseous Cavity 273
6.3.3 Breakdown of Long Oil Gaps 276
6.3.3.1 Direct Breakdown 276
6.3.3.2 Breakdown by Discharges in Streamer Burst 281

6.4 Factors Affecting the Oil Insulation 284
6.4.1 Impurities 284
6.4.2 Dissolved Gases and Hydrostatic Pressure 284
6.4.3 Humidity 285
6.4.4 Dissolved Metals 285
6.4.5 Solid Particle Contamination 285
6.4.5.1 Particle Content 286
6.4.5.2 Effect of Stressed Area and Volume 286
6.4.6 Dielectric Interfaces 294
6.4.6.1 Incipient Fault 294
6.4.6.2 Electrostatic Discharges 295
6.4.7 Aging and Decomposition By-Products of Oils 295
References 295

7. Electric Breakdown in Solid and Composite Materials 299
7.1 Introduction 299
7.1.1 Intrinsic Breakdowns 299
7.1.1.1 Theory of Intrinsic Strength 299
7.1.1.2 Measurement of Intrinsic Strength 300
7.1.2 Initial Breakdown and Strength 301
7.1.3 Aging and Incipient Fault 301
7.1.3.1 Thermal Breakdown 302
7.1.3.2 Breakdown by Electrical Discharges 303
7.1.3.3 Mechanical Aging 304
7.1.3.4 Combined Stress 304
7.1.3.5 Chemical Deterioration 305
7.1.3.6 Electrochemical Deterioration 305
7.1.4 Decomposition By-Products 306
7.1.5 Insulation Systems Reviewed 306
7.2 Polymeric (PE and XLPE) Insulation 306
7.2.1 Physical–Chemical Properties of Insulating Materials 307
7.2.1.1 Natural Rubber 307
7.2.1.2 Ethylene–Propylene Rubber 307
7.2.1.3 Butyl Rubber 308
7.2.1.4 Silicone Rubber 309
7.2.1.5 Neoprene and Polychloroprene 309
7.2.1.6 Polyvinyl Chloride 310
7.2.1.7 Polyethylene and Cross-Linked Polyethylene 310
7.2.2 Dielectric Performance of New Samples 311
7.2.2.1 Initial Breakdown 312
7.2.2.2 Factors Affecting Synthetic Polymer Insulation 313
7.3 Paper–Oil Composite Insulation 316
7.3.1 Lapped Insulation 316
7.3.1.1 Physical–Chemical Properties of Impregnated Paper–Oil Insulation 318
7.3.1.2 Improvement of Insulation Properties 324
7.3.2 Dielectric Performances of New Samples 325
7.3.2.1 Initial Strength 326
7.3.2.2 Factors Affecting the Initial Strength 327
7.4 Gas–Solid (SF_6–Epoxy) Composite Insulation 328
7.4.1 Gas (SF_6) Insulation 329
7.4.1.1 Corona Onset Field 329
7.4.1.2 Limit Withstand Field 331
7.4.1.3 Voltage–Time Breakdown Characteristics 331

7.4.2 Solid (Epoxy) Insulation 335
7.4.2.1 Initial Breakdown Strength 341
7.4.2.2 Voltage–Time Breakdown Characteristics 341
7.4.3 Factors Affecting SF_6–Epoxy Insulation 344
References 349

8. Selection of Overhead Transmission Line Conductors 351
8.1 Development of Overhead Lines 351
8.1.1 AC Power Transmission Lines 351
8.1.2 Bundle Conductor to Improve the Natural Transmission Capability of AC Lines 352
8.1.3 Electrostatic Field Optimization of Conductor Bundle 354
8.2 Average Height of Conductors 356
8.2.1 Electric Field at Ground in the Vicinity of the HV Line 357
8.2.2 Magnetic Field at Ground in the Vicinity of the HV Line 360
8.3 Selection of Conductors 362
8.3.1 Corona Onset Conditions 362
8.3.2 Energy Losses 363
8.3.2.1 Mechanism of Generating Energy Losses from Corona Discharges 363
8.3.2.2 Empirical Formulae for Evaluating Energy Losses 364
8.3.2.3 Corona Loss Characteristics of Bundle Conductors 366
8.3.3 Electromagnetic Interference 366
8.3.3.1 Generation Mechanism of Interference from Corona Discharges 367
8.3.3.2 Interference to the Radio Reception 370
8.3.3.3 Quantification of Electromagnetic Interference 373
8.3.3.4 Measurement of Electromagnetic Interference 375
8.3.3.5 Empirical Formulae for the Calculation of Interference from a Line 379
8.3.3.6 Calculation of Electromagnetic Interference on a Single-Phase Line 380
8.3.3.7 Calculation of Electromagnetic Interference from a Three-Phase Line 385
8.3.3.8 Television Interference 390
8.3.4 Audible Noise 393
8.3.4.1 Static and Acoustic Pressures 394
8.3.4.2 Propagation of Acoustic Wave 394
8.3.4.3 Solution of the Wave Equation 397
8.3.4.4 Specific Acoustic Notions 400
8.3.4.5 Acoustical Characteristics of Corona Discharges 401
8.3.4.6 Measurement of Audible Noise 406
8.3.4.7 Sound Meter 406
8.3.4.8 Methods of Calculation of Audible Noise 408
8.3.5 Selection of Conductors 412
8.3.5.1 Evaluation of the Worst-Case Performances 413
8.3.5.2 Long-Term Corona Performance 421
8.3.6 Emission of Polluting Effluents 422
8.4 Selection of Conductors for HVDC Lines 424
8.4.1 Average Conductor Height 424
8.4.2 Selection of Conductors 425
8.4.2.1 Corona Onset 425
8.4.2.2 Generating Functions 425
8.4.2.3 Corona Losses 425
8.4.2.4 Radio Interference 431
8.4.2.5 Audible Noise 434
8.4.2.6 Experimental Evaluation of Corona Performance of Conductor 436
References 437

9. Lightning Incidence and Lightning Protection 439
9.1 Cloud Charging 439
9.2 Meteorological Data 440
9.3 Lightning Detection and Location 442
9.3.1 Flash Counters 442
9.3.2 Lightning Location Systems 442
9.3.2.1 Direction Finders 442
9.3.2.2 Time-of-Arrival (TOA) Method 443
9.4 Lightning Flash Parameters 444
9.4.1 Flash Classification 444
9.4.2 Return Stroke Current 444
9.4.2.1 Statistical Distribution 444
9.4.2.2 Current Waveform 444
9.4.3 Statistical Parameters 447
9.5 Lightning Attachment 449
9.5.1 Negative Downward Flash 449
9.5.2 Return Stroke 450
9.5.2.1 General 450
9.5.2.2 Return Stroke Models 450
9.5.3 Lightning Attachment Models 452
9.5.3.1 Electrogeometric Model 452
9.5.3.2 Eriksson and Dellera–Garbagnati Models 453
9.5.3.3 Rizk Model 454
9.5.4 Shielding Failure 459
9.5.5 Backflashover 459
9.5.5.1 Tower Top Potential 461
9.5.5.2 Tower Surge Impedance 463
9.5.5.3 Conductor Coupling 465
9.5.5.4 Reflections from Adjacent Towers 466
9.5.5.5 Tower Grounding 466
9.5.5.6 Estimation of Backflashover Rate 467
9.6 Upward Flash 467
9.7 Protective Measures 469
9.7.1 Lightning Rods and Masts 469
9.7.2 Ground Wires 470
9.7.3 Improving Grounding 471
9.7.4 Line Arresters 472
9.7.5 Streamer Inhibition 473
References 474

10. High-Voltage Insulators 479
10.1 Introduction 479
10.2 Insulator Types and Materials 479
10.2.1 Insulator Types 479
10.2.2 Insulator Materials 481
10.2.2.1 Porcelain 481
10.2.2.2 Glass 482
10.2.2.3 Polymers 482
10.3 Electrical Performance of High-Voltage Insulators 484
10.3.1 Lightning Impulse Flashover 484
10.3.2 Switching Impulse Flashover 487
10.3.2.1 Comparison with Air Gaps 487
10.3.2.2 Effect of Rain 487

10.3.3 Pollution Flashover 490
10.3.3.1 Pollution Layer Buildup 490
10.3.3.2 Site Severity 491
10.3.3.3 Effect of Exposure Time 492
10.3.3.4 Pollution Layer Pattern 494
10.3.3.5 Effect of Operating Voltage 495
10.3.3.6 Effect of Distance from Pollution Source 495
10.3.3.7 Effect of Wind Speed 496
10.3.3.8 Insulator Surface Wetting 498
10.3.3.9 Pollution Flashover Mechanism 501
10.3.4 Mechanical Requirements 517
10.4 Insulator Selection 519
10.4.1 Insulator Type and Material 519
10.4.2 Insulator Profile 520
10.4.3 Design Approach 520
10.4.3.1 Flowchart 520
10.4.3.2 Statistical Approach to Insulator Selection 522
References 526

11. High-Voltage (Underground) Cables 531
11.1 Development of High-Voltage Cables 531
11.1.1 Paper–Oil-Insulated Cables 531
11.1.1.1 Pressurized Oil-Filled Paper-Impregnated Cables 532
11.1.1.2 Mass-Impregnated Cables 534
11.1.2 Extruded Insulation Cables 534
11.1.3 Cables with Gas Insulation 535
11.1.3.1 Pressurized-Gas Cables 535
11.1.3.2 Rigid Gas-Insulated Cables (Lines) 535
11.1.4 Future Trends in High-Voltage Cables 536
11.1.4.1 Forced Cooling 536
11.1.4.2 Synthetic Paper and Tape 537
11.1.4.3 Pressure 538
11.1.4.4 Compressed SF_6-Insulated Cable 538
11.2 High-Voltage AC Cables and Accessories 538
11.2.1 Cable Parameters 539
11.2.2 Dimensioning of the Conductor 540
11.2.2.1 Energy Losses 542
11.2.2.2 Thermal Dissipation 545
11.2.3 Dimensioning of the Insulation Based on Limit Field (New Cable) 547
11.2.3.1 Selection of the Withstand Voltage Level 547
11.2.3.2 Determination of the Design Field, E_0 548
11.2.3.3 Determination of the Insulation Thickness 549
11.3 Aging and Incipient Fault 551
11.3.1 Self-Contained Oil-Filled Cables 551
11.3.1.1 Thermal Aging 551
11.3.1.2 Electrical Aging 551
11.3.1.3 Environmental Aging 553
11.3.2 Polymeric (PE and XLPE) Cables 553
11.3.2.1 Thermal Aging 553
11.3.2.2 Electrical Aging 553
11.3.2.3 Environmental Aging 558
11.3.2.4 Decomposition By-Products 560

11.3.3 Gas (SF_6)-Insulated Cables (Lines) ... 560
11.3.3.1 Thermal and Mechanical Aging ... 560
11.3.3.2 Electrical Aging ... 560
11.3.3.3 Environmental Aging ... 562
11.3.4 Experimental Evaluation of Life Function ... 562
11.3.4.1 Accelerated Aging Tests ... 562
11.3.4.2 Analysis of Data ... 563
11.3.4.3 Optimization of Test Parameters ... 564
11.4 Gas-Insulated Substations ... 565
11.4.1 Generation of Fast Transients ... 565
11.4.2 Risk of Burn Through ... 568
11.4.3 Special Considerations for Operating Gas-Insulated Equipment ... 569
11.4.3.1 Temperature ... 569
11.4.3.2 Humidity ... 569
11.5 Accessories ... 571
11.5.1 Impregnated Paper–Oil Accessories ... 571
11.5.1.1 Principal Types of Accessories ... 571
11.5.2 Extruded Insulation ... 573
11.5.3 Gas (SF_6) Insulation ... 575
11.6 High-Voltage DC Cables and Accessories ... 577
11.6.1 Dimensioning of Conductors ... 578
11.6.2 Dimensioning of the Insulation ... 578
11.6.2.1 Field Distribution in Steady-State Regime ... 578
11.6.2.2 Field Distribution in Transient Conditions ... 579
11.6.2.3 Field Enhancement in Butt Gap ... 580
11.6.3 SF_6-Insulated Cable ... 581
11.6.4 Accessories ... 582
11.6.4.1 Impregnated Paper–Oil Insulation ... 582
11.6.4.2 Polymer and SF_6 Insulation ... 582
11.6.4.3 DC Pollution ... 582
11.7 Maintenance Practices Consideration ... 583
11.7.1 Actual State of Insulation ... 583
11.7.2 End of Life ... 583
References ... 584

12. Power Transformers ... 587
12.1 Introduction ... 587
12.2 Transformer Insulation ... 591
12.2.1 Operating Stresses ... 591
12.2.2 Oil–Paper Insulation in Power Transformers ... 592
12.2.2.1 Winding Arrangement ... 592
12.2.2.2 Transformer Insulation Characteristics ... 593
12.2.2.3 Physical–Chemical Properties of Oil-Impregnated Paper ... 595
12.2.2.4 Control of Humidity ... 598
12.2.2.5 Control of Particle Contamination ... 600
12.2.3 SF_6 Insulation ... 604
12.3 Considerations on the Dimensioning of Oil–Paper Insulation ... 606
12.3.1 Cumulative Stress ... 606
12.3.2 Breakdown Probability ... 607
12.3.3 Example of Assessment for Adequacy of a Test Cell ... 610

12.3.3.1 Field Calculation....610
12.3.3.2 Cumulative Stress....613
12.3.3.3 Probability of Breakdown....614
12.4 Audible Noise from Power Transformers....617
12.4.1 Transformer Audible Noise Characteristics....618
12.4.2 Representation of the Audible Noise from Power Transformers....619
12.4.3 Audible Noise in Far Field....621
12.5 Standard HV Testing of Power Transformers....621
12.5.1 Test with AC Voltage....621
12.5.1.1 Applied Potential Test....621
12.5.1.2 Induced Voltage Test....622
12.5.2 Impulse Tests....623
12.5.2.1 Standard Impulse....624
12.5.2.2 Switching Impulse....625
12.5.2.3 Chopped Wave....630
12.5.3 Detection of Failure during Impulse Tests....630
12.6 Aging and Incipient Faults....631
12.6.1 Aging Mechanism....631
12.6.1.1 Thermal Aging....631
12.6.1.2 Electrical Aging....632
12.6.1.3 Environmental Aging....633
12.6.1.4 Decomposition By-Products....634
12.6.2 Assessment of the Actual State of the Insulation....634
12.6.2.1 Measurement of Bulk Parameters....634
12.6.2.2 Measurement of Physical–Chemical Characteristics of the Insulation Components....635
12.6.2.3 Nondestructive Tests....637
12.6.2.4 End of Life....637
12.7 Considerations for Operating and Maintenance....639
12.7.1 Operating....640
12.7.2 Maintenance....642
12.7.2.1 Routine Maintenance....642
12.7.2.2 Diagnostic Maintenance....642
12.7.2.3 Monitoring....645
12.7.2.4 On-Site Evaluation....645
References....645

13. Insulation Coordination....649
13.1 Introduction....649
13.2 Classification of Voltages and Overvoltages....649
13.3 Origin of Overvoltages....650
13.4 Representative Overvoltages....650
13.5 Performance Criterion....651
13.6 Withstand Voltage....651
13.7 Insulation Coordination Procedure....651
13.7.1 Determination of Representative Voltages and Overvoltages....652
13.7.1.1 Continuous Power Frequency Voltage....652
13.7.1.2 Temporary Overvoltages....652
13.7.1.3 Slow-Front Overvoltages....652
13.7.1.4 Fast-Front Overvoltages....662

13.7.2 Determination of Coordination Withstand Voltage (U_{cw}) 667
13.7.2.1 Deterministic Approach 667
13.7.2.2 Statistical Approach: Risk of Failure 667
13.7.3 Determination of Required Withstand Voltage (U_{rw}) 668
13.7.3.1 Altitude Correction Factor 669
13.7.3.2 Safety Factor (K_s) 669
13.7.4 Selection of Standard Withstand Voltage (U_w) 670
13.8 Surge Arresters 670
13.8.1 General 670
13.8.2 Rated Voltage 672
13.8.3 Discharge Current 672
13.8.4 Impulse Current Tests 672
13.8.5 Residual Voltages 672
13.8.6 Arrester Durability Requirements 673
13.8.6.1 Insulation Withstand 673
13.8.6.2 Thermal Stability 673
13.8.6.3 Leakage Test 673
13.8.6.4 Line Discharge Energy 673
13.8.6.5 Operating Duty Test 674
13.8.6.6 Temporary Overvoltages 674
13.8.6.7 Pressure Relief Test 674
References 675

14. High-Voltage Testing and Measuring Techniques 677
14.1 Introduction 677
14.2 Test Categories 677
14.3 Generation of the Test Voltage 680
14.3.1 AC Voltage 680
14.3.1.1 Cascaded Transformers 680
14.3.1.2 Resonant Circuit 690
14.3.1.3 Rotating Machines 696
14.3.2 DC Voltage 696
14.3.2.1 Basic Rectifier Circuit 696
14.3.2.2 Voltage Doubling Circuit 698
14.3.2.3 Cascade Rectifier 699
14.3.3 Impulse Voltage 701
14.3.3.1 Impulse Generators 702
14.3.3.2 Chopped Impulse 709
14.3.4 Long Front Switching Impulse 710
14.3.4.1 Capacitor Discharge 710
14.3.4.2 Short Time Energization 711
14.4 HV Measuring Techniques 717
14.4.1 Grounding and Shielding of Control and Measuring Cables 717
14.4.1.1 Grounding of HV Test Area 717
14.4.1.2 Shielding of Control and Measuring Cables 721
14.4.1.3 Electromagnetic Shielding of HV Laboratory 722
14.4.2 Sphere Gaps as a Voltage Measuring and Protection Device 723
14.4.3 Voltage Measurement 727
14.4.3.1 Voltage Divider 730
14.4.3.2 Low-Voltage Arm 734
14.4.3.3 Connecting Lead 737
14.4.3.4 High Voltage Electrode 737
14.4.3.5 Measuring Instrument 739

14.4.4 Measurement of Current 739
14.4.4.1 Measurement of Fast Transient Corona Pulses 740
14.4.4.2 Measurement of Impulse Current 740
14.4.5 Measurement of Power Losses 743
14.4.5.1 Schering Bridge 744
14.4.5.2 Current Comparator Bridge 746
14.4.5.3 Parallel *R*–*C* Representation 747
14.4.6 Gas-Insulated Capacitor 747
14.4.7 Partial Discharges Measurement 749
14.4.7.1 PD Measurement Using Large Bandwidth Detector Circuit 750
14.4.7.2 PD Measurement with Narrow Bandwidth Detector Circuit 754
14.4.7.3 Calibration 755
14.4.7.4 Capacitive Tap 756
14.4.8 Digital Techniques in HV Measurements 756
14.4.8.1 Inherent Errors in Digital Recorders 757
14.4.8.2 Dynamic Errors 759
References 760

Index 763

Preface

High voltage engineering is a vast subject, extending from basic knowledge in physics, chemistry, and material science to applications in the insulation design of high-voltage transmission lines and substation equipment. Although high voltage engineering applications extend to medicine and nuclear science, these topics are beyond the scope of this book. The book is targeted towards those in the electric power profession. The selection of what material to include is a difficult decision. To limit the scope even further, it was decided to exclude material on the design and testing of high-voltage switchgear, a subject of great scientific and practical interest that is usually dealt with under the designation: high power engineering.

There are some compelling reasons to write a new book on high voltage engineering. Firstly, there is a new revival of worldwide interest in EHV and UHV power transmission. UHV ac transmission lines have been operating for the last two decades in Russia, and more recently, in China. UHV ac lines of 1200 kV are also being planned in India. UHV dc transmission lines of ±750 and ±800 kV have been operating in Russia and, more recently, in China and are presently in the planning stage in India. A ±1000 kV UHV dc line is being designed in China, with commercial operation foreseen in about two years.

Second, many experts in high voltage engineering have retired in the last decade, and it would be helpful for the sake of a new generation of engineers to conserve some of that experience.

The book comprises 14 chapters. Insulation systems of transmission lines and power equipment are exposed to stresses caused by operating voltage as well as those due to internal and external overvoltages. Chapter 1 provides a brief review of power system overvoltages. It starts with simple lumped circuits that can be treated by direct solution of differential equations or by Laplace transforms. Analysis is then extended to long transmission lines with distributed parameters. Temporary overvoltages (TOV) are addressed first, with an emphasis on the effects of neutral grounding and shunt reactor compensation. Symmetrical components are introduced to deal with unsymmetrical faults. Traveling waves follow from the solution of the wave equation of a single lossless line under unit step energization. This was later extended to account for generalized input. Special attention is paid to the important case of energization of an open line with and without surge arrester termination. Three-phase lines are dealt with using modal analysis. However, all through the emphasis is on understanding the overvoltage generation mechanism rather than the completeness or sophistication of the computational procedure, which is covered in more specialized texts. Special attention is paid to overvoltages caused by interruption of small inductive and capacitive currents. The chapter concludes with a brief summary of the EMTP. An example is given on the energization of an open 735 kV transmission line.

Electric field calculations are essential, since ionization phenomena in electrical insulation systems are very sensitive to electrical stresses. This is covered in Chapter 2, which deals with electrostatic fields. In the absence of space charge, the problem amounts to solution of Laplace equation under appropriate boundary conditions. In the presence of space charge, we deal with Poisson's equation. In general, these equations are three dimensional, but considerable simplification results in symmetrical configurations. Analytical solutions for simple geometries are introduced. Uniform field electrodes are also introduced for single and composite dielectrics. Cylindrical geometry is discussed, with a focus on coaxial cables. Prolate spheroidal coordinates are presented, with application to spheroidal electrodes and dielectric particles. A hyperboidal field is introduced with particular reference to the basic rod-plane gap often dealt with in long air gap tests. Different methods of transformation are described, with an emphasis on the method of images. Among the electrodes dealt with is the sphere–sphere configuration, historically used as a high-voltage measuring device. Numerical methods for field computation are briefly reviewed. The method of successive images is of particular importance in handling electric fields of multiconductor systems. This is followed by a discussion of the charge

simulation method, which is applied to a coaxial SF_6 cable with epoxy spacers. Finally, the chapter presents a brief account of the methods of finite differences and finite elements.

Recognition of the statistical nature of ionization and breakdown phenomena is essential for proper planning of high-voltage tests and for interpretation of test results. This is covered in Chapter 3, which describes the characterization of a set of test results. The chapter then introduces discrete and continuous statistical distributions, including the binomial, Poisson, Maxwell, and normal distributions. For low breakdown probability, a number of extreme-value distributions are important. The chapter therefore describes the Gumbel extreme-value distribution as well as the Weibull distribution, which is likely to be more familiar to high voltage engineers. Methods of selection for the appropriate distribution to characterize a certain population are introduced, including the concepts of 50% value, standard deviation, and confidence limits, which are of obvious practical importance. The practical use of special graphic paper, which often simplifies statistical treatment of test results, is also emphasized. Different examples on the planning and interpretation of high-voltage tests are given. Reference is also made to relevant recommendations of international test standards.

Understanding of the mechanism of ionization and breakdown in gases is of fundamental importance in high voltage engineering. Chapter 4 deals with this topic and covers the fundamentals of the kinetic theory of gases. This is followed by an elementary introduction of the atomic structure of elements based on Bohr's model. Different ionization mechanisms are briefly introduced. A detailed analysis of the movement of an ion in an electric field is then presented, introducing the notions of drift velocity and mobility. Sources of free electrons are briefly discussed. The formulation of Townsend ionization and attachment coefficients is then described, which leads to the development of electron avalanches. Onset conditions for a self-sustained discharge are discussed and Paschen's law is introduced. The streamer criterion due to Loeb–Meek–Raether is then introduced, which is useful to account for the breakdown of long gaps, particularly under impulse voltages. The glow is discussed as one of the self-sustained discharges. This is followed by a section that deals with the fundamentals of corona discharge in air, describing the modes of corona discharge in air under positive and negative polarities. AC corona is briefly discussed, followed by an introduction to corona effects on an overhead line conductor, including radio noise, audible noise, and corona losses. Finally, an account of breakdown in electronegative gases with particular reference to SF_6 is presented.

Knowledge of the breakdown characteristics of long air gaps is essential for determining air clearances in transmission lines and substations. Chapter 5 deals with this topic. Air gap breakdown characteristics are presented for lightning and switching impulses, operating dc or ac voltage, as well as under composite stresses. Basic air gap configurations include rod–plane, rod–rod, conductor–plane, conductor–tower leg, etc. Switching impulse breakdown characteristics of long air gaps are addressed in detail due to their importance for EHV and UHV transmission system design. Special attention is paid to modeling of the effect of atmospheric conditions, air density, and humidity on long air gap breakdown. This is then compared with recommendations of international standards.

Chapter 6 deals with the breakdown characteristics of insulating liquids, which assume major importance in transformers, underground cables, capacitors, as well as in some circuit breakers. The chapter includes a brief review of the molecular structure and physical properties of mineral and synthetic oils. It reviews the basic mechanisms of electric conduction and breakdown in pure insulating liquids. This is followed by a description of the breakdown mechanism in commercial oils, with a reference to the role played by gas bubbles and solid particles. Solid–liquid composite systems and short oil gaps are discussed with a focus on streamer breakdown. Breakdown in long oil gaps includes the role of initiation and propagation by leader discharge. Special attention is paid to transformer oil, in particular to the effect of humidity and particle contamination on breakdown strength. Statistical interpretation of the breakdown mechanism in oil accounts for stressed area and stressed volume effects. Finally, the chapter concludes with a discussion on ageing and decomposition of oil by-products.

Chapter 7 includes a review of breakdown mechanism in solid and composite insulation systems. It introduces the concepts of intrinsic breakdown, initial breakdown, and breakdown due to ageing and incipient faults. It also introduces the notion of composite (electrical, thermal, and

mechanical) stress. The chapter deals with the molecular structure and physical and chemical properties of several solid insulating materials, including polyethylene, cross-linked polyethylene, natural rubber, silicon rubber, etc. The structure and physical and chemical properties of the oil–paper system are described. The effect of temperature and water content is introduced. Improvements to the oil–paper insulating system are described, including use of synthetic paper and oil with reduced flammability. The structure of an SF_6-epoxy spacer system is described. Factors affecting breakdown strength such as gas pressure, conductor surface roughness, and particle contamination are also discussed.

Chapter 8 deals with conductor bundle selection for overhead transmission lines, with a focus on corona performance. Electrostatic field optimization of the bundle conductors is introduced, particularly with reference to EHV and UHV ac transmission lines. It accounts for electric and magnetic ground fields in the vicinity of the line. The corona loss (CL) mechanism is presented together with the concept of generating function. The radio interference (RI) mechanism is described with means for both calculation and measurements. RI on three-phase conductor systems is accounted for by modal analysis. TV interference (TVI) mechanism is described briefly. Methods of calculation and measurement of audible noise (AN) are described, with a description of AN performance of some EHV lines. The overall procedure for conductor selection is briefly described, together with long-term corona performance. Finally, HVDC conductor design is presented.

Lightning incidence and lightning protection are covered in Chapter 9. The chapter starts with a brief introduction to the mechanism of cloud charging. This is followed by a review of meteorological data relevant to lightning strikes as well as an introduction to lightning detection and location systems. A section is devoted to lightning flash parameter waveforms, including return stroke current amplitude, with particular reference to such parameters. The mechanism of lightning attachment is introduced with a focus on the negative downward flash. Return stroke models are briefly introduced, including the so-called engineering models. Lightning attachment models are presented including the electrogeometric model as well as the more recent upward positive connecting leader models. Both shielding failure and backflashovers are discussed. Upward flash from tall structures is described, particularly the modeling of such flashes and the prominent role played by the statistical nature of the ground field due to cloud charges, without the participation of a downward stepped leader. Protective measures against exposure to lightning strikes, including lightning rods and masts, are described together with new, passive field-sensitive air terminals as well as the traditional role played by overhead ground wires. An introductory section deals with line arrester applications. Finally, a section introduces the effects of lightning exposure on positive streamer inhibition.

Chapter 10 deals with insulators of high-voltage transmission lines. The chapter begins with a review of insulator types and materials, including ceramic and polymeric insulators. This is followed by a section on the electrical performance of high-voltage insulators under standard and nonstandard lightning impulses as well as standard switching impulses under dry and wet conditions. An extensive section deals with the pollution flashover of insulators under system operating voltage, which is often the designing factor of transmission line insulator strings, particularly under dc voltage. Contamination is presented as an interaction between insulator shape and material and the environment. Examples are given for desert and marine pollution. Polymeric insulator surface is characterized by hydrophobicity that can be assessed by contact angle measurements. Mathematical models for polluted insulator flashover mechanisms are presented for both dc and ac energization. Results of pollution performance of high-voltage insulators are presented on the basis of both laboratory and field tests. The mechanical requirements for high-voltage insulators are briefly introduced with a focus on international standards. Finally, a procedure for selecting insulators is described with due consideration to the statistical nature of the flashover mechanism and with the objective of satisfying a given performance criterion.

Chapter 11 starts with a brief account of underground cable development and construction, which includes paper–oil, pressurized oil-filled paper-impregnated cables, high-pressure oil-filled cables (HPOF), and mass impregnated cables. It deals with the construction of extruded insulation cables and pressurized gas cables, including rigid gas-insulated cables (lines). Future trends are presented including forced cooling and the use of synthetic paper. Electric field distribution in ac cable insulation is

analyzed and electric parameters are presented, including transmission capacity and critical cable length. Examples of conductor and insulation dimensions are provided. AC conductor losses are discussed, with a focus on skin and proximity effects. Sheath losses are presented as well as cross bonding and thermal dissipation. The procedure of insulation dimensioning is discussed based on the notion of a limit withstand field. Ageing and incipient faults in different types of cables are also described. Attention is paid to electrical ageing, particularly partial discharges, water and electrical treeing, as well as charge injection due to contaminants, defects, protrusions, and voids. A brief section deals with gas-insulated substations (GIS), which covers the generation mechanism of very fast transients (VFT). Problems presented include operation at low temperatures and the use of SF_6-N_2 gas mixtures. Cable accessories of different cable designs including joints, terminations, and wall bushings are introduced. A final section deals with HVDC cables and accessories.

Chapter 12 deals with power transformers. After a brief introduction on basic design considerations, the main topic of transformer insulation is presented. The principal insulation system is that of paper–oil, and the basic arrangements of layer winding and disc-type coil winding are introduced. Interwinding insulation, winding to earth insulation, and bushings are discussed. This is followed by a brief introduction to operating voltage and impulse voltage stresses. The physical properties of oil-impregnated paper are presented. Improvements to such traditional insulation systems include the use of polymer-based paper, low inflammability oil, and SF_6 insulation. Dimensioning considerations of oil–paper insulation follow. The concepts of cumulative stress and probabilistic aspects of breakdown lead to area and volume effects. This is followed by a section on audible noise from power transformers, including the notion of acoustic power and near- and far-field audible noise. Standard high-voltage tests, including applied potential, induced voltage, and partial discharge measurement, as well as standard lightning impulse test, chopped wave test, and switching impulse test, are described. Of special importance is fault detection during impulse tests. The transfer function method is also briefly discussed. Ageing and incipient faults, including an introduction to different mechanisms such as thermal, electrical, and environmental ageing, are covered. Finally, diagnostic methods during operation and maintenance including the determination of water content, particle counting, and gas-in-oil analysis are discussed.

Chapter 13 begins with a definition of insulation coordination as provided by IEC. It distinguishes between external and internal insulation and between self-restoring and non-self-restoring insulation. This is followed by a classification of voltages and overvoltages and their origin. The concept of representative overvoltages is introduced. The procedure of insulation coordination is explained with regard to phase-to-earth and phase-to-phase overvoltages. Mathematical modeling of critical switching impulse phase-to-phase air insulation is covered. Phase-to-phase overvoltage distribution is discussed, based on a bivariate normal probability density function, which is used to determine the representative phase-to-phase overvoltage. Fast-front overvoltages are described, with a focus on the impinging surge into a substation. Both the methods of deterministic withstand voltage and the statistical approach based on the risk of failure are introduced. In determining the required withstand voltage, both altitude corrections and the concept of safety factor are briefly reviewed. The selection of standard withstand voltage from IEC standard tables is briefly described, with due consideration to conversion factors between different test techniques. The chapter concludes with a description of surge arresters, which are almost completely of the metal-oxide type.

Chapter 14 deals with the vast topic of high-voltage testing and measuring techniques. It begins with an introduction of test categories, including type, routine, and special tests. Demonstrations as well as on-site and commissioning tests are also presented. Generation of test voltages is also covered in detail. AC test sources include transformer cascades and resonant circuits. Rectifier bridges for the generation of high-voltage dc are described, with a focus on the cascade rectifier circuit. An impulse-generating circuit is described with reference to a multistage generator. Circuit analysis explains the generation of standard and switching impulse voltages. The use of cascade transformers for the generation of long front switching impulses is also described. A review of high-voltage measurement techniques, including ground and electromagnetic shielding and prerequisites for performing interference-free measurements is presented. It covers the classic sphere gap and then describes the response characteristics of voltage dividers. It also describes different divider configurations, including resistive, capacitive, and the widely

used compensated *R–C* divider. The low voltage arm is studied in detail. Current measuring shunts are also discussed. Power loss measurements are described using the Schering bridge. An important element here is the standard compressed gas capacitor. The basic current comparator bridge is introduced followed by a section on partial discharge measurement. The two current approaches of apparent charge and radio influence voltage (RIV) are also discussed. Finally, the chapter ends with an introduction to digital measuring techniques.

Farouk A.M. Rizk

Giao N. Trinh

Acknowledgments

We would like to thank various publishers of technical journals, conference records, standards, and guides, in particular IEEE, CIGRE, and IEC and the respective authors for permitting the reproduction of several tables and figures used in the book. The references listed at the end of each chapter are selected for their representativeness of the state of the art in various areas of high voltage engineering presented in the book, more specifically with an emphasis on providing a basic understanding of the physical phenomena involved and their related analytical modeling for evaluating their impact on practical applications.

Thanks are due to Hydro-Québec for providing the photographs used in the book cover and for various figures illustrating Hydro-Québec's high-voltage testing facilities and equipment and to B. Khodabakhchian of TransEnergie (Hydro-Québec) for providing examples of EMTP study of switching surges on a 300 km, 735 kV line (Chapters 1 and 13).

We are grateful to the late Dr. Lionel Boulet, founder of Hydro-Québec Institute of Research (IREQ), and Nils Hyltén-Cavallius, the first director of the High-Voltage Department, for providing the proper environment to carry out research in the vast field of high voltage engineering. We greatly appreciate the opportunity to have worked, and shared experiences, with our colleagues at IREQ, including D. Train (high-voltage testing), Claire Vincent (internal insulation), Dr. P.S. Maruvada (corona and field effects), Dr. G. Karady (insulators), Dr. R. Malewski (measurement techniques), Dr. Ch. Menemenlis (air insulation), Dr. J. Novak (insulating gases), Dr. D. Couderc (oil-filled cables), and Dr. M. Duval (gas-in-oil analysis).

Last but not least, we would also like to thank Nicole Grenier and Amir Rizk for their invaluable help in the preparation of the manuscript. Special thanks also go to the publisher, CRC Press, in particular Nora Konopka, for inviting us to write a book on the subject of their choice and to the editorial staff at CRC Press—K. Budyk, E. Logan, G. Butler, R. Divakaran, J. Gandour, and M. Smith—for the realization of the book.

Authors

Farouk A.M. Rizk holds a BSc Eng and an MSc from Cairo University; a PhD from the Royal Institute of Technology, Stockholm, Sweden; and a DTech from Chalmers University of Technology, Gothenburg, Sweden.

Dr. Rizk worked as a research engineer with ASEA (ABB), Sweden, in the High Power Laboratory, Ludvika, in 1960–1963 and in the Computer Department, Vasteras, in 1963. He worked for the Egyptian Electricity Authority (1964–1971), becoming manager, High Voltage, in 1968. He joined the Hydro-Québec Institute of Research (IREQ) as a senior research scientist in 1972, subsequently passing from scientific director (1976) to vice president laboratories (1986). He also held the title of fellow research scientist from 1986 to 1996.

Dr. Rizk's research work covers a wide range of topics in high voltage and high power engineering: arc dynamics in circuit breakers, polluted insulators, single-pole switching, electromagnetic shielding, compressed gas and liquid breakdown, long air gaps, and lightning attachment.

Dr. Rizk was elected IEEE fellow in 1982 "for contributions to the science of high voltage technology and for technical leadership in the advancement of the electric power industry." He has served as chairman of the 10th International Symposium on High Voltage Engineering (ISH) in 1997 and as chairman of the ISH Steering Committee. Dr. Rizk received prize paper awards from the IEEE Transmission and Distribution Committee in 1989, 1991, and 1995 and from the Power Engineering Society of IEEE in 1996. He was awarded the IEEE Herman Halperin Electric Transmission Award in 1996 for outstanding contributions to electric power transmission and distribution. He is a distinguished member of the International Council on Large High Voltage Electrical Systems (CIGRE) and a recipient of the CIGRE Technical Committee Award, 1997.

Dr. Rizk made major contributions to standardization work, particularly during his tenure as international chairman of IEC Technical Committee 28: Insulation Co-ordination, 1983–1996. Under his leadership, the whole area of insulation co-ordination was revised, which led to the new standards IEC 71-1 and IEC 71-2. His efforts to promote insulation co-ordination of high-voltage dc transmission led to standardization work now undertaken by IEC TC 28.

Dr. Rizk currently serves as president of Lightning Electrotechnologies Inc, a lightning protection equipment manufacturer, and Expodev Inc., a consulting engineering firm, both of which are in Montreal.

Giao N. Trinh received his BSc in electrical engineering in 1963 and his PhD in high voltage engineering from Laval University, Québec City, Québec, Canada, in 1969. His study of corona discharges in atmospheric air helped establish the various corona discharge modes developed at high-voltage line conductors.

Dr. Trinh joined the Hydro-Québec Institute of Research (IREQ), Varennes, Québec, Canada, in 1968. Until 1977, he participated in various research activities, studying the corona performance of high-voltage transmission lines up to the ultra-high-voltage level of 1 200 kV ac and ±600 kV dc. His main contribution has been to the development of a method for evaluating the corona performance of high-voltage line conductors, based on cage-test results obtained under artificial rain conditions.

In 1978, his research activities shifted to the field of insulation of high-voltage equipment, and until 1997, he carried out studies on practical insulation systems, including the following:

- Gas insulation: He studied the influence of epoxy spacers on dielectric performance and the risk of burn-through of gas-insulated cables. He participated in the commissioning tests of the first few GIS introduced at Hydro-Québec in the Montreal region in the late 1970s.

- Power transformers: He studied the breakdown of large oil volumes, which clearly established the important role of particle contamination with regard to the withstand capability of transformer insulation.
- High-voltage cables: He participated in a study group on the feasibility of a river crossing for Hydro-Québec's 500 kV dc line at Grondines and participated in the testing of the type cable selected for the project.

Dr. Trinh holds two patents and is the author or coauthor of over 80 technical papers in the areas of corona and partial-discharge phenomena; liquid, solid, and gaseous insulation; high-voltage testing; and power equipment insulation. His main contribution has been in the field of gas-insulated cables, where his work on the assessment of the risk of burn-through of gas-insulated cables earned him the 1993 prize-award paper from the Substation Committee.

Dr. Trinh was elected fellow of the IEEE in 1997 for his "contribution to understanding of dielectric and arc phenomena in gas insulated cables." He is a member of the Power Engineers Society (PES), where he participates in the activities of PES-Insulated Conductors and PES Substation Committees, and of the Dielectrics and Electrical Insulation Society (DEIS), where he has served as secretary of DEIS-AdCom from 1993 to 1994 and as chairman of the DEIS Statistics Committee from 1995 to 1997. From 1976 to 2002, he served as an invited professor at École Polytechnique de Montréal, Montréal, Québec, Canada, where he taught a graduate course on high voltage engineering. He currently serves as a consultant in high voltage engineering.

1

Power System Overvoltages

1.1 Introduction

In general, a power system consists of a large number of generators, step-up or step-down transformers, and domestic, commercial, and industrial electrical loads, connected together through a network of overhead transmission lines and underground cables. Connection and disconnection of power system elements are undertaken by power circuit breakers and associated disconnecting switches under both normal operating conditions or to protect the system from occasional faults.

The voltage level of transmission trunk lines is economically determined by the magnitude of transmitted power and by the length of the transmission line. For a given power level, a higher voltage reduces the line current and accordingly the power losses. In ac systems, the steady-state stability limit is proportional to the square of the voltage. A higher voltage, therefore, improves the power system stability margin. On the other hand, system insulation has to be able to sustain the voltage in order to maintain reliability. Obviously, more insulation is more costly, which results in the concept of most economic voltage. Furthermore, for a given conductor size, higher voltage leads to more corona losses and more adverse environmental impact as expressed by radio interference (RI) and audible noise, leading to the necessity of optimizing the conductor bundle and the concept of most economic current density.

Power system insulation is exposed not only to normal stresses associated with steady-state conditions but also to external and internal overvoltages and to occasionally serious deterioration of the insulation due to adverse atmospheric conditions. External overvoltages occur when a transmission line is struck by lightning, while internal overvoltages are generated due to faults and switching operations. For high-voltage transmission systems, only direct strikes to ground wires, towers, or power conductors are important, while at lower voltages, induced lightning overvoltages become also important. Overvoltages generated due to switching operations and ground faults include temporary overvoltages at essentially power frequency as well as transient overvoltages at the system natural frequency and are associated with the redistribution of magnetic energy stored in system inductances and electrostatic energy stored in system capacitances. With respect to the time scale, lightning overvoltages are normally in the microsecond range, temporary internal overvoltage lasts for some tenths of a second, while switching surges cover the hundred microseconds to a few millisecond range. These time durations or the associated frequencies are important in at least two respects: first, in their influence on the withstand characteristics of insulation and, second, in determining the complexity of modeling of any piece of equipment to be used in analytical studies or computer simulation. Moreover, such frequencies will be important in determining the required responses of measuring systems to be used during field tests for recording of such overvoltages.

It is clear from the preceding text that understanding the mechanisms of generation of external and internal overvoltages as well as techniques for assessment of such overvoltages will be essential for the design of power system insulation. This will also be important for selection of appropriate techniques for overvoltage protection. These aspects will be treated in the following sections.

We will start with an introductory section dealing with transients in simple lumped circuits. Although power systems are far more complex, such simple circuits help understanding some of the basic mechanisms of overvoltage generation. These circuits are also used in laboratory simulation of fault interruption. Another section deals with the traveling wave solution of the wave equation of a lossless transmission line and associated lattice diagram. Once again, although real lines obviously have losses,

it is often possible to represent such losses by lumped resistors in the middle and terminals of a loss-free line, which facilitates computation considerably.

A brief description of the electromagnetic transient program (EMTP), which is presently the recognized universal tool for assessment of power system transients, is included. Special sections are dedicated to lightning response of towers and overhead conductors, temporary overvoltages, and switching surges. Practical limits for overvoltage factors are given, based on both simulation results and field experience.

1.2 Lumped Circuits

Consider the simple series damped circuit of Figure 1.1a. A voltage source $U_m \cos \omega t$ is switched at $t = 0$. Variation of the capacitor voltage V is described by the following differential equation:

$$\frac{d^2V}{dt^2} + \frac{R}{L}\frac{dV}{dt} + \frac{V}{LC} = \frac{U_m}{LC}\cos \omega t \tag{1.1}$$

which can be integrated directly or by Laplace transforms to yield

$$V(t) = A\exp\left(-\frac{t}{\tau}\right)\cos \omega_n t + B\exp\left(-\frac{t}{\tau}\right)\sin \omega_n t + \frac{U_m \cos(\omega t - \phi)}{\sqrt{\left(1 - \omega^2 LC\right)^2 + (\omega CR)^2}} \tag{1.2}$$

where

$\tau = 2L/R$

$\omega_0 = 1/\sqrt{LC}$, designate the angular natural frequency with no damping

The angular natural frequency $\omega_n = \sqrt{\omega_0^2 - (1/\tau^2)}$

$$\tau_0 = CR$$

$$\phi = \tan^{-1}\left(\frac{\omega\tau_0}{1 - (\omega^2/\omega_0^2)}\right)$$

$$K_t = \frac{1}{\sqrt{\left(1 - (\omega^2/\omega_0^2)\right)^2 + (\omega\tau_0)^2}}$$

$$A = -K_t \cos\phi . U_m$$

$$B = -K_t\left(\frac{\cos\phi}{\omega_n\tau} - \frac{\omega}{\omega_0}\sin\phi\right)$$

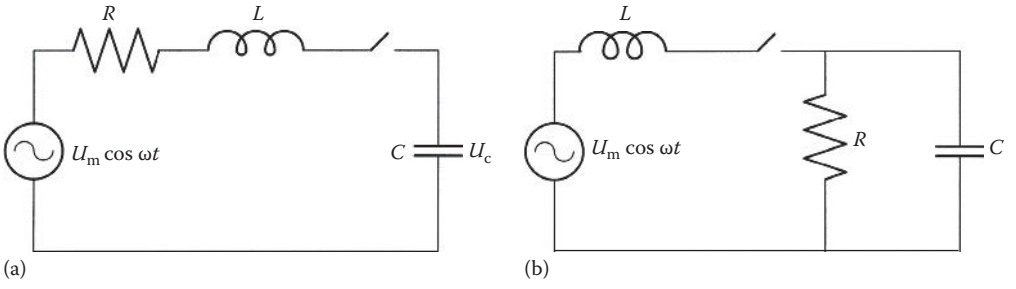


FIGURE 1.1 (a) Simple lumped circuit with series damping. (b) Lumped circuit with parallel damping.

The last term in Equation 1.2 expresses the steady-state solution, from which K_t, defined previously, refers to the temporary overvoltage factor. It is also clear from the preceding text that damping will reduce not only the switching transient amplitude but also the natural frequency of the circuit. An approximation of Equation 1.2, which is valid with $\omega\tau_0$ negligibly small with respect to unity and $\omega_n\tau$ extremely larger than unity, is sometimes used as a simplification:

$$V(t) \approx K_t U_m \left[\cos\omega t - \exp\left(-\frac{t}{\tau}\right)\cos\omega_0 t\right] \tag{1.3}$$

with

$$K_t \approx \frac{1}{1-\left(\omega^2/\omega_0^2\right)}$$

A numerical example of Equation 1.2 is given in Figure 1.2 for a circuit with $f = 50$ Hz, $x = \omega L = 10\ \Omega$, $Z_0 = \sqrt{L/C} = 400\ \Omega$, and $Z_0/R = 8$, which yield $L = 31.83$ mH, $C = 0.1989$ μF, and $R = 50\ \Omega$. Here, the switching surge has an overvoltage amplitude factor of 1.87, reached at a time to crest of 250 μs. The damping effect is quite clear.

Figure 1.1b shows the case of parallel damping, with R placed across the capacitor. The differential equation describing the capacitor voltage $V(t)$ becomes

$$\frac{d^2V}{dt^2} + \frac{1}{RC}\frac{dV}{dt} + \frac{V}{LC} = U_m\cos\omega t \tag{1.4}$$

which is identical to Equation 1.1 earlier with the exception that the time constant L/R will now be replaced by RC and vice versa. Again, by direct integration or Laplace transforms, the solution of Equation 1.4 can be expressed as

$$V(t) = A\exp\left(-\frac{t}{\tau}\right)\cos\omega_n t + B\exp\left(-\frac{t}{\tau}\right)\sin\omega_n t + \frac{U_m\cos(\omega t - \phi)}{\sqrt{\left(1-\omega^2LC\right)^2 + (\omega L/R)^2}}$$

Here, $\tau = 2RC$ and $\tau_0 = L/R$, but in terms of these time constants, the earlier expressions for ϕ, K_t, A, and B remain the same as in the case of the series damped circuit. The temporary overvoltage factor K_t given by

$$K_t = \frac{1}{\sqrt{\left(1-\left(\omega^2/\omega_0^2\right)\right)^2 + (\omega\tau_0)^2}}$$

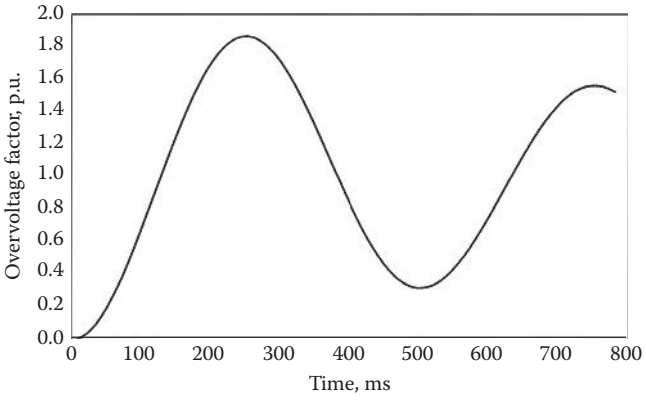


FIGURE 1.2 Transient overvoltage in a series damped circuit with $R = 50\ \Omega$, $L = 31.83$ mH, and $C = 0.1989$ μF.

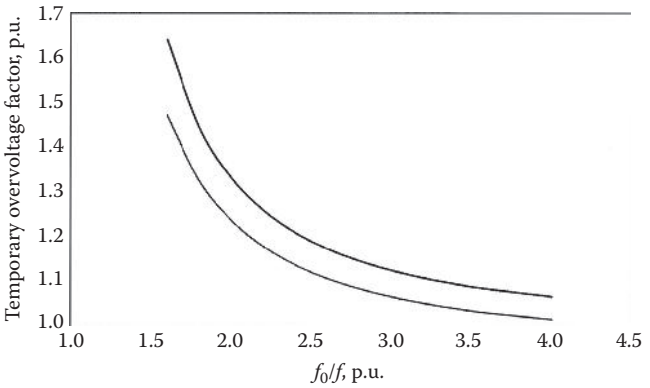


FIGURE 1.3 Dependence of temporary overvoltage factor in parallel damping circuit on natural per unit frequency. Upper, no damping; lower, $X/R = 0.3$.

with $\tau_0 = L/R$, has been evaluated in Figure 1.3 as function of the per unit frequency $f_0/f = \omega_0/\omega$ for two cases. The upper curve refers to a circuit with no damping, while the lower curve refers to $\omega\tau_0 = \omega L/R = X/R = 0.3$. It is shown that the temporary overvoltage factor is quite sensitive to the ratio f_0/f and that as f_0/f decreases towards unity (resonance), damping plays a significant role in limiting the overvoltage. In the practical case of an overhead transmission line, this parallel damping role is played by the nonlinear corona losses, which become quite substantial at high temporary overvoltages (Maruvada et al., 1989).

1.3 Distributed Parameter Circuits

1.3.1 Temporary Overvoltages

1.3.1.1 Ferranti Effect

Consider a long transmission line energized with a sinusoidal voltage at angular frequency ω. The differential equations governing voltage V and current I distributions along the line are

$$\frac{dV}{dx} = -ZI \tag{1.5}$$

$$\frac{dI}{dx} = -YV \tag{1.6}$$

where

$Z = R + j\omega L$

$Y = G + j\omega C$

L and C are the inductance and capacitance per unit length. R and G are the series resistance and shunt conductance per unit length.

Consider a line of length l, with $x = 0$ at the sending end with voltage and current V_s and I_s, respectively. The corresponding values at the receiving end are V_r and I_r, respectively.

With

$$\gamma = \sqrt{ZY} \tag{1.7}$$

and

$$Z_0 = \sqrt{\frac{Z}{Y}} \tag{1.8}$$

Solution of Equations 1.5 and 1.6 yields

$$V_s = V_r \cosh \gamma l + I_r Z_0 \sinh \gamma l \tag{1.9}$$

and

$$I_s = I_r \cosh \gamma l + \frac{V_r}{Z_0} \sinh \gamma l \tag{1.10}$$

If both series and shunt losses are neglected (ideal line), Equations 1.7 and 1.8 simplify to

$$\gamma = j\omega\sqrt{LC} = j\frac{\omega}{v}$$

where v is the speed of wave propagation equal to the velocity of light, $c = 3 \times 10^8$ m/s, and $Z_0 = \sqrt{L/C}$, that is, the surge impedance becomes a resistance. Furthermore, Equations 1.9 and 1.10 simplify to

$$V_s = V_r \cos\frac{\omega l}{v} + jI_r Z_0 \sin\frac{\omega l}{v} \tag{1.11}$$

and

$$I_s = I_r \cos\frac{\omega l}{v} + j\frac{V_r}{Z_0} \sin\frac{\omega l}{v} \tag{1.12}$$

where $\omega l/v$ is termed the electrical length of the line, in radians. For an open line, with $I_r = 0$, the open end temporary overvoltage factor, often referred to as the Ferranti effect, becomes

$$\frac{V_r}{V_s} = \frac{1}{\cos(\omega l/v)} \tag{1.13}$$

with a power frequency f of 50 Hz, $\beta = \omega/v$ becomes 1.047×10^{-6} rad/m or 6°/100 km. For a 400 km line, Equation 1.13 results in a temporary overvoltage factor of 1.095. On the other hand, for a 1000 km line, Equation 1.13 gives a temporary overvoltage factor of 2, which is excessive. In practice though, no such temporary overvoltage factors are allowed to happen, mainly because such long lines are effectively compensated by shunt reactors, as explained in the following. Another limiting factor, as mentioned previously, is corona losses (Maruvada et al., 1989).

A more realistic model to assess the temporary overvoltage factor is shown in Figure 1.4. A transmission of length l is provided with shunt reactors X_r at both ends and energized from a generating station with an equivalent reactance $X_s = X_t + X'_d$, where X_t is the transformer short-circuit reactance and X'_d is the generator transient reactance. U'_d is the equivalent emf behind the transient reactance, assumed constant during the temporary overvoltage duration.

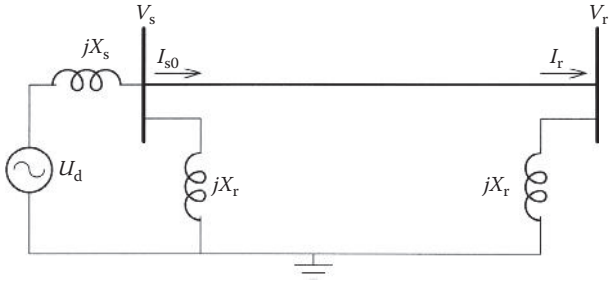


FIGURE 1.4 Circuit of a shunt-compensated line used to calculate temporary overvoltage at the line open end.

From Equations 1.11 and 1.12 earlier and noting that the overvoltage factor K will now be defined as V_r/U'_d, it is found that

$$K = \frac{1}{\left(1 + \frac{X_s}{X_r}\right)\cos\beta l + \left(\frac{Z_0}{X_r} + \frac{X_s}{X_r}\right)\frac{X_s}{Z_0}\sin\beta l} \tag{1.14}$$

If U_n is the nominal voltage of the line, the following power quantities become of interest:

Surge impedance loading

$$P_n = \frac{U_n^2}{Z_0} \tag{1.15}$$

Short-circuit power of the generating station

$$P_{sc} = \frac{U_n^2}{X_s} \tag{1.16}$$

Reactive power compensation

$$P_r = \frac{2U_n^2}{X_r} \tag{1.17}$$

If P_n is used as the base power, P_{sc} and P_r can be expressed in per unit as P^*_{sc} and P^*_r, which when substituted in Equation 1.14 yield

$$K = \frac{1}{\left(1 + \frac{P^*_r}{2P^*_{sc}}\right)\cos\beta l + \left(\frac{P^*_r}{2} + \frac{P^*_r}{2P^*_{sc}}\right)\frac{1}{P^*_{sc}}\sin\beta l} \tag{1.18}$$

If, theoretically, the line is fed from an infinite bus, $P^*_{sc} \to \infty$ and K becomes

$$K = \frac{1}{\cos\beta l + \frac{P^*_r}{2}\sin\beta l}$$

which immediately shows the beneficial effect of shunt reactor compensation on the Ferranti effect.

Also for an uncompensated line, $P^*_r \to 0$, it follows from Equation 1.18 that

$$K = \frac{1}{\cos\beta l - \frac{1}{P^*_{sc}}\sin\beta l}$$

which shows the detrimental effect on temporary overvoltages of feeding the line from a station with a limited short-circuit capacity. A more comprehensive study on a power system simulator would include the effect of the response of the station voltage regulator and even the system frequency rise following the load shedding that has caused the open line situation in the first place. Based on our simplified analysis, Figure 1.5 shows the effect of the short-circuit power of the feeding network on the Ferranti effect for a 600 km transmission line with no shunt reactor compensation. It is shown that excessive temporary overvoltages can, in principle, result at low short-circuit power.

Figure 1.6 shows the dependence of open end temporary overvoltage factor of an 800 km line on shunt reactor compensation P^*_r in per unit of the line surge impedance load, when the line is assumed to be fed from an infinite bus.

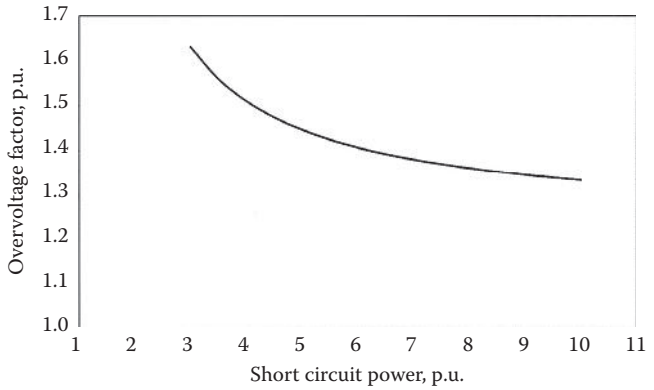


FIGURE 1.5 Effect of short-circuit power of feeding network on open end temporary overvoltage factor of 600 km line.

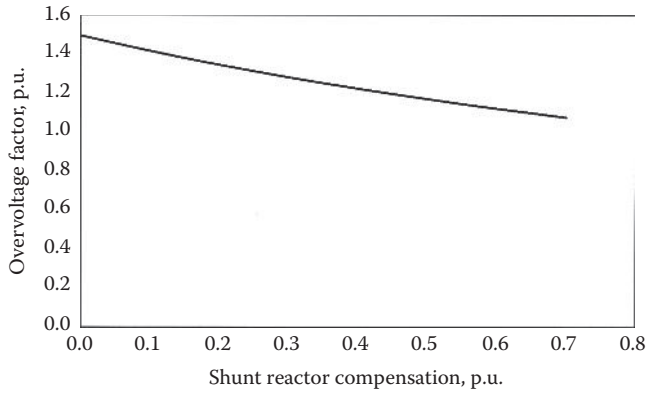


FIGURE 1.6 Variation of open end temporary overvoltage factor on 800 km line with reactive power in per unit of surge impedance loading.

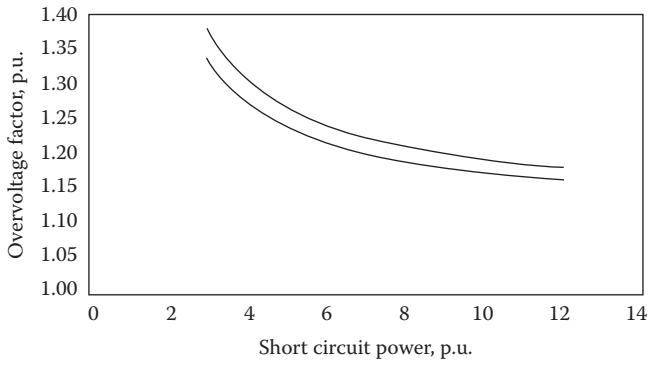


FIGURE 1.7 Dependence of open end temporary overvoltage factor of an 800 km transmission line, with 70% shunt reactor compensation, on short-circuit capacity of feeding network. Upper, reactor at line terminals; lower, uniformly distributed compensation.

Figure 1.7 shows variation of the temporary overvoltage factor at the open end of an 800 km line with 70% reactive compensation of the line capacitive power, with the per unit short-circuit power P_{sc}^{*}. The upper curve refers to shunt reactors equally placed at the line terminals. The lower curve refers to the ideal situation of uniform shunt reactor compensation along the line. It is shown that the results of placement of shunt reactors at line terminals are not much higher than the ideal case of distributed compensation.

1.3.1.2 Voltage Rise on Sound Phases

This section deals with temporary overvoltages on sound phases due to a ground fault on one phase for a system schematically shown in Figure 1.8. The input sequence impedances looking into the system from the fault location are designated Z_1, Z_2, and Z_0 for the positive, negative, and zero sequences. A single-phase-to-ground fault occurs on phase R. It is required to determine the temporary overvoltage factor of the sound phases, using the method of symmetrical components (Clark, 1943).

The terminal conditions neglecting fault resistance at the fault location are

$$V_R = 0$$

$$I_S = 0$$

$$I_T = 0$$

This results in the connection of the sequence networks as per Figure 1.8b, yielding the sequence currents:

$$i_1 = i_2 = i_0 = \frac{U_{ph}}{Z_1 + Z_2 + Z_0}$$

The sequence voltages at the fault location are given by

$$V_1 = U_{ph}\frac{Z_0 + Z_2}{Z_1 + Z_2 + Z_0}$$

$$V_2 = -U_{ph}\frac{Z_2}{Z_1 + Z_2 + Z_0}$$

and

$$V_0 = -U_{ph}\frac{Z_0}{Z_1 + Z_2 + Z_0}$$

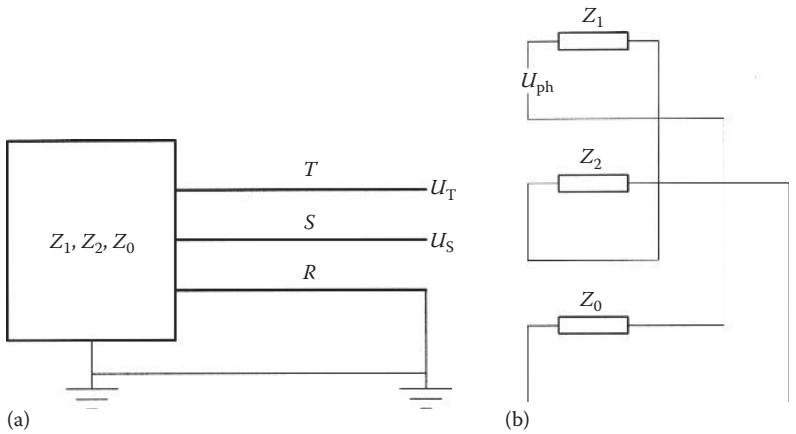


FIGURE 1.8 (a) Schematic diagram of a power system with single-phase-to-ground fault. Z_1, Z_2, and Z_0 are the equivalent positive, negative, and zero sequence impedances as seen from the fault location. (b) Connection of the sequence networks, for a solid single phase-to-ground fault.

The voltage V_{TE} of phase T to ground is given by

$$V_{TE} = V_0 + aV_1 + a^2V_2$$

where

$$a = -\frac{1}{2} + j\frac{\sqrt{3}}{2}$$

$$V_{TE} = \frac{U_{ph}}{Z_1 + Z_2 + Z_0}\left[(a-1)Z_0 + \left(a - a^2\right)Z_2\right]$$

For simplification, we will neglect losses in the positive and negative sequence networks so that

$$Z_1 = jX_1$$

$$Z_2 = jX_2$$

$$Z_0 = R_0 + jX_0$$

The temporary overvoltage factor becomes

$$K_t = \left|\frac{V_{TE}}{U_{ph}}\right| = \frac{\sqrt{\left(-\frac{3}{2}\frac{R_0}{X_1} - \frac{\sqrt{3}}{2}\frac{X_0}{X_1} - \sqrt{3}\frac{X_2}{X_1}\right)^2 + \left(\frac{\sqrt{3}}{2}\frac{R_0}{X_1} - \frac{3}{2}\frac{X_0}{X_1}\right)^2}}{\sqrt{\left(\frac{R_0}{X_1}\right)^2 + \left(1 + \frac{X_2}{X_1} + \frac{X_0}{X_1}\right)^2}} \tag{1.19}$$

which shows that the temporary overvoltage factor K_t is determined by the ratios X_2/X_1, X_0/X_1, and R_0/X_1. Equation 1.19 shows that K_t is sensitive to the ratio X_0/X_1 between the zero sequence and positive sequence reactances. For the special case of $X_0/X_1 = \infty$ (isolated neutral), $K_t = \sqrt{3}$, that is, the sound conductor assumes the full line–line voltage with respect to ground. It is also clear that negative values of X_0/X_1 in the range of –1 to –3 could lead to serious resonance overvoltages.

A numerical evaluation of K_t, Equation 1.19, is shown in Figure 1.9, where the dependence of K_t on X_0/X_1 is shown, for $X_2/X_1 = 1$, and three values of R_0/X_1 of 0.5, 1.0, and 1.5. The sensitivity of the temporary overvoltage factor to X_0/X_1 is evident, while K_t somewhat increases at higher values of R_0/X_1. It is noted that the range $1 < X_0/X_1 < 3$ normally characterizes networks with effective neutral grounding,

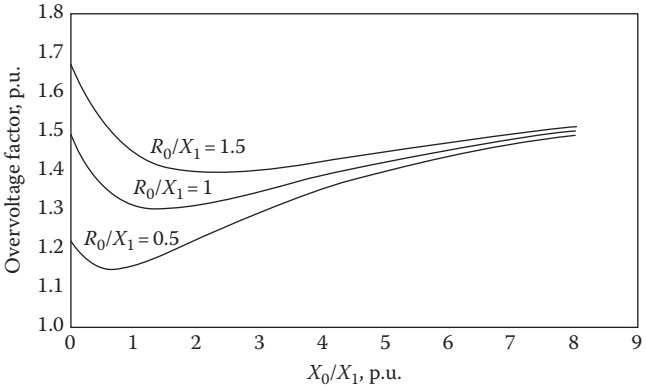


FIGURE 1.9 Variation of sound-phase temporary overvoltage factor with X_0/X_1 for $X_2/X_1 = 1$. Upper, $R_0/X_1 = 1.5$; middle, $R_0/X_1 = 1$; lower, $R_0/X_1 = 0.5$.

which is most relevant to high- and extrahigh-voltage (EHV) transmission, where sound-phase temporary overvoltages are effectively controlled.

It is clear that had we calculated the overvoltage factor on phase S instead of phase T, the results would have been identical.

1.3.2 Transient Overvoltages on Transmission Lines

1.3.2.1 Wave Equations

For transient analysis on lossless transmission lines, a generalization of Equations 1.5 and 1.6 earlier in the time domain becomes

$$\frac{\partial V}{\partial x} = -L\frac{\partial I}{\partial t} \tag{1.20}$$

and

$$\frac{\partial I}{\partial x} = -C\frac{\partial I}{\partial t}$$

which yield the wave equations

$$\frac{\partial^2 V}{\partial t^2} = v^2\frac{\partial^2 V}{\partial x^2} \tag{1.21}$$

and

$$\frac{\partial^2 I}{\partial t^2} = v^2\frac{\partial^2 I}{\partial x^2} \tag{1.22}$$

where $v = 1/\sqrt{LC}$ is the wave propagation speed.

The general solution of Equation 1.21 takes the form

$$V(x,t) = f_1(x - vt) + f_2(x + vt) \tag{1.23}$$

It is noted that f_1 will be constant as $x = vt$, which represents a forward moving wave V_f, while f_2 will be constant as $x = -vt$, representing a wave V_r moving in the reverse direction, so that

$$V(x,t) = V_f + V_r \tag{1.24}$$

From Equation 1.20, differentiating Equation 1.23 with respect to x,

$$\frac{\partial I}{\partial t} = -\frac{1}{L}\left[f_1'(x - vt) + f_2'(x + vt)\right]$$

Integrating with respect to time,

$$I(x,t) = \frac{1}{vL}f_1(x - vt) - \frac{1}{vL}f_2(x + vt)$$

Recognizing that $vL = Z_0$, it follows that

$$I = \frac{V_f}{Z_0} - \frac{V_r}{Z_0}$$

If similar to Equation 1.24, we write

$$I = I_f + I_r \tag{1.25}$$

then $I_f = V_f/Z_0$ and $I_r = -V_r/Z_0$.

It is appropriate to refer to V and I in Equations 1.24 and 1.25 as the transmitted or total V_t and I_t, respectively.

1.3.2.2 Points of Discontinuity

Consider a forward voltage wave V_f and its associated current wave, moving on a transmission line with wave impedance Z_0 and terminated with a load resistance R. At the discontinuity,

$$V_t = I_t.R$$

Substituting for $V_t = V_f + V_r$ and $I_t = I_f + I_r$, with $I_f = V_f/Z_0$ and $I_r = -V_r/Z_0$, the following expressions are obtained:

$$V_r = \frac{R - Z_0}{R + Z_0} V_f$$

or $V_r = a_r V_f$ with the reflection coefficient $a_r = (R - Z_0)/(R + Z_0)$

and

$$V_t = \frac{2R}{R + Z_0} V_f \tag{1.26}$$

or $V_t = a_t V_f$ with the transmission coefficient $a_t = 2R/(R + Z_0)$

$$I_r = -\frac{V_r}{Z_0} = \frac{Z_0 - R}{R + Z_0} \frac{V_f}{Z_0}$$

or $I_r = b_r I_f$ with the current reflection coefficient $b_r = (Z_0 - R)/(R + Z_0)$

and

$$I_t = \frac{2V_f}{R + Z_0} \tag{1.27}$$

or $I_t = b_t I_f$ with the current transmission coefficient $b_t = 2Z_0/(R + Z_0)$.

For an open-circuit line, as $R \to \infty$, $V_t \to 2V_f$, that is, voltage doubling occurs at the open end, while $I_r \to -I_f$ so that $I_t = 0$. For a short-circuited line $R \to 0$ so that $I_t \to 2$ (I/f), that is, current doubles at the short-circuited end, while $V_r \to -V_f$ so that $V_t \to 0$. The case of a line terminated by its wave impedance $R = Z_0$ yields the familiar result that $V_r = 0$ and $I_r = 0$, that is, no reflections.

A simple but powerful consequence of Equations 1.26 and 1.27, pointed out by E.W. Boehne and M. Riyaz, which also follows from the Thevenin theorem, is the equivalent circuit of Figure 1.10. The wave problem is replaced by a lumped element circuit where a source $2V_f$ is impressed on the line wave impedance Z_0 and the load impedance Z, connected in series. The equivalent circuit of Figure 1.10 allows straightforward determination of the transmitted and reflected waves for more complex impedances at the transition point and for other wave forms of the impinging impulse. This can be determined by integrating the relevant differential equation or by using Laplace transforms.

Figure 1.11a shows the case of a transmission line terminated by a shunt reactor with inductance L, subjected to an impinging unit-step impulse of magnitude $V_f = U_0$. The Laplace transform $V_t(s)$ will be given by

$$V_t(s) = \frac{2U_0}{s} . \frac{sL}{sL + Z_0} = 2U_0 \frac{1}{s + (Z_0/L)}$$

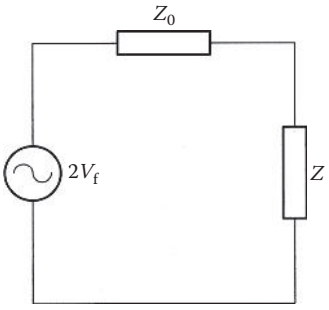


FIGURE 1.10 Equivalent circuit for a wave V_f traveling on a transmission line of wave impedance Z_0, terminated by a load impedance Z.

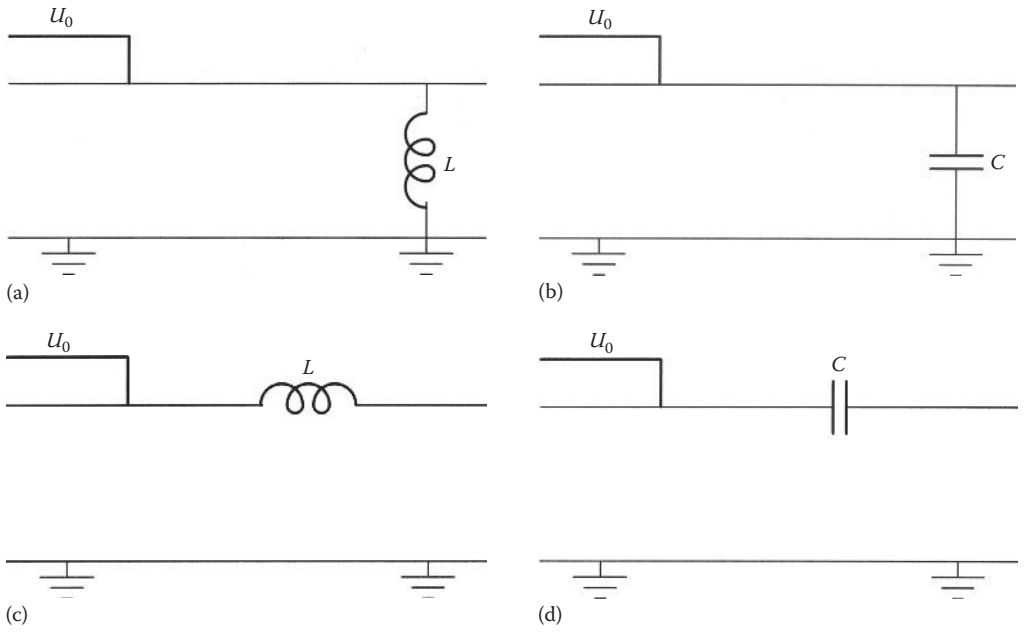


FIGURE 1.11 (a) Line terminated by inductance L. (b) Line terminated with a capacitance C. (c) Current limiting reactor on a long transmission line. (d) Series capacitor on a long transmission line.

and the inverse Laplace transform gives

$$V_t(t) = 2U_0 \left\{ \exp\left[-\frac{t}{\tau} \right] \right.$$

with $\tau = L/Z_0$, which means that the transmission coefficient

$$a_t = \frac{V_t}{V_f} = 2\exp\left[-\frac{t}{\tau} \right] \tag{1.28}$$

and the Laplace transform $I_t(s)$ is given by

$$I_t(s) = \frac{2U_0}{s} \frac{1}{sL + Z_0} = \frac{2U_0}{L} \frac{1}{s\left(s + (1/\tau)\right)}$$

so that

$$I_t(t) = \frac{2U_0}{Z_0}\left(1 - \exp\left(-\frac{t}{\tau}\right)\right)$$

and that the transmission coefficient for the current wave becomes

$$b_t = \frac{I_t}{I_f} = 2\left(1 - \exp\left(-\frac{t}{\tau}\right)\right) \tag{1.29}$$

From Equations 1.28 and 1.29, the corresponding reflection coefficients a_r and b_r will be expressed as

$$a_r = 2\exp\left(-\frac{t}{\tau}\right) - 1$$

and

$$b_r = 1 - 2\exp\left(-\frac{t}{\tau}\right)$$

For a line terminated by a capacitor C (Figure 1.11b), the following expressions are easily obtained:

$$V_t(t) = 2U_0\left(1 - \exp\left(-\frac{t}{\tau}\right)\right)$$

with $\tau = RC$, while the transmitted current

$$I_t(t) = \frac{2U_0}{R}\exp\left(-\frac{t}{\tau}\right)$$

This corresponds to

$$a_t = \frac{V_t}{V_f} = 2\left(1 - \exp\left(-\frac{t}{\tau}\right)\right)$$

and

$$b_t = \frac{I_t}{I_f} = 2\exp\left(-\frac{t}{\tau}\right)$$

In Figure 1.11c of a current limiting reactor installed on a long transmission line, with a unit-step impinging wave U_0, it follows from the equivalent circuit of Figure 1.10 that

$$V_t(s) = \frac{2U_0}{s}\frac{Z_0}{2Z_0 + sL} = \frac{2Z_0}{L}\cdot\frac{U_0}{s\left(s + \frac{2Z_0}{L}\right)} = \frac{1}{\tau}\frac{U_0}{s\left(s + \frac{1}{\tau}\right)}$$

where $\tau = L/2Z_0$, from which

$$V_t(t) = U_0\left(1 - \exp\left(-\frac{t}{\tau}\right)\right) \tag{1.30}$$

giving

$$a_t = \left(1 - \exp\left(-\frac{t}{\tau}\right)\right)$$

and

$$I_t(t) = \frac{U_0}{Z_0}\left(1 - \exp\left(-\frac{t}{\tau}\right)\right)$$

giving

$$b_t = a_t = 1 - \exp\left(-\frac{t}{\tau}\right)$$

For Figure 1.11d with series capacitor compensation, it can similarly be shown that

$$V_t(t) = U_0 \exp\left(-\frac{t}{\tau}\right) \tag{1.31}$$

where $\tau = 2 Z_0 C$ so that

$$a_t = \exp\left(-\frac{t}{\tau}\right)$$

Equation 1.30 shows what could have been deduced by intuition, namely that as $t \to \infty, V_t(t) \to U_0$, which means that the steady-state voltage on L, for a unit-step impinging wave, will vanish. Equation 1.31 on the other hand shows that as $t \to \infty$, the series capacitor will be charged to U_0 and $V_t(t) \to 0$.

For a wave U_0 propagating on a line with surge impedance Z_0 terminated with a nonlinear resistor (surge arrester), having a V–I characteristic,

$$V = AI^{\alpha} \tag{1.32}$$

The equivalent circuit of Figure 1.10 yields

$$2U_0 = Z_0 I_t + A I_t^{\alpha}$$

which can be rewritten as

$$2U_0 - Z_0 I_t = A I_t^{\alpha}$$

and can be solved graphically by the Bergeron method (Baatz, 1956), as shown in Figure 1.12 or by numerical iteration. An example is shown in Figure 1.13 for a nonlinear resistor terminating a transmission line. The V–I characteristic is given by Equation 1.32 with $\alpha = 0.03$. The constant A is determined from the condition that at $V = 600$ kV, $I = 1$ mA. The nonstandard incoming wave is shown.

An exhaustive analysis of different transition elements exposed to traveling waves is included in a classic paper by L.V. Bewley (Bewley, 1963).

1.3.2.3 Traveling Waves of General Form

In the previously mentioned analysis, the response of the transmission line with associated discontinuities was determined under unit-step wave $U_0.u(t)$. In practice, however, it is often required to determine the circuit response under different time-varying waves. For example, the injected current from a lightning impulse may be represented by exponential functions. If under a unit impulse $U_0.u(t)$ the response

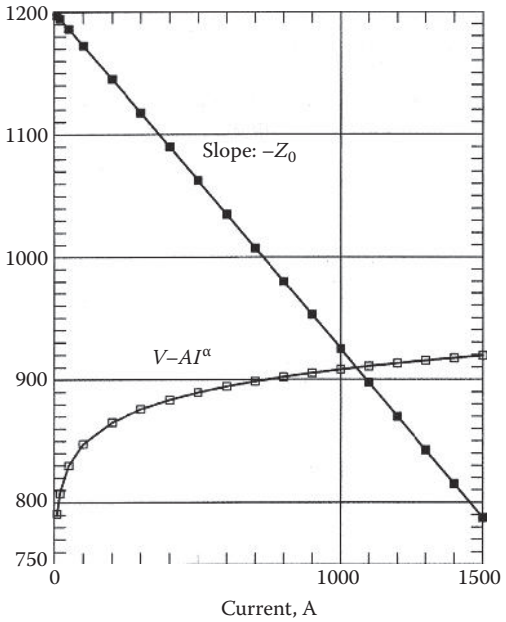


FIGURE 1.12 Schematic diagram for determination of voltage V_t on a nonlinear resistor terminating a transmission line, by the Bergeron method.

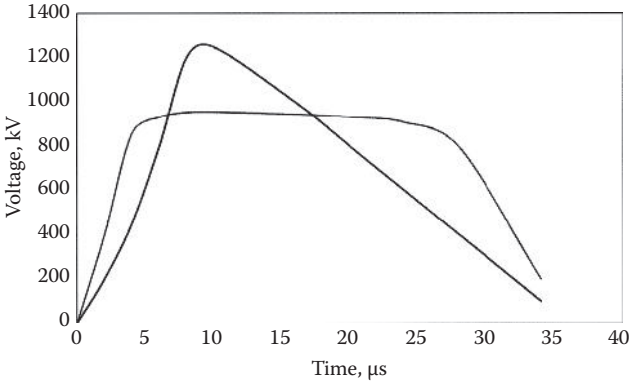


FIGURE 1.13 Voltage V_t on nonlinear resistor terminating a line with $Z_0 = 275\ \Omega$, under nonstandard impinging wave (upper).

$R_u(t)$ of a linear circuit is known, then using Duhamel's integral, the response for an input voltage of the form U_0. $F(t)$ can be determined as

$$R_f(t) = F(0).R_u(t) + \int_0^t F'(T)R_u(t-T)\,dT \tag{1.33}$$

Obviously, another method is to introduce $U_0.F(t)$ as the source voltage in the circuit of Figure 1.10, for direct determination of $R_f(t)$. As an example, consider the case of a transmission line terminated by a shunt reactor earlier. For the transmitted voltage unit-step response, Equation 1.27 gives

$$R_u(t) = a_t = 2\exp\left(-\frac{t}{\tau}\right) \tag{1.34}$$

where $\tau = L/Z_0$.

Consider now a double exponential function:

$$F(t) = \exp\left(-\frac{t}{\tau_q}\right) - \exp\left(-\frac{t}{\tau_f}\right)$$

where τ_q and τ_f are the tail and front time constants, respectively. Substituting in Equation 1.33, the following response function is obtained:

$$R_f(t) = 2\left[\frac{\exp\left(-(t/\tau_q)\right)}{1-(\tau_q/\tau)} + \frac{\exp\left(-(t/\tau)\right)}{1-(\tau/\tau_q)}\right] - 2\left[\frac{\exp\left(-(t/\tau_f)\right)}{1-(\tau_f/\tau)} + \frac{\exp\left(-(t/\tau)\right)}{1-(\tau/\tau_f)}\right] \tag{1.35}$$

The original unit-step response $R_u(t)$ follows from Equation 1.35 as $\tau_f \to 0$ and $\tau_q \to \infty$, yielding $R_u(t) = 2\exp(-(t/\tau))$ as already obtained in Equation 1.34.

1.3.2.4 Lattice Diagram

The lattice diagram, according to L.V. Bewley (Bewley, 1963), is a tool that facilitates auditing of traveling waves in space and time in situations of multiple reflections. An example is shown in Figure 1.14. At the left bus, the transmission and reflection coefficients are designated a_1 and b_1, and those of the right bus are a_3 and b_3, respectively. At the mid bus, two pairs are given: a_2, b_2 for incoming waves from the left section of the line and a_2' and b_2' for incoming waves from the right section, since in general these could be different.

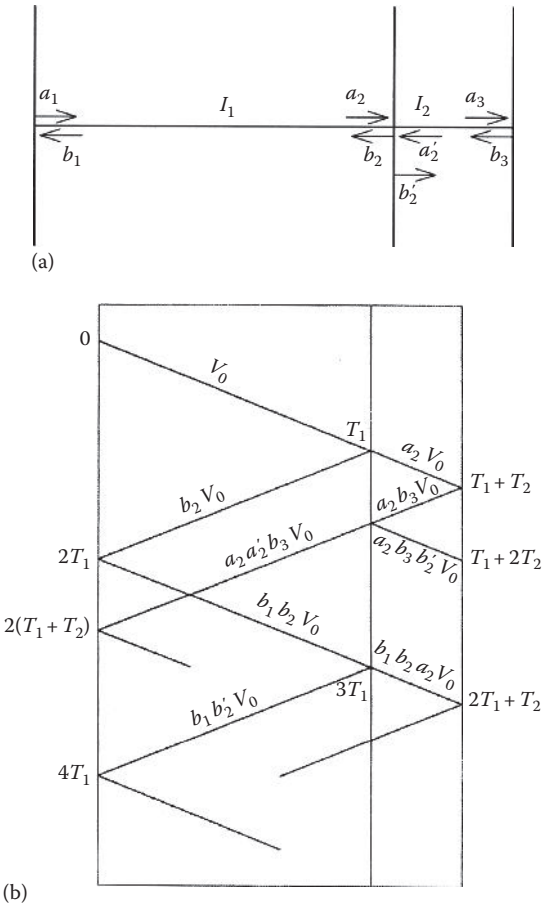


FIGURE 1.14 Lattice diagram for a transmission line with two sections. (a) Line sections. (b) Lattice diagram.

In the lattice diagram, the horizontal axis depicts spacing displacement, while the vertical relates to the time of wave arrival relative to wave first initiation at the left bus. At any point, the waves are added with their corrected magnitude and proper time of arrival (TOA). For example, at the right bus, $V(t)$ will be given by

$$V(t) = V_0\left\{a_2 s\left[t - (T_1 + T_2)\right] + a_2 b_3 b_2 s\left[t - (T_1 + 3T_2)\right] + b_1 b_2 a_2 s\left[t - (3T_1 + T_2)\right] + \cdots\right\}$$

where

s(t) is the unit-step function

T_1 and T_2 are the traveling times of sections 1 and 2, respectively

Theoretically, this process would continue indefinitely, but in practice, after a few reflections, waves are so damped as to warrant no further consideration.

1.3.2.5 Energization of Open Line

As shown previously, energizing an open line could result in overvoltage factors of 2 or more. The overvoltage could even exceed that level if reclosing is performed while the line has trapped charge of opposite polarity to the instantaneous voltage of the feeding side. Because of the importance of this overvoltage type for EHV and UHV transmission lines, it has been the subject of extensive investigations (Wedepohl, 1963; Thoren and Carlsson, 1970; Morched, 1972). This type of overvoltage can be effectively controlled by providing the circuit breaker with a preinsertion resistor. This can be demonstrated by the extremely simplified example of unit-step energization of an ideal line from an infinite bus. If the surge impedance of the transmission line is Z_0 and the preinsertion resistor is R, then the transmission coefficient a_t, which determines the voltage impressed on the line at the sending end, will be

$$a_t = \frac{Z_0}{R + Z_0} \tag{1.36}$$

and the voltage reflection coefficient at the sending end will be

$$a_r = \frac{R - Z_0}{R + Z_0} \tag{1.37}$$

If the source voltage is U_0, then the voltage at the open end can be expressed as

$$v(t) = 2U_0\left[a_t . s(t - T) + a_t a_r . s(t - 3T) + \cdots\right]$$

It should be noted that after an appropriate delay, the preinsertion resistor must be bridged by the main circuit breaker contacts, another traveling (cancellation) voltage will be impressed on the line.

If the preinsertion resistor is selected such that $R \approx Z_0$, it is clear from Equations 1.36 and 1.37 that very effective control of the overvoltage at the open end will be exercised, since the impinging voltage will be effectively reduced and reflections at the sending end will be mild. The preinsertion resistor will obviously be also effective in reducing overvoltages associated with line reclosing.

1.3.2.6 Three-Phase Lines

In the previous section, we only considered single-phase lines. Three-phase lines are obviously more realistic. This can be dealt with by modal analysis (Wedepohl, 1963) as summarized in the following. In matrix form, phase voltages and currents can be presented as

$$[V] = \begin{bmatrix} V_a \\ V_b \\ V_c \end{bmatrix} \tag{1.38}$$

and

$$[I] = \begin{bmatrix} I_a \\ I_b \\ I_c \end{bmatrix} \tag{1.39}$$

It can be shown that wave equations (Equations 1.21 and 1.22) can be replaced by

$$\frac{\partial^2 [V]}{\partial x^2} = [L][C]\frac{\partial^2 [V]}{\partial t^2}$$

where matrices [*L*] and [*C*] comprise self- and mutual inductances and capacitances. For perfect ground and fully transposed line, this yields

$$\frac{\partial^2 [V]}{\partial x^2} = \frac{1}{v^2}[1]\frac{\partial^2 [V]}{\partial t^2}$$

where [1] is a unit diagonal matrix. The phase quantities become uncoupled, with

$$\frac{\partial^2 V_k}{\partial x^2} = \frac{1}{v^2}\frac{\partial^2 V_k}{\partial t^2}$$

which is identical to Equation 1.21 earlier, and therefore, the same solution (1.23) applies. More generally, the wave equation could be written as

$$\frac{\partial^2 [V]}{\partial x^2} = [M]\frac{\partial^2 [V]}{\partial t^2}$$

with

$$[M] = [L][C]$$

The voltage column matrix [*V*] can be transformed into modal quantities [V_m] by

$$[V] = [T][V_m]$$

where [*T*] is a transform matrix so that

$$\frac{\partial^2 [V_m]}{\partial x^2} = [T]^{-1}[M][T]\begin{bmatrix} \\ \\ \end{bmatrix}\frac{\partial^2 V_m}{\partial t^2} \tag{1.40}$$

with proper choice of the transformation matrix [*T*], Equation 1.40 takes the form

$$\frac{\partial^2 [V_m]}{\partial x^2} = [\lambda]\frac{\partial^2 [V_m]}{\partial t^2}$$

where λ is a diagonal matrix. In this case, the modal quantities will again be uncoupled and the simple solution of the wave equation applies. Here, λ values are the eigenvalues of the matrix *M*, and the transformation matrix *T* is formed from the columns of the eigenvectors of *M* (Wedepohl, 1963).

1.3.3 Overvoltages due to Current Interruption

Interruption of fault current obviously generates transient recovery voltages (TRVs), which are important for successful interruption and design and testing of circuit breakers; they are, however, much less significant for power system insulation design, which is the primary objective of this book. In this respect, as explained in the following, interruption of small inductive currents of shunt reactors, reactor-loaded transformers, etc., as well as interruption of capacitive line current, is more significant.

1.3.3.1 Interruption of Small Inductive Currents

Figure 1.15 shows the basic circuit for interruption of small inductive currents. L_t and C_t are the equivalent inductance and self-capacitance of the reactor. L_s and C_s are the equivalent inductance and capacitance of the source. It has been established (Rizk, 1964) that the small inductive current is not interrupted at a natural current zero like short-circuit currents but rather becomes unstable prematurely leading to the so-called current chopping. An extensive investigation of small inductive current interruption is reported in Rizk (1963). If the inductance of the loop formed by the circuit breaker and the source capacitance C_s and load capacitance C_t is designated as L, it has been shown that arc instability criterion is

$$\frac{\theta}{R_d C} - \frac{L}{R_0 \theta} < 1 \tag{1.41}$$

where

- θ is the thermal time constant of the arc, which, for gas-blast circuit breakers, is of the order of a microsecond
- C is the equivalent capacitance across the circuit breaker $C = C_t C_s / C_t C_s$
- L is the loop inductance
- R_0 is the arc resistance

R_d is a dynamic arc resistance, related to R_0 by $R_d = \alpha R_0$, where α is the exponent in the quasistationary V–I characteristic of the arc $VI^{\alpha} = N_0 = \text{const}$.

An example of instability and current chopping is shown in Figure 1.16 (Rizk, 1963), with associated overvoltage. If the chopped current is i_0 and the voltage across C_t at the instant of chopping is u_0, the maximum overvoltage factor occurs when the total associated magnetic and electrostatic energy is transferred to the capacitor C_t, yielding

$$\frac{1}{2} C_t V_{max}^2 = \frac{1}{2} C_t u_0^2 + \frac{1}{2} L_t i_0^2$$

from which

$$V_{max} = \sqrt{u_0^2 + \frac{L_t}{C_t} i_0^2} \tag{1.42}$$

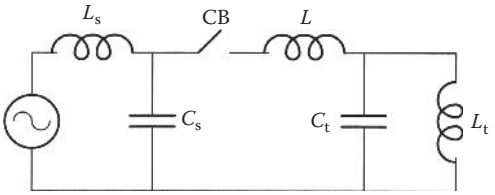


FIGURE 1.15 Basic circuit for interruption of small inductive currents.

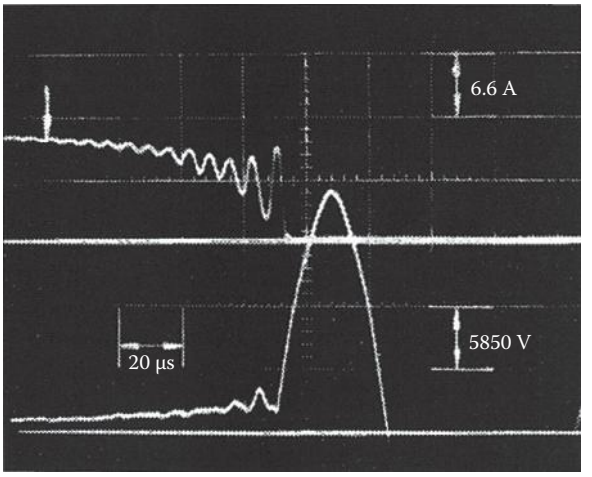


FIGURE 1.16 Example of interruption of small inductive current with associated current instability, chopping and switching overvoltages. (From Rizk, F.A.M., Interruption of small inductive currents with air-blast circuit-breakers, Dr. Tech. dissertation, Chalmers University of Technology, Gothenburg, Sweden, 1963.)

From Equation 1.41, it can be shown that the instability current i_{ins} can be expressed as

$$i_{ins} = N_0 \left(\frac{\hat{E}}{E_a} \sqrt{\frac{q}{C}} - \frac{L}{q}\right)^{-1/(1+a)}$$

which indicates that the instability current significantly increases with the equivalent capacitance C. Laboratory testing has also shown that the chopping current i_0 can be approximately expressed as

$$i_0 = \lambda \sqrt{C}$$

where λ is called the chopping number, which varies with the type of circuit breaker but is numerically of the order of 10^5.

Also, the maximum overvoltage of Equation 1.42 is in practice limited by restrikes in the circuit breaker, when at any instant following current chopping, the voltage across the breaker contacts exceeds the dielectric strength (Rizk, 1963), which sends some of the stored energy into the feeding network.

1.3.3.2 Interruption of Capacitive Current

Figure 1.17a presents the equivalent circuit for interruption of capacitive current. Figure 1.17b shows the associated breaker current as well as the source voltage U_s and the load capacitor (line) voltage U_l. As usual, the capacitive current is leading the voltage U_s by 90°. As the current is interrupted at a zero crossing, the capacitor will be left charged at the peak supply voltage $\hat{U}_s$. If no breaker restrikes take place, this experience will be uneventful and no overvoltages will occur. However, an unfavorable situation will take place if, at the following (negative) peak of the supply voltage, when the breaker contacts are stressed by $2\hat{U}_s$, a restrike occurs and the resulting high-frequency current is interrupted, U_l then be left at $-3\hat{U}_s$. Theoretically, this dangerous process could continue (Slamecka, 1957), where the next restrike at supply voltage peak would leave the capacitor (line) charged to $+5\ \hat{U}_s$.

Fortunately, such dangerous overvoltage levels do not occur in practice as they are based on a series of severe assumptions. It is assumed that charging of the supply capacitor during restrikes is neglected, it is assumed that the high-frequency current at each restrike will be interrupted in one-half cycle, discharge of the line charge between restrikes is neglected, and finally, that restrikes will repeatedly occur at the peak of the supply voltage.

Most importantly though, utilities nowadays require restrike-free circuit breakers and the manufacturers seem to have no major difficulty satisfying that requirement.

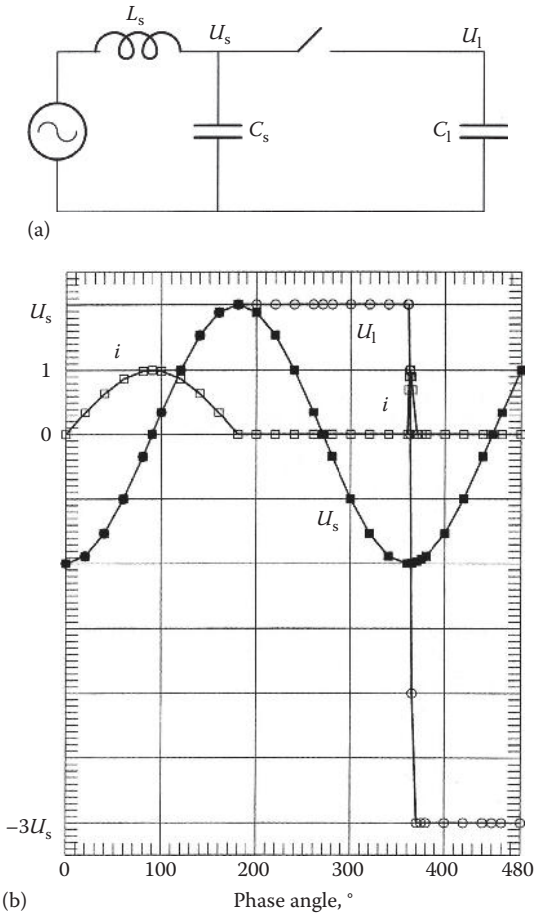


FIGURE 1.17 (a) Equivalent circuit for capacitive circuit interruption. (b) Overvoltage with switching of capacitive current and breaker restrike at supply voltage peak.

1.4 Electromagnetic Transient Program

Presently, the Electromagnetic Transient Program (EMTP) is the universal tool for calculation of power system transients using digital simulation. It is not intended in this chapter to give a detailed review of the EMTP because, on the one hand, this would be a vast job and, secondly, because there exist several expert publications on the subject (Dommel, 1969; Dommel and Meyer, 1974; IEEE 81 EHO 173-5-PWR, 1981). Some brief basic comments on the technique behind the EMTP are given in the following.

First, the EMTP mostly uses time-domain analysis, rather than frequency domain, and the transient analysis problem is defined as finding the values of voltages and currents at any point in the network at any time t, assuming that these were known as a time step Δt previously. Integration through a time step Δt is done using the trapezoidal rule. A fundamental result is that an inductance L and capacitance C can be replaced by resistors $2L/\Delta t$ and $\Delta t/2C$, respectively, in parallel with current sources I, which represent their respective current and voltage conditions.

For an inductance,

$$I = i\left(t - \Delta t\right) + \frac{v\left(t - \Delta t\right)}{R}$$

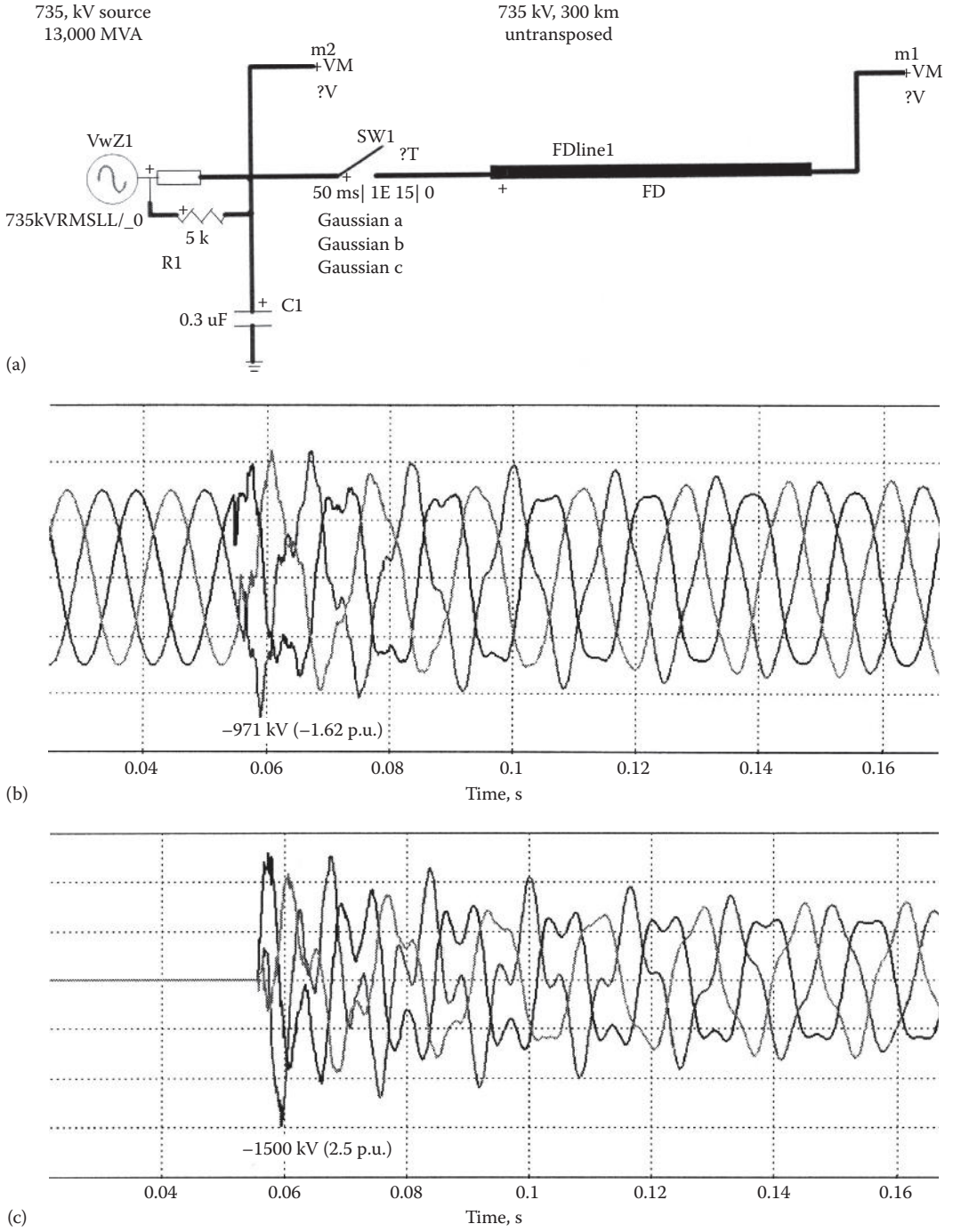


FIGURE 1.18 EMTP switching surge study for a 300 km long nontransposed 735 kV line. (a) Single line diagram. (b) Transient voltage at the sending end. (c) Transient voltage at the open end. (From Khodabakhchian, B., A study case of opening a 735 kV line, private communication, 2013.)

For a capacitance,

$$I = -i\left(t - \Delta t\right) - \frac{v\left(t - \Delta t\right)}{R}$$

Another fundamental point is that for a transmission line of length l between nodes k and m, the Bergeron method is used to obtain

$$i_k\left(t\right) = \frac{v_k\left(t\right)}{Z_0} + I_k$$

where Z_0 is the surge impedance of the line and

$$I_k = -i_m\left(t - T\right) - \frac{v_m\left(t - T\right)}{Z_0}$$

where T is the traveling time of the line. It follows that, at a line terminal, the line is represented by the surge impedance to ground and a parallel current source, without longitudinal connection between the line terminals.

Another interesting aspect is that the line is considered ideal, but lumped resistors at the line terminals and midpoint are used to represent power losses. Details on the methods of solution of the resulting matrix equations are described in IEEE 81 EHO 173-5-PWR (1981).

It is to be noted that the EMTP is an ongoing development project to which many researchers are contributing, particularly with respect to improved models for simulation of power system components. It should be noted that an important part of this research is the validation of computer results by comparison to field tests.

An example of EMTP application is illustrated in Figure 1.18, which shows the results of a switching surge study for a 300 km long nontransposed 735 kV line (private communication with Bahram Khodabakhchian). The line diagram is shown in Figure 1.18a. The transient voltage at the sending and open ends of the line is presented in Figure 1.18b and c, respectively. One can see that while the transient overvoltages remain reasonable at the sending end, –1.62 p.u., they exceed 2.5 p.u. at the open end, reaching some 1500 kV. Such a high level of transient overvoltages is unacceptable for the line insulation, which is designed for an overvoltage level of 2.2 p.u. These results suggest that some measures be taken to limit the transient overvoltages by either using closing resistances or installation of line arresters.

REFERENCES

Baatz, H. *Overvoltages in Power Systems*. Springer-Verlag, Berlin, 1956, pp. 59–62. [In German.]

Bewley, L.V. *Traveling Waves on Transmission Systems*. New York: Dover Publications, 1963.

Clark, E. *Circuit Analysis of A-C Power Systems, Symmetrical and Related Components*, Vol. 1. New York: John Wiley, 1943.

Dommel, H.W. Digital computer solution of electromagnetic transients in single and multi-phase networks. *IEEE Transactions on Power Apparatus and Systems* PAS-88: 388–399, April 1969.

Dommel, H.W. and W.S. Meyer. Computation of electromagnetic transients. *Proceedings of the IEEE* 62: 983–993, July 1974.

IEEE Tutorial Course Digital Simulation of Electrical Transient Phenomena, organized by Arun G. Phadke, 81 EHO 173-5-PWR, 1981.

Khodabakhchian, B. A study case of opening a 735 kV line, private communication, 2013.

Maruvada, P.S., Nguyen, D.H., and H. Hamadani-Zadeh. Studies on modeling of dynamic overvoltages. *IEEE Transactions on Power Delivery* PWRD-4(2): 1441–1449, April 1989.

Morched, A.S. Transmission line energization transients, Thesis, Norwegian Institute of Technology, Trondheim, Norway, February 1972.

Rizk, F.A.M. Arc instability and time-constant in air-blast circuit-breakers, CIGRE, Paper No. 107, 1964.

Rizk, F.A.M. Interruption of small inductive currents with air-blast circuit-breakers, Dr. Tech. dissertation, Chalmers University of Technology, Gothenburg, Sweden, 1963.

Slamecka, E. Interruption of small currents. *AEG Mitteilungen,* 47: 247–264, 1957. [In German.]

Thoren, H.B. and K.L. Carlsson. A digital computer program for the calculation of switching and lightning surges on power systems. *IEEE Transactions on Power Apparatus and Systems* PAS-89(2): 212–218, 1970.

Wedepohl, L.M. Application of matrix methods to the solution of traveling-wave phenomena in polyphase systems. *Proceedings of the IEE* 110: 2200–2212, December 1963.

2

Electrostatic Field Calculation

Electric and magnetic fields are essential in electromagnetism, intervening directly in the transmission of electric energy over long distances, where the lines essentially serve as wave guide for the propagation of the fields. The magnetic field allows the conversion of mechanical energy into electric energy in the alternators and the transformation of the voltage level in power transformers. In electrical insulation, the electric field allows the transfer of energy from the field to the charged particles in the insulating dielectric. In effect, electrostatic field exerts a force **F** on charged particles, free electrons, and ions, according to

$$\mathbf{F} = q \cdot \mathbf{E}$$

where
q is the electric charge of the particle
E is the electrostatic field

Charged particles are accelerated in the direction of the applied field, acquire kinetic energy, and initiate ionization activities leading to partial discharges and, eventually, to breakdown of the discharge gap.

In spite of their fundamental role in electromagnetism, both electric and magnetic fields remain less popular than other engineering terms: voltage, current, power, etc. The reason is, perhaps, related to the complex calculations, often required to determine the field at the surface of electrodes and in stressed gap, while other parameters simply follow from circuit analysis. This chapter reviews the problem of field calculation, starting with the elaboration of the basic equations, Maxwell and Laplace, before discussing the various methods of solution.

2.1 Electromagnetism: Maxwell Equations

Electromagnetism is basically governed by a set of fundamental laws that J.C. Maxwell has integrated in the elaboration of the electromagnetism theory (Becker, 1964). A brief review of the fundamental laws contributing to the establishment of the well-known Maxwell equations is given in the succeeding text, together with the general system of differential equations defining the potential and vector functions, which completely describe the electromagnetic field. The focus will be given to the case of electrostatic field, generally described by the Laplace or Poisson equation and the different methods of solution and, hence, defining the electric field in practical configurations of a discharge gap.

2.1.1 Fundamental Laws

The theory of electromagnetism relies on four fundamental laws that J. Maxwell has summarized in a set of equations known as Maxwell equations:

$$-\nabla \mathbf{H} = \mathbf{J} + \frac{\partial \mathbf{D}}{\partial t} + \rho \mathbf{v} \tag{2.1}$$

which is the statement of Ampere's law for time-varying fields as corrected by Maxwell.

$$\nabla \times \mathbf{E} = -\frac{\partial \mathbf{B}}{\partial t} \tag{2.2}$$

which is the statement of Faraday's law of electromagnetic induction.

$$\nabla \cdot \mathbf{D} = \rho \tag{2.3}$$

which is a statement of Gauss's law.

$$\nabla \cdot \mathbf{B} = 0 \tag{2.4}$$

which states that lines of magnetic flux are continuous.

In these equations, **H** is the magnetic field strength in A/m. **E** is the electric field strength in V/m. **D** is the electric displacement density in C/m^2. **J** is the current density in A/m^2. **B** is the magnetic flux density in Wb/m^2 and ρ is the charge density in C/m^3. **H**, **E**, **D**, **B**, and **J** are vector quantities, while ρ is a scalar quantity.

In addition to the earlier field equations, three equations relate to the characteristics of the medium in which the fields exist:

$$\mathbf{D} = \varepsilon \mathbf{E} \tag{2.5}$$

where $\varepsilon = \varepsilon_r \varepsilon_0$ is the permittivity of the medium expressed in terms of the permittivity of free space $\varepsilon_0 = 8.854 \times 10^{-12}$ F/m, ε_r being the relative permittivity also known as dielectric constant.

$$\mathbf{B} = \mu \mathbf{H} \tag{2.6}$$

where $\mu = \mu_r \mu_0$ is the permeability of the medium expressed in terms of the permeability of free space $\mu_0 = 4\pi \times 10^{-7}$ H/m, μ_r being the relative permeability of the medium.

$$\mathbf{J} = \sigma \mathbf{E} \tag{2.7}$$

where σ is the conductivity of the medium.

The four Maxwell equations are three dimensional partial differential equations in space and time. A magnetic vector potential **A** can be defined through:

$$\mathbf{B} = \nabla \times \mathbf{A} \tag{2.8}$$

And a scalar electric potential *u* to satisfy:

$$\mathbf{E} = -\nabla u - \frac{\partial \mathbf{A}}{\partial t} \tag{2.9}$$

The magnetic vector potential **A** must also satisfy:

$$\nabla \cdot \mathbf{A} = -\mu \varepsilon \frac{\partial u}{\partial t} \tag{2.9b}$$

Maxwell has shown that *the solution thus obtained is unique*. In other words, *there exists only one scalar potential field u and only one vector potential field* **A** *for a given configuration of charge and current densities in space*.

2.1.2 Boundary Conditions

Since any physical system is necessarily bounded and, in addition, can contain one or more dielectrics, it inevitably results in interfaces separating the insulation system in different regions, within which the insulation is homogeneous and the fields are continuous. As a result, the interfaces are the only places where the potential and vector fields may be discontinued. It is then of particular importance to determine the behavior of these fields at the interfaces: behavior that in turn determines the behavior of the

fields inside the adjacent regions of homogeneous dielectric. Let us consider an infinitesimal closed rectangular loop, which intercepts the interface separating two regions of space, having, respectively, a permittivity of ε_1 and ε_2 in such a way as having two sides parallel with the interface. Application of Faraday's law, Equation 2.2, to the closed loop gives

$$\mathbf{n} \times (\mathbf{E}_2 - \mathbf{E}_1) = 0 \quad \text{or} \quad \mathbf{E}_{2t} = \mathbf{E}_{1t} \tag{2.10}$$

where $\mathbf{n}$ is the unit vector normal to the interface separating the two dielectrics, oriented from the region 1 to the region 2, $\mathbf{E}_{1t}$ and $\mathbf{E}_{2t}$ are the tangential components of the electric field.

The last equation indicates that the tangential components of the electric field in the two adjacent dielectrics are equal at the interface. When the interface coincides with an equipotential surface in a coordinate system, the tangential components of the electric field are necessarily zero, and the lines of force representing the variation of the field in the normal direction to the equipotential surface will necessarily be perpendicular to it. In other words, *the equipotential surfaces and the lines of force are orthogonal to one another.*

Metal electrodes, with their high conductivity, constitute naturally equipotential surfaces: the lines of force are necessarily perpendicular to them. This fact explains the importance of choosing an orthogonal coordinate system such as to make the electrode surface coincide with the surfaces with one constant coordinate, which become automatically equipotential. This way of selecting the coordinate system often significantly simplifies the Laplace equation.

Let us consider an infinitesimal cube that intercepts the interface in such a way as having two sides parallel with the interface. Application of Gauss's law, Equation 2.3, to the closed volume that intercepts the interface between two homogeneous media, of permittivity ε_1 and ε_2, respectively, gives

$$\mathbf{n} \cdot (\mathbf{D}_2 - \mathbf{D}_1) = q \quad \text{or} \quad \mathbf{D}_{2n} - \mathbf{D}_{1n} = q \tag{2.11}$$

where $\mathbf{n}$ is the unit vector normal to the interface separating the two dielectrics, oriented from the region 1 to the region 2, and q the surface charge density, $\mathbf{D}_{1n}$ and $\mathbf{D}_{2n}$ the normal components of the displacement vector.

When there is no charge accumulated at the interface, $q = 0$, the preceding equation simplifies to

$$\varepsilon_2 \mathbf{E}_{2n} - \varepsilon_1 \mathbf{E}_{1n} = 0 \quad \text{or} \quad \varepsilon_2 \mathbf{E}_{2n} = \varepsilon_1 \mathbf{E}_{1n} \tag{2.11a}$$

One finds the familiar relationship between the normal components of the electric field at the interface of two dielectrics.

In a similar manner, one can demonstrate the relations between the magnetic field $\mathbf{H}$ and the magnetic flux $\mathbf{B}$ at the interface of two homogeneous media:

$$\mathbf{n} \times (\mathbf{H}_2 - \mathbf{H}_1) = \mathbf{J}_s$$

$$\mathbf{n} \cdot (\mathbf{B}_2 - \mathbf{B}_1) = 0$$

where

$\mathbf{n}$ is the unit vector perpendicular to the interface, oriented from the region 1 to the region 2

$\mathbf{J}_s$, the surface densities of charge and current at the interface

2.2 Electrostatics: Laplace Equation

Electrostatics is a particular case of electromagnetism, when the current density is zero, $\mathbf{J} = 0$, at all points in space and, consequently, $\partial\mathbf{B}/\partial t = 0$. The Maxwell equations simplify to

$$-\nabla \times \mathbf{E} = 0$$

$$-\nabla \cdot \mathbf{D} = \rho$$

The electric field **E** becomes nonrotational; it can be derived from a scalar potential function u such that

$$\mathbf{E} = -\nabla u,$$

since

$$-\nabla \times \mathbf{E} = -\nabla \times (-\nabla u) \equiv 0$$

It follows that the differential equation defining the scalar potential function u is

$$-\nabla^2 u = -\frac{\rho}{\varepsilon} \tag{2.12}$$

usually known as the Poisson equation.

In the particular case where there is no free charge in space, $\rho = 0$, the preceding equation simplifies further and becomes the Laplace equation:

$$-\nabla^2 u = 0 \tag{2.13}$$

The solution of the Poisson or Laplace equation defines completely the scalar potential function u, which complies with the boundary conditions specific to a given problem. The different ways of solving the Laplace equation will be discussed in the following.

2.3 Analytical Solution of the Laplace Equation

The analytical solution of the Laplace equation consists of the following:

- Simplify as much as possible the differential equation to reduce the number of variables to minimum, namely, by adopting an appropriate coordinate system that takes advantage of the natural symmetry of the electrode configuration.
- Decompose the Laplace equation into a set of several differential equations of single variable by using the method of *separation of variables*.
- Find the general solution to the set of differential equations.
- Define the particular solution that satisfies the boundary conditions.

Method of separation of variables: Consists of separating the multivariable differential equations into a set of differential equations, each of a unique variable. A discussion of the separation of variables is given in Moon and Spencer (1960) for the readers who are interested. By assuming that the scalar potential function, u, is the product of several functions, each of a single variable, according to

$$u(x_1, x_2, x_3) = F_1(x_1)\, F_2(x_2)\, F_3(x_3) = \prod_{i=1}^{3} F_i(x_i)$$

the first- and second-order derivatives of u are given by

$$\frac{\partial u}{\partial x_i} = \left[\prod_{\substack{j=1 \\ j \neq i}}^{3} F_j(x_j)\right] \cdot \frac{\mathrm{d}}{\mathrm{d}x_i} F_i(x_i)$$

and

$$\frac{\partial^2 u}{\partial x_i^2} = \sum_{j \neq i} F_j(x_j) \frac{\mathrm{d}^2}{\mathrm{d}x_i^2} F_i(x_i)$$

Replacing the preceding expressions of the derivatives into the Laplace equation and dividing both sides by $u(x_i)$ transforms it to

$$-^2 u(x_i) = \sum \frac{1}{F_i} \frac{\mathrm{d}^2 f_i}{\mathrm{d}x_i^2} = 0$$

which can then be separated into several differential equations of single variable x_i. A few examples of the solution of the Laplace equation are discussed in the following to illustrate the method of separation of variables and the importance of choosing the appropriate coordinate system.

2.3.1 Cartesian Coordinates

In the Cartesian coordinates, x, y, z, equipotential surfaces corresponding to x = const, y = const, and z = const are plane surfaces perpendicular to the x-, y-, and z-axis, respectively. The Laplace equation is expressed as

$$-^2 u(x,y,z) = \frac{\partial^2 u}{\partial x^2} + \frac{\partial^2 u}{\partial y^2} + \frac{\partial^2 u}{\partial z^2} = 0$$

Applying the method of separation of variables, the potential function u is

$$u(x,y,z) = X(x)\, Y(y)\, Z(z)$$

The Laplace equation becomes

$$-^2 u(x,y,z) = \frac{1}{X(x)} \frac{\mathrm{d}^2 X}{\mathrm{d}x^2} + \frac{1}{Y(y)} \frac{\mathrm{d}^2 Y}{\mathrm{d}y^2} + \frac{1}{Z(z)} \frac{\mathrm{d}^2 Z}{\mathrm{d}z^2} = 0 \tag{2.14}$$

The preceding equation can be satisfied only if

$$\frac{1}{Z(z)} \frac{\mathrm{d}^2 Z}{\mathrm{d}z^2} = p^2$$

$$\frac{1}{Y(y)} \frac{\mathrm{d}^2 Y}{\mathrm{d}y^2} = q^2$$

$$\frac{1}{X(x)} \frac{\mathrm{d}^2 X}{\mathrm{d}x^2} + p^2 = -q^2$$

where p^2 and q^2 are positive constants and are effectively separated into three differential equations of single variable. The general solution for y and z is of the exponential type; that for x is sinusoidal.

2.3.1.1 Uniform Field

Consider a gap defined by two parallel plane electrodes of infinite dimensions, separated one from the other by a distance d, and subjected to a potential difference of U. Because of the symmetry of the electrode system, the electric field is a function of the distance along the axis perpendicular to the

electrodes only. By choosing a Cartesian coordinate system having the y–z plane coinciding with one of the electrodes, the Laplace equation has only one variable, x, according to

$$-^2u = \frac{\mathrm{d}^2u}{\mathrm{d}x^2} = 0$$

Taking the successive integration of the preceding differential equation gives

$$\frac{\mathrm{d}u}{\mathrm{d}x} = -E = \text{const},$$

and

$$u(x) = -Ex + \text{const}$$

Applying the boundary conditions at $x = 0$, $u = 0$, and at $x = d$, $u = U$, one obtains the following expressions for the potential $u(x)$ and the electric field $\mathbf{E}(x)$:

$$u(x) = \frac{U}{d}x \tag{2.15}$$

$$E(x) = -\frac{\mathrm{d}u}{\mathrm{d}x} = -\frac{U}{d} \tag{2.16}$$

2.3.1.2 Uniform Field Electrodes

In spite of the apparently simple configuration of the parallel plane gap, the finite dimensions of any physical system make the production of a uniform field a rather delicate matter in practice due to the end effect of the electrodes. A well-designed electrode would ensure a uniform field in the gap between the electrodes and a decreasing field at the edge of the electrodes. Many electrode configurations have been used in practice to produce a uniform field in the gap between two electrodes: from the simple plane electrode with rounded off edges to more elaborated electrode profiles, Rogowski and Bruce, to produce a uniform field in the gap between two electrodes and ensure a better control of the electrode end effect. Their relative effectiveness in producing a uniform field in the gap will be discussed in the following, by comparing the distribution of the field at the electrode surface with emphasis being put on the electrode end effect. In all cases, the electrodes have the same thickness T. The field calculation was made with the charge simulation method (Singer et al., 1974) discussed in Section 2.5.3, for a range of gap length d.

Plane electrode: Figure 2.1a illustrates a simple circular plane electrode having its edge terminated by a circular section of center Ω and radius $R_e = T/2$. Figure 2.1b shows the distribution of the field at the surface of the plane electrode for different ratios of the gap length d by the electrode thickness T. The solid line curves represent the locus of the extremities of the field vectors, perpendicular to the electrode surface. It can be seen that the field remains constant in the central region of the electrodes; it increases towards the end of the electrodes and reaches a maximum value before it decreases again along the circular section of the plane electrode. Varying the gap length does not change the behavior observed for the surface field. This electrode configuration, although simple to achieve, is far from being adequate for producing a uniform field in its gap.

Rogowski profile electrode (Rogowski, 1923; Cobine, 1956): A Rogowski electrode is obtained by the rotation around a vertical axis of a Rogowski profile. The latter corresponds actually to one of the equipotentials produced by a set of two parallel plane electrodes, separated from each other by a distance d, of which one is only a half-plane surface to reproduce the end effect. Rogowski showed that this particular electrode arrangement can be obtained by a conformal transformation of the set of two parallel plane electrodes, in which the upper plane electrode is folded back 180°, along an axis parallel to the z-axis and located at $x = d/\pi$, to produce the half-plane electrode (Figure 2.2a).

In the process, the uniform distribution of the field along the gap axis between the plane electrodes is transformed into a uniform distribution of the field as a function of the rotation angle of the equipotential

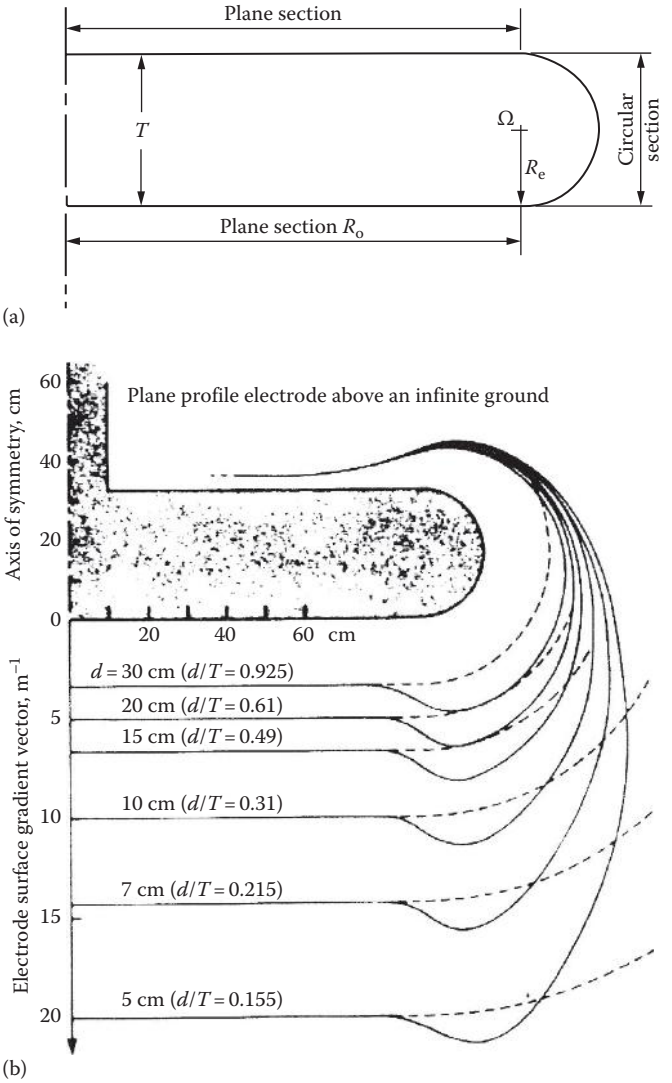


FIGURE 2.1 (a) Plane electrode configuration. (b) Variation of the electrode surface gradient vector at a plane-profile electrode above an infinite ground plane, with d the inter-electrode distance, and T the effective electrode thickness. (From Trinh, N.G., *IEEE Trans. Power Appar. Syst.*, 99, 1235, 1980.)

planes. As a result, the equipotential u also corresponds to the rotation angle of the equipotential plane. In Figure 2.2, the potential of the half plane electrode is set equal to π, which corresponds also to its rotation angle. A point $P(h, u)$ in the gap between the two parallel planes electrodes, with the potential u, between 0 and π, equal to the rotation angle of the equipotential plane, is transformed into a point $P'(x, y)$ in the space between the half-plane electrode and the ground plane according to

$$x = \frac{d}{\pi}\left[h + \exp(h)\cos u\right] \tag{2.17}$$

$$y = \frac{d}{\pi}\left[u + \exp(h)\sin u\right]$$

For the constant value of u, Equations 2.17 define the equipotentials in the half plane to ground space, which are bent upward as illustrated in Figure 2.2b.

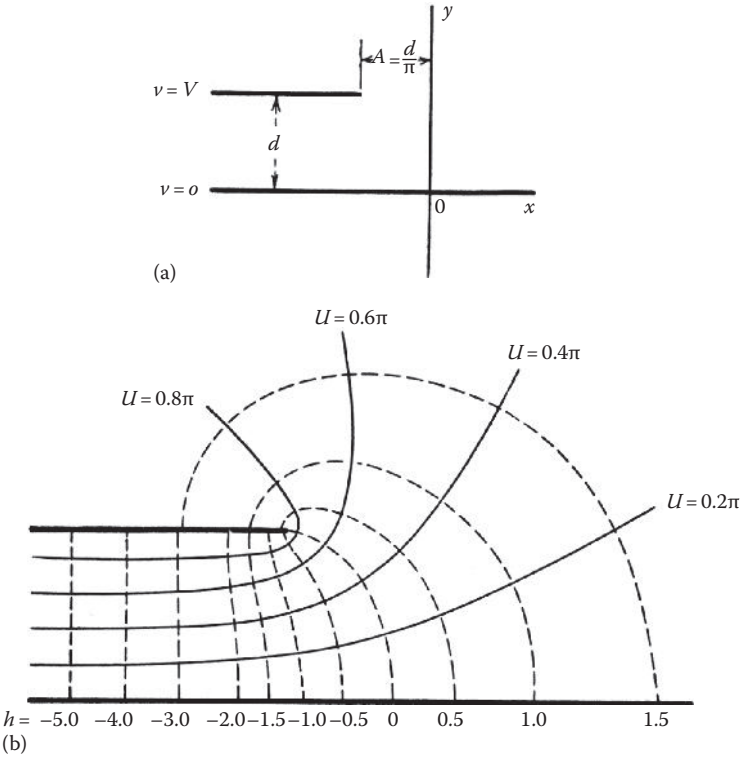


FIGURE 2.2 Rogowski equipotential curves; where d is the inter-electrode distance and A the abscisse of the upper electrode edge. (From Cobine, J.D., *Gaseous Conductors—Theory and Engineering Applications*, Dover Publications Inc., New York, 1956.)

A pronounced end effect can be observed at the edge of the upper electrode associated with the closely spaced equipotential lines for $u \geq \pi/2$, while for $u \leq \pi/2$, the electric field **E** is uniform in the gap between the electrodes and decreases gradually towards the edge of the upper electrode.

For the limiting case corresponding to $u = \pi/2$, the Rogowski profile is defined by

$$x = \frac{d}{\pi} h \tag{2.18}$$

$$y = \frac{d}{\pi}\left(\frac{\pi}{2} + \exp(h)\right) = d\left(\frac{1}{2} + \exp(h)\right)$$

It can be seen that, in this case, the Rogowski profile passes exactly halfway between the electrodes, $y = d/2$, when $h \to -\infty$. Figure 2.3a illustrates a typical Rogowski profile, comprising a central plane section, followed by a Rogowski profile section with $u = \pi/2$ and terminated with a circular section centered at Ω, and having a radius of $R_e = T/2$. Figure 2.3b shows the distribution of the field at the surface of the Rogowski profile plane electrode for different ratios of the gap length d by the electrode thickness T. It can be seen that the field remains constant in the central region of the electrodes and gradually decreases towards the edge of the electrode with no observable end effect.

Bruce profile electrode (Bruce, 1947): Bruce profile electrodes are obtained in a similar way by the rotation of the Bruce profile around the vertical axis. Figure 2.4a shows a typical Bruce profile, composed of a central plane section, followed by a sinusoidal section, and completed by a circular section of center

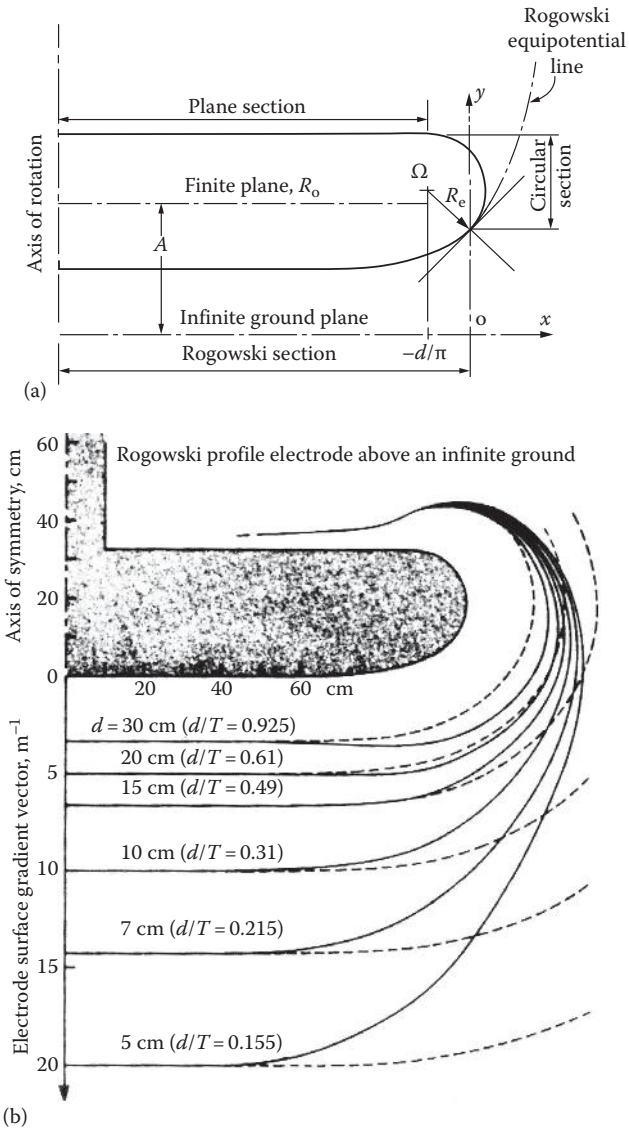


FIGURE 2.3 (a) Illustration of a typical Rogowski profile electrode. (b) Distribution of the electric field at the surface of a Rogowski electrode, with d the inter-electrode distance, and T the effective electrode thickness. (From Trinh, N.G., *IEEE Trans. Power Appar. Syst*., 99, 1235, 1980.)

Ω and radius $R_e = T/2$. The disposition of the different sections is such that the passage from one section to the next is made smoothly. Referring to the coordinate system Ox, Oy in Figure 2.4a, the sinusoidal section can be expressed as

$$y = -R_e \sin(\omega x)$$

Referring to Figure 2.4a, letting X_0 be the abscissa of the center Ω of the circular section, which also corresponds to the abscissa of the maximum of the sinusoidal section, one gets

$$\omega X_0 = \frac{\pi}{2}$$

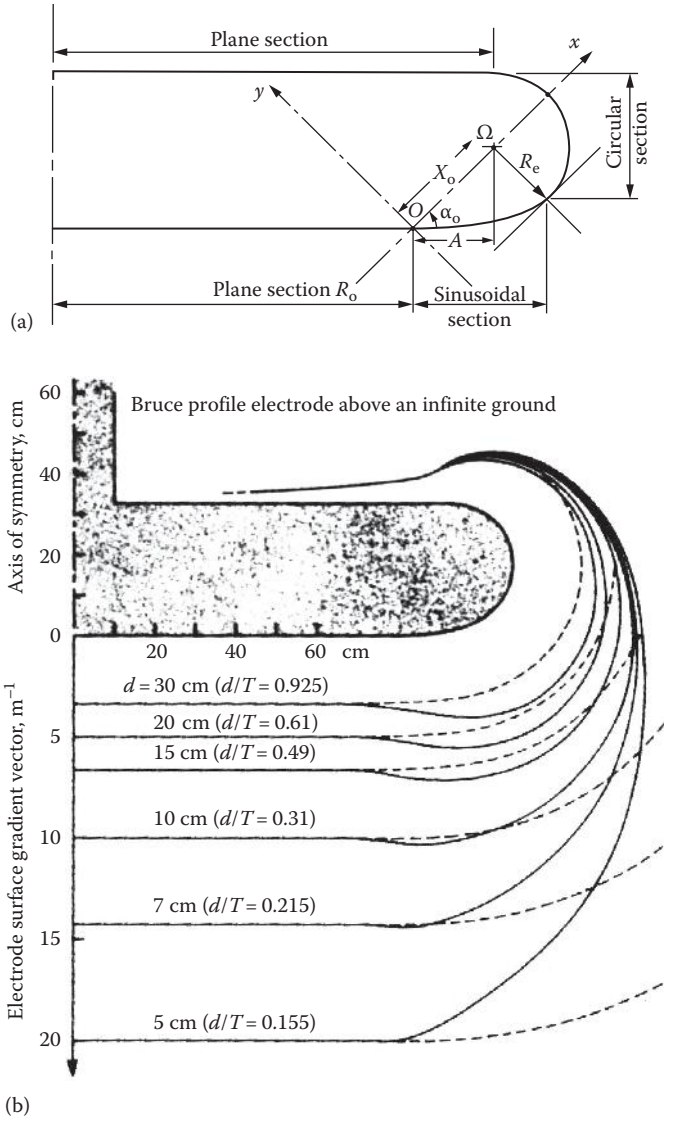


FIGURE 2.4 (a) Illustration of a Bruce profile electrode. (b) Distribution of the electric field at a Bruce profile electrode, with d the inter-electrode distance, and T the effective electrode thickness. (From Trinh, N.G., *IEEE Trans. Power Appar. Syst.*, 99, 1235, 1980.)

It follows that

$$w = \frac{p}{2X_0}$$

The derivate, y', that is, the slope of the tangent at a point on the sinusoidal section, is

$$y' = -wY\cos(wx)$$

At the origin of the coordinates, O, $\omega x = 0$ and the derivate y' becomes

$$y_0' = \tan a = -wR_e\cos(0) = -wR_e$$

which yields

$$R_e = \frac{\tan a}{w} = \frac{2X_0}{p} \tan a \tag{2.19}$$

Figure 2.4b shows the distribution of the field at the surface of the Bruce profile electrode for different ratios of the gap length d by the electrode thickness T. It can be seen that for small values of the ratio d/T, the field remains constant in the central region of the electrodes and gradually decreases towards the edge of the electrode with no observable end effect. However, as the ratio d/T increases, the field at the electrode surface passes by a maximum towards the edge of the electrode. The end effect becomes more pronounced with large values of d/T. Compared with the Rogowski profile, one can see that the Rogowski electrodes provide a better uniformity of the field over a wide range of the ratio d/T. However, for the same overall dimensions, the Bruce profile provides a larger area of uniform field at the electrode.

2.3.1.3 Uniform Field in the Presence of Composite Dielectrics

When the interelectrode space is composed of more than one dielectric, the electric field in each dielectric must respect the boundary conditions at the separating interface. For the case of two dielectrics of thickness a and b, the boundary conditions at the interface are (Equations 2.10 and 2.11)

$$E_{1t} = E_{2t} \quad \text{and} \quad D_{1n} - D_{2n} = q$$

where q is the boundary surface charge density. When there is no charge deposed at the interface, $q = 0$, the last condition simplifies to

$$D_{1n} = D_{2n} \quad \text{or} \quad e_1 E_{1n} = e_2 E_{2n}$$

On the other hand, the sum of the potential differences in the two dielectrics must be equal to the applied voltage U, and one gets

$$aE_1 + bE_2 = U$$

The following expressions can be derived for the electric fields E_1 and E_2:

$$E_1 = \frac{e_2 U}{ae_2 + be_1}$$

and

$$E_2 = \frac{e_1 U}{ae_2 + be_1} \tag{2.20}$$

Figure 2.5 compares the variations of the potential and field in a uniform field gap of length $d = a + b = 1$, subjected to a voltage difference of 1 kV, for the cases of one dielectric and in the presence of two dielectrics of dielectric constants ε_1 and ε_2 with $\varepsilon_1 = 2\varepsilon_2$. In the latter case, one can see that the potential varies linearly with the distance from the cathode and is continuous at the interface between the two dielectrics. The electric field is constant within each dielectric but is discontinued at the interface, giving rise to a sudden jump in the field intensity.

Practical application: An example of a uniform field gap in the presence of two dielectrics is in the elaboration of power capacitors. Here, the plane electrodes are metal foils separated by a sheet of paper or polymer film immersed in insulating oil. Edge effect is inevitable in this case and requires particular care in the setting up of the metal foils. Furthermore, since the dielectric constant of oil is much lower than that of the paper, the field intensity within the oil layer is higher than that inside the paper, making

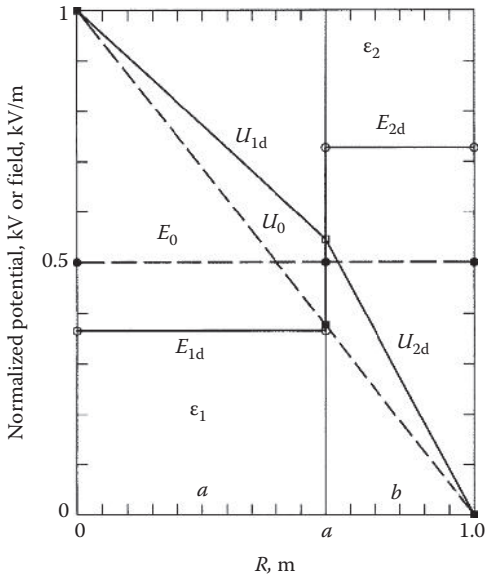


FIGURE 2.5 Distribution of potential and field in a uniform field gap in the presence of two dielectrics. Dashed curves correspond to single dielectric case.

foil edge a potential site for partial discharges. This problem may be partially mitigated by replacing paper with polymer dielectric that has a dielectric constant closer to that of the oil.

2.3.2 Cylindrical Coordinates

In cylindrical coordinates, r, ψ, and z, the equipotential surfaces for constant r are cylinders of radius r, for constant z are plane surfaces perpendicular to the z-axis, and for constant ψ are half-plane surfaces passing by the z-axis. The Laplace equation for potential u is expressed as

$$-^2u = \frac{\partial^2 u}{\partial r^2} + \frac{1}{\mathrm{r}}\frac{\partial u}{\partial r} + \frac{1}{\mathrm{r}^2}\frac{\partial^2 u}{\partial \mathrm{Y}^2} + \frac{\partial^2 u}{\partial z^2} = 0 \tag{2.21}$$

Applying the method of separation of variables with the potential function, one gets

$$u(r, \mathrm{y}, z) = R(r)\ \mathrm{F}(\mathrm{y})\ Z(z)$$

The Laplace equation is converted into three differential equations of single variable as

$$\frac{1}{Z}\frac{\mathrm{d}^2 Z}{\mathrm{d}z^2} = p^2$$

$$\frac{\mathrm{d}^2 \mathrm{F}}{\mathrm{d}\mathrm{y}^2} + q^2 \mathrm{F} = 0$$

$$\frac{\mathrm{d}^2 R}{\mathrm{d}r^2} + \frac{1}{r}\frac{\mathrm{d}R}{\mathrm{d}r} + \frac{(p^2 - q^2)R}{r^2} = 0$$

The constant p^2 must be positive to ensure a realistic solution for $Z(z)$. The equation in ψ and z has a general solution of the circular and exponential type, respectively, while the general solution for the equation of r is of the Bessel type (Moon and Spencer, 1960).

2.3.2.1 Coaxial Cable

Consider the case of a coaxial cable of infinite length; the radii of the central conductor and of the envelope are a and b, respectively, and subjected to a potential difference of U. Because of the axial symmetry of the electrodes, the potential function depends only on the radial distance r, $u(r)$. It is obvious that a cylindrical coordinate system, having the z-axis coinciding with the axis of symmetry of the cable, would be most appropriate. Under these conditions, the Laplace equation in cylindrical coordinates is simplified to

$$-\nabla^2 u = \frac{\mathrm{d}^2 u}{\mathrm{d}r^2} + \frac{1}{r}\frac{\mathrm{d}u}{\mathrm{d}r} = 0 \tag{2.22}$$

The general solution of the preceding differential equation is

$$u(r) = A \ln r + B$$

where A and B are constants. Applying the boundary conditions at $r = b$, $u = 0$, and at $r = a$, $u = U$, one can determine the constants A and B as

$$B = -A \ln b \quad \text{and} \quad A = -\frac{U}{\ln(b/a)}$$

One obtains the following expressions for the potential function $u(r)$ and the electric field $\mathbf{E}(r)$:

$$u(r) = \frac{U}{\ln(b/a)} \ln \frac{b}{r} \tag{2.23}$$

$$\mathbf{E}(r) = -\frac{\mathrm{d}u}{\mathrm{d}r}\mathbf{a}_\mathrm{r} = \frac{U}{\ln(b/a)}\frac{1}{r}\mathbf{a}_\mathrm{r} \tag{2.24}$$

where $\mathbf{a}_\mathrm{r}$ is the unit vector in the radial direction.

Optimal dimensions of a coaxial cable: From Equation 2.24, the expression for the electric field at the surface of the central conductor E_0

$$E_0 = \frac{1}{\ln(b/a)}\frac{U}{a} \tag{2.25}$$

will be minimum when the denominator $f(a, b)$, a function of the cable dimensions a and b, is maximum:

$$f(a, b) = a \ln \frac{b}{a} = a(\ln b - \ln a)$$

For a cable with a given radius b of the envelope, the function $f(a, b)$ will be maximum when its derivative with respect to a is null:

$$\frac{\partial}{\partial a} f(a, b) = \ln b - \ln a - a\frac{1}{a} = \ln \frac{b}{a} - 1 = 0$$

One gets

$$\ln \frac{b}{a} = 1$$

The relationship between the radii of the cable for an optimal design becomes

$$\frac{b}{a} = e = 2.718$$

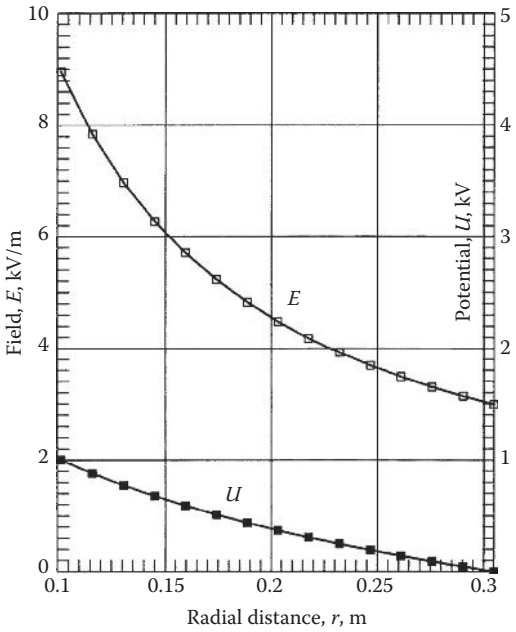


FIGURE 2.6 Variations of normalized potential and field in an SF6-insulated coaxial cable. Conductor radius, 11 cm; envelope radius, 30 cm.

which is currently used for gas-insulated cables and bus bars. Figure 2.6 shows the variations of the normalized potential and electric field at the nominal voltage of 1.0 kV, in an 800 kV SF6-insulated coaxial cable with optimal dimensions $a = 11$ cm and $b = 30$ cm.

Charge and capacitance per unit length: From the preceding expression of E_0, the surface charge density at the conductor, σ_0, is

$$\sigma_0 = \varepsilon E_0 = \frac{\varepsilon}{\ln(b/a)} \frac{U}{a}$$

The linear charge at the conductor is equal to

$$q_1 = 2\pi a \sigma_0 = \frac{\varepsilon}{\ln(b/a)} \frac{U}{a} = \frac{2\pi\varepsilon U}{\ln(b/a)} = C_1 U \quad \text{C/m} \tag{2.26}$$

where q_1 and C_1 are the linear charge and capacitance of the coaxial cable. It follows that the expression of the linear capacitance C_1 is

$$C_1 = \frac{2\pi\varepsilon}{\ln(b/a)} \quad \text{F/m} \tag{2.27}$$

2.3.2.2 Cylindrical Field in the Presence of Composite Dielectrics

When the interelectrode space is composed of more than one dielectric, the electric field in each dielectric must respect the boundary conditions at the interface. For the case of two dielectrics, the boundary conditions at the interface located at a radial distance of $r = d$ are (Equations 2.10 and 2.11)

$$E_{1t} = E_{2t} \quad \text{and} \quad \varepsilon_1 E_{1n} = \varepsilon_2 E_{2n}$$

The electric fields in the dielectrics are

$$E_1(r) = \frac{U_1}{\ln(d/a)}\frac{1}{r}$$

and

$$E_2(r) = \frac{U_2}{\ln(b/a)}\frac{1}{r}$$

At the interface of the dielectrics,

$$\epsilon_1 \frac{U_1}{\ln(d/a)}\frac{1}{d} = \epsilon_2 \frac{U_2}{\ln(b/d)}\frac{1}{d}$$

By noting that the sum of the potential differences U_1 and U_2 in the two dielectrics must be equal to the applied voltage U, $U_1 + U_2 = U$, the solution for the preceding set of equations gives

$$U_1 = \frac{\epsilon_2 \ln(d/a)}{\epsilon_1 \ln(b/d) + \epsilon_2 \ln(d/a)} U \quad \text{and} \quad \mathbf{E}_1(r) = \frac{\epsilon_2}{\epsilon_1 \ln(b/d) + \epsilon_2 \ln(d/a)} \frac{U}{r}\mathbf{a}_r$$

$$U_2 = \frac{\epsilon_1 \ln(b/d)}{\epsilon_1 \ln(b/d) + \epsilon_2 \ln(d/a)} U \quad \text{and} \quad \mathbf{E}_2(r) = \frac{\epsilon_1}{\epsilon_1 \ln(b/d) + \epsilon_2 \ln(d/a)} \frac{U}{r}\mathbf{a}_r$$

where $\mathbf{a}_r$ is the radial unit vector.

Figure 2.7 compares the distributions of normalized potential and electric field in a coaxial cable of optimal dimensions $a = 1$ cm and $b = 2.718$ cm, with single and composite dielectrics of dielectric constants $\varepsilon_2 = 2\varepsilon_1$. In the latter case, one observes that the potential varies according to a logarithmic function within each dielectric and is continued at the interface between the two dielectrics.

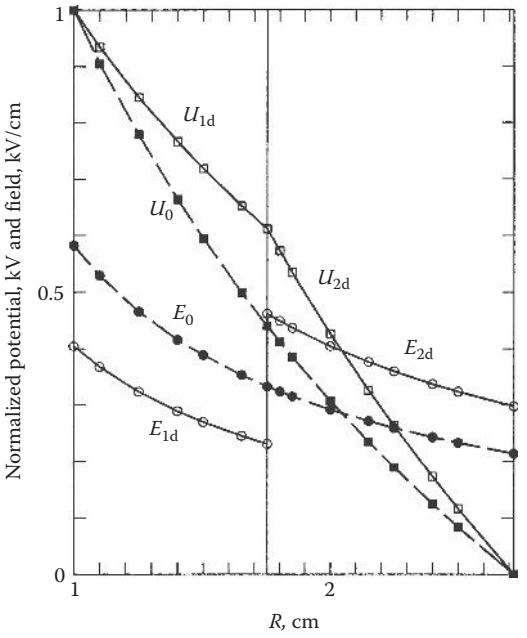


FIGURE 2.7 Variations of the potential and the electric field in a coaxial cable in the presence of two dielectrics. Conductor radius, 1 cm; envelope radius, 2.72 cm. Dashed curves correspond to a single dielectric case. For clarity of the figure, a scale factor of 0.6 has been applied to the normalized field shown.

The electric field varies proportionally to 1/*r*, the radial distance, and is discontinued at the interface, giving rise to a sudden jump in the field intensity.

Practical application: By choosing $\varepsilon_1 > \varepsilon_2$, the electric field at the central conductor in a coaxial cable can be considerably reduced, making the inception of partial discharges more difficult at the central conductor, even if the electric field at the interface between two dielectrics is more pronounced. A practical application is in the elaboration of the entry lead and the conductor of the high-voltage winding of power transformers with several layers of insulating paper tape. The dielectric constant of the paper, $\varepsilon_{pr} = 5$, is significantly higher than that of the insulating oil, $\varepsilon_{hr} = 2.2$, which reduces proportionally the electric field at the conductor surface and minimizes the effect of scratches and other irregularities at the conductor surface. For the same reason, in polymer cables, a semiconducting layer may be first extruded over the central conductor before continued with the main insulation.

2.3.3 Spherical Coordinates

In a spherical coordinate system, *r*, θ and ψ, the equipotential surfaces for constant *r* are spheres of radius *r*, for constant θ are cones with semi-angle θ, and for constant ψ are half-plane surfaces passing by the *z*-axis at an angle ψ. The Laplace equation is

$$-^2 u = \frac{\partial^2 u}{\partial r^2} + \frac{2}{r}\frac{\partial u}{\partial r} + \frac{1}{r^2}\frac{\partial^2 u}{\partial \theta^2} + \frac{\cot \theta}{r^2}\frac{\partial u}{\partial \theta} + \frac{1}{r^2 \sin^2 \theta}\frac{\partial^2 u}{\partial \psi^2} = 0 \tag{2.28}$$

By the method of separation of variables, the potential function *u* is

$$u(r, \theta, \psi) = R(r)\, \Theta(\theta)\, \Psi(\psi)$$

The Laplace equation is decomposed in three differential equations of single variable:

$$\frac{1}{\psi}\frac{d^2 \Psi}{d\psi^2} = -p^2$$

$$\frac{d^2 R}{dr^2} + \frac{2}{r}\frac{dR}{dr} - q(q+1)\frac{R}{r^2} = 0$$

$$\frac{d^2 \Theta}{d\theta^2} + \cot \theta \frac{d\Theta}{d\theta} + \left[q(q+1) - \frac{1}{\sin^2 \theta} p^2\right]\Theta = 0$$

The equation in ψ has a general solution of the circular type; the equation in *r* has a general solution of the type

$$R = Ar^q + Br^{-(q+1)}$$

and the equation for θ has a general solution of the associated Legendre function.

2.3.3.1 Spherical Field

Consider a gap defined by two concentric spherical electrodes of radii *a* and *b* and subjected to a potential difference *U*. Because of the symmetry of the electrodes, the Laplace equation is simplified to

$$-^2 u = \frac{d^2 u}{dr^2} + \frac{2}{r}\frac{du}{dr} = 0 \tag{2.29}$$

The general solution to the preceding differential equation is

$$u(r) = A + \frac{B}{r}$$

where A and B are constants.

Applying the boundary conditions at $r = b$, $u = 0$, and at $r = a$, $u = U$, one obtains

$$A = -\frac{B}{b} \quad \text{and} \quad B = \frac{ab}{b-a}U$$

The potential function $\phi(r)$ is

$$u(r) = \frac{a(b-r)}{b-a}\frac{U}{r} \tag{2.30}$$

The electric field $\mathbf{E}$ is

$$\mathbf{E}(r) = -\frac{\mathrm{d}u}{\mathrm{d}r}\mathbf{a}_r = \frac{ab}{b-a}\frac{U}{r^2}\mathbf{a}_r \tag{2.31}$$

where $\mathbf{a}_r$ is the radial unit vector.

In practice, the configuration of concentric spheres is currently used in metal-clad equipment, in the elaboration of joints at angle, elbows, or *T* connections for gas-insulated buses. Figure 2.8 shows the variations of the normalized potential and field, for an applied voltage of 1.0 kV, in a concentric sphere gap with dimensions of $a = 20.32$ cm and $b = 60.96$ cm. One can see that the potential and the field vary proportionally to $1/r$ and $1/r^2$, respectively.

The field at the inner sphere is

$$E(a) = \frac{b}{a(b-a)}U$$

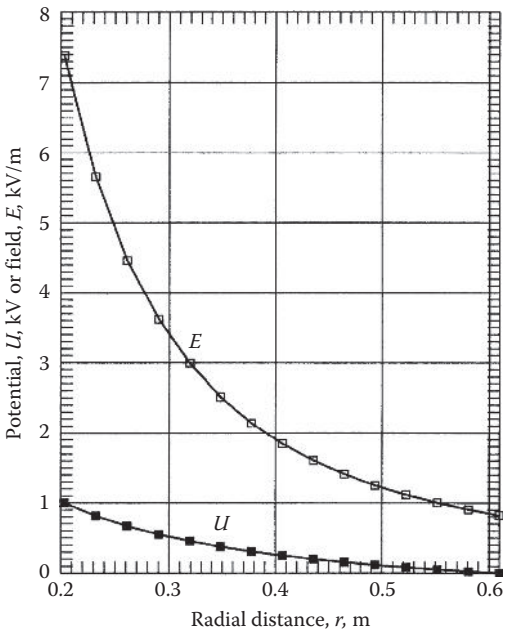


FIGURE 2.8 Distribution of normalized potential and field in a concentric spherical gap. Dimensions: inner sphere radius, $a = 20$ cm; outer sphere radius, $b = 60$ cm.

For a given dimension of the outer sphere b, the field at the inner sphere will be maximum when the denominator $f = a\,(b - a)$ is minimum, that is,

$$\frac{df}{da} = (b - a) - a = b - 2a = 0$$

The optimal dimension of the inner sphere for a given outer sphere is

$$a = \frac{b}{2}$$

2.3.4 Spheroidal Coordinates

Spheroidal coordinates offer a versatile system, which can adapt to objects of different shapes and sizes.

2.3.4.1 Prolate Spheroidal Coordinates

In a prolate spheroidal coordinate system in Figure 2.9, η, θ, and ψ, the equipotential surfaces for constant η are prolate spheroids, for constant θ are hyperbolas, and for constant ψ are half-plane surfaces passing by the *z*-axis at an angle of ψ (Figure 2.9), with a the focal distance on the *z*-axis of the coordinates system. The parameters *b* and *c*, characteristic of the prolate spheroids of constant η, are given by

$$b = a \sinh \eta \quad \text{and} \quad c = a \cosh \eta.$$

The Laplace equation is

$$\nabla^2 u = \frac{1}{a^2 (\sinh^2 \eta - \sin^2 \theta)} \left[\frac{\partial^2 u}{\partial \eta^2} + \coth \eta \frac{\partial u}{\partial \eta} + \frac{\partial^2 u}{\partial \theta^2} + \cot \theta \frac{\partial u}{\partial \theta} + \frac{1}{a^2 \sinh^2 \eta \sin^2 \theta} \frac{\partial^2 u}{\partial \psi^2} \right] = 0$$

By the method of separation of variables, the potential function *u* is

$$u(\eta, \psi, \theta) = H(\eta)\, \Psi(\psi)\, \Theta(\theta)$$

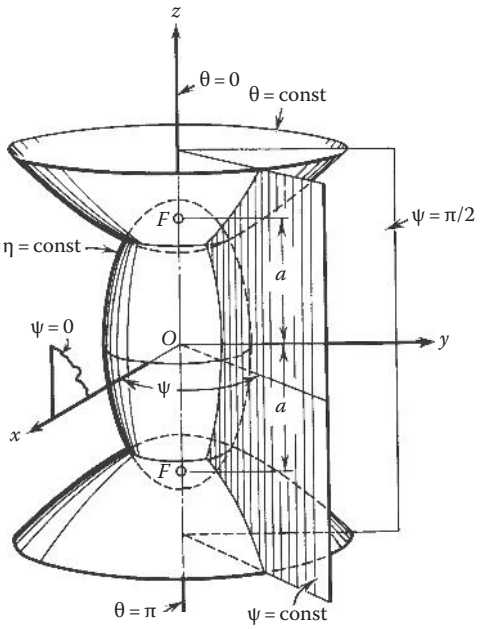


FIGURE 2.9 Prolate spheroidal coordinate system. (From Moon, P. and Spencer, D.E., *Field Theory for Engineers*, D. Van Nostrand, Princeton, NJ, 1961.)

The Laplace equation is decomposed in three differential equations of single variables as follows:

$$\frac{d^2H}{dh^2} + \coth h \frac{dH}{dh} - \left(p(p+1) + \frac{q^2}{\sinh^2 h}\right) H = 0$$

$$\frac{d^2Q}{dq^2} + \cot q \frac{dQ}{dh} - \left(p(p+1) + \frac{q^2}{\sin^2 q}\right) Q = 0$$

$$\frac{d^2Y}{dY^2} + q^2 Y = 0$$

The general solution of the last differential equation is of the sinusoidal type, while the first two differential equations are solved by changing the variable substituting

$$x = \cosh h \quad \text{and} \quad m = \cos q$$

One obtains the following differential equations in ξ and μ:

$$(x^2 - 1)\frac{d^2H}{dx^2} + 2x\frac{dH}{dx} - \left(p(p+1) + \frac{q^2}{x^2 - 1}\right) H = 0$$

$$(m^2 - 1)\frac{d^2Q}{dq^2} + 2q\frac{dQ}{dq} - \left(p(p+1) + \frac{q^2}{m^2 - 1}\right) Q = 0$$

These equations are of the Legendre type, for which the particular solutions are

$$H = P_p^q(\cosh h) \quad \text{and} \quad H = Q_p^q(\cosh h)$$

$$Q = P_p^q(\cos q) \quad \text{and} \quad Q = Q_p^q(\cos q)$$

where $P_p^q(\cos q)$ and $Q_p^q(\cos q)$ are Legendre-associated functions (Moon and Spencer, 1960).

The elementary solutions of the Laplace equation in a spheroidal coordinate system are

$$u = P_p^q(\cosh h) \begin{Bmatrix} P_p^q(\cos q) \sin y \end{Bmatrix}$$

and

$$u = Q_p^q(\cosh h) \begin{Bmatrix} Q_p^q(\cos q) \cos y \end{Bmatrix}$$

Considerable simplifications will result when the boundary conditions contain symmetry and the potential function becomes a function of a single variable.

Field around a charged metal spheroid: When the equipotential surfaces correspond to surfaces of constant η and the potential u is a function of η only, $u = u(\eta)$, as in the case of an isolated metal spheroid at a potential U, the Laplace equation simplifies to

$$\frac{d^2u}{dh^2} + \coth h \frac{du}{dh} = 0, \tag{2.32}$$

The general solution for the preceding differential equation is

$$u = A \ln \left(\coth \frac{h}{2}\right) + B$$

The boundary conditions are at $\eta = \eta_0$, $u = U$, and at $\eta \to \infty$, $u = 0$. The constants A and B are

$$A = \frac{U}{\ln\left[\coth\left(\frac{\eta_0}{2}\right)\right]}$$

and

$$B = 0$$

one gets

$$u = \frac{U}{\ln[\coth(\eta_0/2)]} \ln\left[\coth\left(\frac{\eta}{2}\right)\right] \tag{2.33}$$

The electric field is

$$\mathbf{E} = \frac{U\sqrt{\sinh^2\eta + \sin^2\theta}}{a\ \ln[\coth(\eta/2)]\sinh\eta}\mathbf{a}_\eta \tag{2.34}$$

where $\mathbf{a}_\eta$ is the unit vector perpendicular to the surfaces of constant η.

The field is maximal at the point defined by $\eta = \eta_0$ and $\theta = 0$ and equals to

$$E_{max} = \frac{U}{a\ \sinh^2\eta_0 \ln[\coth(\eta_0/2)]} \tag{2.35}$$

The equipotential surfaces around a charged metal prolate spheroid are shown in Figure 2.10.

The variations of the maximum field at the surface of the spheroid, normalized to the nominal field $E_n = U/a$, are presented in Figure 2.11. When $\eta_0 \to \infty$, the spheroid approaches a sphere, $\coth\eta_0 \to 1$, and E_{max} approaches the nominal field U/a. For slender spheroids, $b/a \to 0$, the field approaches infinity.

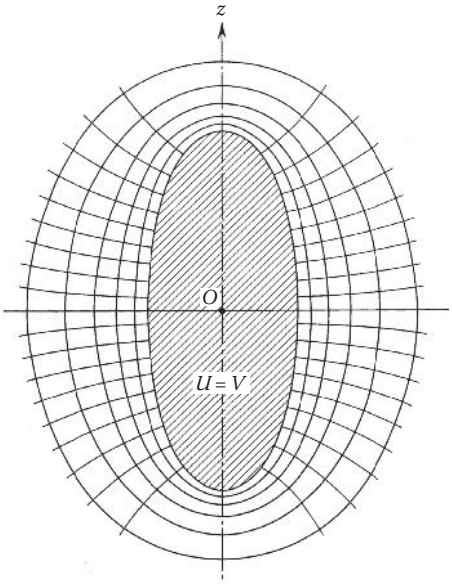


FIGURE 2.10 Potential and field around an isolated metal spheroid at a potential *V*. (From Moon, P. and Spencer, D.E., *Field Theory for Engineers*, D. Van Nostrand, Princeton, NJ, 1961.)

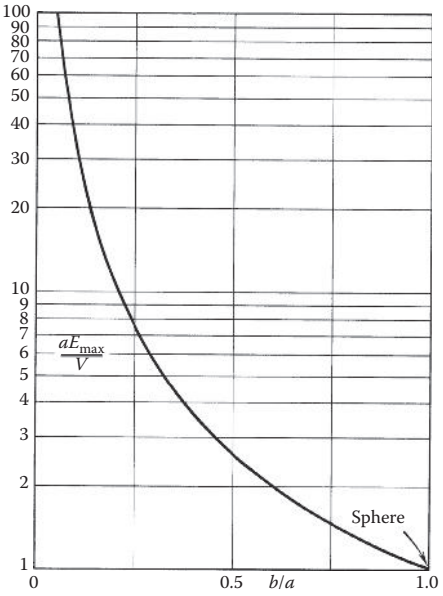


FIGURE 2.11 Variations of the maximum field near a charged spheroid, normalized to the average field $E_{av} = U/a$, as a function of the ratio b/a of the spheroid dimensions. (From Moon, P. and Spencer, D.E., *Field Theory for Engineers*, D. Van Nostrand, Princeton, NJ, 1961.)

Dielectric spheroid in a uniform field: When the potential is a function of η and θ, $u = u(\eta, \theta)$, as in the case of a dielectric spheroid immersed in a uniform field E_0 in air, let u_1 and u_2 be the potentials in the dielectrics of permittivity ε_1 and ε_2, respectively, outside and inside the spheroid. The boundary conditions are

$$\eta \to \infty, \quad u_1 = E_0\, z + A = aE_0 \cosh\eta \cos\theta + A$$

$$\eta = \eta_0, \quad u_1 = u_2 \quad \text{and} \quad \varepsilon_1 E_{\eta 1} = \varepsilon_2 E_{\eta 2}$$

where the constant A represents the potential at $z = 0$ and $\theta = \pi/2$. Because of the axial symmetry, the particular solutions of Laplace equation are

$$u = P_n(\cosh\eta)\, P_n(\cos\theta)$$

and

$$u = Q_n(\cosh\eta)\, Q_n(\cos\theta)$$

where P_n and Q_n are Legendre functions.

As the expression of the potential inside the spheroid contains at the same time $Q_n(\cos\theta)$ and $Q_n(\cosh\eta)$, which become infinite on the z-axis, when $\theta = 0$ and $\eta = 0$, respectively, the function u_2 cannot contain the terms $Q_n(\cos\theta)$ and $Q_n(\cosh\eta)$. As a result

$$u_2 = \sum_{0}^{\infty} A_n P_n(\cosh\eta)\, P_n(\cos\theta)$$

For the same reason, the terms $Q_n(\cos\theta)$ become infinite on the z-axis when $\theta = 0$, are eliminated from the expression of the potential function u_1 outside the spheroid, and

$$u_1 = \sum_{0}^{\infty} \left[B_n P_n(\cosh\eta) + C_n Q_n(\cosh\eta) \right] P_n(\cos\theta)$$

Applying the boundary conditions, one gets the following expressions for the potential functions:

$$u_1 = A + aE_0\left[\cosh\eta + \frac{(\varepsilon_2/\varepsilon_1)-1}{B}\cosh\eta_0 \sinh\eta_0\ Q_1(\cosh\eta)\right]\cos\theta$$

and

$$u_2 = A + \frac{aE_0}{B}\left[Q_1(\cosh\eta_0)\cosh\eta_0 - \sinh\eta_0\ Q_1(\cosh\eta_0)\right]\cosh\eta\cos\theta$$

where A and B are constants, with A equal to the potential at $\theta = \pi/2$ and

$$B = Q_1(\cosh\eta_0)\cosh\eta_0 - \frac{\varepsilon_2}{\varepsilon_1}\sinh\eta_0\ Q_1(\cosh\eta_0) = \text{constant}$$

By noting that $a\cosh\eta\cos\theta = z$, the electric potential inside the spheroid is

$$u_2 = A + \frac{E_0}{B}\left[Q_1(\cosh\eta_0)\cosh\eta_0 - \sinh\eta_0\ Q_1(\cosh\eta_0)\right]z \tag{2.36}$$

This expression (Equation 2.36) shows that *the field inside the spheroid is uniform for all values of* η_0, as illustrated in Figure 2.12, which shows the field and potential distribution around a spheroidal dielectric, with $\varepsilon_2/\varepsilon_1 = 10$ immersed in a uniform field E_0. The field within the dielectric is constant and equal to

$$E_2 = -\frac{du_2}{dz} = -\frac{E_0}{B}\left[Q_1(\cosh\eta_0)\cosh\eta_0 - \sinh\eta_0\ Q_1(\cosh\eta_0)\right] \tag{2.37}$$

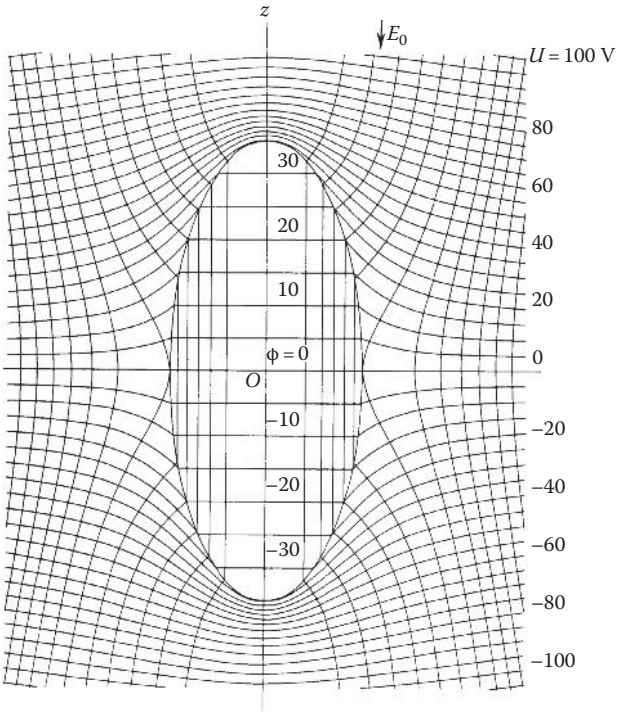


FIGURE 2.12 Distribution of the potential and field around a dielectric spheroid of high permittivity, $\varepsilon_2/\varepsilon_1 = 10$, in a uniform field. (From Moon, P. and Spencer, D.E., *Field Theory for Engineers*, D. Van Nostrand, Princeton, NJ, 1961.)

For the region outside of the spheroid, the electric field is given by

$$\mathbf{E}_1 = -\frac{1}{a\sqrt{\sinh^2 \eta + \sin^2 \theta}} \left(\frac{\partial u_1}{\partial \eta} \mathbf{a}_\eta + \frac{\partial u_1}{\partial \theta} \mathbf{a}_\theta \right)$$

where $\mathbf{a}_\eta$ and $\mathbf{a}_\theta$ are unit vectors perpendicular to the surfaces of constant η and θ, respectively.

With

$$\frac{\partial u_1}{\partial \eta} = aE_0 \left(\sinh \eta + \frac{1}{B} \left(\frac{\varepsilon_2}{\varepsilon_1} - 1 \right) \cosh \eta_0 \sinh \eta_0 Q_1'(\cosh \eta) \right) \cos \theta$$

and

$$\frac{\partial u_1}{\partial \theta} = -aE_0 \left(\cosh \eta + \frac{1}{B} \left(\frac{\varepsilon_2}{\varepsilon_1} - 1 \right) \cosh \eta_0 \sinh \eta_0 Q_1'(\cosh \eta) \right) \sin \theta$$

two particular cases will be discussed in the following.

Spheroid of high permittivity in air: When $\varepsilon_2/\varepsilon_1 \to \infty$, which corresponds to the case of a waterdrop in air and in a uniform electric field, $B \approx -(\varepsilon_2/\varepsilon_1) Q_1(\cosh \eta_0) \sinh \eta_0$, the term $\frac{1}{B}\left((\varepsilon_2/\varepsilon_1) - 1 \right) \sinh \eta_0$ approaches $1/Q_1(\cosh \eta_0)$ and the electric field in air is

$$\mathbf{E}_1 = \frac{E_0}{\sqrt{\sinh^2 \eta + \sin^2 \theta}} \left(\left(\sinh \eta - \frac{\cosh \eta_0}{Q_1(\cosh \eta_0)} Q_1'(\cosh \eta) \right) \cos \theta \mathbf{a}_\eta \right.$$

$$\left. + \left(\cosh \eta - \frac{\cosh \eta_0}{Q_1(\cosh \eta_0)} Q_1(\cosh \eta) \right) \sin \theta \mathbf{a}_\theta \right) \tag{2.38}$$

where $\mathbf{a}_\eta$ and $\mathbf{a}_\theta$ are unit vectors perpendicular to the surfaces of constant η and θ, respectively. The variation of the field and potential around the spheroid is as shown in Figure 2.13. The field is maximum when θ = 0, and $\eta \to \infty$:

$$E_{\max} = E_0 \left(1 - \frac{Q_1'(\cosh \eta_0)}{Q_1(\cosh \eta_0)} \coth \eta_0 \right) \tag{2.39}$$

Figure 2.14 shows the variation of the maximum field at a metal spheroid immersed into a uniform field E_0, with the ratio *b*/*a*, of the spheroid. For large values of η_0, for which the spheroid becomes practically spherical,

$$Q_0(\mu) = \frac{1}{2} \ln \frac{\mu + 1}{\mu - 1} \approx \frac{1}{\mu} + \frac{1}{3\mu^3},$$

with $\mu = \cosh \eta_0$

$$Q_1(\mu) \approx \frac{1}{3\mu^2}$$

and

$$Q_1'(\mu) = -\frac{2}{3\mu^3} \frac{d\mu}{d\eta},$$

or

$$\frac{Q_1'(\cosh \eta_0)}{Q_1(\cosh \eta_0)} \approx -2,$$

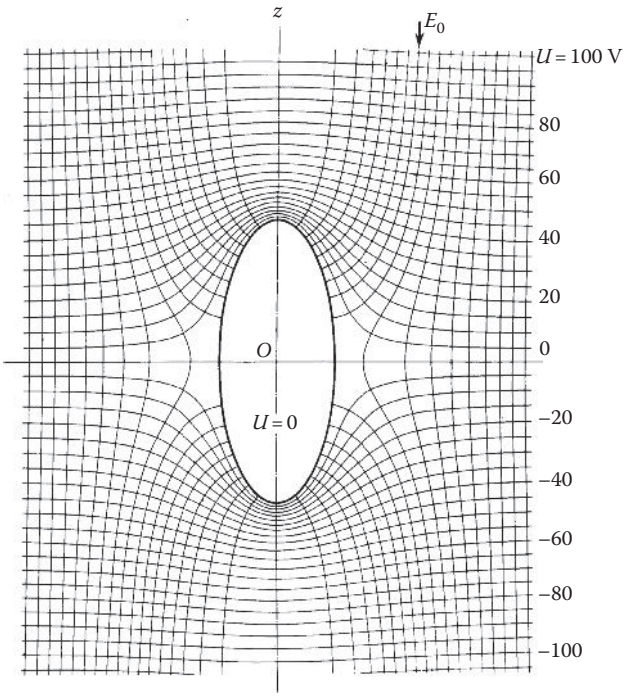


FIGURE 2.13 Field distribution when a spheroid of high permittivity, $\varepsilon_1/\varepsilon_2 \to \infty$, or a metal spheroid, is introduced into a uniform electrostatic field. (From Moon, P. and Spencer, D.E., *Field Theory for Engineers*, D. Van Nostrand, Princeton, NJ, 1961.)

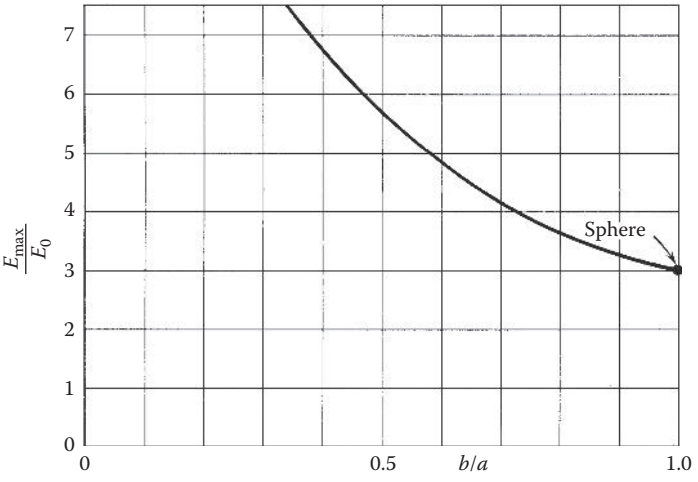


FIGURE 2.14 Maximum normalized field intensity at a metal spheroid introduced into a uniform electric field, E_0. (From Moon, P. and Spencer, D.E., *Field Theory for Engineers*, D. Van Nostrand, Princeton, NJ, 1961.)

and for a sphere

$$E_{\max} = 3E_0$$

Cavity of low permittivity in a dielectric: When $\varepsilon_2/\varepsilon_1 \to 0$, which corresponds to the case where $B \cong Q_1(\cosh\eta_0)\cosh\eta_0$, the field in the dielectric is

$$\mathbf{E}_1 = \frac{E_0}{\sqrt{\sinh^2\eta + \sin^2\theta}}\left[\left(\cosh\eta - \frac{\sinh\eta_0}{Q_1(\cosh\eta_0)}Q_1(\cosh\eta)\right)\cos\theta\,\mathbf{a}_\eta\right.$$

$$\left. + \left(\cosh\eta - \frac{\sinh\eta_0}{Q_1(\cosh\eta_0)}Q_1(\cosh\eta)\right)\sin\theta\,\mathbf{a}_\theta\right] \tag{2.40}$$

where $\mathbf{a}_\eta$ and $\mathbf{a}_\theta$ are unit vectors perpendicular to the surfaces of constant η and θ, respectively.

The field is maximum at $\theta = \pi/2$, and $\eta = \eta_0$

$$E_{\max} = E_0\left[1 - \frac{Q_1(\cosh\eta_0)}{Q_1'(\cosh\eta_0)}\tanh\eta_0\right] \tag{2.41}$$

For large values of η_0, the cavity becomes spherical and the maximum field is equal to

$$E_{\max} = \frac{3}{2}E_0$$

2.3.4.2 Hyperboloidal Field

When the equipotential surfaces correspond to the surfaces of constant θ and the potential is a function of θ only, $u = u(\theta)$, the Laplace equation simplifies to

$$\frac{d^2u}{d\theta^2} + \cot\theta\frac{du}{d\theta} = 0 \tag{2.42}$$

The general expression of the potential is

$$u = A\ln\left[\cot\left(\frac{\theta}{2}\right)\right] + B$$

Applying the boundary conditions,
at $\theta = \pi/2$

$$u = 0 \quad \text{or} \quad u = A\ln\left[\cot\left(\frac{\pi}{4}\right)\right] + B = B = 0$$

at $\theta = \theta_0$

$$u = 1 \quad \text{or} \quad u = A\ln\left[\cot(\theta_0)\right] = 1$$

or

$$A = \frac{1}{\ln\left[\cot(\theta_0)\right]}$$

the potential function ϕ becomes

$$u = \frac{1}{\ln\left[\cot(\theta_0)\right]}\ln[\cot(\theta)] \tag{2.43}$$

The general expression of the electric field in the gap is

$$\mathbf{E}(\theta) = \frac{U}{a}\frac{1}{\sqrt{\sinh^2\eta + \sin^2\theta}}\frac{1}{\ln\left[\cot\frac{\theta_0}{2}\right]}\frac{1}{\sin\theta}\mathbf{a}_\theta \tag{2.44}$$

where

a is the distance of the focus F to the ground plane

$\mathbf{a}_\theta$ is the unit vector perpendicular to the surfaces of constant θ

The field is maximal at the tip of the rod electrode, that is, at $\eta = 0$ and $\theta = \theta_0$, and is equal to

$$E_{max} = \frac{U}{a}\frac{1}{\sin^2\theta_0}\frac{1}{\ln\left[\cot(\theta_0/2)\right]} \tag{2.45}$$

Field in a rod-plane gap: The profile of the tip of a rod in a rod-plane gap can be approximated by a hyperboloid surface, corresponding to the particular case where θ is constant. With the expression of the maximum field as a function of the distance r of the tip from the focus of the hyperbola representing the rod electrode and the interelectrode distance d, according to

$$d = a - r = a\cos\theta_0$$

or

$$r = a(1 - \cos\theta_0)$$

that is

$$\cos\theta_0 = 1 - \frac{r}{a}$$

it follows the expressions

$$\sin^2(\theta_0) = \frac{2r}{a} - \left(\frac{r}{a}\right)^2, \quad \text{and} \quad \cot\frac{\theta_0}{2} = \sqrt{\frac{2a}{r} - 1}$$

Replacing these expressions in Equation 2.45, one obtains the expression of the maximum field, valid for the case where the distance r is much smaller than the interelectrode distance d:

$$E_{max} = \frac{U}{a}\frac{1}{\frac{2r}{a}\left(1 - \frac{r}{2a}\right)}\frac{1}{\ln\left[\sqrt{\frac{2a}{r} - 1}\right]} \approx \frac{U}{2r}\frac{1}{\frac{1}{2}\ln\left[\frac{2a}{r}\right]} \tag{2.46}$$

Since $d = a - r \cong a$ and $r = r_c/2$, where r_c is the radius of curvature of the rod electrode, one finds the familiar expression of the maximum field at the rod electrode:

$$E_{max} = \frac{2}{r_c\ln(4d/r_c)}U \tag{2.47}$$

2.3.4.3 Oblate Spheroidal Metal Protrusion in a Uniform Field

A protrusion can be represented by a surface of constant η. In oblate spheroidal coordinates system as illustrated in Figure 2.15: η, θ and Ψ, the equipotential surfaces for constant Ψ are half plane surfaces

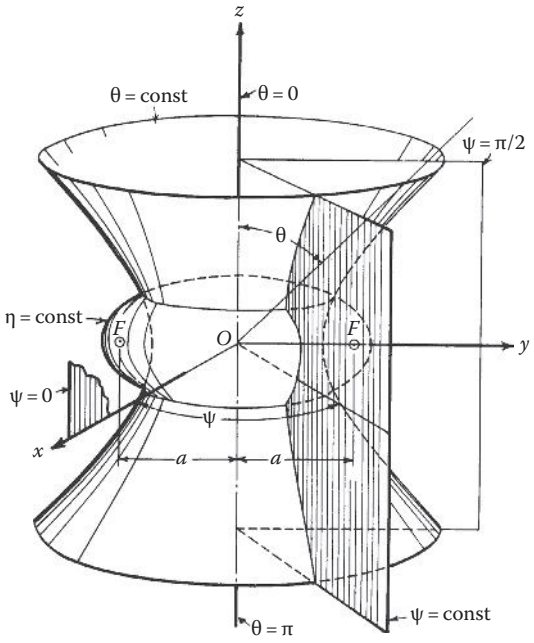


FIGURE 2.15 Oblate spheroidal coordinate system. (From Moon, P. and Spencer, D.E., *Field Theory for Engineers*, D. Van Nostrand, Princeton, NJ, 1961.)

passing by the z-axis at an angle of Ψ; for constant η are oblate spheroids and for constant θ are hyperbolas, with a the focal distance along the y-axis of the coordinates system. The parameters b and c of the oblate spheroids of constant η are given by

$$b = a\cosh\eta \quad \text{and} \quad c = a\sinh\eta.$$

The Laplace equation is

$$\nabla^2 u = \frac{1}{a^2(\cosh^2\eta - \sin^2\theta)}\left[\frac{\partial^2 u}{\partial\eta^2} + \tanh\eta\frac{\partial u}{\partial\eta} + \frac{\partial^2 u}{\partial\theta^2} + \cot\theta\frac{\partial u}{\partial\theta}\right] + \frac{1}{a^2\cosh^2\eta\sin^2\theta}\frac{\partial^2 u}{\partial\psi^2} = 0$$

The electric field without the protrusion is E_0. The boundary conditions are

$$\theta = \frac{\pi}{2}, \quad u = 0$$

$$\eta = \eta_0 \quad \text{and} \quad 0 \le \theta \le \frac{\pi}{2}, \quad u = 0$$

$$\eta \to \infty, \quad u = E_0 z = aE_0\sinh\eta\cos\theta$$

The potential is a function of η and θ. The general solutions of Laplace equation are

$$u = P_m(i\sinh\eta)\,Q_m(\cos\theta)$$

$$u = Q_m(i\sinh\eta)\,Q_m(\cos\theta)$$

as $Q_m(\cos\theta)$ becomes infinite on the z-axis and, consequently, cannot be used. Applying the boundary conditions, one obtains the following expression for the potential function:

$$u = aE_0\sinh\eta\cos\theta\left[1 - \frac{\sinh\eta_0\; Q_1(i\sinh\eta)}{\sinh\eta\; Q_1(i\sinh\eta_0)}\right].$$

By noting that $Q_1(i\sinh\eta) = i\sinh\eta \cdot Q_0(i\sinh\eta) - 1 = \sinh\eta \cdot \cot^{-1}(\sinh\eta) - 1$, the expression of the potential ϕ becomes

$$u = E_0 z\left[1 - \frac{\sinh\eta_0}{\sinh\eta}\left(\frac{\sinh\eta\ \cot^{-1}(\sinh\eta) - 1}{\sinh\eta_0\ \cot^{-1}(\sinh\eta_0) - 1}\right)\right] \tag{2.48}$$

The electric field is given by

$$\mathbf{E} = -\frac{1}{a\sqrt{\cosh^2\eta + \sin^2\theta}}\left(\frac{\partial u}{\partial\eta}\mathbf{a}_\eta + \frac{\partial u}{\partial\theta}\mathbf{a}_\theta\right), \tag{2.49}$$

where $\mathbf{a}_\eta$ and $\mathbf{a}_\theta$ are unit vectors perpendicular to the surfaces of constant η and θ, respectively.

With

$$\frac{\partial u}{\partial\eta} = aE_0\cos\theta\left[\cosh\eta\left(1 - \frac{\sinh\eta_0\ Q_1(i\sinh\eta)}{\sinh\eta\ Q_1(i\sinh\eta_0)}\right)\right.$$

$$\left. - \frac{\sinh\eta_0}{Q_1(i\sinh\eta_0)}\left(Q_1'(i\sinh\eta) - Q_1(i\sinh\eta)\coth\eta\right)\right],$$

$$\frac{\partial u}{\partial\theta} = -aE_0\sinh\eta\ \sin\theta\left(1 - \frac{\sinh\eta_0\ Q_1(i\sinh\eta)}{\sinh\eta\ Q_1(i\sinh\eta_0)}\right)$$

Figure 2.16 shows the distribution of the potential and field around a metal oblate spheroid protuberance in a uniform field. The field is maximum at the top of the protrusion, where $\eta = \eta_0$, and $\theta = 0$:

$$E_{\max} = -\frac{1}{a\cosh\eta_0}\left(\frac{\partial u}{\partial\eta}\right) = -E_0\left(1 - \frac{Q_1'(\sinh\eta_0)}{Q_1(\sinh\eta_0)}\tanh\eta_0\right) \text{ that one can rewrite as}$$

$$E_{\max} = E_0\left(1 + \frac{\sinh\eta_0\cot^{-1}(\sinh\eta_0) - \tanh^2\eta_0}{1 - \sinh\eta_0\cot^{-1}(\sinh\eta_0)}\right) \tag{2.50}$$

One can see that when $\eta_0 = 0$, one obtains the case of a uniform field, $E_{\max} = E_0$. When η_0 tends to infinity, the protrusion becomes hemispherical, and $E_{\max} = 3E_0$.

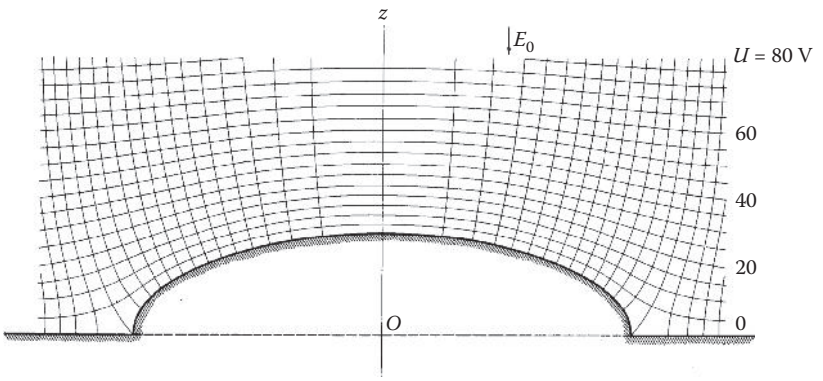


FIGURE 2.16 Distribution of potential and field around a metal oblate spheroid protrusion. (From Moon, P. and Spencer, D.E., *Field Theory for Engineers*, D. Van Nostrand, Princeton, NJ, 1961.)

2.4 Methods of Transformation

The preceding examples of analytical solution of Laplace equation show the latter changes with the coordinate system; as a result, it is of prime importance to properly select the coordinate system used, usually by making the electrode surfaces coincide with the natural equipotential surfaces in the coordinate system. This allows the reduction of the number of independent variables in the set of Maxwell differential equations to be solved. The readers may find in Moon and Spencer (1960) the necessary information on the transfer from one coordinate system to another. Nevertheless, the Maxwell differential equations become rapidly complex with the coordinate system selected to represent practical applications. Transformation methods are sometimes useful to simplify the problem investigated.

2.4.1 Method of Images

2.4.1.1 Images with Respect to a Ground Plane

Consider a set of conductors A_i subjected to potentials U_i, in space above a perfectly conducting plane of infinite dimensions (Figure 2.17). Since the potential function does not have an absolute reference, one can define the potential at the conducting plane as the reference level: $U_p = 0$. If one is interested only in the potential and field in the space above the conducting plane, the configuration of conductor plane can be replaced by two sets of conductors A_i and their images A_{mi} with respect to the conducting plane. The images A_{mi} are located symmetrically with respect to the plane and are subjected to opposite potentials $-U_i$. One can see that the potential U_p at any point P on the conducting plane is

$$U_p = \sum \left[U_i f(r_i) - U_i f(r_{mi}) \right] = 0$$

since, at any point P of the conducting plane,

$$f(r_i) = f(r_{mi})$$

where r_i and r_{mi} are the distances from the point P to the conductor A_i and its image A_{mi}.

Magnetic ground: If for the electric fields the generally conducting ground can be considered as an equipotential surface at potential zero, it remains permeable to the magnetic field produced by a current source in space. Consequently, to calculate the magnetic field produced by the current circulating in a conductor above ground, the application of the method of images must refer to the *magnetic ground* located at a depth δ_p, commonly known as the *depth of penetration of the magnetic field* and is given by

$$\delta_p = \sqrt{\frac{\rho}{\mu p f}} \tag{2.51}$$

where

ρ (Ω m) is the resistivity of the ground
$\mu = 4\pi\ 10^{-7}$ H/m, the permeability
f is in Hz, the frequency of the current

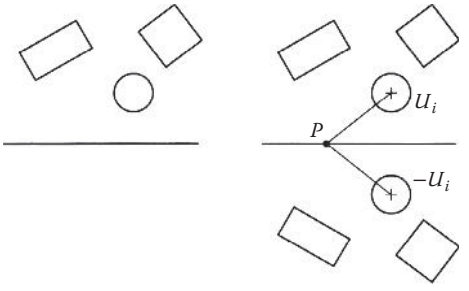


FIGURE 2.17 Method of images.

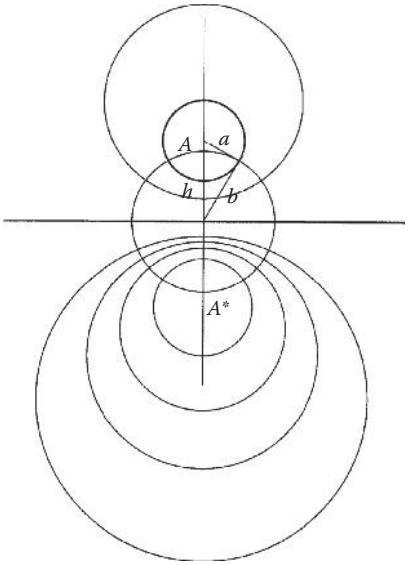


FIGURE 2.18 Bicylindrical coordinate system.

For a typical soil of resistivity 100 Ω m, the depth of penetration is about 5 m at a frequency of 1 MHz and 650 m at the frequency of 60 Hz.

Field around a cylindrical conductor above ground: A practical case corresponds to that of a conductor above ground, subjected to a potential *U*. Applying the method of images with respect to the ground plane, the conductor-plane system is transformed into a system of two conductors located symmetrically with respect to the ground plane and subjected to opposite potentials of *U* and −*U*, respectively. This conductor system can be adapted to a bicylindrical coordinate system, such that the conductor and its image coincide with two of the cylindrical equipotential surfaces and the ground plane with the plane surface, as illustrated in Figure 2.18.

One notes that the two poles *A* and *A** of the coordinate system are located on the axis passing by the centers of the conductor and its image, perpendicular to and at a distance of *b* and −*b* with respect to the ground plane. In such a coordinate system, a set of two line charges, λ and −λ, located at the poles *A* and *A**, will generate equipotential surfaces such that two of which coincide with the surfaces of the conductor and its image. In other words, one can replace the conductor and its image by two line charges located at the poles of the coordinate system, of which the linear charge density ±λ is to be determined to meet the boundary conditions, defined by the potential *U* at the conductor. The potential and the electric field at a point $P(x, y)$ can be evaluated as a function of the linear charges densities λ and −λ as

$$u_p = u_1 + u_2 = \frac{1}{2\pi\varepsilon_0}\left[\ln(r_2) - \ln(r_1)\right] = \frac{1}{2\pi\varepsilon_0}\ln\frac{r_2}{r_1}$$

The components of the electric field at the point *P* are

$$E_{px} = E_{x1} + E_{x2} = E_1\cos\alpha_1 + E_2\cos\alpha_2$$

$$E_{py} = E_{y1} + E_{y2} = E_1\sin\alpha_1 + E_2\sin\alpha_2$$

with

$$E_1 = -\frac{1}{2\pi\varepsilon_0}\frac{1}{r_1}, \quad r_1 = \sqrt{x^2 + (y-b)^2}, \quad \sin\alpha_1 = \frac{y-b}{r_1}, \quad \text{and} \quad \cos\alpha_1 = \frac{x}{r_1}$$

$$E_2 = -\frac{\lambda}{2\pi\varepsilon_0}\frac{1}{r_2}, \quad r_2 = \sqrt{x^2 + (y+b)^2}, \quad \sin\alpha_2 = \frac{y+b}{r_2}, \quad \text{and} \quad \cos\alpha_2 = \frac{x}{r_2}$$

Determination of the linear charge density λ: Consider the two lines of force forming the circle of diameter *AA** (Figure 2.18). Since these lines must be orthogonal to the equipotential surfaces, the circle *AA** is orthogonal to the circles representing the surfaces of the conductors. The position of the poles, *A* and *A**, of the bicylindrical coordinate system is defined as

$$b = \sqrt{h^2 - a^2}$$

For a point *P* located on the surface of the conductor, the potential is known and equal to *U*. By choosing the point *P* on the axis of the conductor centers, one gets

$$x_p = 0 \quad \text{and} \quad y_p = h - a$$

It follows the expression for the potential u_p:

$$u_p = \frac{\lambda}{2\pi\varepsilon_0}\ln\frac{r_2}{r_1} = U$$

or

$$\frac{\lambda}{2\pi\varepsilon_0}\ln\left(h - a + \sqrt{h^2 - a^2}\right) - \ln\left(h - a - \sqrt{h^2 - a^2}\right) = U, \tag{2.52}$$

hence

$$\lambda = \frac{2\pi\varepsilon_0}{\ln\left(h - a + \sqrt{h^2 - a^2}\right) - \ln\left(h - a - \sqrt{h^2 - a^2}\right)}\,U \tag{2.53}$$

For the case where *h* is much larger than *a* as in overhead transmission lines, the preceding expression of the linear charge λ simplifies to

$$\lambda = \frac{2\pi\varepsilon_0}{\ln(2h/a)}\,U = 2\pi a\varepsilon_0 E_0 = CU \tag{2.54}$$

One gets the expressions for the field E_0 at the conductor surface and the capacitance *C* as follows:

$$E_0 = \frac{1}{a\ln(2h/a)}\,U \text{ kV/m} \quad \text{and} \quad C = \frac{2\pi\varepsilon_0}{\ln(2h/a)} \text{ F/m} \tag{2.55}$$

2.4.1.2 Image with Respect to a Cylindrical Conductor

Consider a line charge located in parallel with and at a distance $OA = d$ from the center of a cylindrical conductor of radius *a*, shown in Figure 2.19. One can select a bicylindrical coordinate system such that the line charge passes by one of the two poles, *A*, and the cylindrical conductor coincides with an equipotential surface. Let λ be the linear charge density. One can see that the equipotential condition at the conductor will be met by a set of two line charges of opposite densities and located at the poles of the bicylindrical coordinate system: *A* and *A**. Referring to Figure 2.19, the distance $OA^* = x$ of the conductor center to the image pole is

$$OA \cdot OA^* = d \cdot x = a^2 \quad \text{or} \quad x = \frac{a^2}{d} \tag{2.56}$$

The potential at the conductor is related to the linear charge density according to

$$U = \frac{\lambda}{2\pi\varepsilon_0}\ln\frac{r_1}{r_2} = \frac{\lambda}{2\pi\varepsilon_0}\ln\frac{d-a}{a-x} = \frac{\lambda}{2\pi\varepsilon_0}\ln\frac{d-a}{a-(a^2/d)} = \frac{\lambda}{2\pi\varepsilon_0}\ln\frac{d}{a} \tag{2.57}$$

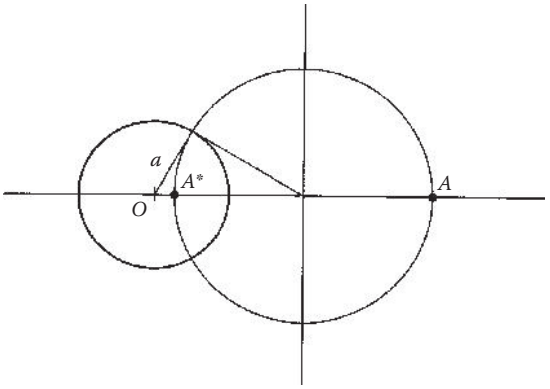


FIGURE 2.19 Definition of the position of the image A^* of a line charge A with respect to the conductor, center O and radius a.

which allows the evaluation of λ as

$$\lambda = 2\pi\varepsilon_0 \frac{U}{\ln(d/a)} \tag{2.58}$$

Inversion—properties of image with respect to a conductor: Noting that Equation 2.56 is the definition of the inversion transformation, the line charge and its image are therefore transformed into each other in an inversion of center O, the center of the conductor, and power of inversion: a^2. A few particular properties are readily derived from the inversion transformation as follows:

- The image of a line charge A of density λ located at infinite distance from a cylindrical conductor is a line charge A^* of density $-\lambda$ located at the center of the conductor.
- The image of a line charge of density λ, with respect to a conductor at ground potential, is a set of three line charges (Figure 2.19): λ is located at A, its image $-\lambda$ located at A^*, and a line charge λ_0 located at the center of the conductor. The charge density $\lambda_0 = \frac{\lambda}{2\pi\varepsilon_0} \ln\frac{a}{d}$ to compensate for the potential resulting from the two line charges λ and $-\lambda$ and thus bring the potential of the conductor to zero.
- The image of a conductor, which does not pass by the center of inversion, is another conductor. Its center is located on the straight line passing by the center of inversion and the center of the original conductor. However, the inversion does not preserve the dimension of the original conductor. The dimension of the transformed conductor can be determined from the images of the intercept points of the axis and the original conductor.

2.4.1.3 Sphere Gap

Another practical case corresponds to that of a sphere above ground, subjected to a potential U. Applying the method of images with respect to the ground plane, the sphere-plane system is transformed into an ensemble of two spheres, located symmetrically with respect to the ground plane, and subjected to opposite potentials of U and $-U$, respectively. Such a two-sphere configuration is currently used as a sphere gap (Figure 2.20), to measure the test voltage, or as a protective device against overvoltages in a test setup. It can be adapted to a bispherical coordinate system η, θ, and ψ illustrated in Figure 2.21 (Moon and Spencer, 1961), such that the surfaces of the spheres coincide with the spherical surfaces of constant η. The surfaces for constant θ are spheres and those for constant ψ are half plane. Because of the axial symmetry, the potential u is independent of ψ. The general solution is

$$u = \sqrt{\cosh\eta - \cos\theta}\ \sum A_n \frac{\sinh(n+1/2)\eta}{\sinh(n+1/2)\eta_0} P_n(\cos\theta)$$



FIGURE 2.20 Sphere gap at Hydro-Québec Institute of research (IREQ). (Photo courtesy from Hydro-Québec.)

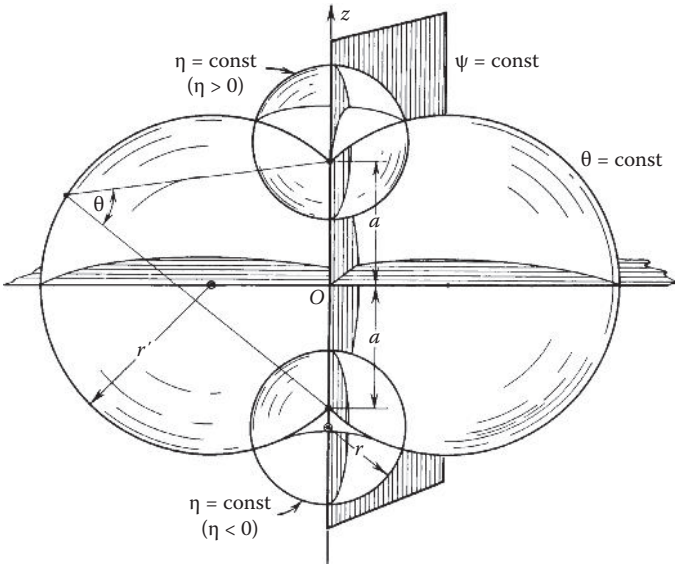


FIGURE 2.21 Bispherical coordinate system. (From Moon, P. and Spencer, D.E., *Field Theory for Engineers*, D. Van Nostrand, Princeton, NJ, 1961.)

The boundary conditions are at $\eta = \eta_0$, $u = U$, and at $\eta = -\eta_0$, $u = -U$, which gives

$$\frac{U}{\sqrt{\cosh \eta_0 - \cos \theta}} = \sum A_n P_n(\cos\theta)$$

The right side of the preceding equation is simply the series development in the Legendre function of the first order of the potential function, expressed by the left side of the equation. One obtains

$$A_n = \frac{2n+1}{2} U \int_{-1}^{1} \frac{P_n(\cos\theta)\,d\theta}{\sqrt{\cosh \eta_0 - \cos\theta}}, \quad n = 1, 2, \ldots \tag{2.59}$$

The first-order Legendre function can be expressed by a series development:

$$P_n(\cos\theta) = \frac{1}{b_n} \sum_{m=1}^{n} c_m (\cos\theta)^m, \text{ with } \quad n = 0, \quad P_0(\cos\theta) = 1$$

The polynomes $P_n(\cos\theta)$ are, on the other hand, related to one another by the following recurrency relation, which defines the coefficients of the Legendre polynomes in terms of $P_0(\cos\theta)$:

$$(n+1)P_{n+1}(\cos\theta) = (2n+1)\cos\theta\, P_n(\cos\theta) - nP_{n-1}(\cos\theta)$$

The electric field $\mathbf{E}(\eta, \theta)$ is given by

$$\mathbf{E} = -\text{grad}\,u = -\frac{1}{a}(\cosh\eta - \cos\theta)\left(\frac{\partial u}{\partial \eta}\mathbf{a}_\eta + \frac{\partial u}{\partial \theta}\mathbf{a}_\theta\right)$$

where $\mathbf{a}_\eta$ and $\mathbf{a}_\theta$ are unit vectors perpendicular to the surfaces of constant η and θ, respectively:

$$\frac{\partial u}{\partial \eta} = \frac{1}{\sqrt{\cosh\eta - \cos\theta}} \sum \frac{A_n}{\sinh\left(n + \frac{1}{2}\right)\eta_0} P_n(\cos\theta)$$

$$\left[\frac{1}{2}\sinh\eta \sinh\left(n + \frac{1}{2}\right)\eta \cdot \eta_0 + \left(n + \frac{1}{2}\right)(\cosh\eta - \cos\theta)\cosh\left(n + \frac{1}{2}\right)\eta \cdot \eta_0\right]$$

where

$$P_n'(\cos\theta) = \frac{d}{d\theta} P_n(\cos\theta) = -\sin\theta \frac{d}{d(\cos\theta)} P_n(\cos\theta)$$

$$\frac{\partial u}{\partial \theta} = \frac{1}{\sqrt{\cosh\eta - \cos\theta}} \sum \frac{A_n}{\sinh\left(n + \frac{1}{2}\right)\eta_0} \sinh\left(n + \frac{1}{2}\right)\eta \cdot$$

$$\left[\frac{1}{2}\sin\theta\, P_n(\cos\theta) + (\cosh\eta - \cos\theta)P_n'(\cos\theta)\right]$$

On the other hand, the coefficients A_n are defined by

$$A_n = \frac{2n+1}{2} U \int_{-1}^{1} \frac{P_n(\cos\theta)\,d\theta}{\sqrt{\cosh h_0 - \cos\theta}}, \quad n = 1, 2, \ldots$$

$$= \frac{2n+1}{2} U \left[\frac{1}{b_n}\right] \sum c_m \int_{-1}^{1} \frac{d\theta}{\sqrt{\cosh h0 - \cos\theta}} (\cos\theta)^m d(\cos\theta) = \frac{2n+1}{2\, b_n} U \sum c_m\, I_m$$

The integral I_m is, on the other hand, evaluated by the following recurrency relation:

$$\int_{-1}^{1} \frac{u^m}{\sqrt{\cosh h_0 - u}} du = \left. \frac{2u^m \sqrt{\cosh h_0 - u}}{(2m+1)(-1)^m} \right|_{-1}^{1} - \frac{2m \cosh h_0}{(2m+1)(-1)^{m-1}} \int_{-1}^{1} \frac{u^{m-1}}{\sqrt{\cosh h_0 - u}} du,$$

with $u = \cos\theta$

$$I_m = \frac{1}{(2m+1)(-1)^m} \left[\sqrt{\cosh h_0 - 1} - (-1)^m \sqrt{\cosh h_0 + 1}\right] - \frac{2m \cosh h_0}{(2m+1)(-1)^{m-1}} I_{m-1}$$

By noting that the polynomials $P_n(\cos\theta)$ and $P_n'(\cos\theta)$ contain terms with even or odd exponents of $\cos\theta$, one can express I_m in terms of I_{m-2}:

$$I_m = \frac{2}{4m^2 - 1} \left\{ \sqrt{\cosh h_0 - 1} - (-1)^m \left[(2m-1) - 2m \cosh h_0\right] \right.$$

$$\left. - \sqrt{\cosh h_0 + 1} \left[(2m-1) + 2m \cosh h_0\right] + 2m(m-1) \cosh^2 h_0 I_{m-2} \right\} \tag{2.60}$$

Figure 2.22 shows the variations of the electric field along the axis of the sphere gap, calculated from the series development in the Legendre function solution in a bispherical coordinate system. One can

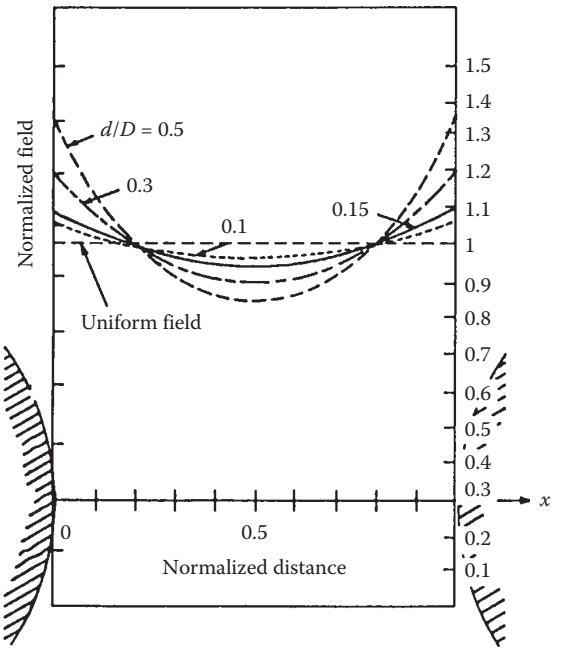


FIGURE 2.22 Distribution of the field in the interelectrode space of a sphere gap, normalized to the uniform field value. (Rizk et al., *CIGRE*, Report No. 13-203, Paris, 1990.)

see that the field distribution is in general not uniform, and the effect is more pronounced with a higher value of the ratio *d/D* of the gap distance by the sphere diameter. For proper operation of sphere gaps as a measuring or/and protection, the device should have a small ratio of *d/D* in order to have a reasonably uniform field distribution, thus minimizing the dispersion in the breakdown voltage.

2.5 Numerical Solution Laplace Equation

In spite of their exact solutions, the analytical solution and the methods of transformation are limited to relatively simple electrode configurations, where the Laplace equation is relatively simple. The development of computers capable of rapidly making a large number of calculations has opened new possibilities of solving the Laplace equation in cases where the analytical solution becomes difficult or impossible. The uniqueness of the solution of the Laplace equation allows an alternative approach to the analytical solution by simply approximating the boundary conditions as much as possible taking advantage of the numerical computation. The adequacy of the solution is assessed by the variation in the potential at the surface of the conductors, which should be an equipotential surface in the exact solution.

An effective approach consists of representing directly the distribution of the surface charge by a set of discrete charges, chosen for their simple representation and known analytical expressions of potential and field: point, line and ring charges, etc. These charges are located outside of the region of interest; their values will be determined to satisfy the specific boundary conditions defined by the known potentials at the electrodes. Generally, this approach leads to a set of n equations for the n unknown charges:

$$[P][1] = [u]$$

where

$[u]$ is a column matrix, $n \times 1$, of potentials of the conductors defining the boundary conditions
$[\lambda]$ a column matrix, $n \times 1$, of the discrete charges
$[P]$ an $n \times n$ matrix of potential coefficients defined as the potential P_i produced at the test point by a unit charge, $q_i = 1$, when all the other charges are null

The solution of the preceding system of n equations for the n unknown charges defines completely the set of discrete charges representing the distribution of the surface charge of the conductors. One can, subsequently, calculate the potential ϕ and the electric field $\mathbf{E}$ at any point P in space around the electrodes, using the values of the discrete charges λ_i newly determined, knowing their position in space. Before presenting a few examples of a numerical solution of the Laplace equation, a review of the analytical expressions of potentials and fields around simple elementary charges currently used in the successive images and the so-called charge simulation methods, presented in the following.

2.5.1 Field and Potential around Elementary Charges

Point charge: The expressions of potential and electric field around a point charge in an appropriate spherical coordinate system are

$$u(r) = \frac{Q}{4\pi\varepsilon} \frac{1}{r} \tag{2.61}$$

$$\mathbf{E} = \frac{Q}{4\pi\varepsilon} \frac{1}{r^2} \mathbf{a}_r \tag{2.62}$$

where

Q is the punctual charge
r is the radial distance of the point P to the charge
$\mathbf{a}_r$ is the radial unit vector

Linear charge element: Consider an element of linear charge located on the z-axis, limited by the ordinates z_a and z_b of its extremities, in a cylindrical coordinate system. Let λ (C/m) be the linear charge density; the potential and field at the point $P(r, z)$ are given by

$$u(r,z) = \frac{\lambda}{4\pi\varepsilon(z_b - z_a)} \ln \frac{(z_b - z + \rho_1)(z_a + z + \rho_2)}{(z_a - z + \delta_1)(z_b + z + \delta_2)} \tag{2.63}$$

$$\mathbf{E} = E_r(r,z)\mathbf{a}_r + E_z(r,z)\mathbf{a}_z \tag{2.64}$$

where $\mathbf{a}_r$ and $\mathbf{a}_z$ are unit vectors in the radial and z-axis, respectively, with

$$E_r(r,z) = \frac{\lambda}{4\pi\varepsilon(z_b - z_a)} \left[\frac{z_b - z}{r\rho_1} - \frac{z_a - z}{r\delta_1} + \frac{z_a + z}{r\rho_2} - \frac{z_b + z}{r\delta_2} \right] \tag{2.65}$$

$$E_z(r,z) = \frac{\lambda}{4\pi\varepsilon(z_b - z_a)} \left[\frac{1}{\rho_1} - \frac{1}{\delta_1} + \frac{1}{\rho_2} - \frac{1}{\delta_2} \right] \tag{2.66}$$

with

$$\rho_1 = \sqrt{r^2 + (z_b - z)^2} \quad \text{and} \quad \rho_2 = \sqrt{r^2 + (z_a + z)^2}$$

$$\delta_1 = \sqrt{r^2 + (z_a - z)^2} \quad \delta_2 = \sqrt{r^2 + (z_b + z)^2}$$

Infinite linear charge: The case of an infinite linear charge is obtained by making the ordinates z_a and z_b tend to infinity. The expressions of potential and electric field become

$$u = -\frac{\lambda}{2\pi\varepsilon} \ln r = \frac{\lambda}{2\pi\varepsilon} \ln \left[\frac{1}{r} \right] \tag{2.67}$$

$$\mathbf{E} = -\frac{du}{dr}\mathbf{a}_r = \frac{\lambda}{2\pi\varepsilon}\frac{1}{r}\mathbf{a}_r \tag{2.68}$$

where

λ is the linear charge density in C/m

$\mathbf{a}_r$ is the radial unit vector

Infinite linear charge above ground: By applying the method of images, one can show that the potential and electric field at a point P in space are

$$u = \frac{\lambda}{2\pi\varepsilon} \ln \left[\frac{r_m}{r} \right] \tag{2.69}$$

and

$$\mathbf{E} = \frac{\lambda}{2\pi\varepsilon} \left[\frac{1}{r} \right] \mathbf{a}_r + \frac{1}{r_m}\mathbf{a}_{rm} \tag{2.70}$$

where

r and r_m are the distances between the point P at the conductor and to its image with respect to the ground

$\mathbf{a}_r$ and $\mathbf{a}_{rm}$ are radial unit vectors with respect to the line charge and its image

Ring charge with uniform charge density: Consider ring charge of radius a located in a plane parallel to the r–θ plane and at a height of z_i, in a cylindrical coordinate system, having the z-axis coincide with that of the ring charge element. The charge density is given by

$$q_0 = \frac{Q_0}{2\pi a}, \text{ with } Q_0 \text{ being the total charge.}$$

The expressions of potential and electric field are

$$u_p = \frac{1}{2p^2e}\frac{Q_0}{a}F\left(\frac{p}{2}, k\right) \tag{2.71}$$

with

$$a = \sqrt{(r + r_j)^2 + (z - z_j)^2}$$

$$\mathbf{E} = E_r(r, z)\mathbf{a}_r + E_z(r, z)\mathbf{a}_z \tag{2.72}$$

where $\mathbf{a}_r$ and $\mathbf{a}_z$ are unit vectors in the radial and z-axis, respectively, with

$$E_r(r, z) = -\frac{1}{4p^2e}\frac{1}{ab^2}\frac{1}{r}Q_0\left[(z^2 + a^2 - r^2)E\left(\frac{p}{2}, k\right) - b^2F\left(\frac{p}{2}, k\right)\right] \tag{2.73}$$

with

$$b = \sqrt{(r - r_j)^2 + (z - z_j)^2}$$

$$E_z(r, z) = \frac{2}{4p^2e}\frac{1}{a\,b^2}Q_0\,E\left(\frac{p}{2}, k\right) \tag{2.74}$$

where E and F are the elliptic functions of first and second order. Figure 2.23 shows the variations of potential and electric field in the x–z plane, around a ring charge of uniform charge density, located in the x–y plane.

2.5.2 Method of Successive Images

The method of images discussed previously can reproduce the equipotential surfaces for a configuration of two parallel cylindrical conductors. It cannot be extended to a set of more than two parallel cylindrical

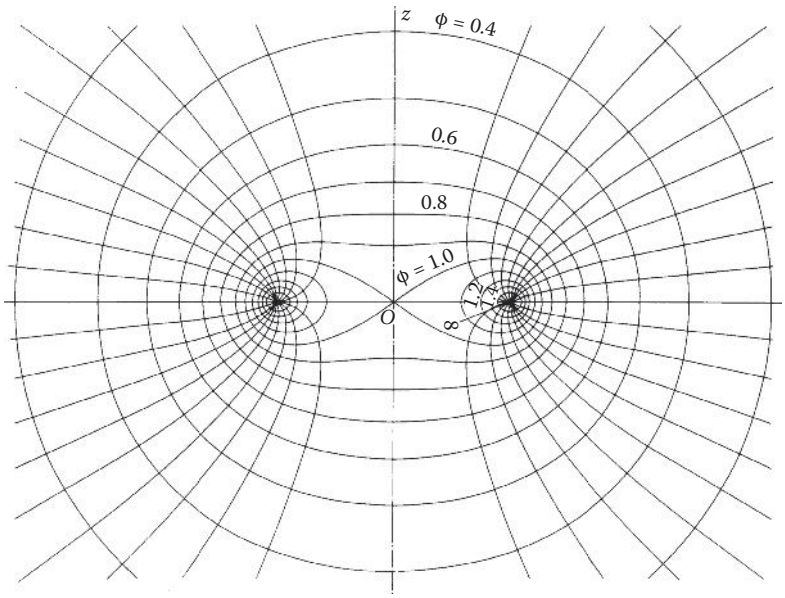


FIGURE 2.23 Distribution of potential and field around a circular charge. (From Moon, P. and Spencer, D.E., *Field Theory for Engineers*, D. Van Nostrand, Princeton, NJ, 1961.)

conductors in space, since in this case it can reproduce the equipotential condition at only one conductor at a time. However, one can apply the method of images successively to each conductor of the configuration and thus gradually approaching the equipotential condition at all the conductors (Maruvada and Janischewskyj, 1969). The method of successive images lends itself to numerical calculation; it minimizes the number of unknown charges by optimizing the position of the image charges and is recognized for its accuracy by IEEE PES-TD-Radio Noise Working Group (IEEE, 1979). Two particular applications of the method of successive images will be discussed in the succeeding text, as related to the cases of overhead lines and of a gas-insulated cable.

2.5.2.1 Overhead Line

Consider the case of an overhead power transmission line. Its conductors form a set of n parallel cylindrical conductors above a ground plane (Figure 2.24a). Let U_i and λ_i be the potential and the linear charge of the ith conductors. The effect of the ground can be represented by a set of n image conductors having potential $-U_i$ and linear charge $-\lambda_i$, giving rise to a set of $2n$ conductors (Figure 2.24b). For each conductor of this new conductor system, the conductors can be represented, at the first approximation, by line charge $\pm\lambda_i$ located at the center of the conductors. The surface of the conductor can be made equipotential by taking the $(2n-1)$ image line charges with respect to the conductor considered (Figure 2.24c). By repeating the procedure for all the conductors, by the end of the first iteration of successive images, one arrives at a set of $(2n-1)$ image charges within each conductor.

One can repeat, subsequently, the same procedure to obtain a new order of successive images and gradually improve the potential distribution at the conductors. The number of new image charges within each conductor at the kth iteration is $(2n-1)^k$. The total number of linear charges in each conductor after k iterations is

$$n_t = \hat{\mathrm{A}}\,(2n-1)^k, \text{ with } \quad k = 0 \text{ to } k,$$

It is to be noted that the iteration order $k = 0$ corresponds to line charges located at the center of each conductor. One arrives, in this manner, to represent the set of $2n$ conductors by a series of theoretically infinite linear charges located within each conductor. In practice, since the distances between the line conductors are much larger than their physical dimensions, an adequate representation is already reached after the first iteration.

Hydro-Québec 735 kV line: Figures 2.25 through 2.28 show the variations of the *gradient factor*, that is, the electric field when the line potential is 1 kV, at the surface of the subconductors and at the ground under a 735 kV of *Hydro-Québec*, using the method of successive images. To obtain the actual field, it suffices to multiply the gradient factor G by the line to ground voltage. The configuration of *Hydro-Québec* 735-kV lines is summarized in Table 2.1. It can be seen that the electric field at the surface of the conductors varies with the position of the conductor in space and for each conductor, with the angular position between the limiting values E_{max} and E_{min}, with the angle corresponding to the maximum

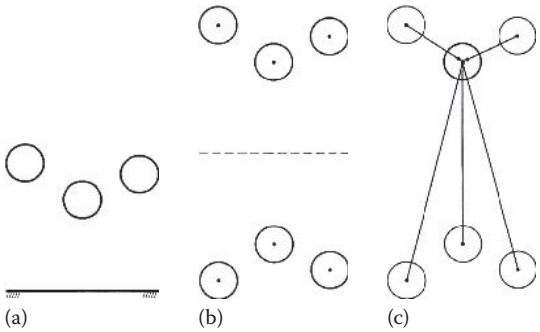


FIGURE 2.24 Representation of successive images method. (a) n-conductor system above ground. (b) Replacement of the ground plane by a $2n$-conductors system using the image method. (c) $2n$-1 image charges in a conductor to make its surface an equipotential.

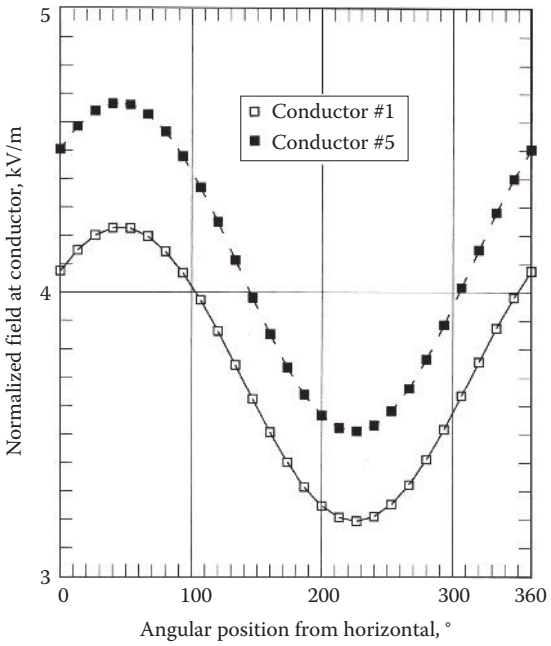


FIGURE 2.25 Variations of the gradient factor at the surface of conductors #1 and #5 as a function of the angular position.

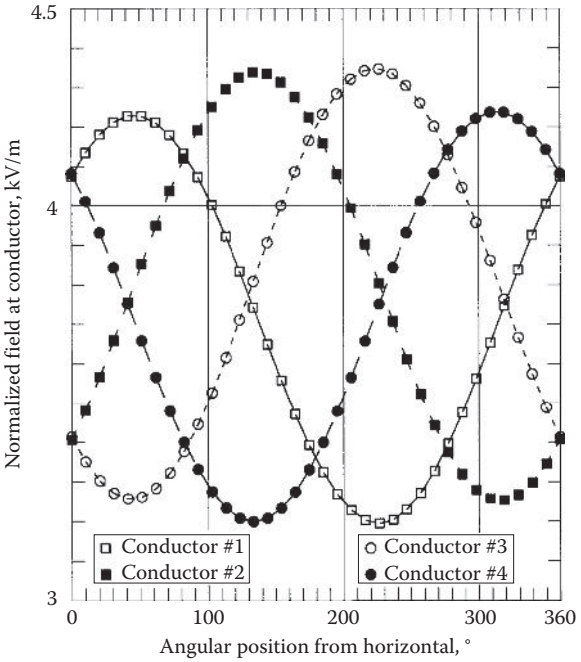


FIGURE 2.26 Variations of the gradient factor G (kV/cm) at conductors #1, #2, #3, and #4—Hydro-Québec's 735 kV line.

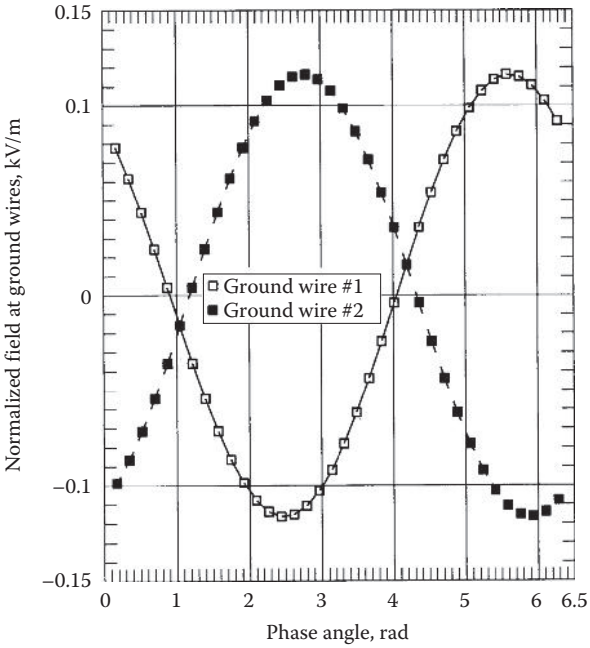


FIGURE 2.27 Variations of the normalized gradient at the ground wires—Hydro-Québec's 735 kV line.

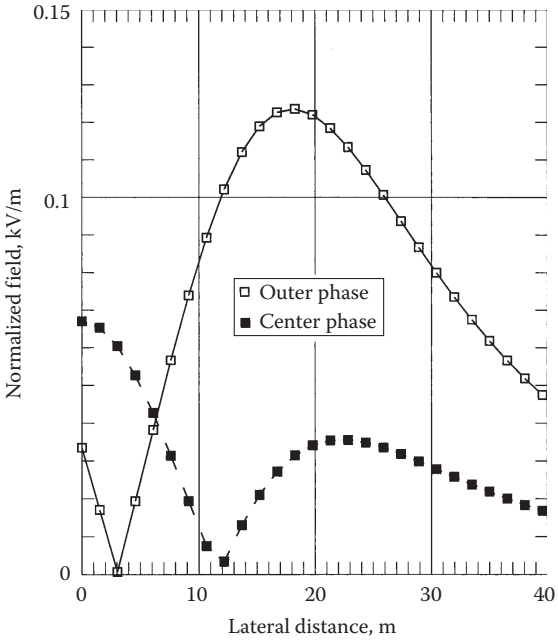


FIGURE 2.28 Variations of the gradient at ground—Hydro-Québec's 735 kV line.

TABLE 2.1

Configuration of the 735 kV Line of *Hydro-Québec*

Parameters	Line Configuration		
Nominal voltage	735 kV		
Number of phases	3		
	Phase 1	*Phase 2* (m)	*Phase 3* (m)
Horizontal position of phases	13.7 m	0	−13.7
Average height of phases	19.8 m	19.8	19.8
Number of subconductors	4		
Radius of subconductors	0.015 m		
Radius of the conductor bundle	0.323 m		
Angular position of the first subconductor	45°		
	Protection against Lightning		
Number of ground wires	2		
Distance between ground wires	17.95 m		
Average height of the ground wires	32.6 m		
Radius of the ground wires	0.0061 m		

TABLE 2.2

Extreme Values of the Gradient Factor at the Subconductors

Conductor #	Angle of G_{max}, deg	G_{max}, /m	G_{min}, /m
1	40	4.2295	3.1976
2	133.33	4.3380	3.2532
3	226.67	4.3466	3.2577
4	320	4.2388	3.1995
5	40	4.6663	3.5121
6	133.33	4.6681	3.5140
7	226.67	4.6681	3.5140
8	320	4.6663	3.5121
9	40	4.3380	3.2532
10	133.33	4.2295	3.1976
11	226.67	4.2388	3.1995
12	320	4.3466	3.2577

field coinciding with the angular position of the subconductor in the bundle (Figures 2.25 and 2.26). The values of the gradient factor G are given in Table 2.2.

Variations of the gradient factor at the ground wires are presented in Figure 2.27.

As for the distribution of the field at ground, one notes that it varies with position with respect to the line conductors: two cases are presented in Figure 2.28, corresponding to when the voltage is maximal at the outer phase and at the center phase, respectively.

2.5.2.2 High-Voltage Cable

A high-voltage cable is formed of several parallel conductors located within a cylindrical envelope. Figure 2.29a is an illustration of a bipolar gas-insulated cable; the parameters of which are given in Table 2.3. Applying the method of images with respect to the cable envelope replaces the latter with two image conductors located outside of the cable. The result is a set of 4 parallel conductors in free space (Figure 2.29b). For the high voltage cable defined in Table 2.3, the image conductors have their centers located at ±61.36 cm, and a diameter of 102.3 cm, considerably larger than the 5 cm diameter

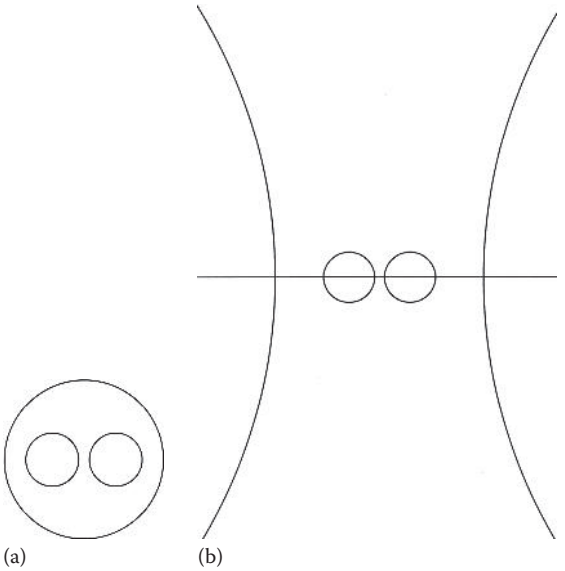


FIGURE 2.29 Image of the conductors with respect to the outer envelope. (a) Bi-polar cable. (b) Images of the conductors with respect to the ground cable sheath, resulting in a set of 4 conductors in space.

TABLE 2.3

Defining Parameters of the High-Voltage Cable

Parameters	
Nominal voltage	±300 kV
Number of phases	2
Dielectric constant ε_r	3
Insulating medium	Polymer
Diameter of the envelope	15 cm
Radial distance of the conductor center	3 cm
Diameter of the conductors	5 cm

TABLE 2.4

Summary of Field and Potential Calculations for an HVDC Cable

Iteration	**Number of Charges**		**Potential, kV**			**Gradient, kV/cm**	
	Conductor/Total		**Minimum**	**Maximum**	**% Error**	**Minimum**	**Maximum**
0	1	4	222.02	300	35.12	123.55	169.3
1	4	16	300	349.7	16.56	164.28	284.64
2	13	52	300	307.03	2.34	152.46	249.66
3	40	160	300	302.44	0.81	152.89	245.43
4	121	484	300	300.54	0.18	152.66	243.75

of the conductors. . The method of successive images can then be used to calculate the potential and field at the conductors and in the space between the conductors and the envelope. At each image order, the potential distribution at the conductor surface is evaluated for its equipotential condition. If the latter is not reached, the calculation is continued to the next image order. This procedure is repeated as many times as needed to obtain the desired accuracy.

A summary of the results of calculation of the potential and electric field at the surface of the conductor #1 is given in Table 2.4. One can see that because of the proximity of the conductors, several iterations

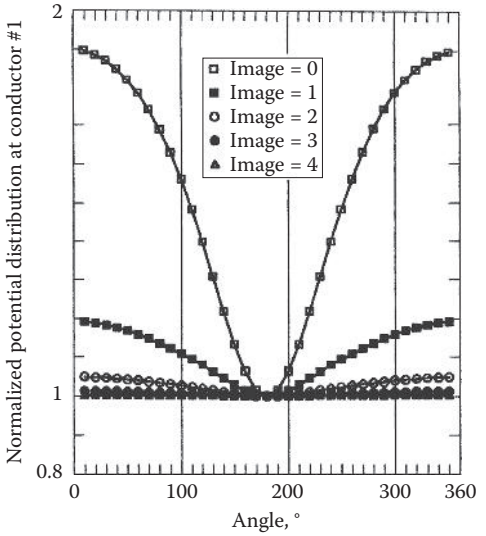


FIGURE 2.30 Improvement of the equipotential condition at the conductor with the successive image orders. Bipolar gas-insulated cable: conductor diameter 3 cm, envelope diameter 15 cm.

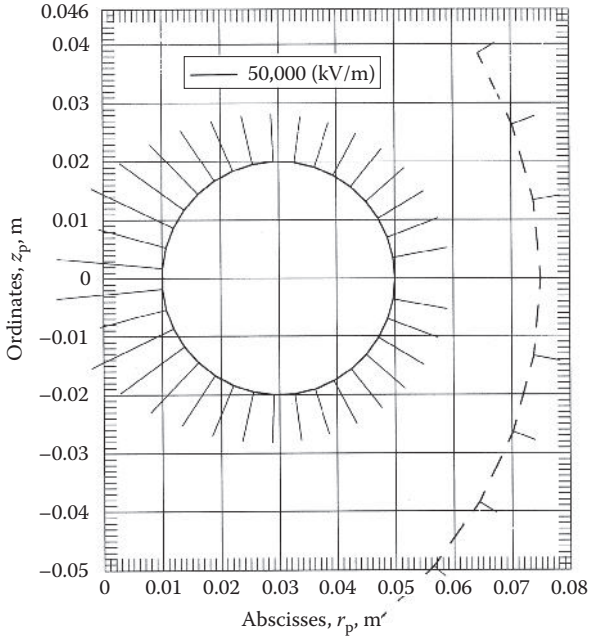


FIGURE 2.31 Variations of the electric field at the surface of the conductor #1 as a function of the angular position. Bipolar gas-insulated cable: conductor diameter 3 cm, envelope diameter 15 cm.

are required to obtain an adequate representation of the equipotential condition at the surface of the conductor. The accuracy of the results is 2.46% at the second image order, 0.83% at the third image order, and 0.18% at the fourth image order. The improvement of the equipotential condition at the conductor #1 with successive image orders is illustrated by the results of Figure 2.30.

With the charges and their successive images thus defined, the field at the surface of the conductors can be evaluated. The variations of the electric field at the surface of conductor #1 are shown in Figure 2.31, as a function of the angular position. In the figure, the field vectors are represented by straight segments, which show both the relative intensity and the orientation of the local field. One notes

that the field is maximal between the conductors, and a local maximum is observed at the opposite point, facing the envelope. Such a situation indicates that some modifications of the cable configuration are still needed to better distribute the maximal fields at the surface of the conductors: a greater separation between the conductors bringing them closer to the envelope. Such a modification reduces the maximum field between the conductor while increasing the field between the conductor and the envelope.

2.5.3 Method of Charge Simulation (Singer et al., 1974)

In this method, the distribution of the surface charge of the electrodes is reproduced by a set of n discrete charges of simple configuration, that is, point, line and ring, etc., located outside of the region of interest, the absolute values of which are to be determined to satisfy the specific boundary conditions.

2.5.3.1 Two-Dimensional Field

When the gap configuration presents an axial symmetry, the potential and field distributions are reduced to two dimensions. An example is presented in Figure 2.32 illustrating the set of ring charges used in the

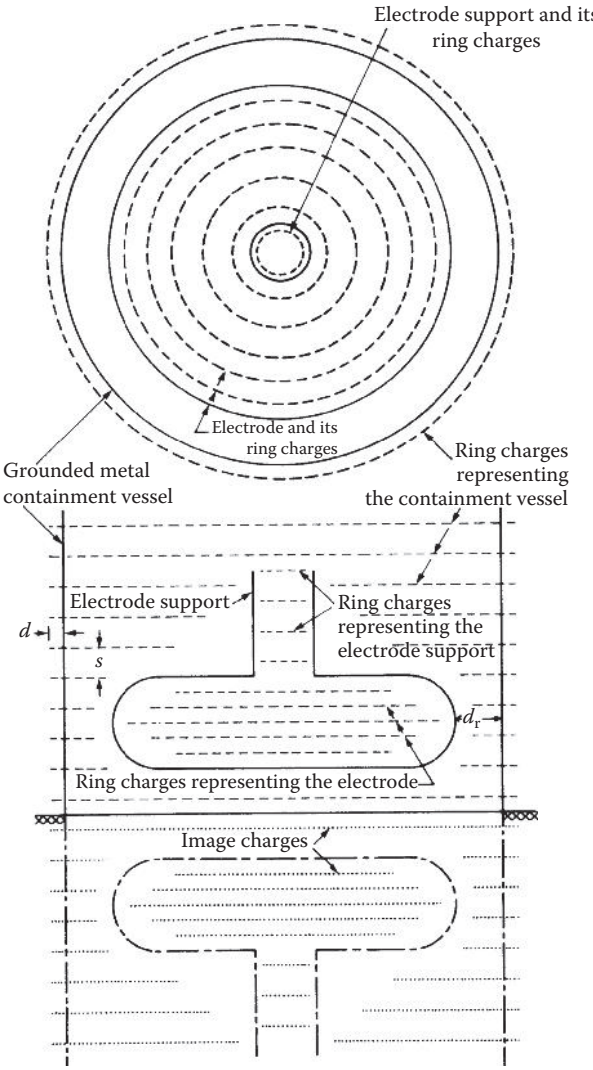


FIGURE 2.32 Representation of charges in electrodes of a uniform field gap. (From Trinh, N.G., *IEEE Trans. Power Appar. Syst*., 99, 1235, 1980.)

evaluation of uniform field electrodes, with respect to their efficiency to produce an adequate distribution of the electric field at their surface discussed in Section 2.3.1.2. The charge elements are located within the plane electrodes and outside of the containment vessel. Evaluation of the efficiency of different uniform field electrodes in producing a uniform field in the gap is evaluated by comparing the distribution of electric field at the electrode surface (Trinh, 1980). The results are presented in Figures 2.1, 2.3, and 2.4 discussed at Section 2.3.1.2 for plane, Rogowski, and Bruce profile electrodes.

2.5.3.2 Field in the Presence of Composite Dielectrics

The method of charge simulation can be readily applied to problems involving two or more dielectrics, by respecting the boundary conditions related to the potential and field at the interface between two dielectrics discussed in Section 2.1.3, namely, for any point at the interface:

- The potential is the same on both sides of the interface: $u_1 = u_2$.
- The tangential electric fields are the same on both sides of the interface: $E_{1t} = E_{2t}$.
- The normal electric fields are related according to $\varepsilon_1 E_{1n} = \varepsilon_2 E_{2n}$

where the indices refer to the two adjacent dielectrics of constants ε_1 and ε_2, respectively.

However, since the charge elements cannot be inside the region where the potential and field are evaluated, the interface between two dielectrics is represented by two sets of charge elements, n_{i1} and n_{i2}, located in the two adjacent dielectrics. The calculation of the potential and field in the dielectric with ε_1 is done with the n_{i2} charge elements located in the dielectric with ε_2, and vice versa. The other charge elements representing the metal interfaces remain the same and are involved in the calculation of potential and field in both dielectrics. One notes that the representation of a dielectric interface adds $2n_i$ charge elements located on either side of the interface, the values of which will be determined by the previously discussed boundary conditions relating the potential and field at the interface between two adjacent dielectrics. Figure 2.33 shows the variations of the electric potential and, hence, illustrates the variation of the field at a cone interface between two dielectrics, SF_6 and epoxy, in a gas-insulated cable (Trinh et al., 1980) discussed in Chapter 6.

2.5.3.3 Three-Dimensional Field: Representation of the Surface Charge by Orthogonal Functions

In this method, the distribution of the surface charge at the conductors is defined by a series development in terms of

Orthogonal functions

$$\sigma = \sigma_0 + \sigma_1 \cos\psi + \sigma_2 \cos 2\psi + \cdots \tag{2.75}$$

Polynomial functions

$$\sigma = \sigma_0 + \sigma_1 x + \sigma_2 x^2 + \cdots \tag{2.76}$$

where σ is the surface charges and ψ and x are the control variables.

For situations where the ring charges are used, the orthogonal functions, $\sin\psi$ and $\cos\psi$, are naturally indicated.

Ring charge with cosinusoidal charge density: Consider a circular charge of radius r_i, located in the plane (r, y) and having a sinusoidal charge density of amplitude q_n such that

$$q(n\psi) = q_n \cos(n\psi)$$

One can demonstrate the following expressions for the potential u_p at the point $P(r, \psi, z)$:

$$u_p = \frac{q_n}{2\pi\varepsilon}\sqrt{\frac{r_i}{r}}\cos(n\psi)Q_{n-1/2}\left(\frac{D^2}{2r_i r}\right) \tag{2.77}$$

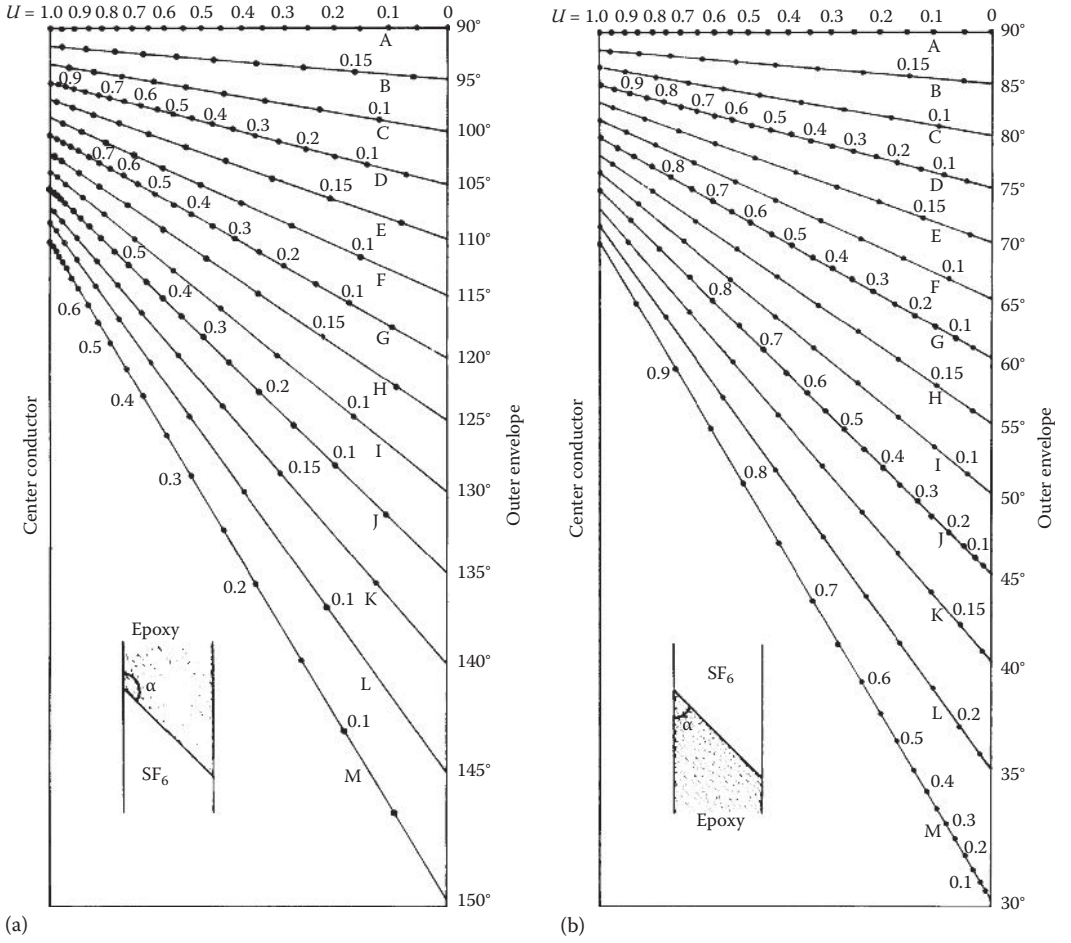


FIGURE 2.33 Potential distribution at a dielectric cone interface in a coaxial conductor. Conductor diameter, 2.54 cm; envelope diameter, 7 cm. (From Trinh, N.G. et al., *IEEE Trans. Power Appar. Syst.*, 99, 2164, 1980.)

where $Q_{n-1/2}(D^2/2r_ir)$ is the second kind Legendre function of order $n - (1/2)$ and defined as

$$Q_{n-1/2}\left(\frac{D^2}{2r_ir}\right) = \frac{1}{\sqrt{2}}\int_0^{\pi}\frac{\cos(n\gamma)}{\sqrt{\dfrac{D^2}{2r_ir_p}-\cos(\gamma)}}\,d\gamma \tag{2.78}$$

with the expression of D^2 defined according to $D^2 = r_i^2 + r^2 + (z - z_i)^2$.

The expressions of the electric field at the point P are

$$E_{nr} = -\frac{\partial u_n}{\partial r} = -\frac{\lambda_n}{2\pi\varepsilon}\cos(n\gamma)\sqrt{\frac{r_i}{r}}\left[-\frac{1}{2r}Q_{n-1/2}\left(\frac{D^2}{2rr_i}\right)\right.$$

$$\left.+\frac{n+\frac{1}{2}}{D^4-4r^2r_i^2}2r_i(2r^2-D^2)\left[Q_{n+1/2}\left(\frac{D^2}{2rr_i}\right)-\frac{D^2}{2rr_i}Q_{n-1/2}\left(\frac{D^2}{2rr_i}\right)\right]\right] \tag{2.79}$$

$$E_{n\gamma} = -\frac{1}{r}\frac{\partial u_n}{\partial \gamma} = \frac{1_n}{2\pi\varepsilon} n\sqrt{\frac{r_i}{r}}\frac{1}{r} Q_{n-1/2}\left(\frac{D^2}{2rr_i}\right)\sin(n\gamma) \tag{2.80}$$

$$E_{nz} = -\frac{\partial u_n}{\partial z} = -\frac{1_n}{2\pi\varepsilon}\sqrt{\frac{r_i}{r}}\cos(n\gamma)\frac{n+\frac{1}{2}}{D^4 - 4r^2 r_i^2} 4rr_i(z - z_i)$$

$$\left[Q_{n+1/2}\left(\frac{D^2}{2rr_i}\right) - \frac{D^2}{2rr_i} Q_{n-1/2}\left(\frac{D^2}{2rr_i}\right)\right] \tag{2.81}$$

Figure 2.34 shows the radial variations of the electric field along the *x*-axis with $\psi = 0$, as a function of the harmonic order of the charge density. The unknowns to be determined in this case are the coefficients σi. For this, one defines once again a set of *n* equations from the *n* test points, chosen at the surface of the electrodes where the potentials are known, defined by the boundary conditions. The solution of the system of *n* equations defines completely the distribution of the surface charge at the electrodes and allows the calculation of potential and electric field at any point in the interelectrode space.

An example of a tridimensional electric field calculation is illustrated in Figure 2.35, which shows a test gap located at 1 m above ground, formed by a 735 kV bushing shield electrode and a circular ground plane located at a right angle with the bushing axis. The absence of axial symmetry in this case requires that ring charges with nonuniform charge distribution be used in the method of charge simulation, in combination with appropriate choices of linear and point charges, to adequately reproduce the boundary conditions at the electrodes. Figure 2.35 illustrates the distribution of the electric field vectors at the surface of the electrodes forming the test gap obtained.

2.5.3.4 Floating Electrode

Figure 2.36 illustrates another example of a tridimensional field calculation. The gap is formed of a spherical terminated rod above ground, taken as the *x*-*y* plane with, in this case, the third electrode not grounded, remaining at a floating potential. When one electrode is floating, its potential is determined by the induced

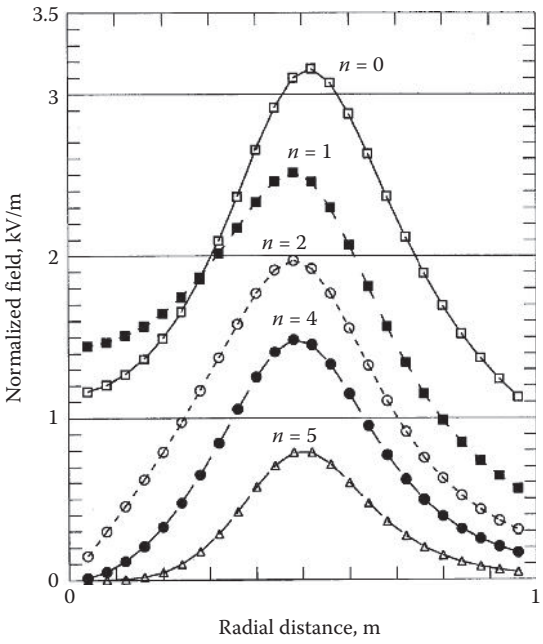


FIGURE 2.34 Radial variations of the field associated with harmonic charges.

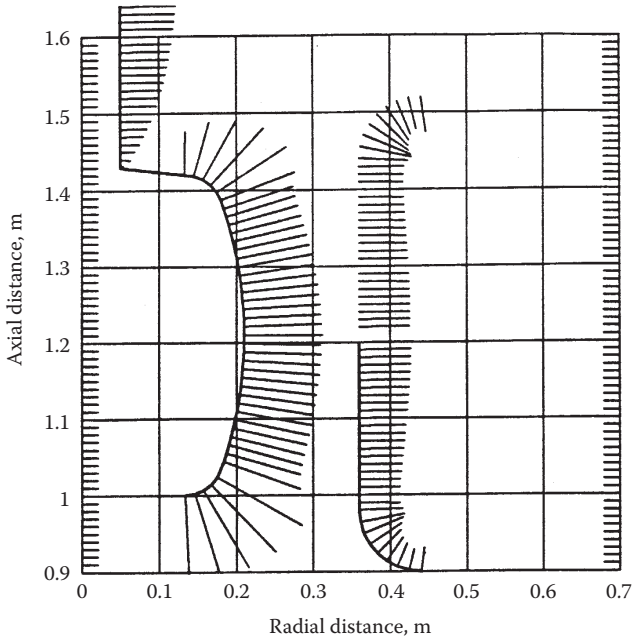


FIGURE 2.35 Field distribution at the surface of the electrodes in a bushing shield plane test gap. Bushing shield electrode radius, 21 cm, height 42 cm; plane electrode radius 30 cm. Gap, 15 cm.

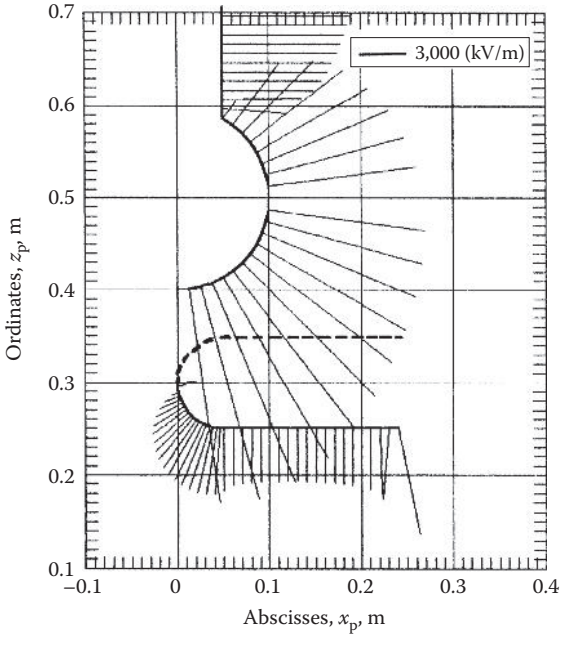


FIGURE 2.36 Field distribution at the surface of the electrodes in a sphere-plane gap with a floating-triggered electrode. Sphere radius, 10 cm; gap 40 cm; floating electrode radius 5 cm, located at 30 cm above ground taken as the x–y plane with $z = 0$. For clarity of the figure, only the distribution of the lower half of the floating electrode is shown in the figure.

charges at its surface, such that the net charge at the floating electrode is zero. The problem is solved in an iteration process: starting with a fixed potential u_0 at the floating electrode, the charges are next calculated and the net charge at the floating electrode evaluated. If the net charge is not equal to zero, a new value for u_1 will be assumed for the floating electrode and the calculation is repeated. The process is continued until the floating potential u_f is determined to the required accuracy. Figure 2.36 illustrates the distribution of the field vectors at the spherical terminated rod and the floating electrode, following the calculation procedure just described.

2.5.4 Method of Global Solution

Different methods of solution of the Laplace equation including numerical calculation, graphical solution, and measurement on reduced scale model can be included in this group; all aims at reconstituting the equipotential surfaces in a specific region of space, usually the interelectrode space. The numerical solutions of the Laplace equation will be discussed in the following.

2.5.4.1 Method of Finite Differences (Moon and Spencer, 1961)

In this approach, the Laplace differential equation is replaced by a finite difference equation that is simpler to resolve. The solution is generally made in a well-defined region in space, often delimited by the boundary where the conditions are known. Consider the Laplace equation in the Cartesian coordinate system:

$$-\nabla^2 u = \frac{\partial^2 u}{\partial x^2} + \frac{\partial^2 u}{\partial y^2} = 0$$

In terms of finite differences, the preceding equation becomes

$$\frac{\Delta^2 u}{\Delta x^2} + \frac{\Delta^2 u}{\Delta y^2} = 0 \tag{2.82}$$

Referring to Figure 2.37 where the space of interest is subdivided into a square grid,

$$\Delta x = \Delta y = h$$

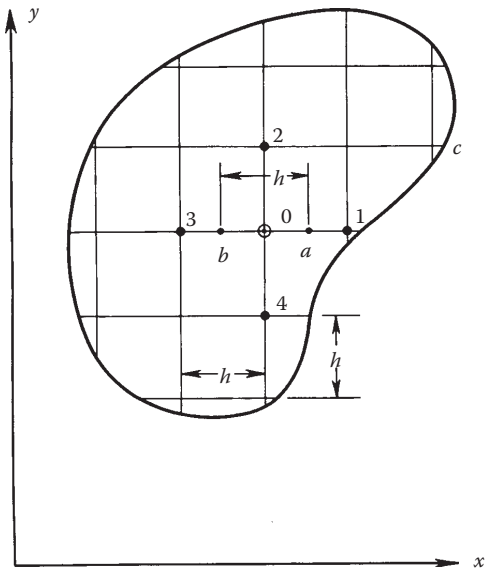


FIGURE 2.37 Method of finite differences.

The expressions of finite differences of the first and second degree are

$$\Delta u_B = (u_B - u_A)$$

$$\Delta u_C = (u_A - u_C)$$

$$\Delta u_D = (u_D - u_A)$$

$$\Delta u_E = (u_A - u_E)$$

and

$$\Delta^2 u_x = \Delta u_B - \Delta u_C = (u_B + u_C - 2u_A)$$

$$\Delta^2 u_y = \Delta u_D - \Delta u_E = (u_D + u_E - 2u_A)$$

The Laplace equation, expressed in terms of finite differences at the point A, simplifies to

$$u_A + u_B + u_C + u_D + u_E = 0, \quad \text{or} \quad u_A = \frac{1}{4}(u_B + u_C + u_D + u_E) \tag{2.83}$$

where u_A, …, u_E are the potentials at points A,…, E.

The preceding relation (Equation 2.83) implies that the solution of the Laplace equation is reduced to a simpler problem, where *the potential at a node is equal to the average value of the potentials at the immediately adjacent nodes*. This numerical solution of the Laplace equation has the advantage of being always convergent. However, the replacement of Laplace differential equation by a finite difference equation inherently limits the computation accuracy, which is directly related to the size of the grid's squares.

2.5.4.2 Method of Finite Elements

The method of finite differences discussed earlier has opened the way to more advanced methods of calculation, generally known as the method of finite elements. However, while the finite difference method aims at finding an approximate solution to the Laplace equation

$$-\nabla^2 u = 0$$

which would meet the boundary conditions associated to a specific problem, the finite element method (FEM) follows the well-known principle of minimum potential energy, which requires that the potential distribution in the region of interest be such as to minimize the stored field energy. For a two-dimensional problem, this energy is (Sylvester and Ferrari, 1990)

$$W(u) = \frac{1}{2}\iint_S |\nabla u|^2 \mathrm{d}S \tag{2.84}$$

the integration being carried out over the region of interest. This minimum energy principle is mathematically equivalent to the Laplace equation in the sense that a potential distribution, which satisfies the latter equation, will also minimize the energy and vice versa. An approximate expression for the stored energy $W(u)$ may be defined by assuming the potential $u(x, y)$ to be given by a combination of suitably chosen, simple functions with as yet undetermined coefficients. Minimization of the stored energy will determine the unknown coefficients and, thereby, implicitly determines an approximation to the potential distribution.

The definition of the region of interest is usually described by the boundary conditions and by symmetry. Let $u(x, y)$ be the true solution of the potential and $h(x, y)$ some sufficiently differentiable function with the following:

- Exactly zero values at the boundary points, where the function u meets the boundary condition.
- The normal derivative vanishes at the symmetry planes.

The combination of $(u + \theta h)$ with θ, a scalar parameter, is an approximate solution for $u(x, y)$. The stored energy $W(u + \theta h)$, associated with the approximate solution for the potential u, is

$$W(u + \theta h) = W(u) + \theta \int_S \nabla u \cdot \nabla h \, dS + \frac{1}{2}\theta^2 \int_S |\nabla h|^2 \, dS$$

Using Green's theorem in two-dimensional form

$$\int_S \nabla^2 v \, dS = \int_C u(-\nabla v) \cdot \mathbf{n} \, dS - \int_S (-\nabla u) \cdot (-\nabla v) dS$$

where C is a close plane curve and S the area in it, the above expression of $W(u + \theta h)$ can be rewritten as:

$$W(u + \theta h) = W(u) + \theta^2 W(h) - \theta \int_S h \nabla^2 u \, dS + \theta \int_C h \frac{du}{dn} \mathbf{n} \, dS \tag{2.85}$$

Since $u(x, y)$ is the exact solution of the Laplace equation: $\nabla^2 u = 0$. In addition, the integral term $\int_C h \frac{du}{dn} \mathbf{n} \, dS$ is also equal to zero at the boundary points due to $h = 0$ and at the symmetry planes due to $\frac{du}{dn} = 0$. Equation 2.85 simplifies to

$$W(u + \theta h) = W(u) + \theta^2 W(h) \tag{2.86}$$

The error on the energy estimate is proportional to θ^2. For small values of θ, as usually is the case, the error on the energy is much smaller than that on the potential.

Definition of the potential grid: The approximate solution of the Laplace equation in FEM is based on the buildup of a potential grid, formed by triangular elements, over the whole region of interest. The essence of the method lies in

- First, approximating the potential u within each element in a standardized fashion
- Second, interrelating the potential distribution to the various elements so as to assure its continuity across the interelement boundaries

Within a typical triangular element illustrated in Figure 2.38, the potential is approximated by

$$U = \alpha_1 + \alpha_2 x + \alpha_3 y \tag{2.87}$$

where α_1, α_2, and α_3 are coefficients to be determined.

The potential along any triangle edge is a linear interpolation between its two vertex values, so that if two elements share the same vertices, the potential will be continuous across the interelement boundary. The surface $U(x, y)$ is therefore piecewise planar but continuous everywhere. Referring to Figure 2.38,

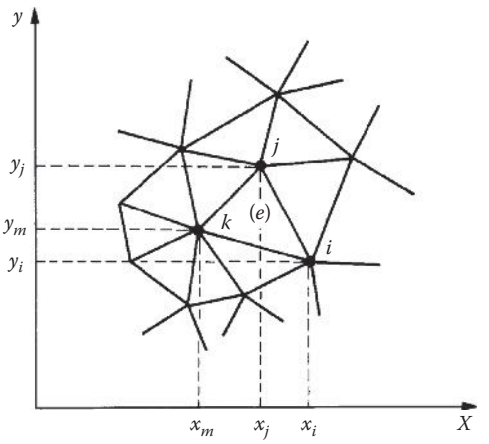


FIGURE 2.38 Triangular element representation in a grid.

which shows a portion of the region of interest, subdivided into triangular elements, the potentials at the nodes of the element e are

$$u_i = a_1 + a_2 x_i + a_3 y_i$$

$$u_j = a_1 + a_2 x_j + a_3 y_j$$

$$u_k = a_1 + a_2 x_k + a_3 y_k$$

The coefficients α_i can be evaluated in terms of the node potentials as

$$\begin{aligned} a_1 &= \frac{1}{2\Delta e}(a_i u_i + a_j u_j + a_k u_k) \\ a_2 &= \frac{1}{2\Delta e}(b_i u_i + b_j u_j + b_k u_k) \\ a_3 &= \frac{1}{2\Delta e}(c_i u_i + c_j u_j + c_k u_k) \end{aligned} \tag{2.88}$$

where

$a_i = x_j y_k - x_k y_j$	$a_j = x_k y_i - x_i y_k$	$a_k = x_i y_j - x_j y_i$
$b_i = y_j - y_k$	$b_j = y_k - y_i$	$b_k = y_i - y_j$
$c_i = x_j - x_k$	$c_j = x_k - x_i$	$c_k = x_i - x_j$

and $2\Delta e = a_i + a_j + a_k = b_i c_j - b_j c_i$, with Δe representing the area of the element e delimited by the nodes i, j, and k.

Replacing the expressions of the coefficients α_i from Equation 2.88, in the Equation 2.87, the potential u_e of the element e is defined by the potentials at the nodes of the element as

$$u_e = u(x,y) = \frac{1}{2\Delta e}\left[(a_i + b_i + c_i)u_i + (a_j + b_j + c_j)u_j + (a_k + b_k + c_k)u_k\right] \tag{2.89}$$

For a 2D field, the energy stored in the region of interest is

$$W = \frac{1}{2}\iint_A |u|^2 \, dA = \frac{1}{2}\iint_A \left[\left(\frac{\partial u}{\partial x}\right)^2 + \left(\frac{\partial u}{\partial y}\right)^2\right] dx dy \tag{2.90}$$

Noting the expression of the potential $u(x, y)$ given in Equation 2.87, the derivatives of u are

$$\frac{\partial u}{\partial x} = a_2 \quad \text{and} \quad \frac{\partial u}{\partial y} = a_3$$

The preceding expression for W becomes

$$W = \frac{1}{2}\iint_A \left[(a_2)^2 + (a_3)^2\right] dx dy = \frac{1}{2}\Delta_e \left[(a_2)^2 + (a_3)^2\right] \tag{2.91}$$

Since the FEM is based on the minimization of the energy, with respect to the potential distribution in the region of interest, this can be expressed as

$$\frac{\partial W_e}{\partial u_i} = 0$$

With the earlier expression of W_e, in Equation 2.91, the minimization condition for W_e is

$$\frac{\partial W_e}{\partial u_i} = \frac{1}{2}\Delta e\left[2a_2\frac{\partial a_2}{\partial u_i} + 2a_3\frac{\partial a_3}{\partial u_i}\right]$$

$$= \frac{1}{4\Delta e}\left[(b_i^2 + c_i^2)u_i + (b_i b_j + c_i c_j)u_j + (b_i b_k + c_i c_k)u_k\right] = 0 \tag{2.92}$$

which can be expressed in matrix form as

$$\frac{\partial W_e}{\partial u_e} = [H_e][u_e] = 0 \tag{2.93}$$

where $[H_e]$ is known as the stiffness matrix and $[\phi_e]$ the node potential matrix of the element e.

Noting that in a triangular grid system, the number of triangular elements around a node in the grid remains small, the minimization condition is limited to a finite system defined by the ensemble of nodes immediately adjacent to the particular node. Figure 2.39 shows four adjacent elements surrounding the node 5 in a triangular grid system. The minimization condition at the node 5 is

$$\frac{\partial W}{\partial u_5} = \sum_1^4 [H_i][u_i] = 0 \tag{2.94}$$

The preceding equation is essentially an algebraic equation relating the potential at the node 5 to those at the immediately adjacent nodes. As a result, its value will be completely defined if the potentials at the surrounding nodes are known. By repeating the same procedure for all the nodes in the region of interest, one obtains a system of N equations for the N unknown node potentials. The solution of which yields the complete distribution of the potential in the region of interest.

The FEM has proven a versatile method for solving field problems. Commercial software has been developed for applications in diverse areas: mechanical, thermal stresses, magnetic and electric fields, etc. For electric field calculation, the FEM can be applied to nonhomogeneous systems with more than one dielectric. The triangular element grid is generated automatically and can be adapted to an optimal representation of the boundaries of two or three dimensions and for adequate accuracy in the results. The main drawbacks of the FEM reside in the requirements for a large memory and fast computing speed, problems that are largely solved with the continuous improvement in both memory and computing time of modern computers.

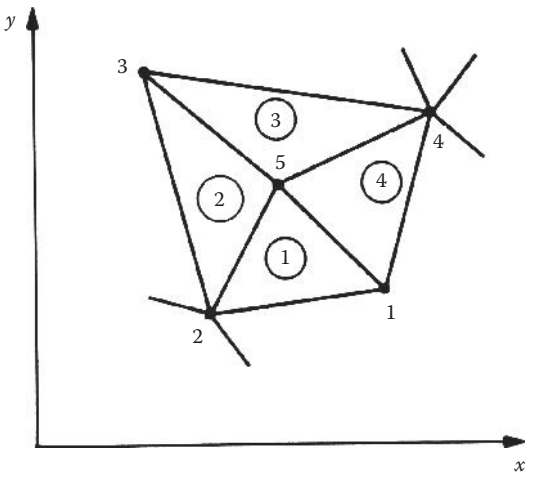


FIGURE 2.39 Localization of node 5 within the grid.

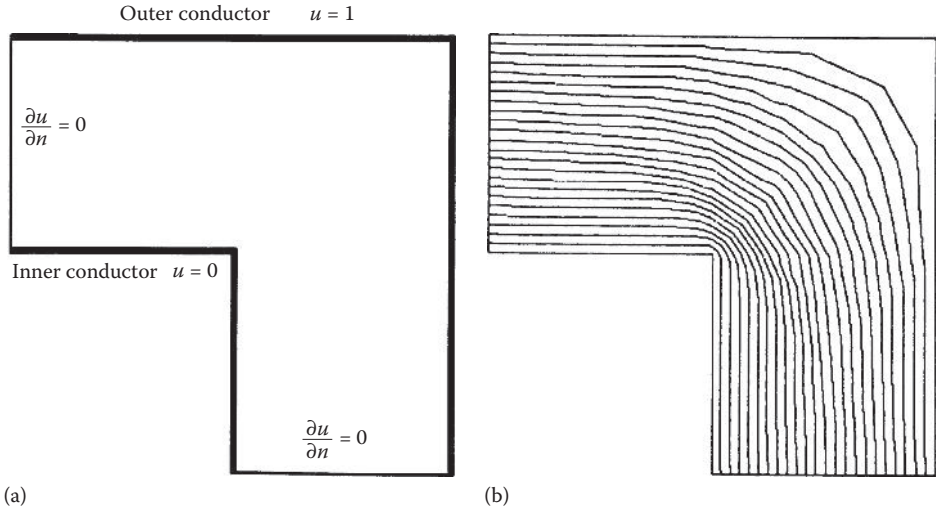


FIGURE 2.40 Distribution of the potential in the interspace of a coaxial transmission line with square conductors obtained with the FEM method. (From Sylvester, P.P. and Ferrari, R.L., *Finite Elements for Electrical Engineers*, Cambridge University Press, New York, 1990.)

An example of field calculation using the FEM method is shown in Figure 2.40 for a coaxial transmission line composed of square conductors (Sylvester and Ferrari, 1990). Because of symmetry, the calculation is limited to a quarter of space as shown in Figure 2.40a, together with the equipotential surfaces and those where the normal derivative is null, $\partial u/\partial n = 0$. Figure 2.40b shows the calculated distribution of the potential in the interspace between the conductors.

REFERENCES

Becker, R. *Electromagnetic Fields and Interactions*. New York: Dover Publications, 1964.

Bruce, F.M. Calibration of uniform-field spark gaps for high voltage measurement at power frequencies. *Journal of IEE* 94(Part II): 138, 1947.

Cobine, J.D. *Gaseous Conductors—Theory and Engineering Applications*. New York: Dover Publications Inc., 1956.

IEEE PES-TD-Radio Noise Working Group. A survey of methods for calculating transmission line conductor surface voltage gradient. *IEEE Transactions on Power Apparatus and Systems* 98: 1996, 1979.

Maruvada, P.S. and W. Janischewskyj. Electrostatic field of a system of parallel cylindrical conductors. *IEEE Transactions on Power Apparatus and Systems* 88: 1069, 1969.

Moon, P. and D.E. Spencer. *Field Theory for Engineers*. Princeton, NJ: D. Van Nostrand, 1961.

Rizk, F.A.M., Trinh, N.G., and C. Melançon. Temporary overvoltage limitation subsequent to load rejection—A new device for shunt reactor reinsertion. CIGRE, Report No. 12-203, Paris, France, 1990.

Rogowski, W. Die elektrische Festigkeit am Rande des Plattenkondensators. Ein Beitrag zur Theorie der Funkenstrecken um Durchfuhrungen. *Archiv fur Electrotechnik* 12: 1, 1923.

Sylvester, P.P. and R.L. Ferrari. *Finite Elements for Electrical Engineers*, 2nd edn. New York: Cambridge University Press, 1990.

Singer, H., Steinbigler, H., and P. Weiss. A charge simulation method for the calculation of high voltage fields. *IEEE Transactions on Power Apparatus and Systems* 93: 1660, 1974.

Trinh, N.G. Electrode design for testing in uniform-field gaps. *IEEE Transactions on Power Apparatus and Systems* PAS-99: 1235, 1980.

Trinh, N.G., Rizk, F.A.M., and C. Vincent. Electrostatic field optimization of the profile of epoxy spacers for compressed SF6-insulated cables. *IEEE Transactions on Power Apparatus and Systems* PAS-99: 2164, 1980.

3

Application of Statistical Analysis in High Voltage Engineering

3.1 Introduction

High voltage engineering relies heavily on experimental data. However, experiments are often costly and time consuming, and in this context, analysis of experimental data has always been of great importance to extract proper information. Because statistical analysis is independent of the phenomenon or objects under investigation, it is applicable to a variety of subjects to sort out their representative parameters and to derive *models* that help make predictions about their performance under different conditions. It is no surprise therefore, that statistical analysis has found its way into high voltage engineering as a means to plan testing and analyze experimental data (Hauschild and Mosch, 1992).

However, precisely *because* it is phenomenon-independent, statistical analysis alone cannot provide a physical explanation on the phenomena under study. It can only present a better, more coherent picture of the set of available data, as well as provide some insight into the phenomenon investigated. Best results are obtained when statistical analysis is paired with an understanding of the physics involved.

Statistical applications to engineering studies are numerous. In the field of high voltage engineering, it has been used to

- Characterize data, for example, to estimate low-probability withstand levels.
- Verify an experimental law.
- Extrapolate the test results on small samples to full-scale insulation system by accounting for length, surface and volume effect, using weak-link statistics.
- Optimize experimental data to separate the component distributions in the data, to improve the amount of experimental data available.
- Estimate the risk of failure and assess breakdown voltage-time characteristics, using joint probability.
- Plan and elaborate more efficient test methodologies aimed at determining low-probability withstand levels.

3.2 Characterization of a Set of Data under Specific Conditions

Anyone who conducts experimental tests is familiar with the fact that repeating the same test many times does not give the same results. Generally the data will be scattered over a finite range of values. This is illustrated by the plot in Figure 3.1. It shows the variations of the ac breakdown field, E_c, of a *bushing shield–plane* gap in oil, in chronological order. It can be seen that though the breakdown field varies from one measurement to the next, it remains within a finite range, bounded by the values 3.1 and 6.5 kV/mm.

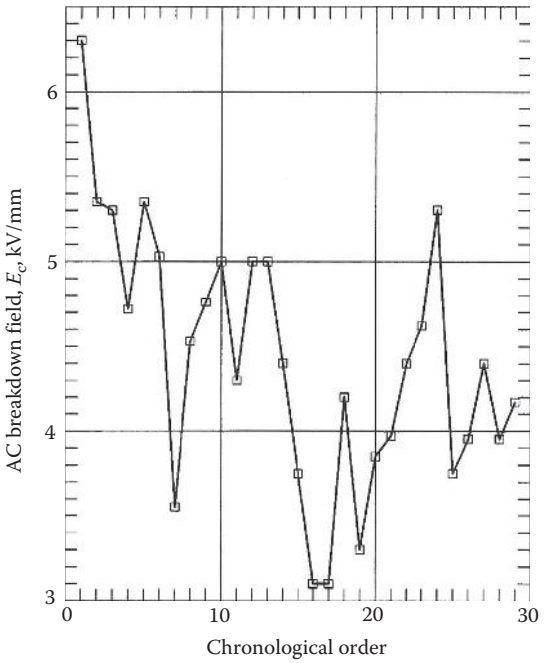


FIGURE 3.1 Variations in chronological order of the ac breakdown field, E_c, of a 20 cm *bushing shield–plane* gap in oil.

3.2.1 Global Statistical Parameters

Two very important parameters are used to describe a set of experimental data points. Those are the *mean value* U_m and the *standard deviation* σ, defined according to (Miller and Freund, 1965)

$$U_m = \frac{1}{N}\sum u_i \tag{3.1}$$

and

$$s^2 = \frac{1}{N-1}\sum (u_i - U_m)^2 \tag{3.2}$$

Here, u_i are the experimental measurements and N is the total number of measurements. The mean value U_m is representative of the population of experimental data, while the variance σ^2, and related standard deviation σ, represents the degree of dispersion of the measurements with respect to the mean and is indicative of the reproducibility of the results. For the set of results in Figure 3.1, the mean breakdown field is $E_m = 4.43$ kV/mm, and the standard deviation is $\sigma = 0.74$ kV/mm, with the coefficient of variation $\sigma/E_m = 0.175$ or 17.5%.

3.2.2 Experimental (Discrete) Distribution

When the volume of experimental data is sufficient, statistical analysis provides an elegant means to evaluate these data, basically by deriving an experimental distribution relating the frequency of occurrence of the measured data expressed as a probability, $P(u)$. Two cases may be distinguished according to the total amount of data gathered.

3.2.2.1 Experimental Distribution with a Small Amount of Data

For most experimental studies, the total number of data is limited, typically in the order of a few tens of measurements. To derive an experimental distribution from a set of breakdown voltage measurements,

one first classifies the results in increasing order of the breakdown voltages. The cumulative probability that the breakdown voltage will be lower than or equal to a specific level U is then defined according to

$$P(u \leq U) = \frac{n(u \leq U)}{N+1} \tag{3.3}$$

where
n is the number of breakdowns occurring at voltages $u \leq U$
N is the total number of measurements

The use of $(N + 1)$ in the preceding definition of the cumulative probability $P(U)$ ensures that the experimental probability distribution is

- Continuously increasing
- Comprised between 0 and 1, more precisely between limiting values of the relative frequencies of $1/(N + 1)$ and $N/(N + 1)$
- The range of probabilities covered by the experimental data is symmetrical with respect to the median value $U_{50\%}$

Figure 3.2 shows the experimental distribution derived from the earlier data set. It can be seen that with a total number of 29 measured breakdown fields, the experimental cumulative distribution is defined between the extreme values of probabilities $P_{\min}$ and $P_{\max}$:

$$P_{\min} = \frac{1}{N+1} \approx 3.333 \times 10^{-2} \quad \text{and} \quad P_{\max} = \frac{N}{N+1} \approx 9.667 \times 10^{-1} \tag{3.4}$$

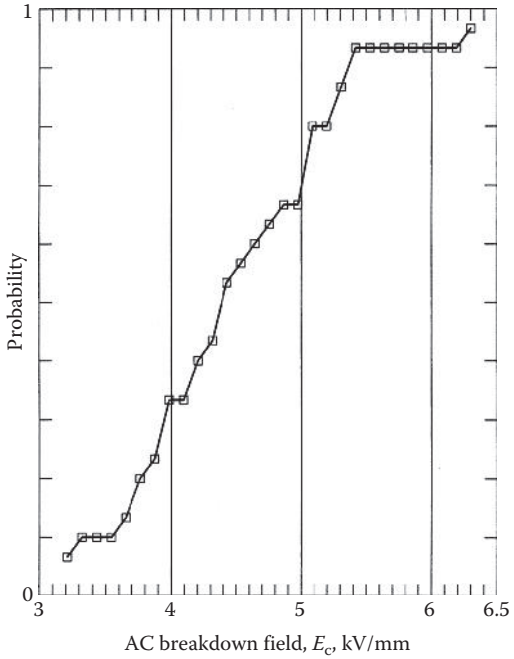


FIGURE 3.2 Experimental cumulative probability distribution of the ac breakdown field, E_c, of a 20 cm *bushing shield–plane* gap in oil.

3.2.2.2 Experimental Distribution with a Large Amount of Data

Statistical analysis is also useful in cases where there is a large amount of data, for example, as is obtained with an automatic data acquisition system over long periods of time. One may be interested to limit the representation of the set of data to m data points, with $m \leq N$, defined as follows:

- Define the extreme limits of the data U_{min} and U_{max}, and reclassify the n experimental data in increasing order.
- Define $m - 1$ equal intervals, $\Delta u = (U_{max} - U_{min})/(m - 1)$, with U_{min} and U_{max} becoming the first and last values.
- The probability density function is defined by $m - 1$ values p:

$$p_j = \frac{dn}{du} = \frac{n_j}{n+1} \tag{3.5}$$

where n_j is the number of measurements comprised in the jth interval.

- The cumulative probability function is defined by m values P_j:

$$P_j(u \leq u_j) = \frac{1}{n+1} \sum_{k=1}^{j} n_k \tag{3.6}$$

with $j = 1, m$, and $\sum n_k$ is the number of measurements comprised in the first j intervals by increasing order.

Figure 3.3 represents the cumulative distribution of corona losses (CL) derived from long-term recordings made at *IREQ* during the evaluation of the corona performances of bundle conductors considered for HVDC transmission lines operating at ±750 kV dc, using the earlier method (Maruvada et al., 1977).

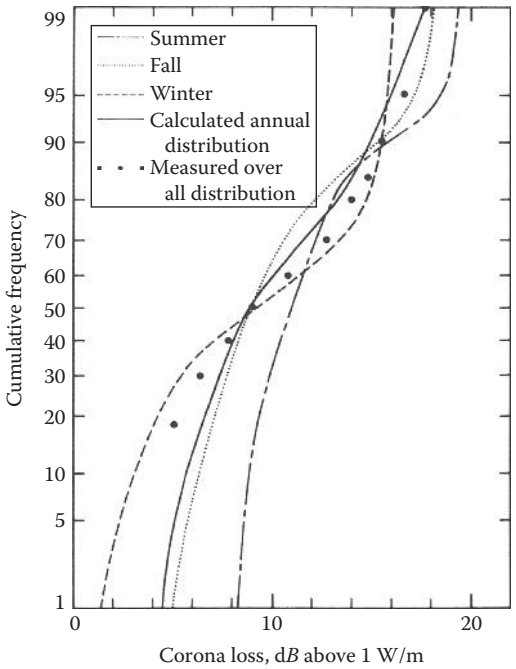


FIGURE 3.3 Distribution of CLs of a bundle conductor considered for power transmission at ± 750 kV dc, obtained with an automatic data acquisition at *IREQ*. (From Maruvada, P.S. et al., *IEEE Trans. Power Appar. Syst.*, PAS-96, 1872, 1977.)

3.2.2.3 Correspondence with the Global Parameters

With the experimental probability density and cumulative probability functions defined earlier, the following correspondence exists with the global parameters defined earlier:

The expectation (mean value)

$$U_{\mathrm{m}} = \hat{\mathrm{A}}\ p_j u_j \tag{3.7}$$

The variance

$$\mathrm{s}^2 = \hat{\mathrm{A}}\ (p_j u_j - U_{\mathrm{m}})^2 \tag{3.8}$$

with σ as the standard deviation.

3.2.2.4 Other Characteristic Parameters

The experimental distributions of the probability density and cumulative probability also allow the definition of several other characteristic parameters, which are currently used in practice, namely,

- *Most probable voltage,* U_{p}: Is the voltage at which the probability density function is maximal.
- *Median voltage,* $U_{50\%}$: Is the voltage at which the cumulative probability of occurrence is equal to 0.5.
- *Withstand voltage of x%*: Is the voltage at which the cumulative probability of occurrence is equal to *x%*.
- *Confidence interval at y%*: Is defined as the range of voltages *u*, which ensures a probability of occurrence of *y%*. The confidence interval is limited by the withstand voltages of (0.5*y*)% and (100–0.5*y*)% and represents a measure of the reproducibility of the phenomenon investigated.
- *Coefficient of variation*: Is defined as the ratio σ/U_{m}.

3.2.3 Statistical Functions (Models)

Because of the limitations of time and cost, experimental data are often obtained under laboratory conditions. As good as they are, laboratory conditions never fully correspond to the operating conditions of the equipment. Therefore, there is a great incentive to extrapolate the results beyond the conditions under which they were obtained. A useful approach consists in defining an analytical distribution function that models the experimental distribution expressed by Equation 3.3 or 3.6, which also satisfy the general conditions for a cumulative probability distribution:

- To be continuously increasing over the range of variations of the independent variable
- To have a value comprised between 0 and 1

By appropriate uses of interpolation or extrapolation, the statistical model thus obtained can be used to determine the behavior of the phenomenon under investigation, for ranges not covered by the experimental data. Several statistical functions exist that are currently used in practice. The most common are presented in detail in the succeeding texts. They are classified in two general categories of discrete and continuous distributions as related to the nature of the variable.

3.2.3.1 Discrete Distributions

In discrete distributions, the variable can take only discrete values, denoted by X_i, for which the relative frequency is defined. Typical discrete distributions are uniform, binomial, and Poisson.

3.2.3.1.1 Uniform Distribution

The random variable can assume n different values:

$$\text{Individual probability} \quad p_i = 1/n \tag{3.9}$$

$$\text{Cumulative probability} \quad P(X \leq X_i) = \sum p_i \tag{3.10}$$

$$\text{Parameters} \quad n, X_i (i = 1, \ldots, n)$$

$$\text{Expectation} \quad \mathrm{EX} = \frac{1}{n} \sum_{1}^{n} X_i \tag{3.11}$$

$$\text{Variance} \quad D^2X = \frac{1}{n} \sum_{1}^{n} (X_i - \mathrm{EX})^2 \tag{3.12}$$

3.2.3.1.2 Binomial Distribution

Binomial distribution applies to the case where the random variable is of Bernoulli type, which can take only one of the two values, 1 and 0, corresponding to the occurrence or nonoccurrence of an event E, for example, breakdown of a test gap. Defining the random variable X as the number of times E occurs in n independent trials, with values 0, 1, …, n, one gets the following expressions:

$$\text{Probability density function} \quad p(k) = P(X = k) = \binom{n}{k} p^k (1 - p)^{n-k} \tag{3.13}$$

$$\text{Cumulative probability} \quad P(X \leq k) = \sum_{m=0}^{k} \binom{n}{k} p^m (1 - p)^{n-m} \tag{3.14}$$

$$\text{Parameters} \quad n \text{ and } p$$

$$\text{Expectation} \quad \mathrm{EX} = np \tag{3.15}$$

$$\text{Variance} \quad D^2X = np(1 - p) \tag{3.16}$$

On the other hand, from a given set of experimental data, one can define the most representative statistical model from

Point estimate for p: $p = k/n$, the relative frequency from n trials in which event E occurs k times.

Confidence estimate for p:

- The F distribution produces the one-sided confidence region with an upper limit as

$$p_0 = \frac{(k+1)F_{m1,m2,\varepsilon}}{n - k + (k+1)F_{m1,m2,\varepsilon}}$$

and the confidence interval

$$I = [0, p_0]$$

where $F_{m1,m2,\varepsilon}$ is the quintile of F distribution of order $q = \varepsilon$, the confidence coefficient and with degrees of freedom $m_1 = 2(k + 1)$ and $m_2 = 2(n - k)$

and one-sided confidence region with a lower limit as

$$p_1 = \frac{k}{k + (n - k + 1)F_{m3,m4,\mathrm{e}}}$$

and the confidence region

$$I = [p_1, 1]$$

with $m_3 = 2(n - k + 1)$; $m_4 = 2k$.

- A two-sided confidence region after Neumann is tabulated in Muller et al. (1973) for $n = 1$ to $n = 30$. These confidence limits are represented in Figure 3.4. Larger values of n are covered by the asymptotic relation

$$\begin{matrix} p_0 \\ p_1 \end{matrix} = \frac{1}{n + \lambda_q^2} \left(k + \frac{\lambda_q^2}{2} \mp \lambda_q \sqrt{\frac{k(n-k)}{n} + \frac{\lambda_q^2}{4}} \right)$$

and the confidence interval

$$I = [P_0, P_1]$$

where λ_q is the quantile of the standardized *normal* distribution of order $q = (1 + \sigma)/2$.

3.2.3.1.3 Poisson Distribution

Poisson distribution is derived from the binomial distribution when n tends towards infinity, and at the same time, $n_p = \lambda$ remains constant:

$$\lim_{n \to \infty,\, np=1} \binom{n}{k} p^k (1-p)^{n-k} = \frac{\lambda}{k!} \exp(-\lambda) \quad \text{with} \quad k = 1,2,\ldots$$

Since the probability p is very small for large n and $n_p = \lambda = \text{constant}$, the Poisson distribution describes rare events.

$$\text{Probability density function} \quad p(k) = P(x = k) = \frac{\lambda^k}{k!} \exp(-\lambda) \tag{3.17}$$

$$\text{Cumulative probability} \quad P(X \leq k) = \sum_{m=0}^{k} \frac{\lambda^m}{m!} \exp(-\lambda) \tag{3.18}$$

$$\text{Parameter} \quad \lambda$$

$$\text{Expectation} \quad EX = \lambda \tag{3.19}$$

$$\text{Variance} \quad D^2X = \lambda, \text{equal to the expectation EX} \tag{3.20}$$

$$\text{Point estimate for } \lambda \quad \lambda = \frac{1}{n} \sum_{1}^{n} x_i \tag{3.21}$$

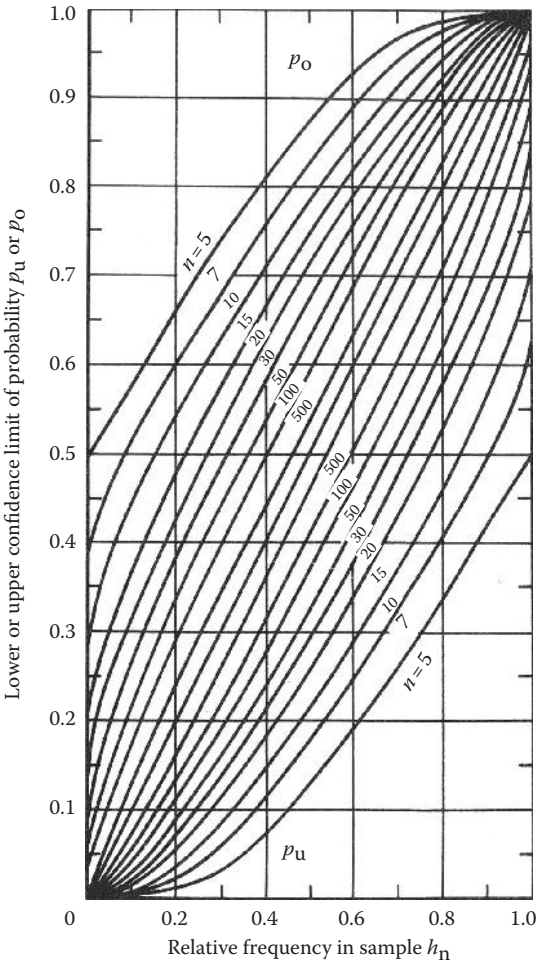


FIGURE 3.4 Confidence limits for unknown probabilities after Neumann, with a confidence coefficient ε = 0.95. (From Muller, H.P. et al., *Tafeln der Mathematischen Statistik*, VEB Fachbuchverlag, Leipzig, Germany, 1973.)

Confidence estimate for λ

- One-sided confidence intervals

$$I = \left[\frac{l_{k,e}}{n}, \bullet\right) \quad \text{and} \quad I = \left[0, \frac{\bar{l}_{k,e}}{n}\right)$$

- Two-sided confidence intervals

$$I = \left[\frac{l_{k,(1+2)/2}}{n}, \frac{\bar{l}_{k,(1+2)/2}}{n}\right)$$

where $l_{k,e}$ and $\bar{l}_{k,e}$ are, respectively, the lower and upper confidence limits.

The confidence factors are related to the quantile of the χ^2 distribution.

3.2.3.2 Continuous Distributions

In continuous distributions, the variable can take any values, the relative frequency of which is defined by a density function $f(x)$. Typical continuous distributions are *Maxwell*, *normal*, *extreme values*, and *Weibull*.

3.2.3.2.1 Maxwell Distribution

Maxwell distribution was introduced by J.C. Maxwell to describe the distribution of velocities of gas molecules under equilibrium conditions, presented in Chapter 4. Maxwell distribution is one of the rare cases where the statistical distribution is derived directly from a physics theory, in this case the kinetic theory of gases. However, it is rarely used as a statistical model, being too specifically identified to gaseous kinetic parameters. The probability density of the velocity of the gas molecules, $f(v)$, can be expressed in terms of the mass and temperature of the gas according to

$$f(v) = \frac{4}{\sqrt{\pi}}\left(\frac{M}{2kT}\right)^{3/2} v^2 \exp\left(-\frac{Mv^2}{2kT}\right) \tag{3.22}$$

The cumulative Maxwell distribution is

$$P(v) = \int_0^c f(v)\mathrm{d}v = \frac{4}{\sqrt{\pi}}\left(\frac{M}{2kT}\right)^{3/2} \int_0^c v^2 \exp\left(-\frac{Mv^2}{2kT}\right)\mathrm{d}v \tag{3.23}$$

where

k is the Boltzmann constant
v is the velocity
M is the mass of the molecule
T is the absolute temperature

One can obtain the following characteristic parameters:

∑ Most probable velocity $c_\mathrm{p} = \sqrt{\frac{2kT}{M}}$

∑Average velocity $c_\mathrm{av} = \frac{2}{\sqrt{\pi}} c_\mathrm{p} = 2\sqrt{\frac{2kT}{\pi M}}$

∑Effective velocity $c_\mathrm{rms} = \sqrt{\frac{3}{2}} c_\mathrm{p} = \sqrt{\frac{3kT}{M}}$

3.2.3.2.2 Normal Distribution

Of the various distribution functions, the *normal* function is probably the most familiar. The probability density, $f(u)$, and the cumulative probability, $P(u)$, are defined according to (Miller and Freund, 1965)

$$f(u) = \frac{1}{\sigma\sqrt{2\pi}} \exp\left[-\frac{1}{2}\left(\frac{x - U_\mathrm{m}}{\sigma}\right)^2\right] \tag{3.24}$$

$$P(u) = \frac{1}{\sigma\sqrt{2\pi}} \int_0^u \exp\left[-\frac{1}{2}\left(\frac{x - U_\mathrm{m}}{\sigma}\right)^2\right]\mathrm{d}x \tag{3.25}$$

where

U_m is the mean value
σ is the standard deviation

By defining a normalized variable as $x_\mathrm{n} = (x - U_\mathrm{m})/\sigma$, the expressions of the probability density and cumulative probability are simplified to

$$f(u_\mathrm{n}) = \frac{1}{\sqrt{2\pi}} \exp\left(-\frac{1}{2} x_\mathrm{n}^2\right) \tag{3.26}$$

$$P(u_n) = \frac{1}{\sqrt{2\pi}} \int_{-\infty}^{u_n} \exp\left(-\frac{1}{2} x_n^2\right) dx_n \tag{3.27}$$

Figure 3.5 illustrates the variations of the probability density and the cumulative probability as a function of the normalized variable u_n, expressed in units of σ, the standard deviation. One can verify the following properties of the *normal* distribution:

- Most probable voltage: $U_p = U_m$.
- Median voltage: $U_{50\%} = U_m$.
- The probability density is symmetrical with respect to U_m.

$$\text{Parameters} \quad \mathtt{m}, \mathtt{s}^2$$

$$\text{Notation} \quad N(m; s_2) = F(x; m; s_2)$$

$$\text{Expectation} \quad \mathrm{EX} = \mathtt{m} \tag{3.28}$$

$$\text{Variance} \quad D^2X = \mathtt{s}^2 \tag{3.29}$$

Point estimate

$$\text{For } \mathtt{m}: \quad \mathtt{m} = \bar{X} = \frac{1}{n} \sum_{i=1}^{n} X_i = X_{50} \tag{3.30}$$

$$\text{For } \mathtt{s}^2: \quad \mathtt{s}^2 = \frac{1}{n-1} \sum_{i=1}^{n} (X_i - \bar{X})^2 = (X_{50} - X_{16})^2 \tag{3.31}$$

where X_{50} and X_{16} are quantiles of the experimental distribution containing n measurements.

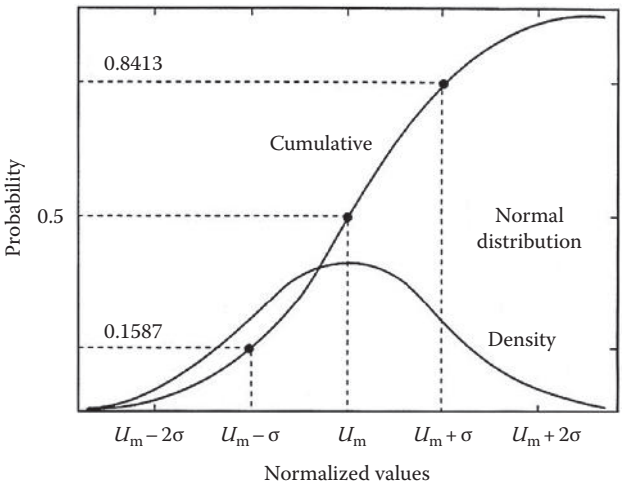


FIGURE 3.5 *Normal* distribution.

Confidence estimate for μ can be defined from the *t* distribution, and for σ^2 from the χ^2 distribution, respectively

- For μ: one-sided with upper limits, $I\,[-\infty, g_0]$, and lower limit, $I\,[g_1, +\infty]$

$$\text{with} \quad g_0 = \bar{X} + t_{n-1,\varepsilon}\frac{s}{\sqrt{n}} \quad \text{and} \quad g_1 = \bar{X} - t_{n-1,\varepsilon}\frac{s}{\sqrt{n}}$$

  Two-sided limits: $I\,[g_1, g_0]$

$$\text{with} \quad g_0 = \bar{X} + t_{n-1,(1+\varepsilon)/2}\frac{s}{\sqrt{n}} \quad \text{and} \quad g_1 = \bar{X} - t_{n-1,(1+\varepsilon)/2}\frac{s}{\sqrt{n}}$$

- For σ^2: one-sided with upper limits, $I\,[-\infty, g_0]$, and lower limit, $I\,[g_1, +\infty]$

$$\text{with} \quad g_0 = \frac{(n-1)s^2}{c^2_{n-1,1-\varepsilon}} \quad \text{and} \quad g_1 = \frac{(n-1)s^2}{c^2_{n-1,\varepsilon}}$$

  Two-sided limits: $I\,[g_1, g_0]$

$$\text{with} \quad g_0 = \frac{(n-1)s^2}{c^2_{n-1,(1-\varepsilon)/2}} \quad \text{and} \quad g_1 = \frac{(n-1)s^2}{c^2_{n-1,(1+\varepsilon)/2}}$$

3.2.3.2.3 Extreme Value Distribution

Introduced by Gumbel E.J. in his study on flooding, this distribution function is suitable for describing phenomena having large return periods. The probability density, $f(u)$, and the cumulative probability, $P(u)$, of the *extreme value* distribution are defined according to (Gumbel, 1954)

$$f(u) = \frac{1}{a}\exp\left\{-\exp\left[\frac{u-U_0}{a}\right]\right\}\cdot\exp\left[\frac{u-U_0}{a}\right] \tag{3.32}$$

$$P(u) = 1 - \exp\left\{-\exp\left[\frac{u-U_0}{a}\right]\right\} \tag{3.33}$$

where

U_0 is the position parameter

α is the form parameter

By defining a normalized variable as $u_n = (u - U_0)/\alpha$, the expressions of the probability density and cumulative probability are simplified to

$$f(u_n) = \exp\{-\exp(u_n)\}\cdot\exp(u_n) \tag{3.34}$$

$$P(u_n) = 1 - \exp[-\exp(u_n)] \tag{3.35}$$

Figure 3.6 illustrates the variations of the probability density and the cumulative probability as a function of the normalized variable, $(u - U_0)/\alpha$. One can verify the following properties of the *extreme value* distribution:

- At $u = U_0$, $P(U_0) = 0.632121$.
- Most probable voltage: $U_p = U_0$.

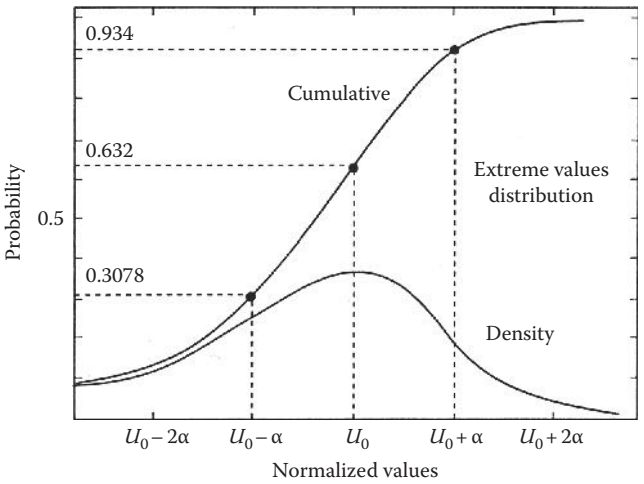


FIGURE 3.6 *Extreme value* distribution.

- Median voltage: $U_{50\%} = U_0 + \alpha \ln(\ln 2)$.
- The density function is not symmetrical but slightly skewed at low probabilities ($U < U_0$).

$$\text{Parameters} \quad U_0 \text{ and } a$$

$$\text{Expectation} \quad EX = U_0 - a\lambda \tag{3.36}$$

with $\lambda = 0.5772$, Euler's constant.

$$\text{Variance} \quad D^2X = \frac{1}{6}\pi^2 a^2 \tag{3.37}$$

$$\text{Point estimate} \quad U_0 = X_{63} \quad \text{and} \quad a = \frac{1}{3}(X_{63} - X_{05}) \tag{3.38}$$

3.2.3.2.4 Weibull Distribution

Introduced by Weibull W., this distribution function is particularly suitable to describe phenomena with a threshold value, U_0, below which the probability of occurrence is identically zero. The probability density, $f(u)$, and the cumulative probability, $P(u)$, of the Weibull distribution are defined according to (Weibull, 1951)

$$f(u) = \frac{b}{a}\left(\frac{u - U_0}{a}\right)^{b-1} \exp\left[-\left(\frac{u - U_0}{a}\right)^{b}\right] \tag{3.39}$$

$$P(u) = 1 - \exp\left[-\left(\frac{u - U_0}{a}\right)^{b}\right] \tag{3.40}$$

where
U_0 is the position parameter
α is the scale parameter
β is the form parameter

By defining a normalized variable as $u_n = (u - U_0)/\alpha$, the expressions of the probability density and cumulative probability are simplified to

$$f(u_n) = \beta(u_n)^{\beta-1} \exp\left[-(u_n)^{\beta}\right] \tag{3.41}$$

$$P(u_n) = 1 - \exp\left[-(u_n)^{\beta}\right] \tag{3.42}$$

Figure 3.7 illustrates the variations of the probability density and the cumulative probability as a function of the normalized variable, $u_n = (u - U_0)/\alpha$. One can verify the following properties of the Weibull distribution:

- There exists a threshold value U_0 such that the probability of occurrence $P(u)$ is identically zero for values of $u \leq U_0$.
- Most probable voltage: $U_p = U_0 + \alpha$.
- Median voltage: $U_{50\%} = U_0 + \alpha \exp\left[\dfrac{\ln(\ln 2)}{\beta}\right]$.
- The scale parameter α is a measure of the dispersion of the distribution.
- The probability density function is not symmetrical.

Special case: Exponential distribution is characterized by $U_0 = 0$, $\beta = 1$, and $\alpha = 1/\lambda$.

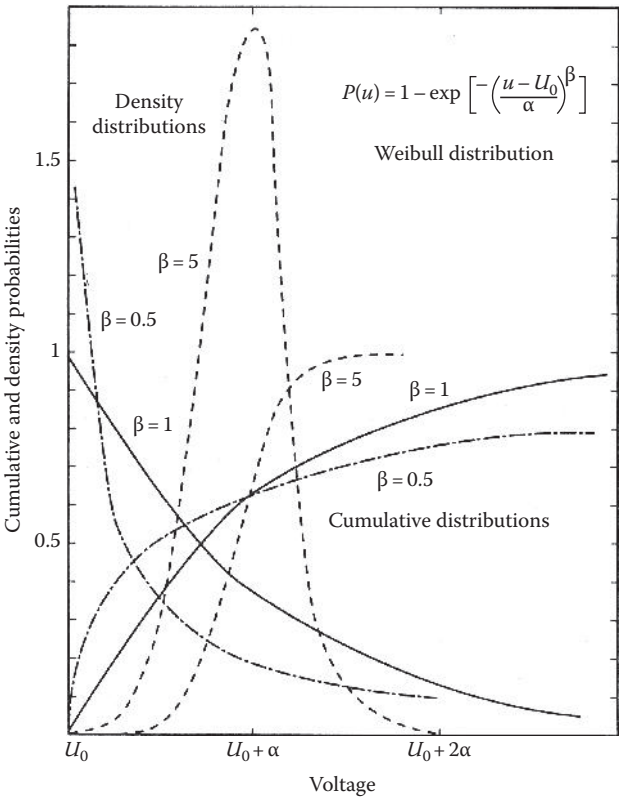


FIGURE 3.7 Weibull distribution.

Parameters U_0, α, and β

$$\text{Expectation} \quad EX = U_0 + a\Gamma\left(\frac{1}{b} + 1\right) \tag{3.43}$$

where $\Gamma\left(\frac{1}{b} + 1\right)$ is the Gamma function.

For the exponential distribution,

$$EX = a = \frac{1}{l} \tag{3.44}$$

$$\text{Variance} \quad D^2X = a^2\left[\Gamma\left(\frac{2}{b} + 1\right) - \Gamma^2\left(\frac{1}{b} + 1\right)\right] \tag{3.45}$$

For the exponential distribution,

$$D^2X = a^2 = \frac{1}{l^2} \tag{3.46}$$

3.3 Estimation of the Population Distribution

One of the main applications of statistical functions is the definition of a statistical model to adequately represent the complete population from a given set of experimental data, termed as sample of the population. In more specific terms, since the experimental sample is known, its statistic parameters are readily defined, and the question becomes how reliable it is to take the sample's statistic parameters as representatives of complete population. In addition, since the type of the population is not known, it is usually assumed and validated with the sample population. These questions are object of a number of statistical tests; the most significant will be discussed in the following:

- Randomness test
- Using the sample's statistic parameters
- Distribution test
- μ-Selection test

3.3.1 Randomness Test

Statistical analysis relies on the assumption that the experimental sample is random, that is, the measured data are independent and identically distributed according to the distribution of the population. This condition can be verified by observing the variation in chronological order of the data. A random sample will show oscillations of the data around a median value, with no tendency to steadily increase or decrease. This can be visualized by graphically representing the data in chronological order of their occurrence.

3.3.2 Using the Sample's Statistic Parameters

Once a test sample has been obtained, a natural approach would be to consider the sample's statistic parameters as representatives of the population statistic distribution. How reliable is this approach? Consider the case where different samples are drawn from the same population and their statistical parameters evaluated. One obtains then new populations for each of the statistic parameters.

3.3.2.1 Sample Means

The population of the sample means $\bar{X}$ will have an expected value:

$$E(\bar{X}) = E\left(\frac{1}{n}\sum (\bar{X}_i)\right) = \frac{1}{n}\sum E(X_i) = \mu \tag{3.47}$$

The mean value of the population of sample means $\bar{X}$ is also the mean value of the population x. Noting that the independence of the sample data permits taking the sum of the variances for the variance of the sum, its variance is

$$\mathrm{var}(\bar{X}) = \mathrm{var}\left(\frac{1}{n}\sum X_i\right) = \frac{1}{n}\sum \mathrm{var}(X_i) = \frac{\sigma^2}{n}$$

The variance of the sample means decreases with n and approaches zero for large values of n. In other words, the mean of a large sample of experimental data is representative of the population mean.

3.3.2.2 Sample Variance

The sample variance σ^2 is defined according to

$$(n-1)\sigma^2 = \sum (X - \bar{X})^2$$

which can be rewritten as

$$(n-1)\sigma^2 = \sum (X-\mu)^2 - n(\bar{X}-\mu)^2$$

Taking the expected value on both sides yields

$$(n-1)E(\sigma^2) = \sum E\left[(X-\mu)^2\right] - nE\left[(\bar{X}-\mu)^2\right]$$

$$= \sum \sigma^2 - n\frac{\sigma^2}{n} = (n-1)\sigma^2$$

and hence, the expected value of the sample variance is the same as the variance of the population x:

$$E(\sigma^2) = \sigma^2 \tag{3.48}$$

The variance of σ^2 can be shown to be (Lindgren and McElrath, 1959)

$$\mathrm{var}\left(\sigma_x^2\right) \approx \frac{n}{n-1}\frac{E\left[(X-\mu)^2\right] - \sigma^2}{n-1}$$

which will approach zero for large values of n. The variance of a large sample is representative of the population variance.

The statistic parameters of the experimental sample will be representatives of the population of x when its size n is sufficiently large. Figure 3.8 shows the influence of the sample size on its distribution. One can see that as the sample size increases, the distribution becomes narrower and little improvement is noticed between samples of sizes between n = 50 and n = 100. A practical approach to define the sample size is to have its cumulative probability distribution cover an adequate range of probabilities. Typically,

- n = 10, the range of relative frequencies is $P_{\min}$ = 9.09% to $P_{\max}$ = 90.91%.
- n = 100, the range of relative frequencies is $P_{\min}$ = 0.990% to $P_{\max}$ = 99.01%.

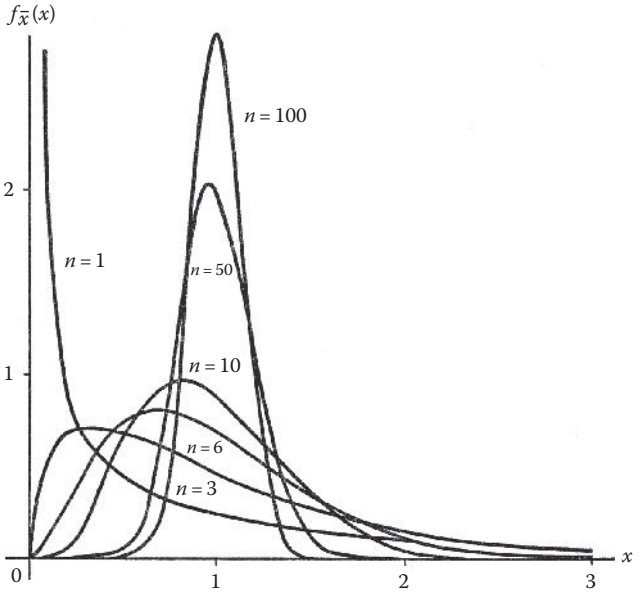


FIGURE 3.8 Illustration of the effect of sample size n on the distribution of the sample mean $\bar{X}$. (From Lindgren, B.W. and McElrath, G.W., *Introduction to Probability and Statistics*, MacMillan Company, New York, 1959.)

3.3.3 Confidence Interval

In order to obtain a measure of the precision of an estimate α* of an unknown parameter α, we try to find two positive parameters δ and ε such that the probability that the parameter a is included between the limits α* ± δ is equal to 1 − ε:

$$P(a^* - \delta < a < a^* + \delta) = 1 - \varepsilon$$

The range ($a^* - \delta$, $a^* + \delta$) is known as the confidence interval. The parameter 1 − ε is the confide NCE coefficient of the interval. And 100 (1 − ε) may be termed the degree of confidence.

3.3.3.1 One-Sided Test

The statistical null hypothesis is

$$H_0: \mu \le \mu_0 \text{ against the alternative of } H_1: \mu > \mu_0$$

The probability of accepting H_0, that is, the probability that the sample mean $\bar{X}$ will not exceed μ_0 in the case of large samples or for *normal* population, is

$$P(\bar{X} < m_0) = 1 - F\left(\frac{m - m_0}{s/\sqrt{n}}\right) = 1 - \frac{1}{s\sqrt{2p/n}} \int_{-\infty}^{m} \exp\left[-\frac{1}{2}\left(\frac{x - m_0}{s/\sqrt{n}}\right)^2\right] dx \tag{3.49}$$

Noting that Equation 3.49 is a *normal* distribution curve reversed, one can verify the effect of n and μ_0 on the characteristic function defined by (3.49):

- Changing μ_0 will shift the characteristic curve horizontally.
- The sample size determines the sampling variability in $\bar{X}$: an increase in n will steepen the characteristic curve around μ_0, approaching a unit impulse for large values of n.

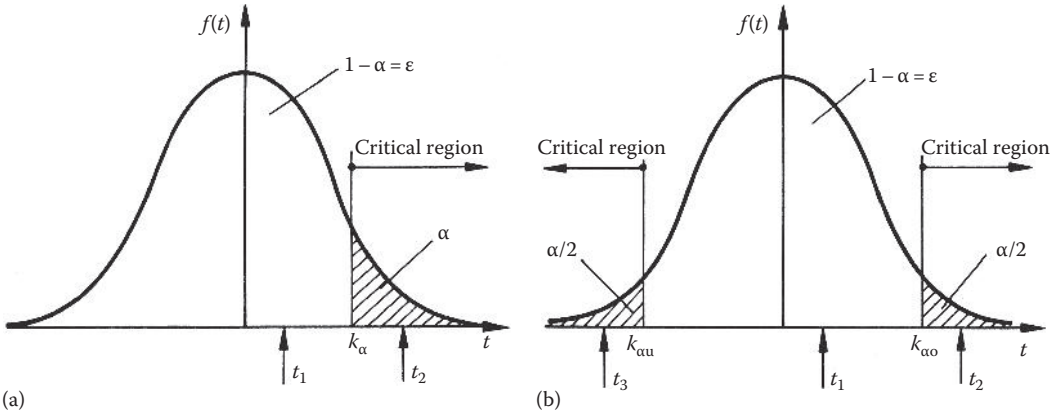


FIGURE 3.9 Illustration of (a) one- and (b) two-sided tests. (From Hauschild, W. and Mosch, W., *Statistical Techniques for High Voltage Engineering*, Peter Peregrinus Ltd., London, U.K., 1992.)

By specifying an accepted level α, taken as the probability of rejection when H_0 is true,

$$a = P(\text{reject } H_0) = P(\bar{X} \geq m_0) = F\left(\frac{m - m_0}{s/\sqrt{n}}\right) = \frac{1}{s\sqrt{2p/n}} \int_{-\infty}^{m} \exp\left[-\frac{1}{2}\left(\frac{x - m_0}{s/\sqrt{n}}\right)\right] dx$$

a critical region will be defined for rejection of μ_0, the population mean, as illustrated in Figure 3.9a.

3.3.3.2 Two-Sided Test

If the statistic null hypothesis is

$$H_0: \quad m = m_0 \quad \text{against the alternative of} \quad H_1: \quad m \neq m_0$$

In this case, the critical region for rejecting H_0 is $|\bar{X} - \mu_0| > K$.
For a large sample or for a *normal* population, the probability of accepting H_0 is

$$P(|\bar{X} - m_0| < K) = F\left(\frac{m_0 + K - m}{s/\sqrt{n}}\right) - F\left(\frac{m_0 - K - m}{s/\sqrt{n}}\right) \tag{3.50}$$

considered as a function of μ for a fixed critical region and fixed sample size. By defining the significance level α, taken as the probability of rejection when H_0 is true, a critical region will be defined for rejection of H_0, which is composed of two parts as illustrated in Figure 3.9b.

$$a = P(\text{reject } H_0) = P(|\bar{X} - m_0| > K) = 2\left[1 - F\left(\frac{K}{s/\sqrt{n}}\right)\right] = 2F\left(-\frac{K}{s/\sqrt{n}}\right) \tag{3.51}$$

From Equations 3.50 and 3.51, one gets the following relation:

$$P\left(\left|\bar{X} - m\right| < K\right) = 1 - a$$

which can be rewritten as

$$P(\bar{X} - K < m < \bar{X} + K) = 1 - a \tag{3.52}$$

which states that the inequality $(\bar{X} - K < \mu < \bar{X} + K)$ has a probability of $(1 - \alpha)$. However, this, by definition, is the $(1 - \alpha)$ confidence interval for the population mean μ as shown in Figure 3.9b.

3.3.4 Distribution Test

A population of experimental data does not, in general, have a specific type of distribution. Therefore, common practice assumes a type of distribution function, and its adequacy to represent the experimental set of data is statistically tested.

3.3.4.1 Chi-Square Test

It is the oldest test *for goodness of fit* still in use today. It allows evaluation whether an assumed population distribution or distribution type is consistent with the data of a random sample. The null hypothesis in this case is as follows:

- For a continuous variable: H_0—the population density function is $f(x)$.
- For a discrete variable: H_0—the population probability function is $p(x)$.

The alternative hypothesis H_1 is the population density or the probability function is not the one considered in H_0.

Consider a random sample of size n; the frequency of the value x_i in the sample is p_{xi}. If the population is discrete and defined by a density probability function $f(x) = P(X = x_i)$, then the expected value of p_{xi} is n $f(x_i)$. The deviations from the population density function can be expressed by a statistical variable χ^2 defined as

$$\chi^2 = \sum_{1}^{k} \frac{[p_{xi} - nf(x_i)]^2}{nf(x_i)} \tag{3.53}$$

It can be shown that for large samples, the variable χ^2 has approximately the chi-square distribution with $(k - 1)$ degrees of freedom, k being the number of distinct possible values. The rejection region is taken to correspond to $\chi^2 > k$. By selecting a significance level α, taken as the probability for rejecting H_0, a critical region for rejection of H_0 can be determined from the tabulated table of the chi-square function. A decision on the adequacy of the representation of the population distribution function by the random sample can be taken based on the value of χ^2 with respect to the rejection limit.

3.3.4.2 Graphical Test

It is another way of evaluating the adequacy of a distribution function to represent a random sample. It has the advantage of being relatively simple and offers a visual evaluation of the adequacy of the model. The graphical test is based on the linearization of a typical distribution by the use of appropriate coordinate scales. An experimental distribution of the same type will be represented by a straight line, whose characteristics determine the parameters of the statistical model, the most representative of the experimental distribution. It should be noted that the graphical solution will require special graphic paper, one for each distribution function. The graphical linearization of a statistical distribution function, $y = P(u)$, transforms the coordinates y and u into new variables z and v, in a way that makes the relation between z and v linear (Figures 3.10 through 3.12) according to

$$z = av + b \tag{3.54}$$

where a and b are characteristic constants defining the straight line.

Let $z = g(y)$ and $v = h(u)$ be the transform functions. A graphical linearization of the function $y = P(u)$ corresponds then to defining these transform functions. By replacing these transform functions in Equation 3.54, one gets

$$z = g(y) = g[P(u)]$$

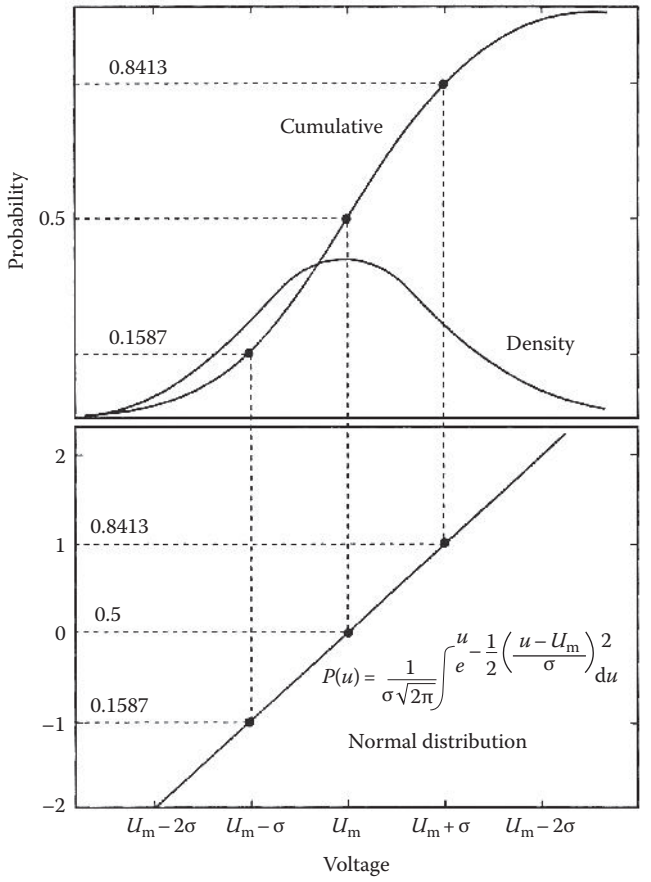


FIGURE 3.10 Graphical representation of the *normal* distribution.

and

$$v = h(u) = \frac{z - b}{a} = \frac{g\left[P(u)\right] - b}{a}$$

For the three statistical distributions discussed, one can observe that

- The normalized variable u_n is given by $u_n = P^{-1}(y)$
- A linear relation already exists between u_n and u according to $u_n = (u - U_0)/\alpha$

One can show that selecting the transform functions $g(y)$ and $h(u)$ to be

$$z = g(y) = P^{-1}(y) = u_n \tag{3.55}$$

and

$$v = h(u) = u \tag{3.56}$$

a linear relation between the two transposed variables z and v is ensured according to Equation 3.54. Equations 3.55 and 3.56 form the basis for defining graphical paper sheets, which are extensively used in statistical analysis; the most widely used graphical papers will be discussed in the following sections.

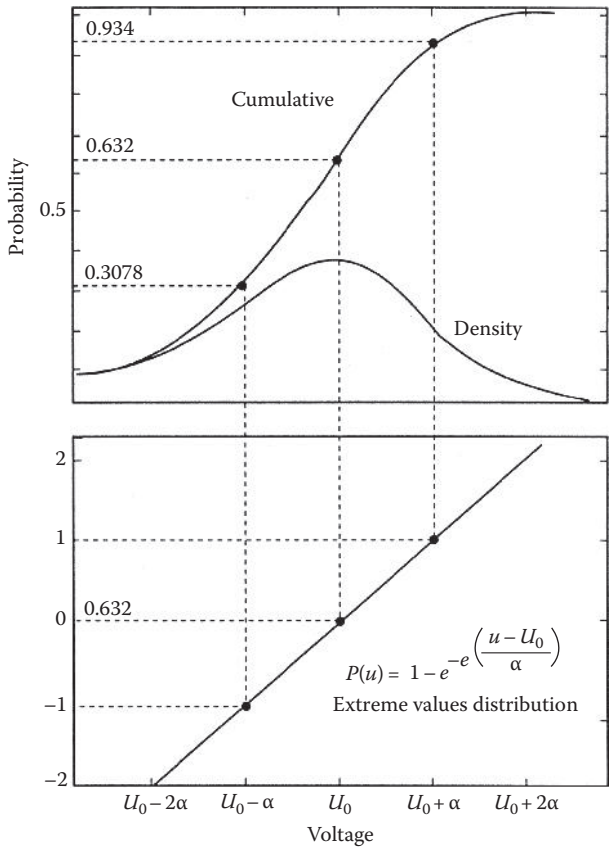


FIGURE 3.11 Graphical representation of the *extreme value* distribution.

3.3.4.2.1 Normal Graphical Paper

When the distribution function is of the *normal* type, the transform functions are

$$z = f^{-1}\left[\frac{1}{\sqrt{2\pi}}\int_{-\infty}^{u_n}\exp\left(-\frac{1}{2}x_n^2\right)dx_n\right] = u_n \tag{3.57a}$$

and

$$v = u \tag{3.57b}$$

where f^{-1} is the inverse function of the distribution f.

Referring to Figure 3.10, the linear relation describing the *normal* distribution that best fits the experimental distribution is

$$z = u_n = \frac{u - U_m}{\sigma} = \frac{1}{\sigma}u - \frac{U_m}{\sigma} = av + b$$

The following observations can also be made:

- At $P = 0.5$, $v = 0$, $u = U_m$
- At $P = 0.8413$, $v = 1$, $u = U_m + \sigma$
- At $P = 0.1587$, $v = -1$, $u = U_m - \sigma$

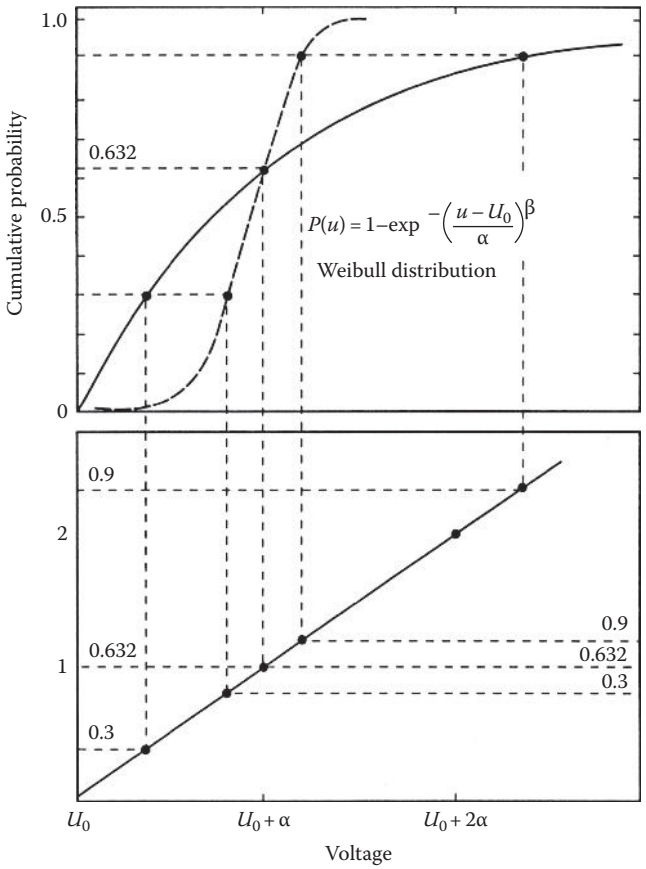


FIGURE 3.12 Graphical representation of the Weibull distribution with known β.

This allows a quick evaluation of the characteristic parameters of a *normal* distribution for a given set of experimental data.

3.3.4.2.2 Extreme Value Graphical Paper

When the distribution function is of the *extreme value* type, the transform functions are

$$z = g^{-1}(y) = \ln[-\ln(1-y)] = u_n \tag{3.58a}$$

and

$$v = u \tag{3.58b}$$

Referring to Figure 3.11, the linear relation describing the *extreme value* distribution that best fits the experimental distribution is

$$z = u_n = \frac{u - U_0}{a} = \frac{1}{a}u - \frac{U_0}{a} = av + b$$

And the following observations can be made:

- At $P = 0.6321$, $v = 0$, $u = U_0$
- At $P = 0.9340$, $v = 1$, $u - U_0 = \alpha$
- At $P = 0.3078$, $v = -1$, $U_0 - u - \alpha$

This allows a quick evaluation of the characteristic parameters of an *extreme value* distribution representing a given set of experimental data.

3.3.4.2.3 Weibull Graphical Paper

When the distribution function is of the Weibull type, the transform functions are

$$z = g^{-1}(y) = \exp\left[\frac{1}{b}\ln[-\ln(1-y)]\right] = u_n \tag{3.59a}$$

and

$$v = u \tag{3.59b}$$

Referring to Equation 3.40, it can be seen that the Weibull distribution is characterized by three parameters: U_0, α, and β. As a result, there is no universal representation for this type of distribution function on graphical paper (which is necessarily bidimensional). Any graphical presentation of the Weibull distribution implies that at least one of the three parameters is known. Two particular cases will be discussed in the following, as related to the cases where the form parameter, β, or the position parameter, U_0, is known.

Form parameter β *is known*: When the form parameter β is known, the transposing functions are defined according to Equation 3.59, the Weibull distribution is represented by a straight line when the probability scale is defined according to Equation 3.59a, and the scale for the independent variable is linear according to Equation 3.59b. The linear equation of the straight line is (Figure 3.12)

$$z = u_n = \frac{u - U_0}{a} = \frac{1}{a}u - \frac{U_0}{a} = av + b$$

The following observations can also be made:

- At $p = 0$, $v = 0$, $u = U_0$
- At $p = 0.6321$, $v = 1$, $u = U_0 + \alpha$

which allows a quick evaluation of the characteristic parameters of a Weibull distribution representing a given set of experimental data, namely, the position and scale parameters, U_0 and α, respectively. The main inconvenience of this representation is that the probability scale varies with the value of β, which means that a different graphical paper will be required for each value of β.

Position parameter U_0 *is known*: If the position parameter U_0 is known, a more convenient representation of the Weibull distribution is obtained by taking the logarithm of z. One then gets (Figure 3.13)

$$\ln z = \frac{1}{b}\ln[-\ln(1-y)] = \ln(u_n) \tag{3.60a}$$

and

$$v = \ln\left[\frac{u - U_0}{a}\right] = \ln(u - U_0) - \ln a \tag{3.60b}$$

The Weibull distribution is again represented by a straight line when the probability scale is according to Equation 3.60a, and the scale for the independent variable is logarithmic according to Equation 3.60b. This linearization of the Weibull distribution assumes that the position parameter U_0 is known, and the linear equation of the straight line is

$$\ln\left[-\ln(1-y)\right] = b\ln(u_n) = b\ln\left[\frac{u - U_0}{a}\right] = b\ln(u - U_0) - b\ln a = av + b$$

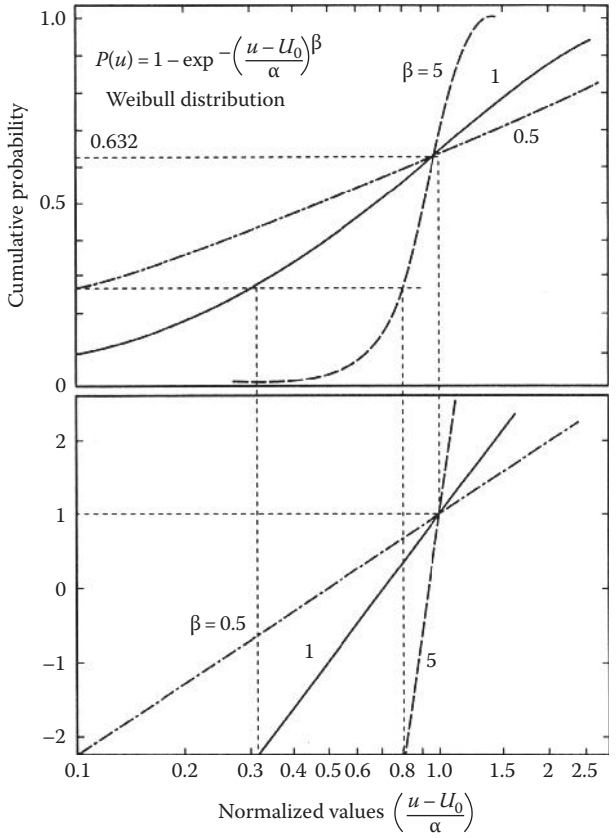


FIGURE 3.13 Graphical representation of Weibull distribution with known U_0.

which allows a quick evaluation of the characteristic parameters of a Weibull distribution representing a given set of experimental data, namely, the scale and form parameters α and β, respectively. In Figure 3.13b, the independent variable is normalized with respect to U_0 and α; the point corresponding to the probable value ($v = 1$, $P = 0.6321$) is common to all distributions represented, while the slope of the straight lines is proportional to the form parameter β. It should be pointed out here that the independent variable is not u, but $(u - U_0)$. Only in the particular case corresponding to $U_0 = 0$, often used and referred to in practice as two-parameter Weibull distribution, the independent variable, u, is represented directly on a logarithmic scale.

3.3.4.3 Linear Regression Analysis

The linearization of the distribution function by means of appropriate coordinate systems allows the use of a powerful tool of statistical analysis, linear regression. This approach is particularly interesting with the widespread use of programmable calculators and personal computers. Indeed, since the graphical representation of the transposed distribution is a straight line,

$$z = av + b$$

linear regression can be put to good use to determine the equation of the straight line that is most representative of the experimental distribution. Using linear regression, we should obtain the parameters a and b according to (Miller and Freund, 1965)

$$a = \frac{\hat{\mathrm{A}}\, v_i z_i - \dfrac{\hat{\mathrm{A}}\, v_i \hat{\mathrm{A}}\, z_i}{n}}{\hat{\mathrm{A}}\, v_i^2 - \dfrac{(\hat{\mathrm{A}}\, v_i)^2}{n}} \quad \text{and} \quad b = \frac{\hat{\mathrm{A}}\, z_i}{n} - a\frac{\hat{\mathrm{A}}\, v_i}{n} \tag{3.61}$$

The quality of the correspondence of the straight line in (i.e., how good a fit we get) representing the experimental distribution is described by the correlation coefficient r^2 that is given by

$$r^2 = \frac{\left[\sum v_i z_i - \frac{\sum v_i \sum z_i}{n}\right]^2}{\left[\sum v_i^2 - \frac{(\sum v_i)^2}{n}\right] \cdot \left[\sum z_i^2 - \frac{(\sum z_i)^2}{n}\right]} \tag{3.62}$$

Regression analysis has the advantage of allowing a rapid and objective comparison of different statistical functions to represent a given set of experimental data.

3.3.4.3.1 Normal Distribution

When the distribution function is of the *normal* type, the transform functions are according to Equation 3.57. The characteristic parameters are derived from

$$U_{\mathrm{m}} = -\frac{b}{a} \quad \text{and} \quad \mathtt{s} = \frac{1}{a} \tag{3.63}$$

3.3.4.3.2 Extreme Value Distribution

When the distribution function is of the *extreme value* type, the transposing functions are according to Equation 3.58. The characteristic parameters are derived from

$$U_0 = -\frac{b}{a} \quad \text{and} \quad \mathtt{a} = \frac{1}{a} \tag{3.64}$$

3.3.4.3.3 Weibull Distribution

When the distribution function is of the Weibull type, the transposing functions are according to Equation 3.58. The form parameter β is known and the other characteristic parameters are derived from

$$U_0 = -\frac{b}{a} \quad \text{and} \quad \mathtt{a} = \frac{1}{a} \tag{3.65}$$

On the other hand, when the transform functions are according to Equations 3.60a and b, the position parameter U_0 is known, and the other characteristic parameters are derived from

$$\mathtt{b} = a \quad \text{and} \quad \mathtt{a} = \exp\left[-\frac{b}{a}\right] \tag{3.66}$$

3.3.5 Adequacy Representation of a Statistical Model

In general, since statistical distribution functions are not dictated by the phenomenon evaluated, they are useful as long as they adequately describe the phenomenon investigated. Furthermore, several statistical models may adequately represent the same set of data. As a result, it is of great interest to define the most suitable statistical distribution for a given set of data. This is particularly true when there is a sufficiently large amount of data available; the adequacy of statistical functions to represent the results may determine the choice of a particular distribution function. Regression analysis then provides a simple means to compare the quality of the representation of the experimental data by different statistical distribution functions.

However, most of the times, the limited amount of data available does not allow a definite differentiation between the models. The choice of a particular statistical function is often arbitrary, dictated by how familiar the user is with the use of the statistical functions. This is why the familiar *normal* distribution is the most often used in statistical analysis of experimental data. Sometimes, a good understanding of

TABLE 3.1

Parameters of the Optimal Distributions

Distribution	U_m (U_0)	Sigma (Alpha)	Beta	Coefficient r^2
Experimental distribution	4.449	0.779	—	
Normal	4.498 kV/mm	0.941 kV/mm	—	0.977
Extreme values	4.967	0.828	—	0.933
Weibull—known U_0	2.5	2.265	2.398	0.985
Weibull—known β	3.133	3.47	3.6	0.99

the phenomenon evaluated can guide the choice of a statistical function. For example, one would use the Weibull distribution to analyze a physical phenomenon that is known to have a threshold value U_0, below which the probability of occurrence is nil.

For the set of data in Figure 3.1, different distribution functions are evaluated with respect to their accuracy in describing the experimental distribution. Their characteristic parameters are shown in Table 3.1 and in Figures 3.14 through 3.17. One can see that although the three distribution functions adequately describe the experimental distribution, the results allow finer discrimination among the distribution functions: The Weibull distribution is the most representative, whereas the *extreme value* distribution is the least representative. Because it is known that the breakdown voltage of an oil gap exhibits a threshold field value, the Weibull distribution represents a better choice.

In this context, it is worthwhile to establish the correspondence between the different most familiar distribution functions. This will help the reader select the most appropriate statistical function for a particular situation. Although a complete correspondence among the different distribution functions is not possible over the whole range of the independent variable, practical experience shows that it is possible to obtain adequate representations for a set of experimental data by different distribution functions. It is only required that the variations of the independent variable stay within a reasonable range, a condition often met in practice.

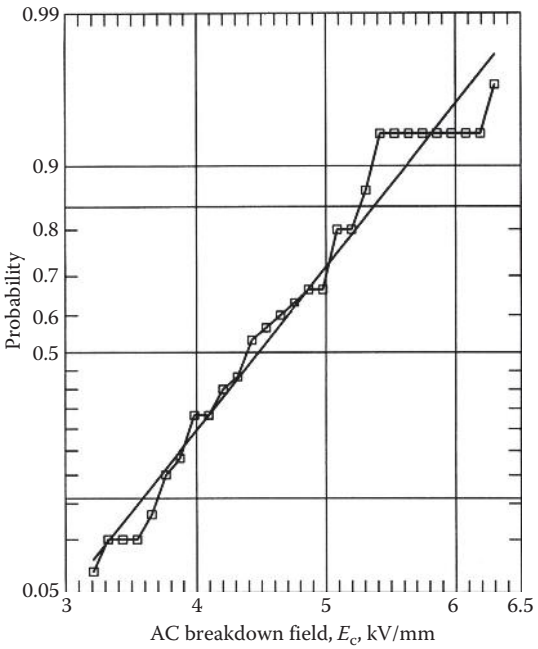


FIGURE 3.14 Representation of the experimental distribution of the ac breakdown field, E_c, of Figure 3.2, with a *normal* function.

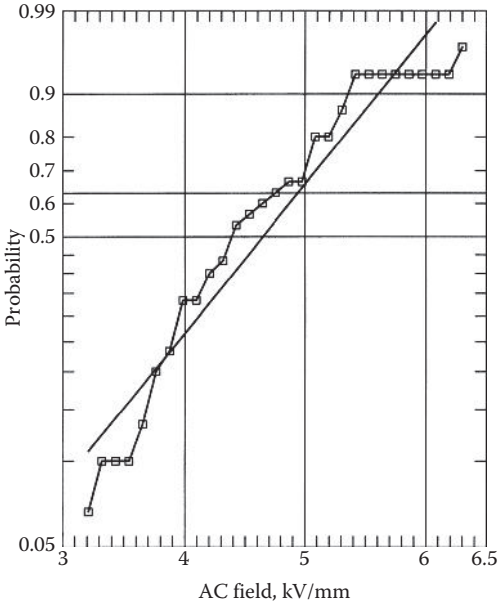


FIGURE 3.15 Representation of the experimental distribution of the ac breakdown field, E_c, of Figure 3.2, with *extreme value* function.

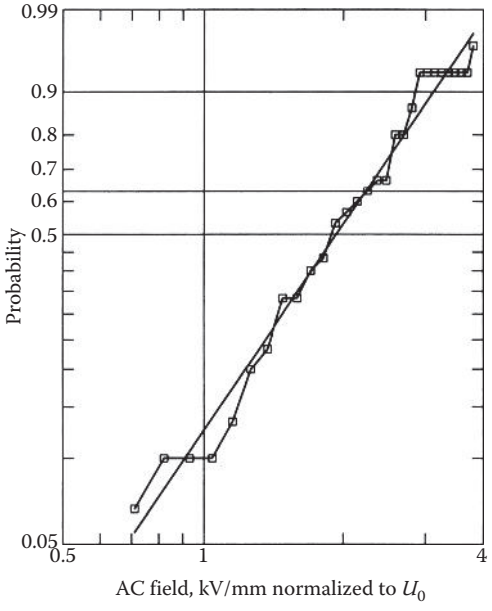


FIGURE 3.16 Representation of the experimental distribution of the ac breakdown field, E_c, of Figure 3.2, with a Weibull function with known U_0.

The problem is illustrated in the following text where we evaluate how adequately a *normal* distribution can be represented by an *extreme value* or Weibull distribution. More specifically, the exercise aims at defining the range of variations of the independent variable over which it is possible to represent the *normal* distribution by another distribution function, of the *extreme value* and Weibull types, and to define how adequate those statistical models are.

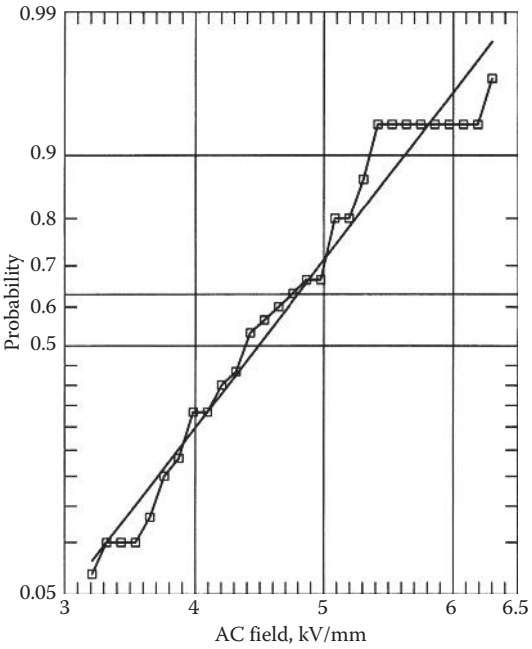


FIGURE 3.17 Representation of the experimental distribution of the ac breakdown field, E_c, of Figure 3.2, with a Weibull function with known β.

3.3.5.1 Extreme Value Distribution

Figure 3.18 compares the different approximations of the *normal* population by a distribution of the *extreme value* type. These distributions are selected in such a way as to intercept the *normal* distribution symmetrically with respect to the 50% probability level. Let U_1, U_2, P_1, and P_2 be, respectively, the voltages and probabilities at the interception points. The following relations may be derived:

$$P_1 = 1 - \exp\left[-\exp\left(\frac{U_1 - U_0}{a}\right)\right] \quad \text{and} \quad P_2 = 1 - \exp\left[-\exp\left(\frac{U_2 - U_0}{a}\right)\right]$$

Therefore,

$$\frac{U_1 - U_0}{a} = \ln[-\ln(1 - P_1)] \quad \text{and} \quad \frac{U_2 - U_0}{a} = \ln[-\ln(1 - P_2)]$$

It follows that

$$a = \frac{\ln[-\ln(1 - P_1)]}{U_1 - U_0} = \frac{\ln[-\ln(1 - P_2)]}{U_2 - U_0} \tag{3.67}$$

and

$$U_0 = \frac{\ln[-\ln(1 - P_2)]U_1 - \ln[-\ln(1 - P_1)]U_2}{\ln[-\ln(1 - P_1)] - \ln[-\ln(1 - P_2)]}$$

Since the interception points are selected symmetrically with respect to the 50% probability,

$$1 - P_2 = P_1$$

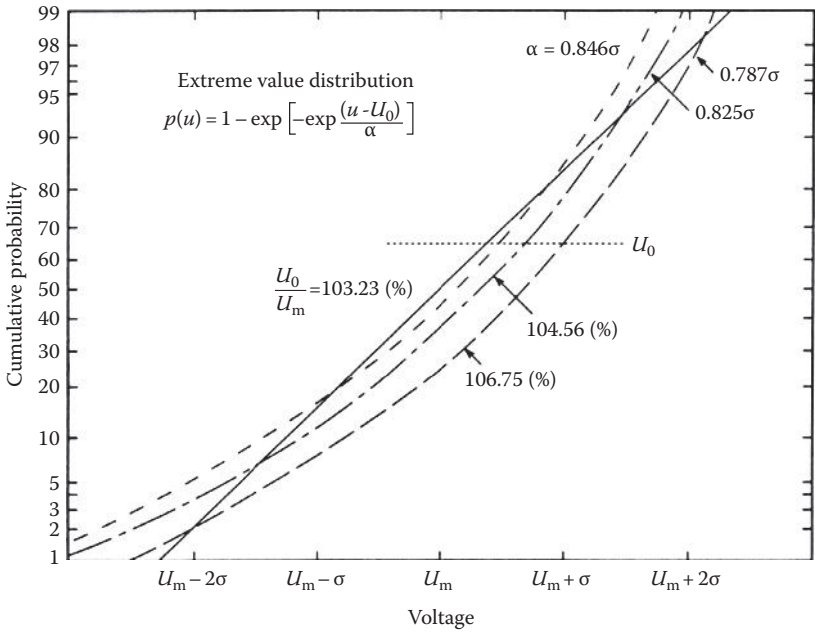


FIGURE 3.18 Adequacy of *extreme value* distributions to represent a *normal* population.

and

$$U_0 = \frac{\ln[-\ln(P_1)]U_1 - \ln[-\ln(1-P_1)]U_2}{\ln[-\ln(1-P_1)] - \ln[-\ln(P_1)]} \tag{3.68}$$

Equations 3.67 and 3.68 define the characteristic parameters of the *extreme value* distributions that best describe the *normal* distribution over the range of probabilities between P_1 and P_2. Table 3.2 compares the probability $P(U_m)$ at the mean value U_m calculated for different *extreme value* distributions. It can be seen that as the interception points occur farther from the 50% probability level, the *extreme value* approximation becomes less adequate. However, the difference with the *normal* distribution, expressed by the ratio U_0/U_m, remains reasonable, in the order of 15%, for the range of probabilities between 5% and 95%.

3.3.5.2 Weibull Distribution

The different Weibull distributions evaluated are selected in such a way as to have the same position parameter U_0 defined by

$$U_0 = U_m - k\mathbf{s}$$

TABLE 3.2

Extreme Value Representation of a Normal Data Population

Probabilities at Interception Points		Probability at U_m
0.15	0.85	0.45
0.06	0.94	0.35
0.02	0.98	0.25

and adjusting the scale parameter, α, so that the 50% probability level coincides with the mean value of the *normal* distribution. By varying k, the optimal position parameter U_0 was found to correspond to

$$U_0 = U_m - 3.33s$$

The corresponding value of the scale parameter α is

$$a = 3.69s$$

Figure 3.19 compares different Weibull distributions for different values of the form parameter β. The best result is obtained with the value of the form parameter:

$$b = 3.6$$

which approximates the *normal* distribution to within 1% over the range of probabilities between 1% and 99%.

3.3.5.3 Discussion

From the preceding analysis, the following observations can be made:

- If accuracy of the order of 5% is sufficient, the three distribution functions are equivalent over the range of probabilities between 5% and 95%.
- To be able to differentiate the different statistical models, the experimental distribution must be defined over a wide range of probabilities, typically between 10^{-3} and 0.999, a requirement that may be difficult to meet in practice due to the generally high cost associated with the acquisition of experimental data.

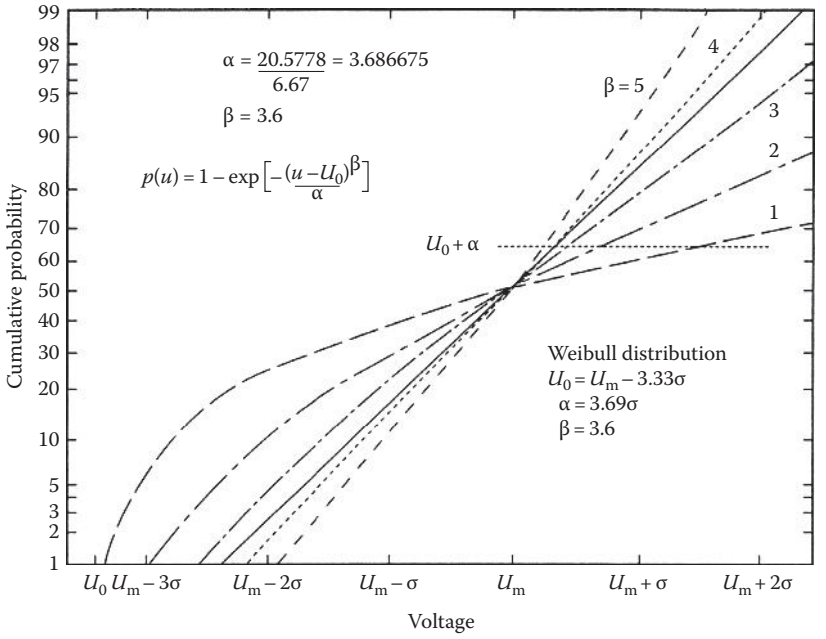


FIGURE 3.19 Adequacy of Weibull distributions to represent a *normal* data population.

- There exists a good correspondence between the *normal* and Weibull distributions, as the characteristic parameters of the latter may be adjusted to provide a good concordance with the *normal* distribution.
- Best results are obtained with $U_0 = U_m - 3.33\sigma$, $\alpha = 0.69\sigma$, and $\beta = 3.6$, which adequately represent a *normal* distribution over the range of probabilities from 1% to 99%.

3.3.5.3.1 International Electrotechnical Commission Procedure for Estimating a Weibull Distribution (IEC 6071-2, 1996)

This procedure determines the equivalent Weibull distribution to fit experimental data which has been presented by a Normal distribution (U_{50}, σ). It requires that the position parameter U_0 be estimated first, usually taken as the withstand voltage:

$$U_0 = U_{50\%} - n\sigma$$

where n is usually taken as $n = 2$, 3, or 4 and σ the standard deviation.

The remaining two parameters, α and β, of the Weibull distribution can then be defined from the condition that the two distributions have the same values at $P = 0.5$ and $P - 0.16$, which results in the following expressions for β and α of the equivalent Weibull distribution:

$$\beta = \frac{1.38}{\ln\left(\frac{n}{n-1}\right)} \quad \text{and} \quad \alpha = \frac{n\sigma}{(\ln 2)^{1/\beta}}$$

As a numerical example, for $n = 2$, $\beta = 2$ and $\alpha = 2.4\,\sigma$ wile for $n = 3$, $\beta = 3.4$ and $\alpha = 3.3\,\sigma$.

3.3.6 Direct Extrapolation of Experimental Data

Once the statistical model has been defined for a set of data, the various characteristic parameters of the experimental distribution can readily be established. However, the main advantage of statistical functions resides in their ability to extrapolate the behavior of a physical system beyond the range covered by the experimental results. Consider, for example, experiments aimed at determining the breakdown probability of an insulation system. Whereas it is relatively easy to obtain experimental data for high-probability events (i.e., events that occur between 10% and 90% of the times), real-world insulation systems must be assessed for much less probable events, down to withstand probabilities of 10^{-3} or even lower. Experimental evaluation of such low breakdown probability distribution often turns out to be simply too expensive.

The usual practice relies on the definition of an appropriate statistical model that can then be used to extrapolate the results to those low-probability levels. The selection of the statistical model is of prime importance in this case since it can have a significant influence on the extrapolated results. By referring to the results of Figures 3.18 and 3.19, it is obvious that if adequate representations of the *normal* population can be obtained by the carefully selected *extreme value* and Weibull distributions over a range of relatively high probabilities, their extrapolations to the low-probability levels of 10^{-3} show considerable differences. The best results are obtained when extrapolation is made in accordance with the physical phenomenon investigated to allow proper extrapolation to very-low-probability withstand levels. The Weibull distribution, for example, which has a threshold value, U_0, below which the probability of occurrence is zero, is particularly suitable to describe many insulation phenomena that usually have an onset field.

3.3.7 Verification of an Experimental Law

Experimental evaluation is often required to validate empirical or semiempirical laws describing the behavior of the physical system under investigation. This implies that experimental data must be obtained for different conditions, selected over a range of the independent variable. The results are presented by data points corresponding to the mean values, with the range of variation of the dependent variable indicated by a linear bar extending on both sides to indicate an experimental error. When sufficient experimental data are available, an experimental distribution and its confidence limits can be defined for each data point, defining the two boundaries within which most of the experimental data are expected to occur.

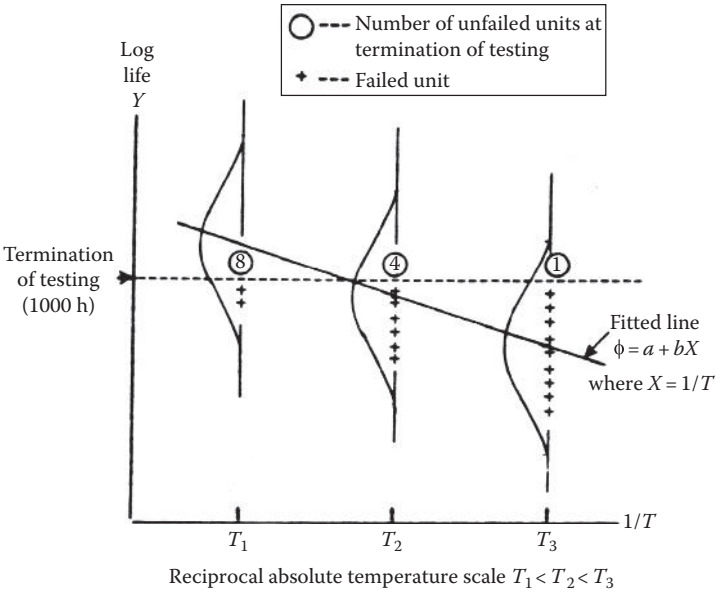


FIGURE 3.20 Thermal aging of paper in oil. (From IEEE Standard 101-1972, IEEE guide for the analysis of thermal life test data, 1972.)

An example is given in Figure 3.20 that illustrates the experimental evaluation of thermal aging of paper in oil: The tests are made on different sample populations of paper, each corresponding to a different temperature. The useful life of the paper was defined as the aging time taken to reach 20% of its initial tensile strength. The results are used to determine the parameters defining the thermal aging process, according to the Arrhenius model:

$$T_b = A\exp\frac{k}{T} \tag{3.69}$$

where
the thermal life T_b is the time to breakdown at constant temperature
T is the temperature in degree K
the constant A is characteristic of the paper aging process

Taking the logarithm of both sides, the preceding relation becomes

$$\ln(T_b) = \frac{k}{T} + \ln A \tag{3.70}$$

Equation 3.70a indicates that the thermal life function will be a straight line when plotted on a graphical paper with $\ln(T_b)$ in ordinates and $(1/T)$ in abscissas. The constant A is then equal to the slope of the experimental function. In Figure 3.20, each sample population is described by its mean and the 90% confidence limits estimated from the experimental sample data. The straight line corresponding to the sample means validates the Arrhenius law, while the confidence region corresponding to the 90% confidence limits represents the adequacy of the experimental data to describe the theoretical law.

Since it is economically unjustified to conduct aging tests at stresses comparable to the operating value, they are generally made under conditions that are significantly more severe than those encountered in operating conditions of the equipment. The results are extrapolated to service conditions following an empirical model. Extrapolation of accelerated aging results assumes that the aging mechanism

remains the same under accelerated aging test as in actual operating conditions, a condition not always met in practice. Furthermore, several aging mechanisms may be active at the same time, which further complicate the interpretation of aging test results.

3.4 Weak Link Statistics

Real insulation systems, because of their size and complexity, are not subjected to extensive dielectric tests. Instead, a typical section or individual components of the system can be evaluated in depth in laboratory and their dielectric performances extrapolated to the real system. Such an extrapolation process assumes that

- The real insulation system is formed by n identical components
- The performance of the individual components are well defined (i.e., there is enough experimental data to derive an adequate statistical model)
- The breakdown phenomenon is the same in laboratory as it is for the system under operating conditions

Weak link statistics are particularly useful to extrapolate the experimental results in this case. Let $P_i(u)$ be the cumulative breakdown probability of a single component at the voltage u. The withstand probability $Q_i(u)$ of that component is given by

$$Q_i(u) = 1 - P_i(u) \tag{3.71a}$$

The withstand of n identical components connected in parallel can be interpreted to mean that each individual component can withstand the test voltage u. Consequently, the withstand probability of the complete system can be expressed as

$$Q(u) = \prod_{i=1}^{n} Q_i(u) = [1 - P_i(u)]^n \tag{3.71b}$$

It follows that the breakdown probability of the complete system of n parallel components is

$$P(u) = 1 - Q(u) = 1 - \prod_{i=1}^{n} Q_i(u) = 1 - [1 - P_i(u)]^n \tag{3.72}$$

with $P_i(u)$ assumed independent.

The breakdown probability of the whole system is readily evaluated from the breakdown probability distribution of the elementary gap. Weak link statistics are particularly useful as they take into account the length effect of high-voltage cables, discussed in Chapter 11, as well as the area and volume effects observed in the breakdown of oil gaps, discussed in Chapter 12. Weak link statistics are also useful in the evaluation of the statistical significance of dielectric test methods, especially when low-probability withstands are required. This last topic will be discussed in Section 3.7.2.

3.5 Optimization of Experimental Data

Until now, the statistical models have assumed that the experimental data evaluated formed one unique and homogeneous population that could be described by a single distribution function. Such a situation does not always occur in practice. Typical real-world experimental data may be made out of several component populations. An indication of this situation is when the experimental distribution cannot be adequately described by a single distribution function. Additionally, the shape of the cumulative distribution of probability will frequently show one or several pronounced inflections.

3.5.1 Determination of the Component Distributions

When there are more than one component populations present, the resulting probability, $P(x)$, can be expressed as a function of the component distributions according to

$$P(x) = \sum k_i \, P_i(x) \quad \text{with} \quad \sum k_i = 1, \quad i = 1,n$$

where

k_i represents the contribution $P_i(x)$ of the ith component population to the resulting probability
n is the number of component distributions

The number of component distributions can be determined from the graphical representation of the experimental distribution as $n = l + 1$, l being the number of inflection points identified in the resulting distribution. The solution of the previously presented system of equations defines completely the n component distributions of the experimental data. The straightforward way to determine the component distributions consists in deriving a system of m equations for the m characteristic parameters, defining the n component distributions according to

$$P(x) = \sum k_i P_i(a_j, x), \quad \text{with} \quad j = 1, m_i$$

where a_j represents the characteristic parameters that define the component distributions $p_i(x)$.

A simplified approach can also be used by subdividing the experimental data into n component populations according to the coordinates of the inflection points. Linear regression analysis can then be used to define the appropriate distribution for each of the component populations. In this approach, the component distributions are directly affected by the subdivision of the experimental data into component populations. By trial and error and using the coefficient of correlation as an objective criterion of selection, the component populations can be gradually adjusted to determine the best representation for the complete set of experimental data. This approach has the advantage of using regression analysis that is relatively simple and rapid to perform. However, knowing the component distributions embedded in a set of data does not by itself provide any explanation of the phenomenon investigated. It does give a better, more coherent view of the data available and, in turn, may help interpret them. The few example cases in the following can illustrate this point.

3.5.1.1 Audible Noise

An example of multiple populations is shown in Figure 3.21, which shows the audible noise (AN) performance of a conductor bundle considered for HVDC power transmission at ±750 kV dc. The AN measured at 15 m from the positive pole was recorded over a period of 12 months during the corona test at IREQ. It can be seen that the distribution of the AN presents two inflection points, which implies that the data are composed of three component populations.

Table 3.3 gives the characteristic parameters of the component distributions for the various seasonal distributions of the AN recorded. Two of these component distributions are related to the corona activities under fair and foul weathers, while the third component distribution was ultimately identified to match the local traffic noise. After removing the traffic noise component distribution, a better interpretation of the remaining experimental data was possible as illustrated by the calculated annual distribution in Figure 3.21.

3.5.1.2 Streamer Length

In the study of discharges in oil, a series of measurements of the streamer lengths was made during a dielectric withstand test (Figure 3.22). The cumulative distribution shows one inflection point, hinting at the presence of two distinct populations in the set of data. Table 3.4 gives the characteristic parameters of the component distributions. Indeed the data set can be broken in two distinct groups, one characterized by frequent and short streamers and a second group of longer streamers. It is apparent that a more

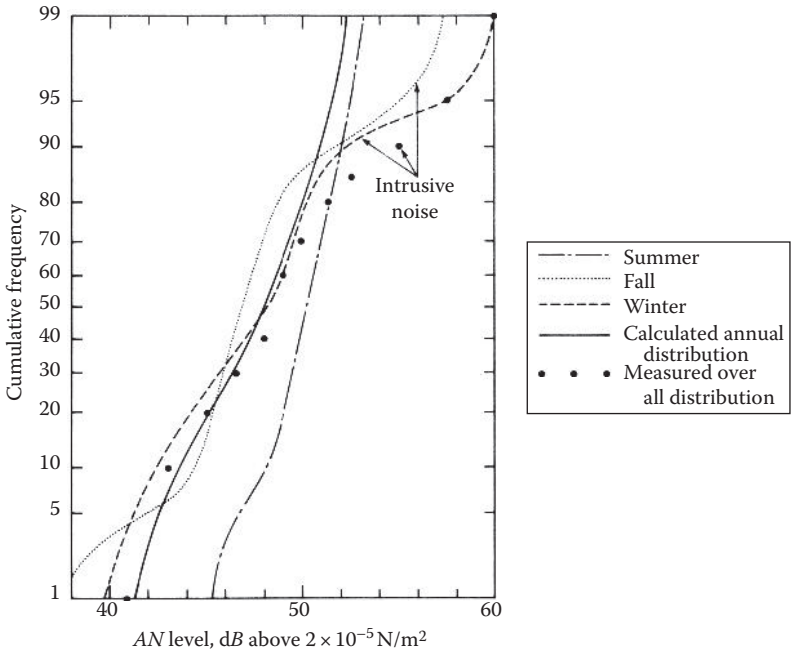


FIGURE 3.21 Distribution of *AN*, measured at 15 m from the positive conductor of the 500 kV dc experimental line during test at *IREQ*. (From Maruvada, P.S. et al., *IEEE Trans. Power Appar. Syst*., PAS-96, 1872, 1977.)

TABLE 3.3

Distribution Components of AN

Distribution #	Mean Value	Standard Deviation	Percentage %	Identification
Summer				
1	50.3	1.2	87	Fair weather
2	47.0	1.1	13	Foul weather
Autumn				
1	47.0	1.9	85.5	Fair weather
2	44.2	2	10	Foul weather
3	57.1	1.5	4.5	Traffic
Winter				
1	48.5	2.2	74.6	Fair weather
2	41.8	1.5	20.6	Foul weather
3	59.4	0.7	4.8	Traffic
Annual				
1	48.2	1.8	83.2	Fair weather
2	44.3	1.65	13.4	Foul weather

Source: Maruvada, P.S. et al., *IEEE Trans. Power Appar. Syst*., PAS-96, 1872, 1977.

vigorous process is present, which generates breakdown streamers that extend further into the oil gap eventually causing its breakdown.

3.5.2 Improvement of Experimental Data

Analysis of experimental data is often limited by the small amount of data available. One can get around this problem by defining new variables that allow grouping data from different tests into a

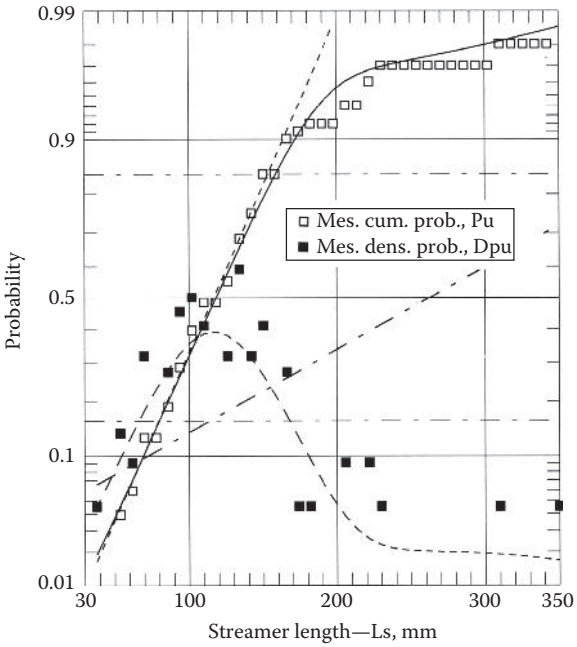


FIGURE 3.22 Distribution of streamer lengths measured in an oil gap.

TABLE 3.4

Distribution Components of Streamer Lengths

Mean Values (mm)	Standard Deviation (mm)	Percentage %	Correlation %	Interpretation
113.55	31.95	93	0.993	
238.66	115.18	7	0.786	Breakdown streamers

larger population, more appropriate for statistical analysis. An example of regrouping data is in the evaluation of the withstand capability of gas-insulated substation (GIS) to internal arc conditions. Under conditions of stationary arc, the time to burn-through of the GIS envelope can be expressed by the functions of the envelope thickness and of the arc current, according to the following empirical relations (Trinh, 1992):

$$T_p = k_i E_p^a \quad \text{and} \quad T_p = \frac{k_t}{I_c^b}$$

where

T_p is the time to burn-through in milliseconds
E_p is the envelope thickness in millimeters
I_c is the arc current in kA
α, β, k_i, and k_t are experimental constants

It has proven difficult to verify these behaviors when experiments were carried out under conditions approaching practical operating conditions of GIS. Despite the large amount of experimental data

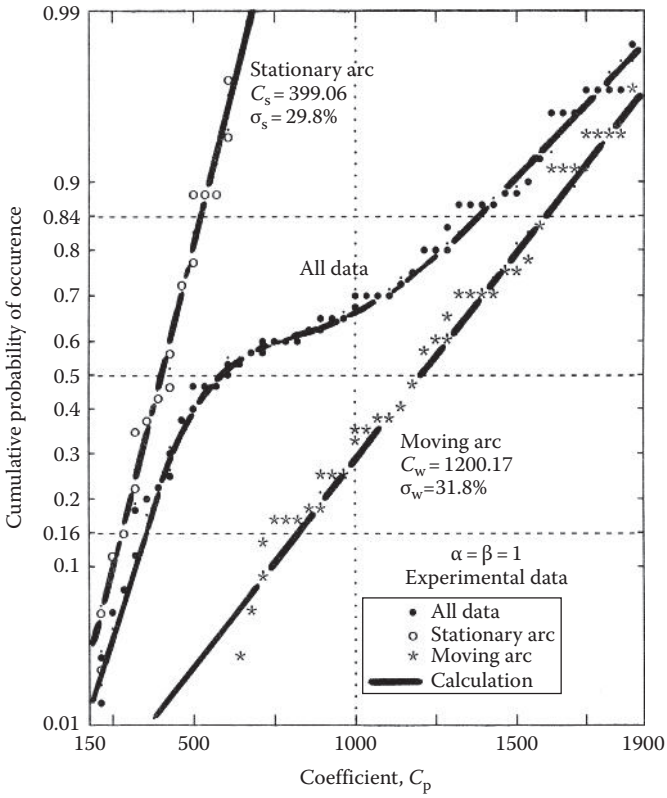


FIGURE 3.23 Statistical distribution of the coefficient C_p. (From Trinh, N.G., *IEEE Trans. Power Deliv.*, PWRD-7, 225, 1992.)

gathered, the measured times to burn-through were widely dispersed due to the wide range of experimental conditions. By defining a new variable C_p according to

$$C_p = T_p \frac{I_c^b}{E_p^a} \tag{3.73}$$

the effect of all three variables, T_p, E_p, and I_c, can be combined and, as a result, allows the regrouping of all experimental data into a single and much larger set of data for the new variable C_p, as illustrated in Figure 3.23. The results show that the set of data for C_p is formed of two distinct populations, implying two different burn-through processes. These are associated with stationary arcs with very short times to burn-through and mobile arcs with much longer time to burn-through and larger standard deviations associated with the traveling time before the arc becomes stationary and cause the burn-through.

3.5.2.1 Breakdown Probability of Elementary Volume

Another example of regrouping data is in the evaluation of the breakdown probability of an elementary volume in large volume oil insulation systems (Wilson, 1953). We saw earlier that Equation 3.72 described the breakdown probability of an oil gap comprised of n unit volumes. We also saw that the breakdown probability of the unit volume, $P_i(u)$, is related to the breakdown probability of the complete oil gap, according to

$$P_i(u) = 1 - \sqrt[n]{1 - P(u)} \tag{3.74}$$

As a result, the breakdown probability distribution of the unit oil volume can be evaluated over a wide range of low probabilities from the available experimental data obtained with oil gaps of different oil volumes, thus taking advantage of a much larger population than is possible with any single experiment.

3.6 Joint Probability

When the outcome of an event depends on two distinct phenomena, the probability of its occurrence can be readily evaluated as follows:

- Let $f(u)$ be the marginal probability density distribution that the marginal variable will have a value of u.
- Let $P(u)$ be the cumulative conditional probability that the marginal variable u will cause the observed outcome.

The elementary joint probability dR is simply the product of the probability density of occurrence $f(u)\,du$ of a marginal variable, u, by the conditional cumulative probability $P(u)$ that it will lead to the outcome of the corresponding event:

$$dR = P(u)\, f(u)du$$

The joint probability R is the sum of all the elementary joint probabilities evaluated over the whole range of the marginal variable:

$$R = \int_0^{\infty} f(u)\, P(u)du \tag{3.75}$$

3.6.1 Risk of Failure

One application of the joint probability is in the evaluation of the risk of failure of a physical system, for example, a line tower, in the normal operating conditions of the line. In this case, $f(u)$ is the marginal probability density that the overvoltages produced by the normal switching operations on the line will have a magnitude of u, and $P(u)$ is the conditional cumulative probability that the overvoltage u will cause breakdown of the tower clearances. Risk of failure is currently used to provide a quantitative evaluation of the quality of an insulation system, discussed in Chapter 13.

3.6.2 *V–t* Breakdown Characteristic

When subjected to impulse voltage of very steep front, for example, under conditions of steep lightning pulses or during disconnect-switch operations in a SF_6-insulated substation, the breakdown of an insulation system tends to occur at voltage above the normal withstand level, following a very short time that the breakdown process needs to be initiated and to develop. Joint probability is used by Rizk and Eteiba to evaluate the *V–t* breakdown characteristic of an insulating gap (Rizk and Eteiba, 1982), discussed in Chapter 7. Here, $f(u)$ is the marginal probability density that the impulse voltage will have a prospective peak of magnitude u, and $P(u|t_d)$ is the conditional probability that the breakdown will occur after a delay time t_d. By evaluating the joint probability of occurrence for various values of u, a region in the *V–t* plane can be delimited between the two boundary curves of 5% and 95% probability where most of the breakdowns will occur.

3.7 Verification of Characteristics or Behavior by Specific Tests

Engineering work requires quantitative assessment of the system performance as well as objective characterization prior to their deployment in service. Specific tests are therefore needed to demonstrate the performance of the system. Statistical analysis provides the tools to help in planning the tests so as to minimize the cost and effort. The following aspects may be considered:

- Optimization of the number of test samples
- Statistical significance of test procedures
- Computer simulation for developing new test methods

3.7.1 Optimization of the Number of Test Samples

Referring to Section 3.2.2.1, the cumulative experimental distribution of a set of experimental data is defined over the range of probabilities comprised between

$$P_{\min} = \frac{1}{N+1} \quad \text{and} \quad P_{\max} = \frac{N}{N+1}$$

3.7.1.1 Minimum Required Number of Tests

The earlier expressions of extreme probabilities provide a simple means to define the minimum number N of tests required to obtain either a given withstand level or an assured breakdown level associated, respectively, with $P_{\min}$ and $P_{\max}$:

$$N = \frac{1}{P_{\min}} - 1 \quad \text{or} \quad N = \frac{1}{1 - P_{\max}}$$

The minimum required number of tests can become very large rapidly as the required withstand level gets lower. This provides a motivation to develop special test methods for low-probability breakdowns and withstand voltages (Trinh and Vincent, 1980). For most practical cases, a probability distribution covering the range of probabilities between 10% and 90% is adequate. By using statistical analysis and extrapolation, the minimum number is $n = 9$ test samples.

It should be borne in mind that this minimum number of test samples will provide only one point on the performance curve corresponding to a specific set of test conditions. This number should be multiplied by the total number of test conditions considered, and the total number of test samples required may rapidly reach levels that become economically unjustified. Specific test procedures may be considered when the emphasis is on the determination of a specific performance, for example, a low-probability withstand level, which allows optimization of the number of test samples as well as the testing time and cost.

3.7.2 Statistical Significance of Test Procedures

Low-probability withstand tests aim at minimizing the number of tests, especially if they are destructive, while determining the withstand levels with very low breakdown probabilities. Most of these tests rely on designing the method of application of the test voltage, using two basic approaches corresponding to

- Test at constant voltage
- Test with increasing voltage

Weak link statistics can be used to evaluate the statistical significance of different test procedures for achieving the desired low-probability withstands (Trinh and Vincent, 1980).

3.7.2.1 Test with Impulse Voltage

When the dielectric performance of an insulating system is evaluated under impulse voltages, a breakdown probability function $P_i(u)$ can be associated to each voltage application of amplitude u.

3.7.2.1.1 Test at Constant Voltage

In this test procedure, the test voltage is kept at the voltage level u and a total of n voltage applications will be made to the test object. Since the breakdown probability of a single application of the voltage u is $P_i(u)$, the corresponding withstand probability is

$$Q_i(u) = 1 - P_i(u)$$

The withstand probability of the insulation system after n voltage applications is

$$Q_n(u) = \prod_n Q_i(u) = [1 - P_i(u)]^n$$

and the breakdown probability of the system after n voltage application is

$$P_n(u) = 1 - Q_n(u) = 1 - \prod_n Q_i(u) = 1 - [1 - P_i(u)]^n \tag{3.76}$$

Figure 3.24 compares the cumulative breakdown probability of tests at constant voltage with different values of n, where n is the number of voltage applications. The breakdown probability of a single voltage application $P_i(u)$ is assumed to be of *normal* type. As expected, the breakdown probability in a test at constant voltage increases with n. This means that tests at constant voltages can be performed at much

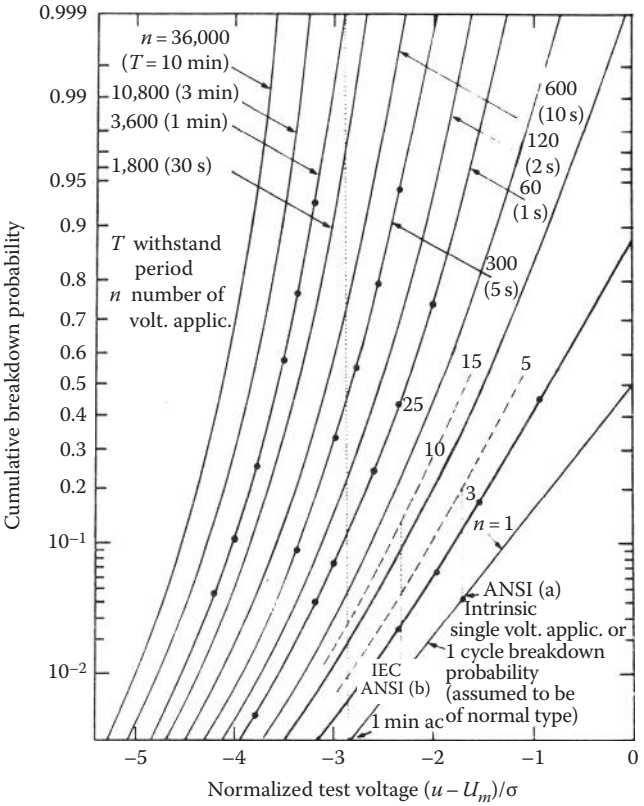


FIGURE 3.24 Breakdown probability under constant impulse and ac voltage—*normal* distribution. (From Trinh, N.G. and Vincent, C., *IEEE Trans. Power Appar. Syst.*, PAS-99, 711, 1980.)

lower voltages while assuring a measured low intrinsic probability withstand level. It also limits at the same time the number of test samples effectively damaged during the test series.

3.7.2.1.2 Test with Increasing Step Voltages (Rizk and Vincent, 1977)

In this test procedure, the test starts at a voltage U_0 with very low breakdown probability; the test voltage is then increased by equal steps Δu with n voltage applications at each level, until breakdown occurs at the voltage u. Let m be the number of voltage steps to reach the test voltage u:

$$u = U_0 + m\Delta u$$

Let $P(u_i)$ be the breakdown probability of a test gap at the voltage level u_i; its withstand probability $Q(u_i)$ is

$$Q(u_i) = 1 - P(u_i)$$

since there are n voltage applications at u_i, the withstand probability $Q_i(u_i)$ at the voltage level u_i is

$$Q_i(u_i) = \left[Q(u_i)\right]^n = \left[1 - P(u_i)\right]^n$$

The withstand of the test gap after m voltage levels implies that the gap withstands all the voltage levels below u. Consequently, the withstand probability of the gap is

$$Q_n(u) = \prod_{i=1}^{m} Q_i(u_i) = \prod_{i=1}^{m} \left[1 - P(u_i)\right]^n$$

It follows that the breakdown probability of the test gap after n voltage levels is

$$P_n(u) = 1 - Q_n(u) = 1 - \prod_{i=1}^{m} Q_i(u_i) = 1 - \prod_{i=1}^{m} \left[1 - P_i(u_i)\right]^n \tag{3.77}$$

and is lower than the breakdown probability of the gap at the voltage u. Figure 3.25 compares the cumulative breakdown probability of tests at increasing voltage with different values of n, the number of voltage applications. The breakdown probability of a single voltage application $P_i(u)$ is assumed to be of the Weibull type. As expected, the breakdown probability in a test with increasing voltage with n voltage applications at each level increases even more than in test at constant voltages. This means that test with increasing voltages can be performed at still much lower voltages while assuring a measured low-probability withstand level. It also limits at the same time the number of test samples effectively damaged during the test series.

3.7.2.2 Practical Test Procedures

Most practical test procedures for low-probability withstands are a combination of the earlier two basic test procedures. Their statistical significance can therefore be readily evaluated from the knowledge of the breakdown probability under single voltage application.

3.7.2.2.1 IEC Rated Withstand Voltage Test (IEC 60060-1, 1989)

In this test, 15 impulses of rated withstand voltage with the specified shape and polarity are applied. The requirements of the test are satisfied if not more than two breakdowns occur. For a given intrinsic probability $p(u)$ of breakdown in one single voltage application at the test voltage, the probability of passing the test P_{test} is (Hauschild and Mosch, 1992)

$$P_{test} = P_0(k = 0,\ n = 15) + P_1(k = 1,\ n = 15) + P_2(k = 2,\ n = 15)$$

where P_0, P_1, and P_2 are, respectively, probabilities to have 0, 1, and 2 breakdowns in a series of 15 tests. For an intrinsic breakdown probability of $p = 0.05$, the binomial distribution probabilities $P_0 = 0.463$, $P_1 = 0.366$, and $P_2 = 0.135$ result in a probability $P_{test} = 0.964$ to pass the test.

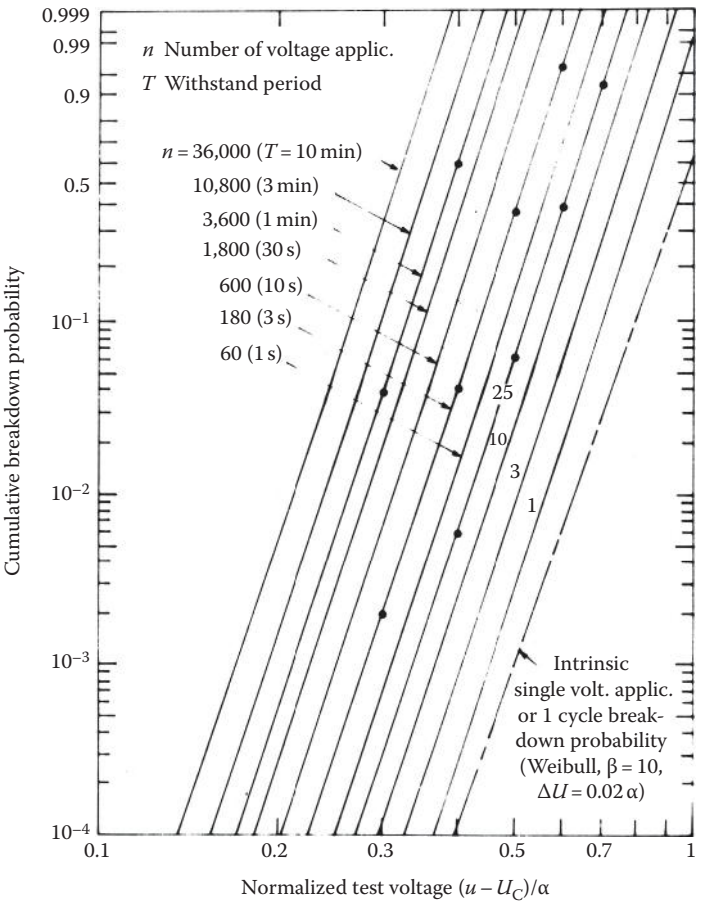


FIGURE 3.25 Breakdown probability in test under increasing voltages—Weibull distribution. (From Trinh, N.G. and Vincent, C., *IEEE Trans. Power Appar. Syst.*, PAS-99, 711, 1980.)

Another interpretation of the IEC rated withstand test, from Equation 3.3, is to associate it to a withstand probability of 2/(15 + 1) or less in a test at constant voltage with 15 voltage applications. Referring to the results of Figure 3.26, the IEC rated withstand voltage test assures an intrinsic breakdown probability of 10^{-2} or less as currently accepted in practice.

3.7.2.2.2 ANSI Rated Withstand Voltage Test (ANSI, 1968)

A different test procedure is proposed by the ANSI for the rated withstand voltage, in two steps.

Five impulses of rated withstand voltage with specified shape and polarity are first applied. If no breakdown occurs, the requirements for the test are satisfied. This corresponds to a withstand probability of 1/(5 + 1) in a test at constant voltage with 5 voltage applications. Referring to the results of Figure 3.26, this ANSI rated withstand voltage assures an intrinsic breakdown probability of a few percent.

If only 1 breakdown occurs, 10 additional impulses are then applied. The test requirements are again satisfied if no breakdown occurs in the additional 10 voltage applications. This corresponds to a withstand probability of 1/(10 + 1) in a test at constant voltage with 10 voltage applications, subjected to the condition that there is only 1 breakdown in the first series of 5 tests. Referring to the results of Figure 3.26, the corresponding intrinsic breakdown probability in this case is 10^{-2} or less.

3.7.2.2.3 Tezner Test Procedures (Tezner, 1958)

It is essentially a test with increasing voltage, with a single voltage application at each level, $n = 1$. Furthermore, the test can start at a voltage level U_0 with a finite probability of breakdown. Figure 3.26

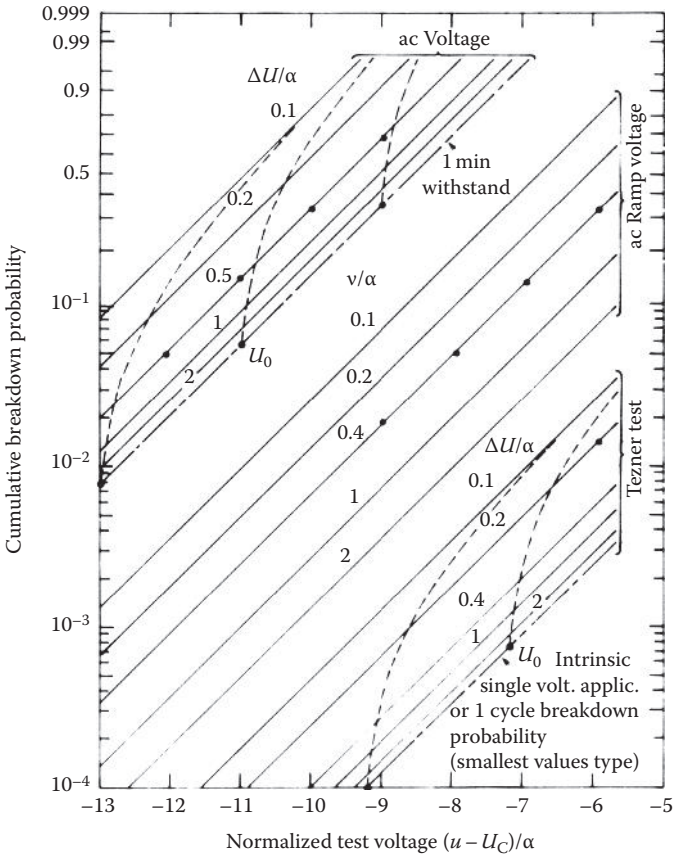


FIGURE 3.26 Breakdown probability obtained in Tezner test—*extreme value* distribution. (From Trinh, N.G. and Vincent, C., *IEEE Trans. Power Appar. Syst.*, PAS-99, 711, 1980.)

illustrates the changes in the breakdown probability with Tezner test procedures with impulse voltages from the breakdown probability under single voltage application $P_i(u)$, assumed to be of the *extreme value* type. Tezner test procedure assures an intrinsic breakdown probability in the range of 0.1–0.3.

3.7.2.3 Test with AC Voltage

In test with ac voltage, a similar evaluation of the statistical performance of test procedures is also possible by defining the *1-cycle breakdown probability*, of the insulation system, and applying weak link statistics as in the case of testing with impulse voltages. Figures 3.24 through 3.26 illustrate also the changes in the breakdown probability with different test procedures from the one-cycle breakdown probability $P_i(u)$, assumed to be of the *normal*, *extreme value*, or Weibull type.

3.7.2.3.1 Rated AC Withstand Voltage Test

In this test, the ac voltage is raised to the rated withstand voltage, maintained at this level for the specified time and then rapidly decreased. The test is satisfied if no breakdown occurs. The currently accepted withstand period is 1 min. Referring to the results of Figure 3.24, the rated ac withstand voltage test assures an intrinsic breakdown probability in one cycle of the applied voltage amounts to 10^{-2} or less.

3.7.2.3.2 AC Test with Ramp Voltages

The corresponding Tezner test with ac voltage is obviously the case of testing with ramp voltages. If ν is the rate of rise of the test voltage and f is the frequency, then the equivalent voltage step is

$$\Delta u = \frac{1}{f}$$

Since the ramp voltage always starts from zero, the measured critical flashover (CFO) voltage is a function of the rate of rise ν of the test voltage. Typical intrinsic breakdown probability of the measured CFO voltage obtained with this test procedure is about 5×10^{-3} to 2×10^{-3} for a rate of rise ν of 0.1–1.0 σ/s, where σ is the estimated standard deviation of the breakdown voltage (Figure 3.27).

3.7.2.3.3 AC Test with Increasing Voltages

In ac test with increasing voltages, the test voltage is raised in steps Δu from a low initial voltage U_0. At each voltage level, the test voltage is kept constant for a time T. If the time required for raising the test voltage is small compared to the withstand time T, this test procedure is essentially a test with increasing voltage and n voltage applications at each level, n being equal to $N = fT$.

To save testing time (and cost), a modified procedure is often used: the test voltage is raised rapidly to the first withstand level close to about 80% of the expected breakdown voltage and then in increasing steps of Δu until breakdown occurs. Referring to the results of Figure 3.26, a typical one-cycle intrinsic breakdown probability of the measured CFO voltage is in the range of 10^{-4} for ac test with increasing voltage and 1 min withstand periods.

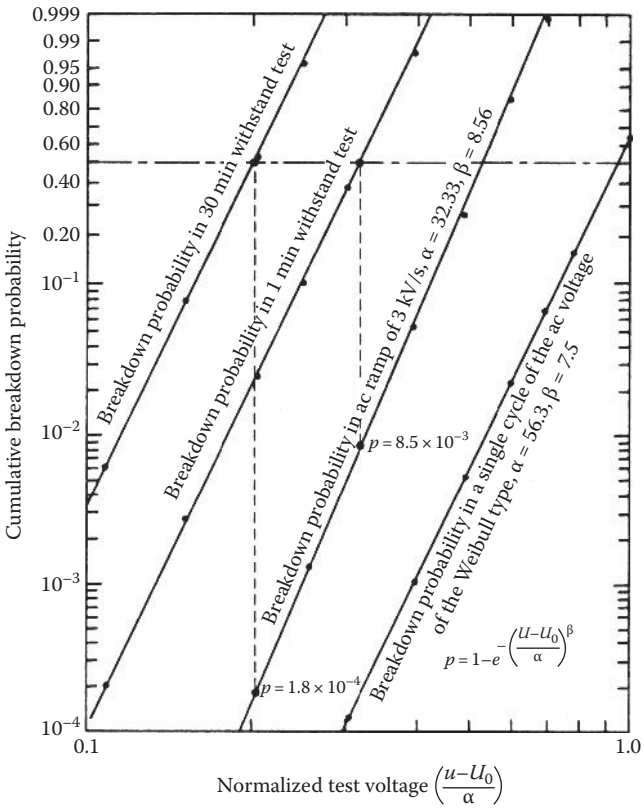


FIGURE 3.27 Correspondence between practical test procedures with ac voltages. (From Trinh, N.G. et al., *IEEE Trans. Power Appar. Syst.*, PAS-101, 3712, 1982.)

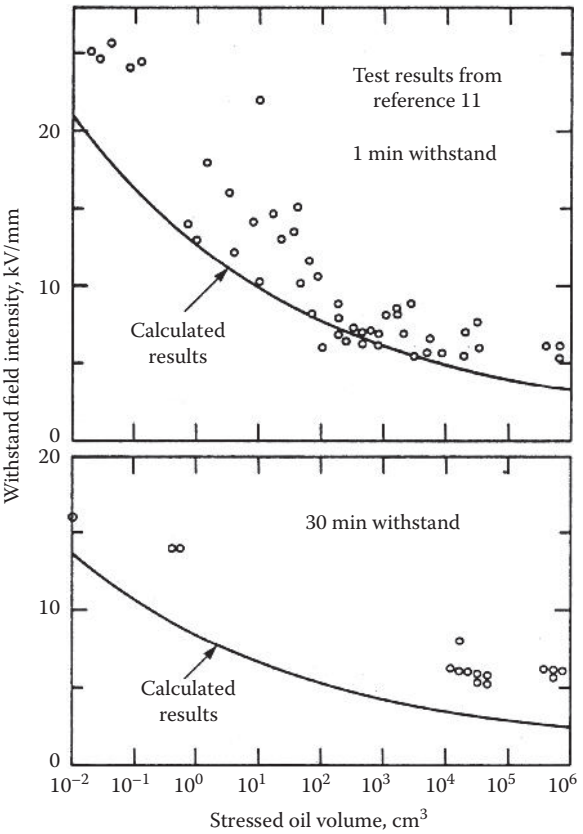


FIGURE 3.28 Estimation of 1 and 30 min withstand voltages of large oil volumes. (From Trinh, N.G. et al., *IEEE Trans. Power Appar. Syst*., PAS-101, 3712, 1982.)

3.7.2.3.4 The 1 and 30 min Withstand Voltage of an Oil Gap

An application of this approach is in the evaluation of the 1 and 30 min. withstand voltages of an oil gap. The results of Figure 3.28 compare the statistical significance of the 1 and 30 min withstand test with the steadily rising voltage test for which the breakdown probability distribution of the unit volume was derived, by assuming a complete correspondence between different test procedures. It can be seen that the 50% withstand level in the 1 and 30 min withstands is equivalent to the 0.85×10^{-2} and 1.8×10^{-4} withstand levels in a test with steadily increasing voltage. As a result, the 1 and 30 min withstand voltages can be readily determined from the breakdown probability distribution curve of the unit volume derived from test results obtained in the test with steadily increasing voltage. Typical results are presented in Figure 3.28 that compares the calculated 1 and 30 min withstand levels with experimental measurements and illustrate the validity of this approach (Trinh et al., 1982).

3.7.3 Computer Simulation of Test Procedures

Weak link statistics provide a simple means of evaluating new test methods, through computer simulation (Rizk and Vincent, 1977). The required test sequence is programmed to the computer, starting with the selection of the test voltage u. The breakdown probability $P(u)$ is then calculated according to the test procedures and the statistical function specified. The decision regarding whether the voltage application results in a breakdown or withstand is made in two steps:

- Generate a pseudorandom number k between 0 and 1.
- By comparing k with the calculated cumulative breakdown probability $P(u)$, a breakdown occurs if $k >= P(u)$, otherwise the gap withstands.

By repeating N times the simulation and noting the simulated result of each computer simulation, the cumulative breakdown probability of the gap is defined as

$$S(u) = \frac{n_f}{N}$$

where n_f represents the number of simulated failures recorded.

Computer simulation is particularly useful in assessing the validity of new and complex test procedures and in comparing the effectiveness of different test procedures. An example is shown in Figure 3.29 that compares different test procedures for low-probability withstand voltages that are briefly described in the following.

3.7.3.1 Hancox Test Procedures (Hancox, 1958)

Hancox test procedures consist of several sequences of increasing voltages to breakdown, with the initial test voltage increased successively by one step at each level until breakdown occurs at the application of the first impulse.

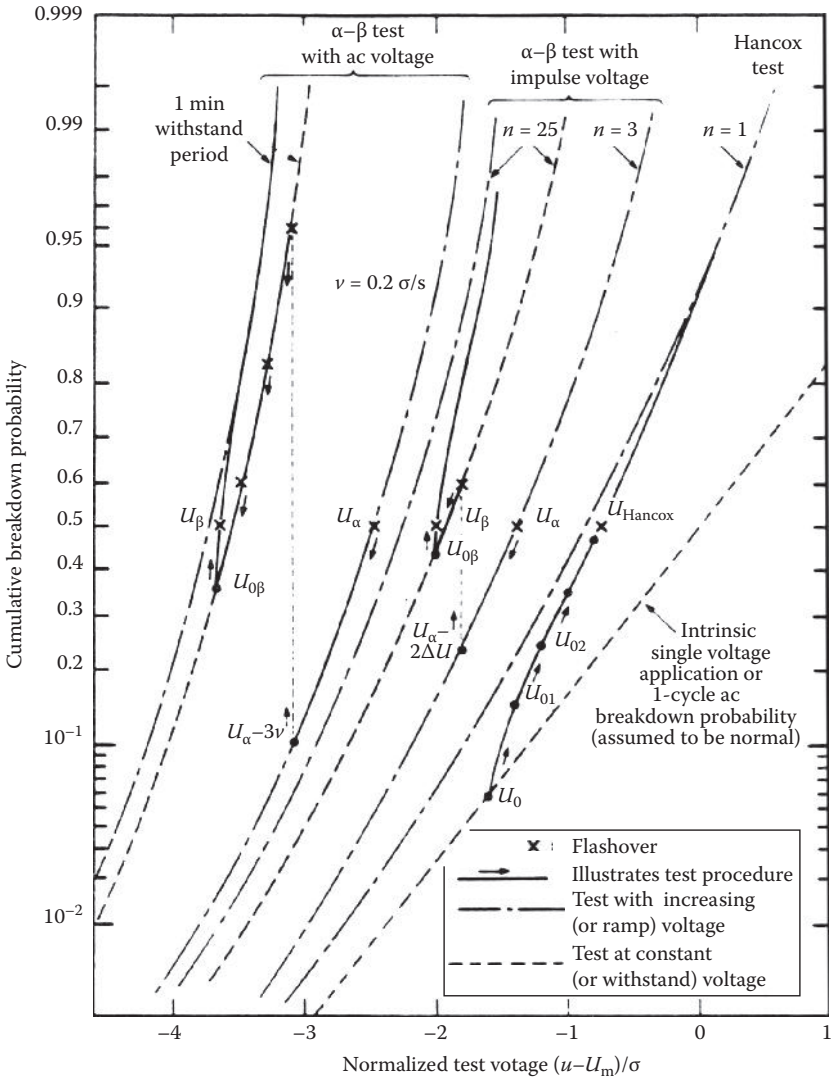


FIGURE 3.29 Computer simulation of special test procedures. (From Trinh, N.G. and Vincent, C., *IEEE Trans. Power Appar. Syst*., PAS-99, 711, 1980.)

3.7.3.2 Fryxell (or α–β) Test Procedures (Fryxell, 1966)

These test procedures consist of two sequences of test with increasing voltages with n voltage applications at each level, with different values for n in the two test sequences:

- In the alpha test series, the test starts from a voltage U_0 of low breakdown probability; the voltage is increased in steps of Δu with α-voltage applications at each level, until breakdown occurs at U_α.
- The beta test series starts at the voltage $U_\alpha - 2\Delta u$; the voltage is increased in steps of Δu with β-voltage applications at each level, until breakdown occurs at U_β. The critical withstand voltage is taken as the highest voltage reached in a beta test series of withstands.

3.7.3.3 Modified α–β Test Procedures (Rizk and Vincent, 1977)

These test procedures follow the same test procedures proposed by Fryxell. However, the critical withstand voltage is taken as the first complete withstand beta test series. The measured critical withstand voltage obtained in this procedure could be slightly lower than the one obtained in a Fryxell test.

Computer simulation, with its ability to make large number of simulations, is also useful in the estimation of the effective number of tests necessary to achieve the required confidence limits, as illustrated in Figure 3.30, which shows the improvement in the confidence limits with increasing number of tests performed. Its main advantage is in the economy of time and cost. The final assessment of a test procedure must be the actual test itself.

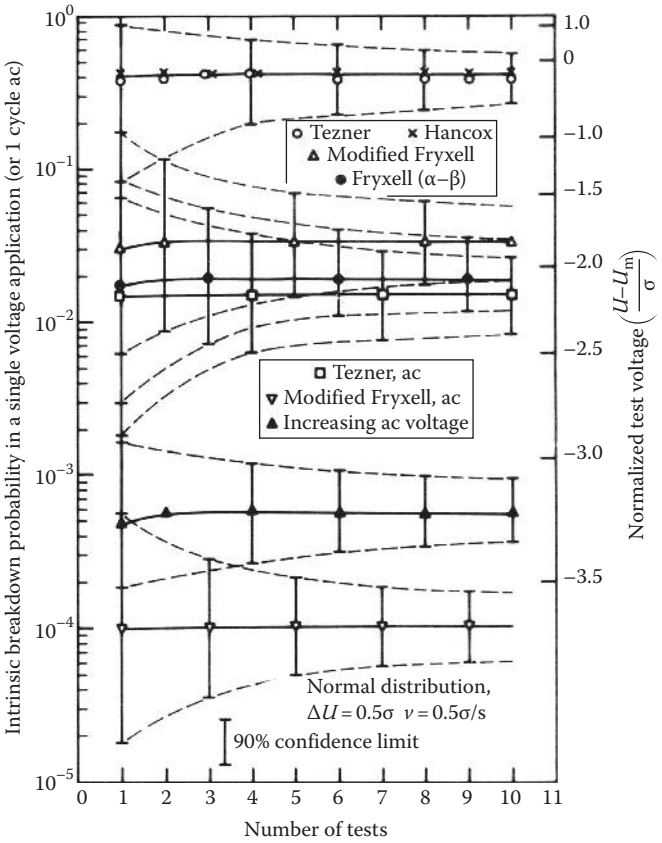


FIGURE 3.30 Variations of the confidence limits with the number of tests. (From Trinh, N.G. and Vincent, C., *IEEE Trans. Power Appar. Syst*., PAS-99, 711, 1980.)

3.8 Conclusions

From the present review of some applications of statistical analysis to high voltage engineering, it may be seen that statistical analysis is foremost a versatile working tool for analyzing test data. When properly applied, statistical analysis can help to

- Identify erroneous data and hence their separation from the main population
- Regroup data from various experiments to improve the total amount of data available and their statistical significance
- Extrapolate the observed behavior to untested conditions
- Provide a quantitative evaluation of the capacity of an insulation system to withstand specified operating conditions
- Sort hidden populations in a set of experimental data, giving a better insight of the phenomenon studied
- Optimize the number of tests and test samples, especially when destructive tests are to be avoided
- Evaluate and compare the statistical significance of test procedures
- Evaluate new test procedures

Its main drawback resides in the implicit assumption that the observed phenomenon remains the same over the whole range of conditions considered, even if they are beyond the effective limits covered by the experimental data, a condition not always met in practice.

REFERENCES

ANSI Standard Techniques for Dielectric Tests. ANSI publication C 60.1, 1968.

Fryxell, J. Determination of the critical withstand voltages. CIGRE, Paper No. 423, Paris, 1966.

Gumbel, E.J. *Statistical Theory of Extreme Values and Some Practical Applications*. Applied Mathematics Series 33, National Bureau of Standards. Washington, DC: U.S. Government Printing Office, 1954.

Hancox, R. The interpretation of the results of impulse breakdown tests. *Proceedings of the IEE* , vol.105, 404, 1958.

Hauschild, W. and W. Mosch. *Statistical Techniques for High-Voltage Engineering*. London, U.K.: Peter Peregrinus Ltd., 1992.

IEC Recommendations—High voltage test techniques. IEC Publication 60060, 1989.

IEC Standard 6071-2. Insulation coordination—Part 2: Application guide, 1996.

IEEE Standard 101-1972. IEEE guide for the statistical analysis of thermal life test data, 1980.

Lindgren, B.W. and G.W. McElrath. *Introduction to Probability and Statistics*. New York: MacMillan Company, 1959.

Maruvada, P.S., Trinh, N.G., Dallaire, D., and N. Rivest. Corona performance of a conductor bundle for bipolar HVDC transmission at ±750 kV. *IEEE Transactions on Power Apparatus and Systems* PAS-96: 1872, 1977.

Miller, I. and J.E. Freund. *Probability and Statistics for Engineers*. Englewood Cliffs, NJ: Prentice Hall Inc., 1965.

Muller, H.P., Neumann, P., and R. Storm. *Tafeln der Mathematischen Statistik*. Leipzig, Germany: VEB Fachbuchverlag, 1973.

Rizk, F.A.M. and M.B. Eteiba. Impulse breakdown voltage-time curves of SF6 and SF6-N2 coaxial-cylinder gaps. *IEEE Transactions on Power Apparatus and Systems* PAS-101: 4452, 1982.

Rizk, F.A.M. and C. Vincent. Testing for low breakdown probability with special reference to liquid insulation. *IEEE Transactions on Power Apparatus and Systems* PAS-96: 1892, 1977.

Tezner, V. Einer bestimmung fur Isolieranordnungen zweckmassige 50% Durchschlag stoss-spannung. *Archiv fur Elektrotechnik* 44: 52, 1958.

Trinh, N.G. Risk of burn-through—A quantitative assessment of the capability of gas-insulated equipment to withstand internal arcs. *IEEE Transactions on Power Delivery* PWRD-7: 225, 1992.

Trinh, N.G. and C. Vincent. Statistical significance of test methods for low-probability breakdown and withstand voltages. *IEEE Transactions on Power Apparatus and Systems* PAS-99: 711, 1980.

Trinh, N.G., Vincent, C., and J. Régis. Statistical dielectric degradation of large volume oil insulation. *IEEE Transactions on Power Apparatus and Systems* PAS-101: 3712, 1982.

Weibull, W. A statistical distribution function of wide applicability. *Journal of Applied Mathematics* 18: 293, 1951.

Wilson, W.R. A fundamental factor controlling the unit dielectric strength of oil. *AIEE Transaction* 72(Part III): 68, 1953.

4

Electrical Breakdown in Gases

4.1 Introduction

Gases as one of the three states of matter are composed of neutral molecules with sufficient kinetic energy to overcome the intermolecular force. They constitute a naturally insulating medium and hence are used in various applications. Extensive studies of gas discharges over the years have contributed significantly to the understanding of the atomic structure of the elements. They also lead to a variety of applications in various fields, lighting, insulation, current interruption, etc. Air, a natural mixture of nitrogen and oxygen, has good dielectric properties and has been extensively used as the insulating medium for overhead lines and other high-voltage equipment, to provide the most economical way of transmitting a large amount of electric energy over long distances, and hence constitutes the backbone of power transmission and distribution systems worldwide. Sulfur hexafluoride (SF_6), on the other hand, is a synthetic gas with superior dielectric properties and good arc-quenching capability. It has been widely used as the insulating medium of gas-insulated equipment and as an arc-quenching medium for current interruption devices. These proprieties of SF_6 have significantly influenced the development of gas-insulated equipment and cables and promoted their application in gas-insulated substations (GIS).

New gases: In spite of the good dielectric performances of SF_6, there is a constant interest to find even better insulating gases for use in electrical equipment (Christophorou et al., 1984). Gases with high degrees of electron affinity like CO_2 and chlorines have been evaluated. The most promising candidates are in the perfluorocarbon group (C_4F_6, C_4F_8, C_5F_8), which all offer a dielectric withstand capability between 1.2 and 2.2 better than SF_6. They open interesting perspectives for gas-insulated power transformers. Their main drawbacks reside in their higher molecular mass, which implies a higher operating temperature than for SF_6. In addition, the presence of carbon gives rise to carbon deposits subsequent to an electric discharge, partial discharges or arcs, with possible detrimental effects in the long term for the insulation, and limits their use in current interrupting apparatus where arcs are present.

Since most of the new gases considered for dielectric insulation are complex molecules, formed from many basic elements, a new aspect must be considered in the selection of new insulating gases: the impact of their decomposition by-products by partial discharges and electric arcs. In effect, energy absorption by these gas molecules causes their fractioning into radicals, smaller and more stable. Decomposed by-products, once at rest, may recombine back to the initial insulating gas. The process is not fully effective, and a small portion of the by-product remains and can react with contaminants (water, O_2, etc.), the metal electrodes, and the insulating structures to form stable by-products. Although most of these by-products are good insulators, certain are toxic and imply severe controls of their presence and concentration to limit their detrimental effects for the workers in maintenance or repair works. The recent efforts to find better insulating gases indicate that when one takes account of all the impacts of the new gas, SF_6 remains the best candidate for insulation of gas-insulated equipment and, more specifically, for current interrupting apparatus (breakers, interrupters, etc.). This chapter reviews the fundamental proprieties of gases and discusses the physical processes that affect their insulating performances and eventually cause the breakdown of a gas gap.

4.2 Gases Composed Uniquely of Neutral Molecules

The physical model of an ideal gas assumes spherical gas molecules in continuous movement in space, exchanging energy in random elastic collisions with one another. Their volumes are negligible with respect to the gas volume; furthermore, their masses are sufficiently small so that one can neglect the gravity effect in interacting among the gas molecules themselves and with the containing walls.

4.2.1 General Laws and Definitions

Consider a gas volume containing only neutral molecules. The gas molecules obey the general laws of Newton kinetic theory.

4.2.1.1 Conservation of Energy

This stipulates that a gas molecule in motion has a kinetic energy equal to

$$E_c = \frac{1}{2} M v^2 \tag{4.1}$$

where
M is the mass of the molecule
v its velocity

and in a collision between two molecules, the total kinetic energy remains unchanged:

$$\sum \frac{1}{2} M_i v_i^2 = \sum \frac{1}{2} M_i V_i^2 \tag{4.2}$$

where v_i and V_i are the velocities of the two molecules before and after their collision.

4.2.1.2 Conservation of Momentum

This stipulates that a molecule in motion has a momentum equal to Mv, and in a collision between two molecules, the total momentum remains unchanged:

$$\sum M_i \mathbf{v_i} = \sum M_i \mathbf{V_i} \tag{4.3}$$

When one molecule is initially at rest, $v_2 = 0$, the preceding equations simplify to

$$\frac{1}{2} M_1 v_1^2 = \frac{1}{2} M_1 V_1^2 + \frac{1}{2} M_2 V_2^2 \tag{4.4}$$

$$M_1 \mathbf{v_1} = M_1 \mathbf{V_1} + M_2 \mathbf{V_2}$$

The preceding equation decomposes in two equations in terms of the velocity components along the coordinate axes (Figure 4.1):

$$M_1 v_1 = M_1 V_{1x} + M_2 V_{2x} = M_1 V_1 \cos \phi_1 + M_2 V_2 \cos \phi_2 \tag{4.5}$$

$$0 = M_1 V_{1y} + M_2 V_{2y} = M_1 V_1 \sin \phi_1 + M_2 V_2 \sin \phi_2$$

where ϕ_1 and ϕ_2 are the angles between the trajectories of the molecules after the collision with respect to the x-axis.

One observes that Equations 4.4 and 4.5 form a set of three equations for four unknowns: V_1, V_2, ϕ_1, and ϕ_2. It is obvious that the collision of the two molecules cannot be solved without additional information

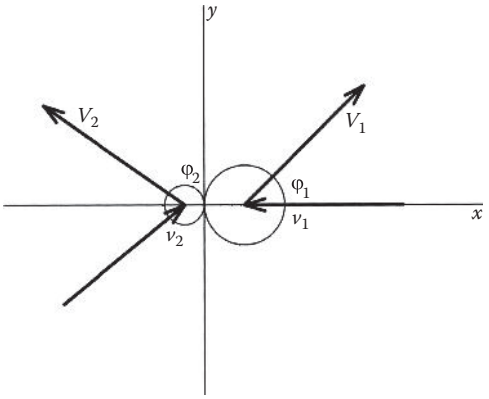


FIGURE 4.1 Collision between two gas molecules.

concerning either the trajectories or the velocities of the molecules after the collision. A particular case corresponds to when the *trajectory after collision coincides with the x-axis*: $\phi_1 = \phi_2 = 0$. Equation 4.5 simplifies to

$$M_1 v_1 = M_1 V_1 + M_2 V_2$$

The solution of Equations 4.4 and 4.5 for V_1 and V_2 gives the following expressions in terms of v_1:

$$\mathbf{V_1} = \left(\frac{M_1 - M_2}{M_1 + M_2}\right)\mathbf{v_1} \quad \text{and} \quad \mathbf{V_2} = 2\left(\frac{M_1}{M_1 + M_2}\right)\mathbf{v_1}$$

It follows that

- If $M_1 > M_2$, the molecule 1 continues its course with a lower velocity
- If $M_1 < M_2$, the first molecule bounces off with a different final velocity. A particular case is when M_1 is much smaller than M_2, for example, collision between electron and atom; the molecule of mass M_1 bounces back with a velocity of $-\mathbf{v_1}$, leaving the second molecule immobile
- If $M_1 = M_2$, $\mathbf{V_1} = 0$ and $\mathbf{V_2} = \mathbf{v_1}$, one has a complete transfer of the kinetic energy between the two molecules. The second molecule continues on the course of the first molecule, leaving the last one on site

4.2.1.3 Inelastic Collisions

When there is absorption of the energy by one of the two molecules, the collision is termed *inelastic*. The energy and momentum laws of the kinetic theory become

$$\sum \frac{1}{2} M_i v_i^2 = \sum \frac{1}{2} M_i V_i^2 + W$$

$$\sum M_i \mathbf{v}_i = \sum M_i \mathbf{V}_i$$

where W is the absorbed energy. When one of the two molecules is initially at rest, the preceding equations simplify to

$$\frac{1}{2} M_1 v_1^2 = \frac{1}{2} M_1 V_1^2 + \frac{1}{2} M_2 V_2^2 + W$$

$$M_1 v_1 = M_1 V_1 + M_2 V_2$$

If one supposes the trajectory of one molecule after collision coincides with the *x*-axis, the solution of the preceding equations yields

$$M_1 v_1^2 = M_1 V_1^2 + M_2 \left(\frac{M_1 v_1 - M_1 V_1}{M_2} \right)^2 + 2W$$

The amount of energy absorbed by one of the molecules in the inelastic collision is maximal when

$$\frac{\mathrm{d}W}{\mathrm{d}V_1} = -M_1 V_1 + \frac{M_1^2}{M_2} (v_1 - V_1) = 0 \quad \text{or} \quad \mathbf{V}_1 = \frac{M_1}{M_1 + M_2} \mathbf{v}_1$$

and the absorbed energy is

$$W_{\max} = \frac{M_2}{M_1 + M_2} \frac{1}{2} M_1 v_1^2$$

It follows that in an inelastic collision, it is impossible for the second molecule to absorb completely the kinetic energy of the first molecule. However, if $M_1 \ll M_2$, practically all the kinetic energy of the first molecule can be absorbed by the second molecule in the collision, if the maximum available energy $W_{\max}$ is greater than the allowed energy of absorption by the second molecule, noting that the energy absorption by a molecule is made by discrete amount only. Furthermore, in a collision, the energy absorption does not necessarily happen each time that the afore mentioned condition is met.

4.2.1.4 Hypothesis of Avogadro

This hypothesis stipulates that under the same conditions of pressure and temperature, *all gases have the same number of molecules per mole*. Under the normal atmospheric conditions, the Avogadro number is equal to

$$N_0 = 6.023 \times 10^{23} \text{ molecules/mol}$$

4.2.1.5 Law of Gay-Lussac

This law stipulates that at constant temperature, *the product pV of the gas pressure* p *by its volume* V *remains constant*:

$$PV = C \quad \text{with C a constant} \tag{4.6}$$

For a gram-mole of gas, the gas volume is V_0, and the preceding expression becomes

$$PV_0 = RT \tag{4.7}$$

where

R is the universal gas constant, R = 83.1436 J/K-mol for all gases
T the gas temperature in K
V_0 = 22.414 L/mol under normal conditions of temperature and pressure

It can be seen that the dimensions of the product $R\,T$ are those of energy: J/mol.

From the Gay-Lussac law, one can derive an expression for the gas pressure in terms of the gas density, n, and absolute temperature, T, as follows:

$$n = \frac{N_0}{V_0} \quad \text{or} \quad V_0 = \frac{N_0}{n}$$

The Gay-Lussac law becomes

$$PV_0 = P \frac{N_0}{n} = RT \quad \text{or} \quad P = \frac{nRT}{N_0} = nkT$$

With k the Boltzmann constant

$$k = \frac{R}{N_0} = 1.3804 \times 10^{-23} \text{ J/K}$$

Effect of a temperature gradient on the repartition of gas molecules (Trinh, 1982): When a volume of gas is subjected to a temperature difference, at equilibrium, the latter imposes a corresponding gradient of the gas density. A typical example is a gas-insulated bus connecting an overhead line to gas-insulated equipment located indoors. A temperature difference exists then between the two ends of the gas-insulated bus. Since the gas pressure must be the same within the gas compartment, a gradient of the gas density must develop according to the Gay-Lussac law as shown in Figure 4.2.

The result is a migration of the gas molecules from the warm part of the gas compartment to the cold one. The effect on the gas insulation is a reduction of its dielectric withstand, which is a function of the lowest gas density in the compartment. The degree of reduction in the gas density depends on the relative length of the indoor portion of the gas compartment. The smaller this portion is, the greater is the reduction of the gas density due to the migration of the gas to the cold portion of the gas compartment (Figure 4.3). For a relative length ratio of 0.5, a temperature difference of 30°C induces a loss of the dielectric withstand in the order of 10%. These considerations underscore the importance of the following:

- Monitoring of the gas density (and not its pressure) to detect the migration of the gas molecules resulting from a temperature gradient
- Avoiding situations where a gas compartment is subjected to a temperature difference: for example, by installing a gas-barrier spacer at the level of the wall separating the indoor from the outdoor environment

4.2.2 Distribution of Velocities of Gas Molecules

Because of the relatively high kinetic energy of the gas molecules, these are continuously in motion and thereby produce collisions with energy exchanges among the molecules. Therefore, there is great interest to determine the distribution of the velocity of the gas molecules.

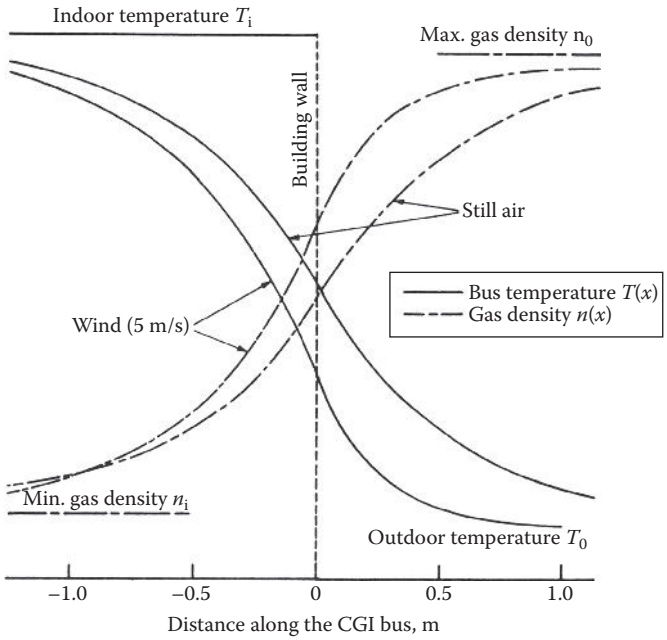


FIGURE 4.2 Distribution of the gas temperature and density in a gas-insulated bus subjected to a temperature difference. (From Trinh, N.G., *IEEE Int. Symp. Electr. Insul.*, 183, 1982.)

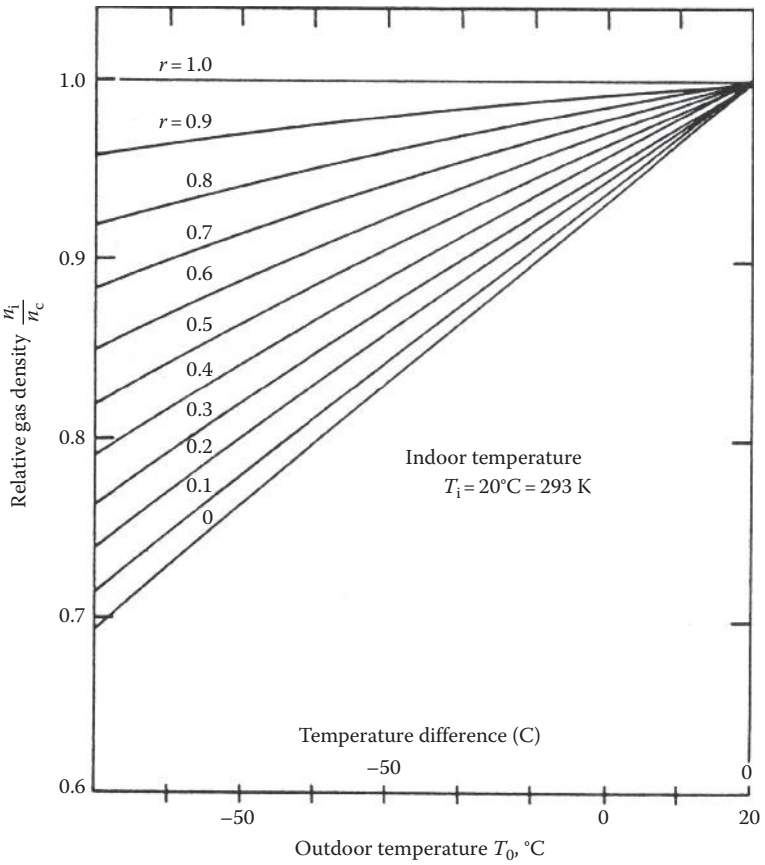


FIGURE 4.3 Variations of the minimum gas density with the temperature difference ΔT and for different value of the ratio r of the indoor portion to the length of the gas compartment. (From Trinh, N.G., *IEEE Int. Symp. Electr. Insul*., 183, 1982.)

4.2.2.1 Distribution Function of the Velocities of Gas Molecules

Since there is no preferred direction for the displacement of the gas molecules, one can conclude that the movement of the gas molecules is completely random. The following hypotheses can be made:

- The number of gas molecules is large.
- There is an equilibrium state in the movement of the molecules in the gas volume.
- All collisions between molecules and, between molecules and wall, are elastic, that is, there is no energy absorption by the gas molecules.

With these considerations, the probability density of the velocity of the gas molecules follows the well-known Maxwell *distribution function*, $f(v)$, according to

$$f(v) = \frac{4}{\sqrt{\pi}} \left(\frac{M}{2kT}\right)^{3/2} v^2 \exp\left(-\frac{M}{2kT} v^2\right) \tag{4.8}$$

where
k is the Boltzmann constant
v is the velocity of gas molecule
M is the mass of the gas
T is the temperature of the gas in K

4.2.2.2 Some Characteristic Values of the Velocity c of Gas Molecules in Air and SF_6

Probable velocity: Corresponds to the velocity at which the velocity distribution function $f(v)$ is maximal. This occurs when

$$\frac{\mathrm{d}f(v)}{\mathrm{d}c} = \frac{4}{\sqrt{\pi}}\left(\frac{M}{2kT}\right)^{3/2} 2v\exp\left(-\frac{M}{2kT}v^2\right) - v^2\left(\frac{M}{2kT}\right) = 0$$

or

$$1 - v^2\left(\frac{M}{2kT}\right) = 0$$

It follows the expression for the probable velocity:

$$c_\mathrm{p} = \sqrt{\frac{2kT}{M}} \tag{4.9}$$

The function $f(v)$ expressed in terms of the probable velocity c_p is

$$f(v) = \frac{4}{\sqrt{\pi}}\frac{v^2}{c_\mathrm{p}^3}\exp\left[-\left(\frac{v}{c_\mathrm{p}}\right)^2\right]$$

which can be rearranged as

$$c_\mathrm{p} f(v) = \frac{4}{\sqrt{\pi}}\frac{v^2}{c_\mathrm{p}^2}\exp\left[-\left(\frac{v}{c_\mathrm{p}}\right)^2\right] \tag{4.10}$$

the quantity $c_\mathrm{p} f(v)$ is a function of v/c_p only and can be applied to any gas. Figure 4.4 shows the density and cumulative probabilities of $c_\mathrm{p} f(v)$ for the range of v/c_p between 0 and 3.

Average velocity: The average velocity c_av of the gas molecules is

$$c_\mathrm{av} = \int_0^\infty \frac{\mathrm{d}N_\mathrm{c}}{N} = \frac{4}{c_\mathrm{p}^3\sqrt{\pi}}\int_0^\infty v^3\exp\left(-\frac{v}{c_\mathrm{p}}\right)^2 \mathrm{d}v$$

Noting that the velocity v is positive and the integral,

$$\int_0^\infty x^{2k+1}\exp\left(-ax^2\right)\mathrm{d}x = \frac{k!}{2a^{k+1}}$$

Integration of the preceding equation yields the following expression for the average velocity:

$$c_\mathrm{av} = 2\sqrt{\frac{2kT}{\pi M}} = \frac{2}{\sqrt{\pi}}c_\mathrm{p} = 1.128c_\mathrm{p} \tag{4.11}$$

Effective velocity of the gas molecules is

$$c_\mathrm{rms} = \sqrt{\frac{3kT}{M}} = \sqrt{\frac{3}{2}}c_\mathrm{p} = 1.224c_\mathrm{p} \tag{4.12}$$

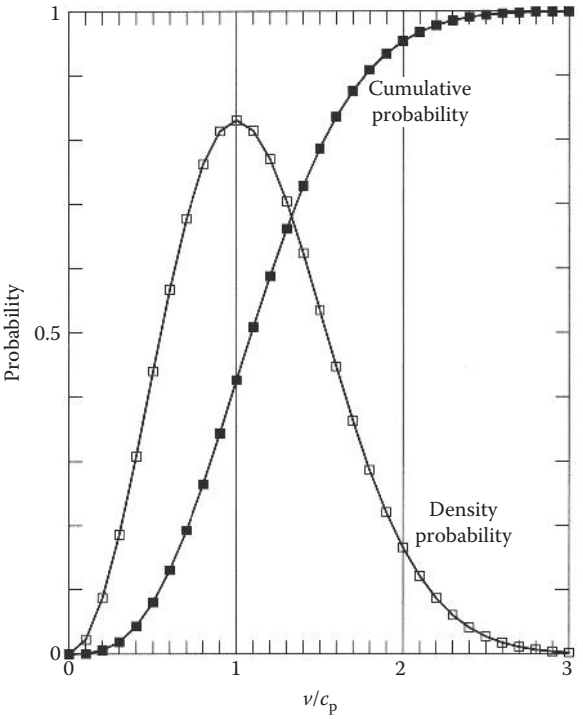


FIGURE 4.4 Distribution of velocities of gas molecules v, normalized to the probable velocity c_p.

Noting that $k = 1.38054 \times 10^{-23}$ J/K, the velocities of gas molecules in common gases, nitrogen, oxygen, and SF_6, under normal conditions of temperature and pressure, are given in Table 4.1. Referring to Figure 4.4, one can make the following observations:

- Because of the widespread shape of the density probability function, most of the gas molecules have a velocity close to c_0. Only 8.1% of the gas molecules have a velocity below $c_p/2$.
- The proportion of gas molecules with a velocity greater than $5c_p$ is only 7.95×10^{-11}.
- The velocities c_p, c_{av}, and c_{rms} are close to one another.

4.2.3 Equal Partition of Energy

Consider 2 g-mol of gases of molecular masses of M_1 and M_2 respectively. At the same temperature T, their pressure must be the same according to the Gay-Lussac law:

$$P_1 = P_2 = P$$

TABLE 4.1

Characteristic Velocities of Gases under Normal Conditions

Parameters	Unit	Nitrogen	Oxygen	SF_6
Molecular mass	Atomic	28	32	146
	kg	3.986×10^{-26}	5.315×10^{-26}	2.425×10^{-25}
Probable velocity, c_0	m/s	450.27	389.95	182.65
Average velocity, c_{av}	m/s	507.91	439.86	206.15
Effective velocity, c_{rms}	m/s	555.13	477.29	223.7

Noting the expressions of the pressures P_1 and P_2 in terms of the number densities and the effective velocities of the gas molecules, it follows that

$$P_1 = \frac{2}{3} n_1 \frac{M_1}{2} \left(c_{\text{rms1}}\right)^2 \quad \text{and} \quad P_2 = \frac{2}{3} n_2 \frac{M_2}{2} \left(c_{\text{rms1}}\right)^2$$

Since for a gram-mole the number of gas molecules is the same and equal to the Avogadro number, the number densities n_1 and n_2 are identical. It follows that

$$\frac{M_1}{2} \left(c_{\text{rms1}}\right)^2 = \frac{M_2}{2} \left(c_{\text{rms2}}\right)^2$$

which means that at the same temperature, *the average energy of the gas molecules is the same in the two gases.*

4.2.4 Mean Free Path

4.2.4.1 Statistical Distribution of Free Paths

Consider a gas volume; let $N(x)$ be the number of gas molecules crossing a distance x without collision. The number of collisions $\mathrm{d}N(x)$ over the distance $\mathrm{d}x$, that is, the rate of variation of $N(x)$, is

$$\mathrm{d}N\left(x\right) = -N\left(x\right) a \, \mathrm{d}x$$

where a is the number of collisions of one molecule crossing 1 cm in the gas. The negative sign in the preceding expression is to underscore the fact that each collision reduces accordingly the number $N(x)$ of gas molecules having crossed the distance x without collision. Integration of the preceding differential equation gives

$$N\left(x\right) = N_0 \exp\left(-ax\right)$$

where N_0 represents the total number of gas molecules at $x = 0$. The probability that a gas molecule makes a free path between x and $x + dx$ is

$$\frac{\mathrm{d}N\left(x\right)}{N_0} = \left| -a \frac{N\left(x\right)}{N_0} \mathrm{d}x \right| = a \exp\left(-ax\right) \mathrm{d}x$$

The use of absolute value of $\mathrm{d}N(x)$ is to give a positive value to the probability. One notes that the probability to find a free path of a given length tends to zero with increasing free path length. It follows the expression for the average value of the free path x:

$$\lambda = \int_0^{\infty} \frac{\mathrm{d}N\left(x\right)}{N_0} = -\int_0^{\infty} a \exp(-ax) \mathrm{d}x,$$

or by changing variable to $u = ax$,

$$\lambda = \frac{1}{a} \int_0^{\infty} \exp(-u) \mathrm{d}u = \frac{1}{a} \exp(-u)\Big|_0^{\infty} = \frac{1}{a}$$

One obtains finally the following expression for the distribution of the free paths of gas molecules as a function of the mean free path λ:

$$N\left(x\right) = N_0 \exp\left(-\frac{x}{\lambda}\right) \tag{4.13}$$

4.2.4.2 Evaluation of the Mean Free Path

Consider a gas molecule moving across the gas volume at a velocity u. The volume covered by the molecule in its course

$$V = uAT$$

where

A is the collision cross section of the molecule; $A = \pi d^2$, with d its diameter

T the time

Assuming that all the other molecules are immobile, the number of collisions made by the molecule in motion is equal to the number of molecules contained in the gas volume covered by the moving molecule (Figure 4.5):

$$N_c = nV = nT\pi d^2 u$$

During the time lapse T, the distance covered is $L = Tu$. It follows that the mean free path, that is, the mean distance covered by a gas molecule between two consecutive collisions, is

$$\lambda_g = \frac{L}{N_c} = \frac{1}{n\pi d^2} \tag{4.14}$$

The denominator of Equation 4.14, $n\,\pi d^2$, is termed *effective cross section for interception* of the gas. Equation 4.14 is valid for neutral gas molecules. In presence of positive ions, which move usually at much higher velocities so that the gas molecules may be considered stationary, the mean free path of ions, λ_i, is longer (Loeb, 1961), (Cobine, 1956) according to:

$$\lambda_i = \sqrt{2}\,\lambda_g \tag{4.14a}$$

In the case of electrons, the small size also increase their mean free path, λ_e, which is given by (Loeb, 1961), (Cobine, 1956)

$$\lambda_e = 4\sqrt{2}\,\lambda_g \tag{4.14b}$$

Distributions of free paths in SF_6: The diameter of a SF_6 molecule is $d_{SF6} = 15.35 \times 10^{-11}$ m. The distributions of the free paths of the gas molecules, its SF_6 ions, and free electrons are shown in Figure 4.6 for the following values of the mean free paths:

$$\lambda_g = \frac{1}{n\pi d^2} = 5.017 \times 10^{-5}\ \text{cm}, \quad \lambda_i = \sqrt{2}\lambda_g = 7.095 \times 10^{-5}\ \text{cm}, \quad \text{and} \quad \lambda_e = 4\sqrt{2}\lambda_g = 2.838 \times 10^{-4}\ \text{cm}$$

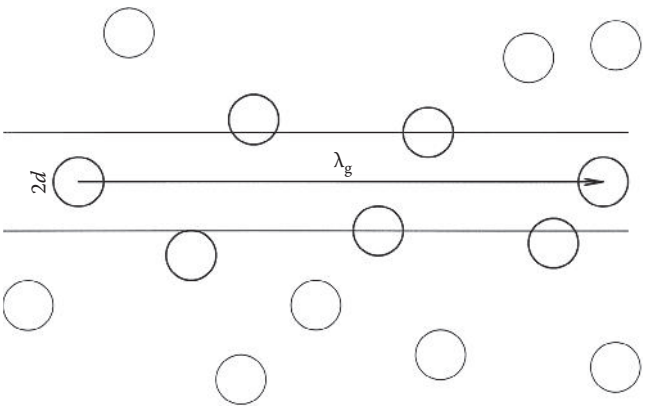


FIGURE 4.5 Free paths of gas molecules, with d the diameter of gas molecule, $2d$ the diameter of the interception cross section and λ_g the free path.

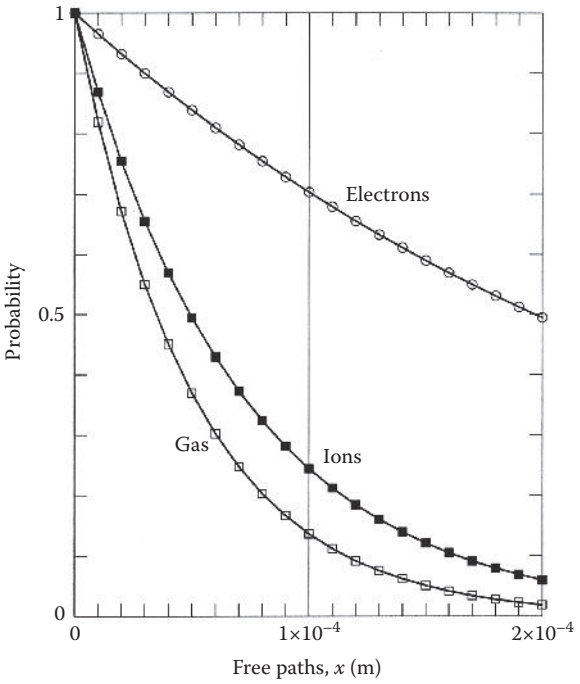


FIGURE 4.6 Distribution of free paths in SF_6.

4.2.5 Diffusion in a Gas

Consider a gas volume and an imaginary plane separating the volume in two. Under normal conditions, there are as many gas molecules traversing the plane in one as in the opposite direction. There is no diffusion in the gas. However, if for some reason, the gas density suddenly increases in one side of the plane, there will be a movement, that is, a net transfer also called diffusion, of gas molecules to the other side of the plane to reestablish an equilibrium state in the gas volume.

4.2.5.1 Number of Molecules Traversing a Unit Area per Second

During the evaluation of the gas pressure on the containing wall, the number of gas molecules having a velocity component in the x-axis between u and $u + du$ that can reach the wall during the time interval T is

$$dN_u = nV_u f(u)du$$

For a velocity between u and $u + du$, the volume $V_u = AT_u$, and

$$dN_u = nATuf(u)du$$

where

A represents the surface of the wall
n the gas number density
$f(u)$ the velocity density distribution function of the gas molecules
V_u the gas volume containing the molecules that can reach the wall

Referring to Figure 4.7, gas molecules with a negative velocity cannot reach the wall; only positive values of u contribute to the integration. The total number, n^*, of gas molecules crossing a unit surface of 1 cm^2 of the wall per second is

$$n^* = \int_0^\infty \frac{dNu}{AT} = \int_0^\infty uf(u)\,du = n\sqrt{\frac{M}{2\pi kT}} \int_0^\infty \exp\left(-\frac{M}{2kT}u^2\right) du$$

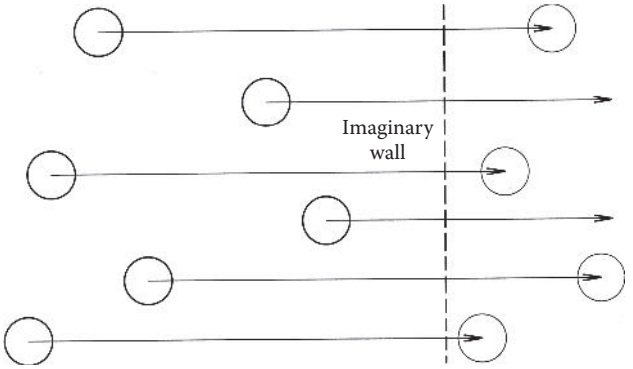


FIGURE 4.7 Diffusion of gas molecules.

Noting that

$$\int_0^{\infty} \exp\left(-\frac{M}{2kT}u^2\right) du = \frac{kT}{M}, \quad c_p = \sqrt{\frac{2kT}{M}}, \quad \text{and} \quad c_{av} = \frac{2}{\sqrt{\pi}} c_p,$$

the preceding expression of the number of gas molecules crossing a unit surface of the wall per second, n^*, becomes

$$n^* = n\sqrt{\frac{M}{2\pi kT}}\frac{kT}{M} = \frac{n}{2\sqrt{\pi}}c_p = \frac{n}{4}\frac{2}{\sqrt{\pi}}c_p = \frac{n}{4}c_{av}$$

4.2.5.2 General Equation of Diffusion

Consider an imaginary wall perpendicular to the x-axis and located at a distance x. By definition, the diffusion along the x-axis at x of a gas is the net transfer of molecules across the imaginary wall. Let $n(x - \lambda)$ be the gas density at $x - \lambda$; the number n_+^* of gas molecules crossing the wall in the positive direction of x per unit surface per second is

$$n_+^* = n(x-\lambda)\frac{c_{\text{av}}}{4} = \left[n(x) - \lambda\frac{dn}{dx}\right]\frac{c_{\text{av}}}{4}$$

In a similar manner, the number of gas molecules n_-^* crossing the imaginary wall in the negative direction of x per unit surface per second is

$$n_-^* = n(x+\lambda)\frac{c_{\text{av}}}{4} = \left[n(x) + \lambda\frac{dn}{dx}\right]\frac{c_{\text{av}}}{4}$$

It follows the expression for the net number n^* of gas molecules crossing the imaginary wall per unit surface per second:

$$n^* = (nx^*_+) - (nx^*_-) = \frac{c_{\text{av}}}{4}\left[n(x-\lambda) - n(x+\lambda)\right]$$

$$= \frac{c_{\text{av}}}{4}\left[n(x) - \lambda\frac{dn}{dx} - n(x) - \lambda\frac{dn}{dx}\right] = -2\lambda\frac{c_{\text{av}}}{4}\frac{dn}{dx} = -D\frac{dn}{dx}$$

The coefficient of diffusion of the gas becomes

$$D = \frac{\lambda}{2}c_{\text{av}} \tag{4.15}$$

The preceding expression of the diffusion coefficient D is only approximate.

A more accurate expression is $D = (\lambda/3)c_{\text{av}}$, with $c_{\text{av}} = 2\sqrt{2kT/\pi M}$ and $\lambda = 1/n\pi d^2$.

Noting that $n = p/kT$, the diffusion coefficient D becomes

$$D = \frac{1}{3pd^2}\frac{1}{\sqrt{M}}\left(\frac{2kT}{p}\right)^{3/2} \tag{4.16}$$

In the case of the diffusion of one gas into another, the mass M becomes $M = M_1M_2/(M_1 + M_2)$.

Consider a gas volume included between two parallel planes, located at x and $x + dx$. The time variation of the gas density $n(x)$ is equal to the difference between the diffusion of the gas at x and $x + dx$; one gets

$$\frac{\partial n}{\partial t}dx = n^*(x) - n^*(x + dx) = n^*(x) - \left[n^*(x) + \frac{\partial}{\partial x}n^*(x)dx\right]$$

or

$$\frac{\partial n}{\partial t} = -\frac{\partial}{\partial x}n^*$$

Noting that $n^* = -D(\partial n/\partial x)$, the preceding equation becomes

$$\frac{\partial n}{\partial t} = -\frac{\partial}{\partial x}n^* = -\frac{\partial}{\partial x}\left[-D\frac{\partial n}{\partial x}\right] = D\frac{\partial^2 n}{\partial x^2}$$

Or in a general manner,

$$\frac{\partial n}{\partial t} = D\nabla^2 n \tag{4.17}$$

which is the general diffusion equation.

4.2.5.3 Diffusion of a Gas in Another Gas

The use of gas mixtures may be advantageous under certain circumstances to improve a specific propriety of the gaseous insulation. However, the gas mixture does not become homogeneous instantaneously as illustrated by the simple case of the diffusion of SF_6 in a gas column of height H. Assuming that initially the SF_6 occupies a volume at the bottom of the column, up to a height h and ignoring the effect of gravity. The equation describing the diffusion of SF_6 in the nitrogen column simplifies to

$$\frac{1}{D}\frac{\partial}{\partial t}n(z,t) = \frac{\partial^2}{\partial z^2}n(z,t) \tag{4.18}$$

where the SF_6 concentration $n(z,t)$ in air is a function of the height z and time t only. Applying the method of separation of variables to the preceding differential equation,

$$n(z,t) = F(z)T(t)$$

$$\frac{1}{D}\frac{\partial}{\partial t}n(z,t) = \mathrm{F}(z)\frac{\mathrm{d}}{\mathrm{d}t}T(t)$$

and

$$\frac{\partial^2}{\partial z^2}n(z,t) = T(t)\frac{\mathrm{d}^2}{\mathrm{d}z^2}F(z)$$

The initial differential equation becomes

$$\frac{1}{D}F(z)\frac{\mathrm{d}}{\mathrm{d}t}T(t)=T(t)\frac{\mathrm{d}^2}{\mathrm{d}z^2}F(z),$$

or by dividing both sides by $F(z)\,T(t)$,

$$\frac{1}{D}\frac{1}{T(t)}\frac{\mathrm{d}}{\mathrm{d}t}T(t)=\frac{1}{F(z)}\frac{\mathrm{d}^2}{\mathrm{d}z^2}F(z)=\text{Constant} \tag{4.19}$$

The only possibility to satisfy the preceding equation is that both members of the equation be equal to a constant. Furthermore, since the time-dependent term must tend to zero for $t \to \infty$, the constant must be negative: $-\gamma^2$. The differential equation (4.19) decomposes in two differential equations, each of a single variable z and t:

$$\frac{1}{D}\frac{1}{T(t)}\frac{\mathrm{d}}{\mathrm{d}t}T(t)=-\gamma^2 \tag{4.20}$$

and

$$\frac{1}{F(z)}\frac{\mathrm{d}^2}{\mathrm{d}z^2}F(z)=-\gamma^2 \tag{4.21}$$

The general solution of Equation 4.20 is of exponential type

$$T(t)=n_0\exp\left(-\gamma^2 Dt\right)$$

where n_0 is a constant representing the initial local concentration of SF_6 in air.

The general solution of Equation 4.21 is of sinusoidal type:

$$F(z)=\sum_{k}\left[A_k\cos(\gamma z)+B_k\sin(\gamma z)\right]$$

The general solution of the diffusion equation is then

$$n(z,t)=A_0+\left\{\sum_{k}\left[A_k\cos(\gamma z)+B_k\sin(\gamma z)\right]\right\}\exp\left(-\gamma^2 Dt\right) \tag{4.22}$$

where the constant A_0 corresponds to the final concentration of SF_6 in the air column, corresponding to the steady state solution of Equation 4.18:

$$A_0=\frac{1}{H}\int_0^h n_0\,\mathrm{d}z=\frac{n_0}{H}h$$

with n_0 being the initial concentration of SF_6.

Since at $t = 0$, the distribution of SF_6 corresponds to the initial distribution with the SF_6 confined at the ground level, up to a height h. Furthermore, the concentration of SF_6 defined by Equation 4.22 is positive only for values of z between 0 and H. The right-hand side of Equation 4.22 represents effectively the development in Fourier series of a periodic function of period $2H$, between $-H$ and H. In these conditions, the coefficients B_k must be null. It follows that

$$\gamma(2H)=2k\pi \quad \text{or} \quad \gamma=\frac{k\pi}{H}$$

On the other hand, the coefficients A_k are determined by multiplying both sides of Equation 4.22 by $\cos\left((k\pi/H)z\right)$, and by integrating over the period of $-H$ to H, one obtains

$$\int_{-H}^{H}F(z)\cos\frac{k\pi}{H}z\,\mathrm{d}z=\int_0^h A_k\cos^2\frac{k\pi}{H}z\,\mathrm{d}z=\pi A_k$$

and

$$A_k = \frac{2}{p}\int_0^H F(z)\cos\frac{kp}{H}z\,dz = \frac{2}{H}\int_0^h n_0\cos\frac{kp}{H}z\,dz = \frac{2n_0}{kp}\sin\frac{kp}{H}h$$

It follows that

$$F(z) = \frac{2n_0}{p}\sum\frac{1}{k}\sin\frac{kp}{H}h\cos\frac{kp}{H}z$$

Finally, the solution to the differential equation for the diffusion of SF_6 in the nitrogen column is

$$n(z,t) = \frac{n_0}{H}h + \frac{2n_0}{p}\sum\frac{1}{k}\sin\frac{kp}{H}h\cos\frac{kp}{H}z\exp\left[-\frac{kp}{H}^2 Dt\right] \tag{4.23}$$

Mixture of SF_6–N_2: The mixture of SF_6–N_2 is a solution to the liquefaction of SF_6 under conditions of low temperatures, without much affecting the dielectric performance of the equipment. Figure 4.8 shows the time variations of the SF_6 concentrations at different levels in the N_2 column of 1 m height, subsequent to the injection of SF_6 at the bottom of the gas column. The final ratio of the gas mixture is 60% SF_6 to 40% N_2. The calculation is made for two different heights, 0.1 and 0.9 m, corresponding to two locations initially in SF_6 and N_2 portion of the gas column. One can see that the diffusion of SF_6 into the N_2 column takes several hours, 20 h in this case, before the mixture becomes completely homogeneous. The effect is directly a function of the dimensions of the gas column and underscores the importance of either to allow a sufficient time for the diffusion process or to use artificial means to accelerate the mixing process in the gas.

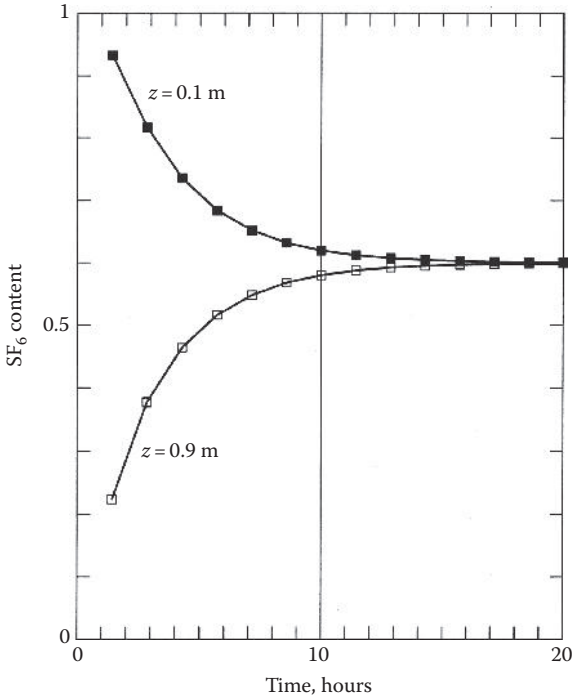


FIGURE 4.8 Time variations of the SF_6 content in a N_2 column subsequent to the injection of SF_6 at the bottom of a 1 m gas column, to make a homogeneous mixture. Calculation was made for two heights in the gas column of $z = 0.1$ and 0.9 m respectively.

Accidental spill of SF_6: Although a rare event, accidental spill of SF_6 can occur following a fault with burn-through of the GIS envelope. Because of its higher specific mass, approximately five times the ambient air, the SF_6 volume first concentrates at the ground level before diffusing slowly into the surrounding air volume. The stagnation of SF_6 in a closed space with little ventilation may be a potential risk of asphyxia for the maintenance personnel. Assuming a burn-through an 800-kV of dimensions 61/20.3 cm, SF_6-insulated compartment of 100 m length and a nominal pressure of 5 atm. abs., the volume of SF_6 spilled out is 105 m^3. Two cases will be evaluated corresponding to a vertical shaft containing a SF_6-insulated bus connecting the underground GIS of a generating station to an overhead line and a tunnel containing a SF_6-insulated bus in an underriver crossing of an overhead line. Both the vertical shaft and the tunnel have a section of 5 m by 5 m; the depth of the vertical shaft is $H = 100$ m. A diffusion coefficient of SF_6 in air of $D = 0.09494$ cm^2/s is used.

In the case of a vertical shaft, it is assumed that the spilled gas occupies initially the bottom of the shaft, up to a height h_0, before diffusing into the volume of the shaft. The initial height of the SF_6 column obviously depends on the length of the damaged GIS compartment. Figure 4.9 shows the time variations of the SF_6 content at a height of $z = 1.5$ m and for different values of the initial height h_0 of SF_6 in the shaft. One observes that it may take many days before the concentration of SF_6 reaches the equilibrium level: h_0/H, which may be several orders of magnitude above the acceptable level of SF_6 in air of 0.001 (or 1000 ppm), the same for a neutral gas other than nitrogen.

For the case of a tunnel for an underriver crossing, because of the length of the tunnel, the spilled SF6 will not immediately spread over the whole tunnel. It is assumed that the spilled gas will first spread on the tunnel floor, over a section of length L_0, up to a height of h_0, before diffusing into the volume of tunnel above L_0. For a given volume of spilled SF_6, the initial height h_0 of the SF_6 column varies with the length L_0 that the gas spreads over the ground. Figure 4.10 shows the time variations of the SF_6 content in the tunnel at two levels of $z = 0.1$ and $z = 1.5$ m and for different values of the initial spreading length L_0, of SF_6 in the tunnel. One observes that it will take several hours before the concentration of SF_6 reaches the equilibrium level, which can be several times the acceptable level for SF_6 in air. It should be noted,

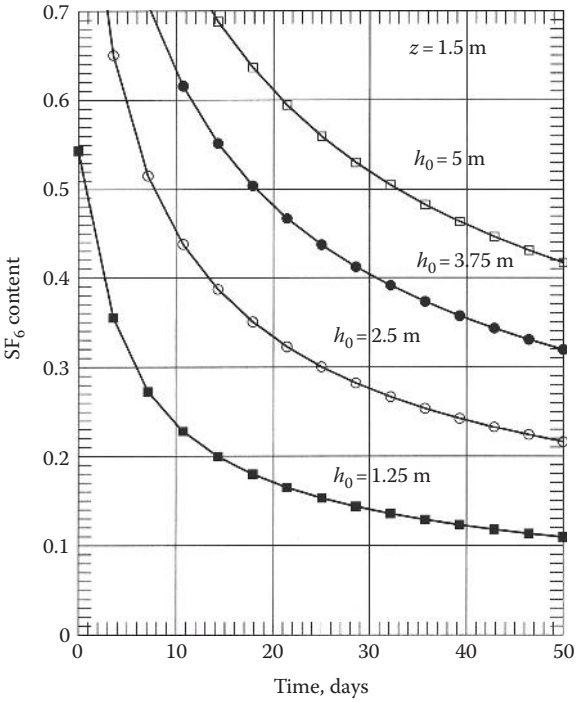


FIGURE 4.9 Variations of the SF_6 concentration in a vertical shaft during a massive spill. Calculations are made for $z = 1.5$ m and different values of h_0, the initial level of SF_6.

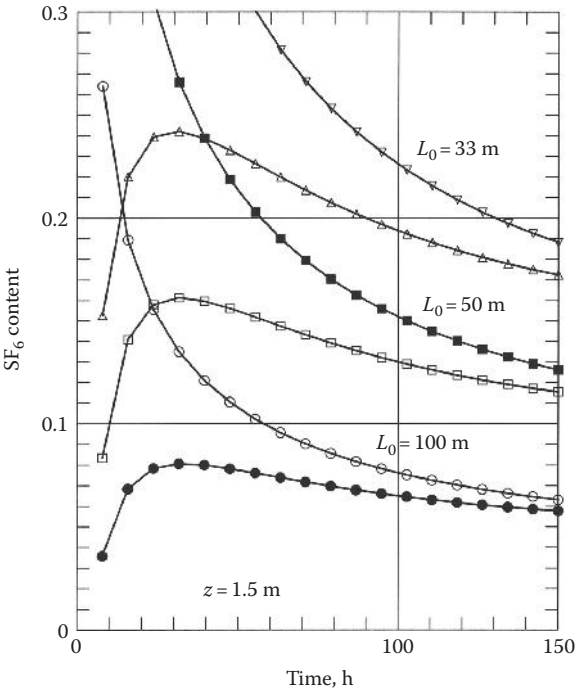


FIGURE 4.10 Time variations of the SF_6 concentration in a tunnel in case of massive spill. Calculations are made for z = 1.5 m and different values of L_0, the initial length occupied by SF_6.

however, that in a real situation, the spreading length L_0 will increase in time, hence reducing the corresponding height h_0 with the consequence that the SF_6 content will be lower than the levels predicted with constant values of L_0 and h_0.

4.3 Atomic Structure of the Elements

The first elaborations of a physical model for the atomic structure of the elements resulted from the observation of the light emissions obtained during electric discharges in various gases. These light emissions consist of discrete line spectra, the frequencies of which are characteristic of each gas (Figure 4.11). One notes that the emission spectra consist of distinct groups of lines, the wave number ν^* of which follows an empirical law. For the emission spectra of hydrogen, the wave number of the lines in the Balmer series follows an empirical formula:

$$\mathrm{n}^* = R\left(\frac{1}{n_1^2} - \frac{1}{n_2^2}\right),$$

where $n_1 = 2$, n_2 is an integer greater than 2, and R = 109,678.28 cm^{-1}, the Rydberg constant.

The wave number ν^* is defined as $\mathrm{n}^* = 1/\mathrm{n}$, $\mathrm{l} = c/\mathrm{n}$ the wavelength of the lines in the spectrum, ν its frequency, and c the speed of light.

4.3.1 Bohr's Atomic Model

Bohr elaborated his atomic model from the works of M. Planck and aimed at improving the Rutherford model consisting of a very small, dense nucleus with a positive charge and one or several electrons gravitating on distinct orbits with the total charge equals that of the central nucleus. This model suffers a number of limitations, the principal being its incapability to explain the great stability of the orbital movements

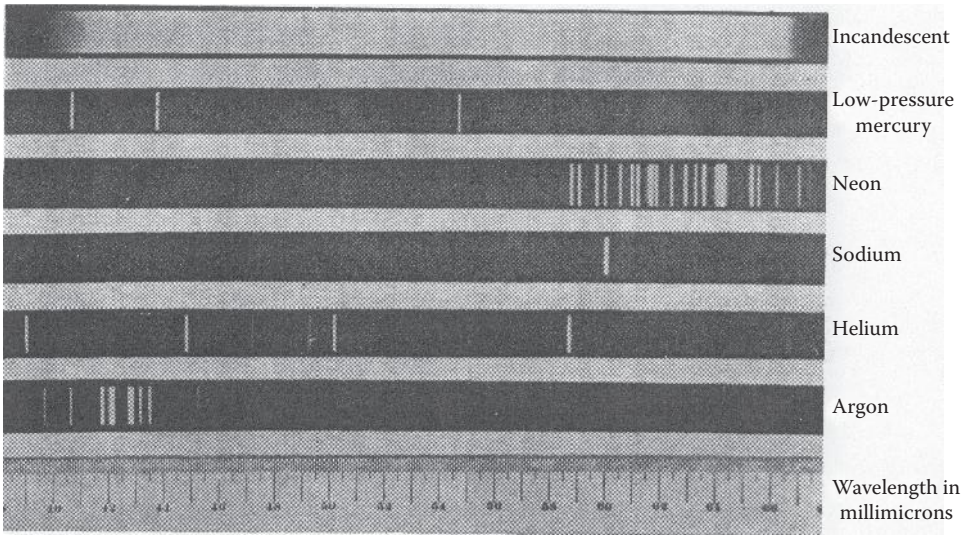


FIGURE 4.11 Emission spectra from an electric arc in different gases. (From Cobine, J.D., *Gaseous Conductors—Theory and Engineering Applications*, Dover Publications Inc., New York, 1958.)

of the electrons around the nucleus. In effect, the orbital movement is justified by the attraction that the nucleus, positively charged, exerts on the electrons of negative charge. The radial force of attraction is

$$eE = \frac{1}{4\pi\varepsilon_0} e\frac{Q}{a^2}$$

where

Q is the electric charge of the nucleus
a the radius of the orbit of the electron

Referring to Figure 4.12, which shows an electron on its orbit, the fact that the electron remains on its circular orbit indicates that the radial force of attraction is equal to the centrifugal force associated with the movement of the electron in its orbit. Without the attraction of the nucleus, the electron would continue its course along a linear trajectory tangential to the orbit. The radial distance that the electron would make during the time t is

$$\delta_r = vt \sin\frac{\omega t}{2}$$

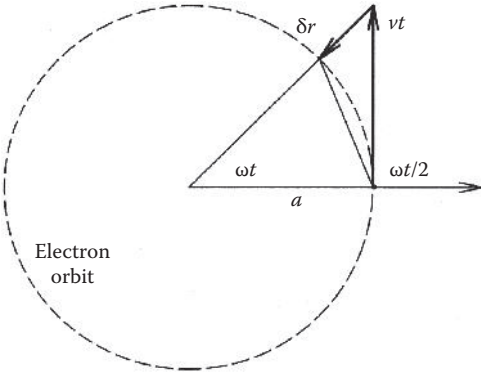


FIGURE 4.12 Orbital movement of an electron.

Since the angle ωt is small, $\sin(\omega t/2)$ is approximately equal to $\omega t/2$. The preceding expression of δ_r becomes $\delta_r = (1/2)\, v\omega t^2$.

The linear velocity v is, on the other hand, related to ω by $v = a\omega$, and it follows that

$$\delta_r = \frac{1}{2}\frac{v^2}{a}t^2 = \frac{1}{2}\gamma_r t^2$$

The centrifuge acceleration, which tries to remove the electron from its orbit, is $\gamma_r = v^2/a$.

The corresponding centrifuge force is $F_r = m\gamma_r = m(v^2/a)$.

Since the electron is maintained in equilibrium on its orbit, the attraction force of the nucleus must equal the centrifuge force. One obtains

$$\frac{Q}{4\pi\varepsilon_0}\frac{e}{a^2} = m\frac{v^2}{a} \tag{4.24}$$

This attraction of the nucleus, which explains the orbital movement of the electron, is in contradiction with the classical theory of electromagnetism, which stipulates that *an electron subjected to a constant acceleration should radiate energy.* In the model of Rutherford, the electron in orbit is constantly subjected to the attraction of the nucleus. It should radiate energy. The electron, losing continuously its energy, must eventually fall to the nucleus of the atom. Furthermore, the continuous radiation of energy by the electron would produce an emission spectrum without lines as observed in practice.

To overcome this limitation of the Rutherford model, Bohr referred to the quantum theory forwarded by M. Planck, which proposes that contrarily to the classical mechanics, energy can be radiated by discrete amounts only, and the basic unit, a photon, has an energy:

$$\Delta w = h\nu$$

where

Δw is the photon energy

ν the frequency of the emitted light

h the universal Planck's constant—$h = 6.625 \times 10^{-34}$ J-s

In the elaboration of his atomic model, N. Bohr modifies the model of Rutherford, by adding two hypotheses based on the quantum theory of M. Planck.

Bohr's first hypothesis: *An electron can only radiate energy when it is on a preferential orbit such that the* ***moment of the momentum****, mva, may be a multiple of* $h/2\pi$.

The kinetic energy, W_c, of an electron in stable equilibrium on an orbit of radius a can be calculated from Equation 4.24, which expresses that the attraction force of the nucleus equals the centrifuge force associated to the movement of the electron on its orbit:

$$W_c = \frac{1}{2}mv^2 = \frac{e}{2a}\frac{Q}{4\pi\varepsilon_0}$$

Since the electron moves in the electric field created by the positive charge of the nucleus, it has also a potential energy W_p. By taking the reference potential as zero at infinite, the potential generated by the nucleus of the atom at a distance a is

$$\varphi = \int_a^{\infty} E\, dr = \frac{1}{4\pi\varepsilon_0}\int_a^{\infty}\frac{Q}{r^2}\, dr = \frac{1}{4\pi\varepsilon_0}\left(-\frac{Q}{r}\right)\Bigg|_a^{\infty} = \frac{1}{4\pi\varepsilon_0}\frac{Q}{a}$$

The potential energy of the electron of charge e and located at a distance a from the nucleus is

$$W_p = q\varphi = -\frac{e}{a}\frac{Q}{4\pi\varepsilon_0}$$

Noting that the charge of the electron is $q = -e$, the total energy of the electron on its orbit is

$$W_e = W_c + W_p = \left(\frac{e}{2a}\right) - \frac{e}{a}\left(\frac{Q}{4\pi\varepsilon_0}\right) = -\frac{e}{2a}\frac{Q}{4\pi\varepsilon_0}$$

With the first hypothesis of Bohr $mva_n = nh/2\pi$, where a_n is the radius of the nth orbit, the velocity of the electron is $v = nh/2\pi ma_n$ or a kinetic energy of

$$W_c = \frac{1}{2}mv^2 = \frac{m}{2}\left(\frac{nh}{2\pi ma_n}\right)^2 = \frac{n^2h^2}{8\pi^2 m a_n^2} = \frac{e}{2a_n}\frac{Q}{4\pi\varepsilon_0}$$

The preceding equation allows the determination of the radius a_n of the preferential orbit as a function of the quantum number n:

$$a_n = \frac{4\pi\varepsilon_0}{4\pi^2}\frac{(nh)^2}{mQe} = \frac{\varepsilon_0 (nh)^2}{\pi mQe}$$

One obtains the following expression for the energy of the electron W_{en}:

$$W_{en} = -\frac{e}{2a_n}\frac{Q}{4\pi\varepsilon_0} = \frac{eQ}{2}\frac{4\pi^2 m\, Qe}{4\pi\varepsilon_0 (nh)^2} = -2m\left(\frac{\pi Qe}{4\pi\varepsilon_0 nh}\right)^2$$

where

Q is the positive charge of the nucleus
m the electron mass

Figure 4.13 illustrates the different energetic levels of the electron in the hydrogen atom for the first few values of the quantum number n. One can see that the total energy of the electron is lowest when the quantum number n is equal to 1. It follows that

$$W_{e1} = -\frac{e}{2a_1}\frac{Q}{4\pi\varepsilon_0} = -2.15 \times 10^{-18}\ \text{J}$$

As the quantum number n increases, the absolute value of the electron energy reduces, implying an increase of its energy in the higher orbits.

Bohr's second hypothesis: *When an electron passes from an allowed orbit to another one of lower energetic level, it radiates energy according to*

$$h\nu = W_{e2} - W_{e1}$$

where

W_{e1} and W_{e2} are the energetic levels of the two orbits of the electron
ν the frequency of the emitted light

It follows that the emission spectrum of a gas is necessarily formed of lines, the frequencies of which are defined according to

$$\nu = \frac{2}{h^3} m (\pi Qe)^2 \left(\frac{1}{n_1^2} - \frac{1}{n_2^2}\right)$$

or in terms of the wave number ν^*

$$\nu^* = \frac{1}{\lambda} = \frac{\nu}{c} = \frac{2}{h^3}\frac{m}{c}(\pi Qe)^2 \left(\frac{1}{n_1^2} - \frac{1}{n_2^2}\right)$$

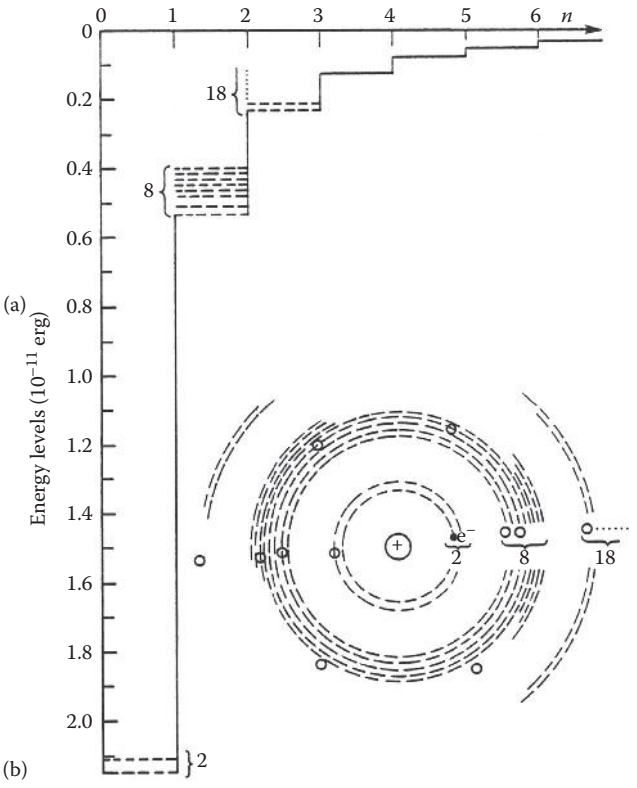


FIGURE 4.13 Potential well of an atom.

where c is the velocity of light. With the empirical expression for the Balmer series of lines, one obtains the Rydberg constant $R = \frac{2m}{h^3 c}\left(\mathrm{p}Qe\right)^2$ = 109,750 cm^{-1} compared with a more accurate value of 109,678.28 cm^{-1}.

The series of lines observed in the emission spectra obtained from electric discharges in gases correspond then to the light radiations accompanying the changes of energetic levels of the electron in orbit around the atom nucleus. The existence of several series of lines in the emission spectrum of a gas is explained by the difference in the terminal energetic levels. Figure 4.14 illustrates the existence of the

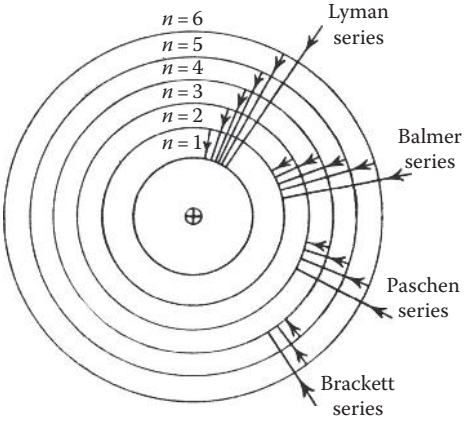


FIGURE 4.14 Illustration of the line series in the light emission spectra of hydrogen. (From Cobine, J.D., *Gaseous Conductors—Theory and Engineering Applications*, Dover Publications Inc., New York, 1958.)

Lyman, Balmer, Paschen, and Brackett series of lines in the emission spectrum of hydrogen. One can see that the terminal energetic levels of these series correspond to the energetic levels for values of the quantum number n of 1, 2, 3, and 4.

4.3.2 Energy States of an Electron in an Atom

From Bohr's theory, there are certain preferential energetic levels, corresponding to the integer values of the quantum number n, such that the electron can stay in stable orbit without radiating energy. These levels are

$$W_{en} = -2m\left(\frac{pQe}{nh}\right)^2$$

In reality, the preceding equation defines only the principal energetic levels. One can show that several electrons, having the same principal energetic level, are actually in slightly different orbits. In fact, a set of four parameters describe the energetic state of a peripheral electron in an atom:

Principal quantum number, n: It defines the energetic level corresponding to different orbits forming the principal layers of the electron around the nucleus. The quantum number n can take positive integer values: $n = 1, 2, 3,\ldots$.

Azimuth quantum number, l: It characterizes the different orbits of the electrons appertaining to the same layer. This quantum number can take integer values defined by $l = n - 1$. At the maximal quantum number, $l = n - 1$ corresponds to the circular orbit with the highest angular moment.

Magnetic quantum number, m: It characterizes the orbital plane of the different trajectories of the electrons of the same layer. It characterizes the movement of orbital electrons when the atom is in a magnetic field. This quantum number can take positive and negative values between $-l$ and l: $m = 0, \pm1, \pm2,\ldots, \pm l$.

Quantum number of spin, s: It defines the direction of rotation of the electron on itself. This quantum number can have only two values: $s = +1/2, -1/2$.

The subject is dealt with more rigorously in solution of Schrodinger's equation described in texts on wave mechanics (Richtmyer et al., 1955).

4.3.3 Exclusion Principle of Pauli

With the energetic states defined earlier for the peripheral electrons in an atom, it follows that a very large number of orbits are available for these electrons. Because of the different energetic levels associated with the electron orbits, an electron will occupy the orbit with the lowest energetic level possible. The arrangement of the electrons around an atom is made according to the following principle of Pauli, which stipulates that *in an atom, it is impossible to have two electrons of exactly the same energetic state defined by the four quantum numbers defined previously.* The consequence of this principle is that the electrons in an atom are grouped in layers:

- The first layer corresponds to $n = 1$; $l = 0$, $m = 0$; and $s = +1/2$ or $-1/2$. This layer can contain only two electrons at most.
- The second layer corresponds to $n = 2$; $l = 1$; $m = 0$, $+1$ or -1; $s = +1/2$ or $-1/2$; and $l = m = 0$, $s = +1/2$ or $-1/2$. One can verify that this second layer contains at most eight electrons, and so on.

4.3.4 Interpretation of the Periodic Table of Elements

The natural elements, as seen earlier, are characterized by their individual atomic structure as represented in the periodic table of natural elements. Figure 4.15 shows the variations of the ionization energy of the first 25 elements in the periodic table with their atomic number. One can see that for elements on the same row or period, of the periodic table, the ionization energy increases with the number of electrons in the peripheral layer. On the other hand, when comparing the elements in different periods, the ionization

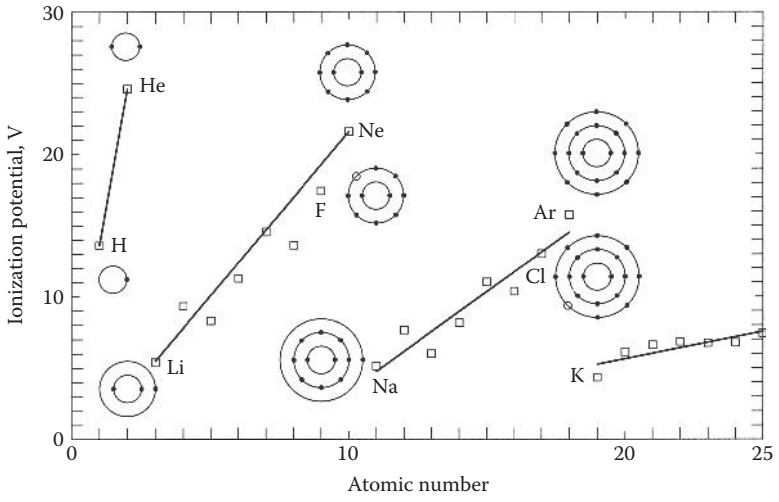


FIGURE 4.15 Influence of the atomic structure on the ionization energy of the elements.

energy decreases as one passes from one period to the next, containing atoms of higher atomic number. This corresponds to the addition of a new shell for the larger number of peripheral electrons, which effectively increases the physical dimensions of the atoms. One can make the following observations:

Noble gases: The elements of the last column of the periodic table form a group characterized by a peripheral layer completely filled with electrons: He, Ar, etc. These elements are particularly stable, chemically neutral, and relatively difficult to ionize.

Active elements: The elements of the first column of the periodic table form a group characterized by a peripheral layer with only one electron, weakly attached to the atom, H_2, Na, etc., making these elements chemically active and easily ionized.

Electronegative gases: The gases in this group have a peripheral layer almost completely filled, leaving available holes for one or two electrons and providing these elements with a high degree of affinity to electrons: F and Cl atoms. These elements can easily capture additional electrons to complete the peripheral layer and form negative ions particularly stable. The electronegative gases are used to improve the dielectric performance of the gas insulation. The most commonly known are air, O_2, SF_6, Cl_2, etc. The most frequently used in dielectric insulation are air and sulfur hexafluoride (SF_6).

4.4 Excitation and Ionization of Atoms

In their normal state, the electrons occupy the orbits of lowest possible energetic level in the atom, in accordance with Pauli's exclusion principle. When the atom absorbs energy, the increase of its internal energy causes the displacement of one or several of its electrons to orbits with higher energetic levels. The atom is then termed excited. However, the state of excitation of the atom is relatively unstable, so that the atom, if left alone, will rapidly release the absorbed energy by light emission at a frequency defined by

$$\nu = \frac{\Delta E}{h}$$

where ΔE is the radiated energy.

When the energy absorbed by the atom is sufficient to move the peripheral electron to an orbit far from the nucleus and eventually remove it from the atom, the atom is ionized. Because of the discrete allowed energy of the orbits, the energy absorbed by the atom corresponds to discrete amounts defined as excitation or ionization energy of the atom. These energies are characteristic for each atom, in direct function

of its atomic structure. Noting that energies are currently expressed in eV, the excitation and ionization energies are often expressed by their *potentials of excitation* and *ionization*, expressed in V.

It should be pointed out that if Pauli's exclusion principle allows the arrangement of the electrons in the atom, it is not an absolute rule. Practical experience shows that certain allowed energetic levels are occupied rarely. This is related to the rules defining the transfer of the electron from one allowed energetic level to another. A few principal rules of transfer are the following:

- The transfer of the electron can take place only between the orbits resulting in a change in the value of the azimuth quantum number l by $\Delta l = \pm 1$.
- The transfer can take place only between the even and odd sums of the azimuth quantum numbers l of the orbits in a layer.
- By defining a quantity J equal to the sum of the azimuth quantum numbers l and the spin s of the electrons in the outer layer, the transfer of the electron is possible only between the orbits resulting in a change in the value of J by $\Delta J = \pm 1$. The transfer is also allowed when there is no change in the value of J, except $J = 0$.
- There is no restriction in the change of n.

The reactions of excitation (and ionization) of an atom can be symbolically represented by the following equations:

For the excitation of the atom

$$W + A \rightarrow A^* + W_c, \quad \text{with } W_c = W - W^*$$

For the ionization of the atom

$$W + A \rightarrow A^+ + e^- + W_c, \quad \text{with } W_c = W - W_i$$

where

A^* represents the atom A in the excitation state
A^+ the positive ion formed during the ionization of the atom A
e^- the free electron removed from the atom A
W represents the amount of energy absorbed by the atom A, causing its excitation or ionization
The energies W^* and W_i correspond to the excitation and ionization energies of the atom A
W_c represents the kinetic energy of the excited atom A^* or of the positive ion A^+

Metastable state: In spite of the general applicability of Pauli's exclusion principle in the definition of the energetic levels of the electrons in orbit around the nucleus of an atom, there exist, in certain gases, electrons with energetic levels corresponding to those excluded by Pauli's exclusion principle. These electrons are said to be in a *metastable state*. Since their energetic level does not correspond to any allowed level, these electrons do not easily lose their energy to return to their neutral state. It follows that atoms in their metastable state have a much longer life then, attaining the order of 10^{-3} s or even seconds, than the normally excited atoms, the life duration of which is in the order of 10^{-8} s.

Absorption of energy by an atom A can be made in various manners, of which, the principal processes are described in the following. It is to be noted that except for their energetic levels, these processes produce essentially the same effect: excitation and ionization of an atom.

4.4.1 Ionization by Electronic Collisions

The symbolic equation describing the reaction is

$$W + e^- + A \rightarrow A^+ + 2e^- + W_c$$

In electronic collisions, the energy exchange between the electron and atom occurs only if the kinetic energy of the electron is greater than the excitation or ionization energy of the atom A. The energy

exchange then causes the excitation or ionization of the atom. If the kinetic energy of the electron is insufficient to excite or ionize the atom, the energetic exchange in the collision is negligible, and the electron conserves essentially all its energy before the collision. On the other hand, electrons with very high energy simply pass through the atom without ejecting any of its peripheral electrons. However, atoms already excited can be ionized in collisions with electrons with relatively low energy. This process requires a sufficiently dense beam of electrons, since the life duration of excited atoms is only in the order of 10^{-8} s.

One way to quantify the efficiency of the electrons to ionize atoms of a gas consists in evaluating the *coefficient of differential ionization* of electrons, defined as the *number of ion pairs formed by an electron of a known energy, crossing a distance of 1 cm in the gas at a pressure of 1 mm Hg.* Figures 4.16 and 4.17 show variations of the ionization efficiency of electrons in the vapor of mercury (Bleakney, 1930) and in air (Engel and Steenbeck, 1930) at a pressure of 1 mm Hg, as a function of the electron energy. One notices that there is an optimal energy, at which the coefficient of ionization of the electrons is maximal: about 70 eV in mercury vapor and 150 eV in air. For electrons with energy below the optimal level, their ionization efficiency can be expressed by the following linear relation:

$$S = a\left(V - V_i\right)$$

where

S represents the differential ionization coefficient
V the energy of the electron in eV
a a constant characteristic of the gas
V_i the ionization potential

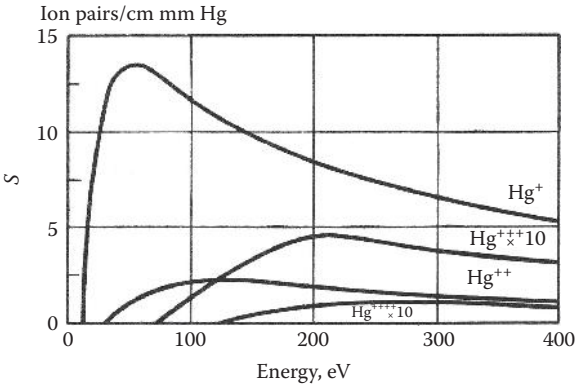


FIGURE 4.16 Coefficients of ionization by electron collisions of mercury vapor. (From Bleakney, W., *Phys. Rev*., 35, 139, 1930; Cobine, J.D., *Gaseous Conductors—Theory and Engineering Applications*, Dover Publications Inc., New York, 1958.)

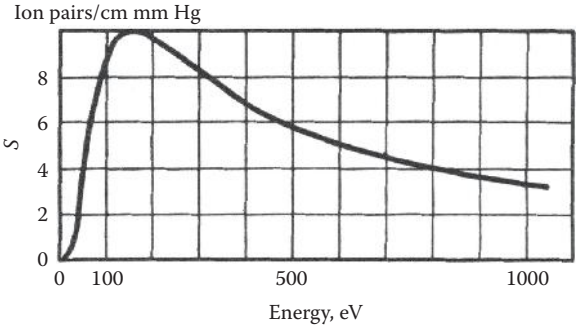


FIGURE 4.17 Differential ionization coefficient for electrons in air. (From Engel, A.V. and Steenbeck, M., Elektrische Gasentladungen, ihre Physik u. Technik, 1, 34, 1930; Cobine, J.D., *Gaseous Conductors—Theory and Engineering Applications*, Dover Publications Inc., New York, 1958.)

One direct consequence of electronic collisions between the electrons and neutral atoms of a gas is the gradual loss of energy by the electrons, subsequent to successive excitations and ionizations of the gas atoms. Eventually, the electron sees its energy reduced below the ionization energy of the gas. The electron reaches its *final state*. The distance d traveled by the electron before reaching its final state is a function of its initial energy according to the following empirical relation (Thompson and Townsend, 1930):

$$d = 1.4 \times 10^{-7} \frac{TV_0^2}{Mp}$$

where

V_0 represents the initial energy of the electron
T, M, and p the temperature, mass, and pressure of the gas
d the critical distance

The residual energy of the electron after crossing a fraction k of the critical distance R is

$$V_k = V_0 \left(1 - k\right)$$

In the case of electric discharges, the electrons gain their energy from the applied electric field. The negligible mass of the electrons compared to that of the neutral atoms cause the electrons to conserve almost all their energies during the elastic collisions. As a result, they can accumulate energy over several consecutive free paths, until the accumulated energy be sufficient to ionize a gas atom. This ability of the electrons to accumulate energy gained from the applied electric field makes this ionization process particularly efficient in electric discharges in gases.

4.4.2 Ionization by Ionic Collisions

In a similar manner to electrons, ionization of neutral gas atoms by collisions with ions is also possible, as described by the following symbolic relation:

$$W + A + B^+ \rightarrow A^+ + B^+ + e^- + W_c$$

However, unlike the electrons, the ion mass is comparable to that of the neutral atoms involved in the collisions. The energy exchange between the molecules is greater than in elastic electron–atom collisions, making the ionization process much less efficient, unless the initial energy of the ions is very high. Figures 4.18 and 4.19 show the ionization efficiency of α-particles in air and argon; one can see that the optimal energy of the α-particles is about 1.5×10^6 eV, compared to 150 eV for the electrons.

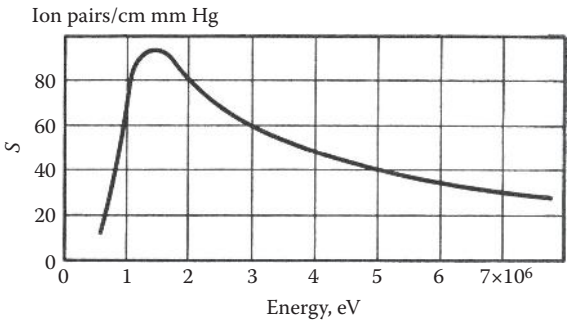


FIGURE 4.18 Differential ionization coefficient for alpha particles in air (1 mm Hg, 0°C). (From Engel, A.V. and Steenbeck, M., Elektrische Gasentladungen, ihre Physik u. Technik, 1, 34, 1930; Cobine, J.D., *Gaseous Conductors—Theory and Engineering Applications*, Dover Publications Inc., New York, 1958.)

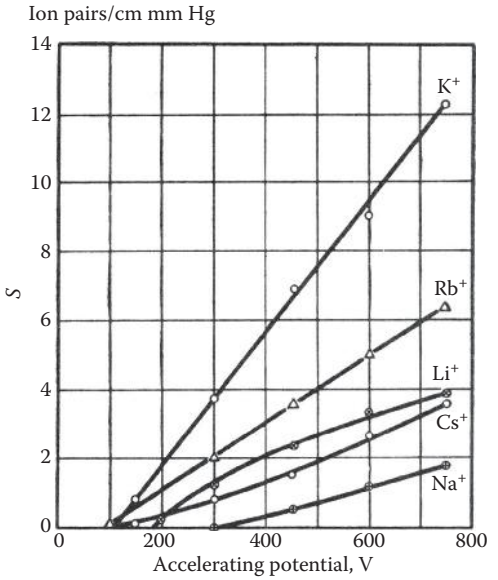


FIGURE 4.19 Differential ionization coefficient for alkali positive ions in argon (ion/cm-mm Hg). Ionization coefficient by ionic collisions in argon. (From Cobine, J.D., *Gaseous Conductors—Theory and Engineering Applications*, Dover Publications Inc., New York, 1958.)

As in the case of electrons, one can describe the ionization efficiency of the ions by their differential ionization coefficient S, expressed by the following empirical relation:

$$S = \frac{2}{3\varphi b\sqrt{V}}$$

where

φ is the effective ionization potential of the gas

b a constant characteristic of the gas

The critical distance d_c for the ions is given by the following empirical relation:

$$d_c = bV_0^{2/3}$$

and the residual energy of the ions after crossing a fraction k of the critical distance d_c is

$$V_k = V_0 \left(1 - k\right)^{2/3}$$

where V_0 is the initial energy of the ions.

4.4.3 Photoionization

The absorption of photon energy is described by the following symbolic reaction:

$$h\nu + A \rightarrow A^+ + e^- + W_c$$

Photoionization is a process particularly efficient when the radiating energy $h\nu$ is close to the ionization energy of the gas. Its efficiency falls off rapidly when the radiating energy differs from the resonant value corresponding to the ionization energy of the gas. Similar to the case of electronic ionization, the direct consequence of the photoionization on the intensity of the photons is a gradual diminution with

the distance traveled by the photons in the gas. Let I be the number of photons emitted per second from the light source; the number of photons lost over a distance dx in the gas is equal to

$$dI = -\mu I dx$$

where μ is the absorption coefficient of the gas. Integration of the preceding equation gives the following expression for the number of residual photons after a distance x in the gas:

$$I(x) = I_0 \exp(-\mu x)$$

where I_0 is the initial number of photons emitted by the source per second. The absorption coefficient μ at the resonant frequency of the gas ν_0 is

$$\mu = \frac{ne^2}{n_0 m} \frac{M}{2kT}$$

where

e is the electronic charge
m and M the electron and gas atom masses
n the number of gas atoms absorbing the radiated energy per cm^3 of gas

4.4.4 Thermal Ionization

Thermal ionization refers to all ionization processes active in a gas at high temperatures, where the collisions of the gas molecules, neutral atoms, ions and electrons, and light radiations contribute to ionization of the gas. This ionization process is the main source of electrons in the electric arc discharge at high pressure.

Let n be the initial concentration of the gas; the proportion $x = n_i/n = n_e/n$, where n_i and n_e are the ion and electron densities supposedly equal, is termed the degree of ionization and given by the Saha equation:

$$\frac{1}{1-x^2} p = 3.16 \times 10^{-7} T^{2.5} \exp\left(-\frac{eV_i}{kT}\right) \tag{4.25}$$

where

p represents the gas pressure
T the absolute temperature
V_i the ionization potential.

Variations of x as a function of the gas temperature are shown in Figure 4.20. The gas consists of mercury vapor at a pressure of 760 mm Hg. It can be seen that the thermal ionization is active only at very high temperature, $T > 4000$ K.

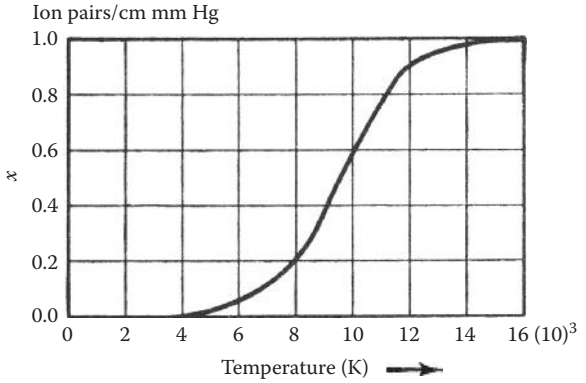


FIGURE 4.20 Thermal ionization. (From Cobine, J.D., *Gaseous Conductors—Theory and Engineering Applications*, Dover Publications Inc., New York, 1958.)

4.4.5 Cumulative Ionization

This ionization process refers to the case where a neutral gas atom gets excited first before being ionized by one of the processes described earlier. The cumulative ionization is particularly efficient in a gas mixture where the excitation energy of one gas is slightly greater than the ionization energy of the other gas.

4.5 Ion Movement in an Electric Field

4.5.1 Ion Mobility

When charged molecules or ions are present in the gas volume subjected to an electric field **E**, an electrostatic force is constantly applied on the ions according to

$$\mathbf{F} = M\frac{\mathrm{d}\mathbf{v}}{\mathrm{d}t} = e\mathbf{E} = M\mathbf{a}$$

It follows that

$$\mathbf{a} = \frac{e\mathbf{E}}{M}$$

where
- M is the mass
- e the electric charge of the ion
- **v** the velocity of the ion in the gas
- **a** the acceleration of the ion under the action of the electrostatic force

Because of the collisions with the neutral gas molecules, the ions do not follow a linear trajectory, but zigzag between the consecutive collisions. Between two successive collisions, the trajectory of the ion is defined by its initial velocity after collisions and the electrostatic force exerted by the applied electric field. Overall, however, the ions move in the direction of the electric field **E**, with a much reduced apparent or drift velocity, $\mathbf{v_d}$, which can be related to the electric field **E** according to

$$\mathbf{v_d} = \mu\mathbf{E} \tag{4.26}$$

where μ is the ion mobility in the gas volume.

Under the influence of the electrostatic force **F**, the distance s covered by *an ion of charge e in the direction of the applied field* in a time t is

$$s = \frac{a}{2}t^2 = \frac{eE}{2M}t^2$$

Taking t as the time between two consecutive collisions,

$$t = \frac{x}{c_{\mathrm{av}}}$$

where
- x is the free path
- c_{av} the average velocity of the gas molecules

It follows that

$$s = \frac{eE}{2M}\frac{\hat{\mathbf{E}}}{\hat{\mathbf{A}}}\frac{x}{c_{\mathrm{av}}}\tilde{}^2$$

The average value of s is

$$S_m = \int_0^{\infty} \frac{dN}{N_0}$$

where dN/N_0 is the probability that a gas molecule has a free path between x and $x + dx$

$$\frac{dN}{N_0} = \frac{1}{\lambda} \exp\left(-\frac{x}{\lambda}\right) dx$$

or

$$S_m = \int_0^{\infty} \frac{Ee}{2M} \frac{x^2}{C_{av}^2} \frac{1}{\lambda} \exp\left(-\frac{x}{\lambda}\right) dx = \frac{Ee}{M} \frac{\lambda^2}{c_{av}^2}$$

Noting that the average time between two collisions is

$$T = \frac{\lambda}{c_{av}},$$

the drift velocity v_d is

$$v_d = \frac{S_m}{T} = \frac{S_m}{\lambda / c_{av}} = \frac{eE\lambda}{Mc_{av}}$$

And the ion mobility, μ, is

$$\mu = \frac{v_d}{E} = \frac{e\lambda}{Mc_{av}} \tag{4.27}$$

A more general expression of the mobility of ions of mass M_1 in a gas with molecular mass M_2 is (Loeb, 1961)

$$\mu = 0.815 \frac{e\lambda_{12}}{M_1 c_1} \sqrt{\frac{M_1 + M_2}{M_2}} \tag{4.28}$$

In the preceding expression of μ, (4.28), c_1 is the effective velocity of the ions. By assuming an equal energy repartition among the ions and the gas molecules, one can express the mobility μ in terms of the gas parameters. In effect, one can write

$$\frac{M_1 c_1^2}{2} = \frac{M_2 c_2^2}{2} = \frac{3kT}{2} \quad \text{and} \quad \mu = 0.815 \frac{e\lambda_{12}}{M_2 c_2} \sqrt{\frac{M_1 + M_2}{M_1}}$$

Noting the relation between the average and effective velocities c_{av} and c_{rms}, $c_{av} = 0.92 c_{rms}$, and the expression of the mobility μ becomes

$$\mu = 0.75 \frac{e\lambda_{12}}{M_2 c_{av2}} \sqrt{\frac{M_1 + M_2}{M_1}} = 0.75 \frac{e\lambda_{12}}{M_1 c_{av1}} \sqrt{\frac{M_1 + M_2}{M_2}} \tag{4.29}$$

In the preceding expressions of μ, λ_{12} is the mean free path of the ions of mass M_1 in a gas with molecular mass M_2 and is related to λ_g, the mean free path of the gas molecules according to

$$\lambda_{12} = \sqrt{2}\lambda_g = \frac{1}{n\pi (r_1 + r_2)^2} \tag{4.30}$$

A more general estimation of the ion mobility by Compton and Langmuir gives the following expression (Compton and Langmuir, 1930):

$$\mu_e = 0.85 \frac{e l_{12}}{M_1 c_{av1}} \sqrt{1 + \frac{M_1 W_2}{M_2 W_1}} \tag{4.31}$$

where W_1 and W_2 are, respectively, the kinetic energies of the ions and gas molecules.

Typical values of the mobility of ions with single charge under normal conditions are presented in Table 4.2, while Figure 4.21 shows the variations of the ion mobility as a function of their molecular mass (Mitchell and Ridler, 1934). It is to be noted that the ion mobility in a gas is much affected by the presence of impurities, which tend to reduce the value of K. A plausible explanation of the influence of impurities is their tendency to form ion agglomerates and hence to increase the ion mass and reduce the mobility. A particular case is that of a mixture of electronegative gases in a neutral gas. The result is the formation of negative ions of higher mass by attachment of electrons to molecules of the electronegative gas, replacing the free electrons as normal charge carriers in the neutral gas.

TABLE 4.2

Mobility of Singly Charged Gaseous Ions at 0°C and 760 mm Hg (cm/s/V/cm)

Gas	μ^-	μ^+
Air (dry)	2.1	1.36
Air very pure	2.5	1.8
A	1.70	1.37
A very pure	206	1.31
Cl_2	0.74	0.74
CCl_4	0.31	0.30
C_2H_2	0.83	0.78
C_2H_5Cl	0.38	0.36
C_2H_5OH	0.37	0.36
CO	1.14	1.10
CO_2 dry	0.98	0.84
H_2	8.15	5.9
H_2 very pure	7900	
HCl	0.62	0.53
H_2O at 100°C	0.95	1.1
H_2S	0.56	0.62
He	6.3	5.09
He very pure	500	5.09
N_2	1.84	1.27
N_2 very pure	145	1.28
NH_3	0.66	0.56
N_2O	0.90	0.82
Ne		9.9
O_2	1.8	1.31
SO_2	0.41	0.41

Sources: Engel, A.V. and Steenbeck, M., Elektrische Gasentladungen, ihre Physik u. Technik, 1, 182, 1930; Landolt et al., *Phys.-Chem. Tabellen*; Thomson, J.J. and Thomson, G.P., *Conduction of Electricity through Gases*, Vol. 1, Cambridge University Press, London, U.K., 1930; Cobine, J.D., *Gaseous Conductors—Theory and Engineering Applications*, Dover Publications Inc., New York, 1958.

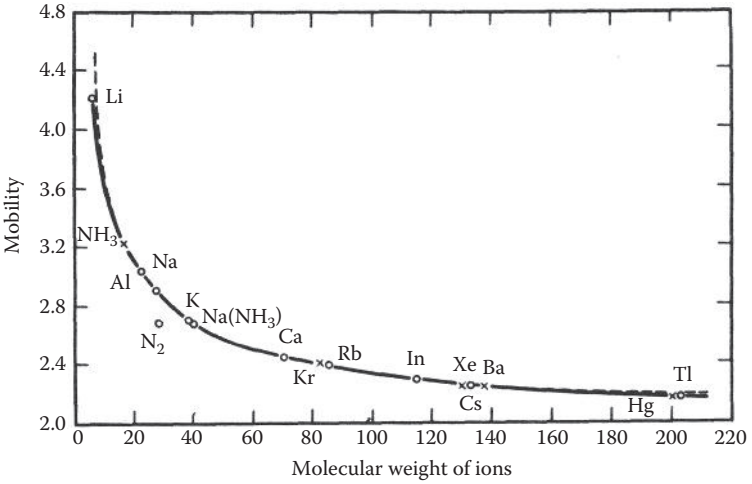


FIGURE 4.21 Variations of the ion mobility μ in cm/s/V/cm as a function of the molecular mass. (From Cobine, J.D., *Gaseous Conductors—Theory and Engineering Applications*, Dover Publications Inc., New York, 1958.)

Ion mobility in SF_6: The ion mobility μ in SF_6 is related to the reduced mobility μ_r according to the following relation:

$$\mu = \mu_r \left(\frac{P_0}{P}\right)\left(\frac{T}{T_0}\right),$$

with $P_0 = 760$ torr and $T_0 = 273.16$ K

The positive and negative reduced mobilities μ_r^+ and μ_r^- for the range of values of *E/N* between 10 and 7000×10^{-21} Vm^2 can be expressed by the following empirical relations for the positive ions (Wiegart et al., 1985):

$$\text{For } E/N < 1.2 \times 10^{-19}\ \text{Vm}^2 \qquad \mu_r^+ = 6 \times 10^{-5} \quad \text{m}^2/\text{V/s}$$

$$\text{For } 1.2 \times 10^{-19} < E/N < 3.35 \times 10^{-19}\ \text{Vm}^2$$

$$\mu_r^+ = 1.216 \times 10^{-5} \ln\left(\frac{E}{N}\right) + 5.89 \times 10^{-4} \quad \text{m}^2/\text{V/s}$$

$$\text{For } E/N > 3.35 \times 10^{-19}\ \text{Vm}^2$$

$$\mu_r^+ = -1.897 \times 10^{-5} \ln\left(\frac{E}{N}\right) - 7.346 \times 10^{-4} \quad \text{m}^2/\text{V/s}$$

For negative ions

$$\text{For } E/N < 5.0 \times 10^{-19}\ \text{Vm}^2 \qquad \mu_r^- = 1.69 \times 10^{32} \left(\frac{E}{N}\right)^2 + 5.3 \times 10^{-5} \quad \text{m}^2/\text{V/s}$$

$$\text{For } E/N > 5.0 \times 10^{-19}\ \text{Vm}^2 \qquad \mu_r^- = 9.52 \times 10^{-5} \quad \text{m}^2/\text{V/s}$$

4.5.2 Electron Mobility

In a neutral gas, the electrons are free and behave in similar way as ions in presence of an applied electric field **E**. As in the case of ions, one can define a mobility for the electron. Evaluation of the electron mobility is discussed below with the following considerations:

- The electrons make inelastic collisions.
- At each collision, the electron loses all its energy to the gas atom.

In these conditions, the drift velocity of the electrons in the direction of the applied field is equal to the average velocity of the electrons in the gas volume. If one considers N_0 electrons starting to move in the gas volume, the number dN of electrons having a free path between x and $x + \mathrm{d}x$ is

$$\mathrm{d}N = \frac{N_0}{\lambda_e}\exp\left(-\frac{x}{\lambda_e}\right)\mathrm{d}x \tag{4.32}$$

These electrons have a kinetic energy of $1/2mv^2 = eEx$. The distance x can be expressed in terms of the terminal velocity of the electron as

$$x = \frac{mv^2}{2eE}$$

Differentiating with respect to the velocity v gives $\mathrm{d}x = (mv/eE)\mathrm{d}v$. Replacing the preceding expression of dx in Equation 4.32 gives the number of electrons having a terminal velocity between v and $v + \mathrm{d}v$ as follows:

$$\mathrm{d}N_v = \frac{N_0}{\lambda_e}\exp\left(-\frac{m}{2eE\lambda_e}v^2\right)\frac{mv}{eE}\mathrm{d}v$$

or

$$\frac{\mathrm{d}N_v}{N_0} = \frac{1}{\lambda_e}\frac{mv}{eE}\exp\left(-\frac{m}{2eE\lambda_e}v^2\right)\mathrm{d}v$$

The average velocity of electrons is

$$v_m = \int_0^\infty \frac{\mathrm{d}N_v}{N_0} = \frac{2m}{\lambda_e Ee}\int_0^\infty v^2\exp\left(-\frac{mv^2}{2Ee\lambda_e}\right)\mathrm{d}v$$

By noting that

$$\int_0^\infty v^2\exp\left(-\frac{mv^2}{2Ee\lambda_e}\right)\mathrm{d}v = \frac{1}{4}\frac{\sqrt{\pi}}{\left(\frac{m}{2Ee\lambda_e}\right)^{3/2}}$$

the average velocity of electrons becomes

$$v_m = \sqrt{\frac{Ee\lambda_e\pi}{2m}}$$

It follows that the electron mobility μ_e is

$$\mu_e = \frac{v_m}{E} = \sqrt{\frac{e\lambda_e\pi}{2mE}} \tag{4.33}$$

where λ_e is the electron mean free path and is related to that of the gas molecules, λ_g, according to

$$\lambda_e = 4\sqrt{2}\lambda_g$$

When the electron energy is so low that the collisions are elastic, the energy transferred to the gas molecules is negligible. The electron mobility is

$$\mu_e = 0.85\ \frac{e\lambda_{12}}{mc_1}\ \sqrt{1+\frac{mW_2}{MW_1}} = 0.85\ \frac{e\lambda_{12}}{mc_1} \tag{4.34}$$

where

λ_{12} is the electron mean free path in the gas of molecular mass M

W_1 and W_2 the kinetic energies of the electrons and gas molecules, respectively

For the case where the electron energy is not sufficient to produce inelastic collisions at each collision but is still sufficiently high to do it from time to time, one has the following expression for the electron mobility (Loeb, 1961):

$$\mu_e = 0.92\frac{e\lambda_{12}}{2meW_{1t}}\ \sqrt{1+\frac{mW_2}{MW_1}} \tag{4.35}$$

where W_{1t} is the kinetic energy at equilibrium of the electron when the energy gained from the applied electric field compensates for the loss from multiple elastic collisions.

Drift velocity of electrons in SF_6: The electron drift velocity v_{ed} in SF_6, for the range of values of E/N between 10 and 2000×10^{-21} Vm^2, can be expressed by the following empirical relations (Wiegart et al., 1985):

$$\text{For } 10^{-20} < E/N < 2 \times 10^{-18}\,\text{Vm}^2 \quad v_{ed} = 1.027 \times 10^{19} \left(\frac{E}{N}\right)^{0.7424} \quad \text{m/s}$$

4.5.3 Ions in a Gas Subjected to an Electric Field

When one applies an electric field to a gas volume containing ions of charge q, the movement of the ions in the gas causes also a change in the concentration of the molecules in the gas volume.

Consider a gas volume limited by two parallel imaginary walls of surface A vertical to the direction of the applied field of surfaces A. The forces applied to the walls by the molecules and ions are

- The electrostatic force: $nqEA\,dx$
- The force to the wall at x: $Ap(x)$
- The force to the wall at $x + dx$: $Ap(x + dx)$

Since the gas volume remains stationary, there is no displacement of the imaginary wall, and it follows that

$$Ap(x) + AnqE\,dx - \left[Ap(x) + A\frac{\partial p}{\partial x}dx\right] = 0$$

or

$$-\frac{\partial p}{\partial x} + nqE = 0$$

Since $p(x) = n(x)kT$

$$\frac{dp}{dx} = kT\frac{dn}{dx},$$

which gives $-kT\left(\mathrm{d}n\left(x\right)/\mathrm{d}x\right)+nqE=0$ that one can rewrite as

$$nq\left(-\frac{kT}{nq}\frac{\mathrm{d}n\left(x\right)}{\mathrm{d}x}+E\right)=0$$

The effect of the increase of the molecular density in the gas volume caused by the movement of ions can be interpreted as an electric field $\mathbf{E}'$ opposite to the applied field and of intensity

$$E'=-\frac{kT}{nq}\frac{\mathrm{d}n\left(x\right)}{\mathrm{d}x}$$

In these conditions, the ion velocity is reduced to

$$v=\mu\left(E+E'\right)=\mu\left(E-\frac{kT}{nq}\frac{\mathrm{d}n\left(x\right)}{\mathrm{d}x}\right).$$

As the accumulation of ions progresses in time, the increased concentration of molecules in the gas tends to slow down the movement of new ions. If the applied electric field is removed suddenly, E becomes null; only the effect of molecular concentration remains, which tends to redistribute the ions in the gas volume by diffusion. One gets

$$v=-\mu\left(\frac{kT}{nq}\frac{\mathrm{d}n\left(x\right)}{\mathrm{d}x}\right)\quad\text{or}\quad nv=-\mu\left(\frac{kT}{q}\frac{\mathrm{d}n\left(x\right)}{\mathrm{d}x}\right).$$

On the other hand, the number of gas molecules crossing the imaginary wall, *nv*, is also equal to

$$nv=n\frac{\mathrm{d}x}{\mathrm{d}t}=\frac{\mathrm{d}n}{\mathrm{d}t}=-D\frac{\mathrm{d}n}{\mathrm{d}x}\tag{4.36}$$

One gets the Einstein relation of the diffusion coefficient *D* in the case of ions with single electronic charge, $q = e$:

$$\frac{D}{\mu}=\frac{kT}{e},\tag{4.37}$$

which constitutes the basis for experimentally determining values of *D* in terms of μ, and *T* for the ions in a gas.

4.5.4 Electric Current Produced by the Movement of a Charged Particle

Consider a gas volume limited by two parallel electrodes subjected to a potential difference *U*. An electric field is created in the gas gap. When a molecule of charge $+q$ leaves the anode and moves towards the cathode (Figure 4.22a), a charge of opposite polarity $-\alpha q$ is induced at the anode, where α is a coefficient < 1. As the charged molecule moves to the cathode, a charge transfer occurs via the external circuit from the anode to the cathode (Figure 4.22b). This charge transfer manifests itself as an electric current such that

$$\int i\,\mathrm{d}t=q$$

It is to be noted that the transfer will be completed when the charge $+q$ reaches the cathode. The current in the external circuit becomes then zero. However, when a charged molecule moves in an electric field, it produces a work according to

$$\mathrm{d}W=q\mathbf{E}\,\mathbf{dx}$$

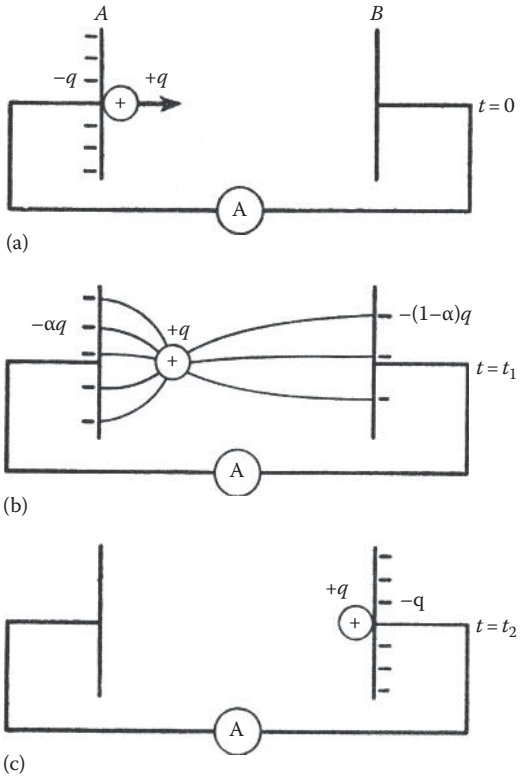


FIGURE 4.22 Electric current produced by the displacement of charges. (a) Charge q leaving the anode; (b) charge at mid gap; (c) charge q at cathode. (Cobine, J.D., *Gaseous Conductors—Theory and Engineering Applications*, Dover Publications Inc., New York, 1958.)

The energy required to do this work is provided by a source such that

$$\mathrm{d}W = Ui\,\mathrm{d}t$$

It follows that $qE\,\mathrm{d}x = Ui\,\mathrm{d}t$ or

$$i = \frac{qE}{U}\frac{\mathrm{d}x}{\mathrm{d}t} = \frac{qE}{U}v_\mathrm{d}$$

where v_d is the ion drift velocity in the electric field. For a uniform field $E = U/d$, with d as the interelectrode distance, the current i is

$$i = \frac{qv_\mathrm{d}}{d} \tag{4.38}$$

It follows that the electric current measured in the external circuit is directly proportional to the drift velocity v_d of the ions in the uniform field (Shokely's theorem). This provides a method to measure the drift velocities of electrons and ions and their mobility in a gas.

4.6 Deionization and Deexcitation

When an excited atom is left alone, the peripheral electrons will return to a lower energetic level while radiating the absorbed energy by emitting photons of various frequencies characteristic for each gas. This process called the deexcitation of the atom is generally rapid, considering that the life duration of excited atoms is of the order of 10^{-8} s.

When an ion is left alone, it will tend to return to its neutral state by recuperating a free electron in the gas. The process by which the ion returns to its neutral state is defined as a deionization process. The symbolic equation describing the deionization process is

$$A^+ + e^- \rightarrow A + W$$

where W is the energy restored from the reaction.

In practice, a direct recombination between ion and electron is not frequent, often because of the high energy of the electron. The latter must spend its excess of energy before being able to recombine with an ion. Such a dissipation of energy can occur in various manners: by collision with neutral molecules or against the containing vessel or by attachment of the electron to a neutral molecule, forming a negative ion, which on a collision with a positive ion produces the recombination of the ions according to the following symbolic relations:

$$e^- + A + W \rightarrow A^-$$

$$A^- + B^+ \rightarrow A + B$$

4.6.1 Recombination

Let n_1 and n_2 be the densities of positive and negative ions in a gas volume. The rate of ion recombination is

$$\frac{dn_1}{dt} = \frac{dn_2}{dt} = -\eta_i n_1 n_2$$

where η_i is the coefficient of ion recombination.

The negative sign underscores the fact that each recombination corresponds to a loss among the ions. When n_1 is equal to n_2, $n_1 = n_2 = n_i$, the preceding equation becomes $dn_i/dt = -\eta_i n_i^2$, which can be rewritten as $-dn_i/n_i^2 = \eta_i\, dt$.

Integrating the preceding equation gives $1/n_i = \eta_i t + C$, C being a constant.

Applying the initial conditions, at $t = 0$, $n_i = n_0$, the integration constant is equal to $1/n_0$. The expression for the ion density becomes

$$n_i = \frac{n_0}{1 + \eta_i n_0 t}$$

In ambient air, ions are produced by radiations from the soil or from space. Let m_i be the number of ions thus produced per cm^3 per second. One has

$$\frac{dn_i}{dt} = m_i - \eta_i n_i^2$$

An equilibrium state is reached when

$$\frac{dn_i}{dt} = 0 \quad \text{or} \quad m_i = \eta_i n_i^2 \tag{4.39}$$

For a value of m_i between 1 and 7 and η_i about 1.5×10^{-6} cm^3/s, an ion density of about 2000 ions per cm^3 of gas per second is obtained.

Coefficient of volume recombination of ions in SF_6: The coefficient of volume recombination, K_r, of ions in SF_6 for the range of gas pressures between 1.0 and 3000 kPa can be expressed by the following empirical relations (Wiegart et al., 1985):

$$\text{For } 1 \leq P \leq 39 \text{ kPa} \quad K_r = 2 \times 10^{-13} (P)^{0.6336} \quad \text{m}^3/\text{s}$$

$$\text{For } 39 \le P \le 270 \text{ kPa} \quad K_r = 2.282 \times 10^{-11} (P)^{-0.659} \quad \text{m}^3/\text{s}$$

$$\text{For } 270 \le P \le 2000 \text{ kPa} \quad K_r = 6.867 \times 10^{-10} (P)^{-1.279} \quad \text{m}^3/\text{s}$$

4.6.2 Attachment

In most gases, N_2, H_2, etc., electrons remain free. However, for electronegative gases, O_2, SF_6, etc., with a high degree of electron affinity, electrons can attach themselves to neutral gas molecules to form stable negative ions according to the following symbolic equation:

$$A + e^- \rightleftharpoons A^-$$

The electron attachment in a gas is characterized by an attachment coefficient η, defined as *the probability that an electron will attach to a neutral gas molecule in crossing a distance of 1 cm in the gas*. In these conditions, the number of negative ions formed by attachment dn over a distance dx in the direction of the applied field is

$$dN(x) = -\eta N(x) dx$$

The negative sign underscores the fact that the formation of a negative ion represents a loss among the free electrons. Integration of the preceding equation gives the following expression for $N(x)$, the number of residual free electrons after traveling a distance x cm in the gas:

$$N(x) = N_0 \exp(-\eta x) \tag{4.40}$$

where N_0 is the initial number of free electrons in the gas.

4.6.3 Deionization by Diffusion

A direct consequence of the diffusion is a natural tendency of the gases to maintain a constant density in the whole gas volume. Applied to the case of ions in presence of a gradient of ion concentration in the gas volume, there is a diffusion of ions from the region of high ion concentrations towards those of low concentrations. This redistribution of the ions in the gas volume effectively produces

- A recombination effect, that is, a diminution of the local ion density, in the regions of high ion concentrations
- An ionization effect, that is, an increase of the local ion density, in the regions of low ion concentrations

Diffusion coefficient of electrons in SF_6: The diffusion coefficient of electrons in SF_6 for the range of values of E/N between 20 and 800 × 10^{-21} Vm^2 can be expressed by the following empiric relation (Wiegart et al., 1985):

$$\text{For } E/N < 7 \times 10^{-19} \text{Vm}^2 \quad \frac{D_t}{\mu} = 7.114 \times 10^{18} \frac{E}{N} + 2.57 \text{V}$$

Diffusion coefficient of negative ions in SF_6: Variations of the diffusion coefficient of negative ions in SF_6 are shown in Table 4.3 for the range of values of E/N between 30 and 220 × 10^{-21} Vm^2 and gas pressures between 1 and 10 torr. The Townsend energy factor, K_t, corresponds to the ratio of the average energy to the average thermal energy (Wiegart et al., 1985)

TABLE 4.3

Diffusion Coefficient of Negative Ions in SF_6

E/N (10^{-21} Vm^2)	K_t	D/μ (V)
30.3	1.0	0.025
60.7	1.2	0.030
91.0	1.7	0.043
121.4	2.6	0.066
151.7	3.5	0.088
182.0	4.6	0.116
212.3	5.9	0.149

Source: Naidu, M.S. and Prasad, A.N., *J. Phys. D*, 3, 1970.

4.7 Sources of Free Electrons

The presence of free electrons in the gas volume is a necessary, though not sufficient, condition to initiate the processes involved in the gaseous discharge. Several mechanisms are able to produce free electrons in the gas volume, the principal ones are summarized in the following.

Natural and artificial sources: Ionization of the gas atoms by natural radiations from the soil or from space constitutes a natural mechanism to generate free electrons in the gas volume. It is a constant source of free electrons and produces some hundreds, or even thousands, of free electrons per cm^3 of gas per second. These natural processes of producing free electrons in the gas volume can be reproduced by artificial means in laboratory, either by the use of radioactive materials presently prohibited or by irradiating the gas with energetic light such as ultraviolet (UV) light.

Detachment of electrons from negative ions: In most gases, the free electrons, present naturally or artificially, are readily available to initiate the ionization processes, necessary in an electric discharge. In electronegative gases like O_2 and SF_6, these electrons attach themselves rapidly to the gas atoms, to form stable negative ions, and are not immediately available for the initiation of an electric discharge. Nevertheless, they constitute a source of free electrons in the gas volume, obtained via detachment of electrons from the negative ions in presence of a sufficiently high electric field. The detachment process can be described by the following reaction:

$$A^- + W \rightarrow A + e^- \tag{4.41}$$

Emissions of electrons from solids: In a solid, the electrons are kept in place by an energetic barrier, which prevents them from being ejected from the surface of the solid into the gas volume. Such an energetic barrier is generally represented by a potential ϕ such that the product $e\phi$ corresponds to the minimal energy quantity that an electron of the solid must acquire to escape from it (Figure 4.23). The potential ϕ is termed *the potential barrier*, and the energy quantity $e\phi$ *the work function* of the solid.

The emission of an electron from the surface of the solid can be represented by the following symbolic equation:

$$e_s^- + W \rightarrow e^- + W_c, \quad \text{with } W \geq e\phi$$

where

e_s^- is an electron located inside the solid
W its absorbed energy
e^- the free electron emitted from the surface of the solid
W_c the kinetic energy of the free electron

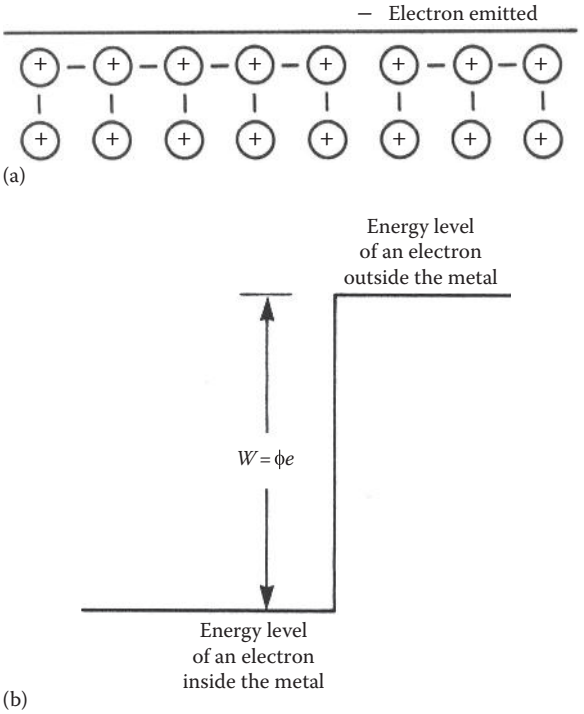


FIGURE 4.23 Potential barrier of an electron at the surface of a metal electrode. (a) Emission of an electron from the metal surface. (b) Illustration of energy state.

Emission of electrons by collisions and by radiations: The work function of most metals being smaller than the ionization energy of gases, the ionization processes in gases discussed previously are also effective in liberating electrons from the surface of metal electrodes, namely,

- Emission by electron bombardment
- Emission by positive ion bombardments
- Emission by meta stable atom bombardments
- Emission by photons

Thermionic emission: When the energy is supplied to the solid by direct heating of the solid, the electrons can be emitted from the solid. The resulting current density J_s is (Richardson, 1921; Dushman, 1923)

$$J_s = AT^2 \exp\left(-\frac{e\phi}{kT}\right) \tag{4.42}$$

where A is a constant characteristic of the emitter. For most metals, A has a value of approximately 60 A/cm^{2}K^2, while for pure surfaces of a single crystal face, A has a value of 120.4 A/cm^{2}K^2.

Field emission: One way to interpret the potential barrier ϕ of a metal is by the action of the electron image. In effect, when an electron is emitted from the surface of a metal electrode, it is subjected to an electric field produced by its image with respect to the surface of the electrode (Figure 4.24). The work function of the metal $e\phi$ corresponds thus to the work required to remove the electron from the electric field of the electron image. Noting that the charge of the electron is negative,

$$-e\phi = -e\int_0^{\infty} E_i(x)\,dx$$

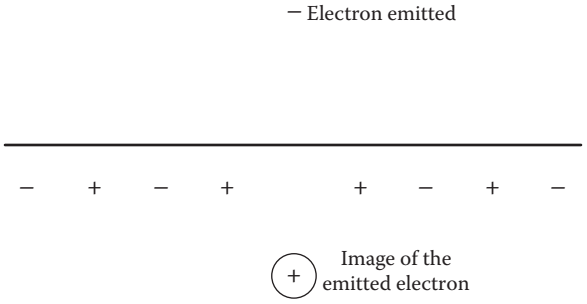


FIGURE 4.24 Illustration of the image of an electron emitted from the cathode.

where $E_i(x)$ represents the electric field of the electron image, and consequently of positive charge, located at a distance x from the surface:

$$E_i(x) = \frac{e}{(2x)^2}$$

The preceding expression takes account of the fact that the charge of the electron image is positive and the distance between the electron and its image is actually twice the distance x between the electron image and the metal surface. In presence of an external uniform electric field **E**, the effect of the electron image can be partially or completely neutralized by the applied field. The condition for the field emission of an electron can be expressed as

$$-e\phi' = -e\int_0^{\infty} E_i(x) - E\,dx = -e\int_0^{x_0} E_i(x) - E\,dx$$

where

ϕ' is the resulting potential subjected to the electron inside the solid
E the applied field
x_0 the distance from the electrode surface where the two fields are equal

One gets

$$E_i(x_0) = E = \frac{e}{4x_0^2} \quad \text{or} \quad x_0 = \frac{1}{2}\sqrt{\frac{e}{E}}$$

The potential barrier can be expressed differently as

$$\phi' = \int_0^{x_0} E_i(x)\,dx - \int_0^{x_0} E\,dx = \int_0^{\infty} E_i(x)\,dx - \int_{x_0}^{\infty} E_i(x)\,dx - \int_0^{x_0} E\,dx$$

$$= \phi - \int_{x_0}^{\infty} \frac{e}{4x^2}\,dx - \int_0^{x_0} E\,dx = \phi - \frac{e}{4}\left[0 + \frac{1}{x_0}\right] - E(x_0 - 0)$$

By replacing the expression of $x_0 = 1/2\sqrt{e/E}$ in the preceding equation, one obtains

$$\phi' = \phi - \frac{e}{4}2\sqrt{\frac{E}{e}} - E\frac{1}{2}2\sqrt{\frac{e}{E}} = \phi - \sqrt{eE}$$

One can see that the effect of an external electric field corresponds to a reduction of the potential barrier ϕ by an amount of $\sqrt{eE}$, which facilitates the emission of the electrons at the surface of the electrodes under stress. The effect is particularly pronounced at high applied fields associated with vacuum insulation where the field is sufficiently high to cause emission of electrons by field effect. The current density due to field emission has been shown by Fowler and Nordheim to be (Fowler and Nordheim, 1928, 1929)

$$j = \frac{e}{2\pi h}\frac{n^{1/2}e^{5/2}}{(\mu + \varepsilon)\varphi^{1/2}}E^2 \exp\left(-\frac{4Ke^{1/2}\varphi^{3/2}}{3E}\right) \tag{4.43}$$

with

$$\mu = \left(\frac{3n}{8\pi}\right)^{2/3}\frac{h^2}{8m} \quad \text{and} \quad K^2 = \frac{8\pi^2 m}{h^2} \quad \text{e.s.u.}$$

where

E is the electric field
e the electronic charge
h Planck's constant
m the mass of electron
n the number of free electrons per cm^3
ϕ the work function of the surface

Equation 4.43 indicates that the field emission current should be measurable at fields of the order of 10^7 V/cm and has been verified experimentally.

4.8 Development of Electron Avalanches

4.8.1 Townsend Discharge

Early studies of electric discharges in a gas showed particular interest in the relationship between discharge current i and applied voltage U. Figure 4.25 shows a typical i–U characteristic illustrating this relationship. The discharge gap consists of two parallel plane electrodes separated by a distance d and subjected to a potential difference U. An external source, irradiating the cathode by UV light, assures a sufficient number of free electrons to initiate the discharge in the gap. One can distinguish essentially three regions, bound by the voltage levels U_0, U_1, and U_2:

- *The region T_0, defined by the voltages below U_0*: In this region, an increase of the applied voltage U gives rise to a proportional increase of the discharge current i, up to a maximal value of i_0. Interpretation of the relationship $i = f(U)$ in this region is based on the displacement of electric charges across the interelectrode space, under the action of the applied electric field. One can show that the measured electric current in the external circuit is directly proportional to the drift velocity of the electric charges in the gap. The discharge current reached saturation when all the charges produced at the cathode are rapidly accelerated to the anode. The saturation current i_0 is a function of the amount of electric charges supplied by the external ionization source.
- *The region T_1*, bounded by the voltages U_0 *and U_1*: In this region, an increase of the applied voltage U gives rise to an exponential increase in the discharge current i. J.S. Townsend interpreted this behavior of the discharge current by the ionization of the neutral atoms in the gas volume, in collisions with the free electrons subjected to the action of the applied electric field.
- *The region T_2, defined by voltages higher than U_1*: In this region, an increase of the applied voltage U gives rise to an increase of the discharge current i, even more rapid than expressed by the exponential law, established in the region T_1. Townsend interpreted this behavior of the discharge current as due to secondary ionization action from the cathode that he associated to positive ions in the gas volume subjected to the action of the applied field.

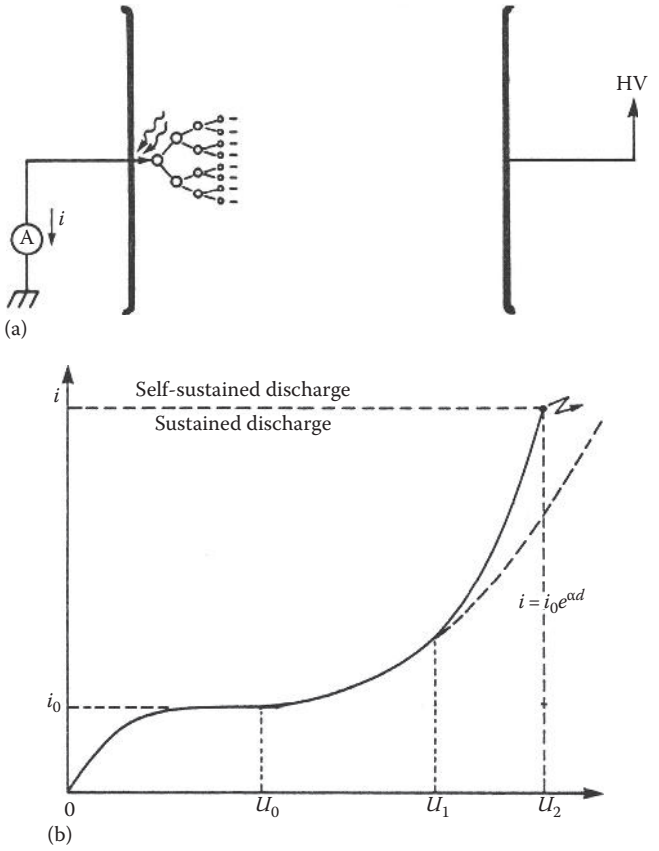


FIGURE 4.25 (a) Arrangement of the discharge gap; (b) i-U characteristics of a discharge gap.

The interpretation by J.S. Townsend of the behavior of the discharge current as a function of the applied voltage U forms the basis of the classical theory of discharge in gases. It recognized, in particular, the action of the free electrons in the ionization of the gas, the active process in the region T_1. It recognizes also the action of the secondary ionization to explain the behavior of the discharge current in the region T_2. However, the association of this process to electron emission due to positive ion bombardment of the cathode was not found possible under some practical conditions of electric discharges. These include breakdown of long gaps as well as breakdown under impulse voltages.

4.8.2 Ionization by Electron Collisions in the Gas Volume

4.8.2.1 Mechanism of Discharge by Electronic Collisions: Electron Avalanche (Loeb, 1961; Raether, 1964; Loeb, 1965)

When an electric field is applied to the gas volume, energy is transferred to the gas molecules via the action of ions and electrons. In effect, the electrostatic field **E** exerts a force **F** on the charged particles, oriented in the direction of the applied field:

$$\mathbf{F} \fallingdotseq e\mathbf{E}$$

where

E is the electric field

e the charge of ions and electrons

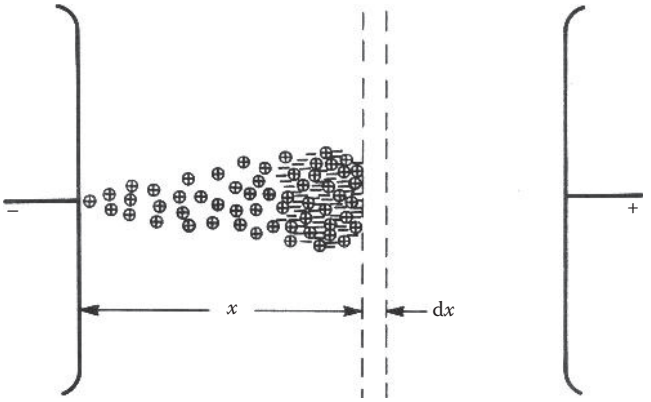


FIGURE 4.26 Development of an electron avalanche.

Thus, these charged particles acquire continuously kinetic energy from the applied field and redistribute it to neutral gas molecules via multiple collisions between charged and neutral molecules. Ions, because of their mass comparable to that of the gas molecules, redistribute at each collision the kinetic energy accumulated in the preceding free path. As a result, the probability that an ion can accumulate sufficient energy to ionize the gas molecules on collision is generally negligible under normal conditions of discharge.

The situation is different for the electrons: they conserve almost the totality of their kinetic energy in elastic collisions with the gas molecules. In this way, they can accumulate energy over several consecutive free paths to eventually ionize on impact a gas molecule, even *at relatively low values of the applied field*. This particularity of the electrons makes the process of ionization by electronic collisions particularly efficient in electric discharges in the gas volume. Referring to Figure 4.26 and letting α be *the number of ionizations made by an electron in crossing a distance of 1 cm in the direction of the applied field*, the number d*n* of electrons produced over a distance d*x* is

$$\mathrm{d}n_{\mathrm{e}}(x) = \alpha n_{\mathrm{e}}(x)\mathrm{d}x$$

or

$$\frac{\mathrm{d}n_{\mathrm{e}}(x)}{n_{\mathrm{e}}(x)} = \alpha\,\mathrm{d}x$$

where $n_e(x)$ is the number of free electrons at a distance x from the cathode.

The coefficient α is termed the coefficient of ionization by electron collisions, also known as Townsend's *first ionization coefficient*. It follows that the number of free electrons $n_e(x)$ produced over a distance of x cm is

$$n_{\mathrm{e}}(x) = n_0 \exp(\alpha x) \tag{4.44}$$

where n_0 is the number of free electrons at the cathode, $x = 0$.

Equation 4.44 shows that the number of free electrons produced by ionization by electron collisions increases exponentially as the initial electron travels across the discharge gap. Such an ionization process is referred to as an electron avalanche process, and the ensemble of the free electrons and positive ions thus produced an *electron avalanche*. Figure 4.27, taken from the work of Reather and Riemann (Raether, 1964), is a photograph of an electron avalanche developing in a mixture of air, alcohol, and water vapor. Such a mixture favors the formation of ion agglomerates, which slow down significantly the avalanche process to allow photographic recording of its development. One can distinguish the typical shape of the electron avalanche, associated with its exponential growth over the distance.

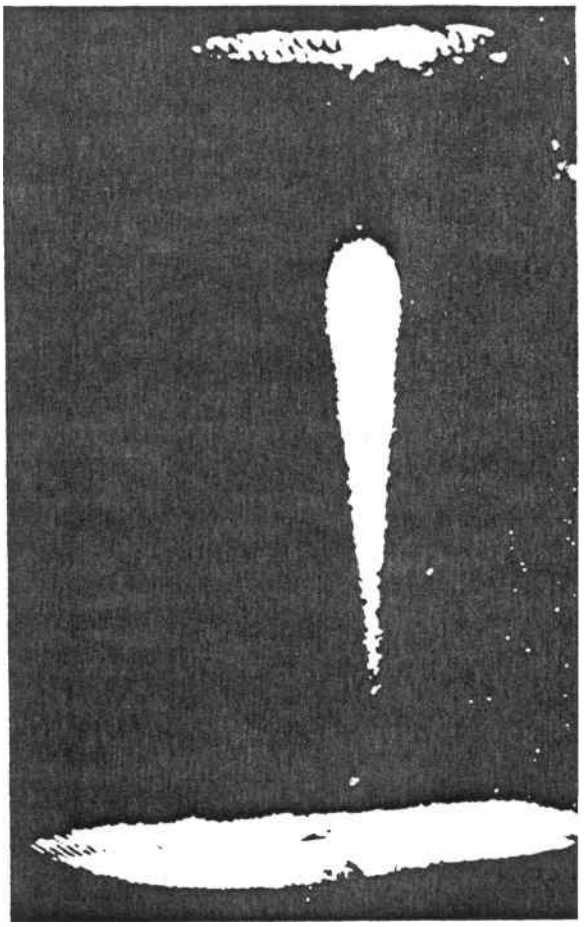


FIGURE 4.27 Photograph of an electron avalanche in the mixture of air, alcohol, and water vapor. Cathode below, anode above, seen by reflected light. (From Raether, H., *Electron Avalanches and Breakdown in Gases*, Butterworth Co., London, U.K., 1964; Loeb, L.B., *Basic Processes of Gaseous Electronics*, University of California Press, Berkeley/Los Angeles, CA, 1961; Loeb, L.B. *Electrical Coronas*, University of California Press, Berkeley/Los Angeles, CA, 1965.)

4.8.2.2 Townsend's First Coefficient of Ionization, α

One can expect that the coefficient α be a function of the electric field **E** and of the electrons mean free path λ in the gas volume. In effect, the following applies:

- The ionization coefficient α is, by definition, *the number of ionizations made by an electron in crossing a distance of 1 cm in the direction of the applied field*. One may expect that α is a function of the kinetic energy accumulated by the electron in a free path, that is, the product **E**λ of the electric field **E** by the length of the mean free path, λ.
- However, a high value of the mean free path λ of the electrons implies a lower collision frequency in the gas volume. α should then be also inversely proportional to λ.

The ionization coefficient α can be expressed as $\alpha = f(E\lambda)/\lambda$. The mean free path λ can be related to the number density n and diameter d of the gas molecules according to

$$\lambda = \frac{1}{n\pi d^2} \quad \text{or} \quad \lambda = \frac{kT}{p\pi d^2}$$

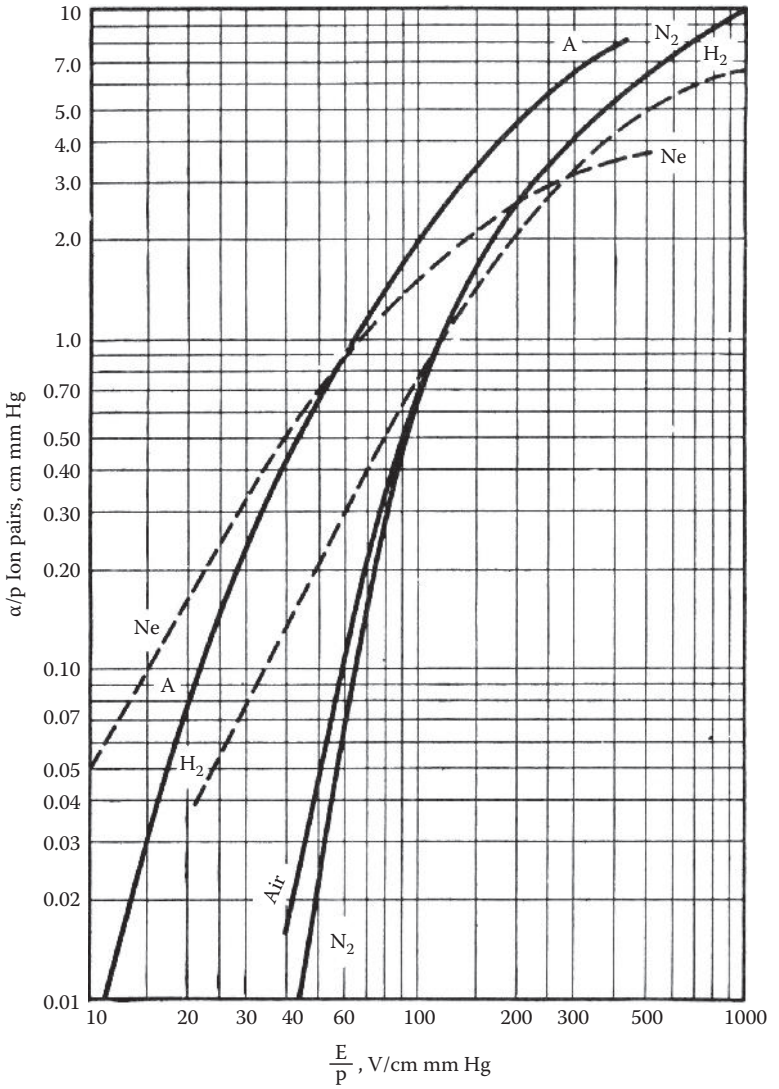


FIGURE 4.28 Ionization coefficients of some common gases. (From Cobine, J.D., *Gaseous Conductors—Theory and Engineering Applications*, Dover Publications Inc., New York, 1958.)

which means that for constant temperature, λ is inversely proportional to p.
It follows that one can express α as

$$\frac{\alpha}{p} = f\left(\frac{E}{p}\right) \tag{4.45}$$

Figure 4.28 shows typical variations of the normalized values of the ionization coefficient α/p as a function of E/p measured in some common gases including N_2 and air.

4.8.2.3 Practical Expressions of Townsend's First Ionization Coefficient

Let n_c be the number of collisions made by an electron over a distance of 1 cm. The number of free electrons produced by an electron advancing a distance of 1 cm in the direction of the applied field, that is, the ionization coefficient α, is

$$\alpha = n_c P_i$$

where P_i represents the probability that a collision leads to the ionization of a gas molecule.

Assuming that the kinetic energy of the free electrons is zero at the beginning of each free path, the ionization by electronic collisions is realized when the length x_0 of the free path allows the electron to accumulate sufficient energy to ionize the gas.

$$e\left(Ex_0\right) = eU_i \quad \text{or} \quad x_0 = \frac{U_i}{E}$$

where U_i represents the ionization potential of the gas.

The probability that an electron can ionize in a collision with a gas molecule is then equal to the probability that the electron can have a free path equal to or exceeding the critical value x_0 given by

$$P_i = \exp\left(-\frac{x_0}{\lambda}\right) = \exp\left(-\frac{U_i}{E\lambda}\right)$$

On the other hand, the collision frequency n_c is equal to $1/\lambda$; it follows the expression for the ionization coefficient α:

$$\alpha = n_c P_i = \frac{1}{\lambda}\exp\left(-\frac{U_i}{E\lambda}\right)$$

Replacing the expression of λ in the preceding equation, one obtains the general expression of the ionization coefficient:

$$\frac{\alpha}{p} = \frac{\pi d^2}{kT}\exp\left(-\frac{U_i p \pi d^2}{EkT}\right) = A\exp\left(-\frac{B}{E/p}\right) \tag{4.46}$$

where $A = \pi d^2/kT$ and $B = U_i \pi d^2/kT$ are characteristic constants of the gas.

Table 4.4 presents values of the constants A and B evaluated for some common gases. It should be noted that the expression of α/p thus derived gives only an approximate value of the ionization coefficient of the gas, valid within certain range of E/p. In most practical calculations, it may be preferable to use experimental values obtained in laboratory.

TABLE 4.4

Ionization Coefficients of Common Gases

Gas	*A* (ion/cm torr)	*B* (V/cm torr)	Limits of *E/p* (V/cm mm Hg)
Air	14.6	365	150–600
Ar	13.6	235	100–600
H_2	5	130	150–400
He	2.8	34	20–150
H_2O	12.9	289	100–1000
CO_2	20	466	500–1000

Source: Cobine, J.D., *Gaseous Conductors—Theory and Engineering Applications*, Dover Publications Inc., New York, 1958.

TABLE 4.5

Ionization, Attachment, and Effective Ionization Coefficients of Air and Oxygen (Ion Pair/cm mmHg)

Geballe and Harrison's Values of α/p and η/p as Functions of E/p for O_2 and Air

	O_2			Air		
E/p	α/p	η/p	$\alpha/p-\eta/p$	α/p	η/p	$\alpha/p-\eta/p$
25.0	0.0215	0.0945	–0.0730	0.00120	0.00495	–0.00375
27.5	0.0293	0.0900	–0.0607	0.00205	0.00473	–0.00268
30.0	0.0400	0.0851	–0.0451	0.00340	0.00460	–0.00120
32.5	0.0532	0.0795	–0.0263	0.00560	0.00460	+0.00100
35.0	0.0697	0.0735	–0.0038	0.00880	0.00475	+0.00405
37.5	0.0862	0.0685	+0.0177	0.0130	0.00497	+0.0080
40.0	0.107	0.0645	+0.043	0.0190	0.00530	+0.0137
42.5	0.128	0.0605	+0.068	0.0260	0.00575	+0.0203
45.0	0.152	0.0570	+0.095	0.0340	0.00635	+0.0277
47.5	0.179	0.0535	+0.126	0.0460	0.00700	+0.0390
50.0	0.206	0.052	+0.154	0.057	0.00780	+0.049
52.5	0.234	0.049	+0.185	0.070	0.00870	+0.061
55.0	0.263	0.047	+0.216	0.087	0.00967	+0.077
57.5	0.292	0.045	+0.247	0.102	0.0108	+0.091
60.0	0.323	0.043	+0.280	0.120	0.0119	+0.108
62.5	0.355	0.0415	+0.314	0.140	—	—
65.0	0.383	0.040	+0.343	0.170	—	—
70.0	0.450	—	—	—	—	—
72,5	0.482	—	—	—	—	—
75.0	0.518	—	—	—	—	—

Source: Loeb, L.B., *Basic Processes of Gaseous Electronics*, University of California Press, Berkeley/Los Angeles, CA, 1961.

4.8.3 Electronegative Gases

Several gases of practical interest, oxygen, air and SF_6, have a high affinity for free electrons. This affinity is generally represented by an attachment coefficient η, defined as *the probability that a free electron be attached to a gas molecule in advancing a distance of 1 cm in the direction of the applied field.* In these conditions, the effective number of ionizations made by an electron crossing a distance of 1 cm in the direction of the applied field is reduced to a value α':

$$a \Leftarrow a - h \tag{4.47}$$

Termed the effective ionization coefficient. Townsend's theory of ionization by electronic collisions developed earlier still applies, with the condition to replace the ionization coefficient α by its effective value α'. Tables 4.5 and 4.6 give the experimental data obtained by Harrisson and Geballe (Loeb, 1961) for the ionization, attachment, and effective ionization coefficients of a few gases of interest.

4.9 Classical Theory of Gaseous Discharges

4.9.1 Influence of Secondary Processes

Consider again the *i–U* characteristics of the electric discharges in a gas gap (Figure 4.25), and, more specifically, the region T_2. Increasing the applied voltage U causes the discharge current to increase faster than predicted by the exponential law, typical of the ionization by electronic collisions in the gas volume. J.S. Townsend interpreted this behavior of the discharge current as due to the action of secondary

TABLE 4.6

Ionization, Attachment, and Effective Ionization Coefficients of SF_6, CCl_2F_2, and Si Cl_4 (Ion Pair/cm mmHg) (Loeb, 1961) Geballe and Harrison's Values of α/p and η/p for CCl_2F_2, SF_6, and $SiCl_4$ as Functions of E/p

	CCl_2F_2			SF_6			$SiCl_4$		
E/p	α/p	η/p	$\alpha/p-\eta/p$	α/p	η/p	$\alpha/p-\eta/p$	α/p	η/p	$\alpha/p-\eta/p$
80	0.2	0.87	−0.67	0.22	1.19	−0.97	—	—	—
85	—	—	—	0.33	1.17	−0.84	—	—	—
90	0.315	0.92	−0.60	0.44	1.15	−0.74	—	—	—
95	—	—	—	0.55	1.14	−0.59	—	—	—
100	0.45	0.95	−0.50	0.67	1.12	−0.45	0.050	0.043	+0.007
105	—	—	—	0.78	1.10	−0.32	0.070	0.053	+0.017
110	0.60	0.96	−0.36	0.90	1.08	−0.18	0.090	0.064	+0.026
115	—	—	—	1.01	1.06	−0.05	0.110	0.074	+0.036
120	0.78	0.94	−0.16	1.11	1.04	+0.07	0.152	0.084	+0.068
125	—	—	—	1.23	1.02	+0.21	0.200	0.094	+0.106
130	0.92	0.87	+0.05	1.34	1.00	+0.34	0.25	0.102	+0.148
135	—	—	—	1.47	0.97	+0.50	0.310	0.110	+0.200
140	1.15	0.77	+0.38	1.59	0.96	+0.63	0.375	0.117	+0.258
145	—	—	—	1.71	0.94	+0.77	0.44	0.123	+0.317
150	1.35	0.70	+0.65	1.84	0.91	+0.93	0.510	0.128	+0.382
155	—	—	—	1.97	0.88	+1.09	0.58	0.131	+0.449
160	1.56	0.63	+0.93	2.1	0.85	+1.25	0.65	0.133	+0.517
165	—	—	—	2.225	0.81	+1.44	—	0.134	—
170	1.75	0.56	+1.19	—	—	—	0.80	0.134	+0.666
175	—	—	—	—	—	—	—	0.132	—
180	1.95	0.50	+1.45	—	—	—	0.95	0.126	+0.824
185	—	—	—	—	—	—	—	—	—
190	2.15	0.45	+1.70	—	—	—	1.11	0.110	+1.00
195	—	—	—	—	—	—	—	—	—
200	2.32	0.39	+1.93	—	—	—	1.26	0.084	+1.18
205	—	—	—	—	—	—	—	—	—
210	2.50	0.34	+2.16	—	—	—	—	—	—

Source: Loeb, L.B., *Basic Processes of Gaseous Electronics*, University of California Press, Berkeley/Los Angeles, CA, 1961.

ionization processes, which adds on the ionization by electronic collisions. He attributed the secondary process to the ionizing action of positive ions produced during the development of the electron avalanche towards the anode. Although such a secondary ionization process is now recognized as improbable in the situation previously described, the action of the secondary ionization processes is certainly the cause of the observed behavior of the discharge current in the region T_2. Several secondary ionization processes have been proposed: photoionization in the gas volume, emission from the cathode by photoemission beside bombardment of positive ions, etc. The action of the secondary ionization will be analyzed in the following for the case of a gas gap subjected to a uniform field. Let

- n_c: the total number of electrons emitted from the cathode
- n_0: the number of electrons emitted per unit of surface of the cathode by the action of an external source, for example, irradiation of the cathode with UV lights
- γ: the *second ionization coefficient (or secondary emission)* at the cathode. γ represents the probability that an electron from the avalanche will emit a secondary electron from the cathode. The physical process may be photoionization, bombardment of positive ions, etc.

In these conditions, the total number of free electrons produced in the gas gap is

$$n_t = n_c \exp(\alpha d)$$

where d is the interelectrode distance.

The number of secondary electrons, n_s, emitted from the cathode is by definition

$$n_s = \gamma n_t = \gamma n_c \exp(\alpha d).$$

It follows that

$$n_c = n_0 + n_s = n_0 + \gamma n_c \exp(\alpha d)$$

one gets

$$n_c = \frac{n_0}{1 - \gamma \exp(\alpha d)} \tag{4.48}$$

and the current density $j(t)$ of the corresponding electric current

$$j = \frac{q}{d} v = \frac{n_t e}{d} \mu_e E$$

where $v(t)$ is the drift velocity of electrons, $\mathbf{v}(t) = \mu_e \mathbf{E}$, and μ_e the electron mobility. It follows that

$$j = \frac{n_0}{1 - \gamma \exp(\alpha d)} \frac{e}{d} \mu_e \exp(\alpha d) E = \frac{j_0}{1 - \gamma \exp(\alpha d)} \tag{4.49}$$

where $j_0 = (n_0 e/d)\mu_e \exp(\alpha d)$ represents the density of the current supplied by the external source.

The preceding equation shows clearly that the discharge current density $j(t)$ can increase faster than is expressed by the exponential law.

4.9.2 Regimes of Sustained and Self-Sustained Discharges

Referring to the expression of the discharge current in the gas gap (Equation 4.49), one can see that the electric discharge depends on the supply of n_0 free electrons from the cathode by the external source. The discharge stops when the external source is removed, reducing the number of initiating electrons n_0 to zero. The electric discharge is in a *regime of sustained discharge*. This regime corresponds essentially to the range of voltages in the regions T_1 and T_2 illustrated in Figure 4.35. The regime of sustained discharge in the region T_2 continues as long as the denominator of Equation 4.49 remains positive:

$$1 - \gamma \exp(\alpha d) > 0$$

A new regime of discharge develops in the gas gap when the preceding expression becomes null, making the discharge current undetermined and independent of the external source. The electric discharge reaches *a self-sustained regime*, since the action of secondary emissions becomes sufficiently important to replace the external source. It is obvious that the self-sustained regime of discharge corresponds to a drastic change in the dielectric proprieties of the gas gap, passing from the state of insulator to conductor. The self-sustained regime of discharge can develop in different forms, depending on the conditions of the applied electric field and the gas pressure in the gap:

- At low pressure, the self-sustained regime of discharge takes the form of a *glow discharge*, the main application of which is in the development of gas discharge lamps, for example, fluorescent tubes and mercury-vapor lamps and rectifiers.

- Another form of self-sustained discharge is the *electric arc* with the main application in arc welding and in the development of high-voltage circuit breakers.
- In overhead transmission lines, the electric field is nonuniform in the air gap between the conductors and the ground or the tower. The self-sustained discharge regime can develop in the form of partial discharges in air, known as *corona discharges*, or to an *electric breakdown*, a transient state leading to the development of an electric arc. The application to overhead transmission lines is limited essentially to the dimensioning of the tower and length of the insulators string and the selection of the line conductors to obtain a good compromise between the dielectric performances of the line and its costs.

4.9.3 Onset Conditions of Self-Sustained Discharge

Because of the practical importance of the self-sustained discharge regime, the conditions for its development in a gas gap are of prime interest to engineers. These conditions are described by the following equation, which makes the discharge current indeterminate:

$$1 - \gamma \exp(\alpha d) = 0 \tag{4.50}$$

4.9.3.1 Breakdown Voltage in Uniform Fields: Paschen's Law

The onset conditions for the self-sustained discharge regime in a uniform field gap are

$$\exp(\alpha d) = \frac{1}{\gamma}$$

Taking the logarithm of both sides of the preceding equation,

$$\alpha d = \ln\left(\frac{1}{\gamma}\right) \tag{4.51}$$

Assuming that the ionization coefficient of the gas can be expressed as (Equation 4.46)

$$\alpha = pA\exp\left(-\frac{Bp}{E}\right)$$

and taking into account the expression of the uniform field $E = U/d$, where U is the applied voltage and d the interelectrode spacing, the onset conditions of the self-sustained discharge, expressed by Equation 4.51, become

$$\ln\left(\frac{1}{\gamma}\right) = \alpha d = pAd\exp\left(-\frac{Bpd}{U_c}\right)$$

or

$$\frac{\ln(1/\gamma)}{Apd} = \exp\left(-\frac{Bpd}{U_c}\right)$$

Taking the logarithm of both sides of the preceding equation gives

$$\ln\left[\frac{\ln(1/\gamma)}{Apd}\right] = -\frac{Bpd}{U_c}$$

The expression for the onset voltage of the self-sustained regime of discharge in a uniform field gap becomes

$$U_c = -\frac{Bpd}{\ln\left[\dfrac{\ln(1/\gamma)}{Apd}\right]} = f(pd) \tag{4.52}$$

It can be seen that *the onset voltage U_c is a function of the product pd, of the gas pressure p by the inter-electrode spacing d*, generally known as Paschen's law. The readers can refer to Dakin et al. (1974) for a detailed review of the uniform field breakdown. Figures 4.29 and 4.30 (Dakin et al., 1974) show the variations of the uniform field breakdown voltage in air and SF_6 as a function of the product *pd*. One can see that the voltage U_c becomes very large for values of *pd* either very high or very small. As a result, there exists a critical value of *pd* where the uniform field breakdown voltage is minimal.

The results also show that the SF_6 has a dielectric strength about 2.5 times that of atmospheric air. This explains the widespread use of SF_6 in the insulation of high-voltage equipment, the dielectric withstand of which is further improved by the use of high pressure. It should be pointed out that because of the approximate value of the expression for the ionization coefficient α, Paschen's law is applicable in practice, for values of the product *pd* below 1000.

4.9.3.2 Streamer Criterion: Onset Condition in Nonuniform Fields

The onset condition for the self-sustained regime of discharge, expressed by Equation 4.50, is derived for the case of a uniform field. Extrapolation to the case of a nonuniform field in an electronegative gas gives

$$1 - \gamma\exp\left[\int_{E}^{\hat{E}} (\alpha - \eta)\,dx\right] = 1 - \gamma\exp\left[\int_{E}^{\hat{E}} (\alpha - \eta)\,dx\right] = 0 \tag{4.52a}$$

where α and η are, respectively, the ionization and attachment coefficients, $\alpha' = (\alpha - \eta)$ the effective ionization coefficient by electron impact of the gas, and γ a coefficient representing the role of secondary

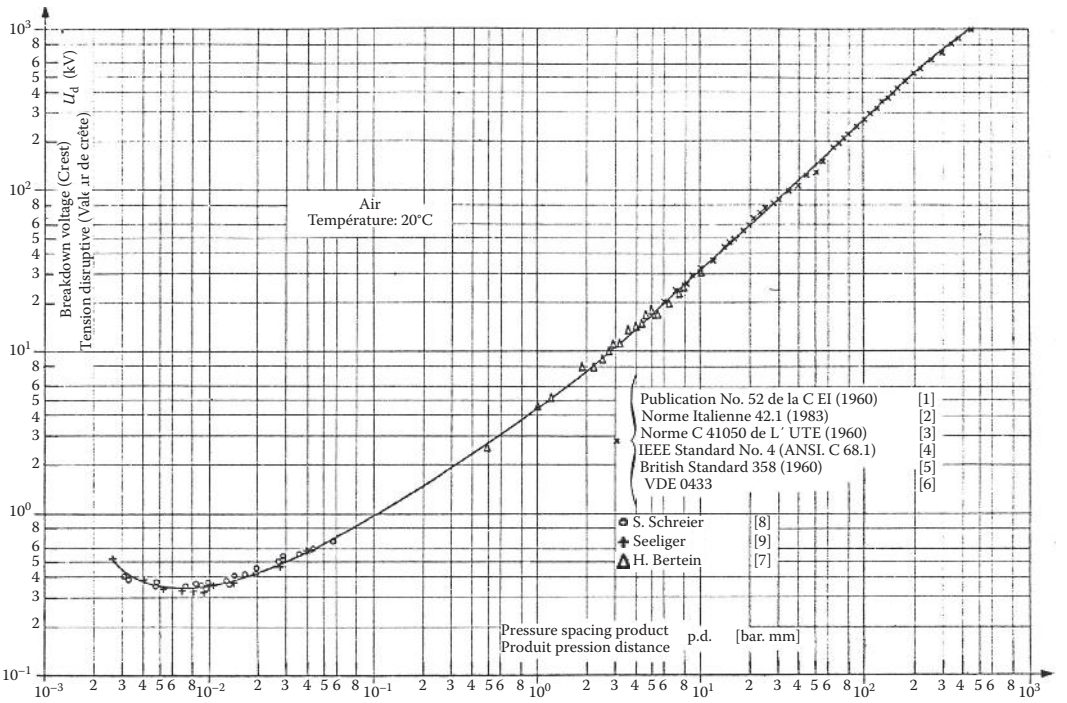


FIGURE 4.29 Paschen's curves in air. (From Dakin, T.W. et al., *Electra*, 32, 61, 1974.)

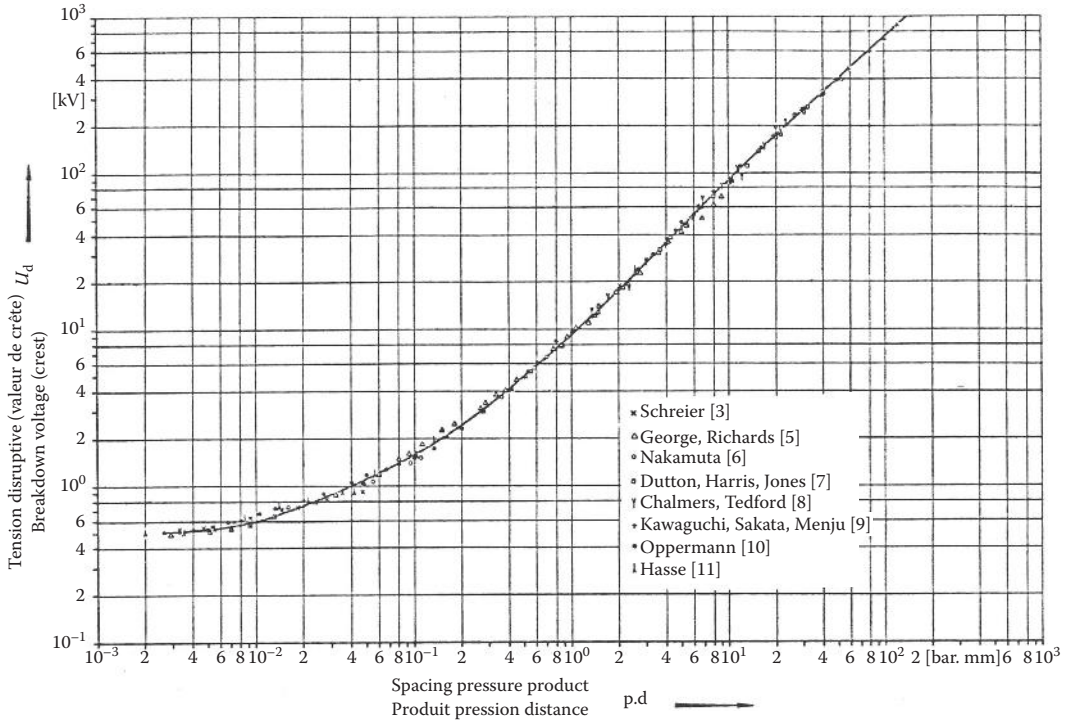


FIGURE 4.30 Paschen's curves in SF_6. (From Dakin, T.W. et al., *Electra*, 32, 61, 1974.)

processes in maintaining the ionization activities in the gap. In a nonuniform field, α' varies with the distance x from the highly stressed electrode, and the integral is evaluated along a hypothetical avalanche path for values of x where the ionization coefficient α' is positive. The onset condition (4.52a) can be rewritten as

$$\exp\left[\int_0 (\alpha - \eta)\,dx\right] = \frac{1}{\gamma} \tag{4.53}$$

The left-hand side represents the avalanche development from a single electron and $1/\gamma$ the critical size of the avalanche to assure stable development of the discharge. The following is a physical meaning to the aforementioned corona onset criteria: *There exists a critical length for the initial electron avalanche equal to 1/γ, such that the action of the secondary processes becomes sufficient to maintain the discharge in the gap in a self-sustained regime of discharge*. It is often accepted that the critical length of the initial electron avalanche corresponds to 10^8 electrons. One obtains the criteria currently used to calculate the onset voltage for the self-sustained regime of discharge, also known as the streamer criterion, referring to the predominant streamers discharge at onset (Cobine, 1958; Pedersen et al., 1984):

$$\exp\left[\int_0 (\alpha - \eta)\,dx\right] = \frac{1}{\gamma} = 10^8 \tag{4.54}$$

An alternative expression is obtained by taking the logarithm of both sides of Equation 4.54:

$$\int (\alpha - \eta)\,dx = \ln 10^8 = 18.42 \tag{4.55}$$

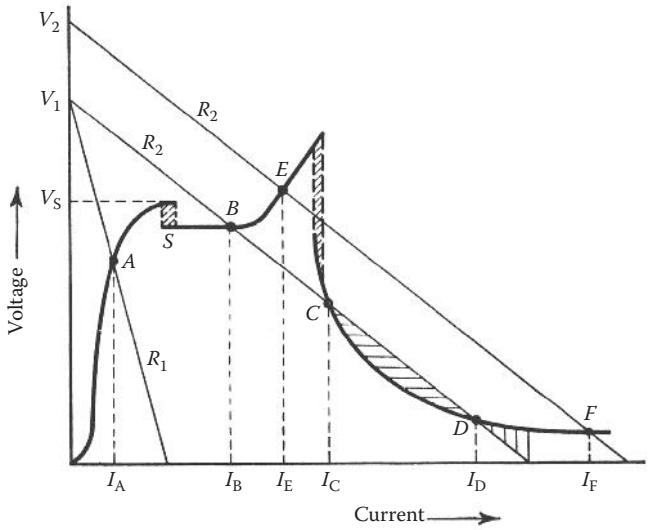


FIGURE 4.31 *U–I* characteristics of a uniform field discharge gap, with I_A in the range of 10^{-5} A. I_C in the range of 10^{-1} A and I_D in the range of *A*. (From Cobine, J.D., *Gaseous Conductors—Theory and Engineering Applications*, Dover Publications Inc., New York, 1958.)

4.10 Examples of Self-Sustained Discharges

A brief review of two common self-sustained discharges will be presented in the following, namely, the glow discharge and electric arc. Consider a uniform field gap, subjected to a dc voltage *U*, with circuit resistance *R*. By varying the resistance *R*, one modifies the operating conditions of the circuit, which define the static characteristics of the discharge gap: the voltage *U* across the gap and current *i* as illustrated in Figure 4.31. One can see that as the circuit current increases (by reducing the circuit resistance *R*), the sustained regime of Townsend's discharge develops up to currents in the order of 10^{-5} A. A first self-sustained regime of discharge, the glow discharge, follows, developing at discharge currents between 10^{-5} and 10^{-1} A and, finally, the electric arc developing at currents of discharge higher than 10^{-1} A.

In Figure 4.31, the straight lines with the slope determined by the circuit resistance *R* represent the operating characteristics of the circuit. The actual operating point is determined by the intersection point of the above line and the *U–I* characteristics of the discharge. For values of the circuit resistance $R = R_1$ higher than a critical value R_m, there is only one stable operating point for the circuit. When $R = R_2$, smaller than R_m, three intersection points exist. One can verify that only two of the three operating points are stable, corresponding to the conditions for the glow discharge (point *B*) and electric arc (point *D*). In effect, a reduction of the circuit current around the operating point *A* (or *B*) would tend to decrease the applied voltage (along the circuit characteristic line) above the value required to maintain discharge in the gap (along the *U–I* characteristics) and to increase the discharge current, thus bringing the operating point back to *A* (or *B*). On the other hand, an increase of the circuit current from the operating point *A* (or *B*) corresponds to a negative difference between the applied voltage and that required to maintain the discharge, which tends to reduce the discharge current and bring the operating point back to *A* (or *B*).

A reduction of the circuit current around the operating point *C* corresponds to a negative difference between the applied voltage and the voltage required to maintain the discharge in the gap, which reduces further the circuit current and moves the operating point to the left and away from *C*. On the other hand, an increase of the circuit current around the operating point *C* corresponds to a positive difference between the applied voltage and that required to maintain the discharge in the gap, which increases further the circuit current and moves the operating point to the right and away from *C*. As a result, although the operating point *C* is possible for the circuit, a small fluctuation in the operating conditions would move the operating point to one of the two stable operating points *B* or *D*. In practice, a glow discharge is usually

initiated by increasing the applied voltage across the gap, while keeping the gap constant. An electric arc is initiated by separating the electrodes of a closed gap or by approaching the electrodes of an open gap while maintaining the circuit conditions the same (opening and closing operations of a circuit breaker).

4.10.1 Glow Discharges

The glow discharge is a self-sustained discharge regime usually developing in a low-pressure gas gap, typically in the order of a few mm of Hg. The discharge extending over the whole gap is characterized by the existence of glow regions. One may distinguish three regions in the discharge: the cathode region, the positive column, and the anode region.
Cathode region: This region of the glow discharge contains a number of luminescent zones alternating with dark spaces of small dimensions. Starting from the cathode, one distinguishes in successive order a first dark space (Aston), a cathode luminescent region, and a second dark space (Faraday) followed by the positive column of the discharge.

Positive column: This is a region extending over almost the whole length of the discharge gap, where the ionization activities remain relatively stable in the gas volume, producing a uniform glow of characteristic color, which corresponds to the emission spectrum of the insulating gas.

The anode region: This is characterized by a glow region, indicating an enhanced ionization activity, followed by the anode dark space adjacent to the anode where the ionization of the gas is clearly reduced.

4.10.1.1 Physical Mechanism of the Discharge

The development of the glow discharge can be explained as follows: The ionization in the gas volume is essentially by electronic collisions, while the discharge is sustained by a *secondary mechanism of producing free electrons by emissions from the cathode by impact of positive ions.* This physical mechanism of the glow discharge is justified by the fact that the cathode phenomena are much more stable as compared to the other regions of the discharge. In effect, reducing the gas pressure causes the dark spaces and the glow regions immediately close to the cathode to extend further into the interelectrode space at the expense of the positive column. One observes the same behavior when approaching the two electrodes one to the other. It is the positive column that absorbs the reduction of the discharge gap while the dimensions of the cathode dark spaces and glow regions remain sensibly unchanged.

The formation of dark spaces alternating with luminescent regions can be explained by the uniform energetic state of the secondary electrons emitted from the cathode. Their energy being insufficient to ionize the gas, the emitted electrons must travel over a certain distance in the direction of the applied field to accumulate the energy required for ionizing the gas molecules. This gives rises to a first dark space of Aston, adjacent to the cathode. On leaving the Aston dark space, the free electrons have acquired sufficient energy to start ionizing the gas atoms, thus giving rise to the first cathode luminescent region.

The ionization by electronic collisions in the cathode luminescent region increases exponentially the number of free electrons in the gas. However, it reduces the electron energy and prevents them from continuing the ionization of the gas. On leaving the cathode luminescent region, the electrons, both primary and secondary, must again accumulate energy from the applied electric field as they cross the second dark space, termed cathode dark space. On leaving the cathode dark space, ionization by electronic collisions is again possible in the gas, giving rise to a second negative luminescent region, termed negative glow, usually the most intense because of the high number of free electrons available, in the order of 10^{11} electrons/cm^3.

On leaving the negative glow region, the electrons are once again discharged of their energy; one observes a third dark space of Faraday, which allows them to acquire energy. This dark space is followed by a region where the ionization activities are more stable and diffuse, identified as the positive column, extending over almost the whole length of the discharge gap. The existence of the positive column is

attributed to the diffusion of the free electrons and by the dispersion in their individual energetic states as they move further from the cathode. The ionization of the gas becomes random in the positive column, where the density of free electrons is in the order of 10^9–10^{10} electrons/cm^3.

The existence of the anodic dark space is explained by the fact that absorption of the electrons at the anode is possible only if the energy of the incident electrons is not too high. An incident electron with too high energy will bounce off the anode back into the gas volume where it can dissipate its energy via inelastic collisions with the neutral molecules of the gas, before its absorption at the anode. This effect leads to the formation of a dark space followed by a luminescent region adjacent to the anode where the ionization activities in the gas are more intense.

4.10.1.2 Electrical Characteristics

The glow discharge is a self-sustained regime of discharge at relatively high voltage and low discharge current. The *U–I* characteristics of the glow discharge (Figure 4.31) present two distinct regions:

- In the first region, known as the *normal glow*, the development of the discharge is at constant voltage: an increase of the ionization activities in the gap causes a corresponding increase of the discharge current.
- In the second region, known as the *abnormal glow*, the development of the discharge is at increasing voltage: an increase of the ionization activities in the gap requires a corresponding increase in both the voltage and current of the discharge.

If one continues to increase the applied voltage across the discharge gap, the abnormal regime of the glow discharge transforms eventually to an electric arc, a self-sustained regime of discharge with low voltage and high current.

Normal glow: This is characterized by a constant and relatively high voltage with low discharge current. The discharge covers only part of the cathode. Noting that the glow discharge relies on the emission of electrons from the cathode via the bombardment of positive ions to sustain the ionization activities in the gap, an increase of the ionization activities in the discharge gap corresponds to an increase in the active area of the cathode covered by the glow discharge. There is no change in the voltage across the discharge gap or its distribution the discharge gap, with the major portion of the applied voltage applied across a small region near the cathode, followed by a gradual increase of the potential along the positive column.

The cathode voltage drop is highly dependent on the nature of the cathode and the insulating gas: it varies from 64 V for potassium electrodes in argon to 490 V for platinum electrodes in carbon monoxide. It is proportional to the work function *W* of the electrode and decreases with the ionization potential of the gas. This behavior is explained by the fact that the glow discharge depends essentially on the emission of electrons from the cathode by bombardment of positive ions produced by ionization activities in the gas volume. One observes also a simple relationship between the length of the region of the cathode voltage drop, δ_n, and the pressure p of the gas so that

$$\delta_n p = \text{constant} \tag{4.56}$$

Furthermore, the cathode voltage drop is related to the length δ_n of the cathode drop by

$$1 + \frac{1}{\gamma} = \exp\left[\int_{E_0}^{E_{\delta_n}} \alpha \, dx\right] \tag{4.57}$$

where γ is the coefficient of secondary emission of free electrons from the cathode by bombardment of positive ions.

Equation 4.57 represents the onset condition of the self-sustained regime in the cathode region of the gap. The integral is limited to the cathode region and must take into account of the local distribution of the electric field, largely determined by the presence of local space charges.

Abnormal regime of discharge: This is characterized by an essentially linear relationship between the voltage and current of the discharge, with the cathode surface being completely covered by the discharge. The observed behavior of the discharge is explained by the fact that the electrons, which are easily emitted from the surface layer of the cathode, are already removed. To increase the number of electrons emitted from the cathode, the incident ions must have higher energy to access the electrons located in the subadjacent layers; therefore, one observes an essentially linear relationship between the discharge voltage and the square root of current density j in the abnormal regime, according to the following empirical relation for the cathode voltage drop:

$$U_{an} = E + F\frac{\sqrt{j}}{p} \tag{4.58}$$

where U_{an} is the cathode voltage drop during the abnormal glow phase E and F are experimental constants. It follows that

$$\sqrt{j} = \frac{(U_{an} - E)}{F}p$$

On the other hand, the length of the region of the cathode voltage drop, δ_n, is given by the following empirical relation:

$$d_{an} = \frac{A}{p} + \frac{B}{\sqrt{j}} \tag{4.59}$$

which can be rewritten as

$$pd_{an} = A + \frac{Bp}{\sqrt{j}}$$

where A and B are experimental constants. By replacing the expression of $\sqrt{j}$ in the preceding equation, one obtains

$$pd_{an} = A + \frac{BF}{U_{an} - E} \tag{4.60}$$

The main application of glow discharge is in the development of lighting industry, namely, gas discharge lamps, taking advantage of the luminous uniformity and the flexibility for adjustment of the positive column. By choosing a gas with appropriate emission spectrum, one can produce a lighting of desired intensity and color.

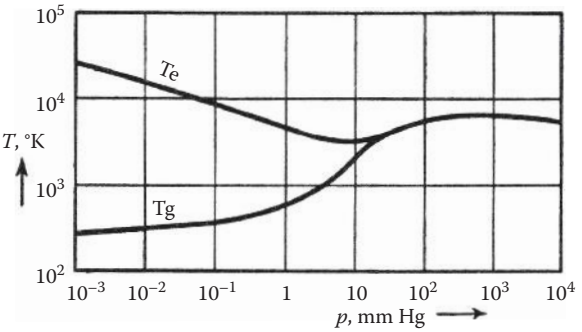


FIGURE 4.32 Distinction between low- and high-pressure arcs. (From Cobine, J.D., *Gaseous Conductors—Theory and Engineering Applications*, Dover Publications Inc., New York, 1958.)

4.10.2 Electric Arc

The electric arc is another self-sustained discharge well known in the development of gas-insulated circuit breakers. Referring to the *U–I* characteristics of a uniform field discharge gap shown in Figure 4.31, the stable operating point *D* corresponds to that of an electric arc, a self-sustained regime of discharge with *a relatively low voltage and a high discharge current*. One distinguishes two forms of electric arc, corresponding to arc regimes at low and high pressures, related to the temperature of the electrons and gas molecules. In a low-pressure arc, the electrons have a higher temperature than that of the gas molecules, while in high-pressure arc, both electrons and gas molecules have the same temperature (Figure 4.32). The separation between the two arc regimes is at a pressure around 20–30 mm Hg.

4.10.2.1 Physical Mechanism

As with the glow discharge, the electric arc is composed of three distinct regions:

- The cathode fall
- The arc column (positive column)
- The anode fall

Cathode phenomena: The region of the cathode fall is characterized by a potential drop in the order of the ionization potential of the gas or vapor in the region adjacent to the cathode. The length of the cathode fall is in the order of a mean free path of the gas molecules. The development of the electric arc corresponds to the establishment of a new mechanism more efficient of electron emission from the cathode. As the current density increases in the abnormal regime of glow discharge, the cathode voltage drop also increases while the region of the cathode fall is reduced. Thus, in the same time that the energy of positive ions increases, the number of collisions with neutral gas atoms in the region of the cathode fall is reduced. The energy absorbed by the cathode is higher, increasing the cathode temperature. With cathodes made of refractory materials, carbon, tungsten, etc., the temperature of the cathode is sufficiently high, in the order of several thousand K, for *the thermionic emission* to take place. The density of the current emitted from the cathode is a function of the cathode temperature, in K:

$$J_s = AT^2 \exp\left(-\frac{e\phi}{kT}\right) \tag{4.61}$$

where ϕ is the potential barrier of the cathode.

The higher current produced by the thermionic emission increases the number of positive ions in the region of the cathode fall and causes further heating of the cathode, requiring a lower cathode voltage to maintain the arc. For cathodes made with materials of low melting temperature, the transition from the glow discharge to the electric arc is sudden, indicating a higher rate of electron emission, associated to the formation of *arc spots*, where the cathode vaporizes into the gas.

Arc column: This is a region of plasma of variable length to allow the circulation of the arc current. In a low-pressure arc, the density of positive ions compensates essentially the effect of space charges. The free electrons are the main charge carrier; their temperature is clearly higher than that of the gas. In high-pressure arcs, the arc column has a smaller cross section and a higher potential gradient along the arc column. The temperature of the arc column is sufficiently high for *thermal ionization* to become the predominant ionization process in the gas, with a quasi-neutral arc column.

Anode fall adjacent to the anode is characterized by the presence of a space charge formed of free electrons. Positive ions produced in the region of the anodic fall move towards the cathode and constitute the main source of positive ions in the arc. The concentration of positive ions in the region of the anode fall increases towards the cathode end, where it becomes sufficiently dense to neutralize the electronic space charge, to form the plasma that one observes in the arc column. It should be noted that the temperature

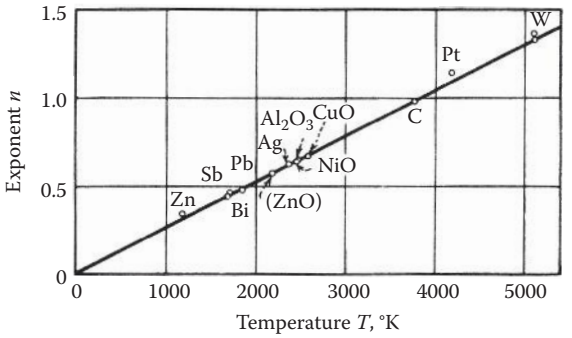


FIGURE 4.33 Variation of the exponent n of the Nottingham equation with the melting temperature of the anode. (From Cobine, J.D., *Gaseous Conductors—Theory and Engineering Applications*, Dover Publications Inc., New York, 1958.)

of the anode is comparable to the melting temperature of the anode material. However, a high temperature at the anode is not essential for maintaining the electric arc, which can develop even if the anode is water-cooled.

4.10.2.2 Arc Characteristics

The stationary U–i characteristics of the electric arc follow an empirical law established by Nottingham (Cobine, 1958):

$$U_a = A + \frac{B}{i^n} \tag{4.62}$$

where A and B are constants. The exponent n of the Nottingham equation in the preceding equation is a linear function of the melting temperature, T in K, of the anode according to

$$n = 2.62 \times 10^{-4} T \tag{4.63}$$

Figure 4.33 shows the variations of the exponent n as a function of the melting temperature of the anode. For carbon electrodes, the melting temperature is 3800 K, and the exponent n is equal to

$$n = 2.62 \times 10^{-4} * 3800 \approx 1,$$

in accord with the results of *H.* Ayrton, who has obtained the following expression for the arc voltage, with carbon electrodes in air at atmospheric pressure (Ayrton, 1902):

$$U_a(x,i) = a + bx + \frac{c + dx}{i} \tag{4.64}$$

where
a, b, c, and d are constants and x is the interelectrode distance in mm
i the arc current in A
U_a the arc voltage in V

The gas pressure affects also the electric arc voltage according to

$$U_a = M \ln(p) + N \tag{4.65}$$

where M and N are constants.

4.11 Fundamentals of Corona Discharges in Atmospheric Air

Air is a particular mixture of different gases, mainly nitrogen (79%), oxygen (20%), and other impurities. Its specific mass is 1.0293 kg/m^3 under normal conditions, pressure of 760 mm Hg, and temperature of 25°C. In spite of by-products produced in discharges, air is a self-renewable gas. However, it is affected by the altitude, which reduces the air density and is subjected to weather conditions, which tend to modify the surface conditions at the electrodes. We will discuss in the following the development of corona discharges, a designated term for partial discharges in atmospheric air, which are the first form of self-sustained discharges in a nonuniform field gap. The case of breakdown of long air gaps is treated in Chapter 5.

Corona discharges follow an electron avalanche process whereby neutral molecules are ionized by electron impacts under the effect of the applied field (Trinh and Jordan, 1968). The discharge development is significantly conditioned by the electronegative nature of oxygen molecules, which can readily capture free electrons to form negative ions and thus hamper the electron avalanche process. The effect is particularly pronounced in nonuniform field gaps where ion space charges of both polarities accumulate. This modifies the local field distribution around the highly stressed electrode and, in turn, affects the discharge development. One can distinguish several modes of corona discharge, resulting from the equilibrium states existing between the buildup and removal of the ion space charges from the highly stressed region at a given applied voltage. This section describes the various corona modes, their specific electrical and light characteristics, and a few practical means of preventing partial discharges in high-voltage test setups.

4.11.1 Empirical Expressions of Onset and Breakdown of Practical Gap Configurations

Although the corona onset can be derived from the streamer onset theory, there exist several empirical expressions for the conditions for the onset of corona discharges, developed by F.W. Peek, Jr. (Peek, 1929) for a number of practical gap configurations and are given in the following:

Sphere–plane gap: The onset field of corona discharges E_c in a sphere of radius R-plane gap is

$$E_c = \frac{18}{\sqrt{R}} \quad \text{(kV/cm, cm)} \tag{4.66}$$

Coaxial conductor: The corona onset field E_c in a coaxial conductor with inner radius a is

$$E_c = 31m\delta\left(1 + \frac{0.308}{\sqrt{\delta a}}\right) \quad \text{(kV/cm, cm)} \tag{4.67}$$

Parallel conductors: The corona onset field E_c and breakdown field E_s of a gap formed of two parallel conductors of the same radius a are

$$E_c = 30m\delta\left(1 + \frac{0.301}{\sqrt{\delta a}}\right) \quad \text{(kV/cm, cm)} \tag{4.68}$$

$$E_s = 30\delta\left(1 + \frac{0.01}{\sqrt{\delta}}\frac{S}{a}\right) \quad \text{(kV/cm, cm)} \tag{4.69}$$

In the earlier expressions, a is the radius of the conductor in cm; R the radius of the spheres in cm; S the distance between the conductor centers in cm; d the interelectrode distance, in cm; m a constant between 0.6 and 1 representing the surface roughness of the conductor; and δ the relative air density factor, given by

$$\delta = \frac{0.392\,p}{273 + \theta} \tag{4.70}$$

where
p is the barometric pressure in mm of Hg
t the temperature in degrees centigrade (°C)
δ is equal to 1 at 760 mm Hg and 25°C

4.11.2 Active Ionization Processes and Source of Free Electrons

Because of the presence of oxygen, air is effectively an electronegative gas where free electrons are readily attached to oxygen molecules to form stable negative ions. The following processes are active in discharges in atmospheric air:

Excitation and ionization by electronic collisions: As previously mentioned, the high efficiency of this ionization process is related to the difference in masses between electrons and air atoms, which allows free electrons to accumulate kinetic energy over several successive free paths, until the accumulated energy is sufficient to excite or ionize the air atom on impact.

Photoexcitation and ionization: During the development of discharges, the number of excited molecules is much larger than that of ion pairs produced. Left alone, the excited atoms must radiate the absorbed energy to get back to their neutral state, by emitting photons, the frequencies of which are characteristic of each gas: N_2 and O_2 in air. The emitted photons can, in turn, excite or ionize other neutral molecules. Photoionization actually plays an important role in the creation of free electrons necessary for maintaining ionization activities in the air gap.

Attachment of electrons: Since air contains 20% of oxygen, a highly electronegative gas, the free electrons attach easily to oxygen atom, forming stable negative ions. Two attachment processes have been identified in the development of corona discharges in air, depending on the energy of the colliding electrons. At low energy levels, between 0.2 and 0.5 eV, negative ions are formed by a direct attachment process:

$$O_2 + O_2 + e^- = O_2^- + O_2 \tag{4.71}$$

At higher energy levels, greater than 2.9 eV, atomic ions are formed by a dissociate attachment process:

$$O_2 + e^- = O^- + O \tag{4.72}$$

The formation of negative ions has a considerable influence on the development of corona discharges, namely, in the establishment of different modes of discharge.

Electron detachment: In air, electron detachment from negative oxygen ions is an active process to provide the free electrons to initiate new avalanches.

Electron emission from the cathode by ionic bombardment: This process can be very active in the development of discharges at the cathode, particularly in presence of a highly divergent field. The positive ions are attracted towards the cathode and can accumulate sufficient energy in the last free paths to emit, on impact, free electrons from the cathode.

4.11.3 Corona Discharges under Negative Polarity

Because of the nonuniform field necessary for the development of corona discharges, the air gap can be separated in two distinct regions by an equigradient surface S_0, where the effective ionization coefficient (α-η) is null. The electronegative nature of air favors the formation of negative ions during the discharge development. Due to their relatively slow mobility, ions of both polarities from several consecutive electron avalanches accumulate in the low-field region of the gap and form ion space charges. To properly interpret the development of corona discharges, the active role of these ion space charges, which continuously modify the local field intensity and hence the development of corona discharges according to their relative buildup and removal from the region around the highly stressed electrode, must be taken into account.

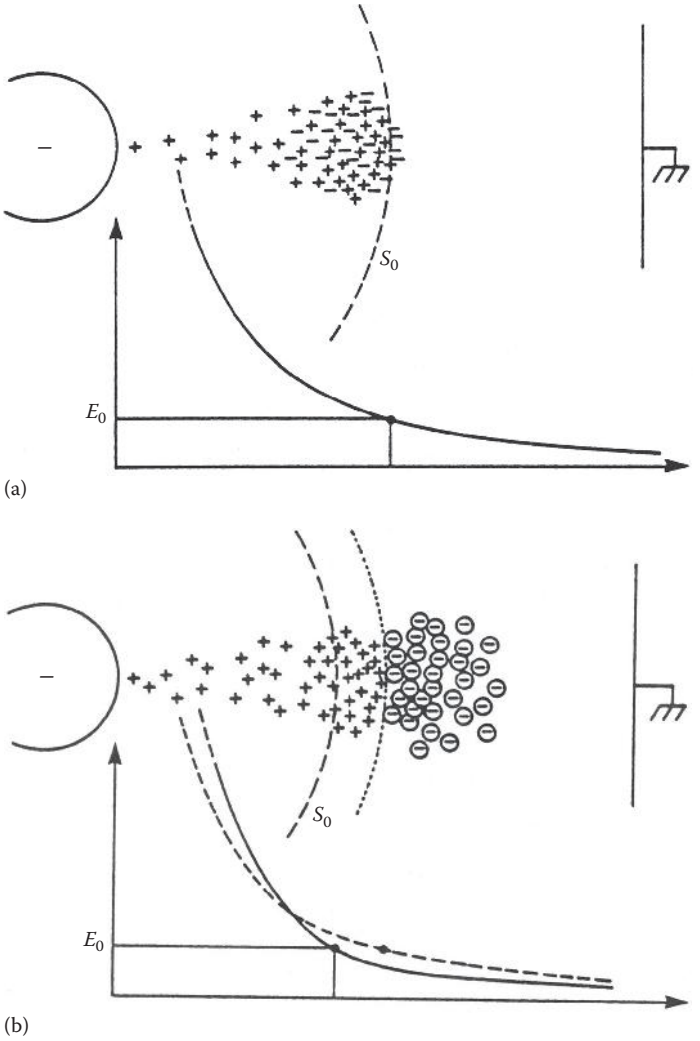


FIGURE 4.34 Development of an electron avalanche from the cathode: (a) schematic diagram of avalanche formation up to a boundary surface S_0 and associated field distribution; (b) space charge movement and modified field distribution with a new position of the boundary surface S_0. (From Trinh, N.G., *IEEE Electr. Insul. Mag*., 11, 23, 1995a.)

4.11.3.1 Electron Avalanche and Space Charges

When the highly stressed electrode is at a negative potential, electron avalanches are initiated at the cathode and develop towards the anode in a continuously decreasing field. Referring to Figure 4.34, the nonuniformity of the field distribution causes the electron avalanche to stop at the boundary surface S_0, where the net ionization coefficient is zero, that is, $\alpha = \eta$. Since free electrons can move much faster than ions under the influence of the applied field, they concentrate at the avalanche head during its progression. The number of ion pairs, electron and positive ions, produced in the avalanche is given by

$$n(x) = n_0 \exp\left[\int_0^x (\alpha - \eta)\, dx\right], \tag{4.73}$$

where n_0 is the initial number of free electrons in the avalanche.

Taking the derivative of the preceding equation with respect to x, one obtains

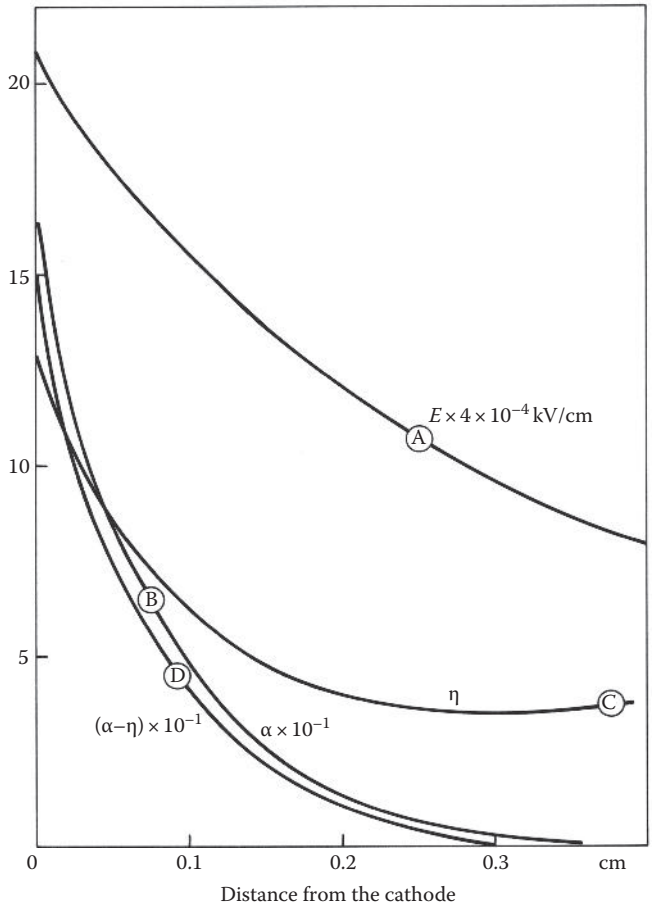


FIGURE 4.35 Distribution of the electric field and ionization parameters near the cathode. Sphere of 0.8 cm diameter, gap length 35 cm. A: Field distribution, B: variation of the ionization coefficient α, C: variation of the attachment coefficient η, D: variation of the effective ionization coefficient (α – η). (From Trinh, N.G., A systematic study of corona discharge in air at atmospheric pressure, PhD Thesis, Laval University, Québec, Canada, 1969.)

$$\frac{dn(x)}{dx} = n_0 \exp\left[\int_0^x (\alpha - \eta)\,dx\right](\alpha - \eta) \tag{4.74}$$

Equation 4.74 represents the net rate of generation of free electrons during the progression of the avalanche. Decomposing the preceding equation shows the contributions of the ionization and attachment processes as follows:

$$\frac{dn(x)}{dx} = \frac{dn^+}{dx} - \frac{dn^-}{dx} = \alpha n_0 \exp\left[\int_0^x (\alpha - \eta)\,dx\right] - \eta n_0 \exp\left[\int_0^x (\alpha - \eta)\,dx\right]$$

With on the one hand, the real rate of generation of positive ions produced by the ionization process in the development of the avalanche is given by

$$\frac{dn^+}{dx} = \alpha n_0 \exp\left[\int_0^x (\alpha - \eta)\,dx\right] \tag{4.75}$$

and on the other hand, that of the formation of negative ions by attachment of free electrons to the atoms of oxygen is expressed by

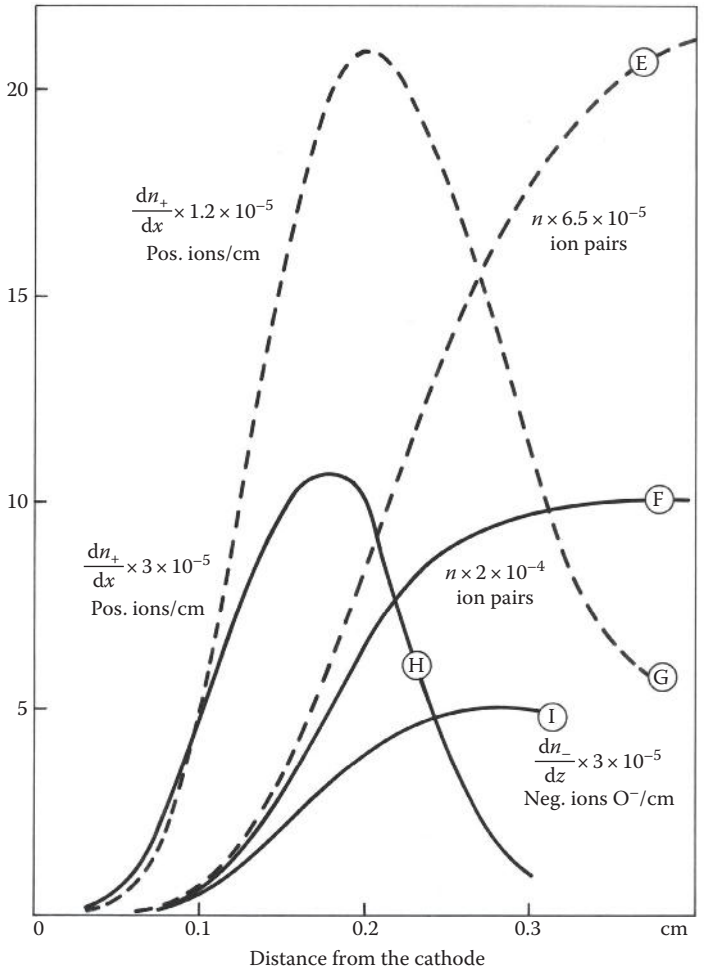


FIGURE 4.36 Distribution of the ion space charges near the cathode: sphere of 0.8 cm diameter, gap length 35 cm. E: avalanche development neglecting electron attachment, F: Avalanche development with electron attachment, G: distribution of positive ions neglecting electron attachment, H: distribution of positive ions with electron attachment, I: distribution of negative ions. (From Trinh, N.G., A systematic study of corona discharge in air at atmospheric pressure, PhD Thesis, Laval University, Québec, Canada, 1969.)

$$\frac{dn^-}{dx} = \eta n_0 \exp\left[\int (\alpha - \eta) dx\right] \tag{4.76}$$

Because of the small mobility of ions, their distribution in space corresponds to the derivative with respect to x, according to Equations 4.75 and 4.76 earlier. Their spatial distributions will be discussed in the following, referring to the sphere–plane gap shown in Figure 4.34a. The variations of the electric field, ionization, and attachment coefficients with the distance x from the cathode are also presented in Figure 4.35.

The development of the electron avalanche stops effectively at the equigradient surface S_0, where the electric field is equal to the threshold value such that the effective ionization coefficient α' is null, $\alpha = \eta$. In the region between the cathode and the surface S_0, the net ionization coefficient α' is greater than zero; the positive ions produced are in greater number than negative ions formed by attachment of free electrons to atoms of oxygen. It results in abundance of positive space charge in this region. Figure 4.36 illustrates the distributions of positive and negative ion space charges in the sphere–plane gap : sphere diameter: 0.8 cm, gap length: 35 cm. The applied voltage is 33 kV, corresponding to the threshold value

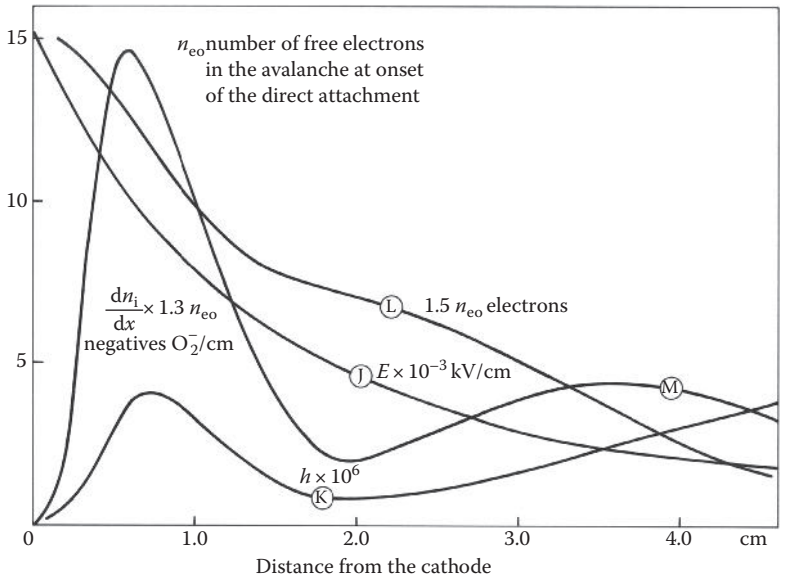


FIGURE 4.37 Distribution of the ion space charges in the interelectrode space : sphere of 0.8 cm diameter, gap length 35 cm. J: Field distribution, K: Variation of the attachment coefficient η, L: Number of negative ions produced, M: Distribution of negative ions. (From Trinh, N.G., A systematic study of corona discharge in air at atmospheric pressure, PhD Thesis, Laval University, Québec, Canada, 1969.)

of the discharges. One notices a pronounced concentration of positive ions close to the cathode, with a maximal concentration at 0.15 cm from the cathode.

Beyond the surface S_0, the net ionization coefficient α' is negative; the free electrons are either captured by atoms of oxygen to form negative ions or neutralized at the anode. The negative ions are in greater number than positive ions produced by ionization in the avalanche. The effect of electron attachment is preponderant and results in a superabundance of negative ion space charges in the region beyond S_0. Figure 4.37 illustrates the distributions of positive and negative ion space charges in the region between

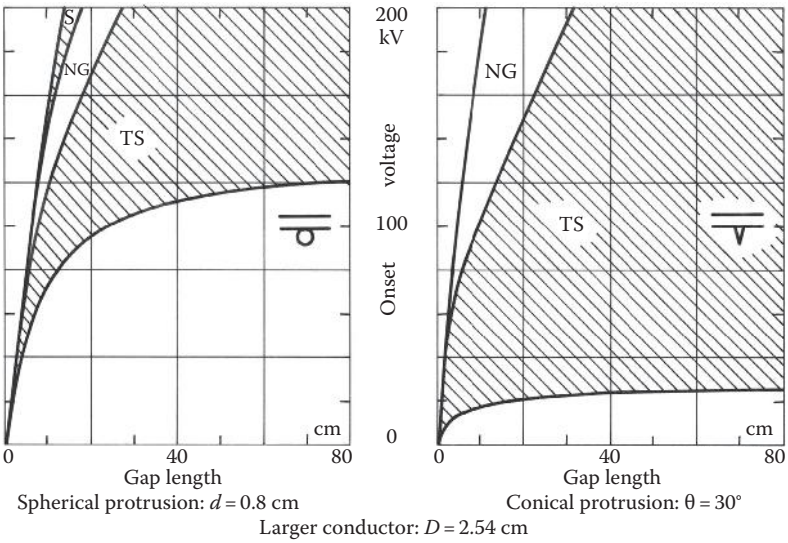


FIGURE 4.38 Onset conditions of corona modes at cathode: a protrusion on a 2.54 cm diameter conductor. Left: spherical protrusion 8 mm in diameter. Right: conical protrusion 8 mm in diameter, α = 30°. TS: Trichel streamers, NG: negative glow, S: negative streamers. (From Trinh, N.G., A systematic study of corona discharge in air at atmospheric pressure, PhD Thesis, Laval University, Québec, Canada, 1969.)

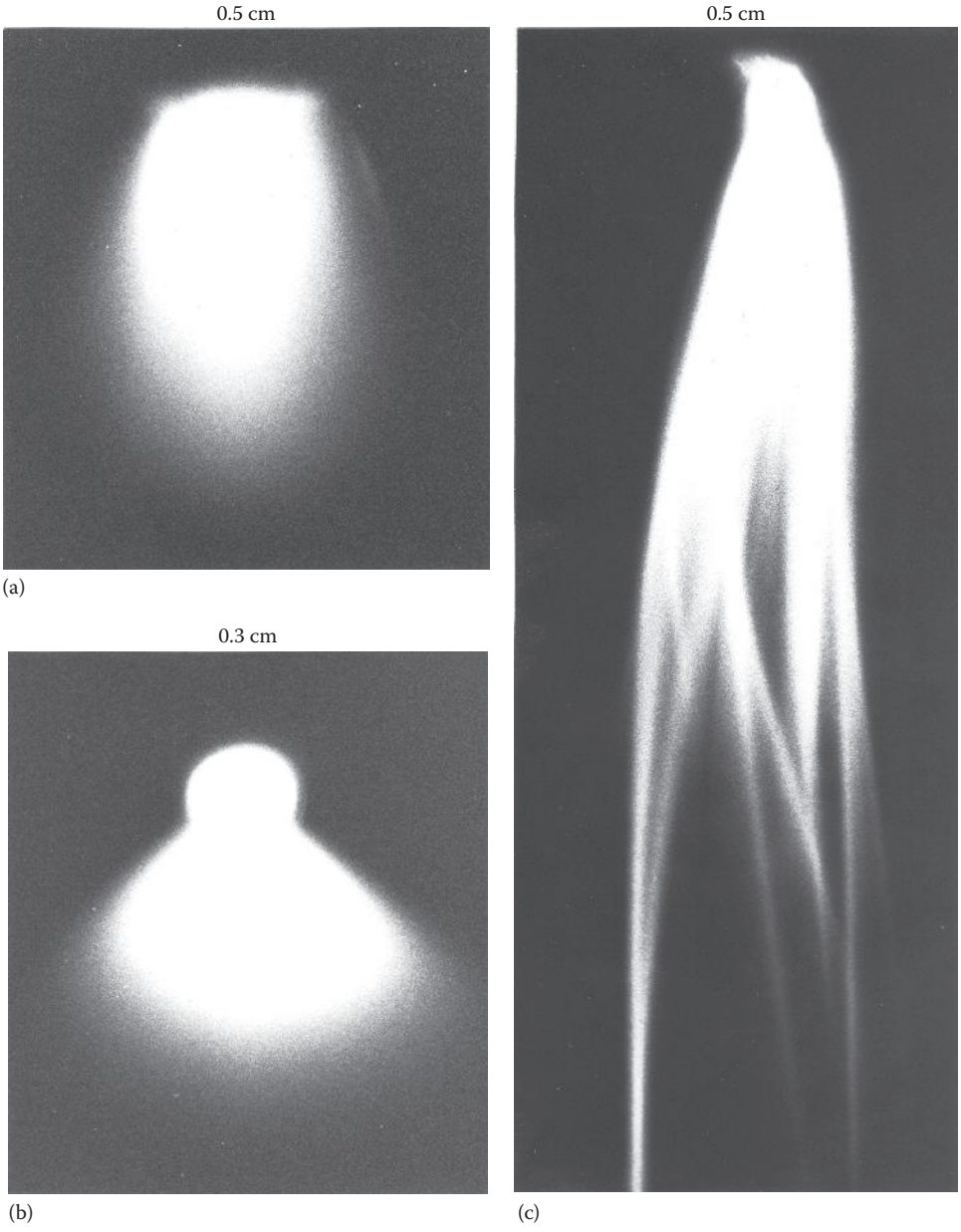


FIGURE 4.39 Corona modes at cathode: (a) Trichel streamers; (b) negative pulseless glow; and (c) negative streamers. Cathode: spherical protrusion (d = 0.8 cm) on a sphere (D = 7 cm); gap 19 cm; time exposure 1/4 s. (From Trinh, N.G. and Jordan, I.B., *IEEE Trans*., PAS-87, 1207, 1968; Trinh, N.G., *IEEE Electr. Insul. Mag*., 11, 23, 1995a. With permission.)

S_0 and the anode of the sphere–plane gap. One notices that most of the free electrons are converted into negative ions within 1 cm from the cathode. Thus, at the end of the first electron avalanche, there exist two ion space charges of opposite polarities in the discharge gap.

4.11.3.2 Negative Corona Modes

The formation of ion space charge of both polarities near the cathode has a direct effect on the local field distribution, as illustrated in Figure 4.34b, which compares field distributions in the gap near the cathode with (dashed curve) and without (solid line curve) ion space charges produced during the development

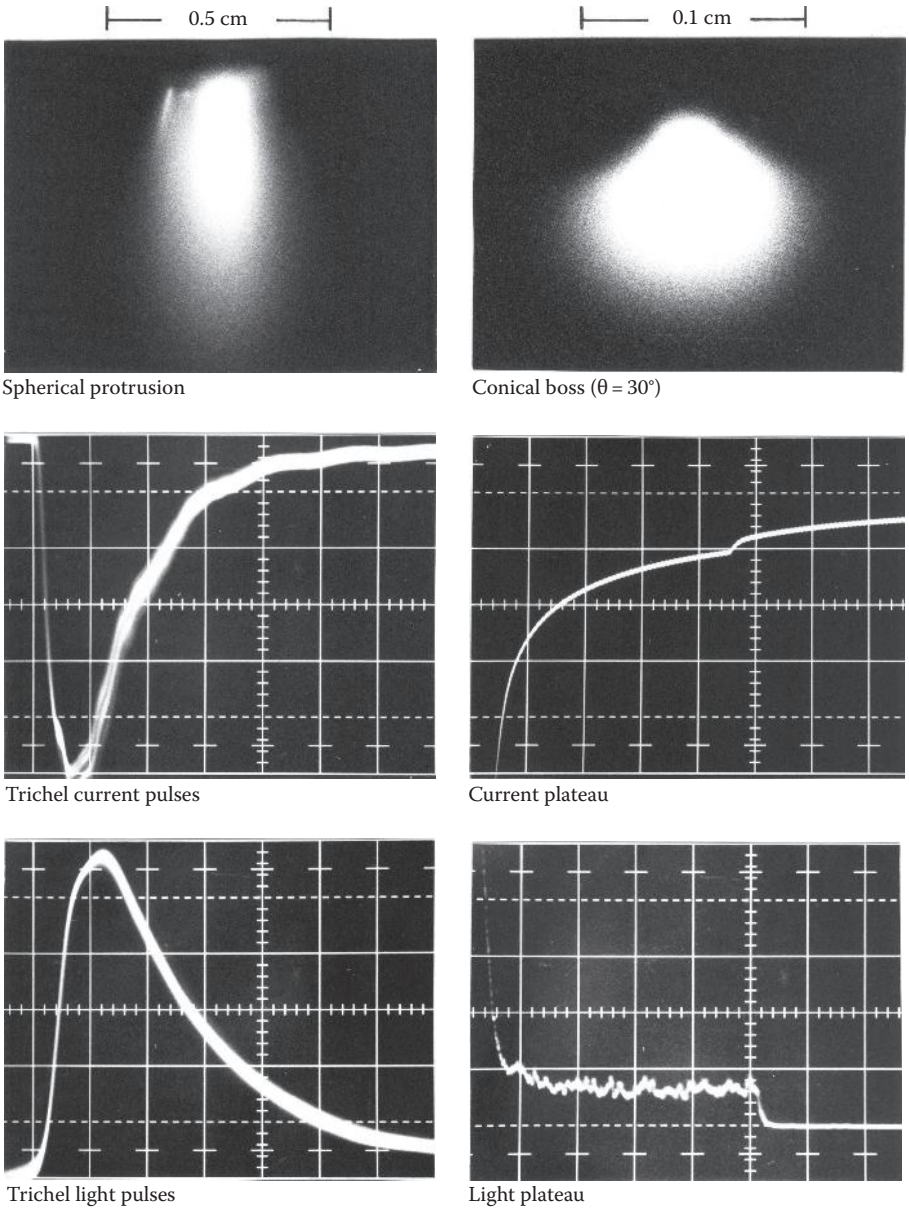


FIGURE 4.40 Current and light characteristics of Trichel streamer. Cathode: spherical protrusion (d = 0.8 cm) on a sphere (D = 7 cm); gap 19 cm. Scales: current 350 μA/div., 50 ns/div. (left), 50 μA/div., 2 μs/div. (right). Light: 0.5 V/div., 20 ns/div. (left), 0.2 V/div., 2 μs/div. (right). (From Trinh, N.G. and Jordan, I.B., *IEEE Trans*., PAS-87, 1207, 1968; Trinh, N.G., *IEEE Electr. Insul. Mag*., 11, 23, 1995a.)

of the initial electron avalanche. The presence of these space charges increases the field near the cathode, but it reduces the field intensity at the anode end of the gap. Therefore, the boundary surface of zero ionization activity S_0 moves towards the cathode. The subsequent electron avalanche develops in a region of slightly higher field intensity but covers a shorter distance than its predecessor covers. The influence of the ion space charge is such that it actually conditions the development of the discharge at the highly stressed electrode, producing three modes of corona discharge, which results from an equilibrium state between the rate of production and removal of ion space charges from the highly stressed region.

Figure 4.38 shows their onset conditions at a protrusion, of spherical and conical shape, on a cylindrical conductor, while their distinct electrical, physical, and visual characteristics are presented in Figure 4.39. These are, respectively, with increasing field intensity: Trichel streamer, negative pulseless glow, and negative streamer. An interpretation of the physical mechanism leading to the development of different corona modes is given in the following texts.

4.11.3.2.1 Trichel Streamers

Figures 4.39a and 4.40a show the visual aspect of the discharge. Its current and light characteristics are shown in Figure 4.40. The discharge develops along a narrow channel from the cathode and follows a regular pattern in which the streamer is initiated, develops, and is suppressed; a short dead time follows before the cycle is repeated. The duration of an individual streamer is very short, a few tens of nanoseconds, while the dead time varies from a few microseconds to a few milliseconds, or even longer. The resulting discharge current consists of regular negative pulses of small amplitude and short duration, succeeding one another at the rate of a few thousand pulses per second. A typical Trichel current pulse is shown in Figure 4.40 (above left) where, it should be noted, the wave shape is somewhat influenced by the time constant of the measuring circuit. The discharge duration may be significantly shorter, as depicted by the light pulse shown in Figure 4.40 (below left).

The development of Trichel streamers cannot be explained without taking account of the active roles of the ion space charges and the applied field. The streamer is initiated from the cathode by a free electron. If the corona onset conditions are met, the secondary emissions are sufficient to trigger new electron avalanches from the cathode and maintain the discharge activity. During the streamer development, several generations of electron avalanches are initiated from the cathode and propagate along the streamer channel. The avalanche process also produces two ion space charges in the gap, which gradually move the boundary surface S_0 closer to the cathode. The positive ion cloud thus finds itself compressed at the cathode and, in addition, partially neutralized at the cathode and by the negative ions produced in subsequent avalanches. This results in a net negative ion space charge, which eventually reduces the local field intensity at the cathode below the onset field and suppresses the discharge. The dead time is a period during which the applied field disperses the remaining ion space charges. A new streamer will develop when the immediate surroundings of the cathode have been cleared of space charges to a sufficient extent.

The preceding Trichel streamer mechanism explains the pulsating nature of the discharge. This mechanism depends on a very effective electron attachment process to suppress the ionization activity within a few tens of nanoseconds following the initiation of the discharge. The streamer repetition rate is essentially a function of the removal rate of ion space charges by the applied field and generally shows a linear dependence on the applied voltage. However, at higher fields, one may observe a reduction in the pulse repetition rate, which corresponds to the transition to a new corona mode.

These stable discharge conditions may be explained by the greater efficiency of the applied field in removing the ion space charges at higher field intensities. Negative ion space charges cannot build up sufficiently close to the cathode to effectively reduce the cathode field and suppress the ionization activities there. This interpretation of the discharge mechanism is further supported by the existence of a plateau in the Trichel streamer current and light pulses (Figure 4.40), which indicates that an equilibrium state exists for a short time between the removal and the creation of the negative ion space charge. Trinh and Jordan (1970) have shown that the transition from the Trichel streamer mode to the negative pulseless glow corresponds to an indefinite prolongation in time of one such current plateau.

4.11.3.2.2 Negative Pulseless Glow

The negative pulseless glow mode is characterized by a constant discharge current. As indicated by the well-defined visual aspect of the discharge (Figures 4.39b and 4.41a), the discharge itself is particularly stable, which shows the basic characteristics of a miniature glow discharge. Referring to Figure 4.48, starting from the cathode, one distinguishes a cathode dark space, followed by a negative glow region, a Faraday dark space, and finally, a positive column of conical shape. As with low-pressure glow discharges, these features of the pulseless glow discharge result from very stable conditions of electron emission from the cathode by ionic bombardment. The electrons, emitted with very low kinetic energy, are first propelled through the cathode dark space, where they acquire sufficient energy to ionize the

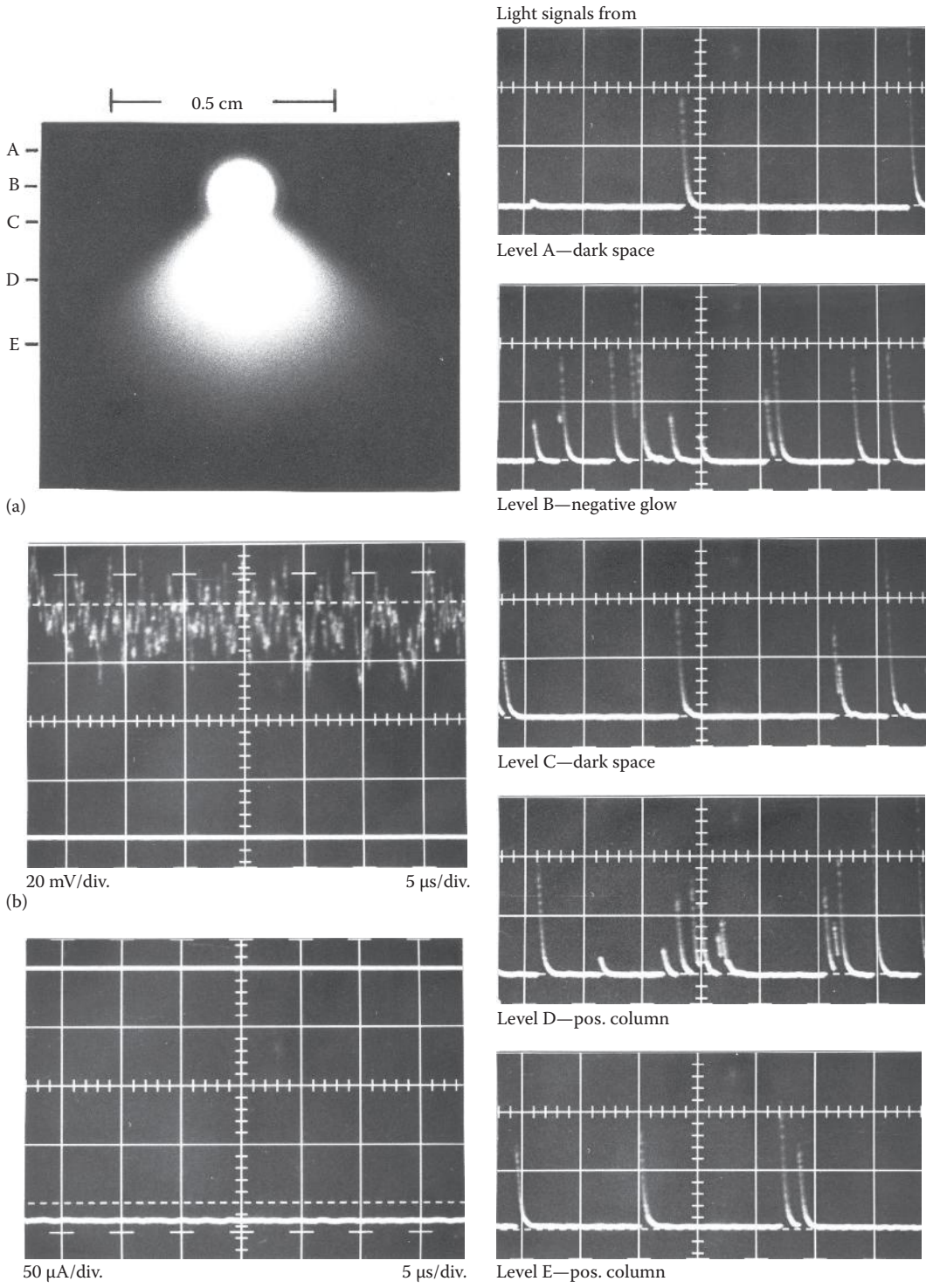


FIGURE 4.41 Characteristics of the negative pulseless glow discharge. Cathode: spherical protrusion (d = 0.8 cm) on a sphere (D = 7 cm); gap 19 cm. (a) Visual aspect of negative glow, (b) light signal. Scales: 20 mV/div., 5 μs/div. (c) Discharge current. Scales: 50 μA/div., 5 μs/div. (right) - Light signals at different observation levels A, B, C, D, E. Scale: 5 mV/div., 2 μs/div. (From Trinh, N.G., A systematic study of corona discharge in air at atmospheric pressure, PhD Thesis, Laval University, Québec, Canada, 1969.)

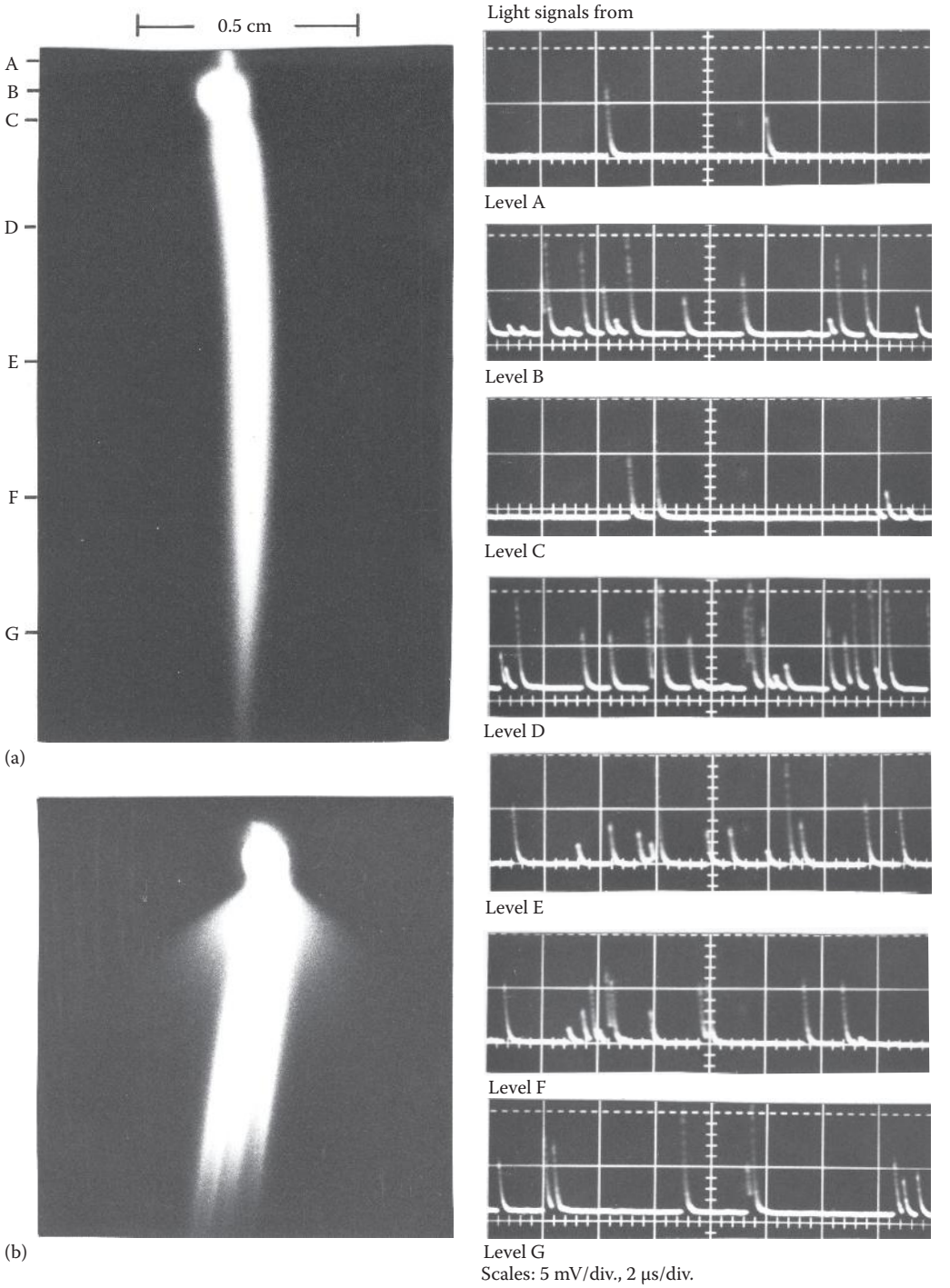


FIGURE 4.42 Characteristics of negative streamers. (a) A streamer channel. (b) Development of streamers from the pulseless glow. Right: light signal at different observation levels: A, B, C, D, E, F, and G. Scales: light: 5 mV/div., 2 μs/div. (From Trinh, N.G., A systematic study of corona discharge in air at atmospheric pressure, PhD Thesis, Laval University, Québec, Canada, 1969.)

gas, and intensive ionization occurs at the negative glow region. At the end of the negative glow region, the electrons lose most of their kinetic energy and are again accelerated across the Faraday dark space, gaining kinetic energy before they can ionize the gas atoms in the positive column. The conical shape of the positive column is attributed to the diffusion of free electrons in the low-field region.

4.11.3.2.3 Negative Streamer

If the applied voltage increases still further, negative streamers may be observed, as illustrated in Figures 4.39c and 4.42. Referring to Figure 4.42, the discharge possesses essentially the same characteristics observed in the negative pulseless glow discharge, but here, the positive column of the glow discharge constricts itself to form the streamer channel, which extends farther into the gap. The glow discharge characteristics observed at the cathode imply that negative streamers depend largely on electron emissions from the cathode by ionic bombardment, while the formation of a streamer channel characterized by intensive ionization denotes an even more effective space charge removal action by the applied field. The streamer channel is fairly stable: it projects from the cathode into the gap and back again, giving rise to a pulsating fluctuation of relatively low frequency in the discharge current. Eventually, the streamer channel extends sufficiently far into the gap to reach the anode and cause the breakdown of the gap.

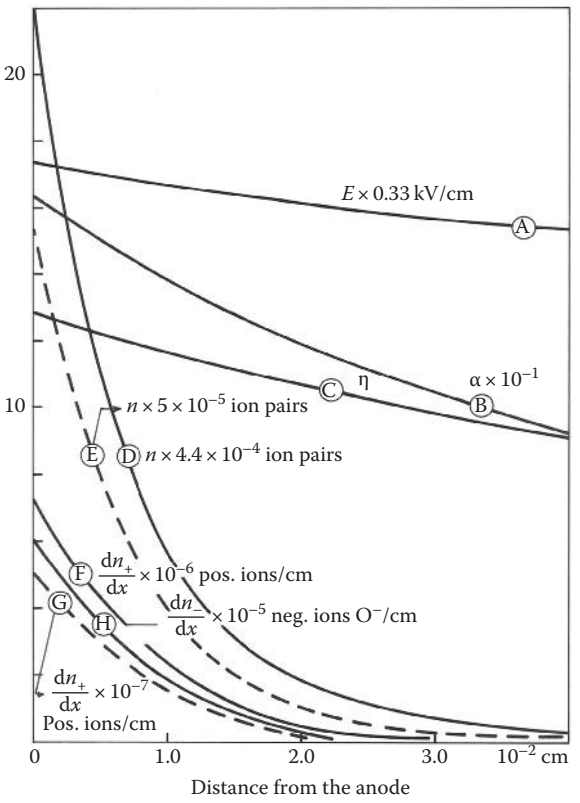


FIGURE 4.43 Distribution of the electric field and ionization parameters near the anode: sphere of 0.8 cm diameter, gap length 35 cm. A: Field distribution, B: variation of the ionization coefficient α, C: Variation of the attachment coefficient η, D: Avalanche development neglecting electron attachment, E: Avalanche development with electron attachment, F: distribution of positive ions neglecting electron attachment, G: distribution of positive ions with electron attachment, H: distribution of negative ions. (From Trinh, N.G., A systematic study of corona discharge in air at atmospheric pressure, PhD Thesis, Laval University, Québec, Canada, 1969.)

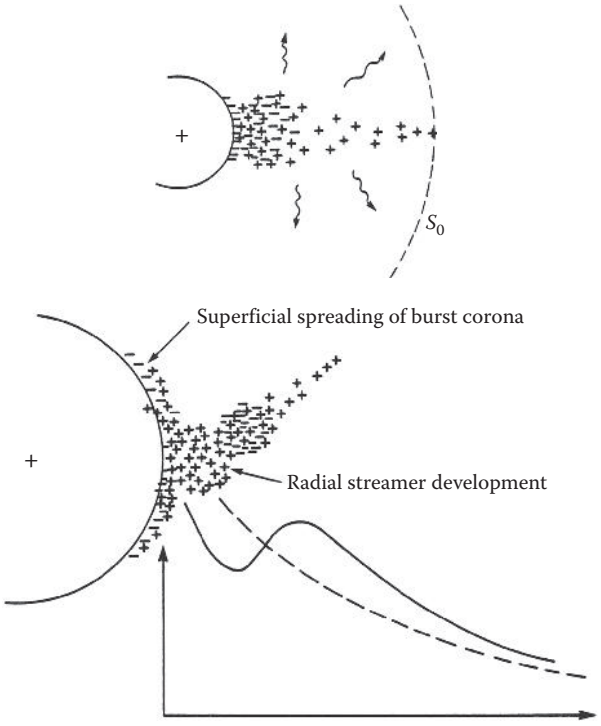


FIGURE 4.44 Development of an electron avalanche towards the anode. (a) Development of the initial electron avalanche. (b) Development of the discharge at the anode surface in burst corona and radially into the gap as streamers. (From Trinh, N.G., *IEEE Electr. Insul. Mag.*, 11, 23, 1995a. With permission.)

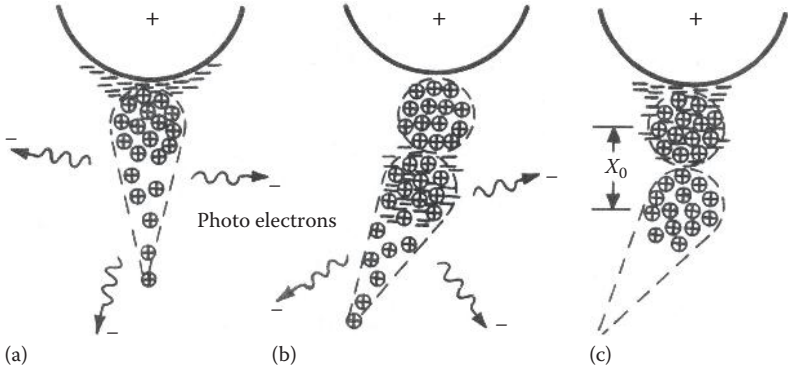


FIGURE 4.45 Propagation mode of corona globules. (a) Emission of photons from the initial electron avalanche. (b) Formation of a corona globule, which attracts a new electron avalanche. (c) Extinction of the old corona globule and formation of a new one. (From Trinh, N.G., A systematic study of corona discharge in air at atmospheric pressure, PhD Thesis, Laval University, Québec, Canada, 1969.)

4.11.4 Corona Discharges under Positive Polarity

4.11.4.1 Electron Avalanche and Ion Space Charge

When the highly stressed electrode is of positive polarity, the electron avalanche is initiated at a point on the boundary surface S_0 of zero net ionization and develops towards the anode in a continuously increasing field (Figure 4.43). As a result, the highest ionization activity occurs at the anode. Here again, due to the lower mobility of the ions, a positive ion space charge is left behind along the development path of the

avalanche. However, because of the high field intensity at the anode, few electron attachments occur and the majority of free electrons created are neutralized at the anode. Negative ions are formed mainly in the low-field region farther in the gap. Figure 4.44 is a schematic illustration of the distribution of the ion space charges during the development of an electron avalanche. One can observe the following discharge behavior (Trinh and Jordan, 1968; Trinh, 1995a):

- The incoming free electrons are highly energetic and cannot be immediately absorbed by the anode. As a result, they tend to spread over the anode surface where they lose their energy through ionization of the gas particles, until they are neutralized at the anode, thus contributing to the development of the discharge over the anode surface.
- Since the positive ions are concentrated immediately next to the anode surface, they may produce a field enhancement in the gap (Figure 4.44b) that attracts secondary electron avalanches and promotes the radial propagation of the discharge into the gap along a streamer channel.
- During streamer discharge, the ionization activity extends considerably into the low-field region of the gap via the formation of corona globules, which propagate owing to the action of the electric field generated by their own positive ion space charge. Figure 4.45 schematically illustrates such a mechanism. Dawson (1965) has shown that if a corona globule is produced containing 10^8 positive ions within a spherical volume of 3×10^{-3} cm in radius, the ion space charge field is such that it attracts sufficient new electron avalanches to create a new corona globule a short distance away. In the meantime, the initial corona globule is neutralized, causing the corona globule to effectively move ahead towards the cathode.

4.11.4.2 Modes of Positive Corona Discharges *(Trinh and Jordan, 1968; Trinh, 1969)*

As in the case of a highly stressed cathode, the presence of ion space charges of both polarities in the anode region greatly affects the local distribution of the field and, consequently, the development of corona discharge at the anode. One can observe four different corona discharge modes resulting from an equilibrium state

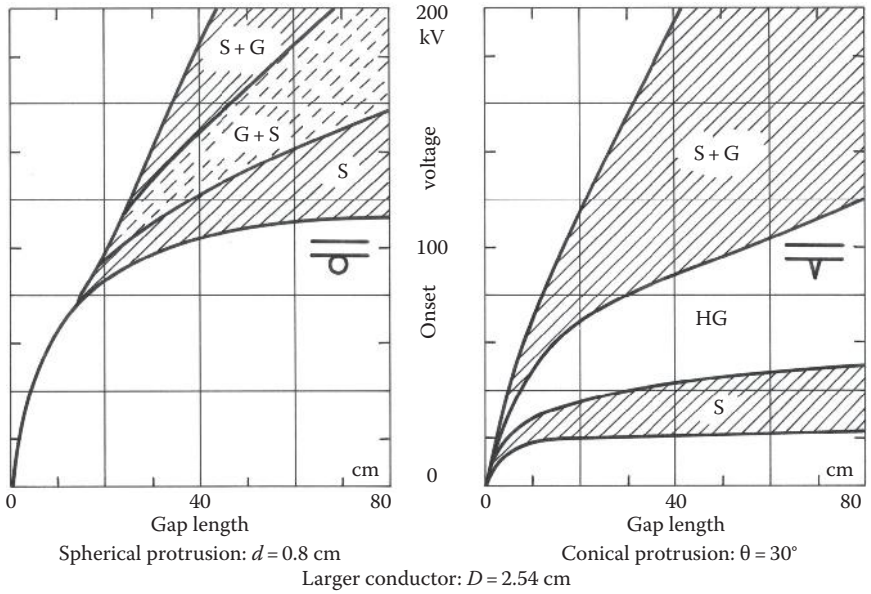


FIGURE 4.46 Onset conditions of corona modes at anode: a protrusion on a 2.54 cm diameter conductor. Left: spherical protrusion 8 mm in diameter. Right: Conical protrusion 8 mm in diameter, θ = 30°. S: streamers at onset and preceding breakdown, HG: positive glow. (From Trinh, N.G. and Jordan, I.B., Modes of corona discharges in air. *IEEE Transactions on Power Apparatus and Systems* PAS-87(5), 1207, 1968; Trinh, N.G., A systematic study of corona discharge in air at atmospheric pressure, PhD Thesis, Laval University, Québec, Canada, 1969.)

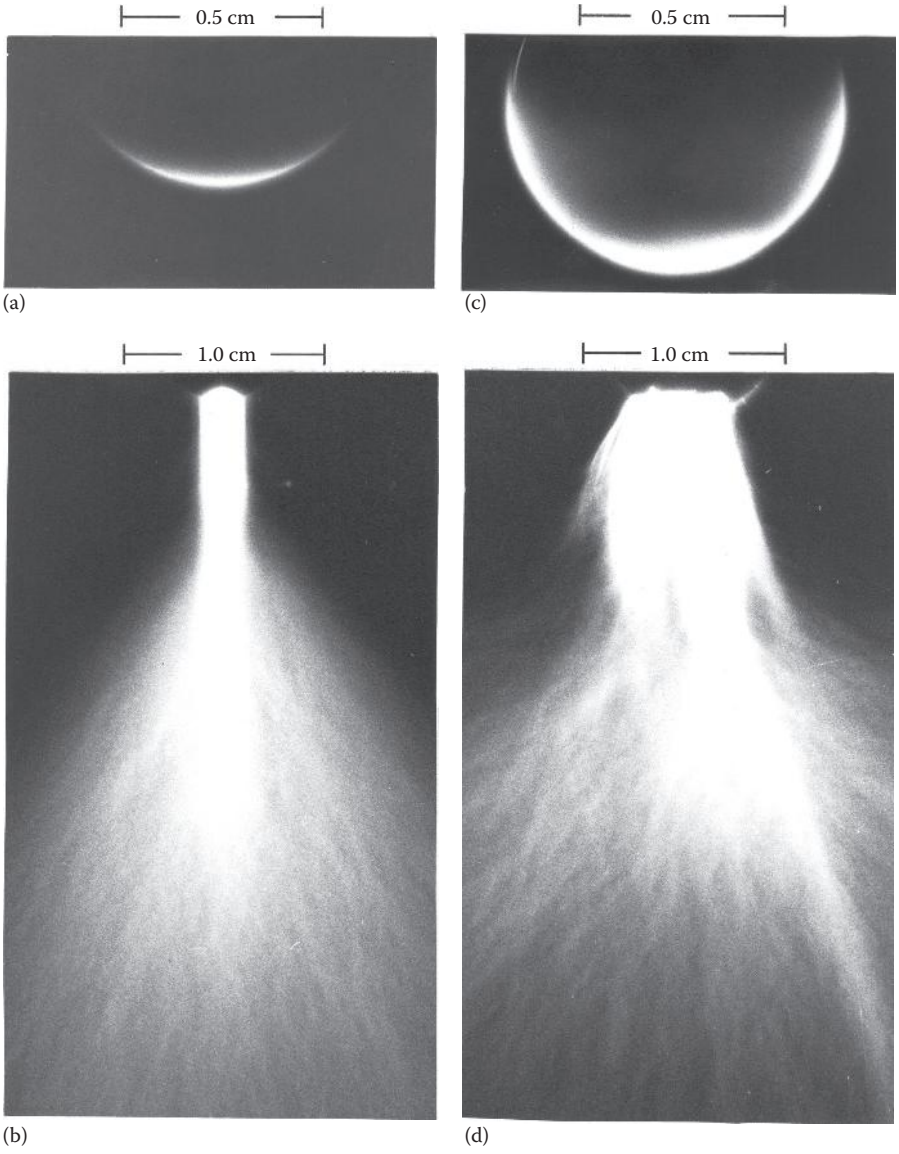


FIGURE 4.47 Corona modes at anode: (a) burst corona; (b) onset streamers; (c) positive glow corona; and (d) breakdown streamers. Anode spherical protrusion (d = 0.8 cm) on a sphere (D = 7 cm); gap 35 cm; time exposure 1/4 s. (From Trinh, N.G. and Jordan, I.B., *IEEE Trans*., PAS-87, 1207, 1968; Trinh, N.G., *IEEE Electr. Insul. Mag*., 11, 23, 1995a.)

between the generation and removal rates of ion space charges in the immediate surroundings of the highly stressed electrode, with distinct electrical, physical, and visual characteristics, prior to flashover of the gap.

Figure 4.46 shows their onset conditions at a protrusion of spherical and conical shape on a conductor, while their visual aspects are presented in Figure 4.47. These are, respectively, with increasing field intensity: burst corona, onset streamers, positive glow, and breakdown streamers. An interpretation of the physical mechanisms leading to the development of these corona modes is given in the following paragraphs, taking into account of the active role of the ion space charges.

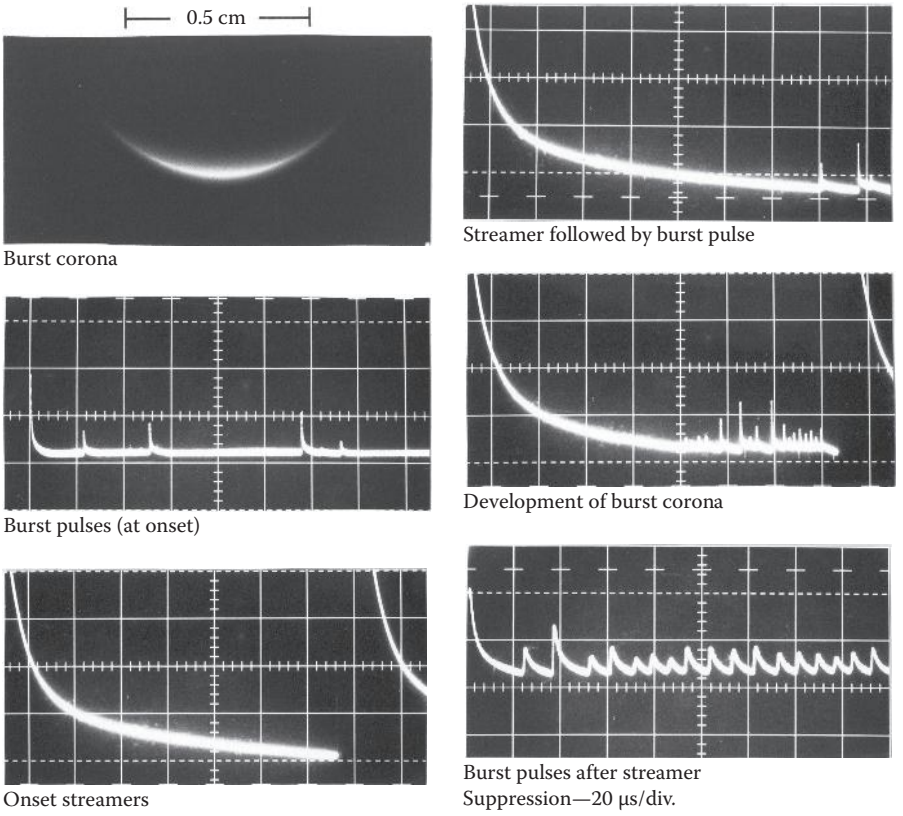


FIGURE 4.48 (a) Burst corona current pulse. Scales: 5 mA/div., 0.2 ms/div. (b) Development of burst corona following a streamer discharge. Scales: 5 mA/div., 20 μs/div. (From Trinh, N.G., A systematic study of corona discharge in air at atmospheric pressure, PhD Thesis, Laval University, Québec, Canada, 1969.)

4.11.4.2.1 Burst Corona

The burst corona appears as a thin luminous sheath adhering closely to the anode surface (Figure 4.47a). The discharge results from the spread of ionization activities at the anode surface, which allows the high-energy incoming electrons to lose their energy before neutralization at the anode. During this process, a number of positive ions are created in a small area over the anode, building up a local positive space charge, which suppresses the discharge. The spread of free electrons then moves to another part of the anode. The resulting discharge current consists of very small positive pulses (Figure 4.48a), each corresponding to the ionization spreading over a small area at the anode and its suppression by the positive ion space charge produced.

4.11.4.2.2 Onset Streamer

The onset streamer results from the radial development of the discharge. The positive ion space charge formed adjacent to the anode surface causes a field enhancement in its immediate vicinity, which attracts subsequent electron avalanches and favors the radial development of onset streamers. This discharge mode is highly effective, and the streamers extend farther into the low-field region of the gap along numerous filamentary channels, all originating from a common stem projecting from the anode (Figure 4.47b).

During this development of the streamers, a considerable number of positive ions are formed in the low-field region. Because of the cumulative effect of the successive electron avalanches and the absorption at the anode of the free electrons created in the discharge, a net residual positive ion space charge forms in front of the anode. The local gradient at the anode then drops below the critical value for ionization and suppresses the streamer discharge. A dead time is consequently required for the applied field to remove the ion space charge and restore the proper conditions for the development of a new streamer.

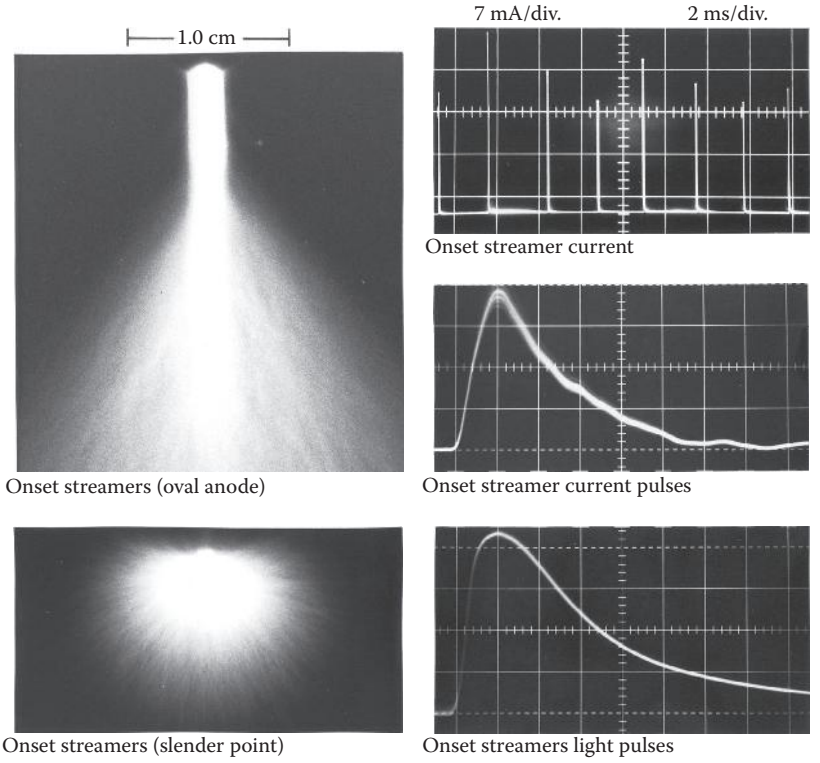


FIGURE 4.49 Characteristics of the onset streamers. Anode: spherical protrusion (d = 0.8 cm) on a sphere (d = 7 cm); gap 35 cm. Scales: current 7 mA/div., 2 ms/div. (upper), 50 ns/div. (middle). Light: 1 V/div., 20 ns/div. (From Trinh, N.G., A systematic study of corona discharge in air at atmospheric pressure, PhD Thesis, Laval University, Québec, Canada, 1969.)

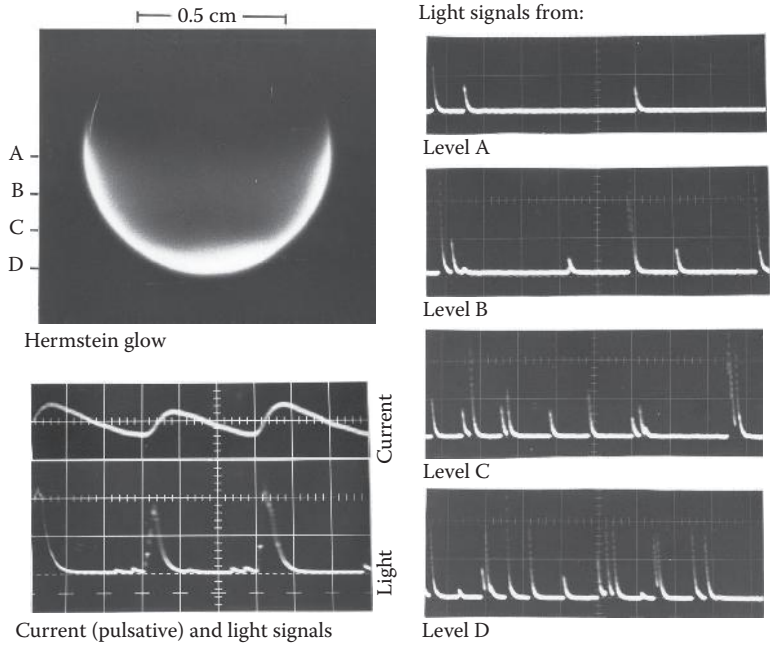


FIGURE 4.50 Characteristics of the positive glow discharge. Anode: sphere (d = 0.8 cm), gap 35 cm. Scales: current: 5 μA/div. Light: 20 mV/div., 1 μs/div.; Right light: 5 mV/div., 2 μs/div. (From Trinh, N.G., A systematic study of corona discharge in air at atmospheric pressure, PhD Thesis, Laval University, Québec, Canada, 1969.)

The discharge develops in a pulsating mode, producing positive current pulses of short duration, high amplitude, and relatively low repetition rate due to the large number of ions created in a single streamer (Figure 4.49c and d).

One can observe these first two discharge modes developing in parallel over a small range of voltages at corona onset. As the voltage is increased, the applied field rapidly becomes more effective in removing the ion space charge in the immediate vicinity of the electrode surface, thus promoting the lateral spread of burst corona at the anode. In fact, burst corona can be triggered just a few microseconds after suppression of the streamer (Figure 4.48b). The rapid clearing of the positive ion space charge at the anode region, combined with the high field intensity, cause the incoming negative ions to shed their electrons. This provides the seeding free electrons to favor the development of new avalanches that sustain the ionization activity over the anode surface in the form of burst corona. The latter will continue to develop until it is again suppressed by its own positive space charge.

As the voltage is raised even higher, the burst corona is further enhanced by a more effective space charge removal action of the field at the anode, which rapidly pushes the positive ions created during burst corona discharges away from the anode. The accumulation of positive ions in front of the anode results in the formation of a stable positive ion space charge that prevents the radial development of the discharge into the gap. Consequently, the burst corona develops more readily, at the expense of the onset streamer, leading to its complete suppression. A new mode, the positive glow discharge, then establishes at the anode.

4.11.4.2.3 Positive Glow

Figures 4.47c and 4.50a present a photograph of a positive glow discharge developing at a spherical protrusion. This discharge is due to the development of the ionization activity over the anode surface, which forms a thin luminous layer immediately adjacent to the anode surface, where intense ionization activity takes place. Referring to Figure 4.50, the discharge current consists of a direct component superimposed by small pulses with a high repetition rate, in the hundreds of kilohertz range. By analyzing the light signals obtained with photomultipliers pointing to different regions of the anode, one can observe that

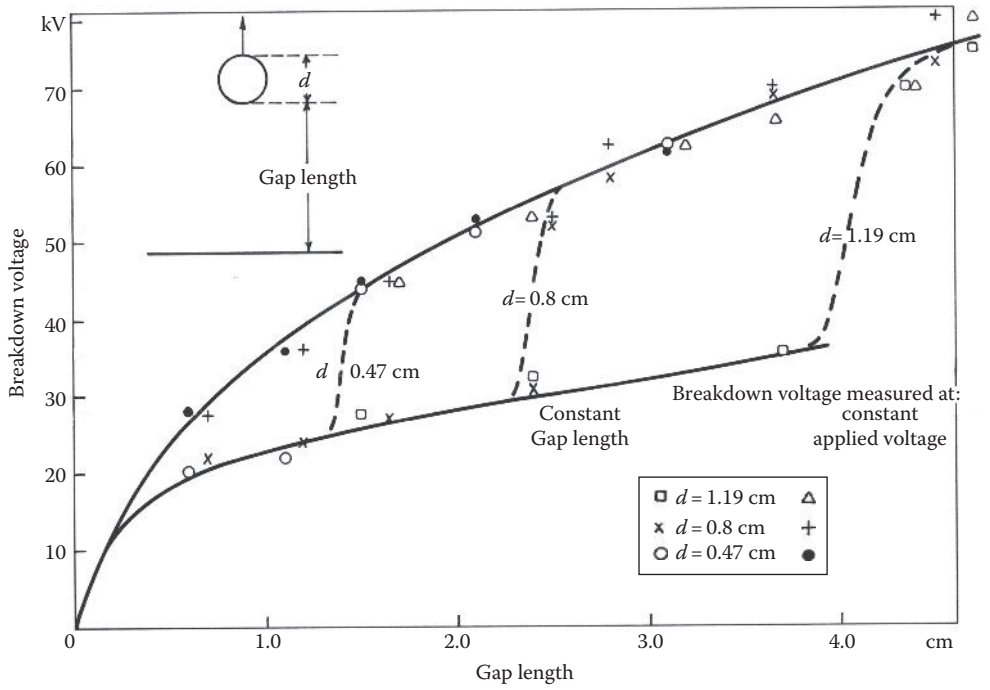


FIGURE 4.51 Improvement of the breakdown voltage by the development of positive glow. (From Trinh, N.G., A systematic study of corona discharge in air at atmospheric pressure, PhD Thesis, Laval University, Québec, Canada, 1969.)

the luminous sheath is composed of a stable central region; from there, bursts of ionization activity may develop and project the ionizing sheath outward and back again, continuously, giving rise to the pulsating current component.

The development of the positive glow discharge may be interpreted as resulting from a particular combination of removal and creation of positive ions in the gap. The high field rapidly removes the positive ion space charge from the anode, thus promoting surface ionization activity. Meanwhile, the field intensity is not sufficient to allow radial development of the discharge and the formation of streamers. The main contribution of the negative ions is to supply the necessary triggering electrons to sustain ionization activity at the anode.

The apparent visual uniformity of the glow is an optical illusion, since the development of the glow discharge occurs over a portion of the anode before a buildup of positive ion space charge forces it to move to an adjacent area. The movement of the discharge is too fast for the eyes (or camera) to record, thus giving rise to a false impression of stability and uniformity of the discharge. The effect of the glow discharge is a significant increase in the breakdown voltage when the glow discharge is present as evidenced by the results of Figure 4.51, which compares the breakdown voltages of short gaps measured under conditions of the following:

- Onset streamer when the voltage is increased at constant gap length
- Breakdown streamer when the glow discharge is first initiated in the gap and breakdown is obtained by reducing gradually the gap length while keeping the applied voltage constant

The improvement obtained in insulation performance is about twice the breakdown voltage. The effect is mainly in short gaps where onset streamers initiate the breakdown. For long gap, the nonuniform field favors the development of the glow prior to breakdown, initiated by breakdown streamers at higher voltages. Practical application of the positive glow discharge has been in the development of streamer-free electrodes for high-voltage tests (Uhlig, 1956).

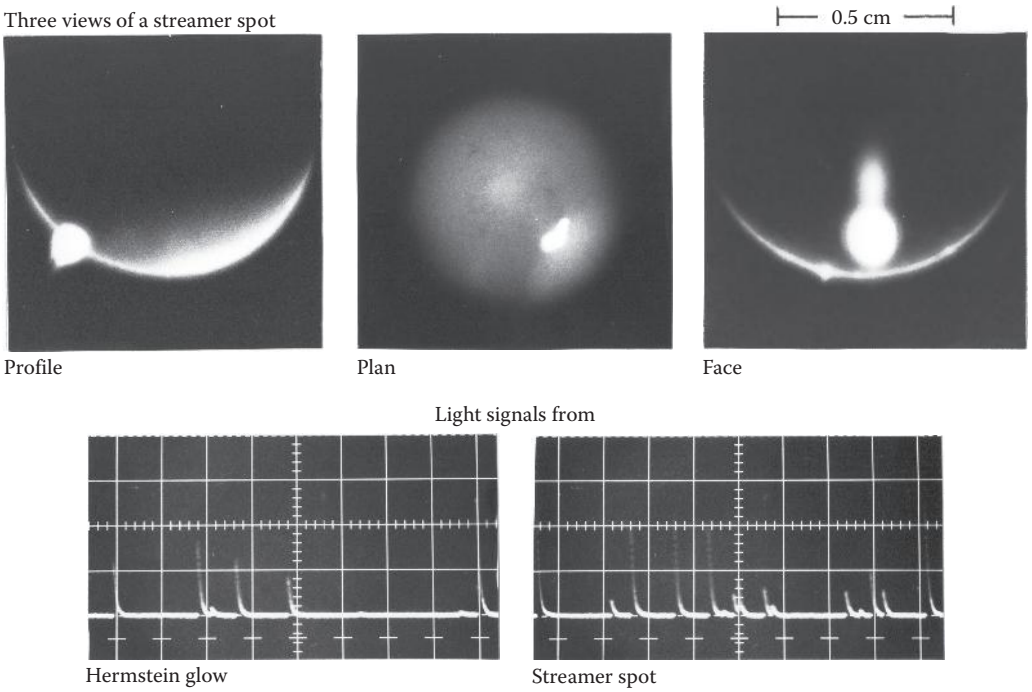


FIGURE 4.52 Formation of a streamer spot. Anode: sphere (d = 0.8 cm), gap: 35 cm. Scales: light, 5 mV/div, 2 μs/div. (From Trinh, N.G., A systematic study of corona discharge in air at atmospheric pressure, PhD Thesis, Laval University, Québec, Canada, 1969.)

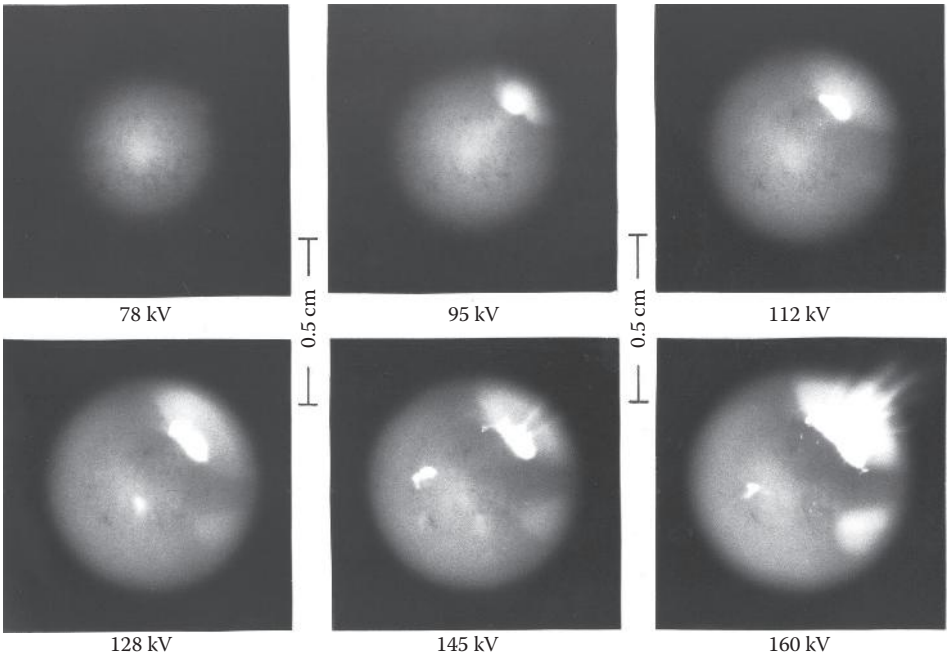


FIGURE 4.53 Development of streamer spots and the initiation of breakdown streamers. Anode: sphere (d = 0.8 cm), gap 35 cm. (From Trinh, N.G., A systematic study of corona discharge in air at atmospheric pressure, PhD Thesis, Laval University, Québec, Canada, 1969.)

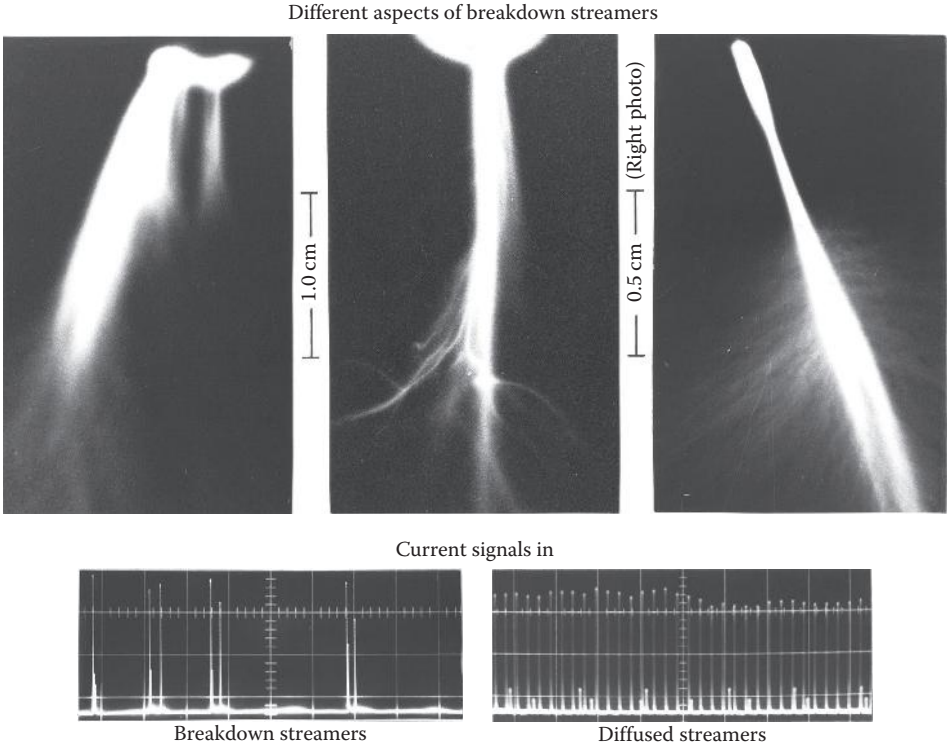


FIGURE 4.54 (a) Scales: left, 10 mA/div.; right, 20 mA/div., 2 ms/div.

(*continued*)

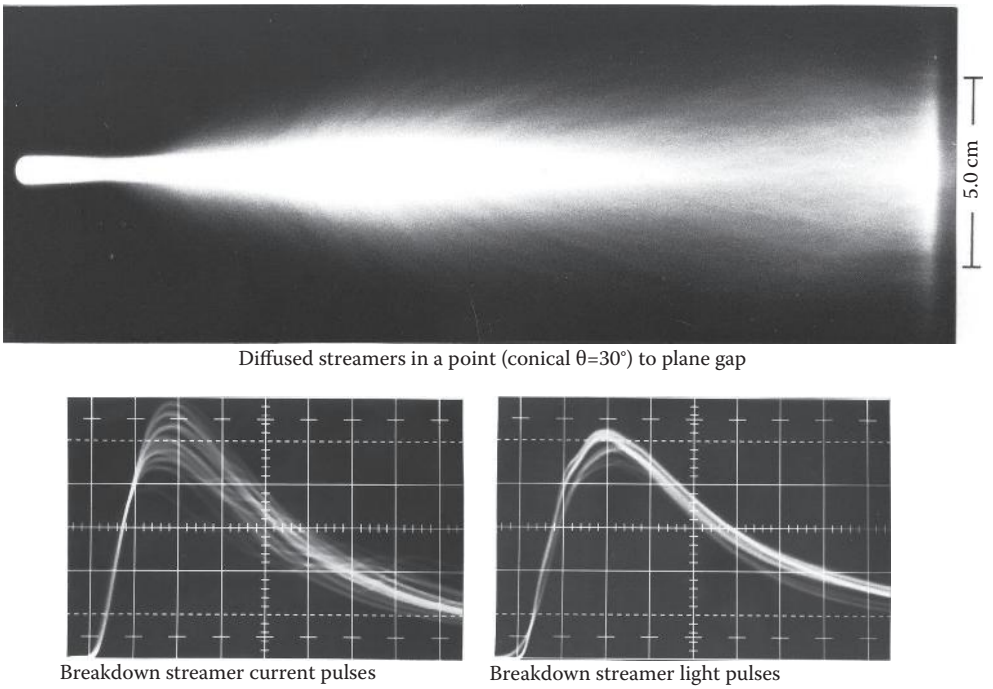


FIGURE 4.54 (continued) (b) Characteristics of breakdown streamers. Anode: spherical protrusion (d = 0.8 cm) on a sphere (D = 7 cm). Gap 35 cm. Scales: current, 10 mA/div., 50 ns/div.; light, 1 V/div., 20 ns/div. (From Trinh, N.G., A systematic study of corona discharge in air at atmospheric pressure, PhD Thesis, Laval University, Québec, Canada, 1969.)

Although the interference-free aspect was achieved also for conductors (Heroux, 1982), the result was greatly affected by the heavy losses associated with the glow discharge. Recent attempts in providing lightning protection for large installations are more promising (Rizk, 2010).

4.11.4.2.4 Breakdown Streamer

If the applied voltage is further increased, streamers develop again and eventually lead to breakdown of the gap. The development of breakdown streamers is preceded by local *streamer spots*, which show intense ionization activity and moves slowly over the anode surface. No marked change in the current or the light signal accompanies the development of streamer spots, implying that the ionization activities at these spots are steady in time (Figure 4.52). The removal rate of the positive ion space charge is still not sufficient to allow the radial development of streamers.

Figure 4.53 shows a series of photographs of the spherical anode, taken at different values of the applied voltage, and illustrates the formation of streamer spots and their transition into breakdown streamers. Only when the applied field becomes sufficiently high to rapidly clear the positive ion space charges from the anode region does radial development of the discharge become possible, resulting in breakdown streamers.

Figure 4.54 illustrates some typical visual aspects of breakdown streamers. The discharge is essentially the same as the onset streamer type but can extend much farther into the gap. The streamer current is more intense and may occur at a higher repetition rate. However, a streamer crossing the gap does not necessarily result in gap breakdown, which proves that the filamentary region of the streamer is not fully conducting. Positive breakdown streamers develop more and more intensively with higher applied voltage and eventually cause the gap to break down. The development of breakdown streamers can be interpreted as resulting from the high efficiency of the applied field in removing the ion space from the region around the anode. This allows the ionization activities to extend further into the discharge gap,

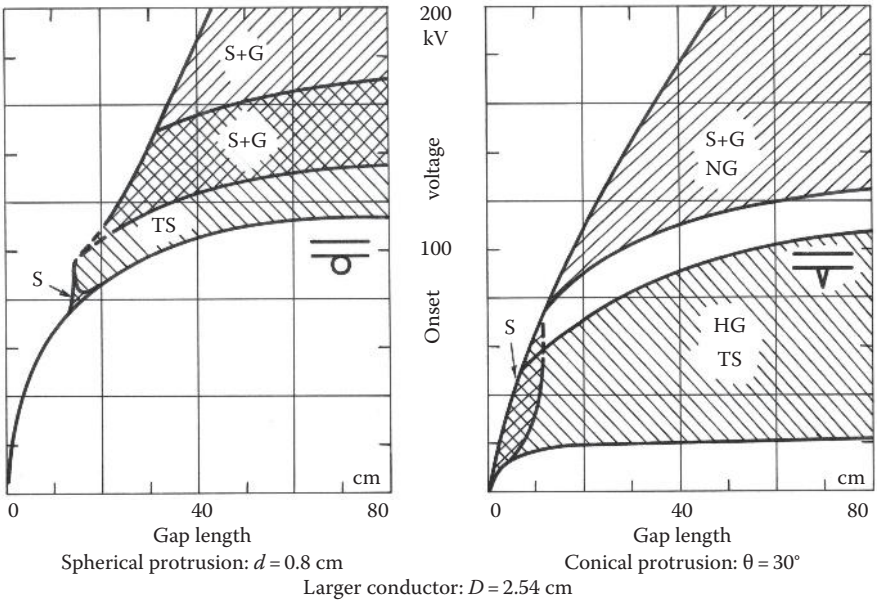


FIGURE 4.55 Corona modes under ac voltage: a protrusion on a 2.54 cm diameter conductor. Left: spherical protrusion 6 mm in diameter. Right: conical protrusion 8 mm in diameter, θ = 30°. TS: Trichel streamers, HG: positive glow, NG: negative glow, S: positive breakdown streamers. (From Trinh, N.G. and Jordan, I.B., Modes of corona discharges in air. *IEEE Transactions on Power Apparatus and Systems* PAS-87(5), 1207, 1968; Trinh, N.G. and Jordan, I.B., *IEEE Trans*., PAS-87, 1207, 1968; Trinh, N.G., *IEEE Electr. Insul. Mag*., 11, 23, 1995a.)

first in small local regions forming streamer spots and, subsequently, along the breakdown streamer channels.

4.11.5 Corona Discharges under Alternating Voltage

Under alternating voltage, the field at the highly stressed electrode varies continuously, both in intensity and in polarity. Different corona modes can develop in the same cycle of the applied voltage. Figure 4.55 illustrates the development of different corona modes at a spherical protrusion as a function of the applied voltage, readily identified by their discharge current.

Their onset conditions under ac voltage are shown in Figure 4.56 for the cases of a protrusion, spherical and conical, at the surface of a conductor, as a function of the interelectrode distance. One can make the following observations:

- For short gaps, the ion space charges created in one half cycle are absorbed by the electrodes in the same half cycle. One observes the same corona modes that develop near onset voltages, namely, negative Trichel streamers, positive onset streamers, and burst corona.
- For long gaps, the ion space charges created in one half cycle are not completely absorbed by the electrodes, leaving residual space charges in the gap. These residual space charges move back to the region of high field intensity in the following half cycle and can influence discharge development. Onset streamers are suppressed in favor of the positive glow discharge. One distinguishes the following corona modes: negative Trichel streamers, negative glow discharge, positive glow discharge, and positive breakdown streamers.
- The critical length separating short and long gaps corresponds to the maximum distance that the ion space charges created in one half cycle can cover within the same half cycle, preventing their neutralization at the ground electrode.

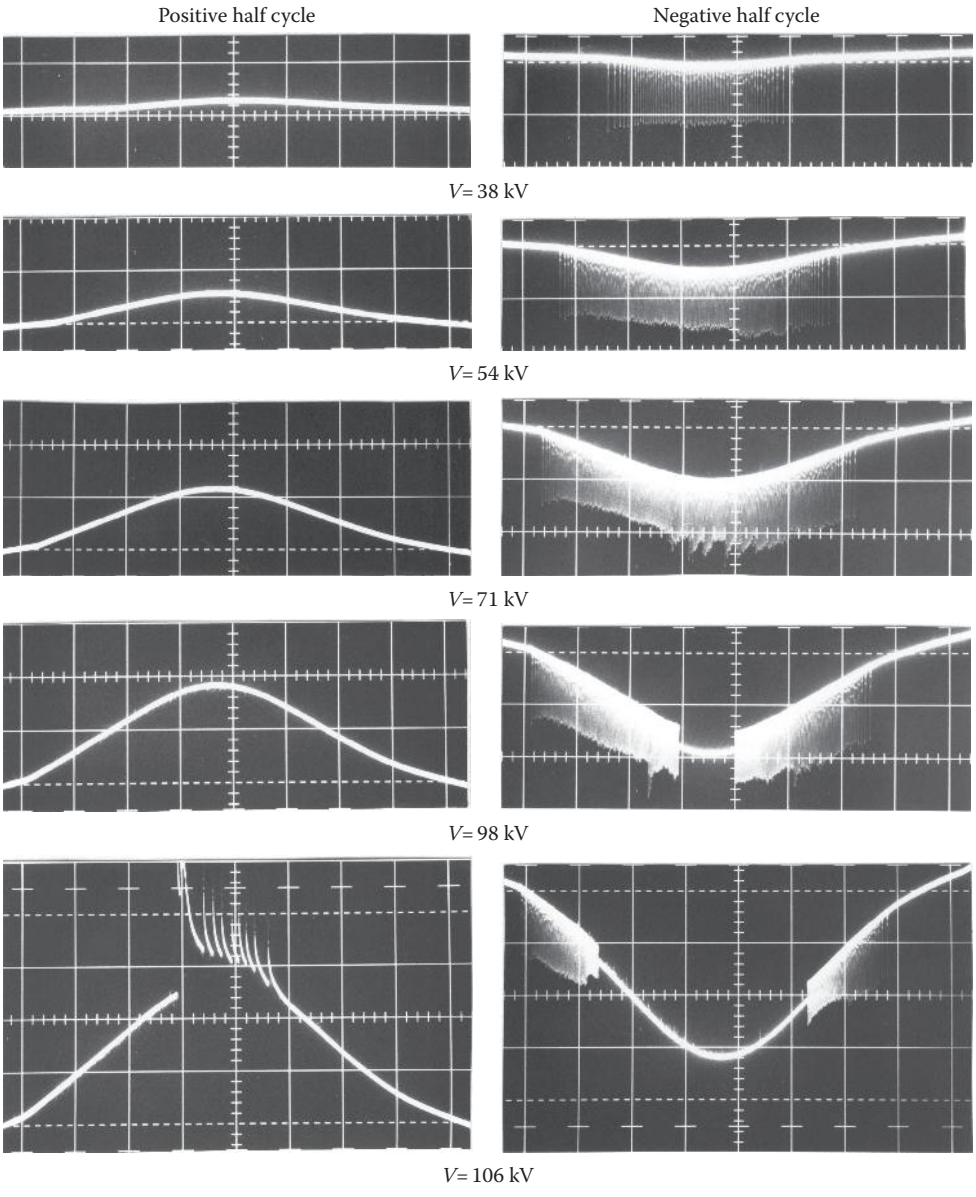


FIGURE 4.56 Discharge currents showing corona modes under ac voltage. (From Trinh, N.G., A systematic study of corona discharge in air at atmospheric pressure, PhD Thesis, Laval University, Québec, Canada, 1969.)

- Negative streamers are not observed under ac voltage, because their onset gradient is higher than the breakdown voltage that occurs during the positive half cycle.

4.11.6 Impact of Corona Discharges

4.11.6.1 Main Effect of Corona Discharges on High-Voltage Testing

The presence of corona discharges in high voltage (HV) test setup usually indicates an inadequate insulation and provides an early warning of possible insulation failure. The current pulses produced by streamer discharges also generate electromagnetic interferences in the hundreds of megahertz range,

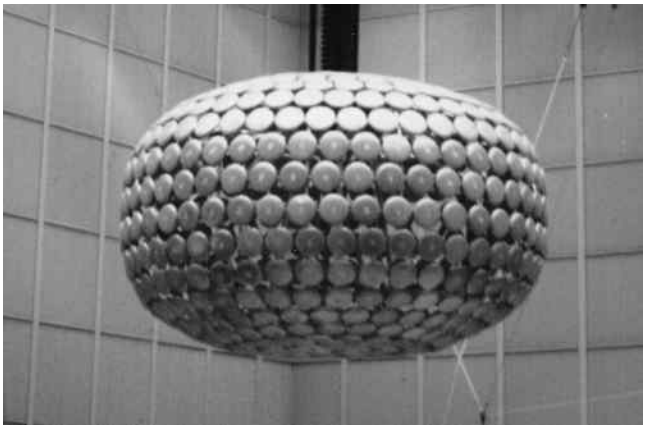


FIGURE 4.57 High-voltage electrode for the 6.4 MV, R–C voltage divider at Hydro-Québec Institute of Research (IREQ) high voltage laboratory. (Photo courtesy from Hydro-Québec.)

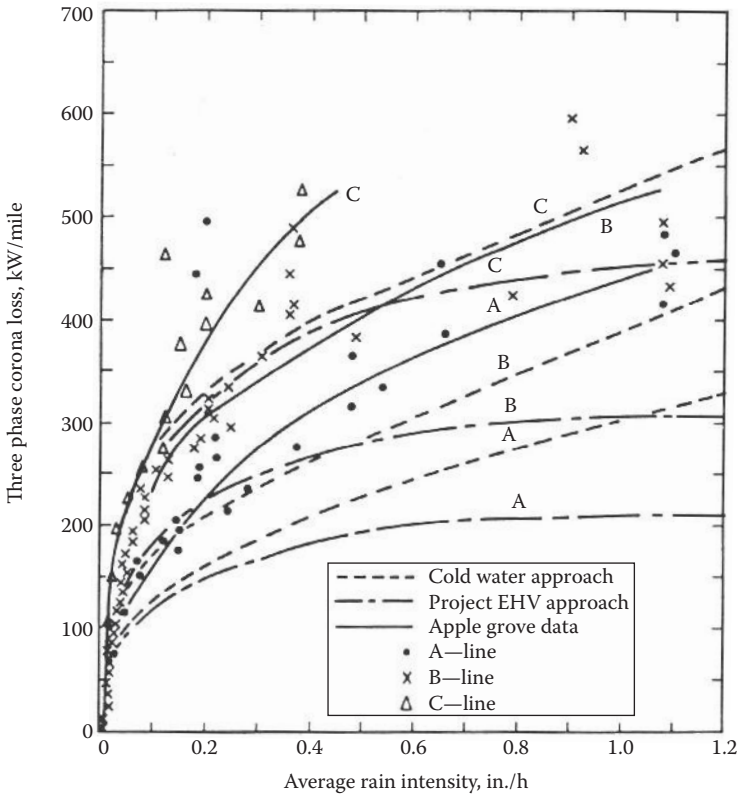


FIGURE 4.58 Typical energy losses on high-voltage transmission lines under foul weather conditions. (From Chartier, V.L. and Shankle, D.F., *IEEE Trans. Power Appar. Syst.,* PAS-89(5), 867, 1970.)

affecting radio and TV reception and measuring instrumentation used in partial discharge (PD) detection. For these reasons, corona discharges should generally be avoided or, at least, kept under control. The most effective means of controlling partial discharges in atmospheric air is to provide a local shielding to critical locations of the HV setup by means of properly designed electrodes, which grade the field intensity at its surface and provide low-field intensities in the protected region inside the electrode.

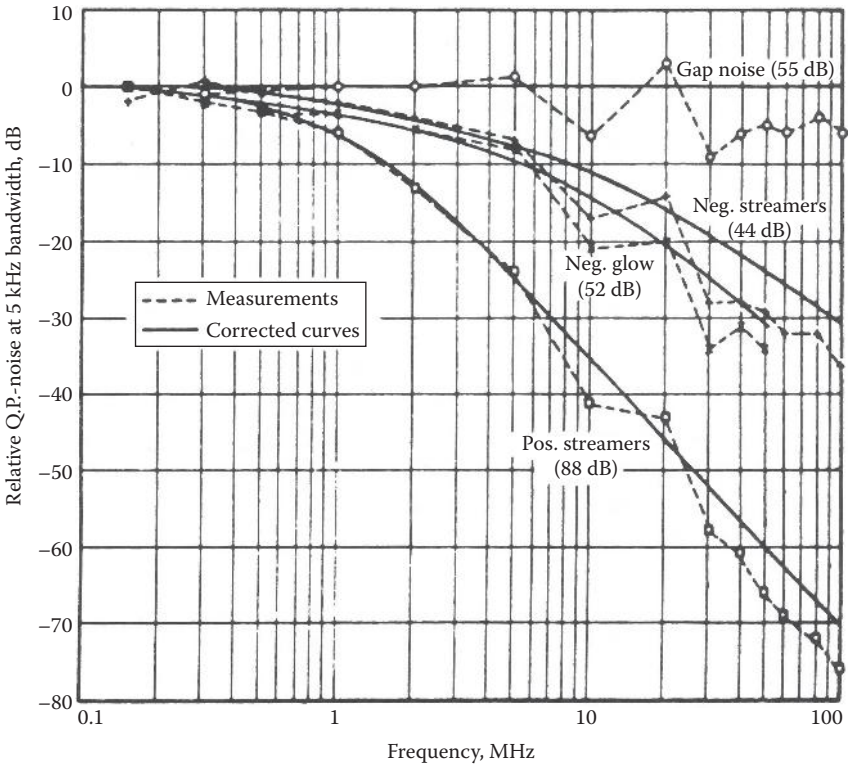


FIGURE 4.59 Frequency spectra of different modes of discharges on transmission line conductors. (From Juette, G.W., *IEEE Trans. Power Appar. Syst*., PAS-91(3), 865, 1972.)

For HV equipment, electrodes of a variety of sizes and shapes can be obtained by fixing small disc-shaped elements on a metallic frame of appropriate size and shape. Figure 4.57 illustrates such an electrode design on a 6.4 MV R–C voltage divider at Hydro-Québec Institute of research (IREQ). These designs are quite effective in grading the field intensity at the electrode surface to ensure a corona-free condition for HV tests with sensitive PD measurements. The use of small disc-shaped elements also simplifies and facilitates the installation of HV connections in practical test setups. Temporary HV electrodes can be made from flexible aluminum and conducting rubber tubes deposed at critical locations (connections, sharp ends, etc.).

For HV lines and hardware, toroidal electrodes are preferred, for their rugged design and simple handling. The installation of two such electrodes facing each other usually provides effective shielding for the line-insulator attachment point. Line conductors and their associated hardware exposed to weather conditions, the main cause of corona discharges, are designed accordingly to minimize their undesirable effects.

4.11.6.2 Main Effects of Corona Discharges on Overhead Lines (Trinh, 1995b)

Impact of corona discharges on design of high-voltage lines has been recognized since the early days of electric power transmission when the corona losses were the limiting factor. This aspect of corona discharges will be treated in details in Chapter 8. We briefly mention here the main factors affecting the design of today's high-voltage line operating at voltages up to 800 kVAC and 500 kVDC with recent extension to 1200 kVAC and 800 kVDC.

4.11.6.2.1 Energy Losses

The generation of charged particles by ionization of neutral molecules in corona discharges and their movement in space under the action of the applied electric field require energy that the power system

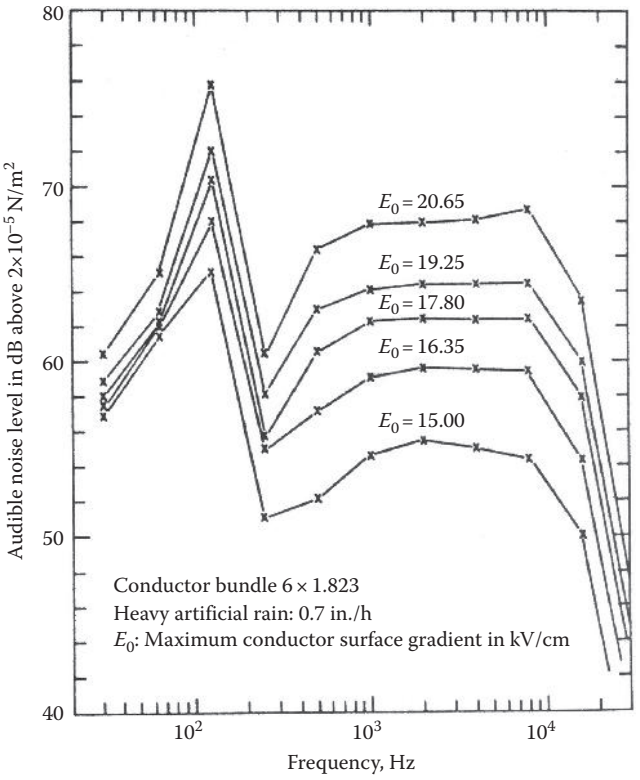


FIGURE 4.60 Audio frequency spectra of corona discharges. (Trinh, N.G. Analysis of the second harmonic (120 Hz) audible noise generated by line corona. *IEEE-PES Summer Meeting paper A* 75 501-7, July 1975.).

must supply, known under the general term of corona losses. Figure 4.58 gives some examples of corona losses measured on different high-voltage transmission lines in operation as a function of the rain rate between 0 and 1.0 mm/min (Chartier and Shankle, 1970). One can observe considerable energy losses, in the order of hundreds of kW/km of line, under foul weather conditions.

4.11.6.2.2 Electromagnetic Interferences

The injection of impulse currents of short duration produced in streamer discharges, particularly positive streamers, on line conductors generates a high-frequency electromagnetic field around the line conductors, which interferes with the reception of radio and television signals. Figure 4.59 shows the frequency spectra of different sources of discharges measured with a noise meter having a bandwidth of 5 kHz. One notices that the positive streamers have a frequency spectrum up to a few MHz (at the level of −30 dB). The negatives (Trichel) streamers of shorter duration have a frequency spectrum up to about 100 MHz (Juette, 1972).

Electromagnetic interference produced by corona discharges on high-voltage transmission lines is limited to their immediate surroundings, where their impact on the reception of the AM radio signal is particularly severe. The television signals have their video and audio components transmitted separately: via AM (bandwidth of 1.5 MHZ) and FM (bandwidth of 4 MHz) respectively. Since electromagnetic interferences affect mainly the AM transmission, video reception is particularly sensitive to television interference. The effect is even more pronounced as the interference level is proportional to the bandwidth of the receiving circuit, larger for television than for radio, and by the greater sensitivity to noise of the image compared to sound.

4.11.6.2.3 Audible Noise

The generation of audible noise by corona discharges on a high-voltage transmission line conductor is related to the sudden heating of the gas to a temperature of some thousand K in the streamer stem. Such a heating

TABLE 4.7

SF_6: Insulating Gas

Physical Properties	Units	Initial Values	ASTM Standard	In Service
Density	kg/m^3	6.518		
Chemical properties		Inert		
		Electronegative		
		Nonflammable		
Toxicity		Nontoxic		
TLV	ppmv	1000		
Impurities in SF_6				
SF_6	% in weight	99.9	99.8	
Air	ppmv	2500	2500	1,000–10,000
H_2O		11	71	100–500
CF_4		800	640	100–500
Hydrolyzable fluorides	ppmw	0.3	0.3	70[a], 7[b]

[a] Maximal concentration of SOF_2 in circuit breakers.
[b] Maximal concentration of SOF_2 in bus bars.
TLV: threshold limiting value; ppmv: parts per million by volume.

causes a corresponding increase of the gas pressure in the streamer channel according to the gas law, perceived by human ears as an acoustic signal. The effect is particularly pronounced under foul weather conditions and mainly on transmission lines operating at the EHV level of 500 kV and higher. Figure 4.60 shows the audio frequency spectra of audible noise generated by high-voltage transmission lines. One notices that the frequency spectra extend up to frequencies of 20 kHz limited by the frequency response of the microphone used and has pronounced pure-tone components of 120 Hz and its harmonics. The latter is generally associated with the movement of ion space charges to-and-fro in the immediate surroundings of the highly stressed conductors.

4.11.6.2.4 Emission of Polluting Effluents

During corona discharges, the absorption of energy by the gas molecules, nitrogen and oxygen, contributes to break their molecular bonds, producing atomic particles, neutral or ionized, which are chemically active (Scherer et al., 1973), while most of the atoms produced will recombine back to the initial gas molecules, a small portion of them react among themselves to form by-products, namely, ozone, O_3, and nitric oxides, NO_x, with potential irritating proprieties. However, the problem is less severe, thanks to the natural ability of atmospheric air to renew itself.

4.12 Electric Breakdown in Compressed Gases: Sulfur Hexafluoride

Because of their high electron affinity to form stable negative ions, electronegative gases are generally sought to improve the dielectric performances of gaseous insulation. Besides the well-established service record of SF_6, CO_2, chlorine, O_2, etc., are among the candidates as gaseous insulation.

4.12.1 Sulfur Hexafluoride

Sulfur hexafluoride (SF_6) is produced by synthesis at a temperature of 300°C of sulfur and fluorine, obtained by electrolysis of fluoride acid according to the reaction

$$S + 3F_2 \rightarrow SF_6$$

The resulting gas has a specific mass of 6.518 kg/m^3, and it is inodorous and colorless and remains inert up to a temperature of 500°C, chemically stable up to temperatures of about 300°C; pure SF_6 is nontoxic.

It is among the insulating gases that are the least damaging to the health of workers and to the environment. The allowed concentration at all times of SF_6 is 1000 ppm (parts per million), the same for any neutral gas other than nitrogen. It is nonflammable, has a higher dielectric strength than atmospheric air, has excellent arc extinction proprieties, and remains in the gaseous state over the range of practical temperatures. Table 4.7 summarizes the principal characteristics of SF_6.

The annual world production of SF_6 in 1990 was about 5000–8000 tons, 80% of which is used electrical apparatus (Niemeyer and Chu, 1992), namely, for insulation of metal-clad equipment and GIS. The advantage of these metal-clad equipment is due partly to the higher dielectric strength of SF_6 compared to atmospheric air (typically by a ratio of 2.5 to 1) and partly to the high operating pressure (typically 4–5 bars). The combined effect allows a reduction of the insulating distances in the order of 1/10 of that required in atmospheric air for the same dielectric stresses. Furthermore, the good arc extinction properties give SF_6 an exclusive place in the development of gas-insulated current interrupting apparatus. Finally, the nonflammability of SF_6 favors the installation of SF_6-insulated equipments in urban areas, which have little spaces and is sensitive to the fire hazards. In this context, a significant amount of work has been made on SF_6 as related to its physical–chemical characteristics. The pertinent data on SF_6 are presented in the following.

4.12.2 Ionization Processes and Source of Free Electrons

Excitation and ionization by electronic collisions: These processes are particularly active in the development of discharges. The ionization coefficient α in SF_6 over the range of values of *E/N* between 100 and 700×10^{-21} Vm^2 can be expressed by the following empirical relations (Wiegart et al., 1985):

$$E/N < 4.6 \times 10^{-19}\ \mathrm{Vm}^2 \quad \frac{\alpha}{N} = 3.4473 \times 10^{34} \left(\frac{E}{N}\right)^{2.985} \quad \mathrm{m}^2$$

$$E/N > 4.6 \times 10^{-19}\ \mathrm{Vm}^2 \quad \frac{\alpha}{N} = 11.269 \times 10^{34} \left(\frac{E}{N}\right)^{1.159} \quad \mathrm{m}^2$$

Attachment of electrons: The formation of negative ions has a considerable influence on the development of corona discharges. The attachment coefficient η in SF_6 over the range of values of *E/N* between 10 and 800 (10^{-21} Vm^2) can be expressed by the following empirical relations (Wiegart et al., 1985):

$$E/N < 2 \times 10^{-19}\ \mathrm{Vm}^2 \quad \frac{\eta}{N} = 10^{-20} \exp\left(-4.09 \times 10^{18} \left(\frac{E}{N}\right)^{-1}\right) \quad \mathrm{m}^2$$

$$E/N > 2 \times 10^{-19}\ \mathrm{Vm}^2 \quad \frac{\eta}{N} = 7\ 10^{-21} \exp\left(-2.25 \times 10^{18} \left(\frac{E}{N}\right)^{-1}\right) \quad \mathrm{m}^2$$

Net coefficient of ionization: The effective ionization coefficient ($\alpha' = \alpha$-η) of SF_6 for the range of *E/N* between 250 and 600×10^{-21} Vm^2. This is adequately expressed as a function of the electric field and the gas pressure according to

$$\alpha' = \alpha - \eta = Cp \left(\frac{E(r)}{p} - \left(\frac{E}{p}\right)_{cr}\right) \tag{4.77}$$

where

$C = 27.7$ is a constant

p the gas pressure in atm. abs.

$\left(E/p\right)_{cr} = 88.5$ kV/cm-atm.abs., the limit field below which the effective ionization coefficient vanishes

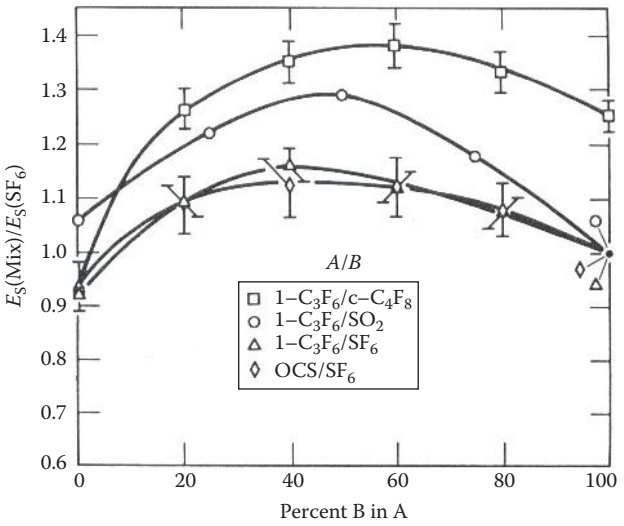


FIGURE 4.61 Synergetic effect of SF_6–carbon perfluoride mixtures. (From Christophorou, I.G. et al., *IEEE Trans. Electr. Insul.,* EI-19, 550, 1984.)

Compared to atmospheric air, the excellent dielectric performance of SF_6 is mainly related to its high affinity to electrons, which provides a limit field about 2.5 times that of atmospheric air. The high value of $C = 27.7$ in the preceding expression of α' implies a high rate of variation in the effective ionization coefficient for fields exceeding the limit value; that is, ionization activities, once initiated, are more intense and rapidly lead to the breakdown of the gap. dependence of α' on the gas pressure p indicates the importance to use SF_6 under pressures to improve the dielectric performances of insulation; the currently used gas pressure in SF_6-insulated equipment is around 4–5 atmospheres absolute.

Photoexcitation and photoionization: Photoionization actually plays an important role in the creation of free electrons necessary for maintaining ionization activities in the gap. The light absorption of SF_6 expressed by the reduced absorption coefficient, μ/p, is equal to

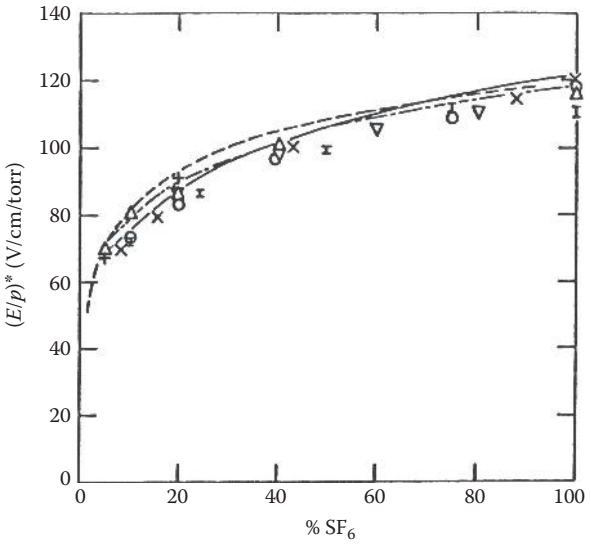


FIGURE 4.62 Variations of the limit field of SF_6–N_2 mixtures. (From Novak, J.P. and Fréchette, M.F., Transport coefficients of SF_6 and SF_6–N_2 mixtures from revised data. *Journal of Applied Physics*, 5(1), 107, 1984.)

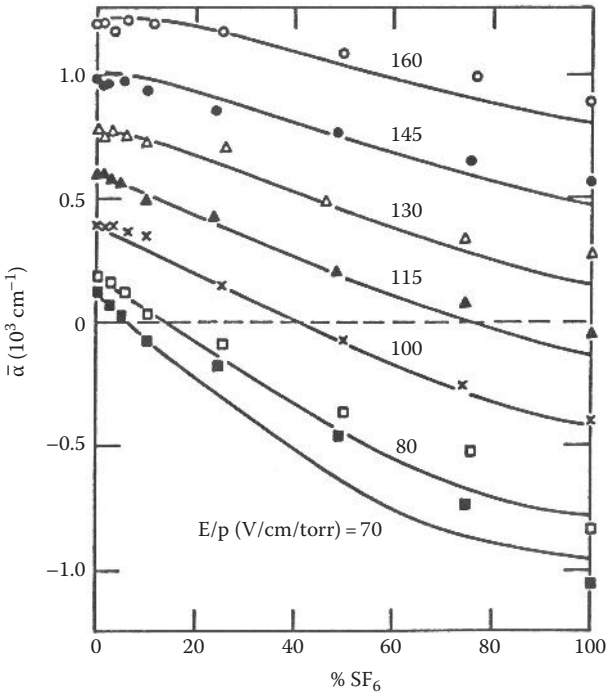


FIGURE 4.63 Effective ionization coefficient of SF_6–N_2 mixtures. (From Novak, J.P. and Fréchette, M.F., Transport coefficients of SF_6 and SF_6–N_2 mixtures from revised data. *Journal of Applied Physics*, 5(1), 107, 1984.)

$$\frac{\text{m}}{p} = 0.026 \pm 0.007 \text{ per cm/torr}$$

for pressure range of 200–1400 torr.

Electron detachment: This process is active to provide the free electrons to initiate new avalanches.

Emission of electrons from the cathode by ionic bombardments: This process can be very active in the development of discharges at the cathode, particularly in presence of a highly divergent field. The positive ions are attracted towards the cathode and can accumulate sufficient energy in the last free paths to emit, on impact, free electrons from the cathode.

4.12.3 Mixtures of SF_6 and Neutral Gases

Gaseous mixtures of SF_6 and a neutral gas such as N_2 are sometimes required to improve the dielectric performances or extend the range of operating conditions of the apparatus. An estimation of the effective ionization coefficient of the gas mixture, α_m, can be made according to

$$\alpha_m = p_1\alpha_1 + p_2\alpha_2 \tag{4.78}$$

where α_m, α_1, and α_2 are the effective ionization coefficients of the mixture and the gas components p_1 and p_2 the respective partial pressures

Mixtures with carbon perfluorides: Mixtures with carbon perfluorides are interesting as they minimize the disadvantages of carbon perfluorides while taking advantage of the synergetic effect of the gas mixtures, which provides a better dielectric strength than expected from the linear relationship with respect

to the proportion of the gas components as illustrated by the results of Figure 4.61 (Christophorou et al., 1984).

Mixture with nitrogen: A simple means of extending the operation of SF_6-insulated equipments to low temperatures consists of using SF_6–N_2 mixtures. The liquefaction of SF_6 is avoided by limiting the partial pressure of SF_6 to the allowed value at the minimal operating temperature.

The required dielectric strength of the gas mixture is obtained by adjusting the partial pressure of nitrogen. For the specific case of a 50% SF_6–50% N_2 mixture, the effective ionization coefficient $\bar{\alpha}$ follows expression (4.77), with the numerical values for $C = 20.9$ kV^{-1} and the limiting field $(E/p)_{cr} = 74.7$ kV/cm.bar.

Figures 4.62 and 4.63 show the variations of the limit field $(E/p)_{cr}$ and effective ionization coefficient $\bar{\alpha}$ of the mixture as a function of the percentage of SF_6. One observes a small synergetic effect of the SF_6–N_2 mixture. However, since the SF_6–N_2 mixture has a lower dielectric strength than pure SF_6, the operating pressure of the mixture will necessarily be higher than with SF_6. Furthermore, the arc extinction ability of the SF_6–N_2 mixture comes essentially from SF_6; the use of such gas mixtures in current interrupting apparatus reduces accordingly their ability for current interruption.

4.12.4 Dielectric Withstand

4.12.4.1 Uniform and Quasiuniform Fields

When the insulating gas is sulfur hexafluoride (SF_6), with the effective ionization coefficient given by Equation 4.77, the onset condition of a self-sustained discharge, Equation 4.79,

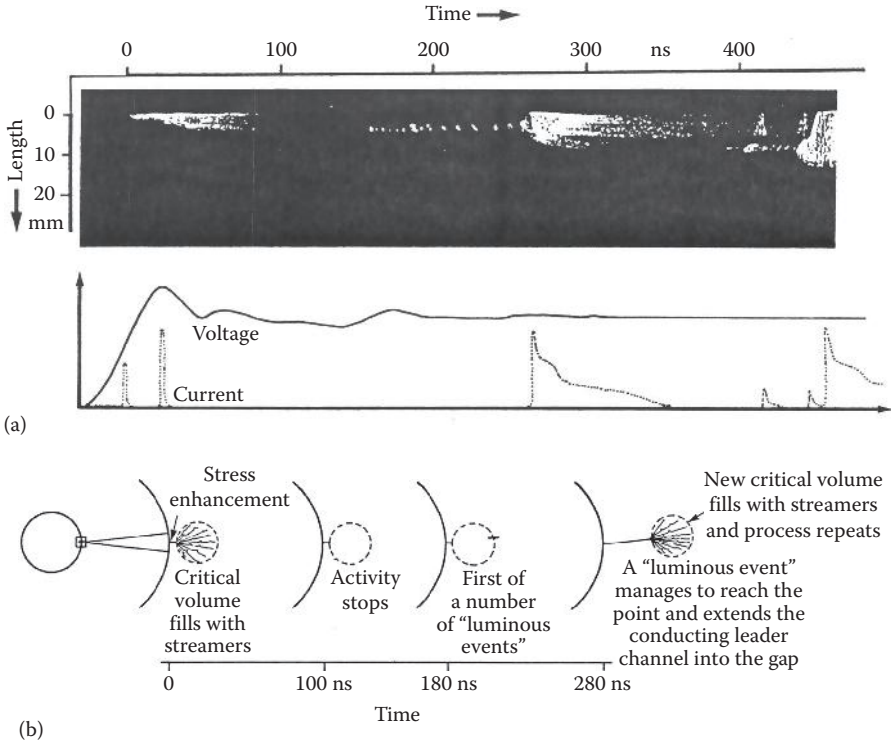


FIGURE 4.64 Development of a leader discharge in SF_6 : (a) Schlieren streak record of leader discharge; (b) time variations of the voltage and discharge current; (c) illustration of the development of leader discharge. (From Wiegart, N. et al. Inhomogeneous field breakdown in GIS - The prediction of breakdown probability and voltages. Part III: Discharge development in SF_6 and computer model of breakdown. *IEEE Trans*., Vol. PWRD-3, 939, 1988c.)

$$\int_{a}^{r_c} (\alpha - \eta)\,dr = \ln 10^8 = 18.42 \tag{4.79}$$

can be expressed as

$$\int_{a}^{r_c} \left(\frac{E}{p} - \left(\frac{E}{p}\right)_{cr}\right) dr = A = \text{Constant} \tag{4.80}$$

which can also be expressed in terms of the potential drop ΔU along the avalanche path

$$\Delta U - p\left(\frac{E}{p}\right)_{cr} (r_c - a) = A \tag{4.81}$$

with the limit field E_c defined as

$$E_c = p\left(\frac{E}{p}\right)_{cr} \tag{4.82}$$

and r_c the radial distance at which the effective ionization coefficient becomes null. This expression of the onset condition of self-sustained partial discharges is particularly useful when the radial distribution of the field is calculated using a computing program.

Weakly divergent fields: When the discharge gap presents a weakly divergent field, the breakdown field can be evaluated according to (Pedersen, 1989)

$$R\left(\frac{E}{\sqrt{E_{max}}} - \sqrt{p\left(\frac{E}{p}\right)_{cr}}\right)^2 = A \tag{4.83}$$

where

E_{max} is the maximal field

R the average radius of curvature of the highly stressed electrode

Coaxial conductor represents another case of weakly divergent field of practical interest. It will be discussed in Chapters 7 and 11.

4.12.4.2 Leader Breakdown in Nonuniform Fields

4.12.4.2.1 Breakdown Mechanism

In a nonuniform field gap, the region with field intensity above the critical value is confined to a small volume around the highly stressed electrode. The nonuniformity of the field and the accumulation of ion space charges in the low-field region of the gap favor the development of streamers at the highly stressed electrode (Wiegart et al., 1988). The breakdown of the gap occurs subsequent to the development of a *leader* discharge (Niemeyer et al., 1989). Figure 4.64 illustrates the dielectric breakdown process by a leader discharge of a nonuniform field SF_6-insulated gap subjected to a steep-front impulse voltage.

The observed phenomenon is very similar to that occurring in the breakdown of long air gap, which has been studied extensively (Les Renardières Group, 1977) under conditions of switching impulse voltage. The leader discharge once initiated from the highly stressed electrode progresses into the gap in distinct steps. At each step of progression, a *streamer* (*leader corona*) is initiated first from the head of the leader channel. The circulation of the discharge current heats up the *streamer* stem, transforms it into a new section of the leader channel, and thus extends it further into the gap. When the applied voltage varies, the development of the leader may be interrupted and reinitiated several times, before

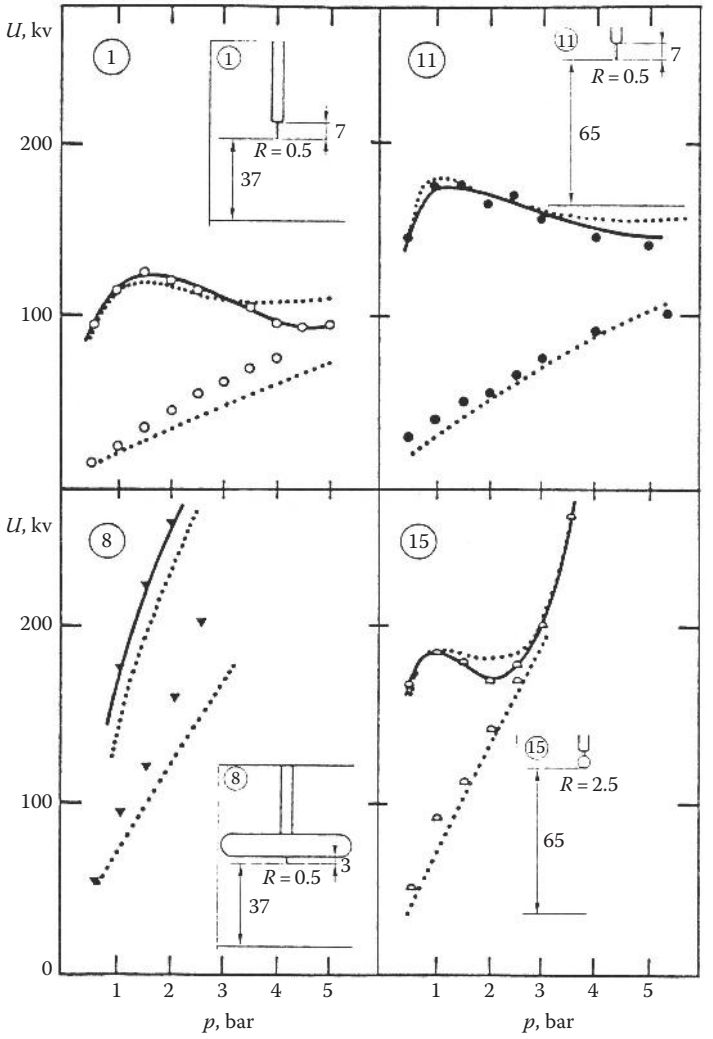


FIGURE 4.65 Comparison of calculated and experimental values of the breakdown voltages in various SF_6-insulated nonuniform field gaps. (Wiegart, N. et al. Inhomogeneous field breakdown in GIS - The prediction of breakdown probability and voltages. Part III: Discharge development in SF_6 and computer model of breakdown. *IEEE Trans.*, Vol. PWRD-3, 939, 1988c.)

a *continuous leader* can establish itself in the gap. As the continuous leader approaches the ground plane, a point will be reached where the streamer succeeds to cross the remaining gap. The streamer–leader transition occurs then rapidly in a process of *final jump* and completes the breakdown of the gap (Wiegart et al., 1988a–c). This sequence of events is similar to that of switching impulse breakdown of long air gaps as explained in Chapter 5.

4.12.4.2.2 Breakdown Criteria

The complexity of the breakdown in nonuniform field gaps excludes practically all possibilities to find a simple breakdown criterion. Such a criterion relies on the definition of the most critical breakdown conditions for discharge gap, followed by empirical formulae relating the breakdown voltage (or field) to the important parameters from experimental data. The main drawback of this approach resides in the large

amount of experimental data required for the derivation of the empirical formulae. Furthermore, empirical formulae are not fully reliable when they are extrapolated to conditions not covered by the experimental data, which requires costly tests on full-scale models.

The preferred approach to estimate the breakdown of nonuniform field gaps relies on the definition of a *breakdown model*, which simulates the physical active breakdown process. For SF_6 insulation, Wiegart et al. (1988c) assume that the inception of the leader discharge occurs when the charge produced in the streamers reaches a critical value, which is a function of the gas pressure only:

$$Q_{cr} = 45\left(\frac{p}{p_0}\right)^{-2.2} \tag{4.84}$$

where

Q_{cr} is the critical charge 10^{-9}C

p_0 the reference gas pressure, $p_0 = 100$ kPa

A computer program calculates the breakdown voltage of nonuniform field gaps subjected to impulse voltages (Wiegart et al. 1988c). The program begins by calculating the streamer onset voltage in the gap, the streamer extension, s_t, and the produced charge Q_s, compares the latter with the critical charge. The inception voltage of the continuous leader is defined as the voltage at which the charge produced in the streamer equals the critical charge at the specific gas pressure. The length of the continuous leader is $l_s = d - s_t$, and the potential drop along the leader channel can be evaluated from the available experimental data on the average voltage gradient along the leader, typically 2–3 kV/cm. Figure 4.65 compares the calculated streamer onset and breakdown voltage obtained by Wiegart et al. for different gap geometries with the experimental data. The results illustrate the adequacy of this approach.

REFERENCES

Ayrton, H. *The Electric Arc*, the Electrician series. New York: D. Van Nostrand Company, Inc., 1902, p. 120.

Bleakney, W. *Physical Review* 35: 139, 1930.

Chartier, V.L. and D.F. Shankle. The Apple Grove 750 kV project: Statistical analysis of radio influence and corona loss performance of conductors at 775 kV. *IEEE Transactions on Power Apparatus and Systems* PAS-89(5): 867, 1970.

Christophorou, I.G., Sauers, I., James, D.R., Rodrigo, H., Pace, M.O., Carter, J.G., and S.R. Hunter. Recent advances in gaseous dielectrics at Oak-Ridge National Laboratory. *IEEE Transactions on Electrical Insulation* EI-19: 550, 1984.

Cobine, J.D. *Gaseous Conductors—Theory and Engineering Applications*. New York: Dover Publications Inc., 1958.

Compton, K.T. Electrical discharges in gases—Part 1: Survey of fundamental processes. *Review of Modern Physics* 2(2): 123–167, April 1930.

Compton, K.T. and I. Langmuir. *Review of Modern Physics* 2: 218, 1930.

Dakin, T.W., Luxa, G., Oppermann, G., Vigreux, J., Wind, G., and H. Winkelnkemper. Breakdown of gases in uniform fields—Paschen curves for nitrogen, air and sulfur hexafluoride. *Electra* 32: 61, 1974.

Dawson, G.A. A model for streamer propagation. *Zeitschrift fur Physics* 183: 159, 1965.

Dushman, S., *Phys. Rev*., 21, 623, 1923.

Engel, A.V. and M. Steenbeck. Elektrische Gasentladungen, ihre Physik u. Technik 1: 34, 1930.

Fowler, R.H. and L. Nordheim. *Proceedings of the Royal Society (London)* A119: 173, 1928.

Fowler, R.H. and L. Nordheim. *Proceedings of the Royal Society (London)* A124: 699, 1929.

Héroux, P., Maruvada, P.S. and G.N. Trinh. High voltage AC transmission lines. Reduction of corona under foul weather. *IEEE Trans*., Vol. PAS-101, 3009–3017, September 1982.

Juette, G.W. Evaluation of television interference from high-voltage transmission lines. *IEEE Transactions on Power Apparatus and Systems* PAS-91(3): 865, 1972.

Les Renardières Group. Positive discharges in long air gaps at Les Renardières. *Electra*, No. 53, 31–151, 1977.

Loeb, L.B. *Basic Processes of Gaseous Electronics*. Berkeley/Los Angeles, CA: University of California Press, 1961.

Loeb, L.B. *Electrical Coronas*. Berkeley/Los Angeles, CA: University of California Press, 1965.

Mitchell, J.H. and K.E.W. Ridler. *Proceedings of the Royal Society (London)* 146A: 911, 1934.

Naidu, M.S. and A.N. Prasad. *Journal of Physics D* 3, 1970.

Niemeyer, L. and F.Y. Chu. SF6 and the atmosphere. *IEEE Transactions on Electrical Insulation* EI-27: 184, 1992.

Niemeyer, L., Ullrich, L., and N. Wiegart. The mechanism of leader breakdown in electronegative gases. *IEEE Transactions on Electrical Insulation* EI-24: 309, 1989.

Nottingham, W.B., *Phys. Rev*., 28, 764, 1926.

Nottingham, W.B. *AIEE Transactions* 42: 302, 1923.

Novak, J.P. and M.F. Fréchette. Transport coefficients of SF_6 and SF_6–N_2 mixtures from revised data. *Journal of Applied Physics*, 5(1), 107–119, 1984.

Pedersen, A. On the electrical breakdown of gaseous dielectrics, 1989 Whitehead Memorial Lecture. *IEEE Transactions on Electrical Insulation* EI-24: 721, 1989.

Pedersen, A., McAllister, I.W., Crichton, G.C., and S. Vibholm. Formulation of the streamer breakdown criterion and its application to strongly electronegative gases and gas mixtures. *Archiv fur Elektrotechnik* 67: 395, 1984.

Peek, F.W. Jr. *Dielectric Phenomena in High Voltage Engineering*. New York: McGraw-Hill, 1929.

Raether, H. *Electron Avalanches and Breakdown in Gases*. London, U.K.: Butterworth Co., 1964.

Richardson, O.W. *Emission of Electricity from Hot Bodies*, Longmans, Green & Co. New York, 1921.

Richtmyer, F.K., Kennard, E.H., and T. Lauritsen. *Introduction to Modern Physics*. New York: McGraw-Hill, 1955, Chapters 5 and 6.

Rizk, F.A.M. Analysis of space charge generating devices for lightning protection: Performance in slow varying fields. *IEEE Transactions on Power Delivery* 25(3): 1996–2006, 2010.

Scherer, H.N., Ware, B.J., and C.H. Shih. Gaseous effluents due to EHV transmission line corona. *IEEE Transactions on Power Apparatus and Systems* PAS-92(3): 1043, 1973.

Thompson, J.J. and G.P. Townsend. *Conduction of Electricity through Gases*, Vol. 2. London, U.K.: Cambridge University Press, 1930, p. 112.

Trinh, N.G. A systematic study of corona discharge in air at atmospheric pressure, PhD Thesis, Laval University, Québec, Canada, 1969.

Trinh, N.G. Analysis of the second harmonic (120 Hz) audible noise generated by line corona. *IEEE-PES Summer Meeting paper A* 75 501–7, July 1975.

Trinh, N.G. Considerations on the effect of a temperature gradient on the dielectric performance of a CGI bus, Philadelphia, Penn. *IEEE International Symposium on Electrical Insulation*, 183, 1982.

Trinh, N.G. Partial XIX: Discharge in air, Part I—Physical mechanisms. *IEEE Electrical Insulation Magazine* 11(2): 23, 1995a.

Trinh, N.G. Partial discharges XX: Discharges in air, Part II—Selection of line conductors. *IEEE Electrical Insulation Magazine* 11(3): 5, 1995b.

Trinh, N.G. and I.B. Jordan. Modes of corona discharges in air. *IEEE Transactions on Power Apparatus and Systems* PAS-87(5): 1207, 1968.

Trinh, N.G. and I.B. Jordan. Trichel streamers and their transition into the pulseless glow discharge. *Journal of Applied Physics* 41(10): 3991–3999, September 1970.

Uhlig, C.A.E. AC corona current and loss on thin wires from onset to spark-over. In: *Proceedings, High Voltage Symposium, National Research Council of Canada*, 1956.

Wiegart, N. and F. Pinnekamp. Corona stabilization to testing of gas-insulated switchgear, Canadian Electrical Association (CEA) report # 153 T 310, 1985.

Wiegart, N., Niemeyer, L., Pinnekamp, F., Boeck, W., Kindersberger, J., Morrow, R., Zaengl, W., Zwicky, M., and I. Gallimberti. Inhomogeneous field breakdown in GIS – The prediction of breakdown probability and voltages. Part I: Overview of a theory for inhomogeneous breakdown in SF_6. *IEEE Trans*., Vol. PWRD-3, 923–930, 1988a.

5

Breakdown Characteristics of Long Air Gaps

5.1 Introduction

Selection of air clearances in power systems in relation to voltage stresses to which such clearances are exposed is a fundamental part of insulation coordination (IEC 60071-1, 1993). This has to consider not only the types and severity of overvoltages and the insulation configuration but also the prevailing environmental conditions, including air density and humidity.

Electric breakdown of a long air gap is a complex process that comprises several stages involving both electrode and gap effects. These in general include ionization in high-field zones, corona formation at the electrodes, onset and propagation of streamers, leader formation and propagation, bridging of the gap, and finally formation of an electric arc between the electrodes. This final stage, traditionally called spark-to-arc transition, represents the complete loss of dielectric integrity of the gap concerned. The relative role played by streamers and leaders in the breakdown process depends on the type and severity of the applied stress, including polarity and time variation, as well as the length of the air gap concerned. In practical air gap configurations, one normally deals with nonuniform fields, where the electric field at one or both electrodes is significantly higher than the mean voltage gradient across the gap.

In classifying voltage stresses, reference is usually made to continuous voltage, temporary overvoltages and transient overvoltages. Transient overvoltages are in turn often divided into slow front, normally referring to switching transients, and fast front in regard to lightning impulses (IEC 60071-1, 1993). Very fast front impulses are not dealt with in this chapter. As explained in Chapter 13, composite overvoltages are dealt with in phase-to-phase and longitudinal insulation configurations. In HVDC systems, we also deal with composite overvoltages, which then mostly refer to a dc component with a superimposed switching impulse. In the present text, reference will frequently be made to streamers and leaders so that a brief description of such discharges is due.

A streamer is a cold, branched, filamentary discharge, where most of the charge resides at the filament tips. It is, at least for positive polarity, characterized by a practically constant mean voltage gradient E_s. Attempts for mathematical modeling of streamers (Gallimberti, 1979; Aleksandrov et al., 1995; Aleksandrov and Bazelyan, 1996; Morrow and Lowke, 1997) contributed to our understanding of the physical process involved. Typical physical parameters of the streamer filament considered in the aforementioned investigations include an electron number density of 10^{14}–10^{15}/cm^3, a radius of the channel of around 100 μm, and electrical resistance per unit length of 10^7 Ω/m. The streamer is also characterized by propagation speeds as high as 10^7 m/s. Despite their complexity, the aforementioned models did not succeed in predicting E_s with sufficient accuracy for engineering application. We will therefore rely on high-voltage tests for the determination of E_s for both polarities.

The leader is an arc-like discharge, with the important characteristic that the voltage gradient E_ℓ is significantly lower than the streamer gradient E_s. Characteristics of the positive leader in switching impulse tests on laboratory rod–plane gaps by Les Renardières Group (1974, 1977) revealed a diameter below 10 mm, yielding a current density of the order of 10 A/cm^2, corresponding to an electron number density of 10^{13}/cm^3. Leader channel temperature has been estimated at 2000 K for a 2 m length and 7000 K for a 6 m length (Gallimberti, 1979). Like the electric arc, the leader has a quasistationary inverse voltage gradient–current characteristic, with E_ℓ of 30–50 kV/m at a current of 1 A. The instantaneous leader gradient however varies with lifetime, starting with a value not much different from the streamer gradient E_s, dropping with time to reach the quasistationary values reported earlier with a time constant θ of 30–60 μs.

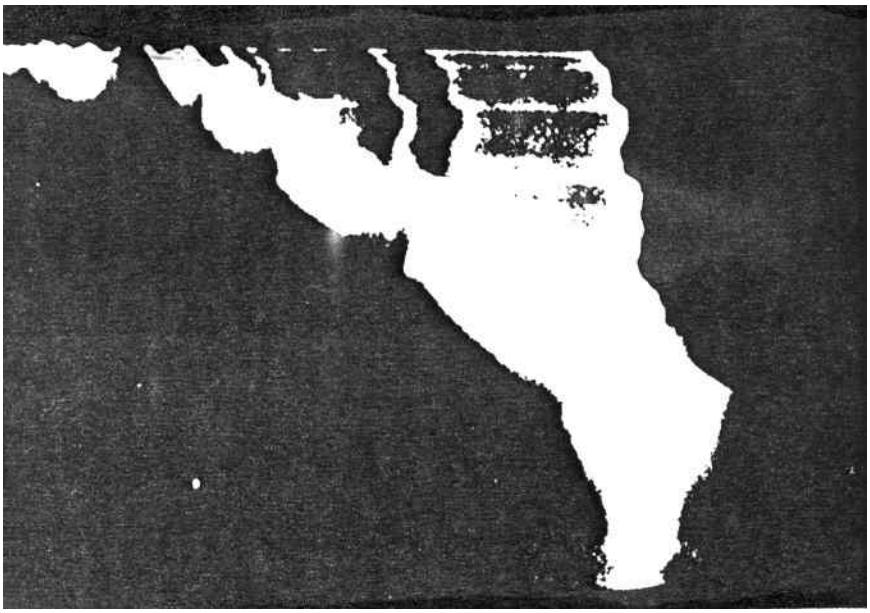


FIGURE 5.1 Streak photograph of breakdown of a 10 m air gap under positive switching impulse. (From Les Renardières Group, *Electra*, 35, 47, 1974.)

The leader propagation speed on the other hand is much lower than that of a streamer, measured in the range 1–2 10^4 m/s for laboratory gaps. Such speed however increases significantly with the overvoltage factor at the leader tip (Baldo et al., 1974; Rizk and Vidal, 2008).

In general, leaders are formed in two distinct situations. The first is when streamers at the high-voltage electrode reach a critical size, leading to the formation of a stem at their root (Rizk, 1989b). If conditions are adequate, such stem continues to grow as a leader propagating towards the counter electrode (Rizk, 1989b).

The other situation is when streamers completely bridge the gap; a leader segment is formed and grows in a stage that precedes transition to an electric arc. This case is referred to as a streamer breakdown mechanism, since the leader phase did not significantly participate in the initial bridging of the gap. This is typical for example of breakdown under lightning impulses. The former case on the other hand, where the leader plays a major role in bridging the gap, is termed a leader breakdown mechanism as is typical of switching impulse breakdown of long air gaps as illustrated in Figure 5.1.

Leaders often grow in a zigzag path, so that the real leader length significantly exceeds the straight line distance covered. Also, particularly in negative polarity, leaders can grow in steps, with time pauses and restrikes as illustrated in Figure 5.2 (Les Renardières Group, 1981; Ortega et al., 1994).

In the following sections, we will deal, respectively, with long air gap strength under fast front impulses, direct voltage, critical switching impulses, and composite and ac voltages. Special attention will be paid to the effect of humidity and altitude.

5.2 Breakdown of Long Air Gaps with Fast Front Impulses

5.2.1 Breakdown Mechanism

For voltages exceeding a minimum value U_0, breakdown of a long air gap under fast front impulses starts with critical electron avalanche formation at the highly stressed electrode leading to streamer onset with subsequent streamer propagation to bridge the whole gap. This is followed by leader onset and spanning of the gap already bridged by streamers. The time to streamer onset could be referred to as



FIGURE 5.2 Streak photograph of negative breakdown of a 10 m air gap under negative switching impulse. (From CIGRE Group 33, Overvoltages and Insulation Coordination, August 1974, CIGRE, 1974.)

the statistical time lag t_s. The sum of streamer propagation and leader formation and propagation times t_{fs} and t_{fl}, respectively, may be termed the formative time lag t_f. Finally, leader transition to an electric arc by thermal ionization will result in completion of the breakdown process and total voltage collapse. The breakdown delay time t_d is taken as the sum of the statistical and formative time lags t_s and t_f. This is illustrated in Figure 5.3 with U_0, occurring at time t_0, below which no breakdown occurs. This corresponds to a mean breakdown onset gradient E_0 with

$$E_0 = \frac{U_0}{d} \tag{5.1}$$

where d is the gap length.

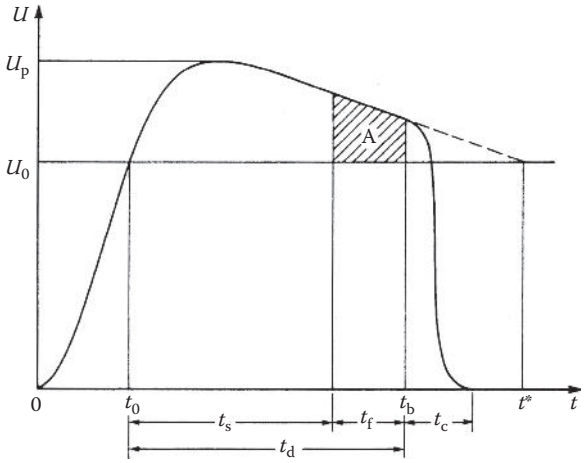


FIGURE 5.3 Schematic representation of an impulse voltage and the different times involved.

For positive polarity, the statistical time lag t_s is determined mostly by electron detachment from negative ions in a critical volume V_c in the vicinity of the highly stressed electrode (Les Renardières Group, 1974). The outer boundary of the critical volume is determined by the condition

$$\alpha = \eta \tag{5.2}$$

where

α is the ionization coefficient
η is the attachment coefficient

The inner boundary surface of the critical volume V_c is determined by the condition that an electron starting from that boundary would be capable through ionization by collision, to produce the number of electrons needed for a critical avalanche (typically 10^8).

The probability function of the statistical time lag t_s can be expressed by (Hutzler and Hutzler-Barre, 1976)

$$P_v(t_s) = 1 - \exp\left[-\int_{t_n}^{\tau_n} n_n \, dV dt\right] \tag{5.3}$$

where

n_n is the negative ion volume density
τ_n is the mean lifetime of a negative ion

The double integration is carried out within the critical volume and in the time interval from t_0 to $t_0 + t_s$. A convenient empirical expression of Equation 5.3, originally developed from the breakdown experiments in SF_6, reads (Rizk and Eteiba, 1982)

$$P_v(t_s) = 1 - \exp(-\lambda F) \tag{5.4}$$

where

$$F = \int_{t_0}^{t_0 + t_s} \left[\frac{U(t) - U_0}{U_0}\right]^k dt \tag{5.5}$$

with λ a constant rate (1/*s*) and *k* is a constant.

The streamer propagation phase was the subject of an investigation by Kind (1958). It was assumed that the speed of streamer propagation $v(x, t)$ at any position x, with $x = 0$ at the highly stressed electrode, can be expressed as

$$v(x, t) = k_1[E(x, t) - E_1(x)] \tag{5.6}$$

where

$E(x, t)$ is the applied electric field at (x, t)
$E_1(x)$ is an electric field at position x, below which no streamer propagation can take place
k_1 is a constant

It was also assumed that space charge has negligible effect on the applied electric field, which remains at the geometric field level, so that it can be related to the applied voltage $u(t)$ by

$$E(x, t) = g(x)u(t) \tag{5.7}$$

where $g(x)$ is a geometric function.

Similarly, it was assumed that $E_1(x)$ is related to a streamer onset voltage u_1 by

$$E_1(x) = g(x)u_1 \tag{5.8}$$

Substituting in Equation 5.2, separating variables and integrating

$$\int_{o}^{d} \frac{dx}{k_1 g(x)} = \int_{t_1}^{t_1 + t_{fs}} \left[u(t) - u_1\right] dt \tag{5.9}$$

where
- d is the gap length
- t_1 is the instant at which $u = u_1$
- t_{fs} is the duration of streamer propagation

It is noted that for a given configuration, the left-hand side of Equation 5.9 becomes a constant and the right-hand side serves as the basis of the so-called equal area criterion, if it is further assumed that $t_1 + t_{fs} = t_b$, where t_b is the breakdown time lag. A generalization of the equal area criterion would be the disruptive effect (DE), which was originally developed by Witzke and Bliss for transformer insulation:

$$DE = \int_{t_0}^{t_b} \left[u(t) - u_1\right]^{k_2} dt \tag{5.10}$$

with u_1, k_2, and DE as constants, needed to establish the breakdown V–t curve.

The application of this integration method to air gaps is reported in Caldwell and Darveniza (1973). For long air gaps, an empirical relationship (Pigini et al., 1989) expressed the streamer propagation time t_{fs} by

$$t_{fs} = \left[1.25\frac{E}{E_{50}} - 0.95\right]^{-1} \quad (\mu s) \tag{5.11}$$

where
- E is the maximum stress to which the gap was stressed (kV/m)
- E_{50} = 500 kV/m, for positive polarity

The leader propagation phase has been modeled using several versions of an empirical expression for the leader propagation speed v_ℓ (Pigini et al., 1989). One such expression is (CIGRE 33.01, 1991)

$$v_\ell(x,t) = k_\ell u(t)\left[\frac{u(t)}{d - x} - E_0\right] \tag{5.12}$$

where
- $u(t)$ is the applied voltage
- x is the leader length
- d is the gap length already bridged by streamers
- E_0 is an onset voltage gradient
- k_ℓ is a constant

One obvious limitation of Equation 5.12 is that the leader speed becomes infinite as the leader bridges the gap ($x \to d$), which is not physically sensible. The aforementioned models for breakdown time lag are used to establish the breakdown voltage–time characteristic of rod–plane and rod–rod gaps mostly under positive polarity, particularly under nonstandard lightning impulses for which relatively limited experimental results are available. The error involved in using the aforementioned models in determination of nonstandard lightning impulse breakdown voltage for different gaps, in both positive and negative polarity, was reported in Pigini et al. (1989). It was shown that for air gaps, the leader progression model was in general more accurate than the integration methods. When an insulator string was present

in the gap, however, errors with both methods could reach levels as high as 30% or more. Nonstandard lightning impulses are dealt with for assessment of backflashovers in lightning performance studies of transmission lines.

5.2.2 Standard Lightning Impulse Breakdown Voltage

Experimental results of 50% positive standard impulse breakdown voltage of 1–10 m rod–plane gaps, under normal atmospheric conditions, can be expressed as (IEC 60071-2, 1996)

$$U_{50\text{rp}} = 530d \quad (\text{kV}_{\text{crest}}, \text{m}) \tag{5.13}$$

Traditionally, the gap factor K (Paris and Cortina, 1968) expresses the ratio of the positive switching impulse breakdown voltage of a certain gap to the corresponding value of a rod–plane configuration. It was later found that the gap factor concept can be generalized, for positive polarity, to apply to fast front impulses with a gap factor K_{ff}, related to K by Pigini et al. (1989) and IEC 60071-2 (1996)

$$K_{\text{ff}} = 0.74 + 0.26K \tag{5.14}$$

No such generalization can be applied to negative polarity (Pigini et al., 1989). Expression 5.13 can therefore be generalized as

$$U_{50} = 530K_{\text{ff}} \langle\rangle d \tag{5.15}$$

The negative standard lightning impulse breakdown voltage of rod–plane gaps, for gaps up to 4 m, can be expressed as (Sirotinski, 1955a; Paris and Cortina, 1968)

$$U_{50\text{rp}} = 215 + 670d \quad (\text{kV}_{\text{crest}}, \text{m}) \tag{5.16}$$

which shows that contrary to the case of positive polarity, the mean negative streamer gradient is not constant but decreases at higher gap spacings. For example, a 50 cm gap would have a mean negative streamer gradient of 1100 kV/m, while for a 2 m gap, the mean negative streamer gradient would drop to 778 kV/m.

For a rod–rod gap, the 50% negative standard lightning impulse breakdown voltage can be expressed as (Sirotinski, 1955a; Paris and Cortina, 1968)

$$U_{50} = 110 + 600d \quad (\text{kV}_{\text{crest}}, \text{m}) \tag{5.17}$$

It is noted that IEC (IEC 60071-2, 1996) recommends that the maximum magnitude of a lightning surge impinging on a substation could be taken as

$$U_{50} = 700d \quad (\text{kV}_{\text{crest}}, \text{m}) \tag{5.18}$$

where d is the length of transmission line insulator string.

5.3 Air Gap Strength under Direct Voltage

DC breakdown of air gaps takes place through streamer mechanism. Due to the ample time involved, ions formed in the vicinity of the highly stressed electrode have time to travel, filling the whole gap, which considerably affects the breakdown gradient. For a 10 cm positive rod–plane gap, the dc breakdown gradient is approximately 700 kV/m (Strigel, 1955a), while at HVTRC, Schneider found the corresponding value for a 1.5 m gap amounts to only 481 kV/m (EPRI TR-102764, 1993). Measurements at IREQ (EPRI EL-963, 1979) on a 4 m positive rod–plane gap yielded 525 kV/m, somewhat higher than the HVTRC value.

Similarly, dc breakdown gradient of a 10 cm rod–rod gap yielded 870 kV/m (Strigel, 1955b), while the corresponding HVTRC value on a 1.5 m rod–rod gap is 493 kV/m (EPRI TR-102764, 1993).

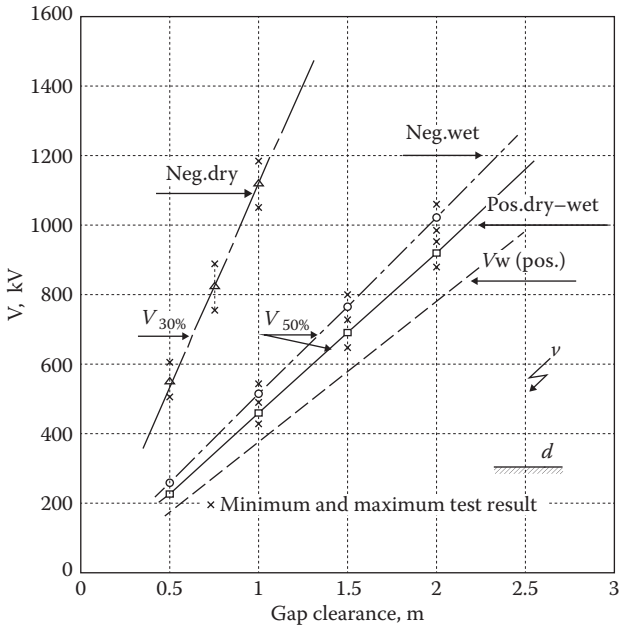


FIGURE 5.4 DC breakdown voltage as a function of gap clearance of rod–plane configuration. (From CIGRE WG 33.07, Guidelines for the evaluation of dielectric strength of external insulation, CIGRE Monograph 72, Chapter 8, 1992).

Under negative polarity, the dc breakdown gradient is significantly higher, reaching 1700 kV/m for a 10 cm rod–plane gap (Strigel, 1955), dropping to 672 kV/m for a 1.5 m gap (EPRI TR-102764, 1993).

Figure 5.4 presents dc breakdown characteristics of 0.5–2.5 m rod–plane gaps from International Council on Large Electric Systems (CIGRE) Guide on External Insulation (CIGRE 33.07, 1992). Again, under dry conditions, the dc breakdown voltage is substantially higher under negative compared to positive polarity. The reduction of the negative breakdown voltage under rain is quite substantial. This could possibly be explained by the adherence of electrons to water droplets, forming heavy negative ions that remain with some positive ions in the vicinity of the highly stressed electrode enhancing electric field elsewhere in the gap. Another possible effect is that negatively charged water drops falling into the vicinity of the ground plane would enhance formation of positive upward streamers from the plane.

Figure 5.5 shows the dependence of breakdown voltage of a rod–rod gap on spacing in the range 0.5–2.5 m, for both polarities under dry and wet conditions (IEC 60060-1, 1989a). The relationship is remarkably linear, with relatively small dispersion, which led the IEC to use the rod–rod gap as a reference measuring device, with the following expression of the disruptive voltage U_0 as function of the gap d (Figure 5.5):

$$U_0 = 2 + 534d \quad (\text{kV, m}) \tag{5.19}$$

for

$$0.25 \leq d \leq 2.5 \text{ m}$$

and

$$1 \text{ g/m}^3 \leq \frac{h}{\delta} \leq 13 \text{ g/m}^3$$

where

h is the absolute humidity

δ is the relative air density

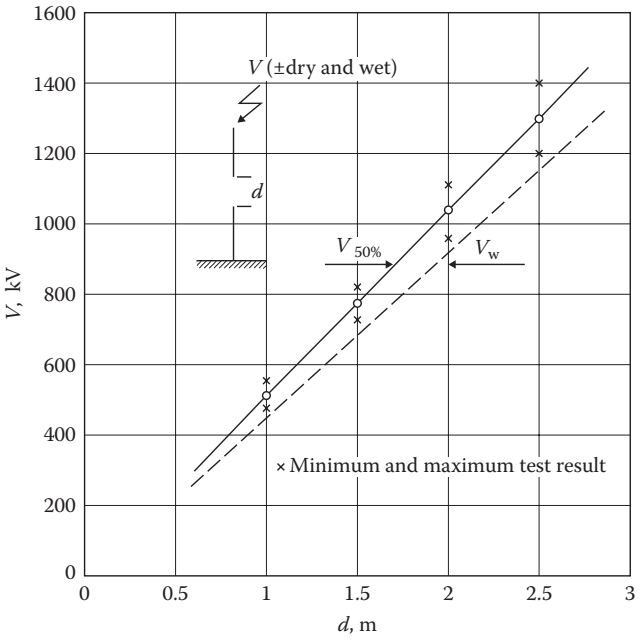


FIGURE 5.5 DC breakdown voltage variation with gap clearance for a rod–rod configuration. (From CIGRE WG 33.07, Guidelines for the evaluation of dielectric strength of external insulation, CIGRE Monograph 72, Chapter 8, 1992).

For a conductor-simulated tower leg lap of 0.33 m, Schneider (EPRI TR-102764, 1993) reported a minimum dc breakdown gradient of 420 kV/m and recommended to use a critical breakdown strength of 400 kV/m for design purpose. It should finally be noted that the dc voltage is often the determining factor for insulator design, particularly in polluted areas, but plays no direct role in establishing tower clearance requirements.

5.4 Positive Switching Surge Strength of Long Gaps

This section will deal with pure switching surge stresses, that is, ignoring the effect any dc bias. A separate section in the following will be dedicated to composite stresses involving a switching impulse superimposed on the pole-to-ground voltage.

5.4.1 System Overvoltages

AC systems switching overvoltages have already been dealt with in Chapter 1.

For a bipolar HVDC transmission line, field measurements and EMTP simulation showed that significant overvoltages occur on the unfaulted pole following a ground fault on the other pole. This overvoltage is caused by capacitive coupling between the two poles, wave propagation, and reflections at the smoothing reactor in the converter station. It has been found that the voltage on the unfaulted pole first drops following ground fault occurrence but then rises to a maximum value that depends on the fault location. In Melvold et al. (1977), it was reported that the maximum measured overvoltage factor was 1.74 p.u. The overvoltage time to crest also varies with the fault location, from hundreds of microseconds to a few milliseconds, typical of slow front impulses. The encountered complex wave shapes can be numerically simulated by reference to positive- and zero-sequence components characterized by different propagation speeds and attenuation factors. In the HV laboratory, however, such complex voltage forms are normally replaced by double exponential impulses with front times in the hundred microsecond range (Knudsen and Iliceto, 1970) or by a standard switching impulse of 250 μs front.

5.4.2 Air Gap Strength Data

An extensive review of switching surge performance of long air gaps has been recently made by Zaffanella (2005). Therefore, only a brief account will be included here. Figure 5.6 shows a vast collection of data on the *V*-curve variation of the switching impulse breakdown voltage of rod–plane gap with time to crest, for gap spacings in the range of 1–25 m (Leroy, 1974). It is shown that the critical front varies in the range 100–1200 μs. The relationship between the gap length d and the critical front t_{cf} may be approximately expressed as

$$t_{cf} = 50 + 40d \quad (\mu s, m) \tag{5.20}$$

On the left branch of the *V*-curve, the rate of rise of the applied voltage is too fast to allow full extension of the leader phase, while on the right of the minimum point, the voltage rate of rise is too slow, leading to discontinuities in leader propagation. Both effects result in less than the optimally critical conditions needed for the minimum point of the *V*-curve (Les Renardières Group, 1974).

It is well known that switching impulse strength of an air gap depends not only on gap spacing but also on electrode configuration (Leroy, 1974). Since the positive switching impulse breakdown of a rod–plane gap results in the lowest breakdown level, it was proposed in Paris and Cortina (1968) to refer to the ratio

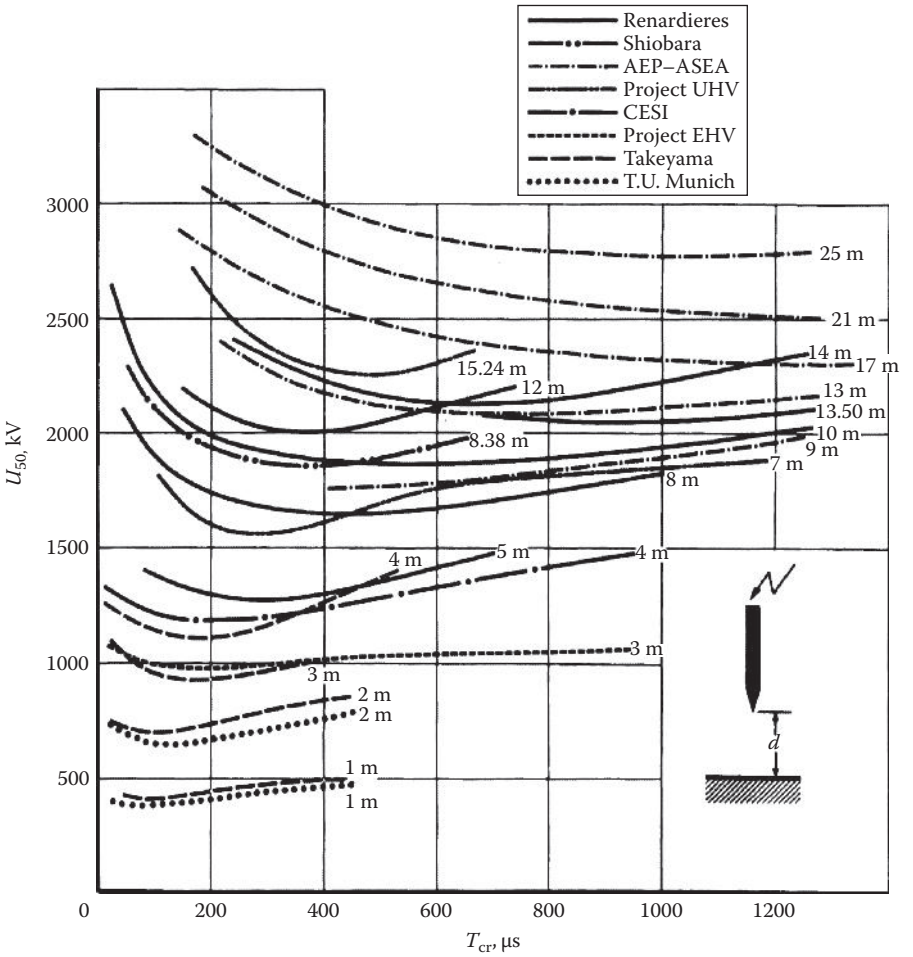


FIGURE 5.6 Data collection of 50% positive switching impulse breakdown voltage as a function of time to crest of rod–plane configuration for different spacings. (From Leroy, G., Recent developments in the physics and engineering of high voltage breakdown, in: *IEE Gas Discharge Conference* (Review Lecture, Opening Session), London, U.K., September 1974.)

of the breakdown voltage of any configuration to that of a rod–plane of equal spacing as the gap factor $K \geq 1$. Some gap factor examples are given in the succeeding text.

For a rod–rod gap d, with the height h of the ground rod, it was found that K can be approximately expressed as (Leroy, 1974)

$$K = 1 + 0.6\frac{h}{h+d} \tag{5.21}$$

For a conductor–tower leg gap, K can be determined from an empirical formula due to CIGRE WG 33.07 (CIGRE 33.07, 1992):

$$K = 1.45 + 0.015\left(\frac{h}{\ell_i}\right) - 6 + 0.35\exp\left(\frac{-8W}{\ell_i}\right) - 0.2 + 0.135\left(\frac{d}{\ell_i}\right) - 1.5 \tag{5.22}$$

where

d is the minimum clearance between the conductor and the tower leg
h is the conductor height aboveground
W is the width of the tower leg
ℓ_i is the insulator string spacing

Consider a 600 kV HVDC transmission line where the maximum overvoltage factor is given as K_0. In a deterministic approach, the maximum overvoltage will be equaled to a $-n\sigma$ insulation level. We will undertake a sensitivity analysis of the conductor bundle–tower leg clearance, for $\sigma = 0.05$. The results are shown in Table 5.1.

From Table 5.1, it can be observed that

- Comparing cases 1 and 2, the minimum clearance is quite sensitive to the maximum overvoltage factor
- Comparing cases 1 and 3, the minimum clearance is rather insensitive to the conductor height aboveground
- Comparing cases 1 and 4, the minimum clearance is rather insensitive to the width of the tower leg
- Comparing cases 1 and 5, the minimum clearance is slightly sensitive to the insulator length. The total gap will of course be sensitive to insulator length due to conductor swing
- Comparing cases 1 and 6, the minimum clearance is sensitive to the insulation withstand level required

An extensive list of recommended gap factors for different electrode configurations is given in CIGRE monograph, No. 72 (CIGRE 33.07, 1992).

TABLE 5.1

Effect of Different Parameters on Minimum Required Conductor–Tower Leg Clearance of a 600 kV HVDC Line

Case No.	K_0, p.u.	h, m	W, m	ℓ_i, m	n, p.u.	d, m
1	1.75	25	2	7	3	3.30
2	1.65	25	2	7	3	3.03
3	1.75	30	2	7	3	3.25
4	1.75	25	3	7	3	3.39
5	1.75	25	2	5	3	3.20
6	1.75	25	2	7	4	3.59

5.4.3 Modeling of Positive Critical Switching Impulse Breakdown

Several attempts have already gone into modeling of critical positive switching impulse breakdown of long air gaps. In this review, only models with practical engineering applications will be considered. Carrara and Thione (1976) introduced the concept of critical electrode radius. For a positive electrode, the 50% breakdown voltage of a given gap remains constant if the electrode radius is maintained below a critical radius corresponding to the gap in question. It increases for radii above the critical radius. From the experimental results, it was shown that for sphere–plane gaps, the critical radius increases with gap length but saturates at approximately 38 cm. The corresponding saturation critical radius of a conductor–plane configuration was reported as approximately 10 cm (Carrara and Thione, 1976).

The continuous leader inception voltage was taken as the corona inception voltage of an electrode with critical radius for the gap concerned. A criterion for equivalence of a rod-type gap to the basic configuration of a rod–plane was based, rather arbitrarily, on a relationship involving field values E_1 and E_2 at radial distances R_1 and R_2 of 20 and 40 cm, respectively. For conductor-type gaps, E_1 and E_2 were determined at R_1 and R_2 of 5 and 15 cm, respectively. The method was applied to rod–rod and conductor–conductor configurations.

A model for critical switching impulse breakdown of long air gaps has been formulated by Rizk (1989a,b). In Rizk (1989a), the analysis is based on the situation at the final jump illustrated in Figure 5.7, which shows the development of a continuous leader in the breakdown of an air gap under the condition of positive switching impulse with critical front. It was assumed that under critical conditions, the leader propagates with practically constant current i, charge per unit length q, speed υ, and tip potential $U_{\ell c}$. For a final jump h_f and a mean positive streamer gradient E_s, it was assumed that the electric field at the plane, largely due to leader space charge, must reach a critical value E_{cr}. Furthermore, at that instant, $U_{\ell c}$ must be equal to $h_f \cdot E_s$. The minimum streamer gradient E_s is normally taken as 400 kV/m.

New expressions were thus obtained for the continuous leader inception voltage $U_{\ell c}$ for rod–plane and conductor–plane gaps of length d. For a rod–plane gap, the following expression for the continuous leader inception voltage was obtained:

$$U_{\ell c} = \frac{1556}{1 + (3.89/d)} \quad \text{(kV, m)} \tag{5.23}$$

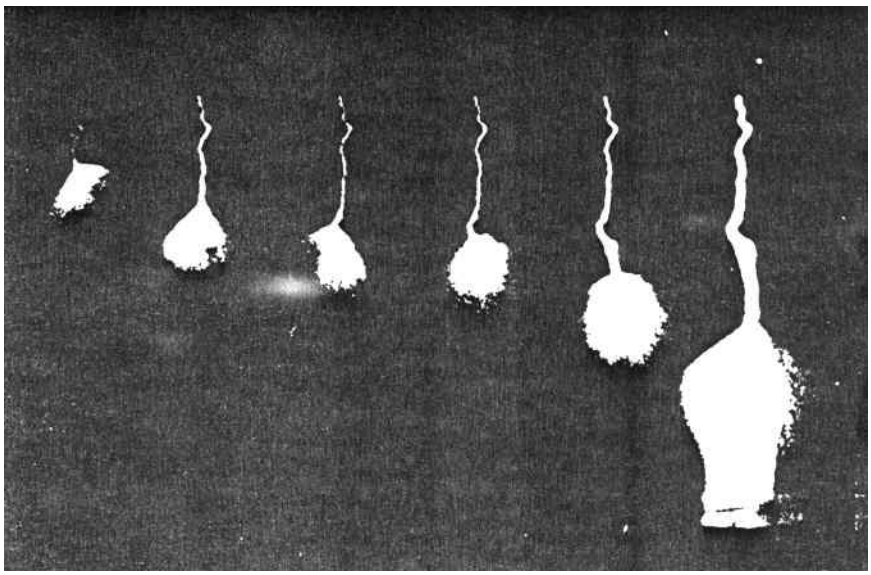


FIGURE 5.7 Steak photographs of the breakdown of a 10 m air gap under positive switching impulse of critical front. (From Gallimberti, I., The mechanism of the long spark formation, *Journal de Physique*, 40(7), 193, 1979.)

It should be emphasized that this expression was not reached using the concept of critical radius as in (Carrara and Thione, 1976) but rather expression 5.23 provides means for calculating the critical radius for any gap length d. In Rizk (1989a), a new expression for the voltage drop ΔU_z of a leader of length ℓ_z was also obtained:

$$\Delta U_z = \ell_z (E_\infty + x_0 (E_\infty \ln \frac{E_i}{E_\infty} - \frac{E_i - E_\infty}{E_\infty} e^{-\ell_z / x_0}) \quad (5.24)$$

where

E_i is the initial leader voltage gradient, taken as 400 kV/m

E_∞ is the ultimate leader voltage gradient for the leader current involved, normally 30–50 kV/m

$x_0 = \upsilon\theta$, where υ is the leader speed, typically 1.5 10^4 m/s and θ a time constant normally assumed in the range 30–60 μs

The leader length ℓ_z was obtained as

$$\ell_z = d - h_f = d - \frac{U_{\ell c}}{E_s} \quad (5.25)$$

As shown in Carrara and Thione (1976), the minimum breakdown voltage U_b of the gap can be expressed as

$$U_b = U_{\ell c} + \Delta U_z \quad (5.26)$$

and the 50% breakdown voltage U_{50} given by

$$U_{50} = \frac{U_b}{1 - 3\sigma} \quad (5.27)$$

where σ is the standard deviation in per unit of U_{50}, normally taken as 0.05 for a rod–plane configuration.

Figure 5.8 shows variation of the critical 50% breakdown voltage of rod–plane gap as function of gap length as determined by Rizk model for gap length of 2–20 m, as compared with the CREIPI formula, which represents the best fit of experimental results (IEC 60071-2, 1996):

$$U_{50} = 1080 \ln(1 + 0.46d) \quad \text{(kV, m)} \quad (5.28)$$

The agreement is very satisfactory.

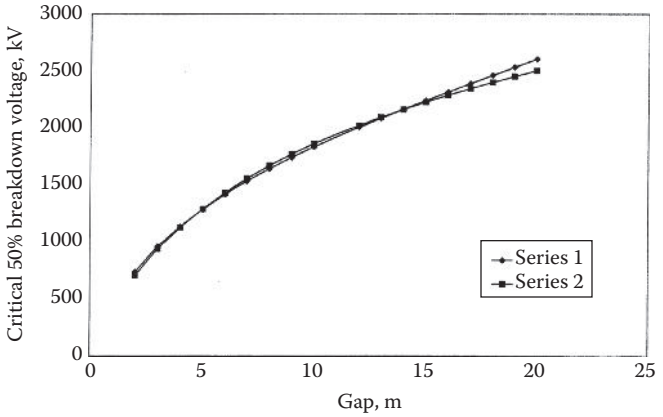


FIGURE 5.8 Variation of critical 50% switching impulse breakdown voltage of rod–plane gap with gap spacing. Series 1 (S1): Rizk model. Series 2 (S2): CREIPI formula.

In Rizk (1989b), the condition for continuous leader inception was deduced on the basis of conditions in the vicinity of the highly stressed electrode. It was assumed that two conditions have to be simultaneously satisfied. The first condition is that for any gap, the streamer (leader corona) charge must reach a critical value Q_0 that is not constant but is proportional to the continuous leader inception voltage $U_{\ell c}$:

$$Q_0 = cU_{\ell c} \tag{5.29}$$

where c is a constant, with dimensions of a capacitance.

The second condition is that for continuous leader progression, the resultant field at the leader tip, comprising the field E_{app} due to the applied voltage and the opposing space charge field E_{sc} due to leader corona (streamers), must reach a critical level E_c:

$$E_{app} - E_{sc} = E_c \tag{5.30}$$

The resulting expression for the continuous leader inception voltage $U_{\ell c}$ of a rod–plane gap was found to be consistent with Equation 5.23 earlier.

For a conductor–plane gap, the following expression for $U_{\ell c}$ was obtained:

$$U_{\ell c} = \frac{2247}{1 + \dfrac{5.15 - 5.49 \ln a}{d \ln(2d/a)}} \quad \text{(kV, m)} \tag{5.31}$$

where

d is the gap spacing, m

a is the equivalent conductor radius, m

The expression of $U_{\ell c}$ in Equation 5.23 could be generalized for a rod-type gap to read

$$U_{\ell c} = \frac{1556}{1 + \dfrac{7.78}{R}} \quad \text{(kV, m)} \tag{5.32}$$

where R is a geometric function that can in general be determined by the charge simulation method (Singer et al., 1974) and that for a rod–plane gap becomes $R = 2d$.

Similarly, for a conductor-type gap where the positive high-voltage electrode is a conductor of radius a and height h aboveground, Equation 5.31 can be generalized as

$$U_{\ell c} = \frac{2247}{1 + \dfrac{F}{R}} \quad \text{(kV, m)} \tag{5.33}$$

where

$$F = \frac{10.30 - 10.98 \ln a}{\ln(2h/a)}$$

and R is a geometric function that can in general be determined by charge simulation, h is the height, while for the base conductor–plane gap, $h = d$, $R = 2d$.

In Rizk (1989b), the model was applied to rod–rod, conductor–rod, and conductor–tower leg gaps. The application of the Rizk model to phase-to-phase insulation was reported in Rizk (1993) and also accounted for the effect of conductor bundle design on critical switching impulse performance of air clearances in Rizk (1996). In all these applications, the agreement between model predictions and experimental results was found to be very satisfactory.

The application of the Rizk model to altitude effects on switching impulse strength of long air gaps will be given in the succeeding text in a special section dealing with that subject.

5.5 Air Gap Breakdown under Composite Stress

Based on literature review, the composite stress referred to in this section will mostly comprise a positive dc voltage, representing the pole-to-ground voltage, with a superimposed positive switching impulse (Watanabe, 1968; Knudsen and Iliceto, 1970). Other polarity combinations exist of course but will usually be less stressful to the air clearances involved. Ideally, the switching impulse should be characterized by a critical front for the air gap concerned, with due consideration to the effect of the dc bias voltage. However, this aspect does not seem to have been rigorously accounted for in previous experimental work as presented in the following.

Other situations involving composite stress, particularly in reference to phase-to-phase insulation, are dealt with in Chapter 13.

5.5.1 Experimental Results

Figure 5.9 shows variation of the critical composite breakdown voltage of a rod–plane gap with gap length for different magnitudes of the dc bias (Knudsen and Iliceto, 1970). It is shown that the positive dc bias leads to an increase in the breakdown voltage over the corresponding value for a 120/4000 μs switching impulse. The relative effect of the dc bias is higher; the lower the gap spacing and, of course, the higher the bias voltage magnitude, within the range of parameters investigated. These results could be explained as follows.

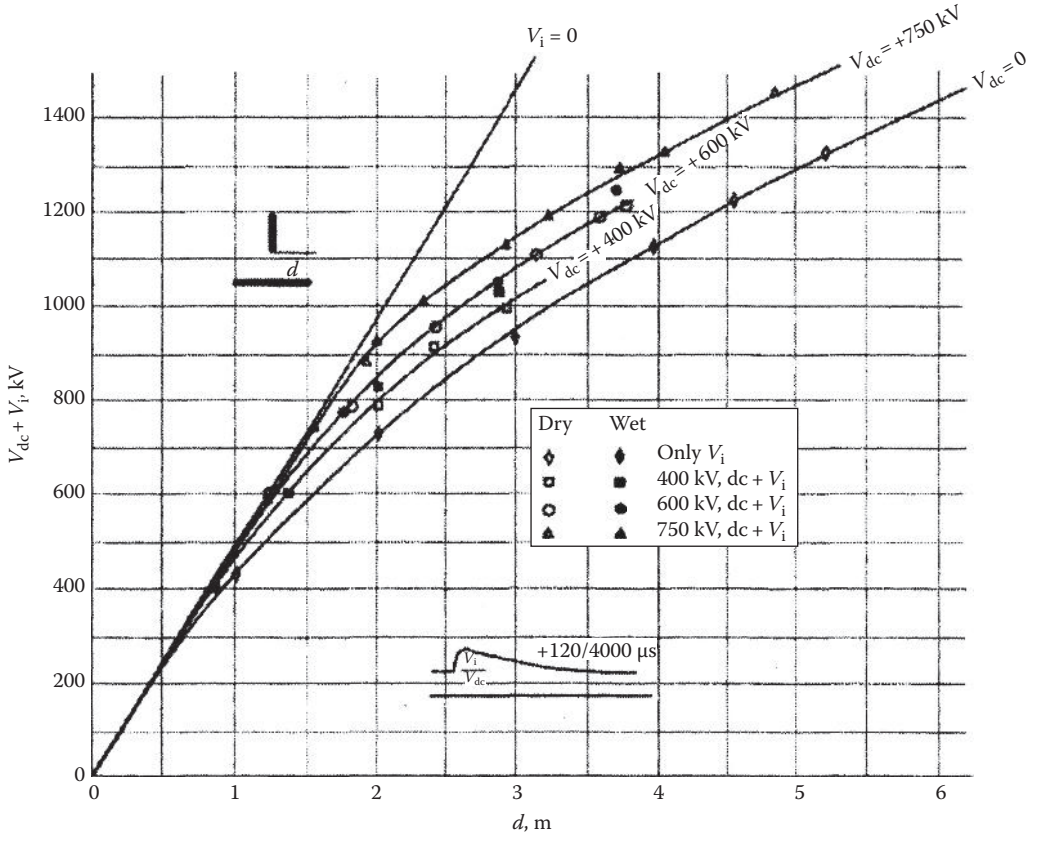


FIGURE 5.9 Variation of breakdown voltage of a rod–plane gap with clearance under switching impulse, composite voltage, and dc. (From Knudsen, N. and Iliceto, F., *IEEE Trans. Power Appar. Syst*., 89(5/6), 781, 1970.)

The positive dc bias voltage, if it exceeds the corona inception voltage of the high-voltage rod, will result in positive space charge that will be present in the gap at the instant of application of the positive switching impulse. Such space charge will induce negative bound charges on the rod electrode and reduce the electric field in its vicinity. This in turn will inhibit positive leader formation resulting in a higher leader onset voltage and consequently a higher breakdown voltage. As the gap length increases, however, the leader onset voltage will constitute a smaller part of the breakdown voltage and accordingly, the relative effect of the dc bias voltage also decreases.

Figure 5.10 shows composite voltage breakdown data for a rod–rod configuration mostly in the range 1–3 m (Knudsen and Iliceto, 1970). In comparison with Figure 5.9, it is clear that the rod–rod gap is much less sensitive to the effect of a positive dc bias than in the corresponding rod–plane. This may be explained by the fact that while positive space charge in the vicinity of the high-voltage rod tends to inhibit positive leader onset, negative space charge generated in the vicinity of the grounded rod will tend to have the opposite effect, enhancing streamer formation from the high-voltage electrode when the switching impulse is applied. It is noted from Figures 5.9 and 5.10 that there is no significant difference between positive composite breakdown voltage under dry and wet conditions.

Figure 5.11 shows the dependence of composite breakdown voltage of a 4-conductor bundle–lattice structure gap as a function of gap spacing (Knudsen and Iliceto, 1970). For comparison, the composite voltage characteristics of rod–plane and rod–rod configurations are indicated. It is shown that the 50% composite breakdown voltage is somewhat closer to the rod–rod characteristics. It is noted that the gap factors of these two configurations are rather close.

Watanabe (1968) investigated the effect of a 400 kV negative dc bias on the 50% composite breakdown voltage, with superimposed positive impulse, of rod–plane and rod–rod configurations. For a 7 m rod–plane gap, the breakdown voltage was about 7% below the corresponding value in the absence of a dc bias. For a 3 m rod–rod gap on the other hand, the 50% composite breakdown voltage with the 400 kV dc negative bias was about 5% above that without dc.

The decrease of the composite 50% breakdown voltage of a rod–plane configuration due to a negative dc bias can be explained in the following. The negative space charge generated by the negative dc bias

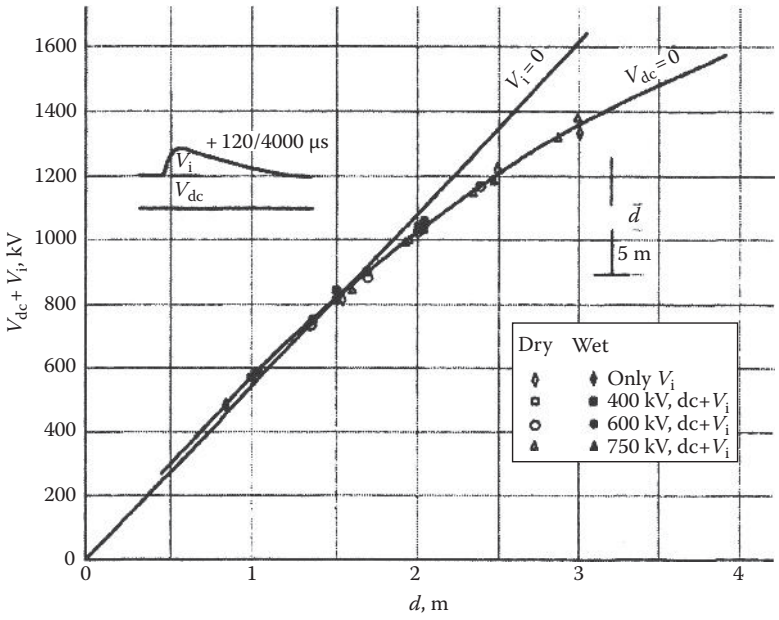


FIGURE 5.10 Breakdown voltage characteristics of rod–rod gaps under switching impulses, composite voltage, and dc. (From Knudsen, N. and Iliceto, F., *IEEE Trans. Power Appar. Syst*., 89(5/6), 781, 1970.)

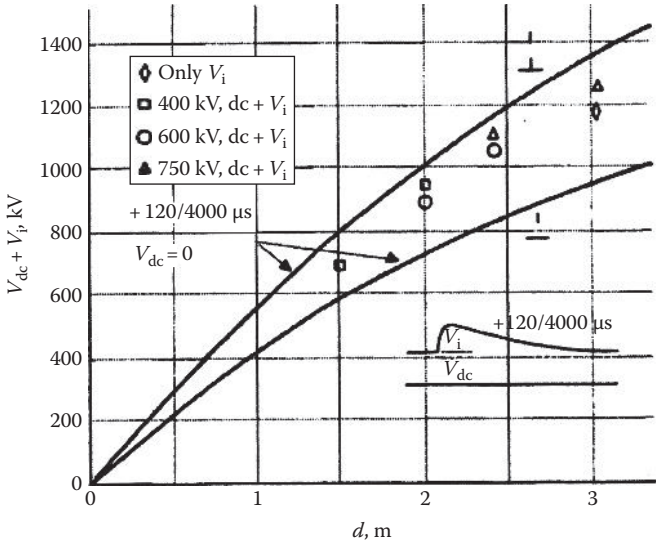


FIGURE 5.11 Comparison of breakdown characteristics of conductor–tower leg gap under composite voltages with that under switching impulse voltage and dc. (From Knudsen, N. and Iliceto, F., *IEEE Trans. Power Appar. Syst*., 89(5/6), 781, 1970.)

will not change position as the rod changes polarity due to application of the positive switching impulse. This will result in electric field enhancement in the rod vicinity, favoring positive leader inception and accordingly reduction of the composite breakdown voltage.

The increase of the composite 50% of a rod–rod gap due to a negative dc bias is more difficult to explain and is likely related to space charge formation in the vicinity of the grounded rod.

5.5.2 Modeling of Air Gap Breakdown under Composite Voltages

In this section, the application of the Rizk model of switching impulse breakdown (Rizk, 1989a,b) to a rod–plane gap under composite voltage (Rizk, 2008) will be reviewed. The analysis of leader inception and propagation in the presence of space charge due to the positive dc bias voltage and subsequent application of a positive switching impulse is quite complex. Simplifying assumptions will therefore be necessary in order to make modeling at all possible.

First, consider the situation at the final jump for the base case of a positive switching impulse without dc bias voltage. For a rod–plane gap of length d, a final jump h_{fo}, the following relationship was established (Rizk, 1989a):

$$\left(\frac{1}{h_{f0}} - \frac{1}{d}\right) = \frac{E_{cr}}{V_{00}} \tag{5.34}$$

where $V_{00} = q_{\ell 0}/2\pi\varepsilon_0$, with the linear leader space charge $q_{\ell 0}$ in the range 40–50 μC/m, and E_{cr} is a critical field at the plane to ensure streamer bridging of the final jump, with E_{cr} = 180–230 kV/m.

With the leader tip potential assumed constant during propagation, the leader inception voltage, without space charge effect due to the bias voltage, will be expressed as

$$U_{\ell c0} = h_{f0}\,E_s = \frac{(E_s/E_{cr})\,V_{00}}{1 + (V_{00}/E_{cr})/d} \tag{5.35}$$

with E_s is the minimum positive streamer gradient taken as 400 kV/m.

If a positive dc voltage is applied to the rod and for levels above the corona inception voltage V_{ci}, positive space charge will not only form in the rod vicinity but will extend to reach the ground plane. The effect of such space charge will be to

1. Reduce the electric field in the rod vicinity, impeding streamer formation and leader onset
2. Increase the electric field at the ground plane by a component E_{sc}

In the presence of space charge due to the bias voltage, the leader inception voltage will assume the higher value $U_{\ell c}$. The linear leader charge q_ℓ may be related to the original value $q_{\ell 0}$ by

$$q_\ell = q_{\ell 0} \left(\frac{U_{\ell c}}{U_{\ell c0}} \right) \tag{5.36}$$

At the final jump, Equation 5.34 will be modified to read

$$V_0 \left(\frac{1}{h_f} \right) - \frac{1}{d} + E_{sc} = E_{cr} \tag{5.37}$$

where
$V_0 = q_\ell / 2\pi\varepsilon_0$
E_{sc} is the space charge field at the ground plane
h_f is the final jump, in the presence of space charge due to the bias voltage

In Equation 5.21, we substitute

$$h_f = \frac{U_{\ell c}}{E_s} \quad \text{and} \quad V_0 = V_{00} \left(\frac{U_{\ell c}}{U_{\ell c0}} \right)$$

It can be shown that

$$U_{\ell c} = U_{\ell c0} + \frac{U_{\ell c0}}{V_{00}} \left(E_{sc} \right) d \tag{5.38}$$

The only unknown in the right-hand side of Equation 5.38 is the space charge field E_{sc} at the ground plane. Unfortunately, analytical determination of E_{sc} in a rod–plane gap will be extremely difficult, if at all possible. A relevant configuration of theoretical interest for which an analytical solution is possible is that of a concentric small sphere–large sphere gap. Let the radius of the small sphere be r_1 and that of the large sphere be r_2 with $r_2 >> r_1$ and $d = r_2 - r_1 \cong r_2$. The applied voltage is designated V_{dc} and the corona inception voltage V_{ci}.

The solution of Poisson and the charge continuity equations gives the following approximate expression for the corona current:

$$i = \frac{3\pi\varepsilon_0 \mu V_{dc} (V_{dc} - V_{ci})}{2r_2} \tag{5.39}$$

with μ the mobility of positive ions: 1.5×10^{-4} m^2/V·s.

This is related to the space charge field $E(r)$ at any radial distance $r >> r_1$ by

$$E(r) = \sqrt{\frac{i}{6\pi\varepsilon_0 \mu r}} \tag{5.40}$$

Substituting for i from Equation 5.39 in Equation 5.40, the space charge field E_{sc} at $r = r_2 = d$ can be expressed as

$$E_{sc} = \frac{1}{2d}\sqrt{V_{dc}(V_{dc} - V_{ci})} \tag{5.41}$$

For the much more complex case of a rod–plane gap, we will assume

$$E_{sc} = \frac{\alpha}{d}\sqrt{V_{dc}(V_{dc} - V_{ci})} \tag{5.42}$$

where α is a constant to be determined from experiment. This will also allow validation of the aforementioned assumption. Substituting from Equation 5.42 in Equation 5.38,

$$U_{\ell c} = U_{\ell co}\left[1 + \frac{\alpha}{V_{00}}\sqrt{V_{dc}(V_{dc} - V_{ci})}\right] \tag{5.43}$$

Following Rizk (1989a) and Equation 5.25 earlier, the leader length ℓ_z at the final jump

$$\ell_z = d - \frac{U_{\ell c}}{E_s} \tag{5.44}$$

The leader voltage drop ΔU_z can be determined from Rizk (1989a) and Equation 5.24 earlier:

$$\Delta U_z = 50\ell_z + 37.5\ln(8 - 7e^{-1.33\ell_z}) \quad \text{(kV, m)} \tag{5.45}$$

from which the minimum breakdown voltage U_b is expressed as follows (Carrara and Thione, 1976; Rizk, 1989a) and as in Equation 5.26:

$$U_b = U_{\ell c} + \Delta U_z \tag{5.46}$$

and the 50% breakdown voltage as in Equation 5.27:

$$U_{50} = \frac{U_b}{1 - 3\sigma} \tag{5.47}$$

with the standard deviation σ in per unit of U_{50} normally taken as 0.05.

From the tests by Knudsen and Ilicato (1970) on a 3 m rod–plane gap, with V_{dc} = 750 kV, U_{50} determined from the Rizk model matched the experimental results for α = 0.35.

In Figure 5.12, the model findings are compared with the results of Watanabe on a rod–plane gap with a wide range of gap spacings with V_{dc} = 400 kV. The agreement is excellent and justifies the assumption

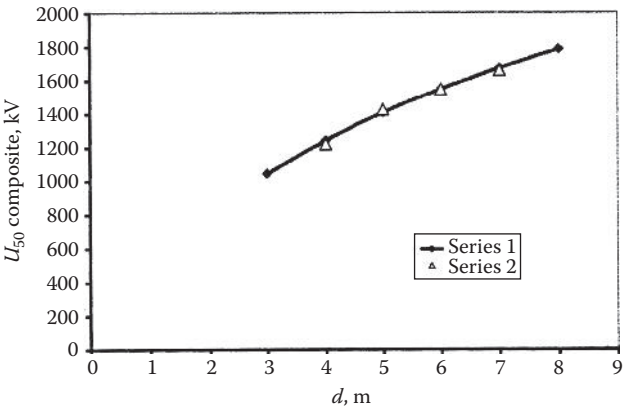


FIGURE 5.12 Variation of 50% breakdown voltage characteristics of a rod–plane configuration under composite voltage, with V_{dc} = 400 kV. S1: Rizk model. S2: measurement. (From Watanabe, Y., *IEEE Trans. Power Appar. Syst.*, 87(4), 964, 1968.)

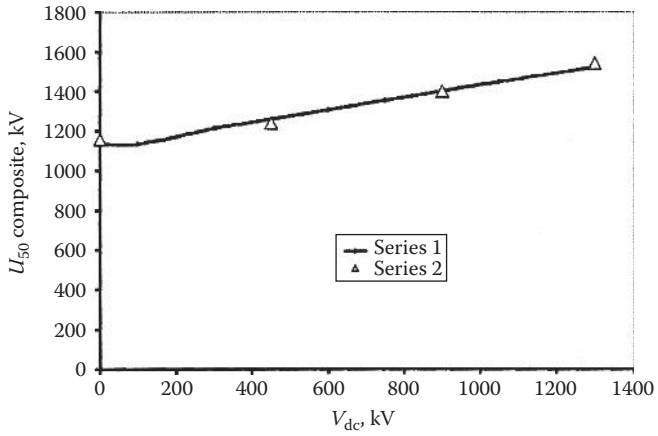


FIGURE 5.13 Variation of U_{50} of a 4 m rod–plane gap with dc bias under composite stress. S1: Rizk model. S2: measurement. (From Electric Power Research Institute, Bipolar HVDC transmission system study between ± 600 kV and ± 1200 kV: Insulation studies, EPRI report EL-963, 1979.)

underlying Equation 5.42 earlier. In Figure 5.13, the model findings are also compared with composite voltage tests (EPRI EL-963, 1979) on a 4 m rod–plane gap, with the dc bias voltage in the extremely wide range of 0–1300 kV. The agreement is extremely satisfactory.

5.6 AC Breakdown of Long Air Gaps

5.6.1 Breakdown Mechanism

It has been shown (Urbain et al., 1981) that the basic mechanism of ac breakdown of long air gaps is the same as that of a long-front switching impulse. It includes the onset of first and subsequent coronas, leader inception and propagation, with associated pauses, restrikes, and then final jump. It was shown that the positive half cycle of a 50 Hz, with 750 kV_{rms} (1061 kV_{peak}), is very close to a 3.3/14.0 ms impulse, with a peak of 1022 kV.

It was earlier shown (Rizk, 1960) that for rod–plane gaps of length up to 1 m, the 50% dry breakdown voltage of a positive power frequency half-cycle impulse was only slightly lower than the corresponding value from a gradual rise ac test. This demonstrates that under such test conditions, accumulated space charge generated due to the extended duration of the ac test had a very limited effect on the breakdown voltage. On the other hand, for gaps up to 4 m and under fog conditions, it has been shown that space charge effects could play a significant role on ac breakdown (Rizk, 1981a).

5.6.2 AC Breakdown Test Procedures

Two ac test procedures are described in IEC Standard 60060-1. The first, commonly known as the 1 min test, comprises a withstand test in which, above 75% of the test voltage U, the rate of rise is about 0.02 U/s, with the voltage subsequently maintained at U for 60 s. In the second procedure, known as the disruptive discharge test, the voltage is applied and raised continuously until a disruptive discharge occurs on the test object. For long air gaps, the statistical implications of such test procedure will be clarified based on Rizk (1960, 1981b). Let the cumulative bivariate breakdown probability $P(u,t)$, where u is the applied voltage and t the test duration, be expressed as

$$P(u,t) = 1 - \exp\left[-\int_0^t h(u,t)\,dt\right] \tag{5.48}$$

where $h(u,t)$ is termed a hazard function.

Of particular interest for air gap breakdown is the assumption that the hazard function $h(u,t)$ is time independent, which applies if the effect of space charge accumulation from one power frequency voltage cycle to another has insignificant effect on breakdown. Furthermore, if the hazard function is defined above a threshold voltage u_0, reached at time t_0, Equation 5.48 could be expressed as

$$P(u,t) = 1 - \exp\left[-\int_{t_0}^{t} h(u)\,\mathrm{d}t\right] \tag{5.49}$$

For a Weibull-type probability distribution, $h(u)$ can be expressed as

$$h(u) = \left[\frac{u - u_0}{u_1}\right]^k \tag{5.50}$$

where

u_1 is the parameter characterizing a test with unit-time duration
k is a constant

Consider a ramp voltage test with

$$u = \lambda t \tag{5.51}$$

where λ is the rate of rise of the applied voltage substituting in Equation 5.49:

$$P(u,t) = 1 - \exp\left[-\int_{u_0}^{u} h(u)\frac{\mathrm{d}u}{\lambda}\right] \tag{5.52}$$

which using Equation 5.50 results in a 50% breakdown voltage

$$u_{50} = u_0 + A u_1^{k/(k+1)} \lambda^{1/(k+1)} \tag{5.53}$$

with

$$A = [(k+1)\ln 2]^{1/(k+1)}, \tag{5.54}$$

which expresses the dependence of the 50% breakdown voltage on the rate of rise of the ramp voltage. From ramp tests (Rizk et al., 1981b) on a 3 m rod–plane gap in dry conditions, it was determined that $u_0 = 706\ \mathrm{kV_{rms}}$. Figure 5.14 shows variation of U_{50} with the rate of voltage rise in the range of 4–50 kV/s resulting in a change of U_{50} from 788 to 830 kV.

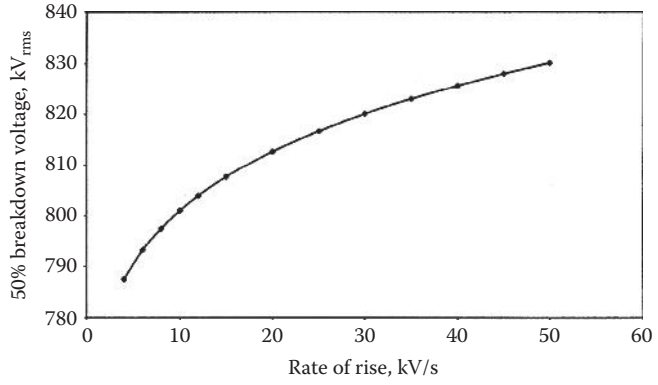


FIGURE 5.14 Effect of rate of rise on $U_{50\%}$ ac breakdown voltage of 3 m rod–plane air gap in a disruptive discharge test.

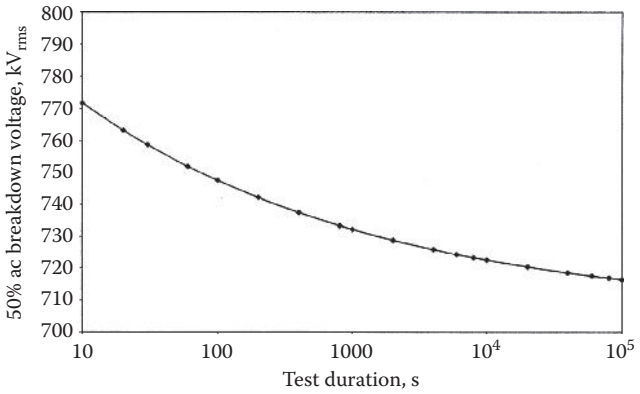


FIGURE 5.15 Variations of the $U_{50\%}$ ac breakdown voltage of a 3 m rod–plane gap with test duration.

For a constant voltage test, using Equation 5.52, it follows that

$$P(u,t) = 1 - \exp\left[-h(u)(t - t_0)\right] \tag{5.55}$$

with $h(u)$ determined from Equation 5.50 and $t - t_0$ taken as the test duration T; the dependence of U_{50} on T can be expressed as

$$u_{50} = u_0 + (\ln 2)^{1/k}\, u_1 T^{-1/k} \tag{5.56}$$

Figure 5.15 shows variation of the 50% ac breakdown voltage of a 3 m rod–plane gap with test duration as determined from Equation 5.56, with the same parameters as earlier. The findings of Figures 5.14 and 5.15 agree with experimental results of a 2.8 m rod–plane gap reported in Lalot and Gallet (1979).

5.6.3 AC Breakdown Test Data

A collection of 50% ac breakdown voltage data on different air gap configurations is given in Pigini et al. (1992). An empirical formula for the dependence of the 50% ac breakdown voltage U_{50} on gap spacing d, under dry conditions, was given as

$$U_{50} = 750 \ln(1 + 0.55 d^{1.2}) \quad (\mathrm{kV_{rms}}, \mathrm{m}) \tag{5.57}$$

for rod–plane gaps with $d > 2$ m.

Figure 5.16 shows a comparison between formula 5.57 and experimental results from Rizk (1981a), Sirotinski (1955b), and Obenaus (1965).

For configurations other than a rod–plane, U_{50} can be related to $U_{50\mathrm{r-p}}$ by an ac gap factor K_{ac}:

$$U_{50} = K_{\mathrm{ac}}\, U_{50\,\mathrm{r-p}} \tag{5.58}$$

where, for any gap d, K_{ac} can, under dry conditions, be approximately determined from (Pigini et al., 1992)

$$K_{\mathrm{ac}} = 1.35 K_{\mathrm{g}} - 0.35 K_{\mathrm{g}}^2 \tag{5.59}$$

where K_{g} is the gap factor under switching impulse voltage.

For example, with a 3 m rod–rod gap having $K_{\mathrm{g}} = 1.3$, K_{ac} is determined at $K_{\mathrm{ac}} = 1.16$. Substituting in Equation 5.57, U_{50} is found as 974 $\mathrm{kV_{rms}}$.

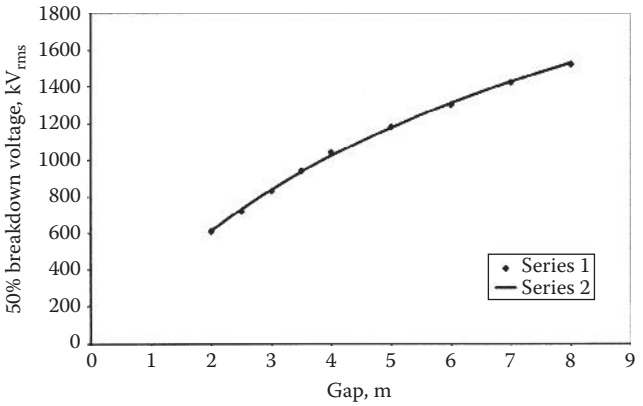


FIGURE 5.16 Variations of the $U_{50\%}$ ac breakdown voltage of rod–plane air gap with gap spacing at standard atmospheric conditions. S1: Experimental results from Rizk (1981), Sirotinski (1955b), and Obenaus (1965). S2: Empirical formula (Pigini et al. 1992).

5.7 Altitude Effect on Air Gap Breakdown

There is a large volume of research work confirming that for a streamer-type breakdown mechanism, associated with lightning impulses of both polarities, power frequency voltage, and dc, the breakdown voltage is proportional to the relative air density δ (Peek, 1914; Strigel, 1955; Philips et al., 1967; Harada et al., 1970). The relative air density δ is related to the altitude H, m, by the relationship (IEC 60071-2, 1996)

$$\delta = e^{-(H/8150)} \tag{5.60}$$

Other formulae are quoted in the literature (Rudakova and Tikhodev, 1989) but agree closely with Equation 5.60 within practical ranges of δ.

For positive switching impulses, on the other hand, it has been found that the breakdown voltage V_a of an air gap at high altitude can be related to the breakdown voltage V_s at sea level (Philips et al., 1967; Pigini et al., 1985; Ramirez et al., 1990) by an air density correction factor K_d:

$$V_a = K_d \, V_s \tag{5.61}$$

with

$$K_d = \delta^n \tag{5.62}$$

where the exponent n varies with the gap length and proximity to ground plane.

For a gap length d, a parameter G was introduced expressing the ratio between the 50% breakdown voltage U_{50} under positive switching impulse to the corresponding breakdown voltage by the streamer mechanism characterized by a 50% gradient E_s taken as 500 kV/m at sea level. It follows that at sea level, G_0 is given by

$$G_0 = \frac{U_{50}}{500d} \quad \text{(kV, m)} \tag{5.63}$$

It was found from the test results that n in Equation 5.62 can be expressed as (Pigini et al., 1985)

$$n = 1.25G_0(G_0 - 0.2) \quad \text{for} \quad 0.3 \leq G_0 \leq 1 \tag{5.64}$$

In IEC Standard 60060-1, the correction was made in terms of

$$G = \frac{U_{50}}{500\delta^k d} \tag{5.65}$$

when no humidity correction is introduced, and G is substituted for G_0 in Equation 5.63.

Modeling of the effect of air density on positive switching impulse breakdown of long air gaps was undertaken by Rizk (1992) and offers a physically based alternative approach for determination of air clearances of transmission lines at high altitudes. It was shown that for a rod-type gap, Equation 5.32 can be generalized at a relative air density δ to take the form

$$U_{\ell c}(\delta) = \frac{1556}{1 + \dfrac{7.78}{\delta \Diamond R}} \quad \text{(kV, m)} \tag{5.66}$$

Similarly, for a conductor-type configuration, Equation 5.33 can be generalized as

$$U_{\ell c}(\delta) = \frac{2247}{1 + \dfrac{F}{\delta \Diamond R}} \quad \text{(kV, m)} \tag{5.67}$$

The length of the final jump $\ell_s(\delta)$ or $h_f(\delta)$ can be determined from

$$\ell_s(\delta) = \frac{U_{\ell c}(\delta)}{\delta E_s} \tag{5.68}$$

from which the leader length $\ell_z(\delta)$ is obtained as

$$\ell_z(\delta) = d - \ell_s(\delta) \tag{5.69}$$

The ultimate leader voltage gradient E_∞ was assumed to be independent of relative air density so that the leader voltage drop ΔU_z can practically be obtained from Equation 5.24 using the proper leader length $\ell_z(\delta)$, although rigorously speaking E_i should be replaced by δE_i.

The minimum breakdown voltage U_b and the 50% value U_{50} are to be obtained from Equations 5.26 and 5.27 in the preceding text. Figure 5.17 shows the relationship between the relative length of final jump of a rod–plane gap and the parameter G_o as determined by the experiment (Pigini et al., 1985; Ramirez et al., 1990) (References [9] and [11] in the figure) and model findings. The agreement is satisfactory. Figure 5.18 shows the dependence of the air density correction factor K_d on the gap length of a rod–plane gap, for different relative air density values. Again, the agreement between the experiments (Ramirez et al., 1990) and the model is satisfactory. Finally, Table 5.2 shows comparison of experimental and Rizk model results of the air density correction factor K_d for different gap configurations and different altitudes. The agreement is again very satisfactory.

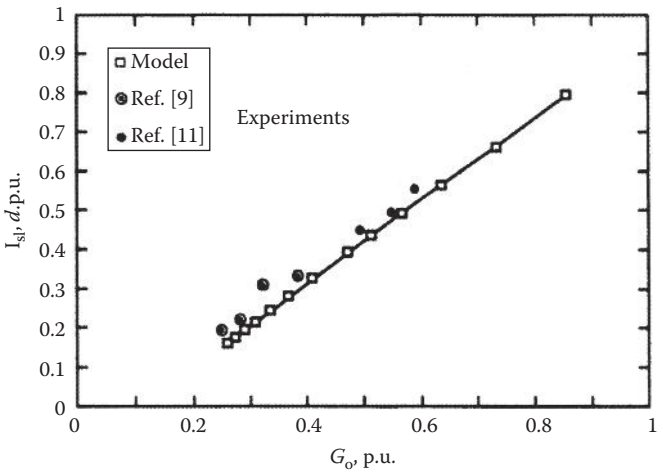


FIGURE 5.17 Variation of the relative length of the final jump of a rod–plane with parameters G_o. References [9] and [11] in the figure correspond to Pigini et al. (1985) and Ramirez et al. (1990).

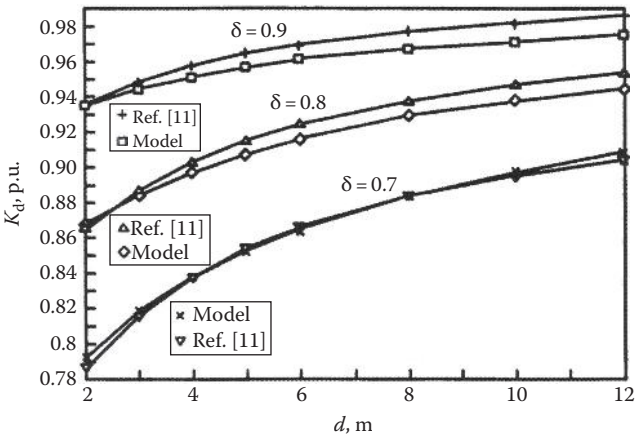


FIGURE 5.18 Variation of the air density correction factor K_d with the length of a rod–plane gap, for different levels of relative air density. Ref. [11] in the figure corresponds to Ramirez et al. (1990).

TABLE 5.2

Comparison between Computed and Measured K_d Values for Different Configurations

Source	Configuration	Gap Parameters, m	δ, p.u.	K_d, p.u.	
				Measured	Model
Philips et al. (1967)	Rod–plane	$d = 5.11$		0.84	0.85
	Rod–rod	$d = 3.66$		0.84	0.86
		$h = 3.66$	0.70		
	Conductor–plane	$d = 3.77$		0.83	0.85
		$a = 0.02$			
Harada et al. (1970)	Rod–plane	$d = 2$		0.87	0.88
		$d = 3$	0.82	0.88	0.90
		$d = 4$		0.93	0.91
		$d = 6$		0.96	0.93
	Rod–rod	$d = 3$	0.82		
		$h = 6$		0.91	0.92

5.8 Humidity Effects on Air Gap Breakdown

An extensive review of the effect of absolute humidity on some basic parameters of air discharge was reported by Busch (1982). Beside the familiar effect on formation of negative ions, the following effects of H_2O molecules in air were stressed:

1. High humidity has a stabilizing effect on negative ions, leading to increased mean lifetime τ_n, which, as previously mentioned, is significant for the determination of the statistical time lag t_s.
2. High humidity results in increased photoabsorption coefficient, a significant parameter in the photoionization process.
3. Humidity was found to have insignificant effect on the critical field E_{crit} at which the ionization coefficient α and the attachment coefficient η coincide and above which effective ionization becomes possible.

5.8.1 Effect of Humidity with Special Reference to Streamer Breakdown

Several investigations have already confirmed that absolute humidity could have a significant effect on streamer breakdown of air gaps (Phelps and Griffiths, 1976; Allen and Dring, 1984; Geldenhuys, 1987; Allen and Boutlandj, 1991). In uniform field gaps, it was found that the electric field E_s required for continuous streamer propagation increases linearly with absolute humidity h_a, taking the form

$$E_s(h_a) = E_s(11)\left[1 + \frac{\varepsilon}{100}(h_a - 11)\right] \tag{5.70}$$

with $E_s(11)$ being the reference value at a standard humidity of 11 g/m^3 and ε is a constant assuming values around 2 for uniform field gaps.

For nonuniform field gaps, Equation 5.70 can be used to express the mean streamer gradient, which for positive polarity results in ε values in the range of 1.0–1.4. More recently, it has been generally accepted that in Equation 5.70, h_a should be replaced by h_a/δ (Zheng and Yang, 1989) so that

$$E_s(h_a) = E_s(11)\left[1 + \frac{\varepsilon}{100}\left(\frac{h_a}{\delta} - 11\right)\right] \tag{5.71}$$

where δ is the relative air density.

From a practical point of view, Equation 5.71 means that under otherwise the same conditions, humidity correction becomes more significant at higher altitudes. For negative polarity, ε was found to be significantly smaller than corresponding values under positive polarity. In IEC Publication 60060-1, First Edition, 1973, a humidity correction factor k_h was included in order to bring the air gap breakdown voltage $V(h_a)$ at absolute humidity h_a to standard conditions of V_0 at $h_a = 11$ g/m^3:

$$V(h_a) = \frac{V_0}{k_h} \tag{5.72}$$

where

$$k_h = k^w \tag{5.73}$$

with the dependence of the variable k on h_a determined from two curves: one applicable to alternating voltage and another curve, less sensitive to humidity, that applies for direct and impulse voltages. Furthermore, for rod–rod and rod–plane gaps under ac or positive switching impulses, the exponent w was taken as unity for clearances below 1 m but decreased linearly with gap spacing to reach a value of 0.4 for a 6 m gap. w was maintained constant at 0.4 for gap lengths between 6 and 10 m.

The aforementioned approach was based on a review of air density and humidity effects published in Electra in 1970 (Kucera and Liao, 1972), which summarized earlier breakdown data (Standring et al., 1963; Vlastos, 1966; Fischer, 1969; Winkelkemper and Baucke, 1969). It should be noted that in the aforementioned early edition of the standard, the exponent w in Equation 5.71 assumed different values for sphere gaps (quasiuniform field), rod–rod, and rod–plane gaps and also varied with polarity. No humidity correction ($w = 0$) was recommended for sphere gaps for all types of voltage stress nor for negative polarity dc, lightning, and switching impulses. It is also noticed that the aforementioned humidity correction procedure is rather complex, varying with the type and polarity of voltage stress, electrode configuration, and gap length. Furthermore, it was not possible to generalize the approach so that a link could be established between the correction factors and the physical breakdown mechanism.

More recently, this has become possible by more advanced research into air gap breakdown mechanism (Les Renardières Group, 1972, 1974), justified by interest in higher transmission voltages and accordingly longer air gaps, particularly under positive switching impulses. Leader inception and propagation plays a major role in positive switching impulse breakdown of long air gaps and, therefore, the humidity effect will be different from that with streamer breakdown, as demonstrated in the next section.

5.8.2 Effect of Humidity on Switching Impulse Breakdown

Figure 5.19 presents results obtained by Les Renardières Group as reported in Busch (1978) and Les Renardières Group (1977) on the dependence of the 50% positive switching impulse breakdown voltage on impulse time to crest, for 5, 10, and 14 m rod–plane gaps at different humidity levels. The familiar increase of the critical front with gap spacing is shown. With regard to humidity effects, the following observations can be made:

- For a fixed gap spacing, the critical front is significantly reduced at higher humidity.
- The effect of humidity on critical front is more substantial the longer the gap, particularly for gaps exceeding 5 m.
- The minimum 50% breakdown voltage increases with humidity, the effect being more significant for longer gaps.
- For a fixed front time, a higher humidity could result in a $U_{50\%}$ substantially higher than when the comparison is made under the relevant critical front, corresponding to each humidity level concerned.

From the test results in different laboratories, Busch (1978) proposed the following empirical formula for the dependence of the critical front t_{fc} on gap length d and absolute humidity h_a:

$$t_{fc} = k_f(d - 4.6) + 200 \quad (\text{ms, m}) \tag{5.74}$$

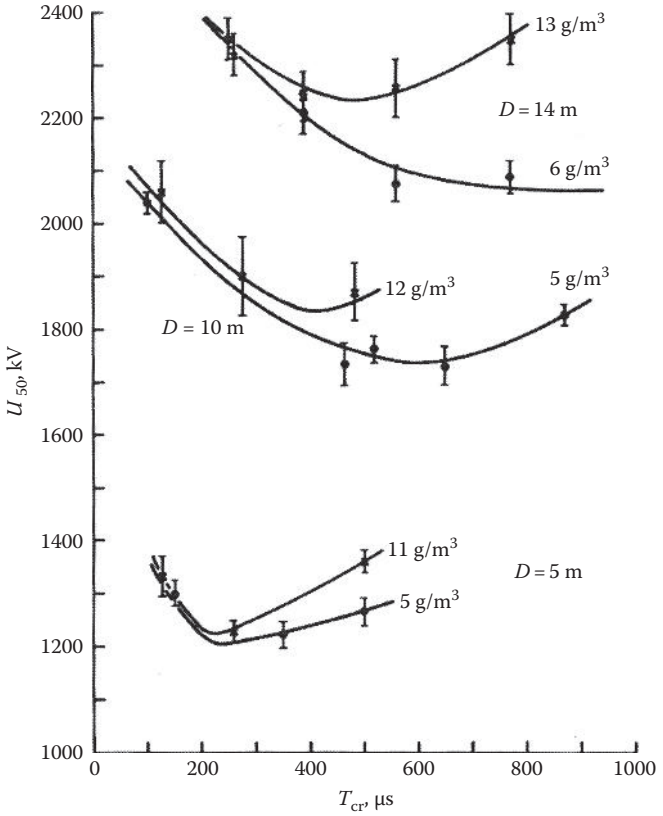


FIGURE 5.19 Switching impulse flashover characteristics for different rod–plane gap spacings and absolute humidity levels. (From Busch, W., *IEEE Trans. Power Appar. Syst*., 97(6), 2086, 1978; Busch, W., Der Einfluss der Luftfeuchtigkeit auf die Schaltspannungsfestigkeit der atmosphärishen Luft im Ultrahochspannungs bereich bei positiver Polarität, Dissertation ETH Nr. 7048, 1982.)

with

$$k_f = 83\left[1 - 0.13\left(\frac{h_a}{10}\right) + 0.083\left(\frac{h_a}{10}\right) - 0.29\left(\frac{h_a}{10}\right)^3\right] \tag{5.75}$$

For $5 < d < 15$ m and $5 < h_a < 15$ g/m^3.

For $d = 10$ m, Equations 5.74 and 5.75 yield a critical front of approximately 600 μs at $h_a = 5$ g/m^3 but only 200 μs at $h_a = 15$ g/m^3.

From measurements on switching impulse breakdown of long rod–plane gaps by Les Renardières Group (1972, 1974), several interesting effects of humidity on basic discharge parameters have been reported. It should be noted, however, that due to the statistical nature of the effects reported, sometimes, the number of tests is quite limited:

- For humidity variation in the range of 5–11 g/m^3, the mean leader speed increases slightly with humidity. Above 11 g/m^3, however, significant increase of leader speed is reported, mostly associated with sudden leader extension steps related to restrikes (Figure 5.20); the phenomenon is more prevalent for gaps above 5 m.
- The aforementioned phenomenon is associated with considerable increase in the 50% breakdown voltage, estimated from prospective peaks of the applied impulses, in the humidity range above 10 g/m^3 (Figure 5.21).
- No such effect is found in the dependence of the real (instantaneous) breakdown voltage U_b, as also shown in Figure 5.21. This is consistent with the finding that the leader inception voltage increases only slightly with humidity (Les Renardières Group, 1977).
- In a constant ambient humidity, the linear leader charge could decrease substantially with the impulse time to crest, as shown in Figure 5.22, particularly at a humidity of 12 g/m^3.
- Decrease of the critical front with humidity will act in opposition to this effect and any large variation of q_l will be inconsistent with the relatively moderate variations of the breakdown voltage and the height of the final jump or leader length l_z with humidity (Figure 5.23).
- The transition zone of humidity above 10–11 g/m^3 with considerable increase in the 50% breakdown voltage reported earlier is also associated with a shift from normal to non-Gaussian S-type probability distribution of the breakdown voltage and a peculiar behavior of the standard deviation.

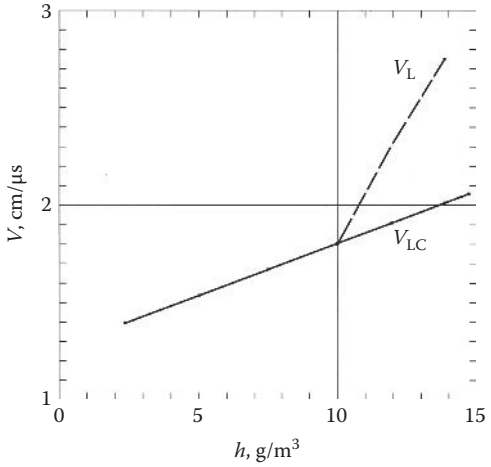


FIGURE 5.20 Variation of leader propagation speed with absolute humidity. 10 m rod–plane gap, 500/10,000 μs impulse. V_{LC}: mean leader speed during continuous propagation phase. V_L: overall mean leader speed. (From Busch, W., *IEEE Trans. Power Appar. Syst.*, 97(6), 2086, 1978; Busch, W., Der Einfluss der Luftfeuchtigkeit auf die Schaltspannungsfestigkeit der atmosphärishen Luft im Ultrahochspannungs Bereich bei positiver Polarität, Dissertation ETH Nr. 7048, Zurich, Switzerland, 1982.)

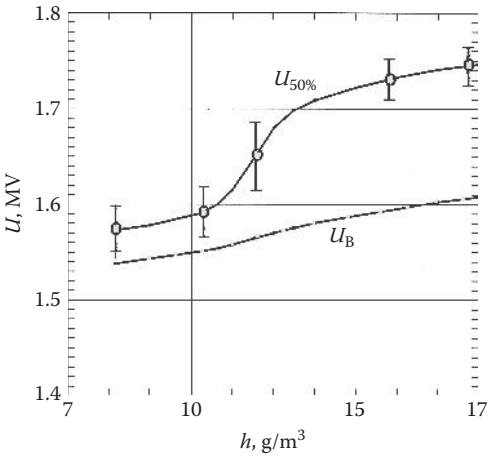


FIGURE 5.21 Variation of switching impulse breakdown voltage with absolute humidity. 8 m rod–plane gap, 390/3200 μs impulse. U_{50}: 50% breakdown voltage based on prospective crest value. U_b: average actual breakdown voltage. (From Busch, W., *IEEE Trans. Power Appar. Syst*., 97(6), 2086, 1978; Busch, W., Der Einfluss der Luftfeuchtigkeit auf die Schaltspannungsfestigkeit der atmosphärishen Luft im Ultrahochspannungs Bereich bei positiver Polarität, Dissertation ETH Nr. 7048, Zurich, Switzerland, 1982.)

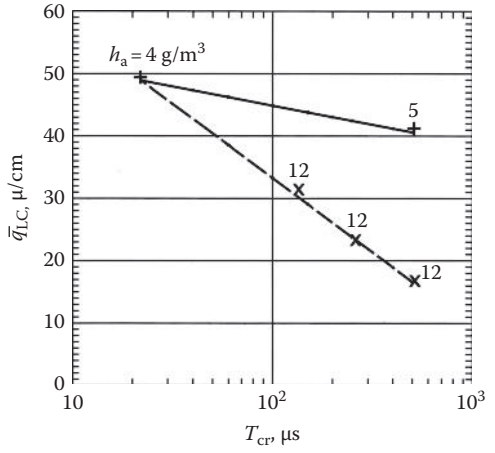


FIGURE 5.22 Variation of leader charge per unit length with impulse time to crest of a 10 m rod–plane gap, for two values of absolute humidity. (From Busch, W., *IEEE Trans. Power Appar. Syst*., 97(6), 2086, 1978; Busch, W., Der Einfluss der Luftfeuchtigkeit auf die Schaltspannungsfestigkeit der atmosphärishen Luft im Ultrahochspannungs bereich bei positiver Polarität, Dissertation ETH Nr. 7048, 1982.)

5.8.3 More Recent Approaches to Humidity Corrections

In the more recent version of IEC Standard 60060-1 (1989b), the humidity correction procedure is similar to that recommended for relative air density δ reported earlier. For a gap of length d, a parameter G is determined from

$$G = \frac{U_{50}}{500\,\delta k d} \quad \text{(kV,m)} \tag{5.76}$$

The exponent w in Equation 5.73 is determined from

$$w = 1.25G(G - 0.2) \quad \text{for} \quad 0.2 \leq G \leq 1.0 \tag{5.77}$$

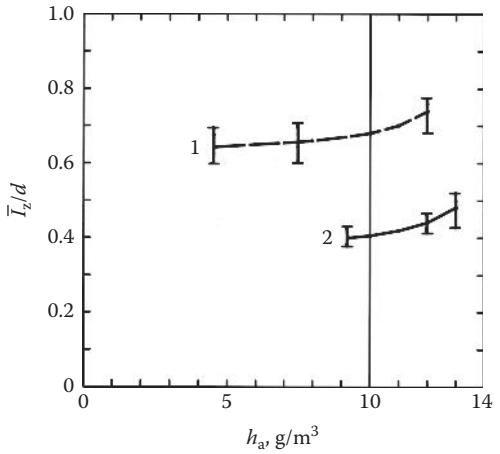


FIGURE 5.23 Variation of mean relative axial leader length with absolute humidity. (1) 10 m rod–plane gap, 500/10,000 μs impulse. (2) 4 m conductor (100 mm diameter) rod–plane gap, 190/10,000 μs impulse. (From Busch, W., *IEEE Trans. Power Appar. Syst*., 97(6), 2086, 1978; Busch, W., Der Einfluss der Luftfeuchtigkeit auf die Schaltspannungsfestigkeit der atmosphärishen Luft im Ultrahochspannungs Bereich bei positiver Polarität, Dissertation ETH Nr. 7048, Zurich, Switzerland, 1982.)

and

$$w = 1.25G(2 - G) \quad \text{for} \quad 1.2 \le G \le 2.0 \tag{5.78}$$

A value G_0 corresponds to the standard conditions $\delta = 1$ and $k = 1$. IEC 60060-1 of 1989 gave the following expressions for k in Equation 5.73:

For impulse voltage and $1 \le h_a/\delta \le 15$ g/m^3,

$$k = 1 + 0.01\left(\frac{h_a}{d}\right) - 11 \tag{5.79}$$

For alternating voltage and $1 \le h_a/\delta \le 15$ g/m^3,

$$k = 1 + 0.012\left(\frac{h_a}{d}\right) - 11 \tag{5.80}$$

and for direct voltage $1 \le h_a/\delta \le 13$ g/m^3,

$$k = 1 + 0.014\left(\frac{h_a}{d}\right) - 11 \tag{5.81}$$

within the above ranges of h_a/δ, the humidity correction factor k_h of Equation 5.73 could be approximated by

$$k_h = 1 + \frac{w}{100}\left(\frac{h_a}{d}\right) - 11 \tag{5.82}$$

with the corresponding humidity correction k_{hg} in % per g/m^3 at $\delta = 1$ given by

$k_{hg} = w$ %/(g/m^3), for impulse voltage
$k_{hg} = 1.2\ w$ %/(g/m^3), for alternating voltage
$k_{hg} = 1.4\ w$ %/(g/m^3), for direct voltage

Table 5.3 (Busch, 1978) presents a comparison between humidity correction factor k_{hg} for rod–plane gaps under switching impulse voltages, based on U_{50}, as obtained from tests in Busch (1978) and Aihara et al. (1978) and as obtained from IEC 60060-1 (1989). It is shown that, in general, correction factors from Busch (1978) are higher than those obtained from Aihara et al. (1978) or from

TABLE 5.3

Humidity Correction Coefficient for Rod–Plane Gaps under Switching Impulses (Busch, 1978) δ = 1

	k_{hg}, %/(g/m³)					
	$5 < h_a < 11$ g/m³			$11 < h_a < 15$ g/m³		
d, m	Busch (1978)	Aihara (1978)	IEC 60060-1 (1973, Edit.)	Busch (1978)	Aihara (1978)	IEC 60060-1 (1973)
8	0.52	0.25	0.33	2.10	0.25	0.33
10	0.54	0.24	0.33	2.13	0.24	0.33
14	0.69	0.23	—	2.32	0.23	—

IEC Standard. In particular, for such large gaps and for the humidity range above 11 g/m³, associated with frequent restrikes, reilluminations, and sudden leader extensions, the disagreements between correction factors from different sources become excessive. It is in this range that, as mentioned earlier, the breakdown probability curve shifts to S-type and the standard deviation becomes irregular. Such complex behavior, however, is limited to U_{50} determined from prospective peaks of the applied impulses, while as mentioned earlier, the real breakdown voltage U_b is stable, with no transition zone and standard deviation not exceeding 2%. A way out of the previously mentioned excessive discrepancies, particularly in the range above 11 g/m³, therefore, is to carry out the humidity correction, not for U_{50} but at a withstand level associated with low breakdown probability, which after all is the final objective of insulation design.

5.8.4 Modeling of Humidity Effects on Switching Impulse Breakdown

In this section, the Rizk model for positive switching impulse breakdown of long air gaps (Rizk, 1989a,b) will be extended in order to include humidity effects. It should first be noted that the analysis applies specifically to critical impulse breakdown voltage corresponding to the critical front for each gap length and humidity level concerned. Furthermore, corrections refer to the minimum breakdown voltage U_b and not to the 50% value U_{50}, due to the irregularities mentioned previously. The following basic assumptions are introduced:

- The dependence of the mean streamer gradient E_s and the critical (stability) field for streamer extension in nonuniform fields E_{cr} on absolute humidity h_a can be determined from Equation 5.71.
- The critical field E_c at the leader tip, which bears some analogy to a corona onset gradient, is taken as practically independent of humidity. Actually, what is of interest for the model is the product of equivalent radius r_e at the leader tip and E_c (Rizk, 1989b). This product was assumed independent of humidity at continuous leader inception.

Under the previously mentioned assumptions, it follows that under critical impulse front for the gap length and humidity concerned, the linear leader charge q_l becomes practically independent of humidity. This does not contradict the experimental fact that, for a fixed impulse time to crest, q_l decreases substantially with humidity (Busch, 1982), noting that the critical front decreases substantially with increased humidity.

The aforementioned assumptions result in the following general expressions for the continuous positive leader inception voltage, including both relative air density and humidity effects:

For a rod-type gap,

$$U_{lc} = \frac{1556}{1 + \dfrac{7.78}{d\sqrt{k}\sqrt{R}}} \quad \text{(kV,m)} \tag{5.83}$$

with R = a geometric parameter, which, in general, can be determined by charge simulation and which can be used to determine the gap factor (Rizk, 1989b), δ = relative air density, and

$$k = 1 + 0.01\left(\frac{h_a}{d} - 11\right) \tag{5.84}$$

For a rod–plane gap $R = 2d$, Equation 5.83 reduces to

$$U_{lc} = \frac{1556}{1 + \dfrac{3.89}{k\sqrt{d}}} \tag{5.85}$$

Similarly, for a conductor-type gap,

$$U_{lc} = \frac{2247}{1 + \dfrac{F}{k\sqrt{R}}} \quad \text{(kV,m)} \tag{5.86}$$

with $F = (10.30 - 10.98 \ln a)/(\ln (2h/a))$, a is the conductor radius, h is the conductor height

For a conductor–plane gap, this reduces to

$$U_{lc} = \frac{2247}{1 + \dfrac{5.15 - 5.49 \ln a}{k\sqrt{d}\ln(2d/a)}} \quad \text{(kV,m)} \tag{5.87}$$

The final jump h_f is determined from

$$h_f = d - \frac{U_{lc}}{k E_s} \tag{5.88}$$

with the minimum leader length l_z:

$$l_z = d - h_f \tag{5.89}$$

Taking the leader voltage drop U_z as (Rizk, 1989a)

$$U_z = l_z E_\bullet + x_0 E_\bullet \ln\frac{E_i}{E_\bullet} - \frac{E_i - E_\bullet}{E_\bullet}\exp\left(-\frac{l_z}{x_0}\right) \tag{5.90}$$

where E_∞ is taken as 50 kV/m at 1 A, independent of atmospheric conditions; E_i = 400 δ·k kV/m; θ = 50 μs; and $x_0 = \theta v$, with v is the mean continuous leader speed, which slightly increases with humidity, an effect that will have insignificant effect on U_z.

Figure 5.24 shows model results for variation of the continuous critical leader inception voltage, under critical from switching impulses, for an 8 m rod–plane gap with absolute humidity in the range of 5–17 g/m^3. It is shown that the continuous critical leader inception voltage varies from 1047 to 1087 kV for the wide humidity range investigated.

Figure 5.25 shows model findings of the decrease of the final jump of the 8 m rod–plane gap with humidity from 2.62 to 2.41 m in the same range. A corresponding increase in the leader length l_z will result. Figure 5.26 shows corresponding variation of the minimum breakdown voltage U_b with humidity for the 8 m rod–plane gap. U_b values from experimental values of actual breakdown values (Les Renardières Group, 1977), obtained as $U_{50} - 3\sigma$, with σ = 2% are also indicated. The agreement between model and experiment is satisfactory.

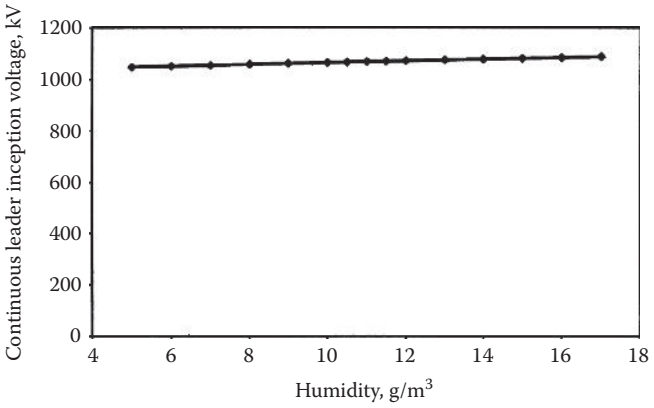


FIGURE 5.24 Variation of the continuous leader inception voltage of an 8 m rod–plane gap with humidity under condition of critical switching impulse according to the Rizk model.

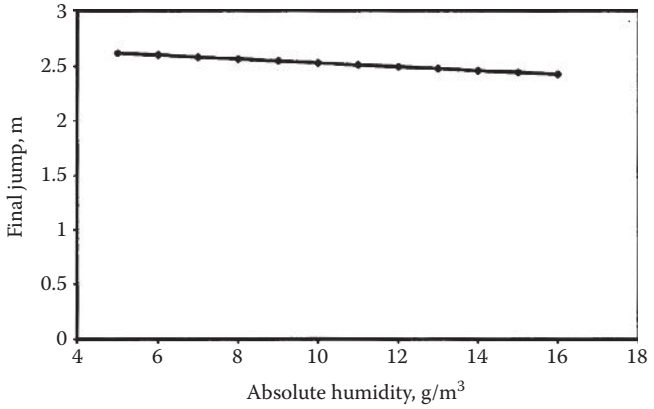


FIGURE 5.25 Variations of the length of the final jump with humidity, rod–plane gap. d = 8 m, according to the Rizk model.

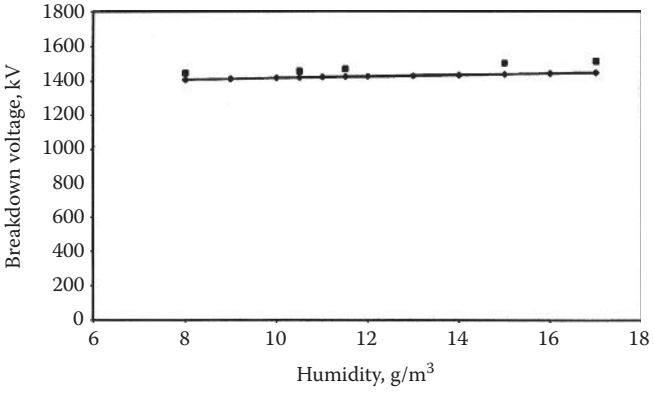


FIGURE 5.26 Variations of the switching impulse breakdown voltage with absolute humidity. Lower: U_b, Rizk model. Upper: experimental results. (From Geldenhuys, H.J., The breakdown voltage of air in rod-plane gap over a practical range of air density and humidity, in: *5th International Symposium on High Voltage Engineering*, Braunschweig, Germany, 1987, Paper 14.02).

5.8.5 Comparison of Correction Factors

Figure 5.27 shows a comparison between variation of the humidity correction factor k_h with humidity for a 3 m rod–plane gap under critical switching impulses as obtained from the present work and using IEC Standard 60060-1 (1989b). The agreement is very satisfactory, in particular since the gap concerned is within the range for which there is ample experimental results, as indicated in the previous review by Busch (1982).

Table 5.4 includes a comparison of humidity correction factors for switching impulse breakdown voltage obtained from the present model and results from Busch (1978), Aihara et al. (1978), and IEC 60-1 (1989), for rod–plane gaps in the range 2–14 m.

The following are noted:

- Model results obtained from the minimum breakdown voltage U_b agree reasonably well with Aihara (Aihara et al., 1978) and with IEC Standards (IEC 60060-1, 1989) for gaps up to 5 m. It is noted that it is in this range that the application of IEC Standard has been recommended (CIGRE 33.07, 1992).
- For gaps of 8 m and above, and humidity in the range of $5 < h_a < 11$ g/m^3, the present model agrees well with recommendations of Aihara (Aihara et al., 1978) based on the review of experimental results. On the other hand, IEC Standard corrections are generally on the low side, while those of Busch (1978, 1982) are on the high side.
- The discrepancies between the different approaches are exacerbated above 8 m gap for the humidity range of $11 < h_a < 15$ g/m^3. The low corrections in IEC Standard 60060-1 could probably be explained by the fact that it is based on experimental results for gaps in the 5 m

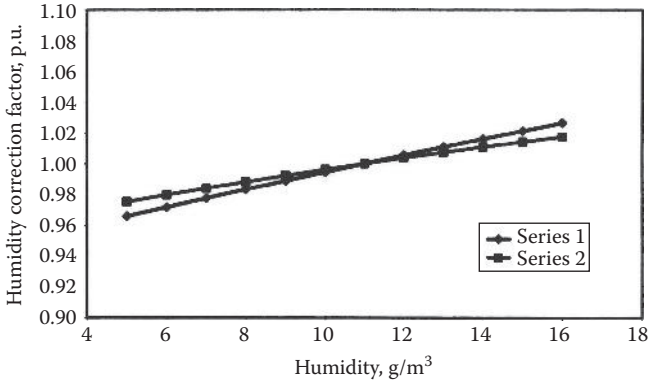


FIGURE 5.27 Variation of positive switching impulse humidity correction factor with absolute humidity, rod–plane gap: $d = 3$ m. S1: Rizk model. S2: IEC 60060-1 (1989).

TABLE 5.4

Comparison of Humidity Correction k_{hg} for Switching Impulse Breakdown Voltage of Rod–Plane Gaps δ = 1

	k_{hg}, %/(g/m^3)							
	$5 < h_a < 11$ g/m^3				$11 < h_a < 15$ g/m^3			
d, m	Model	Aihara	Busch	IEC	Model	Aihara	Busch	IEC
2	0.66	0.40	—	0.55	0.66	0.40	—	0.53
3	0.56	0.35	—	0.39	0.55	0.35	—	0.37
5	0.43	0.31	—	0.23	0.42	0.31	—	0.21
8	0.33	0.25	0.52	0.23	0.32	0.25	2.10	0.21
10	0.28	0.24	0.54	0.09	0.28	0.24	2.13	0.08
14	0.22	0.23	0.69	0.05	0.22	0.23	2.32	0.04

range (CIGRE 33.07, 1992). The high corrections recommended in Busch (1978) can be explained by the fact that they are based on prospective peak measurements of U_{50}, which, as mentioned earlier, is quite sensitive to restrikes with associated sudden extensions of the leader discharge.

5.8.6 Further Application of Generalized Correction Approach

In this section, the generalized approach presented earlier will first be used to gaps other than a rod–plane. Furthermore, the situation of combined air density and humidity correction will be addressed. As a first example, a rod–rod gap is considered. The gap $d = 3$ m and the height of the ground rod $h = 3$ m. From Rizk (1989b), $R = 11.2$ m, with the gap factor K_g calculated from the model as 1.33. The relative air density $\delta = 1$. Figure 5.28 shows a comparison between the humidity correction factor as determined by the model and from IEC Standard 60060-1 (1989). As a second example, a conductor–rod gap is considered, with a gap $d = 4$ m, height of ground rod $h = 4$ m, and conductor radius $a = 0.05$ m. Results are shown in Figure 5.29.

The agreement between the model and IEC standards is reasonably good for the gap range for which most experimental results are available. However, one limitation of the IEC correction, as mentioned previously, is that it does not agree closely with experimental results for gaps of interest in the UHV range

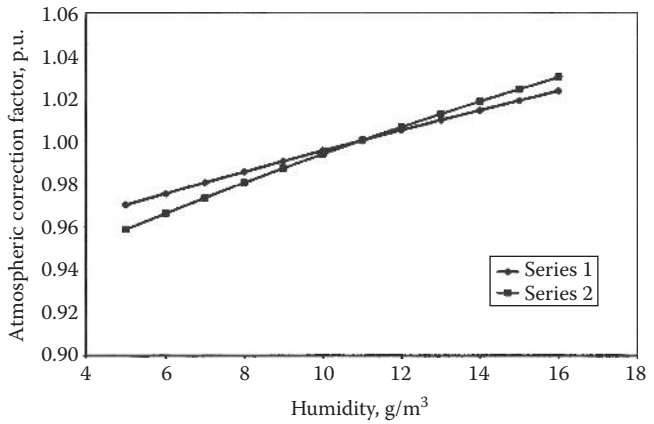


FIGURE 5.28 Critical switching impulse breakdown voltage of 3 m rod–rod gap. Variation of the atmospheric correction factor with humidity. S1: model. S2: from IEC 60060-1 (1989).

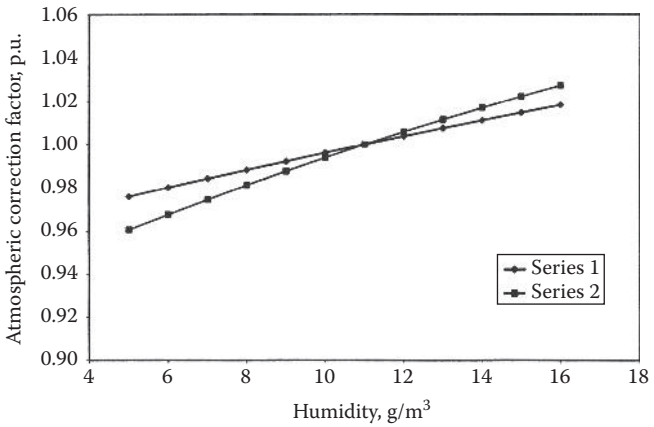


FIGURE 5.29 Critical switching impulse breakdown of conductor–rod gap, $d = 4$ m, $h = 4$ m, $a = 0.05$ cm. Variations of the atmospheric correction factor with humidity. $\delta = 1$. S1: model. S2: from IEC 60060-1 (1989).

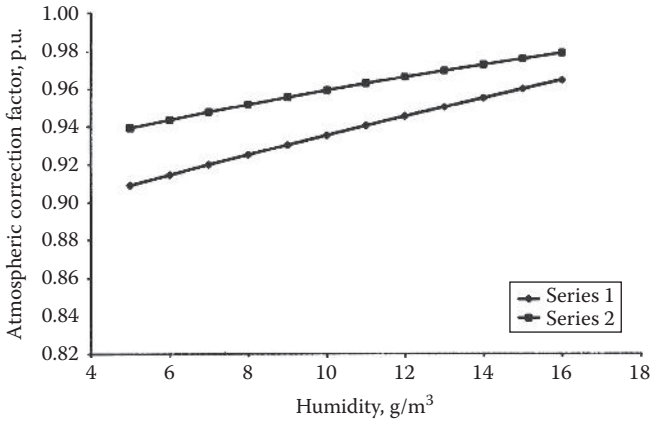


FIGURE 5.30 Critical switching impulse breakdown of 5 m rod–plane gap. Variations of the atmospheric correction factor with h, $\delta = 0.85$. S1: model. S2: from IEC 60060-1 (1989).

as confirmed in Table 5.4. Another fundamental point is the lack of physical justification to the proposed unique dependence of the correction factor on the parameter G. It is clear that the same value of G can be obtained at different gap lengths, for different electrode configurations and it is far from obvious why the correction factors would be identical for all such configurations, since the relative lengths of streamer and leader discharges would be different.

Finally, an example where both the relative air density δ and humidity h_a are different from standard conditions is addressed. This refers to a 5 m rod–plane gap at $\delta = 0.85$ (altitude of 1325 m). Figure 5.30 shows variation of the atmospheric correction factor with absolute humidity in the range of 5–16 g/m^3. Also shown is the correction obtained from IEC Standard (IEC 60060-1, 1989).

REFERENCES

Aihara, Y., Harada, T., Aoshima, T., and Y. Ito. Impulse flashover characteristics of long air gaps and atmospheric correction. *IEEE Transactions on Power Apparatus and Systems* PAS-97(2): 342, 1978.

Aleksandrov, N.L., Bazelyan, A.E., Bazelyan, E.M., and I.V. Kochetov. Modeling of long streamers in atmospheric-pressure air. *Plasma Physics Reports* 21(1): 57, 1995.

Aleksandrov, N.L. and E.M. Bazelyan. Simulation of long-streamer propagation in air at atmospheric pressure. *Journal of Physics D: Applied Physics* 29: 740, 1996.

Allen, N.L. and M. Boutlandj. A study of the electric fields required for streamer propagation in air. *Proceedings of the IEE* A-138: 37, 1991.

Allen, N.L. and D. Dring. Effect of humidity on the properties of corona in a rod-plane gap under positive impulse voltage. *Proceedings of the Royal Society A* 396: 285, 1984.

Baldo, G., Gallimberti, I., Garcia, H.N., Hutzler, B., Jouaire, J., and M.F. Simon. Breakdown phenomena of long air gaps under switching impulse conditions: Influence of distance and voltage level, Presented at the *1974 Summer Power Meeting*, IEEE Publication 74 CH0910-0-PWR, 1974, p. 50.

Busch, W. Air humidity: An important factor for UHV design. *IEEE Transactions on Power Apparatus and Systems* PAS-97(6): 2086, 1978.

Busch, W. Der Einfluss der Luftfeuchtigkeit auf die Schaltspannungsfestigkeit der atmosphärishen Luft im Ultrahochspannungs Bereich bei positiver Polarität, Dissertation ETH Nr. 7048, Zurich, Switzerland, 1982.

Caldwell, R.O. and M. Darveniza. Experimental and analytical studies of the effects of non-standard waveshapes on the impulse strength of external insulation. *IEEE Transactions on Power Apparatus and Systems* PAS-92: 1420, 1973.

Carrara, G. and L. Thione. Switching surge strength of large air gaps: A physical approach. *IEEE Transactions on Power Apparatus and Systems* PAS-95(2): 512–524, March/April 1976.

CIGRE Group 33. Overvoltages and Insulation Coordination, August 1974.

CIGRE WG 33.01. Guide to procedures for estimation of the lightning performance of transmission lines, CIGRE Monograph, No. 63, 1991.

CIGRE WG 33.07. Guidelines for the evaluation of dielectric strength of external insulation, CIGRE Monograph 72, Chapter 8, 1992.

Electric Power Research Institute. Bipolar HVDC transmission system study between ± 600 kV and ± 1200 kV: Insulation studies. EPRI Report EL-963, 1979.

Electric Power Research Institute. HVDC transmission line reference book, EPRI Report TR-102764, Chapter 5, 1993.

Fischer, A. The influence of humidity on DC and AC breakdown voltage of air gaps. *Electra* 10: 65, 1969.

Gallimberti, I. The mechanism of the long spark formation. *Journal de Physique* 40(7): 193, 1979.

Geldenhuys, H.J. The breakdown voltage of air in rod-plane gap over a practical range of air density and humidity. In: *5th International Symposium on High Voltage Engineering*, Braunschweig, Germany, Paper 14.02, 1987.

Harada, T., Aoshima, T., Ishida, T., Ichihara, Y., Anjo, K., and N. Nimura. Influence of air density on flashover voltages of air gaps and insulators. *IEEE Transactions on Power Apparatus and Systems* PAS-89(6): 1192, 1970.

Hutzler, B. and D. Hutzler-Barre. Dielectric breakdown of gases: Analytic expression of "S" curve. In: *Proceedings of the 4th International Conference on Gas Discharges*, Swansea, U.K., 1976, IEE Publication No. 143, pp. 283–286.

IEC Standard 60060-1. High voltage test techniques, Part 1: General definitions and test requirements, 2nd edn., 1989a.

IEC Standard 60060-1. High voltage test techniques, 2nd edn., 1989b, p. 111.

IEC Standard 60071-1. Insulation coordination, part 1: Definitions, principles and rules, 1993.

IEC Standard 60071-2. Insulation coordination, part 2: Application guide, 1996.

Kind, D. The formative area of technical electrodes under impulse voltage stress. *ETZ* 79-A: 65, 1958 (in German).

Knudsen, N. and F. Iliceto. Flashover tests on large air gaps with DC voltages and with switching surges superimposed on DC voltage. *IEEE Transactions on Power Apparatus and Systems* PAS-89(5/6): 781, 1970.

Kucera, J., Liao, T.W., and A.F. Rohlfs. Atmospheric correction factors for high voltage testing. *Electra* 21: 74, 1972.

Lalot, J. and G. Gallet. Breakdown phenomena at power frequency. In: *3rd ISH*, Milan, MI, 1979.

Leroy, G., Recent developments in the physics and engineering of high voltage breakdown,. In: *IEE Gas Discharge Conference* (Review Lecture, Opening Session), London, U.K., September 1974.

Les Renardières Group. Research on long air gap discharges at Les Renardières. *Electra* 23: 53, 1972.

Les Renardières Group. Research on long air gap discharges at Les Renardières – 1973 results. *Electra* 35: 49, 1974.

Les Renardières Group. Positive discharges in long air gaps at Les Renardières – 1975 results and conclusions. *Electra* 53: 31, 1977.

Les Renardières Group. Negative discharges in long air gaps at Les Renardières – 1978 results. *Electra*, 74: 67–216, 1981.

Melvold, D.J., Odam, P.C., and J.J. Vithayathil. Transient overvoltages on an HVDC bipolar line during monopolar line faults. *IEEE Transactions on Power Apparatus and Systems* PAS-96(2): 591, 1977.

Morrow, R. and J.J. Lowke. Streamer propagation in air. *Journal of Physics D: Applied Physics* 30: 614, 1997.

Obenaus, F. Elektrische Isolatoren und Isolierungen. In: E. Philippow (ed.), *Taschenbuch Elektrotechnik*. Berlin, Germany: VEB Verlag Technik, 1965, Chapter 5.

Ortega, P., Domens, P., Gilbert, A., Hutzler, B., and G. Riquel. Performance of a 16.7 m air rod-plane gap under a negative switching impulse. *Journal of Physics D: Applied Physics* 27: 2379, 1994.

Paris, L. and R. Cortina. Switching and lightning impulse discharge characteristics of large air gaps and insulator strings. *IEEE Transactions on Power Apparatus and Systems* PAS-87: 947, 1968.

Peek Jr., F.W. Effect of altitude on the sparkover voltages of bushings, leads and insulators. *Journal of AIEE* 33: 1721, 1914.

Phelps, C.T. and R.F. Griffiths. Dependence of positive streamer propagation on air pressure and water vapor content. *Journal of Applied Physics* 47: 2929, 1976.

Philips, T.A., Robertson, L.M., Rohlfs, A.F., and R.L. Thompson. Influence of air density on electrical strength of transmission line insulation. *IEEE Transactions on Power Apparatus and Systems* PAS-86(8): 948, 1967.

Pigini, A., Rizzi, G., Garbagnati, E., Porrino, A., Baldo, G., and G. Pesavento. Performance of large air gaps under lightning overvoltages: Experimental study and analysis of predetermination methods. *IEEE Transactions on Power Delivery* 4(2): 1379, 1989.

Pigini, A., Sartorio, G., Moreno, M., Ramirez, M., Cortina, R., Garbagnati, E., Britten, A.C., and K.J. Sadurski. Influence of air density on impulse strength of air insulation. *IEEE Transactions on Power Apparatus and Systems* PAS-104(10): 2888, October 1985.

Pigini, A., Thione, L., and F.A.M. Rizk. Dielectric Strength under AC and DC Voltages, Chapter 6, in Guidelines for the Evaluation of the Dielectric Strength of External Insulation, CIGRE Technical Brochure No. 72, CIGRE, Paris, France, 1992.

Ramirez, M., Moreno, M., Pigini, A., Rizzi, G., and E. Garbagnati. Air density influence on the strength of external insulation: experimental investigation up to an altitude of 3000 m a.s.l. *IEEE Transaction on Power Delivery* 4(1): 730, 1990.

Rizk, F.A.M. Flashover characteristics of insulators and spark-gaps with a power-frequency half-cycle pulse, Thesis, Royal Institute of Technology, Stockholm, Sweden, June 1960.

Rizk, F.A.M. Statistical stress-duration characteristics of high voltage insulation. *IEEE Transactions on Power Apparatus and Systems* PAS-100(1): 400, 1981.

Rizk, F.A.M. A model for switching impulse leader inception and breakdown of long air gaps. *IEEE Transactions on Power Delivery* 4(1): 596, 1989a.

Rizk, F.A.M. Switching impulse strength of air insulation: Leader inception criterion. *IEEE Transactions on Power Delivery* 4(4): 2187, 1989b.

Rizk, F.A.M. Critical switching impulse strength of long air gaps: Modeling of air density effects. *IEEE Transactions on Power Delivery* 7(3): 1507, 1992.

Rizk, F.A.M. Critical switching impulse strength of phase-to-phase air insulation. *IEEE Transactions on Power Delivery* PWRD-8(3): 1492, 1993.

Rizk, F.A.M. Critical switching impulse breakdown of long bundle-conductor gaps. *IEEE Transactions on Power Delivery* PWRD-11(1): 373, 1996.

Rizk, F.A.M. Air insulation. In: *EPRI HVDC Reference Book: Overhead Lines for HVDC Transmission*. Palo Alto, CA: EPRI, 2008, Chapter 2.

Rizk, F.A.M., Beausejour, Y., and Hu Shi Xiong. Sparkover characteristics of long fog-contaminated air gaps. *IEEE Transactions on Power Apparatus and Systems* 100(11): 4604, 1981.

Rizk, F.A.M. and M.B. Eteiba. Impulse breakdown voltage—Time curves of SF_6 and $SF_6 - N_2$ coaxial cylinder gaps. *IEEE Transactions on Power Apparatus and Systems* 101: 4460, 1982.

Rizk, F.A.M. and F. Vidal. Modeling of positive leader speed under slow front voltages—Part 1: Long air gaps. *IEEE Transactions on Power Delivery* 23(1): 296, 2008.

Rudakova, V.M. and N.N. Tikhodeev. Influence of low pressure air on flashover voltages of polluted insulators: Test data, generalization attempts and some recommendations. *IEEE Transactions on Power Delivery* 4(1): 607, 1989.

Singer, H., Steinbigler, H., and P. Weiss. A charge simulation method for the calculation of high voltage fields. *IEEE Transactions on Power Apparatus and Systems* PAS-93(5): 1660, 1974.

Sirotinski, L.I. *Hochspannungstechnik*, Vol. 1, Part 1. Berlin, Germany: VEB Verlag Technik, 1955a, p. 140.

Sirotinski, L.I. (ed.). *Hochspannungstechnik*, Part I. Berlin, Germany: VEB Verlag Technik, 1955b, Chapter 5.

Standring, W.G., Browning, D.H., Hughes, R.C., and W.J. Roberts. Effect of humidity on flashover of air gaps and insulators under alternating and impulse voltages. *Proceedings of the IEE* 6: 1077, 1963.

Strigel, R. *Elektrische Stossfestigkeit*. Berlin, Germany: Springer Verlag, 1955a, Chapter 1.

Strigel, R. *Elektrische Stossfestigkeit*, 2nd edn. Berlin, Germany: Springer Verlag, 1955b, p. 292.

Urbain, J.P., Lalot, J., and G. Gallet. Influence of AC test procedure of air insulations: comparison with switching impulse tests. *IEEE Transactions on Power Apparatus and Systems* PAS-100(7): 3451, 1981.

Vlastos, A.E. Breakdown of air in nonhomogeneous field. *Proceedings IEE* 6: 921, 1966.

Watanabe, Y. Influence of pre-existing DC voltage on switching surge flashover characteristics. *IEEE Transactions on Power Apparatus and Systems* PAS-87(4): 964, 1968.

Winkelkemper, H. and W. Baucke. Feuchtigkeitseinfluss auf den durchlag in luft bei Hoher Wechselspannung. *ETZ-A* 25: 667, 1969.

Zaffanella, L. Switching surge performance, EPRI AC transmission line reference book—200 kV and above, 3rd edn. Palo Alto, CA: EPRI, 2005, Chapter 5.

Zheng, J.C. and Y.M. Yang. Influence of humidity on the dielectric strength of large air gaps under AC voltages. In: *6th ISH*, New Orleans, LA, 1989.

6

Electric Breakdown in Liquids

Oil–paper, the relative order of the words corresponding to the preponderance of the oil with respect to paper in the insulation, is among the most widely used insulation systems after atmospheric air. Developed since the discovery of electricity, and thanks to its excellent dielectric, thermal, and arc-quenching properties, the oil–paper insulation is used in high-voltage power apparatus, from power transformation equipment to circuit interrupters and breakers at various voltage levels. The oil–paper insulation has reached the level of 735 kV in the 1960s, 1000 kV in the 1990s, and touching the 1200 kV level at present. The main drawback resides in the high fire hazards associated with failure of oil–paper insulation, which has gradually removed the oil insulation from circuit interrupters and breakers and triggered several attempts to find a replacement to mineral oil with less flammable liquids. At present, the use of oil–paper insulation is limited to power equipment, mainly transformers and inductances, where the high energy losses required an effective cooling system that cannot be found with other insulation systems. In the oil–paper insulation, the main component is the mineral oil, which serves at the same time as the main insulating material and a cooling liquid. The cellulose paper, mainly in the form of pressboard, is also required mainly to provide a mechanical support to the high-voltage windings. This chapter reviews the various aspects of oil–paper insulation, namely, its physicochemical properties and the breakdown mechanisms active in this insulation system.

6.1 Chemical Composition of Mineral Oil

The successful historic application of mineral oil for insulation of power apparatus has been based on management of several characteristics (Zaky, 1955; Wilson, 1980). The viscosity of the oil plays an important role. The flash point defines an upper temperature limit for the oil to minimize fire hazards. The pouring point determines the lower temperature limit for the oil, at which one observes the formation of wax, which prevents free circulation of the oil. The content of dissolved gas is particularly important to avoid the formation of gas bubbles during sudden changes in temperature. The oxidation of the oil is another determining parameter for the adequate operating of the oil in service, its control is ensured by the addition of antioxidants, and the formation of mud is a sure index of corrosion. The oil must also be free of sulfur, organic chlorides, and sulfites, introduced either by contamination or by an inadequate refining of the oil. The insulating oils used at present are petroleum based and contain naphthenic, paraffinic, and aromatic constituents (Fournié, 1990). Typically, an insulating oil for electrical apparatus contains 12.9% aromatics, 42.9% naphthenic, and 44.2% paraffin. Figure 6.1 illustrates the molecular structure of an oil molecule and of its constituents. The oil contains a variety of these molecules, both the length and structure of which can vary considerably. As a result, the molecular mass of the oil is only an average value. The aromatic components in the oil tend to increase the dielectric loss, tanδ; their presence is, however, necessary to inhibit the evolution of dissolved gas in the oil subjected to electrical stresses. The dielectric constant ε of the oil is about 2.2, the dielectric losses are lower than 10^{-3}, and the viscosity can vary between 10 and 1000 centipoises.

In addition to a high volume resistivity and low dielectric losses, the insulating oil must have a good capacity to absorb the gases. In effect, in a new transformer, the oil contains very small percentage of residual dissolved gas. With the gradual aging of the insulation, CO and CO_2 are formed (thermal aging of the cellulose). Combustible gases (mainly H_2) are also formed due to cracking of the oil under the

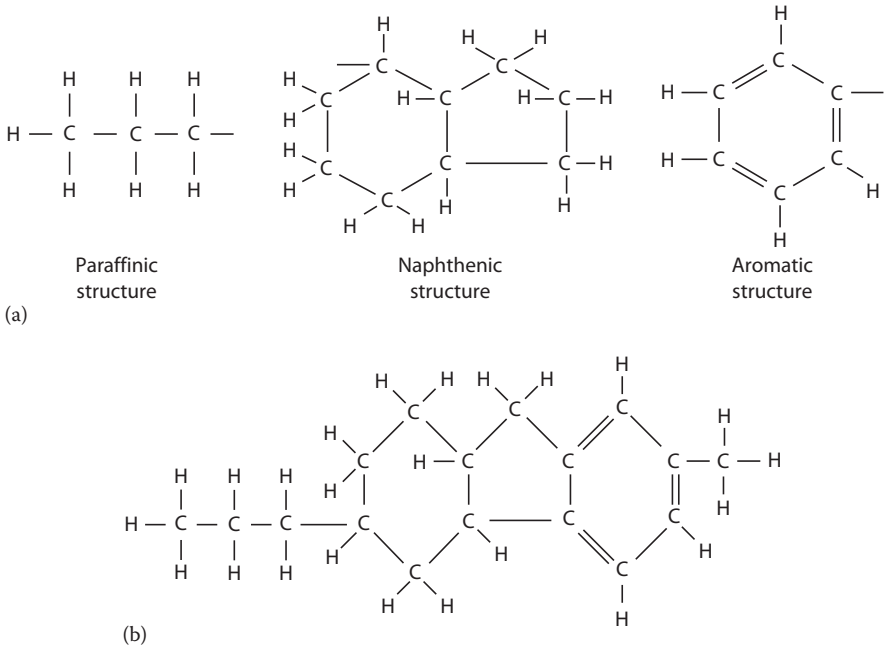


FIGURE 6.1 Molecular structure of oil and its constituents. (a) Paraffinic, naphthenic and aromatic structures. (b) A typical oil molecule.

combined effect of an electric field and high temperature. The concentration of these gases increases in time, in particular CO and CO_2. A good oil–paper insulation should not have PD sites producing combustible gases. To avoid the concentration of these gases to reach, under normal aging conditions, the saturation level of the oil, which would cause the formation of gas bubbles, the oil must have an adequate content of aromatic constituents. The main parameter describing the aging of oils is then *the content of dissolved gas in oil*, which can be directly evaluated from oil samples. Additives are added to the oils to delay the oxidation process, di-*t*-butyl-*p*-cresol (DBPC) or DBP to decompose the peroxides and prevent the formation of sludge in transformer oil, and aromatic components are necessary to absorb the gaseous by-products, in particular hydrogen, and inhibit the evolution of gas in oil subjected to aging.

6.2 Interest in Synthetic Oils

Mineral oil has been successfully used since many decades as the main insulating fluid for oil–paper insulation. The advantages related to its utilization are mainly good dielectric performances and thermal properties, favorable cost, good experience in service, and relatively minor impact on the environment.

Its utilization has extended widely in the electrical industry, from large power equipment, transformers, and shunt inductances to small components, namely, condensers for capacitive compensation or measuring apparatus and capacitive voltage transformers. However, oil–paper insulation has also drawbacks and limitations, which become evident with the development of high-voltage equipment operating at the level of 800 kV and above: high risks of fire subsequent to a failure, high dielectric losses of oil insulation.

Considerable research effort has therefore been devoted to find new insulating fluids, highly purified oils, and synthetic oils such as silicone oil, per-fluorocarbons, and esters, having equivalent or better properties than mineral oil, more specifically with respect to low risks of fire hazards, a better compatibility with new insulating materials (polymers), higher dielectric strength, and low energy losses.

6.2.1 Required Properties for Synthetic Oils

Any dielectric considered for replacing mineral oil must have particular characteristics; the most important are the following:

- A good dielectric strength
- High volume resistivity
- Low dielectric losses at power frequency
- Availability and economy
- High degree of purity
- Good resistance to oxidation and hydrolysis
- High flash point, preferably nonflammable
- Low pouring point
- Good resistance to PDs
- Good absorption ability of gas (H_2) produced by PDs
- Good compatibility with insulating materials
- Nontoxicity
- Low impact on environment

The insulating oil considered must meet the quality standards to ensure its adequacy for use in power apparatus. Being the main impregnating fluid of oil–paper insulation used in electrical equipment, mineral oil serves as reference value to any new insulating fluid considered to replace it. Table 6.1 summarizes the principal properties required by utilities of synthetic oils and those of the mineral oil (*Voltesso* 35). One can see that the requirements from utilities are still largely inspired by the properties of the oil–paper insulation and should represent the minimal conditions required for the dielectric and physicochemical properties.

6.2.2 Principal Synthetic Oils Presently Available

Up to the present, the development of synthetic oils is oriented along two main groups of power equipment:

1. Large power apparatus, transformers, and shunt inductances, the insulation of which is determined by the insulating liquid
2. High-voltage cables and condensers used in capacitive compensation and capacitive voltage transformers, the insulation of which is determined by the impregnated paper, paper–polypropylene film, or polypropylene film

This chapter is confined to the synthetic oils considered for large power equipment, the insulation of which is characterized by

- The preponderance of oil with respect to paper
- The relatively low operating stresses, in the order of 2–5 kV/mm, related to the relatively nonuniform distribution of the electric field and to the large volume of oil (Trinh et al., 1982)

Because of the low operating stresses, combined with the excellent service experience of the oil–paper insulation in transformers and shunt reactors, the principal motivation to find a new fluid to replace mineral oil in the insulation of large power equipment is to minimize the risks of fire hazard subsequent to a failure with internal arc. In the 1930s, the discovery of biphenyl polychlorides (*BPCs*), inert insulating fluids, with very little flammable and superior dielectric properties, seems to be the ideal solution for replacing mineral oil in the oil–paper insulation. This is, however, without counting the environmental impact of *BPC* discovered in the 1970s, which has led to the complete prohibition of this product since 1978.

TABLE 6.1

Properties of Mineral and Synthetic Oil

Dielectric Properties	Conditions	Units	Utility 1	Utility 2	Voltesso 35
Dielectric strength	AC	kV_{rms}/mm	30	35	35
	Impulse				150
Tangent delta	5 C		5×10^{-4}		2.85×10^{-3}
	90			5×10^{-3}	
	100		5×10^{-3}		5×10^{-3}
Volume resistivity	100 C				1.0×10^{13}
Relative permittivity	ε_r		2.2–2.3		2.2
Gassing 50 min	65 C, 10 kV	µL/min	−13.1		Negative
Density, max	15 C	g/mL	0.998	<0.895	0.866
Interfacial tension	Minimum	mN/m	40		45
Viscosity at	−45°C	mm^2/s			5000
	−40		6000		2000/1550
	−15			<800	
	0		75		50/49
	20			<40	
	40		10	<16.5	8/10
Water content at	0 C	ppm			16
	10				27
	20	Max	10		45
Pouring point	Max	C	−50	−30	−51
Cloud point			−35		
Boiling point					300
Flash point	Min		146	140	150–160
Fire point					177–180
Specific heat		J/g C			1.04
Coef. thermal expansion		C^{-1}			$7–8 \times 10^{-4}$
Thermal conduction	20°C–100°C	Cal/cm s C			$3–4 \times 10^{-4}$
		W/m C			0.137
Acid index	Max	mg KOH/g	0.025	0.03	0.03
Corrosion—copper	Sulfur		Noncorrosive	Noncorrosive	Noncorrosive
Oxidation test		h		72	164
	Mud	% by weight		0.1	0.2
	Acidity	mg KOH/g		0.3	0.5
Toxicity			Nontoxic	Nontoxic	Nontoxic
Biodegradability			High	High	High
BPC content			Nondetectable	Nondetectable	Nondetectable

The interdiction of the *BPC* has triggered research efforts for new insulating fluids for the replacement of mineral oil, aiming at minimizing the risk of fire hazard in fault conditions (Rouse, 1987). The main properties required to these new fluids are a comparable or better dielectric performance than the mineral oil with little or no flammability. Also, because of the large amount of oil required for power transformer insulation, the replacement fluids should not be expensive. Finally, the risks of accidental spilling being nonnegligible, the replacement fluids must be environmentally nonaggressive, nontoxic, biodegradable, and nonaccumulative. Several insulating liquids have been developed since the 1980s in response to the replacement of *BPC*. They are essentially in four groups: aliphatic hydrocarbons, silicone oils, perfluorocarbons, and synthetic esters (Bartnikas and Srivastava, 1980). The properties of the principal insulating liquids considered for insulation of large power apparatus are presented in Table 6.2 and discussed in the following.

TABLE 6.2

Properties of Synthetic Oils for Power Transformers

			Oil			PEC[b]	Esters
Typical Product	**Notes**	**Units**	**RTEmp**	**POA[a]**	**Silicone**	**FC–75**	**Midel**
Dielectric strength	AC	kV/mm	43	43			
Tangent delta	25 C				$<10^{-4}$	$<5 \times 10^{-4}$	$<10^{-3}$
Volume resistivity			100		1.0×10^{15}		1.0×10^{15}
Relative permittivity	ɛr		2.2		2.7	1.85	4–6.3
Gassing[c]		µL/min	Positive	Positive		no H_2	
Density		g/mL	0.87	0.85–0.87	0.96	1.76	0.975
Interfacial tension		mN/m				12	
Viscosity	–40 C	mm^2/s			50		330
	0				15		100
	20–25		100–140	33	6.5	0.85	50
	100		13	6	2		6
Water content		ppm	89	70–75	200–250		>1000
Pour point		°C	–24	–30, –50	–55	–113	–30, –50
Boiling point			430	240	101		>400
Flash point			285	265–280	300–305	none	250–260
Fire point			310	305–310	340–360	none	310–330
Combustion			High flammability	High flammability			High flammability
Specific heat		J/g C	1.9	1.51	1.04		1.8–2.1
Coef. thermal expansion		C^{-1}	7.3×10^{-4}	7.1×10^{-4}			8×10^{-4}
Thermal conductivity	20,100	W/m C	0.13		0.15		0.16
Decomposition by-products			H_2, CO, CO_2, HC	H_2, CO, CO_2, HC	H_2, CO_2, HC, SiO_2		H_2, CO, CO_2, HC
Toxicity			Nontoxic	Nontoxic	Nontoxic		Nontoxic
Biodegradability			High	High	Very low		Very good

[a] POA, polyalphaolefin.
[b] PEC, perfluorocarbon.
[c] At 65°C, 10 kV, 50 min H_2.

6.2.2.1 Aliphatic Hydrocarbons

The first attempt to improve the mineral oil is made by improving the purification process. One obtains a highly purified oil, the *RTEmp*. Other fluids of the same aliphatic hydrocarbon group are obtained by the polymerization of the alphaolefins, commonly called polyalphaolefins with dielectric and environmental characteristics very close to that of mineral oil. The chains of hydrocarbons are highly ramified, which allows them to remain in the liquid state over a wide range of temperatures, with very low degree of volatility and improved thermal characteristics. This qualifies them as oils with reduced flammability. The main drawbacks are their high price, a higher viscosity, a positive tendency to gassing, and a dielectric strength sensitive to humidity. These oils are used mainly in transformers in traction systems for electric trains (Castonguay, 1992).

6.2.2.2 Silicone Oil

Silicon oil is a generic term to identify a mixture of *polydimethylsiloxane* (*PDMS*). It is the length of the molecular chains and the proportion of each components in the mixture that determine the physicochemical properties and the degree of flammability of a silicone oil. The mixture currently

used has a viscosity of 50 cS and presents the best compromise with its dielectric properties. The advantages of silicone oils are their high chemical and thermal stability, good resistance to oxidation and low flammability, high compatibility with the usual materials, and being biologically inert with negligible impact on the environment. Their drawbacks are their significantly higher costs, about 10 times that of mineral oil, being a poor lubricant, affinity to humidity with consequences on its dielectric withstand capability, formation of gel under PDs, and nonbiodegradability. Silicone oils are probably the most used as replacement for mineral oil in low-voltage transformers. Their service experience to date is excellent. The low dielectric strength of silicone oils remains the principal obstacle to their utilization in high-voltage power transformers (Castonguay, 1992).

6.2.2.3 Perfluorocarbons (Castonguay, 1992)

Perfluorocarbons were developed since the 1950s, and used in prototype transformers that were totally nonflammable under the name of *FC-75*. Their utilization was then left aside, probably due to their prohibitive cost, up to the introduction of SF6-insulated transformers, where they are used principally as cooling fluid (Narbut et al., 1959; Mukaiyama et al., 1991). The advantages of perfluorocarbons are their very high thermal stability and nonflammability, high capacity for heat transfer, very little toxicity, and a good environmental compatibility. The drawbacks are very high cost and the possibility of formation of toxic by-products (HF, C_2F_4, F_2CO) under certain conditions of fault or fire (Castonguay, 1992).

In the group of halogen hydrocarbons are the aliphatic chlorofluorocarbons (CFC, Formel NF, C_2Cl_4, $C_2F_3Cl_3$) and the aromatic chlorohydrocarbons (trichlorobenzene, *Ugilec-T*). Although their dielectric and thermal properties are interesting, these products are potentially problematic regarding their environmental impact, which tend to make their use highly improbable. In *France*, the *Ugilec-T* is no longer used since 1984.

6.2.2.4 Synthetic Esters

Synthetic esters are constituted of a mixture of chemical compounds from the group of *pentaerythritol esters* (Midel). Their development is essentially in *Europe*, in the 1980s, and their utilization was limited to Germany and England. The advantages of esters are high chemical and thermal stability, good resistance to oxidation and low flammability, high compatibility with mineral oil and usual materials, excellent lubricant properties, dielectric strength little affected by humidity, and being nontoxic and biologically inert with negligible environmental impact. The drawbacks are very high affinity to humidity and not fully nonflammable (Castonguay, 1992).

6.3 Breakdown Mechanisms

Although ionization and excitation processes similar to those active in gases are present in liquids, considerable differences are observed between the two media, with consequences on the development of discharges. The principal difference resides in the fact that liquids are denser than gases. As a result, the molecular bonds between liquid molecules are stronger than in gases. The free paths of the electrons are, consequently, smaller and contribute to limit the accumulation of energy from the applied field.

6.3.1 Early Studies

Early investigations on breakdown in liquids have provided a basic understanding of the phenomena involved. They are reviewed in Lewis (1968) and Krasucki (1968) in terms of pure and commercial insulating liquids that are summarized in the following.

6.3.1.1 Electrical Conduction and Strength of Pure Liquids (Lewis, 1968)

Pure liquids refer to those containing simple molecules of known shape and reasonably well-known impurities. The most frequently studied liquids are paraffinic hydrocarbons with straight chain structure: pentane to decane and in particular *n*-hexane, C_6H_{14}. It has a convenient boiling point of 67°C and a low viscosity and is relatively stable. Furthermore, its electrical characteristics are not far from those of the insulating oils of commercial use that involve the same C–C and C–H bonds as in *n*-hexane.

The liquids are purified to remove dust and ionic impurities and to control the amount of dissolved gases, in particular oxygen and carbon dioxide that can affect the strength of the liquid. A closed glass system is illustrated in Figure 6.2, which allows the cycling of the liquid and incorporates the test cell into its purification system. Small spherical and plane electrodes are used with small gap spacing. Under such conditions, liquid dielectrics exhibit high resistivities, 10^{15}–10^{20} Ω-cm, and have dielectric strength of the order of 1 MV/cm.

Natural conduction: Figure 6.3 illustrates the current–field characteristics of an oil gap. Three distinct regions can be distinguished as the applied field is increased. At low fields, the conduction is largely ionic and due to dissociation. This current saturates at intermediate fields, and at higher fields, the current increases exponentially by field-aided electron emissions from the cathode either by Schottky effect from local field enhancement sites at the cathode or by collision of positive ions returning to the cathode—the γ-process.

The rapid increase in the current as the breakdown stress is approached may imply a collision ionization process in the oil volume—the α-process. No clear evidence was obtained however, and Lewis attributed it to the small spacing of the gap that prevented observation of the process.

Breakdown: It is initiated from local sites of intense electron emission from the cathode, which interacts with the liquid, and imparting energy to it in a very localized way could lead to an instability in the liquid. The liquid becomes vaporized due to local heating, forming microbubbles, which have

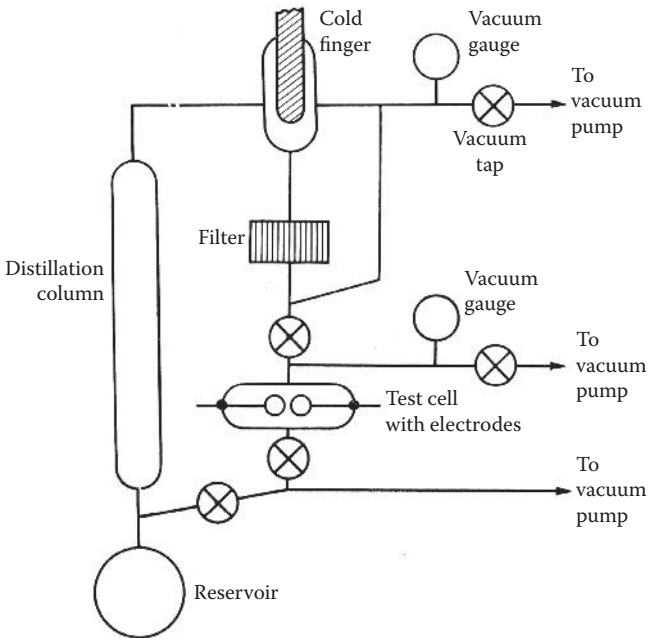


FIGURE 6.2 Closed-cycle liquid purification system. (From Lewis, T.J., The electrical conduction and strength of pure liquids, in: L.L. Alston (ed.), *High Voltage Technology*, Oxford University Press, Oxford, U.K., 1968, Chapter 6.)

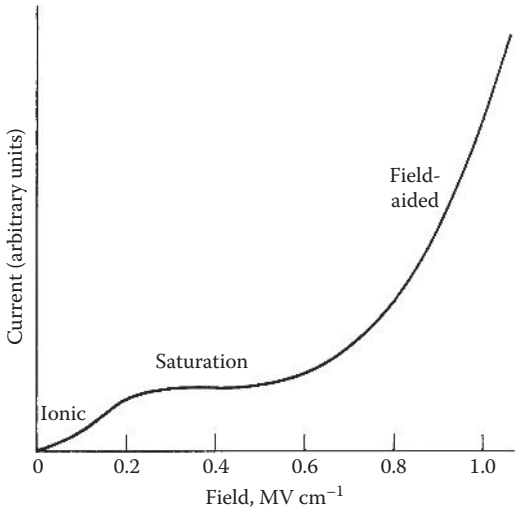


FIGURE 6.3 Current–field characteristic for a hydrocarbon liquid showing three current conduction regimes. (From Lewis, T.J., The electrical conduction and strength of pure liquids, in: L.L. Alston (ed.), *High Voltage Technology*, Oxford University Press, Oxford, U.K., 1968, Chapter 6.)

lower withstand strength than the surrounding liquid. Ultimately, a spark discharge could ensue by growth and extension of one of these vapor regions across the liquid, probably by a gaseous type of ionization within the vapor.

6.3.1.2 Conduction and Breakdown Processes

Different processes are involved in the conduction and breakdown of the liquids. The most important are summarized as follows.

Cathode processes: Electron emission from the cathode can occur by a field-aided process, Schottky emission or Fowler–Nordheim field emission, from asperities at the electrode surface since the fields are easily sufficient for these processes. Emission of this type can be extremely local and further enhanced by the positive ions and dust particles returning to the cathode. There is evidence that a single positive ion arriving at the cathode can cause emission of several electrons. Intense and local emission of electrons will excite molecular vibrations in the liquid and produce a highly localized heat input, which can initiate the growth of a vapor phase or microbubble, an important process in the breakdown of liquid.

Collision processes: In their displacement across the gap, electrons will restitute their energy acquired from the applied field to the liquid through collisions. The most likely process in hydrocarbon liquids would be the excitation of molecular vibrations of the C–C and C–H bonds. The frequencies of such vibrations lie in the infrared with corresponding energy quanta of 0.2–0.4 eV.

The processes of dissociation, excitation, and ionization need energies in the 3–10 eV range. The evidences for such processes are visible scintillations and weak luminescence in the oil. Prolonged exposure to electrical stress can produce wax formation, which involves dissociation and other bond breakages.

Anode processes: At the anode, electrons and negative ions have to be neutralized. If the incoming charges are not easily neutralized, a space charge can be build up and the anode becomes a blocking electrode. Field distortion can occur and could lead to an increased possibility of ionization. Evidence suggests that anodes in hydrocarbon liquids are most likely in blocking condition, especially when the liquid contains a small amount of dissolved oxygen, which forms stable negative ions not easily neutralized.

6.3.1.3 Breakdown of Commercial Liquids (Krasucki, 1968)

Insulating oils, like pure liquids, can exhibit breakdown strength higher than 1 MV/cm when extreme precaution is taken to keep the electrode surface free from oxide film; the liquids themselves are highly degassed and carefully filtered. Test results obtained with highly purified transformer oil show that

- Breakdown strength has a small but definite dependence on the electrode material
- It decreases with increasing gap spacing
- Breakdown strength is independent of the hydrostatic pressure (0–800 mm Hg) for degassed oils, but increases with pressure if the oil contains dissolved gases like nitrogen or oxygen

A commercial liquid as used in industrial equipment cannot be subjected to a very elaborated purification treatment. Its breakdown strength will depend more on the nature of impurities that it contains than on the nature of the liquid itself. Impurities can be divided in three categories according to their physical nature: gaseous, liquid, and solid.

6.3.1.3.1 Breakdown due to Gaseous Inclusion

Because of dissolved gases in oil, gas bubbles are liable to form if the liquid is subjected to changes of temperature and pressure or to agitation. The electric field in a gas bubble immersed in a liquid of permittivity ε is

$$E_b = \frac{3\varepsilon E_0}{2\varepsilon + 1} \tag{6.1}$$

where E_0 is the field in the liquid in the absence of the bubble.

When the field E_b becomes equal to the limiting field for gaseous ionization, a discharge will take place through the bubble. This will result in gas formation through decomposition of oil molecules and may lead to breakdown of the gap. If on the electrodes there are spots at which current density is very high, at sufficiently high fields, vaporization of the liquid may take place at these points. A discharge through the vapor bubble will result in formation of a stable gas volume and may lead to breakdown when the bubble bridges the gap.

6.3.1.3.2 Breakdown due to Liquid Globules

Garton has shown that when an incompressible liquid globule of permittivity ε_2 is immersed in a liquid of permittivity ε_1 and the gap is subjected to an electric field E, it will elongate in the direction of the field (Garton et al., 1964), taking the shape of a prolate spheroid. An expression for the critical field, which causes instability in the liquid, is given for the case where the ratio $\varepsilon_2/\varepsilon_1 \to \infty$ as

$$E_c = 487.7\sqrt{\frac{\sigma}{\varepsilon_1 R}} \text{ V/cm} \tag{6.2}$$

where

σ is the surface tension in dyne/cm

R the radius of the spherical globule

For a critical field of 1 MV/cm that corresponds to the breakdown strength of highly purified oil and assuming a surface tension of $\sigma = 43$ dyne/cm and a permittivity of the oil of $\varepsilon_1 = 2$, Equation 6.2 gives a globule radius of about 5 μm. Breakdown will occur when the globule becomes unstable and elongates rapidly reaching about two-thirds of the gap and breakdown channels developed at the end of the globule. Propagation of the channels across the remaining gap result in total breakdown (Krasucki, 1962).

6.3.1.3.3 Breakdown due to Solid Particles

Solid impurities may exist in a liquid either as fibers or as dispersed solid particles. When the liquid is subjected to an electric field E, it will experience a force according to

$$F = \frac{1}{2} r^3 \frac{\varepsilon_2 - \varepsilon_1}{2\varepsilon_1 + \varepsilon_2} \operatorname{grad} E^2 \tag{6.3}$$

where
- r is the radius of the particle
- ε_1 permittivity of the liquid
- ε_2 permittivity of the particle

For a conducting particle, $\varepsilon_2 \to \infty$ and Equation 6.3 simplifies to

$$F = \frac{1}{2} r^3 \operatorname{grad} E^2 \tag{6.3a}$$

Equations 6.3 and 6.3a indicate that solid particles will be drawn to the region of high field in the gap. A local field enhancement will result and attract additional particles to it. Their accumulation will form a stable chain of particles. Breakdown of the gap will occur when the chain of particles completely bridges the gap.

6.3.1.4 Breakdown of Liquid–Solid Dielectrics (Krasucki, 1968)

Composite insulation, for example, oil–impregnated paper, is widely used in insulation of power transformers and cables. When the paper is not completely impregnated, gaseous inclusions are present and result in PD inception at very low stresses. All the voids in the dielectric can be removed by careful impregnation; this results in an increase in the PD inception stress, E_i. The final value of E_i depends on electrical processes that lead to gas formation. In oil–impregnated paper, these are

- Decomposition of moisture present in paper
- Local electric breakdown of the oil

Except in very dry conditions, the gas first formed arises from electrochemical decomposition of water held in the paper, the nature of the impregnant having little effect. The onset of gassing coincides with the discharge inception. The gas bubbles move rapidly away from the high-field region and, in degassed oil, are dissolved in a few minutes. This process tends to dry out the oil–impregnated paper insulation and increases the discharge inception stress E_i as illustrated in Figure 6.4 that shows the variations of E_i of oil–impregnated paper with the resistivity taken as a measure of the moisture content. In the ideal case of a completely dry paper, gas formation results from local breakdown of the oil in the region of highest stress.

When a gas bubble is formed in an oil–paper dielectric, at the discharge inception stress E_i, discharges in the bubble decompose the molecules of the oil, resulting in further gas formation and a rapid growth of the bubble. As long as the bubble remains in the dielectric, E_i is low, until the bubble dissolves in the liquid and restores the initial high discharge inception stress. This, however, does not prevent permanent damages to the dielectric and an increase in the loss angle tanδ due to formation of ions by the discharges (Krasucki, 1960).

Investigations made with oil–impregnated paper capacitors indicate that even a short period of discharge (15 min) in a capacitor results, after a subsequent rest period, in a large increase in the stress—dependent loss angle as illustrated in Figure 6.5—and can only be explained by the production of ionic impurities.

Since the 1970s, a considerable amount of work has been made on a variety of insulating liquids and, in particular, insulating oil for use in power transformers and shunt reactors. They have led to a better understanding of the processes involved in the development of discharges and breakdown in liquids. They will be discussed in the following with reference to the cases of short and long gaps.

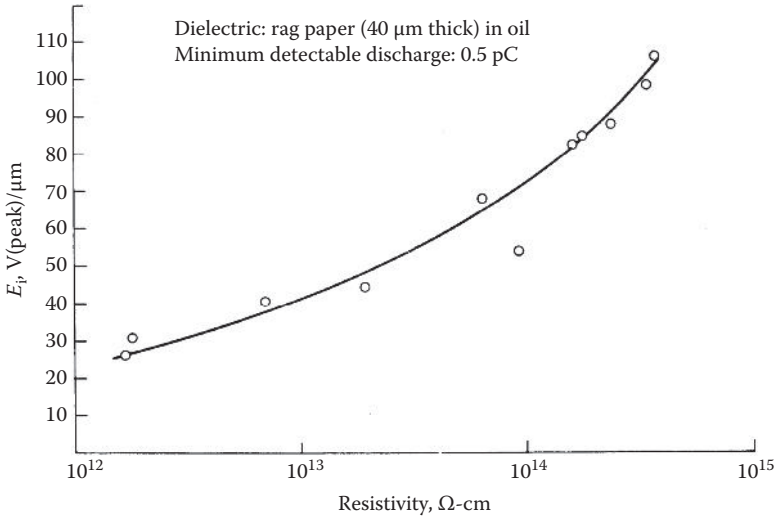


FIGURE 6.4 Variation of discharge inception stress E_i with resistivity of the oil–paper insulation. (From Krasucki, Z., Breakdown of commercial liquid and liquid-solid dielectrics, in: L.L. Alston (ed.), *High Voltage Technology*, Oxford University Press, Oxford, U.K., 1968.)

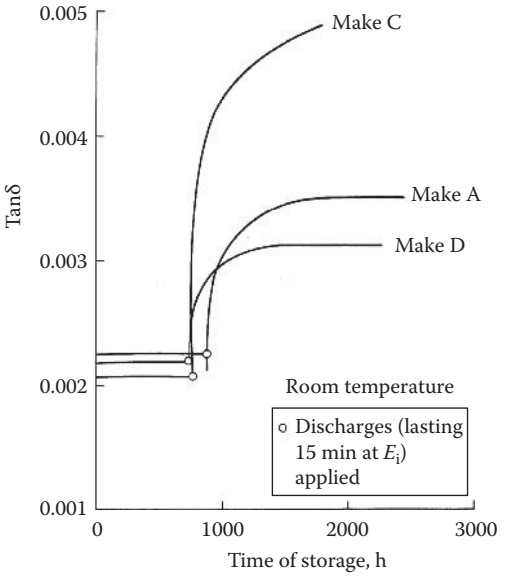


FIGURE 6.5 Effect of 15 min discharges at E_i, on subsequent tanδ of oil–impregnated paper capacitors. (From Krasucki, 1960.)

6.3.2 Breakdown in Short Gaps

Studies of discharges resulting to breakdown of a liquid gap are often made on short gaps, using pure insulating liquids, *n-hexane*, *toluene*, and Marcol 70, the quality of which can be easily controlled (Hebner et al., 1985; Tobazeon, 1994). The main findings are reviewed in the following.

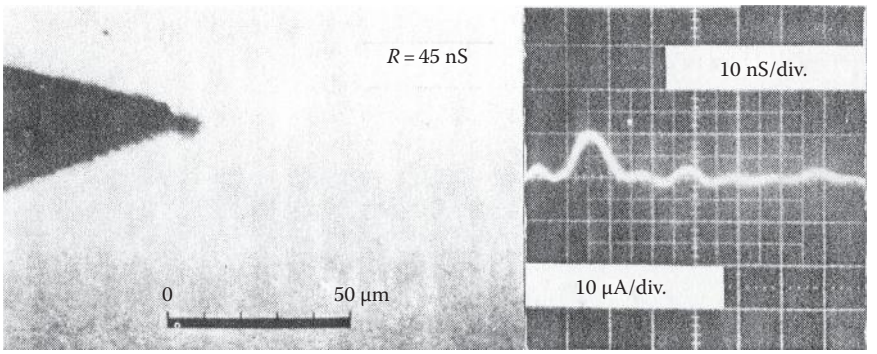
6.3.2.1 Streamer Discharges in Oil

Although the avalanche process, similar to the electron avalanches in gas discharges, is possible for liquids, it is not possible to extend the similarity to define the onset conditions for discharges in liquids

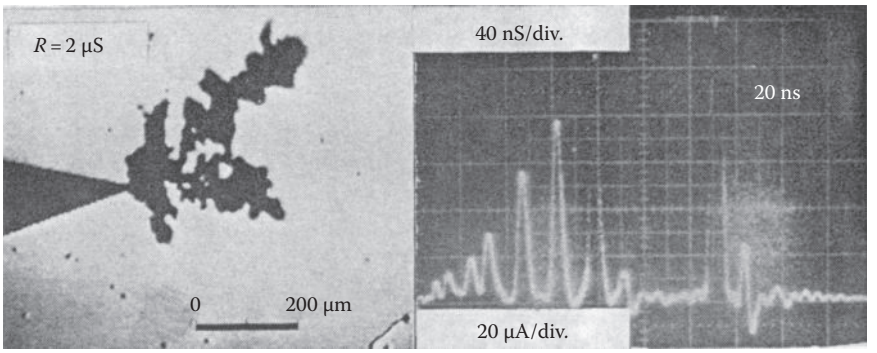
by simple criteria in the same way as for gases. At most, the studies by Hebner et al. (1985) have shown some similarity with the streamer discharges in gases. The term *streamer* is abundantly used to describe discharge phenomena in liquids.

Typical discharges observed in *n-hexane*, *toluene,* and Marcol 70 by Forster (Hebner et al., 1985) using the method of *shadowgraph*, where the shadow of the discharge is projected on a screen for observation, are presented in Figures 6.6 and 6.7 for a point–plane gap, with the point electrode, respectively, at negative and positive potential. The visual aspect of the shadowgraphs shows clear resemblance with the streamer discharges observed in gases. The discharge development is fast, with a propagation velocity in the order of 10^3–10^6 m/s, which indicates that the discharge process is governed by electron ionization. The discharges have many branching, having different visual aspects for negative and positive polarities: more dense for negative streamers (*bush-type*) and filamentary for positive streamers. For the point–plane configuration, the breakdown is caused by a fast streamer, initiated from the peripheral region of the initial streamer, and propagates across the gap at supersonic velocity; the breakdown voltage is lower under positive polarity.

Forster interprets the development of the positive streamer in oil by the extraction of charges from the oil volume by the high electric field around the highly stressed point electrode (Hebner et al., 1985). These charges ionize the oil molecules to form a conducting channel, which extends towards the plane electrode. In so doing, it extends the anode into the oil volume and allows the process to repeat itself and hence the progression of the streamer into the adjacent oil volume. The propagation velocity is subsonic with this mode of propagation, and the initial streamer does not cross the oil gap to cause its breakdown. Under negative potential, the charge injection is caused by the electrons

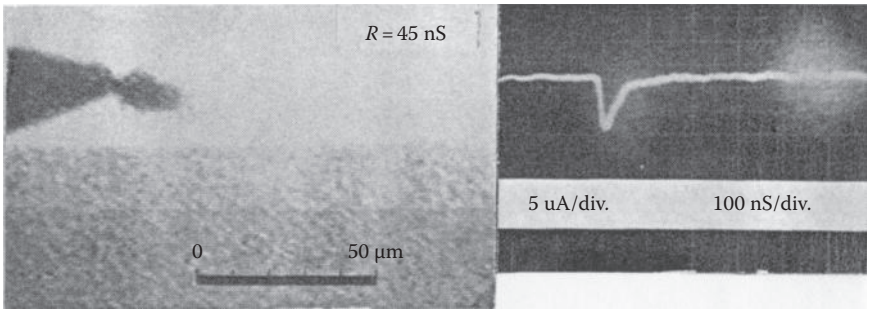


(a)

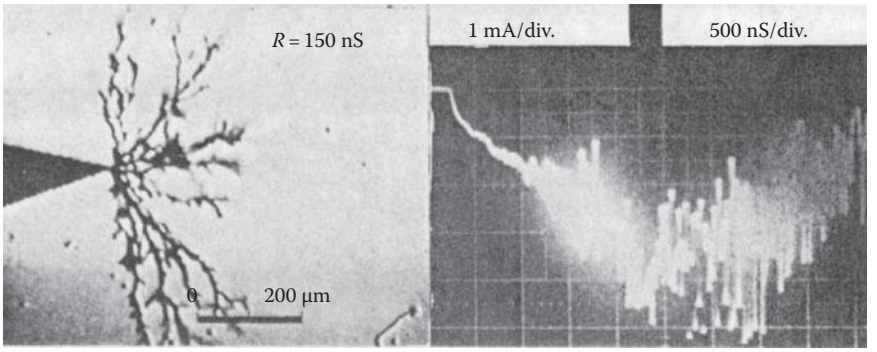


(b)

FIGURE 6.6 Development of streamers from a negative point electrode. (From Hebner, R.E. et al., *IEEE Trans. Electr. Insul*., EI-20(2), 282, 1985.)



(a)



(b)

FIGURE 6.7 Development of streamers from a positive point electrode. (From Hebner, R.E. et al., *IEEE Trans. Electr. Insul*., EI-20(2), 282, 1985.)

emission from the cathode under high field intensity and initiates the ionization of the oil and the development of the initial streamer.

The breakdown of the oil gap is caused by a fast streamer, which develops from the peripheral region of the initial streamer, attributed by Forster to an interfacial instability. The propagation of the fast streamer is supersonic, reaching a velocity in the tens of km/s. The difference in the behavior of streamers under positive and negative polarities is attributed to the mechanism of charge injection, which is easier when the point electrode is at negative polarity. Under positive polarity, the development of the electronic ionization process is largely dependent on the existence of a primary electron in the stressed oil volume surrounding the point electrode.

6.3.2.2 Formation of a Gaseous Cavity

Recent studies by Lesaint et al. (Kattan et al., 1989; Lesaint et al., 1991) have identified a specific mechanism to discharges in liquids: the formation of a gaseous cavity preceding and accompanying the development of streamers. The formation of the gaseous cavity is observed under both polarities of the discharge. It results from the evaporation of the oil by electron impacts in the oil volume subjected to an appropriate electric field. Thus, the development of streamer is made essentially in a gas volume formed by the vaporization of the oil. Figure 6.8 shows such a gaseous cavity (Lesaint and Gournay, 1994a,b). This mechanism reconciles the rather slow development of the discharge with the fast ionization processes within the gaseous cavity. It allows a better interpretation of the prebreakdown phenomena in insulating liquids (Tobazeon, 1994; Trinh and Saker, 1996) that we summarize in the following. The breakdown of an oil gap is made in three stages: the initiation of the discharge, the propagation of the streamer in the gap, and finally, the transition of the streamer into breakdown.

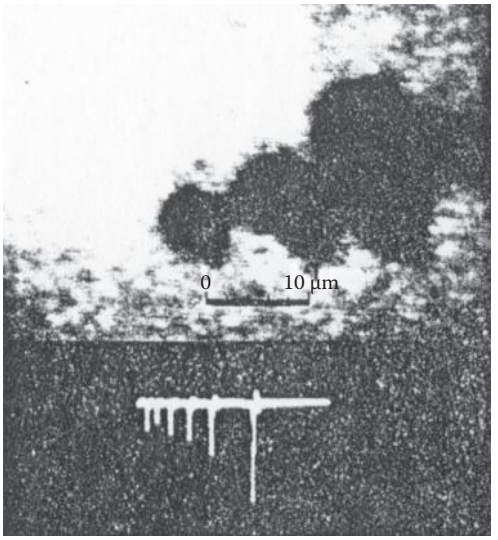


FIGURE 6.8 Formation of a gaseous cavity during the development of streamer in oil. (From Kattan, R. et al., *J. Appl. Phys*., 66(9), 4062, 1989.)

6.3.2.2.1 Initiation of the Discharge

Several mechanisms are active in the initiation of the discharge: charge injection, electron avalanches, and gas bubbles, which will be discussed in the following.

Injection of charge: The fundamental work in this domain was realized by Halpern and Gomer (1969). Field emission was shown to be the mechanism allowing the tunnel effect between the metallic cathode and the liquid across the potential barrier, according to the Fowler–Nordheim law.

Development of avalanches: The ionization by electronic collisions constitutes the principal mechanism allowing the multiplication of charges in the liquid (Hebner et al., 1985). The phenomenon is similar to the development of electron avalanches in gases, and one can determine an effective ionization coefficient for atomic and molecular liquids.

Generation of gas bubbles: It is observed under both polarities subsequent to the evaporation of the liquid in the stressed volume. It is easily observable when the point electrode is negative and is accompanied by a measured impulse current. When the pressure at the tip of the point electrode is below a critical value p_c, each gas bubble follows the same sequence of events: generation, development, and collapse, generating shock waves, the velocity of which is close to sound velocity and the attenuation of these oscillations being caused by heat exchange at the liquid/vapor interface. When the pressure at the tip of the point electrode is higher than p_c, the shock wave is only observed for each measured current pulse. The evolution of the diameter of the gas bubble follows the Raleigh model (Raleigh, 1917). Gas bubbles are observed at energy levels as low as 10^{-8}–10^{-11} J, with a diameter of the order of 10^{-6} m.

The generation of a gas bubble has two immediate consequences: the increase of the electric field and the increase of the pressure within the gaseous cavity. The increase in the electric field is directly related to the difference between the permittivities of the gas and the oil, in the range of 2.2–2.6. The increase of the local electric field, combined with the lower ionization potential of the gas, tends to favor the development of subsequent ionization activities in the gaseous cavity. On the other hand, the increase of the gas pressure within the cavity tends to make the same ionization activities more difficult.

6.3.2.2.2 Propagation of the Discharge

When the conditions are propitious, several current pulses follow the initial pulse; each corresponds to the generation of a new gas bubble ahead of the last, forming a streamer channel, and the dimensions and the propagation velocity correspond to a *bush-type* streamer. The development of the discharge depends

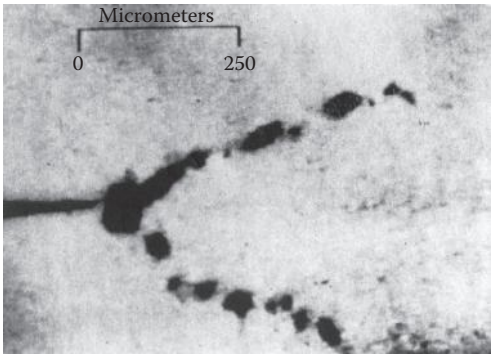


FIGURE 6.9 Breaking up of a streamer channel into microbubbles. (From Lesaint, O. and Gournay, P., *J. Appl. Phys*., 27, 2111, 1994a; Lesaint, O. and Gournay, P. *J. Appl. Phys*., 27, 2117, 1994b.)

essentially on the sustainment of the gas channel. In effect, the discharge stops when the gas channel collapses, disintegrating into multiple bubbles shown in Figure 6.9 (Lesaint and Gourmay, 1994a). This particularity of the discharge mechanism in oil explains the influence of the hydrostatic pressure on development of the discharges. The interpretation of the discharge development must consequently take account of the formation of the gas channel and its sustainment, probably by ionization activities in the gas volume.

Negative streamer: When the point electrode is under negative polarity, the charge injection is made from the cathode and the avalanches develop in a continuously decreasing field within the gas channel formed by the evaporation of the oil. As in the case of gas discharges, neutralization of the positive ions at the cathode results in the formation of a negative ion space charge within the gas cavity, which reduces the local field and eventually suppresses the ionization within the gas cavity. The ionization activities are reactivated when the ion space charge is dispersed into the surrounding oil volume. One observes then a new gas bubble, which extends the gas channel farther into the oil volume. This behavior of the discharge gives rise to a current pulse, similar to *Trichel* pulses, well known in gas discharges. Since the development of negative streamer is made in a decreasing field, the streamer progression eventually stops and the gas channel collapses in a series of microbubbles.

Positive streamer: When the point electrode is under positive polarity, the generation of a free electron in the oil volume within the stressed volume initiates a first electron avalanche developing towards the anode and, at the same time, forming a gas bubble by evaporation of the oil. The subsequent avalanches develop essentially within the gas cavity and contribute to its growth. Since the positive avalanches develop in an increasing field, the great majority of the ionization activity is towards the anode where the electrons are eventually absorbed, leaving in their path a positive ion space charge. The accumulation of positive ion space charges effectively extends the anode farther into the oil volume in the form of a streamer channel (Figure 6.10).

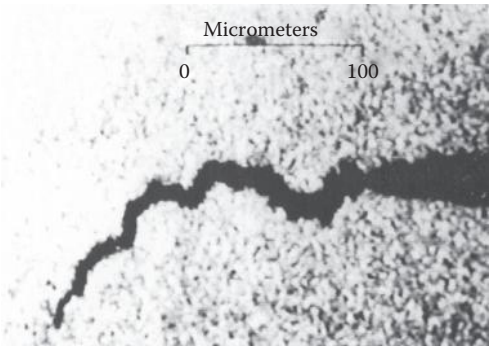


FIGURE 6.10 Progression of a streamer into the oil volume. (From Lesaint, O. and Gournay, P., *J. Appl. Phys*., 27, 2111, 1994a; Lesaint, O. and Gournay, P. *J. Appl. Phys*., 27, 2117, 1994b.)

This mechanism of propagation of the positive streamer is efficient since the development of the subsequent avalanches provides the free electrons, which follows the same path towards the anode and contributes to sustaining the gas channel. It gives the filamentary structure, typical of positive streamers. The extension of positive streamers into the low-field regions contributes eventually to the accumulation of a positive ion space charge, which reduces the local field and stops the streamer development. The gas channels collapse into a series of microbubbles. A new streamer will be initiated when the positive ion space charge is dispersed and an initiating free electron is present in the stressed oil volume.

Fast streamer (supersonic): The ionization activities within the gas cavity produce an increase in the gas pressure associated to the high temperature in the discharges. Two effects are possible: On the one hand, the increase in the gas pressure makes the development of the discharge more difficult; on the other hand, it contributes to facilitate the growth of the gas cavity and, consequently, to sustain the discharge within the gas cavity. It is possible that it is the mechanical stress from the internal gas pressure, which is at the origin of the interfacial instability, observed during the development of fast streamers leading to the breakdown of short gaps.

6.3.2.2.3 Transition to Breakdown

The breakdown occurs when the streamers succeed to cross the discharge gap, forming a conducting path between the electrodes. In uniform and quasi-uniform field gaps, the breakdown often results from the simultaneous development of streamers of both polarities originating from different sites (Hebner et al., 1985). Generally, the negative streamers do not propagate beyond half of the gap. The breakdown results from a positive streamer, which cross the remaining gap to reach the negative streamer.

6.3.3 Breakdown of Long Oil Gaps

Because of the high dielectric strength of the insulating oil, most of the studies of oil insulation are done in relatively short gaps, limited by the test facilities. As a result, there are relatively few studies of breakdown of long oil gaps in nonuniform fields. From the early studies of Anderson and Liao (1955), the resemblance to leader breakdown processes of long air gaps has been observed. The question remains controversial and is still not completely resolved (Kamata and Kato, 1980; Rain et al., 1991). We present in the following the main findings of a joint project, *IREQ–LEMD* (*Jeumont Schneider-Laboratoire d'Électrostatique et de Materiaux Diélectriques*), on the breakdown of long oil gaps (Saker et al., 1994; Massala et al., 1995; Aubin et al., 1996; Trinh and Saker, 1996). The extensive use of photographs in *streak* mode has allowed an interpretation of the physical mechanism of discharges leading to the breakdown of a point–plane gap in typical transformer oil. Two modes of breakdown can be distinguished as

1. Direct breakdown
2. Breakdown by streamer burst

6.3.3.1 Direct Breakdown

The direct breakdown of an oil gap is observed subsequent to the development of a leader discharge, which extends from the stressed electrode to the plane electrode. After its initiation, the leader development is characterized by a succession of reilluminations followed by extinctions of the leader channel all along its progression across the discharge gap. Figure 6.11 shows the photos in streak mode of the leader development and the corresponding light signal under positive and negative polarities (Trinh and Saker, 1996). The following observations can be made:

- In addition to the complete reilluminations of the leader channel, one observes also partial reilluminations with only a portion of the *leader* channel that is reilluminated.
- The reillumination of the leader channel may or may not be followed by a diffuse discharge, referred to as *streamer*, which develops from the tip of the *leader* channel.
- In the case where one observes a *streamer* discharge, it is rapidly suppressed to transform into a new segment of the leader channel during the rest period separating two reilluminations. This is particularly visible in the case of partial reilluminations.

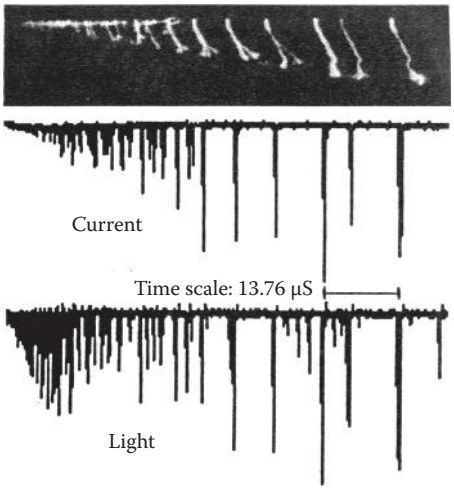


FIGURE 6.11 Leader direct breakdown under positive polarity in a 60 cm oil gap at 380 kV. (From Trinh, N.G. and Saker, A., Interpretation of the physical mechanism in the breakdown of long gaps in transformer oil, in: *International Conference on Conduction and Breakdown in Dielectric Liquids*, Rome, Italy, 1996, pp. 287–291.)

- The dead time separating two consecutive reilluminations increases with the progression of the leader into the gap.
- The apparent average velocity of progression of the leader is in the order of 3 km/s.
- No significant difference is observed under ac and impulse voltage and between positive and negative polarities on the development of the discharge, both in the visual aspect as shown in Figure 6.12 (Trinh and Saker, 1996) and in the measured withstand voltages. For a 28 cm diameter sphere-plane gap of 60 cm, the direct ac breakdown occurs at –608 kV (in the negative half cycle) and +636 kV (in the positive half cycle). It is –543 kV and +535 kV in streamer burst breakdown.

The interpretation of the results obtained is presented in the following, concerning the physical mechanism in the preceding two-mode breakdown. The gaseous leader channel explains the observed similarities with the leader discharge in air, namely, the reillumination of the leader and its constant progression, in successive steps, until it either stops or causes breakdown of the gap. One can formulate the mechanism for the direct breakdown composed of three stages:

1. Formation (progression) of the gaseous channel (of the leader)
2. Gas discharge (reillumination) within the leader channel
3. Extension of the gaseous channel

6.3.3.1.1 Formation of the Gaseous Channel (of the Leader)

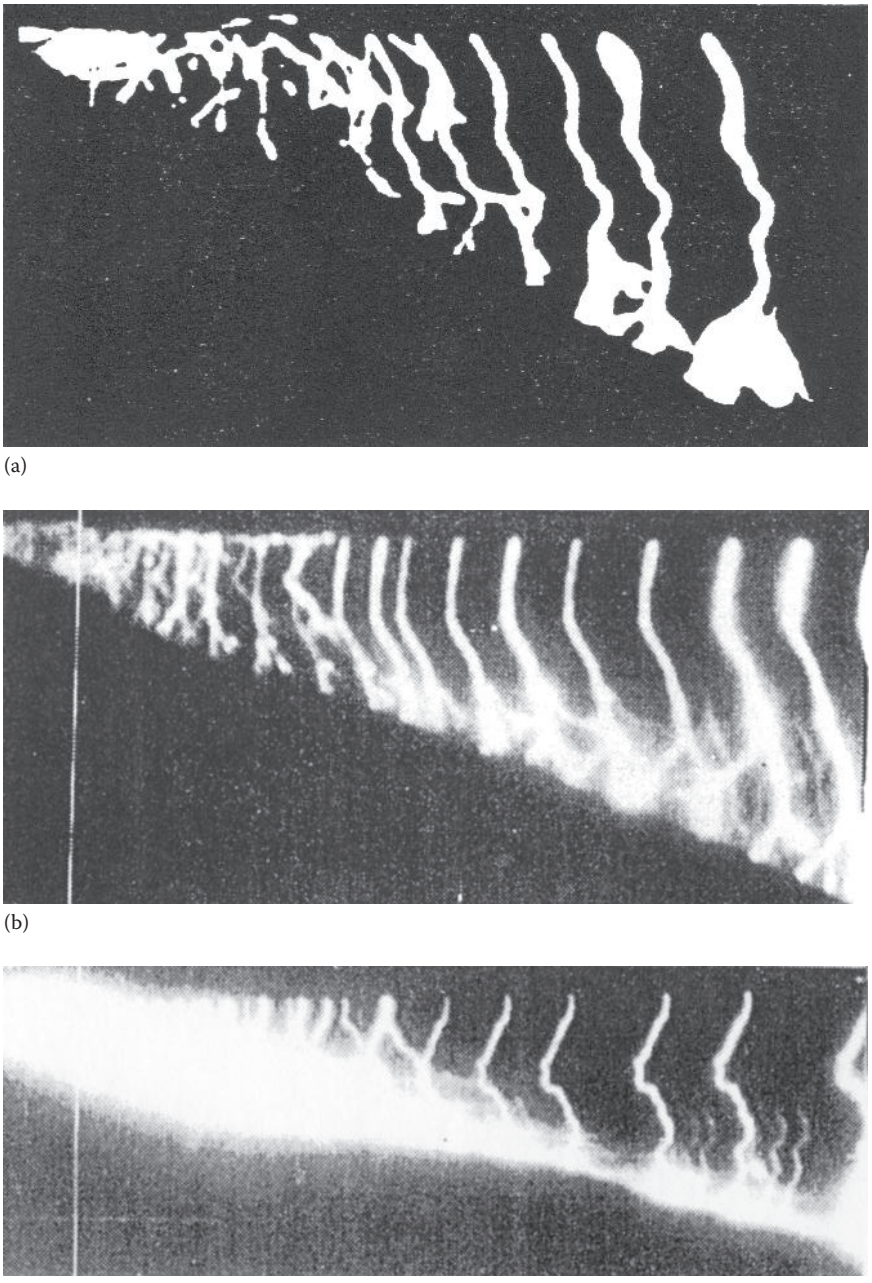
It is initially produced by an electronic discharge (streamer) under the action of an electric field sufficiently high at the stressed electrode (Trinh and Saker, 1996). This discharge is rapidly suppressed by its own ion space charges. It is created by evaporation of the oil microbubbles, which after coalescing form a gaseous channel adjacent to the electrode. The longitudinal field along the gas volume is approximately

$$E_m = \frac{du_l}{dl} \tag{6.4}$$

where

l is the length

u_l the voltage drop across the gas channel formed, determined by the applied electric field and ion space charges deposed on the wall of the gaseous channel



(a)

(b)

(c)

FIGURE 6.12 Visual aspect of Leader direct breakdown under positive ac and impulse voltage of both polarities. (a) Development of positive leader under ac voltage; (b) development of positive leader under impulse voltage; (c) development of negative leader under impulse voltage. (From Trinh, N.G. and Saker, A., Interpretation of the physical mechanism in the breakdown of long gaps in transformer oil, in: *International Conference on Conduction and Breakdown in Dielectric Liquids*, Rome, Italy, 1996, pp. 287–291.)

6.3.3.1.2 Gas Discharge (Reillumination) of the Leader Channel

If the voltage drop u_1 is sufficiently high, a gas breakdown occurs within the gas volume and completely ionizes the gas, emitting intense light signal, corresponding to the initiation (or reillumination) of the leader channel. The consequences of the gas breakdown are as follows:

- The leader channel becomes highly conducting, with a voltage drop Δu_1 much smaller than u_1 determined by the applied field. A local field enhancement occurs at the tip of the leader channel and initiates a new electronic discharge in the region ahead of the leader channel.
- Sustaining the gas discharge within the volume of the leader channel requires a steady supply of free electrons to ionize the gas. Since the gas volume is limited, the ionization activities will stop when supply of electrons becomes insufficient. The gas discharge is suppressed and the reillumination is completed.
- The reillumination of the *leader* also increases the gas pressure within the gaseous channel, preventing it from collapsing. The duration of a gas cavity in oil is typically in the order of microseconds (Raleigh, 1917; Lesaint and Gournay, 1994b).

6.3.3.1.3 Extension of the Gaseous Channel

At the end of the gas discharge phase, the gas within the leader channel cools down, its conductivity is reduced, and the voltage drop across the gaseous channel increases to eventually equal the value determined by the applied voltage. In the mean time, the electronic discharge, developing under the action of the field enhancement at the tip of the leader channel, produces microbubbles, which transform into a small gas volume of length δl, and effectively extends the initial gaseous channel further in the discharge gap. At the end of this phase, if the voltage drop across the extended gaseous channel (determined by the applied voltage) is sufficient, a new gas discharge occurs within the gas volume and reilluminates the leader, which progresses effectively by a distance δl into the discharge gap.

As previously mentioned, the photos in *streak* mode of the leader development show also cases of partial reillumination of the gaseous channel. This phenomenon can be explained by the nonuniform cooling of the leader channel subsequent to its extinction. The voltage drop is insufficient to initiate the gas breakdown across the whole gas volume, although it is sufficient for a partial breakdown of a portion of the gaseous channel. These partial reilluminations seem to correspond to the transformation of the streamer discharge into a segment of the channel. It is to be noted that the development of the streamer (diffuse) and, consequently, the extension of the gaseous channel are dependent on the local electric field at the tip of the leader. In effect, Figures 6.11 and 6.12 show cases where the reillumination of the *leader* does not produce a streamer discharge nor increase in the leader length. One observes in this case a branching of the leader, probably due to a mutual screening effect, which reduces the electric field at the tip of these branches of the leader below the threshold value to initiate a streamer discharges. This process continues and allows the leader to progress into the oil gap until the occurrence of one of the two conditions:

1. The leader bridges the oil gap and causes its breakdown.
2. The voltage drop u_l along the leader is insufficient to initiate the gas breakdown within the gas volume. The leader is then stopped and the oil gap withstands the applied voltage.

6.3.3.1.4 Discussions

This model of leader discharge, based on the sustaining of a gaseous channel by successive reillumination, provides qualitative answer to several experimental observations:

- *Effect of polarity*: Although present, the observed polarity effect is not pronounced, both in the visual aspect shown in Figures 6.11 and 6.12 (Trinh and Saker, 1996) and in the measured withstand voltages. The results of Kamata and Kako (Kamata and Kako, 1980) show a difference in the order of 10%–20% for the gaps up to 1 m. For short gaps, the onset voltage of the streamer is higher under negative polarity, while for long gaps, the onset voltage is higher under positive polarity.

The leader mechanism with its gaseous channel sustained by successive reilluminations should not show a significant effect of polarity, which may influence the initiation of the reilluminations but does not change the basic mechanism. The difference in the onset voltage of the streamer can be explained by the difficulty to find the initiating electron, which must be emitted from the cathode when the applied voltage is negative and from the oil volume around the stressed electrode when the applied voltage is positive. In short gaps, the lower positive onset voltage is explained by the relative facility to find the initiating electron in the stressed oil volume around the anode. In long gaps, the high electric field at the cathode is sufficient to activate the electron emissions from the cathode and eventually makes the onset voltage lower in negative polarity.

- *Evolution of the leader channel*: Saker has shown that the probable representation of the leader channel is a volume of essentially neutral gas, slightly conducting and having ion space charges deposed on the leader–oil interface (Saker, 1993). The model presented here is not in conflict with the representation suggested by Saker. With the exception of the period of reillumination where the leader channel can have a high conductivity, it loses rapidly this conductivity during the dead time between two consecutive reilluminations, subjecting the gaseous channel to a high electric field to initiate the next reillumination.
- *Existence of a critical front for the switching impulse for which the breakdown voltage is minimal*: The existence of a critical front for the switching impulse, in the order of 50–100 μs (Figure 6.13), seems observable from the results of Kamata and Kako (1980). The minimal breakdown voltage can be explained by the fact that the voltage rises during the front of a switching impulse of critical front, is sufficient to compensate for the increase in the voltage drop along the leader, necessary to ensure its progression into the discharge gap. The development of the leader is continuous from its initiation to breakdown of the oil gap. For impulses with front shorter than critical, a higher voltage is required by the leader to bridge the gap in a shorter time. For impulses with front longer than critical, the leader does not progress continuously, and higher applied voltage is required to break the gap.

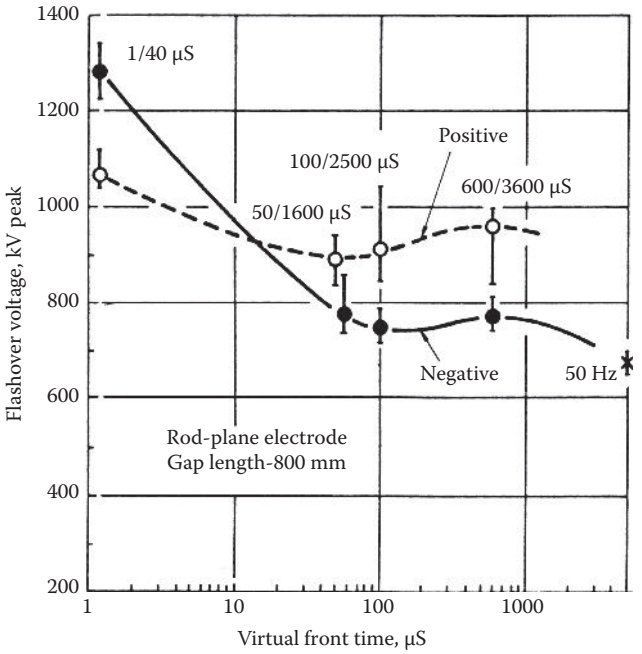


FIGURE 6.13 Variations of the breakdown voltage with the front time of the switching impulse. (From Kamata, Y. and Kako, Y., *IEEE Trans. Electr. Insul.*, EI-15(1), 18, 1980.)

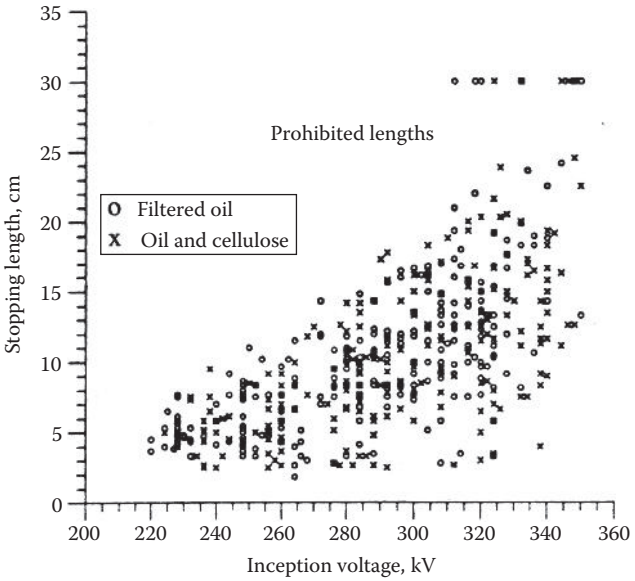


FIGURE 6.14 Distribution of the length of leaders in oil, showing a range of excluded lengths. (From Trinh, N.G. and Saker, A., Interpretation of the physical mechanism in the breakdown of long gaps in transformer oil, in: *International Conference on Conduction and Breakdown in Dielectric Liquids*, Rome, Italy, 1996, pp. 287–291.)

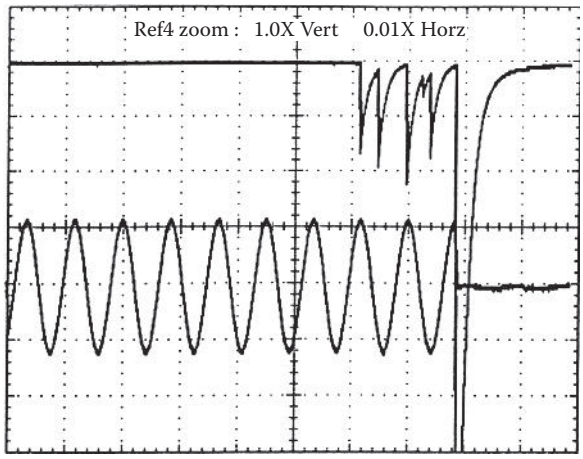
- *Existence of a final jump* seems indicated by the results obtained in measuring the length of the leader shown in Figure 6.14 (Saker et al., 1994). They show a range of forbidden lengths to the leader. This may be related to the fact that the distribution of the electric field in the space between the streamer head and the plane electrode becomes more uniform as the streamer approaches the latter. It follows that for a given applied voltage, there exists a critical distance at which the streamer can extend over the space separating the leader tip and the plane electrode, resulting in a rapid extension of the gaseous channel to bridge this space and cause the breakdown of the oil gap. The consequence is that a stable leader cannot extend within this range of distances.

6.3.3.2 Breakdown by Discharges in Streamer Burst

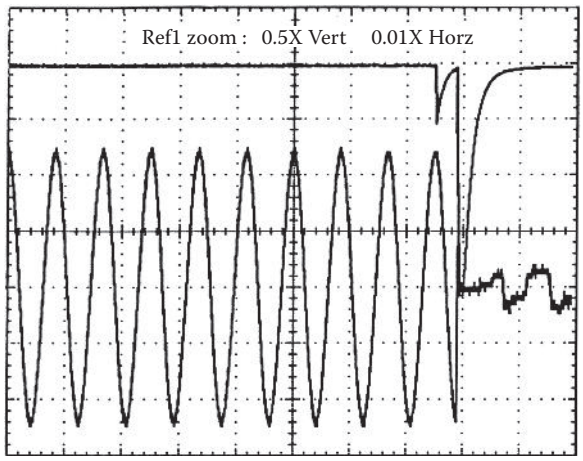
In the case of an ac voltage, the breakdown of the oil gap may occur subsequent to a discharge in streamer burst (Saker et al., 1994), where the leader is extinguished and reignited over several consecutive half cycles of the applied ac voltage, until the last discharge bridges completely the gap and causes its breakdown (Trinh and Saker, 1996). Figure 6.15 shows the light signal and the applied voltage, recorded during a streamer burst discharge causing the breakdown of the oil gap.

The video visualization of the streamer burst discharge at *LEMD* shows a similarity in the paths followed by the discharge in successive half cycles. This signifies a *certain influence of the leader discharge in one half cycle on the development of the leader discharge in the next half cycle, without being systematic*, as illustrated by the sequences of photos taken during a discharge in streamer burst shown in Figure 6.16. The interest in this mechanism of breakdown resides in the fact that it is specific to the ac voltage, allowing the streamer to continue its progression over a much longer time and to cause the breakdown of long oil gaps at voltages relatively low.

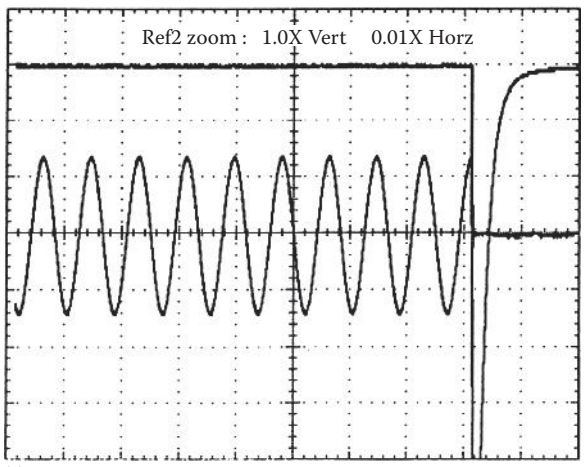
One can expect, in the case of discharges in streamer burst, that the final breakdown (at the last half cycle of the streamer burst) follows a leader process as in the case of a direct breakdown. However, a new mechanism must be found to explain the reignition of the leader channel after a long dead time, during which the applied field passes by zero and changes polarity. Two mechanisms are possible for the reignition of the discharge in streamer burst: by microbubbles and residual ion space charges.



(a)



(b)



(c)

FIGURE 6.15 Breakdown of an oil gap caused by a discharge in streamer burst under ac voltage. (a) Streamer burst lasting over 5 half cycles at 552 kV. (b) Streamer burst lasting over 2 half cycles at 565 kV. (c) Direct breakdown in one half cycle at 890 kV. (From Trinh, N.G. and Saker, A., Interpretation of the physical mechanism in the breakdown of long gaps in transformer oil, in: *International Conference on Conduction and Breakdown in Dielectric Liquids*, Rome, Italy, 1996, pp. 287–291.)

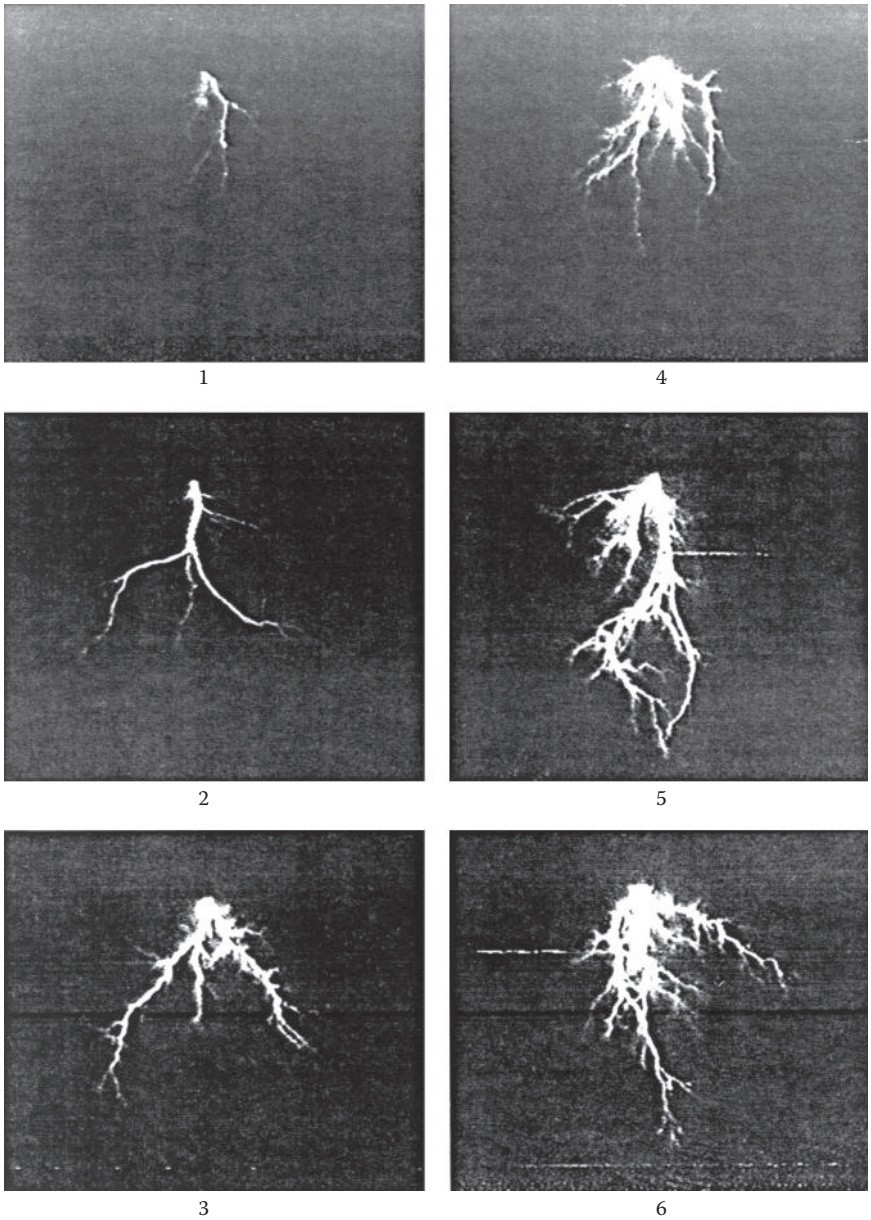


FIGURE 6.16 Sequences of the development of a discharge in streamer burst. (From Lesaint, O. and Saker, A., Études des mécanismes de claquage des grands volumes d'huile, LEMD and IREQ, Grenoble, France, 1993.)

- The duration of the gaseous cavities in oil being in the order of microseconds, it would be difficult to imagine that the gaseous channel is preserved during several milliseconds between two consecutive reilluminations. One can suppose that, during the dead time, the gaseous channel begins to break up into a series of microbubbles illustrated in Figure 6.9 (Saker, 1993).

  In these conditions, the reignition of the leader corresponds to a discharge initiated within the microbubbles which reactivate the leader channel. Since the applied field passes by zero between two consecutive reignitions of the leader, one can assume that at each half cycle, it resumes its development from the stressed electrode. The reignition starts probably in a

microbubble adjacent to the electrode and propagates rapidly to the other microbubbles forming the residual gaseous channel. The initiation of the discharges in the microbubbles results from the enhancement of the electric field in the microbubbles as compared to the nominal field within the oil in the absence of the microbubbles.

This mechanism suffers, however, of the short duration of the microbubbles. In the life duration of the microbubbles observed by Saker is in the order of microseconds but may extend up to a half millisecond (500 μs) observed by Watson (Watson et al., 1985).

- The reignition of the leader channel is caused by the residual space charges from the preceding half cycle (Figure 6.15). If the microbubbles are absorbed by the oil, the ion space charges are left within the oil volume around the stressed electrode. Under the action of the applied field, these space charges are either pushed away from or attracted to and partly neutralized at the stressed electrode. At the end of a half cycle, the voltage reverses its polarity, causing the residual charges to reverse their movement within the oil volume. As a result, the charges not neutralized at the stressed electrode are pushed away into the oil volume, while those previously in the oil volume at the end of the preceding half cycle are now attracted to the stressed electrode. Their arrival close to the electrode increases the local field and facilitates the reignition of the leader.

6.4 Factors Affecting the Oil Insulation

Because of its dielectric, thermal properties and long service experience, the oil insulation is widely used in electrical apparatus and, almost exclusively, in power transformers and inductances. However, a number of parameters can affect its insulating performances (Zaky and Hawley, 1955), namely, impurities, dissolved gas content, humidity, hydrostatic pressure, stressed areas and volumes, and solid particle contamination.

6.4.1 Impurities

The presence of impurities with low ionization and excitation potentials can affect the development of the discharges. This is particularly important for a pure liquid. The question is relatively irrelevant for mineral oil, which is a mixture of hydrocarbons from different origins and diverse additives.

6.4.2 Dissolved Gases and Hydrostatic Pressure

Gases can dissolve into insulating oils to different degrees, depending on the nature of the gas, the hydrostatic pressure, and the temperature of the oil (Zaky and Hawley, 1955; Bartnikas and Srivastava, 1980). The effect of dissolved gases on the dielectric performances of the insulation is relatively minor if the content remains below the saturation level. When the saturation is reached, the excess of dissolved gas in the oil is released and forms gas bubbles. Such a behavior can occur during sudden change of the loading conditions, which causes a rapid increase in the local temperature, for example, close to the windings. Because of the low permittivity of the gas, the electric field in the gas bubbles is two to three times the field in the adjacent oil. This favors the development of PDs in the gas bubbles, which can ultimately affect the dielectric performances of the oil insulation. The presence of gas bubbles in the insulation is particularly critical when they are formed in high-field regions.

As for the hydrostatic pressure, it has a direct influence on the dielectric strength of the oil, providing a better dielectric performance at higher pressures. The effect is related to the fact that the breakdown of the oil gap passes by a gaseous phase, for which the generation of a gaseous cavity is more difficult the higher the hydrostatic pressure is. Hydrostatic pressures are unavoidable in oil-insulated equipment; their effect must be taken into account in the insulation design of the equipment.

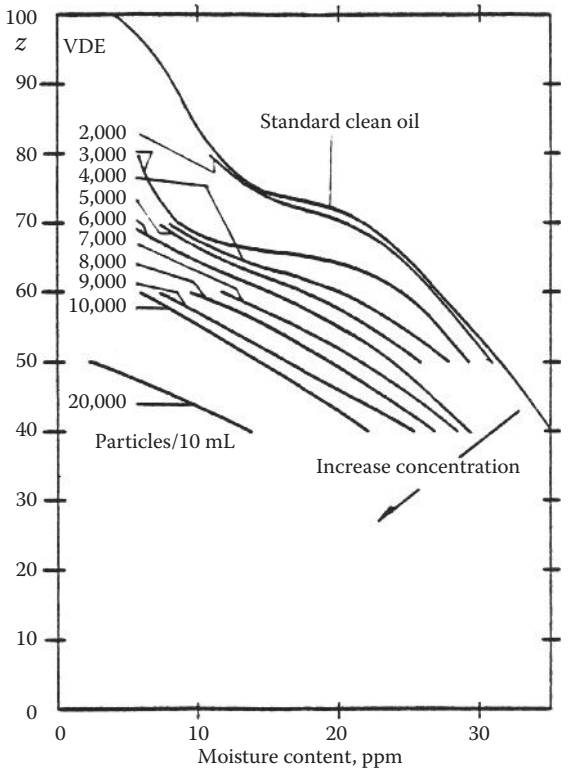


FIGURE 6.17 Effect of humidity on the dielectric strength of oil evaluated with VDE electrode gap z: % strength in reference to dry oil, for different particle content levels. (From Miners, K., *IEEE Trans. Power Appar. Syst*., PAS-101(3), 751, 1982.)

6.4.3 Humidity

Water is also absorbed by the oil in power transformers and reduces significantly the dielectric strength of the insulating oil (Miners, 1982). Figure 6.17 illustrates the effect of humidity on the dielectric strength of mineral oil measured with Verband Deutscher Electrotechniker (*VDE*) electrodes. One notices a slight reduction of the dielectric strength, about 15%, at a water content of 10 ppm. It passes by a plateau at 70% at a water content of 20 ppm before it reduces notably at water contents higher than 20 ppm.

6.4.4 Dissolved Metals

Under normal operating conditions, minute quantities of metals used in the fabrication of power transformers, in particular copper, are dissolved in the oil (Lamarre et al., 1987). The typical content of dissolved copper in oil of power transformers is of the order of *ppb* and tends to increase with time in service and can ultimately affect the dielectric loss factor, tanδ, of the insulating oil. It is a specific propriety of the oxidation of the insulating oil and an indication of its aging state and may be used in the location of incipient faults (Skog et al., 1980).

6.4.5 Solid Particle Contamination

The dielectric strength of transformer oil can be significantly reduced by the contamination of solid particles, in particular carbon and fiber particles.

In the presence of the applied electric field, particles are subjected to different forces related to the following: electrostatic, electrophoretic, dielectrophoretic, and electrohydrodynamic forces (Pickard, 1965). The electrostatic force on a charged particle drives the particle into the low field regions while the electrophoretic forces drive the particle into the high field regions. The electrohydrodynamic force imposes a circular movement on the particles that may, in some cases, counter the effect of the previously

mentioned forces (Denegri et al., 1977). In a short gap, the particles can accumulate in the high-field region to eventually short-circuit the gap and cause its breakdown (Darveniza, 1969).

Such a breakdown mechanism is unlikely in long gaps and under conditions of steady oil circulation. The effect of particle contamination is then more restraint, corresponding to an accrued probability to initiate the breakdown of the oil gap. One observes that the breakdown voltage is a function of the electrode dimensions, namely, its stressed area and oil volume. The effect of the stressed oil volume on the breakdown voltage of oil has been recognized since the 1950s when Wilson proposed the theory of volume effect to explain the behavior of oil insulation (Wilson, 1953, 1955). The theory was rapidly contested by Weber and Endicott, who observed rather an effect of the stressed electrode area (Weber and Endicott, 1956; Endicott and Weber, 1957; Weber and Endicott, 1957). As the majority of experimental data available are obtained under conditions of uniform and quasi-uniform fields, the controversy between the stressed areas and volumes lasted for several years.

Since then and particularly during the 1970s–1980s, considerable works have been made, covering a wide range of stressed areas and volumes, 10^5 cm^2 and 10^7 cm^3, respectively (Trinh et al., 1982). The correlation between the particle contamination and the volume effect was established by Palmer and Sharpley who clearly show that an improvement in the dielectric strength of the oil occurs when the oil is well filtered to eliminate the contaminating particles (Palmer and Sharpley, 1969, 1970). Trinh et al. have shown that the distinction between the stressed area and volume effect is closely related to the particle content in the oil (Trinh et al., 1982). In a well-filtered oil, the breakdown is initiated from asperities at the electrode surface, producing a predominant effect of the stressed electrode areas. In a particle-contaminated oil, the breakdown of the oil is initiated from the solid particles within the oil volume, producing a predominant effect of the stressed oil volume. It is, at present, accepted that solid particle contamination is unavoidable in power transformers and reactors in normal operating conditions. The effect of particle contamination on the dielectric performance of an oil gap will be discussed in the following.

6.4.5.1 Particle Content

The practical way to determine the particle content in oil is to measure the particle density, that is, the number of particles of dimensions greater than a threshold value in a known volume of oil, typically 100 mL. Most particle counters count the particles by optical means: the oil is circulated in a glass tube of known diameter. An intense light is directed transversally to the oil circulation and projects a shadow of any solid particle passing in front of the observation window, on a photodiode opposite to the light source. By measuring the current of the photodiode, the number and dimensions of the particles can be evaluated. Figure 6.18 compares the results obtained by different laboratories in a round-robin test for the measurement of particle content of transformer oil for CIGRE Study Committee 15.

Index of particle content, δ_p (Trinh et al., 1982): In an effort to simplify the representation of the particle contamination in oil, an index of particle content δ_p was introduced. Noting that the distribution of the particle content follows approximately a power law, the index δ_p was defined as

$$\delta_p = \ln(n_0 * d_1) \tag{6.5}$$

where

n_0 is the number of particles larger than 1 μm

d_1 the maximal diameter possible of the particles in the oil sample, in μm.

An oil with $n_0 = 10^5$ particles larger than 1 μm per 10 ml of oil, and $d_1 = 100$ μm has an index of particle content δ_p of 13.8. Typical oils in transformers have an index of particle content between 13 and 15; a contaminated oil has an index higher than 15, while a well-filtered oil has an index less than 13.

6.4.5.2 Effect of Stressed Area and Volume

As previously mentioned, it is a known fact that the dielectric withstand voltage of an oil gap is reduced considerably with the increase of either the stressed area or volume. The latter parameters are defined, respectively, as the region at the surface of the electrode and the volume oil where the electric field is

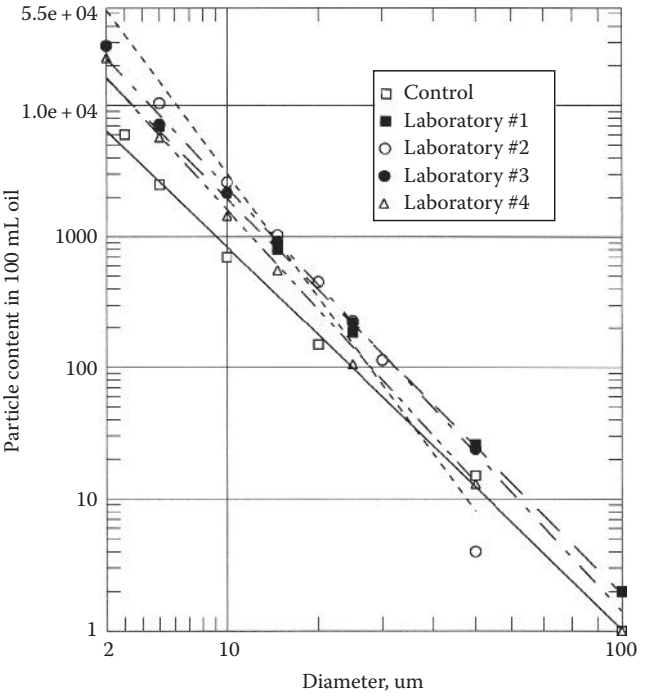


FIGURE 6.18 Typical particle contents of transformer oil.

higher than 90% of the maximal field in the gap (Wilson, 1953; Weber and Endicott, 1956). One can subdivide the electrode surface and the oil volume in small elementary surfaces and volumes of dimensions taken arbitrarily as 0.1 cm^2 and 0.02 cm^3. The stressed area and volume are, consequently, formed by N_s and N_v elementary surfaces and volumes.

The area and volume effects are directly related to the statistical nature of initiating the breakdown of the oil gap. By associating to each elementary surface and volume a finite probability to initiate the breakdown of the oil gap, the breakdown probability of the oil gap can be evaluated from the known breakdown probability distribution functions of the elementary surface and volume (Trinh et al., 1982). In effect, let $p_s(u)$ and $p_v(u)$ be the probability of an elementary surface and volume to initiate the breakdown of the gap; the probabilities that the breakdown will not be initiated from these same elementary surface and volume are $1 - p_s(u)$ and $1 - p_v(u)$, respectively. Then the withstand probability of the oil gap corresponds to the case where breakdown is not initiated from any of the elementary surface and volume:

$$1 - P_n(u) = \prod_{N_s} [1 - p_s(u)] \prod_{N_v} [1 - p_v(u)],$$

and the breakdown probability of the oil gap is

$$P_n(u) = 1 - \prod_{N_s} [1 - p_s(u)] \prod_{N_v} [1 - p_v(u)] \tag{6.6}$$

where $p_s(u)$ and $p_v(u)$ are, respectively, the probabilities that the breakdown of the oil gap is initiated from an elementary surface and volume at the voltage u.

Noting that the stressed area and volume correspond to region in the oil gap where the field is normally higher than 90% of the maximal field, a simplification can be introduced by assuming the same probability of initiating breakdown from an elementary surface or volume. One gets

$$P_n(u) = 1 - [1 - p_s(u)]^{N_s} [1 - p_v(u)]^{N_v} \tag{6.7}$$

From the previous expressions for the breakdown probability of an oil gap, one can see that a pure area effect exists when $p_v(u)$ is null, a condition obtained in well-filtered oil. On the other hand, a pure volume effect implies that $p_s(u)$ is null, a condition prevailing in a particle-contaminated oil:

$$P_n(u) = 1 - [1 - p(u)]^n \tag{6.8}$$

where

$P_n(u)$ is the breakdown probability of the oil gap
$p(u)$ is the probability to initiate the breakdown from an elementary surface or volume
n is the number of elementary surfaces or volumes forming the stressed electrode area or oil volume

The stressed electrode area or oil volume effect is therefore a simplified but convenient way to interpret oil breakdown data. We will discuss in the following how appropriate these simplified approaches are.

Evaluation of the probability function of the elementary surface and volume: From the preceding expression, one can derive the probability to initiate the breakdown from an elementary surface or volume, according to

$$p(u) = 1 - \sqrt[n]{1 - P_n(u)} \tag{6.9}$$

This last equation (6.9) provides a convenient means to determine the distribution function of the probability that an elementary surface or volume to initiate the breakdown of the oil gap using the vast amount of from experimental data available in studies of large oil gap breakdown. In effect, note that the measured breakdown probability can be taken as $P(u) = 0.5$ unless a special low-probability test procedure is used. The relation (6.9) determines the breakdown probability of an elementary surface or volume at the voltage u, knowing the number of elementary surfaces or volumes forming the discharge gap. The larger the number n of elementary surfaces or volumes, the lower the breakdown probability of the elementary surface or volume. As a result, the distribution function of the breakdown probability of the elementary surface or volume can be readily determined over a wide range of breakdown probabilities from available test results obtained on oil gaps with different stressed areas and volumes.

Typical results are presented in Figures 6.19 and 6.20 showing the distribution function of an elementary surface and volume under conditions of breakdown test with increasing ac voltages. On the other hand, Tables 6.3 through 6.6 present the parameters defining the distribution functions of probabilities to initiate the breakdown of an elementary surface and volume for different classes of oil quality under conditions of ac and impulse voltages. The weibull distributions are derived from the Normal distributions according to the CIGRE procedure, with a value of n = 3, discussed in Chapter 3 (Trinh et al., 1982).

Evaluation of the breakdown voltage of an oil gap: These probability distribution functions can then be used to calculate the breakdown voltage of an oil gap, knowing its stressed area or volume and the desired breakdown probability, P_b. In effect, from the breakdown probability P_b, the corresponding breakdown probability of the elementary surface or volume is readily obtained from the equation (6.9) and the corresponding breakdown voltage from the experimental distribution function of the breakdown probability of the elementary surface or volume. Figures 6.21 through 6.24 compare the calculated breakdown voltages with the experimental values for the range of stressed surfaces and volumes. These results illustrate well the adequacy of this approach to evaluate the withstand capability of an oil gap from its stressed surface or volume.

Evaluation of the ac withstand voltage: Noting that the distribution of the breakdown probability of an elementary surface or volume is derived for a steady rising voltage, it may be taken as approximately representing the breakdown probability of the elementary surface or volume in an ac cycle of the applied voltage. The ac withstand voltage of an oil gap can then be readily evaluated for different values of the withstand duration (Trinh and Vincent, 1980). In effect, with the equivalent breakdown probability of an elementary surface or volume, p_n, taken as the breakdown probability in one cycle of the applied voltage, the corresponding withstand probability in one cycle of the ac voltage is

$$P_W = 1 - p_n$$

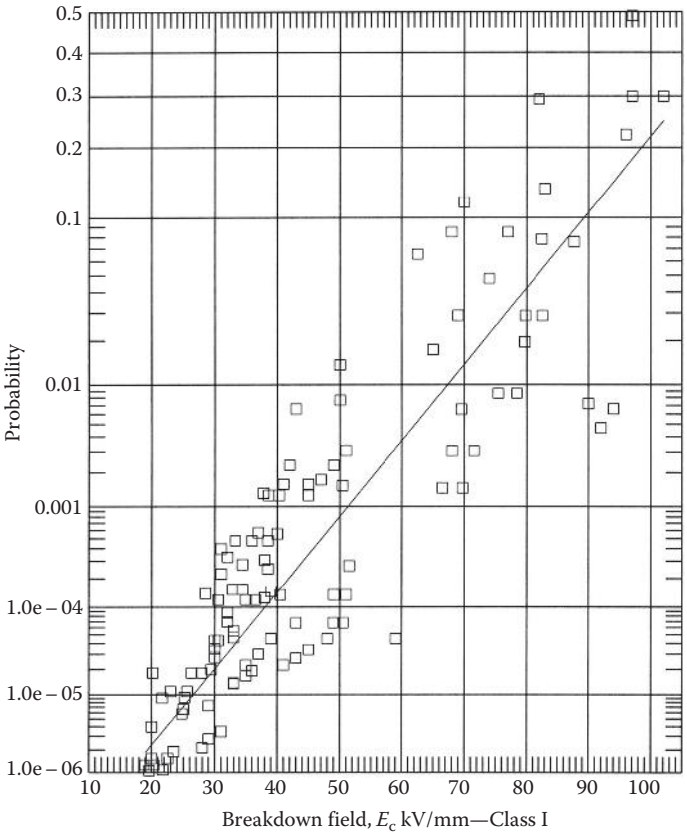


FIGURE 6.19 Typical distribution of the breakdown probability of an elementary volume, of normal type, in class I oil, and under condition of steady rising impulse voltage.

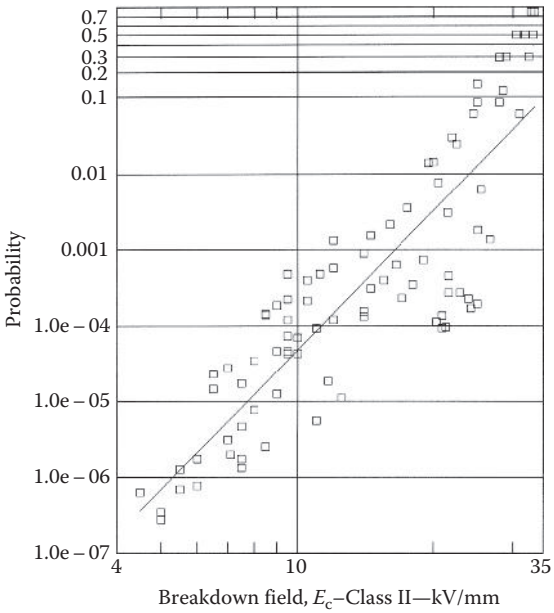


FIGURE 6.20 Typical distribution of the breakdown probability of an elementary volume, of Weibull type, in class II oil, and under condition of steady rising ac voltage.

TABLE 6.3

Distribution of Probability to Initiate Breakdown from an Elementary Volume, $W_0 = 2 \times 10^{-2}$ cm^3 under Condition of Steady Increasing AC Voltage

Parameters	Units	Normal	Extreme Values	Weibull CIGRE Procedure
Class I oil				
Mean E_m, position E_0		34.93	33.0	24.52
Sigma σ, scale α		3.47	1.29	11.45
Form β				3.4
r^2, coefficient of correlation		0.98	0.89	
Class II oil				
Mean E_m, position E_0	kV/mm	31.48	26.67	16.15
Sigma σ, scale α	kV/mm	5.11	1.44	16.86
Form β				3.4
r^2, coefficient of correlation		0.91	0.67	
Class III oil				
Mean E_m, position E_0	kV/mm	16.98	15.78	8.22
Sigma σ, scale α	kV/mm	2.92	1.02	9.63
Form β				3.4
r^2, coefficient of correlation		0.95	0.69	

Sources: Trinh, N.G. et al., Electrode area, stressed-volume: Two apparent effects of large-volume oil-insulation, in: *IEEE International Symposium on Electrical Insulation*, Philadelphia, PA, June 6–9, 1982a, pp. 115–118; Trinh, N.G. et al., *IEEE Trans. Power Appar. Syst*., PAS-101(10), 3712, 1982b.

TABLE 6.4

Distribution of Probability to Initiate Breakdown from an Elementary Volume, $W_0 = 2 \times 10^{-2}$ cm^3 under Condition of Steady Rising Impulse Voltage

Parameters	Units	Normal	Extreme Values	Weibull CIGRE Procedure
Class I oil				
Mean E_m, position E_0		136.47	119.05	60.66
Sigma σ, scale α		25.27	8.72	83.39
Form β				3.4
r^2, coefficient of correlation		0.89	1.0	
Class II oil				
Mean E_m, position E_0	kV/mm	94.25	76.83	47.57
Sigma σ, scale α	kV/mm	15.56	4.1	51.35
Form β				3.4
r^2, coefficient of correlation		0.54	0.23	

Sources: Trinh, N.G. et al., Electrode area, stressed-volume: Two apparent effects of large-volume oil-insulation, in: *IEEE International Symposium on Electrical Insulation*, Philadelphia, PA, June 6–9, 1982a, pp. 115–118; Trinh, N.G. et al., *IEEE Trans. Power Appar. Syst*., PAS-101(10), 3712, 1982b.

the corresponding withstand probability in m consecutive cycles of the ac voltage is

$$P_{wm} = 1 - p_m = \left(1 - p_n\right)^m \tag{6.10}$$

and the corresponding equivalent breakdown probability of an elementary surface or volume is

$$p_m = 1 - P_{wm} = 1 - \left(1 - p_n\right)^m \tag{6.11}$$

TABLE 6.5

Distribution of Probability to Initiate Breakdown from an Elementary Surface, A_0 = 0.1 cm^2 under Condition of Steady Rising Impulse Voltage

Parameters	Units	Normal	Extreme Values	Weibull CIGRE Procedure
Class I oil				
Mean E_m, position E_0		143.0	124.32	57.86
Sigma σ, scale α		28.38	9.98	93.65
Form β				3.4
r^2, coefficient of correlation		0.82	1.0	
Class II oil				
Mean E_m, position E_0	kV/mm	108.7	86.48	46.38
Sigma σ, scale α	kV/mm	20.54	5.69	67.78
Form β				3.4
r^2, coefficient of correlation		0.92	0.74	

Sources: Trinh, N.G. et al., Electrode area, stressed-volume: Two apparent effects of large-volume oil-insulation, in: *IEEE International Symposium on Electrical Insulation*, Philadelphia, PA, June 6–9, 1982a, pp. 115–118; Trinh, N.G. et al., *IEEE Trans. Power Appar. Syst*., PAS-101(10), 3712, 1982b.

TABLE 6.6

Distribution of Probability to Initiate Breakdown from an Elementary Surface, A_0 = 0.1 cm^2 under Steady Rising AC Voltage

Parameters	Units	Normal	Extreme Values	Weibull CIGRE Procedure
Class I oil				
Mean E_m, position E_0		35.92	34.14	24.04
Sigma σ, scale α		3.96	1.49	13.07
Form β				3.4
r^2, coefficient of correlation		0.96	0.87	
Class II oil				
Mean E_m, position E_0	kV/mm	36.31	30.36	16.21
Sigma σ, scale α	kV/mm	6.7	2.01	22.11
Form β				3.4
r^2, coefficient of correlation		0.99	0.96	
Class III oil				
Mean E_m, position E_0	kV/mm	22.05	18.45	7.89
Sigma σ, scale α	kV/mm	4.72	1.53	15.57
Form β				3.4
r^2, coefficient of correlation		0.89	0.73	

Sources: Trinh, N.G. et al., Electrode area, stressed-volume: Two apparent effects of large-volume oil-insulation, in: *IEEE International Symposium on Electrical Insulation*, Philadelphia, PA, June 6–9, 1982a, pp. 115–118; Trinh, N.G. et al., *IEEE Trans. Power Appar. Syst*., PAS-101(10), 3712, 1982b.

The corresponding withstand voltage is then readily determined from the experimental distribution function of the breakdown probability of the elementary surface or volume. Figure 6.25 compares the calculated 1 and 30 min withstand voltages of oil gaps of different stressed oil volumes from 10^{-2} to 10^6 cm^3 with experimental data and illustrates the validity of this approach. The main drawback of this approach resides in the necessary extrapolation of the experimental distribution function for

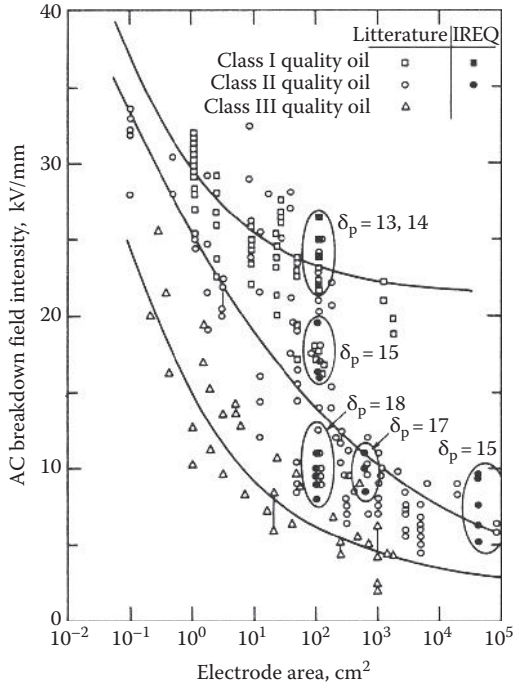


FIGURE 6.21 Electrode area effect under ac voltage. (From Trinh, N.G. et al., Electrode area, stressed-volume: Two apparent effects of large-volume oil-insulation, in: *IEEE International Symposium on Electrical Insulation*, Philadelphia, PA, June 6–9, 1982a, pp. 115–118; Trinh, N.G. et al., *IEEE Trans. Power Appar. Syst*., PAS-101(10), 3712, 1982b.)

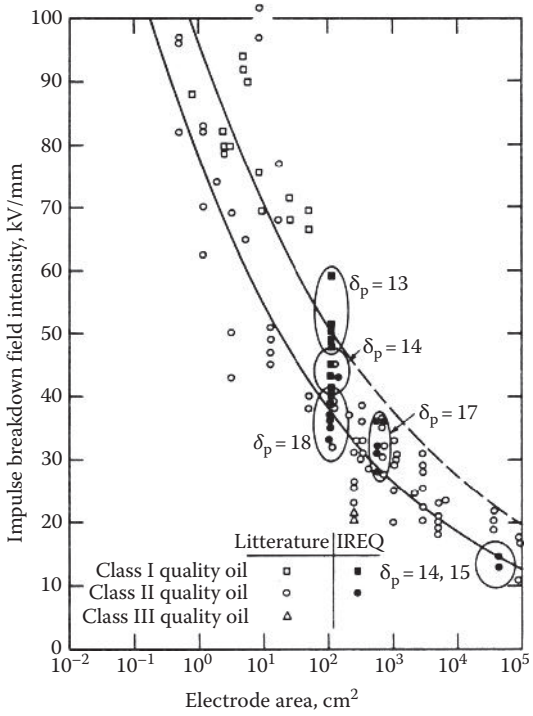


FIGURE 6.22 Electrode area effect under impulse voltage. (From Trinh, N.G. et al., Electrode area, stressed-volume: Two apparent effects of large-volume oil-insulation, in: *IEEE International Symposium on Electrical Insulation*, Philadelphia, PA, June 6–9, 1982a, pp. 115–118; Trinh, N.G. et al., *IEEE Trans. Power Appar. Syst*., PAS-101(10), 3712, 1982b.)

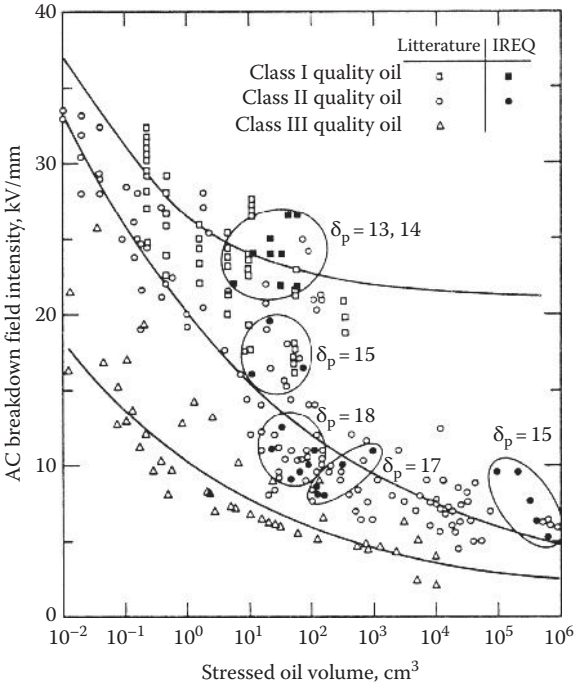


FIGURE 6.23 Stressed volume effect under ac voltage. (From Trinh, N.G. et al., Electrode area, stressed-volume: Two apparent effects of large-volume oil-insulation, in: *IEEE International Symposium on Electrical Insulation*, Philadelphia, PA, June 6–9, 1982a, pp. 115–118; Trinh, N.G. et al., *IEEE Trans. Power Appar. Syst.*, PAS-101(10), 3712, 1982b.)

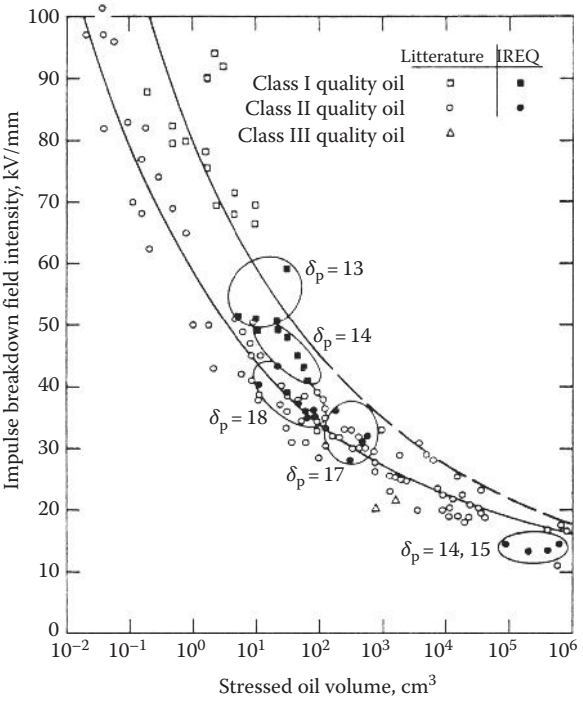


FIGURE 6.24 Stressed volume effect under impulse voltage. (From Trinh, N.G. et al., Electrode area, stressed-volume: Two apparent effects of large-volume oil-insulation, in: *IEEE International Symposium on Electrical Insulation*, Philadelphia, PA, June 6–9, 1982a, pp. 115–118; Trinh, N.G. et al., *IEEE Trans. Power Appar. Syst.*, PAS-101(10), 3712, 1982b.)

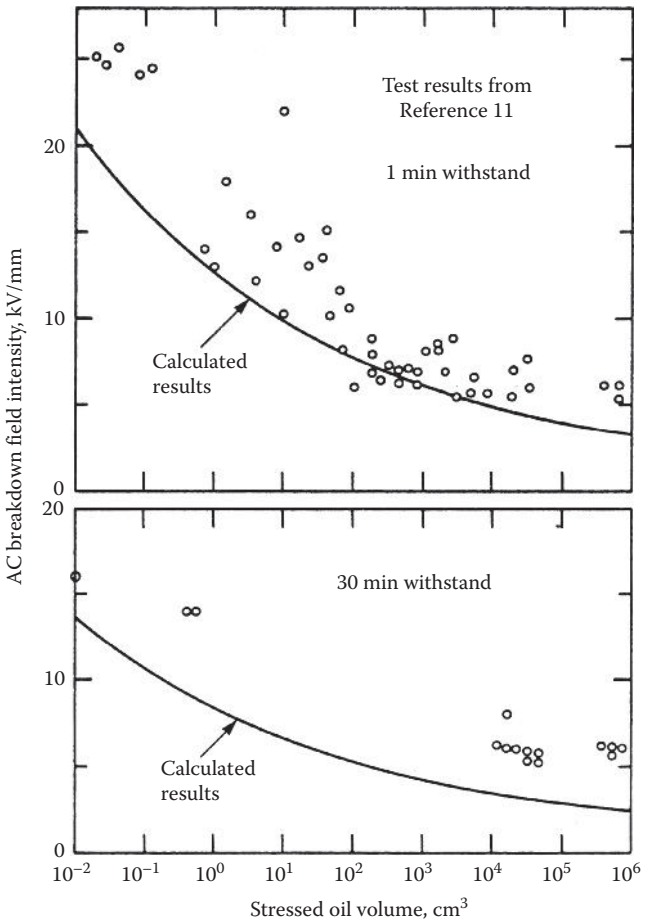


FIGURE 6.25 Variations of the 1 and 30 min ac withstand field with the stressed oil volume. (From Trinh, N.G. et al., Electrode area, stressed-volume: Two apparent effects of large-volume oil-insulation, in: *IEEE International Symposium on Electrical Insulation*, Philadelphia, PA, June 6–9, 1982a, pp. 115–118; Trinh, N.G. et al., *IEEE Trans. Power Appar. Syst*., PAS-101(10), 3712, 1982b.)

the breakdown probability of the elementary surface or volume to very low values. Fortunately, with breakdown data obtained in oil gaps with large stressed electrode areas and volumes, the experimental distribution of breakdown probability of the elementary surface and volume is determined for probabilities as low as 10^{-7} and ensures a reasonable assessment of the breakdown of practical oil gaps. One important conclusion from Figures 6.21–6.24 is that the ac breakdown voltage is much more sensitive to oil quality than the corresponding impulse breakdown voltage.

6.4.6 Dielectric Interfaces

Any practical oil insulation system is effectively a composite insulation with the oil forming the main component of the insulation and a solid insulating structure to mainly handle the mechanical stresses.

6.4.6.1 Incipient Fault

The presence of a dielectric interface allows failure to occur along the interface discussed in Section 6.3.1.3. It causes gradual deterioration of the insulation under the action of prolonged PDs, producing carbon particles as a result of the decomposition of oil molecules. In oil, these carbon particles are dispersed and their cumulative effect remains marginal. The presence of a dielectric interface provides a

substrate on which the carbon particles are deposed and accumulate with time. The effect is accentuated by the erosion of the cellulose, creating a preferential path for the discharge, which gradually becomes conducting with the deposit of carbon particles and extends the stressed electrode further into the oil gap. PDs can then develop from the tip of the carbonized path and propagate farther in the insulation, until the oil gap is bridged and causes failure of the insulation.

6.4.6.2 Electrostatic Discharges

Electrostatic discharge is another breakdown mechanism, observed in the presence of pressboard and under condition of high circulation of the oil (Higaki et al., 1979; Shimisu et al., 1979). Electrons are removed from the oil molecules and deposed on the pressboard, where their accumulation can affect the local field distribution to eventually initiate an electrostatic discharge and breakdown of the oil gap.

6.4.7 Aging and Decomposition By-Products of Oils

Aging of oil–paper composite insulations is discussed in Chapters 7 and 12; it suffices to mention here that aging of the insulating oil is due to

- Oxidation when the oil is exposed to high temperatures over long period of time
- Decomposition of the oil molecules due to hot spots and PDs

Oxidation: When oil is heated, oxidation sets in, produces typical polar compounds, increases the soluble acidity and the peroxide content, and reduces the interfacial tension. When no additive is added to the oil, the oxidation continues until saturation; when the soluble acidity exceeds 0.2 mg KOH/g oil, the interfacial tension drops below 10 mN/m and the formation of solid oxidation compounds or sludge starts. The degree of oxidation of transformer oil is usually determined by its soluble acidity, peroxide contents, and interfacial tension. To delay oxidation, inhibitors such as 2.6-DBPC are usually added to new and reclaimed oils. The oxidation is then under control as long as the inhibitor is present. Sharp increases in the soluble acidity and polar compounds accompanied by a sharp drop in the interfacial tension occur when the DBPC is depleted. Sludge formation begins shortly after, accompanied by a reduction in the dissolved copper and followed by saturation of the oil with oxidation by-products.

Decomposition of oil molecules: Hot spots, PDs, electric arc, etc., due to their higher temperatures, can degrade the insulating oil to a higher degree and generate decomposition by-products, which are specific to the insulating fluid. Low-level PDs produce large amounts of hydrogen H_2 with small amount of methane CH_4. Overheating of the oil produces ethylene C_2H_4, while arcing in oil generates acetylene C_2H_2. The oil reclaim must be done quickly after the complete depletion of the additives to avoid permanent damage to the oil due to oxidation.

In oil-filled cable, aromatic additives are used to increase the gas absorption of the oil. Here again, measurement of the aromatic additives can be used as a means to assess the adequacy of the insulating fluid to prevent saturation of the dissolved gases in oil.

REFERENCES

Anderson, J.G. and T.W. Liao. The propagation mechanism of impulse creepage discharges over oil-immersed surfaces. *AIEE Transactions* 74: 218–226, 1955.

Aubin, J., Saker, A., Lesaint, O., Tobazéon, R., and C. Boisdon. Propagation des décharges à grandes distances dans l'huile minérale. Influence des particules. Rapport CIGRE, 1996.

Bartnikas, R. and K.D. Srivastava. *Elements of Cable Engineering*. Waterloo, Ontario, Canada: Standford Educational Press, 1980.

Castonguay, J. Nouveaux fluides isolants: Étude bibliographique. Rapport IREQ No. 92-070, Avril 1992.

Darveniza, M. The effect of carbon particles on the AC strength of transformer oil. *Electrical Engineering Transactions*, *The Institution of Engineers, Australia* 284–289, September 1969.

Denegri, G.B., Liberti, G., Molinari, G., and A. Viviani. Field enhanced motion of impurity particles in fluid dielectrics under linear conditions. *IEEE Transactions on Electrical Insulation* EI-12(2): 114–124, 1977.

Endicott, H.S. and K.H. Weber. Electrode area effect for the impulse breakdown of transformer oil. *AIEE Transactions* 76: 393–398, 1957.

Fournié, R. *Les isolants en électrotechnique—Essais, Mécanismes de dégradation et applications industrielles*. Collection de la Direction des Études et Recherche d'Électricité de France, No. 73. Paris, France: Eyrolles, 1990.

Garton C.G. and Z. Krasucki. Bubbles in insulating liquids: stability in an electric field, *Proc. Royal Soc. A*., Vol. 280, 211–226, 1964.

Halpern, B. and R. Gomer. Field ionization in liquids. *Journal of Chemical Physics* 51(3): 1048–1056, 1969.

Hebner, R.E., Kelley, E.F., Forster, E.O., and G.J. FitzPatrick. Observation of prebreakdown phenomena in hydrocarbons II. *IEEE Transactions Electrical Insulation* EI-20(2): 282–292, 1985.

Higaki, M., Miyao, H., Endou, K., and H. Ohtani. A calculation of potential distribution caused by static electrification owing to oil flow in a oil-paper insulation system. *IEEE Transactions on Power Apparatus and Systems* PAS-98(4): 1275–1282, July/August 1979.

Kamata, Y. and Y. Kako. Flashover characteristics of extremely long gaps in transformer oil under non-uniform field conditions. *IEEE Transactions Electrical Insulation* EI-15(1): 18–26, 1980.

Kattan, R., Denat, A., and O. Lesaint. Generation, growth and collapse of vapor bubbles in hydrocarbon liquids under a high divergent electric field. *Journal of Applied Physics* 66(9): 4062–4066, 1989.

Krasucki, Z. The loss angle of impregnated paper capacitors. Electrical Research Association report L/T 400, 1960.

Krasucki, Z. Processes leading to discharges in oil-impregnated paper. *Proceedings of IEE*, 109(Part B, Suppl. 22): 435, 1962.

Krasucki, Z. Breakdown of commercial liquid and liquid-solid dielectrics. In: L.L. Alston (ed.), *High Voltage Technology*. Oxford, U.K.: Oxford University Press, 1968.

Lamarre, C., Crine, J.P., and M. Duval. Influence of oxidation on the electrical properties of inhibited naphthenic and paraffinic transformer oils. *IEEE Transactions on Electrical Insulation* EI-22: 57–62, 1987.

Lesaint, O. and A. Saker. Études des mécanismes de claquage des grands volumes d'huile, LEMD and IREQ, Grenoble, France, 1993.

Lesaint, O., Gournay, P., and R. Tobazéon. Investigation on transient currents associated with streamer propagation in dielectric liquids. *IEEE Transactions on Electrical Insulation* EI-26(4): 699–707, 1991.

Lesaint, O. and P. Gournay. On the gaseous nature of positive filamentary streamers in hydrocarbon liquids. I: Influence of the hydrostatic pressure on the propagation. *Journal of Applied Physics* 27: 2111–2116, 1994a.

Lesaint, O. and P. Gournay. On the gaseous nature of positive filamentary streamers in hydrocarbon liquids. II: Propagation, growth and collapse of gaseous filaments in Pentane. *Journal of Applied Physics* 27: 2117–2127, 1994b.

Lewis, T.J. The electrical conduction and strength of pure liquids. In: L.L. Alston (ed.), *High Voltage Technology*. Oxford, U.K.: Oxford University Press, 1968, Chapter 6.

Massala, G., Saker, A., and O. Lesaint. Study of streamer propagation in mineral oil in overvolted gaps under impulse voltages. In: *Conference on Electrical Insulation and Dielectric Phenomena (CEIDP)*, 1995.

Miners, K. Particles and moisture effect on dielectric strength of transformer oil using VDE electrodes. *IEEE Transactions on Power Apparatus and Systems* PAS-101(3): 751–756, 1982.

Mukaiyama, Y., Nonaka, F., Tagaki, I., Higaki, M., Endo, K., Sakamoto, T., Hiraishi, K., and K. Kawashima. Development of a perfluorocarbon liquid immersed prototype large power transformer with compressed SF6 gas insulation. *IEEE Transactions on Power Delivery* PWRD-6(3): 1108–1116, 1991.

Narbut, P., Maslin, A.J., and C. Wasserman. Vaporization cooling for power transformer. *AIEE Transactions on Power Apparatus and Systems, Part III B* 1319–1327, December 1959.

Palmer, S. and W.A. Sharpley. Electrical strength of transformer insulation. *Proceedings of IEE* 116(12): 2029–2037, 1969.

Palmer, S. and W.A. Sharpley. Electrical strength of transformer insulation, conference on dielectric materials measurement and application. *IEE Conference Publications* 67: 20–24, 1970.

Pickard, W.F. Electrical forces in dielectric liquids. *Progress in Dielectrics*, 6, 1–39, 1965.

Rain, P., Boisdon, C., Lesaint, O., and R. Tobazéon. Behavior of streamers under divergent AC fields in transformer oils at large gaps. *IEEE Transactions on Electrical Insulation* EI-26(4): 715–725, 1991.

Raleigh, L. On the pressure developed in a liquid during the collapse of a spherical cavity. *Philosophical Magazine* 34: 94, 1917; also *Scientific Papers VI*. New York: Dover Publications, 1964, p. 504.

Rouse, T.O. Technical requirements dielectric liquids. In: *Proceedings of Workshop on Substitute Insulation for Polychlorinated Biphenyls*, *EPRI*, Palo Alto, CA, April 1987.

Saker, A. Caractérisation des décharges rampantes à l'interface liquide diélectrique-solide isolant, Thèse de Doctorat, Institut National Polytechnique de Grenoble, France, 1993.

Saker, A., Lesaint, O., and R. Tobazéon. Propagation of streamers in mineral oil at large distances. In: *Annual Report Conference on Electrical Insulation and Dielectric Phenomena*, Arlington, TX, 1994, pp. 889–894.

Shimisu, S., Murata, H., and N. Honda. Electrostatics in power transformers. *IEEE Transactions on Power Apparatus and Systems* PAS-98(4): 1244–1250, 1979.

Skog, J.E., de Giorgio, J.B., Jakob, F., and T. Haupert. Location of incipient transformer faults by metal in oil analysis, 1980. In: *DOBLE Conference*, Section 601, 1980.

Tobazéon, R. Prebreakdown phenomena in dielectric liquids. *IEEE Transactions on Dielectrics and Electrical Insulation* 1(6): 1132–1146, 1994.

Trinh, N.G. and A. Saker. Interpretation of the physical mechanism in the breakdown of long gaps in transformer oil. In: *International Conference on Conduction and Breakdown in Dielectric Liquids*, Rome, Italy, 1996, pp. 287–291.

Trinh, N.G. and C. Vincent. Statistical significance of test methods for low probability breakdown and withstand voltages. *IEEE Transactions on Power Apparatus and Systems* PAS-99: 711, 1980.

Trinh, N.G., Vincent, C., and J. Régis. Electrode area, stressed-volume: Two apparent effects of large-volume oil-insulation, 1982. In: *IEEE International Symposium on Electrical Insulation*, Philadelphia, PA, June 6–9, 1982a, pp. 115–118.

Trinh, N.G., Vincent, C., and J. Régis. Statistical dielectric degradation of large-volume oil-insulation. *IEEE Transactions on Power Apparatus and Systems* PAS-101(10): 3712–3721, 1982b.

Watson, P.K., Chadband, W.G. and W.Y. Mak. Bubble growth following a localized electrical discharge and its relationship to the breakdown of triggered spark gaps in liquids. *IEEE Trans*., EI-20, 275–280, April 1985.

Weber, K.H. and H.S. Endicott. Area effect and its extremal basis for the electric breakdown of transformer oil. *AIEE Transactions on Power Apparatus and Systems* 75: 371–381, 1956.

Weber, K.H. and H.S. Endicott. Extremal area effect for large area electrodes for the electric breakdown of transformer oil. *AIEE Transactions on Power Apparatus and Systems* 76: 1091–1098, 1957.

Wilson, W.R., Streater, A.L., and E.J.Tuohy. Application of volume theory of dielectric strength to oil circuit breakers. *AIEE Trans*., 74, 677–688, August 1955.

Wilson, A.C.M. *Insulating Liquids: Their Use, Manufacture and Properties*, IEE Electrical and Electronic Materials and Devices Series 1. Stevenage, U.K.: Peter Peregrinus Ltd., 1980.

Wilson, W.R. A fundamental factor controlling the unit dielectric strength of oil. *AIEE Transactions on Power Apparatus and Systems* 72: 68–74, 1953.

Wilson, W.R., Streater, A.L., and E.J. Tuohy. Application of volume theory of dielectric strength to oil circuit breakers. *AIEE Trans.,* 74: 677–688, 1955.

Zaky, A.A. and R. Hawley. *Conduction and Breakdown in Mineral Oil*. London, U.K.: Peter Peregrinus Ltd., 1955.

Zaky, A.A. and R. Hawley. *Conduction and Breakdown in Mineral Oil*, Peter Peregrinus Ltd, 1955.

7

Electric Breakdown in Solid and Composite Materials

7.1 Introduction

The need for a compact insulation system for high-voltage equipment has led to the development of a variety of insulating materials, which are combined to form practical insulation systems: solid, composite solid–liquid, and solid–gas insulation. Solid and composite materials are characterized by the fact that they are non-self-restoring; see *Chapter 13.* The breakdown processes in solid and composite materials may be classified in two broad categories: direct breakdown as measured in new materials and breakdown by incipient fault, typical in practical insulation systems.

7.1.1 Intrinsic Breakdowns (Garton, 1968)

Intrinsic breakdown refers to the situation when breakdown occurs to new samples of homogeneous material, usually at high voltage and in relatively short time. They are useful to compare the various insulating materials. They usually correspond to the highest insulating performance that can ever be expected with a given insulating material and usually are far beyond the actual values currently used in practical insulation.

The intended meaning is the field intensity at which free electrons in the material are accelerated without limit by the electrostatic action of the field. The exact mechanism of intrinsic breakdown is still unresolved; however, it seems likely that any catastrophic acceleration of electrons must be preceded by an unlimited increase in the conductivity of the material, termed as stress-enhanced conductivity. As a result, intrinsic breakdown is sometimes not distinguishable from the thermal instability, since the numerical difference may be small, if the final rise of conduction occurs over a narrow range of voltage (Garton, 1968).

7.1.1.1 Theory of Intrinsic Strength

The earliest theory based on the collective stability of conduction electrons is due to von Hippel (von Hippel, 1934, 1935), who calculated the field necessary to render the thermal distribution of electron energy unstable, so that a thermal electron might be indefinitely accelerated in the field, a condition termed as low-energy criterion. Fröhlich considered, on the other hand, that electrons of more energy than average are more easily accelerated and are always present in sufficient number to cause instability, a condition termed high-energy criterion.

Figure 7.1 illustrates the high-energy criterion for intrinsic breakdown. Curve *B* shows the rate of energy loss from the electron by collision with lattice vibrations as a function of its energy. The electrons are present with all energies up to a limit I set by the ionization potential of the lattice. Electrons of mean thermal energy would occupy the extreme left-hand portion of the curve. Curves F_1, F_c, and F_2 show the rate of gain of energy by an electron from the field. The condition of instability for an electron at a given field strength is that it should find itself with an energy w above the curve *B* as with curve F_2. For the curve F_1, this cannot occur, since it implies $w > I$ and there are no such electrons. The critical field is thus that one, F_c, which intersects *B* at the energy level *I*.

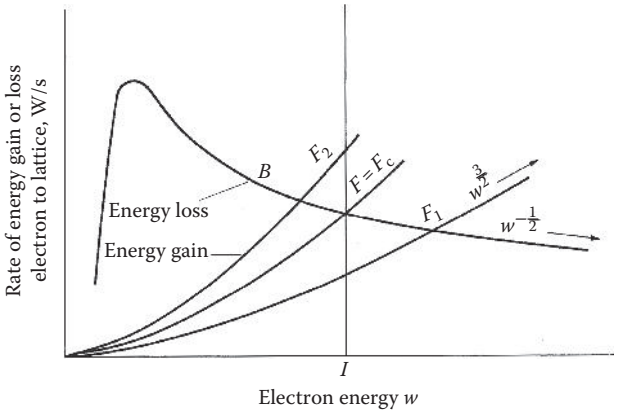


FIGURE 7.1 Fröhlich's high-energy criterion. F is the field strength, F_c the critical field strength, and I the ionization potential of the lattice. (From Garton, C.G., High Voltage Technology – Chapter 8, *Intrinsic and Related Forms of Breakdown in Solids*, L.L. Alston (ed.), Oxford University Press, 1968.)

7.1.1.2 Measurement of Intrinsic Strength

This is not a simple task. Two methods are described in the following: the recessed specimen and the McKeown technique.

Recessed specimen method: Illustrated in Figure 7.2, it consists of a plane disc into which a spherical depression is either pressed, machined, or ground, leaving only a thickness of 30–200 μm for evaluation of breakdown.

The spherical radius should be such that stress concentration at the apex of the depression is negligible, typical value is about 1 cm. The surface of the recess and of the opposite plane is then made conducting by any technique, which gives extremely good contact with the dielectric: evaporated film of aluminum or graphite coating. There are two limitations to this method: the cooling of the stressed area is not very good, and the thin apex of the specimen is mechanically unsupported, tends to buckle, and becomes thinner under the compressive force from the electrodes.

McKeown method: Illustrated in Figure 7.3, it uses as electrodes two ball bearings, located within a cylindrical hole in a disc of any convenient plastic. The lower ball is cemented into position with an epoxy resin, and the hole is filled with the same resin in liquid form and gently heated in vacuum until it is degassed. The sample in the form of a thin disc is placed in the hole on top of the ball and the liquid degassed again. The top ball is then inserted and the hole cured until solidified.

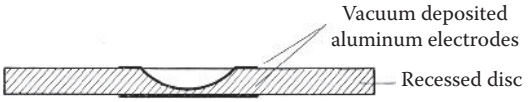


FIGURE 7.2 The recess specimen. (From Garton, C.G., High Voltage Technology – Chapter 8, *Intrinsic and Related Forms of Breakdown in Solids*, L.L. Alston (ed.), Oxford University Press, 1968.)

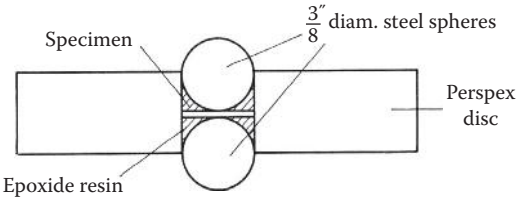


FIGURE 7.3 The McKeown technique. (From Garton, C.G., High Voltage Technology – Chapter 8, *Intrinsic and Related Forms of Breakdown in Solids*, L.L. Alston (ed.), Oxford University Press, 1968.)

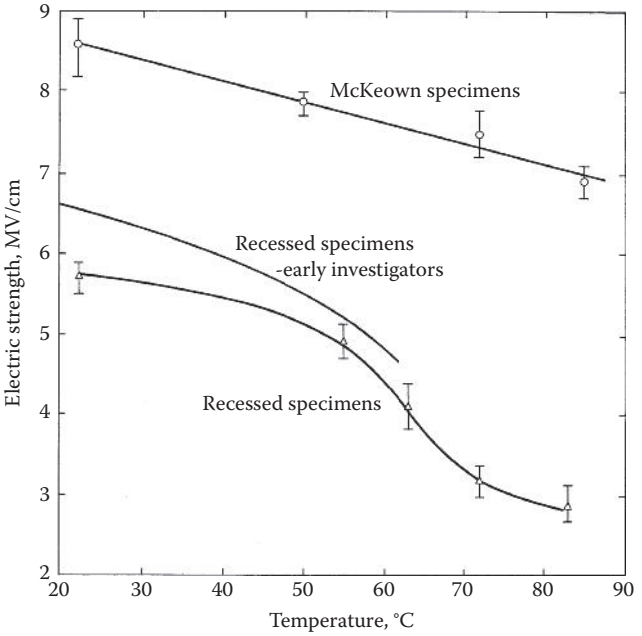


FIGURE 7.4 Variation of the intrinsic electric strength with temperature of polythene recess specimens and McKeown specimens, showing 95% confidence limits of the means. (From Lawson, W.G., Effects of temperature and techniques of measurement of the intrinsic electric strength of polyethylene, *IEE Proc*., 113, 197, 1966.)

This technique has proved extremely satisfactory at room temperature for measuring the intrinsic strength of low-loss polymers but tends to give higher values than those obtained with the recess specimens, as illustrated by the results shown in Figure 7.4 obtained by Lawson for the intrinsic strength of polythene at temperature up to 85°C (Lawson, 1966). The reason seems to be related to the elimination of electromechanical distortion of the specimen.

7.1.2 Initial Breakdown and Strength

Intrinsic strength has meaning only for a limited range of substances. The material must be homogeneous, so that breakdown cannot occur through interstices. The material must be mechanically strong to withstand the large forces setup by the field. Its conductivity must be low so that suitable conditions of temperature and frequency can be chosen to eliminate thermal instability at fields below the intrinsic value.

Interesting as it is, intrinsic strength is an unreachable limit for practical insulation systems, due to their size and manufacturing limitations. Of more practical interest are *initial breakdown voltage and strength* obtained on small laboratory model or sample of the practical insulation system. They are measured by raising the voltage until breakdown occurs on a new sample, with no aging of the insulation involved. Initial breakdown voltage and strength are affected by different factors, namely, pressure, insulation thickness, electrode surface condition, voids and impurities within the sample, and preparation of the model or sample. They reveal the inherent limitations of the insulation system and can serve as a basis to define realistic design values for practical insulation systems, namely, by means of some safety margin for the operating stress, see Chapter 13.

7.1.3 Aging and Incipient Fault

Once a piece of equipment is put in service, operating conditions can affect its insulation properties and performance and may result eventually in insulation failure. Deterioration of the insulation properties is generally referred to as aging while failure is termed incipient faults.

Aging basically results from the absorption of energy by the insulation system, which breaks the molecular bonds, causes irreversible changes in the molecular structure of the insulating material

forming the constituent components of the insulation system. Chemical radicals are also liberated in the process and trigger chemical reactions to produce more stable by-products. These changes in turn affect the properties of the insulation system, so as to eventually make it unsuitable for use.

Incipient faults develop from local failure, which causes permanent damage to the insulation system. This becomes a discharge site, which extends further its progression into the insulation system and eventually causes its complete failure. Failure of the insulation occurs only after a certain time, termed as *life of the insulation*, which should be long enough to ensure adequate service of power equipment over a period of several tens of years.

A number of factors are responsible for aging of the insulation; the most important are thermal, electrical, mechanical, and environmental.

7.1.3.1 Thermal Breakdown

Because of conduction currents or other forms of dielectric loss, heat is generated continuously in electrically stressed insulation.

Under dc stress, the generated heat P per unit volume is given by

$$P = \frac{E^2}{\rho} \quad \text{per cm}^3 \tag{7.1}$$

where

E is the dc stress in V/cm

ρ the resistivity of the insulation in Ω-cm

Under ac stress, the heat loss is given by

$$P = \frac{E^2}{X}\tan\delta \tag{7.2}$$

where

X is the reactance

δ the loss angle of the material

The reactance X is related to the capacitance C of the gap by

$$X = \frac{1}{2\pi fC} \quad \text{for 1 cm}^3$$

where f is the frequency of the ac stress.

It follows that

$$P = \frac{E^2 f\varepsilon}{1.8 \times 10^{12}}\tan\delta \tag{7.2a}$$

where ε is the relative permittivity.

These losses are due to the motions of ions and to vibrations of dipoles within the insulation. Under ac stress, the energy losses arising from the motion of ions increase rapidly with temperature, following an exponential law $P \propto \exp\left(-\frac{\alpha}{T}\right)$, where T is absolute temperature and α an experimental constant.

In cases of stable operation of the insulation, the temperature rises until the heat generated is balanced by the heat removal by cooling process. If the latter process is not adequate, it is possible for an unstable state to arise in which temperature increases indefinitely and the insulation burns out. Figure 7.5 illustrates the cases of thermal instability. When the heat removal is adequate as with stress E_2, an equilibrium temperature is reached at T_A while a thermal instability situation corresponds to stress E_1 or at increased operating temperature as in T_B.

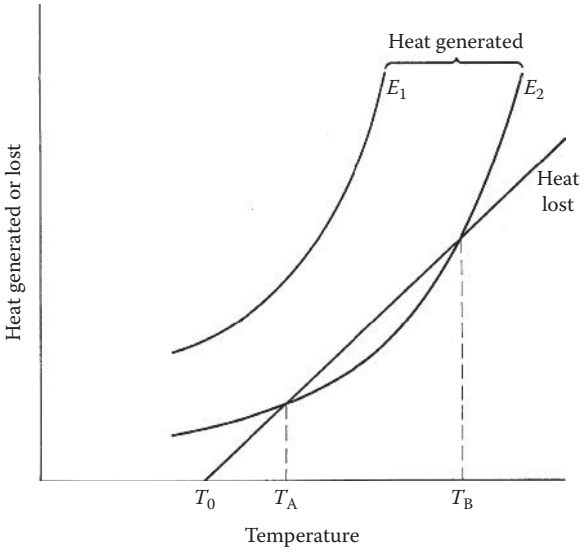


FIGURE 7.5 Thermal instability of insulation. (From Garton, C.G., High Voltage Technology – Chapter 8, *Intrinsic and Related Forms of Breakdown in Solids,* L.L. Alston (ed.), Oxford University Press, 1968.)

The maximum voltage a given insulating material can withstand cannot be increased indefinitely simply by increasing its thickness, because with thick insulation, the internal temperature is little affected by the surface condition. There is an upper limit of voltage independent of thickness, known as the maximum thermal voltage V_t, beyond which it is not possible to go without thermal instability.

7.1.3.2 Breakdown by Electrical Discharges (Day, 1968)

Two types of breakdown are distinguished, depending on the interelectrode space, which is made of a single or more dielectrics with interfaces between different dielectrics. In the former case, breakdown is caused by discharges in the gas-filled cavities within the insulation, while in latter case, breakdown is caused by a creep discharge on the gas/solid interface and termed surface tracking.

Surface tracking occurs when a sufficiently high potential difference exists along the interface of two dielectrics; it develops in the side of the dielectric of low withstand strength and is generally initiated from a local field enhancement. The tendency to track, according to Parr and Scarisbrick (1965), depends on the proportion of the bonds that produce free carbon on pyrolysis to the total bond energy of the molecule. The lower the ratio, the less likely is the material to track.

Discharges within a gas-filled cavity in the dielectric occur when the field within the cavity exceeds the critical stress, which corresponds to Paschen's minimum for the gas. For a plane-parallel cavity of thickness d_g in an insulation of thickness $d_g + d_d$, the discharge inception voltage V_i is

$$V_i = E_g \left(d_g + \frac{d_d}{\varepsilon} \right) \tag{7.3}$$

where

E_g is the breakdown stress of the gas of thickness d_g at the appropriate pressure
d_d the thickness of the dielectric
ε is the relative permittivity

Initially, the impact of the discharges is erosion over a comparatively large area. This erosion roughens the surface and slowly penetrates the insulation, but it is not the cause of the rapid failure. At some stage, the erosion gives way to channel formation and dendritic growth through the remaining of the insulation.

7.1.3.3 Mechanical Aging

Mechanical aging is mostly present in equipment with moving parts, where mechanical stresses may wear off the metal parts by frictions producing metallic particles, damage insulation, and weaken its mechanical strength (Mitsui, 1981). It is not the direct cause of insulation failure, but can enhance other active aging processes such as thermal and electrical aging. In polymer-insulated cables, mechanical stresses can cause snaking of the cable and separation of the extruded layers forming voids, which become sites of PDs and initiate the incipient fault process.

Zurkov et al. (Zhurkov, 1965, 1974, 1975) assume that chemical bonds are broken by thermal motion and fluctuation and their strength is reduced by the applied mechanical stress according to

$$t_b = t_0 \exp\left(\frac{u_0 - \gamma\sigma}{kT}\right) \tag{7.4}$$

where

t_b is the time to breakdown under a stress σ
k is the Boltzmann constant
T is the temperature in K
t_0 is an adjustable parameter
u_0 is an energy barrier typical of the bonds strength
γ is an activation volume

The breakdown is obtained in three steps:

1. Stretching of bonds by stress
2. Scission of the overstressed bonds by thermal fluctuations with formation of two end radicals
3. Formation of microcracks following bonds rupture

Tobolsky and Eyring (1943) assume that failure results from breakage of bonds and the slippage of chain molecules past each other. The time to breakdown under stress σ can be described according to

$$t_b = \frac{2h}{kT} \exp\left(\frac{\Delta G}{kT}\right) \operatorname{csch}\left(\frac{\lambda\sigma}{2NkT}\right) \tag{7.5}$$

where

h is Planck's constant
ΔG the Gibbs free energy of the process
λ the barrier width
N the number of bonds per unit area

7.1.3.4 Combined Stress

Normal operation of power equipment subjects their insulation to several stresses at the same time: thermal, electrical, mechanical, etc. Life estimation under multistress conditions is much more complex (Cygan and Laghari, 1990) due to possible synergism among the different aging mechanisms involved. Under multistress conditions, the time to breakdown t_b is a multivariable function (Montanari, 1984):

$$t_b = f(s_i)$$

with s_i being the various stresses involved in the aging process.

Experimental data are generally obtained with all stresses remaining constant except one or two, usually corresponding to thermal and electrical stresses. The time to breakdown t_b is a function of two variables, thermal stress T and electrical stress E:

$$t_b = f(T, E) \tag{7.6}$$

The time to breakdown t_b is then represented by a failure surface in the three-dimensional space: time to breakdown t_b, thermal stress T, and electrical stress E. Special cases correspond to situations with one of the three variables being constant, corresponding to the following familiar cases:

- Thermal endurance test: $t_b = f(T)$
- Electrical endurance test: $t_b = f(E)$
- Constant time to failure: $t_b = f(T,E) = L$

Synergism corresponds then to the situation when one defining parameter in one process is dependent on the other aging process. The subject is still far from being fully explored, and no established theory exists today to adequately estimate the insulation life under multistress conditions, which still relies on experimental data obtained in multistress tests.

7.1.3.5 Chemical Deterioration (Church, 1968)

Progressive chemical degradation of insulating material can occur in the absence of electric stress from a number of causes.

Chemical instability: Many insulating materials, especially organic materials, show chemical instability, which should be very low under normal operating conditions but is strongly temperature dependent. Such chemical changes may result from spontaneous breakdown of the structure of the material as in the depolymerization and carbonization of cellulose and synthetic materials.

Oxidation: Oxidation of insulating materials occurs in the presence of oxygen and in particular ozone. The materials become brittle and develop cracks.

Hydrolysis: Hydrolysis occurs in the presence of humidity and heat, causing loss of mechanical and electrical properties of the materials.

Leaching of chemically active substances: Under warm damp conditions, glass fabrics made from glass of high sodium content lose mechanical strength rapidly as a result of migration of sodium to the surface of the fibers and subsequent chemical attacks on the glass surface.

Incompatibility of materials: Component materials in an electrical equipment may be chemically incompatible and insulation may be contaminated by unsuitable materials surrounding it. Cellulose degrades much more rapidly in the presence of traces of acidic substances. Rubber and polypropylene age more rapidly at elevated temperature when in contact with copper.

7.1.3.6 Electrochemical Deterioration (Church, 1968)

No insulation is completely free from ions, and under electric stress, this results in leakage current.

Nature of electrochemical deterioration: Ions may arise from dissociation of impurities or from slight ionization of the insulation itself. On arrival at the electrodes, ions lose their charge and electrode reaction ensues. The insulation and electrode metal may be attacked, gas evolved, or substances deposited on the electrode. The products of electrode reactions may be chemically or electrically harmful and can lead to rapid failure of the insulation. The process follows Faraday's law of electrolysis. The rate of electrolysis is usually much greater with dc stress than with ac stress, since in the latter case, the reaction may be partially reversed when the polarity changes. Clearly, the rate of electrochemical deterioration is determined by the leakage current, and any factor that may affect the leakage current also affects the reaction rate, namely, concentration of impurity ions in the insulation, temperature, and polar materials. A few examples of electrochemical effect in insulation are the following:

Gassing of impregnated hygroscopic insulation: Water absorbed by the insulation can be electrolyzed to form gas. Except in very dry condition, the gas first formed arises from electrochemical decomposition of the water held in paper.

Migration of metals: Under moist conditions, some metals migrate over the surface of solid insulating materials or through porous ones under dc stress and may lead to short circuit.

Stabilizers: Stabilizers are used to absorb hydrogen and extend the life of the impregnant. The hydrogen ions discharged at the cathode readily react with the stabilizer rather than with the impregnant, a more difficult chemical process.

7.1.4 Decomposition By-Products

Chemical reactions within the insulation produce decomposition by-products, which may be solid or dissolved gases. Their presence in the insulation is a clear indication of aging. They are currently used to assess the state of the insulation, a crucial step to diagnostics and maintenance of power equipment.

7.1.5 Insulation Systems Reviewed

In this chapter, we review insulation characteristics, initial breakdown processes, and the various factors affecting the initial breakdown voltage in various insulation systems currently used in high-voltage equipment and, in particular, high-voltage cables:

- Polymer–polyethylene (PE) and cross-linked polyethylene (XLPE)–insulation
- Paper–oil insulation
- Gas (SF_6)–epoxy insulation

Insulation aging and development of incipient faults will be discussed in *Chapter 11*. However, it should be borne in mind that solid and composite insulation systems comprise an ongoing developing science, which depends on the introduction of new and better performing materials and on the improvement in the manufacturing processes. What we know today represents the achievements of today's technologies and set the basic requirements for tomorrow's insulation systems, yet to be invented.

7.2 Polymeric (PE and XLPE) Insulation

Dry insulation has always presented a great interest for high-voltage cables, namely, because of their simple handling, installation, and compact dimensions. Several types of dry insulation are available, from natural and synthetic rubbers to butyl rubber and ethylene propylene rubber and, more recently, natural or cross-linked polyethylene (XLPE). We review, in the following, the various solid insulations regarding their dielectric properties appropriate to high-voltage cables, with specific reference to PE and XLPE. They have very low ac dielectric losses, which are practically independent of temperature ($\tan\delta \approx 10^{-4}$), a low relative permittivity ($\varepsilon_r = 2.3$), relatively good thermal resistivity (400 C cm/W), and, above all, high intrinsic dielectric strength.

TABLE 7.1

Physical–Chemical Properties of Polymers

Properties	Units	PE	XLPE	Butyl Rubber	EPR
Density	kg/m^3	0.91–0.925	0.91–0.925	0.91	0.86
Permittivity		2.3	2.3–3	2.1–2.4	3–3.5
Dielectric losses, tanδ		0.0002	0.0007	0.003	0.0004
AC strength	kV/mm	23	35	23	35–41
Lightning impulse strength	kV/mm		75		40
Volume resistivity	Ohm-m^3	>10^{16}	10^{15}–10^{17}	10^{17}	10^{15}–10^{17}
Melting temperature	°C	115	105		
Maximum temperature	°C	90	90–130	150	150–175
Minimum temperature	°C	−55	−45 to −65		

7.2.1 Physical–Chemical Properties of Insulating Materials

The variety of insulating materials allows better adaptation of the type of cables to the specific needs in each situation: cables with a better fire resistance in cars, good resistance to radiations in nuclear generating stations, better chemical resistance in difficult environments, etc. We will focus on PE (natural and cross-linked) insulation, which presents the best dielectric properties and makes them particularly suitable for high-voltage applications. Table 7.1 summarizes the physical–chemical properties of the principal polymers used in cable insulation.

7.2.1.1 Natural Rubber

The general chemical formula of which is $(C_5H_8)_x$ was used extensively in high-voltage cables up to 25 kV. Figure 7.6 illustrates the molecules of natural rubber and of gutta-percha. The natural rubber must be transformed into sheets, which are continuously washed to remove organic and inorganic solid impurities. The rubber sheets are dried to acquire a smooth and elastic texture. Natural rubber is then mixed with softeners and *fillers*, which can be of inert materials: mica, quartz, glass, clay, and ceramic. The final stage to produce natural rubber insulation consists of mixing it with accelerators and vulcanizing agents like sulfur. Vulcanization is a chemical process, which changes the properties of natural rubber; accelerators only increase the rate of chemical reaction. Finally, the rubber sheets are heated, softened in mixing rolls prior to its extrusion on the conductor. Natural rubber insulation is vulnerable to exposure to ozone and high temperatures. This favors the development of synthetic *elastomers*, materials that can extend up to twice their length at ambient temperature and return back to their initial length, and their utilization in the manufacture of high-voltage cables.

7.2.1.2 Ethylene–Propylene Rubber

It is perhaps the main concurrent to XLPE for the insulation of distribution cables up to 35 kV, mainly because of its greater mechanical flexibility. Contrary to PE, natural and cross-linked, which contains about

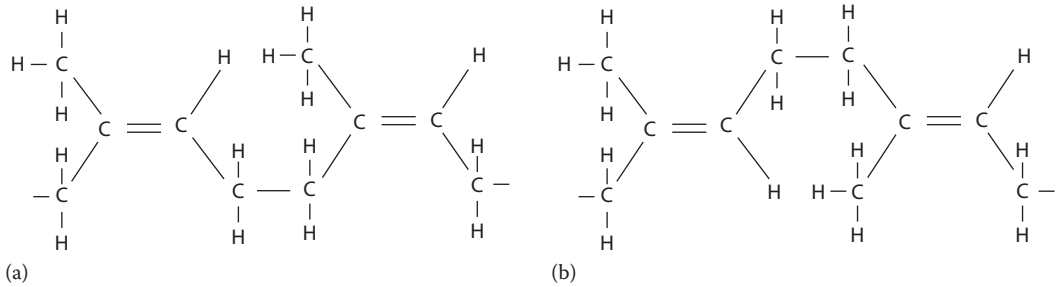


FIGURE 7.6 Molecular structures of natural rubber and gutta-percha. (a) Molecular structure of natural rubber, *cis*-$(C_5H_8)_x$ with substituent groups on the double-bond carbons on the same side of the chain. (From Rosen, L.S., *Fundamental Principles of Polymeric Materials*, Book, Barnes & Noble, New York, 1971.) (b) Molecular structure of gutta-percha, *trans*-$(C_5H_8)_x$ with substituent groups on the double-bond carbons on the opposite sides of the chain. (From Rosen, L.S., *Fundamental Principles of Polymeric Materials*, Book, Barnes & Noble, New York, 1971.)

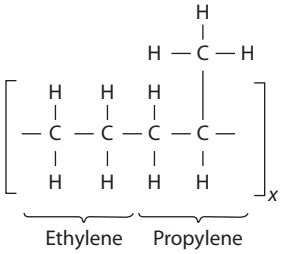


FIGURE 7.7 Molecular structure of *EPR*. (Rosen, L.S., *Fundamental Principles of Polymeric Materials*, Barnes & Noble, New York, 1971.)

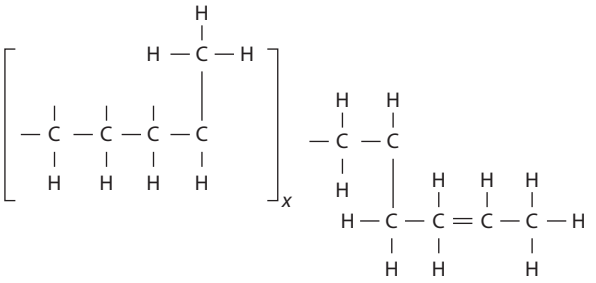


FIGURE 7.8 Molecular structure of *EPR* with 1.4 hexadiene unit; the numerical figure corresponds to the order of the carbon atom in the chain. (From Rosen, L.S., *Fundamental Principles of Polymeric Materials*, Book, Barnes & Noble, New York, 1971.)

50% of crystallization, ethylene–propylene rubber (EPR) is completely amorphous. It is an elastomer synthesized from ethylene and propylene, in a ratio of 1:1. Molecular structure of *EPR* is shown in Figure 7.7, where x is the repetition unit, which can vary between 2×10^3 and 5×10^3. The average molecular mass of EPR used in the cables can vary between 1.5×10^5 and 2.5×10^5. In this form, *EPR* can be vulcanized with peroxide.

For vulcanization with sulfur agents, the *EPR* molecule must contain 1.4 hexadiene units as illustrated in the molecular structure shown in Figure 7.8; the percentage of a third component or nonconjugated diene units does not generally exceed 6%, for a ratio of 47 % ethylene to propylene, respectively. The other advantage of such terpolymer resides in the more efficient utilization of the *curing* agents, easier processing, and improved coloring. The *filler* content in *EPR* is relatively high, exceeding 50%, and comprises either clay or silicate. Dielectric losses in *EPR* are principally determined by the *fillers*.

EPR copolymer is a low-cost elastomer, which can be processed by equipment used for processing natural rubber. It can be used at temperatures up to 150°C (300°F). It has a high resistance to ozone and environmental factors, good resilience and stress–strain properties, and good mechanical properties at low temperatures: it becomes brittle at temperatures between −45°C and −65°C. *EPR* has good electrical properties: a volume resistivity of 10^{15}–10^{17} Ω-cm, a loss factor tanδ of 0.007, a dielectric strength of 35 kV/mm (900 V/mil), and a dielectric constant of 3.2. It suffers, however, from a poor oil and flame resistance, and like PE, it is susceptible to degradation by PDs, giving rise to treeing.

Because of their high dielectric losses, *EPR* cannot compete with XLPE for insulation of high-voltage cables, above 35 kV. Its withstand level for impulse voltage of 40 kV/mm is considerably lower than PE and paper–oil insulation.

7.2.1.3 Butyl Rubber

It offers electrical and physical properties superior to natural rubber. Butyl rubber is composed of long molecular chains, polymerized from isobutylene with a small quantity of isoprene, the molecular structures of which are illustrated in Figure 7.9. During the polymerization process, sulfur is used as cross-linking agent.

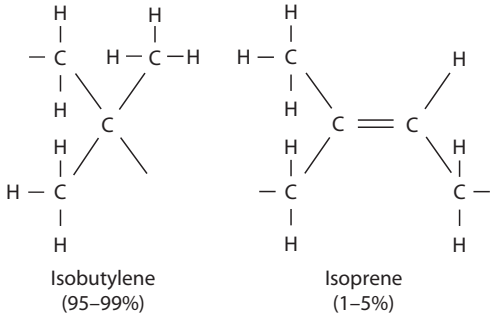


FIGURE 7.9 Molecular structure of base elements in butyl rubber. (Rosen, L.S., *Fundamental Principles of Polymeric Materials*, Barnes & Noble, New York, 1971.)

Because of its low degree of nonsaturation, vulcanization of butyl rubber must be made at temperatures higher than those used with the natural rubber for the same duration of curing. Butyl rubber presents a good environmental and resistance to PDs, UV radiations, oil, and tearing and thermal aging, while having good electrical properties. It is used as insulating and protective *jacketing* materials of cables.

Butyl rubber can also be composed with *plasticizers*, a chemical agent added to polymers to increase their flexibility and softness, to provide a flexibility at low temperatures of −45°C (−60°F). Although butyl rubber is good resistant to acids, it *swells* in petroleum base solvents; it is particularly sensitive to alkaline, high temperatures, and humidity; and it offers poor flame resistance. It has a volume resistivity of 10^{17} Ω-m at ambient temperature, a dielectric constant of 2.9 at 1000 Hz, a dielectric strength of 23 kV/mm (600 V/mil), and a loss factor tanδ of 0.003. Butyl rubber can be used at high temperatures, up to 150°C (300°F), and becomes brittle at the temperature of −55°C (−80°F).

7.2.1.4 Silicone Rubber

It is classified as an organic–inorganic elastomer, obtained by polymerization of organic siloxanes. The silicone rubbers were developed in 1943 and used in situations requiring a high degree of thermal stability. Its basic structure is shown in Figure 7.10. The properties of silicone rubber are determined by the length of its molecular chains and by the nature of R-substitutes in silicone atoms. Silicone rubbers are composed of units of dimethyl-siloxane $(CH_3)_2\ SiO^-$, the R-substitutes being simple groups of methyl.

Silicone rubbers are made by hydrolysis and subsequent condensation of the silicone fluids of low molecular masses. Fillers like silica, calcium carbonate, titanium oxide, or iron oxides and catalysts are added to obtain the desired formulation. Cross-linking or vulcanization is made generally with *peroxide*, such as *benzoyl peroxide* or *dichlorobenzoyl peroxide*. Electrons and gamma rays can be used to obtain cross-linking, which, often, is a function of the intensity of radiation.

Since silicone rubber does not contain plasticizers or softeners, it is more resistant to embrittlement caused by aging. For low-temperature applications, silicone rubber remains flexible to temperatures of −75°C (−120°F), becoming brittle only at −100°C (−180°F). At high temperature, silicone rubber can operate continuously at temperatures up to 250°C (500°F) and to 350°C (700°F) in intermittent operation. It has a low absorption coefficient for humidity and an excellent resistance to PDs. Because of its capacity to maintain good electric properties at high temperatures, it is well adapted to particularly severe operating conditions.

7.2.1.5 Neoprene and Polychloroprene

The neoprene is a synthetic rubber made from polychloroprene, with metal oxides serving as cross-linking agent. Figure 7.11 shows the molecular structure of the chloroprene monomer, which is the base

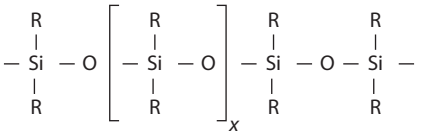


FIGURE 7.10 Base elements of the molecular structure of silicone rubber. (Rosen, L.S., *Fundamental Principles of Polymeric Materials*, Barnes & Noble, New York, 1971.)

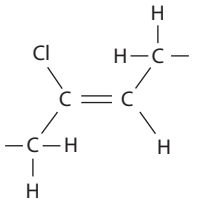


FIGURE 7.11 Molecular structure of chloroprene. (Rosen, L.S., *Fundamental Principles of Polymeric Materials*, Barnes & Noble, New York, 1971.)

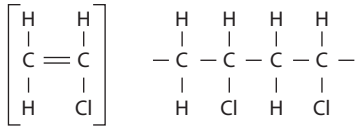


FIGURE 7.12 Molecular structure of vinyl chloride and PVC. (Rosen, L.S., *Fundamental Principles of Polymeric Materials*, Barnes & Noble, New York, 1971.)

element for neoprene and polychloroprene. Its use is essentially in the manufacture of the protective jacket of cables since 1933. The neoprene has the advantage of being more resistant than natural rubber to aging and to ozone, *UV* radiations, oil, etc., and above all, to its properties of flame resistance.

7.2.1.6 Polyvinyl Chloride

It is a *thermoplastic* compound, which conserves the property of softening under the effect of temperature and hardening again at ambient temperature, in contrast with a *thermoset* polymer, which can do this cycle only once. It has a molecular structure similar to that of PE with one hydrogen atom out of two replaced by a chloride atom. Figure 7.12 illustrates the base molecules of vinyl chloride and polyvinyl chloride (PVC).

7.2.1.7 Polyethylene and Cross-Linked Polyethylene

PE is a long plastic hydrocarbon chain, produced by polymerization of the ethylene (C_4H_4) under high or low pressure. The high-pressure process (1000–2000 atm. at 200°C) produces low-density PE, which has an appearance of wax and a texture of rubber. The product obtained is *thermoplastic*, that is, the material can undergo several times the heating–cooling cycles without losing its property of softening under the effect of temperature and hardening again at ambient temperature.

Figure 7.13 illustrates the molecular structure of linear PE, the length of which can vary between a few hundred and several tens of thousands of molecules with lateral branching as illustrated in Figure 7.14a. The structure of the PE chain is illustrated schematically in Figure 7.14b. The crystalline regions, where the PE chains are parallel (Region A), can be distinguished from the amorphous regions, where the PE chains are in disorder (Region B). It is the percentage of the crystalline regions to the amorphous regions that determines the physical–chemical properties of the final product.

Table 7.2 gives a summary of the effect of the crystallization on the properties of the PE. Low-density PE has a crystallization between 40% and 60% and its molecular mass is between 10^4 and 5×10^5. High-density PE is produced at lower pressure (60 atm.), its crystallization is higher than 60%, and its molecular mass can reach 10^6. A high degree of crystallization gives a higher rigidity to PE but makes it brittle. The dielectric strength also increases with the degree of crystallization. The main drawback of PE is its relatively low melting temperature, which limits its utilization to temperatures in the range of 75°C–90°C to avoid problems related to the displacement of the conductors, which modifies the concentric geometry of the cable.

Cross-linked polyethylene (*XLPE*): Cross-linking is a process that allows linking of two adjacent PE chains. Several processes exist for polymer cross-linking: by radiation, which extracts two hydrogen atoms to joint two lateral branches, with peroxide and even water as cross-linking agent, processes that replace the hydrogen atom in two lateral branches by a radical to allow their junction. *XLPE* is produced from low-density PE, to which is added a minute quantity of dicumyl peroxide and other organic

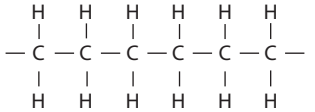


FIGURE 7.13 Molecular structure of linear PE. (Rosen, L.S., *Fundamental Principles of Polymeric Materials*, Barnes & Noble, New York, 1971.)

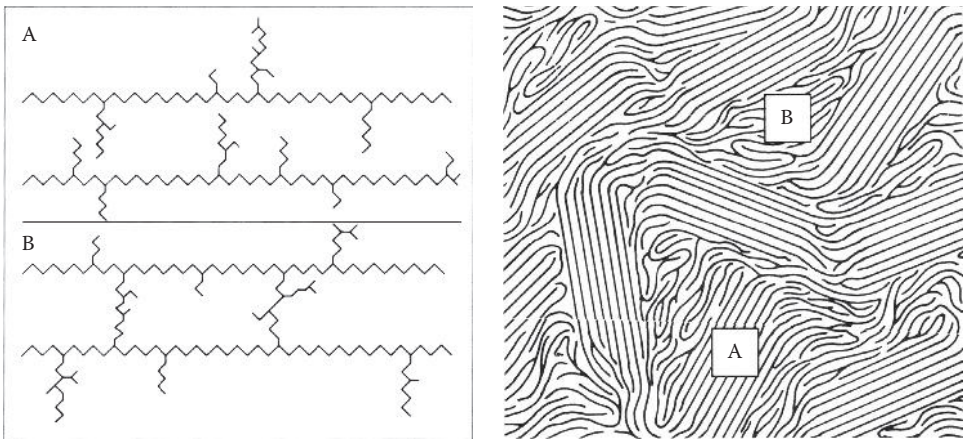


FIGURE 7.14 Illustration of the molecular structure of PE. (a) Molecular structure of PE and XLPE chains. (b) Macroscopic structure of PE showing crystalline and amorphous regions. (From Barlow, A., The chemistry of polyethylene insulation, *IEEE Electrical Insulation Magazine*, 7, 8, 1991.)

peroxides. The mixture is then *thermally cured* to allow the *cross-linking*. The effect of cross-linking is to produce a large number of interchain links, which make the product more rigid and give it better thermal properties, with an operating temperature between 90°C and 130°C. XLPE becomes, however, *thermoset*. The advantages of *XLPE* reside in its much lower thermal deformation coefficient at high temperatures and an elasticity comparable to rubber.

7.2.2 Dielectric Performance of New Samples

Figure 7.15 shows a typical design of polymer-insulated cable: The insulation is extruded directly on the conductor. It is then cured to complete the chemical process. A metal sheath fixes the ground potential, and the cable is completed with a protective jacket.

TABLE 7.2

Effect of Changes in Density and Melt Index on PE Properties

Physical Properties	Increasing Density	Increasing Melt Index
Melt viscosity		Lower
Surface hardness	Higher	Slightly lower
Tensile strength yield	Much higher	Slightly lower
Tensile strength—break	Slightly lower	Lower
Tensile strength—elongation	Lower	Lower
Resistance to creep	Higher	Slightly lower
Flexural stiffness	Much higher	Slightly lower
Flexibility	Lower	
Resistance to brittleness	Lower	Lower
Resistance to environmental stresses	Lower	Lower
Barrier properties—MVT rate	Lower	
Barrier properties—gas and liquid transmission	Much lower	
Barrier properties—grease resistance	Much higher	Slightly lower
Substrate adhesion	Slightly lower	Slightly higher
Shrinkage	Higher	Lower
Electrical properties	Slightly higher	No effect

Source: Fukuda, T., *Electr. Insul. Mag*., 4(5), 9, September/October 1988a; Fukuda, T., *Electr. Insul. Mag*., 4(6), 15, November/December 1988b.

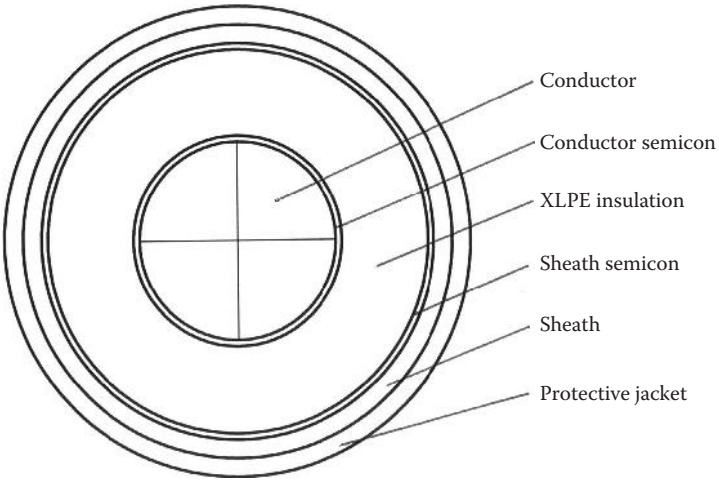


FIGURE 7.15 Typical design of solid insulation cable.

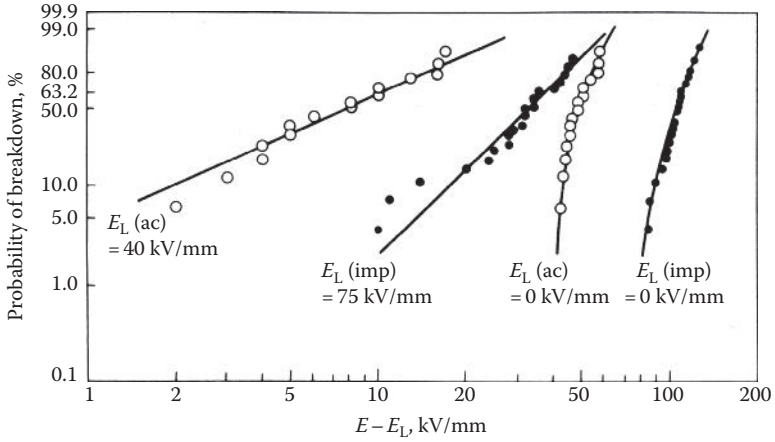


FIGURE 7.16 AC and impulse breakdown field obtained with 66 kV cable samples. (From Fukuda, T., *Electr. Insul. Mag.*, 4(5), 9, September/October 1988a.)

7.2.2.1 Initial Breakdown

This is obtained on new cable samples with no aging when the voltage is raised steadily until breakdown. Under such conditions, breakdown assumes an electron avalanche process and ion space charges similar to those active in gas breakdown, accompanied by the development of microcracks in the insulation. Breakdown fields obtained in this way are much higher than normally encountered in high-voltage cables. Figure 7.16 shows the variations of the initial breakdown fields of an XLPE-insulated 66 kV cable subjected to ac and impulse voltages (Fukuda, 1988a). It can be seen that the breakdown distributions are of Weibull type with position parameters of $E_{0AC} = 40$ kV/mm and $E_{0imp} = 75$ kV/mm, which can be defined as the *limit withstand fields* E_{lAC} and E_{limp}, respectively, for ac and impulse voltages, a propriety of the polymer used. It depends on the choice of the materials used, the quality control, and the manufacturing procedures.

The initial breakdown strength varies with insulation thickness of the test sample. Figures 7.17 and 7.18 show the range of variation of initial ac and impulse breakdown stresses as a function of the insulation thickness (Fukuda, 1988). The lower curves in the figures correspond to the limit withstand fields E_{lAC} and E_{limp}. An important reduction of the dielectric strength of the PE is observed with increasing insulation thickness under both ac and impulse voltages, which may reach some 30% of the value measured on thin samples.

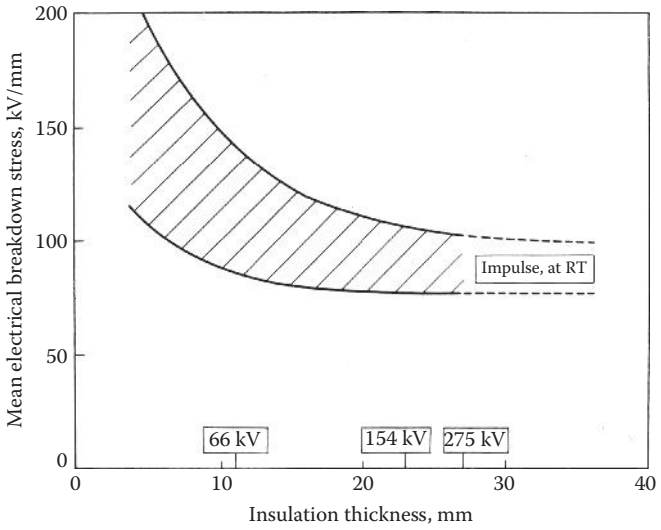


FIGURE 7.17 Influence of the insulation thickness on the ac breakdown voltage. (From Fukuda, T., *Electr. Insul. Mag.*, 4(5), 9, September/October 1988a.)

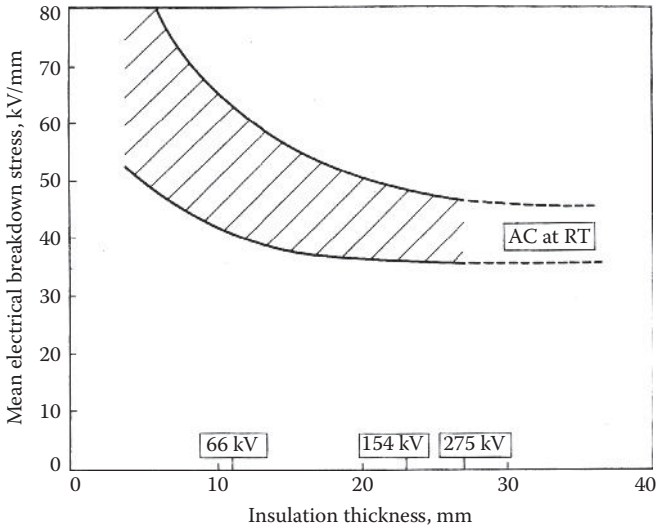


FIGURE 7.18 Influence of the insulation thickness on the impulse breakdown voltage. (From Fukuda, T., *Electr. Insul. Mag.*, 4(5), 9, September/October 1988a.)

7.2.2.2 Factors Affecting Synthetic Polymer Insulation

The dielectric performance of polymer insulation depends largely on the care taken in the selection of the base materials and the method of extrusion. Improvements in the quality control of the material used and in the extrusion techniques have contributed to the continuous improvement in the dielectric performances of polymer insulation. Several factors can affect the dielectric performance of new samples. The main factors are discussed in the following.

Protrusions at conductor surface: Protrusions create local field enhancement of several times the nominal field intensity, which favors initiation of discharges and subsequent breakdown of the sample. Figure 7.19 illustrates the effect of protrusions at the conductor surface defined by their height, on the

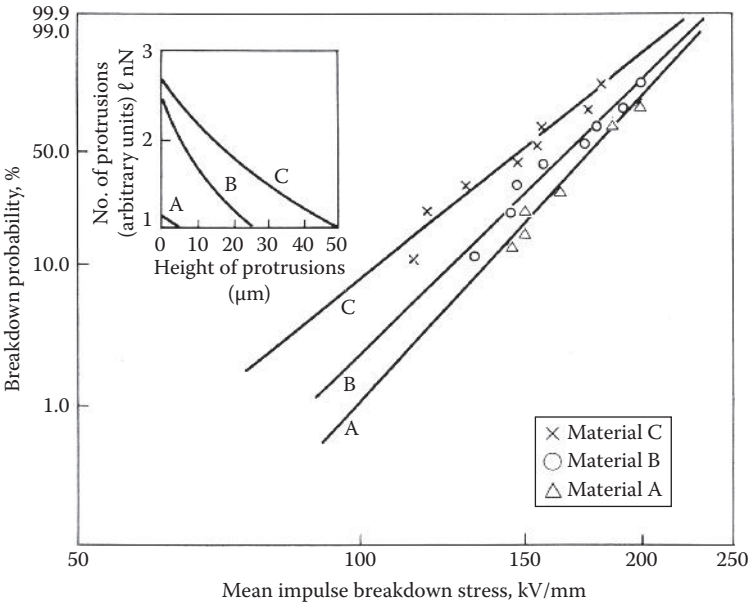


FIGURE 7.19 Effect of protrusions at conductor surface on dielectric breakdown voltage. (From Fukuda, T., *Electr. Insul. Mag*., 4(5), 9, September/October 1988a.)

distributions of the breakdown voltage measured on three different test samples. Small protrusions result in higher values of the breakdown voltage, although with a higher dispersion in the measured values. The utilization of semiconducting layers reduces the local field intensity at the conductor and sheath and, hence, the effect of the conductor surface roughness.

Cavities and solid contaminants: The presence of solid particle contamination and gas- and liquid-filled cavities in the cable insulation also produce local field enhancement, favorable to the development of PDs and eventual breakdown of the insulation. Solid particles come from the base material and can be improved by adequate quality control of the material used. Figure 7.20 illustrates the improvement obtained in the reduction of the impurities in PE insulation over the period from 1974 to 1984.

Gas- and liquid-filled voids are produced during curing of the insulation and are directly related to the curing process: steamed and dry cures. Dry cure uses pressurized nitrogen and high temperature and

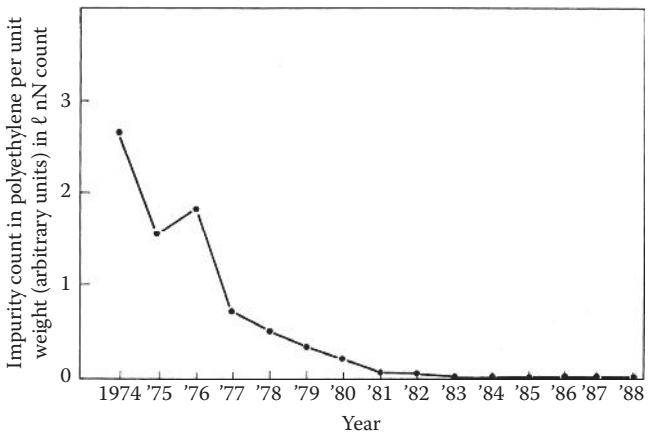


FIGURE 7.20 Effect of the quality control on the content of impurities. (From Fukuda, T., *Electr. Insul. Mag*., 4(5), 9, September/October 1988a.)

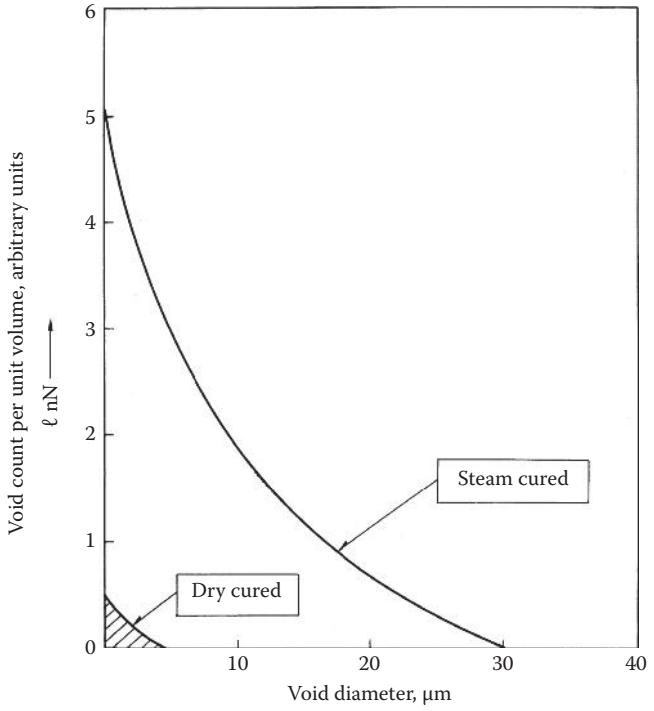


FIGURE 7.21 Effect of dry cure on the control of voids within the insulation. (From Fukuda, T., *Electr. Insul. Mag.*, 4(5), 9, September/October 1988a.)

reduces considerably the number and the dimensions of the voids present in the insulation, as illustrated in Figure 7.21, by at least an order of magnitude.

Separation of insulation layers: The extrusion of the semiconducting layers was initially made in several stages in tandem. The contraction and dilatation of the dielectric during the load cycles of the cable produce shear stress in the dielectric, making the dielectric and semiconducting layers around the central conductor vulnerable to layer separation both at the conductor and main insulation, forming voids at these locations. The problem is solved when improvement in the extrusion technique allows the coextrusion of several layers, which provides a better adhesion between the semiconducting layers and the main insulation and minimizes the risks of separation at their interfaces.

Migration of solid contaminants: It is observed for carbon particles at the interface of the semiconducting layers and the main insulation. This problem has led to the replacement of the carbon black used in the extrusion of the semiconducting layers, by the acetylene black containing less carbon particles and, above all, particles of very small dimensions.

Humidity: For long time, the use of an impermeable sheath to protect the main insulation against ingress of humidity was not considered necessary in North America. This has resulted in a large number of premature failures, related to the development of water trees. The use of an impermeable sheath is now encouraged to minimize the risk of humidity ingress and the development of water trees within the insulation. Additional improvement is also obtained by the use of additives and voltage stabilizers, which retard and slow down the development of trees.

The many solutions adopted by the cable manufacturers to minimize the effect of these factors affecting the solid insulations have greatly improved their dielectric performances, as illustrated by a continuous increase in the dielectric strength of PE and XLPE insulations since their introduction to electrical insulation. Figure 7.22 summarizes the progress obtained and their impact on the dielectric performances of PE and XLPE insulation as described by the limit withstand fields E_{lAC} and E_{limp} under ac and impulse voltages, which reach the level of 35 and 70 kV/mm, respectively, in the 1980s.

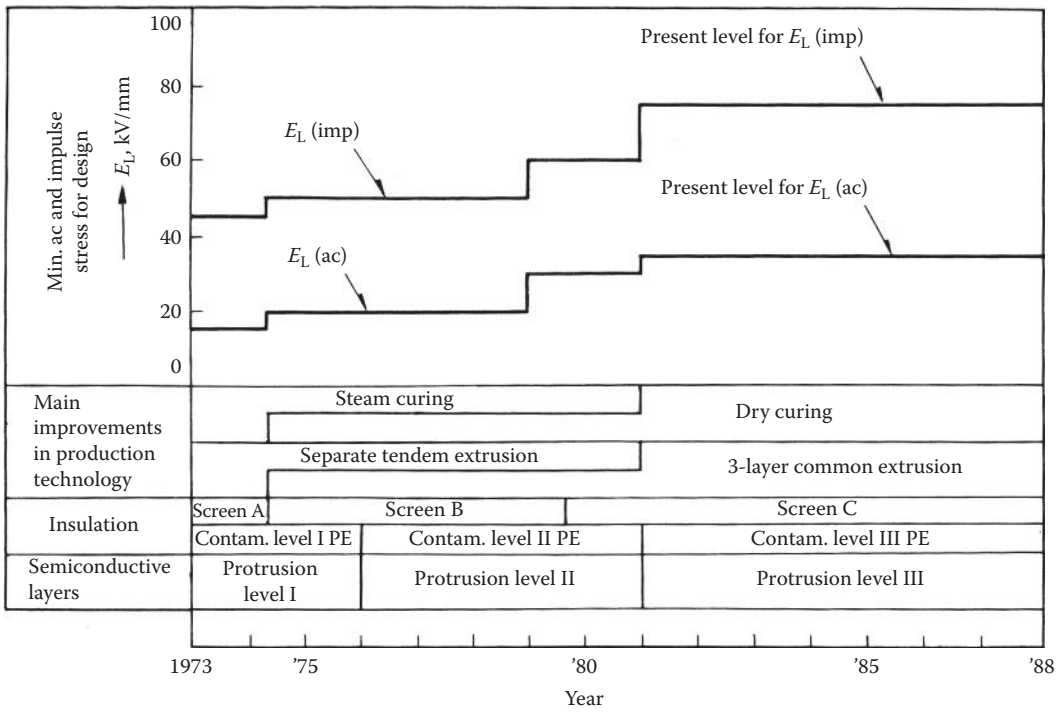


FIGURE 7.22 Key development stages of extruded *PE* and *XLPE* insulation cables. (From Fukuda, T., *Electr. Insul. Mag*., 4(5), 9, September/October 1988a)

7.3 Paper–Oil Composite Insulation

Oil–paper composite insulation varies considerably with the type of equipment: power transformers, shunt reactors, and high-voltage cables. In power transformers and shunt reactors, the oil is predominant and plays a significant role in insulation performance, since failure of the insulation is ultimately related to breakdown of the oil space between the winding, high-voltage leads, etc., to ground. This specific aspect of oil–paper insulation is treated in *Chapter 12 on Power transformers*. This chapter deals principally with the paper–oil insulation, where the paper is the predominant component as used in high-voltage cables.

Figure 7.23 illustrates a typical design of a paper-impregnated oil-filled cable. The conductor shown is composed of seven segments forming a central channel for the circulation of the impregnating oil. The cable insulation is built up around the conductor with *kraft* paper tapes to the required insulation thickness. A metal sheath fixes the reference (ground) potential and completes the cable. Self-contained oil-filled (SCOF) cables, because of the high pressure of the impregnating oil, must be hermetic and able to withstand the oil pressure. Additional layers of lead or/and PVC are added to protect the cable against ingression of water and leaks and mechanical damages.

7.3.1 Lapped Insulation

Introduced by S. Ferranti in 1891, the impregnated paper–oil cables have seen a continuous development, which led to application at all voltage levels, for both ac and dc power transmission. The insulation uses impregnated paper tape, wound around the cable central conductor in successive layers, until the desired insulation thickness is reached. The tapes in the same layer do not touch one another to allow the layers sliding one upon the other without crumpling up or tearing the paper during bending of the cable. The resulting butt gap, an artificial void, is the main weak point of lapped insulation. Figure 7.24 illustrates different *overlays* of the paper tape: the ratio of the proportion of paper tape to free space between two

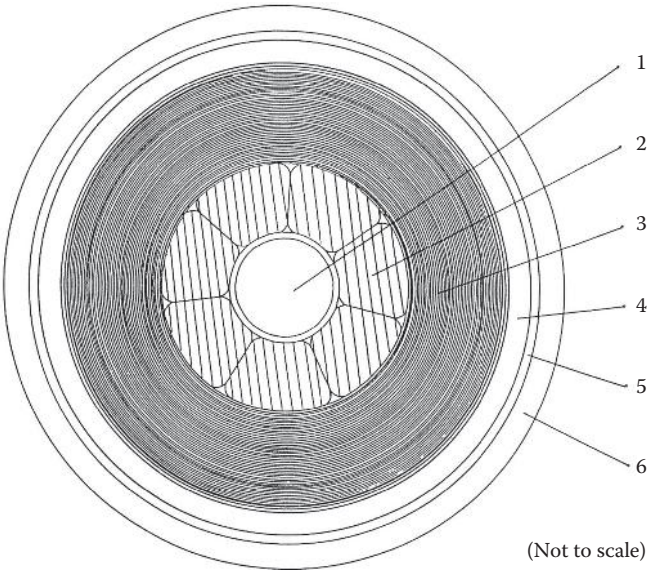


FIGURE 7.23 Typical design of paper-impregnated–oil cable. 1—Oil circulation channel; 2—conductor; 3—paper–oil insulation; 4—lead sheath; 5—reinforcement; and 6—protection jacket.

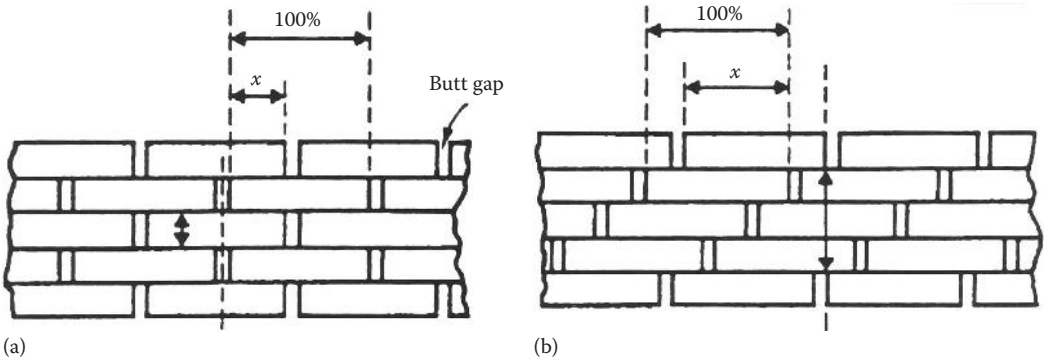
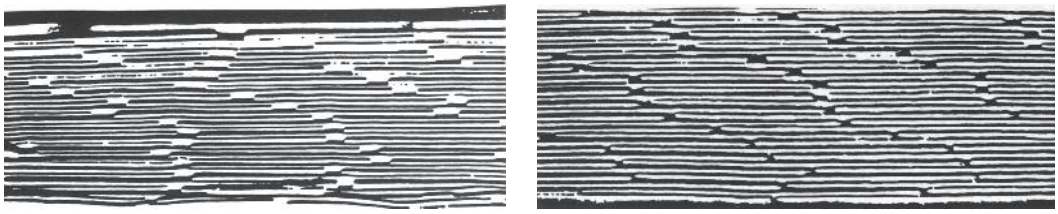


FIGURE 7.24 Illustration of different overlay ratio of taped paper. (a) x = 50%, 50/50 and (b) x = 70%, 70/30.

consecutive tapes in a layer. The most commonly used is 70/30, which allows a maximum of three layers of tapes between two consecutive butt gaps in the radial direction (Figure 7.24b).

In all lapped tape insulations, the butt gaps must be filled with an impregnating fluid to prevent initiation of PDs by the local electric field. For many years, this phenomenon of PDs has forbidden the use of impregnated paper–oil cables beyond voltages of 30–35 kV. In 1926, Emmanueli introduced the principle of pressurization of the insulation, which prevents the formation of gas bubbles and eliminates the initiation of PDs, which are important factors in the aging of the cable insulation. The higher is the internal pressure, the higher is the permissible operating voltage gradient of the cable.

Control of taping process: The main problem with paper insulation resides in the flexibility required by the cable, which is obtained only by accurate control of numerous parameters during the taping process. The tape in the same layer must not touch one another to allow sliding of the tapes without overlapping, crumpling, or tearing during flexion of the cable. The inherent butt gap between the paper tapes, an artificial void, is the weak point in lapped insulation, and in particular, the way that the butt gaps are aligned in the radial direction is critical for the dielectric withstand of the insulation. Figure 7.25 illustrates



(a) (b)

FIGURE 7.25 Examples of (a) a non-uniform poorly taped and (b) reasonably well-taped cable. (From Greenfield, W.E., *Paper Cable Taping Patterns*, Washington State Institute of Technology, Bulletin 268, Power Technologies Inc., 1963.)

the cases of a reasonably well-taped (Figure 7.25b) and a poorly taped (Figure 7.25a) cable insulation, which results in radial alignment of several butt gaps. If the accuracy in maintaining a constant overlay is important for ac cables, it is more so for dc cables: A slight variation in the overlay ratio can reduce by 5%–7% the ac and impulse breakdown voltage; the reduction is about 30% under dc voltage.

Since the cable insulation must be as compact as possible while allowing adequate bending of the cable, the taping must be made with a traction force sufficiently high without exceeding the tearing limit of the paper tape (≈77 and 35 MPa in the longitudinal and transversal directions, respectively). The actual traction is adjusted in terms of the mechanical performances of the paper, usually identified by a factor *A* defined according to

$$A = \frac{1}{\mathrm{h}} \sqrt[4]{4\, E_{\mathrm{l}}\, E_{\mathrm{t}}\, G^2} \tag{7.7}$$

where

E_{l} and E_{t} are the elastic modulus of the paper in the longitudinal and transversal directions
G is the shearing modulus
η is the coefficient of static de friction

The coefficient *A* allows a comparison of the mechanical characteristics of different paper tapes, based on their coefficient of friction and elastic and shearing modulus. These parameters depend on the process of manufacture of the paper and determine its permeability and density, having a direct incidence on the relative dielectric constant ε_{r} and the loss factor tanδ of the cable insulation. An increase in the density of the paper increases its dielectric strength at the expense of an increase in ε_{r} and tanδ that one would like to keep as low as possible to preserve the critical length of the cable and its transmission capacity.

For large cables at EHV level, a value of *A* higher than 10 MPa is normally required. Figure 7.26 illustrates the variation of the interlayer pressure within the insulation, starting at the conductor, having the shape of an *S*. This distribution of the interlayer pressure allows all the tapes to safely slide one upon the other while ensuring good compactness to the insulation. If the slope of the central (or plateau) portion of the pressure curve becomes negative, a loosening may result among the tape layers and affect the insulation performance. These mechanical criteria limit, in practice, the thickness of the paper tape to 0.075 mm. An exhaustive study of the mechanical aspects of the taping was carried out by Pirelli, which has made public its theory on taping, still followed in the manufacture of modern cables (Gazzana Priaroggia et al., 1961).

7.3.1.1 Physical–Chemical Properties of Impregnated Paper–Oil Insulation

Since its introduction, impregnated paper–oil insulation has undergone tremendous improvement and now reached its maturity, with little improvement expected in the future.

Paper: *Kraft* paper is the most utilized in the cable insulation. It is composed essentially of cellulose fibers, produced in sheet, with good mechanical properties. Well dried and impregnated with oil, *kraft* paper presents also good dielectric properties with acceptable losses for the manufacture of high-voltage cables at both ac and dc voltages. *Kraft* paper tapes have a variety of useful properties, lightness, flexibility, compatibility

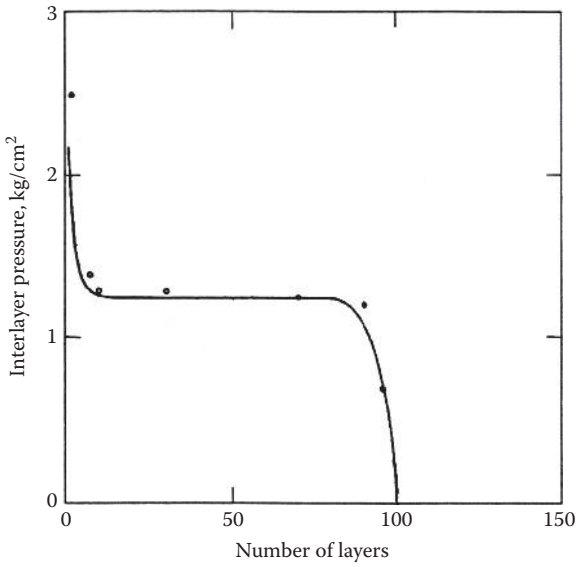


FIGURE 7.26 Variation of the interlayer pressure of paper-taped insulation. (From Gazzana Priaroggia et al., *Fundamentals of the theory of paper lapping of a single core HV cable*, Pirelli S.p.a., Milan, 1961.)

with various impregnating fluids, and can be produced with controlled parameters, density, superficial friction, rigidity, and thickness. The tapes used in the manufacture of cables have a thickness between 60 and 190 μm (2.5–7.5 mil), with typical value of 125 μm (5 mil). The mechanical properties of the paper are rigorously controlled, to avoid tearing during the taping process. Mechanical strength is typically around 75 and 35 Mpa (11,000 and 5,000 psi), in the longitudinal and transversal directions respectively.

The cellulose paper is defined by the general chemical formula $C_{12}H_{20}O_{10}$. The cellulose molecules in the paper fibers are formed from units of glucose disposed in pairs, as illustrated in Figure 7.27. The elementary unit has a length in the order of 10 Angstrom, a width of 9 Angstrom, and a thickness of 5 Angstrom.

The molecular structure of the cellulose contains also groups of carboxyl (-COOH), which appear at about every hundred of glucose units. Its presence gives the cellulose a low degree of acidity and can contribute to the ionic losses in the paper at industrial frequencies. The pores of the paper can vary from a few hundred μm for the minuscule holes down to about 10 Angstrom for the small pores in the cellulose fiber. The fibers form a complex tangle in the paper and facilitate the migration of ions over long distances in the paper–oil insulation, as long as the dimensions of the ions are smaller than the smallest of the pores in the paper.

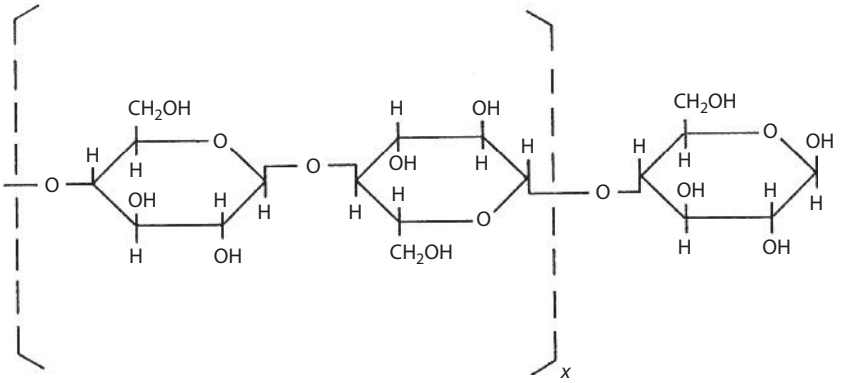


FIGURE 7.27 Molecular structure of cellulose. (Bartnikas, R. and Srivastava, K.D., *Elements of Cable Engineering*. Standford Education Press, 1980.)

The density of *kraft* paper tapes is about 0.75 g/cm^3. Since the density of the paper is also a measure of the cellulose fiber content in the insulation, the density of which is 1.54 g/cm^3, paper–oil insulation contains about half of the volume in impregnating fluid. The porosity of the paper determines the effectiveness of drying and impregnation of the paper. Paper of higher density contains more water and tends to produce more dielectric losses. On the other hand, being less porous, they have a better strength in traction and, when impregnated in oil, provide a better dielectric strength. Since the paper tapes of high density have also a higher dielectric constant, the distribution of the electric field in the cable insulation can be graded uniformly by an appropriate arrangement of paper density in the radial direction of the cable insulation.

To minimize the ionic content, associated with dielectric losses, the paper is washed normally in demineralized water. This process removes the majority of chemical residues left by the manufacturing. These residues are of electrolytic nature and can be basic by-products, acids and salts or a combination of these, and can be established by measuring the conductivity of water sample used in measurement of its acidity.

The paper alone has a very low dielectric strength (≈5 kV/mm), which makes it unsuitable for high-voltage insulation. Its impregnation with an insulating oil and pressurization provides a highly effective insulation (50 kV/mm under ac voltage). The dielectric constant of cellulose is about 7.5 and that of *kraft* paper varies from 1.7 to 3.2 for a density between 0.6 and 1.2 g/cm^3. *Kraft* paper is the only type used in high-voltage cable insulation. Table 7.3 gives the proportion of different constituents of this paper.

Oil: Mineral oils are widely used in insulation of power transformers and oil-filled cables. Their compositions vary to suit specific requirements in power transformers and cables. The selection of an oil for the cable impregnation must take into account several characteristics:

- The viscosity of the impregnating fluid plays an important role: it determines the rate of impregnation during the cable manufacturing and, in service, the circulation of the oil within the insulation system. When the electric load is removed from the system, cable insulation cools down. The impregnating fluid, which has dilated under load conditions, must have a viscosity sufficiently low to reintegrate the insulation and avoid the formation of voids. The thermal expansion coefficient of the oil influences the dimensioning of the pressurized oil reservoir.
- The flash point of the oil establishes an upper limit for the temperature to avoid the risks of fire.
- The pouring point determines the lower limit for the temperature at which one observes the formation of wax, which prevents the free circulation of the oil within the insulation.
- The dissolved gas content is particularly important in low oil pressure cables to avoid the formation of gas bubbles.

Insulating oils used as impregnating fluid for *kraft* paper are refined from petroleum and have naphthalene, paraffin, and aromatic constituents. Typically, a cable oil contains 12% of aromatic, 38% of naphthalene, and 50% of paraffin. Each oil contains molecules of a variety of dimension and structure. The molecular mass of the oil is an average value. The length and the structure of oil molecules can vary considerably. The aromatic components in the oil tend to increase dielectric losses; their presence is, however, necessary to inhibit the evolution of gas in oil subjected to electrical stresses. The dielectric

TABLE 7.3

Typical Composition of *Kraft* Paper

Constituent	Percentage (%)
α-Cellulose	88.3
Hemicellulose	2.9
Lignin	4.3
Ashes	0.5
Sulfate content	0.02
Chloride content	0.02
Other impurities	3.96

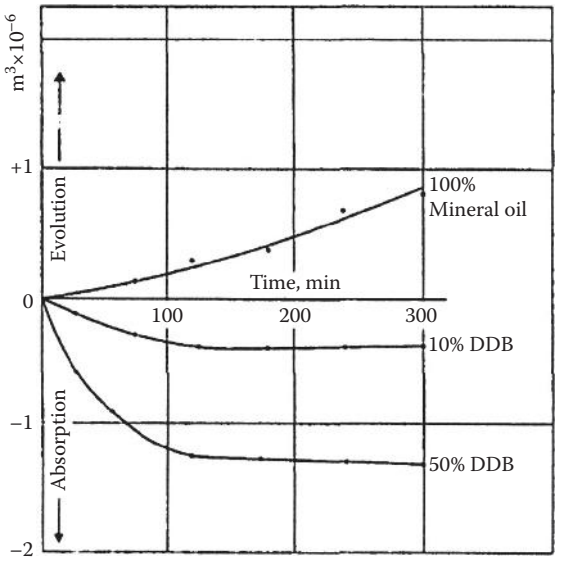


FIGURE 7.28 Effect of the addition of DDB to mineral oil on its capacity to absorb hydrogen. (From Miranda, F.J. et al., *Proc. IEE*, 123(3), 229, March 1976.)

constant ε_h of oil is about 2.2, the loss factor tanδ is below 10^{-4}, and the viscosity can vary between 10 and 1000 centistokes.

Highly refined mineral oil is more and more replaced by synthetic oil (alkylates) because of their superior properties. SCOF cables of 500 kV (ac and dc) and above are almost exclusively impregnated with synthetic oil dodecylbenzene (*DDB*) where the low viscosity of oil is required. Recently, polybutyl fluids having a viscosity between 10.6 and 11.1 centistokes have been used in pipe-type cables. The polybutyls are polymer hydrocarbons, which have a low dissipation factor, a high volume resistivity, and a good dielectric strength. They are relatively free of ionic impurities and little affected by oxidation. In the same group, nonylbenzene (NB), very fluid, is used in long submarine cables, and at the other end of the viscosity range, octadecyl-benzene is used in pipe-type cables as well as the synthetic oil polybutene. Figure 7.28 shows the effect of the addition of *DDB* in mineral oil on its capacity to absorb hydrogen in a gassing test. It can be seen that while the hydrogen is in constant evolution in the mineral oil, the addition of a small percentage of DDB was sufficient to change the degassing from evolution to absorption.

Figure 7.29 compares the evolutions in time of the dielectric losses tanδ of two cables, one impregnated with mineral oil and the other with *DDB*. The temperature of 120°C used in the accelerated aging test is clearly higher than the operating temperature of paper–oil cables (85°C to 90°C). It can be seen that, beyond 800 days, the *DDB*-impregnated cable is still operating adequately, while the cable impregnated with mineral oil has reached its saturation in gas. The insulation generates intense PDs, which cause a sudden increase in the tanδ.

In addition to a high volume resistivity and low losses, cable oil must have a good capacity to absorb gas. In effect, when the cable is new, the oil contains a very small percentage of residual dissolved gas. Due to insulation aging, CO and CO_2 are formed (thermal aging of cellulose) as well as combustible gases (namely, H_2) due to *cracking* of the oil, under the combined effect of electric field and temperature. The concentration of these gases increases regularly with time, in particular for CO and CO_2. An insulation well impregnated and pressurized should not have PDs generating combustible gases. To prevent the concentration of these gases in normal insulation aging, to reach the level of saturation of the oil, which causes the formation of gas bubbles, the cable oil must have a high content of aromatics.

Impurities and humidity: Figure 7.30 shows the influence of the ionic contamination of paper on the loss factor tanδ. It can be seen that tanδ remains relatively stable, passes by a minimum before increasing rapidly at temperatures exceeding 90°C.

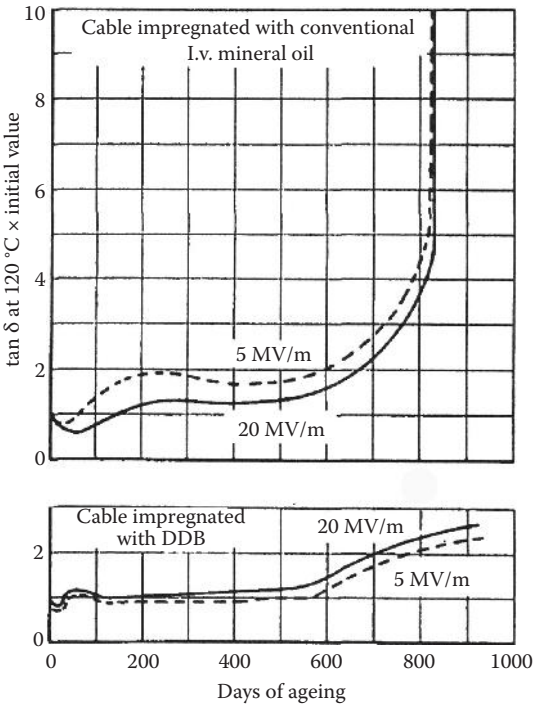


FIGURE 7.29 Evolution in time of tanδ of paper–oil and paper–DDB insulation. (From Miranda, F.J. et al., *Proc. IEE*, 123(3), 229, March 1976.)

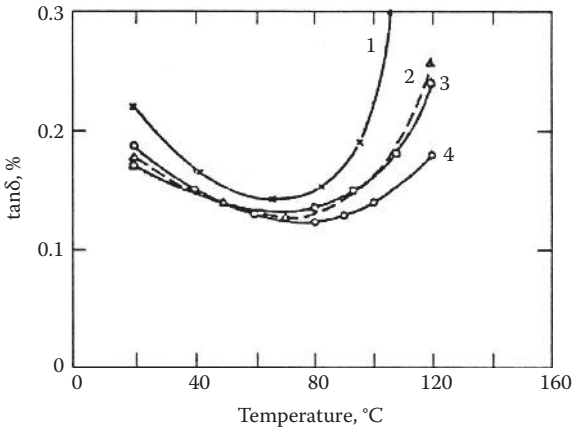


FIGURE 7.30 Influence of the temperature on the tanδ in% of paper for different levels of ionic content. Curve 1: 0.62% ash content, 220×10^{-6} Na^+ content, and 2200×10^{-6} Ca^{++} content. Curve 2: 0.41% ash content, 38×10^{-6} Na^+ content, and 2300×10^{-6} Ca^{++} content. Curve 3: 0.5% ash content, 44×10^{-6} Na^+ content, and 2000×10^{-6} Ca^{++} content. Curve 4: 0.22% ash content, 26×10^{-6} Na^+ content, and 90×10^{-6} Ca^{++} content. (Bouvier, B., *Papier et papier imprégné*", Techniques de l'ingénieur, D-280, pp. 1–26, 1977.)

Humidity is another factor, which can affect the insulation loss factor tanδ as illustrated by the results in Figures 7.31 and 7.32.

It is observed in Figure 7.31 that at 85°C, the impregnated paper has a tanδ varying from 3×10^{-3} to 1.6×10^{-1} for values of the water content varying from 0.1% to 4.7%. To obtain such a low level of water content in the paper–oil insulation, the paper must be dried and the insulating fluid degassed under

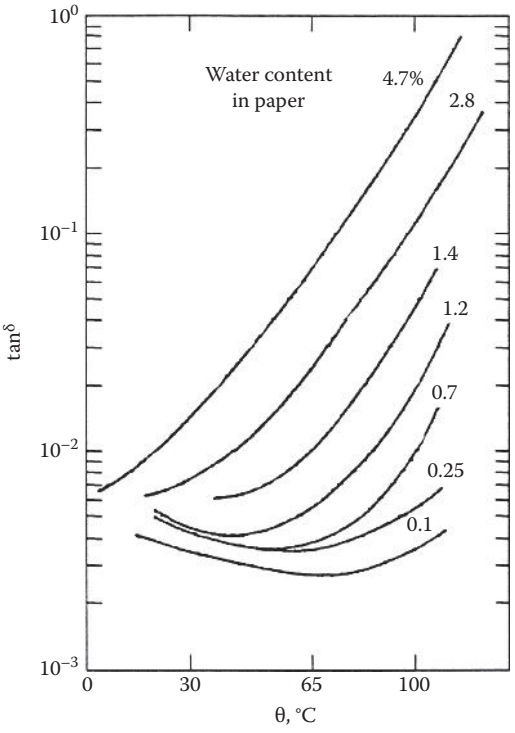


FIGURE 7.31 Variations of tanδ of cable impregnated paper, with temperature for different water contents in paper. (From (Bouvier, B., *Papier et papier imprégné*", Techniques de l'ingénieur, D-280, pp. 1–26, 1977.)

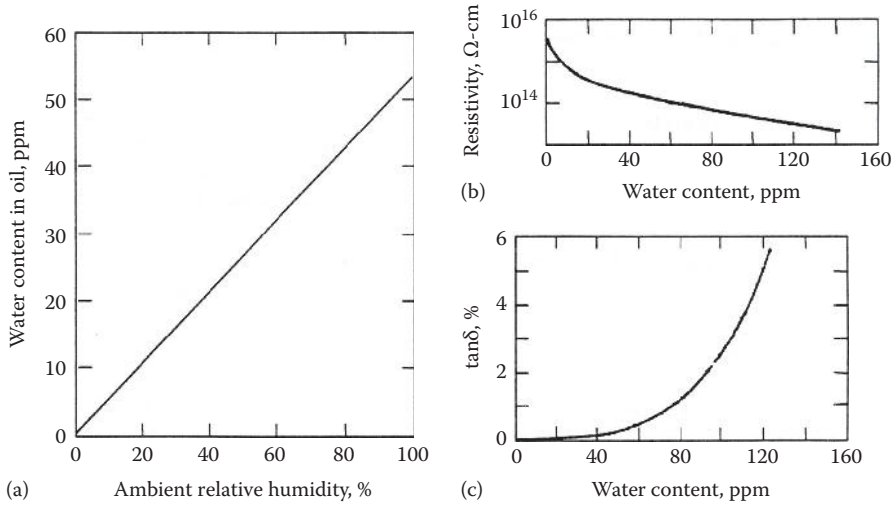


FIGURE 7.32 Influence of water content on resistivity and tanδ of oil. (a) Variation in the water content in oil, in ppm, with the ambient relative humidity in %. (b) Variation in the resistivity, in Q-cm, with the water content in oil, in ppm. (c) Variation of tanδ with the water content in oil, in ppm. (From Bouvier, B., *Papier et papier imprégné*", Techniques de l'ingénieur, D-280, pp. 1–26, 1977.))

vacuum before impregnation to eliminate water and residual dissolved gases coming from the ambient air in contact with the impregnating fluid.

Figure 7.32a through c shows, respectively, the water content in new oil as a function of the relative humidity of the ambient air and its influence on the resistivity and tanδ of the oil.

7.3.1.2 Improvement of Insulation Properties

Several attempts have been made to improve paper–oil insulation, namely, by the use of synthetic paper and oils with reduced flammability.

Synthetic paper: Impregnated *kraft* paper–oil insulation has now reached its full maturity with little possibility of improvement in sight due to the complex molecular structure of cellulose. Among the many candidates investigated to find a synthetic substitute with improved dielectric properties, *polypropylene–paper–laminate* (PPL) stands out as the most promising.

PPL is composed of a polypropylene film inserted between two *kraft* paper tape layers, the total thickness of the tape remains comparable to an equivalent paper tape, and it represents a good compromise between the required mechanical qualities of the cellulose paper and the excellent electric properties of polypropylene. Table 7.4 gives the main characteristics of *PPL* as compared with that of *kraft* paper. It can be noticed that the *PPL* is superior concerning the dielectric constant, losses, and dielectric strength under ac and impulse voltages.

The main inconvenience of *PPL* resides in its restricted chemical compatibility with most of the insulating fluids, in particular *DDB*, which swells the polypropylene and lets the oil penetrate into the PPL film between the crystalline zones. The swelling of the PPL tapes increases the interlayer pressure and affects the sliding of the tape layers one upon the other during bending of the cable, normally controlled by the *kraft* paper barriers. Furthermore, the effect of chemical action of the impregnating fluid on the amorphous zone in polypropylene is still not fully understood, which leaves some doubts on the long-term behavior, both mechanical and electrical, of this type of insulation.

Japanese cable manufacturers seem to have developed a complex method of taping PPL to control swelling (Hata et al., 1985): the tape is humidified during the taping process, which causes swelling of the *kraft* paper. During the drying under vacuum phase of the insulation, the paper shrinks, leaving free space for the swelling of *PPL* after impregnation. It is the control of these processes of shrinking/swelling of insulation that allows the commercialization of *PPL*–oil-insulated cables of 275 kV in 1982 and of 525 kV in 1985.

Ionic impurities: The polypropylene used has a crystallinity of about 60%. Umemura and Couderc (1986) have shown that aging of the polypropylene increases the crystallinity and reduces proportionally the amorphous phase, since the latter always contains a certain amount of impurities coming from residues of catalysts used in the synthesis of the material and antioxidants. During aging, these impurities are pushed to the surface of the film and can be extracted by the impregnating fluid. The phenomenon of extraction is even more important when the oil penetrates deeply into the film, as in the case with DDB. It increases the ion concentration in oil over a long period of time. The extracted impurities contribute to ac dielectric losses. In dc, they increase the conductivity of the insulation and participate in the formation of ion space charges. *Kraft* papers also let go of their residual ionic impurities into the oil. However, the ion concentration in oil does not increase with time.

On the other hand, free ions in oil tend to settle down, thus reducing dielectric losses with the time under constant electric field conditions as illustrated by the results shown in Figure 7.33 for PPL–silicone

TABLE 7.4

Constitution and Characteristics of Laminate PPL and *Kraft* Paper

Description	Units	PPL	PPL	PPL	*Kraft* Paper
Total thickness	mm	0.12	0.17	0.22	0.2
Kraft paper thickness	mm	0.03	0.04	0.04	
Polypropylene thickness	mm	0.06	0.09	0.11	
Kraft paper thickness	mm	0.03	0.09	0.07	
Dielectric constant		2.57	2.58	2.61	3.4
tanδ (80 C–20 kV/mm)	%	0.054	0.053	0.059	0.2
AC dielectric strength[a]	kV/mm	172	150	139	80
Impulsion dielectric strength[a]	kV/mm	284	256	245	150

[a] Measured on one sheet of each type of insulation.

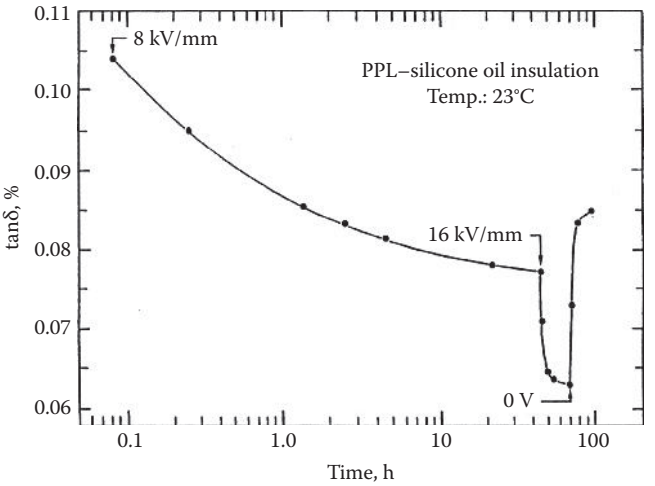


FIGURE 7.33 Influence of the time under constant ac stress on the dielectric losses of a PPL–silicone oil insulation. (From Couderc, D., Revue de l'état des recherches des câbles de transport à très haute tension de courant alternative et continu, IREQ report, November 1987.)

oil insulation, where the measured value of tanδ level off in time to a stable level. The effect is more pronounced with high value of the applied field. This is indicated by a substantial reduction of the stable level of tanδ when the applied field increases from 8 to 16 kV/mm. However, removal of the applied field produces the reverse effect, subsequent to the liberation of the ions trapped in the insulation, and increases the dielectric losses.

Oil with reduced flammability: Major fires in *France* (*Lyon* and *Paris*) and in the *United States* (*Grande Coulée*) involving mineral oil cables, combined with the fact that the synthetic alkylbenzene oils (*DDB*) with their excellent properties of gas absorption are as flammable as conventional mineral oil, have raised interest to develop an inflammable oil for cable insulation. Silicone oil is much less flammable than mineral and synthetic alkylbenzene oils; it can even extinguish on its own if there is not enough heat generated to sustain the fire. It has, however, relatively low dielectric properties as compared with mineral oil. In 1986, Pirelli developed a silicone-based fluid for cable insulation, which has adequate dielectric properties with the reduced flammability of the silicone oil (Lanfranconi and Vecellio, 1986). Long-duration test on ac cables made by Pirelli over a period of 2 years showed that the proposed fluid has performances at least identical to the DDB widely used in high-voltage cables.

7.3.2 Dielectric Performances of New Samples

Impregnated paper–oil insulation used in high-voltage cables has an inherent weak point corresponding to the presence of butt gaps within the paper tape layers, which constitute artificial voids. In ac voltage, a field enhancement occurs in the butt gap, which can facilitate initiation of PDs and eventually causes the breakdown of the insulation.

Modes of failure: Two modes of failure have been observed either in tests on laboratory samples or in practical operating conditions of impregnated paper–oil cables, illustrated in Figure 7.34.

Breakdown with puncture of the paper tapes: In this breakdown process, the discharge is initiated in a butt gap, develops through the paper tapes in a straight path, the shortest to reach the opposite electrode, and causes breakdown of the gap. The radial progression of the breakdown may be attributed to a cascade effect, which, following the breakdown of the butt gap or puncture of a tape layer, redistributes the applied voltage across the remaining sound tape layers. The redistributed voltage being higher than the initial value can cause the breakdown of the next butt gap or tape layer, and the process continues.

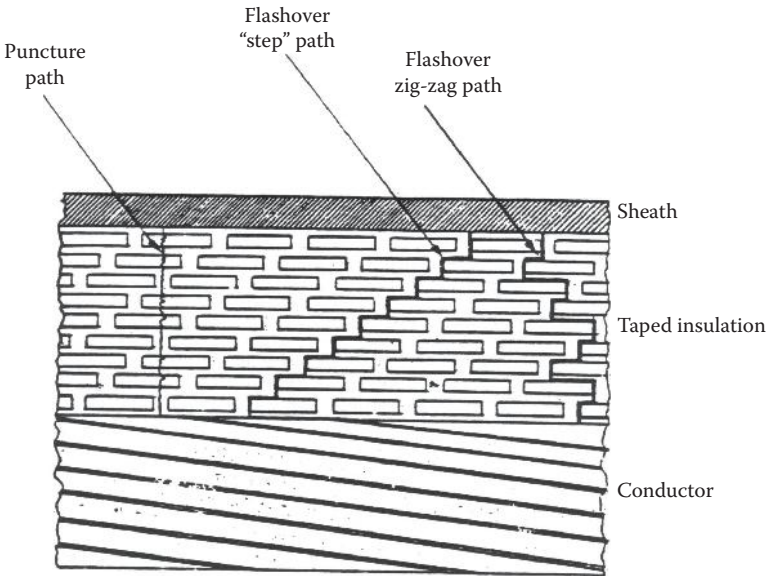


FIGURE 7.34 Illustrations of failure modes in cable impregnated paper–oil insulation. (From Greenfield, W.E., *Paper Cable Taping Patterns*, Washington State Institute of Technology, Bulletin 268, Power Technologies Inc., 1963.)

Flashover through the oil-filled butt gaps: In this breakdown process, the discharges initiated in a butt gap develop uniquely through the oil-filled butt gaps following a stepwise or zigzag path, passing by the interlayer spaces. Breakdown occurs when the discharge reaches the opposite electrode. The flashover process implies a longitudinal progression of the breakdown, which can be attributed to the voltage difference between two consecutive butt gaps due to the enhancement of the field within the butt gap and the lower breakdown field in the oil compared to puncture field through the paper tape.

7.3.2.1 Initial Strength

As previously mentioned, due to its physical layout, butt gaps are present within the lapped insulation of oil-impregnated paper. The effect is an enhancement of the field distribution, which favors the development of discharge within the oil-filled gap and determines the dielectric strength of the paper–oil insulation.

Field enhancement in the butt gap: Referring to the overlay shown in Figure 7.24, let n be the number of paper tape layers between two consecutive butt gaps in the radial direction. For a paper tape thickness, dr, considerably smaller than the total insulation thickness, the field within a tape layer can be considered as uniform and the corresponding voltage drop is $\mathrm{d}u_\mathrm{p} = E_\mathrm{p}\,\mathrm{d}r$. The voltage drop across the $n + 1$ layers of taped insulation, comprising n layers of paper tapes and one butt gap, is

$$\mathrm{D}u = n\,\mathrm{d}u_\mathrm{p} + \mathrm{d}u_\mathrm{h} = n\,E_\mathrm{p}\mathrm{d}r + E_\mathrm{h}\mathrm{d}r \tag{7.8}$$

where du_p and du_h are the voltage drop across one layer of paper tape and across the butt gap respectively.

The radial fields in the oil and paper are related to each other according to the following boundary condition:

$$\varepsilon_\mathrm{h}E_\mathrm{h} = \varepsilon_\mathrm{p}E_\mathrm{p} \quad \text{or} \quad E_\mathrm{p} = \frac{\varepsilon_\mathrm{h}}{\varepsilon_\mathrm{p}}E_\mathrm{h}$$

where ε_p and ε_h are relative permittivities of paper and oil, respectively.

Replacing the preceding expression of E_p in Equation 7.8 gives

$$\Delta u = E_h dr + n\frac{\varepsilon_h}{\varepsilon_p} E_h dr = \left(1 + n\frac{\varepsilon_h}{\varepsilon_p}\right) E_h dr = (n+1) E\, dr$$

where E is the field in a homogeneous insulation. It follows the expression for the field enhancement in the butt gap as

$$\frac{E_h}{E} = \frac{n+1}{1 + n(\varepsilon_h/\varepsilon_p)} \tag{7.9}$$

For a typical overlay ratio of 70/30, $n = 3$, and the dielectric constants of $\varepsilon_h = 2.2$ and $\varepsilon_p = 3.5$, the field enhancement in the butt gap amounts to 1.386 or 40% higher than the corresponding field in a homogeneous insulation. Such a field enhancement explains the pronounced effect of butt gaps in the initiation of PDs in paper–oil insulation.

Figure 7.35 shows the steady improvement in the dielectric strength of paper–oil insulation obtained on laboratory model samples, with increase in the oil pressure for both ac and impulse voltages. A limit withstand field E_l is found to be about 60 and 150 kV/mm for ac and impulse voltage, respectively, and increasing with the pressure. Test on oil-filled cable samples established a limit withstand field of 100 kV/mm under impulse voltage (Kaneko, 1975).

7.3.2.2 Factors Affecting the Initial Strength

The dimension of butt gaps and oil pressure are the two factors affecting the initial strength of new cable samples.

Dimensions of butt gaps: Control of the dimensions of the butt gaps is important to the dielectric performances of the cable insulation. In effect, the butt gaps being filled with oil, the dielectric strength of

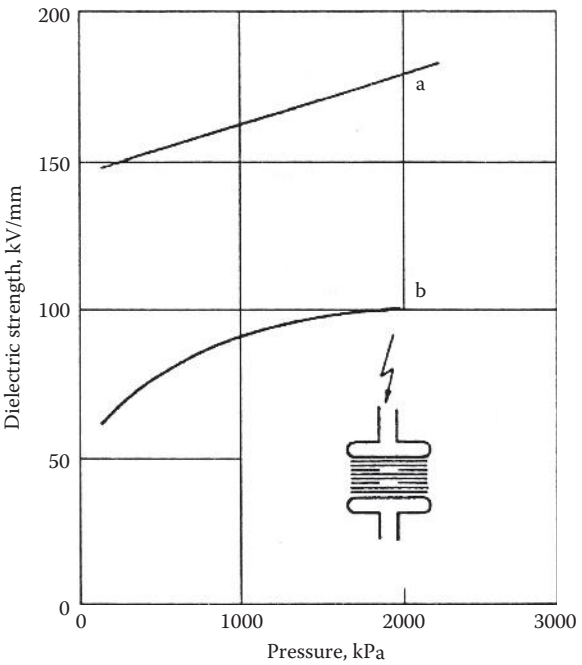


FIGURE 7.35 Effect of the oil pressure at 20°C on the dielectric strength of the oil-impregnated paper (Ochini et al., 1978): a—under lightning impulses and b—under ac voltage.

the insulation is also related to the dielectric strength of oil, which depends on the dimensions of the butt gaps and, in particular, its depth. Cable manufacturers use the following empirical expression for the ac withstand of insulating oil:

$$E = a\,d^{-0.2085} \quad \text{(kV/mm)} \tag{7.10}$$

where
a is a coefficient depending on the nature, purity, and pressure of the oil
d is the thickness of the oil film

Both the depth and width of butt gaps influence the impulse performance of the insulation:

- The reduction in the impulse strength is up to 15% with an increase in the width of the butt gap to 3 mm, which is generally adopted by cable manufacturers to allow proper bending of the cable.
- The use of thin paper tapes can improve considerably the impulse dielectric strength of the paper–oil insulation. However, this will increase the number of paper tape layers in the insulation. A compromise is generally adopted by grading the paper tape thickness with the local field in the cable insulation.

Conductor surface roughness: Protrusions at the surface of the conductor can produce local enhancement of the electric field and initiate PDs. To control this effect, the manufacturers apply one or several layers of conducting or semiconducting paper to the conductor before taping the insulation. The procedure is repeated at the insulation before making the cable sheath. However, this tends to increase the size of the conductor and cable.

Additional improvement to the field grading within paper–oil insulation can be obtained by varying the paper tape thickness with thin paper tapes with higher dielectric constant, in the high-field region to reduce the effect of the butt gaps. In practice, the cable manufacturers optimize the cable insulation in three to four layers: the first is composed of paper tapes of 0.08 mm and the last of paper tapes of 0.15–0.2 mm thick.

Impurities and humidity: Paper–oil insulation is sensitive to impurities and humidity. To maintain an adequate level of dielectric losses, the paper insulation must be dried and the oil degassed under vacuum prior to the impregnation. These processes made on long lengths of cable require complex industrial operations, which are little covered in the technical literature. The publication of Russek (1967) remains pertinent with regard to the present drying and impregnation techniques of paper–oil-insulated cables. To meet the absolute necessity to maintain the pressure and prevent the ingress of water and air into the insulation, cables are either sealed in a lead or aluminum sheath for SCOF cables or laid inside a steel tube for pipe-type cables. The oil pressure is kept constant with a pump station or reservoirs containing hermetic compressed cells, with no contact with the ambient air.

7.4 Gas–Solid (SF_6–Epoxy) Composite Insulation

All practical gas-insulated systems, overhead lines and SF_6-insulated cables and equipment, use composite insulations, consisting of two insulation systems—gaseous and solid—in parallel to provide the adequate insulation and mechanical performances required by the system. Table 7.5 presents the main characteristics of SF_6 and epoxy used in gas insulation. Figure 7.36 illustrates a typical design of a coaxial SF_6-insulated cable, with epoxy spacers placed at regular intervals along the cable. In its current form, the central conductor and the envelope are rigid tubes, which give the familiar terminology of *rigid cable* to make it distinct from the usual term *cable*, which implies a high degree of flexibility.

In such a system, the gaseous insulation provides the main insulation performances, while the solid insulation provides the necessary mechanical strength, with as little impact as possible on the insulation performance of the gaseous insulation. In addition, because of the large insulation clearances of the gas

TABLE 7.5

Characteristics of SF_6 and Epoxy

	Units	SF_6	Epoxy
Density	kg/m³	6.07	
Operating gas pressure	atm-abs	4–5	
Dielectric constant		1	5
Limit field	kV/cm atm.	86.1	
Practical operating field	kV/mm atm.	20.5	7.7
Dielectric losses, tanδ			10^{-3}–10^{-2}

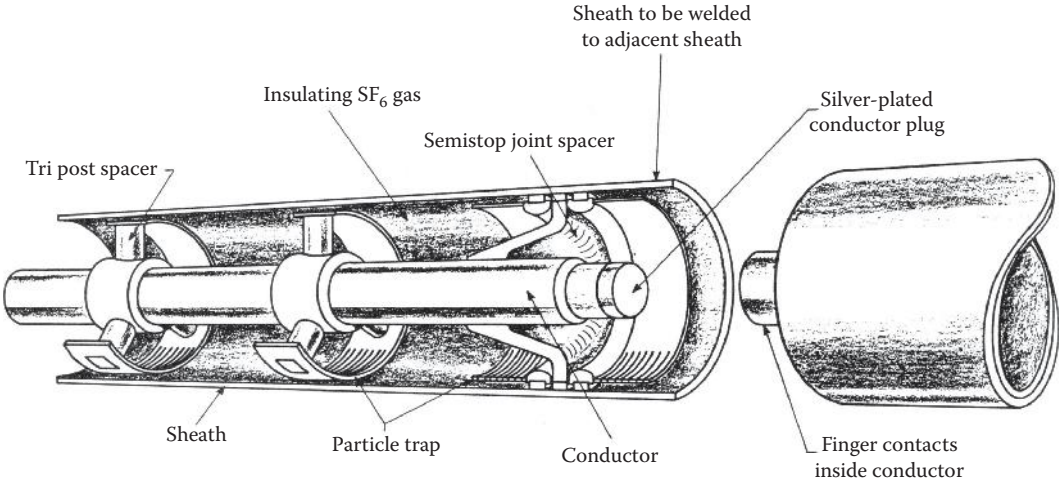


FIGURE 7.36 Typical design of a rigid SF_6-insulated cable. (From Cookson, A., Gas-insulated cables, *IEEE Trans*., Vol. EI-20, No. 5, 859, 1985.)

insulation, the operating gradient within the solid insulation is generally much below the intrinsic breakdown field of the solid insulation.

Failure mode: Failure of practical gas-insulated system often results from flashover occurring at the interface between the gas and solid insulations.

7.4.1 Gas (SF_6) Insulation

Electronegative gases are preferred candidates for the gas insulation part of the gas–solid composite insulation. SF_6 is so far the most adequate electronegative gas: In addition to having good dielectric properties, SF_6 has also good arc-quenching ability and is chemically neutral with relatively low environmental impact. However, its intrinsic dielectric strength is about 2.5 times better than atmospheric air; as a result, gas-insulated cable and equipment use pressurized SF_6, usually at 4–5 atm. abs., to achieve the required reduction in insulation clearance. Gas breakdown has been discussed in *Chapter 4*; it suffices to focus in the following, on the specific aspects of breakdown in pressurized SF_6 insulation used in high-voltage cables.

7.4.1.1 Corona Onset Field

The dimensions of the conductor and outer envelope determine the dielectric performance of the gas-insulated cable. For a coaxial configuration, taking account of the effective ionization coefficient α′ in SF_6,

$$\alpha = Cp\left(\frac{E}{p} - \left(\frac{E}{p}\right)_{cr}\right). \tag{7.11}$$

The minimal radius, a, of the central conductor can be evaluated from the streamer criteria, expressed as (Trinh and Vincent, 1978)

$$E_c\, r_c\, \ln\frac{r_c}{a} - E_c\,(r_c - a) = \frac{k}{C} \tag{7.12}$$

where E_c is the limit field $E_c = p(E/p)_{cr}$ with $(E/p)_{cr} = 86.1$ kV/cm atm. abs., $k = 18.3$, and $C = 27.7$.

The solution of the aforementioned equation yields the value of r_c, the length of the critical electron avalanche at onset of the streamer discharge in the coaxial gap. On the other hand, with the critical distance r_c thus determined, the applied voltage U_0 corresponding to the streamer onset can be evaluated according to

$$U_0 = E_c\, r_c \ln\frac{b}{a} \tag{7.13}$$

and the corona onset field, E_0,

$$E_0 = \frac{1}{\ln(b/a)}\frac{U_0}{a} = E_c\frac{r_c}{a} \tag{7.14}$$

With the conductor radius a determined, the envelope radius can be derived, assuming an optimal configuration of the cable, according to

$$\frac{b}{a} = 1 \tag{7.15}$$

Figure 7.37 compares the variations of corona onset field as a function of gas pressure evaluated for different coaxial conductor configurations (Trinh and Vincent, 1978). It can be observed that corona onset gradient varies slightly with the conductor dimension and follows a nearly linear relationship between corona onset field and gas pressure.

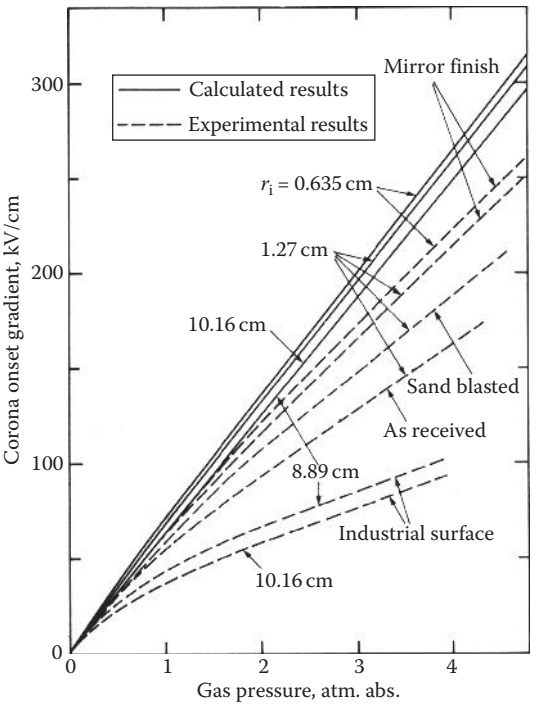


FIGURE 7.37 Corona onset and breakdown field of SF_6-insulated coaxial conductors. (From Trinh, N.G. and Vincent, C., *IEEE Trans. Power Appar. Syst.*, 97(6), 2198, November–December 1978.)

7.4.1.2 Limit Withstand Field

Noting that corona discharge are indicative of the first ionization activities in the gap, its onset voltage corresponds then to the limit withstand field of the gap. Furthermore, because of the moderate degree of nonuniformity of the radial field in a coaxial gap, corona onset in SF_6 coaxial conductor almost coincides with the breakdown value. Therefore, it corresponds to the best dielectric performance of a coaxial SF_6-insulated cable. Figure 7.37 compares such a limit withstand field with breakdown fields measured in coaxial conductors with different surface finish conditions: mirror finish, sandblasted, and industrial surface conditions. Although some measured breakdowns are close to the calculated performance according to Equation 7.14, the difference increases with the gas pressure and is attributed to the sizes of protrusions on conductor surface discussed in Section 7.4.3.

Figure 7.38 shows the variations of the normalized limit withstand (or corona onset) field with the conductor radius for different gas pressures as compared with experimental data. It can be seen that the normalized limit withstand field decreases with increasing conductor radius and gas pressure. In addition, the measured breakdown field is about 90% of the calculated limit withstand field values.

7.4.1.3 Voltage–Time Breakdown Characteristics

Breakdown in SF_6 occurs very fast and generates overvoltages with front time in the nanoseconds range. Therefore, there is a great interest to investigate the behavior of an insulation system to such steep front pulses. The streamer breakdown criterion implies the following:

- Free electrons are present in the high-field region to initiate the electron avalanche process.
- A finite time is necessary for the streamer development and its transition to breakdown of the gap.

With dc and low-frequency ac voltages, these conditions are generally satisfied, and the breakdown voltage is relatively independent of the voltage wave shape. However, this is no longer the case with impulse voltages, where the fast time variations in the voltage can affect the breakdown process. Breakdown of the gap depends on the availability of free electrons in the high-field region and the probability that they can initiate the breakdown. The instantaneous breakdown voltage is generally higher than the static value U_0, obtained under dc or ac voltages. For an impulse voltage of a given shape and prospective

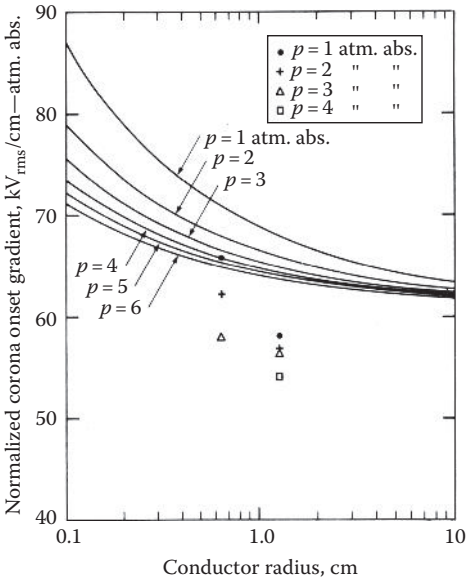


FIGURE 7.38 Variations of the normalized limit withstand field of SF_6-insulated coaxial conductors. (From Trinh, N.G. and Vincent, C., *IEEE Trans. Power Appar. Syst*., 97(6), 2198, November–December 1978.)

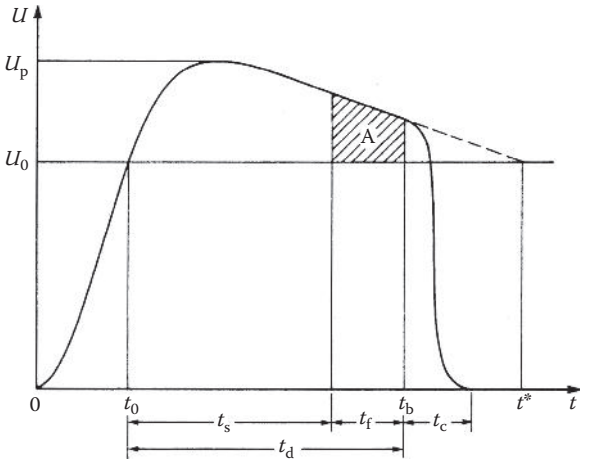


FIGURE 7.39 Definition of time lags. (From Rizk, F.A.M. and Eteiba, M.B., *IEEE Trans. Power Appar. Syst.*, 101, 4460, 1982.)

amplitude, the breakdown can occur at different points on the impulse wave. Referring to Figure 7.39, the delay time to breakdown t_d has two components t_s and t_f such that $t_d = t_s + t_f$. The *statistical time lag* t_s is the time required, once the applied voltage has reached the threshold value U_0, for a free electron to appear at a favorable position in the gap to initiate an electron avalanche of critical size. The *formative time lag* t_f is the time required for the avalanche–streamer transition to occur. A third time lag t_c, corresponding to the streamer–arc transition, can also be defined; the latter is much shorter than the preceding two time lags and is not taken into account in the evaluation of t_d.

Rizk and Eteiba (1982) have extensively investigated the short-time breakdown in SF_6 and SF_6–N_2 mixture, considering both the statistical and formative time lags as statistical variables. For a double exponential impulse voltage of prospective peak U_p, the probability that breakdown occurs at a time shorter than t_d is

$$P(t_b \le t_d) = P(U_p, t_d) = \int_0^{t_d} f(t_s)\, P_c[(t_d - t_s) \mid t_s]\, dt_s \tag{7.16}$$

where

$f(t_s)$ is the marginal density probability function of the statistical time lag

$Pc[(t_d - t_s)|t_s]$ is the conditional probability of the formative time lag

7.4.1.3.1 Statistical Time Lag

This depends on the number of free electrons produced per unit time in the high-field region, which, for positive impulse voltage, corresponds to the gas volume V_c around the highly stressed electrode where the effective ionization coefficient is positive. In electronegative gases, part of the electrons produced is captured by SF_6 molecules to form negative ions. The probability that an electron will attach to SF_6 molecule after crossing a distance x in the nonuniform field is

$$P_0(x) = \frac{\int_0^x h \exp\left[-\int_0^x (a - h)\, dx\right] dx}{1 + \int_0^x h \exp\left[-\int_0^x (a - h)\, dx\right] dx} \tag{7.17}$$

The probability that an electron crossing a distance x in the field remains free is then $1 - P_0(x)$. To take account of the effective number of free electrons produced, Rizk and Eteiba introduced a weighted volume defined as

$$V_w = \int_{V_c} (1 - P_0)\,dv \tag{7.18}$$

For a cylindrical geometry, the weighted volume is a function of $(U - U_0)/U_0$ so that

$$V_w = 1 \left[\frac{U - U_0}{U_0} \right]^{K_1} \tag{7.19}$$

where U_0 is the breakdown inception voltage.

For the 2.54/7.0 cm diameter 60 cm long coaxial cylindrical gap used by the authors, $\lambda = 413$ cm^3, $K_1 = 1.76$ in SF_6 and $\lambda = 447$ cm^3, $K_1 = 1.73$ in 50% SF_6–50% N_2 mixture. The effective number of free electrons produced in the critical volume around the highly stressed electrode is

$$N_e = n_0 V_w \tag{7.20}$$

where n_0 is the average rate of production of free electron per unit volume and unit time in the gas, which is given by Knorr (1979):

$$n_0 = \frac{\ln 2}{\int_{t_0}^{t_{50\%} - t_f} V_w\,dt} \tag{7.21}$$

Figure 7.40 gives the variations of n_0 as a function of the overvoltage ratio $(U - U_0)/U_0$ for two gas pressures.

The probability to have a statistical time lag t_s is

$$P_v(t_s) = 1 - \exp\left[-n_0 \int_{t_0}^{t_0 + t_s} V_w\,dt \right] \tag{7.22}$$

For negative impulse voltage, free electrons are also produced at the highly stressed cathode to initiate electron avalanche. A similar expression is used:

$$N_e = A_s\, n_{e0} \left[\frac{U - U_0}{U_0} \right]^{K_2} \tag{7.23}$$

where n_{e0} is a constant rate of electron production per unit time and unit cathode area.

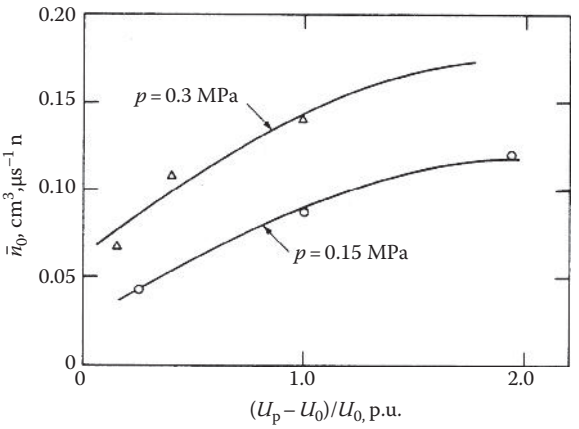


FIGURE 7.40 Rate of production of free electron in the gas volume. (From Rizk, F.A.M. and Eteiba, M.B., *IEEE Trans. Power Appar. Syst.*, 101, 4460, 1982.)

The total probability of statistical time lag due to both mechanism of electron production is

$$P(t_s) = 1 - \exp\left[-n_{e0} A_s \int_{t_0}^{t_0 + t_s} \left(\frac{U - U_0}{U_0}\right)^{K_2} dt - n0 \int_{t_0}^{t_0 + t_s} V_w \, dt\right] \tag{7.24}$$

Typical values for n_{e0} are 14.4×10^{-3} cm^{-2} μs^{-1} for SF_6 at 0.3 MPa and 16.7×10^{-3} cm^{-2} μs^{-1} for the 50% SF_6–50% N_2 mixture at the same pressure. K_2 has a value close to unity.

7.4.1.3.2 Formative Time Lag

This is determined by the area A between the impulse voltage wave and the inception level U_0 as shown in Figure 7.39. The probability to have a formative time lag corresponding to an area less than or equal to A, once an effective electron avalanche is initiated, is

$$P_c(t_f(A) \mid t_s) = 1 - \exp\left[-\frac{A - F}{CF}\right] \tag{7.25}$$

where F is a minimal value of the area A, determined from the experimental test results yielding the minimal value of time to breakdown t_{bm}:

$$F = \int_{t_0}^{t_{bm}} [u(t) - U_0] \, dt \tag{7.26}$$

Typical values obtained from experimental data give $C = 0.1$, while F varies with the stress as shown in Figure 7.41.

7.4.1.3.3 Joint Time Lag Probability Distribution

With both time lags considered as statistical variables, the bivariate probability distribution $P(t_{s0}, t_{f0})$ is

$$P(t_{s0}, t_{f0}) = \int_0^{t_{s0}} \int_0^{t_{f0}} f(t_s, t_f) \, dt_f \, dt_s \tag{7.27}$$

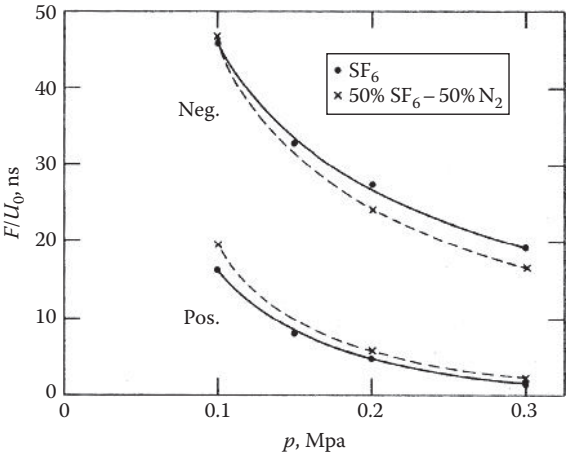


FIGURE 7.41 Variation of the reduced minimum area F/U_0 with the gas pressure. (From Rizk, F.A.M. and Eteiba, M.B., *IEEE Trans. Power Appar. Syst*., 101, 4460, 1982.)

with the joint density function $f(t_s, t_f)$ expressed as

$$f(t_s,t_f) = f(t_s) \lozenge f(t_f|t_s) \tag{7.28}$$

where
$f(t_s)$ is the marginal density function of the statistical time lag
$f(t_f|t_s)$ is the conditional density function of the formative time lag

Since the delay time to breakdown is the sum of the statistical and formative time lags, expression (7.27) becomes

$$P(t_d) = \int_0^{t_d} f(t_s) P_c((t_d - t_s) \mid t_s) dt_s \tag{7.29}$$

On the other hand, for a given impulse wave shape, both the statistical and formative time lags will vary with the applied voltage, and the preceding expression can be rewritten as

$$P(U_p,t_d) = \int_0^{t_d} f(t_s) P_c((t_d - t_s) \mid t_s) dt_s \tag{7.30}$$

where $f(t_s)$ is derived from Equations 7.22 and 7.24, respectively, as

$$f(t_s) = \frac{dP_v(t_s)}{dt_s} \quad \text{for the positive impulse and}$$

$$f(t_s) = \frac{dP(t_s)}{dt_s} \quad \text{for the negative impulse}$$

Furthermore, it can be shown that the distribution function $P(t_d|U_p)$ of t_d for an impulse with a prospective peak U_p can be expressed as

$$P(t_d|U_p) = \frac{P(U_p,t_d)}{P(U_p)} = \frac{P(U_p,t_d)}{P(U_p,t^*)} \tag{7.31}$$

Where $P(U_p)$ is the marginal breakdown probability independent of the delay time involved and assuming that no breakdown can ever occur beyond the point on the wave tail, where the voltage impulse wave intersects the inception level U_0.

Figures 7.42 and 7.43 compare the calculated and measured probability distribution of breakdown delays in SF_6 at 0.3 MPa, respectively, under a 358 kV positive impulse and a 314 kV negative impulse. A visual way to present the short-time breakdown of a gap is via its voltage–time characteristics, defined by two boundary curves representing constant breakdown probabilities, typically 5% and 95%, which include a large proportion of the measured breakdowns.

Figures 7.44 and 7.45 show two such voltage–time characteristics of a coaxial cylinder gap of SF_6 at 0.3 MPa, respectively, for positive and negative impulses. It can be seen that as the applied voltage is raised above the inception level U_0, breakdown occurs at higher values with shorter time to breakdown. Such a behavior of the SF_6-insulated coaxial cylinder gap is largely attributed to the lack of free electrons to initiate the electron avalanche at the moment the impulse wave exceeds the inception level U_0.

7.4.2 Solid (Epoxy) Insulation

The solid insulation corresponds to the set of insulating spacers, which are essential to maintain the proper clearances in the SF_6-insulated equipment and, sometimes, to serve as gas barrier to subdivide

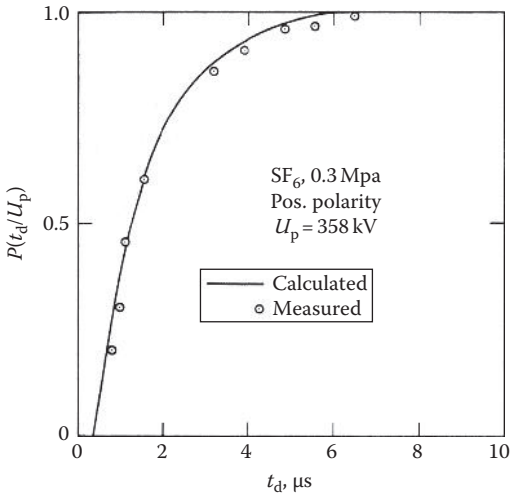


FIGURE 7.42 Probability of breakdown delays in SF_6 at 0.3 MPa under 358 kV positive impulse. (From Rizk, F.A.M. and Eteiba, M.B., *IEEE Trans. Power Appar. Syst*., 101, 4460, 1982.)

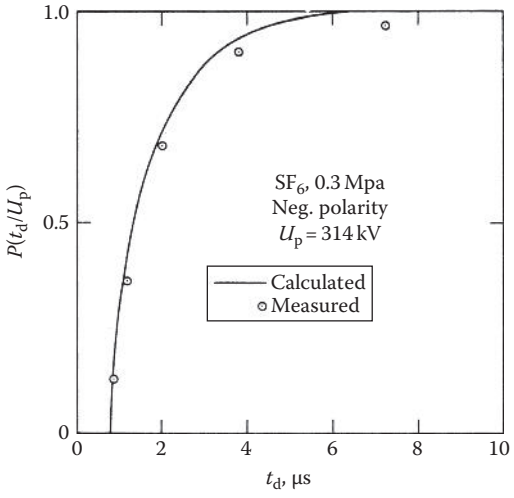


FIGURE 7.43 Probability of breakdown delays in SF_6 at 0.3 MPa under 314 kV negative impulse. (From Rizk, F.A.M. and Eteiba, M.B., *IEEE Trans. Power Appar. Syst*., 101, 4460, 1982.)

the system into small compartments. Epoxy is generally used in the manufacture of insulating spacers, mainly because of its mechanical strength, good dielectric performance and the facility to mold spacers of various sizes and shapes.

Epoxy: Several commercial epoxy formulations are available. They are all derived from the nonpolymerized epoxy shown in Figure 7.46. Organic and inorganic compounds are used as catalysts to open the oxygen bonds and allow the cross-linking, which binds the epoxy molecules together to form larger polymerized molecules. By controlling the duration and rate of chemical reactions with the use of appropriate accelerators, hardeners, and catalysts, a variety of epoxy formulations is obtained.

The density of epoxy is controlled by the amount of polymerized molecules. During the polymerization process, agglomeration of epoxy molecules subsequent to the establishment of the interatom bonds increases the density while contracting the volume of epoxy, which can cause separation of the molded epoxy from the metal substrate. The use of fillers made of noncontracting materials, such as silica, can compensate for the contraction of epoxy and contribute to reduce the density of the final epoxy product.

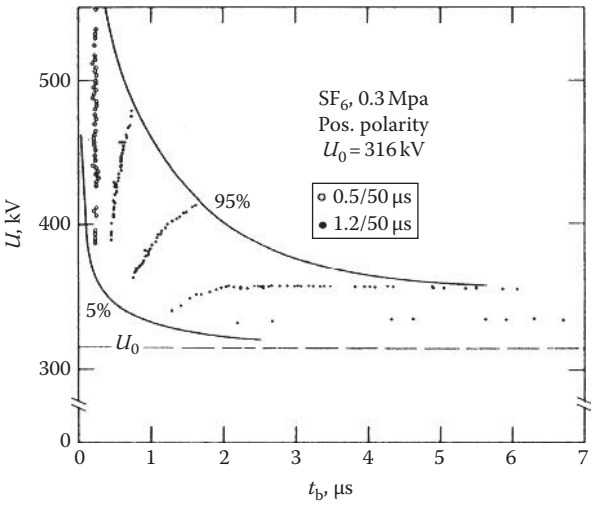


FIGURE 7.44 Voltage–time characteristics in SF_6 at 0.3 MPa under positive impulse. (From Rizk, F.A.M. and Eteiba, M.B., *IEEE Trans. Power Appar. Syst*., 101, 4460, 1982.)

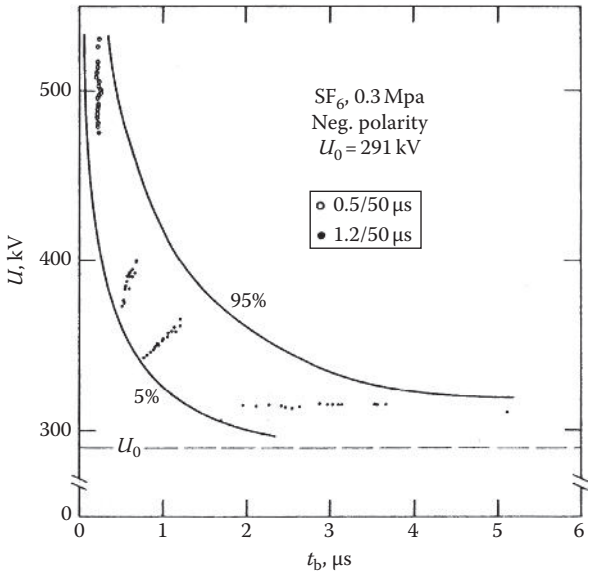


FIGURE 7.45 Voltage–time characteristics in SF_6 at 0.3 MPa under negative impulses. (From Rizk, F.A.M. and Eteiba, M.B., *IEEE Trans. Power Appar. Syst*., 101, 4460, 1982.)

Spacer: Because of the high permittivity of epoxy, the presence of a solid insulating spacer creates a dielectric discontinuity, which modifies the distribution of the local electric field and affects the dielectric withstand. The effect is particularly pronounced at the triple junction between the metal electrode, spacer, and gas (Trinh et al., 1980; Takuma and Kawamoto, 1984), where the enhanced local field can initiate PDs in the gas. Furthermore, the presence of the spacer tends to favor the development of the discharges along the gas–dielectric interface, as illustrated by the photographs of the breakdown path shown in Figure 7.47 obtained by Giesselmann and Pfeifer (1984) using a cylindrical insulator placed in a uniform-field gap, oriented along the gap axis. Both front and side views of the breakdown path are presented in the figure. It can be seen that even if breakdown is initiated away from the insulator and its cylindrical geometry does not modify the applied field, the breakdown path follows closely the gas-insulator surface.

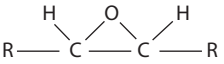
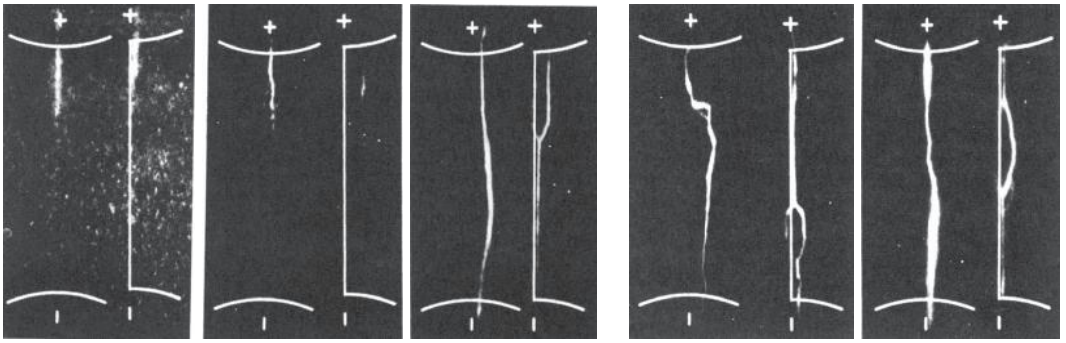


FIGURE 7.46 Epoxy molecule in its nonpolymerized form.



(a) (b)

FIGURE 7.47 Front and side views of breakdown path showing the influence of a spacer on the breakdown development in SF_6. (a) and (b) Discharge initiated from the anode without crossing the gap. (c) (d) and (e) Discharge initiated from the anode and crossing the gap, with part of the breakdown path in the gas as shown by the side views of the discharges. (From Giesselmann, M. and Pfeiffer, W., Influence of solid dielectrics upon break-down voltage and predischarge development in compressed gases, in *Gaseous Dielectrics IV*, 1984, pp. 431–436.)

It is generally accepted that dimensions of a rigid *SF_6-insulated* cable are determined by the dielectric performance of the spacers. Furthermore, because of the relatively large dimensions and the high permittivity of epoxy, the operating field within the epoxy spacer is lower than that prevailing in the gas at its interface and considerably below the intrinsic breakdown field of epoxy. As a result, breakdown in SF_6–epoxy insulation generally occurs along the gas–dielectric interface of the spacer. The design of the spacer constitutes, consequently, an important aspect of the design of a SF_6-insulated cable, usually proprietary to manufacturers. In spite of the numerous spacer designs found in operating GIS, they belong to three broad categories: cone, disc, and composite-profile spacers. Their relative merit and dielectric performance are discussed in the following.

Spacer profile: Since the majority of failure occurs along the gas–dielectric interface, the spacer profile is generally designed to prevent such a failure mode by forcing the breakdown, if any, to occur across the gas gap rather than along the gas–dielectric interface. This is achieved, in general, by properly choosing the spacer profile to reproduce a specific field distribution and, hence, controlling the development of breakdown at the gas–dielectric interface.

Potential distributions at the gas-dielectric interface: Figure 7.48 compares the potential distribution in a coaxial conductor without spacer (curve A) with distributions at different epoxy/*SF_6* interfaces. It can be seen that the electric potential distribution is somewhat nonuniform along the gas–dielectric interface.

For conical interfaces, a dielectric cone angle α_c exists for which the electric potential distribution is quasi-uniform along the interface (curve B). The value of the critical angle α_c is a function of the permittivity of the solid dielectric. For epoxy with a relative permittivity about 5, the optimal angle is 75°. For dielectric cone angles α greater than α_c, an increase in the local field is noticed close to the central conductor (curve F), whereas for dielectric cone angles α smaller than the optimal value, the electric field increase occurs close to the outer envelope. This nonuniform distribution of the potential along the gas–dielectric interface favors the initiation of PDs in the gas at the triple junction and is the main reason for a relatively lower dielectric strength of the spacers as compared to that of the gas gap alone.

Disc-profile spacers: Disc-profile spacers have their interfaces located symmetrically with a central plane. The interfaces have a dielectric cone angle equal to the optimal value α_c to produce a uniform distribution of the electric potential along the spacer interfaces. The lower tangential field along the spacer interfaces at the triple junction on the central conductor as compared to the radial field in the gas tends to inhibit the

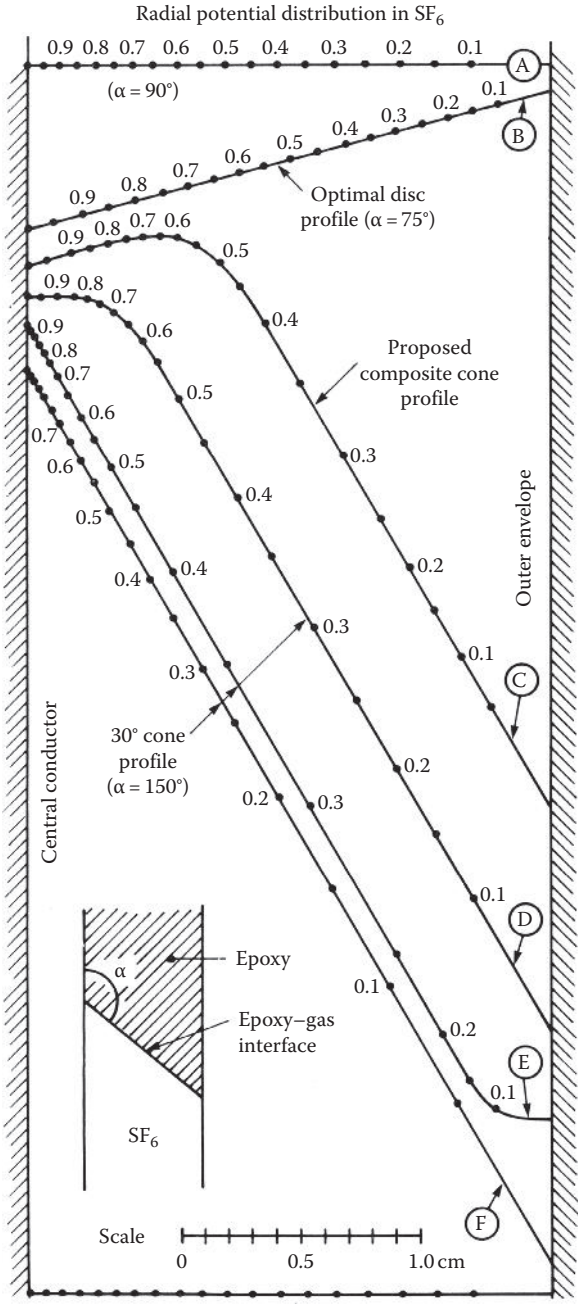


FIGURE 7.48 Distribution of the electric potential along the epoxy/SF_6 interface. (From Trinh, N.G. et al., *IEEE Trans. Power Appar. Syst.*, 99(6), 2164, November–December 1980.)

initiation of the PDs and thus improves the dielectric performance of the spacer. However, this design suffers of a high sensitivity to surface protrusions near the triple junctions, in particular at the central conductor, since a PD initiated from one of these protrusions develops easily into breakdown of the gas along the gas–dielectric interface, favored by the uniform distribution of the tangential electric field at the interface.

Cone-profile spacers: Cone-profile spacers have parallel interfaces that do not have the optimal dielectric cone angle but aim at providing a long interface as physically feasible. Pure cone-profile spacers, in spite

of their long leakage path, are not used in practice because of the nonuniform distribution of the potential along the gas–dielectric interfaces, which results in local concentrations of the electric fields near the triple junctions: close to the central conductor (lower interface) and at the envelope (upper interface). PDs are readily initiated at relatively low voltages and considerably affect the dielectric performance of the cone spacers.

Composite profile spacers: Composite-profile spacers combine the advantages of a uniform distribution of the electric potential in a disc profile with that of a long leakage path in a cone profile. Figure 7.49 illustrates such a composite-profile spacer: The disc sections close to the central conductor and the outer envelope ensure a uniform distribution of the tangential field close to the triple junctions, thus delaying the initiation of PDs from these triple junctions (curves C, D, and E). The cone section, on the other hand, provides a region of low tangential field to prevent the development of PDs along the gas–dielectric interface. Breakdown then preferably occurs across the gas gap and provides a spacer dielectric performance comparable to the gas gap itself.

The triple junction: Between the conductor, the gas, and the epoxy spacer constitutes a point ill-defined in term of the electric field, where PDs can be initiated and are susceptible to cause breakdown of the gas along the spacer interface (Trinh et al., 1980; Takuma and Kawamoto, 1984). Metal electrodes can be used to provide an electrostatic shield to triple junctions. They are either embedded within the spacer or incorporated in the modular design of the conductor and envelope, which, once assembled, serve as guard rings adjacent to the spacer. However, the latter approach tends to increase the overall dimensions of the cable.

Metal insert constitutes an elegant alternative to control the field at the triple junction since it does not modify the external shape and size of the spacer. It makes the molding process more delicate to avoid cracks and separation of the epoxy from the metal insert. The effect can be attenuated by a proper choice

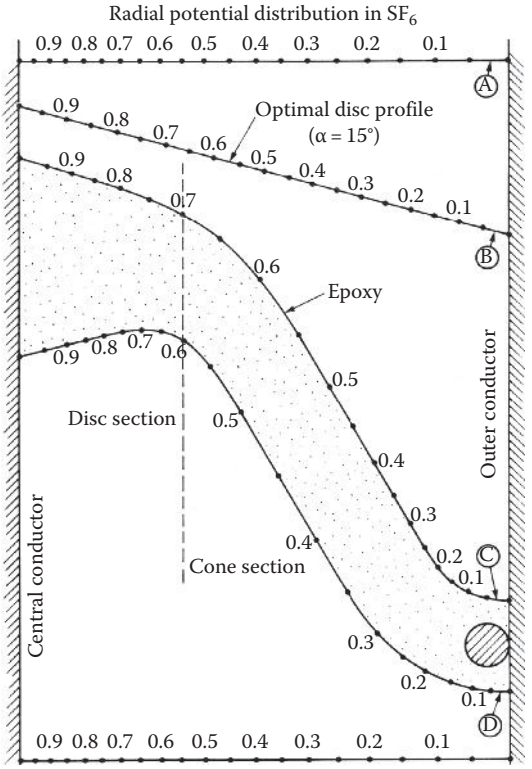


FIGURE 7.49 Disc and composite-profile spacers. (From Trinh, N.G. et al., *IEEE Trans. Power Appar. Syst*., 99(6), 2164, November–December 1980.)

of the *filler* such as silica and alumina and their relative proportion in the epoxy formulation. Increase in the filler provides a higher thermal conductivity to the epoxy and, consequently, reduces the thermal expansion coefficient of epoxy, bringing it closer to that of the metal insert. It also allows the cables to operate at higher temperatures, which are presently limited to about 100°C. However, epoxy formulations with a percentage of filler higher than 80% are difficult to prepare and to mold.

7.4.2.1 Initial Breakdown Strength

Figures 7.50 through 7.52 compare the dielectric performances under ac and impulse voltages obtained with different spacer designs with that of a 2.5/7 cm coaxial conductor without the spacer taken as reference. The following observations can be made:

- As expected, the cone shape spacer has the lowest ac dielectric performance, about 50% of the reference coaxial conductor without spacer.
- The disc-profile spacer performs better than the cone profile. Its ac dielectric performance is about 75% of the reference performance at 4 atm. abs.
- Best ac dielectric performances are obtained with the composite-profile spacer, which is within a few percent of the reference values.

  These results illustrate the efficiency of the composite profile in preventing the development of the breakdown to occur along the spacer interface, thus limiting the effect of the spacer on breakdown of the coaxial conductor to within a few percent of its ac performance.
- Under impulse voltages, both lightning and switching, the performances of both disc and composite profiles are relatively close to the reference values. This behavior may be attributed to the inability of the asperities at the triple junction to initiate PDs within the short duration of the impulse voltages.

7.4.2.2 Voltage–Time Breakdown Characteristics

Figures 7.53 and 7.54 compare the *V–t* characteristics of the coaxial gap without the spacer represented by solid line curves, with measured breakdown points in presence of an insulating spacer of disc and composite-profile cone spacers, which show promising dielectric performances (Trinh et al., 1988a). The following observations can be made:

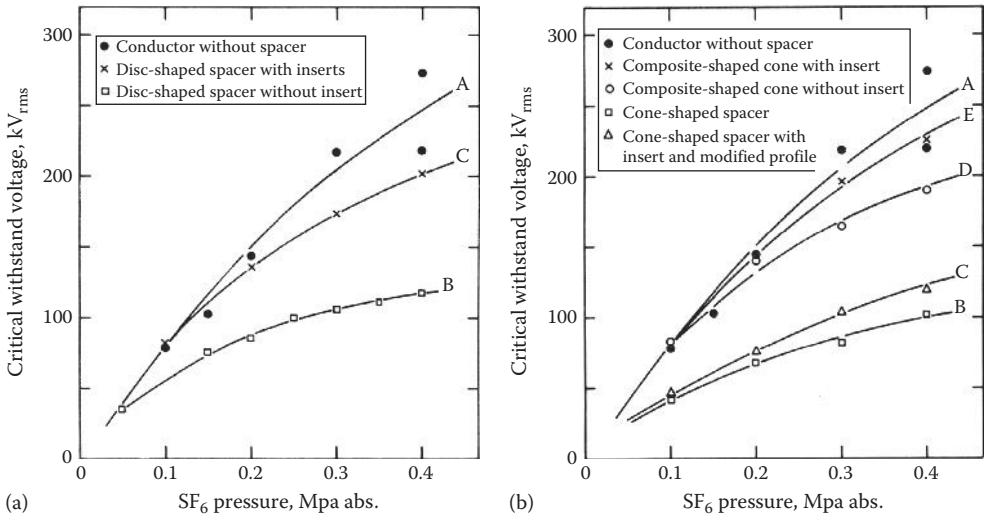


FIGURE 7.50 Dielectric performances under ac voltage of spacers of various profiles. (a) Disc-shaped spacers. (b) Composite profile cone- and cone-shaped spacers. (From Trinh, N.G. et al., *IEEE Trans. Power Appar. Syst.*, 99(6), 2164, November–December 1980.)

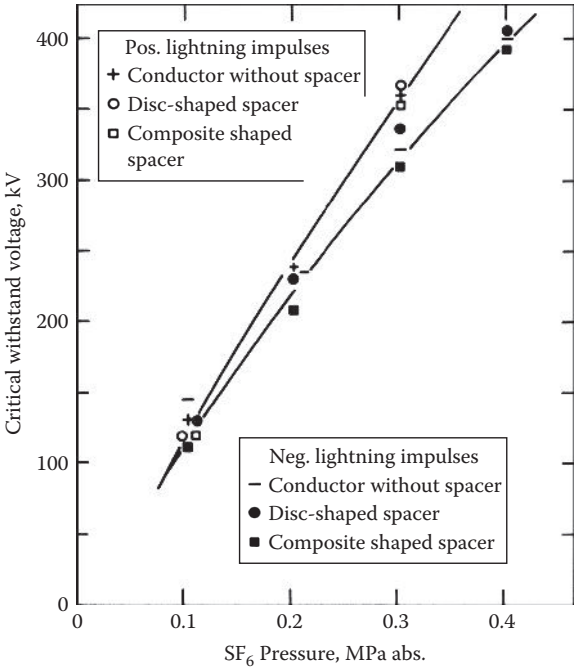


FIGURE 7.51 Dielectric performances under lightning impulses of spacers of disc and composite profiles. (From Trinh, N.G. et al., *IEEE Trans. Power Appar. Syst*., 99(6), 2164, November–December 1980.)

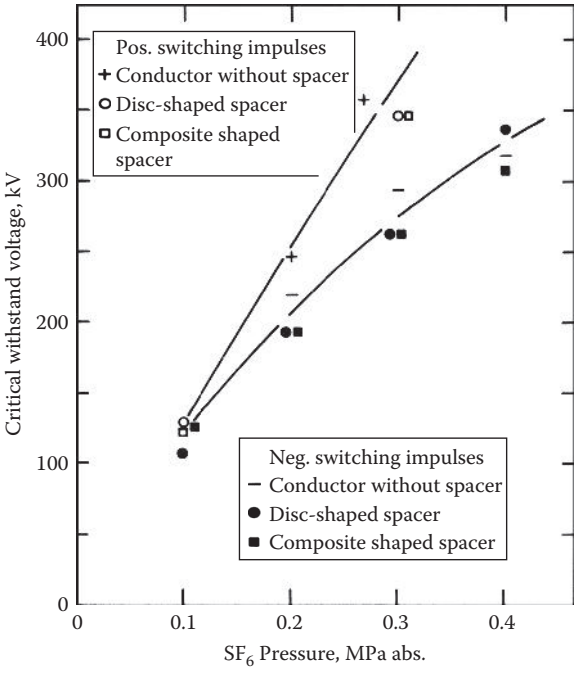


FIGURE 7.52 Dielectric performances under switching impulses of disc and composite profiles. (From Trinh, N.G. et al., *IEEE Trans. Power Appar. Syst*., 99(6), 2164, November–December 1980.)

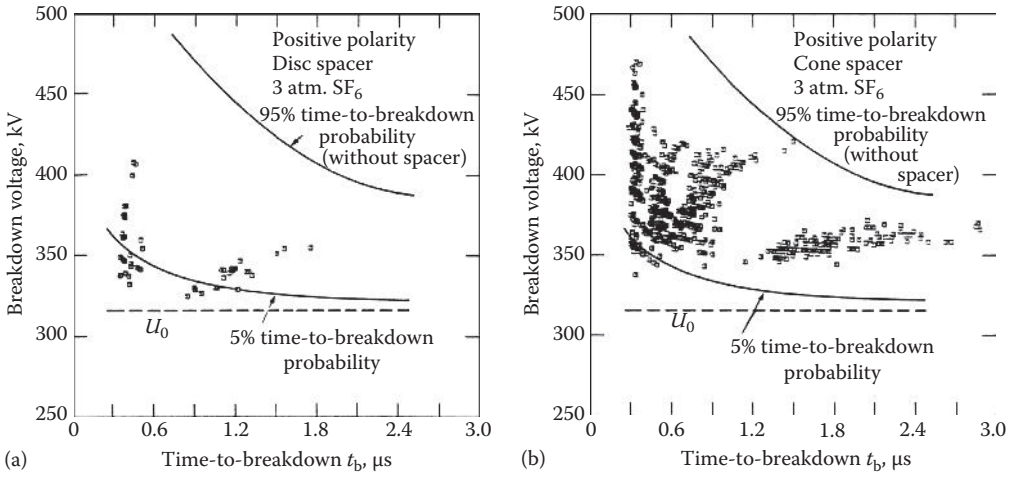


FIGURE 7.53 Positive polarity *V–t* characteristics in presence of an insulating spacer. (a) Disc-shaped spacers. (b) Composite profile cone-shaped spacers. (From Trinh, G.N. et al., *IEEE Trans. Power Deliv.*, 3(1), 16, January 1988a; Trinh, N.G. et al., *IEEE Trans. Power Deliv.*, 3(1), 26, January 1988b.)

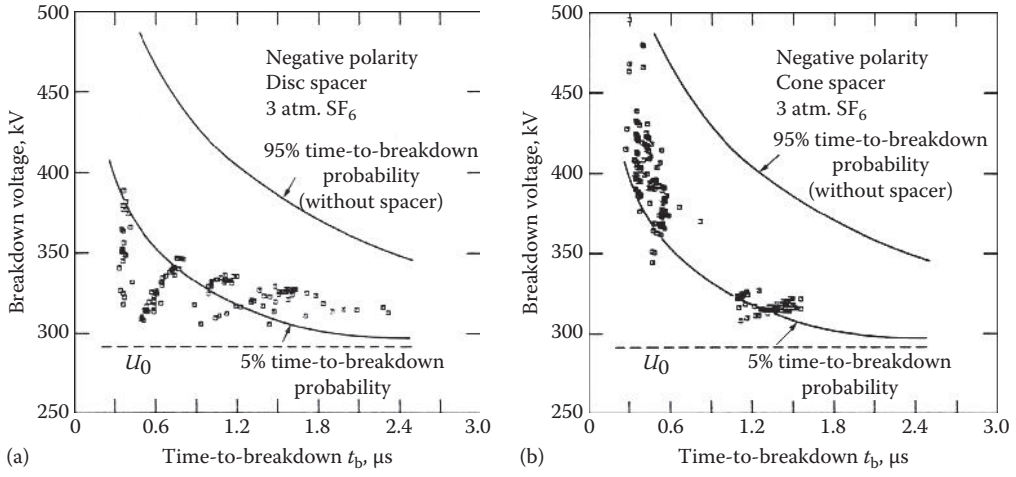


FIGURE 7.54 Negative polarity *V–t* characteristics in presence of an insulating spacer. (a) Disc-shaped spacers. (b) Composite profile cone-shaped spacers. (From Trinh, G.N. et al., *IEEE Trans. Power Deliv.*, 3(1), 16, January 1988a; Trinh, N.G. et al., *IEEE Trans. Power Deliv.*, 3(1), 26, January 1988b.)

- The presence of an insulating spacer can modify considerably the behavior of the insulation.
- A significant reduction of the withstand voltage is observed together with a smaller dispersion of the measured breakdown voltages and flattening of the *V–t* curves. The effect is more pronounced under positive polarity.
- The disc-shape spacer is less performing than the composite-profile spacer: most of the breakdown points fall below the 5% breakdown level of the coaxial conductor without spacer.
- The large majority of composite-profile cone spacer breakdown points fall within the 5% and 95% boundary curves of the coaxial conductor without spacer.

Such a dielectric performance of the composite-profile cone spacer may be attributed to its ability to force the breakdown to occur through the gas gap rather than along the spacer–gas interface as illustrated in Figure 7.55, which shows the breakdown marks left on the central conductor at the end of the

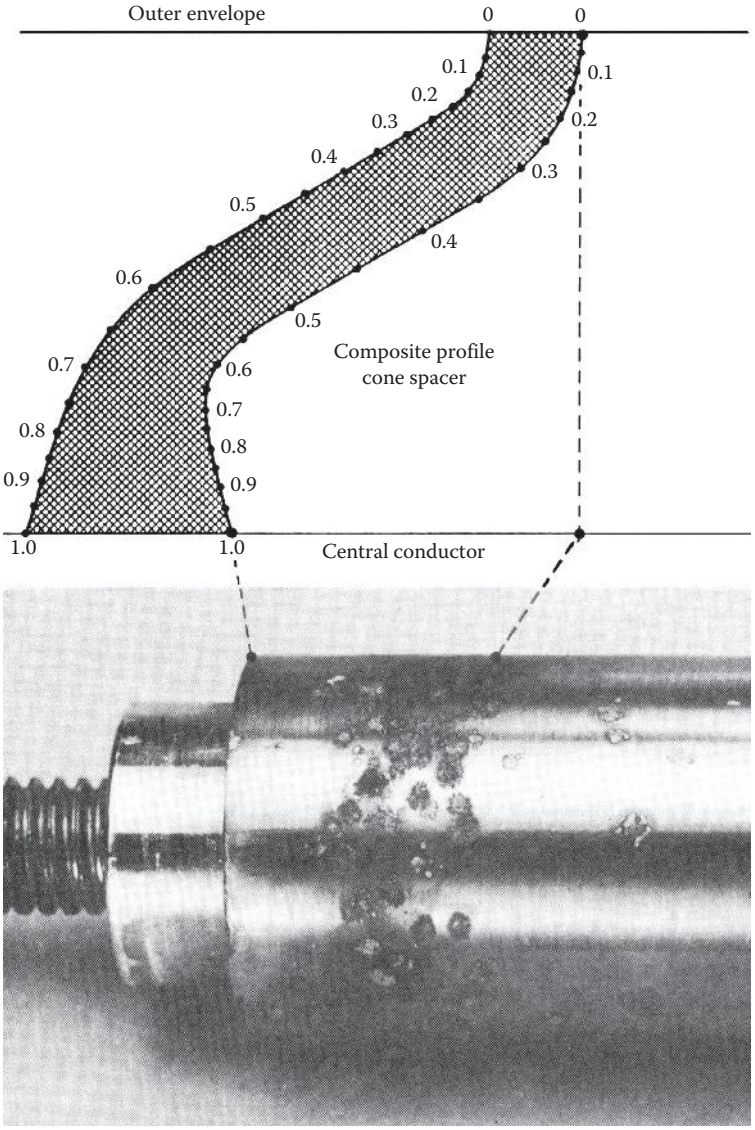


FIGURE 7.55 Breakdown marks left on the center conductor after the series of tests with composite-profile cone spacer. (From Trinh, G.N. et al., *IEEE Trans. Power Deliv.*, 3(1), 16, January 1988a; Trinh, N.G. et al., *IEEE Trans. Power Deliv.*, 3(1), 26, January 1988b.)

test series. It can be seen that while breakdowns were initiated from the triple junction at the envelope, they did not reach the triple junction on the central conductor. The lower tangential field along the center portion of the spacer profile has diverted the breakdown through the gas gap.

The slightly lower breakdown voltages of the composite-profile cone spacer may be attributed to the effect of the triple junction at the envelope, which triggered breakdown more easily compared to the case of coaxial conductor without spacer.

7.4.3 Factors Affecting SF_6–Epoxy Insulation

Several factors can affect the dielectric performance of the SF_6–epoxy insulation. They are discussed in the following.

Gas pressure: Gas pressure has a direct effect on the dielectric performance of the SF_6 insulation. In effect, from expression (7.25) of the effective ionization coefficient α' of SF_6, it can be seen that the ionization in the SF_6 stops when the local field becomes less than the limit field E_c, defined according to

$$E_c = p \left(\frac{E}{p}\right)_{cr} \tag{7.32}$$

An increase in the gas pressure raises the limit field proportionally. On the other hand, from corona onset conditions for a SF_6-insulated coaxial conductor, Equation 7.12, the critical distance r_c at which the initial electron avalanche stops can be evaluated. Figure 7.56 shows variations of r_c with the radius of the central conductor and for different gas pressures. It can be seen that r_c increases with the conductor radius but decreases with increasing pressure. Furthermore, the small absolute value of r_c implies that the avalanche development is sensitive to the increase of the local electric field due to the presence of a protrusion, a metal or dielectric particle. This behavior of the critical avalanche length r_c explains the high sensitivity of gas insulation to the finish conditions of the electrode and the cleanliness required for the installation of the gas-insulated equipment, especially under high pressure of the gas as explained in the following.

Electrode surface conditions: Many authors have investigated the effect of surface condition on the breakdown voltage of a SF_6 gap. The results show that the surface of practical electrodes contains protrusions of diverse shapes and sizes (Figure 7.57), typically in the order of 25–100 μm (Berger, 1976).

Protrusions at the electrode surface can statistically reduce the dielectric performance of the SF_6 gap. The effect is explained by the increase in the local electric field, which favors early development of electron avalanches and initiation of the breakdown process. Figure 7.58 illustrates the reduction of the limit field E_c as a function of the product $p \cdot h$, with p being the gas pressure (in bar) and h the maximal height of the protrusion (in μm). The surface roughness can reduce the limit field up to 30% of its nominal value. Careful control of the surface finish of the electrodes is necessary to minimize the deterioration of the

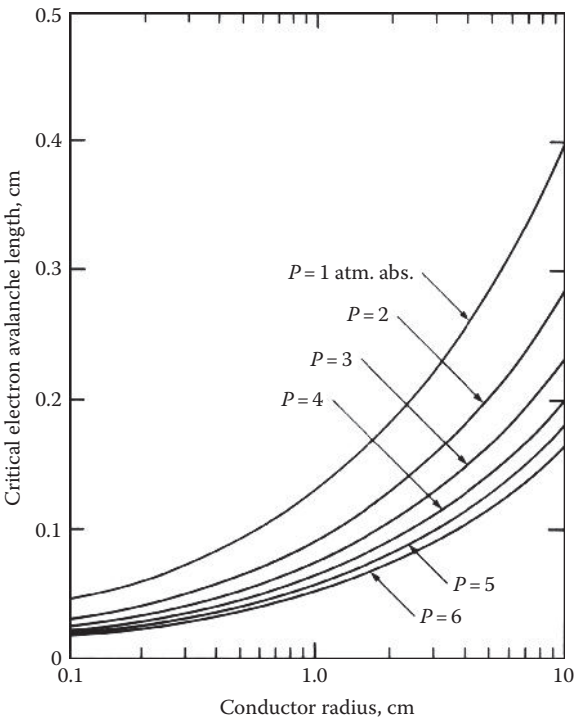


FIGURE 7.56 Variations of the avalanche length in a coaxial cable as a function of the gas pressure. (From Trinh, N.G. and Vincent, C., *IEEE Trans. Power Appar. Syst*., 97(6), 2198, November–December 1978.)

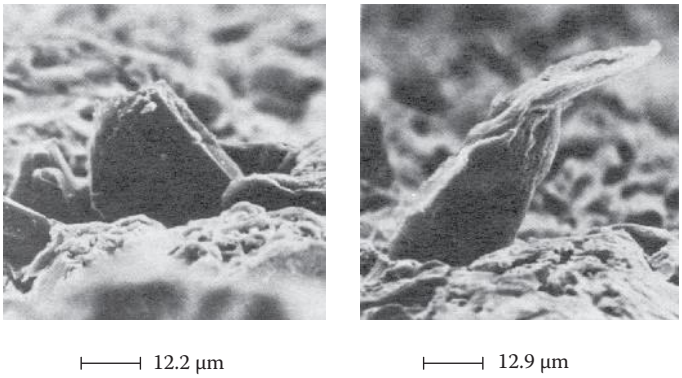


FIGURE 7.57 Examples of surface roughness observed on electrodes of metal-clad equipment. (From Berger, S., *IEEE Trans. Power Appar. Syst*., 95(4), 1073, July/August 1976.)

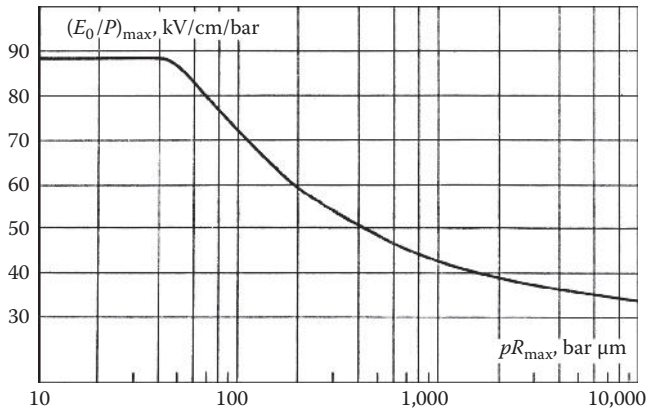


FIGURE 7.58 Effect of the surface roughness on the limit field. (From Pedersen, A., The effect of surface roughness on breakdown in SF_6, *IEEE Trans., Vol. PAS-94*, No. 5, 1749, 1975.)

dielectric performance of gas-insulated equipment. A surface roughness factor k of 0.6 is representative of the surface conditions of most practical surfaces (Pedersen, 1975).

Particle contamination: The presence of solid contaminants in gas-insulated equipment is generally accepted as unavoidable, and its effect is recognized as detrimental to the dielectric performances of the SF_6 insulation. In presence of an electric field, metallic particles get charged and can be lifted from the envelope. The movement of a particle of simple geometry can be predicted from basic differential equations (Cookson and Farish, 1973). The height reached by the particle during its displacement can constitute a significant portion of the interelectrode distance, depending on its dimensions and the applied voltage.

Solid particles are introduced in gas insulation during on-site installation. Metallic particles are also generated by frictions between conductors, during their expansion and contraction in load cycles. Vibrations associated with operations of circuit breakers also release particles from their natural traps to contaminate the main gas insulation with detrimental effect on its dielectric performances.

Under ac voltage, variation of the electric field attracts and pushes the particles from the central conductor, lifting the particles to considerable heights, depending on the time it remains hovering in the gas (Figure 7.59). The final effect is that the particles are gradually displaced to areas of low electric fields, where they remain trapped. Movement of particles in the interelectrode space is particularly detrimental to gaseous insulation. In short gaps, the simple fact that the conducting particle short-circuits partially the gas gap can substantially reduce the breakdown voltage. In long gaps, when the particle approaches the central conductor, the field enhancement at the particle can exceed the limit field and initiate electron avalanches. Streamers were observed crossing the distance separating the particle in motion and the

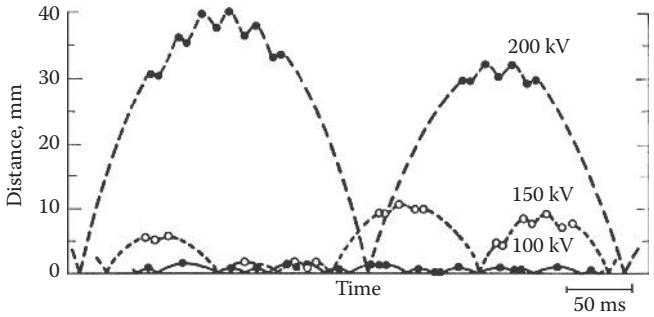


FIGURE 7.59 Movement of particles in a SF_6-insulated gap. (From Cookson, A.H. and Farish, O., *IEEE Trans. Power Appar. Syst*., 92, 871, 1973.)

high-voltage electrode, before bridging the entire gas gap, and cause its breakdown (Rizk et al., 1979; Anis and Srivastava, 1982). Because of the random nature of the particle movement in the interelectrode space, the particle-initiated breakdown voltage varies considerably under the same test conditions (Cookson and Farish, 1973). The results of Figure 7.60 illustrate the effect of solid particle contamination on the dielectric withstand of a coaxial gap, reducing it to 30% of its nominal value (without solid particle contamination).

The effect of a particle deposed on the insulator/gas interface varies with its relative position with respect to the stressed electrode and is more pronounced when the particle is located close to the central conductor. Breakdown is then initiated by a streamer discharge between the particle and the conductor, before it crosses the gap and causes its breakdown, usually along the surface of the spacer.

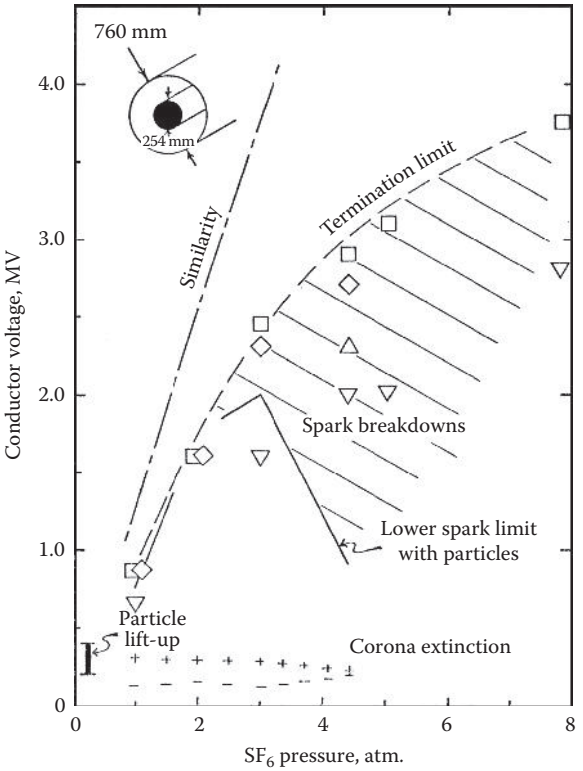


FIGURE 7.60 Effect of particle contamination on the breakdown voltage of a coaxial gap. (From Cooke, C.M. and Velasquez, R., *IEEE Trans. Power Appar. Syst*., 96(5), 1491, 1977.)

The behavior of SF_6 insulation in presence of particle contamination requires severe quality control, which must be ensured during manufacturing and installation to minimize the amount of particles left behind in the equipment. It induces changes in the design of gas-insulated equipment: specifically designed covers are installed around sliding contacts to collect particles detached during cyclic expansion and contraction of the contacts. Since particles are naturally deposited on horizontal surfaces, such a position for insulating spacers should be avoided whenever possible in gas-insulated equipment. Finally, special test procedures developed to condition the equipment have become part of their commissioning tests: voltage is raised in steps, of durations varying from 30 min to 1 h, to displace the particles to natural or specifically designed traps, neutralizing their effect in the local near-zero electric field within the traps.

Humidity: Moisture is introduced in gas-insulated equipment during their manufacture and on-site installation. Often, moisture is absorbed in polymer insulation of the supporting structure, which can absorb a significant amount of moisture. During operation, an equilibrium state will be established between the gas and polymer, which causes a seasonal variation of humidity (Chu and Braun, 1989).

Figure 7.61 (Schmidt and Szente, 1974) illustrates the effect of humidity on the dielectric withstand of SF_6 insulation. It is noticed that the dielectric withstand of gaseous insulation is only slightly influenced by humidity. Dielectric withstand, however, is reduced considerably by the presence of an insulating spacer (curve 3) and, in particular, the presence of water condensation on its surface. In this case, dielectric withstand is reduced to 50% of the withstand value of the gas at 70% relative humidity. The effect is, however, limited to temperatures above zero when the condensation results in liquid water.

Accumulation of electrostatic charges: One of the problems specific to insulating spacer is the possibility of accumulating electrostatic charges at their surface by migration of charges, either across the bulk of the dielectric spacer or across the gas. The absence of a conducting path to evacuate the deposed charges causes their gradual accumulation at the gas/spacer interface. The accumulated charges gradually modify the electric field distribution at the spacer–gas interface, which may eventually initiate a streamer discharge along the interface, resulting in the breakdown of the spacer. The exact mechanism of failure by accumulation of electrostatic charges is still not fully understood. However, accumulation of electrostatic charges appears to be the cause of breakdowns occurring at very low voltages (below its critical withstand voltage), which are observed when an insulating spacer is repeatedly subjected to breakdown under impulse voltages (Trinh et al. 1988a,b). Electrostatic charge accumulation is also suspected to be

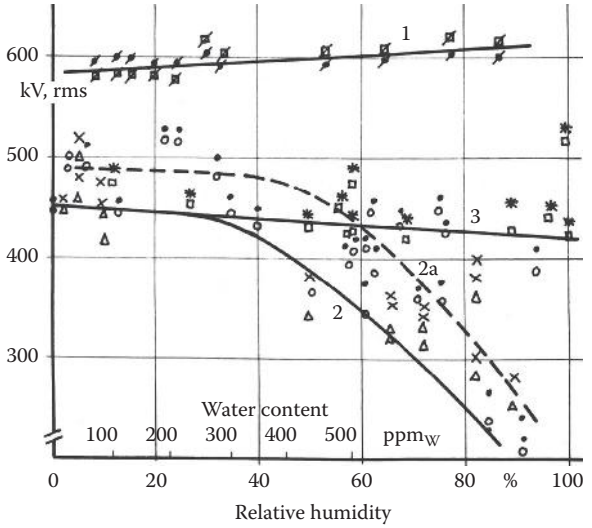


FIGURE 7.61 Influence of humidity on the dielectric withstand of SF_6 insulation. 1—Average 1 min withstand and breakdown without insulator; 2—withstand with insulator; 2a—average breakdown with insulator at temperatures above freezing point; and 3—average breakdown with insulator at temperature below freezing point. (From Schmidt, W. and Szente, V., Effect of humidity on the electrical strength of SF_6 gas-insulated H. V. equipment, in: *IEEE Canadian Conference on Power & Communication*, Montreal, Canada, 1974, pp. 241–242.)

the cause of certain spacer failures occurring under operating service voltage. The explanation in this case assumes the possibility that charges, generated by steady PDs developing at protrusions close to the spacer, are deposed on the spacer and their accumulation eventually causes the failure of the spacer.

REFERENCES

Anis, H. and K.D. Srivastava. Nonuniform field breakdown of SF6 insulation under combined AC and switching impulse voltages. *IEEE Transactions on Power Apparatus and Systems*PAS-101: 537–546, September 1982.

Barlow, A. The chemistry of polyethylene insulation. *IEEE Electrical Insulation Magazine* 7: 8–19, 1991.

Bartnikas, R. and K.D. Srivastava. *Elements of Cable Engineering*. Standford Education Press, 1980.

Bouvier, B. Papier et Papier imprégné. *Techniques de l'ingénieur*, D-280, pp. 1–26, 1977.

Berger, S. Onset or breakdown voltage reduction by electrode surface roughness in air and *SF6. IEEE Transactions on Power Apparatus and Systems* PAS-95(4): 1073–1079, July/August 1976.

Bouvier, B. Papier et Papier imprégné. *Techniques de l'ingénieur* D-280: 1–26, 1977.

Chu, F.Y. and J.M. Braun. Assessment of moisture in gas-insulated substations. Final report to the CEA, No. 217-T-434, 1989.

Church, H.F. Thermal breakdown, chemical and electrochemical deterioration. In: L.L. Alston (ed.), *High Voltage Technology*. Oxford, U.K.: Oxford University Press, 1968, Chapter 10.

Cooke, C.M. and R. Velasquez. The insulation of ultra high voltage in coaxial systems using compressed SF6 gas. *IEEE Transactions on Power Apparatus and Systems* PAS-96(5): 1491–1497, 1977.

Cookson, A.H. and O. Farish. Effect of conducting particles on AC corona and breakdown in compressed SF6. *IEEE Transactions on Power Apparatus and Systems*PAS-91: 1329–1338, 1972.

Cookson, A.H. and O. Farish. Particle-initiated breakdown between coaxial electrodes in compressed SF6. *IEEE Transactions on Power Apparatus and Systems*PAS-92: 871–876, 1973.

Cygan, P. and Laghari, J.R. Models for insulation aging under electrical and thermal multistress. *IEEE Transactions* EI-25(5): 923–934, October 1990.

Cookson, A. Gas-insulated cables. *IEEE Transactions* EI-20(5): 859–890, October 1985.

Couderc, D. Revue de l'état des recherches des câbles de transport à très haute tension de courant alternative et continu. IREQ report, November 1987.

Day, A.G. Tracking and breakdown of solids due to discharges. In: L.L. Alston (ed.), *High Voltage Technology*. Oxford, U.K.: Oxford University Press, 1968, Chapter 9.

Fukuda, T. Technological progress in high-voltage XLPE power cables in Japan—Part I. *Electrical Insulation Magazine* 4(5): 9–16, September/October 1988a.

Fukuda, T. Technological progress in high-voltage XLPE power cables in Japan—Part II. *Electrical Insulation Magazine* 4(6): 15–20, November/December 1988b.

Garton, C.G. Intrinsic and related forms of breakdown in solids. In: L.L. Alston (ed.), *High Voltage Technology*. Oxford, U.K.: Oxford University Press, 1968, Chapter 8.

Giesselmann, M. and W. Pfeiffer. Influence of solid dielectrics upon break-down voltage and predischarge development in compressed gases. *Gaseous Dielectrics IV*, pp. 431–436, 1984.

Greenfield, W.E. *Paper Cable Taping Patterns*. Washington State Institute of Technology, Bulletin 268, Power Technologies Inc., 1963.

Gazzana Priaroggia, P. et al. *Fundamentals of the Theory of Paper Lapping of a Single Core HV Cable*. Milan, Italy: Pirelli S.p.a., 1961.

Hata, R. et al. Properties of polypropylene laminated paper and study of applicability of PPLP insulated self-contained oil cable to EHV and UHV underground transmission line, IEEE paper No. CH2115-4/85, pp. 725–728, 1985.

Kaneko, R. and Sugiyama, K. Statistical considerations on impulse breakdown characteristics of cross-linked polyethylene-insulated cables. *IEEE Transaction*s PAS-94: 367–377, March/April 1975.

Knorr, W. Der Zundversug Schwach Inhomogener Elektrodenanordnungen in SF6, PhD thesis, University of Aachen, Aachen, Germany, 1979.

Lanfranconi, G.M. and B. Vecellio. Câbles à huile ininflammable, Rapport CIGRE No. 21-11, Paris, France, 1986.

Lawson, W.G. Effects of temperature and techniques of measurement of the intrinsic electric strength of polyethylene. *IEE Proceedings* 113: 197, 1966.

Miranda, F.J. et al. Self-contained oil-filled cables—A review of progress. *Proceeding of the IEE* 123(3): 229–238, March 1976.

Mitsui, H., Yoshida, K., Inoue, Y., and Kawahara, K. Mechanical degradation of high voltage rotating machine insulation. *IEEE Transactions* EI-16(4): 351–359, August 1981.

Montanari, G.C., Pattini, P., and Simoni, L. Voltage endurance of XLPE insulated cable models. In: *IEEE International Symposium on Electrical Insulation*, Montreal, Québec, Canada, 1984, pp. 54–57.

Occhini, E. et al. High Voltage Transmission Systems at 750 and 1100 kV with Oil-filled Cables – Construction and Tests. CIGRE 21-08; 1978.

Parr, D. and Scarisbrick, R.M. Performance of synthetic insulation materials under polluted conditions. *IEE Proceedings* 112: 1625–1632, 1965.

Pedersen, A. The effect of surface roughness on breakdown in *SF6. IEEE Transactions on Power Apparatus and Systems* PAS-94(5): 1749–1754, September–October 1975.

Pedersen, A. The effect of surface roughness on breakdown in SF6. *IEEE Transactions* PAS-94(5): 1749–1754, September–October 1975.

Rizk, F.A.M. and M.B. Eteiba. Impulse breakdown voltage time curves of *SF6* and *SF6*-N2 coaxial cylinder gaps. *IEEE Transactions on Power Apparatus and Systems*PAS-101: 4460–4471, 1982.

Rizk, F.A.M., Masetti, C., and R.P. Comsa. Particle initiated breakdown in SF6-insulated system under high direct voltage. *IEEE Transactions on Power Apparatus and Systems*PAS-98: 825–836, May/June 1979.

Rosen, L.S. *Fundamental Principles of Polymeric Materials*. New York: Book, Barnes & Noble, 1971.

Russek, R.M. Drying and impregnation of paper-insulated power cables. *IEEE Transactions on Power Apparatus and Systems* PAS-86(1): 34–48, January. 1967.

Schmidt, W. and V. Szente. Effect of humidity on the electrical strength of SF6 gas-insulated H. V. equipment. In: *IEEE Canadian Conference on Power & Communication*, Montreal, Canada, 1974, pp. 241–242.

Takuma, T. and T. Kawamoto. Field intensification near various points of contact with a zero contact angle between a solid dielectric and an electrode. *IEEE Transactions on Power Apparatus and Systems* PAS-104: 2486–2494, 1984.

Tobolsky, A. and H. Eyring. Mechanical properties of polymeric materials. *Journal of Chemical Physics* 11: 125–134, 1943.

Trinh, G.N., Mitchel, G., and C. Vincent. Influence of an insulating spacer on the V-t characteristics of a coaxial gas-insulated cable—Part I: Study on a reduced-scale coaxial conductor. *IEEE Transactions on Power Delivery* PWRD-3(1): 16–25, January 1988a.

Trinh, N.G., Mitchel, G., and Vincent, C. Influence of an insulating spacer on the V-t characteristics of a coaxial gas-insulated cable, Part I—Study on a reduced-scale coaxial-conductor. *IEEE Transactions* PWRD-3(1): 16–25, January 1988a.

Trinh, N.G., Rizk, F.A.M., and C. Vincent. Electrostatic-field optimization of the profile of epoxy spacers for compressed *SF6*-insulated cables. *IEEE Transactions on Power Apparatus and Systems* PAS-99(6), 2164–2174, November–December 1980.

Trinh, N.G. and C. Vincent. Bundled-conductors for EHV transmission systems with compressed SF6 insulation. *IEEE Transactions on Power Apparatus and Systems* PAS-97(6): 2198–2206, November–December 1978.

Trinh, N.G., Vincent, C., and G. Mitchel. Influence of an insulating spacer on the V-t characteristics of a coaxial gas-insulated cable—Part II; Tests on EHV buses. *IEEE Transactions on Power Delivery* PWRD-3(1): 26–34, January 1988b.

Trinh, N.G., Vincent, C. and Mitchel, G. Influence of an insulating spacer on the V-t characteristics of a coaxial gas-insulated cable, Part II—Test on EHV buses. *IEEE Transactions* PWRD-3(1): 26–34, January 1988b.

Von Hippel, A. A mechanism of electric breakdown in solid insulators. Part I. *Zeitschrift für Physik* 67: 707, 1931.

Von Hippel, A. A mechanism of electric breakdown in solid insulators. Part II. *Zeitschrift für Physik* 68: 309, 1931.

Von Hippel, A. Electrical breakdown of alkali halides. *Zeitschrift für Physik* 88: 358, 1934.

Von Hippel, A. Electrical breakdown in solid insulators. *Ergebn. Exakt. Naturw*. 14: 79, 1935.

Umemura, T. and D. Couderc. Morphology and electrical properties of polypropylene films. *IEEE Transactions on Electrical Insulation*EI-21(2): 137–144, April 1986.

Zurkov, S.N. Kinetic concept of the strength of solids. *International Journal of Fracture* 1: 311–323, 1965.

Zurkov, S.N. and Korsukov, V.E. Atomic mechanisms of fracture of solid polymers. *Journal of Polymer Science, Polymer Physics Edition* 12: 385–398, 1974.

Zurkov, S.N. and Kuksenko, V.S. The micromechanics of polymer fracture. *International Journal of Fracture* 11: 629–639, 1975.

8

Selection of Overhead Transmission Line Conductors

8.1 Development of Overhead Lines

Since the introduction of the first overhead line in the end of the nineteenth century, the development of overhead power transmission lines has been a continuous process. Although both approaches of ac and dc power transmission were considered at the start, the former has rapidly gained its predominance. Favored by the flexibility of power transformers in modulating the power supply to the local needs and the favorable conditions for the development of current interrupting apparatus, ac transmission system has reached the level of 200–300 kV and extended over distances of several hundred of kilometers during the first part of the twentieth century.

Modern electric power systems often have generating stations located far away from the consumption centers, with long overhead transmission lines to transmit the energy from the generating sites to the load centers. From the few tens of kilovolts in the early years of the twentieth century, the line voltage has reached 400 kV in Europe and 500 kV in North America in the 1950s. It reached the EHV levels of 800 kV ac in the late 1960s with Hydro-Québec's 735 kV and AEP's 765 kV transmission systems and touched the ultrahigh-voltage (UHV) levels of 1200 kV ac in the former USSR, by the end of the twentieth century (Bortnik et al., 1988).

On the other hand, being frequency-independent, dc power transmission does not require compensation for inductive loads. However, it depends heavily on the development of converter technology and lacks the flexibility provided by power transformers and circuit interrupting devices. As a result, it is mainly used for point-to-point transmission of bulk power between the generating station and the consumption centers. Early dc transmission system relied on mercury arc valves: in Sweden, United States with BPA's 500 kV dc system, and Canada with Manitoba's 450 kV dc system. With the development of thyristor valves in the 1970s, dc power transmission has gained wide interest, reaching 500 kV dc level with multiterminals, Hydro-Québec 450 kV dc lines, and touched the 600 kV dc (Krishnayya et al., 1988). Finally, it has to be mentioned the many dc projects of back-to-back converter stations with no overhead lines provide means for energy transfer between neighboring systems.

Although overhead lines operating at high voltages are the most economical means of transmitting large amounts of energy over long distances, their exposure to atmospheric conditions alters the surface conditions of the conductors, reducing the dielectric withstand of the insulator strings, and causes large variations in the corona activities on the line conductors. These factors are determining in the design of line tower and the selection of line conductors, which have to ensure an adequate power transmission capability while minimizing their environmental impact, namely, with respect to electric and magnetic fields and corona effect. Electrical performance of conductors is the subject of the present chapter, while transmission line insulators are dealt with in Chapter 10.

8.1.1 AC Power Transmission Lines

A number of parameters characterize ac power transmission lines, relating their physical dimension to electrical parameters, which, for reason of simplicity, are derived for the case of a single-phase line:

The capacitance and inductance per unit conductor length are given by

$$C = \frac{2\pi\varepsilon}{\ln\left(2h/a\right)} \quad \text{F/m} \tag{8.1}$$

$$L = \frac{1}{c^2 C} \quad \text{H/m} \tag{8.2}$$

Characteristic impedance, Z_0, is determined as:

$$Z_0 = \sqrt{\frac{L}{C}} \tag{8.3}$$

Surge impedance loading, P_n:

$$P_n = \frac{U_n{}^2}{Z_0} \tag{8.4}$$

Nominal current, I_n:

$$I_n = \frac{P_n}{U_n} = \frac{U_n}{Z_0} \tag{8.5}$$

Critical length, L_c:

$$L_c = \frac{1}{f\sqrt{LC}} \tag{8.6}$$

where
- a is the conductor radius
- c is the speed of light
- h is the average conductor height
- ε is the permeability
- μ is the susceptibility in air
- f is the frequency of the ac voltage

To increase the natural transmission capability of the line, it is necessary to either increase the line voltage U_n, which is system dependent, or reduce the characteristic impedance, which is dependent on the conductor bundle design. In practice, both these actions are linked together.

8.1.2 Bundle Conductor to Improve the Natural Transmission Capability of AC Lines

The development of HV transmission lines as we know today is largely related to the concept of the bundle conductor introduced at the beginning of the twentieth century. In effect, the single-conductor design, which was adequate up to the voltage level of 300 kV, starts to show shortcomings as the line voltage is increased further to meet the need of higher natural power transmission capabilities. Increasing the line voltage is the best way to increase the power transmission capability. This also increases the surface gradient at the conductor, which must be kept below the corona onset levels for the line to operate properly.

With single conductors, the only way to control the surface gradient is to increase its diameter, which becomes rapidly a limiting factor. Several attempts were made to increase the size of the line conductor and, hence, reduce the characteristic impedance. A breakthrough was made in 1909 with the

TABLE 8.1

Comparison of Performances between Single and Bundle Conductors

Parameters	Units	400 kV	735 kV	1 100 kV
Number of subconductors		2	4	8
Diameter of the bundle	cm	45	65	84
Diameter of the conductor	cm	3.2	3.05	3.2
Maximum gradient	kV_{rms}/cm	16.3	19.79	17.3
Corona onset gradient	kV_{rms}/cm	22.32	22.04	22.32
Characteristic impedance	Ohm	311	268	246
Surge impedance loading	GW	0.5	2.0	4.9
Phase distance	m	12	13.7	17
Single conductor to meet the transmission capability of bundle conductor				
Diameter of the conductor	cm	8.5	22	64
Simple conductor to meet the maximum gradient of the bundle conductor				
Diameter of the conductor	cm	4.7	8.5	13.8

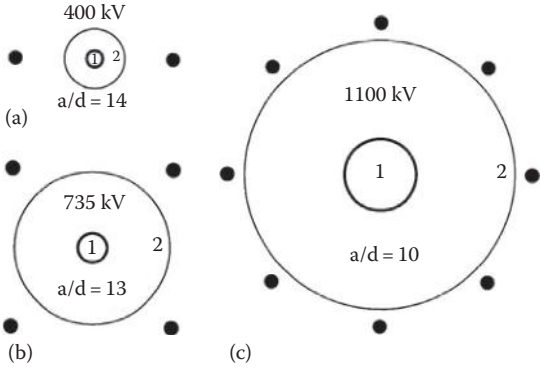
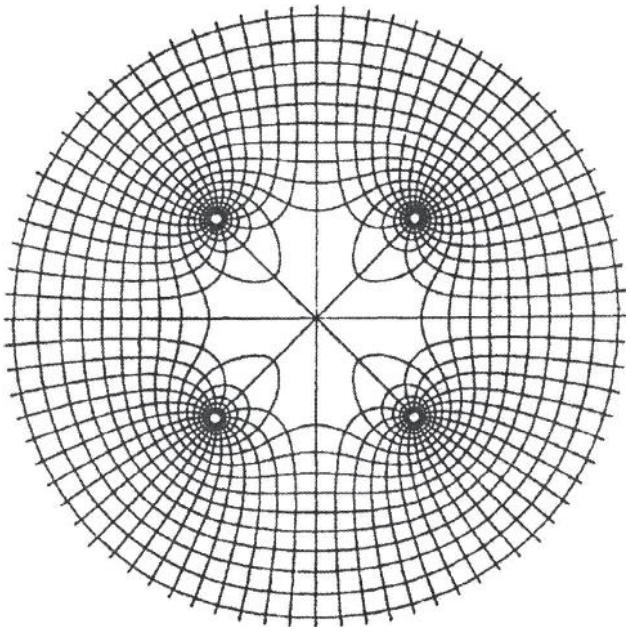


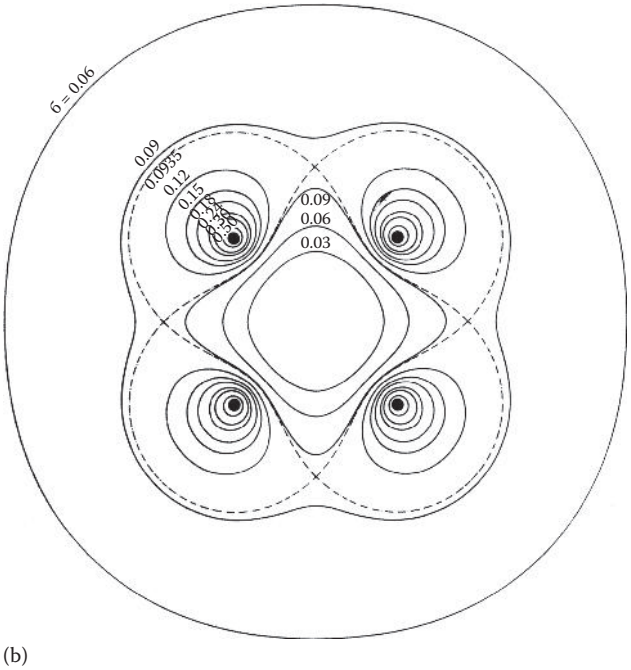
FIGURE 8.1 Comparison of single and bundle conductors for EHV and UHV lines. (1) Single conductor having same maximum gradient; (2) single conductor having same natural power transmission capability; *a* and *d* are, respectively, the subconductor spacing and diameter. (a) 2-Conductor bundle for 400 kV line. (b) 4-Conductor bundle for 735 kV line. (c) 8-Conductor bundle for 1100 kV line.

introduction of the concept of bundle conductor by P.H. Thomas (Thomas, 1909), which consists of *n* parallel subconductors placed around a large circumference to form the bundle conductor. Such a bundle effectively increases the conductor size without significantly changing the physical dimensions of the subconductors, which are determined in accordance with the current carrying capacity of the line. Bundle conductor was quickly found to be also effective in controlling the surface gradient at the conductors (Whitehead, 1910) and, hence, the line corona activities.

The results shown in Table 8.1 and Figure 8.1 compare the required dimensions of single conductors to match the performances obtained with bundle conductors: with respect to either the power transmission capability or the surface gradient. It is obvious that at such voltages and power levels, single conductors become completely impractical. The bundle conductors are however particularly effective in increasing the power transmission capability, which can be directly associated with the potential and field distribution around the bundle conductor, which approach those of a single conductor of diameter comparable to the bundle dimension, as shown in Figure 8.2 for the case of a four-conductor bundle.



(a)



(b)

FIGURE 8.2 Distribution of potential and field around a four-conductor bundle: (a) equipotential and lines of force; (b) equigradient surfaces. (From Tismascheff, A., Field patterns of bundle conductors and their electrostatic properties, *AIEE Trans*., 80, 590, 1961; Timascheff, A., Equigradient lines in the vicinity of bundle conductors, *AIEE Trans*, 82, 104, 1963.)

8.1.3 Electrostatic Field Optimization of Conductor Bundle

The characteristic parameters of bundle conductors are the bundle diameter, number, and diameter of subconductors. They all affect the surface gradient at the subconductors and the natural power transmission capacity of the line. Figure 8.3 shows variations of the natural power transmission capacity of

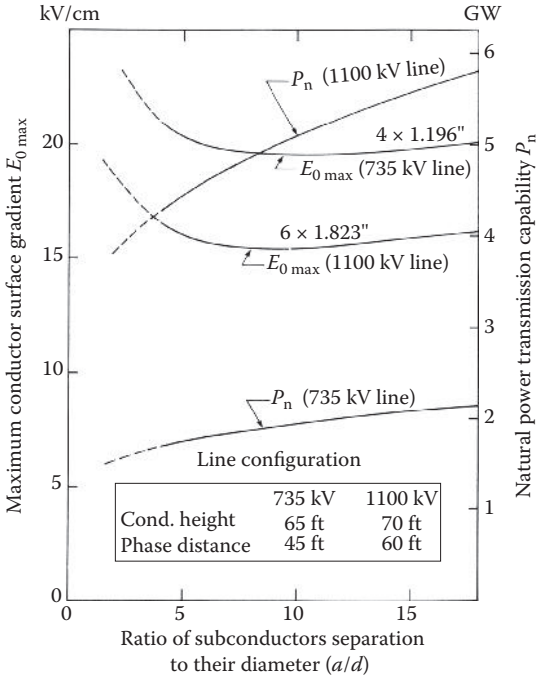


FIGURE 8.3 Variations of the maximum subconductor field with the ratio *a*/*d*.

the line, P_n, and maximal electric field at the subconductor surface, E_0, as a function of the ratio *a*/*d* of the subconductor spacing a to their diameter *d*, evaluated for two conductor bundles considered for the 735 and 1100 kV lines, respectively. It can be seen that

- Although the natural power transmission capacity of HV line is primarily a dependent on the line voltage, it is also affected by the actual bundle configuration. For the range of *a*/*d* between 5 and 20, the natural power transmission capacity varies almost linearly with the ratio *a*/*d*, which has a direct influence on the bundle diameter and, hence, the capacitance of the line conductor.
- At small values of *a*/*d*, the maximal electric field at the surface of the subconductor approaches the field at a single conductor of diameter *nd*, *n* being the number of subconductors in the bundle, obtained when the subconductors touch one another. With increasing values of the ratio *a*/*d*, the surface field decreases and passes by a minimum before it increases again, approaching the field at a single subconductor.
- The range of *a*/*d* values around the minimum field is reasonably large. As a result, there is no need to match the actual size of the bundle conductor to fit the optimal ratio. Most bundle conductors use an *a*/*d* ratio between 10 and 15 to favor a higher natural power transmission capacity for the line and improve wake-induced subconductor vibrations at the cost of a marginally higher value for the maximal field intensity at the subconductor surface.

The design of HV lines implies the dimensioning of the tower, the average height of the phase conductor bundles and their configuration, in order to ensure a continuous and reliable operation of the line with minimal impact on the environment. Referring to Figure 8.4 showing a schematic drawing of a 735 kV tower, two key parameters are involved in its dimensioning, namely, the clearance distances and the average height of line conductors, respectively, for its basic width and height. The final dimensions of the tower are also affected by the length of the insulator chains, the height of the ground wires, and, to some extent, the dimension of the conductor bundles. The latter are, on the other hand, selected mainly with respect to their corona performances in fair- and foul-weather conditions.

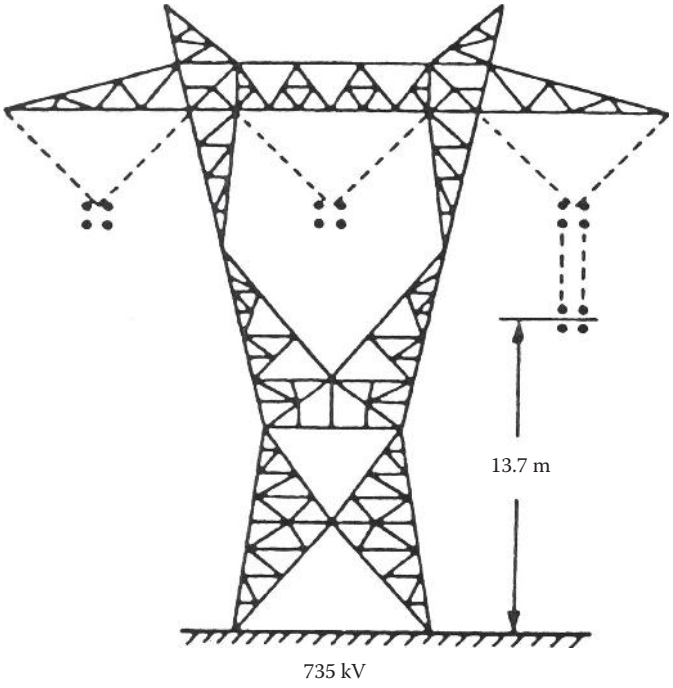


FIGURE 8.4 735 kV line tower.

The current approach to the design of HV lines aims at dimensioning the line with regard to the following aspects:

- The phase-to-ground and phase-to-phase insulation distances treated in Chapter 13
- The selection of the insulators, treated in Chapter 10
- The protection of the line against lightning, treated in Chapter 9
- The average height of the line conductors to ensure an acceptable level of the electric and magnetic fields in the immediate vicinity of the line
- The selection of the conductor bundles to minimize the environmental impacts: the energy losses, the radio interference (RI), and the audible noise (AN), produced by corona discharges

Only the last two aspects will be discussed in this chapter.

8.2 Average Height of Conductors

Since the 1980s, a novel aspect has been considered in designing HV lines: the possible effect on the health of people living close to the HV lines, associated to electric and mainly magnetic fields in the immediate surrounding of the lines. The problem was first raised by Wertheimer and Leeper (1979) in their epidemiological study, which revealed a slightly higher rate of cancer incidences among the children living close to the HV lines. For the line design, the control of both electric and magnetic fields at ground level is achieved by adequate adjustment of the height of the conductors and of the width of the right-of-way of the lines. These measures are generally costly and have relatively poor efficiency because of the gradual decrease of the fields with the lateral distance from the line (approximately proportional to $1/r$). Thus, to reduce by half the field intensity at the limit of the rights-of-way of the line, the latter must be doubled. A realistic approach, which compensates for the gradual decrease of the fields, consists of maximizing the utilization of the existing rights-of-way, namely, with multi-phase and multi-circuit lines sharing the same tower, and regrouping lines of different voltages in the same rights-of-way.

8.2.1 Electric Field at Ground in the Vicinity of the HV Line

The biomedical aspect of electric and magnetic fields being beyond the scope of the present book, we limit ourselves to the field intensities at the ground level, which constitute important parameters for the line design, namely, in the establishment of the average height of the conductors. Their calculation is detailed in the following.

Calculation of the electric field at ground: Is relatively simple and straightforward. A number of simplifications can be made, namely, in the representation of the bundled conductors by a single conductor of diameter equal to the geometric mean value of the bundle. The electric field at ground is

$$\mathbf{E} = \frac{1}{2\pi\varepsilon_0} \hat{\mathbf{A}} \frac{q_i}{r_i} \mathbf{a}_r \tag{8.7}$$

where

q_i is the linear charge density

r_i the direct distance from the measuring point to the individual phase conductors

Figures 8.5 and 8.6 show lateral profiles of the electric field at ground in the immediate surrounding of HV lines. The typical electric field in the surrounding of HV lines is calculated with the average height of the conductors (Figure 8.5), while the maximal fields are obtained with the minimal height (Figure 8.6).

In substations, there are little variations in the height of the bus bars, because of their stiffness, which keeps them at constant height above ground. As expected, the electric field at ground is higher near a line of higher voltage. For the 735 kV lines of Hydro-Québec, the field is maximal below the outer phase, at the point corresponding to the maximal sag of the phase conductor and amounts to 10 kV/m (Figure 8.6). At the limit of the right of way, usually 15 m from the outer phases, it is 4 kV/m and decreases gradually with the lateral distance from the line. One notes also the efficiency of control of the field at ground by the use of double-tern, because of the field cancellation (Figure 8.6). The electric field at ground in the substations is in the same range as that below the lines (Figures 8.7 and 8.8).

Effect of an ac field: The electric model of a person is a parallel *R–C* circuit (Figure 8.9), where R_0 is the body resistance, typically in the order of a few kΩ, and C_0 its capacitance to ground, typically around 100 pF. Because the relatively low body resistance prevents the effective charging of the body capacitance C_0, a person is generally at ground potential. When a person enters into an electric field, he may experience the following two phenomena: the charging (or discharging) of his body capacitance and the circulation of an induced current through his body resistance.

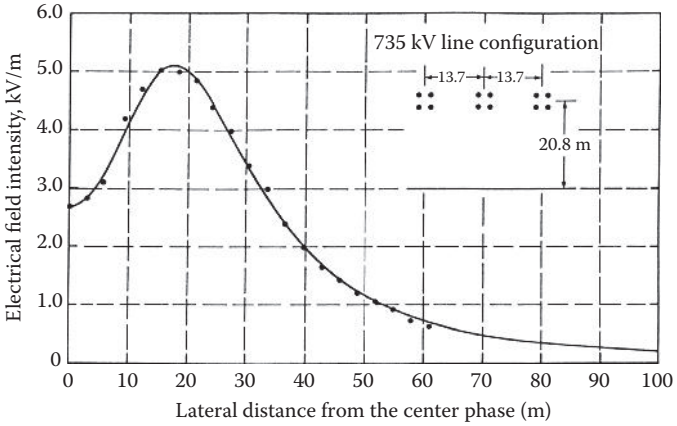


FIGURE 8.5 Lateral profile of typical electrostatic field under *Hydro-Québec* 735-kV lines calculated with average heights. (From Maruvada, P.S. et al., Electrostatic field effects from high voltage power lines and in substations, CIGRE Report No. 36-04, Paris, France, 1976.)

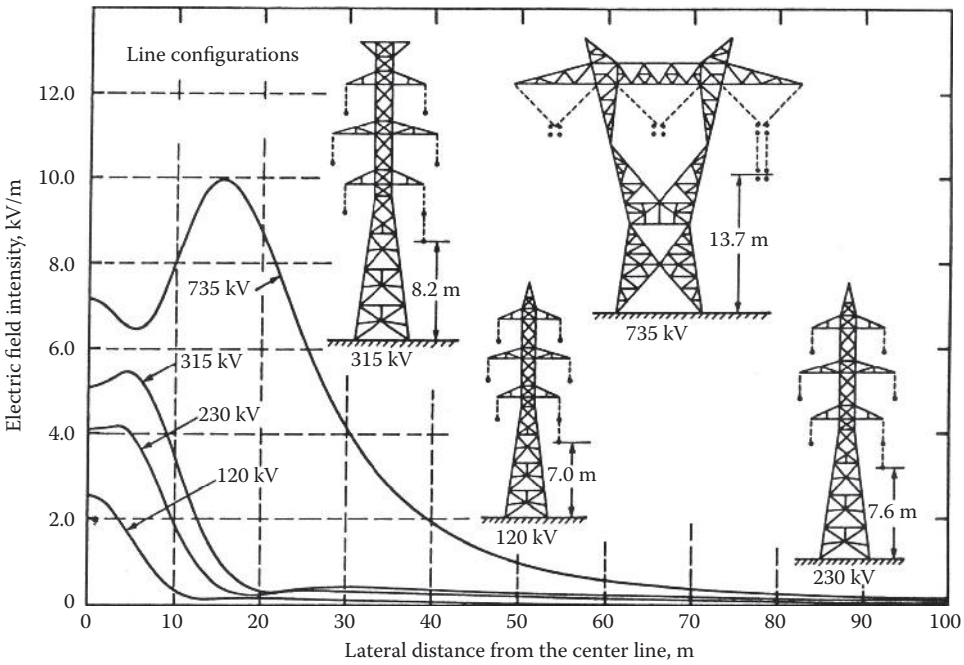


FIGURE 8.6 Lateral profile of maximum electrostatic field of high-voltage transmission lines calculated with minimum heights. (From Maruvada, P.S. et al., Electrostatic field effects from high voltage power lines and in substations, CIGRE Report No. 36-04, Paris, France, 1976.)

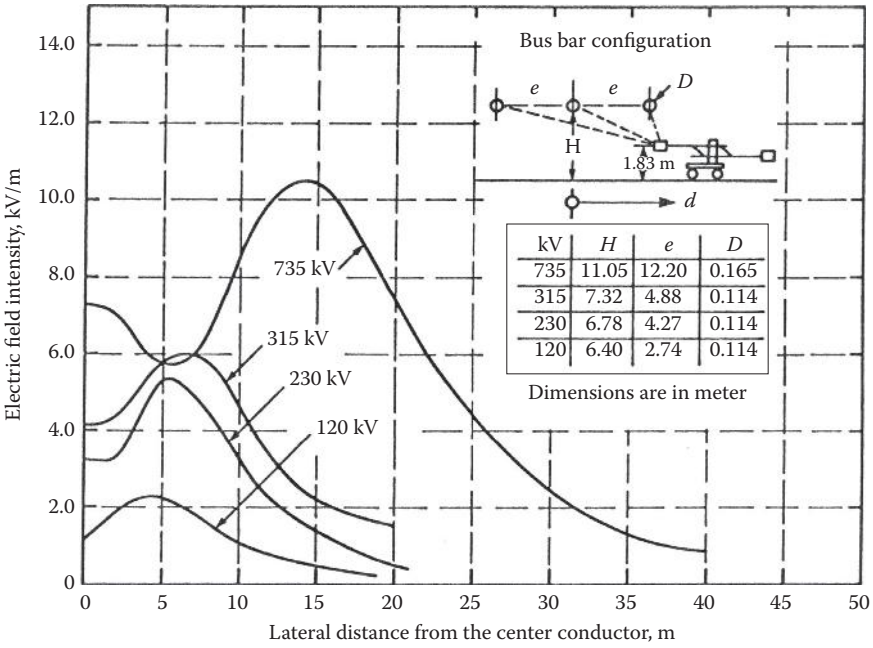


FIGURE 8.7 Lateral profile of electrostatic field below bus bars in a 735-kV substation of *Hydro-Québec*. (From Maruvada, P.S. et al., Electrostatic field effects from high voltage power lines and in substations, CIGRE Report No. 36-04, Paris, France, 1976.)

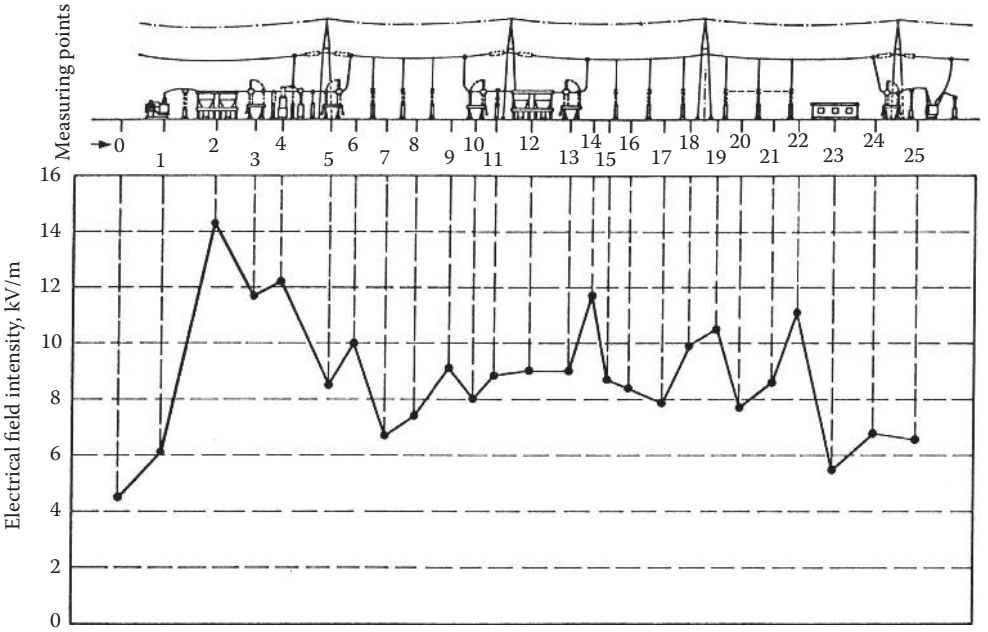


FIGURE 8.8 Distribution of electrostatic field in a 735-kV substation of *Hydro-Québec*. (From Maruvada, P.S. et al., Electrostatic field effects from high voltage power lines and in substations, CIGRE Report No. 36-04, Paris, France, 1976.)

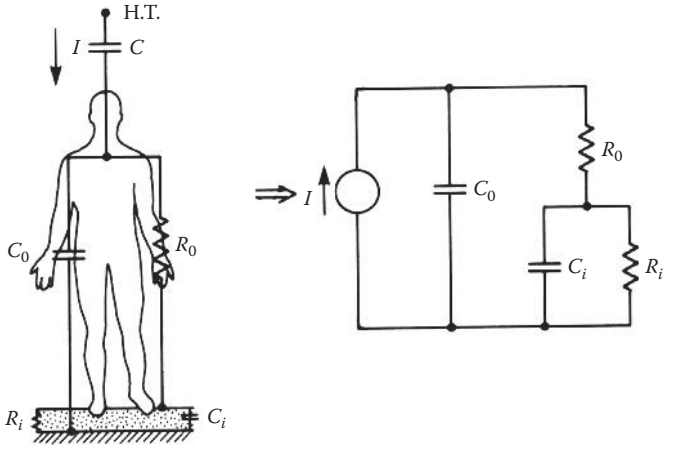


FIGURE 8.9 Representation of a human person in an electric field. R_0, C_0 are body resistance and capacitance. R_i, C_i are insulation resistance and capacitance. (From Maruvada, P.S. et al., Electrostatic field effects from high voltage power lines and in substations, CIGRE Report No. 36-04, Paris, France, 1976.)

Charging (or discharging) of the body capacitance: When a person is well insulated from the ground, for example, by wearing good insulating shoes, his body resistance is increased, the induced voltage establishes at the value determined by the ratio between the capacitances of the person with respect to ground and to the line conductors (Maruvada et al., 1976). A charging current circulates through the body during the transient period when the body capacitance is charged up to the induced voltage, which can reach several tens of kV when the person is well insulated from ground.

On the other hand, a discharging current will circulate through the body when the person touches a structure solidly grounded, and discharge his body capacitance C_0. A discharging current also occurs when a well-grounded person touches a floating object, thus discharges its capacitance C.

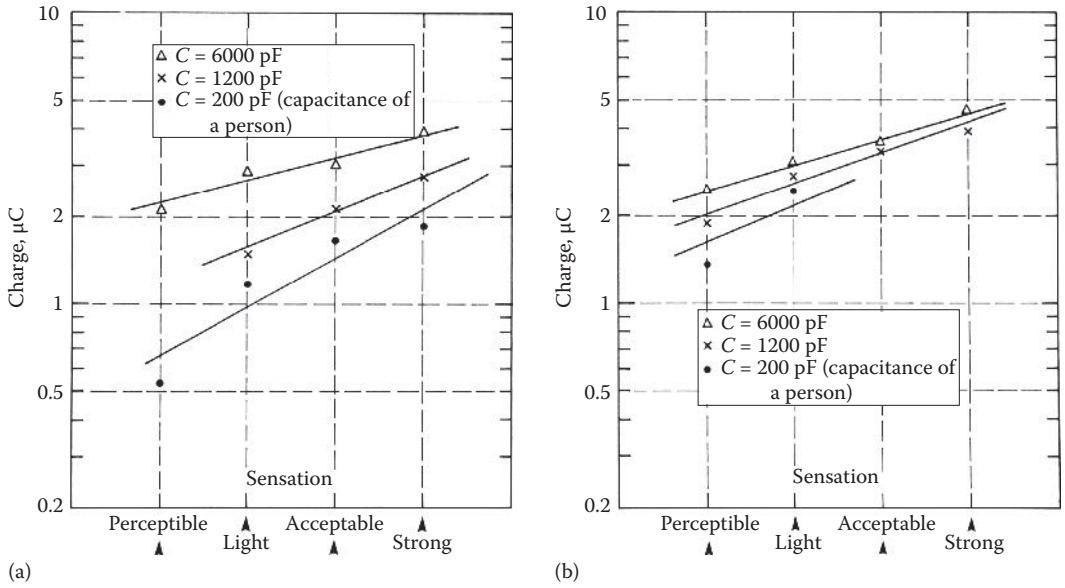


FIGURE 8.10 Human reaction to an electrostatic discharge represented by their received electric charge. (a) Charging. (b) Discharging. (From Maruvada, P.S. et al., Electrostatic field effects from high voltage power lines and in substations, CIGRE Report No. 36-04, Paris, France, 1976.)

Both charging and discharging currents are transient pulses of short duration. The effect of such a charging (or discharging) capacitive current is generally without consequence. It depends on the duration of the current and is more disagreeable when the duration is short, in the order of microseconds. It is perceptible only when the absorbed (or discharging) charge is in the order of 0.5–2 μC and becomes clearly disagreeable when the charge reaches values around 5 μC (Figure 8.10).

Induced current: Is the steady-state ac current that circulated through the person's body and is essentially limited by the capacitance between the person and the line conductors, typically in the order of a few tens of pF, and does not exceed 1–2 mA under a 735 kV line (Figure 8.11). Such an induced current is barely perceptible by most people and is considerably below the level of *let-go*, typically between 7–10 mA, which prevents the person to release the charged object (Dalziel, 1954). The danger of the induced current increases when one touches a charged object of large dimensions, well insulated from the ground, for example, a vehicle and fences. The induced current can then exceed the threshold level of let-go. Simple means to evaluate the capacitance to ground of objects having practical shapes and sizes are provided in Maruvada and Hyltén-Cavallius (1975); thus help evaluating the potential risk of touching these objects.

8.2.2 Magnetic Field at Ground in the Vicinity of the HV Line

Calculation of the magnetic field at ground: The calculation of the magnetic field **H** and the magnetic induction flux **B** at ground, in the immediate surrounding of HV lines, can be made using the same simplifications in the representation of the line conductors according to

$$\mathbf{H} = \frac{1}{2\pi} \sum \frac{I_i}{r_i} \mathbf{a}_r \quad \text{and} \quad \mathbf{B} = \frac{\mu_0}{2\pi} \sum \frac{I_i}{r_i} \mathbf{a}_r \tag{8.8}$$

where I_i is the current circulating in the line conductors.

It should be noted that the calculation of the magnetic field must take into account the penetration of the magnetic field into the soil, which results in placing the magnetic ground plane at a depth d_p given by

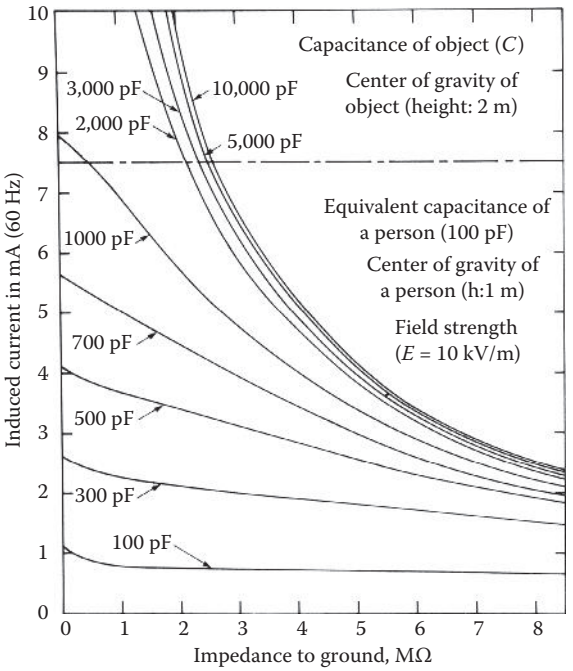


FIGURE 8.11 Induced current as a function of the ground impedance. (From Maruvada, P.S. et al., Electrostatic field effects from high voltage power lines and in substations, CIGRE Report No. 36-04, Paris, France, 1976.)

$$d_p = 2\sqrt{\frac{r}{mw}} \tag{8.9}$$

where

ρ is the resistivity of the soil in Ohm-m
μ is the permeability
ω is the frequency of the current

For typical values of ρ = 100 Ohm-m, $\mu = 4\pi \times 10^{-7}$, and $\omega = 2\pi 60$, the depth of the magnetic ground plane is dp = 918 m.

Figure 8.12 shows the variations of the magnetic field at the ground, in the immediate surroundings of 735 kV lines of Hydro-Québec. Finally, it should be noted that the electric and magnetic fields around transmission lines vary in time and with the distance from the line. The lateral profiles of the electric field (Figures 8.5 through 8.7) and magnetic fields (Figure 8.12) represent the maximal levels reached at a given location near the line.

Effect of a magnetic field: At the actual levels of the magnetic field in the immediate surrounding of HV lines, its presence is generally not perceptible. The effect of the magnetic field on health, namely, with respect to the possible cancer incidence, is mainly related to a prolonged exposition to an ac magnetic field of high intensity, during tests on animals in the laboratory. These levels of the magnetic field are, however, several orders of magnitude higher than the field levels prevailing near HV lines. The many epidemiological studies realized to the present have not established beyond any doubt a cause to effect relationship between the magnetic field from HV lines and the health of people living in the immediate vicinity of the lines. They have sensitized the public to the effects of magnetic field and contributed to the elimination from the market of the electric blankets, which produce much more intense magnetic fields.

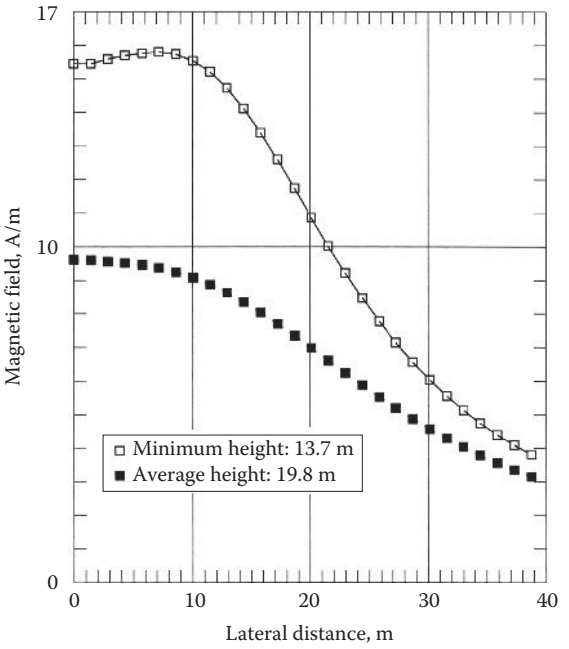


FIGURE 8.12 Lateral profile of magnetic field at ground, below a 735 kV line of *Hydro-Québec*.

8.3 Selection of Conductors

8.3.1 Corona Onset Conditions

Impact of corona discharges on the design of HV lines has been recognized since the early days of electric power transmission. Corona discharges occur on the line conductor when the local electric field exceeds an onset value, usually according to the Peek empirical formula:

$$E_c = m\delta\left(21.1 + \frac{0.301}{\sqrt{\delta a}}\right) \tag{8.10}$$

where

E_c is the onset field, in kV_{rms}/cm

m is a coefficient characteristic of the surface conditions of the conductors, in the range of 0.6 and 0.9, typically m = 0.7 for fair weather condition

δ is the relative air density given by

$$\delta = \frac{3.92b}{273 + \theta}$$

With b the barometric pressure in cm Hg and θ the temperature in *C*.

Corona performance is a general term used to characterize the energy loss and environmental impact of an HV line in its immediate vicinity. It generally refers to the following main effects of corona discharges developing on the line conductors and their related hardware, namely, corona losses (CL), electromagnetic interference (RI) and TVI, audible noise (AN), and polluting effluents, which are stable by-products of corona discharges in air, namely, ozone, O_3, and the nitrite oxides, NO_x. All parameters are sensitive to weather conditions, which dictate the corona activities.

Of these parameters, only the CLs can be described by a lump number equal to the total energy losses per kilometer of the line, associated with the corona activities. Both electromagnetic interference and AN levels vary with the distance from the line and are best described by lateral profiles, which show variations in the RI and AN levels with the lateral distance from the line. For convenience, the interference and noise levels at the edge of the right-of-way, typically 15 m from the outside phases of the line, are generally used to quantify the interference and noise level.

The time variations in the corona performance of HV lines is best described in terms of a statistical distribution, which shows the proportion of time that energy losses, electromagnetic interference, and AN exceed their specified levels. The physical mechanisms of these phenomena and their current evaluation methods are discussed in the following.

8.3.2 Energy Losses

For many years, when the technological development limited the power transmission to relatively low-voltage levels, below 300 kV, CLs were the limiting factor in the selection of line conductors. CLs are generally described in terms of the energy losses per kilometer of the line. They are generally negligible under fair-weather conditions but can reach values of several hundreds of kilowatts per kilometer of line during foul weather. Direct measurement of CLs is relatively complex, but foul-weather losses can be readily evaluated in *test cages* under artificial rain conditions, which yield the highest energy loss. The results are expressed in terms of the *loss generation function*, a characteristic of the conductor to produce CL under given operating conditions.

8.3.2.1 Mechanism of Generating Energy Losses from Corona Discharges

The movement of ion space charges of both polarities generated by corona discharges, and subjected to the applied field around the line conductors, is the main source of energy loss. In effect, the work realized by a charge q, moving across a distance dx in the direction of the applied field, is

$$\mathrm{d}W = \mathbf{F}\,\mathbf{dx} = q\mathbf{E}\,\mathbf{dx} \tag{8.11}$$

On the other hand, the energy supplied by the source is

$$\mathrm{d}W = U\,i\,\mathrm{d}t, \tag{8.12}$$

It follows that

$$q\,E\,\mathrm{d}x = U\,i\,\mathrm{d}t$$

or

$$i\left(t\right) = \frac{qE}{U}\frac{\mathrm{d}x\left(t\right)}{\mathrm{d}t} = \frac{qE}{U}v\left(t\right) \tag{8.13}$$

where v is the speed of the charged particle.

The movement of the ion space charges across the interelectrode space causes energy losses that the source must supply via the applied electric field, which can be determined by measuring the electric current circulating in the external circuit. For ac lines, the movement of the ion space charges, illustrated in Figure 8.13, is limited to the immediate vicinity of the line conductors corresponding to their maximum displacement during one half cycle, typically a few tens of centimeters before the voltage changes polarity and reverses the ionic movement. This particular characteristic of ac corona makes it possible to evaluate the generated losses of conductor bundles in experimental test cages, which effectively reproduce the electric field conditions around the test conductor bundle.

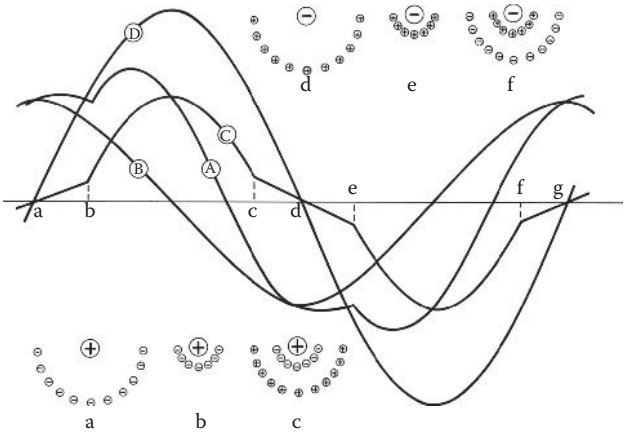


FIGURE 8.13 Corona discharge current. (A) Total current. (B) Capacitive current. (C) Corona current. (D) Conductor voltage. b, e: Instant of corona onset and c, f: instants of corona extinction during positive and negative half cycles and schematic diagrams for corresponding space charge positions.

8.3.2.2 Empirical Formulae for Evaluating Energy Losses

In the absence of an accurate method of calculation of the energy losses by corona discharges, several empiric formulae have been developed and used in the evaluation of CLs on power transmission lines. Some of these empirical formulae are presented in the following.

Two parallel conductors: The CLs in a system of two parallel conductors are expressed by the empirical formula proposed by Peek:

$$P = \frac{241}{\delta}(f + 25)\sqrt{\frac{a}{s}}(U_e - U_0)^2 10^{-5} \quad (\text{kW/km}) \tag{8.14}$$

where
f is the frequency of the voltage, in Hz
a is the radius of the conductors, in cm
s is the distance between the conductors, in cm
U_e and U_0 are the effective values of the applied and onset voltages, in kV
δ is a correction factor for the air density

Single-phase line with single conductor: The semiempirical formula developed by *Hydro-Ontario* assumes that the ionization produced by corona discharges forms a conducting layer of radius r_c around the conductor. The presence of such a conducting layer around the line conductor has two effects:

- It increases the effective radius of the conductor and, hence, its capacitance to ground, C.
- It presents a resistance, R, producing energy losses corresponding to the CLs.

The development of corona discharges can then be represented by an electrical R–C series circuit illustrated in Figure 8.14. The calculation of CLs is reduced to calculating the energy losses in the circuit, of which the values of the resistance, R, and the capacitance, C, are

$$R = k_1 \ln\frac{r_c}{a} \quad \text{and} \quad C = \frac{2\pi\varepsilon_0}{\ln(2h/r_c)}$$

where
a is the radius of the conductor
$k_1 = \rho/2\pi$ is a constant characteristic of the ionized space inside the conducting corona layer

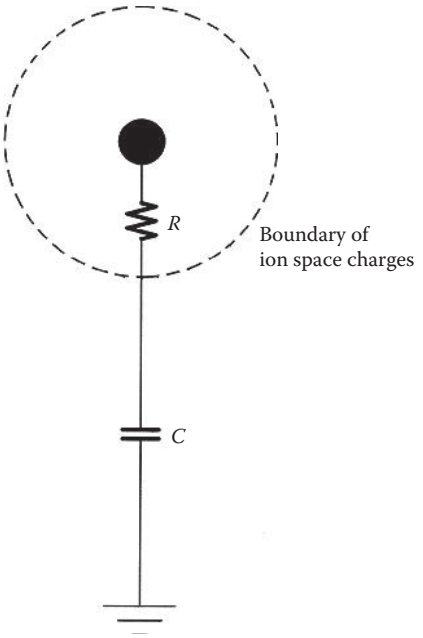


FIGURE 8.14 Model for calculation of CLs.

The impedance of the *R–C* series circuit is

$$Z = \sqrt{R^2 + \frac{1}{\omega^2 C^2}} = \sqrt{\left(k_1 \ln \frac{r_c}{a}\right)^2 + \left(k_2 \ln \frac{2h}{r_c}\right)^2}, \quad \text{with } k_2 = \frac{1}{2\pi\varepsilon_0}$$

The discharge current is $I = U/Z$, and the CLs are

$$P = RI^2 = R\left(\frac{U}{Z}\right)^2 = \frac{k_1 \ln(r_c/a)}{\left[k_1 \ln(r_c/a)\right]^2 + \left[k_2 \ln\left(2h/r_c\right)\right]^2} U^2 \tag{8.15}$$

Since r_c/a is generally much smaller than $2h/r_c$, the preceding expression simplifies to

$$P = \frac{k \ln(r_c/a)}{\left[\ln(2h/r_c)\right]^2} U^2, \quad \text{with } k = \frac{k_1}{k_s^2}$$

Noting that for a cylindrical field,

$$E_c r_c = aE_0 = \frac{U}{\ln(2h/r_c)} \tag{8.16}$$

$$\frac{r_c}{a} = \frac{E_0}{E_c} \quad \text{and} \quad \ln\frac{2h}{r_c} = \frac{U}{r_c E_c} = \frac{U}{aE_0}$$

In the preceding equation, E_0 is the field at the surface of the conductor and E_c the corona onset field given by the Peek formula. It follows that the expression for the applied voltage:

$$U = E_c r_c \ln\frac{2h}{r_c}$$

Replacing the expression for U in Equation 8.15 gives the following expression for the CLs as a function of the applied field, E_0, and corona onset field, E_c:

$$P = \frac{k \ln(r_c/a)}{\left[\ln(2h/r_c)\right]^2} U^2 = \frac{k}{(U/aE_0)^2} \ln\frac{E_0}{E_c} U^2 = ka^2 E_0^2 \ln\frac{E_0}{E_c} \quad (8.17)$$

The preceding formula depends only on the physical parameters of the line, and the coefficient k has typical values between 0.002 and 0.003.

Three-phase lines: For a three-phase line, the energy losses are simply equal to the sum of the losses generated in each phase of the line, according to the electric field at the conductors.

8.3.2.3 Corona Loss Characteristics of Bundle Conductors

Current evaluation of CLs is based on experimental data on the corona-*generated loss* characteristics in W/m of the bundle conductors. These energy losses are usually obtained in tests on full-size bundle conductors in test cages, under conditions of heavy artificial rain, which yield the highest losses. The generated losses are measured over a range of practical electric field intensities, so that the CLs can be readily obtained for the actual values of the field at the line conductors. The line parameters of a 735 kV line are given in Table 8.2, together with the various corona-generated parameters taken from Trinh and Maruvada (1977). The CLs are the sum of the losses generated at the three phases of the line, which amount to 127.63 kW/km.

8.3.3 Electromagnetic Interference

One of the consequences of corona discharges is the generation of electromagnetic interferences, which disturb the reception of radio and television signals in the immediate surrounding of the line, where the interference levels can be particularly high under foul-weather conditions. Electromagnetic interference is associated with streamer discharges that inject current pulses into the conductor. These pulses of steep front and short duration have a high harmonic content, reaching the tens of megahertz range (Juette, 1972). A tremendous research effort was devoted to the subject during the years 1950–1980, starting with the work of Adams (1956), in an effort to evaluate the electromagnetic interference from HV lines. The most comprehensive contributions comes from Moreau and Gary (1972a,b) of *Électricité de France (EDF),* who introduced the concept of excitation function to characterize the ability of a line conductor to generate electromagnetic interference under a given operating condition. These aspects of electromagnetic interference will be discussed in the following, namely, the physical mechanism of the generation of electromagnetic interference and the methods of calculation of the interference levels produced by HV transmission lines.

TABLE 8.2

Parameters of the 735 kV Line of Hydro-Québec

Parameters		
Phase spacing (m)	13.7	
Number of subconductors	4	
Diameter of subconductors (cm)	3.05	
Phase	**Central**	**Outer**
Capacitance per unit length (pF/m)	10.57	
Maximal gradient factor, G_{max} (/m)	4.6663	4.2267
Minimal gradient factor, G_{min} (/m)	3.5140	3.1976
Maximal field, E_0 (kV/m)	19.832	17.963
Generated loss W (W/m)	59.773	33.926
Excitation function, Γ (dB above 1.0 $\mu A/\sqrt{m}$)	43.527	39.593
Subcond. generated acoustic power density A (dBA above 1 μW/m)	3.284	–0.2387

8.3.3.1 Generation Mechanism of Interference from Corona Discharges

The development of corona discharges on the line conductors can occur in different modes having distinct visual, electric, and audible characteristics, discussed in Chapter 4. The streamer modes are characterized by the generation of current pulses of very short duration, typically of a hundred of nanoseconds. Their amplitude varies between a few mA up to amperes, depending on the mode of discharge and the local electric field in the immediate surrounding of the discharge site. Electrically, the development of streamers corresponds to the injection of a discharge current pulse into the line conductor. At injection, facing two identical long half lines, the current pulse divides itself in two current pulses of amplitude equal to half of the injected current pulse, progressing in the opposite directions. Since the corona discharge current pulses have a large harmonic content, the line conductors actually act as an emitting antenna of electromagnetic waves of diverse frequencies, which can interfere with the reception of radio and television signals.

Correspondence between the time and frequency domains: It is well known that, for all time-varying electrical signals, there exists a total correspondence in the frequency domain. Such a correspondence is expressed by the Fourier transforms. For a function of time $f(t)$, the corresponding frequency spectrum $F(\omega)$ is given by

$$F(\omega) = \int_{-\infty}^{\infty} f(t)\exp(-j\omega t)\,dt \tag{8.18}$$

Inversely, the function $f(t)$ can be derived from the frequency spectrum $F(\omega)$ according to

$$f(t) = \frac{1}{2\pi}\int_{-\infty}^{\infty} F(\omega)\exp(j\omega t)\,d\omega \tag{8.19}$$

Physical interpretation: The Fourier transforms (8.18) and (8.19) means that to a time-varying signal, can be associated with a series of periodic signals, each represented by a vector $\boldsymbol{F}(\omega)$ rotating around its origin in the complex frequency plane. With this vector representation of the components of the Fourier series, it can be seen that the vector $\boldsymbol{F}(\omega)$ is equal to its conjugate vector $\boldsymbol{F}^*(-\omega)$.

The relation (8.19) can be rewritten as

$$f(t) = \frac{1}{2\pi}\int_{-\infty}^{0} F(\omega)\exp(j\omega t)\,d\omega + \frac{1}{2\pi}\int_{0}^{\infty} F(\omega)\exp(j\omega t)\,d\omega$$

Applying the change of variable $\omega \to -\omega$ to the first integral, one obtains the following:

$$f(t) = \frac{1}{2\pi}\int_{0}^{\infty} F(-\omega)\exp(-j\omega t)\,d\omega + \frac{1}{2\pi}\int_{0}^{\infty} F(\omega)\exp(j\omega t)\,d\omega$$

Noting that $\boldsymbol{F}(-\omega) = \boldsymbol{F}^*(\omega)$, the expression of $f(t)$ becomes

$$f(t) = \frac{1}{2\pi}\int_{0}^{\infty} \left[\mathbf{F}^*(\omega)\exp(-j\omega t) + \mathbf{F}(\omega)\exp(j\omega t)\right] d\omega \tag{8.20}$$

Referring to the vector representation in Figure 8.15, the integrand in the preceding equation is represented by the vectors $\boldsymbol{F}(\omega)$ rotating around their origin at an angular velocity of ω rad/s and their conjugates $\boldsymbol{F}^*(\omega)$ rotating at an angular velocity of $-\omega$ rad/s, that is, in the reverse direction. It follows the expression for the integrand of Equation 8.20:

$$\mathbf{F}(\omega)\exp(j\omega t) + \mathbf{F}^*(\omega)\exp(-j\omega t) = 2\left|F(\omega)\right|\cos\left[\omega t + \alpha(\omega)\right]$$

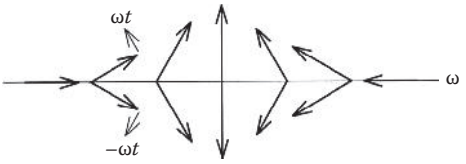


FIGURE 8.15 Correspondence between the time and frequency domains.

The function $f(t)$ becomes

$$f(t) = \frac{1}{\pi}\int_0^{\infty} |F(\omega)| \cos\{\omega t + \alpha(\omega)\}\, d\omega \tag{8.21}$$

where $\alpha(\omega)$ is the phase angle at frequency ω.

Harmonic content of corona discharge current: When streamer discharges develop, the discharge current is constituted of pulses of short duration, with amplitude varying between 10^{-3} and a few amperes (Figure 8.16). The wave shape of the current pulses can be adequately represented by a double exponential function according to

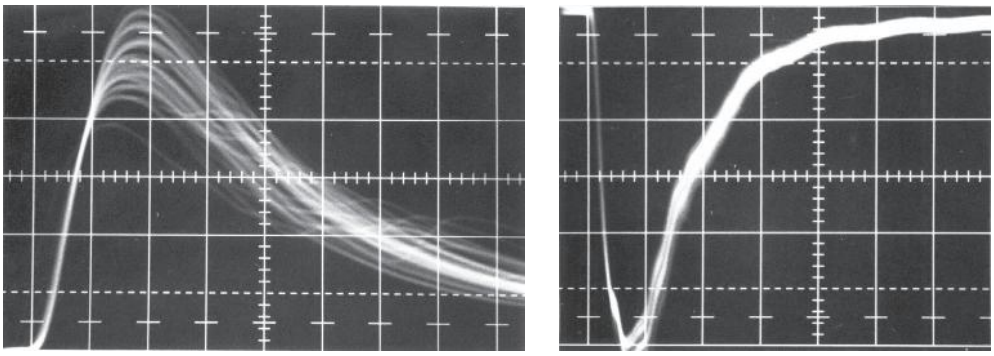
$$i(t) = A\{\exp(-at) - \exp(-bt)\}$$

The duration δ of the current pulse can be defined as the time it decreases to half of its amplitude. For Trichel streamers, the current pulses have an amplitude of mA, with a typical duration between 100 and 150 ns, while the positive streamers generate current pulses of amplitude of 10^{-1} *A* to a few amperes, with a typical duration between 250 and 500 ns.

For the present analysis, the corona discharge current pulses are represented by a square wave of amplitude *A* and duration δ. Applying the Fourier transforms to such a square wave current, one obtains the following frequency spectrum:

$$F(\omega) = \int_{-\infty}^{\infty} f(t)\exp(-j\omega t)\,dt = A\int_{-\delta/2}^{\delta/2} \exp(-j\omega t)\,dt = \frac{A}{-j\omega}\exp(-j\omega t)\Big|_{-\delta/2}^{\delta/2}$$

$$= \frac{2A}{\omega}\left\{\frac{\exp(j\omega\delta/2) - \exp(-j\omega\delta/2)}{2j}\right\}.$$



(a) (b)

FIGURE 8.16 Wave shape of corona discharge current pulses: (a) positive streamer current, scales: 10 mA/div, time 50 ns/div; (b) Trichel streamer current, scales: 350 μA/div, time 50 ns/div.

or

$$F(\omega) = \frac{2A}{\omega}\sin\left(\frac{\omega\delta}{2}\right)$$

that can be rewritten as

$$F(\omega) = A\delta\frac{\sin(\omega\delta/2)}{\omega\delta/2} = A\delta S_a\left(\frac{\omega\delta}{2}\right) \tag{8.22}$$

where the product $A\delta$ defines the *impulse strength* and S_a *the sampling function* defined as

$$S_a\left(\frac{\omega\delta}{2}\right) = \frac{\sin(\omega\delta/2)}{\omega\delta/2} \tag{8.23}$$

Figure 8.17 shows the frequency spectrum of a square wave corona discharge current pulse, defined by the preceding equation. The frequency spectrum contains successive lobes, limited by the frequencies where the amplitude of $|F(\omega)|$ is null or when $\omega\delta/2 = n\pi$. In practice, the range of frequencies of interest is often limited to the first lobe of the spectrum, of which the cutoff frequency f_c corresponds to the first frequency at which the amplitude of $|F(\omega)|$ is null, $n = 1$:

$$\omega_c = \frac{2\pi}{\delta} = 2\pi f_c \quad \text{or} \quad f_c = \frac{1}{\delta} \tag{8.24}$$

It can be seen that when the duration of the current pulse δ tends to zero, the cut-off frequency f_c tends to infinite, one approaches the conditions of *white noises*. For corona discharges, the typical durations of the current pulses determine the range of frequencies where the disturbing effect of the discharge may be present. For Trichel streamers, the duration of the discharge pulses is 100–150 ns, which corresponds to a cutoff frequency in the order of 6–10 MHz. For positive streamers, the duration of the discharge pulses is 250–500 ns, corresponding to a cutoff frequency in the order of 2–4 MHz.

Harmonic content of corona discharge current on a line: When an HV line is exposed to adverse climatic conditions, the corona discharges can become intense, because of the multitude of discharge sites along the line conductors. The corona discharge current is composed of a train of pulses of essentially random frequency and amplitude, depending on the discharge activities at the individual discharge sites. The effect of a train of pulses on the frequency spectrum will be examined in the following, for the case of a train of square wave pulses of duration δ. Such a signal can be represented by the Fourier integral as

$$F(t) = \int_0^\infty [A(\omega)\cos(\omega t) + B(\omega)\sin(\omega t)]\,d\omega$$

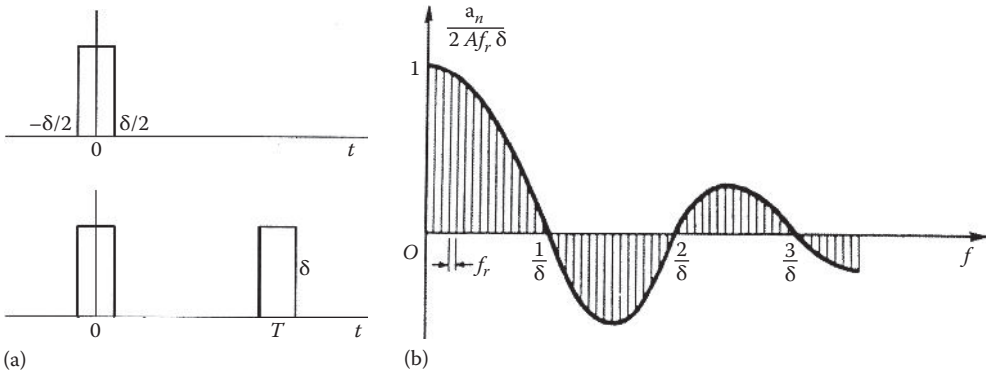


FIGURE 8.17 Frequency spectra of a square wave pulse and a train of square wave pulses. (a) Characteristics of a single square wave impulse, and a train of square wave impulses. (b) Frequency spectra corresponding to a single impulse (solid line curve) and a train of impulses (discrete lines).

The coefficients A and B are functions of the frequency ω and are defined by the following expressions:

$$A(\omega) = \frac{1}{\pi}\int_{-\infty}^{\infty} f(t)\cos(\omega t)\,dt \quad \text{and} \quad B(\omega) = \frac{1}{\pi}\int_{-\infty}^{\infty} f(t)\sin(\omega t)\,dt$$

For square wave pulses, the function $f(t)$ can be made even by properly choosing the time origin; in these conditions, the coefficient $B(\omega)$ is null and the coefficient $A(\omega)$ is

$$A(\omega) = \frac{\sin \omega d}{\pi \omega}$$

It can be demonstrated that the Fourier transforms of a train of pulses $F(t)$ are

$$G(\omega) = \frac{2\pi}{T}\sum_{n} g(n\omega_0)\,\delta(\omega - n\omega_0) \tag{8.25}$$

where

$g(\omega)$ is the Fourier transforms of the single pulse $f(t)$
T is the time period between two consecutive pulses
$\delta(\omega - n\omega_0)$ the Kronecker delta function, with $\delta = 1$ for $\delta = n\omega_0$ and $\delta = 0$ for $\delta \neq n\omega_0$

For the case of a train of square wave pulses, the value of the function $g(\omega)$ at frequencies multiple of ω_0 is

$$g(n\omega_0) = A_n = \frac{2A}{n\pi\omega_0}\sin\left(n\omega_0 \frac{d}{2}\right) = \frac{Ad}{\pi}\frac{\sin(n\omega_0 d/2)}{n\omega_0 d/2} = \frac{Ad}{\pi} S_a\left(n\omega_0 \frac{d}{2}\right) \tag{8.26}$$

Two effects of the pulse repetition can be observed (Figure 8.17):

- The frequency spectrum of a train of pulses is discrete, composed of frequencies equal to multiple of the fundamental frequency, ω_0: $\omega_0 = 2\pi/T$.
- The amplitude of the envelope of the frequency spectrum of a train of pulses is the spectrum of the single pulse, amplified by a factor $2\pi/T$.

Thus, the higher is the repetition frequency of the pulses, the closer are the frequency lines and the higher is the amplification factor.

8.3.3.2 Interference to the Radio Reception

The reception of a radio signal is generally made by the capture of an electromagnetic wave of a specific frequency by a local tuning circuit in the receiver. The signal transmitted by the electromagnetic wave is next decoded and amplified to be restituted in the form of an audio signal. The tuning of a radio signal can then be represented by a filter circuit with a transfer function $T(\omega)$, which is that of a band-pass filter, of central frequency ω_0, the tuning frequency, and bandwidth $\Delta\omega$. By adjusting the tuning circuit to the carrier wave frequency of a radio station, the radio signal is transmitted without attenuation across the tuning circuit (filter).

When corona discharges develop on the conductors of an HV transmission line, current pulses of short duration are injected in the conductors and propagate along the line. An electromagnetic field is generated around the conductor, which has a wide frequency spectrum (Figure 8.18a), a portion of it can be captured by the antenna of the radio receiver. Let $f(t)$ be the captured electromagnetic signal and $F(\omega)$ its frequency spectrum. The frequency spectrum $R(\omega)$ of the signal at the output of the tuning circuit is

$$R(\omega) = T(\omega)F(\omega) \tag{8.27}$$

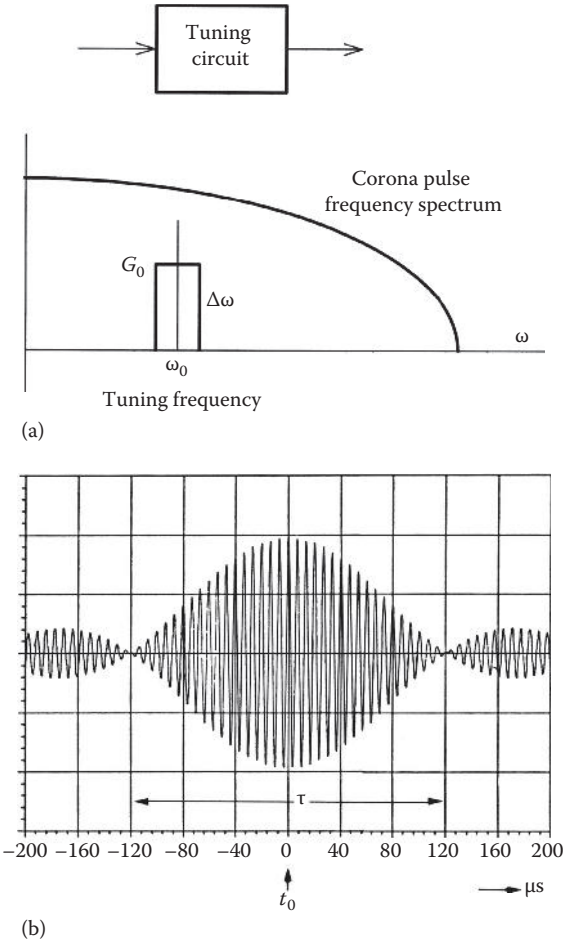


FIGURE 8.18 Interference signal received by an AM radio receiver. (a) Tuning circuit. (b) Frequency spectra of the noise and the tuning circuit. (c) Signal at the output of the tuning circuit.

The corresponding signal $r(t)$ is

$$r(t) = \frac{1}{2\pi}\int_{-\infty}^{\infty} F(\omega)T(\omega)\exp(j\omega t)\,d\omega \tag{8.28}$$

and, for a real signal $f(t)$, the output signal $r(t)$ is given by

$$r(t) = \frac{1}{2\pi}\int_{-\infty}^{\infty} \mathrm{Re}\left[F(\omega)T(\omega)\exp(j\omega t)\right]d\omega = \frac{1}{\pi}\int_{0}^{\infty} F(\omega)T(\omega)\cos\left[\omega t + a(\omega)\right]d\omega \tag{8.29}$$

Since the bandwidth $\Delta\omega$ of the tuning circuit is generally small with respect to the tuning frequency ω_0, the phase shift $\alpha(\omega)$ can be assumed as constant and, consequently, represents simply a time delay in the signal. To simplify the analysis, the effect of the phase shift can be neglected in the following, by assuming that $\alpha(\omega) = 0$. Assuming an ideal tuning circuit has a constant transfer function, equal to 1.0 over the whole bandwidth and zero elsewhere (Figure 8.22), the signal $r(t)$ at the output of the tuning circuit is

$$r(t) = \frac{1}{\pi}\int_{0}^{\infty} F(\omega)\,T(\omega)\cos(\omega t)\,d\omega \tag{8.30}$$

with

$$\left|F(\omega)\right| = \left|Ad\delta S_a\left(\omega\frac{d}{2}\right)\right|$$

and

$$\begin{aligned}|T(\omega)| &= 0 \quad \text{at the frequencies below} \quad \omega_0 - \frac{\Delta\omega}{2}\\ &= 1 \quad \text{at frequencies between} \quad \omega_0 - \frac{\Delta\omega}{2} \text{ and } \omega_0 + \frac{\Delta\omega}{2}\\ &= 0 \quad \text{at frequencies higher than} \quad \omega_0 + \frac{\Delta\omega}{2}\end{aligned}$$

It follows:

$$r(t) = \frac{Ad}{\pi}\int_{\omega_0-\Delta\omega/2}^{\omega_0+\Delta\omega/2} S_a(\omega d/2)\cos(\omega t)\,d\omega \tag{8.31}$$

For the range of AM radio frequencies, the interference level produced by corona discharges is relatively constant, that is, the term $\omega_0\delta/2$ is much smaller than 1.0, the value of the function $S_a(\omega_0\delta/2)$ is close to 1.0. In these conditions,

$$r(t) = \frac{Ad}{\pi}\int_{\omega_0-\Delta\omega/2}^{\omega_0+\Delta\omega/2} \cos(\omega t)\,d\omega \tag{8.32}$$

Noting that the integration is made with respect to the frequency ω, consequently, the time t is a constant, one gets

$$\begin{aligned}r(t) &= \frac{Ad}{\pi t}\sin(\omega t)\Big|_{\omega_0-\Delta\omega/2}^{\omega_0+\Delta\omega/2} = \frac{Ad}{\pi t}\left[\sin\left(\omega_0 + \frac{\Delta\omega}{2}\right)t + \cos\left(\omega_0 - \frac{\Delta\omega}{2}\right)t\right]\\ &= \frac{Ad}{\pi t}\left[\sin(\omega_0 t)\cos\left(\frac{\Delta\omega}{2}t\right) + \cos(\omega_0 t)\sin\left(\frac{\Delta\omega}{2}t\right)\right.\\ &\quad \left. - \sin(\omega_0 t)\cos\left(\frac{\Delta\omega}{2}t\right) + \cos(\omega_0 t)\sin\left(\frac{\Delta\omega}{2}t\right)\right]\\ &= \frac{Ad}{\pi t}2\cos(\omega_0 t)\sin\left(\frac{\Delta\omega}{2}t\right) = \frac{Ad}{\pi t}2\cos(\omega_0 t)\frac{\sin(\Delta\omega t/2)}{\Delta\omega t/2}\frac{\Delta\omega t}{2}\end{aligned}$$

that can be expressed in terms of the bandwidth Δf of the tuning circuit as

$$r(t) = 2Ad\delta\Delta f S_a\left(\frac{\Delta\omega}{2}t\right)\cos(\omega_0 t) \tag{8.33}$$

Figure 8.18 illustrates the response of the tuning circuit to a corona pulse. It can be seen that a short-duration pulse causes a distortion in the amplitude of the carrier wave of frequency ω_0 according to the function $2A\delta\Delta f S_a(\Delta\omega t/2)$, corresponding to the envelope of the response $r(t)$, which has its first crossing by zero at a time $t = 1/\Delta f$. For all practical purposes, a short-duration pulse received by the tuning circuit of the radio receiver is transformed into a pulse of amplitude $(2A\delta\Delta f)$ and duration $2/\Delta f$. When the

electromagnetic interference is produced by a train of pulses of short duration, the interference signal received by the radio is also a train of pulses of the same frequency and of a constant shape.

For AM radio, the information of the transmitted signal is contained in the variations of the amplitude of the carrier wave of frequency ω_0. This distortion of the amplitude of the carrier wave effectively adds to the signal and appears as *a distortion of the received signal, that is, a background noise that can be heard when one passes below an HV line during foul weather* and one is interested to quantify and measure.

8.3.3.3 Quantification of Electromagnetic Interference

The usual parameters for a quantitative evaluation of an electric signal are the voltage, the current, and the power. For electromagnetic interferences, *the random nature of the signal tends to favor the emitted power of the interference signal as the quantification parameter.*

Stationary random signal: When a random signal is such that its average power measured over a sufficiently long period remains constant, it is termed as a *stationary random signal*. The electromagnetic interference associated to corona discharges on HV lines fits well to this definition: its power remains relatively constant in time, depending on the actual atmospheric conditions. Let P be the emitted power of the electromagnetic interference of the line. P represents, by definition, the rate of dissipation of the electromagnetic interference energy, which can be expressed as a function of the interference signal $f(t)$ as

$$P = \lim_{T\to\infty} \cdot \frac{1}{T} \int_{-T/2}^{T/2} f^2(t)\,dt = \overline{f^2(t)} = (F_{\text{rms}})^2 = Constant \tag{8.34}$$

The preceding equation with $P = C$ applies to a stationary random signal, where F_{rms} represents the effective value of the signal $f(t)$.

Percival theorem: The Percival theorem stipulates that *for a stationary random signal, the total power measured in the time domain $P(t)$ is equal to that measured in the frequency domain $P(\omega)$*:

$$P(t) = \int_{-\infty}^{\infty} f^2(t)\,dt = \frac{1}{2\pi} \int_{-\infty}^{\infty} |\mathbf{F}(\omega)|^2\,d\omega = P(\omega) \tag{8.35}$$

Spectral power density: Applying the Percival theorem to the case of an electromagnetic interference signal $f(t)$, of which the average power P is constant in time, yields

$$P(t) = \lim_{T\to\infty} \cdot \frac{1}{T} \int_{-T/2}^{T/2} f^2(t)\,dt = \frac{1}{2\pi} \int_{-\infty}^{\infty} \lim_{T\to\infty} \cdot \frac{|\mathbf{F}(\omega)|^2}{T}\,d\omega$$

Noting that the integrand is an even function of ω, the preceding expression of $P(t)$ becomes

$$P(t) = \frac{1}{\pi} \int_{0}^{\infty} \lim_{T\to\infty} \cdot \frac{|\mathbf{F}(\omega)|^2}{T}\,d\omega = P(\omega) \tag{8.36}$$

Thus, by measuring the power $P(\omega)$ and integrating over all the frequencies, one obtains the power $P(t)$. This practice of measuring the interference power in the frequency domain is simple and more adapted to the evaluation of the interference at the reception of the radio signal. The preceding expression of $P(t)$ can also be expressed as

$$P(t) = \frac{1}{2\pi} \int_{-\infty}^{\infty} \lim_{T\to\infty} \cdot \frac{|\mathbf{F}(\omega)|^2}{T}\,d\omega = \frac{1}{2\pi} \int_{-\infty}^{\infty} F(\omega)\,d\omega$$

by defining the *spectral power density* Φ(ω) of the electromagnetic interference signal $f(t)$ as

$$\Phi(\omega) = \lim_{T \to \infty} \frac{|F(\omega)|^2}{T} = |f(\omega)|^2 \tag{8.37}$$

which represents the dissipation of the interference energy at the frequency ω. For corona discharges on an HV line, electromagnetic interference is related to the discharge current injected in the line conductor; the spectral power density Φ(ω) has dimensions A^2. The emitted power of the interference can be expressed as a function of the spectral power density Φ(ω) as

$$P = \frac{1}{2\pi}\int_{-\infty}^{\infty} \Phi(\omega)\,d\omega = \int_{-\infty}^{\infty} \Phi(f)\,df = \frac{1}{2\pi}\int_{-\infty}^{\infty} |f(\omega)|^2\,d\omega$$

or

$$|f(\omega)|^2 = f(\omega)\, f^*(\omega) = f(\omega)\, f(-\omega)$$

Noting that $f(\omega)$ is an even function, one obtains

$$P = \frac{1}{\pi}\int_0^{\infty} |f(\omega)|^2\,d\omega = \frac{2}{2\pi}\int_0^{\infty} \Phi(\omega)\,d\omega = 2\int_0^{\infty} \Phi(f)\,df \tag{8.38}$$

It can be seen that the average power P is uniquely a function of the amplitude spectrum of the signal. The phase information does not exist due to the random nature of the phenomenon.

Some properties of the spectral power density: Two properties of the spectral power density are mentioned, without demonstration:

- For a linear filter (Figure 8.19), with a transfer function $T(\omega)$, and $f_i(t)$ a stationary random signal applied at the input of the filter circuit. The spectral power density $\Phi_o(\omega)$ of the output signal $f_o(t)$ is given by

$$\Phi_o(\omega) = |T(\omega)|^2 \Phi_i(\omega) \tag{8.39}$$

  $\Phi_i(\omega)$ being the spectral power density of the input signal $f_i(t)$.

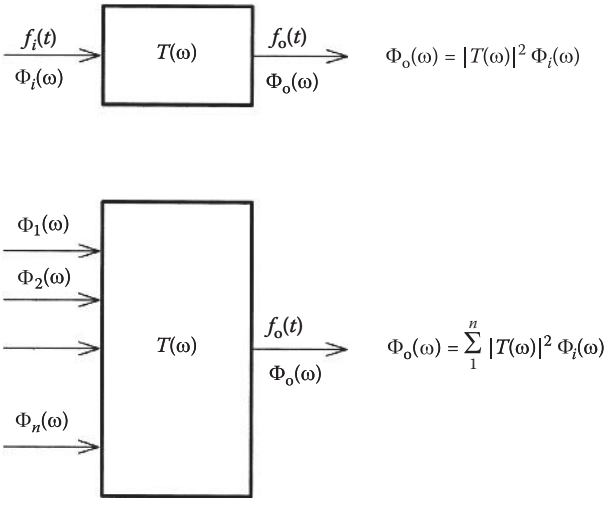


FIGURE 8.19 Percival theorem.

- When several signals are applied simultaneously to the input of the linear filter of Figure 8.19, the spectral power density $\Phi_o(\omega)$ of the output signal is equal to

$$\Phi_o(\omega) = \sum |T(\omega)|^2 \Phi_i(\omega) \tag{8.40}$$

Note that for *nonrandom* signals at the input of the linear filter, the spectral power density of the output signal will be the algebraic sum of the transformed signals:

$$\Phi_o(\omega) = \sum |T(\omega)| \Phi_i(\omega)$$

8.3.3.4 Measurement of Electromagnetic Interference

The preceding considerations show clearly that the electromagnetic interference can be defined by its spectral components and can be measured by appropriate apparatus, as long as they can be represented by a linear filter circuit.

Characteristics of a noise meter for electromagnetic interference: Consider an RI meter, with a transfer function $H(\omega)$, the spectral power density of the measured signal, $\Phi_o(\omega)$, is related to the input signal according to

$$\Phi_o(\omega) = |T(\omega)|^2 \Phi_i(\omega) \tag{8.41}$$

By the Percival theorem, the effective value, F_{rms}, of the output signal is related to the input spectral power density according to

$$F_{rms}^2 = \overline{f_o^2(t)} = \frac{1}{\pi} \int_0^{\infty} \Phi_o(\omega) d\omega = \frac{1}{\pi} \int_0^{\infty} |T(\omega)|^2 \Phi_i(\omega) d\omega \tag{8.42}$$

If the transfer function $T(\omega)$ of the measuring meter is an ideal band-pass circuit, of amplitude $|T(\omega)| = 1.0$ and bandwidth $\Delta\omega$, the average power of the output signal is given by:

$$\overline{f_o^2(t)} = \frac{1}{\pi} \int_{\omega_0 - \Delta\omega/2}^{\omega_0 + \Delta\omega/2} \Phi_i(\omega) d\omega \tag{8.43}$$

If $\Delta\omega$ is much smaller than ω_0 and $\Phi_i(\omega)$ is constant and equal to $\Phi_i(\omega_0)$, the preceding equation becomes

$$F_{rms}^2 = \frac{1}{\pi} |T(\omega_0)|^2 \Phi_i(\omega_0) \int_{\omega_0 - \Delta\omega/2}^{\omega_0 + \Delta\omega/2} d\omega \tag{8.44}$$

with $|T(\omega_0)| = 1.0$, the preceding expression becomes

$$F_{rms}^2 = \frac{1}{\pi} \Phi_i(\omega_0) \Delta\omega = 2\Phi_i(f_0) \Delta f$$

and the effective value of the output signal at the measuring frequency is

$$F_{rms} = \sqrt{2\Phi_i(f_0)\Delta f} = \sqrt{\frac{1}{\pi} \Phi_i(\omega_0) \Delta\omega} \tag{8.45}$$

that can be measured with a voltmeter. In the preceding expression of F_{rms}, $\Phi_i(f_0)$ is a function of the frequency f_0 (Hz), commonly used in the measurement of the RI. Knowing the bandwidth, Δf, of the RI measuring meter, the value of the spectral power density $\Phi_i(f_0)$ at the measuring frequency f_0 can be deduced. Scanning over all frequencies with the measuring meter, one obtains the frequency spectrum of spectral power density of the input signal.

From the preceding considerations, the main characteristics of the measuring meter for electromagnetic interference are as follows:

- To be able to tune and scan over a range of defined frequencies
- To have a detection circuit of defined bandwidth and transfer function $H(\omega)$

Measurement apparatus for radio interference: Commonly used RI meters operate on the principle of a radio receiver, with the output modified to allow the quantitative measurement of the signal. Figure 8.20 gives the operating scheme of such a measuring device for RI:

- The input is constituted of an antenna or simply a probe of appropriate impedance.
- The received signal is amplified at the radio frequency, passed by a mixer having a local oscillator for tuning and frequency scanning, and amplified again at the intermediate frequency.
- To quantify the measured RI, a detection circuit, weighting circuit, and measuring circuit complete the RI measuring meter.

Figure 8.21c shows the circuit used for the detection and measurement of the RI. The detection of the signal envelope is simply a rectifier circuit, composed of a diode D. An $R-C$ series-parallel circuit is used for the weighting of the detected signal. Finally, the average value of the signal at the output of the weighting circuit is measured with an $R-C$ series circuit, having a time constant R_mC_m much larger than that of the weighting circuit. The latter is defined by a charging time constant R_0C and a discharging time constant RC.

Referring to Figure 8.21, different types of measurement are possible, depending on the characteristics of the weighting circuit:

- *Mean value*: Is possible when the discharging time constant RC is sufficiently small so that the weighting circuit can follow the variations of the signal at the output of the detector.
- *Quasi-peak value*: When the discharging time constant RC is in the order of a few hundred milliseconds, the signal at the output of the weighting circuit does not closely follow the variations of the detected signal. The measured value approaches without being equal to the peak value.
- *Peak value*: When the discharging time constant RC is very large, the measured value is determined by the maximal value reached by the detected signal.

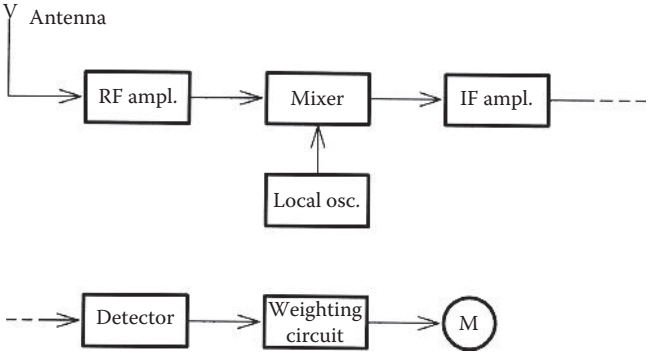


FIGURE 8.20 Measurement of RI—weighting circuit.

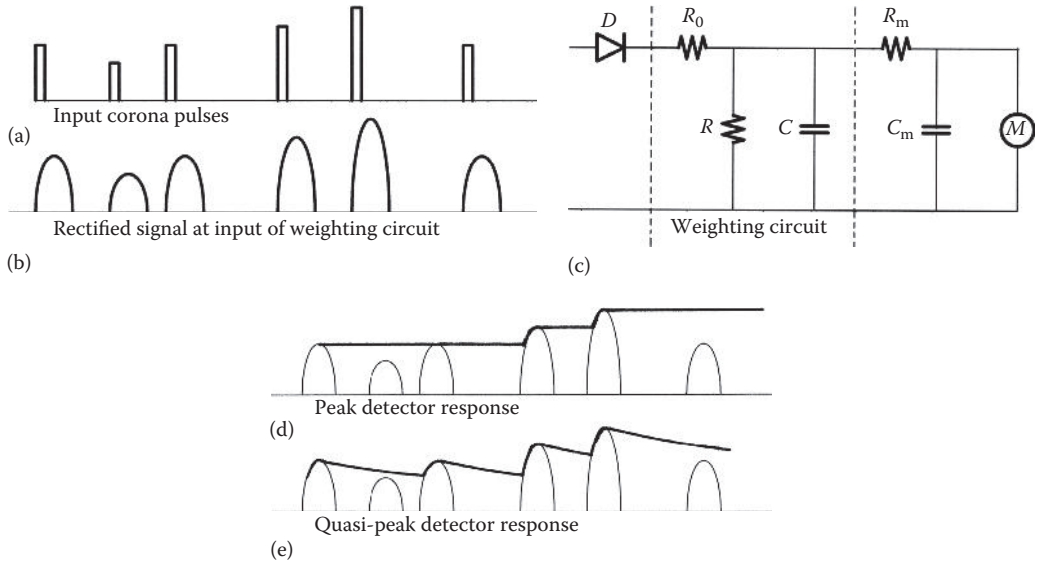


FIGURE 8.21 Responses of weighting circuits as a function of repetition rate of the input pulses.

Of the previous three types of measurement, the quasi-peak value is mostly used. The standardized characteristics of the weighting circuit are as follows:

- *ANSI* (America): charging time, 1 ms; discharging time, 600 ms; bandwidth, 5 kHz
- *CISPR* (Europe): charging time, 1 ms; discharging time, 160 ms; bandwidth, 9 kHz

The two circuits differ by their discharging time constant: higher in the *ANSI* circuit, and their bandwidth: larger for *CISPR* meter. These characteristics of the weighting circuit directly affect the measured signal level, which is higher with *ANSI* circuit, as shown by the results of Figure 8.22, comparing responses of the two weighting circuits as a function of the repetition rate of the input pulses.

The use of quasi-peak measurements, however, poses a problem when one would like to compare the measurements with calculated values, because the latter are expressed in effective values, which, strictly

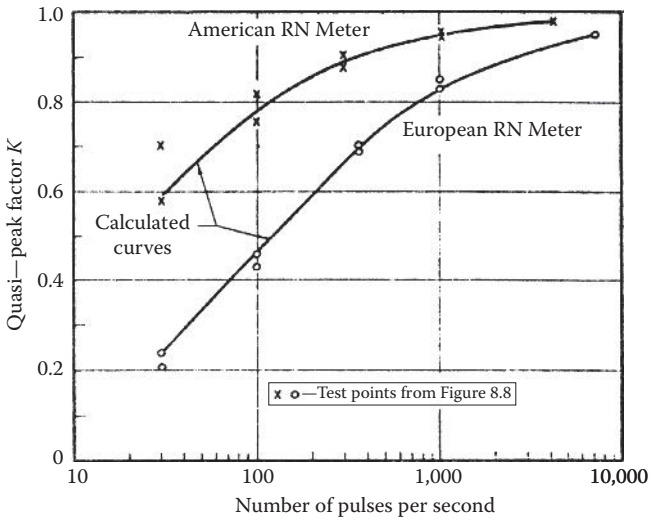


FIGURE 8.22 Correction for the response of the RI measuring circuit to the pulse repetition rate. (From Nigol, O., IEEE Trans., PAS-83(5), 524, 1964.)

speaking, do not compare with measurements made in quasi-peak values. Fortunately, the difference is not significant to affect such comparisons and to maintain the current use of quasi-peak in RI measurements.

Quality of radio reception: The choice of the quasi-peak values for measuring the RI resides mainly in the fact that they represent adequately the subjective evaluation of the degree of acceptability of RI in the radio reception. It was shown that adequate listening of the radio signal is obtained when the signal to noise ratio S/N is higher than 22 dB, with S/N defined as

$$\frac{S}{N} = 20\log\frac{\text{Signal}}{\text{Noise}} \tag{8.46}$$

Measurement of magnetic and electric interference field: The electric and magnetic components of the interference field are related according to

$$Z_0 = \frac{E}{H} = \sqrt{\frac{\mu_0}{\varepsilon_0}} = 120\pi \tag{8.47}$$

where Z_0 is the *characteristic impedance*, also known as *wave impedance*, of free space.

The electromagnetic interference field can thus be defined either by its magnetic or electric components, with the latter being most often used. The magnetic interference field can be measured with a loop antenna, while the electric field is measured with a rod antenna. Referring to Figure 8.23, showing the electric and magnetic interference field at ground, it can be seen that the rod antenna, normally vertical, is already in the direction of the electric field and does not require any orientation. For the loop antenna, since the magnetic field is parallel to ground, one must orientate the antenna in order to obtain a maximal reading of the magnetic interference field. It should be noted that because of the finite depth of the magnetic ground, the magnetic field measured at ground does have a small vertical component, which is generally neglected.

Some practical aspects of the measurement of radio interference from power lines

Unit of measure: The measured electric field intensity is expressed in μV/m. The meter is calibrated in terms of the input field, via a rod antenna (for the measurement of electric field) or a loop antenna (for the measurement of the magnetic component). Rod antenna is generally preferred to the loop antenna for its greater sensitivity, in spite of the fact that it is easily disturbed by the ambient environment.

Radio interference level: Because of its wide range of variations, it is generally expressed in decibel (dB) above a reference level, arbitrarily set at RI_{re} = 1 μV/m according to

$$\text{RI (dB)} = 20\log\frac{\text{RI}}{\text{RI}_{re}} \tag{8.48}$$

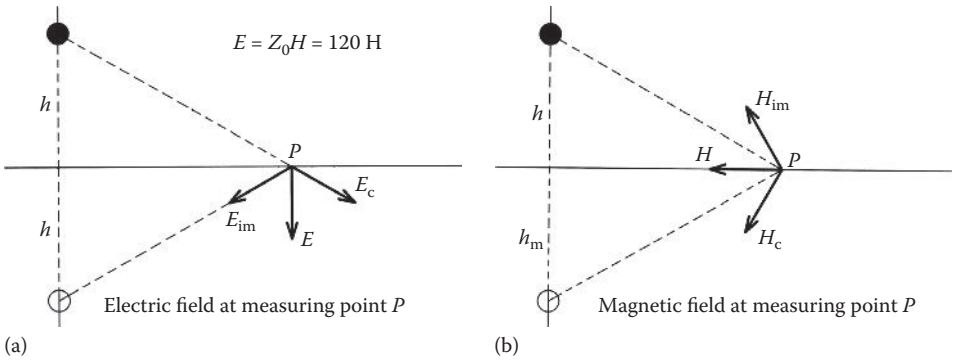


FIGURE 8.23 Measurements of RI interference field. $\mathbf{H}_c$ and $\mathbf{E}_c$ are magnetic and electric field components from the conductor, $\mathbf{H}_{im}$ and $\mathbf{E}_{im}$ are field components from the image conductor, and $\mathbf{H}$ and $\mathbf{E}$ the resulting magnetic and electric fields. h is the height of the conductor above ground, h_m is the depth of the magnetic image of the conductor below ground.

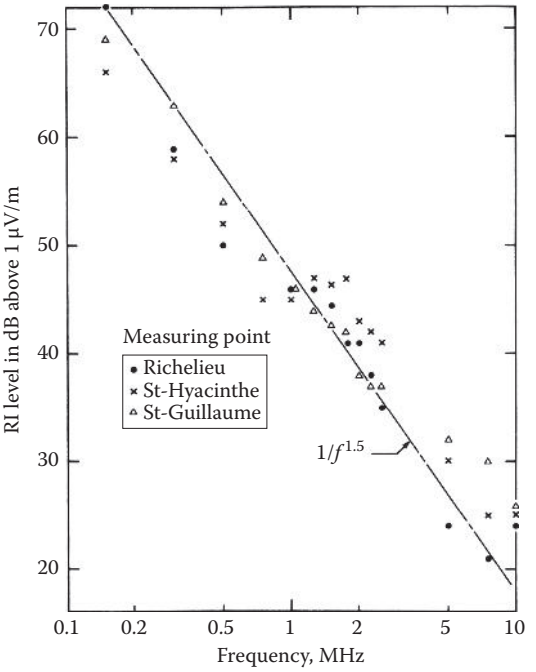


FIGURE 8.24 Frequency spectrum of RI from 735 kV lines of *Hydro-Québec*. (From Maruvada, P.S. and Trinh, N.G., *IEEE Trans*., PAS-94(5), 1714, 1975.)

Factors affecting the measurement of radio interference

Measuring frequency: The frequency spectrum of RI from HV transmission lines, when presented in dB versus log(f), decreases with the frequency with a slope of $1/f^{1.5}$, as illustrated by the results in Figure 8.24, showing the frequency spectrum of the RIs measured close to a 735 kV line of *Hydro-Québec* (Maruvada and Trinh, 1975). Consequently, the measuring frequency of RI is usually selected to be within the AM frequency range, typically 1.0 MHz in North America and 500 kHz in Europe.

Distance from the line: The effect of distance is best described by the lateral profile of the interference level, which represents variations of the interference level measured at midspan, and following a perpendicular path to the line.

Atmospheric conditions: Rain and snow, etc. can affect the surface conditions of the conductors and hence, the RI performance of the line. The effect of weather conditions is best represented by the statistical distribution of the interference level RI measured at a fixed distance from the line, usually 15 m. from the external phase, over a long period of time, at least one year, to cover all the atmospheric conditions encountered by the line.

8.3.3.5 Empirical Formulae for the Calculation of Interference from a Line

In the early days of RI, the lack of an adequate theory to evaluate the electromagnetic interference from HV lines has favored the use of experimental data obtained from operating lines to predict the RI of new lines. The establishment of an empirical formula generally begins with the definition of the principal parameters affecting the phenomenon studied. For the radio interference, RI, these are the electric field E_0 at the conductor surface, in kV/cm; the diameter d of the conductor, in cm; and the lateral distance r from the measuring point to the outer phase of the line, in m. One obtains

$$\mathrm{RI} = f\left(E_0, d, r\right)$$

Assuming a function of the exponential type, the preceding equation can be rewritten as

$$\mathrm{RI} = AE_0^{\,a} d^{b} r^{g}$$

Expressing the RI level in dB above 1 μV/m, one obtains

$$\mathrm{RI}\ (\mathrm{dB}) = 20\log\left(AE_0^{\,a}d^{b}r^{g}\right) = \mathrm{RI}_0 + 20a\log\left(E_0\right) + 20b\log\left(d\right) + 20g\log\left(r\right)$$

With appropriate experimental data, the values of RI_0, α, β, and γ can be determined to best represent the calculated RI with respect to the available experimental data. A number of empirical formulae have been derived during the 1970s. They are summarized in the IEEE review on the subject (IEEE Radio Noise Committee, 1973). A typical formula is introduced by *Ontario-Hydro*:

$$\mathrm{RI} = \mathrm{RI}_0 + A\log\left(\frac{E_0}{18.8}\right) + 40\log\left(\frac{d}{2.54}\right) + B\log\left(\frac{30.5}{r}\right) + 20\log\left(\frac{C+1}{C+f^2}\right) \tag{8.49}$$

with the parameters A and B given in Table 8.3 for different line configurations, weather conditions and measuring frequencies. C is a correction parameter for the measuring frequency $C = 1$ for $f \geq 1$ MHz, and $C = 0.5$ for $f < 1$ MHz.

It is to be noted that dimensions of the bundle do not significantly modify the RI of the line and are not taken into account in the formula. The accuracy obtained with the empirical formula of *Ontario-Hydro* is about 6 dB. For a specific line, most of the specific terms in the preceding equations are constant, and the empirical formula simplifies significantly, becoming a function of the lateral distal x from the outer phase. Thus, for the 735 kV line of Hydro-Québec, the empirical formula for the RI under conditions of fair weather simplifies to

$$\mathrm{RI}\left(x\right) = 63.1 - 40\log\left(\frac{x}{15}\right)$$

Depicting the variations of the RI level with respect to the lateral distance x from the outer phase of the line. The reference lateral distance is 15 m, corresponding to the limit of the right of way. Figure 8.25 compares the calculated lateral profile with different profiles of the RI level under various weather conditions. It can be seen that the empirical formula applies to maximum fair weather conditions and mainly for distances beyond the rights-of-way. At close distances, considerable differences can be observed between calculated and actual measured values of the RI levels.

8.3.3.6 Calculation of Electromagnetic Interference on a Single-Phase Line

Although the RI field is often referred to by its electric component, its calculation is generally made via its magnetic component, since the corona interference field is generated by the discharge current circulating in the line conductors. The electric component of the interference field is next obtained from Equation 8.47 relating the magnitude of the two field components.

The development of a streamer discharge corresponds to the injection of a current impulse into the line conductor. At the injection, the current pulse sees two long half lines of equal impedance. It divides itself in two identical pulses of amplitude, equal to half-value of the injected pulse, and propagates in opposite directions. Furthermore, in a multiphase line, the capacitive coupling between the phase conductors also induces current pulses on the other line conductors. These currents, injected and induced,

TABLE 8.3

Parameters used in the RI Empirical Formula of Ontario Hydro

	Fair	**Foul**	
Parameters	RI_0	RI_0	Coeff. B
Horizontal	34	63	40
Vertical	37	66	32
Coefficient A	146	120	
Measuring frequency	≥1 MHz	<1 MHz	
Coefficient C	1	0.5	

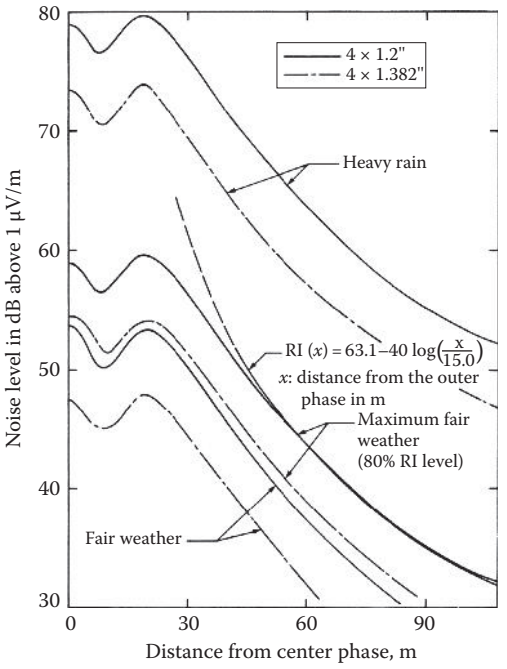


FIGURE 8.25 Lateral profile of 735 kV line—Empirical formula. (From Maruvada, P.S. and Trinh, N.G., *IEEE Trans.*, PAS-94(5), 1714, 1975.)

propagate along the line conductors, which serve as emitting antenna for the interference generated by corona discharges. Calculations of the electromagnetic interference of a HV transmission line must take into account these aspects. Their amplitude decreases with the traveled distance following an exponential function:

Propagation of interference along the line: Propagation of a transient wave along HV line is discussed in Chapter 1. It suffices to mention here the main findings: upon injection, the current pulse is divided in two current pulses of same form propagating in opposite directions of the line from the injection point at a propagation velocity of v m/s.

Their amplitude decreases with the traveled distance following an exponential function: $\exp\left(-\alpha\left|\frac{x}{v}\right|\right)$ according to:

$$i(x,t) = \exp\left(-\alpha\left|\frac{x}{v}\right|\right) i_0(x,t) = \exp(-\alpha x) i_0(x,t) \tag{8.50}$$

where α is an attenuation constant.

Power spectral density of the interference current on a single-phase line: For an HV line under corona, there exist a multitude of discharge sites uniformly distributed along the line. It can be assumed that the injection of the electromagnetic interference is defined by a discharge current density J_0, having a spectral power density $\phi_0(\omega)$, related to each other by

$$J_0(\omega) = \sqrt{\frac{1}{\pi}\phi_0(\omega)\Delta\omega} = \sqrt{2\phi_0(f)\Delta f} \tag{8.51}$$

where ω is the measuring frequency. In addition, since one assumes a uniform distribution of spectral power density of the interference current, the unit of the spectral power density $\phi_0(\omega)$ is $\mu A^2/m$. Consequently, the unit of the interference current density J_0 must be $mA/\sqrt{m}$.

The interference current injected at the point $P(x)$ located at a distance x from the measuring point, taken as origin of the abscissa, is

$$\Delta I_0(\omega) = \frac{1}{2} J_0(\omega)\,dx \tag{8.52}$$

The factor 1/2 takes account of the fact that the interference current pulse is dividing in two upon injections (Figure 8.26). The interference current at the measuring point can then be evaluated by taking into account the contributions of the injected interference currents $\Delta I_0(\omega)$ over the line. However, it must be noted that because of the random nature of the injected interference currents $\Delta I_0(\omega)$, their contributions to the interference current cannot be directly added at the measuring point, but rather by adding the spectral power density of the injected interference currents.

Due to the attenuation occurring during their travel along the line, the injected interference current $\Delta I_0(\omega)$ is reduced to $\Delta I(\omega)$ at the measuring point:

$$\Delta I(\omega) = \frac{1}{2} J_0(\omega)\exp(-\gamma|x|)\,dx \tag{8.53}$$

with a spectral power density of $\Delta\Phi(\omega)$.

Expressing $\Delta I(\omega)$ as

$$\Delta I(\omega) = K(\omega) J_0(\omega)\,dx$$

with the transfer function $K(\omega)$ defined as $K(\omega) = \frac{1}{2}\exp(-\gamma|x|)$, the following relation between the spectral power density of the interference is obtained:

$$\Delta F(\omega) = |K(\omega)|^2 f_0(\omega)\,dx \tag{8.54}$$

The spectral power density of the RI at the measuring point $F(\omega)$ is the integration of all the contributions from the discharge sites distributed along the line. One obtains by integrating the preceding equation for the values of x from $-\infty$ to $+\infty$:

$$F(\omega) = \int_{-\infty}^{+\infty} |K(\omega)|^2 f_0(\omega)\,dx = 2\int_{0}^{+\infty} |K(\omega)|^2 f_0(\omega)\,dx = 2\int_{0}^{+\infty} \left(\frac{1}{2}\exp(-\gamma|x|)\right)^2 f_0(\omega)\,dx$$

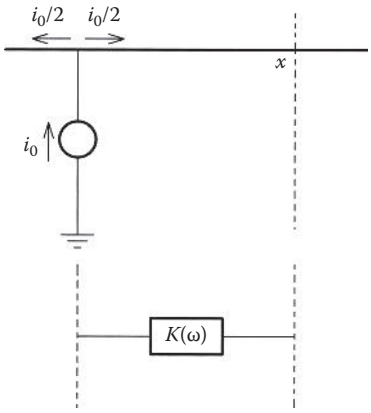


FIGURE 8.26 Measurements of RI on a HV line.

If one neglects the phase angle introduced by the propagation of the current wave, the propagation constant γ is reduced to $\gamma = \alpha$ and

$$F(\omega) = \frac{1}{4a} f_0(\omega) \tag{8.55}$$

Since the characteristics of a RI meter are that of a band-pass filter, there exists a correspondence between the effective value of the injected interference current $I(\omega)$ and the spectral power density $\Phi(\omega)$ at the input of measuring apparatus. According to Equation 8.45, the interference current at the measuring point is

$$I(\omega) = \sqrt{\frac{1}{p} F(\omega) \Delta\omega} = \sqrt{\frac{1}{p} \frac{f_0(\omega)}{4a} \Delta\omega} \tag{8.56}$$

By noting that the relation between the spectral power density $\phi_0(\omega)$ and the density of the interference current is

$$J_0(\omega) = \sqrt{\frac{1}{p} f_0(\omega) \Delta\omega} \tag{8.57}$$

it follows that the relation between the interference current $I(\omega)$ and the density of the injected interference current $J_0(\omega)$ is

$$I(\omega) = \frac{J_0(\omega)}{2\sqrt{a}} \tag{8.58}$$

The RI from an HV transmission line can be evaluated from the characteristic parameters defining the line and knowing the spectral power density of the injected current per unit of length of the line, under condition of corona discharge.

Excitation function of radio interference: In spite of the simple relation between the interference current at the point $P(x)$ and the injected interference current J_0 per unit length of the line conductor, the latter is a function of the line parameters, in particular of the capacitance C to ground, which further complicates the evaluation of the RI. A breakthrough was made with the concept of *excitation function* $\Gamma(\omega)$, introduced by Moreau and Gary of *EDF* in the 1970 (Gary, 1972; Moreau and Gary, 1972a) according to

$$G(\omega) = \frac{2\pi\varepsilon_0}{C} J_0(\omega) \quad \left[\frac{\hat{E}\ \mathrm{mA}}{\hat{A}\sqrt{\mathrm{m}}}\right] \tag{8.59}$$

The excitation function thus defined is a characteristic defining the capacity of generating electromagnetic interference of the line conductor only. Such a parameter can be determined for different conductors and used for the calculation of RI from a HV line that uses the same conductor.

Radio interference from a single-phase line: The calculation of RI from a single-phase line is made in four stages as follows:

- From the known excitation function of the conductor, calculate the density of the interference current $J_0(\omega)$ at the measuring frequency.
- Calculate the resulting RI current at the measuring point.
- Calculate the magnetic interference field at the measuring point.
- Convert the magnetic interference field into an electric interference field.
- Calculate the RI level in dB.

The contribution to the electromagnetic interference at the measuring frequency ω from corona discharges developing over a section dx of the conductor is

$$J_0(\omega) = \frac{C}{2\pi\varepsilon_0} G(\omega)\,dx \tag{8.60}$$

where C is the capacitance per unit length of the line conductor to ground.

Upon injection, the discharge current divides itself in two identical current pulses of half amplitude and propagating in opposite directions from the discharge site. At the measuring point located at a distance x along the line from the discharge site, the interference current is distorted according to

$$I(\omega,x)\,dx = I_0(\omega)\exp(-\alpha x)\,dx = \frac{1}{2} J_0(\omega)\exp(-\alpha x)\,dx$$

where the propagation constant is represented approximately by its real component

The total interference current circulating in the line conductor is the sum of all contributions from the different corona sites along the line conductor and is given by

$$I(\omega) = \sqrt{\int_{-\infty}^{\infty} |I(\omega,x)|^2\,dx} = \frac{J_0(\omega)}{2\sqrt{\alpha}} \tag{8.61}$$

The circulation of the interference current in the line conductor generates an electromagnetic field around the conductor, which can be captured by an antenna of a radio and/or television receiver located in the immediate surrounding of the line. The current practices characterize the interference field in terms of its electric component, $E(\omega)$, expressed in decibels (dB) above the reference level of 1.0 μV/m. The evaluation of the electromagnetic interference is made generally by calculating at first the magnetic interference field $H(\omega)$ at the measuring point, taking into account the magnetic image of the conductors, with respect to a fictive magnetic ground plane:

$$\mathbf{H}(\omega) = \sum_j \frac{1}{2\pi r_j} I_j(\omega)\,\mathbf{a}_r \tag{8.62}$$

For a typical soil of resistivity of ρ = 100 Ohm-m, a permeability of $\mu_0 = 4\pi\ 10^{-7}$, the penetration depth of the magnetic field d_p is equal to 7.11 m at the measuring frequency of f = 1 MHz (in North America—*ANSI/IEEE*). It increases to 10.07 m when the measuring frequency is reduced to 500 kHz (in Europe—*CISPR*).

The summation is made for all the phase conductors of the line and their images with respect to the magnetic ground. The electric interference field can then be determined according to the following relation:

$$E(\omega) = \sqrt{\frac{\mu_0}{\varepsilon_0}} H(\omega) \tag{8.63}$$

Radio interference from a phase (central) conductor: The 735 kV line of *Hydro-Québec* uses a bundle of four conductors of d_c = 3.05 cm in diameter. The electric field at the surface of conductors is E_c = 19.79 kV/cm (on the central phase), and the average height of the conductors is h_c = 19.8 m. The capacitance of the bundle conductor to ground is C_1 = 10.57 pF/m.

We will calculate the contribution from the central phase to RI level at a lateral distance of 28.7 m (at the edge of the rights-of-way) by considering it as a single-phase line. Consider a unit excitation function of $G(\omega) = 1.0\ \mu A/\sqrt{m}$. It follows that the density of the injected interference current into the conductor is

$$J_0(\omega) = \frac{C_1 G}{2\pi\varepsilon_0} = 1.901 \times 10^{-7} \quad \frac{\mu A}{\sqrt{m}}$$

TABLE 8.4

Modal Attenuation Coefficients

Line Configuration	**Triangle**		**Horizontal Flat**	
f_0 = 500 kHz [6.13]	**(dB/km)**	**(10^{-6} Np/m)**	**(dB/km)**	**(10^{-6} Np/m)**
Mode 1	0.2	21.5	0.1	11.1
Mode 2	0.2	21.5	0.5	54
Mode 3	3.0	342	3.0	342
f_0 = 1.0 MHz	**(dB/km)**	**(10^{-6} Np/m)**	**(dB/km)**	**(10^{-6} Np/m)**
Mode 1	—	—	0.15	17.3
Mode 2	—	—	1.0	115
Mode 3	—	—	6.0	691

Source: Moreau, M.R. and Gary, C.H., *IEEE Trans*., PAS-91, 292, 1972b.

Assuming a value for the attenuation coefficient of $\alpha = 691\ 10^{-6}$ Np/m (Table 8.4, mode 3), the interference current $I(\omega)$ at the measuring point is

$$I(\omega) = \frac{J_0(\omega)}{2\sqrt{a}} = 3.616 \times 10^{-6} \tag{A}$$

The magnetic field generated by the interference current, I, and its image with respect to the magnetic ground, I^*, at the measuring point P located at a lateral distance of 28.5 m (or 15 m from the outer phase of a 735-kV line) is

$$H = \frac{I}{2\pi\sqrt{R^2 + h^2}}\cos\theta + \frac{I_m}{2\pi\sqrt{R^2 + h_m^2}}\cos\theta_m$$

where θ is the angle between the line relating P to the conductor and the vertical (Figure 8.6).

It follows:

$$H = 9.461\ 10^{-9} + 9.938\ 10^{-9} = 1.939\ 10^{-8} \quad \text{A/m}$$

The corresponding electric field component is

$$E = \sqrt{\frac{\mu_0}{\varepsilon_0}}\, H = 120\pi H = 7.313 \times 10^{-6} \quad \text{V/m}$$

Finally, the RI level produced by the line is

$$\text{RI}\ (\text{dB}) = 20\log\left(\frac{E}{10^{-6}}\right) = 17.3\ \text{dB}$$

For the central phase of the 735 kV line, the excitation function is 43.52 dB above $1\ \text{mA}/\sqrt{\text{m}}$. The calculated RI level is 60.80 dB. Compared to the measured RI of 71 dB at 15 m from the outer phase of the 735-kV line of *Hydro-Québec* (Figure 8.25), the calculated interference level from the central phase alone is 10 dB lower and illustrates the effect of the contribution of the other two phases of the line to the overall level of RI.

8.3.3.7 Calculation of Electromagnetic Interference from a Three-Phase Line

Because of the high-frequency nature of the interference current, the calculation of the interference field from a three-phase line must take into account the mutual capacitive coupling among the phase conductors, which significantly complicates the calculation. Consider a section dx of a line conductor with a RI excitation function Γ (Moreau and Gary, 1972a), the RI current generated by the corona discharge is

$$i_0(\omega)\,dx = \frac{1}{2\pi\varepsilon_0} C G(\omega)\,dx \tag{8.64}$$

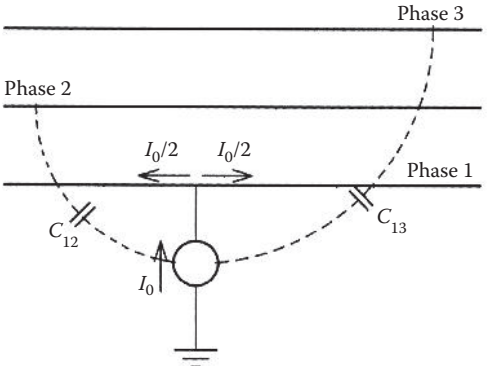


FIGURE 8.27 Propagation of the interference current on a three-phase line.

Because of the capacitive coupling among the line conductors (Figure 8.27), the injected current $i_0(\omega)\mathrm{d}x$ induces RI current to be injected in the other phases of the line as well and can be expressed in a matrix form as

$$\left[\mathrm{d}I_0(\omega)\right] = \frac{1}{2\pi\varepsilon_0}[C][G(\omega)]\mathrm{d}x \tag{8.65}$$

Direct calculation of the interference current is rather complex. The modal analysis provides a practical means to evaluate the interference current circulating in the line conductors and their corresponding interference field. In this approach, the interference current is first transformed into its modal components, which propagate without distortion along the line, each at its own velocity. This property of the modal currents allows the evaluation of the modal components in an independent manner and their reconstitution of the interference wave at the measuring point. The reader can find an extensive analysis of this approach to calculate the RI from HV lines in Maruvada (2000). We present in the following a simplified approach of Moreau and Gary (1972b), which focuses on the RI current associated with the concept of excitation function Γ.

The calculation of the RI current is made in three stages:

- Decomposition of the interference current into its modal components can be expressed as

$$\left[\mathrm{d}I_0(\omega)\right] = [M]\left[\mathrm{d}I_0(\omega)\right]$$

  It follows the expression for the modal current:

$$\left[\mathrm{d}I_0(\omega)\right] = [M]^{-1}\left[\mathrm{d}I_0(\omega)\right] \tag{8.66}$$

  where

  $[M]$ is the modal transformation matrix

  $j_0(\omega)$ is the modal components of the injected interference current

- Evaluate the modal components at the measuring point, taking into account the propagation characteristics proper to each modal component. As discussed previously, the modal component $[J(\omega)]$ at the measuring point located at a distance x from the injection point is given by

$$\left[\mathrm{d}J(\omega)\right] = \frac{1}{\left[2\sqrt{\alpha}\right]}\left[\mathrm{d}I_0(\omega)\right] = \frac{1}{2\left[\sqrt{\alpha}\right]}[M]^{-1}\left[\mathrm{d}I_0(\omega)\right] = \frac{1}{4\pi\varepsilon_0}\frac{1}{\left[\sqrt{\alpha}\right]}[M]^{-1}[C][G] \tag{8.67}$$

- Reconstitute the interference wave at the measuring point according to

$$\left[J(\omega)\right] = [M]\,\left[J(\omega)\right] \tag{8.68}$$

The magnetic and electric field at the measuring point, produced by the interference current, can then be evaluated according to Equations 8.62 and 8.63.

Modal transformation matrix: Several modal transformation matrices can be defined for a given line configuration. Moreau and Gary (1972b) obtained good concordance between the calculated and experimental results with the symmetric component modes of *Clarke*, of which the transformation matrix is

$$[M] = \begin{bmatrix} 1/\sqrt{6} & 1/2 & 1/\sqrt{3} \\ -2/\sqrt{6} & 0 & 1/\sqrt{3} \\ 1/\sqrt{6} & -1/2 & 1/\sqrt{3} \end{bmatrix} \tag{8.69}$$

Another modal transformation matrix can be derived from the geometric matrix [*P*] of the line, using the following relationship (Trinh et al., 1974):

$$[M]^{-1}\,[P]\,[M] = [\lambda]_d$$

which can be rewritten as

$$[P]\,[M] = [\lambda]_d\,[M]$$

or

$$\left\{[P] - [\lambda]_d\right\}\,[M] = 0 \tag{8.70}$$

where

[*P*] is the matrix of the potential coefficients

$[\lambda]_d$ is the diagonal spectral matrix, which is related to the matrix of modal characteristic impedances, according to

$$[Z_m] = 60\,[\lambda]_d . \tag{8.71}$$

The preceding equation can be rewritten as

$$\begin{bmatrix} p_{11}-1 & p_{12} & p_{13} \\ p_{21} & p_{22}-1 & p_{23} \\ p_{31} & p_{32} & p_{33}-1 \end{bmatrix} \begin{bmatrix} m_{11} & m_{12} & m_{13} \\ m_{21} & m_{22} & m_{23} \\ m_{31} & m_{32} & m_{33} \end{bmatrix} = 0$$

which has a nontrivial solution only if the determinant of the first matrix is null:

$$\begin{vmatrix} p_{11}-1 & p_{12} & p_{13} \\ p_{21} & p_{22}-1 & p_{23} \\ p_{31} & p_{32} & p_{33}-1 \end{vmatrix} = 0 \tag{8.72}$$

Equation 8.72 is reduced to a third-degree equation of λ, the solution of which determines the coefficients of the geometric modal transformation matrix. For a three-phase line, the modal transformation matrix is

$$[M] = \begin{bmatrix} \dfrac{1}{\sqrt{2+p^2}} & \dfrac{p}{\sqrt{2+p^2}} & \dfrac{1}{\sqrt{2+p^2}} \\ \dfrac{1}{\sqrt{2}} & 0 & \dfrac{1}{\sqrt{2}} \\ \dfrac{1}{\sqrt{2+q^2}} & \dfrac{q}{\sqrt{2+q^2}} & \dfrac{1}{\sqrt{2+q^2}} \end{bmatrix} \tag{8.73}$$

with $p = 2p_{12}/(\lambda_1 - p_{22})$ and $q = 2p_{12}/(\lambda_3 - p_{22})$, and λ_i the eigenvalue of the matrix [*P*].

Coefficients of modal attenuation, α: Are generally a function of the line configuration, the resistivity of the soil, and the measuring frequency *f*. Typical values of α are presented in Table 8.4. They are adjusted to the measuring frequency according to (Moreau and Gary, 1972b)

$$\alpha(f) = \alpha(f_0)\left(\frac{f}{f_0}\right)^{0.8} \tag{8.74}$$

where f_0 is the reference frequency at which the data are obtained.

Example of calculation: The case of the 735-kV line of *Hydro-Québec*, the parameters of which are presented in Table 8.2, will be considered below to illustrate this approach to the calculation of RI from HV transmission lines. This requires that the noise current be first transformed into its modal components. Consider a noise current of unit excitation function $G(w) = 1.0\ \text{mA}/\sqrt{\text{m}}$ circulating in phase A of the line. Because of the capacitive coupling, it induces currents to the other two phases of the line as well. For *Hydro-Québec*'s 735 kV line,

the capacitance matrix is

$$C = \begin{bmatrix} 11.204 & -2.241 & -0.73 \\ -2.241 & 11.605 & -2.241 \\ -0.73 & -2.241 & 11.204 \end{bmatrix} \text{ pF/m}$$

and the noise current in phase A and its induced currents to phases B and C are

$$i_a(w) = \begin{bmatrix} 11.204 \\ -2.241 \\ -0.73 \end{bmatrix} \text{ mA}$$

The modal transformation matrix is

$$[M] = \begin{bmatrix} 0.45399 & 0.70711 & 0.542122 \\ -0.76667 & 0 & 0.64204 \\ 0.45399 & -0.70711 & 0.54212 \end{bmatrix}$$

The inverse modal matrix, more precisely, the product of $\left(\frac{1}{\sqrt{a}}\right)[M^{-1}]$ is

$$\left(\frac{1}{\sqrt{a}}\right)[M^{-1}] = \begin{bmatrix} 103.334 & -174.514 & 103.339 \\ 72.925 & 0 & -72.925 \\ 22.216 & 26.313 & 22.216 \end{bmatrix}$$

Using Equations 8.65–8.67 gives the following unit modal noise currents at the measuring point, taking into account the different attenuations of modal currents:

$$[u_m] = \begin{bmatrix} 13.24 & -22.35 & 13.24 \\ 7.82 & 11.08 & -7.82 \\ 1.56 & 1.85 & 1.56 \end{bmatrix}$$

These modal currents, once transformed back to the injected and induced interference currents, Equation 8.68, gives the modal components of the noise currents flowing in the line conductors at the measuring point, as related to the noise current injected to phase A:

$$I_a(\omega)=[M][u_{ma}]$$

where $[u_{ma}]$ is the diagonal matrix of the modal coefficients associate with the noise current in phase A.

$$I_a(w) = \begin{bmatrix} 12.39 \\ -9.15 \\ 1.328 \end{bmatrix} = \begin{bmatrix} 6.012 & -5.531 & 0.846 \\ -1.015 & 0 & 1.003 \\ 6.012 & -5.531 & 0.846 \end{bmatrix} \text{ mA}$$

These currents can then be used to calculate the normalized magnetic and electric interference fields, using Equations 8.62 and 8.63. For the interference injected in phase A and its induced interference currents in phase B and C, the resultant magnetic field at the measuring point is simply the algebraic sum of the three field components, according to:

$$H_a(\omega) = H_{a1}(\omega) + H_{a2}(\omega) + H_{a3}(\omega)$$

with

$$H_{ai} = \frac{I_{ai}}{2\pi}\left[\frac{h}{(x_i + h)^2} + \frac{h + d_p}{(x_i + h + 2d_p)^2}\right]$$

where

h is the height of the conductor above ground in m

d_p the penetration depth of the magnetic field in m, given by Equation 8.9

$(h + 2d_p)$ corresponds to the depth of the magnetic image of the conductor below ground

The normalized electric interference field $E_a(\omega)$ is

$$E_a(\omega) = 120\ \pi H_a(\omega)$$

For a point located at the edge of the right of way of the case of the *Hydro-Québec* 735-kV line, a lateral distance of $x_p = 28.7$ m from the center phase, the contribution to the measured RI from the interference current injected in phase A is

$$H_a = 7.118 \text{ mA} \quad \text{and} \quad E_a = 26.83 \text{ μV/m} \quad \text{or} \quad 28.57 \text{ dB above 1 μV/m}$$

The measuring frequency is 1.0 MHz, the penetration depth of the magnetic interference field in the ground is $\delta_p = 5.03$ m. The above electric interference field and interference level are obtained assuming a noise excitation function of 1.0 $\mu A/\sqrt{m}$. For the case of interest, the excitation function at phase A is 39.59 dB and the corresponding interference level is 68.16 dB.

By repeating the same process for the noise currents injected in phases B and C, one obtains effectively two additional sets of magnetic and electric field components generated by the circulation of the interference currents injected in the line conductors B and C. However, since the interference currents are essentially random pulses, the resultant magnetic field at the measuring point is:

$$H_a(\omega) = \sqrt{H_a^2 + H_b^2 + H_c^2}$$

And the corresponding electric field $E_a(\omega)$ is:

$$E_a(\omega) = 120\pi H_a(\omega) = \sqrt{E_a^2 + E_b^2 + E_c^2}$$

For the preceding measuring point, their contributions to the interference level are, respectively, 59.50 and 40.91 dB, resulting in a total noise level of 68.72 dB at the measuring point as compared with the measured interference level of 70 dB. Figure 8.28 shows the complete lateral profiles of *Hydro-Québec* 735-kV lines under foul weather conditions.

8.3.3.8 Television Interference

As for the case of RI, the television receiver can also be represented by a band-pass filter of fixed bandwidth and a tunable central frequency. The problem of interference to the television reception is, therefore, essentially the same as for the radio reception. The preceding analysis of the RI applies also to the television interference, taking into account the fact that the video and audio information are transmitted, respectively, by amplitude and frequency modulation, and the carrier frequencies for

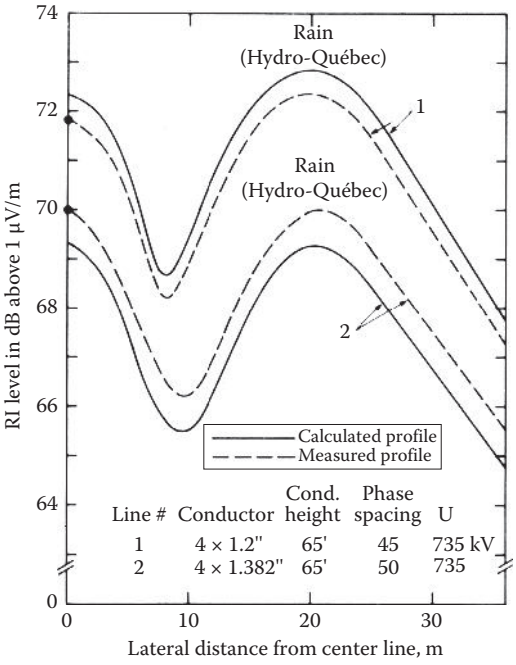


FIGURE 8.28 Comparison of calculated lateral profiles of RI with measurements made under *Hydro-Québec* 735 kV lines.

television signal are in the range of 100 MHz, which are much higher than the MHz frequency range for AM radio signals.

Mechanism of television interference: The functioning of television relies on the separated transmission of the video and audio information: amplitude modulation (bandwidth of 1.5 MHz) for the video signal and frequency modulation (bandwidth of 4 MHz) for the audio signal, respectively. In North America, the television receiver uses an ensemble of 525 horizontal lines to compose the image on the screen, renewed at a rate of 60 times per second. Since electromagnetic interference affects mainly the transmission by amplitude modulation, television interference is more pronounced on the video reception than audio. The effect is further enhanced by the fact that the interference is proportional to the bandwidth of the receiver, larger in television than for radio, and by the accrued sensitivity to noise in images than in sound.

The television interference is caused by streamer discharges, which impinge interference pulses superposed to the video signal. The perceived effect is then a black space on the screen (Figure 8.29). The high carrier frequency used in television, above 54 MHz, has a beneficial effect to the television reception.

Figure 8.30 shows the frequency spectra of corona discharge pulses of positive and negative polarities. It can be seen that both spectra decrease at high frequencies, at a rate of approximately 35 dB per decade. The positive streamers generate current pulses of high amplitude, thus giving rise to a more important interference signal. However, the frequency range associated with these discharges is relatively narrow, of about 1 MHz. Their importance is therefore more pronounced in the radio reception than for television. The negative (Trichel) streamers generate current pulses of small amplitude and produce a lower interference signal; the range of frequencies associated with these discharges is larger, of the order of up to 30–50 MHz.

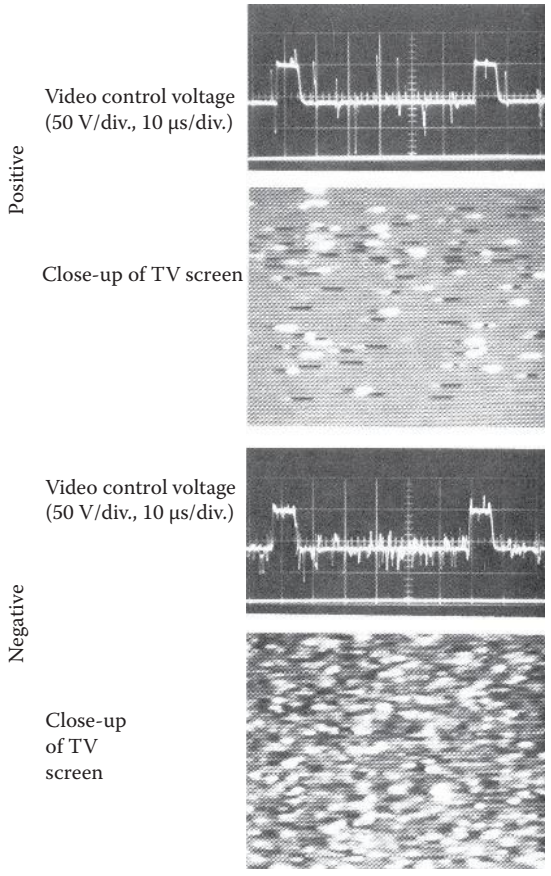


FIGURE 8.29 Interference to the video reception caused by corona discharges. (From Juette, G.W., *IEEE Trans*., PAS-91, 865, 1972.)

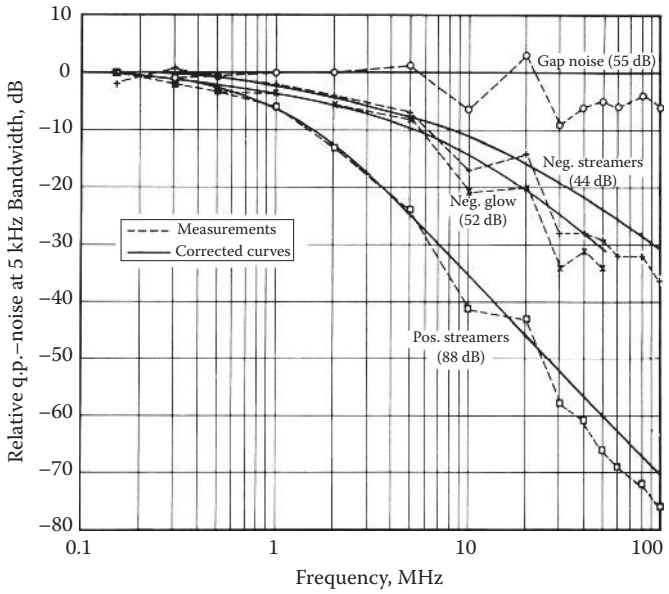


FIGURE 8.30 Frequency spectra of different modes of discharge. (From Juette, G.W., *IEEE Trans*., PAS-91, 865, 1972.)

Their importance is more evident to the television reception and even more so due to the high repetition rate of Trichel streamers, of several tens of kHz.

In summary, because of cutoff frequencies around a few tens of megahertz, of the frequency spectrum of corona discharges, the interference levels at the television frequencies are very much attenuated. Figure 8.30 also shows the frequency spectrum of a spark or *gap discharge*. One notices that this type of discharge has at the same time a strong interference signal and a large frequency spectrum, extending up to frequencies of several hundreds of MHz and can therefore, significantly affect the reception of television signals.

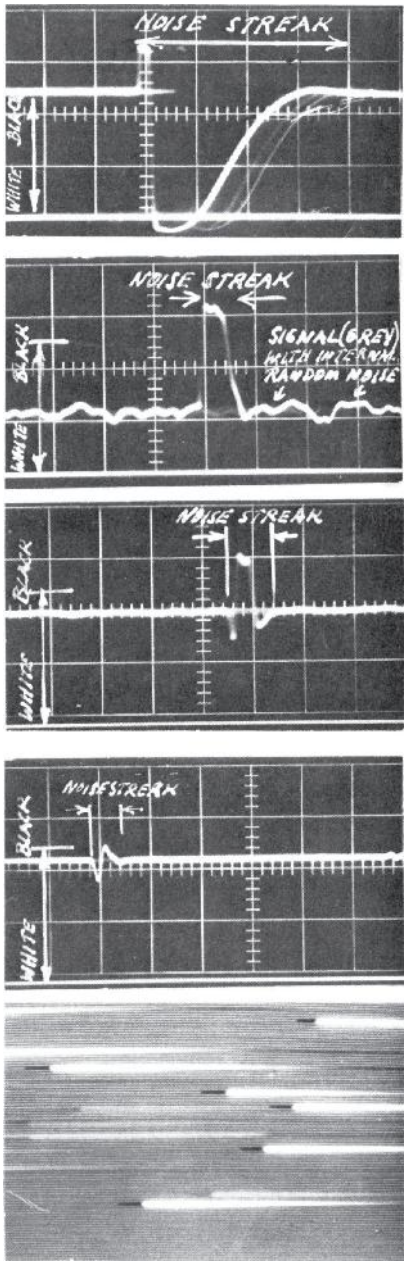
The strong interference pulses can also saturate the video amplifier, which will take a certain time to recover its initial state. The saturation of the video amplifier is characterized by a white space, often referred to as *snow*, on the screen (Figure 8.31) (Juette, 1972). In fact, gap discharges, which generate sharp current pulse with nanosecond rise times, are the principal discharges that effectively interfere with the television reception. These discharges are produced by loose connections, which are a common problem on low-voltage distribution lines, but rarely observed on HV transmission lines of 300 kV and above.

At *UHV* lines of 1000 kV ac and higher, the large diameter of the conductors can introduce new discharge phenomena similar to gap discharge, which produce more intense electromagnetic interference. Figure 8.32 shows the results of an evaluation of the quality of television reception as a function of the signal-to-noise ratio. It can be seen that a ratio of about −10 dB is necessary to ensure a good reception of television in the presence of interferences from corona discharges on HV lines. The signal-to-noise ratio must be increased up to −30 dB in the presence of interferences from the *gap discharges*.

Finally, another source of interferences is related to reflections of television signals at HV line towers, producing ghost images. However, the problem is not related in any way to corona activities on the line conductors.

Measurement of television interference: Is similar to that of RI, with nuances related to the measuring frequencies and the bandwidth of detection circuit, which is of 4 MHz, as compared to 100–150 kHz for the RI meters. The use of certain RI measuring apparatus capable of tuning to television frequencies for measuring television interference is possible. One has to make a correction for the narrow bandwidth of the circuit used, by multiplying the measured value by a factor k_f:

$$k_f = \sqrt{\frac{\Delta f\,(\text{tv})}{\Delta f\,(\text{radio})}} = \sqrt{\frac{4}{0.15}} = 5.16 \tag{8.75}$$



(a)

Signal	58.5 dB
Noise	78.5 dB
Ratio	−20 dB

50 V/div.
5 μs/div.

(b)

Signal	20 dB
Noise	30 dB
Ratio	−10 dB

50 V/div.
2 μs/div.

(c)

Signal	40 dB
Noise	30 dB
Ratio	+10 dB

50 V/div.
2 μs/div.

(d)

Signal	58 dB
Noise	30 dB
Ratio	+28 dB

50 V/div.
2 μs/div.

(e)

Signal	58 dB
Noise	76 dB
Ratio	−18 dB

FIGURE 8.31 Video signals of television interference caused by gap discharges. (From Juette, G.W., *IEEE Trans*., PAS-91, 865, 1972.)

As for the nature of the weighting circuit, peak, quasi-peak, effective, or average value, the discussion is still open.

8.3.4 Audible Noise

The importance of AN in the selection of conductors for HV lines dates back to the years 1970s, with the introduction of lines operating at voltages of 800 kV and higher, for which the corona AN reaches considerable levels under adverse atmospheric conditions: rain, snow, etc. The AN is associated with the

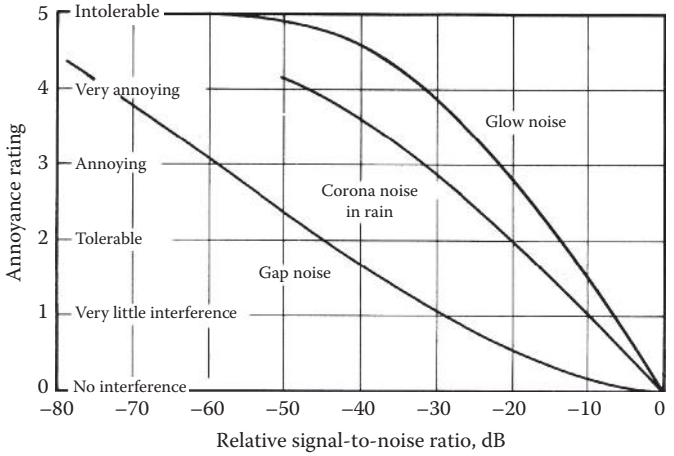


FIGURE 8.32 Subjective evaluation of the image quality in presence of television interference. (From Juette, G.W., Evaluation of television interference from high-voltage transmission lines, IEEE Trans PAS-91, 865, 1972.)

streamer discharges, which cause a sudden temperature rise in the discharge channel and create a corresponding increase in the local air pressure. Consequently, a pulsating sound wave is generated from the discharge site, propagates through the surrounding ambient air, and is perfectly audible in the immediate vicinity of HV lines. The perceived noise is a regular hissing sound related to the high repetition rate of Trichel streamers and a cracking sound accompanying the positive streamers. Different aspects of AN will be discussed in the following.

8.3.4.1 Static and Acoustic Pressures

Consider a gas volume V, the random movement of the gas molecules creates a static pressure P_0 at all points in the gas volume. Because of the random nature of the movement, the static pressure thus created is constant, is omnidirectional, and depends only on the gas temperature, according to the general gas law. When a local disturbance $p(r, t)$ occurs to the static gas pressure, it propagates across the gas volume, generating an acoustic pressure wave to which the human ear may be sensitive. The resulting pressure $P(r, t)$ at any point in the gas volume may be expressed as

$$P(r,t) = P_0 + p(r,t)$$

8.3.4.2 Propagation of Acoustic Wave

The propagation of the acoustic wave across the gas volume is regulated by a differential *wave equation* that can be derived from the fundamental laws of physics.

Newton law: Stipulates that an object of mass m subjected to a force $\mathbf{F}$ is propelled in the direction of the applied force with an acceleration $\mathbf{a}$ according to

$$\mathbf{F} = m\mathbf{a} \tag{8.76}$$

Applying the Newton law to an elementary gas volume ΔV of density ρ_0, subjected to an acoustic pressure $p(r, t)$, the total force applied to the volume ΔV is

$$\mathbf{F} = m\mathbf{a} = \rho_0 \Delta V \frac{\mathrm{d}}{\mathrm{d}t}\mathbf{q}(r,t) \tag{8.77}$$

where $q(r, t)$ represents the apparent velocity of the gas volume ΔV.

On the other hand, in an appropriate Cartesian coordinates system, the force applied to the elementary gas volume ΔV is

$$\mathbf{F} = F_x\mathbf{a}_x + F_y\mathbf{a}_y + F_z\mathbf{a}_z$$

Noting that

$$P_x(r,t) = P_0 + p_x(r,t)$$

it follows

$$dP_x(r,t) = \frac{\partial}{\partial x}P(r,t)dx = \frac{\partial}{\partial x}p(r,t)dx$$

and

$$F_x = -\frac{\partial}{\partial x}p(r,t)dxdydz = -\frac{\partial}{\partial x}p(r,t)\Delta V \tag{8.78}$$

By proceeding in similar manner for the other two components, F_y and F_z, one obtains the expression for the force applied by the acoustic pressure $p(r, t)$ on the elementary gas volume ΔV:

$$\mathbf{F}(r,t) = -\hat{\mathbf{A}}\left(\frac{\partial}{\partial xi}p(r,t)\mathbf{a}_{xi}\right)\Delta V = -\mathbf{grad}\,p(r,t)\Delta V \tag{8.79}$$

Combining Equations 8.77 and 8.79, one obtains the following relation between the velocity of the gas molecules $q(r, t)$ and the acoustic pressure $p(r, t)$:

$$\frac{d}{dt}\mathbf{q}(r,t) = -\frac{1}{\rho_0}\mathbf{grad}\,p(r,t) \tag{8.80}$$

where

ρ_0 is the gas density

$\mathbf{q}(r, t)$ is the velocity of the gas molecules

Gas law: In its most general form, the gas law can be expressed as

$$PV^{\gamma} = Const \tag{8.81}$$

Taking the logarithm of both sides of the preceding equation,

$$\ln P(r,t) + \gamma \ln V(r,t) = Const$$

Taking the derivative of both sides of the preceding equation, one gets

$$\frac{dP(r,t)}{P(r,t)} + \gamma\frac{dV(r,t)}{V(r,t)} = 0 \tag{8.82}$$

The pressure $P(r, t)$ and the volume $V(r, t)$ can be expressed by

$$P(r,t) = P_0 + p(r,t) \approx P_0$$

and

$$V(r,t) = V_0 + \varepsilon(r,t) \approx V_0$$

where V_0 is the static gas volume, that is, $P(r, t) = P_0$, and $\zeta(r, t)$ the variation in the gas volume caused by the acoustic pressure $p(r, t)$. In these conditions, Equation 8.82 becomes

$$\frac{p(r,t)}{P_0} + \gamma \frac{\zeta(r,t)}{V_0} = 0$$

Differentiating both sides of the preceding equation with respect to time, *t,*

$$\frac{1}{P_0}\frac{\partial}{\partial t} p(r,t) = -\frac{\gamma}{V_0}\frac{\partial}{\partial t}\zeta(r,t)$$

or

$$\frac{\partial}{\partial t}\zeta(r,t) = -\frac{V_0}{\gamma P_0}\frac{\partial}{\partial t} p(r,t) \tag{8.83}$$

Law of mass conservation: Stipulates that the total mass of a deformable gas volume must remain the same. It allows the establishment of a unique relation between the rate of variation in time of the volume $\zeta(r, t)$ and the velocity of displacement of the surfaces of the static gas volume V_0. In effect, if the mass of the gas volume V_0 remains constant, the time variations $\zeta(r, t)$ of the gas volume depend only on the difference in the displacement $\xi(r, t)$ of the surfaces defining the elementary gas volume V_0. It follows

$$\frac{\partial \zeta}{\partial t} = V_0 \frac{\partial}{\partial t}(\text{div}\,\xi) = V_0 \,\text{div}\frac{\partial \xi}{\partial t} \tag{8.84}$$

or

$$\frac{\partial \zeta}{\partial t} = V_0 \,\text{div}\frac{\partial \xi}{\partial t} = V_0 \,\text{div}(\mathbf{q}) \tag{8.85}$$

known as the continuity equation, where ξ is the displacement and $\mathbf{q}$ is the velocity of the gas molecules.

Wave equation: Differentiating once again the preceding equation of continuity with respect to time *t*, one obtains

$$\frac{\partial^2 \zeta}{\partial t^2} = V_0 \,\text{div}\frac{\partial q}{\partial t} \tag{8.86}$$

By the Newton laws,

$$\frac{\mathrm{d}}{\mathrm{d}t}\mathbf{q}(r,t) = -\frac{1}{\rho_0}\mathbf{grad}\, p(r,t)$$

which gives

$$\frac{\partial^2 \zeta}{\partial t^2} = -\frac{V_0}{\rho_0}\text{div}\ \mathbf{grad}\, p(r,t) = -\frac{V_0}{\rho_0}\nabla^2 p(r,t)$$

or

$$\nabla^2 p(r,t) = -\frac{\rho_0}{V_0}\ \frac{\partial^2}{\partial t^2}\ \zeta(r,t) \tag{8.87}$$

On the other hand, by the gas law, and differentiating with respect to time, Equation 8.83 gives

$$\frac{\partial^2}{\partial t^2}\zeta(r,t) = -\frac{V_0}{\gamma P_0}\frac{\partial^2}{\partial t^2}p(r,t) \tag{8.88}$$

which with (8.87) finally results in the following differential equation:

$$-\nabla^2 p(r,t) = \frac{\rho_0}{\gamma P_0}\frac{\partial^2}{\partial t^2}p(r,t) \tag{8.89}$$

known as the *wave equation*, which governs the propagation of the acoustic wave in the gas volume. One notices that the term $\gamma(P_0/\rho_0)$ depends only on the characteristics of the gas. It has the dimensions of m^2/s^2 and corresponds to the square of the velocity of propagation C of the acoustic wave in the gas volume. The wave equation can then be written as

$$-\nabla^2 p(r,t) = \frac{1}{C^2}\frac{\partial^2}{\partial t^2}p(r,t) \tag{8.90}$$

with

$$C^2 = \gamma\frac{P_0}{\rho_0}$$

In atmospheric air, $P_0 = 1.013\,2 \times 10^5$ N/m^2, and with the values of $\gamma = 1.4$, the density $\rho_0 = 1.18$ kg/m^3, the velocity of propagation of sound is equal to $C = 346.7$ m/s.

8.3.4.3 Solution of the Wave Equation

The solution of differential equation (8.60) defines completely the variations of the acoustic pressure $p(r, t)$ in time and space. In the general case, this solution is not always possible; we limit ourselves to two simple cases of plane and spherical waves, for which the analytical solution is relatively simple.

Plane wave: An acoustic wave is plane when the acoustic pressure $p(r, t)$ is identical for all points located in a plane perpendicular to its direction of propagation. By choosing the x-axis coinciding with the direction of propagation of the acoustic wave, the wave equation simplifies to differential of a single variable x:

$$\frac{\partial^2}{\partial x^2}p(x,t) = \frac{1}{C^2}\frac{\partial^2}{\partial t^2}p(x,t) \tag{8.91}$$

It can be verified that the general solution to the preceding differential equation is the sum of two functions $f_1(x, t)$ and $f_2(x, t)$ such that

$$p(x,t) = f_1\left(t - \frac{x}{C}\vec{n}\right) + f_2\left(t + \frac{x}{C}\vec{n}\right) \tag{8.92}$$

where f_1 and f_2 are arbitrary functions with continuous derivatives of first and second orders. In effect, taking the first- and second-order derivatives of Equation 8.92,

$$\frac{\partial}{\partial x}p(x,t) = \frac{1}{C}\left[f_1'\left(t - \frac{x}{C}\vec{n}\right) + f_2'\left(t + \frac{x}{C}\vec{n}\right)\right]\vec{n}.$$

and

$$\frac{\partial^2}{\partial x^2} p(x,t) = \frac{1}{C^2} \left[f_1'' \left(t - \frac{x}{C} \right) + f_2'' \left(t + \frac{x}{C} \right) \right] = \frac{1}{C^2} \frac{\partial^2}{\partial t^2} p(x,t)$$

which is the wave equation (8.91).

General properties: From this general solution of the wave equation for the case of a plane wave, the following general properties can be observed:

- At any point x, the acoustic pressure wave can be decomposed in two components $f_1(x, t)$ and $f_2(x, t)$, propagating in opposite directions from the point x.
- Considering only the incident wave and making the change of variable, $t' = t + \frac{x}{C}$, yields

$$p(x,t) = f_1 \left(t - \frac{x}{C} \right) = f_1(x,t')$$

which is independent of x. The incident acoustic wave $f_1(x, t)$ at the point x is the same as $f_1(t)$ at $x = 0$, with a delay of x/C. In other words, the propagation of the acoustic wave produces a delay time, but does not change its wave shape; an essential condition to allow proper vocal communication.

When the acoustic pressure is a sinusoidal function of time (a pure-tone sound), it can be expressed as the real component of the complex exponential function according to

$$p(x,t) = \sqrt{2}\, \mathrm{Re} \left[\mathbf{P}(x) \exp(j\omega t) \right] \tag{8.93}$$

The solution of the preceding wave equation becomes

$$\begin{aligned} p(x,t) &= \sqrt{2}\, \mathrm{Re} \left[\mathbf{P}_1 \left(t - \frac{x}{C} \right) + \mathbf{P}_2 \left(t + \frac{x}{C} \right) \right] \\ &= \sqrt{2}\, \mathrm{Re} \left[\mathbf{P}_1 \exp\left(-j\omega \frac{x}{C} \right) + \mathbf{P}_2 \exp\left(j\omega \frac{x}{C} \right) \exp(j\omega t) \right] \end{aligned} \tag{8.94}$$

where $\mathbf{P}_1$ and $\mathbf{P}_2$ are the complex amplitudes of the pressure waves $p_1(x, t)$ and $p_2(x, t)$.

The velocity of the gas molecules is given by

$$\begin{aligned} \frac{\mathrm{d}}{\mathrm{d}t} \mathbf{q}(x,t) &= -\frac{1}{\rho_0} \mathbf{grad}\, p(r,t) = -\frac{1}{\rho_0} \frac{\mathrm{d}}{\mathrm{d}x} \left[f_1 \left(t - \frac{x}{C} \right) + f_2 \left(t + \frac{x}{C} \right) \right] \\ &= -\frac{1}{\rho_0 C} \left[f_1' \left(t - \frac{x}{C} \right) + f_2' \left(t + \frac{x}{C} \right) \right] \end{aligned} \tag{8.95}$$

It follows the expression for the velocity $q(x, t)$:

$$\begin{aligned} q(x,t) &= \int \frac{\partial q(x,t)}{\partial t} \mathrm{d}t = \frac{1}{\rho_0 C} \int \left[f_1' \left(t - \frac{x}{C} \right) + f_2' \left(t + \frac{x}{C} \right) \right] \mathrm{d}t \\ &= \frac{1}{\rho_0 C} \left[f_1 \left(t - \frac{x}{C} \right) + f_2 \left(t + \frac{x}{C} \right) \right] = \frac{1}{\rho_0 C} p(x,t) \end{aligned} \tag{8.96}$$

which is directly proportional to the acoustic pressure.

Spherical wave: When a local disturbance occurs in air, it propagates across space in the form of a spherical wave, with a velocity *C*. In an appropriate spherical coordinates system, the differential equation governing the propagation of the acoustic wave is

$$-^2 p(r,t) = \frac{\partial^2}{\partial r^2} p(r,t) + \frac{2}{r}\frac{\partial}{\partial r} p(r,t) = \frac{1}{C^2}\frac{\partial^2}{\partial t^2} p(r,t) \tag{8.97}$$

Noting that

$$\frac{\partial^2}{\partial r^2}\left[r p(r,t)\right] = \frac{\partial}{\partial r}\left[\frac{\partial}{\partial r}\left[r p(r,t)\right]\right] = \frac{\partial}{\partial r}\left[p(r,t) + r\frac{\partial p(r,t)}{\partial r}\right]$$

$$= \frac{\partial p(r,t)}{\partial r} + \frac{\partial}{\partial r}\left[r\frac{\partial p(r,t)}{\partial r}\right] = 2\frac{\partial p(r,t)}{\partial r} + r\frac{\partial^2 p(r,t)}{\partial r^2}$$

$$= r\left[\frac{\partial^2 p(r,t)}{\partial r^2} + \frac{2}{r}\frac{\partial p(r,t)}{\partial r}\right] = r-^2 p(r,t)$$

the wave equation becomes

$$-^2 p(r,t) = \frac{1}{r}\frac{\partial^2}{\partial r^2}\left[r p(r,t)\right] = \frac{1}{C^2}\frac{\partial^2}{\partial t^2} p(r,t)$$

or

$$\frac{\partial^2}{\partial r^2}\left[r p(r,t)\right] = \frac{r}{C^2}\frac{\partial^2}{\partial t^2} p(r,t) = \frac{1}{C^2}\frac{\partial^2}{\partial t^2}\left[r p(r,t)\right] \tag{8.98}$$

where

$p(r, t)$ is the acoustic pressure expressed in N/m^2

r is the radial distance from the measuring point to the source

Equation 8.98 is of the same form as of Equation 8.91 for a plane wave.

General properties: When the acoustic disturbance is a pure-tone sound, of frequency ω, the solution of the wave equation for the case of an acoustic point source is

$$p(r,t) = \left[\frac{A^+}{r}\exp(-jkr) + \frac{A^-}{r}\exp(jkr)\right]\exp(j\omega t) \tag{8.99}$$

where A^+ and A^- are, respectively, the amplitudes of the incident and reflected waves and $k = \frac{\omega}{C} = \frac{2\pi}{\lambda}$ the wave number.

When there is no reflection of the acoustic wave, the preceding expression of the acoustic pressure simplifies to

$$p(r,t) = \frac{A^+}{r}\exp(-jkr)\exp(j\omega t) \tag{8.100}$$

The velocity $q(r, t)$ of the gas molecules in air is governed by the differential equation:

$$\frac{\partial}{\partial t}\mathbf{q}(\mathbf{r},\mathbf{t}) = -\frac{1}{\rho_0}\nabla p(r,t) = -\frac{1}{\rho_0}\frac{\partial}{\partial r}A^{+}\exp(j\omega t)\left(-\frac{1}{r^2} - \frac{jk}{r}\right)\exp(-jkr)$$

$$= \frac{A^{+}}{\rho_0}\left(\frac{1}{r^2} + \frac{jk}{r}\right)\exp(j\omega t)\exp(-jkr)$$

It follows the expression for the radial velocity $q(r, t)$ of a spherical acoustic wave:

$$q(r,t) = \int \frac{\partial q(r,t)}{\partial t}dt = \frac{A^{+}}{\rho_0}\left(\frac{1}{r^2} + \frac{jk}{r}\right)\exp(-jkr)\int \exp(j\omega t)dt$$

$$= \frac{A^{+}}{\rho_0}\left(\frac{1}{r^2} + \frac{jk}{r}\right)\frac{1}{j\omega}\exp(-jkr)\exp(j\omega t)$$

$$= \frac{1}{\rho_0}\left(\frac{1}{jkr} + \frac{1}{r^2}\right)\frac{jk}{j\omega}\frac{A^{+}}{r}\exp(-jkr)\exp(j\omega t)$$

$$= \frac{1}{\rho_0 C}\left(1 + \frac{1}{jkr}\right)p(r,t) \tag{8.101}$$

8.3.4.4 Specific Acoustic Notions

Acoustic impedance: By definition, the acoustic impedance of the medium, Z_a, is the ratio between the acoustic pressure $p(r, t)$ and the velocity of the gas molecules:

$$Z_a = \frac{p}{q} \tag{8.102}$$

For a plane wave,

$$Z_a = \rho_0 C \tag{8.103}$$

For a spherical wave,

$$Z_a = \rho_0 C = \frac{jkr}{1 + jkr} = \frac{\rho_0 C}{\sqrt{1 + (kr)^2}} \tag{8.104}$$

Acoustic intensity: Represents the flow of acoustic energy across the system. The general expression of acoustic intensity at a given location is

$$I = \mathrm{Re}\left(\frac{1}{2}p^{*}q\cos\phi\right) \tag{8.105}$$

where

p^* represents the conjugate of the acoustic pressure
ϕ is the angle between the direction of propagation of the acoustic pressure wave
q is the velocity of the air molecules

For a plane wave,

$$I = \frac{1}{\rho_0 C} p^2(r,t) = \frac{1}{\rho_0 C} p_{\text{rms}}{}^2 \tag{8.106}$$

For a spherical wave,

$$I = \text{Re}\left[\frac{p_r^* p_r}{2\rho_0 C}\left(1 - \frac{j}{kr}\right)\cos\theta\right] = \frac{1}{2\rho_0 C} p_r{}^2 \cos\theta$$

with

$$p_r = \frac{A^+}{r}\exp(-jkr)$$

For a point source, the acoustic intensity in the radial direction, $\phi = 0$, is

$$I = \frac{1}{2\rho_0 C} pr^2 = \frac{1}{2\rho_0 C}\left(A^+\right)^2 \frac{1}{r^2} \tag{8.107}$$

Furthermore, since the total acoustic power of the source must be equal to the sum of acoustic energy flowing across a closed surface surrounding the source, one has for a spherical surface

$$4\pi r^2 I = W \tag{8.108}$$

It follows from the preceding expressions of the acoustic intensity that

$$I = \frac{W}{4\pi r^2} = \frac{1}{2\rho_0 C} pr^2 = \frac{1}{\rho_0 C} p_{\text{rms}}^2$$

and, inversely, the acoustic pressure is

$$p = p_{\text{rms}} = \sqrt{\rho_0 C I} \tag{8.109}$$

Audible noise: Because of the wide range of variations of the acoustic pressure in absolute value, N/m^2, the AN level is usually expressed in terms of dB, defined as

$$\text{AN}(\text{dB}) = 20\log\left[\frac{p}{p_{\text{re}}}\right] \tag{8.110}$$

where $p_{\text{re}} = 2 \times 10^{-5}$ N/m^2 is a reference acoustic pressure corresponding to the sound perception threshold of the ear.

8.3.4.5 Acoustical Characteristics of Corona Discharges

Acoustical characteristics of a single corona source: It is evident that the acoustic characteristics of a single corona source depend largely on the active discharge mode. The glow discharges, positive and negative, due to their continuous development, give rise to an equilibrium state of the ion flow and, consequently, to an essentially spatial pressure gradient. The generated AN is a low-frequency sound, associated with the movement of ion space charges across the discharge gap.

The generation of AN is generally typical of streamers discharges, Trichel and positive streamers, and is associated to the rapid heating of the discharge channel, causing a sudden variation of the local air pressure, that is, an acoustic wave perceptible by the human ear. Figure 8.33 shows the wave shape of the acoustic pulses associated with positive and negative streamers (Héroux and Trinh, 1976). The acoustic wave is delayed with respect to the electric one by the traveling time of

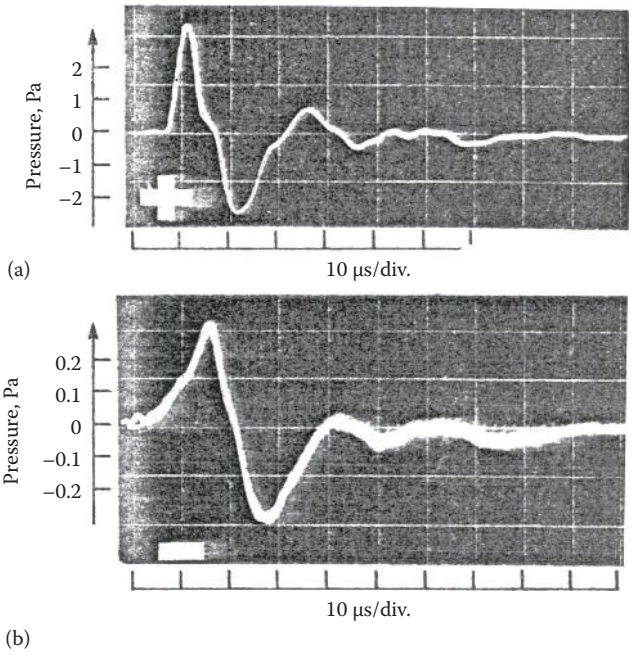


FIGURE 8.33 Acoustic characteristics. (a) Positive streamer discharges. (b) Negative *Trichel* streamers. (From Héroux, P. and Trinh, N.G., A statistical study of electrical and acoustical characteristics of pulsative corona, IEEE Paper No A-76 122-2, *IEEE–PES Winter Meeting*, New York, January 1976.)

the acoustic wave from the discharge site to the microphone. In addition, even if the electric phenomenon lasts only a fraction of microseconds, the acoustic wave persists over several tens of microseconds. This definitely limits the frequency spectra of AN pulses to a few tens of kilohertz, estimated from square wave pulses of duration corresponding to those of positive and negative streamer pulses.

Because of this characteristic of the acoustic pressure wave generated by streamer discharges, the acoustic wave is audible only when the streamer repetition rate remains relatively low. In effect, by representing the individual acoustic pulse by a pulse of constant amplitude A and a duration δ, the time variations of a train of acoustic pressure waves can be expressed by its harmonic components, according to

$$f(t) = A\delta\omega + \sum_{n=1}^{\infty} A_n \cos(n\omega t)$$

with

$$A_n = \frac{1}{\pi}\int_{-\pi}^{\pi} f(t)\cos(n\omega t)\,dt = \frac{2A}{\pi n\omega_0}\sin\frac{n\omega_0\delta}{2} = \frac{A\delta}{\pi}\frac{\sin(n\omega_0\delta/2)}{n\omega_0\delta/2}$$

$$= \frac{A\delta}{\pi} S_a\frac{n\omega_0\delta}{2}$$

and its frequency spectrum is

$$G(\omega) = \frac{2\pi}{T}\sum_{n=-\infty}^{\infty} g(\omega)\,\delta(\omega - n\omega_0) \tag{8.111}$$

where

$f = \omega_0/2\pi = 1/T$ is the streamer repetition rate

$\delta(\omega - n\omega_0)$ is the Kronecker delta function

The generated AN is composed of the fundamental frequency ω and its harmonics, the amplitude of which is modulated according to the sampling function:

$$\frac{Ad}{p} S_a\left(n\omega_0 \frac{d}{2}\right) = \frac{Ad}{p} \frac{\sin\left(n\omega_0 \frac{d}{2}\right)}{n\omega_0 \frac{d}{2}}$$

The harmonic content of the AN is thus limited to those within the main lobe of the function $g(f)$, with the cutoff frequency given by

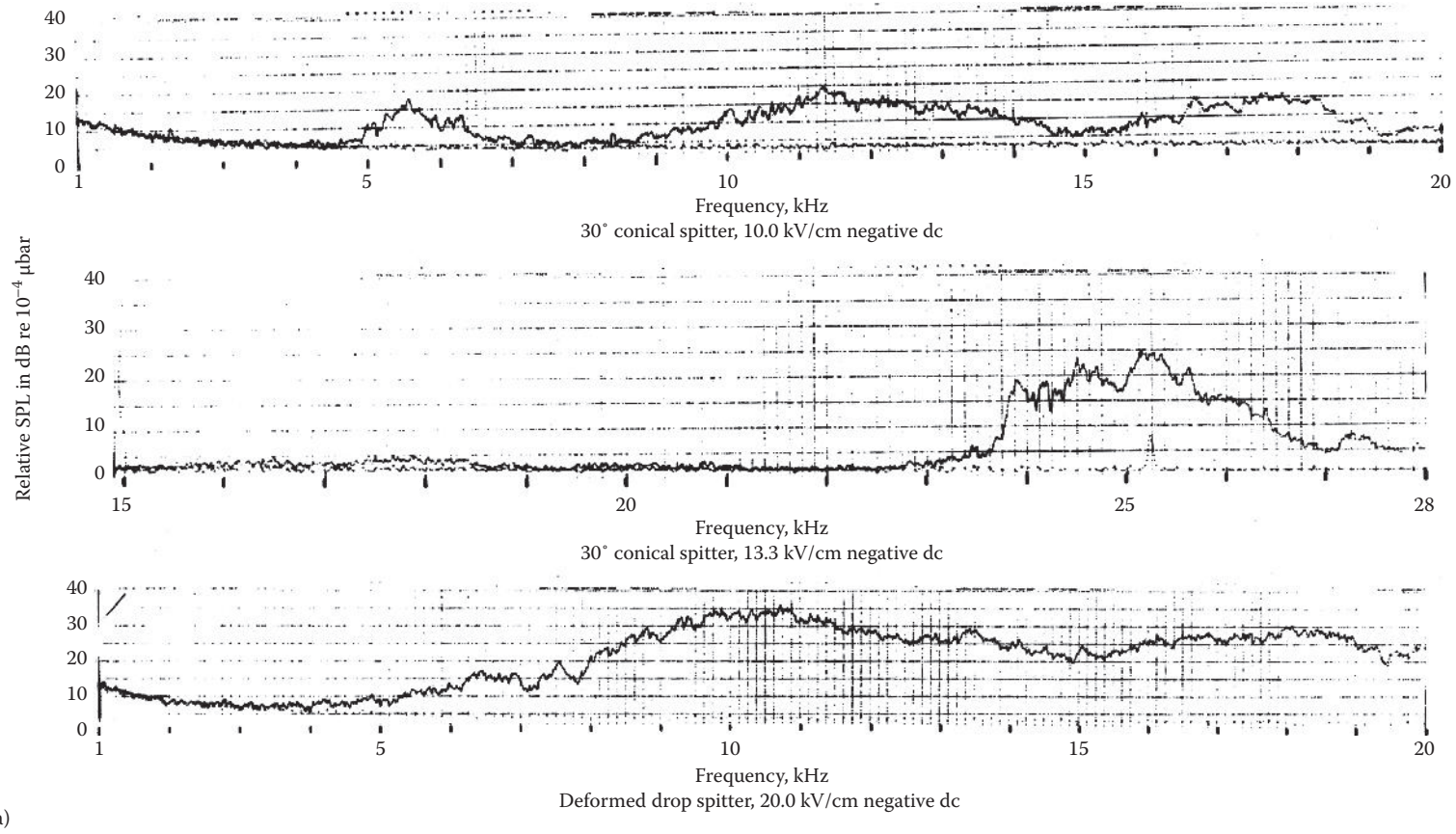
$$f_c = \frac{1}{d}$$

It can be seen that for identical acoustic pressure pulses, as the streamer repetition rate increases, there are less acoustic harmonics within the main lobe of the spectrum, which is a characteristic of the generated acoustic pressure wave. For a positive streamer, the duration of acoustic waves is typically of 35 μs; the cutoff frequency of the main lobe of the spectrum is 28.5 kHz. For a negative Trichel streamer, the duration of acoustic waves is of 25 μs, and the cutoff frequency of the main lobe is 40 kHz.

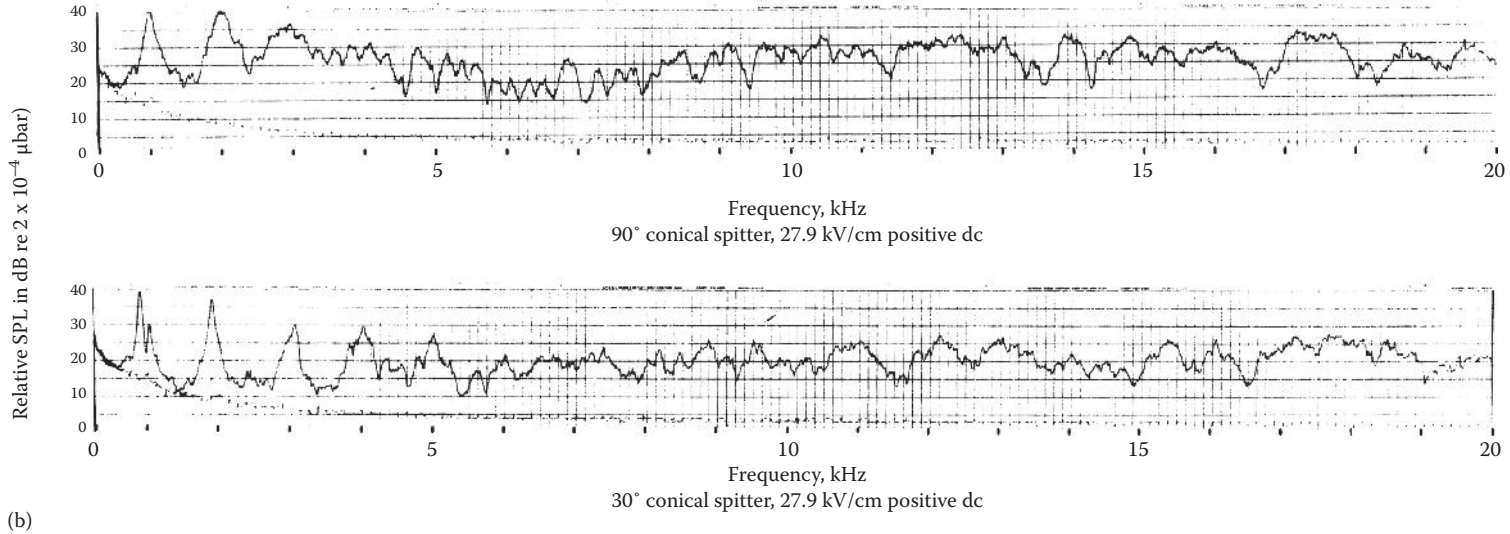
It follows that the generation of AN is particularly important when the streamers are repeated at a rate of kHz. The positive streamers are thus particularly noisy due to a repetition rate not too high combined with a high amplitude of the generated acoustic pulse. The Trichel streamers are, in comparison, less noisy, having lower intensity and higher repetition rate. This is illustrated by the frequency spectra of the AN generated by a single corona source, presented in Figure 8.34 for negative Trichel and positive streamers (Ianna et al., 1974).

Acoustical characteristics of an HV line: The AN generated from a transmission line is the resulting effect of a multitude of corona sites distributed along the line conductors. This is particularly true under conditions of foul weather where each waterdrop, snowflake, or ice deposited on the conductor can be an effective corona source. The perceived effect is thus the integration of the contributions from different corona sources along the conductors. The typical octave-band frequency spectra of line corona in Figure 8.35 contains discrete components, corresponding to the second and higher harmonics of the line voltage superimposed on a relatively broadband noise, extending well into the ultrasonic range (Trinh, 1974). The octave-band measurements in this figure show a sharp drop at frequencies over 20 kHz, due principally to the limited frequency response of the microphone and associated sound-level meter.

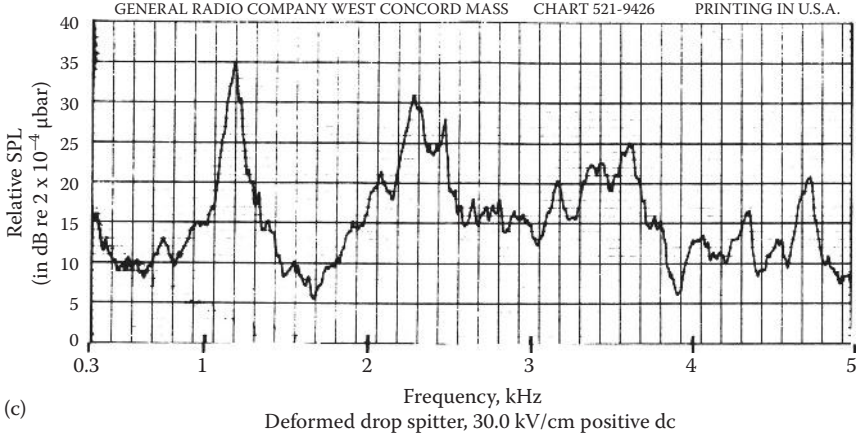
Standing waves: The existence of pure-tone sounds is generally associated with the movement of ion space charges in the immediate surroundings of HV conductors. Because of their opposite polarities, the ion space charges are alternatively attracted to and pushed away from the line conductors, giving rise to a periodic variation in the local air pressure around the conductors, at twice the frequency of the line voltage. Furthermore, the harmonic oscillation of the sound pressure wave can also form standing acoustic pressure waves when several sources of AN are at close proximity of one another. This is observed in tests in a corona test cage where the effect of reflection of the acoustic waves by the ground can be represented by a second acoustic source, located symmetrically with respect to the ground. For a three-phase line, each phase also acts as an acoustic source, delayed in time by the phase shift in the line voltage. Figure 8.36 shows the effect of standing waves in the immediate surrounding of 735 kV lines of different phase spacing. One notices that the acoustic intensity at 120 Hz can fluctuate considerably as a result of standing wave. The phenomenon decreases rapidly as one get away from the sources.


Relative SPL in dB re 10^{-4} μbar
40
30
20
10
0
1
5
10
15
20
Frequency, kHz
30° conical spitter, 10.0 kV/cm negative dc
40
30
20
10
0
15
20
25
28
Frequency, kHz
30° conical spitter, 13.3 kV/cm negative dc
40
30
20
10
0
1
5
10
15
20
Frequency, kHz
Deformed drop spitter, 20.0 kV/cm negative dc

(a)



(b)



(c)

FIGURE 8.34 (continued) Frequency spectra of corona discharges from a single source. (From Ianna, F. et al., *IEEE Trans*., PAS-93, 1787, 1974.) (a) Frequency spectrum of negative corona discharges—single discharge source. (b) Frequency spectrum of positive corona discharges. (c) Frequency spectrum of positive corona from a waterdrop.

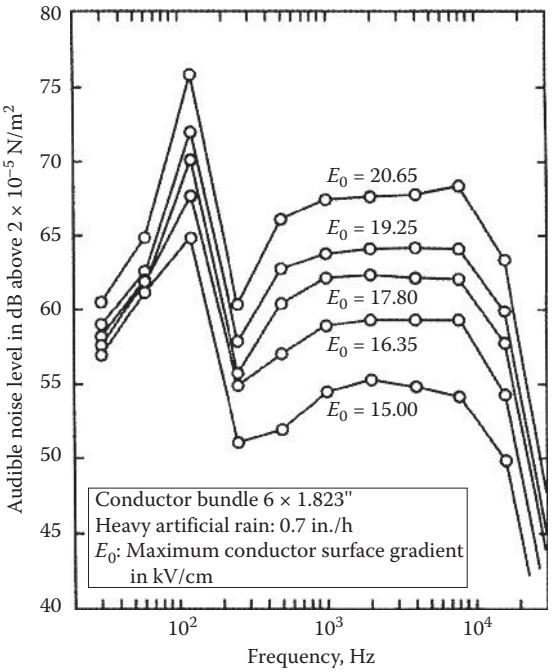


FIGURE 8.35 Frequency spectrum of AN from HV line. (From Trinh, N.G., Analysis of the second harmonic (120 Hz) audible noise generated by line corona, *IEEE-PES Summer Meet. Pap. A*, 75, 501, 1975.)

8.3.4.6 Measurement of Audible Noise

Acoustical characteristics of the human ear: The human ear is the interface allowing us to recognize variations in the ambient air pressure, perceived as sound. A human ear can be described as an acoustic transducer comprising

- The eardrum
- The ossicles, the hammer, and anvil
- The cochlea

The pressure of the inner ear is normally maintained in equilibrium with the ambient pressure by the channel of *Eustache*; as a result, the eardrum responds only to the variations in the ambient pressure, that is, to the acoustic pressure. The vibrations of eardrum are transmitted by the ossicles, hammer, and anvil to the cochlea. The latter have acoustic sensors distributed along a membrane and are excited by different harmonic components of the acoustic pressure perceived that the brain interprets as a sound. Typical frequency response of human ear, in the form of equiphonic curves over the range of acoustic pressures from 1 to 130 dB above the threshold of 2×10^{-5} N/m^2, covers frequency range between 20 Hz and 20 kHz, with maximum sensitivity at frequencies of kHz.

8.3.4.7 Sound Meter

Figure 8.37 shows the typical scheme of a sound meter, composing of three parts:

- The detection of sound and its transformation into an electric signal
- The weighting of the signal and its amplification and/or attenuation
- The measurement of the electric signal

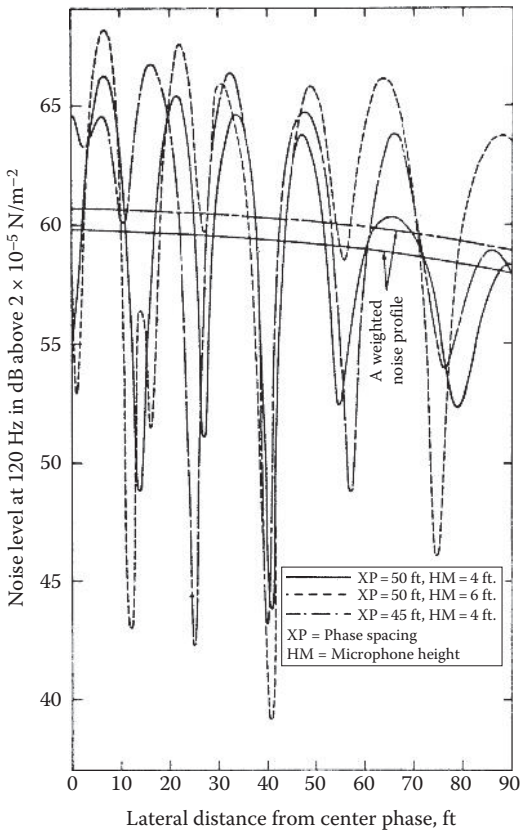


FIGURE 8.36 Lateral profiles of AN measured in dBA at 120 Hz of *Hydro-Québec* 735 kV lines. (From Trinh, N.G., Analysis of the second harmonic (120 Hz) audible noise generated by line corona, *IEEE-PES Summer Meet. Pap. A*, 75, 501, 1975.)

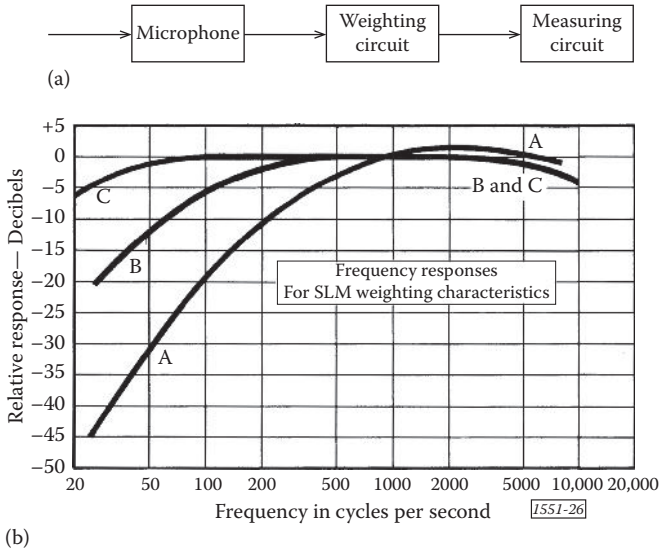


FIGURE 8.37 Operating principle of a sound meter and weighting circuit. (Peterson, A.P.G. and Gross Jr., E.E., *Handbook of Noise Measurement*, 6th edn., General Radio Company, West Concord, MA, 1963.)

Noise detection: Is made by an electro-acoustic transducer or microphone, which gives an electric signal proportional to the received acoustic signal. The main types of microphones used are condenser and piezoelectric microphones.

Weighting of signal: To give the sound meter a response similar to human ear, the electric signal from the transducer is modified by a weighting circuit, which has a frequency response essentially the inverse that of the human ear. Such a weighting circuit is of type A and is most frequently used in measurement of the AN. Figure 8.37b also shows the frequency response of different weighting circuits available for diverse applications, namely, the measurement of impact noise (type B) and noise with low-frequency harmonics (type C).

Measurement of signal: The acoustic pressure is measured in terms of the effective value. The measuring circuit has, consequently, a quadratic circuit, which gives an output signal proportional to the square of the input signal. By measuring the average value of the quadratic signal, one obtains a reading proportional to the effective value of the AN, which is then converted in dB with respect to the reference pressure of $p_{re} = 2 \times 10^{-5}$ N/m^2.

8.3.4.8 Methods of Calculation of Audible Noise

Empirical formulae: The interest in empirical formulae resides in their simplicity, which compensates largely for the lack of rigor of a well-developed theory. In this approach, one defines a function from experimental data, which expresses the acoustic pressure $p(r)$ as a function of different parameters, namely,

- The electric field, E (kV_{rms}/cm)
- The number of subconductors, n, in the bundle
- The diameter of the subconductors, d (cm)
- The distance R (m) from the measuring point to the conductor

The acoustic pressure $p(R)$ can be expressed as

$$p(R) = f(E,n,d,R) = p_0 E^{a} d^{b} n^{g} \frac{1}{R^{d}} \tag{8.112}$$

where p_0 is a constant characteristic of the conductor.

The AN of a single-phase line AN (dBA) is, by definition, given by (8.110). The general expression follows

$$\text{AN}(\text{dBA}) = AN_0 + A\log E + B\log d + C\log n - D\log R$$

with

$$AN_0 = 20\log \left(\frac{p_0}{p_{re}} \right)_A$$

The index A indicates that the measurements are made with the weighting circuit of type A.

The parameters AN_0, A, B, C, and D are determined from experimental data, namely, from tests made in corona test cages on a large number of configurations of bundle conductors and for the range of electric fields comparable to those encountered on the transmission lines. A number of empirical formulae have been developed in the late 1970s (IEEE Corona and Field Effect Subcommittee, 1982). The empirical formula, developed from results obtained in test cages at Hydro Québec Institute of Research (IREQ), under conditions of artificial rain, has the following parameters (Trinh and Maruvada, 1972; Trinh et al., 1974):

$$AN_0 = -57.6\ A = 72.\ B = 45.8\ C = 22.7\ D = -11.39$$

The expression of AN from a single-phase line under conditions of heavy rain is

$$\mathrm{AN}\,(\mathrm{dBA}) = -57.6 + 72\log E + 45.8\log d + 22.7\log n - 11.39\log R \tag{8.113}$$

Empirical formulae are also useful to compare the performances between two transmission lines of similar design. Let AN (dBA) and AN_{re} (dBA) be the two AN levels from the two lines, of which one is used as reference. From Equation 8.113, the AN from the reference line can be expressed as

$$\mathrm{AN}_{re}\,(\mathrm{dBA}) = -57.6 + 72\log E_{re} + 45.8\log d_{re} + 22.7\log n_{re} - 11.39\log R_{re}$$

Combined with Equation 8.113 gives

$$\mathrm{AN} - \mathrm{AN}_{re} = 72\log\frac{E}{E_{re}} + 45.8\log\frac{d}{d_{re}} + 22.7\log\frac{n}{n_{re}} - 11.39\log\frac{R}{R_{re}}$$

Theoretical calculation of audible noise from a single-phase line: Referring to Figure 8.38, which shows a single-phase line with an average height h. The microphone is located at a lateral distance y from the line and at a height h above ground. Similar to the case of electromagnetic interference, the ability of the line conductors to produce AN is characterized by the *generated acoustic power density A*, defined as the acoustic power produced per unit length of the line conductor, under specific operating conditions. The acoustic power generated by corona discharges developing in a portion dx of the conductor is then

$$\mathrm{d}A = A\,\mathrm{d}x$$

Its contribution to the acoustic intensity at the measuring point is

$$\mathrm{d}I = \frac{A}{4\pi r^2}\mathrm{d}x$$

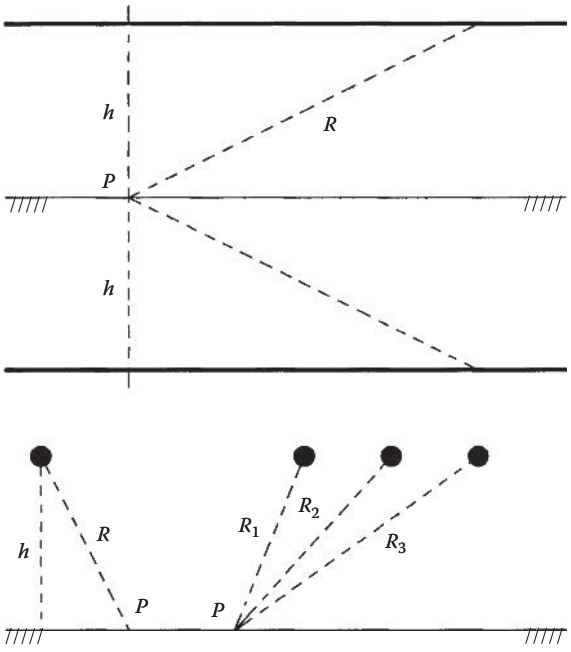


FIGURE 8.38 Calculations of AN. Representation of the measuring point *P* for single- and three-phase lines.

with

$$r^2 = y^2 + (H - h)^2 + x^2 = R^2 + x^2$$

where

r represents the direct distance from dx to the measuring point
R is the distance between the conductor and the measuring point

The reflection of the acoustic wave from the ground can be taken into account by an image source located symmetrically with respect to the ground, with an acoustic power density of KA, $K \leq 1$. The acoustic intensity at the measuring point is obtained by integrating the contributions from all the elementary sections dx along the conductor and its image:

$$I(R) = \int_{-L_1}^{L_2} \mathrm{d}I + \int_{-L_1}^{L_2} \mathrm{d}I_{\mathrm{m}} = \int_{-L_1}^{L_2} \frac{A}{4\pi} \frac{\mathrm{d}x}{R^2 + x^2} + \int_{-L_1}^{L_2} \frac{KA}{4\pi} \frac{\mathrm{d}x}{R_m{}^2 + x^2} \tag{8.114}$$

where

L_1 and L_2, for a short line, are the distances along the line from the measuring point to its extremities
R and R_{m} the distances from the measuring point to the conductor and its image

When the measurements are made close to the ground, $R = R_{\mathrm{m}}$, Equation 8.76 simplifies to

$$I(R) = \frac{(1+K)A}{4\pi} \int_{-L_1}^{L_2} \frac{\mathrm{d}x}{R^2 + x^2} = \frac{(1+K)}{4\pi} \frac{A}{R^2} \int_{-L_1/R}^{L_2/R} \frac{\mathrm{d}(x/R)}{1 + (x/R)^2} \tag{8.115}$$

Integration of Equation 8.115, with a change of variable $u = x/R$, gives the following expression, for the acoustic intensity $I(R)$ at the measuring point:

$$I(R) = \frac{(1+K)A}{4\pi R} \left[\tan^{-1} \frac{L_2}{R} + \tan^{-1} \frac{L_1}{R} \right]$$

For a long line and assuming a coefficient of reflection of the ground of $K = 1$, the expression of the acoustic intensity at the measuring point simplifies to

$$I(R) = \frac{A}{2R} \tag{8.116}$$

In general, the measurements of AN being made in function of the acoustic pressure, it is necessary to evaluate the corresponding acoustic pressure and AN level, according to (8.109) and (8.110), respectively.

Calculation of the audible noise of a three-phase line: Is made by considering each phase of the line as an independent noise source, as well as evaluating the contribution of each phase to the acoustic pressure and, consequently, the AN level at the measuring point. The acoustic pressure produced by a single-phase line at the measuring point p_i is by definition

$$p_i = 2 \times 10^{-5} \times 10^{\frac{\mathrm{AN_i\,(dB)}}{20}} \tag{8.117}$$

Since acoustic pressures do not add algebraically, the resulting acoustic pressure p_{t} is

$$p_{\mathrm{t}} = \sqrt{\sum p_{\mathrm{i}}{}^2} = 2 \times 10^{-5} \sqrt{\sum 10^{\left[\mathrm{AN_i\,(dB)}/10\right]}} \tag{8.118}$$

and finally, in terms of dBA,

$$\mathrm{AN}\,(\mathrm{dBA}) = 20\log\left(\frac{p_t}{2\times10^{-5}}\right) = 20\log\left(\sqrt{\sum 10^{\mathrm{AN_i\,(dB)}/10}}\right) \tag{8.119}$$

Another way to evaluate the AN level from a three-phase line is to directly calculate the acoustic intensity at the measuring point, according to Equation 8.116:

$$I_{\mathrm{i}}\,(R_{\mathrm{i}}) = \frac{A_{\mathrm{i}}}{2R_{\mathrm{i}}}$$

When the generated acoustic power density is expressed in dBA, the acoustic intensity in dBA is

$$I_{\mathrm{i}}\,(\mathrm{dBA}) = A_{\mathrm{i}}\,(\mathrm{dBA}) - 10\log(2R_{\mathrm{i}})$$

Its absolute value is

$$I_{\mathrm{i}}\,(R_{\mathrm{i}}) = A_{\mathrm{re}}\,10^{A_{\mathrm{i}}\,(\mathrm{dBA})/10}$$

Finally, the acoustic intensity at the measuring point is the sum of the contributions from different phase conductors of the line:

$$I\,(R) = \sum_i I_i\,(R_i) \quad \text{or} \quad I_{\mathrm{t}} = 10^{-6}\sum 10^{A_{\mathrm{i}}\,(\mathrm{dBA})/10} \tag{8.120}$$

The sound pressure and the corresponding AN level are evaluated according to (8.109) and (8.110).

Example of calculation: The case of a 735 kV line of *Hydro-Québec*, of which the parameters are presented in Table 8.2, will be considered in the following to illustrate this approach to the calculation of the AN level from HV transmission lines. The subconductor generating acoustic power density, A_{s}, is

- At the central phase: 3.284 dBA, or 2.130 μW/m
- At the outer phases: −0.239 dBA, or 0.946 μW/m

Noting that the generated acoustic power density of the bundle conductors A_{b} is related to that of its subconductors A_{s}, and the number of subconductors n, according to

$$A_{\mathrm{b}} = n^2 A_{\mathrm{s}}$$

with $n = 4$, the generated acoustic power density of the conductor bundles is

- At the central phase: 34.081 μW/m
- At the outer phases: 15.144 μW/m

At the measuring point P, located at 15 m from the outer phases, the direct distances to the bundle conductors are, respectively, 24.84, 34.86, and 46.79 m. The acoustic intensity at the measuring point is

$$I = \sum I_{\mathrm{i}} = \sum \frac{A_{\mathrm{i}}}{2R_{\mathrm{i}}} = 0.305 + 0.489 + 0.162 = 0.956 \quad \mathrm{mW/m^2}$$

The corresponding acoustic pressure is

$$p = \sqrt{\rho_0 C I} = \sqrt{1.18\times344.2\times0.956\times10^{-6}} = 19.699\times10^{-3} \quad \mathrm{N/m^2}$$

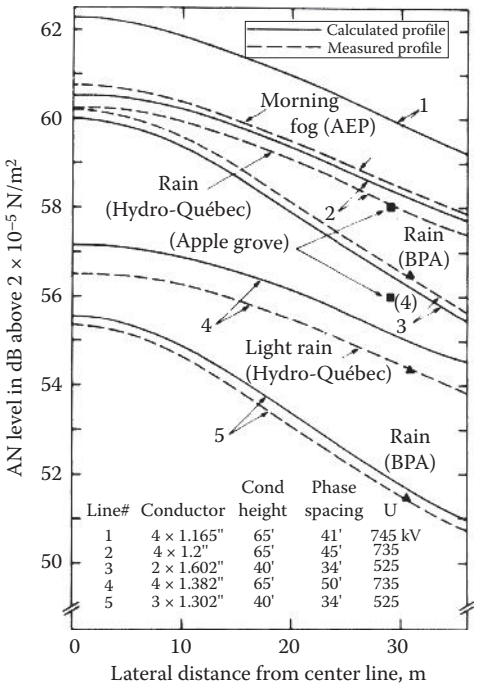


FIGURE 8.39 Lateral profiles of AN from transmission lines.

Or, in terms of dBA,

$$\text{AN}\,(\text{dBA}) = 20\log\left(\frac{19.699\times10^{-3}}{2\times10^{-5}}\right) = 59.87 \quad \text{dBA}$$

Figure 8.39 shows typical lateral profiles of the AN calculated for different line configurations and bundle conductors and compared with the actual measurements. It can be seen as the good concordance between the calculated and measured AN levels. For the case of the 735 kV line, the calculated AN level is 1 dBA higher than the measured value.

8.3.5 Selection of Conductors

The occurrence of corona discharges on line conductors is dictated essentially by the local field intensity, which, in turn, is greatly affected by the surface conditions, for example, rugosity, waterdrops, and snow and ice particles. For a smooth cylindrical conductor, the corona onset field is well described by the Peek experimental law; see Chapter 4:

$$E_c = 30m\delta\left(1 + \frac{0.301}{\sqrt{\delta a}}\right) \tag{8.121}$$

where

E_c is the corona onset field in kV_{peak}/cm
a is the radius of the conductor in cm
m is an experimental factor to take account of the surface conditions

Typical values of m are 0.8–0.9 for a dry-aged conductor, 0.5–0.7 for a conductor under foul-weather conditions, and δ is the relative air density factor.

The previous corona onset condition emphasizes the great sensitivity of corona activities to the conductor surface condition and, hence, to changes in weather conditions. In effect, although the line voltage and the nominal conductor surface gradient remain constant, the surface condition factor varies

continuously due to the exposure of line conductors to atmospheric conditions. The changes are particularly pronounced during foul weather as a result of the numerous discharge sites associated with waterdrops and snow and ice particles deposited on the conductor surface.

Adequate corona performance of HV lines is generally achieved by a proper control of the field intensity at the surface of the conductor. Current practices for selecting HV line conductors usually call for a corona-free performance in fair weather, with limited proportions of time when the corona performance may exceed the design levels. This is well illustrated by the simple case of a single-phase, single-conductor line for which the field intensity around the conductor is expressed as

$$E(r) = \frac{1}{\ln\left(\frac{2h}{a}\right)} \frac{U}{r} \tag{8.122}$$

where

U is the line-to-ground voltage
h is the height of the conductor above ground
a is the conductor radius
r is the radial distance to the center of the line conductor

At the conductor surface, $r = a$, the field is maximum and equal to

$$E_0 = \frac{1}{\ln\left(\frac{2h}{a}\right)} \frac{U}{a} \leq E_c \tag{8.123}$$

It can be seen that the field intensity at the conductor surface is primarily dependent on its radius and, to a lesser extent, on the height of the conductor above ground. By properly dimensioning the conductor, the field intensity at its surface can be kept below the fair-weather corona onset field for an adequate control of the corona activities and their undesirable effects. Even with the use of bundled conductors, it is not economically justified to design line conductors that would be corona-free under all weather conditions.

Selection of line conductors is therefore made in terms of them being relatively corona-free under fair weather, with minimum effects under foul weather. For ac lines, the design levels of 65 dB for RI and 60 dBA for AN at the edge of the right-of-way are often used (Maruvada and Trinh, 1975). These levels may be exceeded during periods of foul weather, and for a specified annual proportion of time, typically 15%–20%, depending on the local distribution of the weather pattern. It requires field calculations and tests on conductor samples to determine the number and dimensions of the conductors to minimize the undesirable effects of corona discharges. In this context, it is important to be able to evaluate the corona performances of the bundle conductors, which are used for EHV and UHV lines. Current practices in selection of HV line conductors usually involve two stages of selection: a preselection in terms of the worst-case performances under adverse atmospheric conditions, followed by a final selection among the configurations of the most promising as a function of their long-term performances.

8.3.5.1 Evaluation of the Worst-Case Performances

As already seen, the corona performance of an HV line, CL, RI, and AN can be readily evaluated from their respective generating quantities:

- The generated losses W
- The excitation function $\Gamma(\omega)$
- The generated acoustic power density A

These parameters are intrinsic characteristics of the bundle conductors and, for a specific weather condition, *are functions only of the electric field at the surface of the conductors*. As a result, they can be

determined experimentally from tests on the full-scale bundle conductors, either in test cages or on an experimental test line. One of the key factors in the evaluation of the worst-case corona performances of HVAC lines resides in the possibility to evaluate the generating functions of bundle conductors under conditions of artificial heavy rain, which correspond to the worst-case conditions for ac corona (Moreau and Gary, 1972a). By varying the test voltage, the generating functions of the bundle conductors can be established as a function of the electric field at the surface of the conductors over a range of applied field intensities. The results can then be used to derive the appropriate generating functions, corresponding to the electric field at the surface of the line conductors, and to evaluate their worst-case corona performances.

Experimental evaluation of the generating functions under artificial rain: Evaluation of the conductor worst-case performances is best done in *test cages* under artificial heavy rain conditions (Trinh and Maruvada, 1977). Figure 8.53 shows the test cages at IREQ, located side by side. Each test cage is made up of three sections. The central insulated section of 100 m long is embedded between two grounded sections to control the end effect of the field distributions. The cross section is a square of 3 m by 3 m. The test cages are equipped with an artificial rain system, which can produce a rain rate of 17.5 mm/h to simulate the worst-case heavy rain conditions. They are adequate for evaluating full-size conductor bundles located along its central axis, for lines up to the 1500 kV class. The main advantage of this experimental setup is the relatively modest test voltage required to reproduce the same field distribution on real-size bundled conductors. The worst-case corona performance of various bundled conductors can then be determined over a wide range of surface gradients.

Generated losses: Are evaluated by measuring the corona current collected at the central section of the cages. The measured generated losses are defined as the power losses per unit length of the conductor, P (W/m). During tests in corona cages, the discharge current is measured, which allows the evaluation of the corresponding power losses, P_t, and evaluates the generated losses:

$$P = \frac{P_t}{L} \tag{8.124}$$

where L is the effective length of the test cage.

Excitation function: The current way to measure the excitation function of a bundle conductor consists of measuring the high-frequency corona discharge current, with the test conductor terminated at one

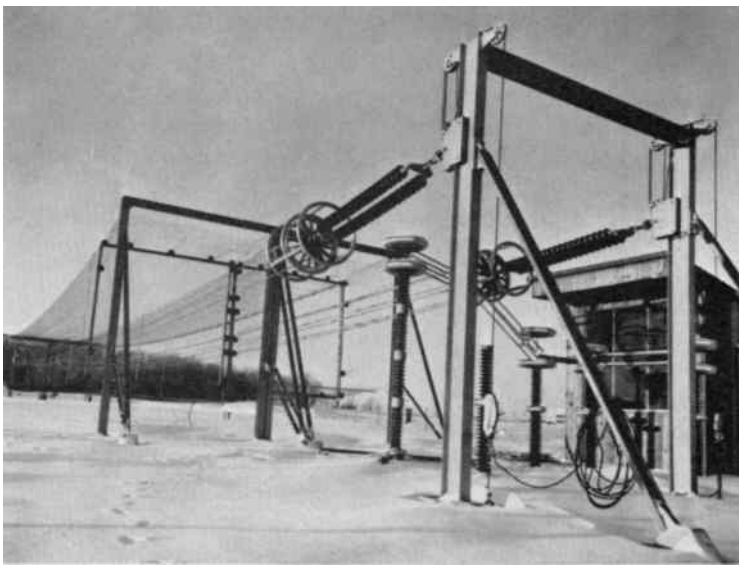


FIGURE 8.40 Corona test cages at IREQ. (Photo Coutesy of Hydro-Québec.)

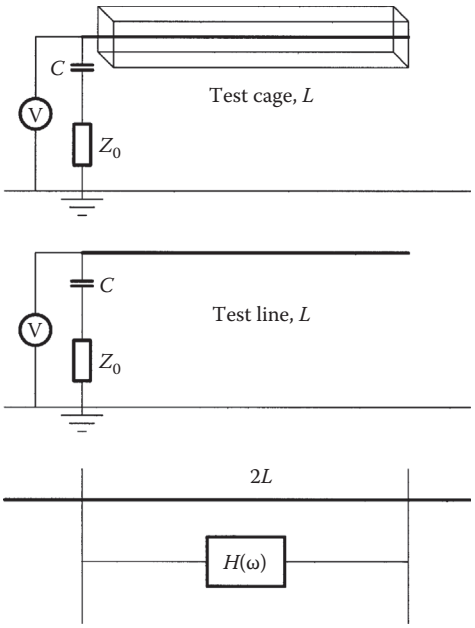


FIGURE 8.41 Determination of the excitation function of a bundle conductor.

end by its characteristic impedance Z_0. The measuring circuit must be isolated from the test conductor by a coupling capacitor, which presents a low impedance at the measuring frequency, between 0.5 and 1. MHz. Referring to Figure 8.41 showing the electric scheme of the corona test cage and line of effective length L, it can be seen that using an impedance equal to the characteristic impedance of the conductor eliminates the reflection to interference current pulses at the measuring end. However, the current pulses reaching the open end of the test conductor will be reflected with a coefficient of reflection of 1.0. It follows that the contribution to the interference current at the measuring point, at terminated end of the test conductor, is equivalent to that of corona discharges on section of length $2L$ of a long line. As already explained, because of the random nature of interference current, the spectral density of the measured interference current is obtained by adding up the spectral densities of the injected interference currents:

$$F(\omega) = \int_0^{2L} \Phi f(\omega)\,dx = \int_0^{2L} \frac{f_0(\omega)}{2} \left[\exp(-\gamma|x|)\right]^2 dx \tag{8.125}$$

Neglecting the phase coefficient, β, one obtains

$$F(\omega) = f_0(\omega)\left[\frac{1-\exp(-2\alpha L)}{4\alpha}\right] \tag{8.126}$$

Applying the relation between the effective value of the signal and its spectral density, the following expression can be derived for the effective value of the discharge current:

$$I(\omega) = \sqrt{2F(\omega)\Delta f} = J_0(\omega)\sqrt{\frac{1-\exp(-2\alpha L)}{4\alpha}} \tag{8.127}$$

The expression for the density of the injected interference current $J_0(\omega)$ is

$$J_0(\omega) = \frac{2\sqrt{\alpha} I(\omega)}{\sqrt{1 - \exp(-2\alpha L)}} \tag{8.128}$$

and the excitation function Γ:

$$\Gamma(\omega) = \frac{2\pi\varepsilon_0}{C_n} J_0(\omega) = \frac{2\pi\varepsilon_0}{C_n} \frac{2\sqrt{\alpha}\, I(\omega)}{\sqrt{1 - \exp(-2\alpha L)}} \tag{8.129}$$

where C_n is the capacitance of the conductor in the test cage, in pF/m; the attenuation constant α is in the range of 2–6 dB/km or 0.23×10^{-3} to 0.691×10^{-3} m^{-1}. A value of $\alpha = 0.691 \times 10^{-3}$ m^{-1} will be used in the following.

Generated acoustic power density: A (μW/m) can be determined by measuring the AN level produced by the test conductor. For a test conductor of length L, the generated acoustic power density A is related to the acoustic intensity measured at a distance R from the conductor, according to

$$I(R) = \frac{A(1+K)}{4\pi R^2}\left[\tan^{-1}\frac{L_2}{r} + \tan^{-1}\frac{L_1}{r}\right] = \frac{1}{r_0 C}\left[p(R)\right]^2 \tag{8.130}$$

where

K is the coefficient of reflection of the sound from the ground
$p(R)$ is the acoustic pressure at the measuring point

For a bundle of n subconductors, there exists a simple relation between the generated acoustic power density of the bundle and that of the subconductors:

$$A_b = n^2 A_s \tag{8.131}$$

where A_b and A_s are the generated acoustic power density of the bundle and subconductors.

This relation simplifies the representation of the experimental data, which are expressed in terms of the generated acoustic power density of the subconductors, A_s. Typical experimental results obtained from cage tests are presented in Figures 8.42 to 8.44 for single conductors and 8.46 to 8.48 for a bundle of four conductors.

Predetermination of the corona generating quantities of bundle conductors: Although the generating functions of bundle conductors can be readily obtained in cage tests, these tests require special installation and testing equipment. Therefore, there is a strong incentive to analytically predetermine the corona generating functions. These characteristic properties of the bundle conductors are function of the subconductor dimensions and of the local field distribution:

$$W = w(E, d),\ \Gamma = \gamma(E, d) \text{ and } A = a(E, d)$$

These complex functions, however, can be determined experimentally by evaluating the generating functions of single conductors, which present a uniform distribution of the electric field at their surface. The results can subsequently be used to evaluate the generating functions of bundle conductors, taking into account the actual field distribution at the surface of subconductors.

Corona performances of single conductors: In the 1970s, considerable efforts were made at IREQ to the predetermination of the corona performances of conductors for HV lines. A large number of tests were made on single conductors of diameters between 2.45 and 7.62 cm under condition of artificial rain and over a range of electric field intensities between 10 and 30 kV/cm. The results are presented in Figures 8.42 to 8.44, respectively, for the generated losses W_s, the excitation function Γ_s, and the generated acoustic power density A_s and can be expressed by the following empirical formula:

$$W_s = w(E,d) = e^{-17.41} E^{5.80} d^{2.46} \tag{8.132}$$

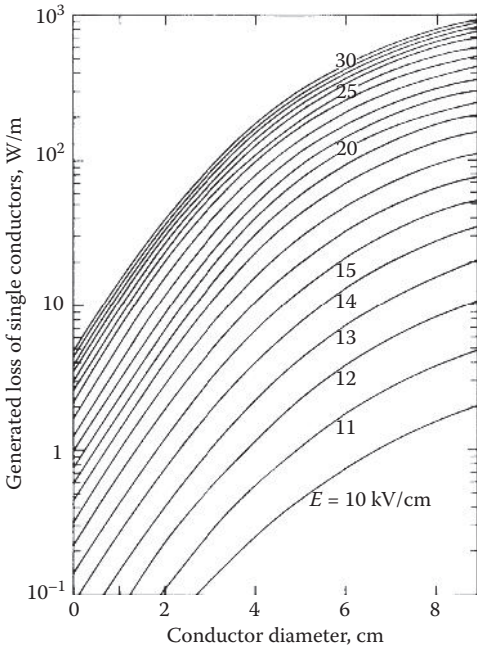


FIGURE 8.42 Generated losses W_s of single conductors. (From Trinh, N.G. and Maruvada, P.S., A method of predicting the corona performance of conductor bundles based on cage test results, *IEEE Trans* PAS-96, 312, 1977.)

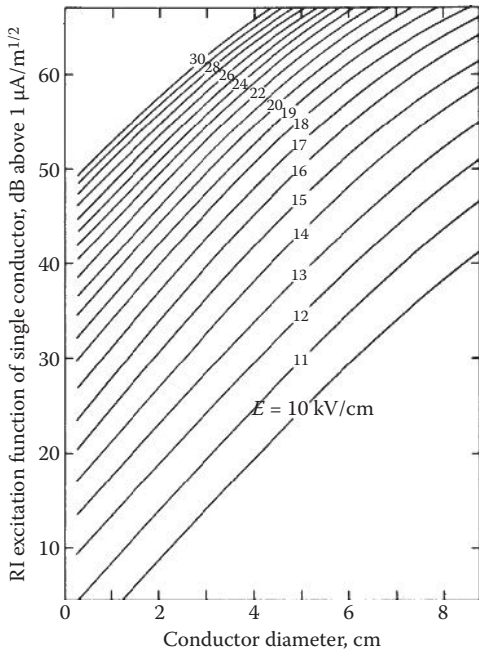


FIGURE 8.43 Excitation functions of single conductors. (From Trinh, N.G. and Maruvada, P.S., A method of predicting the corona performance of conductor bundles based on cage test results, *IEEE Trans* PAS-96, 312, 1977.)

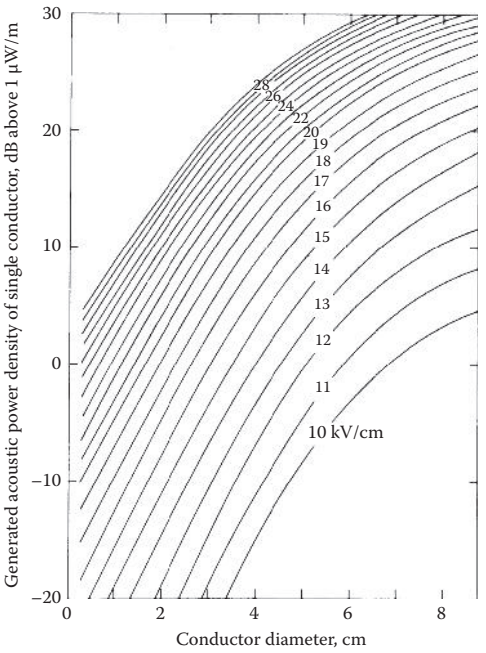


FIGURE 8.44 Generated acoustic power density of single conductors. (From Trinh, N.G. and Maruvada, P.S., A method of predicting the corona performance of conductor bundles based on cage test results, *IEEE Trans* PAS-96, 312, 1977.)

$$G_s\,(\mathrm{dB}) = g(E,d) = -93.35 + 92.42\log(E) + 43.03\log(d) \tag{8.133}$$

$$A_s\,(\mathrm{dB}) = a(E,d) = -123.94 + 82.84\log(E) + 48.28\log(d) \tag{8.134}$$

where

E is the effective field intensity in kV_{rms}/cm

d is the conductor diameter in cm

Corona performances of bundle conductors: For a bundle conductor, the subconductor diameter d is known, which defines a specific set of functions $w(E, d)$, $\gamma(E, d)$, and $a(E, d)$. The generating function of the bundle conductor then depends only on the local electric field at the surface of the conductors. Figure 8.45 (Trinh and Maruvada, 1977) shows the field distribution at the subconductor of different bundle configurations. It can be seen that the field intensity at the surface of a subconductor in a bundle varies with its position and can be expressed as

$$E(\theta) = E_a + \frac{\Delta E}{2}\cos(\varphi - \alpha) \tag{8.135}$$

where

θ is the angle defining a point at the subconductor surface with respect to the point of maximum field intensity

φ is the angle defining a point at the subconductor surface with respect to the horizontal axis

α is the angle of the point of maximum field intensity at the subconductor surface, with respect to the horizontal axis

E_a is the average field intensity

ΔE is the difference between the extreme field intensities at the subconductor surface

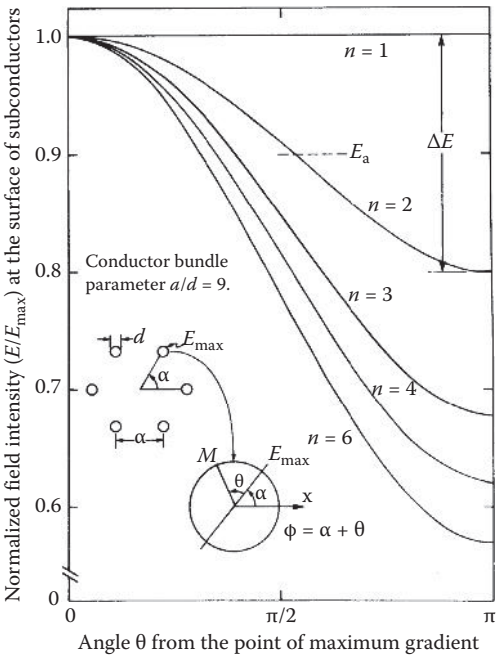


FIGURE 8.45 Variations of the electric field at the surface of subconductors for different values of n. (Trinh, N.G. and Maruvada, P.S., A method of predicting the corona performance of conductor bundles based on cage test results, IEEE Trans PAS-96, 312, 1977.)

The generating functions of a bundle conductor are obtained by integrating, over the contours of the subconductors, the contributions coming from the local discharges and taking into account the distribution of the electric field at the surface of the subconductors.

For generated losses, W_b,

$$W_b = \frac{C_b}{C_s}\left[\sum_{1}^{n}\frac{1}{2\pi}\int_{0}^{2\pi} W_s(E,d)\,df\right] \tag{8.136}$$

For the RI excitation function, Γ_b,

$$G_b = \frac{C_s}{C_b}\left[\sum_{1}^{n}\sqrt{\frac{1}{2\pi}\int_{0}^{2\pi} \Gamma_s^{\,2}(E,d)\,df}\right] \tag{8.137}$$

For the generated acoustic power density, A_b,

$$A_b = \left[\sum_{1}^{n}\sqrt{\frac{1}{2\pi}\int_{0}^{2\pi} A_s(E,d)\,df}\right]^2 \tag{8.138}$$

where C_s and C_b are, respectively, the capacitances of the single conductor and the bundle conductor in the test cage.

Since $\Gamma_s(E, d)$, $A_s(E, d)$, and $W_s(E, d)$ vary with the local field at the surface of the subconductors, this approach takes account of the actual field distribution at the surface of the subconductors in the bundle. It requires an accurate evaluation of the field distribution at the surface of the subconductors. Figures 8.46 through 8.48 show variations of the generating functions of four-conductor bundles, as a function of the

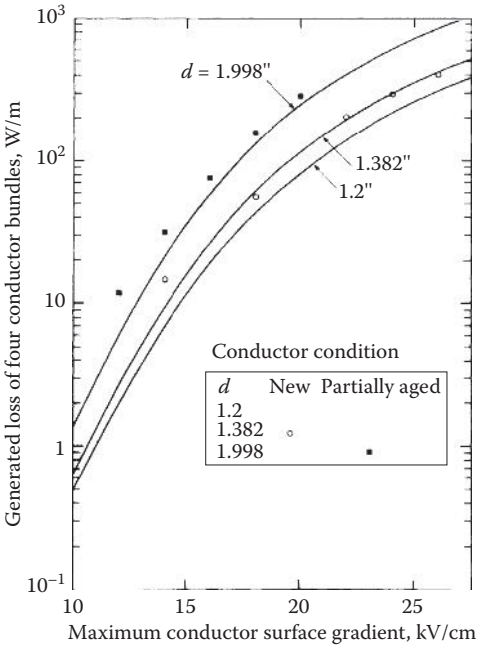


FIGURE 8.46 Generated losses *W* of four-conductor bundles. (From Trinh, N.G. and Maruvada, P.S., A method of predicting the corona performance of conductor bundles based on cage test results, *IEEE Trans* PAS-96, 312, 1977.)

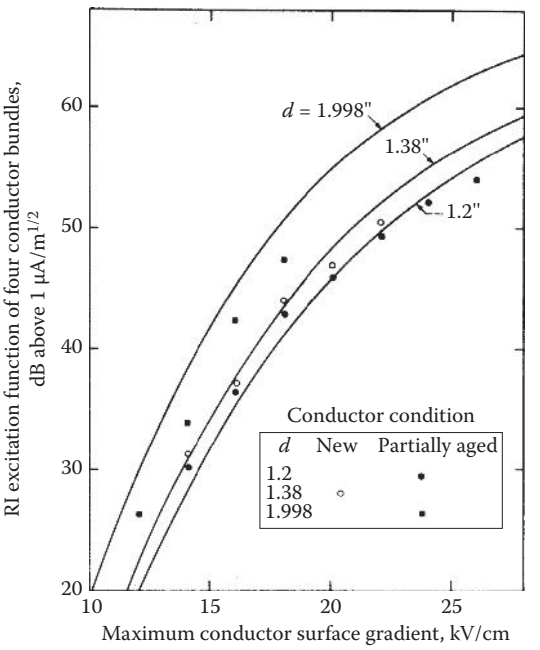


FIGURE 8.47 Excitation functions of four-conductor bundles. (From Trinh, N.G. and Maruvada, P.S., A method of predicting the corona performance of conductor bundles based on cage test results, IEEE Trans PAS-96, 312, 1977.)

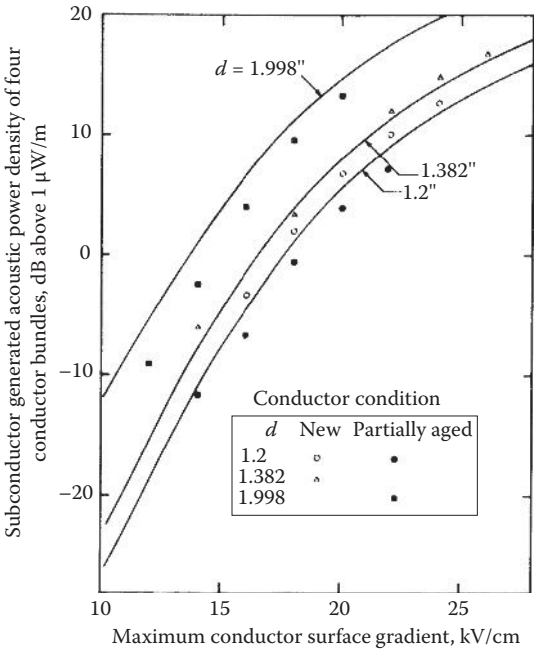


FIGURE 8.48 Generated acoustic power densities of four-conductor bundles. (From Trinh, N.G. and Maruvada, P.S., A method of predicting the corona performance of conductor bundles based on cage test results, *IEEE Trans* PAS-96, 312, 1977.)

field intensity at the surface of the conductors. Numerical values of the field intensities and of the generating functions for a 735 kV line of Hydro-Québec are given in Table 8.2.

Once the generating quantities are determined, the worst-case corona performances of the line can be evaluated as described in previous sections. The results presented in Figures 8.28 and 8.39, which compare the calculated and measured lateral RI and AN profiles of a number of HV lines, illustrate the good agreement obtained. In the preliminary stage of a project, analytical evaluation of the worst-case performances of HV line conductors, using available experimental data obtained in cage tests under conditions of artificial heavy rain, makes it possible to avoid tedious and expensive tests to help select the best configurations of line conductors to meet a given rating of the line.

8.3.5.2 Long-Term Corona Performance

Because of its wide range of variations with weather conditions, representative corona performances of HV line are best evaluated in their natural environment.

Experimental evaluation of long-term corona performance: Test lines are generally used, which involves energizing the conductors for a sufficiently long period, usually one year, to cover most of the weather conditions and recording their corona performances together with the weather conditions. The necessarily higher cost of evaluation of the long-term corona performance usually limits its application to a small number of conductor configurations already selected from their worst-case performances. It should be noted that best results for the long-term corona performance evaluated on test lines are obtained when the weather pattern at the site is similar to that existing along the projected HV line. A direct transposition of the results is then possible. If this condition is not met, some interpretation of the experimental data is needed. This is done by first decomposing the recorded long-term data into two groups, corresponding to the fair and foul-weather conditions, then recombining these data according to the local weather pattern to predict the long-term corona performance along the line; see Chapter 3.

Analytical estimation of the annual variations of corona performance: Evaluation of the annual statistic variations of the corona performances assumes that distributions of the corona performances, as energy losses, RI and AN, under fair and foul-weather conditions, are known. Generally, the distributions of the annual statistical variations of the RI and AN, are evaluated at the edge of the rights-of-way of the line (usually 15 m from the outer phase). For the distribution of the energy losses, the absolute values of W are converted in dB above a reference value W_{re} = 1 kW/km, before proceeding to the statistical analysis:

$$\mathrm{CL}\,(\mathrm{dB}) = 10\log(W) \tag{8.139}$$

Since heavy rain conditions correspond to the worst weather conditions, the results obtained in test cages under artificial rain are assumed to correspond to the level of the following:

$U_{50\%} + \sigma$ for a *normal* distribution and

$U_0 + \alpha$ for an *extreme values* and Weibull distributions

RI and AN levels under fair-weather conditions are assumed to be negligible compared to ambient noise, typical of the *Montréal* rural region, and the energy losses under fair weather are estimated to be at 10% of the heavy rain value.

Table 8.5 gives the suggested parameters for the fair and foul-weather distributions, which are used in the evaluation of the annual statistical distribution of the corona performance of a 735 kV line of *Hydro-Québec* shown in Figures 8.49 through 8.51.

8.3.6 Emission of Polluting Effluents

Mechanism of emission of effluents: During corona discharges, the absorption of energy by the air molecules, nitrogen N_2 and oxygen O_2, contributes to break the molecular link between the atoms in the gas molecule, giving rise to atomic particles, neutral or ionized, which are chemically actives. While the large majority of these atoms will recombine to form the initial gas molecules, a small portion of them will react among themselves to form stable by-products, namely, ozone O_3 and nitric oxides NO_x, according to the following chemical reactions:

- Under the action of UV radiations emitted from corona discharges,

$$O_2 \rightarrow O + O$$

$$NO_2 \rightarrow NO + O$$

- The formation of ozone is made in a three-way collision, according to

$$O + O_2 + M \rightarrow O_3 + M$$

$$O_2^* + O_2 \rightarrow O_3 + O$$

- The oxidants O_3 and NO are not stable substances; they recombine together to restitute the molecules NO_2 and O_2, according to

$$O_3 + NO \rightarrow NO_2 + O_2$$

TABLE 8.5

Suggested Parameters for the Statistical Distributions of Corona Performance

	Foul Weather		Fair Weather	
Parameters	**Mean Value**	**Std Deviation**	**Mean Value**	**Std Deviation**
RI (dB)	RI_f = 70.01	5% RI_f	RI_b = 50	20% RI_b
Energy losses (dB)	CL_f = 16.06	5% CL_f	CL_b = 0.1 * CL_f	20% CL_b
AN (dBA)	AN_f = 55.13	5% AN_f	AN_b = 45	20% AN_b

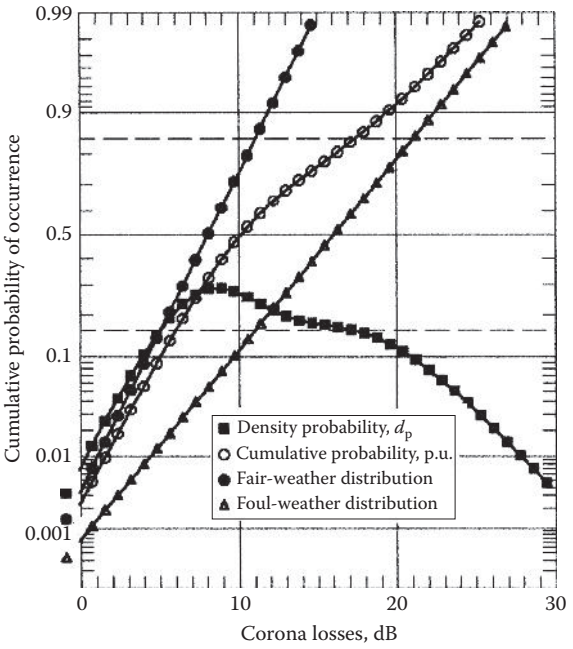


FIGURE 8.49 Annual statistical distributions of energy losses—735 kV line of *Hydro-Québec*.

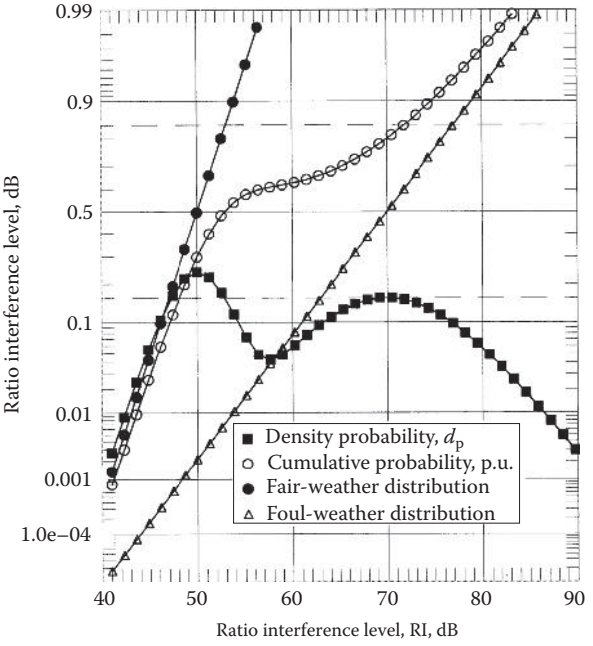


FIGURE 8.50 Annual statistical distributions of RI—735 kV line of *Hydro-Québec*.

The irritating and corrosive nature of these by-products, in particular ozone, has raised some concerns regarding construction of transmission lines in the proximity of urban zones. The calculations based on measurements in laboratories (Scherer et al., 1973) show that a maximal concentration of ozone, in the order of a few parts per billion (ppb), can be attributed to corona discharges on the AEP 765 kV lines, while the natural ambient concentration of ozone measured by AEP near 765 kV lines can reach

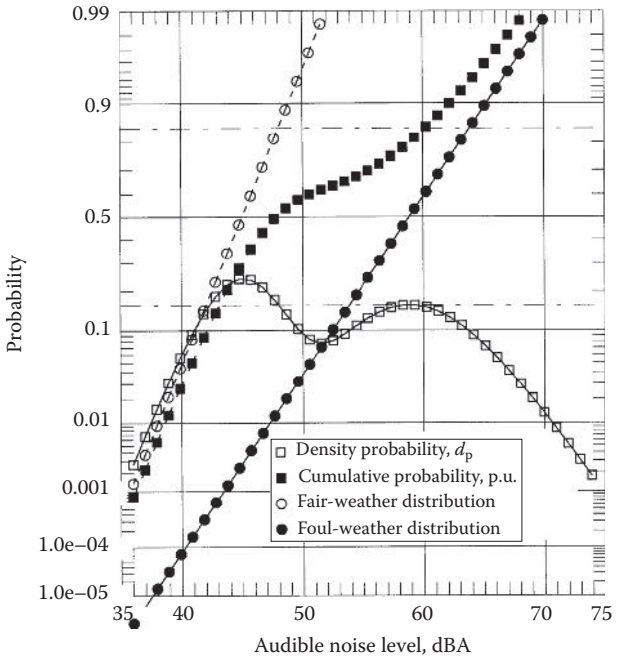


FIGURE 8.51 Annual statistical distributions of AN—735 kV line of *Hydro-Québec*.

several tens ppb. As a result, no substantial variations in the ozone level can be detected, confirming at the same time the low contribution from corona discharges on the HV lines already predicted by the calculation (Frydman et al., 1973). This aspect of the secondary effect of corona discharges appears presently of little concern and does not constitute a criterion for the selection of conductors for HV lines.

8.4 Selection of Conductors for HVDC Lines

Generally speaking, there is no significant difference in the selection of conductors for ac and dc power transmission. The discussion on HVAC line design so far can be extended to HVDC lines, as long as one takes into account the specificities associated with the latter mode of power transmission. These aspects of HVDC power transmission will be discussed in the following.

8.4.1 Average Conductor Height

A brief review for solution of ionized field equations (Maruvada, 2000) is given in the section dealing with dc corona losses below. Average conductor height is generally determined from criterion on ionized ground field and ion current density at ground. Typical design values under the line are 25 kV/m and 100 nA/m^2.

Electric field effect: In presence of a dc electric field, both phenomena related to the charging (or discharging) of the body capacitance and to the induced current are present. However, since the induced current is limited by the resistance (and not the capacitance) of the air space between the person and the line conductors, it is much lower than in the case of an ac field. The effect of charging (or discharging) of the body capacitance, on the other hand, is more disagreeable due to the presence of ionic currents in the immediate surrounding of HVDC lines. These ionic currents continuously charge the body capacitance C, gradually increasing the induced voltage of the person. Eventually, the induced voltage reaches a value sufficiently high to cause the breakdown of the air gap separating the person

from the ground, thus discharging the body capacitance. Exposing a person to a dc electric field subjects him to charging (or discharging) currents, which occur at regular intervals. The phenomenon is without consequence, although it can be quite disagreeable. It is more pronounced in fair weather as a result of the improved natural insulation of the air space between the person and the ground, that is, a higher breakdown voltage and a lower induced current, which favor the accumulation of charge on the person.

8.4.2 Selection of Conductors

Conductor selection is made to achieve a most economic cross section, with due considerations to power losses and resistive voltage drop along the line. The selection of conductor bundle on the other hand, is determined by corona performances, Several differences exist with the dc voltages, namely.

The ion displacement covers the whole distance separating the line conductors and between the conductors and the ground. As a result, under corona discharge conditions, the space between the line conductors and ground is partially filled with ion space charges, which affect the field distribution in the gap so as to considerably increase the field at ground and reduce it in the conductor vicinity. This can be evaluated by solving the Poisson equation.

The dc field tends to stabilize the waterdrops on the conductors. Their shape and size are determined by the equilibrium state between the water supply and removal of the drops. At low rain rate, streamer discharges can develop at the tip of the waterdrops as the waterdrops break up into small droplets. Under heavy rain, however, the waterdrops are extended further into the lower field region, causing waterdrop breaking up in the low field region, away from the conductor, with the result that positive streamers are replaced by a glow discharge developing at the surface of the extended waterdrops (Hoburg and Melcher, 1975).

The collection of charged particles at the conductors: The unipolar field produces different effects on the two poles. The negative pole is subjected to bombardment of positive ions produced in corona discharges, which tend to clean up the conductor. The positive pole also attracts negative ions, which are often of aggregated forms of larger dimensions and, therefore, move more slowly with the result that the positive pole tends to collect dusts and aerosols.

8.4.2.1 Corona Onset

The corona onset on a cylindrical conductor is given by the Peek formula (8.121). For a smooth conductor, the surface condition factor m is close to 1, being slightly lower for negative corona than positive discharges. However, for practical stranded conductors, the surface condition factor is between 0.6 and 0.7 in fair weather, and below 0.6 in foul weather, with a value between 0.3 and 0.4 for snow and rain conditions, and no difference between the onset fields at the two polarities. An extensive analysis of the corona performances of HV dc transmission lines was carried out in Maruvada (2000). The highlights are presented in the following.

8.4.2.2 Generating Functions

Generating functions are also used to evaluate the corona performances of dc lines. However, because of the distinct polarities, the corona discharge activities are also different on the two poles, consisting of Trichel streamers and negative glow discharge on the negative conductor, positive streamers, and positive glow on the positive conductor. Therefore, the generating functions are generally different for the positive and negative conductors.

8.4.2.3 Corona Losses

Corona losses are generated by displacement of the ions produced in the discharges across the interconductor and conductor-ground spaces. For ac lines, the regular reversal of the line voltage polarity limits the ion displacement within a few tens of centimeters around the conductors, with the result that

each phase conductor can be considered as an independent source of energy losses. The concept of a generating function, the generated losses, characteristic of the conductor is fully justified.

For dc lines, the ion displacement covers the whole distance separating the line conductors and between the conductors and ground. The concept of generated losses is still valid for a single-phase dc line. Its extension to the case of a bipolar dc line is, however, not possible: the total losses are higher than the sum of two single-phase lines as can be seen from the results of Figures 8.52 and 8.53, which compare unipolar and bipolar losses from lines of comparable voltages and using similar conductor configurations.

This can be visualized by noting that, for a bipolar dc line (Figure 8.54), in addition to the natural ground, there is also a virtual vertical ground located at midway between the two poles. If the latter is replaced by a solid vertical ground plane, then the line CLs will be equal to the sum of the two single-phase lines associated with the two poles. The additional bipolar losses correspond then to the additional travel distance that ions of both polarities have to complete to reach the pole of opposite polarity when the solid ground plane is replaced by the virtual vertical ground plane. Bipolar losses must be taken as a whole, which can be evaluated either theoretically or from experimental data obtained from tests on an experimental test line.

Empirical formulae: Early attempt to derive an empirical formula for dc CL was made by Knudsen and Illiceto (1974), which gives the following formula for unipolar lines:

$$P = U k_c n r 2^{0.23(g-g_0)} 10^{-3} \tag{8.140}$$

where

P is the corona loss in kW/km
U is the line voltage in kV
n is the number of sub conductors in the bundle
r is the sub-conductor radius in cm
g is the maximum bundle gradient in kV/cm
g_0 is the reference value of g and
k_c is an empirical constant

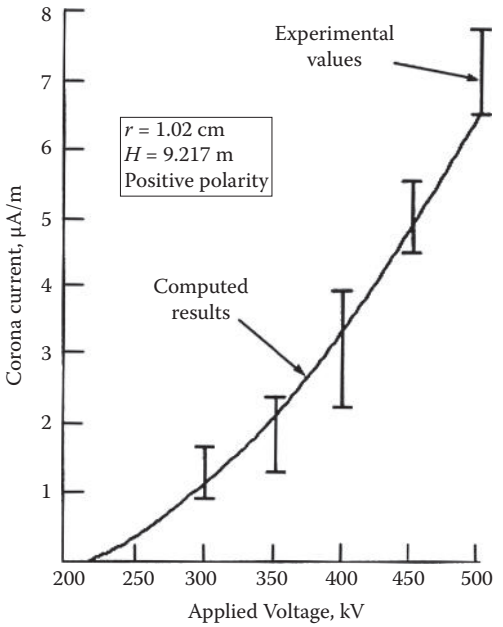


FIGURE 8.52 Variation of corona current from a positive pole with applied voltage. (From Janischewskyj, W. et al., Corona losses and ionized fields of HVDC transmission lines, CIGRE Paper No. 36-09, Paris, France, 1982.)

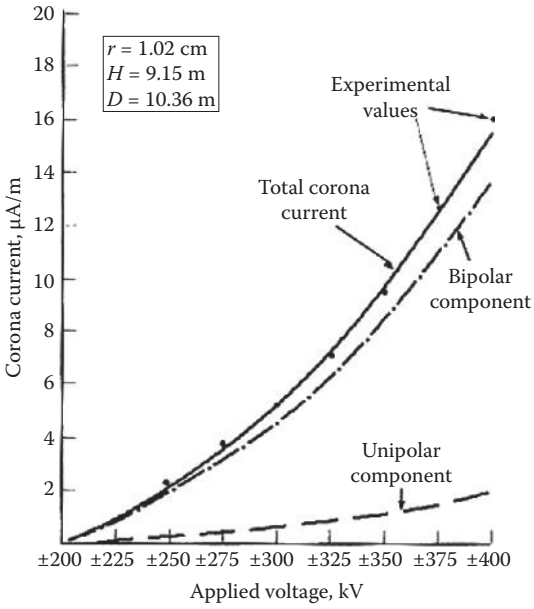


FIGURE 8.53 Variation of corona current of a bipole with applied voltage. (From Janischewskyj, W. et al., Corona losses and ionized fields of HVDC transmission lines, CIGRE Paper No. 36-09, Paris, France, 1982.)

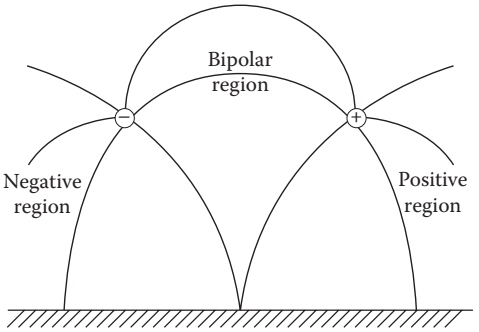


FIGURE 8.54 Components of dc corona discharge current. (From Maruvada, P.S., *Corona Performance of High Voltage Transmission Lines*, Research Studies Press, Hertfordshire, England, 2000.)

and for bipolar line:

$$P = 2U\left[\frac{2}{\pi}\tan^{-1}\left(\frac{2h}{S}\right)\right]k_c\, n r\, 2^{0.25(g-g_0)}\, 10^{-3} \tag{8.141}$$

where

P is the corona loss in kW/km
U is the voltage applied to the bipolar line in kV
h is the average conductor height in m
S is the pole spacing in m
n is the number of sub conductors in the bundle
r is the sub-conductor radius in cm
g is the maximum bundle gradient in kV/cm
g_0 is the reference value of g and
k_c is an empirical constant

More recent studies have proposed formulae for bipolar lines by Maruvada et al. (1982) for line voltages between ±600 kV and ±1200 kV:

$$P = P_0 + k_1 (g - g_0) + k2 \log \left(\frac{n}{n_0} \right) + 20 \log \left(\frac{d}{d_0} \right) \tag{8.142}$$

where P and P_0 are CLs expressed in dB above 1 W/m. With $n_0 = 6$, $d_0 = 4.064$ cm, $g_0 = 25$ kV/cm, the values for P_0, k_1, and k_2 are given in Table 8.6.

It can be seen that the CLs are higher in foul weather than in fair, with highest losses occurring in summer and lowest losses in winter.

For HVDC lines between ±150 kV and ±1200 kV, Corbellini and Pellaci (1996) introduced

For fair weather

$$P = P0 + 50 \log \left(\frac{g}{g_0} \right) + 30 \log \left(\frac{d}{d_0} \right) + 20 \log \left(\frac{n}{n_0} \right) - 10 \log \left(\frac{HS}{H_0 S_0} \right)$$

For foul weather

$$P = P0 + 40 \log \left(\frac{g}{g_0} \right) + 20 \log \left(\frac{d}{d_0} \right) + 15 \log \left(\frac{n}{n_0} \right) - 10 \log \left(\frac{HS}{H_0 S_0} \right)$$

where P and P_0 are CLs expressed in dB above 1 W/m, with $g_0 = 25$ kV/cm, $d_0 = 3.05$ cm, $n_0 = 3$, $H_0 = 15$ m, and $S_0 = 15$ m. The values for P_0 are 2.9 dB for fair weather and 11 for foul weather.

Theoretical calculation of corona losses: Theoretical evaluation of the CLs in dc transmission lines is complex. However, adequate results are obtained with some simplifications. The reader can find a detailed analysis of CLs from unipolar and bipolar dc lines in the reference (Maruvada, 2000). We summarize in the following the main approach used in the calculation of CLs, based on the following assumptions:

- Space charges affect only the magnitude and not the direction of the electric field.
- For voltages above corona onset, the magnitude of the electric field at the surface of the conductor in corona remains constant at the onset values.

The first assumption is the so-called Deutsch's first assumption, which makes it possible to convert an essentially 2D problem into an equivalent 1D problem. Physically, this assumption implies that the geometric

TABLE 8.6

Parameters for Evaluation of Bipolar CLs

Season	Weather	P_0 (dB)	k_1	k_2
Summer	Fair	13.7	0.8	28.1
	Foul	19.3	0.63	9.7
Fall/spring	Fair	12.3	0.88	36.9
	Foul	17.9	0.72	12.8
Winter	Fair	9.6	1.0	44.3
	Foul	14.9	0.85	10.2

pattern of the electric field remains unaffected by the presence of ion space charges, which means that the electric fields with and without space charges are related by a scalar point function according to

$$\mathbf{E} = x\mathbf{E}' \tag{8.143}$$

The flux lines are unchanged while the potential lines are shifted; a condition not always satisfied under conditions of intense corona activities. The magnitudes of the electric field in both cases are

$$\mathbf{E} = -\frac{dF}{ds} \quad \mathbf{E}' = -\frac{df}{ds} \tag{8.144}$$

where

E and E' and Φ and φ are, respectively, the fields and potentials with and without space charge
s is the distance measured along the flux line of the space charge-free field

The second assumption does find some justifications for conditions normally encountered in overhead transmission lines. Combining Equations 8.143 and 8.144 yields

$$\frac{dF}{df} = x \tag{8.145}$$

Unipolar line (Maruvada and Janischewskyj, 1969a): For unipolar dc space charge field, the Maxwell equations are

$$-\nabla \cdot \mathbf{E} = \frac{r}{\varepsilon_0} \tag{8.146}$$

$$\mathbf{j} = mr\mathbf{E} \tag{8.147}$$

$$-\mathbf{j} = 0 \tag{8.148}$$

Substituting Equation 8.143 into 8.146 gives

$$\mathbf{E}' \cdot \nabla x = \frac{r}{\varepsilon_0}$$

Since $E' \cdot \nabla\xi$ represents the projection of the vector $\nabla\xi$ in the direction of $\mathbf{E}'$, one has

$$\mathbf{E}' \cdot \nabla x = E' \frac{dx}{ds} = \frac{r}{\varepsilon_0}$$

that can be transformed into

$$\frac{dx}{df} = -\frac{r}{\varepsilon_0 (E')^2} \tag{8.149}$$

In a similar way, substituting Equations 8.146 and 8.143 into (8.147) gives

$$\frac{dr}{df} = \frac{r^2}{\varepsilon_0 x (E')^2} \tag{8.150}$$

Equations 8.145 through 8.150 describe the distributions of electric field and charge density along the flux line, which can be solved in an iterative process, for the charge density ρ, which would respect the boundary conditions as

$$\Phi = U \quad \text{at} \quad \phi = U$$

$$\Phi = 0 \quad \text{at} \quad \phi = 0$$

$$x_- = \frac{U_{0-}}{U} \quad \text{at} \quad f = -U$$

Once the charge density ρ has been determined, the current density at the surface of the conductor is obtained from Equation 8.147. By subdividing the surface of the conductor into a number of segments, the charge and current density associated with each segment can be defined. The total corona current is then the total sum of various current densities and allows the calculation of the CLs. Figure 8.52 compares the calculated and measured values of corona current for a unipolar line (Janischewskyj et al., 1982) and illustrates the validity of this approach.

Bipolar lines (Maruvada and Janischewskyj, 1969): Are characterized by the division of the space around the lines into unipolar and bipolar regions. In the unipolar region, the charge density *r* can be determined following the approach described above for unipolar lines. In the bipolar region, the Maxwell equations are

$$-\nabla \mathbf{E} = \frac{r_+ - r_-}{\varepsilon_0} \tag{8.151}$$

$$\mathbf{j}_+ = \mu_+ r_+ \mathbf{E}$$

$$\mathbf{j}_- = \mu_- r_- \mathbf{E}$$

$$\mathbf{j} = \mathbf{j}_+ + \mathbf{j}_- = (\mu_+ r_+ + \mu_- r_-)\mathbf{E} \tag{8.152}$$

Noting that ion recombination can take place in the bipolar region, as described by the following equations, with *R* being the ions recombination coefficient in air, $R = 1.2 \times 10^{-12}$ m^3/s:

$$-\nabla \cdot \mathbf{j}_+ = -\frac{R r_+ r_-}{e}$$

$$-\nabla \cdot \mathbf{j}_- = \frac{R r_+ r_-}{e}$$

$$-\nabla \cdot \mathbf{j} = 0 \tag{8.153}$$

Substituting Equation 8.143 in (8.151), and changing the independent variable to ξ, yields

$$\frac{dx}{df} = \frac{r_+ - r_-}{\varepsilon_0 (E\phi)^2} \tag{8.154}$$

$$\frac{dr_+}{df} = \frac{1}{\varepsilon_0 x (E\phi)^2} \left[r_+^2 - r_+ r_- \left(1 - \frac{\varepsilon_0 R}{\mu_+ e} \right) \right] \tag{8.155}$$

and

$$\frac{d\rho_-}{d\phi} = -\frac{1}{\varepsilon_0 x (E\Phi)^2}\left(\frac{E}{r}\rho_-^2 - r_+\rho_- E\right) - \frac{\varepsilon_0 R}{m_- e}\rho_- \tag{8.156}$$

Equations 8.143, 8.154, and 8.156 describe the distributions of electric field and charge density along the flux line. These equations can be solved using an iterative process, for the charge density ρ_+ and ρ_-, using an iterative process, which would respect the boundary conditions as

$$\Phi = U \quad \text{at} \quad \phi = U$$

$$\Phi = -U \quad \text{at} \quad \phi = -U$$

$$x_+ = \frac{U_{0+}}{U} \quad \text{at} \quad \phi = U$$

$$x_- = \frac{U_{0-}}{U} \quad \text{at} \quad \phi = -U$$

Once the charge densities ρ_+ and ρ_- have been defined, the current densities at the surface of the line conductors are obtained from Equation 8.152. By subdividing the surface of the conductor into a number of segments, the charge and current densities associated with each segment can be defined. The total corona current is then the total sum of the various currents, and allows the calculation of the CLs. Figure 8.53 compares the calculated and measured values of corona currents on a bipolar line (Janischewskyj et al., 1982) and illustrates the validity of this approach.

8.4.2.4 Radio Interference

RI is reduced under heavy rain conditions, due to the effect of dc field on the shape and size of waterdrops on the conductors (Hoburg and Melcher, 1975). RI is more pronounced under conditions of snow, dust deposits, etc., favorable to the development of streamer discharges. As a result, heavy rain is not the worst condition for RI, which occurs rather under light rain, fog, snow, and even fair weather. In addition, positive streamers generate current pulses of several orders of magnitude higher than negative Trichel streamers. As a result, for an HVDC bipolar line, the positive pole is the only contributor to the RI generation.

Empirical formulae
Hirsch and Schaffer (1969):

$$\mathrm{RI} = RI_0 - 29.4\log\frac{D}{D_0} - 20\log\frac{1+f^2}{1+f_0^2} \tag{8.157}$$

where
D is the radial distance between the conductor and the measuring antenna in m
f is the measuring frequency in MHz
RI_0, D_0 and f_0 are reference values

Knudsen and Illiceto (1974):

$$\mathrm{RI} = 25 + 10\log(n) + 20\log(r) + 1.5(g - g_0) - 40\log\frac{D}{D_0} \tag{8.158}$$

where
n is the number of sub conductors
r the sub-conductor radius in cm
g is the maximum gradient in kV/cm
D is the radial distance between the positive conductor and the measuring antenna in m with $D_0 = 30$ m and $g_0 = 22\,\delta$ where δ is the relative air density

BPA for average fair weather RI

$$\mathrm{RI} = 51.7 + 86 \log \frac{g}{g_0} + 40 \log \frac{d}{d_0} \tag{8.159}$$

where
g is the maximum bundle gradient in kV/cm
d is the conductor diameter in cm with $d_0 = 4.62$ cm and $g_0 = 25.6$ kV/cm

Maruvada et al. (1979) derive an empirical formula for the excitation function Γ, based on test results at IREQ for lines between ±600 and ±1200 kV:

$$\Gamma = \Gamma_0 + k_1 (g - g_0) = k_2 \log \frac{n}{n_0} + 40 \log \frac{d}{d_0} \tag{8.160}$$

where Γ and Γ_0 are the excitation functions expressed in dB above 1 $\mu A/\sqrt{m}$. With $n_0 = 6$, $d_0 = 4.064$ cm, and $g_0 = 25$ kV/cm, the values for Γ_0, k_1, and k_2 are given in Table 8.7.

It can be seen that the spring, summer, and fall excitation functions are lower under foul weather than fair, a direct result of the low level of RI from rain, while the winter excitation function is higher in foul weather than fair resulting from the higher RI level from snow.

Theoretical calculation: Of the RI from a bipolar HVDC line is made using the concept of the excitation function. The matrix of line parameters is only of the order 2 by 2. Furthermore, the positive pole being the sole contributor to RI, the column matrix of the excitation function has only one positive term. As for the case of a three-phase line, the calculation of RI current is made in three stages:

- Decomposition of the interference wave into its modal components:

$$[J_0(\omega)]\,dx = [M]^{-1}[I_0(\omega)]\,dx \tag{8.161}$$

  where
  $[M]$ is the modal matrix
  $[I_0(\omega)]$ is the matrix of the injected corona noise current
  $[J_0(\omega)]$ is the matrix of its modal components
- Evaluate the modal components at the measuring point, taking into account the propagation characteristics proper to each modal component:

$$[J(\omega)] = \frac{1}{\sqrt{\alpha}}[J_0(\omega)] = \frac{1}{4\pi\varepsilon_0}\frac{1}{\sqrt{\alpha}}[M]^{-1}[C][\Gamma] \tag{8.162}$$

  where
  $\sqrt{\alpha}$ is the matrix of attenuation coefficient
  $[C]$ is the line capacitance matrix
  $[\Gamma]$ is the matrix of the excitation function
- Reconstitute the interference wave at the measuring point:

$$[I(\omega)] = [M][J(\omega)] \tag{8.163}$$

The magnetic and electric field at the measuring point, produced by the interference current, can then be evaluated for the calculation of RI of the line.

TABLE 8.7

Parameters for Evaluation of the Excitation Function Γ

Season	Weather	Γ_0 (dB)	k_1	k_2
Summer	Fair	27.0	1.83	45.8
	Foul	20.4	1.39	48.0
Fall/spring	Fair	23.4	1.68	29.0
	Foul	19.8	1.68	63.5
Winter	Fair	18.7	1.63	19.7
	Foul	19.5	1.47	10.0

Modal transformation matrix: Can be derived from the geometric matrix [*P*] of the line, using the following relationship (Trinh et al., 1974):

$$[M]^{-1}[P][M] = [\lambda]_d$$

which can be rewritten as

$$[P][M] = [\lambda]_d[M]$$

or

$$\{[P] - [\lambda]_d\}[M] = 0 \tag{8.164}$$

where

[*P*] is the matrix of the potential coefficients

$[\lambda]_d$ is the diagonal spectral matrix, which is related to the matrix of modal characteristic impedances, according to $[Z_m] = 60[\lambda]_d$

The preceding equation can be rewritten as

$$\begin{bmatrix} p_{11} - 1 & p_{12} \\ p_{21} & p_{22} - 1 \end{bmatrix} \begin{bmatrix} m_{11} & m_{12} \\ m_{21} & m_{22} \end{bmatrix} = 0 \tag{8.165}$$

which has a nontrivial solution only if the determinant of the first matrix is null:

$$\begin{vmatrix} p_{11} - 1 & p_{12} \\ p_{21} & p_{22} - 1 \end{vmatrix} = 0 \tag{8.166}$$

Equation 8.164 is reduced to a second-degree equation of λ, the solution of which determines the coefficients of the geometric modal transformation matrix. For a bipolar dc line, the modal transformation matrix is

$$[M] = \frac{1}{\sqrt{2}} \begin{bmatrix} 1 & 1 \\ -1 & 1 \end{bmatrix} \tag{8.167}$$

The physical interpretation of modal current components associates them to the line-to-line and line-to-ground modes. In the first mode, the modal current flows through one conductor and returns via the second line conductor. In the second mode, the modal current flows in both conductors and returns through the ground.

Coefficients of modal attenuation, α: Are generally a function of the line configuration, the resistivity of the soil, and the measuring frequency *f*. The line-to-line and line-to-ground modes of the bipolar dc line are

similar to the corresponding modes 2 and 3 of a horizontal three-phase line. Typical values of α are presented in Table 8.8. They are adjusted to the measuring frequency according to (Moreau and Gary, 1972b)

$$\alpha(f) = \alpha(f_0)\left(\frac{f}{f_0}\right)^{0.8} \tag{8.168}$$

where f_0 is the reference frequency at which the data are obtained.

Noting that for a dc line, the RI comes mainly from the positive pole. This is illustrated by the results of Figure 8.55, which show a typical lateral profile of RI from an HVDC line, with a marked dissymmetry in the RI profile. The RI from DC transmission lines is generally lower than that of a three-phase line using the same conductor bundles at comparable field intensity.

8.4.2.5 Audible Noise

AN is reduced under heavy rain conditions, due to the effect of the dc field on the shape and size of waterdrops on the conductors (Hoburg and Melcher, 1975). As for the case of RI, heavy rain is not the worst condition for AN, which occurs rather under light rain, fog, snow, and even fair weather, and the positive pole is the sole contributor to AN. In addition, the AN frequency spectrum does not contain any pure-tone noise and standing wave phenomenon associated with the oscillating movement of the ion space charges, as illustrated by the typical AN frequency spectrum of Figure 8.56 (IEEE Corona and Field Effect Subcommittee, 1981). As for the case of the RI, the AN of dc transmission lines comes mainly from the streamers discharge on the positive pole and is essentially that of a unipolar line. The AN level is, therefore, considerably lower than that of a three-phase line having the same conductor bundle at comparable field intensities.

Empirical Formulae

Chartier (Chartier and Stearn, 1981):

$$\mathrm{AN} = \mathrm{AN}_0 + 86\log(\mathrm{g}) + k\log(\mathrm{n}) + 40\log(\mathrm{d}) - 11.4\log(\mathrm{R}) \tag{8.169}$$

where

n is the number of sub conductors

d the sub-conductor diameter in cm

R the radial distance between the positive pole and the measuring microphone

with $k = 25.6$ for $n > 2$ and 0 for $n = 1$ and 2, $\mathrm{AN}_0 = -100.62$ for $n > 2$ and -93.4 for $n = 1$ and 2.

Maruvada et al. (1979) derive an empirical formula for the generated acoustic power density A:

$$A = A_0 + k_1(g - g_0) + 40\log\left(\frac{d}{d_0}\right) + 10\log\left(\frac{n}{n_0}\right) \tag{8.170}$$

where A and A_0 are the generated acoustic power densities expressed in dB above 1 μW/m. With $n_0 = 6$, $d_0 = 4.064$ cm, $g_0 = 25$ kV/cm, the values for A_0, k_1, and k_2 are given in Table 8.9.

TABLE 8.8

Modal Attenuation Coefficients

Line Configuration	**Bipolar DC Lines**	
f_0 **= 500 kHz**	**(dB/km)**	**(10^{-6} Np/m)**
Mode 1	0.5	54
Mode 2	3.0	342
f_0 **= 1.0 MHz**	**(dB/km)**	**(10^{-6} Np/m)**
Mode 1	1.0	115
Mode 2	6.0	691

Source: Moreau, M.R. and Gary, C.H., *IEEE Trans.*, PAS-91, 292, 1972b.

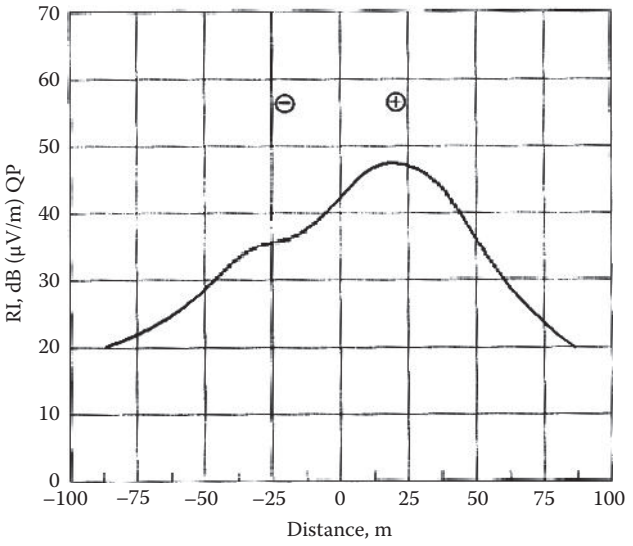


FIGURE 8.55 Lateral profile of RI from a HVDC line. (From Maruvada, P.S., *Corona Performance of High Voltage Transmission Lines*, Research Studies Press, Hertfordshire, England, 2000.)

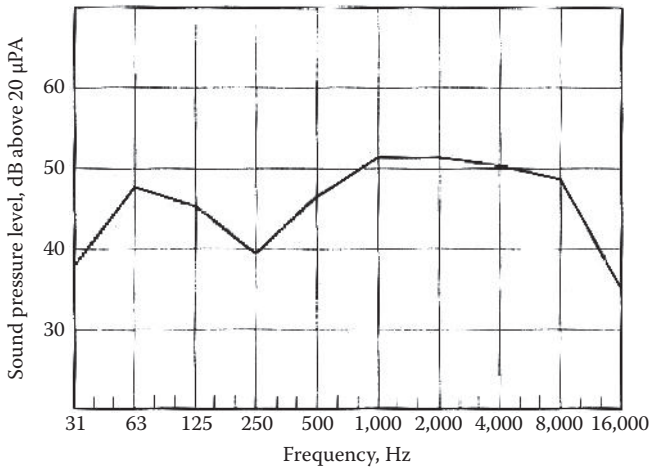


FIGURE 8.56 Typical frequency spectrum of HVDC line corona AN. (From IEEE Corona and Field Effect Subcommittee, *IEEE Trans*., PAS-100(3), 1440, 1981.)

TABLE 8.9

Parameters for the Evaluation of the Generated Acoustic Power Density A

Season	Weather	A_0(dB)	k_1
Summer	Fair	4.3	1.54
	Foul	1.48	1.52
Fall/spring	Fair	4.43	0.84
	Foul	4.06	0.84
Winter	Fair	1.84	0.51
	Foul	5.65	1.04

As for the case of RI, the summer-generated acoustic power density A_0 is higher in fair weather than in foul, a direct result of the low noise level associated mainly with rain, while the reverse effect was observed in winter corresponding to the effect of snow.

Theoretical calculation: The calculation of the AN is straightforward and corresponds to the addition of acoustic sound pressures generated from the individual discharge sources. In addition, since the positive pole is the only contributor to the AN, the AN from an HVDC line is reduced to the case of a single-phase line.

For a long line and assuming a coefficient of reflection of the ground of $K = 1$, the expression of the acoustic intensity at the measuring point simplifies to

$$I(R) = \frac{A}{2R}$$

The measurements of AN being generally made in function of the acoustic pressure, it is necessary then to evaluate the corresponding acoustic pressure, according to

$$p = \sqrt{\pi_0 C I(R)}$$

where

ρ_0 is the air density
C is the velocity of sound
R is the direct distance from the measuring point to the positive pole

The audible noise level AN is

$$\mathrm{AN}(\mathrm{dB}) = 20\log\frac{p}{p_{\mathrm{re}}}$$

8.4.2.6 Experimental Evaluation of Corona Performance of Conductor

Test cage: Has been a useful tool to evaluate the worst-case corona performances of bundle conductors under artificial heavy rain conditions. Its usefulness for evaluating the corona performances under dc voltages is much reduced, since there is not a single worst-case conditions for dc corona as for ac lines. The conditions for the highest RI and AN, snow, fog, or light rain, are not easily produced artificially. This tends to favor the long-term evaluation of dc corona on a test line over a long period of time to cover all the weather conditions of interest.

Attempts to use test cages to evaluate the dc corona performance under heavy rain conditions turn out to be unsuccessful. The problem is related to the difference in field distributions in test cages as compared to that under a dc line, mono- or bipolar. In a test cage, the field distribution is similar to that of a coaxial cylindrical conductor while the field distribution under a single-phase dc line is that of a bi-cylindrical configuration (Chapter 2). The field distribution in a test cage is thus representative of that prevailing in the high field region around the bundle conductor.

Under ac voltage, this situation is fully adequate since the movement of ion space charge is limited to a few tens of centimeters around the conductor bundle. The corona generating functions measured in test cages can be correlated to those prevailing in the line conductors, to evaluate the corona performance of HVAC lines.

The situation is different under dc voltage where the movement of charged particles across the whole conductor-to-ground gap contributes to the corona losses. It is further complicated in bipolar lines where a significant part of the corona losses is related to the movement of charged particles in the space between the two poles. As a result, the bipolar losses are not equal to the sum of corona losses from the two poles taking as monopolar lines. Cage test results, from both single and bipolar test cages, are inadequate to predict corona losses under dc voltage (Maruvada et al., 1981b), due to their limitation in reproducing the actual field distribution under HVDC lines.

Experimental test line: Essentially corresponds to a short span of the HVDC line, usually in the range of a few hundred meters. The line is energized at its nominal voltage over a long period of time, typically one full year, to cover all the weather conditions. Corona performances of the line conductors are recorded over the whole time period, which allows appropriate analysis of the long-term corona performance of the line conductor.

REFERENCES

Bortnik, I.M., Belyakov, N.N., Djakov, A.F., Horoshev, M.I., Ilynichin, V.V., Kartashev, I.I., Nikitin, O.A., Rashkes, V.S., Tikhodeyev, N.N., and O.V. Volkova. 1200 kV transmission line in the USSR: The first results of operation. CIGRE Report No. 38-09, Paris, France, August 1988.

Chartier, V.L. and R.D. Stearns. Formulas for predicting audible noise from overhead high voltage AC and DC lines. *IEEE Transactions* PAS-100: 121, 1981.

Corbellini, U. and P. Pelachi. Corona losses on HVDC bipolar lines. *IEEE Transactions* PWRD-11: 1475, 1996.

Dalziel, C.F. The threshold of perception currents. *AIEE Transactions on Power Apparatus & Systems* 73: 990–996, 1954.

Frydman, M., Levy, A., and S.E. Miller. Oxidant measurements in the vicinity of energized 765 kV lines. *IEEE Transactions* PAS-92(3): 1141–1048, 1973.

Gary, C.H. The theory of the excitation function: A demonstration of its physical meaning. *IEEE Transactions* PAS-91: 305, 1972.

Héroux, P., and N.G. Trinh. A statistical study of electrical and acoustical characteristics of pulsative corona. IEEE Paper No A-76 122-2, IEEE–PES Winter Meeting, New York, January 1976.

Hirsch, F.W. and E. Schaffer. Progress report on the HVDC test line of the 400 kV-Forschungsgemeinschaft: Corona losses and radio interference. *IEEE Transactions* PAS-88: 1061, 1969.

Hoburg, J.F. and J.R. Melcher. Current driven, corona terminated water jets as source of charged droplets and audible noise. *IEEE Transactions* PAS-94: 128, 1975.

Ianna, F., Wilson, G.L., and D.J. Bosak. Spectral characteristics of acoustic noise from metallic protrusion and water droplets in high electric fields. *IEEE Transactions*, PAS-93: 1787, 1974.

IEEE Corona and Field Effect Subcommittee. Measurement of audible noise from transmission lines. *IEEE Transactions* PAS-100(3): 1440, 1981.

IEEE Corona and Field Effect Subcommittee. A comparison of methods for calculating audible noise of high voltage transmission lines. *IEEE Transactions* PAS-101(10): 4090–4099, 1982.

IEEE Radio-Noise Subcommittee. CIGRE/IEEE survey of extra-high voltage transmission line radio noise. *IEEE Transactions* PAS-92(3): 1019–1028, 1973a.

IEEE Radio-Noise Subcommittee. Comparison of radio noise prediction methods with CIGRE/IEEE results. *IEEE Transactions* PAS-92(3): 1029–1042, 1973b.

Janischewskyj, W., Maruvada, P.S., and G. Gela. Corona losses and ionized fields of HVDC transmission lines. CIGRE Paper No. 36-09, Paris, France, 1982.

Juette, G.W. Evaluation of television interference from high-voltage transmission lines. *IEEE Transactions* PAS-91: 865, 1972.

Knudsen, N. and F. Illiceto. Contribution to the electrical design of HVDC overhead lines. *IEEE Transactions* PAS-93: 233, 1974.

Krishnayya, P.C.S., Lambeth, P.J., Maruvada, P.S., Trinh, N.G., and G. Désilets. An evaluation of the R&D requirements for developing HVDC converter stations for voltages above ± 600 kV. CIGRE Report No. 14-07, Paris, France, 1988.

Maruvada, P.S. *Corona Performance of High Voltage Transmission Lines*. Hertfordshire, England: Research Studies Press, 2000.

Maruvada, P.S., Dallaire, R.D., Héroux, P., Rivest, N. and R. Pedneault. Corona studies for bipolar HVDC transmission at voltages between ± 600 kV and ±1200 kV—Part 2: Special bipolar lines, bipolar cages and bus studies. *IEEE Transactions* PAS-100: 1462, 1981a.

Maruvada, P.S. and N. Hyltén-Cavallius. Capacitance calculation for some basic high voltage electrode configurations. *IEEE Transactions on Power Apparatus & Systems* PAS-94: 1708–1713, 1975.

Maruvada, P.S., Hyltén-Cavallius, N.R., Trinh, N.G., and M. De Vizio. Electrostatic field effects from high voltage power lines and in substations. CIGRE Report No. 36-04, Paris, France, 1976.

Maruvada, P.S. and W. Janischewskyj. Analysis of corona losses on DC transmission lines: I—Unipolar lines. *IEEE Transactions on Power Apparatus & Systems* PAS-88(5): 718–731, 1969a.

Maruvada, P.S. and W. Janischewskyj. Analysis of corona losses on DC transmission lines: II—Bipolar lines. *IEEE Transactions on Power Apparatus & Systems* PAS-88(10): 1476–1491, 1969b.

Maruvada, P.S. and N.G. Trinh. A basis for setting limits to radio interference from high voltage transmission lines. *IEEE Transactions* PAS-94(5): 1714–1724, 1975.

Maruvada, P.S., Trinh, N.G., Dallaire, R.D., Rivest, N., and P. Héroux. Corona studies for bipolar HVDC transmission at voltages between ± 600 kV and ± 1200 kV—Part 1: Long-term bipolar studies. *IEEE Transactions* PAS-100: 1453, 1981b.

Moreau, M.R. and C.H. Gary. Predetermination of the radio-interference level of high voltage transmission lines—I: Predetermination of the excitation function. *IEEE Transactions* PAS-91: 284, 1972a.

Moreau, M.R. and C.H. Gary. Predetermination of the radio-interference level of high voltage transmission lines—II: Field calculating method. *IEEE Transactions* PAS-91: 292, 1972b.

Nigol, O. Analysis of radio noise from high voltage lines: I—Meter response to corona pulses. *IEEE Transactions* PAS-83(5): 524–533, 1964.

Peterson, A.P.G. and E.E. Gross Jr. *Handbook of Noise Measurement*, 6th edn., General Radio Company, West Concord, MA, 1963.

Scherer, H.N., Ware, B.J., and C.H. Shih. Gaseous effluents due to EHV transmission line corona. *IEEE Transactions* PAS-92(3): 1043–1049, 1973.

Thomas, P.H. Output and regulation in long distance lines, calculation of the high tension line. *AIEE Transactions on Power Apparatus & Systems* 28, Part I: 615–685, discussion: 716–722, 1909.

Timacheff, A. Field patterns of bundle conductors and their electrostatic properties. *AIEE Transactions on Power Apparatus & Systems* 80: 590–597, 1961.

Timascheff, A. Equigradient lines in the vicinity of bundle conductors. *AIEE Transactions on Power Apparatus & Systems* 82: 104–110, April 1963.

Trinh, N.G. Analysis of the second harmonic (120 Hz) audible noise generated by line corona. *IEEE-PES Summer Meeting Paper A* 75: 501–507, 1975.

Trinh, N.G., and P.S. Maruvada. A semi-empirical formula for evaluation of audible noise from line corona. In: *IEEE Canadian Communications & EHV Conference*, Montréal, Québec, Canada, pp. 166–167, November 9–10, 1972.

Trinh, N.G. and P.S. Maruvada. A method of predicting the corona performance of conductor bundles based on cage test results. *IEEE Transactions* PAS-96: 312, 1977.

Trinh, N.G., Maruvada, P.S., and B. Poirier. A comparative study of the corona performance of conductor bundles for 1200-kV transmission lines. *IEEE Transactions* PAS-93: 940, 1974.

Wertheimer, N. and E. Leeper. Electrical wiring configurations and childhood cancer. *American Journal of Epidemiology* 109: 273–284, 1979.

Whitehead, J.B., Systems of electrical transmission. U.S. Patent No. 1,078,711, 1910.

9

Lightning Incidence and Lightning Protection

Interest in lightning by high voltage engineers is justified by the fact that lightning strikes generally constitute a major cause of high-voltage transmission line outages and of occasional substation equipment damage (Hileman, 1999).

9.1 Cloud Charging

Cloud formation and charging are obvious prerequisites for incidence of lightning. There seems to be broad agreement that the following phenomena are significant although no consensus exists on their exact quantitative role in the charging mechanism (Simpson and Scrase, 1937; Mason, 1958; Williams, 1989; Saunders, 1993):

- Updraft of warm air due to heating at ground surface or due to encounter between cold and warm fronts
- Formation at different ambient temperatures (altitudes) of water drops, small ice crystals and large graupels, and collisions among those particles with resulting charge separation
- Smaller particles being blown upward by wind and heavier particles falling down under gravity
- Formation and upward movement of space charge due to corona from plants and bushes (point discharge)
- Electric induction and polarization of particles under the effect of electric field within the cloud
- Elongation and disintegration of water drops, which set an upper limit on water drop size
- Disintegration of water drops due to strong wind speeds

A schematic diagram of cloud charge zones (Simpson and Scrase, 1937) is shown in Figure 9.1. It should be noted, however, that this is necessarily a simplified picture due to the following arguments:

- Charge is more likely to be localized in discrete centers rather than the continuous volume charge distributions implied.
- The real situation is not static but time dependent with continuous interaction between charge centers and ultimate local breakdowns.
- A resulting static charge model will obviously comprise a main dipole with positive charge at the cloud top, negative charge lower down, and a much smaller positive point charge near the cloud base. Such model is probably valid for electric field estimates at ground level but will be of limited validity for assessment of conditions within the cloud.
- It is not clear how the charge redistribution and recovery process following a lightning strike, normally characterized by times of roughly 10 s, really takes place.

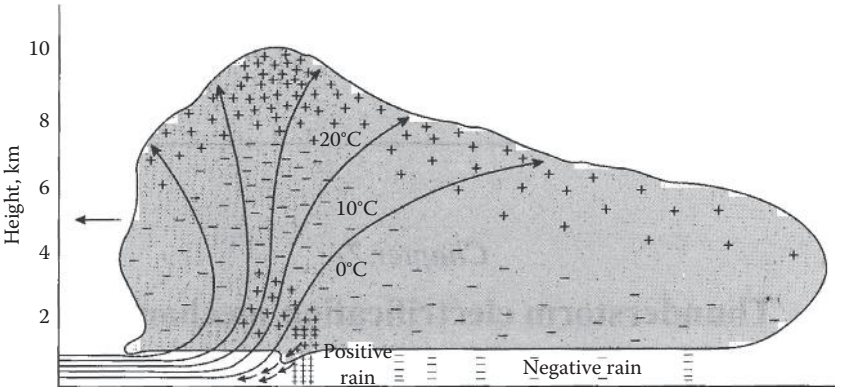


FIGURE 9.1 Schematic diagram of cloud charge zones. (From Simpson, G. and Scrase, F.J., *Proc. R. Soc. Lond. A*, 161, 309, 1937.)

9.2 Meteorological Data

Traditionally, lightning activity in a given region has been characterized by the number of thunder storm days T_d, the keraunic level. By definition, this refers to the number of days on which thunder has been heard in any given location during 1 year. This number is a statistical variable that varies widely from 1 year to another and, therefore, to be meaningful it has to be averaged over several years. It also varies widely among different regions, being highest in tropicals as shown in Figure 9.2. It should also be noted that

- Thunder is heard in an area of roughly 1500 km^2 (about 20 km radius) around the incidence location
- The keraunic level does not distinguish between strikes to ground and strikes within the cloud
- The keraunic level does not account for the number of storms occurring in any given day, that is, storm multiplicity

It has long been recognized that the more significant index for lightning performance of ground objects is the ground flash density, that is, the average number of strikes per km^2 per year. Based mostly on lightning flash counter records, several empirical formulae were developed in different countries relating the ground flash density N_g to the keraunic level T_d.

In South Africa (Anderson et al., 1984), such relationship takes the following form:

$$N_g = 0.04 T_d^{1.25} \tag{9.1}$$

which is valid for $0.1 < N_g < 12$ km^{-2}/year.

A similar relationship established in Australia reads (Makerras, 1978)

$$N_g = 0.01 T_d^{1.4} \tag{9.2}$$

which applies for $10 < T_d < 100$.

To reduce the multiplicity effect referred to earlier, a relationship has been established between storm duration T_h, in hours per year, and ground flash density N_g (MacGorman et al., 1984):

$$N_g = 0.054 T_h^{1.1} \tag{9.3}$$

which was further simplified by CIGRE (CIGRE 33-01, 1991) as

$$N_g = 0.05 T_h \tag{9.3a}$$

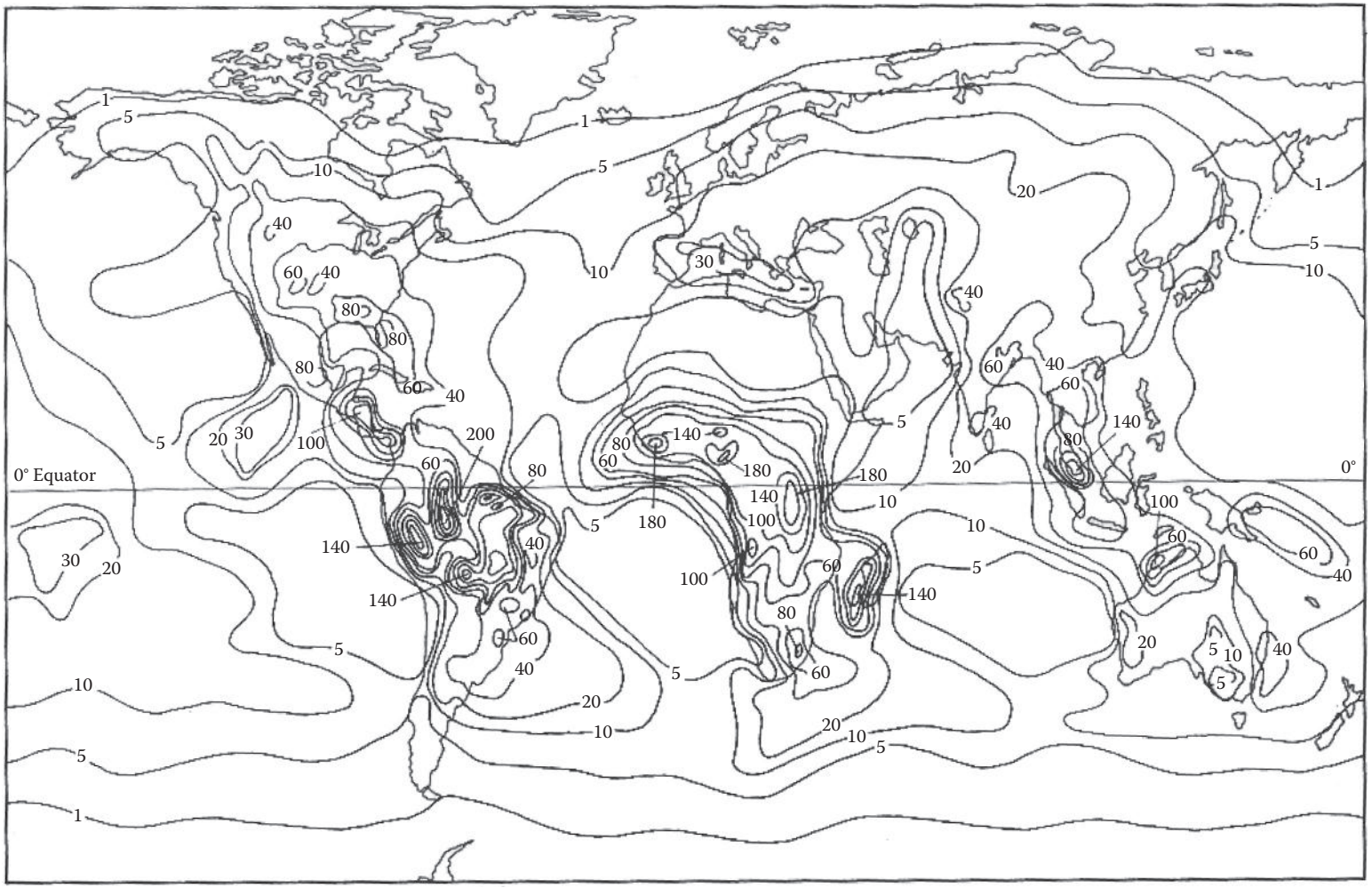


FIGURE 9.2 A typical world mapping of the keraunic level. (From Golde R.H., *Lightning Protection*, Edward Arnold, London, U.K., 1973.)

It may be noted that one reason for the different expressions like (9.1) and (9.2) is that the ratio between cloud discharges N_c and cloud-to-ground discharges N_g varies among different regions. A trend line, with substantial dispersions, was established (Prentice and Makerras, 1977) for the dependence of the ratio N_c/N_g on latitude λ:

$$\frac{N_c}{N_g} = 4.16 + 2.16\cos 3\lambda \tag{9.4}$$

for $0 \le \lambda \le 60°$, which results in a ratio N_c/N_g of 6.3 at the equator and 2 at $\lambda = 60°$.

Another formula suggested by Pierce (1970) could be expressed as

$$\frac{N_c}{N_g} = \frac{1}{0.1 + 0.25\sin\lambda} - 1 \tag{9.5}$$

which results in $N_c/N_g = 9$ at the equator and $N_c/N_g = 2.2$ at $\lambda = 60°$.

9.3 Lightning Detection and Location

9.3.1 Flash Counters

Most of the aforementioned observations, which date back to the 1970s or earlier, are based on flash counter records (Anderson et al., 1984). Effectively, a return stroke flows from ground to cloud with 1/3 of the speed of light to neutralize charge associated with the negative descending leader, resulting in a collapse of the electric field, which can be sensed by a lightning flash counter. Such counter, in principle, comprises a vertical rod antenna, a preprocessing filter, an electronic trigger circuit characterized by a threshold voltage and a dead time, and an electromechanical counter.

For a given return stroke current and cloud height above ground, the distance of the detector from the strike point determines the electric field change and, accordingly, the ability of the detector to respond to the flash in question. Since lightning parameters vary randomly, for example, charge and current amplitude, the range of a lightning flash counter is also a statistical variable. Practically, however, a range may be defined as the maximum distance from the counter where a ground flash with a median return stroke current of 25–30 kA will have a high probability of detection. An example is the CIGRE 10 kHz counter (Anderson et al., 1984) having a limited range of approximately 20 km but a good ability to reject cloud flashes. An obvious advantage of such counter is its low price; on the other hand, many counters have to be used to cover a large region.

Detection efficiency of flash counters, and other techniques for lightning detection, can be determined by comparison with direct photographic or video records.

9.3.2 Lightning Location Systems

9.3.2.1 Direction Finders

Under some simplifying assumptions, namely, that the lightning channel follows a straight line path perpendicular to the earth surface and that the return stroke speed is constant, the azimuthal radiated magnetic field **H** at a distance r far from the strike point can be expressed as (Rakov and Uman, 2003)

$$\mathbf{H}\left(r, t + \frac{r}{c}\right) = \frac{\upsilon I(t)}{2\pi c r} \tag{9.6}$$

where

I is the return stroke current, function of time
υ is the return stroke speed
c is the speed of light: $c = 3 \times 10^8$ m/s.

If a magnetic loop antenna is installed at this location, the open circuit voltage induced by the magnetic field will be

$$V_{oc} = \mu_0 NA \sin\theta \frac{d\mathbf{H}}{dt} \tag{9.7}$$

where

θ is the angle between the normal to the plane of the loop antenna and the incident magnetic field
A is the area of the loop
N is the number of turns
μ_0 is the magnetic permeability of air

Based on the earlier equations, methods are being used to determine the location of a lightning strike, as explained in the following. It is also obvious that, under the earlier assumptions, magnetic field measurements would permit an estimate of lightning stroke current.

At any particular location, two crossed-loop broadband (Krider et al., 1976) electrically shielded antennas are placed so that one is oriented north–south (NS) and the other east–west (EW). A distant lightning flash at a bearing angle θ from the north will, through its radiated magnetic field, induce a voltage proportional to $(d\mathbf{H}/dt)\cos\theta$ in the NS and $(d\mathbf{H}/dt)\sin\theta$ in the EW loops. The bearing angle θ can then be determined from

$$\theta = \arctan\left(\frac{V_{EW}}{V_{NS}}\right) \tag{9.8}$$

which constitutes the principle of the cathode ray direction finder. If two such stations are placed at a certain base line distance apart (several hundred kilometers), then by triangulation, taking into consideration the spherical nature of the earth, the stroke location can be determined.

The method experiences the so-called site errors due to, among other things, reradiation from nearby objects. Such errors could be substantially reduced if three, four, or more stations are used. A numerical algorithm is also used to minimize such errors.

9.3.2.2 Time-of-Arrival (TOA) Method

In this method (Lewis et al., 1960; Lee, 1986), several stations receive, through vertical rod antennas, electric field signals from the same lightning stroke. The signal will obviously be first received at the station nearest to the strike location, while the farthest station will receive the signal last. The differences in the TOA will be in the range of a few tens of microseconds to a few milliseconds, depending on the distances involved. In order to measure these time differences, an extremely accurate clock is needed as a reference (resolution 0.1 μs) in every site.

Synchronization of the clock at every site is provided by satellite. Also the exact location of each station is determined by satellite-based Global Positioning System (GPS). When the difference in the TOA at two stations is accurately measured, a hyperbola then represents the locus of the possible positions of the lightning flash. With three stations, the flash location can be determined.

Furthermore, electric field measurements provide means for estimating stroke current. It should be noted, however, that in both the direction finder (DF) and TOA methods described earlier, estimation of lightning current from field measurement could still suffer from significant inaccuracies caused by the complex structure of the lightning channel, variation of return stroke speed with height above ground, effect of lossy ground on wave propagation, as well as electromagnetic field reradiation effects.

It has been claimed (Rakov and Uman, 2003) that location accuracies in the earlier two methods of the order of 1 km, and detection efficiencies approaching 90%, are possible. The National American Lightning Detection Network (NALDN) is an example of combining both the DF and TOA techniques (Cumming et al., 1998).

9.4 Lightning Flash Parameters

9.4.1 Flash Classification

A lightning flash can be classified into different categories. One distinguishes between a downward flash that involves a downward leader and an upward flash that is initiated normally from tall structures without the presence of a downward leader. Detailed descriptions of the criteria involved for initiation of such flashes are given in the following.

Another classification relates to polarity. In a negative flash, negative charge is lowered from cloud to ground, while in a positive flash, positive charge is lowered instead. In summer lightning, almost 90% of strikes are of negative polarity and only 10% are positive (Anderson and Eriksson, 1980). In winter lightning in Japan, the proportion of positive flashes assumes more significance than in summer lightning (Miyaka et al., 1992). It is also worth noting that winter lightning in Japan also includes upward flashes from structures that are only of moderate height. This also occurs in mountainous regions even with summer lightning (Berger, 1968).

Another classification relates to whether the flash comprises a single or a multiple of individual strokes. Measurements in South Africa showed a mean number of strokes per flash of four with a median interval of approximately 50 ms in between (Schonland, 1956). Normally, the current amplitudes in the second and subsequent strokes are lower and front steepness significantly higher than the first.

9.4.2 Return Stroke Current

9.4.2.1 Statistical Distribution

The analysis of peak current measurements from structures less than 60 m in height (Anderson and Eriksson, 1980) yields a lognormal distribution with a median current of 31 kA and a natural logarithmic standard deviation of 0.484. It was also noted that the measured distribution may be better approximated by two straight lines, characterizing currents below and above 20 kA, as presented in Figure 9.3. Also shown in Figure 9.3 is the IEEE current amplitude distribution originally proposed by John G. Anderson (IEEE Standard 1243-1, 1997):

$$P(I) = \frac{1}{1 + (I/31)^{2.6}}, \quad \text{with } I \text{ in kA.} \tag{9.9}$$

It is shown that the discrepancy between the CIGRE and IEEE distributions becomes significant for currents below 20 kA and also above 100 kA.

9.4.2.2 Current Waveform

The analysis of measured return stroke current (Anderson and Eriksson, 1980; CIGRE 33-01, 1991) shows very significant concavity of the front, with maximum steepness S_m at a current value as high as 90% of the peak. This makes a double exponential function, which has a maximum steepness at $I = 0$, unsuitable for representing this wave form. CIGRE (CIGRE 33-01, 1991) has therefore recommended separate analytical expressions for the front and tail under the assumption that four basic parameters are known:

1. The current peak I, kA
2. The maximum steepness S_m, kA/μs
3. The front duration t_f, μs
4. The tail duration t_h, μs

It is recommended to determine t_f from

$$t_f = 1.67[t_{90} - t_{30}] \tag{9.10}$$

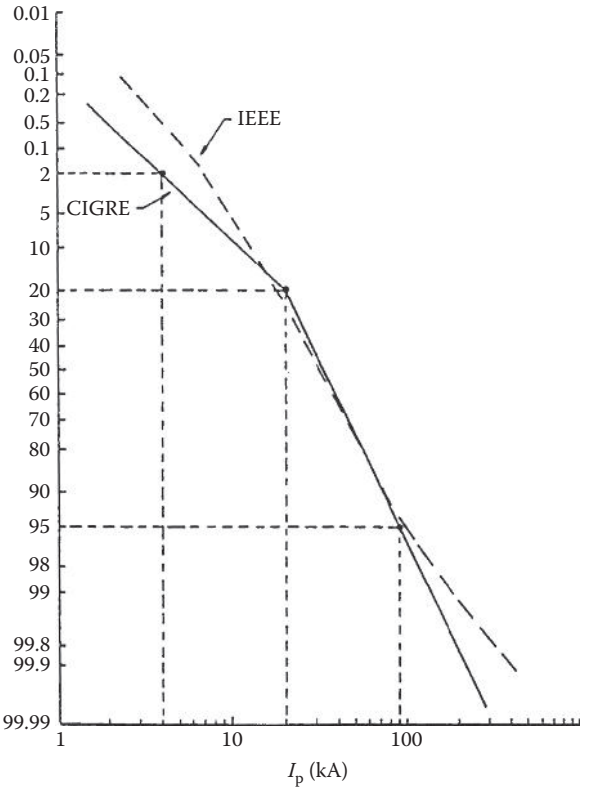


FIGURE 9.3 Distribution of the lightning current amplitude. (From IEEE Standard 1243-1, 1997.)

where t_{90} and t_{30} refer to the instants on the current impulse front at which the instantaneous current corresponds to 90% and 30% of the peak value, respectively. This is in agreement with the procedure to determine an impulse front recommended in IEC Standard 60060-1 (1989).
In the CIGRE wave form, the front is represented by

$$i(t) = At + Bt^n \tag{9.11}$$

Formulae for determining A, B, and n in terms of I, S_m, and t_f are given in CIGRE 33-01 (1991). A formula is also given to determine t_n, the time corresponding to the maximum rate of rise S_m.
For $t > t_n$, variation of the current is expressed by

$$i(t) = I_1 \exp\left[-\frac{(t-t_n)}{t_1}\right] - I_2 \exp\left[-\frac{(t-t_n)}{t_2}\right] \tag{9.12}$$

Expressions for I_1, I_2, t_1, and t_2 in terms of the four basic parameters stated earlier are also given in CIGRE 33-01 (1991).

Figure 9.4 shows an example of the CIGRE current waveform for the four basic parameters: $I = 31$ kA, $S_m = 26$ kA/μs, $t_f = 3$ μs, and $t_h = 75$ μs. The resulting parameters characterizing the front were determined at

$$n = 8.27,\ A = 3.23 \text{ kA/μs},\ B = 3.79 \times 10^{-5} \text{ kA/(μs)}^n, \text{ and } t_n = 4.66 \text{ μs}$$

For the wave tail, the relevant parameters were found to be

$$t_1 = 101.5 \text{ μs},\ t_2 = 0.119 \text{ ms},\ I_1 = 31.04 \text{ kA, and } I_2 = 3.14 \text{ kA}.$$

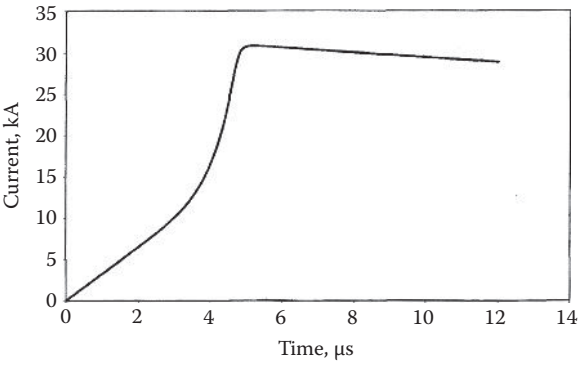


FIGURE 9.4 CIGRE current wave form. (From CIGRE WG 33.01 (Lightning), Guide to procedures for estimating the lightning performance of transmission lines, CIGRE Technical Brochure, No. 63, October 1991.) I = 31 kA, t_f = 3 μs, S_m = 26 kA/μs, t_h = 75 μs.

Another wave shape that allows for the concavity of the impulse current front was proposed by Heidler (1987) and Heidler et al. (1999), which, for a peak current I reads

$$i(t) = \frac{I}{\eta}\frac{(t/\tau_1)^n}{(t/\tau_2)^n + 1}\exp\left(-\frac{t}{\tau_2}\right) \tag{9.13}$$

where

τ_1 is the rise time constant
τ_2 the tail time constant
n the current steepness factor
η the peak current correction factor, expressed as

$$\eta = \exp\left[-\left(\frac{\tau_1}{\tau_2}\right)\left(\frac{n\tau_2}{\tau_1}\right)^{1/(n+1)}\right] \tag{9.14}$$

Unfortunately, the parameters τ_1, τ_2, and n have not been related to the four basic parameters adopted by CIGRE earlier. Usually, the factor n is taken as five or more. If we denote the time at which the maximum steepness S_m is achieved, by t_n similar to the CIGRE formula, then it was shown (Heidler, 1987) that for large values of n, the following approximations apply:

$$t_n \approx \tau_1 \tag{9.15}$$

and

$$S_m \approx \frac{nI}{4\tau_1\eta} \tag{9.16}$$

It can also be shown that

$$t_n \approx \tau_2 \ln\left(\frac{2}{\eta}\right) \tag{9.17}$$

Furthermore, in (Heidler, 1987), it was shown that the current i_n at which the maximum steepness occurs is related to the peak current I by the approximate relationship:

$$\frac{i_n}{I} = \frac{n-1}{2n\eta} \tag{9.18}$$

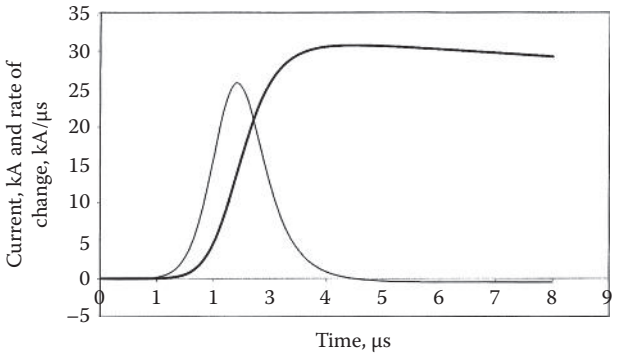


FIGURE 9.5 Return stroke current and rate of change represented by the Heidler function. (From Heidler, F., Lightning electromagnetic pulse, theory and measurement, PhD thesis, Federal Armed Forces University, Munich, Germany, 1987.) $I = 31$ kA, $\tau_1 = 2.5$ μs, $\tau_2 = 60$ μs, $n = 8$.

This clearly shows that the Heidler formula cannot allow for maximum steepness to occur at an instantaneous current as high as 0.9 of the peak current, as required in the CIGRE waveform, since from (9.18) the ultimate value would be 0.5/η. Figure 9.5 shows an example for the representation of the current waveform by the Heidler function, for $I = 31$ kA, $\tau_1 = 2.5$ μs, $\tau_2 = 60$ μs, and $n = 8$. η was obtained at 0.928. A maximum steepness $S_m = 25.8$ kA/μs was also achieved, which took place at $t_n = 2.42$ μs corresponding to $i_n = 13.97$ kA, that is, 45% of the peak current, far from the 90% value required by CIGRE Working Group (CIGRE 33-01, 1991). In comparison, S_m obtained from the approximate formula (9.15) amounted to 26.7 kA/μs, a discrepancy of only 3.6%.

9.4.3 Statistical Parameters

As previously mentioned, CIGRE (CIGRE 33-01, 1991) adopted a lognormal distribution for the current peak of the first negative downward stroke and recommended to use t_{90}–t_{30} to evaluate the front. Table 9.1 summarizes the mean values M of some significant parameters and their corresponding natural logarithmic coefficient of variation β (CIGRE 33-01, 1991). Much of the parameters analyzed by the CIGRE Working Group are in fact based on original measurements by Berger (1968).

Similar parameters for subsequent negative downward strokes are summarized in Table 9.2 (CIGRE 33-01, 1991). Comparison between Tables 9.1 and 9.2 confirms the fact that in general, subsequent strokes are characterized by lower current peak but higher maximum steepness.

TABLE 9.1

Statistical Parameters of the First Negative Downward Stroke

	Application Range			
	$3 \le I \le 20$ kA		**$I > 20$ kA**	
Parameter	***M***	**β**	***M***	**β**
Final crest current, I_F, kA	61.1	1.33	33.3	0.605
Maximum front steepness S_m, kA/μs	24.3	0.599	24.3	0.599
Front time t_f, μs	3.83	0.553	3.83	0.553
Minimal equivalent front I/S_m, μs	2.51		1.37	

Source: CIGRE WG 33.01 (Lightning), Guide to procedures for estimating the lightning performance of transmission lines, CIGRE Technical Brochure, No. 63, October 1991.

TABLE 9.2

Statistical Parameters of Subsequent Negative Downward Strokes

Parameter	*M*	β
Crest current I_F, kA	12.3	0.530
Maximum steepness, kA/μs	39.9	0.852
Minimum equivalent front I_F/S_m, μs	0.308	

Source: CIGRE WG 33.01 (Lightning). Guide to procedures for estimating the lightning performance of transmission lines, CIGRE Technical Brochure, No. 63, October 1991.

Based mostly on Berger's data (Berger, 1977), some statistical distributions relating to the maximum rate of current rise S_m, kA/μs and charge content Q, C, in negative downward first stroke have been expressed as

$$P(S_m) = \frac{1}{1 + (S_m/24)^4} \tag{9.19}$$

and

$$P(Q) = \frac{1}{1 + (Q/5)^2} \tag{9.20}$$

Statistical distributions relating to peak current I, kA, maximum current steepness S_m, kA/μs, and charge content Q, C, in subsequent strokes can be expressed as (Anderson and Eriksson, 1980)

$$P(I) = \frac{1}{1 + (I/12)^{2.7}} \tag{9.21}$$

$$P(S_m) = \frac{1}{1 + (S_m/40)^{2.1}} \tag{9.22}$$

and

$$P(Q) = \frac{1}{1 + (Q/1)^{2.2}} \tag{9.23}$$

All the data reported so far relate to negative downward flash. Measurements with positive return stroke are scarce, making any statistical distributions relating to positive stroke parameters much less reliable. Nevertheless, the following distributions for positive first stroke current kA and charge content Q, C, have been put forward (Anderson and Eriksson, 1980):

$$P(I) = \frac{1}{1 + (I/34)^{1.5}} \tag{9.24}$$

and

$$P(Q) = \frac{1}{1 + (Q/19)^{1.34}} \tag{9.25}$$

In (9.19) through (9.25), it is recalled that these represent probabilities that the variable in question is exceeded.

Comparison between (9.9) and (9.24) indicates that extremely high currents are significantly more likely for a positive than a negative first stroke. For example, according to (9.9), the probability that a 200 kA current is exceeded in a negative first stroke is 0.8%. From (9.24), however, the corresponding probability of occurrence for a positive first stroke is 6.6%. The same conclusion can be reached with regard to extremely high charge content by comparing the (9.20) and (9.25), where the probability of exceeding 100 C in a first negative stroke amounts to 0.25%, while the corresponding value for a positive first stroke is 9.7%.

9.5 Lightning Attachment

9.5.1 Negative Downward Flash

Under thunderstorm conditions, integration of the electric field from ground to the cloud base obviously yields the value of the potential at the cloud base. In the presence of space charge due to corona from plants, bushes, etc., such field assumes lower values near ground and increases progressively with height. For illustration, if the cloud base is at 2500 m above ground and the average electric field is 40 kV/m, the cloud base potential will be 100 MV. It is generally assumed that a downward stepped leader is initiated by a preliminary breakdown between charge centers within the cloud itself.

The negative downward leader, a faint plasma channel, moves towards ground in discrete steps of roughly 50 m in length, covered in a time duration of a few microseconds. A pause of some tens of microseconds elapses before the leader moves again, creating another individual step. While the general leader motion is downward towards ground, successive steps assume different orientations, so that the real leader length becomes longer than the minimum vertical distance from cloud to ground. The mean downward leader speed varies but a representative value frequently cited is 2×10^5 m/s. This means that a distance of 2.5 km from cloud base to ground will be crossed by the negative stepped leader in roughly 12.5 ms.

The downward leader comprises a conducting core, with a radius of roughly 1 cm and a negative corona space charge sheath of a few meters in radius. A negative streamer discharge emanates from the leader tip and extends tens of meters ahead. This streamer corona is responsible for maintaining the stepped leader through injection of corona current. It is estimated that the resulting leader current is of the order of 100 A and the leader voltage gradient varies with time from an initial value of several hundreds kV/m to an ultimate value of the order of 1 kV/m. The negative streamer gradient, however, is constant at several hundreds kV/m. On the other hand, the negative streamer space charge creates a field at the leader tip opposing the applied electric field associated with the tip potential. If the tip potential and its resulting field are not sufficient to counter the opposing field due to negative streamer space charge, the leader stops.

The mechanism of formation of individual steps is most likely, in similarity, to long laboratory gaps under a negative switching impulse, associated with the formation of a so-called space leader (Les Renardières Group, 1981). This is followed by positive and negative leaders bridging the gap between the negative descending leader tip and the space leader, previously occupied by streamers.

The complex interaction between the negative descending leader and the negative streamer ahead can explain the formation of long pauses between steps as well as the continuous variation of the orientation of successive steps.

Such interaction can also explain leader branching, although this and the stepping phenomenon have been traditionally explained by the presence of positive space charge pockets due to point discharges from ground, which exert electrostatic forces on the descending leader. So far, the effect of such space charge pockets has not been quantitatively accounted for.

It should be mentioned, however, that earlier small-scale laboratory experiments showed that space charge generated by needle electrodes at the ground plane appears to enhance leader stepping in a negative rod–plane gap (Schonland and Allibone, 1931). However, more recent negative switching impulse tests on

rod–plane gaps of up to 16.7 m demonstrated that stepping takes place without any generation of prior space charge pockets (Ortega et al., 1994).

Before negative leader descent, ground objects are exposed to enhanced electric field, due to cloud charges, that can reach values as high as 20 kV/m within a time interval of several seconds. Such field, under negative cloud charge, will induce positive charge on conducting ground objects and can cause sharp objects to go into corona. This phenomenon will be more pronounced the taller the ground object. As the negative stepped leader moves towards ground, associated negative space charge will induce substantial positive charge on ground objects in proximity of its path. This could result in significant streamer activity and, eventually, upward positive leader initiation simultaneously from several ground structures. This will be more likely if such structures are not so close as to result in mutual space charge shielding.

With further downward travel of the stepped leader, such positive upward leaders further elongate and, eventually, at least one upward leader may meet the descending leader in a streamer breakdown in a so-called final jump. In a way, there is a race among ground objects, through their upward positive leader generation, so that the one that *wins* such race is the one that gets struck. Such race is of course strongly influenced by proximity to the downward stepped leader path as well as geometric characteristics of the ground object, primarily height. More complex characteristics involve space charge generation from the ground object due to electric field caused by cloud charge, prior to stepped leader descent.

9.5.2 Return Stroke

9.5.2.1 General

Mathematical modeling of the attachment process due to negative descending leader is accounted for in the following separate section.

Following the final jump between the negative stepped leader and the positive upward connecting leader, the situation is such that a continuous plasma exists between a charge center in the cloud and ground. However, the negative space charge in the negative leader sheath is still available and exerts a strong electric field on the tip of the positive leader, which is connected to ground. Long positive streamers are therefore formed, which extend to neutralize such negative space charge, resulting in a high current discharge regime, termed the return stroke. This extends upward towards the cloud with very high speed, typically one third of the speed of light. The resulting current and released negative charge to ground constitute the first stroke, the characteristics of which have been briefly summarized in a previous section. As also previously mentioned, this can be followed by one or more subsequent strokes, separated by some tens of milliseconds intervals that are generally characterized by lower current amplitude but higher front steepness. The impulse current that lasts for typically some tens of microseconds can be followed by a long duration continuous current, for example, hundreds of milliseconds, and much smaller amplitude, for example, hundreds of amperes. Due to its long duration, the continuous current regime could cause significant damage to the struck object due to thermal effects.

9.5.2.2 Return Stroke Models

Some early mathematical models have been put forward to account for the return stroke phase (Lundholm, 1957; Rusck, 1958; Wagner, 1963). It should be noted that the physics of return stroke are very complex and certain aspects are not fully understood. For example, streamers from the return stroke leader tip extend, in presence of a partially conducting core ahead left by the descending stepped leader. The streamers extend into a negative space charge zone associated with the descending leader corona sheath. Little information is available on positive streamer speeds in the presence of negative space charge, and the nature and extent of the charge neutralization is not fully accounted for, even at present time. It is therefore not surprising that simplifying assumptions are necessary if a model is to be formulated at all.

In the models of Lundholm (1957) and Rusck (1958), it was assumed that the descending leader charge per unit length is constant and that return stroke progress is governed by the well-known

Toepler's theorem with Toepler's constant taken as 0.05 Vs/m. A relationship between return stroke speed and return stroke current was first deduced by Lundholm and is later modified by Rusck to take the form

$$\upsilon_r = \frac{1}{\sqrt{1+\dfrac{500}{I_0}}} \tag{9.26}$$

where

υ_r is the return stroke speed in per unit of the speed of light $c = 3 \times 10^8$ m/s
I_0 is the peak return stroke current, kA.

Similarly, Wagner (1963) assumed that, in analogy with laboratory experiments, a specific energy dissipation per unit length and unit current amounting to 0.2 Vs/m is needed for return stroke extension. The following relationship was obtained:

$$\upsilon_r = \frac{0.555}{\sqrt{1+\dfrac{115}{I_0}}} \tag{9.27}$$

with the units as in (9.26). Wagner also deduced the following expression for the so-called stroke potential as function of υ_r:

$$V = 120\frac{\upsilon_r}{1-2.2\upsilon_r^2} \tag{9.28}$$

with V in MV and υ_r in per unit of the speed of light. As an example, for I_0 = 50 kA, from (9.27), $\upsilon_r = 0.306$ and substituting in (9.28) V = 46 MV.

Expressions like (9.26) could be used to deduce the negative downward leader charge q per unit length as function of the return stroke current I_0. As an example, for I_0 = 30 kA, q is obtained at 420 μC/m.

More recently, some return stroke models were formulated whose main objective was to account for electromagnetic field measurements at different distances from the strike location, an excellent summary of which is given in Rakov and Uman (2003). It should be noted that such models do not explain the mechanism of upward propagation of the return stroke. The engineering return stroke models are broadly classified into transmission line type and traveling-current-source type.

In the former type, it is assumed that current is injected from ground into the channel base, travels upward along the channel with a front speed υ, assumed constant, and is attenuated as it propagates (Wagner, 1963; Rakov and Dulson, 1991). In the traveling current source, the channel progresses upward with a speed υ_f but the injected current propagates towards ground with the speed of light c (Heidler, 1985). Concentrating on the transmission line types, the general dependence of current on time t and height z above ground could be expressed as (Rakov and Uman, 2003)

$$I(z,t) = u\left(t - \frac{z}{\upsilon}\right)P(z)I\left(0,t - \frac{z}{\upsilon}\right) \tag{9.29}$$

where

$P(z)$ is the current attenuation function
u is a unit-step function

The current at the base $I(0, t)$ is assumed to be known.
In Nucci et al. (1988), $P(z)$ is assumed to take the form

$$P(z) = \exp\left(-\frac{z}{\lambda}\right) \tag{9.30}$$

where λ is a constant taken as 2000 m, while in Rakov and Dulson (1991),

$$P(z) = 1 - \frac{z}{H} \tag{9.31}$$

where H is the channel length.

It can be shown from expression (9.29) that the distribution of charge q per unit length, as function of time t and height z above ground, can be expressed as

$$q(z,t) = \frac{P(z)}{u} I\left(0, t - \frac{z}{u}\right) - \frac{dP(z)}{dz} \int_{z/u}^{t} I\left(0, t - \frac{z}{u}\right) dt \tag{9.32}$$

which could be put as

$$q(z,t) = \frac{P(z)}{u} I\left(0, t - \frac{z}{u}\right) - \frac{dP(z)}{dz} Q(z,t) \tag{9.32a}$$

where $Q(z, t)$ is the charge that passed through the channel section at a height z above ground, at time $t > z/\upsilon$.

Comparison with measured field waveforms at a distance of 5 km from the strike location led Rakov and Uman (2003) to conclude that all such models are less than adequate. Based, however, on all available results at different distances and on mathematical simplicity, the model in Rakov and Dulson (1991) was ranked highest, while the original simple transmission line model by Uman and McLain (1969) was ranked lowest.

It should be noted, however, that probably due to the lack of relevant measurements, the earlier models have not been examined on the basis of validity of their fundamental physical assumptions.

9.5.3 Lightning Attachment Models

Until the 1980s, the tools available for assessment of lightning exposure of ground objects comprised the constant angle approach and the electrogeometric model (EGM) and its offshoot, the rolling sphere method.

The constant angle approach assumes the existence of a conical protected zone around a mast, the base radius of which is a multiple of the mast height. The semiangle of the cone was termed the protective angle, often taken in the range of 30°–60°, and was originally obtained from reduced-scale high-voltage laboratory tests (Peek, 1929).

9.5.3.1 Electrogeometric Model

In the original EGM (Young et al., 1963), the striking distance was determined, assuming a streamer-type breakdown between the downward leader tip and the ground structure, with a mean streamer gradient of 500–600 kV/m. The more recent and widely used version of the EGM due to Armstrong–Whitehead is described in Armstrong and Whitehead (1968). Recognizing that the relevant interval of increase of ground fields due to a descending leader is in the hundreds of microseconds to a few milliseconds, Whitehead and his associates considered breakdown between the negative leader tip and ground objects as a negative switching impulse breakdown.

The first fundamental formula behind the EGM is an approximate relationship between the negative descending leader tip potential V_s, MV, and the return stroke peak current I_0, kA:

$$V_s = 3.7 I^{2/3} \tag{9.33}$$

Note that V_s is taken as independent of the descending leader tip height above ground.

Furthermore, it was mentioned (Armstrong and Whitehead, 1968) that "to determine the strike distance, there is no recourse but to extrapolate the laboratory strike distances for the highest voltages available."

TABLE 9.3

Rolling Sphere Radius for Different Peak Return Stroke Currents

IEC Protection Levels	I_0, kA	Probability, %		r_s, m
		CIGRE	IEEE	
I	2.9	99	99.8	20
II	5.4	97	98.9	30
III	10.1	91	94.9	45
IV	15.1	84	85.4	60

From negative switching impulse test results in the gap range of 1.5–5.0 m, the following empirical formula was obtained (Armstrong and Whitehead, 1968):

$$r_s = 1.4V_s^{1.2} \quad (\text{m, MV}) \tag{9.34}$$

Combining (9.33) and (9.34), the following relationship between the striking distance r_s, m, and the peak return stroke current I_0 was obtained:

$$r_s = 6.72\,I_0{}^{0.8} \quad (\text{m, kA}) \tag{9.35}$$

It is clear from the previous texts that it would be totally meaningless to accept the EGM, on the one hand, and, on the other, to claim that laboratory tests on long air gaps do not apply for lightning exposure models. Over the years, (9.35) has undergone some changes, based on the claim of better agreement with field experience. One such widely applied version is (Chisholm and Anderson, 2005)

$$r_s = 10\,I_0{}^{0.65} \quad (\text{m, kA}) \tag{9.35a}$$

This expression is used to calculate the rolling sphere radius for different return stroke currents, presently used in some international standards (IEC Standard 62305-1).

Also shown in Table 9.3 is the IEC protection class corresponding to each current level and the probability that such current can be exceeded according to both the CIGRE lognormal and the IEEE distributions.

It should finally be noted that the EGM, based on laboratory rod–rod gaps breakdown data, strictly speaking applies only for masts but has nevertheless been also applied to conductors and ground wires, sometimes by introducing geometric correction factors (Mousa and Srivastava, 1990).

9.5.3.2 Eriksson and Dellera–Garbagnati Models

In more recent models of lightning attractiveness (Eriksson, 1987a,b; Dellera and Garbagnati, 1990a,b), it has been recognized that inception of a positive upward leader from the ground structure and its subsequent propagation to encounter the downward leader can play a predominant role in the attachment process. A fundamental point in such models is the criterion used for upward positive leader onset from the ground object. For that purpose, the aforementioned models use the critical radius concept due to Carrara–Thione (1976). While the Eriksson and Dellera–Garbagnati models are based on more detailed physical grounds than the EGM rolling sphere methods, there is certainly room for significant improvement. For example, the critical radius in Carrara and Thione (1976) was originally determined as function of the laboratory gap spacing. It is not clear how the critical radius will be determined in relation to ground objects with different heights above ground. There is in fact experimental evidence (Gary and Hutzler, 1989) that the critical radius of a vertical ground rod can be quite different from that of a conventional rod–plane gap. More recently, this has been theoretically accounted for on the basis of proximity effect (Rizk, 2009).

As a result, the earlier models, particularly Dellera and Garbagnati (1990a,b), result in strong dependence of lightning exposure on the ground structure height (see Fig. 10 of Dellera and Garbagnati (1990a)). Furthermore, Eriksson (1987a,b) did not model lightning exposure of a conductor but simply assumed that the conductor lateral attractive distance amounts to 80% of that of a mast of the same height.

There are some differences between the Eriksson (1987a,b) and Dellera–Garbagnati models (Dellera and Garbagnati, 1990a,b). In the former, it is assumed that the negative downward leader descends vertically towards ground unperturbed by the presence of ground objects. In Dellera and Garbagnati (1990a,b), however, the downward leader follows geometric electric field lines from the instant it leaves the cloud base, being therefore attracted to the predominant ground object. In this respect, the downward leader movement is traced in more detail by Dellera–Garbagnati, but the model becomes much more complex. In reality, however, downward leader descent is much more complex still due to stepping and branching so that simplifying assumptions are necessary to make modeling at all possible. It is not evident, therefore, that tracing the geometric field lines, in the absence of space charge, would make the Dellera–Garbagnati model more realistic in this respect. In the leader trajectories following positive leader inception, it was found (Eriksson, 1987a,b) that the significant parameter is the ratio between the propagation velocity of negative and positive leaders υ^-/υ^+, rather than their absolute values. Eriksson assumed $\upsilon^-/\upsilon^+ = 1$, while Dellera–Garbagnati assumed that the aforementioned ratio starts with 4 at positive upward leader onset but decreases to unity at the final jump.

9.5.3.3 Rizk Model

A model by Rizk (1990) was formulated to address some of the limitations of the aforementioned models as described in some detail in the following.

In contrast to the condition of corona onset field on an electrode with critical radius referred to earlier, the Rizk model makes reference to the critical space potential U_{ic}, defined as the critical induced voltage at the position of the tip of the ground object, with the object removed, at positive upward leader onset. The space potential U_1 can in general be defined as

$$U_1 = \int_0^h E_i \, dz \tag{9.36}$$

where

E_i is the induced electric field, in the absence of the ground object
z is the vertical distance above ground
h is the height of the ground object

It was shown (Rizk, 1990) that for a slender mast of height h, the critical continuous upward positive leader inception space potential U_{lc} is given by

$$U_{lc} = \frac{1556}{1 + \dfrac{3.89}{h}} \quad \text{(kV, m)} \tag{9.37}$$

The word slender mentioned earlier becomes clear when it is recognized that buildings and massive structures tend to inhibit upward leader inception (Rizk, 2009).

For a cylindrical conductor of radius a, m, and height h, m, above ground (Rizk, 1990),

$$U_{lc} = \frac{2247}{1 + \dfrac{5.15 - 5.49 \ln a}{h \ln(2h/a)}} \quad \text{(kV, m)} \tag{9.38}$$

A fundamental point is that the critical upward leader onset space potential, according to (9.37) and (9.38), is determined by the height h above ground and not the distance d between the structure tip and the descending negative leader. It should be noted that, for bundle conductors, the radius a in (9.38) should be replaced by the equivalent bundle radius r_e (Rizk, 1996). Another basic point is that U_{lc} in both (9.37) and (9.38) saturates with height h, asymptotically reaching 1556 and 2247 kV, respectively.

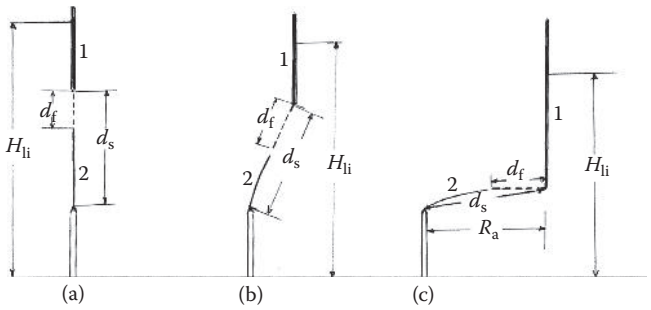


FIGURE 9.6 Schematic diagram illustrating a negative downward strike. (a) Downward leader directly above the struck mast; (b) downward leader displaced laterally from struck mast; (c) downward leader at the limit of the attractive zone. With (1) negative downward leader; (2) upward positive leader; H_{li}, height of the negative leader at inception of positive leader from ground structure; d_f, final jump by streamer breakdown; R_a, maximum attractive distance; d_s, striking distance.

In this model, following positive leader inception, the downward leader continues its descent unperturbed while the upward leader travels on a trajectory seeking the negative leader tip. It has been assumed that during this stage, the downward leader travels continuously, without space leaders or stepping and therefore with reduced speed. In the original version of the model, it was assumed that, in agreement with Eriksson, $\upsilon^-/\upsilon^+ = 1$. However, results were also presented with $\upsilon^-/\upsilon^+ = 2$ (Rizk, 1990). In a more recent version of the model (Rizk, 2010), both υ^- and υ^+ were calculated continuously during the leader trajectories, where it was assumed that the leader speed is basically determined by the overvoltage factor at the leader tip (Rizk and Vidal, 2008).

Figure 9.6 shows a schematic diagram illustrating a negative downward strike. Figure 9.6a represents the idealized and unlikely case of a negative leader descending vertically along the axis of the ground mast. Figure 9.6b shows a more realistic case with the downward leader displaced laterally from the ground mast. Figure 9.6c shows the limiting case, when the downward leader descends at the boundary of the exposure area, limited by the maximum attractive radius r_a, for the prospective return stroke current involved.

In Figure 9.6, H_{li} refers to the height of the negative leader at the instant of positive upward leader onset from the ground structure. It is shown that H_{li} varies with the lateral displacement of the descending leader, being highest for the unrealistic case of direct descent along the axis of the ground structure (Figure 9.6a).

The striking distance in Figure 9.6 is defined as the distance between the negative leader tip and the ground structure tip at the instant of the final jump. The value of d_s will in general be different depending on the lateral position of the downward leader. The difference between the maximum attractive R_a and striking distance d_s is clear from Figure 9.6c.

Sample calculation results are given in Table 9.4 for both a slender mast and a horizontal conductor, each of 40 m height on flat ground and a return stroke current of 31 kA. It is shown that positive leader onset takes place with the downward leader height H_{li}, significantly larger for the mast case. It is also clear that the striking distance d_s and attractive radius R_a for the mast, or lateral attractive distance D_a for the conductor, are significantly different.

Furthermore, it is shown that the lateral attractive distance D_a of the conductor is significantly lower than the attractive radius R_a of the mast, for the same height and current. In this case, $D_a/R_a = 0.84$, not far from the ratio of 0.8 assumed by Eriksson (1987b).

TABLE 9.4

Illustrative Numerical Examples

Configuration	***I*, kA**	***h*, m**	***R*$_a$, m**	***D*$_a$, m**	***H*$_{li}$, m**	***d*$_s$, m**
Slender mast	31	40	107		197	123
Horizontal conductor	31	40	—	90	141	96

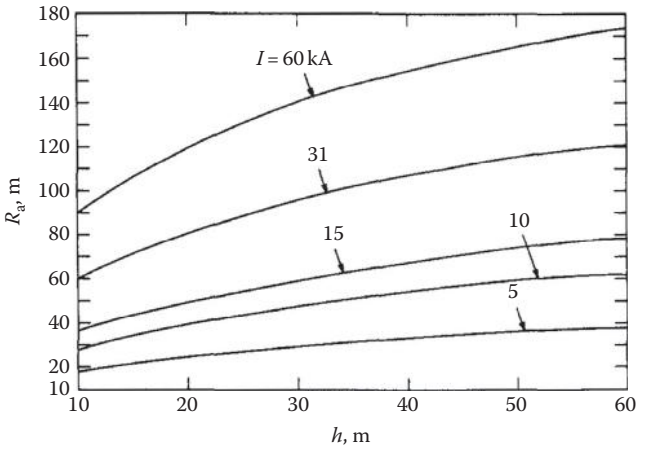


FIGURE 9.7 Variation of the attractive distance R_a with the mast height h for different values of the prospective return stroke current I, according to Rizk and Vidal. (From Rizk, F.A.M. and F. Vidal, *IEEE Trans. Power Deliv.*, 23(1), 296, 2008.)

Figure 9.7 shows model results of the dependence of the attractive radius R_a on mast height h for different values of the prospective return stroke current I. Figure 9.8 shows the dependence of R_a on I for different values of mast height.

These results could be expressed by the approximate regression formula:

$$R_a = 2.57 I^{0.615} h^{0.422} \quad \text{(m, kA)} \tag{9.39}$$

which is valid for $5 \leq I \leq 31$ kA and $10 \leq h \leq 50$ m.

An overall attractive radius R_{ao} can be defined from the average annual number of strikes N_s corresponding to a ground flash density N_g:

$$N_s = \pi R_{ao}^2 N_g 10^{-6} \tag{9.40}$$

with R_{ao}, m, and N_g, 1/km^2.

It can be shown that with the IEEE current distribution, for a mast height h,

$$R_{ao} = 1.23 R_a(31, h) \tag{9.41}$$

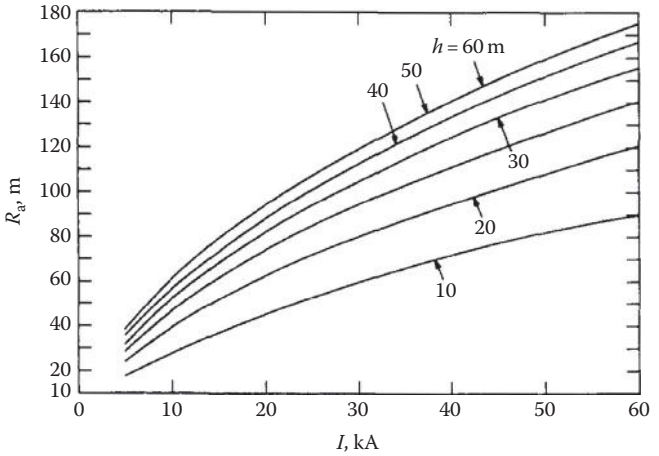


FIGURE 9.8 Variation of the attractive distance R_a with the prospective return stroke current I for different values of mast height h, according to Rizk and Vidal. (From Rizk, F.A.M. and F. Vidal, *IEEE Trans. Power Deliv.*, 23(1), 296, 2008.)

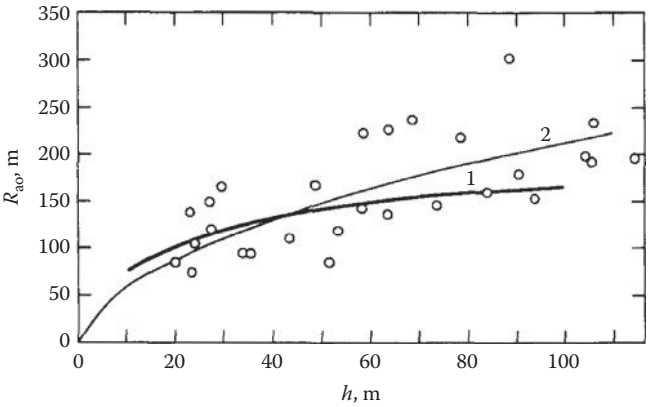


FIGURE 9.9 Variation of R_{ao} with the mast height h—Comparison of calculated results with field data. (1) The Rizk model. (From Rizk, F.A.M., *IEEE Trans. Power Deliv.*, PWRD-5(4), 1983, 1990); (2) the Eriksson model. (From Eriksson, 1987b.)

A comparison of the dependence of R_{ao} on h predicted by the model and field experience is shown in Figure 9.9. Note that some of the field points do not relate to flat ground and may include upward flashes.

Similar model results for the conductor lateral attractive distance D_a are presented in Figures 9.10 and 9.11. The results could be accounted for by an approximate regression formula:

$$D_a = 1.57 I^{0.694} h^{0.454} \tag{9.42}$$

which is valid for $5 \le I \le 31$ kA and $10 \le h \le 50$ m.

Similar to (9.41), an overall lateral attractive distance D_{ao} is obtained:

$$D_{ao} = 1.13 D_a(31, h) \tag{9.43}$$

which is valid for $5 \le I \le 60$ kA, $10 \le h \le 60$ m.

Figure 9.12 shows comparison between model findings regarding variation of D_{ao} with prospective return stroke current I and field experience derived by Eriksson (1987b). As mentioned previously,

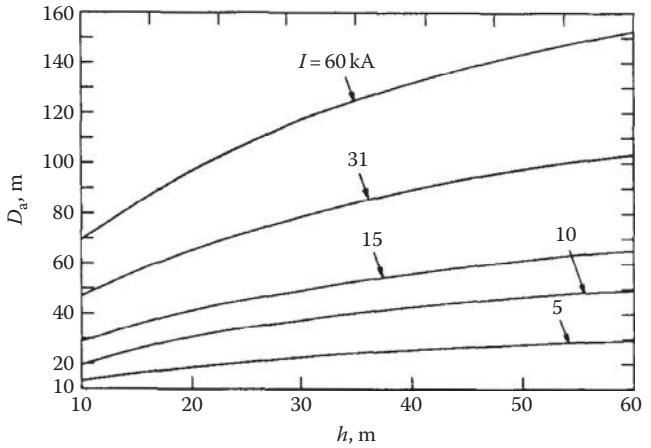


FIGURE 9.10 Variation of the attractive distance D_a with the conductor height h for different values of the prospective return stroke current I, according to the Rizk model. (From Rizk, F.A.M., *IEEE Trans. Power Deliv.*, PWRD-5(4), 1983, 1990.)

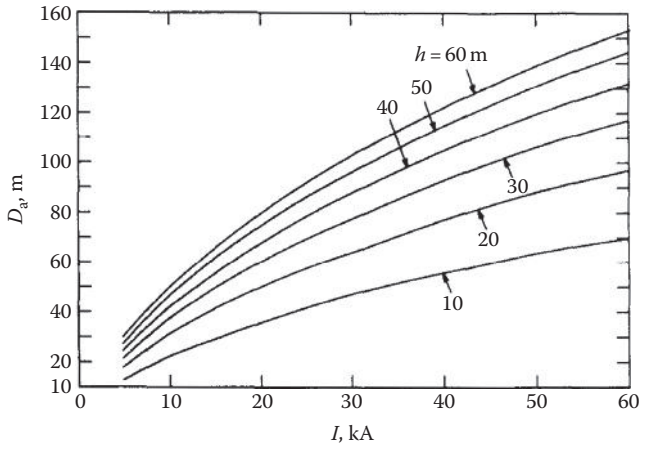


FIGURE 9.11 Variation of the attractive distance D_a with the prospective return stroke current I for different values of conductor height h, according to the Rizk model. (From Rizk, F.A.M., *IEEE Trans. Power Deliv.*, PWRD-5(4), 1983, 1990.)

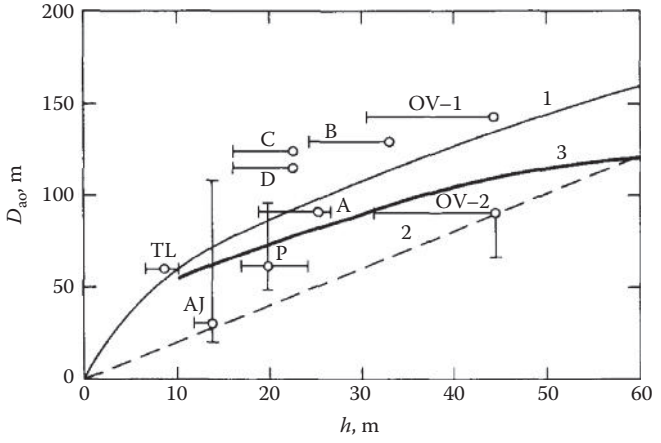


FIGURE 9.12 Variations of D_{ao} with conductor height h—comparison of calculated results and field. (Data from Eriksson, A.J., *IEEE Trans. Power Deliv.*, PWRD-2(3), 859, 1987b.) (1) The Eriksson model; (2) $D_{ao} = 2h$; (3) the Rizk model.

the earlier calculations are made with $\upsilon^-/\upsilon^+ = 1$. If it is assumed that $\upsilon^-/\upsilon^+ = 2$ instead, the following regression formula for D_a was obtained (Rizk, 1990):

$$D_a(I,h) = 2.0\, I^{0.62}\, h^{0.37} \tag{9.44}$$

Over the whole practical current range, the overall lateral attractive distance $D_{ao}(h)$ can be expressed in terms of conductor height as

$$D_{ao}(h) = 19 h^{0.445}, \quad \text{m} \tag{9.45}$$

A similar expression deduced previously by Eriksson (Erickson, 1987a) reads

$$D_{ao}(h) = 14 h^{0.6}, \quad \text{m} \tag{9.46}$$

which is used to determine the so-called electrical shadow.

9.5.4 Shielding Failure

Shielding failure occurs when a phase conductor is struck instead of the ground wire. It should be noted that not all shielding failures lead to flashover. Such flashovers occur in a current range, the lower limit of which, I_c, can be expressed as

$$I_c = 2\frac{U_b}{Z_0} \tag{9.47}$$

where

U_b is the negative lightning impulse withstand voltage of the insulator string
Z_0 is the line surge impedance

The upper limit current I_m characterizes the situation where the lateral attractive distance of the overhead shield wire D_{agw} just covers the sum of the lateral attractive distance of the phase conductor D_{ac} and the lateral displacement a between the conductor and shield wire:

$$D_{agw}(I_m) = D_{ac}(I_m) + a \tag{9.48}$$

which can be solved for I_m.

For a ground wire of height h_{gw} and a conductor of height h_c, in a region characterized by a ground flash density N_g, the shielding failure flashover rate (SFFOR) N_{sf} of a transmission line (two vulnerable conductors) per 100 km/year is given by

$$N_{sf} = 2N_g 10^{-1}\int_{I_c}^{I_m}[D_{ac}(I,h_c) + a - D_{agw}(I,h_{gw})]f(I)\,dI \tag{9.49}$$

where $f(I)$ is the statistical frequency function of the return stroke current I.

The condition $I_m = I_c$ corresponds to the ideal situation where theoretically no shielding failure flashover is possible, which defines the critical lateral displacement a_c from (9.48):

$$a_c = D_{agw}(I_c) - D_{ac}(I_c) \tag{9.50}$$

which results in the critical (perfect) shielding angle δ_c, determined from

$$\delta_c = \tan^{-1}\left(\frac{a_c}{h_{gw} - h_c}\right) \tag{9.51}$$

Figure 9.13 shows variation, according to the Rizk model, of δ_c with h_c for a transmission line with I_c = 5 kA and $h_{gw} - h_c$ of 5, 10, and 15 m. Figure 9.14 presents similar results for a high-voltage line with I_c = 10 kA. From these results, one observes that the critical protective angle decreases significantly with conductor height, but for a given height, δ_c decreases slightly with the height difference $h_{gw} - h_c$. It is also clear that for higher critical current I_c, significantly larger values of δ_c are permissible.

It may be more practical to design transmission line shielding not on the basis of a perfect shielding angle but rather on the basis of a shielding failure flashover rate (SFFOR) or N_{sf}, as previously suggested by Hileman (1999). Figure 9.15 shows the Rizk model results for variation of SFFOR, with shielding angle for a transmission line with h_{gw} = 25 m, h_c = 20 m, I_c = 5 kA, and N_g = 1/km^2 year. It is shown that, at least for the relatively low values of N_g, the shielding angle can be significantly higher than the perfect angle without much adverse effect on line performance. Similar results for h_{gw} = 30 m, h_c = 20 m, I_c = 10 kA, and N_g = 1/km^2 year are shown in Figure 9.16.

9.5.5 Backflashover

The term backflashover characterizes the situation when, as a result of a direct strike to the tower or ground wire, an insulator string flashover takes place. In general, backflashovers are associated with

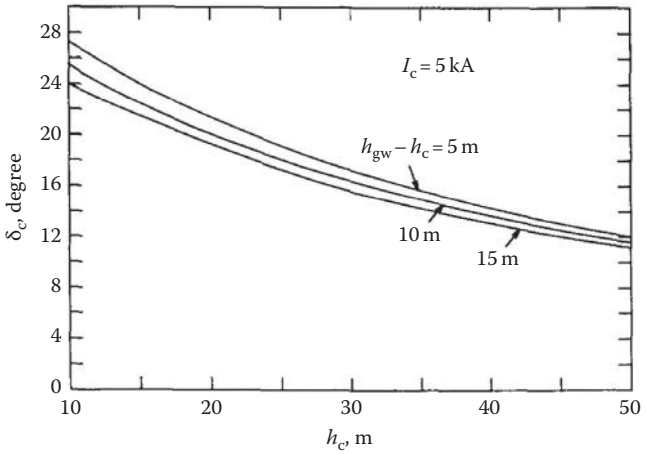


FIGURE 9.13 Variation of δ_c with h_c for a transmission line with I_c = 5 kA and $h_{gw} - h_c$ of 5, 10, and 15 m, according to the Rizk model.

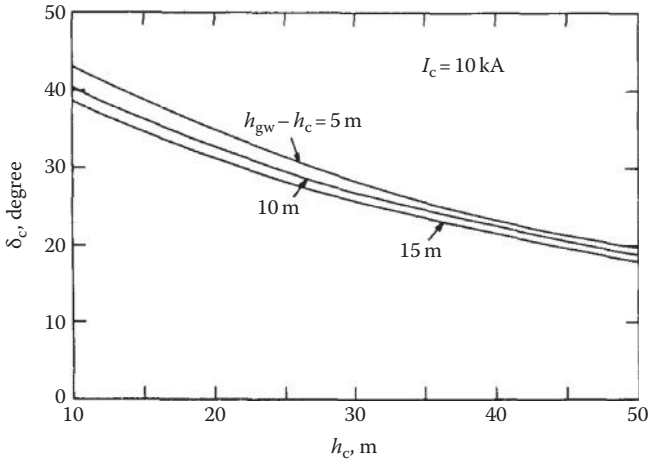


FIGURE 9.14 Variation of δ_c with h_c for a transmission line, with I_c = 10 kA and $h_{gw} - h_c$ of 5, 10, and 15 m, according to the Rizk model.

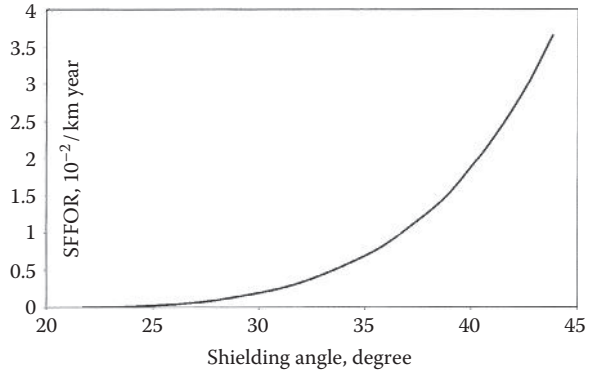


FIGURE 9.15 Variation of the SFFOR, with the protective angle by the Rizk model. h_{gw} = 25 m; h_c = 20 m; I_c = 5 kA; N_g = 1/km^2 year.

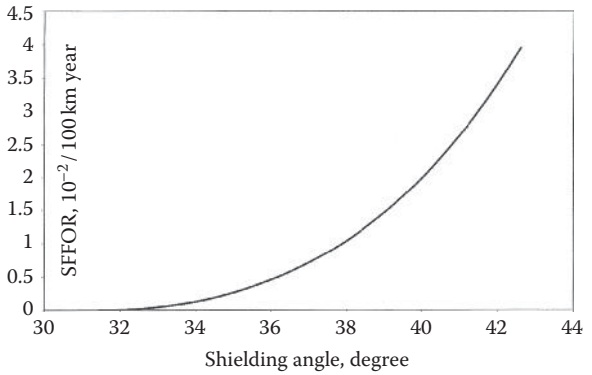


FIGURE 9.16 Variation of the SFFOR, with protective angle by the Rizk model. h_{gw} = 30 m; h_c = 20 m; I_c = 10 kA; N_g = 1/km^2 year.

very high return stroke currents or poor tower grounding. Backflashover has been the subject of several excellent extensive reviews (CIGRE 33-01, 1991; Hileman, 1999; Chisholm and Anderson, 2005), so that only a brief account of the essential points will be included in the present text.

Assessment of backflashover includes

1. Impulse response analysis of tower, footing resistance, and ground wires, using traveling wave methods
2. Accounting for soil ionization phenomena associated with high impulse currents
3. Study of the coupling between ground wires and phase conductors, with due consideration to transient corona effects as well as damping of traveling waves due to corona
4. Analysis of the response of the insulator string to nonstandard impulse voltages

It is obvious that a rigorous treatment of the subject would be very complex and that several simplifying assumptions will be necessary to make the analysis manageable.

9.5.5.1 Tower Top Potential

For outlining the calculation of the tower tip potential, consider the schematic diagram of Figure 9.17 and its equivalent circuit of Figure 9.18. Here, the tower is represented by a simple surge impedance Z_t (discussed later), the ground wire with Z_g, and the tower footing resistance R_i (discussed later). The tower top is struck by lightning, which in the simplest case is characterized by the impulse current of amplitude I and front time t_f. With this notation, it is implicit that lightning is represented by a current source (very high surge impedance) so that the lightning current is independent of the impedances of the struck object.

At the struck point, the equivalent surge impedance Z_e is given by

$$Z_e = \frac{Z_g Z_t}{Z_g + 2Z_t} \tag{9.52}$$

A surge of magnitude u flows into the tower towards ground and also away along the ground wires with

$$u = Z_e I \tag{9.53}$$

After twice the tower travel time T_t, a reflected wave will come back to the tower top, governed by the reflection coefficient α_t at the tower base with

$$\alpha_t = \frac{Z_t - R_i}{Z_t + R_i} \tag{9.54}$$

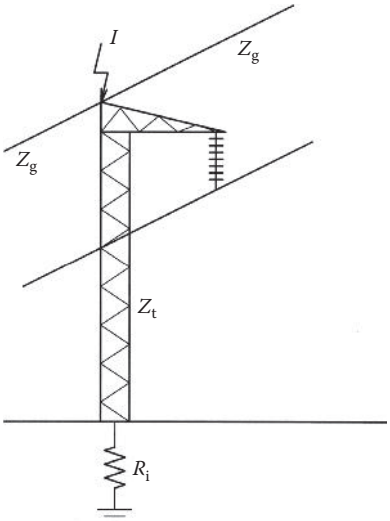


FIGURE 9.17 Schematic diagram for a tower struck by lightning.

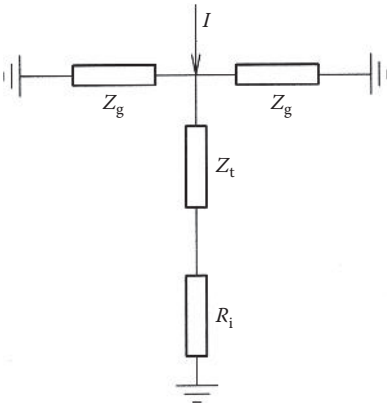


FIGURE 9.18 Equivalent circuit of schematic diagram in Figure 9.17.

Hileman (1999) introduced three voltage magnitudes of interest at the tower top:

1. V_t, which is the voltage at $t = 2T_t$, where T_t is the tower travel time
2. V_{tt}, which is the peak voltage
3. V_F, which is the final voltage

For a linearly rising current with front time t_f and peak value I, it can be shown that

$$V_t = \frac{2T_t}{t_f} Z_e I \tag{9.55}$$

$$V_{tt} = \left(1 - \alpha_t \frac{\hat{E}}{\hat{I}}\right) \left(1 - \frac{2T_t}{t_f}\right) \hat{I} Z_e \tag{9.56}$$

and

$$V_F = (1 - \alpha_t) Z_e I \tag{9.57}$$

with Z_e expressed by (9.52).

Hileman (1999) simplified the earlier expressions further by making the practical assumption

$$Z_t \approx \frac{Z_g}{2}$$

If instead of a linear front the concave front recommended by CIGRE (CIGRE 33-01, 1991) is adopted, and assuming that

$$T_t \ll \frac{I}{S_m}$$

where S_m is the maximum steepness, the tower can be roughly treated as a distributed inductance and the following estimate of the maximum tower top potential can be made:

$$V_{tt} = R_i I + \frac{Z_t}{u} h_t S_m \tag{9.58}$$

where

h_t is the tower height

υ is the propagation speed

In (9.58), the first term is obviously the resistive component due to the footing resistance, and the second is the inductive component due to the tower.

As a numerical example, let $R_i = 10\ \Omega$, $I = 100$ kA, $Z_t = 200\ \Omega$, $\upsilon = 2.4 \times 10^8$ m/s, $h_t = 30$ m, and $S_m = 24$ kA/μs. The footing resistance term in (9.58) would be 1000 kV and the tower term would be 600 kV. In general, the ratio V_{tt}/I may be referred to as K_{tt}, the tower top potential factor.

9.5.5.2 Tower Surge Impedance

Wagner and Hileman used field theory to demonstrate that when a vertical cylindrical tower of radius r and height h is struck by lightning, the surge impedance Z_t is a function of time (Wagner and Hileman, 1960):

$$Z_t = 60 \ln\left[\sqrt{2}\frac{ct}{r}\right] \tag{9.59}$$

where c is the speed of light. Z_t therefore increases with time and at $t = 2\ h/c$, it reaches the value

$$Z_t = 60 \ln\left[\sqrt{2}\frac{2h}{r}\right] \tag{9.60}$$

Sargent and Darveniza used the unit-step response (9.59) to obtain tower response to a linearly rising current and obtained (Sargent and Darveniza, 1969)

$$Z_t = 60\left[\ln\sqrt{2}\frac{2h}{r} - 1\right] \tag{9.61}$$

which also happens to be the mean value of Z over the height h. Expression (9.61) is widely used for cylindrical towers. For a conical tower with semiangle θ at the apex, Sargent and Darveniza also obtained (Sargent and Darveniza, 1969)

$$Z_t = 60 \ln\left[\frac{\sqrt{2}}{\sin\theta}\right] \tag{9.62}$$

Chisholm and Chow (1983) showed that the tower surge impedance differs depending on whether the tower is directly struck or receives a traveling wave current along the overhead ground wire.

For a tower characterized by upper and lower conical sections, a mean radius r_{mean} was obtained and for a tower height h, the following expression for Z_t was recommended (Chisholm and Chow, 1983):

$$Z_t = 60 \ln \cot\left(0.5 \tan^{-1} \frac{r_{mean}}{h}\right) \tag{9.63}$$

For an H-frame tower, with each leg of height h and radius r, spaced by a distance d, the tower surge impedance forms a self-surge impedance Z_s and a mutual surge impedance Z_m. Formulae based on early work by Jordan (1934; Anderson, 1982) are

$$Z_s = 60 \ln \frac{h}{r} + 90 \frac{r}{h} - 60 \tag{9.64}$$

and

$$Z_m = 60 \ln \frac{h}{d} + 90 \frac{d}{h} - 60 \tag{9.65}$$

with

$$Z_t = \frac{1}{2}(Z_s + Z_m) \tag{9.66}$$

As an example, for h = 20 m, d = 8 m, r = 0.5 m, Z_s = 163.6 Ω, and Z_m = 31.0 Ω, the resulting surge impedance is Z_t = 97.3 Ω.

If Z_s and Z_m are formulated instead following (9.61) by replacing h/r in (9.64) and (9.65) by $\sqrt{2}(2h/r)$, Z_s is obtained at 223.5 Ω and Z_m at 57.4 Ω resulting in Z_t = 140.4 Ω.

Variation of the tower surge impedance with height z above ground can be obtained from

$$Z_t(z) = \frac{1}{\upsilon C_t(z)} \tag{9.67}$$

where

υ is the wave propagation speed, often taken as the speed of light

C_t is the tower capacitance per unit length as function of height z above ground

Unpublished work by F.A.M. Rizk shows that $C_t(z)$ can be determined by the charge simulation method. This shows that Z_t is highest near the tower top and lowest near ground. A suitable mean value can be obtained from (9.67). Figure 9.19 shows variation of Z_t for the H-frame tower example

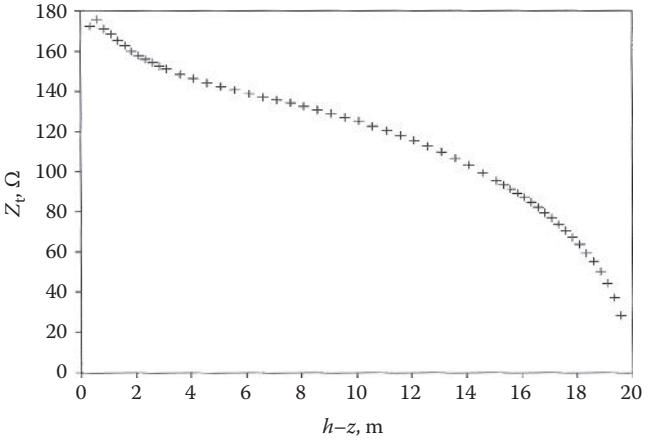


FIGURE 9.19 Variation of Z_t (for the H-frame tower example) with height above ground, as obtained by charge simulation technique. A mean value of Z_t was determined at 119 Ω.

considered earlier, with height above ground, as obtained by charge simulation technique. A mean value of Z_t was determined at 119 Ω.

9.5.5.3 Conductor Coupling

Traditional traveling wave equations on a two-conductor system, for example, ground wire and phase conductor, take the form

$$u_1 = Z_{11} i_1 + Z_{12} i_2 \tag{9.68}$$

and

$$u_2 = Z_{12} i_1 + Z_{22} i_2 \tag{9.69}$$

where

Z_{11} and Z_{22} are the self-surge impedances of the ground wire and the phase conductor, respectively
Z_{12} is the mutual surge impedance

With $i_2 = 0$, it follows that

$$u_2 = u_1 \frac{Z_{12}}{Z_{11}} = C_0 u_1 \tag{9.70}$$

where C_0 is the geometric coupling factor.

Here

$$Z_{11} = 60 \ln \frac{2h_{gw}}{r_0} \tag{9.71}$$

where

r_0 is the ground wire radius
h_{gw} its mean height above ground

The mutual surge impedance is practically given by

$$Z_{12} = 60 \ln \frac{2h_{gw}}{d} \tag{9.72}$$

where d is the distance between the two conductors.

When the ground wire is struck by lightning, it goes into corona, leading to significant increase of its capacitance per unit length. In (CIGRE 33-01, 1991), empirical formulae are provided to calculate the increase of a conductor capacitance due to corona. In Anderson (1982), a procedure for estimation of an increased conductor radius r_c is provided, under the assumption that the ionization zone is limited by an electric field of 1500 kV/m. As shown in (Hileman, 1999), the values of r_c obtained from CIGRE method are several times larger than those calculated according to John Anderson. However, due to the logarithmic dependence of the coupling factor on r_c, the resultant effect is not as pronounced.

Table 9.5 shows some estimated coupling factors, with and without corona for a ground wire of 1.2 cm diameter, by Anderson's method. The negative lightning impulse amplitude varies between 1000 and 3000 kV. It is shown that at 3000 kV the coupling factor due to corona is 39% above the corresponding value without corona. It should be noted, however, that the voltage stressing the insulator string is proportional to (1 – coupling factor). It is therefore shown, in the last column of Table 9.5, that corona on the ground wire at 3000 kV would reduce the voltage stressing the insulator string by 16%. A comparison undertaken by Hileman (1999), however, showed that if the CIGRE method is adopted, the effect of corona in reducing the insulator string stress, at a lightning impulse of 3000 kV, can be as high as 20%–35%, depending on the corona constants adopted.

TABLE 9.5

Calculated Coupling Factors between Ground Wire and Phase Conductor. $R_0 = 0.6$ cm, $h_{gw} = 30$ m, $d = 7$ m

V, kV	R_c, m	C_0, p.u.	C_c, p.u.	Ratio $\frac{1-C_c}{1-C_0}$
1000	0.105	0.23	0.28	0.89
2000	0.242	0.23	0.30	0.86
3000	0.399	0.23	0.32	0.84

9.5.5.4 Reflections from Adjacent Towers

Wave reflection from adjacent towers will reduce the tower top potential. In the analysis, normally one span on each side of the struck tower is considered. If the two spans and adjacent tower equivalents are taken in parallel and a reflection coefficient α_s is obtained, the reduction factor K_s can be expressed as (Hileman, 1999)

$$K_s = 1 - a_s(1 - a_t)\left[1 - \frac{2T_s}{t_f} + a_s a_t\left[1 - \frac{4T_s}{t_f} + \cdots\right]\right] \tag{9.73}$$

where T_s is the span traveling time, which is valid for $nT_s < t_f$.

It is noted that α_s is calculated with the geometric footing resistance R_0, assuming that the current in the adjacent tower will not cause significant soil ionization. It is clear from (9.73), since α_t and α_s are less than unity, that long spans, that is, larger T_s values, will be detrimental to backflashover performance.

9.5.5.5 Tower Grounding

Extensive tables of low-frequency ground resistances for electrodes of different geometries, including multiple rods, radial wires, and rings, were given by Sunde (1968). For the simplest geometry of a hemisphere of radius r,

$$R_0 = \frac{\rho}{2\pi r} \tag{9.74}$$

where ρ is the earth resistivity, assumed uniform. For a ground rod of length l and radius r,

$$R_0 = \frac{\rho}{2\pi l}\left[\ln\frac{4l}{r} - 1\right] \tag{9.75}$$

A particular aspect for lightning application is that for currents exceeding a critical level I_g, ionization phenomena in the soil act to reduce the footing resistance of a tower, effectively as if the dimensions of the ground electrodes were increased.

If the initial geometrical resistance is R_0 and earth resistivity is ρ, then I_g for a hemisphere can be expressed as (CIGRE 33-01, 1991)

$$I_g = \frac{1}{2\pi}\frac{\rho E_0}{R_0^2} \tag{9.76}$$

where E_0 is a critical voltage gradient, characterizing soil ionization, usually taken in the range 400–1000 kV/m. It can be shown that, for a hemispherical ground electrode, the resistance R_i at a current $I > I_g$ is given by

$$R_i = R_0\sqrt{\frac{I_g}{I}} \tag{9.77}$$

Assuming that the same expression (9.76) for I_g also applies for a rod, K.H. Weck obtained the following empirical expression (Weck, 1989):

$$R_i = \frac{R_0}{\sqrt{1 + (I/I_g)}} \tag{9.78}$$

As a numerical example, if ρ = 100 Ωm, R_0 = 20 Ω, and assuming E_0 = 600 kV/m, I_g = 23.9 kA. If the footing resistance R_i is evaluated from (9.78) at 100 kA, R_i = 8.8 Ω, which constitutes over a 50% reduction from the initial geometrical resistance R_0.

9.5.5.6 Estimation of Backflashover Rate

In estimating the backflashover rate (BFR), the critical current I_c for insulator flashover is determined:

$$I_c = \frac{V_{ns} - V_{pf}}{(K_{ta} - C\,K_{tt})K_s} \tag{9.79}$$

where

V_{ns} is the string flashover voltage under nonstandard lightning impulse
V_{pf} the sinusoidal power frequency voltage on the phase conductor
K_{tt} the tower top potential factor
K_{ta} the potential coefficient at insulator attachment point, $K_{ta} \approx K_{tt}$
K_s the factor due to reflection from adjacent towers
C the corona coupling factor

This procedure is repeated for all three phases, and since K_{tt} will in general be different for each phase, the corona coupling factors will also be different and the instantaneous power frequency voltage will obviously be different. In this way, the phase for which I_c is lowest will be determined. With view of soil ionization effects, some iteration will be necessary to determine I_c. Let N_l be the total number of flashovers to the tower, ground wire, as determined from the electrical shadow and the ground flash density. The number of backflashovers per 100 km year, the *BFR*, can be expressed as

$$\text{BFR} = N_l \int_{I_c}^{\infty} f(I)\,\mathrm{d}I \tag{9.80}$$

where $f(I)$ is the frequency function of the current amplitudes.

It should be noted, however, that (9.80) is too conservative since N_l comprises direct strikes to the tower as well as strikes occurring along the ground wire span. Mid-span flashovers between conductor and ground wire are rare. Furthermore, surges reaching the tower due to strikes to the ground wire span are less severe than direct strikes to the tower. Accordingly, the BFR of (9.80) should be reduced to get a more realistic flashover level. Based on calculations by Hileman, a reduction factor of 0.6 was introduced in (9.80).

9.6 Upward Flash

As previously mentioned, upward flash normally takes place through formation of an upward leader from a tall structure, with no existence of a downward stepped leader. Such flashes have also been reported on structures of moderate heights on mountain tops. Initiation of an upward leader may lead to a negative flash occurring under the effect of electric field caused by cloud charges, with or without the presence of remote downward or cloud discharges. The analysis of previous measurements of ground field E_g in

thunderstorm conditions, before downward stepped leader descent, showed that E_g follows an exponential statistical distribution of the form (Rizk, 1994)

$$P(E_g > E_{gc}) = \exp\left[-\frac{(E_{gc} - E_{g0})}{E_{g1}}\right] \tag{9.81}$$

where
E_{g0} is a threshold gradient
E_{g1} a shape field parameter

These parameters were shown to depend on region and topology. Measurements by Simpson (1949) in England could be characterized by E_{g0} = 2 kV/m and E_{g1} = 2 kV/m. For this statistical distribution, the probability of a ground field exceeding 10 kV/m is as low as 2%.

Ground field measurements by Eriksson in South Africa (Anderson, 1977) at a plateau of 1400 m altitude, on the other hand, were characterized by E_{g0} = 3 kV/m and E_{g1} = 6 kV/m. In this case, the probability of reaching a ground field as high as 20 kV/m is 6%.

Two criteria were formulated for inception of continuous upward leader from a slender mast of height h ($h/r \gg 1$) on flat ground (Rizk, 1994):

$$E_g h \geq 1600 \quad (\text{m, kV}) \tag{9.82}$$

and

$$E_{gt} \geq E_{\bullet} \tag{9.83}$$

where
E_g is the mean ground field along a height h above ground, in the absence of the structure
E_{gt} is the ambient field at the mast top height
E_{∞} is a steady-state leader gradient, which decreases with current and is in the range of 30–50 kV/m at 1 A.

Criterion (9.82) relates to the onset of the upward positive leader from a slender structure, while (9.83) expresses the condition that once leader propagation starts it will in fact continue, resulting in an upward flash.

Criteria formulating continuous upward leader onset from a massive structure, for which the slenderness condition is not satisfied, are given in Rizk (2009a).

If the number of thunderstorms per year in a given location is taken as T_d, then the number of upward flashes N_u per year can be calculated from

$$N_u = T_d P(E_g > E_{gc}) \tag{9.84}$$

For the same structure, the number of direct downward flashes per year, N_d, can be obtained from

$$N_d = \pi R_{ao}^2 N_g \tag{9.85}$$

where
R_{ao} is the overall attractive radius
N_g is the ground flash density

The conditional probability P_u that once a structure is struck by lightning, such a strike would be an upward flash can be expressed as

$$P_u = \frac{N_u}{N_u + N_d} \tag{9.86}$$

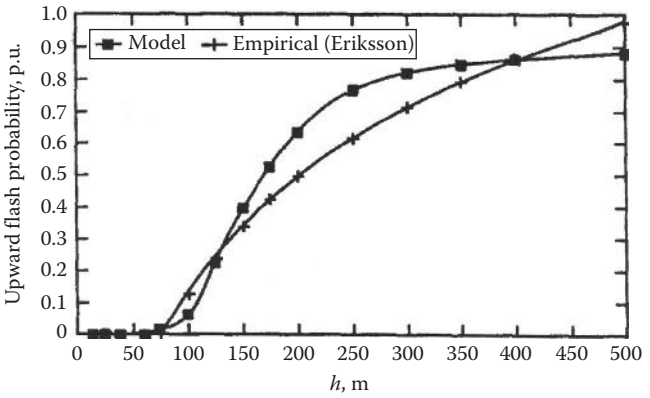


FIGURE 9.20 Comparison of calculated conditional probability P_u that once a structure is struck by lightning, such a strike would initiate an upward flash with results from Eriksson's empirical formula. (From Eriksson, A.J., *IEEE Trans. Power Deliv.*, PWRD-2(3), 859, 1987a.)

Such probability is shown in Figure 9.20 (Rizk, 1994) as function of mast height for a location with $N_g = 1/km^2$ year and indicates that upward flashes become significant for structures above 100 m height. It also shows that for $h = 500$ m, 90% of strikes would comprise upward flashes. The results of the model are compared with empirical formula by Eriksson (1987a).

It should be noted that formula (9.84) for determination of the number of upward flashes assumes one storm per thunderstorm day. As previously mentioned, such assumption is not always valid and storm multiplicity can occur, so that estimates from (9.84) would constitute a lower limit.

9.7 Protective Measures

9.7.1 Lightning Rods and Masts

Since the invention of the lightning rod by Benjamin Franklin in 1753, it found very wide application (Golde, 1973; NFPA 780, 2004; Uman, 2008) and in general, the experience has been satisfactory. A meaningful analysis by McEachron in 1950 (McEachron, 1950) of statistics from Iowa showed that "91% of buildings damaged by lightning were unrodded." This means that 9% of buildings, which were damaged due to lightning, were provided with lightning rods. Another statistic was quoted based on the Ontario Fire Marshal reports (Federal Interagency Lightning Protection User Group, 2001). Here, it was reported that among 66,282 structures protected under the Rod Act, only 17 rodded after 1922 were damaged. This was interpreted as 99.975% efficiency. Such conclusion, however, is misleading, since it should have been based not on the total number of structures installed but rather on the number of structures, protected by lightning rods or not, which suffered lightning damage. In other words, most of the 66,282 structures have probably never been struck by lightning and should not be included in the estimation of the rod efficiency. This argument has obviously been understood by McEachron (1950).

Although the notion of discharging clouds with a rod having a sharp tip, originally adopted by Franklin, was later abandoned, the rod shape remained basically unchanged. Recommendations to use air terminals with large exposed surfaces were made by Nicola Tesla (1918) and Aleksandrov and Kadzov (1987). The subject came again to the forefront with comparative tests on lightning rods of different geometries carried out near 3288 m high summit of South Baldy Peak, New Mexico (Moore et al., 2000). It was found in 7 years of exposure that none of the sharp rods nor the so-called early streamer emitters (ESE) have been struck by lightning (Moore et al., 2000). All strikes went to blunt rods with diameters of 12.7–25.4 mm, with most hits to the 19 mm diameter rod.

It can be concluded that the air terminal geometry plays a significant role in its exposure to lightning and, accordingly, in its performance as a protective device. While the results of New Mexico have not

satisfactorily been explained in Moore et al. (2000), they were the subject of detailed physical analysis in Rizk (2010). The following conclusions were reached:

- Cloud charge field intensification at the tip of a slender lightning rod makes such a rod susceptible to corona formation in the absence of or prior to negative leader descent. The resulting space charge tends to suppress the electric field in the tip vicinity.
- Corona onset of lightning rods due to cloud charge fields prior to leader descent is not restricted to tall rods but applies as well to rods of practical height installed on top of tall structures due to local field intensification.
- In the absence of corona formation at the rod tip due to cloud charge fields prior to negative leader descent, the rod diameter has no significant effect on upward connecting leader inception.
- Laboratory tests to compare the performance of competing lightning rods would be meaningful only if performed with composite voltages comprising a dc component with a superimposed switching impulse. This is necessary to simulate ground field due to cloud charges.
- A new analytical approach has been introduced to estimate the self-shielding effect of corona space charge due to cloud charge fields prior to negative leader descent on continuous upward leader inception.
- Under otherwise the same conditions, the effect of corona space charge produced by cloud charge fields on inhibiting upward leader inception will be more significant: the taller the rod, the higher the maximum ambient ground field will be and the lower the corona inception field.
- It has been found that for lightning rods of height in the 10 m range, the corona space charge prior to leader descent will have a limited effect on the attractive radius of a solitary rod but will have a determining effect on the competition of adjacent objects exposed to the same atmospheric conditions.
- Based on the physics of electrical discharges, the characteristics of a non-self-shielding air terminal were formulated.
- Due to the effects of protrusions and water drops on large electrodes, a dc corona-free rod, prior to the negative leader descent, with the smallest practical diameter is preferable.
- The preferred rod slenderness ratio h/r is not a constant but varies with rod height, maximum ground field, and ambient relative air density.
- For rods or masts of heights above flat ground in the tens of meters range, corona-free performance prior to negative leader descent requires impractically large rod diameters, which are moreover susceptible to deteriorated corona performance due to protrusions and water drops.
- Both theory and field experience demonstrate the advantage of a lightning rod that is less prone to corona formation under cloud charge fields prior to negative leader descent.

An air terminal designed to minimize self-protection due to space charge shielding due to corona caused by cloud charge fields prior to negative leader descent is shown in Figure 9.21 (Rizk, 2011). This design has the advantage of being insensitive to protrusions caused by rain drops (Rizk, 1976). This air terminal could be placed at the top of a mast in a substation, on a transmission tower, to enhance their lightning protection performance, or in a corner of a high building, which is often the most vulnerable location (Rizk, 2009).

9.7.2 Ground Wires

The shielding effect of overhead ground wires has already been analyzed in Section 9.5.3. Appropriate selection of the number and placement of overhead ground wires generally reduces shielding failure rate to acceptable levels. Shielding wire application can be problematic, however, in large spans under severe icing conditions. This could lead to significant risk of shield wire breakage and fall on the phase conductors, resulting in a prolonged line outage since such fault cannot obviously be cleared by autoreclosure.



FIGURE 9.21 An air terminal designed to minimize self-protection by space charge shielding due to corona caused by cloud charge fields prior to negative leader descent. (From Rizk, F.A.M., Lightning protective device, wet/dry field sensitive air terminal, US Patent, US 7960647 B2, June 14, 2011.)

Despite advances in our understanding of the attachment mechanism, there are still some situations where the shielding performance does not fully meet expectations such as

- Multicircuit lines with exceptionally high towers (Taniguchi et al., 2009)
- UHV lines (Tikhodev, 1993)
- The positive pole of an HVDC transmission line (Rizk, 2008)

These topics are presently the subject of ongoing research. Finally, an additional shield wire built under the phase conductors can in principle reduce the BFR by increasing the coupling factors (Hileman, 1999). Electric utilities, however, do not seem to be keen on this application, due to difficulties in coordinating different conductor heights under diverse climatic conditions.

9.7.3 Improving Grounding

Utilities normally strive to control BFR by controlling tower footing resistance R_0. Design values as low as 10 Ω are common. However, in zones of high soil resistivity, such as rocky ground, it is not easy or economic to meet such requirement. It should also be mentioned that soil resistivity is a statistical variable that varies due to seasonal and climatic changes, corrosion of embedded conductors, etc. One of the means to reduce tower footing resistance is through the use of counterpoise. It is noted that for a wire of length l, radius a, and depth d, with soil resistivity ρ, the footing resistance is given by (Sunde, 1968)

$$R_c = \frac{\rho}{\pi l}\left(\ln\frac{2l}{\sqrt{2ad}} - 1\right) \tag{9.87}$$

For example, with ρ = 1000 Ω m, l = 150 m, a = 0.01 m, and d = 0.5 m, R_0 = 14 Ω.

With a span of 300 m and a continuous counterpoise, the footing resistance from (9.87) and (9.88) will be practically divided by 2, due to the two counterpoises each with a 150 m length. However, Bewley has shown (Bewley, 1951) that the unit-step response of a counterpoise starts with a surge impedance Z_{0c} of 120–220 Ω, which decays exponentially to reach the steady-state leakage resistance R_c:

$$R_c(t) = R_c + (Z_{0c} - R_c)\exp\left(-\frac{t}{\tau_c}\right) \tag{9.88}$$

where $\tau_c \approx \frac{2}{3}T_c$, with T_c the traveling time of the length with a propagation speed of 1/3 the speed of light. In the earlier example, therefore, $T_c = 1.5$ μs and $\tau_c = 1.0$ μs. In other words, the resistance R_c is not reached instantaneously but after a delay that depends on the span length. It should be added however that for large stroke current, the aforementioned resistances will be significantly reduced due to soil ionization.

9.7.4 Line Arresters

Another means for improving lightning performance of transmission lines is the application of line arresters, which have now been available for 25 years (Koch et al., 1985). Early applications were mostly for line voltages in the range of 72–145 kV (Koch et al., 1985; Sadovic et al., 1997). The development of 275 and 500 kV line arresters was undertaken in Japan (Ishida et al., 1992).

Simple calculations would show that for a zinc oxide arrester in parallel with an insulator string, a sufficient margin can easily be maintained between the arrester protective level, or residual voltage, and the string lightning impulse flashover voltage. As an example, consider a 245 kV transmission line, in a solidly grounded system, with an earthing factor of 1.4. The maximum continuous operating voltage of the arrester can be chosen as

$$\text{MCOV} = \frac{245}{\sqrt{3}}1.4 = 198\ \text{kV}_{\text{rms}}$$

For an arrester rated 5 kA, a protective level V_{pl} for an 8/20 μs impulse current can be selected as

$$V_{pl} = 780\ \text{kV}_{\text{peak}}$$

A realistic value for the lightning impulse flashover voltage of the 245 kV insulator string is 950 kV_{peak}, which has a 22% margin above the arrester protective level.

In practice, insulation coordination between the arrester and insulator string should be based on maintaining an adequate margin between the *V–t* curves over a sufficient range of time to flashover. The previously mentioned simplistic analysis is certainly not sufficient to decide line arrester application to a specific transmission line. A list, not exhaustive, of questions that have to be settled is given in the following:

1. Is application of line arresters economically viable, if compared to other measures, such as improvement of tower footing resistance?
2. The question of energy requirement made of the arrester has to be analyzed carefully. The arrester energy requirement will normally be manageable if the transmission line is provided with ground wires, since the maximum stroke current associated with shielding failure is usually limited to 5–15 kA. With no shield wires, the stroke current and associated energy dissipation in the arrester will be much higher. Even if the energy capability is not exceeded, this is likely to have a detrimental effect on arrester reliability and lifetime. An example of analyzing the arrester energy requirement is given in Sadovic et al. (1997), for shielded and unshielded lines.

3. A line arrester application strategy has to be decided. What will be the extent of line arrester application
   a. On a line section or on the whole line?
   b. On all phases or on some phases only?
   c. On every tower or, say, every second tower?
4. Such decisions will have significant impact on both economics and the degree of improvement of lightning performance of the line. Transient analysis is presently done by an electromagnetic transient software such as the EMTP or ATP.
5. A decision has to be taken on whether to use gapless or gapped line arrester. Each has its advantages and problems:
   a. A gapless arrester is simpler but stressed all the time, which may influence reliability. If an arrester fails shorted, it introduces a permanent fault that will require immediate replacement, unless energized through a disconnecting device, which in itself introduces a further complexity.
   b. A gapped arrester is more complex. It makes insulation coordination more involved. The gap is more susceptible to environmental conditions. Successful interruption of power follow current is essential.
   c. The external arrester gap has to cope not only with power frequency voltages but with the maximum switching overvoltages that the system may produce.
6. Insulation coordination for line arresters involves dealing with pollution, icing, heavy rain, etc.
7. Arrester failure, though not frequent, should not lead to fragmentation, especially when used near populated areas.

With view of the earlier texts, the tendency is to use gapless line arresters for distribution and medium-voltage lines and gapped line arrester at higher voltages of 245 and 525 kV. No line arrester application has been reported for 765 kV or UHV transmission lines.

Finally, arrester testing, an essential part of the coordination process, is carried out according to national or international specifications (IEC Standard 99-4, 1991; IEEE Standard C62-22, 1991; IEEE Standard C62-11, 1993).

9.7.5 Streamer Inhibition

As explained in Section 9.5.3, formation of an upward connecting leader plays a major role in the attachment process. The distance bridged by the upward leader comprises a very significant part of the attractive radius of a mast or the lateral attractive distance of a conductor. Initiation of a streamer of critical size is in fact a prerequisite for upward leader inception (Rizk, 1989). It has long been known that thin wires energized at HVDC or HVAC tend to suppress formation of streamers in favor of glow, or ultracorona (Uhlig, 1956). Based on extensive high-voltage tests on air gaps, Uhlig concluded that the cylindrical part of a thin wire, not points, comprises the ideal electrode shape to produce ultracorona (Uhlig, 1956). In a test series on small thin wire-plane gaps with positive impulses, Uhlig determined (Uhlig, 1956) that there exists a critical rate of rise of the impulse voltage (impulse front) above which the breakdown occurs due to streamer formation. For a 1 mm diameter wire, the critical rate for streamer formation was measured at 0.1 kV/μs, which increased to 1.0 kV/μs for a 0.1 mm diameter wire.

More recently, it was shown (Rizk, 2010) that for a horizontal wire of radius r at a height h above ground, the critical rate of voltage rise A, below which stable ultracorona prevails, can be expressed as

$$A = \mathrm{m} E_{\mathrm{ci}}^2 \ln \frac{2h}{r} \tag{9.89}$$

where

E_{ci} is the corona inception field for the thin wire

μ is the positive ion mobility in air, normally taken as $1.5–2.0 \times 10^{-4}$ m²/V s.



FIGURE 9.22 Streamer inhibitor electrode used as air terminal. (From Rizk, F.A.M., Lightning protective device, wet/dry field sensitive air terminal, US Patent, US 7960647 B2, June 14, 2011.)

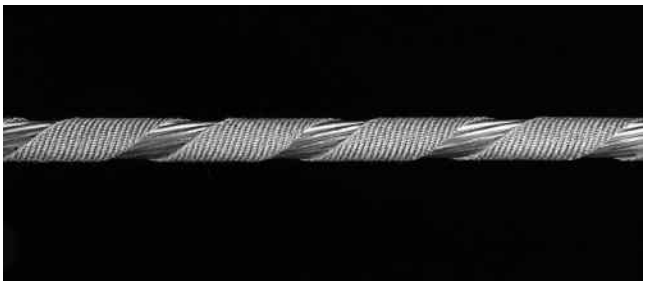


FIGURE 9.23 Streamer-inhibited conductor. (From Rizk, F.A.M., Lightning protective device, wet/dry field sensitive air terminal, US Patent, US 7960647 B2, June 14, 2011.)

The corona inception field E_{ci} can be expressed as

$$E_{ci} = 2300\left(1 + \frac{0.224}{(2r)^{0.37}}\right) \quad \text{kV/m, m} \tag{9.90}$$

which accounts for the well-known increased corona onset gradient for thin wires. From (9.89) and (9.90), it is also clear that the thinner the wire, the higher the critical rate of rise, that is, the more favorable the wire will be for ultracorona formation and streamer suppression.

Based on the earlier texts as well as extensive high-voltage tests (Rizk, 2010), a streamer-suppressing electrode, consisting of a thin-wire, woven tape–clad toroid, was introduced for use as an air terminal (Rizk, 2011). This novel air terminal is particularly intended to suppress upward flashes from tall structures. A picture of a streamer inhibitor electrode is shown in Figure 9.22.

A streamer-inhibiting cylindrical conductor based on the same ultracorona principle was also introduced. The application of this novel conductor was analyzed in Rizk (2011). This conductor can be used as a ground wire, a down conductor inside a wind turbine blade or along the side of a tall structure to inhibit side flashes. A photograph of a streamer-inhibited conductor is shown in Figure 9.23.

REFERENCES

Aleksandrov, G.M. and G.D. Kadzov. On increased effectiveness of lightning protection. *Electric Technology U.S.S.R.* 1: 75–82, 1987.

Anderson, J.G. Lightning performance of transmission lines. *EPRI Transmission Line Reference Book, 345 kV and Above*, Chapter 12, EPRI, Palo Alto, CA, 1982.

Anderson, R.B. Measuring techniques. In: R.H. Golde (ed.), *Lightning*, London, U.K.: Academic Press, London, 1977, Chapter 13, p. 441.

Anderson, R.B. and A.J. Eriksson. Lightning parameters for engineering applications. *Electra* 69: 65–102, 1980.

Anderson, R.B., Eriksson, A.J., Kroninger, H., Meal, D.V., and M.A. Smith. Lightning and thunderstorm parameters. In: *IEE Conference Publication, No. 326*, *Lightning and Power Systems*, London, U.K., June 1984.

Armstrong, H.R. and E.R. Whitehead. Field and analytical studies of transmission line shielding. *IEEE Transactions on Power Apparatus and Systems* PAS-87(1): 270–281, 1968.

Berger, K. Discussion of SC 33 on "lightning and surges". In: *CIGRE Proceedings, Vol. II*, CIGRE, Paris, France, 1968, pp. 10–11.

Berger, K. Methods and results of lightning research at Monte San Salvatore by Lugano in the years 1963–1971. *Bulletin SEV* 63: 1403–1422, 1977.

Bewley, L.V. *Traveling Waves on Transmission Lines*. New York: John Wiley, 1951.

Carrara, G. and L. Thione. Switching surge strength of large air gaps: A physical approach. *IEEE Transactions on Power Apparatus and Systems* PAS-95(2): 512–524, 1976.

Chisholm, W.A. and J.G. Anderson. Lightning and grounding. In: *EPRI AC Transmission Line Reference Book—200 kV and Above*, 3rd edn., EPRI, 2005, Chapter 6.

Chisholm, W.A. and Y.L. Chow. Lightning surge response of transmission towers. *IEEE Transactions on Power Apparatus and Systems* PAS-102(9): 3232–3242, 1983.

CIGRE WG 33.01 (Lightning). Guide to procedures for estimating the lightning performance of transmission lines. CIGRE Technical Brochure, No. 63, CIGRE Paris, France, October 1991.

Cummins, K.L., Murphy, M.J., Bardo, E.A., Hiscox, W.L., Pyle, R.B., and A.E. Pifer. A combined TOA/MDF technology upgrade of the US national detection network. *Journal of Geophysical Research* 103: 9035–9044, 1998.

Dellera, L. and E. Garbagnati. Lightning stroke simulation by means of the leader progression model. Part I: Description of the model and evaluation of free-standing structures. *IEEE Transactions of Power Delivery* PWRD-5(4): 2009–2022, 1990a.

Dellera, L. and E. Garbagnati. Lightning stroke simulation by means of the leader progression model. Part II: Exposure and shielding failure evaluation of overhead lines with assessment of application graphs. *IEEE Transactions of Power Delivery* PWRD-5(4): 2023–2029, 1990b.

Eriksson, A.J. The incidence of lightning strikes to power lines. *IEEE Transactions of Power Delivery* PWRD-2(3): 859–870, 1987a.

Eriksson, A.J. An improved electrogeometric model for transmission line shielding analysis. *IEEE Transactions of Power Delivery* PWRD-2(3): 859–870.

Federal Interagency Lightning Protection User Group. The basis of conventional lightning protection technology, NFFA, June 2001.

Gary, C. and B. Hutzler. Simulation en laboratoire de l'impact au sol. RGE, Paris, France, No. 3, March 1989, pp. 18–24.

Golde, R.H. *Lightning Protection*. London, U.K.: Edward Arnold, 1973.

Heidler, F. Traveling current source model for LEMP calculations. In: *Proceedings of Sixth International Symposium on EMC*, Zurich, Switzerland, 1985, pp. 157–162.

Heidler, F. Lightning electromagnetic pulse, theory and measurement, PhD thesis, Federal Armed Forces University, Munich, Germany, 1987.

Heidler, F., Cvetic, J.M., and B.V. Stanic. Calculation of lightning current parameters. *IEEE Transactions on Power Delivery* 14(2): 399–404, 1999.

Hileman, A.R. *Insulation Coordination for Power Systems*. New York: Marcel Dekker, 1999.

IEC Standard 60060-1. *High Voltage Test Techniques, Part 1: General Definitions and Test Requirements*, IEC, Geneva, Switzerland, 1989.

IEC Standard 62305-1. *Protection against Lightning*.

IEC Standard 99-4. *Metal-oxide Surge Arresters without Gaps for AC Systems*, 1991–2011.

IEEE Standard C 62.11. *IEEE Standard for Metal Oxide Surge Arrester for Alternating Current Circuits*, 1993.

IEEE Standard C 62.22. *IEEE Guide for the Application of Metal Oxide Surge Arrester for Alternating Current Power Systems*, 1991.

IEEE Standard 1243–1997. *IEEE Guide for Improving the Lightning Performance of Transmissioin Lines*, 1997.

Ishida, K., Dokai, K., Isozaki, T., Irie, T., Nakayama, T., Fujita, H., Arakawa, K., and Y. Aihara. Development of a 500 kV line arrester and its characteristics. *IEEE Transactions on Power Delivery* PWRD-7(3): 1265–1274, 1992.

Jordan, C.A. Lightning computations for transmission lines with overhead ground wires, Part II. *General Electric Review* 37(3): 180–186, March 1934.

Koch, R.E., Timoshenko, J.A., Anderson, J.G., and C.H. Shih. Design of zinc oxide transmission line arresters for application on 138 kV towers. *IEEE Transactions on Power Apparatus and Systems*PAS-104(10): 2675–2680, 1985.

Krider, E.P., Noggle, R.C., and M.A. Uman. A gated wideband magnetic direction finder for lightning return strokes. *Journal of Applied Meteorology* 15(3): 301–306, 1976.

Lee, A.C.L. An operational system for the remote location of lightning flashes using VLF arrival time difference technique. *Journal of Atmospheric and Oceanic Technology* 3: 630–642, 1986.

Les Renardieres Group. Negative discharges in long air gaps at Les Renardieres—1978 results. *Electra* 74: 67–216, 1981.

Lewis, E.A., Harvey, R.B., and J.E. Rasmussen. Hyperbolic direction finding with sferics of transatlantic origin. *Journal of Geophysics Research* 65: 1879–1905, 1960.

Lundholm, R. Induced overvoltage-surges on transmission lines and their bearing on the lightning performance of medium voltage networks. Trans. Chalmers University of Technology, Gothenburg, Sweden, 1957, p. 15.

MacGorman, D.R., Maier, M.W., and W.D. Rust. Lightning strike density for the contiguous United States from thunderstorm duration reports. U.S. Nuclear Regulatory Commission Report NUREG/CR-3759, May 1984.

Makerras, D. Prediction of lightning incidence and effects in electrical systems. In: *Electric Energy Conference 1978*, Vol. EE 14, Institution of Engineers, Barton, Australia, 1978, pp. 73–78.

Mason, B.J. A critical examination of theories of charge generation in thunderstorms. *Tellus* 5: 446–498, 1953.

McEachron, K.B. Lightning protection since Franklin's day. *Journal of the Franklin Institute* 253: 441–470, 1950.

Miyake, K., Suzuki, T., and K. Shinjou. Characteristics of winter lightning current on Japan sea coast. *IEEE Transactions on Power Delivery* 7: 1450–1456, 1992.

Moore, C.B., Rison, W., Mathis, J., and G. Aulich. Lightning rod improvement studies. *Journal of Applied Meteorology* 39: 593–609, 2000.

Mousa, A.M. and K.D. Srivastava. Modelling of power lines in lightning incidence calculations. *IEEE Transactions on Power Delivery* 5: 303–310, 1990.

NFPA 780. *Standard for the Installation of Lightning Protection Systems*, 2004.

Nucci, C.A., Mazetti, C., Rachidi, F., and M. Ianoz. On lightning return stroke models for LEMP calculations. In: *International Conference on Lighting Protection*, Graz, Austria, 1988, pp. 463–469.

Ortega, P., Domens, P., Gilbert, A., Hutzler, B., and G. Riquel. Performance of a 16.7 m air rod-plane gap under a negative switching impulse. *Journal of Physics D: Applied Physics* 27: 2379–2387, 1994.

Peek, F.W. *Dielectric Phenomena in High Voltage Engineering*. New York: McGraw Hill, 1929.

Pierce, E.T. Latitudinal variation of lightning parameters. *Journal of Applied Meteorology* 9: 194–195, 1970.

Prentice, S.A. and D. Makerras. The ratio of cloud to cloud-ground lightning flashes in thunderstorms. *Journal of Applied Meteorology* 16: 545–550, 1977.

Rakov, V.A. and A.A. Dulzon. A modified transmission line model for lightning return stroke field calculations. In: *Proceedings Ninth International Symposium on EMC*, Zurich, Switzerland, 1991.

Rakov, V.A. and M.A. Uman. *Lightning: Physics and Effects*, Cambridge, U.K.: Cambridge University Press, 2003.

Rizk, F.A.M. Lightning protection device: Wet/dry glow based streamer inhibitor, US Patent 7 468 879, 2006.

Rizk, F.A.M. Influence of rain on switching impulse sparkover voltage of large-electrode air gaps. *IEEE Transactions on Power Apparatus and Systems Part 1* 95(4): 1394–1402, 1976.

Rizk, F.A.M. Switching impulse strength of air insulation: Leader inception criterion. *IEEE Transactions on Power Delivery* 4(4): 2187–2195, 1989.

Rizk, F.A.M. Modeling of transmission line exposure to direct lightning strokes. *IEEE Transactions on Power Delivery* PWRD-5(4): 1983–1997, 1990.

Rizk, F.A.M. Modeling of lightning incidence to tall structures—Part I: Theory. *IEEE Transactions on Power Delivery* 9(1): 162–171, 1994.

Rizk, F.A.M. Critical switching impulse breakdown of long bundle-conductor gaps. *IEEE Transactions on Power Delivery* PWRD-11(1): 373–383, 1996.

Rizk, F.A.M. Lightning performance. *EPRI HVDC Reference Book: Overhead Lines for HVDC Transmission*, EPRI, Palo Alto, CA, June 2008, Chapter 4.

Rizk, F.A.M. Modeling of lightning exposure of buildings and massive structures. *IEEE Transactions on Power Delivery* 24(4): 1987–1998, 2009a.

Rizk, F.A.M. Modeling of proximity effect on positive leader inception and breakdown of long air gaps. *IEEE Transactions on Power Delivery* 24(4): 2311–2318, 2009b.

Rizk, F.A.M. Modeling of substation shielding against direct lightning strikes. *IEEE Transactions on Electromagnetic Compatibility* 52(3): 664–675, 2010.

Rizk, F.A.M. Analysis of space charge generating devices for lightning protection: Performance in slowly varying fields. *IEEE Transactions on Power Delivery* 25(3): 1996–2006, 2010.

Rizk, F.A.M. Modeling of lightning exposure of sharp and blunt rods. *IEEE Transactions on Power Delivery* 25(4): 3122–3132, 2010.

Rizk, F.A.M. Lightning protective device, wet/dry field sensitive air terminal, US Patent: US 7960647 B2, June 14, 2011.

Rizk, F.A.M. Effect of positive streamer inhibition on exposure of overhead conductors to direct lightning strikes. *IEEE Transactions on Power Delivery* PWRD-26(2): 1156–1165, 2011.

Rizk, F.A.M. and F. Vidal. Modeling of positive leader speed under slow front voltages—Part I: Long air gaps. *IEEE Transactions on Power Delivery* 23(1): 296–301, 2008.

Rusck, S. Induced lightning overvoltages on power transmission lines with special reference to the overvoltage protection of low voltage networks. Trans. Royal Institute of Technology, Stockholm, Sweden, 1958, p. 39.

Sadovic, S., Joulie, R., Tartier, S., and E. Brocard. Use of line surge arresters for improvement of the lightning performance of 63 kV and 90 kV shielded and unshielded transmission lines. *IEEE Transactions on Power Delivery* PWRD-12(3): 1232–1240, 1997.

Sargent, M.A. and M. Darveniza, Tower surge impedance. *IEEE Transactions on Power Apparatus and Systems* PAS-88: 680–687, 1969.

Saunders, C.P.R. A review of thunderstorm electrification processes. *Journal of Applied Meteorology* 32: 642–655, 1993.

Schonland, B.F.J. The lightning discharge. *Handbuck der Physik*, Vol. 22. Berlin, Germany: Springer-Verlag, pp. 576–638, 1956.

Schonland, B.F.J. and T.E. Allibone. Branching of lightning. *Nature* 128: 794–795, 1931.

Simpson, G. Atmospheric electricity during disturbed weather. *Geophysical Memoirs*, No. 84, Meteorological Office, London, 1949, pp. 1–51.

Simpson, G. and F.J. Scrase. The distribution of electricity in thunderclouds. *Proceedings of Royal Society of London A* 161: 309–352, 1937.

Sunde, E.O. *Earth Conductor Effects in Transmission Systems*. New York: Dover Publications, 1968.

Taniguchi, S., Tsuboi, T., and S. Okabe. Observation results of lightning shielding for large-scale transmission lines. *IEEE Transactions on Dielectrics and Electrical Insulation* DEI-16(2): 552–559, 2009.

Tesla, N. Lightning protector, US Patent 1266175, May 14, 1918.

Tikhodeev, N.N. *Operational Lightning Performance of EHV and UHV Overhead Lines and Its Enhancement*, Lecture Series, Hydro-Québec Institute of Research (IREQ), Varennes, Québec, Canada, 1993.

Uhlig, C.A.E. The ultra corona discharge: A new phenomenon occurring on thin wires. In: *High Voltage Symposium*, National Research Council of Canada, Ottawa, Ontario, Canada, 1956.

Uman, M.A. *The Art and Science of Lightning Protection*. Cambridge, U.K.: Cambridge University Press, 2008.

Uman, M.A. and D.K. McLain. Magnetic field of the lightning return stroke. *Journal of Geophysical Research* 74: 6899–6910, 1969.

Wagner, C.F. The relation between stroke current and velocity of the return stroke. *AIEE Transactions Part III* 82: 609–617, 1963.

Wagner, C.F. and A.R. Hileman. A new approach to the calculation of the lightning performance of transmission lines III—A simplified method—Stroke to tower. *AIEE Transactions of Power Apparatus System* PAS-79(3): 589–603, 1960.

Weck, K.H. The current dependence of tower footing resistance. CIGRE WG 33.01, 7 IWD, 1989.

Williams, E.R. The tripole structure of thunderstorms. *Journal of Geophysical Research* 94: 13151–13167, 1989.

Young, F.S., Clayton J.M., and A.R. Hileman. Shielding of transmission lines. *IEEE Transactions on Power Apparatus and Systems* S 82: 132–154, 1963.

10

High-Voltage Insulators

10.1 Introduction

The basic role of high-voltage insulators is to ensure proper attachment of the line conductors to grounded support structures. In this respect, the insulators play two essential roles:

1. To ensure the electrical integrity of the system, under diverse weather conditions, by withstanding electrical stresses associated with system voltage as well as related temporary and switching overvoltages. While flashovers due to direct lightning strikes cannot be practically eliminated, these can certainly be managed down to acceptable levels.
2. To maintain the mechanical integrity of the system by withstanding mechanical stresses associated with conductor weight and related overstressing due to icing, wind load, broken conductor conditions, etc.

With the progressive increase of transmission line voltage from 33 to 1100 kV during the twentieth century, both the electrical stresses associated with the line voltage and the mechanical loads due to the massive conductor bundles represented a challenge to the insulator designer. It is obvious that EHV and UHV transmission lines with power transfer capacity of thousands of MW have to meet the highest standards of electrical and mechanical reliability. Such reliability has to be maintained over the prospective lifetime of the line, which designers take to be as long as 50 years or more. Present-day insulator designs have met this challenge satisfactorily. While the failure rate of individual glass or porcelain disc insulators may be typically 10^{-4} to 10^{-3} units per year, failures involving total mechanical collapse are very rare, in the order of 10^{-7} per year.

In the following, we will be reviewing the different materials and designs of high-voltage insulators, with special reference to high-voltage transmission lines. Specific sections deal with electrical and mechanical insulator performance, with due consideration to adverse weather conditions including the effects of rain and pollution. Insulator standards and testing are also addressed. Finally, both deterministic and statistical design approaches are discussed.

10.2 Insulator Types and Materials

10.2.1 Insulator Types

There are different basis to classify high-voltage insulators. On the basis of mechanical function, insulators can be classified into suspension or support insulators. Apart from medium-voltage lines where post insulators are used, suspension insulators on transmission towers prevail for high-voltage lines. On the other hand, insulator columns are widely used in high-voltage substations to carry tubular bus bars or other electrical equipment such as disconnecting switches or capacitor banks. Based on orientation, transmission line insulators can be classified into suspension strings in tangent or small-angle towers and tension strings in large-angle or terminal towers. For suspension strings, distinction could further be made between single or multiple I-strings or V-strings. The justification for applying

multiple I- or V-strings is normally based on mechanical or safety requirements, such as long spans associated with river or highway crossings.

Based on the profile of suspension insulators, distinction can be made among disc type and long-rod type, as shown in Figure 10.1 (Rizk et al., 1972), for a set of porcelain insulators. In Figure 10.1, three profiles A, B, and D show disc insulators, while C and E represent long rods. Figure 10.1(type A) shows a basically regular profile, while Figure 10.1(type D) represents a so-called antifog disc with deep ribs and long leakage path from the cap to the pin along the insulator surface. Figure 10.1(type B) shows a

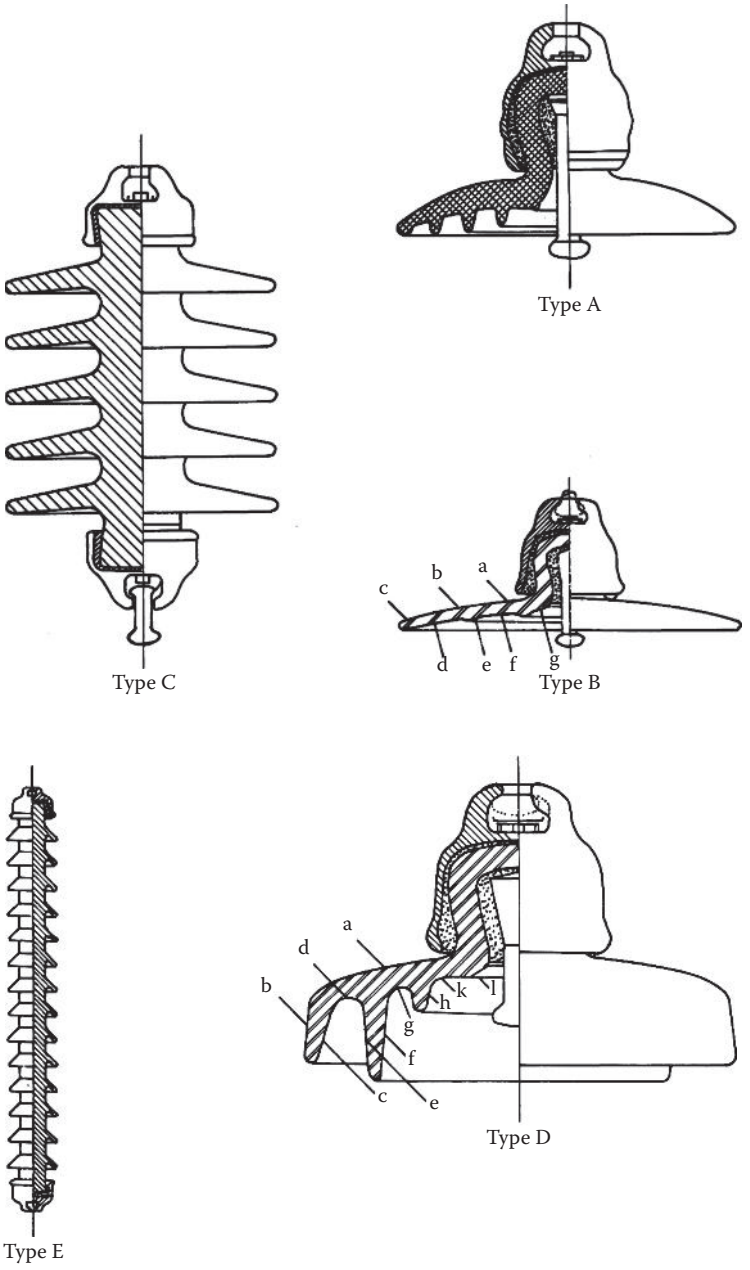


FIGURE 10.1 Profile of different cap and pin and long-rod porcelain insulators. (From Rizk, F.A.M. et al., Comparative tests on contaminated insulators with reference to desert conditions, CIGRE, Paper No. 33-03, 1972.)

TABLE 10.1

Basic Parameters of Insulators in Figure 10.1

Type	Leakage Path, mm	Spacing, mm	No. of Sheds	Outside Diameter, mm	Leakage Path/Spacing
A	384	183	—	320	2.10
B	419	178	—	483	2.54
C	1100	450	5	270	2.45
D	533	171	—	356	3.05
E	1850	1270	14	150	1.46

so-called aerodynamic disc, characterized by a relatively smooth profile and large overall diameter. Type E is a regular 75/14 long rod, while type C represents an aerodynamic long rod. Table 10.1 shows the basic parameters of the insulators shown in Figure 10.1.

In the following, we will return to the significance of these parameters and their effect on insulator performance, particularly under pollution conditions.

10.2.2 Insulator Materials

As far as insulator material is concerned, distinction should be made between ceramic insulators of porcelain and glass and polymeric or composite insulators. Material aspects are discussed in the following.

10.2.2.1 Porcelain

Electrical porcelain is made of a mixture of roughly 50% clay, 25% quartz or alumina, and 25% feldspar (Callister, 1994). Clays constitute some combination of hydrated aluminum silicate of one or more crystalline form, of a wide range of alumina (Al_2O_3) to silica (SiO_2) ratio. Quartz is chemically pure silica (SiO_2), while feldspar is a class of alkali–alumina–silicate minerals, for example, potash feldspar comprises $K_2O \cdot Al_2O_3\ 6SiO_2$ (Young, 1954). The raw materials are mixed together and ground to the desired particle size. In the wet preparation process, these materials are mixed with water, and the resulting mixture is filtered to remove foreign particles. Actual forming is carried out by casting, extrusion, jiggering, and plunging (Young, 1954). For the dry preparation process, forming is performed by dry and vacuum pressing (Young, 1954). Forming is followed by drying, finishing, glazing, and firing, which is probably the most important operation in porcelain manufacturing (Young, 1954). It is obvious that the quality of porcelain depends not only on the raw materials but also on the skill of the manufacturer and on quality control.

Metal fittings are attached to porcelain by cementing. Fitting materials include malleable cast iron, ductile iron, and steel. The types of cement used include alumina cement, Portland cement and sulfur cement. Experience has shown that some problems could be encountered with sulfur cement in hot climates, while Portland cement could suffer in industrial environment that includes sulfates. Tables on physical properties of electrical porcelain are available in material science texts (Young, 1954; Callister, 1994) and in IEC 60672. Some properties are summarized in the following:

- Density: ≈ 2.5 g/cm^3.
- Tensile strength of porcelain depends on composition and varies in the range of 40–80 MPa.
- Compressive strength of porcelain is about an order of magnitude higher than its tensile strength.
- Volume resistivity is of the order of $10^{11}\ \Omega \cdot$ m.
- Relative permittivity ε_r at room temperature and power frequency: 6–7.
- Dielectric strength is typically 200 kV/cm but depends on the thickness of the specimen.
- Maximum safe operating temperature is approximately 160°C.

- Coefficient of linear expansion $\approx 5 \times 10^{-6}$ (1/K).
- Thermal conductivity ≈1–4 W/m · K.
- Tan δ at power frequency: $1–3 \times 10^{-2}$.

The aforementioned properties lead to many advantages and some limitations of porcelain insulators (Vosloo et al., 2004). On the positive side, porcelain insulators are immune to degradation due to environmental factors, are resistant to surface damage due to leakage current, and have high compressive strength. They are, however, vulnerable to breakage and cracking due to power arcs and, when punctured, take specialized techniques (Vaillancourt and Rizk, 1988) to detect.

10.2.2.2 Glass

The soda lime glass consists of a melt of a mix of silica (SiO_2), limestone (CaO), feldspar ($Na_2O \cdot Al_2O_3 \cdot 6SiO_2$), and soda ash ($Na_2O$). Difference from porcelain arises primarily from its method of forming rather than from its ultimate composition (Young, 1954). In glass manufacturing, raw material mix is melted in a suitable furnace and then cooled to a lower temperature to become more viscous and can be worked into the desired shape. For cap and pin glass insulators, a heat treatment process called toughening is applied. This comprises reheating to a uniform temperature between transition and softening temperatures, followed by rapid quenching by exposing the surface to jets of cold air.

Relevant physical properties of toughened glass are summarized in the following:

- Density: ≈2.5 g/cm^3.
- Tensile strength is in the range of 100–120 MPa, somewhat higher than porcelain.
- Similar to porcelain, the compressive strength is considerably higher, reaching 700 MPa.
- Volume resistivity is similar to porcelain: $\approx 10^{11}\ \Omega \cdot$ m.
- Relative permittivity at room temperature and power frequency: ≈7, close to porcelain.
- Dielectric strength somewhat higher than porcelain and, as other solids, decreases with sample thickness.
- Maximum operating temperature is somewhat lower than porcelain and could be as low as 110°C (Bartnikas, 1993).
- Coefficient of linear expansion: $\approx 9 \times 10^{-6}$, significantly higher than porcelain.
- Thermal conductivity: ≈1 W/m · K, significantly lower than porcelain.
- Tan δ at power frequency: up to 6×10^{-2}, significantly higher than porcelain.

The positive features of glass insulators (Vosloo et al., 2004) include high dielectric strength and resistance to puncture, easy detection of damaged insulators due to shattering, and good compressive strength. On the other hand, glass insulators constitute a target for vandalism and are susceptible to erosion due to leakage current, which can precipitate shattering. Cap and pin glass insulators assume similar shapes to porcelain discs shown in Figure 10.1.

10.2.2.3 Polymers

Polymeric insulators for high-voltage transmission lines comprise a resin-embedded fiberglass core, which provides mechanical strength and a polymeric cover for protection from adverse weather conditions. Two housing materials are presently in use: ethylene propylene diene monomer (EPDM) and silicone rubber. Silicone rubber is resistant to UV radiation and has hydrophobic property. This makes composite insulators with silicone rubber sheds a viable alternative to ceramic insulators in polluted regions. Silicone rubber is made from polydimethylsiloxane with the mer structure shown in Figure 10.2 (Young, 1954; Rosen, 1971; Callister, 2004), which, as elastomers, are cross-linked.

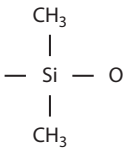


FIGURE 10.2 Chemical structure of polydimethylsiloxane.

Some relevant physical properties of silicone rubber material are given in the following (Young, 1954; Rosen, 1971; Bartnikas, 1993; Callister, 2004; Vosloo et al., 2004):

- Density: ≈1.15 g/cm^3.
- Glass transition temperature T_g: −120°C. This means that the material retains its rubber behavior in very low temperatures.
- Maximum operating temperature: ≈350°C.
- Relative permittivity at room temperature under power frequency: ≈4.
- Tan δ at room temperature under power frequency: 2–3 × 10^{-2}.
- Dielectric strength at power frequency: 160–200 kV/cm.
- Volume resistivity: 10^{12} Ω · m.
- Elongation to rupture: 150%–300%.

Note that these numbers, as those given for porcelain and glass earlier, are material properties. Accordingly, figures such as maximum operating temperature cannot obviously be applied to characterize an insulator unit, which results from application of different materials and manufacturing processes.

A typical design of a composite silicone rubber insulator (Dietz et al., 1986) is shown in Figure 10.3. It includes a fiber reinforced polymer (FRP) rod, which is chemically bonded to a high-temperature vulcanized (HTV) silicone rubber sheath. HTV silicone rubber sheds are vulcanized to the sheath. The FRP rod is attached to the end metal fittings by a cleaving wedge. The techniques used to attach the FRP rod to the end fittings include crimping, use of a cleaving wedge as in Figure 10.3, or application of an epoxy wedge within the end fitting.

It is important to ensure proper sealing between the end fitting and the silicone rubber sheath to avoid ingress of moisture. This and the chemical bond between the FRP rod and the sheath are intended to produce a puncture-free interface zone (Dietz et al., 1986). Typical dimensions of a silicone rubber composite

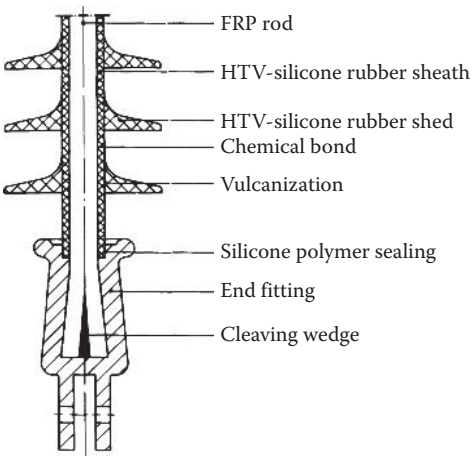


FIGURE 10.3 Typical details of a composite long-rod insulator. (From Dietz, H. et al., Latest developments and experience with composite long-rod insulators, CIGRE, Paper No. 15-09, 1986.)

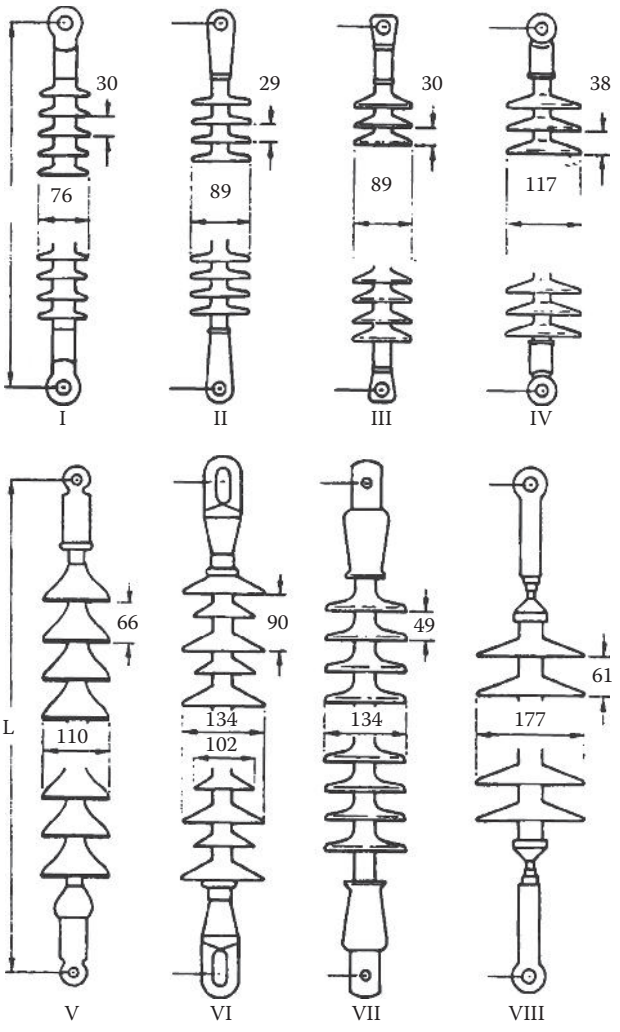


FIGURE 10.4 Profile of different nonceramic insulators. (From Houlgate and Swift, 1990.)

insulator are shown in Figure 10.4 (Houlgate and Smith, 1990). For type VII insulator, the shed spacing is 49 mm, outside diameter 134 mm, length L of 2.46 m, and leakage path length L_c 5.93 m. Using such insulator unit at a system voltage U_m of 245 kV results in a specific leakage path $l_{sp} = L_c/U_m$ of 24 mm/kV.

For system voltages of 245 kV and above, it is often recommended to provide polymeric insulators with protective rings. Such rings serve different purposes, including RI control, protection of end fittings from power arcs, as well as inhibiting housing material erosion due to surface discharge activity (Cherney et al., 1983; Phillips et al., 1999). Definitions, test methods, and acceptance criteria for composite insulators are given in IEC Standard 61109 (1992).

10.3 Electrical Performance of High-Voltage Insulators

10.3.1 Lightning Impulse Flashover

As mentioned in the chapter on long air gaps, lightning impulse sparkover takes place according to a streamer breakdown mechanism, since impulse duration is too short to allow any significant leader growth. Lightning impulse flashover of insulator strings is effectively a streamer breakdown of the air

gap between the conductor and the cross arm or between the guard rings or along the string arcing distance, whichever is shorter.

For strings of 2–6 standard cap and pin discs, Figure 10.5 (Rizk, 1960) shows a linear relationship between the number of insulator units and lightning impulse flashover voltage. As shown, negative impulse flashover voltage is only about 5% higher than with positive polarity. Figure 10.6 (Paris and Cortina, 1968) shows positive and negative standard lightning impulse flashover voltage of an insulator string, with conductor crossarm gap in the range of 2–6 m. Again, a linear relationship is shown with

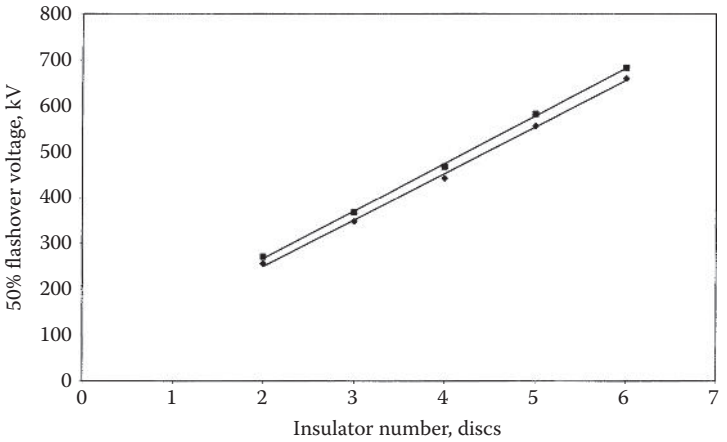


FIGURE 10.5 Standard lightning impulse flashover characteristics of short insulator strings. Upper: negative; lower: positive. (From Rizk, F.A.M., Flashover characteristics of insulators and spark-gaps with a power frequency half-cycle pulse, Thesis, Royal Institute of Technology, Stockholm, Sweden, 1960.)

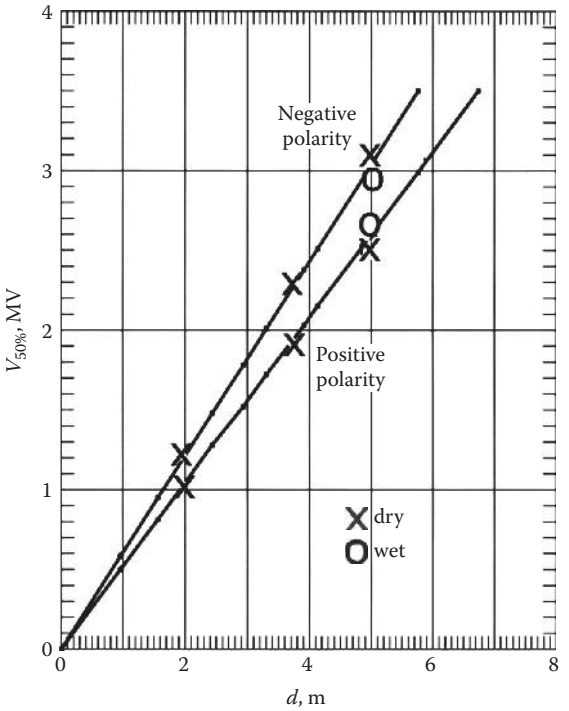


FIGURE 10.6 Lightning impulse flashover characteristics of dry and wet insulator strings. (From Paris, L. and Cortina, R., *IEEE Trans. Power Appar. Syst*., 87(4), 947, April 1968.)

the negative impulse flashover voltage slightly higher than the positive. The mean positive breakdown gradient amounts to approximately 525 kV/m, while the negative is approximately 600 kV/m. Note that these numbers would be affected by design and positioning of guard rings.

It is also noted in Figure 10.6 that the flashover results of dry and wet insulator strings under standard lightning impulse practically coincide. This confirms that rain has practically no effect on lightning impulse flashover. In fact, international standards do not require a lightning impulse wet test on insulator strings (IEC Standard 60305, 1995).

Lightning impulse flashover of transmission line insulators can influence lightning performance of the line in two ways. First, as mentioned in Chapter 9 on lightning, the minimum stroke current that can lead to flashover following a shielding failure is given by:

$$I_c = \frac{2U_b}{Z_0} \tag{10.1}$$

where

U_b is the negative lightning impulse flashover voltage of the line insulation
Z_0 is the line surge impedance

Since, as explained previously, there is a maximum current I_m at which shielding failure can occur, increasing I_c by reinforcing line insulation will result in reducing SFFOR.

Ultimately, if $I_c = I_m$, SFFOR will vanish. It is an economic question, whether it would be more advantageous to reduce I_m by proper positioning of the overhead ground wire, or increase I_c by reinforcing line insulation.

The second aspect, also treated in the Chapter 9 on lightning, is the effect of line insulation of backflashover. Here, the critical current level I_{cb} for backflashover was expressed by (Hileman, 1999)

$$I_{cb} = \frac{V_{NS} - K_{PF}V_{LN}}{(1 - C)K_{TT}} \tag{10.2}$$

where

V_{NS} is the critical nonstandard lightning impulse flashover voltage of the insulator string
V_{LN} is the phase-to-ground power frequency voltage
K_{PF} is the power frequency voltage factor
K_{TT} is the tower top potential coefficient
C is the coupling factor between the phase conductor and ground wire

It is clear from (10.2) that reinforcing line insulation will increase V_{NS} and accordingly I_{cb}. Under otherwise the same conditions of tower design and tower grounding, it is obvious that reinforcing of line insulation will then lead to reduction of the backflashover rate.

An illustrative simplified example is shown in Figure 10.7, based on Monteith et al. (1964), which presents variation of the backflashover rate per 100 km · year with the tower footing resistance of a 138 kV line, with 8, 10, and 12 insulators. Here, the span is 275 m and the keraunic level is 30. The backflashover rate is sensitive to both the footing resistance and the number of insulator discs. Again, the choice in order to satisfy the line performance criterion is economic. If it is required, for example, to limit the backflashover rate to 1.0/100 km · year, then with a 10 Ω footing resistance an 8-disc string will be adequate. For a 20 Ω footing resistance, on the other hand, the performance criterion can only be met with a 12-disc string. In this example, the insulator-specific leakage path amounted to 17, 21, and 26 mm/kV for 8, 10, and 12 discs, respectively. As will be shown later in this chapter, the line insulation is often dictated by insulator pollution requirements. In such situations, it may be found that the backflashover performance criterion is met even for nonrestrictive values of the tower footing resistance.

Finally, another effect of the lightning impulse flashover characteristics of line insulation is that it sets the upper limit for the amplitude of impinging impulses into the substation (Hileman, 1999).

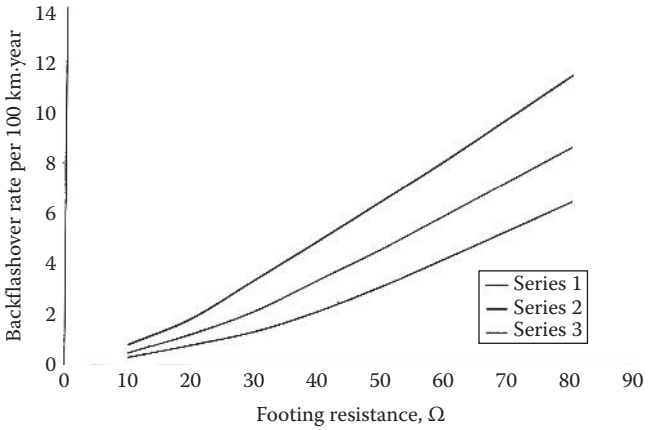


FIGURE 10.7 Variation of backflashover rate with tower footing resistance for different numbers of disc insulators in a 138 kV line. Span: 275 m; keraunic level: 30. S1: 8 insulators; S2: 10 insulators; S3: 12 insulators. (From Monteith, A.C. et al., Line design based upon direct strokes, in: *Electrical Transmission and Distribution Reference Book*, Westinghouse Electric Corporation, East Pittsburg, PA, 1964, pp. 578–609, Chapter 17.)

TABLE 10.2

Effect of Insulator String on Switching Impulse Flashover of a Conductor: Tower Crossarm Gap

	U_{50}, kV	
Applied Impulse	**Gap without Insulators**	**19-Disc String**
Positive switching	1160	1132
Negative switching	1478	1449

Source: LeRoy, G. et al., *Les propriétés diélectriques de l'air et les très hautes tensions*, Eyrolles, Paris, France, 1984, Chapter 16.

10.3.2 Switching Impulse Flashover

10.3.2.1 Comparison with Air Gaps

Here again, switching impulse flashover of an insulator string under dry conditions is basically a breakdown of the corresponding air gap. This occurs with the stages explained earlier of critical streamer formation, continuous leader inception and propagation, and final jump. Table 10.2 extracted from LeRoy et al. (1984) shows that there is little difference between the switching impulse strength of an insulator string, here consisting of 19 cap and pin discs, and the corresponding air gap without insulators.

10.3.2.2 Effect of Rain

An extensive experimental study on the effect of rain on switching impulse flashover of both insulator strings and supporting porcelain columns is reported in Rizk (1975). It was found that for positive polarity, the discharge path is displaced away from the insulator position (Figure 10.8). This explains the finding that positive switching impulse flashover voltage of both insulator strings and supporting columns is rather insensitive to rain intensity and resistivity within the ranges investigated. On the other hand, negative switching impulse discharge path takes place in proximity of the insulator and, accordingly, is more sensitive to rain parameters.

These points are illustrated in Figure 10.9 (Rizk, 1975). It is shown that, for a 25-disc insulator string, the positive switching impulse flashover voltage, apart from statistical scatter, is independent of the rain resistivity. Negative switching impulse flashover voltage, however, increases slightly with the increase of

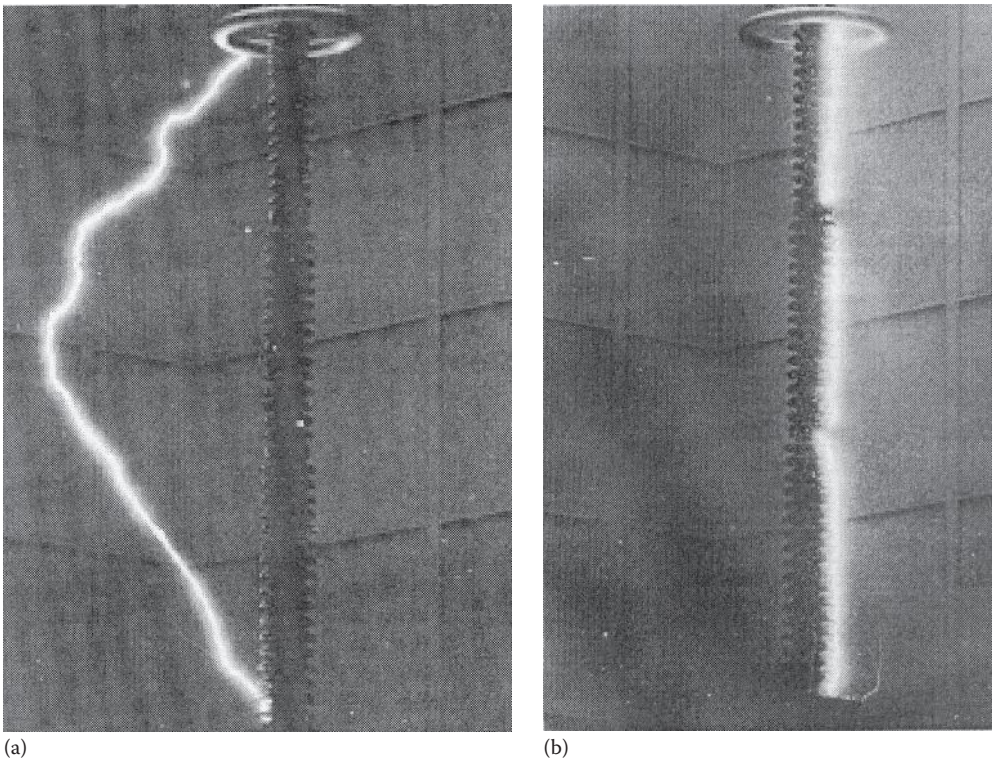


FIGURE 10.8 Typical switching impulse flashover path on an insulator column. (a) Positive polarity and (b) negative polarity. (From Rizk, F.A.M., *Proc. IEE*, 122(4), 449, April 1975.)

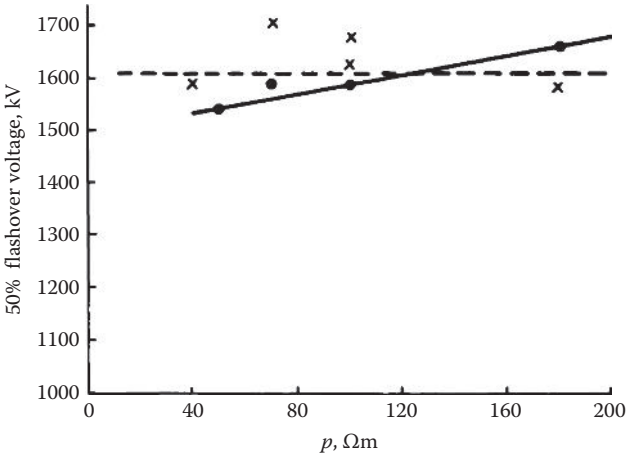


FIGURE 10.9 Variation of wet switching impulse flashover voltage of a disc string with water resistivity. x—Positive and *—negative. (From Rizk, F.A.M., *Proc. IEE*, 122(4), 449, April 1975.)

rain resistivity. The same trend is confirmed in Table 10.3 (Rizk, 1975), which presents the ratio of wet to dry switching impulse flashover voltage for a 25-disc string.

Similar results are presented in Table 10.4 for a 4.7 m supporting porcelain insulator column. Here again, there is practically no effect of rain on positive switching impulse flashover voltage, while there is a significant decrease for negative polarity. Finally, it should be mentioned that, in general, high-voltage rain tests are notorious for their relatively large dispersion, particularly for short wetting time (Figures 10.10 and 10.11) (Rizk and Hyltén-Cavallius, 1974).

TABLE 10.3

Effect of Rain of 50% Flashover Voltage of a 25-Disc String on Polarity of Switching Impulse

Applied Impulse	Rain Parameters Intensity, mm/min	Resistivity, Ω · m	Wet FOV, % Dry FOV
Positive switching	5	100	103
Negative switching	5	100	87

Source: Rizk, F.A.M., *Proc. IEE*, 122(4), 449, April 1975.

TABLE 10.4

Effect of Rain on Switching Impulse Flashover of 4.7 m Insulator Column

Test Condition	Rain Parameters Intensity, mm/min	Resistivity, Ω · m	U_{50}, kV Positive	U_{50}, kV Negative
Dry	—	—	1654	>2400
Wet	5	100	1637	1855

Source: Rizk, F.A.M., *Proc. IEE*, 122(4), 449, April 1975.

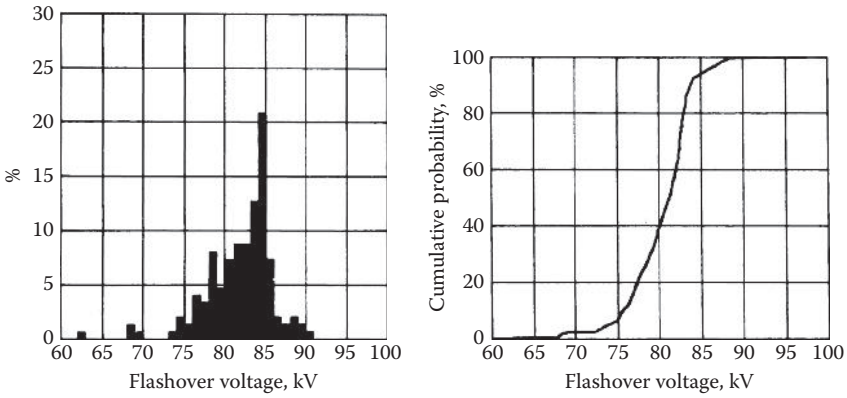


FIGURE 10.10 Frequency histogram and cumulative distribution curve of wet switching impulse flashover of a standard disc insulator. Wetting time: 0–18 min. (From Rizk, F.A.M. and N. Hyltén-Cavallius, Wetting of high-voltage insulators by artificial rain, IEEE Conference Paper C74 074-1, Winter Power Meeting, New York, 1974.)

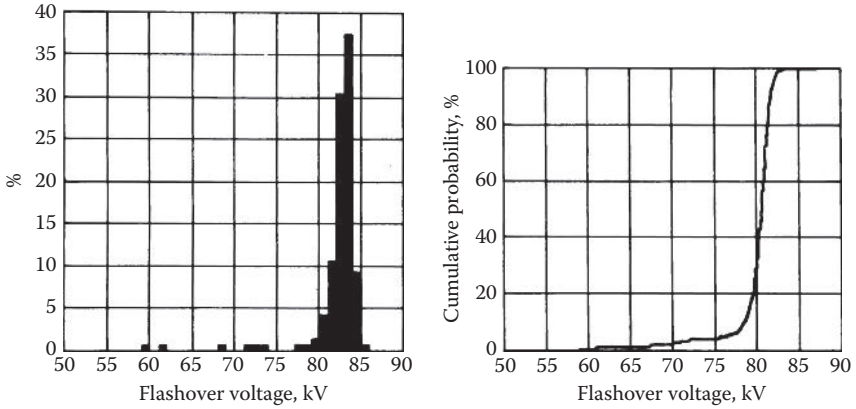


FIGURE 10.11 Frequency histogram and cumulative distribution curve of wet switching impulse flashover of a standard disc insulator. Wetting time: 18–45 min. (From Rizk, F.A.M. and N. Hyltén-Cavallius, Wetting of high-voltage insulators by artificial rain, IEEE Conference Paper C74 074-1, Winter Power Meeting, New York, 1974.)

10.3.3 Pollution Flashover

Flashover of insulators under system operating voltage has been experienced in heavily polluted industrial environment, near the seacoast, and in the desert. It is now recognized that pollution flashover mechanism is characterized by different stages: contamination layer buildup, insulator wetting, leakage current surging, formation of dry-band arcs, and eventual extension of such arcs to span the whole leakage path. In this chapter, such stages are dealt with and pollution flashover characteristics of insulators of different materials and designs are presented. High-voltage laboratory testing of polluted insulators is also included.

10.3.3.1 Pollution Layer Buildup

A pollution layer is formed when airborne particles settle on the insulator surface. The forces governing the motion of airborne particles involve wind forces, gravitational forces, and forces due to the electric field distribution in the insulator vicinity (Witt, 1961). The resultant force **F** is the vector sum of these forces. It may be instructive to look at these individual forces.

As we are dealing with fog and dust particle sizes in the range of 10–100 μm (Humphreys, 1964; Rizk et al., 1975), motion under gravity will be governed by Stoke's equation (Rouse, 1961; Kikoin and Kikoin, 1978). For a spherical particle of radius r and density ρ, the terminal speed v_t is reached when the viscous frictional force is equated to the gravitational force:

$$6\pi r\eta v_t = \frac{4}{3}\pi r^3 (\rho - \rho_a)g \tag{10.3}$$

where
ρ_a is the air density
η is the viscosity of air
g is the gravitational constant, 9.81 m/s^2

This yields the following expression for the terminal velocity v_t:

$$v_t = \frac{2}{9} g r^2 \frac{(\rho - \rho_a)}{\eta} \tag{10.4}$$

Using (10.4) with $\rho_a = 1.29$ kg/m^3 and $\eta = 1.72 \times 10^{-5}$ kg/m · s, Table 10.5 gives estimates, for $10 \le r \le 80$ μm, of v_t, for both dust particles of different dimensions and for fog.

It is shown that for most particle sizes in the earlier range, the terminal velocity under gravity is much lower than any practical wind speed.

Under wind conditions, with a wind speed v_w, motion of particles in the earlier size range can also be described by Stoke's equation. For a spherical particle of radius r, the wind force F_w can be expressed as

$$F_w = 6\pi r\eta (v_w - v) \tag{10.5}$$

where v is the particle speed at any instant, in the direction of v_w.

TABLE 10.5

Calculated Terminal Velocity under Gravity of Different Airborne Particles

Particle	Diameter, μm	Density ρ, kg/m^3	Velocity v_t, m/s
	10	1500	0.0048
	20		0.019
Dust	40		0.076
	60		0.171
	80		0.304
Fog	10	1000	0.003

Only for $v = 0$ would $F_w \to 6\pi r\eta v_w$, while F_w would vanish if $v \to v_w$, since then there would be no viscous frictional force applied to the particle.

The acceleration of the particle exposed to wind could be obtained from (10.5) as

$$\frac{dv}{dt} = \frac{9}{2}\frac{\eta}{r^2\rho}(v_w - v) \tag{10.6}$$

When integrated, this equation shows that $v \to v_w$ with a time constant $\tau = (2r^2\rho)/9\eta$. For a dust particle with a 50 μm diameter and $\rho = 1500$ kg/m^3, τ is determined at 12 ms. As expected, it does not take long before the particle assumes the wind speed v_w and there will be no more acceleration.

The present analysis for gravitational and wind forces on 10–100 μm particles and resulting accelerations differs from the approach described in Witt (1961).

The first electrical force $\mathbf{F}_{e1}$ acts on particles charged by corona in the insulator vicinity:

$$\mathbf{F}_{e1} = qE \tag{10.7}$$

where

q is the particle charge

E is the electric field at any point

The second is the dielectrophoretic force $\mathbf{F}_{e2}$ due to polarization of dust particles. Such force also depends on the particle shape and, for a spherical particle of radius r, can be expressed as

$$\mathbf{F}_{e2} = 2\pi r^3 \varepsilon_0 \frac{\varepsilon_r - 1}{\varepsilon_r + 2}\operatorname{grad}|E|^2 \tag{10.8}$$

where ε_r is the relative permittivity of the particle and

$$|E|^2 = E_x^2 + E_y^2 + E_z^2 \tag{10.9}$$

where E_x, E_y, and E_z are the x, y, and z components of the electric field at any point.

It is interesting to note that the force $\mathbf{F}_{e1}$ that acts on charged particles tends to drive the particles to zones of lower electric field. On the other hand, the dielectrophoretic force $\mathbf{F}_{e2}$ tends to drive the particles to zones of high electric field (Witt, 1961). It should also be noted that the force $\mathbf{F}_{e1}$ on charged particles may be relevant only under direct voltages, while the dielectrophoretic force $\mathbf{F}_{e2}$ applies for both ac and dc.

It should be noted that the pollution layer on the insulator surface is the result of complex interaction between the insulator shape and material and prevailing atmospheric conditions. In this respect, the site severity (CIGRE 33.04, 1979) does not become an abstract term characterizing the site alone but must account for the aforementioned interaction. This will be addressed in the following.

10.3.3.2 Site Severity

We should perhaps start with definition of equivalent salt deposit density (ESDD), which is often used to characterize pollution severity. The ESDD is the equivalent surface density of sodium chloride NaCl/cm^2, measured in mg/cm^2, which, when subjected to the same wetting, will produce the same surface conductivity χ_s in μS as the actual pollution layer. The procedure to measure ESDD is described in IEC 60507 (IEC Standard 60507, 1991). Another term used is the NSDD, which is the nonconducting surface deposit density, also measured in mg/cm^2. While nonconducting by itself, NSDD contributes indirectly to actual surface conductivity through its ability to absorb water. This will also influence drying of the pollution layer through leakage current surging as well as washing the layer off when exposed to prolonged wetting.

Methods used to assess site pollution severity include the following (CIGRE 33.04, 1979):

- Measurement of ESDD on different insulator types and design after certain exposure periods.
- Monitoring of the surface conductance of a sample insulator. The applied voltage level and duration have to be such as to avoid dry-band formation.
- Counting of leakage current surges exceeding a certain preset level.
- Recording to the highest leakage current I_h on a certain insulator, which does not lead to flashover (Verma, 1973).
- Measurement of the maximum current level I_{max} attained just before flashover (Verma, 1973).
- Measurement of the flashover stress, which is defined as the power frequency flashover voltage divided by the overall insulator length.
- Use of directional dust deposit gauges is described in Vosloo et al. (2004). This method does not account for the interaction between the insulator and the environment and will not be treated here further.

10.3.3.3 Effect of Exposure Time

As mentioned earlier, pollution layer buildup is a result of a complex interaction between the insulator and the environment. Pollution layer pattern is discussed in the following texts. An obvious factor influencing pollution layer buildup is the time of exposure. Also, self-cleaning due to wind and rain usually sets an upper limit for pollution severity but also depends on insulator shape. Open aerodynamic profiles have better self-cleaning quality than long leakage path profiles with deep under ribs. Also, frequency and intensity of dew formation influence layer buildup.

The rate of pollution accumulation, even for the same insulator design, clearly depends on location as shown in Figure 10.12 (Rizk et al., 1975). This refers to field tests on a 500 kV transmission of 800 km length in desert environment. The line is divided in four sections, each of which was considered to repre-

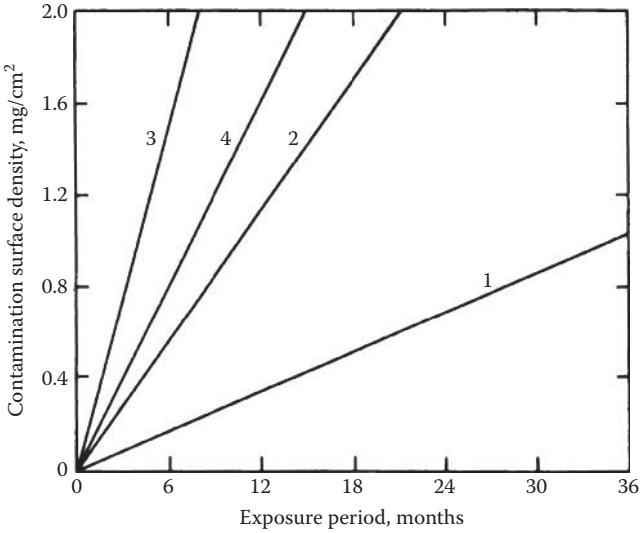


FIGURE 10.12 Contamination layer buildup on insulator surface with exposure period in the desert for different line sections. (From Rizk, F.A.M. et al., *IEEE Trans. Power Appar. Syst*., 94(5), 1170, September/October 1975.)

sent distinct environmental conditions. The straight lines in Figure 10.12 represent the best fit of highly dispersed material. Several observations can be made:

- Different line sections have distinct rates of pollution accumulation.
- While section 3 reaches 2 mg/cm^2 of deposit (conducting and nonconducting) in 6 months, section 1 has apparently not reached saturation after 36 months of exposure. This is rather unfortunate since it necessitates long exposure periods during field tests in order to reach realistic severity levels for line design.

Chemical analysis of this natural contaminant showed that soluble salts amount to 18% by weight, mostly consisting of sulfates and chlorides: $CaSO_4 \sim 10\%$, $NaCl \sim 3\%$, and $KCl \sim 0.5\%$. This means that for section 3 of the line, a total deposit of 2 mg/cm^2, reached in 6 months of exposure, corresponds to 0.36 mg/cm^2 of soluble salt, which is extremely severe. This high content of soluble salts in the natural contaminant was quite surprising, since analysis of salt content from sand samples taken along the line route varied in the range of 1%–4%. This discrepancy was explained when grain size analysis of the contaminant and the soil samples were undertaken.

It was established that 95% by weight of the natural contaminant comprise a grain size less than 44 μm, and all grains were below 74 μm. Figure 10.13 shows variation of soluble salt content as a function of grain size in soil samples from the desert sand. It is observed that, for grain size above 100 μm, salt content is relatively small. On the other hand, for the small grains of the size found on the insulator surface, the salt content was excessive. It was then visualized that a grain selection process occurs on the insulator surface, whereby small grains stick while large grains are blown away by wind. Dew formation is likely to play an important role in this process.

It should be noted that the gradual buildup of pollution layer on insulator surface presented in Figure 10.12 does not apply to all regions. For example, stormy conditions from the sea, like typhoons in Japan, dump large amounts of salty water on the insulators in a matter of hours (Higashimori et al., 1995). Even in the desert, sandstorms dump large amounts of dry contaminants on transmission line insulators in a single day. In case of storms near the seashore, the phases of contamination buildup and insulator surface wetting are combined and, therefore, represent a serious hazard. As to sandstorms, the hazard depends on whether the sandstorm is quickly followed by drizzle. If no insulator surface wetting follows, however, the dry sand due to the storm is gradually blown away by wind with no serious consequences.

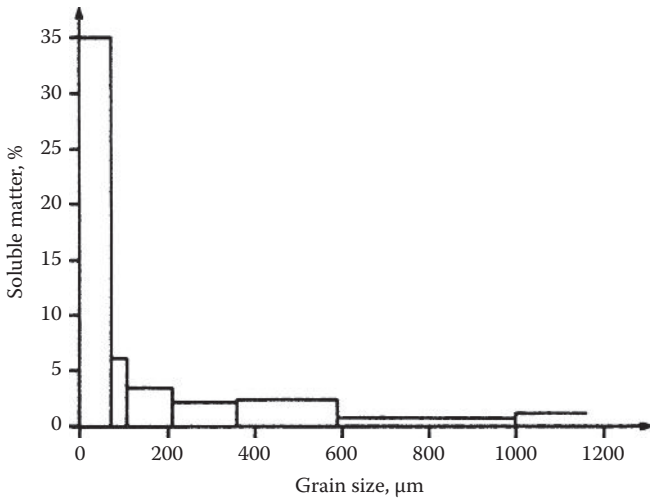


FIGURE 10.13 Variation of soluble salt content with grain size of a solid sample in the desert. (From Rizk, F.A.M. et al., *IEEE Trans. Power Appar. Syst*., 94(5), 1170, September/October 1975.)

10.3.3.4 Pollution Layer Pattern

It has often been reported that for ceramic cap and pin insulators, the contamination surface density on the bottom ribbed surface can be as high as 5–10 times that of the upper surface (Rizk et al., 1975). The value depends of course on insulator profile and on the prevailing self-cleaning effect. Figure 10.14 (Rizk et al., 1975) shows the distribution of ESDD along the leakage path of antifog disc type D of Figure 10.1 after 24 months of exposure in desert environment, confirming the extremely high pollution captured in the deepest groove, points *c*, *d*, and *e*. The following groove, point *g*, was clearly protected by the first rib.

Figure 10.15 (Rizk et al., 1975) shows the corresponding ESDD distribution along the leakage path of the aerodynamic profile of insulator B of Figure 10.1. There is still extremely high pollution in the part *d*–*e*–*f* of the bottom surface. It is clear, however, that by integration over the surface, the total amount of pollution collected by the aerodynamic profile will be much lower than the antifog profile.

Pollution buildup on silicone rubber insulators has not been as extensively studied as on ceramic insulators. It has been reported (Higashimori et al., 1995) that marine-type pollution forms in isolated spots on the surface of a new silicone rubber insulator. However, with aging, as hydrophobicity is lost, the pollution layer becomes more uniform. For inland, it was reported that dust is deposited evenly on the polymeric insulator surface (Karady et al., 1995).

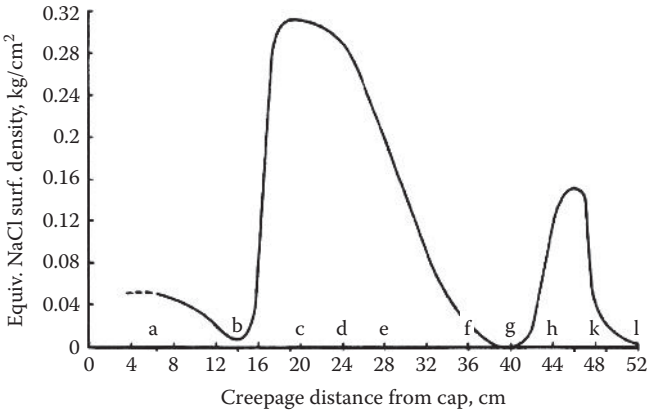


FIGURE 10.14 Distribution of ESDD along a path on the surface of an antifog disc—type D. (From Rizk, F.A.M. et al., *IEEE Trans. Power Appar. Syst*., 94(5), 1170, September/October 1975.)

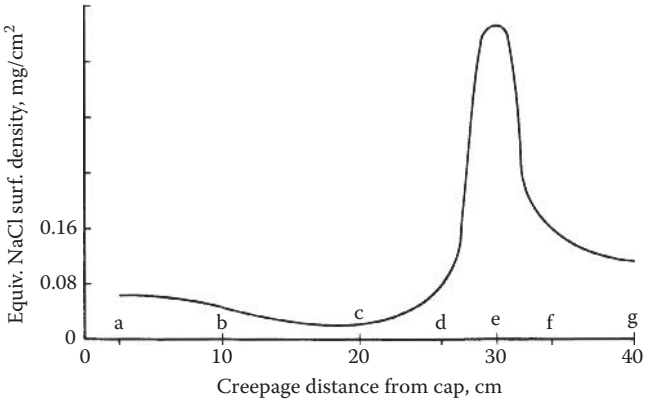


FIGURE 10.15 Distribution of ESDD on the surface of aerodynamic type B insulator. Cap: point a; pin: point g. (From Rizk, F.A.M. et al., *IEEE Trans. Power Appar. Syst*., 94(5), 1170, September/October 1975.)

10.3.3.5 Effect of Operating Voltage

As previously mentioned in Section 10.3.3.1, the operating voltage effect on pollution layer buildup will manifest itself in the electric force $\mathbf{F}_{e1}$ exerted on charged particles and the dielectrophoretic force $\mathbf{F}_{e2}$. Estimates in Hall and Mauldin (1981) show that the force $\mathbf{F}_{e2}$ is small compared to gravitational and wind forces even for the not particularly high wind speed of 0.8 m/s (2.9 km/h). This is in agreement with long-standing field experience, which shows that, for ac lines, the operating voltage has little influence on pollution layer buildup. This in turn led to building of exposure tests stands sometimes with unenergized insulators to collect pollution deposit data for ac transmission line design (Akbar et al., 1995).

On the other hand, the effect of the force $\mathbf{F}_e$ on charged particles, associated with dc energization, is more complex. This effect can be assessed by comparison of severity with dc and ac energization. Such review was undertaken by Schneider (1993) and presented in Figure 10.16. It is shown that for moderately polluted zones, with ESDD $\sim$ 0.01 mg/cm^2, dc energization could lead to intensification of pollution layer buildup by a factor of 8. For zones with extremely high severity, for example, of ESDD $>$ 0.1 mg/cm^2 on the other hand, dc energization has practically no effect on layer buildup. This can be interpreted that for low pollution severity zones, the wind and gravitational effects are relatively small, which makes the effect of particle charging very significant. On the other hand, where wind and gravitational forces are large, dumping excessive pollution deposit on the insulator, the relative value of $\mathbf{F}_e$, becomes insignificant.

10.3.3.6 Effect of Distance from Pollution Source

Experience has shown that transmission line insulators in the vicinity of the seacoast may be exposed to severe marine pollution (Houlgate et al., 1982). However, this appears to be dependent on the direction of the prevailing wind. If the prevailing wind is from the sea into the land, the situation is most severe near the seacoast but improves with distance as we move inland.

Figure 10.17 shows the relationship between ESDD on standard porcelain disc insulators and distance from the seacoast, as reported from a Japanese investigation (Kimoto et al., 1972). There is substantial scatter in the ESDD results, but the definite trend is for reduction of severity with longer distance from the coast. It appears from Figure 10.17 that it takes a distance of about 50 km from the coast for the ESDD to stabilize to the inland level. This pollution buildup was attributed to calm wind, meaning that it was not caused by typhoons, but unfortunately the wind speed range involved was not reported (Kimoto et al., 1972). From the analysis of forces acting on airborne deposit particles given in Section 10.3.3.1, it is clear

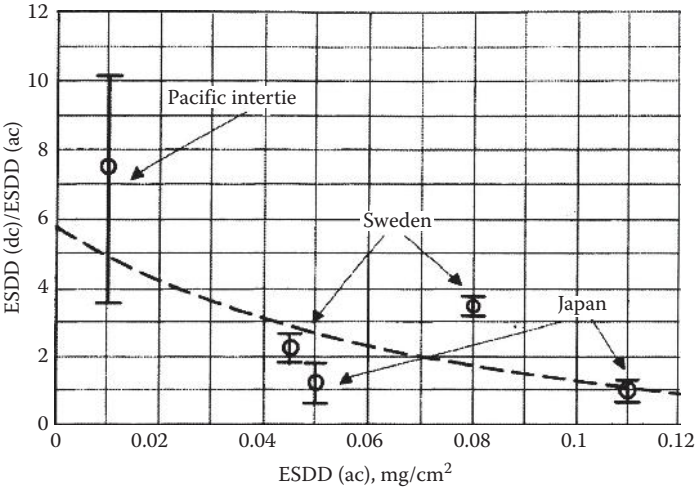


FIGURE 10.16 Ratio of ESDD collected on insulators energized with dc to that collected on ac—energized insulators. (From Schneider, H.M., *Insulation for HVDC Transmission Lines*. EPRI HVDC Reference Book, Chapter 5, September 1993.)

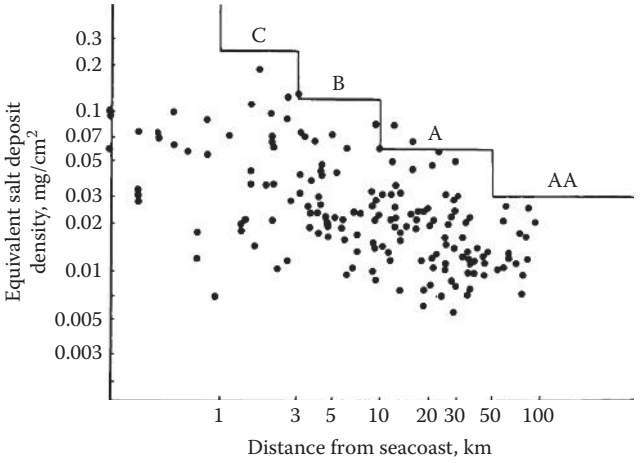


FIGURE 10.17 Variation of ESDD on insulators with distance from the seacoast. (From Kimoto, I. et al., *IEEE Trans. Power Appar. Syst*., 91, 317, January 1972.)

that the distance affected by proximity to the seacoast will depend on wind speed and also on the particle size. Such distance will generally increase; the higher the wind speed, and the smaller the size of the pollutants. In this respect, salt fog particles will travel longer distance from the sea than heavier dust particles characterizing, for example, a combined marine and desert condition since the terminal gravitational terminal speed, Equation 10.3, is proportional to r^2. A lower prevailing wind speed will have the same effect.

Figure 10.18 (Kimoto et al., 1972) shows variation of ESDD on standard cap and pin discs, with distance from an industrial pollution source emitting soot and smoke. It is shown that pollution severity stabilizes at distance from the source below 5 km, which is an order of magnitude shorter than corresponding distances from the seacoast reported earlier. This may be attributed to the fact that for a point source, the pollutant content in air decays with approximately the square of the distance from the source.

10.3.3.7 Effect of Wind Speed

As mentioned previously, the effect of wind on insulator pollution buildup is quite complex acting both as the medium carrying airborne deposit and as a self-cleaning agent. Let us assume that the salt deposit density, ESDD mg/cm^2, for any insulator design, is a function of the salt density per unit volume in air, D_s, g/m^3; mean wind speed v_w, m/s; and exposure time t:

$$\text{ESDD} = F\left(D_s, v_w, t\right) \tag{10.10}$$

By dimensional analysis (Langhaar, 1951), intuition yields one dimensionless variable so that

$$Y\left(\frac{\text{ESDD}}{D_s v_w t}\right) = 0 \tag{10.11}$$

or

$$\text{ESDD} = K_s D_s \cdot v_w \cdot t \tag{10.12}$$

where K_s is a constant depending on insulator profile, which can only be determined by experiment.

From (10.12), if the volume density of salt in air is independent of v_w, then ESDD will be proportional to both mean wind speed and exposure time t. An investigation of marine pollution in Japan (Taniguchi et al., 1979), however, has shown that D_s is proportional to the square of mean wind speed so that in such situation:

$$\text{ESDD} = K_s v_w^3 \, t \tag{10.13}$$

The trend expressed by (10.13) is shown in Figure 10.19 (Taniguchi et al., 1979).

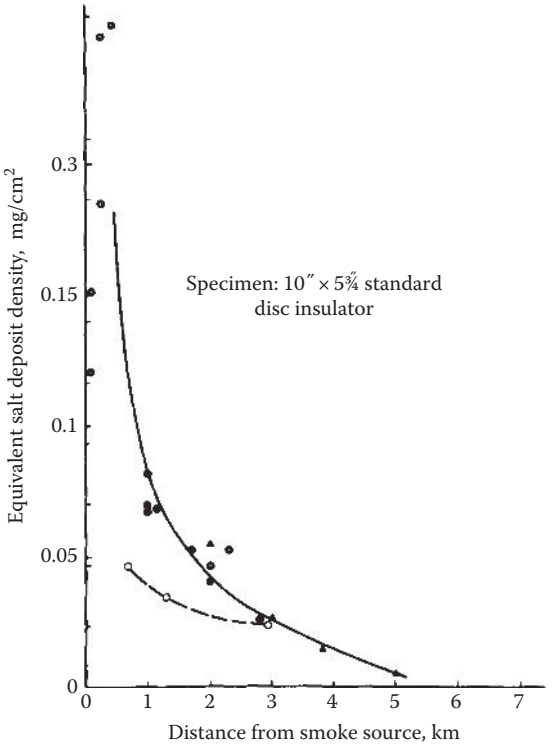


FIGURE 10.18 Example of relation of ESDD to the distance from smoke source under industrial pollution measured at various places. (From Kimoto, I. et al., *IEEE Trans. Power Appar. Syst*., 91, 317, January 1972.)

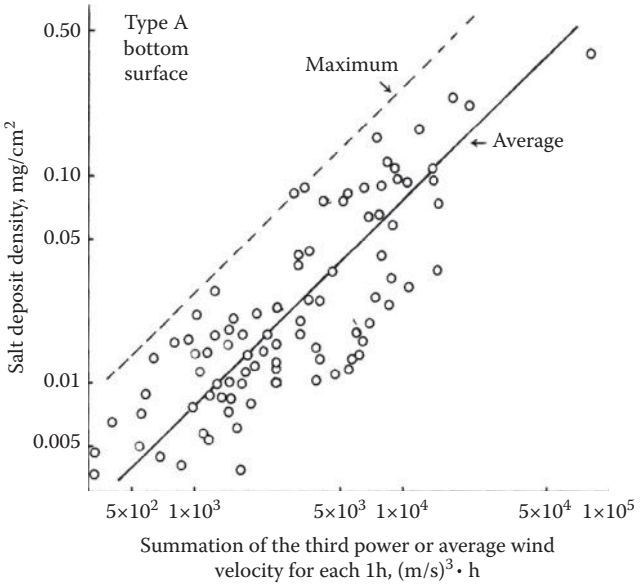


FIGURE 10.19 Variation of salt deposit density with average wind speed in marine environment. (From Taniguchi, Y. et al., *IEEE Trans. Power Appar. Syst*., 98(1), 239, January/February 1979.)

Unfortunately, no similar field investigation of the dependence of ESDD on v_w was reported for other environmental conditions nor was such investigation undertaken in wind tunnel experiments (Hall and Mauldin, 1981). The effect of wind speed on wetting and insulator flashover will be treated in other sections.

10.3.3.8 Insulator Surface Wetting

10.3.3.8.1 Ceramic Insulator

As previously mentioned, wetting of the contamination layer is a prerequisite for flashover to occur. The most significant mechanisms for wetting of a predeposited layer include

- Adsorption of water from humid air due to the hygroscopic nature of salt contaminants
- Condensation by contact cooling leading to dew formation
- Precipitation in the form of drizzle

A systematic investigation *of wetting due* to the two first earlier mechanisms was reported in Rizk et al. (1975). Hygroscopic wetting was produced by exposing a contamination layer deposited on a glass plate to humidity in a special chamber. Constant humidity was maintained in the chamber by using different saturated aqueous solutions. A sample of the results is presented in Figure 10.20 showing variation of the specific layer conductivity of two contamination layers with exposure time in a constant relative humidity of 96%, at an ambient temperature of 20°C. The 40 and 72 μS values correspond to saturation values of these two layers when exposed for sufficient time to 100% relative humidity at 20°C. It is shown that the specific layer conductivity first increases rapidly, followed by a much slower rate to reach saturation. It is concluded that, when the contamination layer temperature is in equilibrium with the ambient atmosphere, hygroscopic absorption is a slow process with maximum surface conductivity reached in 1 h or more.

Figure 10.21 (Rizk et al., 1975) shows variation of the final surface layer conductivity, for the two layers mentioned earlier, with ambient relative humidity in the range of 67%–100%. It is shown that adsorption will lead to significant specific layer conductivity if the ambient humidity exceeds 85%.

Figure 10.22 (Rizk et al., 1975) shows a typical daily variation of ambient and insulator surface temperature of cap and pin and long-rod porcelain insulators in a desert environment. It is shown that in the early morning hours, insulator temperature can drop below the ambient temperature due to thermal inertia of the insulator. Although such temperature difference is around 2°C, this will be sufficient to cause dew formation on the insulator surface for ambient humidity below 90%, as shown in leakage current measurements of Figure 10.23 (Rizk et al., 1975). Here, a 2.2°C undercooling leads to very significant increase in the leakage current, starting with ambient relative humidity of 80%. Dew point was reached on the insulator surface at a relative humidity of 87.5% and saturation of the leakage current was attained at 92% of relative humidity. It is concluded that, in desert environment, undercooling of insulators in the early morning hours can lead to severe wetting of the pollution layer by dew formation, constituting a serious hazard for insulator flashover.

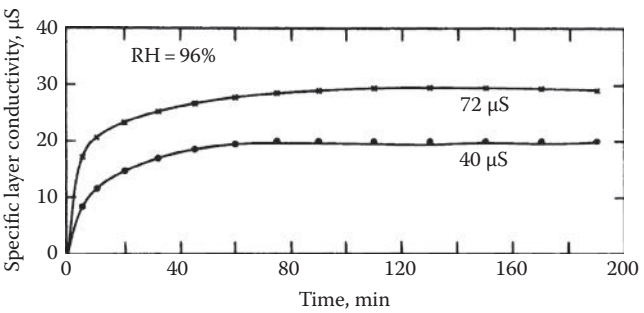


FIGURE 10.20 Response of natural desert contamination layers to ambient relative humidity at 20°C, relative humidity 96%. (From Rizk, F.A.M. et al., *IEEE Trans. Power Appar. Syst*., 94(5), 1170, September/October 1975.)

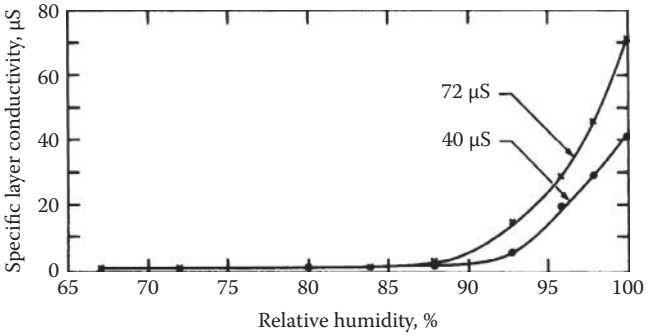


FIGURE 10.21 Variation of ultimate specific layer conductivity with ambient relative humidity at 20°C. (From Rizk, F.A.M. et al., *IEEE Trans. Power Appar. Syst*., 94(5), 1170, September/October 1975.)

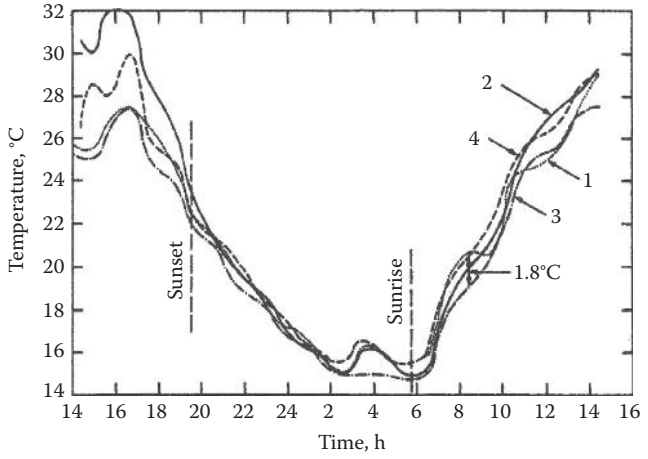


FIGURE 10.22 Typical daily variation of ambient and insulator temperature in the desert. 1—ambient temperature; 2—shed of disc insulator; 3—stem of 75/14 long rod; 4—shed of 75/14 long rod. (From Rizk, F.A.M. et al., *IEEE Trans. Power Appar. Syst*., 94(5), 1170, September/October 1975.)

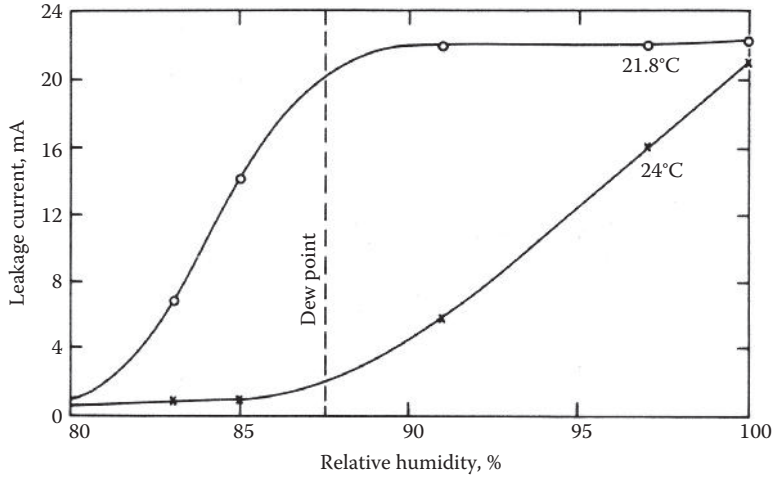


FIGURE 10.23 Variation of leakage current with relative humidity with and without under cooling. (From Rizk, F.A.M. et al. Laboratory and field experience with EHV transmission line experience in the desert. *IEEE Trans*., Vol. PAS-94, No. 5, pp. 1770–1776, September/ October 1975.)

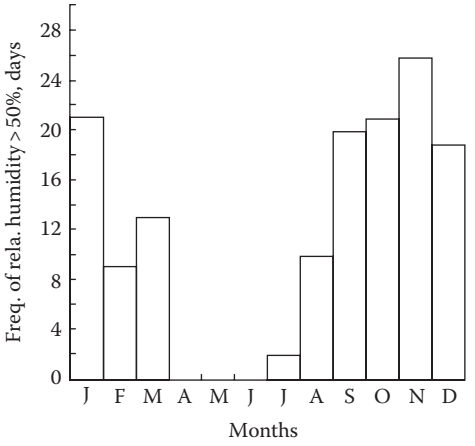


FIGURE 10.24 Days with relative humidity exceeding 90% at El-Minya, Egypt. (From El-Koshairy, M.A.B. and Rizk, F.A.M., Performance of EHV transmission line insulators under desert pollution conditions, CIGRE, Paper No. 33-05, 1970.)

Insulator wetting in a clean fog chamber used for high-voltage testing of polluted insulators was analyzed by Karady (1975). It was shown that for cold fog, the major wetting factor is the collision of water drops with the insulator surface. For steam fog, on the other hand, condensation is the major factor. In case of warm fog, both condensation and water drop collision play a role in the wetting process. It was also shown that the condensation becomes more effective the lower the ratio between the insulator surface area and insulator thermal capacity (Karady, 1975).

Drizzle also can constitute a hazardous wetting agent for contaminated insulators. Typical parameters of drizzle (Humphreys, 1964) include a precipitation rate of 0.25 mm/h, yielding 0.4 mg/cm^2/min, a droplet radius of 100 μm, and water content in air of 90 mg/m^3. It may be interesting to compare these drizzle parameters with corresponding parameters in a fog chamber described in Karady (1975).

The following are noted:

- The drop size in drizzle is an order of magnitude larger than that of condensation water drops in the fog chamber.
- The drizzle precipitation rate of 0.4 mg/cm^2/min is smaller than the typical rate of 1 mg/cm^2/min in the fog chamber (Karady, 1975).
- The water content of typically 40 g/m^3 in the fog chamber (Naito and Nagasaka, 1975) is three orders of magnitude higher than the corresponding value of 90 mg/m^3 in atmospheric air associated with drizzle.

It should be noted that the effect of dew formation on polluted insulators is by no means confined to desert conditions and has been earlier accounted for in Europe (Wittenzellner, 1962).

It can be understood from the earlier texts that the frequency of occurrence of days with 90% relative humidity can be used as a measure of wetting events on polluted insulators (El-Koshairy and Rizk, 1970). Figure 10.24 shows a histogram of days of relative humidity exceeding 90% at El-Minya, Egypt. It should be noted that pollution flashover is a slow process and, accordingly, it is not sufficient that high-humidity conditions occur but that such conditions last for 1–2 h to constitute a serious hazard (Rizk et al., 1975).

10.3.3.8.2 Nonceramic Insulators

It is obvious that the wetting agents of fog, dew, drizzle, etc., will be the same for polymeric insulators as for porcelain and glass. The justification of treating this in a separate section, however, is the different response of the polymeric surface to wetting. When a clean high-energy surface like porcelain or glass is exposed to sufficient wetting, it forms a continuous layer of water (Rizk, 1974; Rizk and Hyltén-Cavallius, 1974). A polymeric surface, on the other hand, forms isolated drops manifesting a property termed hydrophobicity (Vlastos and Sherif, 1990). One index for evaluating hydrophobicity is

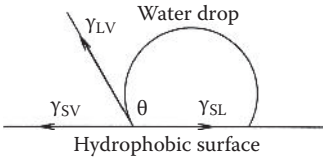


FIGURE 10.25 Schematic diagram of a water drop on a hydrophobic surface.

the contact angle θ at the triple point between a water drop, a solid substrate (polymer), and vapor (air) in Figure 10.25. The contact angle is determined by the balance of surface tension γ_{LV} (liquid/vapor), γ_{SL} (solid/liquid), and γ_{SV} (solid/vapor) as expressed by the Young–Dupré equation (Adamson, 1967):

$$g_{LV}\cos q = g_{SV} - g_{SL} \tag{10.14}$$

which is valid for a perfectly smooth surface.

Ultimately, for full wetting as $\theta \to 180°$, (10.14) yields

$$g_{LV} + g_{SV} = g_{SL} \tag{10.15}$$

The practical problem with (10.14) is that both γ_{SV} and γ_{SL} cannot be measured or calculated. The contact angle θ can be measured by

- Direct photography of small droplets (~10 μm) placed on a horizontal substrate (Vlastos and Sherif, 1990)
- Direct photographic determination as the difference between advancing and receding contact angles on an inclined plane substrate (Pigini and Tomba, 1993)
- Direct photography of the meniscus rise *h* (Morcos and Rizk, 1977) at a substrate plate or cylindrical solid (polymer) partially immersed in a liquid (water) expressed by

$$\sin q = 1 - \frac{rg}{g_{LV}}h^2 \tag{10.16}$$

where
ρ is the liquid density
g is the acceleration of gravity

- Practical evaluation of hydrophobicity by visual comparison of the pattern of water drop formation on an insulating surface to a given set of seven classes HC1 to HC7 (STRI, 1992)

It is presently understood that hydrophobicity is related to the presence of a layer of low molecular weight (LMW) silicon oil on the insulator surface (Chang and Gorur, 1994). Hydrophobicity is lost by corona and dry-band arcing but can be recovered as the LMW oil diffuses back to the surface from the polymer bulk (Chang and Gorur, 1994). It is clear that in the field at least temporary loss of hydrophobicity could also take place due to heavy rain, sandstorms, etc. It is also clear that if hydrophobicity is lost, wetting of polymeric insulators becomes similar to wetting of ceramic insulators. In this respect, it may be mentioned that in artificial pollution testing, several methods are used to *condition* the polymeric insulator in order to facilitate application of the wet contaminant. In effect, conditioning induces a temporary loss of hydrophobicity.

10.3.3.9 Pollution Flashover Mechanism

10.3.3.9.1 General Description

Excellent descriptions of the different phases involved in the pollution flashover mechanism, with special reference to ceramic insulators, were presented by Nasser (1962, 1972). This starts with a conducting layer already formed on the insulator surface and accounts for the complex interaction between

TABLE 10.6

Phases of Contamination Flashover Based on Nasser's Results

Phase	Layer	Discharge Form	Leakage Current
Heating of surface layer	Conductivity increases	None	Increases
Drying of surface layer	Conductivity decreases locally	None	Decreases
Dry zone formation	Lateral drying locally	None	Stops
Onset of dry zone arcing	Conductivity decreases	Bright laterally moving arcs	Intermittent surges
Glow and streamer discharges	Conductivity increases	Hardly visible discharges, radio noise	Very small and pulsating
Slow arc growth	Dry zones enlarged	Merging of arcs and slow arc growth	Increases slowly, intermittent
Fast arc growth	No further drying	Arc spans half of the insulator	Continuous, rapidly increasing
Flashover	Partly dried out	Arc	Short-circuit current

Source: Nasser, E., *ETZ-A*, 93(6), 321, 1972.

such layer and the applied voltage. Under critical conditions, such interaction will lead to full flashover. Table 10.6 is based on Nasser (1972) and summarizes the different phases, state of the contamination layer, form of electrical discharges, and corresponding leakage current.

In the more practical situation, layer formation and wetting take place under voltage, but most of the phases described in Table 10.6 remain valid, with differences only in the initial phases before maximum layer conductivity is reached.

In another publication (Nasser, 1968), Nasser described a systematic investigation involving synchronized photographic and oscillographic recording of the glow, streamer, and arc discharges on polluted surfaces.

There are some fundamental differences in the phases of pollution flashover of silicone rubber insulators. Firstly, it should be noted that the pollutant will be embedded in the LMW silicon oil on the insulator surface. The second point is that the initial wetting mostly comprises isolated water drops on the surface of the energized insulator. Karady et al. (1995) suggested a sequence of events that may lead to flashover of silicone rubber insulators:

- The first phase involves migration of the pollutant to the water droplets or migration of water into the dry pollutant.
- In both previous cases, a continuous layer is formed and, through the flow of a relatively small leakage current, ohmic heating occurs.
- As wetting continues, the surface density of the droplets increases and the interdroplet distance is reduced.
- Also under the effect of the electric field, droplets may elongate forming conducting filaments.
- Filaments intensify the electric field at their tips and initiate spot discharges.
- Discharges lead to loss of the LMW polymer layer and results in loss of hydrophobicity.
- Wet regions start to form as a result of local hydrophobicity loss.
- Formation of the wet regions and elongation of the filaments create a path for arc propagation similar to the ceramic insulators.

10.3.3.9.2 Pollution Layer Resistance

Consider an insulator with a wet pollution layer having a volume resistivity ρ, in Ω · m, and layer height *h*; the surface conductivity χ_s will then be given by

$$\chi_s = \frac{h}{\rho} \tag{10.17}$$

The layer resistance per unit leakage path length $r(s)$ will be expressed as

$$r(s) = \frac{1}{\pi D(s)\sigma_s} \tag{10.18}$$

where $D(s)$ is the insulator diameter at a leakage distance S from one end. The total pollution resistance R_p can be expressed as

$$R_p = \int_0^L \frac{ds}{\pi D(s)\sigma_s} \tag{10.19}$$

where L is the total leakage path.

If χ_s is assumed constant along the leakage path,

$$R_p = \frac{1}{\sigma_s} \int_0^L \frac{ds}{\pi D(s)} \tag{10.20}$$

The integral in (10.20) is a geometric parameter termed the insulator form factor f with

$$f = \int_0^L \frac{ds}{\pi D(s)} \tag{10.21}$$

which can also be expressed as

$$f = \frac{L}{\pi D_{av}} \tag{10.22}$$

where D_{av} is the insulator average diameter.

It is clear that the form factor is proportional to the leakage path and inversely proportional to the average diameter. From (10.20) and (10.21), we get

$$R_p = \frac{f}{\sigma_s} \tag{10.23}$$

relating the total pollution resistance to the form factor and surface conductivity.

When the pollution layer is characterized by the ESDD, mg/cm^2, it would be helpful to correlate ESDD with the specific layer conductivity χ_s. Such equivalence can only be established on the basis of equality of the insulator withstand voltage under a defined test technique.

It should be noted that the electrical conductivity of an electrolytic solution increases substantially with temperature so that at 100°C, it is roughly three times higher than at 20°C.

10.3.3.9.3 Slow Arc Growth

As indicated in Table 10.6, heating of the surface layer due to leakage current flow results in increased conductivity. Energy dissipation is obviously more intense in regions of smallest diameter. As boiling temperature is reached in those reasons, intense evaporation occurs resulting in substantial reduction in the layer thickness, leading to dry-band formation. Modeling of dry-band formation and growth is reported in Loberg (1971) and Raghuveer and Kuffel (1974). Dry-band arcing is a prerequisite for pollution flashover under service voltage. However, under field conditions, it normally takes place at leakage current levels substantially lower than the critical levels required for flashover. In Table 10.6, thermal growth of dry-band arcs is referred to as slow, resulting in merging of arcs and characterized by slow increase of intermittent leakage current. Only when this phase is followed by fast arc growth can a significant risk of flashover be expected.

10.3.3.9.4 Fast Arc Growth

The mechanism of fast arc growth over the surface of a polluted insulator has been the subject of several investigations. It may be helpful to start reviewing the different types of forces that could be exerted on an electric arc. We will then reflect on which among those forces could be a plausible cause for arc propagation:

- Thermal buoyancy forces are particularly relevant to horizontal arcs, driving the arc upward, making the actual arc length significantly longer than the shortest distance between terminal electrodes. It would be difficult, however, to see how buoyancy forces could be responsible for arc propagation on a contaminated insulator surface.
- Magnetic (Lorentz) forces can in principle displace electric arcs. However, the low levels of leakage current, in the range of a fraction of an ampere to a few amps, make such forces unlikely to play a significant role in arc propagation over a polluted insulator surface.
- Electrostatic forces have been proposed as responsible for the fast arc growth phase (Nasser, 1972). This will be discussed further in the following. It should be mentioned, however, that the arc column is quasi-neutral, with practically equal density of electrons and positive ions. Electrostatic forces, therefore, can only act on the arc cathode or anode regions where a net charge is available (Engel, 1955). A net electrostatic force on such charge would drag the arc cathode or anode region towards the counter electrode over the polluted insulator surface.
- Ionization in air in the vicinity of the arc root, although not constituting a mechanical force acting on the arc, has been suggested as a viable mechanism for arc extension (Obenaus et al., 1965; Wilkins and Baghdadi, 1971).

Hampton (1964) conducted flashover experiments on a uniform water column with practically constant resistance per unit length. The criterion for arc motion was formulated as

$$E_a < E_p \tag{10.24}$$

where

E_a is the (mean) arc voltage gradient
E_p is the (mean) voltage gradient in the pollution layer

Hesketh (1967) suggested that an arc burning in series with a wet pollution layer will adjust itself, without specifying the mechanism, to draw maximum current from the supply. The criterion for arc propagation then reads

$$\frac{di}{dx} > 0 \tag{10.25}$$

where

i is the arc current
x is the arc length

Consider a source with voltage U and internal resistance R_s, applied to a polluted insulator. The circuit equation will be

$$U = (R_s + R_p)i + xE_a \tag{10.26}$$

where

x is the arc length
E_a is the arc voltage gradient
R_p is the pollution resistance
i is the leakage current

Differentiating (10.26) with respect to x, Hesketh used (10.25) to obtain

$$\frac{E_a + i(dR_p/dx)}{x(dE_a/di) + R_p + R_s} < 0 \tag{10.27}$$

If the denominator in (10.27) is positive, the numerator results in

$$E_a < -i\frac{dR_p}{dx} \tag{10.28}$$

Since $E_p(x) = -i(dR_p/dx)$, Hesketh's criterion becomes

$$E_a < E_p(x) \tag{10.29}$$

The difference from (10.24) is that (10.29) applies to the case of a nonuniform pollution resistance and expresses a local condition for arc propagation.

10.3.3.9.5 Pollution Resistance during Arc Growth

Consider a polluted insulator energized with a voltage U. An arc of length x is burning in series with a layer resistance R_{px}. The simple circuit equation will show that the value and distribution of R_{px} will be determining both the arc current i and the pollution voltage gradient E_p, which, according to the earlier criterion, will decide whether the criterion for arc propagation will be satisfied. Furthermore, as will be shown in the following, R_{px} will also be decisive for determining the critical voltage U_c needed to maintain the arc of any length on the insulator surface. Knowing R_{px} is therefore essential for modeling the flashover process. Exact knowledge of the value and distribution of the dynamic layer resistance R_{px} during the arc propagation is difficult due to the following reasons:

- Even with a uniform pollution surface conductivity or salt deposit density, the insulator geometry makes the distribution of R_{px} quite complex (IEC Standard 60507, 1991).
- Under field conditions, the surface conductivity is usually far from uniform (Rizk et al., 1975) with at least vastly different values on the upper and bottom insulator surfaces.
- The arc itself contributes to the complexity of the situation: firstly, through constriction at the arc foot points, and, secondly, through the resulting thermal effects influencing the layer conductivity.
- For insulators with large diameter, particularly supporting columns, parallel arcing may persist resulting in a complex pattern.

It is therefore understandable that, for modeling of the flashover process, several models were put forward to represent the pollution surface resistance. These models differ widely in their complexity. Even with much simplification, such models contribute to our basic understanding of the underlying phenomena and interpretation of test results.

The simplest model was suggested by Neumärker (1959), with a constant pollution resistance r_p per unit leakage length yielding R_{px} as

$$R_{px} = r_p(L - x) \tag{10.30}$$

where

L is the leakage path length
x the arc length

From a practical point of view, r_p can be taken as the average pollution resistance per unit length:

$$\overline{r_p} = \frac{R_p}{L} = \frac{f}{\sigma_s L} \tag{10.31}$$

where

R_p is the total pollution resistance for the length L
χ_s is the layer surface conductivity, assumed constant
f is the insulator form factor

Böhme and Obenaus (1966) considered two series resistive layers characterizing the stem and shed zones of a long-rod insulator with leakage lengths l_1 and l_2 and corresponding to mean surface resistances per unit leakage length, $\overline{r_{p1}}$ and $\overline{r_{p2}}$, respectively.

Here the total leakage path $L = l_1 + l_2$. The total pollution layer resistance R_p is given by

$$R_p = \overline{r_{p1}}\,l_1 + \overline{r_{p2}}\,l_2 \tag{10.32}$$

If arcs with total length x are burning on the stem region, the series layer resistance R_{px} will be expressed as

$$R_{px} = \overline{r_{p1}}\,(l_1 - x) + \overline{r_{p2}}\,l_2 \tag{10.33}$$

For a circular insulating disc model, using the symbols of this chapter, Woodson and McElroy reported that pollution resistance R_{px} in series with an arc of length x may be expressed as

$$R_{px} = \frac{\text{const}}{c_s}(L - x)^m \tag{10.34}$$

with the exponent $m = 1.4$.

A possible reformulation of (10.34) suggested is

$$R_{px} = R_p\left(1 - \frac{x}{L}\right)^m \tag{10.35}$$

where R_p is the total pollution resistance as $x \to 0$.

Similarly, Claverie (1971) made measurements on a long-rod insulator and presented a relationship between R/ρ and the length x, as shown in Figure 10.26. Here, R is what has been designated R_{px} earlier and ρ is the volume resistivity of the liquid polluted of height h. As indicated in (10.17), $\chi_s = h/\rho$. Here again, the variation of R_{px} with x may be approximated as

$$R_{px} = R_p\left(1 - \frac{x}{L}\right)^m \tag{10.36}$$

where

R_p is the total pollution resistance

m is a constant

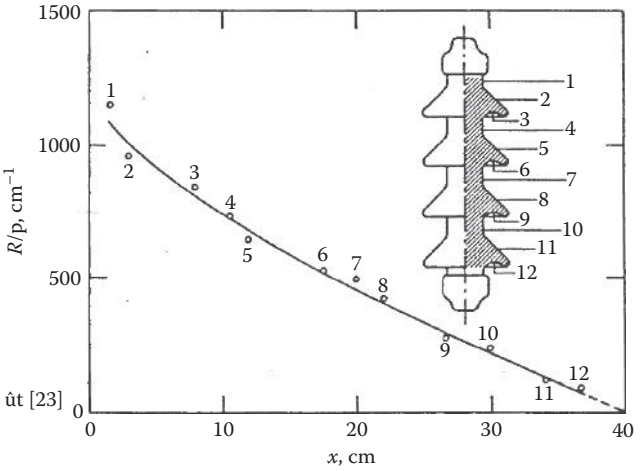


FIGURE 10.26 Distribution of pollution surface resistance of a long-rod insulator. (From Claverie, *IEEE Trans. Power Appar. Syst*., 90(4), 1902, July/August 1971.)

It should be noted that in Woodson and McElroy (1970) and Claverie (1971), the resistance distribution and m value were necessarily determined using a metallic electrode, not an arc, so that the results may not be fully representative. In case of a cap and pin insulator unit, Claverie (1971) found that, due to under ribs, the variation of R_{px} with x is quite complex. It should be noted, however, that for long insulator strings during the phase of fast arc growth, the arc often bridges several insulator units, and the series pollution resistance R_{px} also refers to several discs. Under these circumstances, the variation of R_{px} with x will not be disturbed by the under ribs to the same extent as measurements on a single unit tend to indicate.

The effect of constriction of leakage current at the arc foot point was explicitly analyzed by Näcke (1969) and Wilkins (1969). Näcke (1969) considered a rectangular pollution strip of length x_p and width b with arc foot points represented by two semicircles of radius r_b.

For a narrow strip, the pollution layer resistance R_{px} can be expressed as

$$R_{px} = \frac{1}{\pi c_s} + \bar{r}_p x_p + \frac{2}{\pi c_s} \ln\left(\frac{b}{2\pi r_d}\right) \tag{10.37}$$

According to Näcke's analysis (Näcke, 1969), the first term in (10.37) refers to the internal resistance at the semicircular arc foot points, while the two other terms are referred to as the external resistance. For a wide strip, Näcke's results (Näcke, 1969) could be expressed as

$$R_{px} = \frac{1}{\pi c_s} + \frac{2}{\pi c_s}\left(0.3 + \ln\frac{x_p}{r_d}\right) \tag{10.37a}$$

From (10.37), it is clear that the wide strip pollution resistance is much less dependent on the strip length x_p than for a narrow strip (10.36).

Wilkins (1969) considered circular arc foot points and obtained results that are very similar to Näcke's. For a narrow strip, Wilkins obtained the following:

$$R_{px} = \bar{r}_p (L - x) + \frac{1}{\pi c_s} \ln\left(\frac{b}{2\pi r_d}\right) \tag{10.38}$$

The major difference with (10.37) due to Näcke (1969) is the absence of the internal resistance term at the arc foot points.

Substituting for $c_s = 1/(b\bar{r}_p)$, (10.38) becomes

$$R_{px} = \bar{r}_p (L - x) + \frac{b\bar{r}_p}{\pi} \ln\left(\frac{b}{2\pi r_d}\right) \tag{10.39}$$

To estimate the relative values of the two resistance terms on the right-hand side of (10.39), we will consider a numerical example. Consider a simple cylindrical insulator with length 100 cm and diameter 5 cm (b = 15.7 cm), with a uniform pollution layer of χ_s = 40 μS. The arc diameter is assumed as 4 mm (r_d = 2 mm) and the arc length 50 cm.

$\bar{r}_p$ is obtained at 1592 Ω/cm. Substituting in (10.39),

$$\bar{r}_p (L - x) = 79.6 \text{ k}\Omega$$

and

$$\frac{b\bar{r}_p}{\pi} \ln\left(\frac{b}{2\pi r_d}\right) = 20.1 \text{ k}\Omega$$

The example shows that the increase in the pollution layer resistance due to constriction at the arc roots can be quite significant. An anode and cathode voltage drop of about 800 kV per arc could be added (Wilkins, 1969). This effect could be substantial if it is assumed that many arcs are simultaneously burning in series.

It should be noted that, during the dry-band phase, many arcs will be burning in series. Gradually, however, as the critical phase of fast arc propagation is reached, the number of series burning arcs drops substantially. Another point is that the region of high current density in the vicinity of the arc foot

point will necessarily have a higher temperature and, accordingly, increased electrical conductivity that will tend to suppress the earlier effect.

10.3.3.9.6 Modeling of Flashover Characteristics

10.3.3.9.6.1 DC Model There are two conditions necessary for pollution flashover to occur: a mechanism for arc growth and sufficient applied voltage to maintain the arc in series with the pollution layer resistance. The first condition was expressed by (10.24). Consider the simple dc circuit of an arc of length x and current i burning in series with a pollution surface resistance R_{px} under an applied voltage U as in (10.26):

$$U(x,i) = xE_a + iR_{px} \tag{10.40}$$

Let

$$E_a = \frac{N_0}{i^n}$$

and

$$R_{px} = R_p \left(F\left(\frac{x}{L}\right)\right) \tag{10.41}$$

with $F(0) = 1$ and $F(1) = 0$.

Substituting in (10.40),

$$U(x,i) = \frac{xN_0}{i^n} + i\left(R_p F\left(\frac{x}{L}\right)\right) \tag{10.40a}$$

To maximize U, the following conditions must be satisfied:

$$\frac{dU}{dx} = 0 = \frac{N_0}{i^n} + iR_p\left(\frac{1}{L}F'\left(\frac{x}{L}\right)\right) \tag{10.42}$$

$$\frac{dU}{di} = 0 = -n\frac{xN_0}{i^{n+1}} + R_p\left(F\left(\frac{x}{L}\right)\right) \tag{10.43}$$

Note that from (10.41)

$$\frac{dR_{px}}{dx} = -r_{px} = \frac{R_p}{L}\left(F'\left(\frac{x}{L}\right)\right) \tag{10.44}$$

where r_{px} is the local pollution resistance per unit length about to be bridged by the arc of length x. It follows that (10.42) for critical conditions can be expressed as

$$\frac{N_o}{i_c^n} - r_{px}i_c = 0$$

that is,

$$\frac{N_o}{i_c^n} = r_{px}i_c \tag{10.45}$$

or

$$E_a = E_p$$

which agrees with the criterion for arc motion (10.24).

Equations 10.42 and 10.43 should be solved to obtain the critical arc length x_c and critical leakage current i_c from which the critical flashover voltage U_c is determined.

Substituting from Equation 10.42 into Equation 10.43,

$$x_c = -\frac{L\,F\left(x_c/L\right)}{n\,F'\left(x_c/L\right)} \tag{10.46}$$

For the simplest case of a uniform pollution resistance r_p per unit leakage length,

$$F\left(\frac{x}{L}\right) = 1 - \frac{x}{L}$$

$$F'\left(\frac{x}{L}\right) = -1 \tag{10.47}$$

Substituting in (10.46),

$$x_c = \frac{L}{n}\left(1 - \frac{x_c}{L}\right)$$

or

$$x_c = \frac{L}{n+1} \tag{10.48}$$

With $n = 0.76$ (Wilkins, 1969),

$$x_c = 0.57L \tag{10.49}$$

which means that the arc has to span more than half of the leakage path for a flashover to occur.

Substituting for $F'(x/L) = -1$ in Equation 10.42, we get

$$\frac{N_o}{i_c^n} = i_c r_p \tag{10.50}$$

which is exactly the condition for arc motion (10.24), yielding

$$i_c = \left(\frac{N_o}{r_p}\right)^{1/(n+1)} \tag{10.51}$$

It is interesting to note that the critical current is independent of the leakage path.

Substituting for R_{px}, x_c, and i_c into (10.40), an expression for the critical flashover voltage U_c is obtained as

$$U_c = N_o^{1/(n+1)}\, r_p^{n/(n+1)}\, L \tag{10.52}$$

as previously obtained by Neumärker (1959).

Consider now the more general distribution of pollution layer resistance expressed by (10.35)

$$F\left(\frac{x}{L}\right) = \left(1 - \frac{x}{L}\right)^m$$

$$F'\left(\frac{x}{L}\right) = -m\left(1 - \frac{x}{L}\right)^{m-1} \tag{10.53}$$

which, when substituted in (10.46), gives

$$x_c = \frac{L - x_c}{n\,m} \quad \text{or} \quad x_c = \frac{L}{1 + n\,m} \tag{10.54}$$

As a numerical example, take as before $n = 0.76$ and $m = 1.4$:

$$x_c = 0.48\,L$$

which is slightly less than the critical arc length of the uniform pollution resistance case (10.49) but still close to half of the leakage path.

Substituting for x_c in (10.45), an expression for the critical current i_c is obtained as

$$i_c = K_i \left(\frac{N_o}{r_p}\right)^{1/(n+1)} \tag{10.55}$$

where

$$K_i = \frac{1}{m^{m/(n+1)}} \left(\frac{1+n}{n}m\right)^{(m-1)/(n+1)} \tag{10.56}$$

so that i_c differs from the uniform pollution case by the constant K_i. It is obvious that the uniform pollution case follows by letting $m = 1$, which yields $K = 1$.

As a numerical example, with $N = 0.76$ and $m = 1.4$, the constant K_i is obtained at 0.96 so that the critical leakage current has been reduced insignificantly by the generalized distribution of pollution resistance (10.35).

Substituting for x_c and i_c in (10.40), the critical voltage U_c is obtained at

$$U_c = K_u N_o^{1/(n+1)} r_p^{-n/(n+1)} L \tag{10.57}$$

where K_u is a constant expressed as

$$K_u = \frac{1}{(1+n)m} \left(1 + \frac{1}{K_i^n}\right)^{m} \tag{10.58}$$

With $n = 0.76$ and $m = 1.4$ as earlier, $K_i = 0.96$ and $K_u = 1.016$. This indicates that, with the earlier constants, the critical flashover voltage was slightly changed by using the nonlinear pollution resistance distribution (10.35) rather than the simple uniform distribution. It is clear from (10.58) that as $m \to 1$, $K_u \to 1$ as to be expected.

10.3.3.9.6.2 AC Models It has long been known that the withstand level of a polluted insulator under alternating voltage (ac) is substantially higher than under direct voltage (dc) (Forrest, 1969; Lambeth, 1971). The basic reason is that while the condition of arc propagation may be satisfied, extinctions at current zeros require a higher voltage to maintain an ac arc. The analysis of the mechanism of recovery and reignition of ac arcs on a polluted insulator has first been undertaken by Rizk (1971). A review of this analysis is further included in Rizk (1981) and Rizk and Nguyen (1984). The significance of the reignition characteristics of ac arcs on polluted insulators has also been stressed by Claverie (1971), based on tests of cap and pin and long-rod insulators.

In Rizk (1971), dielectric recovery of a free-burning arc in air was analyzed on the basis of an approximate solution of the energy balance equation of the residual arc plasma subsequent to a current zero. For an arc peak current i, length x, and time t after current zero, the instantaneous dielectric recovery voltage U_d (x, i, t), from the Rizk model with updated thermal conductivity values for air, can be expressed as (Rizk and Rezazada, 1997)

$$U_d(x,i,t) = xE_d(t) = xE_{d0}\left(1 + \frac{64.69}{1 + \left(211.3t/i^{1.326}\right)}\right)^{-0.562} \tag{10.59}$$

where E_{d0} is the power frequency dielectric strength of the arc gap, without current, at room temperature, assumed to be in the range of 5–6 kV_{peak}/cm.

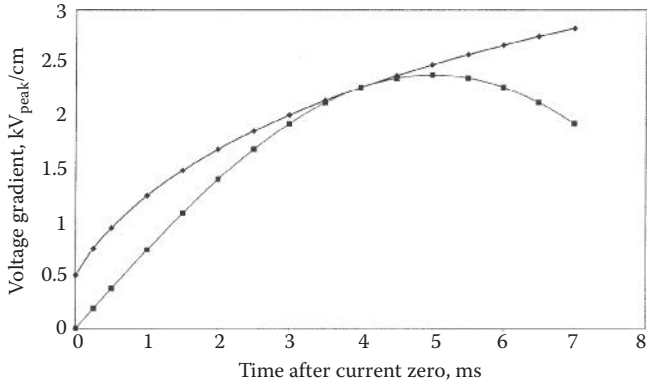


FIGURE 10.27 Determination of arc reignition characteristics: upper curve dielectric strength $E_d(t)$; lower curve: 50 Hz applied recovery voltage gradient $E_{ds}(t)$. $I = 0.1$ A; $E_{sc} = 2395$ V_{peak}/cm.

Variation of the instantaneous reignition voltage gradient $E_d(t)$ can, by definition, be obtained from (10.59) as $U_d(t)/x$. This equation has to be solved with the sinusoidal applied voltage to determine the critical reignition supply peak voltage (Figure 10.27).

Figure 10.28 shows variation of the reignition peak supply voltage gradient E_{ds} with arc current in the range 0.1–2.0 A, assuming $E_{do} = 5.25$ kV_{peak}/cm. It is shown that, for a leakage current of 0.1 A, $E_{ds} = 2395$ V_{peak}/cm or 1694 V_{rms}/cm, while the corresponding values for a 2.0 A arc are $E_{ds} = 604$ V_{peak}/cm or 427 V_{rms}/cm.

Within a certain range of leakage current, the peak reignition supply voltage gradient E_{ds} can be expressed in the form

$$E_{ds} = \frac{A}{i^{\alpha}} \tag{10.60}$$

where A and α are constants. It should be noted that our interest is in the minimum values of the reignition supply voltage gradient needed to reestablish the arc, leading to continued arc propagation.

Regression analysis of the results of Figure 10.28 shows that for $0.1 \leq i \leq 1$ A, with R-square of 0.996, $\alpha = 0.52$ and $A = 698$ V_{peak}/cm. Extending the regression range to $0.1 \leq i \leq 2$ A, it was found that R-square was reduced to 0.984, with also a lower $\alpha = 0.47$ while $A = 751$ V_{peak}/cm.

Experimental results in Claverie (1971) yielded an exponent α of the reignition characteristics amounting to 0.5, in good agreement with the Rizk model results. In Claverie (1971), the constant A was determined as 940 V_{peak}/cm, but in Claverie and Porcheron (1973), this constant was reduced

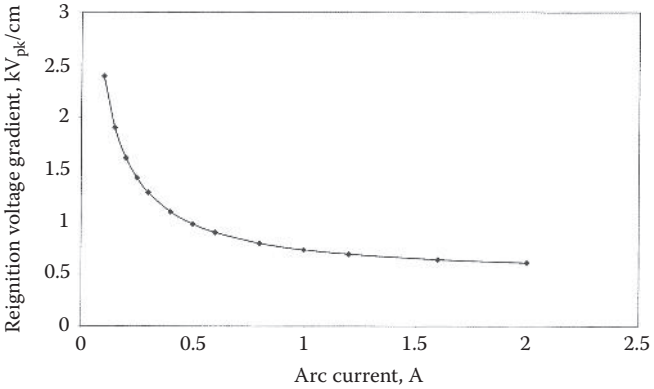


FIGURE 10.28 Variation of power frequency reignition voltage gradient E_{ds} of free-burning arc in air with arc current according to the Rizk model.

to 800 V_{peak}/cm. These values were based on fitting of flashover characteristics of different insulator designs. It was previously suggested (Rizk, 1981) that fitting should have been made in Claverie and Porcheron (1973) with minimum instead of mean flashover voltages, which would have resulted in A close to 700 V_{peak}/cm. The earlier values are in reasonably good agreement with the model.

For the determination of the critical ac supply voltage for flashover of polluted insulators, two equations have to be considered. The first is the circuit equation at the peak arc current i and length x in series with the pollution surface resistance R_{px} under the peak supply voltage $U_s(i, x)$:

$$U_s(i,x) = \frac{xN_o}{i^n} + iR_{px} \tag{10.61}$$

The second equation to be satisfied is the arc reignition condition:

$$U_s(i,x) = \frac{xA}{i^a} \tag{10.62}$$

As mentioned previously, R_{px} will be expressed as

$$R_{px} = R_p\left(1 - \frac{x}{L}\right)^m = \bar{r}_p L\left(1 - \frac{x}{L}\right)^m \tag{10.63}$$

where

$\bar{r}_p$ is the average pollution resistance per unit leakage length

L is the leakage path

Equations 10.61 and 10.62 can be solved numerically, but with some minor simplification, an analytic solution could be obtained. Since the arc voltage drop is much lower than its dielectric reignition voltage, it can be taken as an approximation that $n = \alpha$. Substituting for U_s from (10.62) into (10.61),

$$\frac{(A - N_o)x}{i^a} = i\bar{r}_p L\left(1 - \frac{x}{L}\right)^m \tag{10.64}$$

yielding an expression for the variation of i as function of x:

$$i^{a+1} = \frac{(A - N_o)x}{\bar{r}_p L\left(1 - \frac{x}{L}\right)^m} \tag{10.65}$$

Substituting from (10.65) into (10.62), an expression for the required supply voltage to maintain an arc of length x over this insulator is obtained:

$$U_s(x) = \frac{A}{(A - N_o)^{a/(1+a)}} x^{1/(1+a)} \bar{r}_p^{-a/(1+a)} L^{a/(1+a)}\left(1 - \frac{x}{L}\right)^{(ma)/(1+a)} \tag{10.66}$$

The critical flashover voltage U_{sc} can be obtained by maximizing U_s with respect to x, which will first result in an expression for the critical arc length x_c:

$$x_c = \frac{L}{(1 + ma)} \tag{10.67}$$

which, for the linear model with $m = 1$, yields the familiar expression

$$x_c = \frac{L}{(1 + a)} \tag{10.67a}$$

Substituting for x_c in (10.35) results in an expression for the critical leakage current i_c:

$$i_c = K_i \left(\frac{A - N_o}{\bar{r}_p}\right)^{1/(1+a)} \cdot \tag{10.68}$$

where for ac

$$K_i = \frac{(1+ma)^{(m-1)/(1+a)}}{(ma)^{m/(1+a)}} \tag{10.69}$$

which, for the linear model with $m = 1$, becomes

$$K_i = \frac{1}{a^{1/(1+a)}} \tag{10.69a}$$

If $m = 1.4$ and $\alpha = 0.5$, (10.67) yields $x_c/L = 0.588$ while for the linear model of pollution resistance with $m = 1$, $x/L = 0.667$. It can therefore be concluded by comparison with dc model that the relative critical arc length is in general somewhat longer for ac than for dc and, here again, the nonlinear distribution of pollution resistance reduces the relative critical arc length.

Substituting for i_c and x_c in (10.62), an expression for the ac critical flashover (withstand) voltage is obtained:

$$U_{sc} = K_u A^{1/(1+a)} \bar{r}_p^{a/(1+a)} L \tag{10.70}$$

where for ac

$$K_u = \frac{1}{\left(1 - \frac{N_o}{A}\right)^{a/(1+a)} K_i^a (1+ma)} \tag{10.71}$$

which, for the linear model with $m = 1$, becomes

$$K_u = \frac{a^{a/(1+a)}}{(1+a)\left(1 - \frac{N_o}{A}\right)^{a/(1+a)}} \tag{10.71a}$$

Some examples for the application of the model are given in the following.

Figure 10.29 shows the dependence of the critical leakage current on the average pollution surface resistance, with the linear model, $m = 1$, according to (10.68). It is shown that the critical leakage current

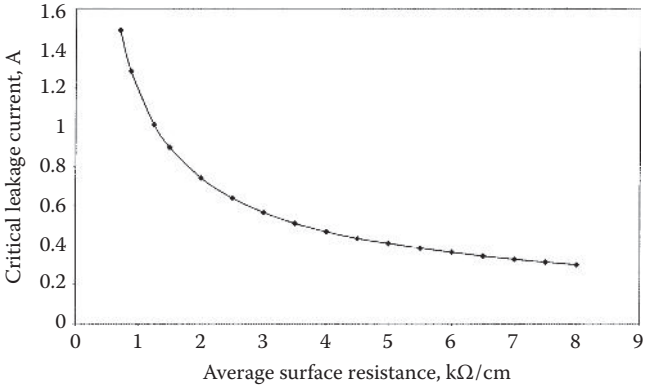


FIGURE 10.29 Variation of critical ac leakage current with average pollution surface resistance per unit leakage length.

is sensitive to pollution severity. For $\overline{r_p} = 700\ \Omega$/cm, i_c = 1.49 A, while for $\overline{r_p} = 7000\ \Omega$/cm, i_c = 0.30 A. This is consistent with the long established practice of using leakage current level to characterize pollution severity, as mentioned previously.

Figure 10.30 shows variation, again for the linear model, of the critical flashover voltage gradient E_{sc} with r_p in the range 700–8000 Ω/cm, according to (10.70). It is shown that E_{sc} varied from 382 V_{peak}/cm at $\overline{r_p} = 700\ \Omega$/cm to 861 V_{peak}/cm for $\overline{r_p} = 8000\ \Omega$/cm.

Finally, the linear model was used to predict pollution performance of a porcelain long-rod insulator-type VKL 75/14 with leakage path L = 180 cm and a form factor f = 6.3. Figure 10.31 resulted from (10.70). It is shown that, for a specific layer conductivity χ_s = 5 μS, the critical flashover (withstand) voltage amounts to 105 kV, while for χ_s = 50 μS, the corresponding value is only 49 kV. Model results were compared with experiments reported in the following. At χ_s = 10 μS, the critical flashover voltage U_c, determined by the model, amounts to 83.2 kV, while the measured value is 90.9 kV. At χ_s, = 40 μS, the model value is 52.4 kV while the experimental value is practically identical.

It should be noted, however, that the model is not intended as a substitute for laboratory or field testing. However, the model can be extremely helpful in rationalizing testing and in interpretation of experimental results (Rizk and Rezazada, 1997). It has also proven its validity in establishing the required high-voltage test source capacity for pollution flashover tests (Rizk and Nguyen, 1984, 1988; Rizk and Bourdages, 1985).

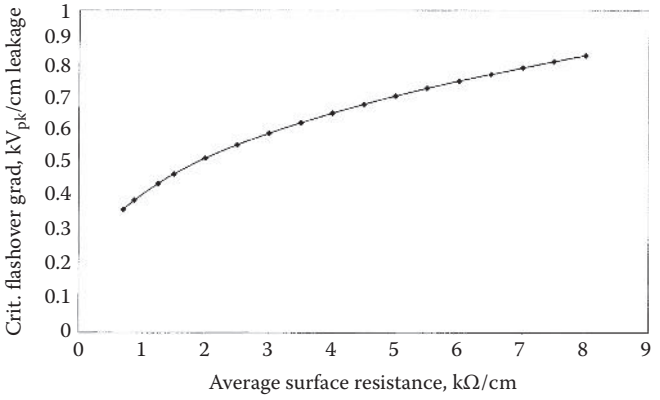


FIGURE 10.30 Variation of critical ac flashover voltage per unit leakage path as a function of average pollution surface resistance per unit leakage path.

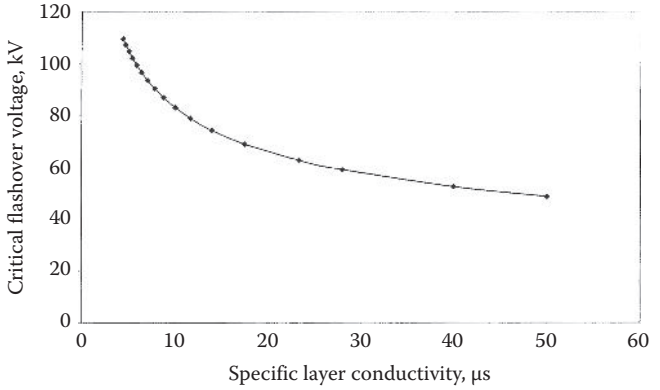


FIGURE 10.31 Variation of critical flashover voltage of long-rod insulator VKL 75/14 with surface layer conductivity as predicted by the Rizk model. L = 180 cm; f = 6.3.

10.3.3.9.7 Experimental Flashover Characteristics

Pollution flashover test techniques have been specified in IEC 60507 for ac tests (IEC Standards 60507, 1991) and IEC 61245 for dc (IEC Standards 61245, 1993). In the salt fog test, a specified number of nozzles are used to atomize and spray a solution, having a salinity that can be set in the range 2.5–224 kg/m^3, towards an energized insulator string. The test can be performed to produce either a withstand voltage or a withstand salinity. This technique produces withstand voltage stresses, kV/m, and order of merit of different insulator designs that appear to be consistent with experience with marine pollution test site results (Lambeth, 1971; Houlgate and Swift, 1990). The solid layer method, on the other hand, produces a predeposited pollution layer that is subsequently wetted, often by steam fog. In the clean fog version, wetting occurs under voltage, which is maintained for a specific duration or until flashover occurs. Again, this technique produces either a withstand salt deposit density at a given voltage or a withstand voltage under a given severity. In an earlier version of this test, the so-called kieselguhr method, the voltage is suddenly applied to an already polluted and wetted insulator at maximum specific layer conductivity. This test was intended to simulate the situation of line energization on already polluted and wetted insulators.

Another practical approach is to expose insulators to natural pollution for varying long durations and, subsequently, perform wetting under voltage in the laboratory to determine the withstand voltage (Rizk et al. 1972). This method is certainly more representative of field conditions but is far more time consuming and expensive than artificial pollution tests.

Still another technique is to expose different insulators to natural pollution under voltage and vary the string length to determine the withstand characteristics and order of merit (Lambeth, 1971; Houlgate and Swift, 1990). Again, this is representative of the environment but also very time consuming.

Some typical flashover test results will be presented for insulators A, B, C, D, and E shown in Figure 10.1 with dimensions included in Table 10.1 (Rizk et al. 1972). It should be noted that insulators are usually compared on the basis of their flashover (withstand) characteristics per unit suspension length. This is more relevant to transmission tower design.

Figure 10.32 (Rizk et al. 1972) shows how the different insulator designs are performed in laboratory flashover tests subsequent to field exposure in desert environment for periods extending up to 24 months. It is indicated that, in general, the antifog disc type D had the best flashover voltage per unit suspension length. Although this insulator collected significant pollution due to the deep under ribs, its high ratio of leakage path to spacing (3.05) proved quite favorable. The worst performance was that by type E long-rod VKL 75/14, having the lowest ratio of leakage path/spacing (1.46). It should be noted, however, that

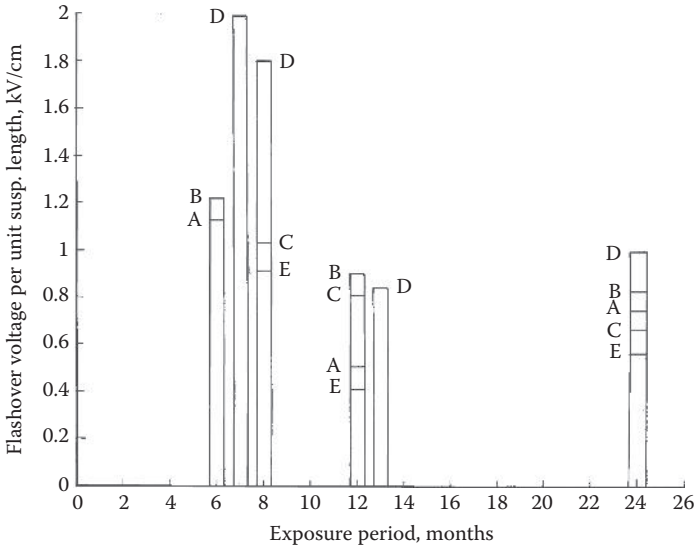


FIGURE 10.32 Flashover voltage per unit suspension length of different insulator designs in laboratory flashover tests subsequent to field exposure in desert environment for periods extending up to 24 months. (From Rizk et al. 1972.)

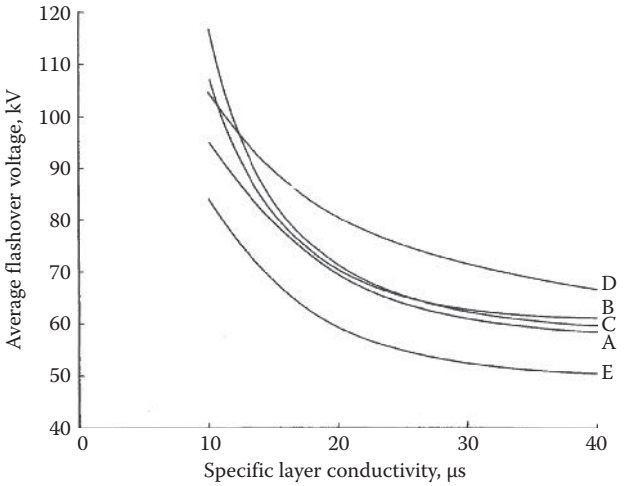


FIGURE 10.33 Variation of average flashover voltage with specific layer conductivity of different insulator strings in a dust deposit test. (From Rizk and El-Sarky, 1972.)

the comparative performance among different insulator designs, in terms of flashover voltage per unit suspension length, was not proportional to the leakage path/suspension length ratio. This is because the critical flashover voltage per unit leakage path length was not the same among different insulator designs exposed to field conditions. For example, after 1-year exposure, the flashover voltage per unit creepage length was 368, 329, 274, and 239 V/cm for insulator types B, C, D, and A, respectively (Rizk et al. 1972). This means that the flat aerodynamic designs B and C had superior critical flashover voltage per unit leakage path, as such designs collect less contaminant in a desert environment.

Figure 10.33 shows variation of the 50% flashover voltage with specific layer conductivity χ_s in the range 10–40 μS for the earlier insulator types in high-voltage dust deposit tests (Rizk et al. 1972). The insulator string length was kept constant at 127 cm ± 6%. Several interesting results were observed. First, artificial tests, at heavy pollution, showed little difference in performance among types B, C, and A, while under field exposure, type B demonstrated clear advantage. Furthermore, the dependence of U_{50} on χ_s can in general for each type, be expressed as

$$U_{50} = \text{const.}\ \sigma_s^{-b} \tag{10.72}$$

It was found that β amounted to 0.48, 0.40, 0.39, 0.36, and 0.35 for insulator types C, B, A, D, and E, respectively (Rizk et al. 1972).

Salt fog tests according to IEC 60507 were carried out on the same strings. The results are shown in Table 10.7, where the withstand salinities are reported at a test voltage of 63.5 kV $\left(110/\sqrt{3}\ \text{kV}\right)$ and withstand voltages at a salinity of 33.6 g/L. It is observed that the same order of merit is obtained from withstand salinity test as from the U_{50} at constant salinity. The order of merit, however, differs from that

TABLE 10.7

Salt Fog Test Results

String Type	Withstand Salinity at 63.5 kV, g/L	U_{50}, kV at 33.6 g/L Salinity	Order of Merit
A	28	69	3
B	14	60	4
C	40	71	2
D	47.5	86	1
E	7	49	5

Source: Rizk et al., CIGRE, Paper No. 33-03, Paris, France, 1972.

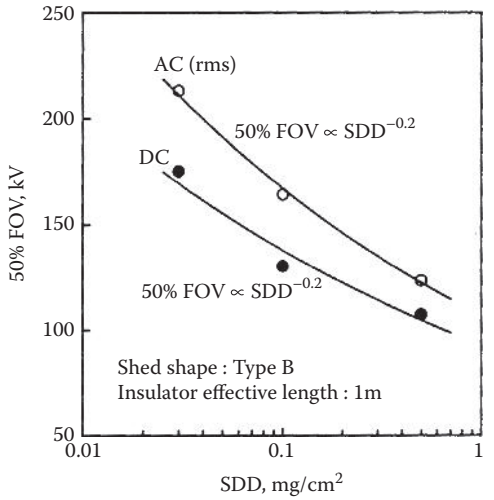


FIGURE 10.34 Variation of 50% flashover voltage of silicone rubber insulators with salt deposit density under ac and dc energization. (From Matsuoka, R. et al. Contamination withstand voltage characteristics of polymer insulators, in: *10th ISH*, Vol. 3, Montréal, Québec, Canada, 1997, pp. 81–84.)

obtained from the dust deposit test or from field exposure tests. In particular, the flat aerodynamic disc behaved significantly unfavorably under salt fog.

The aforementioned results confirm that, for transmission line design, insulator selection should be based on a test technique appropriate for the environment.

So far in this section, we dealt with porcelain insulators. It has long been known that polymeric insulators such as silicone rubber, when new, outperform ceramic insulators under pollution. If polymeric insulators completely lose their hydrophobicity, however, they practically behave like ceramic insulators. It has also been known that, in the laboratory, it is difficult to apply and maintain a wet contamination layer on a silicone rubber insulator unless such surface is deliberately deprived from its hydrophobicity in a so-called conditioning process. It is also well known that silicone rubber insulators lose their hydrophobicity, at least temporarily, in service due to surface discharges, sandstorms, heavy rain, and UV radiation (Karady et al., 1994; Rizk et al., 1997). Unless the insulator has seriously aged, hydrophobicity will be recovered in a matter of hours. If exposed to severe pollution and wetting conditions before hydrophobicity is recovered, flashover can take place.

Matsuoka et al. (1997) reported on laboratory contamination tests on different profiles of silicone rubber insulators. It has been shown that insulator performance, for an ESDD = 0.03 mg/cm^2, can be improved by increasing the ratio l/p between the leakage distance l per shed and the shed pitch p up to approximately 4. For a profile with l = 140 mm and p = 50 mm, Figure 10.34 (Matsuoka et al., 1997) shows the effect of salt deposit density on 50% flashover voltage for both ac and dc energization. It is confirmed that under otherwise the same conditions, dc stress is significantly more severe than ac, as predicted by the earlier model work. It is also shown that, for these unaged polymeric insulators and for the extreme severity of 0.5 mg/cm^2, the 50% flashover stress amounts to approximately 110 kV/m for dc and 125 kV$_{rms}$/m for dc. If comparison is made on the basis of peak voltage, this shows that the ac 50% flashover voltage is 60% higher than dc for the polymeric insulator in question. For a severity of 0.03 mg/cm^2, the ac peak flashover voltage is almost 90% higher than the dc.

10.3.4 Mechanical Requirements

As mentioned in the introduction to this chapter, the importance of mechanical integrity of the line insulators cannot be overemphasized. It should be quite clear that a mechanical failure of the string could lead to conductor dropping and long period out of service. Certainly, this is far more serious than a flashover that can be dealt with by system protection.

In general, the insulator will be subjected to a vertical force F_v due to the conductor weight plus any ice load. A horizontal wind force F_w will also be vectorially added, leading to a resultant force F_r. The vertical load F_v, N could be expressed as

$$F_v = (M_c + M_i) \lozenge g \tag{10.73}$$

where
M_c is the conductor mass for a weight span L_m
M_i is the mass of the ice accumulated
g is the acceleration of gravity

The wind force can be obtained from the design wind speed v_s, which is related to the basic wind speed v_w by (Bayless, 1999)

$$v_s = f_1 \lozenge f_2 \, v_w \tag{10.74}$$

where
f_1 is a topology factor
f_2 is a ground roughness factor

The dynamic pressure q, N/m^2 is obtained from

$$q = k_p v_s^2 \tag{10.75}$$

with $k_p = 0.613$, using SI units (Bayless, 1999).
The wind force F_w can be expressed as

$$F_w = C_f \lozenge q \lozenge A_e \tag{10.76}$$

where
C_f is a force coefficient that depends on conductor shape
A_e is the exposed conductor area for a wind span, with due consideration to possible ice accretion

The resultant force F_r is then given by

$$F_r = \sqrt{F_v^2 + F_w^2} \tag{10.77}$$

For a cap and pin insulator, the electromechanical failing load EMFL is defined as the maximum tensile force reached prior to breakage of the insulator or hardware. Statistically, this is taken as the 50% level minus 3 standard deviations. EMFL is then related to the resultant force F_r by a factor of safety K_s:

$$\text{EMFL} = K_s \lozenge F_r \tag{10.78}$$

The safety factor K_s is usually defined for a set of stringing conditions. Examples are as follows:

- $K_s = 5$ at 20° without wind or ice. This means that the everyday working load is 20% of the electromechanical failing load.
- $K_s = 2.5$ at −20°C without wind or ice.
- $K_s = 2.5$ at −5°C with specified wind pressure and ice accretion.
- $K_s = 2.5$ at 5°C at a more severe wind pressure but obviously no ice.

Application to nonceramic insulators is made more complex by the fact that mechanical strength is not a constant but decreases with time due to creep of the core materials (IEC Standard 60815, 2008; Vosloo et al., 2002). In the IEC Standard 60815 (2008), the strength of a polymeric rod is presented as a decaying linear function of the logarithm of the load duration, in minutes. It requires that the slope of

the straight-line relationship be less than 8% of the 1 min failing load per decade of time (a factor of 10). The IEC strength curve $F(t)$ can be expressed as

$$F(t) = F(1) - 0.08 \log_{10}(t) \tag{10.79}$$

where

$F(t)$ is the residual strength after a duration t

$F(1)$ is the 1 min strength, which means that after 50 years of service, the residual mechanical strength should be above approximately 40% of the initial 1 min strength

It was argued in Vosloo et al. (2004), however, that actual tests show that after such period, about 65% of the original 1 min strength is retained. Obviously, laboratory test results were substantially extrapolated to 50 years (de Tourreil et al., 1985).

The 1 min strength specified by the manufacturer is referred to as the *specified mechanical load*, SML, of the polymeric insulator. Similar to the case of ceramic insulators, here, SML is related to the resultant force F_r by

$$\text{SML} = K_s \cdot F_r \tag{10.80}$$

where, as mentioned earlier, K_s is the factor of safety.

Standard IEEE cap and pin insulators (5′(3/4)/10′/or 146/254 mm) are commercially available with electromechanical ratings of 70–160 kN (15,000–36,000 lb). Antifog discs are available for up to 530 kN (120,000 lb). Silicone rubber long-rod insulators are also available for SML ratings of 110–350 kN (25,000–80,000 lb).

10.4 Insulator Selection

10.4.1 Insulator Type and Material

The selection of transmission line insulators includes the determination of the type, material, and insulator characteristics. Reference should be made to treatment of these aspects earlier in this chapter and elsewhere. A summary is included in the following.

The first decision is regarding the use of ceramic or polymeric insulators (Papaliou and Schmuck, 2013). The following are reiterated:

- Polymeric insulators have favorable mechanical strength to weight ratio. However, deterioration of failing mechanical load over the insulator lifetime must be considered.
- Polymeric insulators are less vulnerable to vandalism.
- Polymeric insulators have favorable pollution performance when new. However, they are exposed to occasional loss and recovery of hydrophobicity. The designer has to consider suitability of such insulators to the particular environment.
- Ultimately, under aging factors, nonceramic insulators are bound to lose their hydrophobicity as the LMW silicon oil that diffuses to the surface and is responsible for hydrophobicity will be practically depleted. The designer has therefore to decide whether to take advantage of the superior performance of nonceramics when new and accept replacement at an earlier time. The other choice, which may be more prudent, is to use the same design stress as for porcelain or glass.
- Also, consideration must be given to the effect of aging not only on electrical characteristics but also on mechanical integrity, which may dictate a shorter lifetime compared to porcelain or glass.
- At system voltage of 245 kV and above, special care must be given to the design of corona rings in order to inhibit surface discharges that would otherwise accelerate aging of the polymeric insulator.
- The user has to be aware that application of polymeric insulators requires a follow-up in service that is more demanding than would be the case for porcelain (puncture) or glass (shattering).

If the decision is made to use conventional ceramic insulators, the designer has to choose between porcelain and glass. As mentioned earlier in this chapter,

- In high-voltage laboratory, pollution tests porcelain and glass insulator performance is practically identical
- In service, glass insulators may be more vulnerable to surface cracks induced by erosion due to severe flow of leakage current in polluted environment
- In service, the detection of punctured porcelain units requires specialized techniques, while shattering of glass units is easily identified

The earlier arguments apply for new designs of conventional transmission lines. For compact line design or for mechanical or electrical upgrading of operating lines, the lack of air clearances and the necessity of supporting heavier conductor bundles may favor the application of polymeric insulators (Papaliou and Schmuck, 2013).

10.4.2 Insulator Profile

The IEC Standard 60815 (2008) defines four levels of pollution: I, light; II, medium; III, heavy; and IV, very heavy, with minimum nominal specific creepage distance of 16, 20, 25, and 31 mm/kV$_{LL}$, respectively. When referred to phase-to-ground voltage, the specific leakage distances become 28, 35, 43, and 54 mm/kV, respectively. Several parameters are given to characterize the insulator or a complete string:

- The minimum distance between sheds
- The ratio between spacing and shed overhang
- The local, as distinct from overall, ratio between creepage distance and clearance
- Alternating sheds
- Inclination of sheds
- Two parameters characterizing the entire insulator (string):

1. Creepage factor (CF): defined as the ratio between the total leakage distance and the arcing distance
2. Profile factor (PF): defined as the ratio between the so-called *simplified* and real leakage path between consecutive sheds and insulator units

For reference to detailed drawings, please refer to the IEC Standard 60815 (2008).

Some recommendations are given concerning the limits of the aforementioned parameters. For example, it is advised to keep CF ≤ 3.5 for pollution levels I and II and CF ≤ 4.0 for pollution levels III and IV. Experience has shown that increasing CF beyond these limits is not effective in improving insulator performance.

The standard (IEC Standard 60815, 2008) recognizes, as can be deduced from the earlier model, that pollution performance can deteriorate for insulators with large average diameter (lower r_p for the same χ_s or ESDD). For a mean diameter d_m below 300 mm, no increase of the specific leakage path is recommended. However, for $300 \leq d_m \leq 500$ mm, a 10% increase in the specific leakage path is recommended. For $d_m > 500$ mm, a 20% reinforcement of the specific leakage path is recommended.

It is considered that, while IEC 60815 (IEC Standard 60815, 2008) contains useful general classifications and recommendations, it is by no means adequate for insulator selection in polluted environment. The subject will be treated in more depth in the following.

10.4.3 Design Approach

10.4.3.1 Flowchart

Figure 10.35 shows a proposed flow chart (Rizk, 1997) for the selection of high-voltage insulators in polluted environment. The chart will be briefly explained in this section, but details of the different stages in the selection process will be dealt with in later sections.

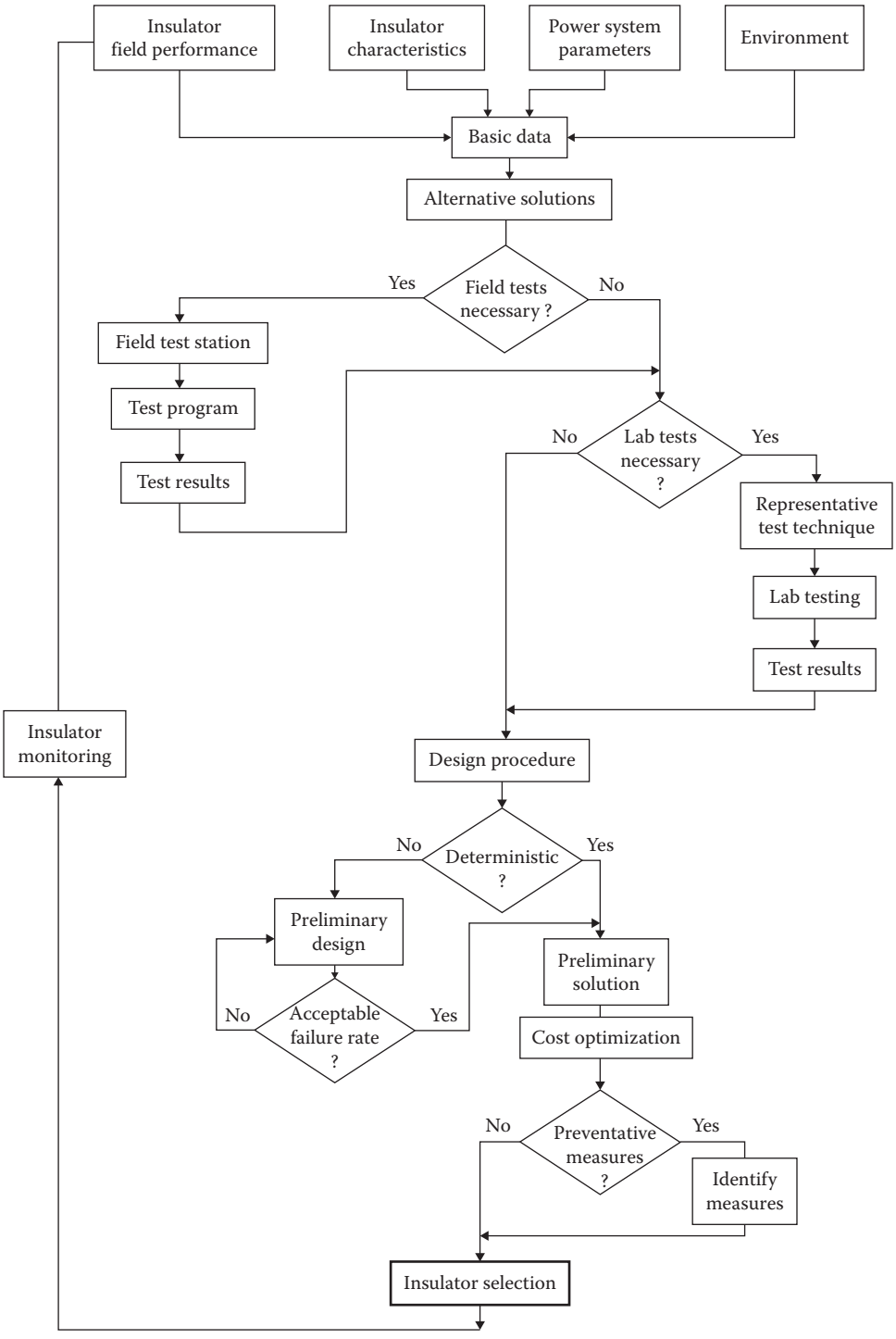


FIGURE 10.35 Flow chart for insulator selection in polluted environment.

The chart starts with the basic data available to the design engineer related to relevant power system parameters: ac or dc, line voltage, frequency, transmission line length, level of overvoltages, environmental parameters (type of environment, pollutants, rain, wind, fog, dew, etc.), as well as any available information on insulator type, designs, and pollution performance both from the field and in the laboratory. At this stage, some alternative solutions could be envisaged, for example, different profiles of porcelain cap and pin insulators and different designs of silicone rubber rods. A decision has to be made early on whether field tests on the selected alternative designs would be necessary. That decision should be based on adequacy of field and laboratory results on the performance of the alternative designs in the specific or similar environment to that of the proposed route. It is essential to reach the decision on field tests early, since field tests would normally require 2–4 years. If such time is not available, the decision is simple: no meaningful field testing program could be undertaken. Otherwise, a field test station has to be designed and a test program prepared and implemented.

The other question that has to be settled as early as possible is that of the necessity of high-voltage pollution tests in a laboratory. Again, this will be based on the adequacy of available material on the performance of the different insulators considered. If the decision is taken to test, a test most representative of the environment concerned has to be selected. It could suitably be one of the standard tests of salt fog or clean fog or some modified variance thereof.

In the design procedure, a decision has to be made on whether to follow a deterministic approach, in which a safety margin between the operating voltage and the withstand voltage of the polluted string is adopted, or a statistical approach, in which insulators are selected to meet a predetermined performance criterion. While the statistical approach is more scientifically appealing, it requires more complete information on the environmental *events* and flashover characteristics of polluted insulators as well as a sensible determination of what an *acceptable* failure rate is.

Once the selected insulators are installed, a follow-up of their performance in service will provide necessary information for any remedial or maintenance procedures needed as well as input for selection of insulators for future lines and installations.

10.4.3.2 Statistical Approach to Insulator Selection

It is well known that, for a given pollution severity expressed by equivalent deposit density ESDD, specific layer conductivity χ_s, or mean surface resistance r_p per unit leakage length and adequate wetting, for example, caused by dew formation or light drizzle, the flashover voltage of an insulator string is a statistical variable often described by a normal distribution:

$$P(V) = \Phi\left(\frac{V - U_{50}}{\sigma}\right) \tag{10.81}$$

where

V is the applied voltage
U_{50} is the 50% flashover voltage
σ is the standard deviation, all expressed in kV
ϕ is the cumulative normal distribution function

In dealing with many strings in service and considering that, for adequately insulated lines, we are facing low-probability situations, it is important to realize that for physical reasons, flashover cannot occur below a certain threshold voltage U_o, which can be related to U_{50} by

$$U_o = U_{50} - n\sigma \tag{10.82}$$

where n is a number usually assumed as 2, 3, or 4. This means that instead of (10.81), we should have

$$P(V) = \frac{\Phi\left(\frac{V - U_{50}}{\sigma}\right) - \Phi(-n)}{1 - \Phi(-n)} \tag{10.83}$$

The truncation will obviously influence the low-probability region only and (10.81) will still be practically valid at higher probabilities. In the earlier equations, U_{50} and σ, which usually is proportional to U_{50}, are functions of pollution severity.

Another statistical distribution, the Weibull distribution, has the built-in truncation property mentioned earlier and, moreover, provides a simple manipulation when dealing with multiple stressed objects assumed to act as independent statistical variables. Instead of (10.81), we may then have

$$P(V) = 1 - \exp\left[-\left(\frac{V - U_o}{\beta U_o}\right)^k\right] \tag{10.84}$$

where U_o, β, and k are the Weibull distribution parameters and U_o is determined from (10.82), once n has been selected.

Since most available high-voltage test results are expressed in terms of the normal distribution, it is required to determine the equivalent Weibull distribution. The parameters β and k can then be determined if we impose two conditions of equivalence. In reference (IEC Standard 60071-2, 1996), these two conditions require that the two distribution functions have the same values so that $P(V) = 0.5$ at $V = U_{50}$ and $P(V) = 0.16$ at $V = U_{50} - \sigma$.

These constraints result in the following formulae:

$$k = \frac{1.38}{\ln\left(n/(n-1)\right)} \tag{10.85}$$

and

$$\beta = \frac{n \diamond c}{(1 - n \diamond c)(\ln 2)^{1/k}} \tag{10.86}$$

where the coefficient of variation $c = \sigma/U_{50}$ is obtained from the normal distribution. Table 10.8 shows the values of k for different values of n.

As numerical examples, for $c = 0.10$ and $n = 2$, (10.86) yields $\beta = 0.30$, while for $c = 0.08$ and $n = 3$, β is determined at 0.352.

For a number of strings N stressed simultaneously and assumed statistically independent, the probability of flashover becomes

$$P_N(V) = 1 - \exp\left[-N\left(\frac{V - U_o}{\beta U_o}\right)^k\right] \tag{10.87}$$

which, for $NP \ll 1$, yields

$$P_N(V) \approx N\left(\frac{V - U_o}{\beta U_o}\right)^k \tag{10.88}$$

Dividing the applied voltage V and the withstand voltage U_o by the string length to obtain E and E_o, respectively, (10.88) when referred to one string becomes

$$P_N(V) \approx \left(\frac{E - E_o}{\beta E_o}\right)^k = \text{const.}\left(\frac{E - E_o}{E_o}\right)^k \tag{10.89}$$

where the constant amounts to $(1/\beta)^k$.

TABLE 10.8

Exponent k of the Equivalent Weibull Distribution

n	2	3	4
k	2.0	3.4	4.8

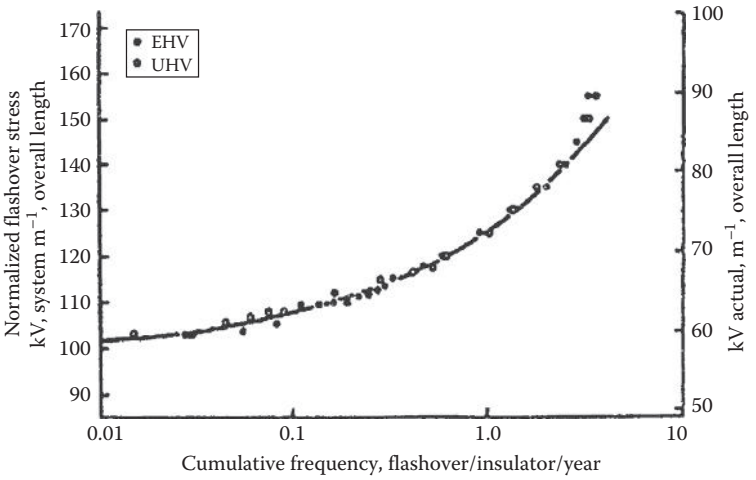


FIGURE 10.36 Cumulative flashover distribution of an insulator string in marine environment. (From Houlgate, R.G. et al., The performance of insulators at extra and ultra high voltage in a coastal environment, CIGRE, Paper 33-01, 1982.)

Figure 10.36 shows cumulative flashover distribution curve, referred to one string, of insulator exposed to marine pollution at the Brighton test station (Houlgate et al., 1982). The results fit expression (10.89) with $E_o = 99$ kV/m (referred to system voltage, actual stress $E_o = 99/\sqrt{2}$ kV/m) and $k = 2.1$, which from Table 10.8 corresponds to $n = 2$ (Houlgate et al., 1982).

Having shown that field experience substantiates the statistical approach developed so far on the basis of a Weibull distribution, we will extend the approach to predict line performance.

The information needed for such an approach comprise the variation of pollution severity along the line route as well as the frequency of dangerous wettings (Rizk et al., 1975) constituting the statistical events. Figure 10.37 shows the variation of ESDD on three types of insulators during 32 months exposure at Ghazlan, Saudi Arabia (Akbar and Zedan, 1991). SPI is a standard porcelain, FP1 is antifog

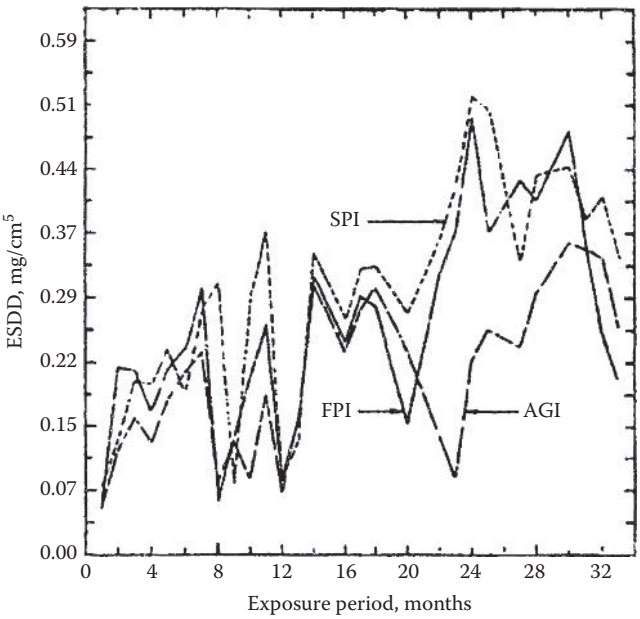


FIGURE 10.37 Variation of ESDD with exposure period for different insulators in desert environment. (From Akbar, M. and Zedan, F.M.., *IEEE Trans. Power Deliv.*, 6(1), 429, January 1991.)

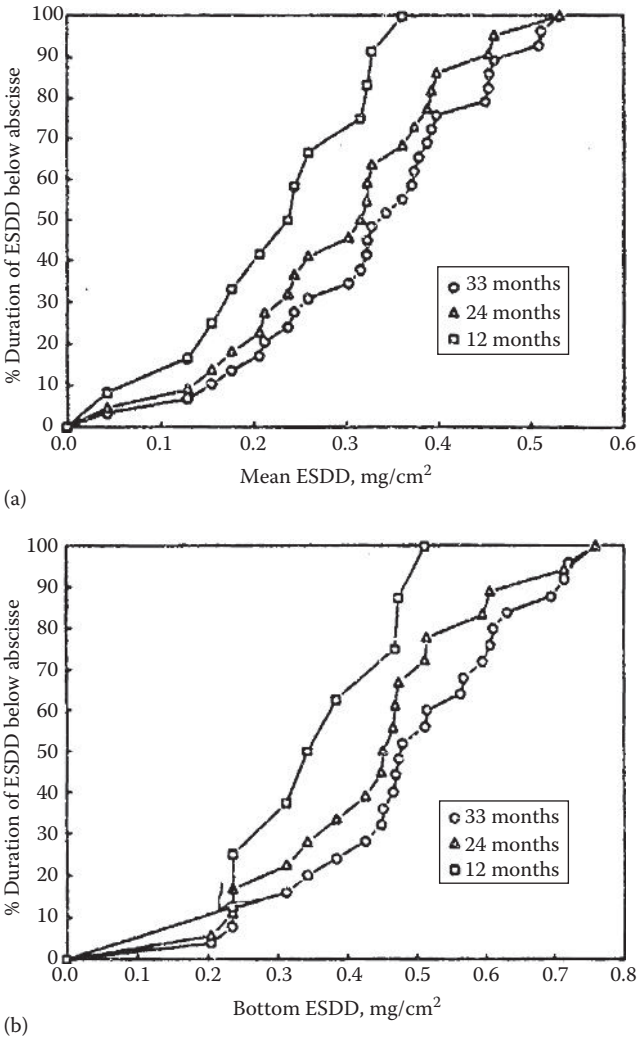


FIGURE 10.38 Cumulative severity–duration curves for different insulators in desert environment. (From Akbar, M. and Zedan, F.M.., *IEEE Trans. Power Deliv*., 6(1), 429, January 1991.)

porcelain, and AG1 is aerodynamic glass insulators. It is once more confirmed that severity varies with the insulator profile (Figure 10.37).

It was suggested by Rizk that severity measurements could be more readily interpreted if presented as severity–duration curves as shown in Figure 10.38. It is shown that the difference between the 24 and 33 months curves is much less significant than between the 12 and 24 months characteristics, confirming that a minimum exposure period of 2–3 years is needed for meaningful results in this environment. It is also evident that the 50% severity values are more stable than the extreme ESDD values.

Let us consider a section of a high-voltage transmission line where both pollution severity and wetting conditions could be considered reasonably uniform. Let the number of strings in this section be N_i. Also, divide the exposure period T into subintervals ΔT_v, so that within such subinterval, the pollution severity does not vary significantly and the number of dangerous wetting events be w_{iv}. From (10.87), the number of flashovers in this section within this time subinterval will be

$$n_{fiv} = w_{iv}\left[1 - \exp\left(-N_i \frac{V - U_{oiv}}{bU_{oiv}}\right)^k\right] \tag{10.90}$$

which, if the condition leading to (10.88) is satisfied, becomes

$$n_{\text{fiv}} = w_{\text{iv}} N_{\text{i}} \left(\frac{V - U_{\text{oiv}}}{U_{\text{oiv}}} \right)^{k} \tag{10.91}$$

Here, the letter i refers to the section and v to the subinterval, so that n_{fiv} is the number of flashovers in section i during subinterval v and U_{oiv} is the corresponding withstand voltage. Over the whole exposure period considered, the total number of flashovers n_{f} is obtained by a double summation overtime and line sections:

$$n_{\text{f}} = \sum_{\text{i}} \sum_{\text{v}} w_{\text{iv}} N_{\text{i}} \left(\frac{V - U_{\text{oiv}}}{U_{\text{oiv}}} \right)^{k} \tag{10.92}$$

As mentioned earlier, this could be expressed in terms of the applied and withstand gradients E and E_{oiv}:

$$n_{\text{f}} = \sum_{\text{i}} \sum_{\text{v}} w_{\text{iv}} N_{\text{i}} \left(\frac{E - E_{\text{oiv}}}{E_{\text{oiv}}} \right)^{k} \tag{10.93}$$

This equation represents a dynamic statistical model of line performance since both E_{oiv} and w_{iv} are functions of time.

For any section or subsection of the line, the specific number of faults can be introduced as the number of faults per string per wetting event, that is, $n_{\text{f}}/(w \cdot N)$.

For any time subinterval, from (10.91), this could be expressed as

$$\frac{n_{\text{f}}}{(w \cdot N)} = \left(\frac{E - E_{\text{o}}}{E_{\text{o}}} \right)^{k} \tag{10.94}$$

As an example, consider a 60 km section of a 525 kV transmission line. The nominal span is 400 m, so that the number of strings per section $N = 450$. The number of dangerous wettings per year is given as $w = 10$. The type of insulator tested at the relevant pollution severity showed a 50% flashover gradient $E_{50} = 60$ kV/m of suspension length. Based on experience, the distribution parameters were taken as $n = 3$ and $c = 0.08$. The earlier expressions resulted in $E_{\text{o}} = 45.6$ kV/m and the Weibull distribution parameter $\beta = 0.35$. The performance criterion of 1F/100 km · year results in $n_{\text{f}} = 0.6$ faults/year for the 60 km section.

From (10.94), the operating voltage gradient is determined at $E = 47.0$ kV/m, which, from the operating phase-to-ground voltage of 303 kV, results in a design suspension string length of 6.46 m. The cap and pin insulator in question had a unit spacing of 170 mm, so that the number of string units required becomes 38.

REFERENCES

Adamson, A.W. *Physical Chemistry of Surfaces*, 2nd edn. New York: Wiley-Interscience, 1967, Chapter 7.

Akbar, M., Ahmed, Z., Matsuoka, R., Sakanishi, K., and N. Okada. Insulation contamination study in Pakistan (Part I). In: *9th ISH*, Graz, Austria, 1995, Paper 3208.

Akbar, M. and F.M. Zedan. Performance of HV transmission line insulators in desert conditions. Part III: Pollution measurements at a coastal site in the eastern region of Saudi Arabia. *IEEE Transactions on Power Delivery* 6(1): 429–438, January 1991.

Akbar, M., Zedan, F.M., Abdul-Majeed, M.A., and K.T. Al-Soufi. Design of HV lines to combat insulator pollution problems in the eastern region of Saudi Arabia. *IEEE Transactions on Power Delivery* 6(4): 1912–1921, October 1991.

Bartnikas, R. Dielectrics and insulators. In: R.C. Dorf (ed.), *Electrical Engineering Handbook*. Boca Raton, FL: CRC Press, 1993, Chapter 52.

Bayless, C. *Transmission and Distribution Electrical Engineering*, 2nd edn. Oxford, U.K.: Newness, 1999.

Böhme, H. and F. Obenaus. Pollution flashover tests on insulators in the laboratory and in systems and the model concept of creepage path flashover, CIGRE, Paper No. 407, Paris, France, 1966.

Callister, Jr., W.D. *Materials Science and Engineering*, 3rd edn. New York: John Wiley & Sons Inc., 1994.

Chang, J.W. and R.S. Gorur. Surface recovery of silicon rubber used for HV outdoor insulation. *IEEE Transactions on Dielectrics and Electrical Insulation Society* DEIS-1(6): 1039–1046, December 1994.

Cherney, E.A., Karady, G., Brown, R.L., Nicholls, J.L., Orbeck T., and L. Pargamin. Application of composite insulators to transmission lines. *IEEE Transactions on Power Apparatus and Systems* PAS-102(5): 1226–1234, May 1983.

CIGRE Working Group 33.04. The measurement of site pollution severity and its application to insulator dimensioning for AC systems. *Electra* 64: 101–116, 1979.

Claverie, P. Predetermination of the behaviour of polluted insulators. *IEEE Transactions on Power Apparatus and Systems* PAS-90(4): 1902–1908, July/August 1971.

Claverie, P. and Y. Porcheron. How to choose insulators for polluted areas. *IEEE Transactions on Power Apparatus and Systems* PAS-92(3): 1121–1131, May/June 1973.

Dietz, H., Kärner, H., Müller, K.H., Patrunky, H., Schenk, G., Verma, P., and H.J. Voss. Latest developments and experience with composite long-rod insulators, CIGRE, Paper No. 15-09, Paris, France, 1986.

El-Koshairy, M.A.B. and F.A.M. Rizk. Performance of EHV transmission line insulators under desert pollution conditions, CIGRE, Paper No. 33-05, Paris, France, 1970.

von Engel, A. *Ionized Gases*. Oxford, U.K.: Clarendon Press, 1955, Chapter 9.

Forrest, J.S. The performance of high-voltage insulators in polluted atmospheres. In: IEEE Conference Paper No. 69 CP7-PWR, presented at the *IEEE Winter Power Meeting*, New York, January 26–31, 1969.

Hall, J.F. and T.P. Mauldin. Wind tunnel studies of the insulation contamination process. *IEEE Transactions on Electrical Insulation* EI-16(3): 180–188, June 1981.

Hampton, B.F. Flashover mechanism of polluted insulation. *Proceedings of IEE* III(5): 985–990, July 1964.

Hesketh, S. General criterion for prediction of pollution flashover. *Proceedings of IEE* 114(4): 531–532, April 1967.

Hileman, A.R. *Insulation Coordination for Power Systems*. New York: Marcel Dekker Inc., 1999.

Higashimori, Y., Nakao, Z., and S. Nishimura. Rapid salt contamination of insulator surfaces by typhoons. In: *9th ISH*, Graz, Austria, 1995, Paper 3882.

Houlgate, R.G., Lambeth, P.J., and W.J. Roberts. The performance of insulators at extra and ultra high voltage in a coastal environment, CIGRE, Paper 33-01, Paris, France, 1982.

Houlgate, R.G. and D.A. Swift. Composite rod insulators for AC power lines: Electrical performance of various designs at a coastal testing station. *IEEE Trans. on Power Delivery* 5(4): 1944–1955, 1990.

Humphreys, W.J. *Physics of the Air*. New York: Dover Publications, 1964, pp. 279–280.

IEC Standard 60507. Artificial pollution tests on high-voltage insulators to be used on AC systems, 2nd edn., 1991.

IEC Standard 61109. Composite insulators for AC overhead lines with a nominal voltage greater than 1000 V-definitions, test methods and acceptance criteria, 1992.

IEC Standard 61245. Artificial pollution tests on high-voltage insulators to be used on DC systems, 1993.

IEC Standard 60305. Insulators for overhead lines with a nominal voltage above 1000 V-ceramic or glass insulator units for AC systems—Characteristics of insulator units of the cap and pin type, 4th edn., 1995.

IEC Standard 60071-2. Insulation coordination, Part 2: Application guide, 1996.

IEC Standard 60815. Selection and dimensioning of high-voltage insulators intended for use in polluted conditions—Part 1: Definitions, information and general principles. Part 2: ceramic and glass insulators for AC systems—Part 3: Polymer insulators for AC systems, 2008.

Karady, G. The effect of fog parameters on the testing of artificially contaminated insulators in a fog chamber. *IEEE Transactions on Power Apparatus and Systems* PAS-94(2): 378–387, March/April 1975.

Karady, G.G., Schneider, H.M., and F.A.M. Rizk. Review of CIGRE and IEEE research into pollution performance of non-ceramic insulators: Field aging effects and laboratory test techniques, CIGRE, Paper No. 33-103, Paris, France, 1994.

Karady, G.G., Shah, M., and R.L. Brown. Flashover mechanism of silicon rubber insulators used for outdoor insulation. *IEEE Transactions on Power Delivery* 10(4): 1965–1971, October 1995.

Kikoin, A. and I. Kikoin. *Molecular Physics*. Moscow, Russia: MIR Publications, 1978, pp. 173–176.

Kimoto, I., Kito, K., and T. Takatori. Anti-pollution design criteria for line and station insulators. *IEEE Transactions on Power Apparatus and Systems* PAS-91: 317–327, January 1972.

Lambeth, P.J. The effect of pollution on high-voltage outdoor insulators. *IEE Reviews* 118: 1107–1130, September 1971.

Langhaar, H.L. *Dimensional Analysis and Theory of Models*. New York: John Wiley & Sons Inc., 1951.

LeRoy, G., Gary, C., Hutzler, B., Lalot, J., and C. Dubanton. *Les propriétés diélectriques de l'air et les très hautes tensions*. Paris, France: Eyrolles, 1984, Chapter 16.

Loberg, J.O. and E.C. Salthouse. Dry-band growth on polluted insulation. *IEEE Transactions on Electrical Insulation* EI-6(3): 136–141, September 1971.

Matsuoka, R., Ito, S., Tanaka, K., and K. Kondo. Contamination withstand voltage characteristics of polymer insulators. In: *10th ISH*, Vol. 3, Montréal, Québec, Canada, 1997, pp. 81–84.

Monteith, A.C., Harder, E.L., and J.M. Clayton. Line design based upon direct strokes. In: *Electrical Transmission and Distribution Reference Book*. Westinghouse Electric Corporation, East Pittsburg, PA: Westinghouse Electric Corporation, 1964, pp. 578–609, Chapter 17.

Morcos, I. and F.A.M. Rizk. A surface chemistry approach to the study of solid electrodes in insulating liquids. *IEEE Transactions on Electrical Insulation* EI-12(4): 309–312, August 1977.

Näcke, H. Stabilität der Fremdschichtenladungen und Theorie des Fremdsschichtüberschlags, ETZ-A, No. 16, pp. 577–585, 1966.

Naito, K. and H. Nagasaka. Discussion of (Karady, 1975). *IEEE Trans*. PAS-94(2), 1975.

Nasser, E. Zum Problem des Fremdschictüberschlages an Isolatoren. *ETZ* 83: 356–365, 1962.

Nasser, E. Some physical properties of electrical discharges on contaminated surfaces. *IEEE Transactions on Power Apparatus and Systems* PAS-87(4): 957–963, 1968.

Nasser, E. Contamination flashover of outdoor insulation. *ETZ-A* 93(6): 321–325, 1972.

Neumärker, G. Verschmutzungszustand und Kriechweg, Monatsber. *Deutsche Akad. Wiss, Berlin* 1: 352–359, 1959.

Obenaus, F., Böhme, H., Fiebig, R., Hoppadietz, F., and D. Rösler. Elektrische Isolatoren und Isolerungen. In: *Taschenbuch Elektrotechnik*, Vol. 2. Starkstromtechnik. Berlin, Germany: VEB Verlag Technik, 1965.

Papaliou, K.O. and F. Schmuck. *Silicon Composite Insulators, Materials, Design, Applications*. Berlin, Germany: Springer-Verlag, 2013.

Paris, L. and R. Cortina. Switching and lightning impulse discharge characteristics of large air gaps and long insulator strings. *IEEE Transactions on Power Apparatus and Systems* PAS-87(4): 947–957, April 1968.

Phillips, A.J., Childs, D.J., and H.M. Schneider. Water drop corona effects on full-scale 500 kV non-ceramic insulators. *IEEE Transactions on Power Delivery* 14(1): 258–265, January 1999.

Pigini, A. and A. Tomba. Setup of a method to evaluate the surface hydrophobicity of insulators. In: *8th International Symposium on High-Voltage Engineering*, Yokohama, Japan, 1993, Paper No. 41-03.

Raghuveer, M.R. and E. Kuffel. Experimental and analytical studies of factors which affect flashover voltage of polluted insulation surfaces. *IEEE Transactions on Power Apparatus and Systems* PAS-74: 312–320, January/February 1974.

Rizk, F.A.M. Flashover characteristics of insulators and spark-gaps with a power frequency half-cycle pulse, Thesis, Royal Institute of Technology, Stockholm, Sweden, 1960.

Rizk, F.A.M. Analysis of dielectric recovery with reference to dry-zone arcs on polluted insulators. In: IEEE Conference Paper No. 71 CP 134-PWR, presented at the *IEEE Winter Power Meeting*, New York, January 31–February 5, 1971.

Rizk, F.A.M. Electrical resistance of an insulating surface under artificial rain. *Proceedings of IEE* 121(2): 154–160, February 1974.

Rizk, F.A.M. Mechanism of insulator flashover under artificial rain. *Proceedings of IEE* 122(4): 449–454, April 1975.

Rizk, F.A.M. Mathematical models for pollution flashover. *Electra* 78: 71–103, October 1981.

Rizk, F.A.M. A systematic approach to high-voltage insulator selection for polluted environment. In: *Second Regional Conference of CIGRE Committees in Arab Countries*, Amman, Jordan, Keynote Session #2, 1997.

Rizk, F.A.M. and M. Bourdages. Influence of AC source parameters on flashover characteristics of polluted insulators. *IEEE Transactions on Power Apparatus and Systems* PAS-104(4): 948–958, July 1985.

Rizk, F.A.M., El-Arabaty, A., and A. El-Sarky. Laboratory and field experience with EHV transmission line experience in the desert. *IEEE Transactions on Power Apparatus and Systems* PAS-94(5): 1170–1176, September/October 1975.

Rizk, F.A.M., El-Sarky, A.A., Assaad, A.A., and M.M. Awad. Comparative tests on contaminated insulators with reference to desert conditions. CIGRE, Paper No. 33-03, Paris, France, 1972.

Rizk, F.A.M. and N. Hyltén-Cavallius. Wetting of high-voltage insulators by artificial rain. In: IEEE Conference Paper C74 074-1, *Winter Power Meeting*, New York, 1974.

Rizk, F.A.M. and D.H. Nguyen. AC source-insulator interaction in HV pollution tests. *IEEE Transactions on Power Apparatus and Systems* PAS-103(4): 723–732, April 1984.

Rizk, F.A.M. and D.H. Nguyen. Digital simulation of source-insulator interaction in HVDC pollution tests. *IEEE Transactions on Power Delivery* PWRD-3(1): 405–410, January 1988.

Rizk, F.A.M. and A.Q. Rezazada. Modeling of altitude effects on AC flashover of polluted high-voltage insulators. *IEEE Transactions on Power Delivery* PWRD-12(2): 810–822, April 1997.

Rizk, M.S., Nosseir, A., Arafa, B.A., Elgendy, O., and M. Awad. Effect of desert environment on the electrical performance of silicon rubber insulators. In: *10th ISH*, Montréal, Québec, Canada, 1997, Vol. 3, pp. 133–136.

Rosen, S.L. *Fundamental Principles of Polymeric Materials for Practicing Engineers*. New York: Barnes & Noble Inc., 1971.

Rouse, H. *Fluid Mechanics for Hydraulic Engineers*, Dover Publications, New York, pp. 210–213, 1961.

Schneider, H.M. *Insulation for HVDC Transmission Lines*. EPRI HVDC Reference Book, Chapter 5, EPRI, Palo Alto, September 1993.

STRI. Hydrophobicity classification guide, Swedish Transmission Research Institute, 1992.

Taniguchi, Y., Arai, N., and Y. Imano. Natural contamination test of insulators at Noto testing station near Japan Sea. *IEEE Transactions on Power Apparatus and Systems* PAS-98(1): 239–245, January/February 1979.

de Tourreil, C., Roberge, C., and P. Bourdon. Long-term mechanical properties of high-voltage composite insulators. *IEEE Transactions on Power Apparatus and Systems* PAS-104(10): 2918–2921, 1985.

Vaillancourt, G.H. and F.A.M. Rizk. Apparatus for detecting defective insulators in an insulating column supporting an electrical conductor in a power circuit line. US Patent 4760343, July 26, 1988.

Verma, M.P. Höchster Ableit-Stromimpuls als Kenngrösse fur das Isolierverhalten Verschmutzter Isolatoren. *ETZ-A*, 94: 302–303, 1973.

Vlastos, A.E. and E. Sherif. Experience from insulators with RTV silicon rubber sheds and shed coatings. *IEEE Transactions on Power Delivery* 5(4): 2030–2038, October 1990.

Vosloo, W.L., Macey, R.E., and C. de Tourreil. *The Practical Guide to Outdoor High-Voltage Insulators*. Johannesburg, South Africa: ESKOM, 2004.

Wilkins, R. Flashover voltage of high-voltage insulators with uniform surface-pollution films. *Proceedings of IEE* 116(3): 457–465, March 1969.

Wilkins, R. and A.A.J. Al-Baghdadi. Arc propagation along an electrolytic surface. *Proceedinhd of IEE* 118(12): 1886–1892, December 1971.

Witt, H. *Insulation Levels and Corona Phenomena on HVDC Transmission Lines*. Gothenburg, Sweden: Chalmers University Books, Gumperts, 1961, p. 45.

Wittenzellner, Th. Klimatische Einflüsse auf das Isoliervermögen von Freiluftisolatoren. *Elektrizitätswirtschaft* 61(8): 212–217, 1962.

Woodson, H.H. and A.J. McElroy. Insulators with contaminated surfaces. Part II: Modeling of discharge mechanisms. *IEEE Transactions on Power Apparatus and Systems* PAS-89(8): 1858–1867, November/December 1970.

Young, J.F. *Materials and Processes*, 2nd edn. New York: John Wiley & Sons Inc., 1954.

11

High-Voltage (Underground) Cables

In spite of their economic advantage and wide application, overhead transmission lines suffer two inherent drawbacks:

1. Their exposure to atmospheric conditions that may considerably hamper their performance and therefore has to be taken into account in their design.
2. Their rather large insulation clearances, which result in line towers of considerable sizes, require large corridors for the entire length of the line.

High-voltage cables provide answers to these drawbacks by providing

- A contained insulating environment that ensures stable operating conditions and protects the insulation against atmospheric conditions
- Compact dimensions that compare advantageously with overhead lines, even at high voltages

This comes, however, at a substantially higher price, an order of magnitude compared to that of the overhead lines, and has also their own drawbacks. As a result, the use of high-voltage cables is limited to particular applications when the constraints, either natural (water crossings, mountains, etc.) or social (restrained space, city environment, etc.), exclude the application of overhead lines.

11.1 Development of High-Voltage Cables

The interest in high-voltage cables dated back to the beginning of the twentieth century—the first high-voltage cable was developed by S. de Ferranti in 1891—and contributed to sustain their constant evolution towards higher voltages and power transmission capacities. Unlike overhead lines, the development of high-voltage cables has a wide diversification depending on the development of new insulating materials and competition between different cable technologies. Actually, high-voltage cables exist in one of the three categories, identified by the mode of insulation: impregnated paper–oil, solid (extruded), and compressed gas–epoxy.

11.1.1 Paper–Oil-Insulated Cables (Couderc, 1987)

Introduced in 1891 by S. de Ferranti, the insulation by paper impregnated with ozokerite, a by-product of the candle wax, offers an elegant solution to the problem of cable insulation and is precursor to the paper–oil insulation used in modern cables. The paper–oil insulation suffered, however, of partial discharges (PDs) developing in the voids formed between the layers of paper tapes, which caused premature failures of the initial cables using this type of insulation. For many years, the utilization of these cables was limited to voltages below 30–35 kV. The use of pressurization with nitrogen at pressures of 1.1–1.38 MPa (160–200 psi) partly solved the PD problem and gave rise to the pressurized-gas paper-impregnated cable developed in 1943. This solution reached its full potential only with the introduction of lapped paper for the flexibility of the cable and pressurized fluid oil, introduced by Emmanuelli in 1926, to improve the dielectric performance, namely, by the elimination of voids containing air (or gas), constituting sites of PDs responsible for the slow degradation of the impregnated paper insulation. Figure 11.1 gives an overview of the development of cables with pressurized insulation made of lapped impregnated paper. The bold characters indicate the current types of cable.

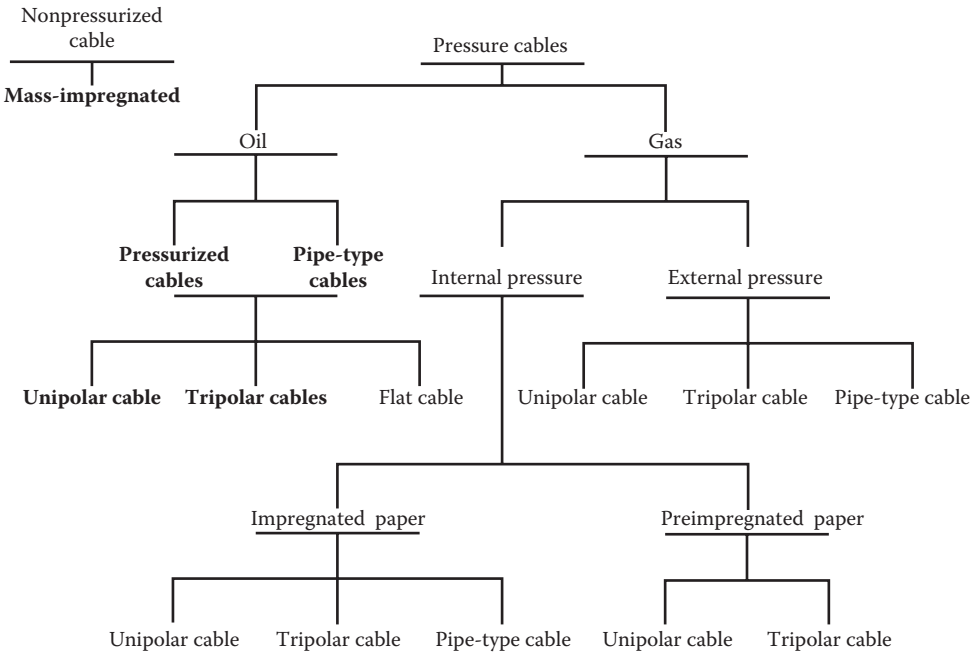
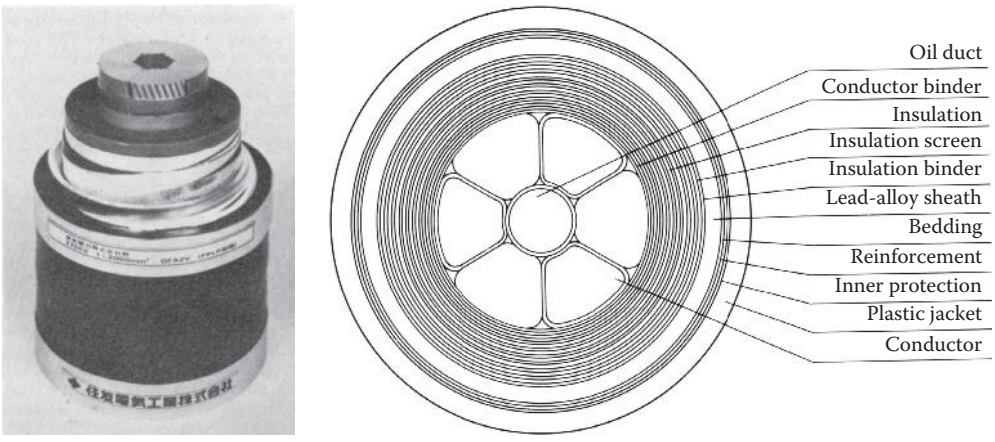


FIGURE 11.1 Cables with pressurized lapped paper insulation. (Couderc, D. Revue de l'État des Technologies des Câbles de Transport a Très Haute tension en Courant Alternatif et Continu, IREQ report, IREQ, Varennes QC, Canada, November 1987.)

11.1.1.1 Pressurized Oil-Filled Paper-Impregnated Cables

Pressurized oil-filled paper-impregnated cables are presently the most widely used because of their proven reliability, their availability over a wide range of voltages and power transmission capability, and above all, the long experience of manufacturers and users with this type of cable. Two main categories of paper–oil insulation exist for ac cables: self-contained oil-filled (SCOF) and high-pressure oil-filled (HPOF).

Self-contained oil-filled cable: In SCOF cables with internal oil pressure (Figure 11.2), the hollow conductor is filled with pressurized oil, typically at 450 kPa, which diffuses from the center to the insulation periphery. The latter comprises several layers of paper tapes of high purity, with a thickness varying from



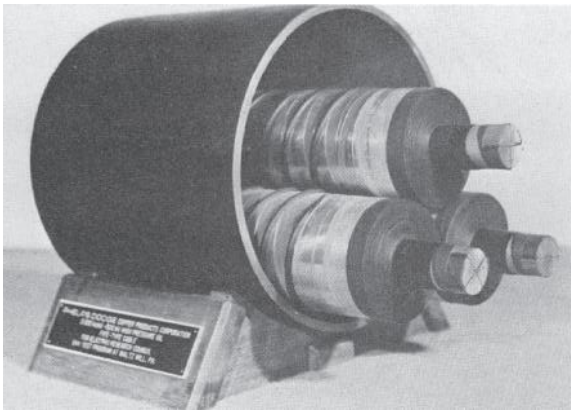
(a) (b)

FIGURE 11.2 Single-phase oil-filled cable. (a) SCOF cable; (b) schematic representation. (From Kubo, H. et al., *IEEE Trans*., PAS-101(12), 4472, 1982.)

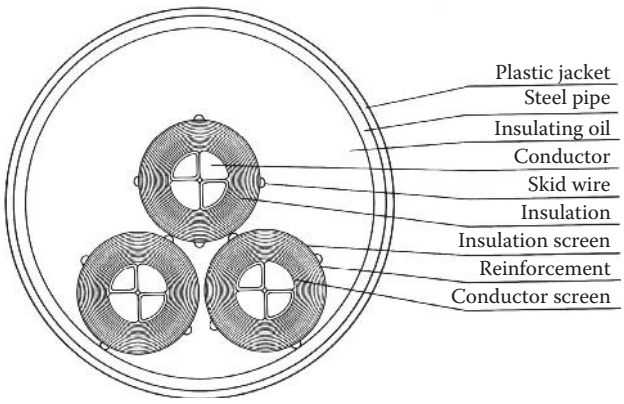
25 to 250 μm and width that varies with the distance from the conductor. An outer metal sheath maintains the oil pressure in the cable and protects the insulation against contamination. The SCOF cable is predominantly used in high-voltage cable circuits worldwide, at voltages up to 500 kV ac and ±500 kV dc.

Impregnation of paper insulation is made by filling the central channel with oil of low viscosity, allowing the oil to diffuse across the cable insulation during thermal cycles. This is done by connecting the central channel to sealed underground reservoirs with expansion bellows to compensate the variations in the oil volume during the thermal cycles of the cable while maintaining a constant pressure in the oil. The majority of existing cables use mineral oil as impregnating fluid. The introduction of synthetic oils has gradually changed the situation in favor of the latter as impregnating oil in paper–oil cables. In the 1960s, it was dodecylbenzene (DDB); more recently, *alkylate* oils like the decylbenzene (DB) and the *nonylbenzene* (NB) are becoming popular due to their low viscosity and good capacity to absorb water vapor liberated during aging of cellulose fibers. SCOF cables are widely used in Europe where cable circuits operate at voltages of 400 and 500 kV. In North America, 525 kV is the highest voltage reached by SCOF cables (Bellport, 1970). Sections of 750 kV cables have been successfully tested. The maximum admissible transmission power can reach, with forced cooling, the level of 10,000 MVA at 1,100 kV ac (Farnetti et al., 1984b).

High pressure oil-filled cables: In HPOF cables with external oil pressure, three or more paper-taped cables are placed inside a rigid steel pipe maintained under oil pressure (Figure 11.3). Each of the elementary cables is of similar structure to those in SCOF cables, except for the viscous impregnating fluid. The insulation, also of taped cellulose paper, is covered with a metal screen, which fixes the potential at the periphery of the cable, while protecting the insulation against humidity during storage and cable laying.



(a)



(b)

FIGURE 11.3 Three-phase oil-filled cable. (a) HPOF pipe-type paper–oil cables; (b) schematic representation. (From McKean, A.L. et al., IEEE Trans., PAS-90(1), 224, 1971.)

Maintaining an external oil pressure does not require a central channel for the oil circulation. The cables and their paper insulation are impregnated in factory. To facilitate cable laying into the pipe, sliding wires with D-shape cross section, of metal or high-density polyethylene (PE), are wound in long pace around each elementary cable. HPOF cables are widely used in North America up to voltages of 345 kV. Cables of 550 kV are available, and tests have been made on sections of 765 kV (Allam et al., 1986).

In spite of the various options used by different cable manufacturers, paper–oil insulation has the following typical characteristics: a relative permittivity of 3.5, a loss factor between 0.3% and 0.5%, and a thermal resistivity of about 500 m°C/W. The oil pressure is between 520 and 620 kPa (75–90 psi) for SCOF cables and about 1.38 MPa (200 psi) in pipe-type cables. This difference in the oil pressure gives pipe-type cables a slightly better dielectric performance, of around 10%, as compared to SCOF cables.

The principal limitation of impregnated paper–oil insulation resides in their high dielectric losses, which tends to favor thermal breakdown. Thermal breakdown can occur even if the high-voltage cable does not carry any current, and the sheath is at ambient temperature, making their utilization at voltages above 800 kV ac almost impossible. This, even if a prototype 1100 kV ac cable by Pirelli, has successfully passed a long-duration demonstration program by *ENEL*. The 1100 kV ac cable is, in fact, a 750 kV ac cable for which the internal oil pressure was increased to 1.3 MPa to enhance the operating gradient to 30 kV/mm. The length of the test cable, at Suvereto, was about 200 m, comprising joints and terminations as well as an external cooling system (Farnetti et al., 1984).

Practical experience shows that paper–oil insulation develops permanent deformations at temperatures higher than 120°C, and it is not recommended to operate the cable at 100°C, corresponding to a temperature difference of about 80°C between the central conductor and the sheath. The current practice favors a range of operating temperature of 70°C–90°C for paper–oil-insulated cables.

11.1.1.2 Mass-Impregnated Cables

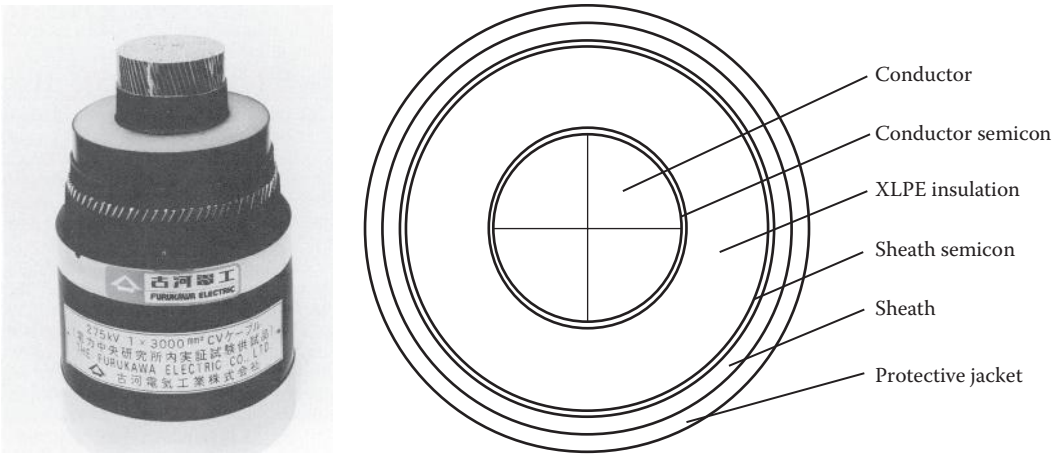
Mass-impregnated cables use an impregnating material, which is viscous at ambient temperature and gives the impression of a solid insulation when the cable is dissected. Under load condition, where the cable heats up, the impregnating material liquefies and diffuses into the paper insulation. However, the dilatation of the materials sustains a temporary pressurization, which disappears when the cable cools down, producing gaseous voids in the butt gaps. The existence of gas voids, which becomes PD sites, is a major handicap in ac voltage application, limiting its use to voltages below 63 kV ac. The effect of gas voids is somewhat less severe in dc voltage where the utilization of mass-impregnated cable extends up to voltages of 400 kV dc and is under consideration for the level of 500 kV dc. They are presently the only candidate for long submarine crossings where the cables are subjected to considerable hydrostatic pressures and a serious competitor to internal oil pressure cables, even at high-voltage levels.

11.1.2 Extruded Insulation Cables

The first application of solid insulation in high-voltage cables dates back to 1888 with the use of vulcanized rubber. The low dielectric strength of the rubber however limits its use to low-voltage cables. The copolymerization of synthetic rubber with ethylene and propylene improves the dielectric performance of rubber while keeping good flexibility and high deformation temperature up to 135°C. The use of EPR is limited to voltages below 100 kV.

The principal breakthrough in solid insulation cables was obtained by the use of polymers PE and XLPE. Practical experience shows that the extrusion of polymers in thick layers is delicate to ensure that the insulation is free of voids and solid impurities, which can initiate PDs, particularly damaging to both PE and XLPE. The development of extruded cables was largely dependent on progress realized in the techniques of extrusion and quality control processes. From a nominal voltage of 25 kV in the 1960, extruded cables have reached the level of 225 kV ac and then 400 kV ac in 1986 with the commissioning of an EDF cable system using natural PE of SILEC (Jocteur et al., 1986).

Figure 11.4 illustrates the typical construction of the solid insulation cable. The central copper conductor has a cross section chosen for the required power transmission capacity. The PE insulation is coextruded in sandwich between two layers of semiconducting (carbon-filled) PE to ensure good adhesion between the different layers and, thus, minimize the risk of separation of the layers during thermal



(a) (b)

FIGURE 11.4 Polymer-insulated cable. (a) XLPE-insulated cable; (b) schematic representation. (From Fukuda, T., *IEEE Electric. Insul. Mag.*, 4(6), 15, 1988.)

cycles. A lead sheath covers the insulation to protect against the water infiltration. Finally, a PVC protective jacket is extruded on the lead sheath to protect against corrosion.

Cross-linked polyethylene (XLPE), more economical than PE with better mechanical properties and a higher operating temperature (90°C compared to 65°C–70°C for PE), is widely used in low and medium voltages. Improved methods of manufacture have provided a high homogeneity of the insulating material, minimizing migration of impurities and simplicity of manufacture that allowed XLPE cable to reach the level of 500 kV ac in the 1990's with the commissioning of 500 kV cable system by Tokyo Electric Power Co.

11.1.3 Cables with Gas Insulation

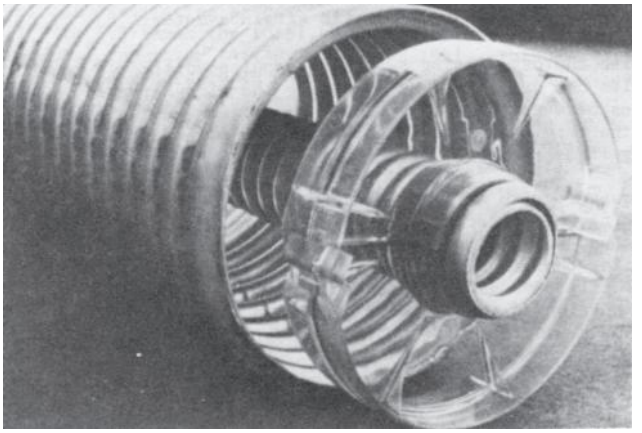
11.1.3.1 Pressurized-Gas Cables

The first application of compressed gas insulation was introduced to minimize the effect of voids on the dielectric strength of the paper–oil insulation. The individual cables with paper–oil insulation are placed in an external envelope capable to sustain a high gas pressure, usually nitrogen at a pressure of 1100–1380 kPa (160–200 psi). Pressurizing the paper–oil insulation reduces the size and increases the inception voltage of PDs in the gas voids, thus improves the dielectric performance of the insulation. These cables are used mainly in submarine crossings; two important achievements are as follows: the three-phase link of British Columbia to Vancouver Island using unipolar 138 kV cables, with a hollow conductor for the gas to propagate over long distance. The other is the 48 km crossing at the strait of Cook, in New Zealand, with a 600 MW, 250 kV dc link.

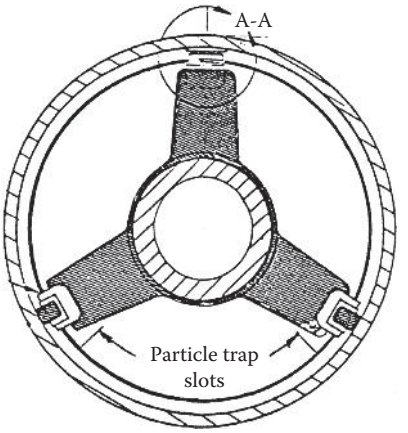
The rapid development of the SCOF and pipe-type cables has made pressurized-gas cables less appropriate for ac voltage, while for dc voltage, they are replaced by nonpressurized mass-impregnated cables. Obviously, it is much more difficult to maintain a gas pressure of 1400 kPa than an equivalent oil pressure. This situation also favors the development of the rigid gas-insulated cables, also known as gas-insulated lines (GIL), because of the rigid structure of the cable.

11.1.3.2 Rigid Gas-Insulated Cables (Lines)

Gas insulation, because of its less competitive dielectric strength, has traditionally been neglected by the cable industry, for which compactness and flexibility are the key parameters. In effect, even with a clearance distance of 1/10 of air insulation, SF_6-insulated cables operating at 4–5 atm abs are still several times larger than conventional paper–oil-insulated cables of the same voltage rating. Instead, it is the combination of the good arc-quenching propriety of SF_6, its adequate insulating performances, and



(a)



(b)

FIGURE 11.5 Gas-insulated cables. (a) Flexible SF_6-insulated cable; (b) rigid cable with tripod spacer. (From Cookson A.H., *IEEE Trans. Electr. Insul*., EI-20, 859, 1985.)

above all, its nonflammability, which promotes development of SF_6-insulated switchgear, at first as single pieces of equipment and then their integration into a full-scale substation.

It is only when the development of gas-insulated stations (GISs) has reached 345 kV that gas-insulated cables, with their high power transmission capacity with critical length comparable to that of overhead lines and hence its designation as GIL and low dielectric losses, gain their competitive edge over conventional cables. The combination of compact GIS with long gas-insulated cables provides an elegant solution to transmit the output power of underground generating stations to overhead lines, which has been used by several utilities (Cookson, 1985). It reached 420 kV in Europe (Wehr station) and 500 kV ac level in Japan and in North America: the underground link in the Cascades (United States) in 1975 (De Maris, 1975) and the Mica project of BC Hydro in 1976. Short lengths of 800 kV ac cables are operating in the Guri Central in Venezuela since 1984.

The design of rigid gas-insulated cables is relatively simple: insulating spacers maintain the metal conductors in place within a cylindrical tube, containing compressed SF_6, at 0.3–0.5 MPa. To make gas-insulated cables more competitive, flexible and semiflexible cables have been evaluated. The conductor is composed of aluminum strands, the outer sheath is of corrugated aluminum, and spacers, in greater number, are molded from more economic plastic shown in Figure 11.5. A short length of a 1200 kV ac flexible gas-insulated cable has been tested by EPRI in the 1990s (Bolin et al., 1982; Gnadt and Walldorf, 1995).

11.1.4 Future Trends in High-Voltage Cables

With the current trend for high-voltage power transmission systems to 1200 kV ac in Russia and China and ±800 kV dc in China, development of high-voltage cables will turn to improve the current technology to make them more economical to produce and operate, namely, to increase the power transmission capability and to reduce dielectric losses.

11.1.4.1 Forced Cooling

Forced cooling can almost double the power transmission capacity of cable circuits. Table 11.1 illustrates, in effect, the potential ac power transmission capacity reached by high-voltage cables with appropriate forced cooling technologies (Morello et al., 1985). The adaptation to forced cooling requires the installation of a channel for the circulation of the cooling liquid and stations of heat exchange at regular intervals, a few kilometers, along the cable circuit. Early installations of forced cooling used water circulating in conduits installed in parallel to the cables. The current trend is to circulate the cooling fluid in a channel within the conductor. Oil-filled cables, both SCOF and HPOF, are easily adapted to forced cooling with the insulating oil serving at the same time as cooling liquid. Forced cooling of solid XLPE insulation cable with water circulating in a central channel was evaluated in Japan in 1987 (Kobayashi et al., 1985; Ogawa et al., 1989).

TABLE 11.1

Power Transmission Capacity (in MVA) of HVAC Cables with Forced Cooling

Cable	Cooling	Length, km	110 kV	220 kV	400 kV	800 kV	1000 kV
SCOF	Ext./Water	0.5	1,700	3,500	5,000	5,000	
SCOF	Ext./Water	2.5	800	1,500	2,200[a]	2,200	
SCOF	Surf./Water	0.5	2,300	4,500	6,500	6,500	4,500[a]
SCOF	Surf./Water	2.5	1,000	1,900	2,900	2,900	2,000
SCOF	Cond./Oil	0.5	3,500	7,000	10,000	10,000	6
SCOF	Cond./Oil	2.5	1,000	2,000	3,000[a]	3,000	2,600
SCOF	Cond./Water	0.5	4,700	10,000	10,000	10,000	10,000[a]
SCOF	Cond./Water	2.5	1,400[a]	3,000	3,000	3,000	3,000
HPOF	Surf./Oil	0.5	1,200	2,400	3,200	4,200	10,000
HPOF	Surf./Oil	2.5	550	1,100	1,500[a]	2,000[a]	3,000
PE	Cond./Water	0.5	2,500	5,000			
PE	Cond./Water	2.5	750	1,500[a]			
XLPE	Cond./Water	0.25			1,500[b]		
SF_6	N/A		1,400	3,000	7,000[a]	13,000	18,000[a]

Source: Morello et al. 1985.

[a] Values obtained by measurement or by calculation.

[b] Results from long-term tests on 275 kV cable.

The use of forced cooling may cause certain problems related to the overheating of cable joints, their insulation built in site, that are generally thicker and dissipate the generated heat less efficiently.

11.1.4.2 Synthetic Paper and Tape

The main limitation of oil-impregnated paper cables resides in their high dielectric losses, which makes their use at voltages higher than 800 kV ac almost impossible. Several attempts to reduce the dielectric losses have been made, using synthetic tapes, polypropylene films, and composite films formed of a polypropylene film in sandwich between two cellulose tapes. Table 11.2 gives the main characteristics of these synthetic insulations, considered for use in high-voltage cables. Among many candidates investigated, the polypropylene paper laminate (PPL) composed of a polypropylene film inserted between two *kraft* paper tape layers, the total thickness of the PPL tape being comparable to that of an equivalent paper tape, stands out as the most promising. The PPL represents a good compromise between the required mechanical qualities of the cellulose paper and the excellent electric properties of polypropylene. It can be seen from Table 11.2 that the PPL is superior concerning the dielectric constant, the losses, and the dielectric strength in ac and impulse voltages. PPL–oil-insulated cables are in service in Japan at 275 kV

TABLE 11.2

Characteristics of Synthetic Lapped Insulation

Parameters	Units	PPL	Polypropylene	Kraft
Thickness	mm	100	125	100
Resistance to traction	MN/m^2	76	22–35	110
Elongation at rupture	%	2.7	4–6	3.1
Density		0.9	0.75	0.95
Relative dielectric constant		2.7	2.2	3.4
Loss factor tanδ		8×10^{-4}	3×10^{-4}	2.3×10^{-3}
Positive impulse	kV/mm	190		135
Negative impulse		150		135
AC dielectric strength	kV_{rms}/mm	55	60	50
Permeability to air	Gurley-s	3,000	15,000	

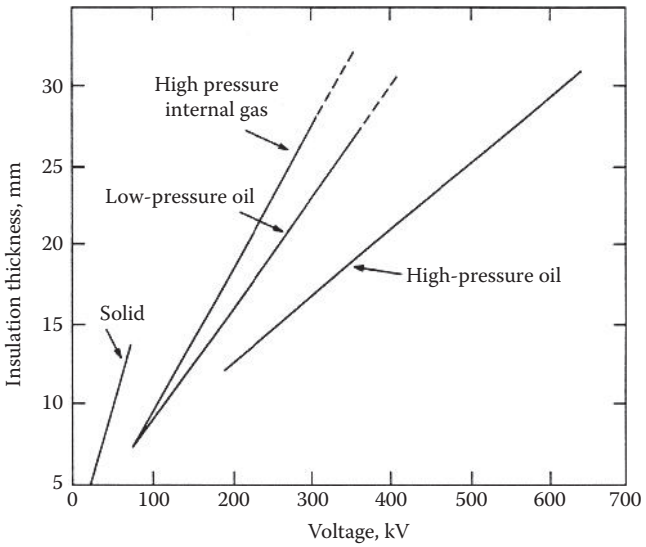


FIGURE 11.6 Influence of the pressure on the insulation thickness of different types of ac cables. (From Couderc, D. Revue de l'État des Technologies des Câbles de Transport a Très Haute tension en Courant Alternatif et Continu, IREQ report, IREQ, Varennes QC, Canada, November 1987.)

since 1980 and 525 kV since 1985. In the United States, a pipe-type PPL–oil-insulated cable of 345 kV is in service since 1985, while a prototype of 765 kV is under evaluation by Phelps Dodge (Cablec).

11.1.4.3 Pressure

Figure 11.6 illustrates the influence of pressure on dielectric strength and thickness of the insulation of different types of cables. It can be seen that pressurized-gas cables cannot compete with oil-filled cables due to the lower dielectric strength of gases. The higher the internal pressure of the cable, the higher the operating gradient can be. This gradient is 10–12 kV/mm for low-oil-pressure cables (≤500 kPa). It increases to 15–28 kV/mm for higher oil pressures up to 1500 kPa in cables of 400 kV and higher. As for the nonpressurized mass-impregnated cable, the presence of gas voids as PD sites limits its use to dc voltages only, particularly in applications requiring the immersion of great lengths of cables, when they are subjected to considerable hydrostatic pressures.

11.1.4.4 Compressed SF_6-Insulated Cable

Penalized by its relatively large size, compressed SF_6-insulated cables offer an alternative to transmission of large bulk power at high voltage, above 500 kV ac, where the dielectric losses become a serious drawback to oil-filled cables. The low losses of SF_6-insulated cables allow their use over long distances up to several hundreds of kilometers without compensation. Their large size also minimizes the need of forced cooling and allows operating at close to their natural power transmission capacity.

11.2 High-Voltage AC Cables and Accessories

Electric field distribution: High-voltage ac cables, those operating at EHV levels in particular, are single-core, coaxial configuration. The field distribution in the cable insulation is

$$E(r) = \frac{U}{\ln(b/a)} \frac{1}{r} \tag{11.1}$$

where a and b are the radii of the center conductor and envelope.

The following expressions are for the field at the central conductor E_0 and at the outer sheath E_s:

$$E_0 = \frac{U}{\ln(b/a)}\frac{1}{a} \tag{11.2}$$

$$E_s = \frac{U}{\ln(b/a)}\frac{1}{b} \tag{11.3}$$

11.2.1 Cable Parameters

A number of parameters characterize ac cable in coaxial configuration, relating their physical dimensions to their electrical parameters as follows:

The cable capacitance C per unit length is

$$C = 2\pi\varepsilon\frac{1}{\ln(b/a)} \quad \text{F/m} \tag{11.4}$$

The cable inductance L per unit length is

$$L = \frac{\mu}{2\pi}\ln\frac{b}{a} \quad \text{H/m} \tag{11.5}$$

The propagation velocity of electromagnetic wave is

$$v = \frac{1}{\sqrt{LC}} = \sqrt{\frac{1}{\mu\varepsilon}} \quad \text{m/s} \tag{11.6}$$

Characteristic impedance Z_0 is

$$Z_0 = \sqrt{\frac{L}{C}}\ \Omega \tag{11.7}$$

Natural transmission capacity P_p is

$$P_p = \frac{U_p^2}{Z_0}\ \text{MVA} \tag{11.8}$$

where

P_p is the natural transmission capacity per phase of the line (MVA)
U_p is the nominal phase-to-ground voltage (kV)
ε is the permeability
μ is the susceptibility

Because of the excellent dielectric performance of cable insulation systems, the insulation thickness is often less than the optimal value for a minimum gradient at the central conductor. The capacitance is in the range of a few tens of pF/m, and the cable characteristic impedance a few tens of Ohms, compared to a value of a few hundreds of Ohms for overhead lines. As a result, high-voltage cables have a natural power transmission capacity many times higher than an overhead line operating at the same voltage.

Effective power transmission capacity P_l *and critical length* L_l: For overhead lines, the natural transmission capacity is a determining parameter; it is much less so for high-voltage cables, where the high dielectric losses combined with the low efficiency of heat transfer of the soil limit the load current to an effective value I_L. Except for the case of unburied gas-insulated cables, power transmission of

high-voltage cables is reduced considerably below their natural transmission capacity defined from Equation 11.7, according to

$$P_L = U_p I_L \tag{11.9}$$

and the critical length to

$$L_c = \frac{I_L}{\omega C U_p} \tag{11.10}$$

SF_6-insulated cables, with their low permittivity and high ampacity, have longer critical lengths, reaching several hundreds of kilometers. Solid polymer-insulated cables follow with critical lengths in the range of a few hundreds of kilometers. The impregnated paper–oil-insulated cables, penalized by a high permittivity and notable dielectric losses, have a critical length of a few tens of kilometers only. However, except for submarine link, which can reach several tens of kilometers, cable circuits are usually part of a larger overhead line transmission system, and their lengths are kept to minimum, in the range of a few kilometers.

11.2.2 Dimensioning of the Conductor

In spite of the wide variety of insulating materials and insulation systems available, the dimensioning of high-voltage cables follows a few general rules presented in the following for the selection of the conductor and cable insulation.

Table 11.3 compares typical characteristics of high-voltage cables. Although the natural load current I_n given by

$$I_n = \frac{P_n}{U_n} = \frac{U_n}{Z_0} \tag{11.11}$$

can be high, it may not correspond to the maximum admissible current in a high-voltage cable, determined by the limit temperature at which the cable can operate without danger. This limit temperature is in the range between 70°C and 85°C for most cables and provides an adequate safety margin below the temperatures causing thermal instability to the insulation, in the range of 100°C–135°C. For buried cables, a second limit temperature exists and corresponds to the local temperature of the soil, which must be maintained at a safe level, of about 85°C, to avoid drying of the soil and thermal runaway, which might follow.

It should be noted that often, a cable circuit is only a part of a transmission system largely composed of overhead lines, which determine both the load current and the nominal voltage for the cable circuit. Dimensioning the cable conductor consists of minimizing the total losses, taking into account the available heat dissipation system. The designing parameters are the resistive heat generated by the conductor, the dielectric losses in the cable insulation and sheath, and the characteristic of the thermal dissipation system. Since the insulation thickness is determined by the electrical stresses to the cable, its dielectric losses are a function of the conductor dimension. An iterative process results in which the cable conductor is varied to adjust the generated resistive heat to limit the maximum temperature at the conductor below the selected safe value. These aspects are discussed in the following.

Conductor design: To provide the required flexibility, the conductor, copper or aluminum, is built up from small metal strands. The conductor for SCOF cables is hollow to make up a channel for the circulation of the impregnating oil. Conductors of small section are made of several layers of copper or aluminum wires around a steel spiral to form the oil channel. Conductors of large section, above 800 mm^2 (1580 kcmil), use one of the two designs, *Conci* or *Milliken*.

The *Conci* design shown in Figure 11.7 uses strands of trapezoidal section, imbricated one to another to form a self-supporting arch. The conductor has several layers, three in the case of 800 mm^2 conductor, with the strands spiraled in opposite directions in two adjacent layers to provide better mechanical behavior. The *Conci* conductor provides a high degree of compactness, of about 98%, and forms naturally a channel for the circulation of the impregnating oil of SCOF cables. Hollow conductors are also

TABLE 11.3

Typical Characteristics of High-Voltage Cables

	Units	SCOF/HPOF	Polymer	SF_6 Insulation
Conductor				
Section maximum	mm^2	3040/1270	2500	
Radius	cm	3.5/2.5	3	10–25
Thickness	mm			12.7
Nominal field				
AC	kV_{rms}/mm	150/170		100
DC	kV/mm	270/310		150
Temperature	C	70–90	70	70–90
Ampacity	kA		0.6–1.5	4
Insulation				
Thickness	cm	0.5–2.5	2.5	10–25
AC dielectric strength	kV_{rms}/mm	50–55	16–25	
Impulse dielectric strength	kV/mm	95–135	50–75	
Relative dielectric constant		3.5	2.5	1
Loss factor		2.5×10^{-3}	3×10^{-4}	
Loss factor		8.8×10^{-3}	0.7×10^{-3}	
Thermal resistivity	m C/W	500	350	
Deformation temperature	C	120	90–135	105–135
Sheath				
Material		Lead, aluminum		Aluminum
Thickness	mm	6		5–10
Cable Parameters				
Capacitance	pF/m	200–500	150–250	55
Critical length	km	50–90	70–150	500
Soil Characteristics				
Thermal conductivity	W/m C	1–2.5		
Thermal resistivity	m C/W	100		

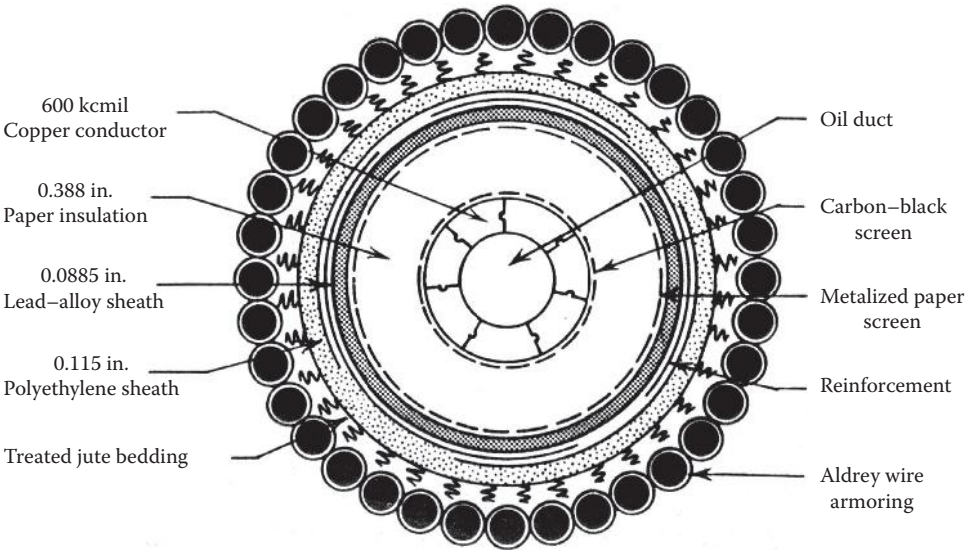


FIGURE 11.7 *Conci* conductors in pressurized oil-impregnated paper submarine cables. (From Gazzana Priaroggia, P. et al. The long island sound submarine cable interconnection, *IEEE Trans*., PAS-90(4): 1863, 1971.)

effective to counter skin effect in large conductors, and *Conci* conductors are quite effective to adjust the diameter of the oil channel to needs. Thus, a 1600 mm^2 *Conci* conductor reduces the skin effect from 10% to 6% for an increase of the channel diameter from 12 to 40 mm.

Regrouping the strands in segments is another means to counter the skin and proximity effect. The *Milliken* design (Figure 11.4) subdivides the conductor into segments, built up from small strands. The segments are disposed around a steel spiral to form the central channel, kept in place by bronze tapes. Each segment is formed of round wires highly compacted to increase the proportion of metal per unit area of the conductor's cross section. This technique provides a high degree of flexibility to the conductor and is particularly adapted to manufacturing conductors of very large cross section, up to 1300 mm^2, even for pipe-type and polymer cables where the central channel for oil circulation is not required. Increasing the diameter of the central channel of Milliken conductors has little impact on the losses by skin effect since the transposition of the insulated segments (Milliken patent) ensures a uniform distribution of the current within the conductor's cross section.

For gas-insulated cables, the conductor is generally an aluminum tube of appropriate cross section, the dimensions of which are defined by the electric field allowed at the surface of the conductor, while its thickness is optimized with respect to skin effect. An optimal ratio between the radii of the conductor and envelope is generally used. In the case of the semiflexible cable, the conductor is of stranded aluminum wires, while the outer envelope is of corrugated aluminum.

11.2.2.1 Energy Losses

Power transmission by high-voltage cables produces energy losses, which must be kept at an acceptable level. These losses come from different parts of the cable, namely, the conductor, the insulation, as well as the sheath (or pipe). The high power transmission capacity of modern cables requires conductors of very large sections, 3000 mm^2 being the actual limit. They must be economical and meet specific needs of different cable types: flexible, accommodating a channel for the circulation of oil, etc.

Conductor losses: The main source of energy losses comes from the flow of the load current in the conductor, according to

$$W = R_{ac}\, I^2 \tag{11.12}$$

R_{ac} is the ac resistance of the cable conductor, which can be expressed as

$$R_{ac} = R_{dc}\left[1 + K\left(Y_{pe} + Y_{pr}\right)\right] \tag{11.13}$$

where

R_{dc} is the dc resistance of the conductor
Y_{pe} is a factor related to the skin effect
Y_{pr} is a factor related to the effect of proximity
K is a factor characteristic of the type of cable: $K = 1$ for SCOF and 1.7 for HPOF cable

The high value of K in HPOF cable is due to the large magnetic field prevailing in the containing pipe. The dc resistance of the conductor, R_{dc}, is given by

$$R_{dc} = \frac{\rho_0}{S}\left[1 + \alpha_{20}\left(\theta_{cmax} - 20\right)\right]\left(1 + Z\right)(\Omega\ \mathrm{m}^{-1}) \tag{11.14}$$

where

ρ_0 is the resistivity of the metal at 20°C in Ω–m
S is the cross section of the conductor in mm^2
α_{20} is the coefficient of increment per °C at 20°C
θ_{cmax} is the maximum temperature of the conductor in C
Z is a factor related to the type of conductor ($Z = 0.04$ for large conductors)

Material: From Equation 11.14, it is evident that minimizing the resistive losses requires the use of metals of low resistivity. Among these, copper and aluminum are currently used. The abundance and the relatively light weight of aluminum make it more economical and provide a predominant place in the cable industry. Sodium is another candidate for conductor in high-voltage cables. Its abundance offers interesting possibilities to future high-voltage cables. Its malleability at ambient temperatures allows the sodium conductor to better adapt to deformations subjected to the solid insulation and explains, in part, the good performance of the first sodium cable in the Lima project (Graneau, 1976). However, the highly reactive nature of sodium limits the application of sodium conductor cable to specific cases.

Skin effect: It can be demonstrated that the resistance of a conductor is minimum when the current is uniformly distributed over the entire cross section of the conductor, obtained with dc current. Any operating condition, which modifies the uniformity of the current distribution, necessarily increases the resistance of the conductor and proportionally the resistive energy losses. Due to skin effect, the circulation of an ac current in a conductor forces the current towards the conductor surface. The current density follows an exponential law, having the maximum density at the surface of the conductor, according to

$$J(x) = J_0 \exp\left(-\frac{x}{\delta}\right) \tag{11.15}$$

where
- J_0 is the current density at the surface of the conductor
- δ is the penetration depth
- x is the distance below the conductor surface

The penetration depth δ is a characteristic of the metal and function of frequency f of the ac current, expressed as

$$\delta = \frac{1}{\sqrt{\pi \sigma \mu f}}$$

where
- σ is the conductivity of the metal
- μ is its permeability
- f is the frequency of the current

At power frequencies, the penetration depth in the metals currently used is in the range of centimeter.

The influence of skin effect is particularly significant on large conductors of a radius comparable to the penetration depth at power frequency, reaching 20% increase in the ac losses in a conductor of 1600 mm^2. As mentioned earlier, two approaches are currently used to minimize skin effect: hollow conductor in *Conci* design and segmentation of the conductor in *Milliken* design.

Effect of proximity: Current distribution in the conductors of ac cables, single or tripolar, is affected by the resulting magnetic field produced by current flow in the adjacent conductors, which modifies current distribution in the conductor's cross section, increasing its effective resistance, expressed by a proximity coefficient k_p. Significant proximity effect occurs in pipe-type cables where the high voltage cables are adjacent to one another. To counter proximity effect on the current distribution, the cable conductor is fragmented into segments, which are twisted in range to alternate the position of the cable segments with respect to the adjacent segments, thus redistributing the circulation of the current in the conductor's cross section.

Dielectric losses: Result from the movement of ions across the dielectric insulation and the deformation of the dielectric molecules due to polarization. Good insulating dielectrics leave few ions for the leakage current so that the dielectric loss W_d is mainly related to the polarization of the dielectric molecules, expressed as

$$W_d = UI \cos \varphi \tag{11.16}$$

where φ is the phase angle between the applied voltage U and the leakage current I.

With the following expression of the current, $I = \omega C U$, the dielectric losses can be expressed as

$$W_d = \omega C U^2 \cos\varphi$$

Noting that the angles φ and δ are complementary, for small dielectric losses, one has

$$\cos\varphi = \sin\delta \approx \tan\delta$$

$$W_d = \omega C U^2 \sin\delta \approx \omega C U^2 \tan\delta \tag{11.17}$$

The loss factor tanδ can be expressed as

$$\tan\delta = -\frac{1}{\omega C R} \tag{11.18}$$

where R and C are parallel elements of the insulation impedance.

Equation 11.17 indicates that dielectric losses are proportional to the square of the applied voltage, the cable capacitance per meter, and the frequency of the applied voltage. Gas insulation, less subjected to polarization, gives minimum dielectric losses, related mainly to the presence of epoxy spacers. Polymers, PE and its derivatives, have a loss factor in the range of $1–5 \times 10^{-4}$. Cross-linking of the PE doubles approximately the PE dielectric losses. Oil-impregnated paper insulation gives highest dielectric losses with a loss factor of about 3×10^{-3}.

Sheath and pipe losses: High-voltage cables are provided with a metal sheath to control the distribution of the electric field within the insulation and provide a protective screen against the ingress of humidity and other contaminants. For oil-filled cables, the sheath must also maintain the oil or gas pressure, in the range of 345–450 kPa (50–65 psi). Bronze, copper, aluminum, and lead are among the materials currently used in the manufacture of cable sheath. Lead, in particular, can be made in a continuous sheath to withstand high pressure and to serve as a barrier against infiltration of humidity into the cable insulation. The cable sheath can be made of metal tapes as in the pipe-type cables. Finally, for SF_6-insulated cables, the sheath is usually a rigid steel or aluminum tube, of length of a few tens of meters, fitted with flanges and O-rings at both ends to facilitate their mounting.

Although the cable sheath is not designed to carry load current, proximity of conductors, sheath, or other cables, as well as the multiple grounding points, can give rise to significant induced and ground return currents circulating in the sheath. Practical experience tends to show that significant energy losses are associated with the circulation of leakage currents, which affect the power transmission capacity of the cable.

Ground return current: Occurs when the metal sheath is grounded at more than one point and the low resistance of the metal sheath diverts part of the ground return current through the metal sheath. The ground return current can be significant in single-phase cables, especially if they are well spaced from one another. Grounding the cable sheath at one point only would eliminate the ground return current in the sheath. However, this can result in unacceptable voltage differences along the sheath.

Sheath transposition provides a simple and economical means to reduce the ground return current. Referring to Figure 11.8, showing three consecutive spans of a three-phase cable circuit, the cable sheaths are solidly grounded, at every three joints, and transposed at intermediate ones. Thus, the voltage induced to the cable sheath between two grounding points is the vector sum of three voltage drops Δu_j out of phase by 120° from each other. This voltage will be zero if the cable spans between two joints are equal, resulting in equal induced voltage drops Δu_j, and the ground return current in the sheath would be null. The induced voltage at the sheath increases linearly with the distance from the grounding point to a maximum value at the first intermediate joint; it remains constant between the two intermediate joints and reduces gradually to zero at the next grounding point. In practice, because of the unequal lengths of cable spans between two consecutive joints, the voltages drops Δu_j are not equal, although their vector sum remains small and minimizes the losses from the circulation of ground return current in the cable sheaths. Because of obvious difficulties, this method does not apply to submarine cables. Their sheaths are generally grounded only at both ends of the cable.

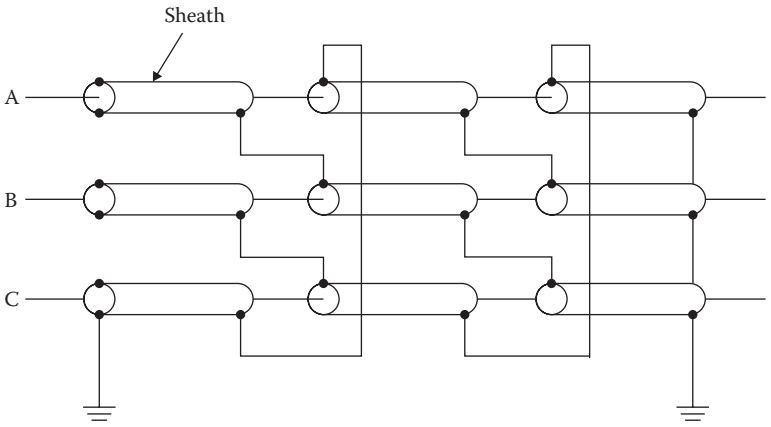


FIGURE 11.8 Cross-bonding transposition of cable sheaths.

TABLE 11.4

Losses (W/m) at Full Capacity of a Three-Phase Circuit Using SCOF Cables

Voltage, kV	Conductor	Sheath	Insulation	Total Losses
33	112.76	14.4	1.2	128.38
66	109.53	14.08	4.41	128.02
132	99.31	15.17	11.62	126.11
275	74.95	21.87	22.61	123.43
400	55.72	22.05	44.58	122.35

Source: Couderc, D. Revue de l'État des Technologies des Câbles de Transport a Très Haute tension en Courant Alternatif et Continu, IREQ report, IREQ, Varennes QC, Canada, November 1987.

Induced currents: Occur when the cable sheath is in proximity of current-carrying conductors and intercepts a part of the generated magnetic flux. The phenomenon is particularly pronounced with magnetic material sheath as in pipe-type HPOF cables. In this case, hysteresis of the metal produces additional losses. These losses by induced currents do not depend on the circuit configuration and can be comparable to the resistive losses in the conductor, thus limiting the transmission capacity of the pipe-type HPOF cables as compared to SCOF cables. Submarine cables are protected by a single- or double-layer armor formed of steel wires to sustain the mechanical stress during the cable laying or removal and protect the cable against mechanical impacts from ship anchors and commercial fishing equipment. Hysteresis losses comparable to those in the cable sheath may develop and reach sufficiently high levels to forbid the use of ferromagnetic materials in the manufacture of the armor.

Table 11.4 gives values of losses originating from different parts in a three-phase cable circuit, composed of three SCOF cables having aluminum conductors of 2000 mm^2 and located at 150 mm center to center from one another. The cables are buried directly in the soil at a depth of 1 m. Corrugated aluminum sheath is transposed and covered with protective PVC sheath (Tareev, 1975). It is noticed that the losses in the insulation increase rapidly with the voltage to reach about 36% of the total losses in a 400 kV cable. Therefore, the temperature rise in the conductor due to dielectric losses becomes a significant factor defining the transmission capacity of a high-voltage cable.

11.2.2.2 Thermal Dissipation

To avoid overheating of the high-voltage cable, it is necessary to ensure adequate dissipation of the losses generated by the cables to the ambient environment. Analysis of the thermal dissipation is made

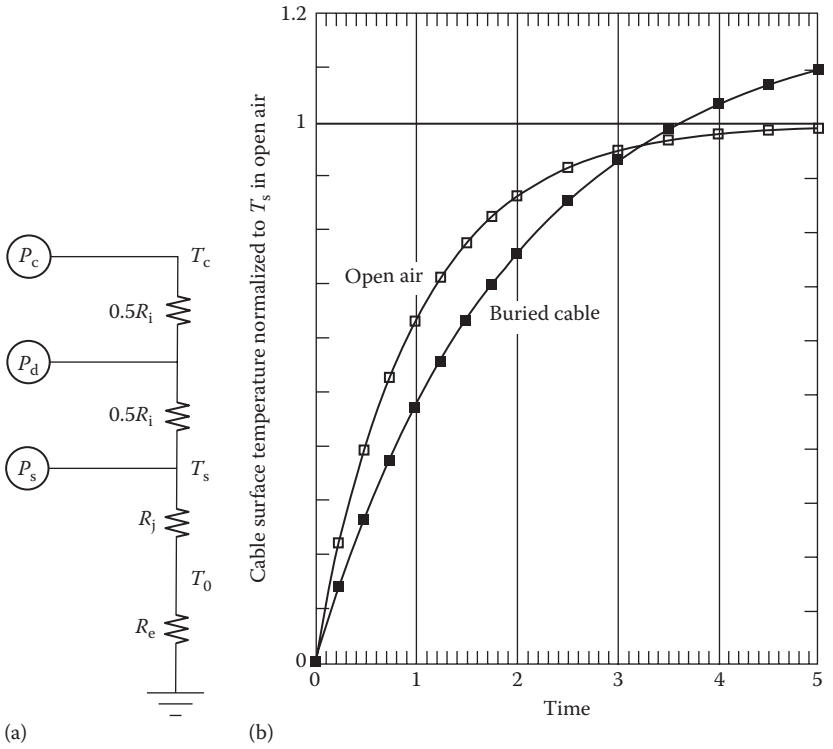


FIGURE 11.9 (a) Thermal equivalent circuit for a cable. (b) Transient responses to a step function energization.

with thermal circuits established from the characteristics of the cable and the soil. Figure 11.9a shows a typical thermal circuit of a buried cable. Thermal sources are identified to the conductor P_c, insulation P_d, and the covering sheath P_s. Thermal resistance of the insulation R_i is divided in two equal parts, separating the three thermal sources. R_j and R_e are thermal resistances of the jacket and soil. Thermal resistances of the metal parts—conductor, sheath, and pipe—are neglected. The solution of the thermal circuit in Figure 11.9a to a step function is of exponential type:

$$\theta(t) = T_f \left(1 - \exp\left(-\frac{t}{\tau}\right)\right)$$

where

θ is the temperature at the conductor
T_f is the terminal temperature
τ is the thermal time constant

Figure 11.9b compares the transient temperature rises of a cable in air with a buried cable following energization of the cable, represented by a step function. It can be seen that the problem is generally more critical to buried cables than those in ambient air: The terminal temperature is higher, and the thermal time constant is longer for the buried cables.

Ampacity: The solution of the thermal circuit determines the ampacity of the high-voltage cable or, inversely, the required dimensions of the conductor corresponding to its transmission capacity. This is out of cope for this book which deals with high voltage phenomena.

Fault conditions: Are rarely determining for dimensioning of cables; it is prudent, however, to verify the cable limits under these conditions. Fault currents expose the cable insulation to the risk of permanent damages, either by electromechanical impacts or by accrued heating of the cable. It is not recommended

to use automatic reclosure in circuits containing high-voltage cables to avoid multiple energization of the fault current. The ampacity of the conductor under fault conditions can be determined by calculating the temperature rise in the conductor according to

$$I_c^2 R_{ac} t_f = A_c \delta C_v \Delta T_c \tag{11.19}$$

where

I_c is the fault current
R_{ac} is the ac resistance of the conductor
t_f is the fault duration
A_c is the cross section of the conductor
δ is the density of the conductor metal
C_v is the specific heat of the conductor metal
ΔT_c is the allowed temperature rise

The thermal dissipation of the soil is neglected due to the short duration of the fault. Furthermore, the limit temperature for thermal instability in the insulation is used as the allowed temperature rise. The resulting cable ampacity under fault condition, in the range of hundreds of kA, is adequate most of the time.

11.2.3 Dimensioning of the Insulation Based on Limit Field (New Cable)

The principal role of the insulation of a high-voltage cable is to maintain the voltage difference between the conductor and sheath over the useful life of the cable. At the same time, it allows the heat generated in the conductor and the dielectric to dissipate in the ambient environment and provides a mechanical support to keep the cable configuration the same over the whole length of the cable. This implies that in addition to the nominal service voltage, cable insulation must withstand transients including lightning and switching overvoltages, which can occur during normal operation. Dimensioning of high-voltage cable insulation is relatively straightforward, namely, by choosing the insulation thickness so that the maximum field intensity within the insulation is maintained below a level selected to meet various stresses related to the operating conditions. It involves three basic steps: selection of the withstand voltage levels, a design field E_0, and determination of the insulation thickness.

11.2.3.1 Selection of the Withstand Voltage Level

It is often the responsibility of the utilities to determine the withstand voltage level in concordance with the operating conditions of the system and various standards available: IEC and ANSI as discussed in Chapter 13. The withstand voltage varies with the nature of the voltage: ac and lightning and switching impulse voltages. However, a specific value for the withstand voltage level can be specified if one knows all the factors contributing to the buildup of overvoltages in the system.

For ac voltage, the designed withstand voltage U_1 is (King and Halfter, 1982)

$$U_1 = k_{sys} \frac{U_n}{\sqrt{3}} = k_1 \, k_2 \, k_3 \, \frac{U_n}{\sqrt{3}} \tag{11.20}$$

where

U_n is the system nominal voltage
k_{sys} is a factor representing the overvoltage that can occur to the cable. k_{sys} can be decomposed into several components k_1, k_2 and k_s explained below.

Typical values of k_i are as follows: $k_1 = 1.15$, a coefficient for the maximum ac overvoltage; k_2, between 1.25 and 1.5, is a factor for the possible variations in the dielectric strength of the insulating material; and for pressurized paper–oil-insulated cables, k_3, between 1.1 and 1.2, is a factor for the variations of the breakdown voltage with the pressure of the impregnating fluid.

TABLE 11.5

Design Impulse Withstand Voltage U_2 for the Calculation of the Insulation of an AC Cable

Nominal Voltage	U_2, kV		
U_n, kV_{rms}	Minimum[a]	Normal	Reduced
110	421	550	450
132	497	650	550
150	560	750	650
220	802	1050	900
380	1356	1550	1425

[a] Minimum values calculated from Equation 11.21.

The withstand voltage for lightning impulse (BIL) as specified by the standard IEC 60141.1 should not be lower than (IEC 60141-1)

$$V_p = 6U_0 + 40 \ (\text{kV}) \tag{11.21}$$

where

V_p is the peak value of the minimum impulse voltage

U_0 is the voltage between the conductor and cable sheath, usually corresponding to the nominal phase-to-ground voltage U_p

However, when the cable is connected to an overhead line, the withstand value V_p according to Equation 11.21 may not be sufficient, and a higher withstand level specified by the standard IEC 60071.1 should be used for the insulation coordination (IEC 60071.1). The designed impulse voltage U_2 used for high-voltage cable is

$$U_2 = k_p \ V_p \tag{11.22}$$

where the coefficient k_p takes account of the nonhomogeneity of the insulation and of the effect of repeated application of impulse voltages on the dielectric strength. The coefficient k_p has generally a value between 1.1 and 1.35 (King and Halfter, 1982).

Table 11.5 gives the values of U_2 for several values of the nominal system voltages U_n. The minimum value is recommended by the IEC for cables with no direct connection to an overhead line, while the reduced values apply to cables directly connected to an overhead line in a system with grounded neutral.

11.2.3.2 Determination of the Design Field, E_0

The insulation thickness can be determined to ensure an adequate distribution of the electric field within the insulation. For a coaxial cable, the field within the insulation is a function of the radial distance according to Equation 11.1 and its maximum value, at the conductor surface by Equation 11.2. Because of the variation of the breakdown field in polymer with the thickness of the insulation and time, the design of cable aims at ensuring a maximum in-service field that the cable insulation can withstand over its whole service life. Let E_1 be the *limit withstand field* measured on new cable samples, discussed in Chapter 7, then the design field E_0 can be defined as

$$E_0 = m_{des} E_1 \tag{11.23}$$

where m_{des} is an empirical coefficient representing the manufacturer's experience in dealing with various factors that affect the limit withstand field of the insulation. m_{des} can be decomposed into several components m_j, less than 1.0. Typical values for m_{des} vary between 0.5 and 0.7.

The limit withstand field E_1 is a propriety of the insulation system used. It depends on the choice of the materials used, quality control, and manufacturing processes and often is manufacturer's proprietary.

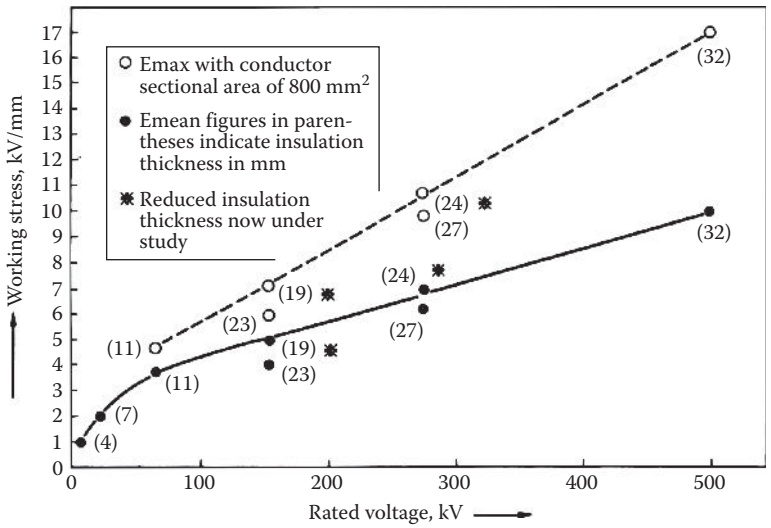


FIGURE 11.10 Variation of working stress as a function of the cable rated voltage. (From Fukuda, T., *IEEE Electr. Insul. Mag*., 4(6), 15, 1988.)

TABLE 11.6

Typical Design Electric Fields (kV/mm) in High-Voltage Cables

Cable Type	AC, rms	DC Voltage	Lightning	Switching
Paper–Oil	20	35	95	95
PPLP	22		98	
Mass impreg.	—	25	95	90
PE	15		70	
SF_6-insulated	12		25	18
Epoxy	5			

It is possible to have a good idea of the design field E_0 from existing cables, whose dimensions and withstand voltage levels are known. An example is illustrated in Figure 11.10 (Fukuda, 1988a) where the working stress of XLPE cables is given as a function of the rated voltage and insulation thickness (in bracket).

Table 11.6 gives typical limit fields in high-voltage cables for the different types of voltages: ac, dc, and lightning and switching impulse voltages. It can be seen that these typical design fields are significantly below their initial breakdown levels of the insulation to take account of the reduction of the insulation dielectric performances in time.

11.2.3.3 Determination of the Insulation Thickness

Knowing the required withstand levels, the design field E_0 of the cable and conductor dimensions, and noting that for coaxial cables, the maximum field occurs usually at the conductor, given by Equation 11.2, the radius of the envelope can be derived by setting

$$E_{\max} = \frac{U}{\ln\left(b/a\right)}\frac{1}{a} = E_0$$

It follows

$$\ln\frac{b}{a} = \frac{U}{aE_0},$$

which yields

$$b = a\exp\left(\frac{U}{aE_0}\right) \quad \text{and} \tag{11.24}$$

The insulation thickness, e_p, is

$$e_p = b - a = a\left[\exp\left(\frac{U}{aE_0}\right) - 1\right] \tag{11.25}$$

Since both technical specifications and insulation performance vary with the type of voltage stress, Equation 11.25 yields different values for the required insulation thickness. Obviously, the largest insulation thickness should be selected.

Table 11.7 gives typical dimensions of 800 kV cables with different types of insulation and their related characteristic parameters to meet the technical specifications shown in Table 11.8. It can be seen that the design field E_0 evaluated from the cable dimensions and their specified withstand voltages are considerably below the estimated limit field of Table 11.6, to take account of the reduction of insulation dielectric performance due to aging with time in service. These aspects will be discussed in more detail for the three types of cable insulation, namely: Paper-oil in SCOF cables, Polymer in Polyethylene and Cross-link Polyethylene cables and gas in SF_6-insulated cables.

TABLE 11.7

General Characteristics of an 800 kV AC Cable

Cable Design[a]	Unit	SF_6	XLPE	PPL	Paper-Oil
Diameter of central conductor	mm	203.2	60	60	60
Diameter of cable sheath	mm	609	148	121.2	129.3
AC Insulation thickness	mm	203.2	44	30.6	34.65
AC limit withstand field	kV/mm	12	15	22	20
LI limit withstand field	kV/mm	25	70	98	95
SI limit withstand field	kV/mm	18			95
Gas pressure	atm abs	4.5			
Dielectric constant		1	2.2	2.78	3.6
Capacitance per unit length	pF/m	50	135	231	310
tanδ				10×10^{-4}	2.3×10^{-3}
Dielectric losses	W/m			14.53	30
Resistive losses—nominal current	W/m	80		45.2	84.5
Power transmission capacity[b]	MVA	3500	2100	1500	800

[a] Estimated from submissions of manufacturers.
[b] Single phase with natural cooling.

TABLE 11.8

Cable Specifications

General Characteristics	Units	Spec.	SF_6	XLPE	PPL	Paper-Oil
Nominal voltage	kV	765				
Nominal current	A	3000	3000	1500	1500	1500
			Withstand Field (kV/mm)			
AC withstand voltage and withstand field	kV_{rms}	960	4.7	15.8	15.8	15.8
Phase to ground voltage and withstand field	kV	440	2.3	7.6	7.6	7.6
LI withstand voltage and withstand field	kV	1800	8.8	29.5	29.6	29.6
32.58 BIL + 10% and withstand field	kV	1980	9.7	32.5	32.6	32.6
SI withstand voltage and withstand field	kV	1550	7.6	24.5	25.5	25.5

11.3 Aging and Incipient Fault

Operating conditions of high-voltage cables subject their insulation to a variety of stresses, thermal, mechanical, and electrical, which cause irreversible changes in the materials termed as aging discussed in Chapter 7. Insulation failure is caused by incipient faults developing from local failure, causing permanent damage to the insulation system. The net effect is a gradual loss of dielectric withstand, which is generally expressed by the time to failure of the insulation T_b, which is a function of applied stresses, thermal θ, electrical E, etc.:

$$T_b = f(\theta, E) \tag{11.26}$$

The direct consequence to cable design is that cable dimensioning based on the initial dielectric performance of new cable must be validated with respect to insulation aging to ensure an acceptable life expectation T_b. Aging process and hence Equation 11.26 vary, however, with the insulation. This will be further discussed in the following regarding the main aging processes: thermal, electrical and environmental with reference to the three general insulation systems currently used in high-voltage cables.

11.3.1 Self-Contained Oil-Filled Cables

11.3.1.1 Thermal Aging

Early studies of thermal aging by Montsinger (1930), followed by Dakin (1948) discussed in Chapter 12, have shown that thermal aging follows the Arrhenius' chemical rate theory, according to

$$T_b = A\exp\left(\frac{B}{\theta}\right) \tag{11.27}$$

where

T_b is life expectation
θ is the temperature in K
A and B are constants determined by the activation energy of the particular chemical reaction responsible for thermal aging

Equation 11.27 shows up as a straight line when the logarithm of the insulation life is plotted against the reciprocal of the absolute temperature, known as the Arrhenius' life curve.

Decomposition by-products: Thermal aging breaks chemical bonds, gradually reducing the structure of the cellulose molecules to H_2O, CO_2, CO, and furans or furfuraldehydes (Burton et al., 1984; Shroff and Stanett, 1985). Furans are uniquely related to the degradation of paper and, hence, can be effectively used to monitor its aging process in paper. The decomposition of the insulating oil produces a variety of by-products, namely, carbon, H_2, CH_4, C_2H_2, C_2H_4, and C_2H_8. They are currently used in their diagnostics. The degradation rate depends on the presence of moisture, oxygen, ions, metal, reaction products, and additives.

11.3.1.2 Electrical Aging

Electrical aging is caused by development of PDs, which erode the insulating material, forming a permanent path along the discharge channel in the paper insulation. Even that filling with the impregnating fluid, provides improved dielectric strength, discharge channel constitutes a weak point of the insulation, by which subsequent discharges can develop in a treeing process. The discharge channel extends gradually in time to eventually bridge the gap and cause the final breakdown of the insulation, at voltages much lower than the initial value obtained in new samples.

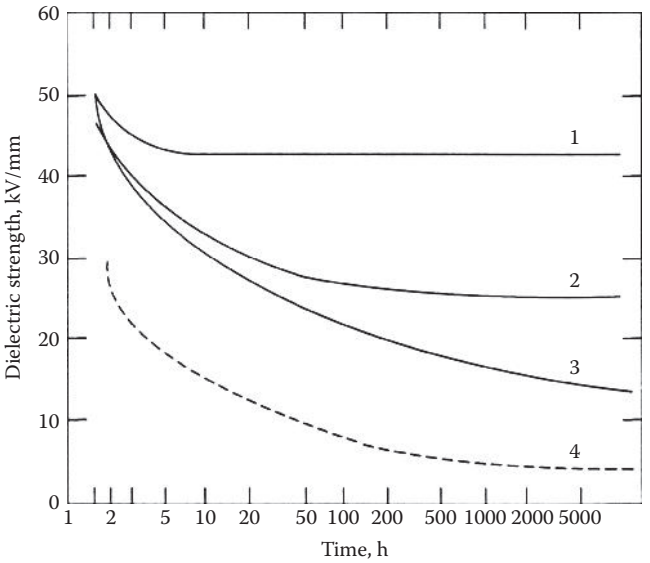


FIGURE 11.11 Life curves of different types of ac-impregnated paper–oil cables. (1) SCOF cable (130 kPa), (2) pressurized gas cable (1500 kPa), (3) mass-impregnated cable, and (4) nonpressurized three-phase cable (nonradial field). (From Couderc, D. Revue de l'État des Technologies des Câbles de Transport a Très Haute tension en Courant Alternatif et Continu, IREQ report, IREQ, Varennes QC, Canada, November 1987.)

Figure 11.11 shows life curves of different types of paper–oil insulation. It can be seen that there is a decrease in the breakdown field with time, from the initial short-term breakdown field E_d to a final long-term value E_∞, which may be expressed by the following empirical relation (Couderc, 1987), a variant of the inverse power law, applied to the paper–oil insulation of oil-filled cables subjected to a constant ac voltage:

$$E_d = E_\bullet + \frac{\Delta E}{\sqrt[n]{t_b}}, \text{ which can be rewritten as} \tag{11.28}$$

$$\frac{E_d - E_\bullet}{\Delta E} = \frac{1}{\sqrt[n]{t_b}} \tag{11.29}$$

where
E_d is the disruptive field
E_∞ is the withstand field
ΔE and n are experimental constants depending on the properties of the insulation
t_b is the time to breakdown

Equation 11.29 expresses the reduction of the residual dielectric strength $E_d - E_\infty$ with time, which is more convenient to determine the end of life of the insulation system: the service life of the equipment is completed when the residual dielectric strength of its insulation is lower than an acceptable level above the operating stresses to minimize in-service failure.

Figure 11.12 shows variations of the final values of the breakdown field E_∞ of paper insulations pressurized in oil and gas, as a function of pressure for different values of paper thickness. It illustrates the effectiveness of oil impregnation in improving the dielectric strength of the impregnated paper–oil insulation, as discovered early by Emmanuelli.

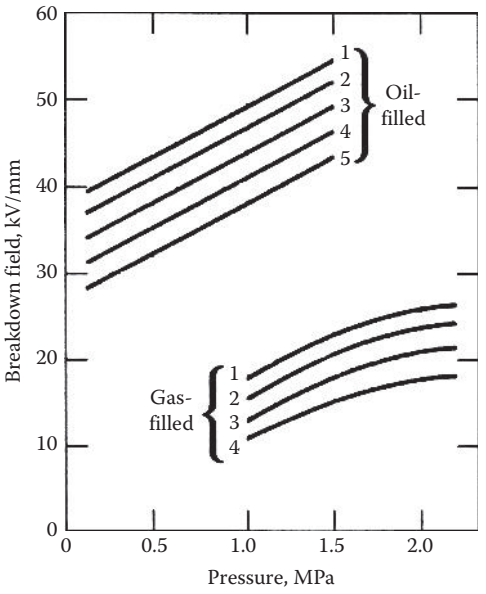


FIGURE 11.12 Long-term ac dielectric strength of paper–oil as a function of the pressure, for different paper thickness: (1) 0.03, (2) 0.045, (3) 0.075, (4) 0.125, and (5) 0.175 mm. (From Couderc, D. Revue de l'État des Technologies des Câbles de Transport a Très Haute tension en Courant Alternatif et Continu, IREQ report, IREQ, Varennes QC, Canada, November 1987.)

11.3.1.3 Environmental Aging

Oil-filled cable forms a closed system, usually by means of a lead or aluminum sheath, which can withstand the high oil pressure of several thousands of kPa. The metallic sheath also constitutes a protective barrier against environmental aging and, in particular, ingress of moisture. However, it also favors accumulation of the PD decomposition by-products within the insulation. Saturation of the dissolved gas in oil must be avoided to prevent the development of PDs within the cable insulation and further enhance the aging process.

11.3.2 Polymeric (PE and XLPE) Cables

11.3.2.1 Thermal Aging

The low loss factor tanδ of polymeric insulation, such as PE and XLPE, tends to minimize the effect of thermal aging. However, the compact design of cables may favor local thermal aging in areas with poor cooling for the cables. Furthermore, the morphological structure of the material also influences the aging process. PE, which is thermoplastic, may soften under heat. This, in turn, tends to favor the displacement of the cable conductors subjected to a local mechanical stress, and failure may occur as a result of the loss of adequate insulating clearance. XLPE, which is thermoset, will harden under heat and becomes brittle as a result of aging.

11.3.2.2 Electrical Aging

The electrical aging mechanisms—PDs, electrical treeing (ET), water treeing (WT), and charge injection—occur at contaminants, defects, protrusions, and voids (CDPV) and tend to be localized. The development of electrical trees starts from one of CDPV sites, erodes the dielectric forming voids in the insulation, grows within the bulk of the insulation until it bridges the gap separating the electrodes, and causes breakdown (Denseley, 2001). In the process, it generates PDs, the signature of which may be detected at terminal points for diagnostic purpose.

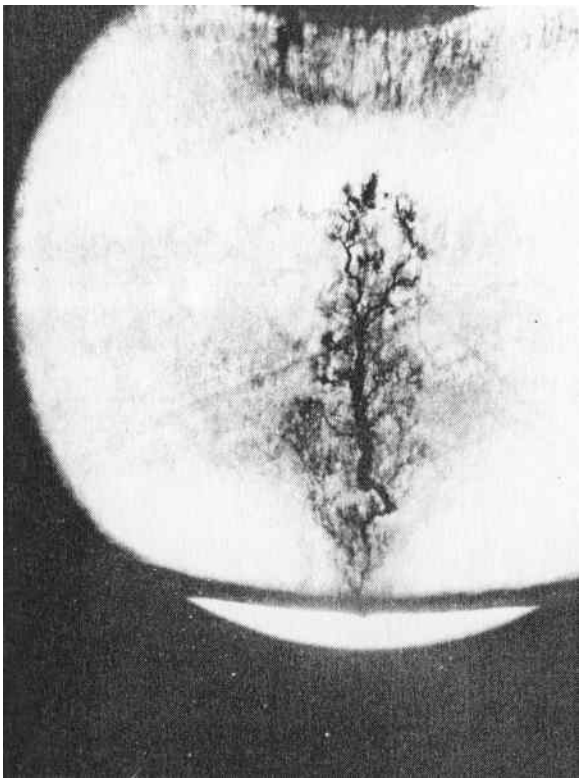


FIGURE 11.13 Electrical trees. (From Lawson, J.H. and Thue, W.A., Summary of service failure of high voltage extruded dielectric insulated cables in the United States, in *IEEE International Symposium on Electrical Insulation*, Boston, MA, June 1980, pp. 100–104.)

Electrical tree: Two mechanisms tend to explain the development of trees in polymer dielectrics (Figure 11.13):

1. One assumes that breakdown of the chemical bonds in the molecules liberates enough energy to form a gas-filled channel in the dielectric, which eventually joins the two electrodes. Breakdown of the gas channel follows and leads to failure of the solid dielectric.
2. The other theory assumes that treeing results from PDs developing within the gas-filled voids in the dielectric. The action of PDs contributes to erosion of the dielectric and formation of channels.

Contradictory observations tend, however, to minimize the importance of PDs in the treeing process, in favor of the combined action of electric charges captured within the dielectric and the breakdown of molecular bonds.

Three phases of tree development related to initiation, propagation, and final breakdown of the insulation can be distinguished:

Initiation of tree: An electrical tree can develop from a protrusion at the surface of the conductor or cable shield, or a contaminant, or void within the insulation, which causes local enhancement of the electric field sufficiently high to initiate PDs. Eventually, the insulation may be locally destroyed, forming an empty channel along the discharge paths.

Propagation of tree: The mechanism of propagation of an electrical tree may be explained by the formation of gas-filled cavities by the PDs. Such a channel constitutes a cavity of low dielectric

constant, which accentuates the local electric field and perpetuates the development of PDs within the cavity. Decomposition of the insulation gives rise to carbon deposits on the wall of the discharge channels, which tends to extend the conductor potential into the insulation or to accentuate the field enhancement ahead of the tree branching, thus favoring the progression of the tree further into the insulation.

Final breakdown: Occurs when the electrical tree completely bridges the insulation to form a conducting path and hence a short circuit between the central conductor and the cable sheath. The fault current that follows is sufficiently high to permanently damage the insulation. It is probable that the development of incipient faults is accompanied with PDs sufficiently high to be detected outside the cable insulation and constitutes a subject of discussion still open. The difficulty to detect incipient faults resides in the intermittent nature of PDs. In effect, the development of PDs also deposits charges on the walls of the cavities forming tree branches. It reduces the local electric field within the cavities and suppresses PDs. The process can resume again when the deposited charges are sufficiently neutralized.

Life estimation: The aging of polymer-insulated cables, corresponding to a gradual reduction of the dielectric withstand of the cable insulation, follows an inverse power law

$$E(t) = E_0 \frac{1}{t^n} \tag{11.30}$$

where

$E(t)$ is the withstand field for a stress duration t

E_0 is the withstand value for a unit duration

Taking the logarithm of both sides of the preceding equation yields

$$\ln\left[E(t)\right] - \ln\left(E_0\right) = -n \ln t \tag{11.31}$$

which expresses a linear relationship between the logarithm of the ratio $E(t)/E_0$ and the time t that the insulation is subjected to the ac stress.

Figure 11.14 shows the variations of the withstand field of a 66 kV XLPE cable, as a function of time under a constant ac voltage (Fukuda, 1988a). It can be seen that the withstand field is reduced by a factor of 1.4 over a period of 30 years, passing from an initial value of 40 kV/mm to 25 kV/mm. The corresponding value of the exponent n is 15 for the XLPE-insulated cable insulation. Similar results were obtained with impulse voltage.

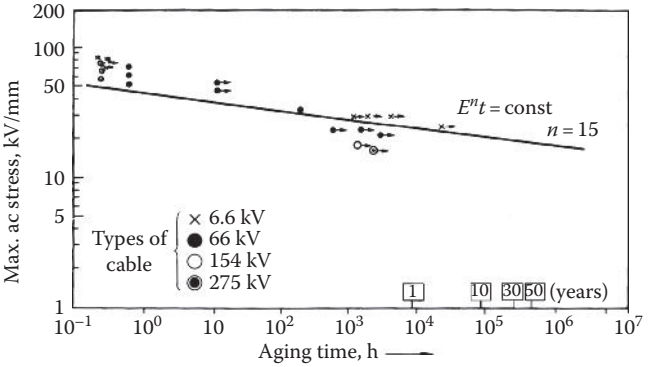


FIGURE 11.14 Aging test of XLPE-insulated cables. (From Fukuda, T., *Electr. Insul. Mag.*, 4(5), 9, 1988a.)

Possible mechanisms for electrical aging in polymer: In spite of the general consensus about development of incipient faults via water and electrical trees, there is still no adequate physical mechanism explaining the inverse power relationship observed in electrical aging data. Several mechanisms have been advanced for the initiation of the aging processes in polymeric insulation.

Bahder et al. (1982) proposed a model based on the scission of molecular chains and the formation of craters at discharging voids to explain the aging of polymer. The development of PDs in microvoids of dimensions less than 100 μm, already present within the bulk polymer, produces ion space charges that penetrate the polymeric insulation in the immediate surroundings of the microvoid. It is the back and forth movement of the ion space charges dictated by the applied ac field that causes the breaking of molecular chains to form microcracks, branching outwardly from a stem. The same process contributes to enlarge the stem and cause the microcrack branching to extend farther into the polymer and transform it into an electric tree. The time to breakdown of polymer-insulated cables may be expressed as

$$t_b = \frac{1}{f b_1 \left\{ \exp\left(b_2 \left(E - E_{th}\right)\right) - 1 \right\} \exp\left(b_3 E_b\right) + b_4} \tag{11.32}$$

where

f is the frequency of the ac test voltage

b_1, b_2, b_3, and b_4 are constants representing the dependence of polymeric material on temperature, shape, and frequency of the applied voltage (ac, dc, or impulse)

E and E_b are the applied and breakdown field, respectively

The threshold stress E_{th} is influenced by the type and shape of the imperfection and by the temperature of the insulation.

Figure 11.15 illustrates the variations of the logarithm of voltage stress as a function of logarithm of time to breakdown. It can be seen that the breakdown field follows the inverse power law at high stresses. However, at low stresses close to the operating values, the breakdown occurs at shorter times than predicted by the inverse power law.

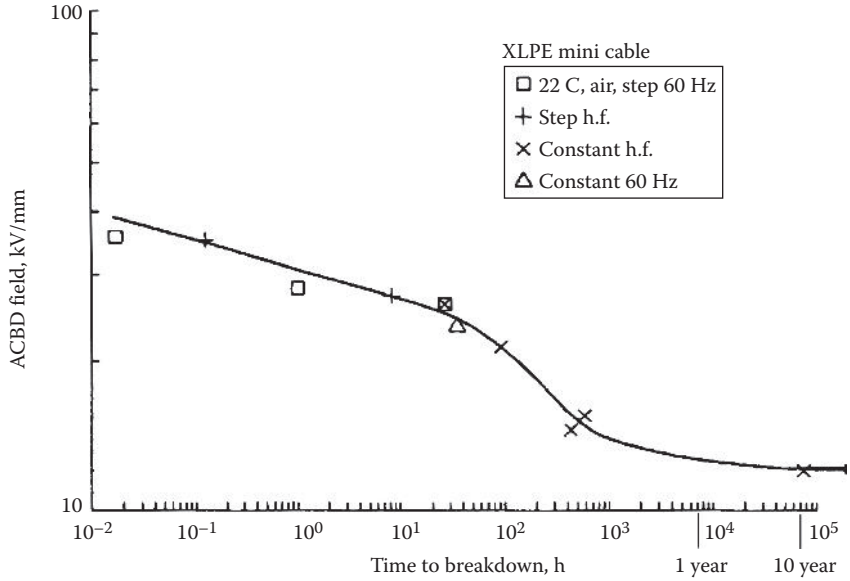


FIGURE 11.15 Variation of the ac breakdown field with time to breakdown—results from Bahder et al. (1982). (From Dang, C. et al., *IEEE Trans. Dielectr. Electr. Insul.*, DEI-3(2), 237, 1996.)

Crine (Crine, 1987; Dang et al., 1996; Parpal et al., 1997) proposed the rate theory to explain the aging process in polymers, especially regarding its behavior at field intensities close to the normal operating value of the cable. Crine assumed the following:

- The final breakdown occurs when charge carriers go over an energy barrier of height ΔG and width λ. The nature of the energy barrier is typical of the insulation tested.
- The electric field reduces the height of the energy barrier and affects the barrier width λ.
- Breakdown is a thermally activated process.
- A general relationship was derived for the time to breakdown t_b as related to the field E, the energy barrier ΔG, and λ:

$$t_b = \frac{2h}{kT}\exp\left(\frac{\Delta G}{kT}\right)\csc h\left(\frac{e\lambda E}{2kT}\right) \tag{11.33}$$

At high field intensities, the preceding expression simplifies to

$$t_b = \frac{4h}{kT}\exp\left(\frac{\Delta G}{kT} - \frac{e\lambda E}{2kT}\right) \tag{11.34}$$

where
k is the Boltzmann constant
h the Planck constant
e the electron charge

which predicts an exponential relation between field and time to breakdown.

Thus, ΔG and λ can be readily deduced from the intercept and the slope of the curve E as a function of the logarithm of time. Figure 11.16 presents the results of Figure 11.15 using semilogarithmic paper however, showing variation of the breakdown field as a function of logarithm of time. It can be seen that the breakdown field follows an exponential law at high fields before it tapers off at low stresses.

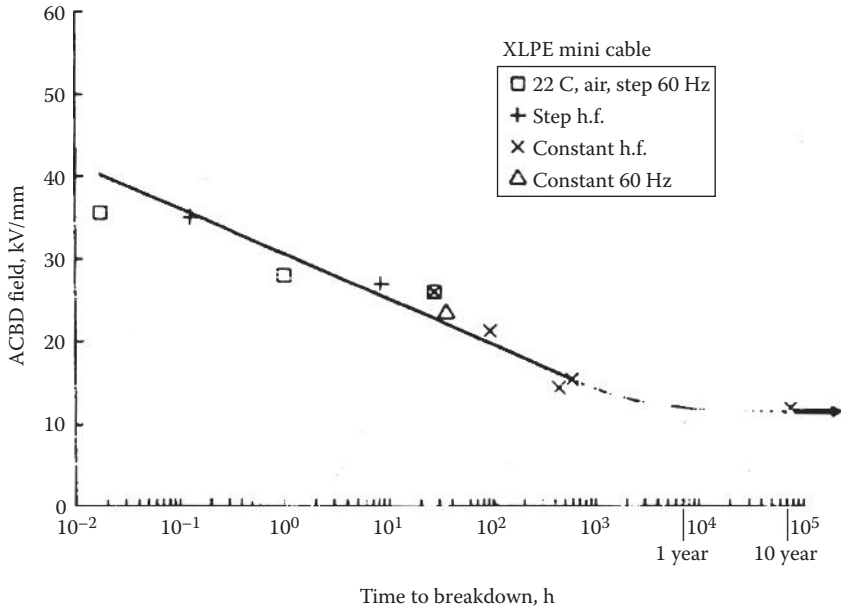


FIGURE 11.16 Variations of the ac breakdown field with time to breakdown—results from Bahder et al. (1982). (From Dang, C. et al., *IEEE Trans. Dielectr. Electr. Insul.*, DEI-3(2), 237, 1996.)

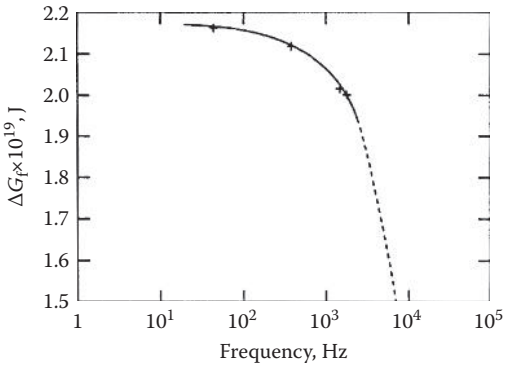


FIGURE 11.17 Variations of ΔG as a function of the frequency of the applied field at 22°C by Bahder et al. (From Parpal, J.L. et al., *IEEE Trans. Electr. Insul*., EI-4(2), 197, 1997.)

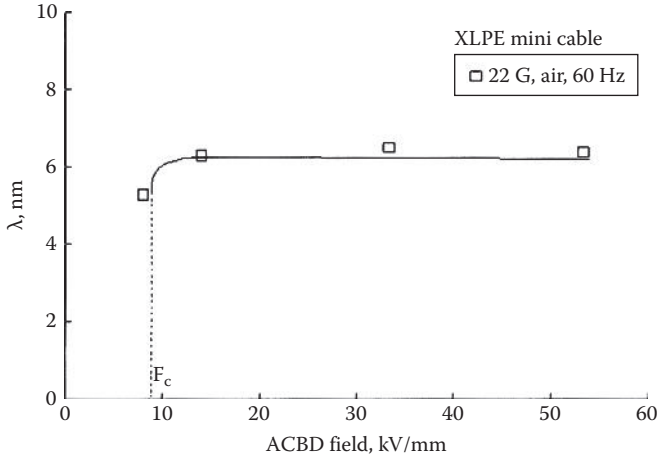


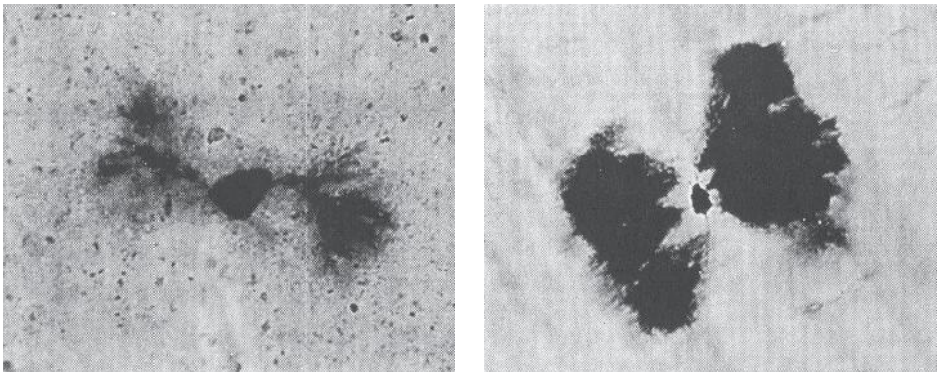
FIGURE 11.18 Variations of λ as a function of the applied field. (From Parpal, J.L. et al., *IEEE Trans. Electr. Insul*., EI-4(2), 197, 1997.)

Evaluation of Δ*G* and λ (Figures 11.17 and 11.18) shows that at high field intensities, λ is constant while it sharply decreases at low field values. This variation of λ at low fields explains the taper off observed in the curve of electrical aging as a function of aging time.

11.3.2.3 Environmental Aging

Polymeric insulation is particularly sensitive to humidity, which favors development of water trees within the insulation. Steamed cure seems to produce water-filled voids within the insulation, thus favoring development of water trees. Migration of humidity through the protecting jacket into the main polymeric insulation of power cables is another cause, which is particularly present in distribution cables, due to the flooding of the cable manhole, which can immerse the cable insulation over long periods. The best way to counter the ingress of humidity is to use a hermetic metallic, lead or aluminum, sheath. The solution comes with a price and is limited to high-voltage cables of 200 kV and higher. Finally, on-site installation of cable joints and terminations is still the weak points in a cable system regarding ingress of moisture.

Water trees: When cables are in a humid environment, as often is the case with underground cables, the development of electrical trees is often preceded by the development of water trees (or chemical trees when chemical substances are present in the water). The development of water trees seems related to the migration of water molecules through the protective jacket into the main PE insulation. Like electrical trees, water trees are attracted by the electric field: they develop from protrusions at the conductor and metal sheath or from



(a) (b)

FIGURE 11.19 Water trees developing from a solid contaminant. (a) A typical bowtie tree in XLPE cable insulation aged eight months at three times rated voltage. (b) A bowtie tree in clay filled EPR cable insulation, initiating from a contaminant. (From Boggs, S. and Xu, J., *Electr. Insul. Mag.*, 17(1), 23, 2001.)

solid impurities within the dielectric, giving rise to butterfly tie trees. Water trees are diffuse, however, with no clear evidence of forming well-defined channels (Figure 11.19). The structure of the water trees takes the form of a series of water-filled voids, which are interrelated by oxidized tracks (Moreau et al., 1993).

Water trees seem to be not as permanent as electrical trees. In effect, drying the insulation can temporarily remove water trees and allow the insulation to recover most of its dielectric strength. However, water trees will quickly reemerge when the dried cable is put back into a humid environment, indicating that water trees do weaken the insulation, making their paths easy for the migration of water molecules within the insulation. Water trees do not directly cause failure of cable insulation, which occurs after a transition of water trees into electrical trees. Four development phases of water trees can therefore be distinguished, related to the initiation, propagation, transition to an electrical tree, and final breakdown of the insulation (Figure 11.20).

Initiation of water tree: Starts from a location in the insulation where the local field enhancement is sufficiently high to attract water molecules, probably due to their dipole polarization, to initiate water trees. The natural locations for field enhancement are protrusions at the conductor and cable sheath, empty or gas- or liquid-filled cavities formed during the curing process, especially steam cured, or subsequent to a separation of insulation at the interface with the conductor or cable shield.

Propagation: It may be expected that the high permittivity of water also creates local concentration of the electric field in the dielectric around the water-filled void, which is comparable to field enhancement around a conducting contaminant of the same shape and size. Field enhancement around water-filled void attracts new water molecules and allows the water tree to grow. However, the high dielectric constant of water also reduces proportionally the electric field within the water-filled void, making the development of PDs within the water-filled voids practically impossible. As a result, water trees can progress further into the insulation but do not directly cause breakdown.

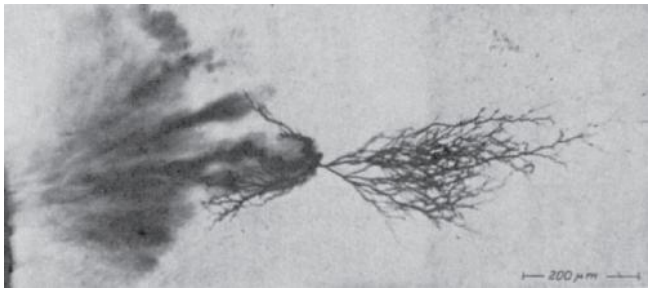


FIGURE 11.20 Transition of water tree to electrical tree from a vented water tree. (From Kalkner, W. et al. Water treeing in PE and XLPE insulated high voltage cables, *International Conference on Large High Voltage Systems*, CIGRE, paper no. 21-07, 1982.)

Transition to electrical tree: It may be assumed that once a water tree succeeds to bridge the two electrodes, a conduction current may flow in the water-filled channel, causing vaporization of the water and thus transforming it into a gas-filled channel. Water vapor having a lower dielectric strength, combined with the high electric field across the tree channel, can initiate PDs, transforming it into an electrical tree.

Final breakdown: Once the transition from water to electrical tree has occurred, the final breakdown phase is identical to that of an electrical tree when it completely crosses the insulation to form a conducting path and hence a short circuit between the central conductor and the cable sheath. The fault current that follows is sufficiently high to permanently damage the insulation.

11.3.2.4 Decomposition By-Products

Although PDs and chemical reactions do produce decomposition by-products in polymeric insulation, they cannot be collected or measured and hence cannot be used in assessment of the polymeric insulation.

11.3.3 Gas (SF_6)-Insulated Cables (Lines)

Due to their great ability to regenerate from their decomposition by-products, and since the majority of the decomposition by-products associated with PDs are in gaseous state and have comparable dielectric performances as the gas itself, gases do not practically age. Aging of gas–solid insulation is therefore determined by the aging of insulating spacers and other supporting structures, forming an integrant part of the insulation.

11.3.3.1 Thermal and Mechanical Aging

Gas insulation is little affected by thermal aging due to the low value of the loss factor tanδ and the usually large physical dimensions of gas-insulated equipment, which provides adequate heat transfer to ambient air. However, the cyclic expansions and contractions of the conductor with loading conditions do wear off the metal, producing particles, which may be detrimental to the insulation.

11.3.3.2 Electrical Aging

Since breakdown of gas–solid insulation generally occurs along the gas–solid interface, incipient fault in solid insulation, normally associated with the development of electrical trees within the bulk of the solid insulation, although a possible cause for failure of insulating spacers, is rather unlikely to occur due to the low electric field in the bulk of epoxy spacer. A more likely cause of failure is associated with the development of surface tracking, related to the development of steady PDs at the spacer–gas interface. Erosion of the epoxy resin leaves a path partially covered by carbon deposits, which constitutes an easy path to PDs to propagate along the interface and, eventually, cause the breakdown of the spacer. Surface tracking is dependent on the formulation of epoxy resin and of the type of filler used. Resistance to surface tracking is generally used as a criterion for evaluating insulating material used in the manufacture of spacers.

Life estimation: Several investigations have been made to evaluate the long-term behavior of epoxy insulators in full size as well as reduced-scale samples (Crucius and Luxa, 1980; Honda, 1984). Figure 11.21 shows the voltage–time characteristics of reduced-scale epoxy postinsulators, subjected to accelerated aging with the applied voltage being the accelerating parameter (Nitta and Kuwahara, 1981). The results evaluated over a period of several hundred hours show a reduction rate of the dielectric withstand of the insulators of about 3% per decade of time. The aging seems to follow an exponential law corresponding to the linear relationship between the breakdown field and the logarithm of time to breakdown.

Possible aging mechanism: Several mechanisms have been advanced for the aging mechanism in polymeric insulation, principally for PE and XLPE. For SF_6–epoxy insulation, Dakin and Studniarz (Dakin and Studniarz, 1978; Studniarz and Dakin, 1982) observe that aging of cast epoxy resin may be associated with the development of PDs in the bulk epoxy volume. This mechanism explains the existence of

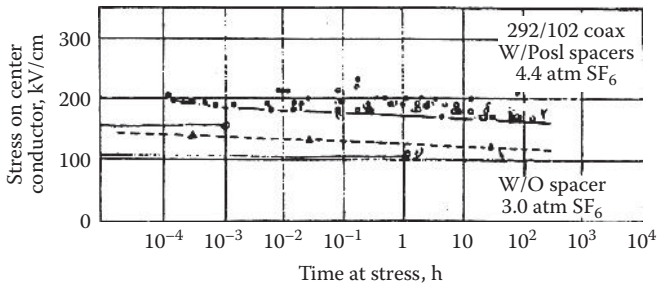


FIGURE 11.21 *V–t* characteristics of molded epoxy spacers. (From Nitta, T. and Kuwahara H., *IEEE Trans. Power Appar. Syst*., 100(6), 3055, 1981.)

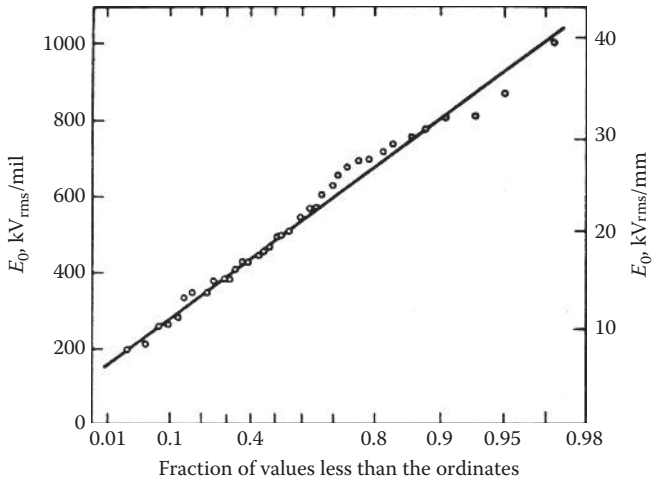


FIGURE 11.22 Extreme value distribution of the onset fields for PDs E_0 in epoxy spacers. (From Dakin, T.W. and Studniarz, S.A., The voltage endurance of cast epoxy resins. *IEEE International Symposium of Electrical Insulation*, 1978.)

a threshold field E_0 below which no PD can be initiated and hence no aging is experienced by the epoxy at fields below E_0.

Figure 11.22 shows variations of the onset field E_0 for PDs plotted in extreme value statistics graph paper. The threshold field for epoxy is estimated to be about $E_0 = 6$ kV/mm. The time to failure can be expressed as a function of the electrical stress E, or more precisely the differential field $(E - E_0)$, according to

$$t = \left(\frac{1}{E - E_0}\right) K_2 \exp\left[-K_1 (E - E_0)\right] \tag{11.35}$$

taking the logarithm of both sides gives

$\ln t = \log\left(\frac{1}{E - E_0}\right) + \ln(K_2) - K_1 (E - E_0)$, which can be rewritten as

$$\ln t = K_2 - K_1 (E - E_0) + \ln (E - E_0) \tag{11.36}$$

where K_1 and K_2 are experimental constants.

Figure 11.23 illustrates variations of electric field as a function of time to breakdown, using a semilog graph paper. A linear relationship between the two parameters for high values of the electric field can be observed. However, the curve tapers off at low field intensities approaching the normal operating stress.

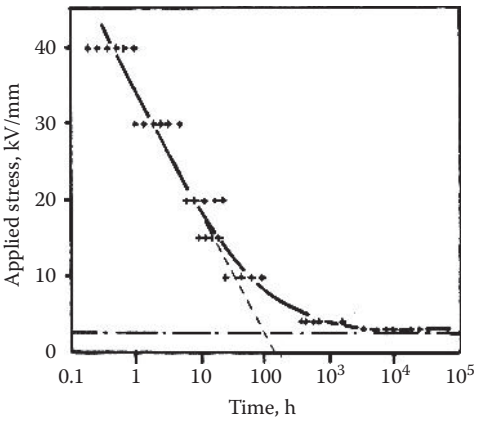


FIGURE 11.23 Electrical aging—semilog. (From Cygan, P. and Laghari, J.R., *IEEE Trans. Electr. Insul.*, EI-25(5), 923, 1990.)

11.3.3.3 Environmental Aging

Compressed gas insulation is subjected to ingress of humidity through the joints and particle contamination associated with the cyclic expansion–contraction of the conductor, producing metallic particles and mechanical vibrations, which may set loose particles from their natural traps.

Decomposition by-products: There are no significant gaseous by-products associated with the degradation of SF_6 and epoxy insulators. As a result, there has been little interest to develop methods for assessing the aging state of gas insulation via their decomposition by-products. Analysis of the gas is, however, made prior to major work requiring the opening of the gas-insulated equipment, especially current interrupting devices such as circuit breakers and disconnecting switches.

11.3.4 Experimental Evaluation of Life Function

The lack of satisfactory theories for various aging processes combined with the fact that practical insulation systems are simultaneously subjected to multiple aging processes has promoted alternative approaches to estimate the life, or remaining life, of the insulation from experimental tests. However, the problem turns out to be one of the most difficult and has not been fully mastered in spite of the considerable research work already undertaken in this field.

11.3.4.1 Accelerated Aging Tests

Accelerated aging tests are frequently used to evaluate the long-term performance of an insulation system. Introduced some 60 years ago by Mathes (1948), the concept of evaluating insulating materials in their operating environment with one or two accelerating parameters is well accepted and widely used nowadays. The objective is to obtain experimentally the life curve of the insulation system subjected to high stresses and to extrapolate the results to the operating conditions. It assumes basically that the failure mechanism under the specific test conditions will remain the same over the range of variations of the accelerating parameters.

Electrical and thermal stresses are the most commonly used as accelerating aging parameters. Time to breakdown was measured as a function of the accelerated parameters, starting at high stresses while keeping the other parameters constant. The source frequency is another accelerating parameter. The logic behind this approach is the assumption that PDs are sensitive to being alternately initiated and suppressed within a half cycle of the applied voltage. Increasing the frequency of the test voltage would then accelerate the aging process in a proportional manner. Aging tests are regularly conducted with ac voltage frequency ranging up to several kHz.

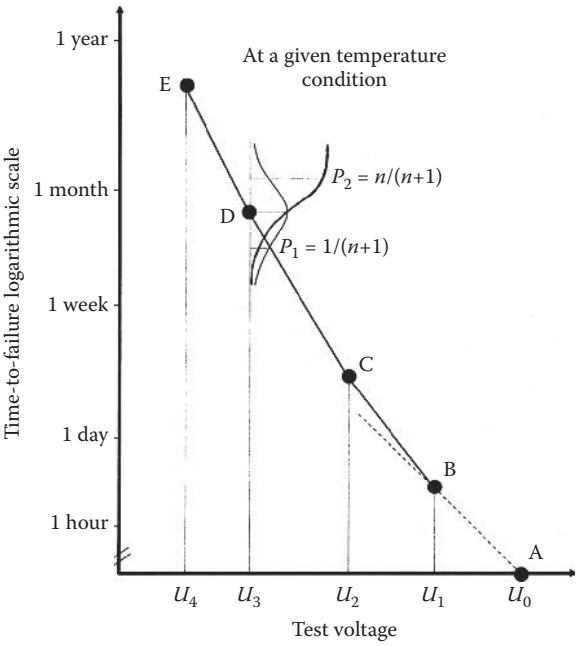


FIGURE 11.24 Typical schedule for a conventional endurance test program. (Dang, C. et al., Dielectric performance of distribution XLPE-cable accessories at high temperatures, CEA report 139-D-505A, 1990.)

Typical endurance test method: Referring to the schematic test schedule of Figure 11.24, the life curve is obtained in *M* test series; each consists of subjecting *N* test samples to constant stresses and measure the time (or number of voltage applications for impulse voltage) to failure of all the samples. The accelerating parameter (applied voltage) is then changed to the next level, and the test repeated with a new group of *N* samples. For practical reasons, the aging test usually starts with the highest voltage level, which produces failures of test samples in relatively short time. The test voltage is then reduced in subsequent test series to gradually approach the operating stress. At each test voltage level, the measured population of *N* values of the time to breakdown can be evaluated for its defining parameters, for example, mean value and standard deviation. The experimental life curve is defined by the set of *M* mean times to breakdown. It is then extrapolated for the service life of the insulation system.

11.3.4.2 Analysis of Data

With the previously mentioned test procedure, the time to failure at any test voltage is defined by a statistical distribution for a population of *N* samples. Two situations are possible, corresponding to uncensored and censored data.

Uncensored data: Correspond to the situation when all the samples in a test series fail, usually corresponding to test under relatively high stresses. The data are termed uncensored, and the probability distribution of the time to breakdown is defined between the two extreme probabilities (Chapter 3):

$$P_{\min} = \frac{1}{N+1} \quad \text{and} \quad P_{\max} = \frac{N}{N+1}$$

Different statistical functions can be evaluated regarding their adequacy to represent the experimental data. *Normal* and *Weibull* distributions are most frequently used. Their parameters are determined from the experimental distribution of the time to failure.

Censored data: As the voltage level is reduced, the test duration and the possibility that a test series will contain samples that do not breakdown both increase. The data are then termed censored (Nelson, 1978), and the probability distribution of the time to failure is defined between the two extreme probabilities:

$$P_{\min} = \frac{1}{N+1} \quad \text{and} \quad P_{\max} = \frac{N_b}{N+1}$$

where $N_b < N$ is the number of failed samples in the test series.

The distribution of the time to failure of censored data is necessarily less accurate as N_b is smaller than N. For practical reasons, N_b should be at least equal to the number of parameters defining the specific statistical distribution function: two in general for *normal* and *extreme value* functions and three for *Weibull* distribution.

To avoid censored data, several alternatives have been considered, namely, residual dielectric strength and residual life.

Residual dielectric strength: Provides an alternative to remedy the unpredictable duration of the conventional endurance test. In this approach, the endurance test is carried out in the same manner as with conventional endurance test. However, the residual strength of the insulation is evaluated at the end of an aging test series, determined by the schedule test duration or the time until the first failure occurs, whichever event coming first (Montanari et al., 1984). In this way, variation of the aging state of the insulation defined by its residual dielectric strength with the aging duration can be derived. The advantage of this approach is obviously the possibility to set a time limit to the endurance test. Also, since the residual strength is evaluated for all the test samples of the series, there are no censored data involved, and the analysis of the test data may be simplified.

Residual life: Although both the time to breakdown and the residual strength are complementary parameters for assessing the aging process of an insulation system, there is no simple relationship between the two. Evaluation of both the actual state of the insulation and its residual life of polymer-insulated cable after it experiences a (first) failure in service provides an interesting approach to estimate the remaining service life of a practical cable system (Gotoh et al., 1984). It provides some correlation among the actual in-service aging (up to the first failure), the actual state of the insulation, and the estimated remaining life established by accelerated aging tests (which necessarily take less time than a conventional endurance test on new cable samples).

11.3.4.3 Optimization of Test Parameters

The destructive nature of aging tests, combined with the fact that the test samples may be limited in number, has promoted the need to optimize the aging test procedure. The following considerations should be made:

- Aging test corresponds essentially to extrapolation of test results obtained under high-stress conditions to estimate the service life of the insulation at the normal operating stresses. It assumes that the breakdown at low stresses follows the same mechanism at high stresses.
- The total number of test samples, $N_t = N \times M$, depends on the desired accuracy of the distribution of the time to breakdown, limited between the extreme probabilities $P_{\min}$ and $P_{\max}$, which determine the number of test samples for each test series, and the number M of test voltages, which determines the effective extent of the experimental life curve.
- The testing time increases with reduced test voltage. In conventional endurance tests, where the time to breakdown is measured, a test voltage selected too close to the normal operating stress may easily result in testing time exceeding the scheduled limits, with consequences either on the test budget or as most often is the case the termination of the test with censored data.
- Minimize the number of censored data.
- Real-time update of the experimental life curve may be made and allows proper adjustment of the next test voltage level to maximize the chance of completing the test series within the allowed time.

11.4 Gas-Insulated Substations

Gas-insulated substations (GIS) are the natural outcome of the development of a variety of gas-insulated switchgear in the first half of the twentieth century. Figure 11.25 illustrates the basic scheme for a GIS: a set of disconnecting and measuring equipment, which allow appropriate changes of circuit configuration. All equipment shares the same insulation system, which also includes bushings for connections to power transformers, overhead lines, and/or underground cables. Connections between the various pieces of equipment are made with short bus sections. Gas barriers are used to isolate the breakers and disconnecting switches from the main gas insulation, protecting it from particles produced during switching operations. GISs are usually arranged in breaker bays, disposed in two areas of high and low voltages, located at both sides of power transformers.

While the operation of GIS is no different from a conventional substation, the good dielectric performance of gas insulation allows a reduction in size by a ratio of about 1/10. Combined with the low risk of fire hazards and minimum visual impact, GIS can be installed in urban areas, where the high cost of land has practically forbidden the installation of conventional substations. However, GIS does have some particular problems related to operation of disconnecting switches, namely, fast transients, ground potential rise, and trapped charges. These aspects of GIS will be discussed in the following.

11.4.1 Generation of Fast Transients

One of the features of SF_6 insulation is that breakdown time is much shorter in SF_6 than in air, which generates transient voltages with very fast front (Boggs et al., 1982). The problems are particularly prevalent in GISs during operations of disconnecting switches because of the high number of restrikes, and the reduced dimensions of GIS cause transient reflections occurring at higher rate with little attenuation.

Figure 11.26 compares voltages at the source and load sides of the switch during an opening operation. It can be seen that, as the contacts of the switch are separated, restrikes occur each time the voltage difference between the source and the load exceeds the withstand level of the gap between the contacts, increasing with the gap distance until it withstands the source voltage.

Short-time breakdown characteristics: Referring to Figure 11.27, each restrike between the contacts of the switch corresponds to the injection of a step voltage V_0 equal to the restrike voltage, which separates into two transient waves of half amplitude, propagating away from the injection point (Fujimoto et al., 1982). The transient wave and its subsequent reflections within the GIS can build up substantial overvoltages of short front times, in the range of tens of nanoseconds, that are applied to the GIS insulation. Two principal problems are related to the fast transient voltages: the breakdown characteristics of SF_6 insulation at a short time to breakdown and the transient ground potential rise higher in GIS than in conventional substations.

Because of the rather flat V–t characteristics of SF_6 insulation, the choice of protection devices for gas-insulated equipment is made assuming a V–t curve remaining constant at the BIL level of the equipment down to breakdown times around 1 μs, before an increase in the breakdown voltage at shorter time to breakdown. This explains the tendency to use SF_6-insulated metal-oxide lightning arresters for the overvoltage protection of gas-insulated equipment.

Transient potential ground rise: Because of the very fast front transient impulses, the penetration depth into the metal conductor and envelope is small (Fujimoto et al., 1982). The internal and external surfaces of the envelope behave as two distinct concentric conductors connected together at the open end of a connection to the overhead line, which constitutes a triple junction access point (Figure 11.28). In presence of the inductance of the ground loop, the circulation of such a ground current generates a transient ground potential rise higher than those encountered in conventional substations. Research work sponsored by the Canadian Electrical Association (CEA) on the subject led to the conclusion that with appropriate means to limit the inductance of the ground loop, this situation does not constitute a danger to maintenance personnel (Ford et al., 1982). On the other hand, these potential rises can be critical to substation control and measuring equipment (Dick et al., 1982).

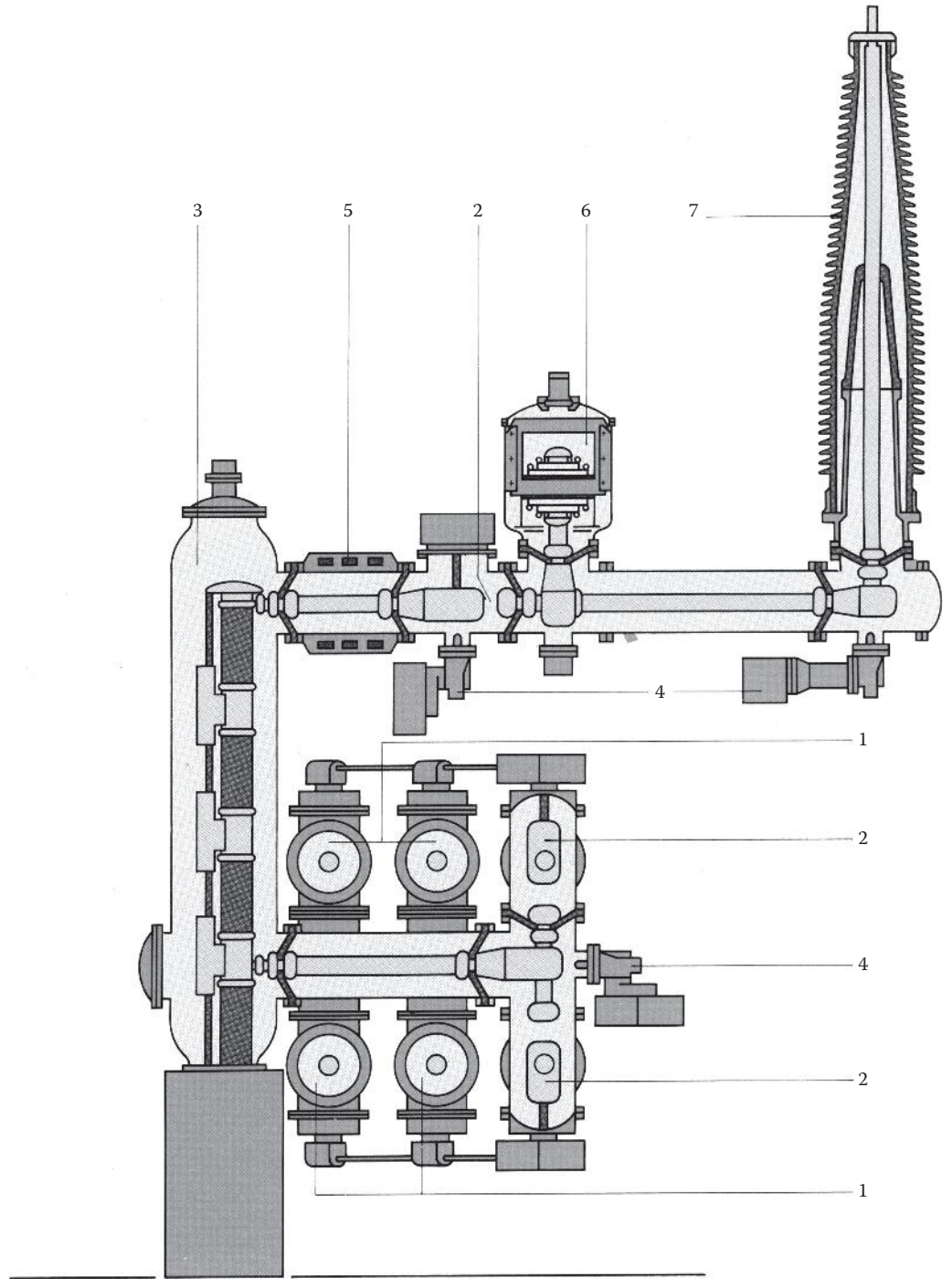


FIGURE 11.25 Basic components of a GIS. (1) Busbar, (2) disconnecting switch, (3) circuit breaker, (4) earthing switch, (5) current transformer, (6) voltage transformer, and (7) outdoor bushing. (From ABB Ltd., SF_6 Gas-insulated switchgear—Type ELK, 1990.)

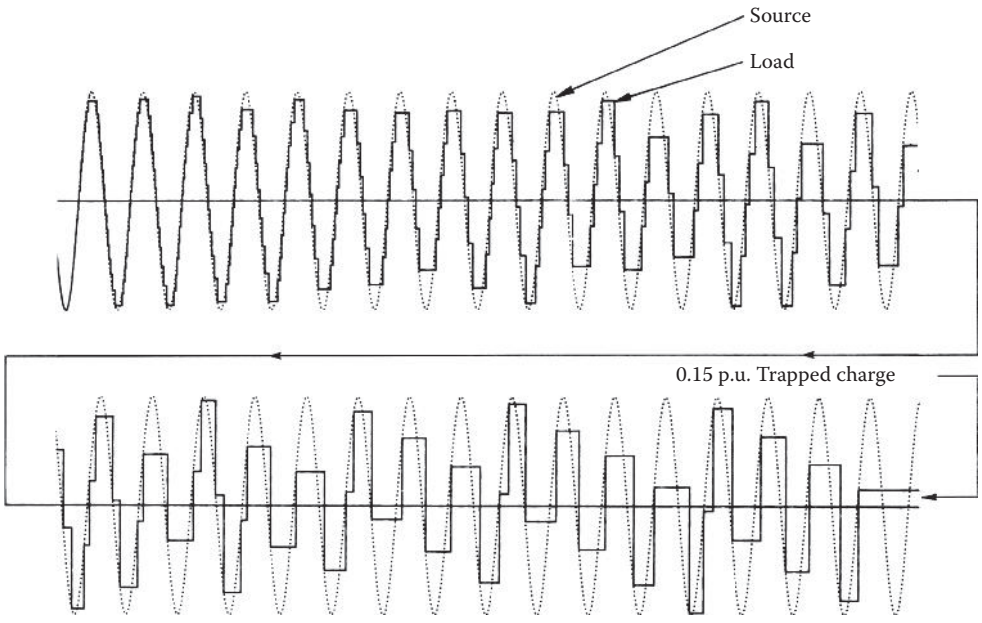


FIGURE 11.26 Restrikes between contacts during opening of a disconnecting switch. (From Boggs, S.A. et al., *IEEE Trans. Power Apparatus Syst*., PAS-101, 3593, 1982.)

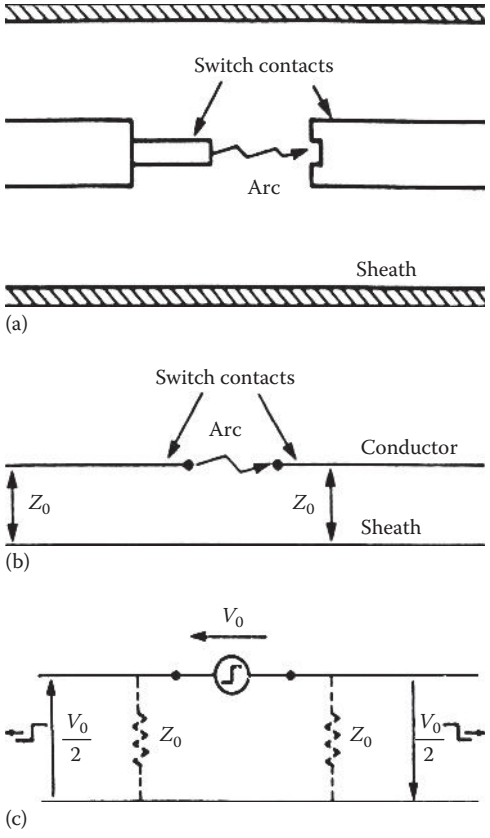


FIGURE 11.27 Generation of fast transients. (a) Arcing between contacts. (b) Circuit representation of arcing between contacts. (c) Propagation of transient voltage. (From Fujimoto, N. et al., *IEEE Trans. Power Apparatus Syst*., 101, 3603, 1982.)

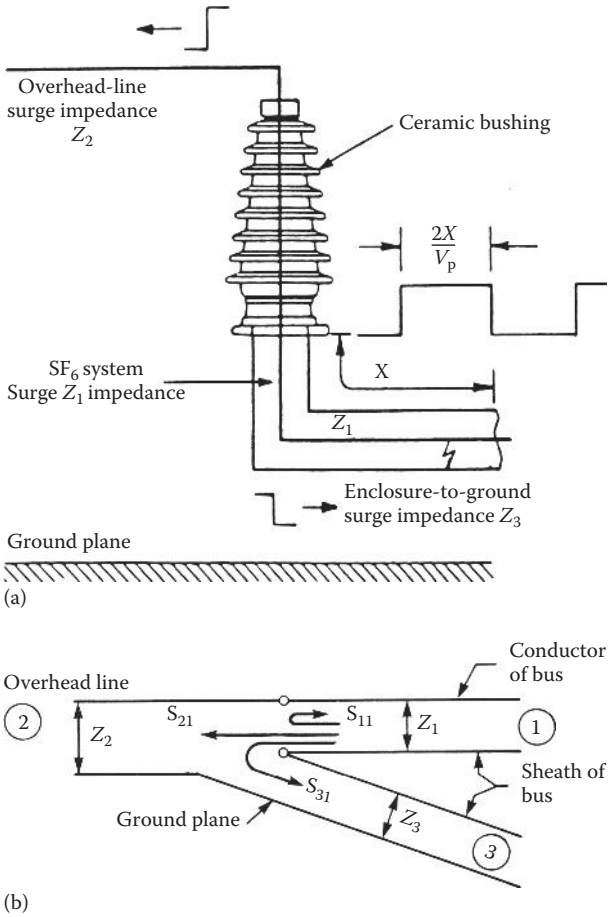


FIGURE 11.28 Mechanism of ground potential rise. (a) Physical arrangement of GIS connection to overhead line. (b) Circuit representation by a three-port transmission line. (From Fujimoto, N. et al., *IEEE Trans. Power Apparatus Syst*., 101, 3603, 1982.)

Grounding: Solutions have been proposed and some are already incorporated in the grounding design of GISs (Dick et al., 1982):

- Grounding at several points, with shorter spacing between the grounding points near the terminations to overhead lines where the highest overvoltages (of the range of several kV) are possible (Dick et al., 1982).
- Special grounding, using a ground plane, is installed at the base of wall bushings and cable terminations.

Trapped charge: Because of the random nature of arc quenching in SF_6-insulated disconnecting switches, electrostatic charges may be trapped at the conductor and insulating spacers after the opening of the switch, as illustrated by the recording of the voltage across the contacts shown in Figure 11.29 (Boggs et al., 1982). The presence of trapped charge at or near the insulating spacer may affect the local distribution of the electric field and cause its failure.

11.4.2 Risk of Burn Through

Operating SF_6-insulated equipment raises some concerns regarding the possibility of burn through of the envelope, subsequent to a phase-to-ground fault. Service experience to date has shown that the design of

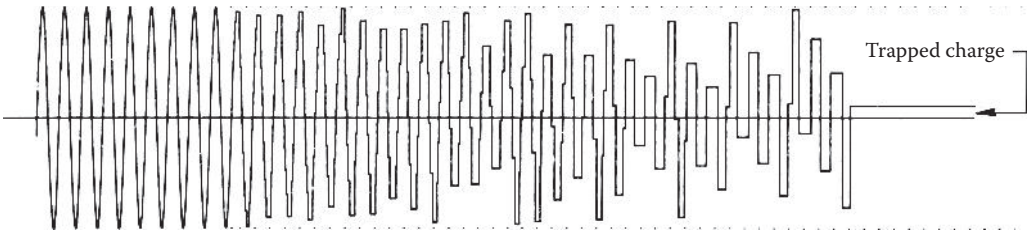


FIGURE 11.29 Trapped charge. (From Boggs, S.A. et al., *IEEE Trans. Power Apparatus Syst*., 101, 3593, 1982.)

gas-insulated equipment is secure in this respect. Burn through is a rare incident, which, even if potentially dangerous due to the spilling of SF_6 (discussed in Chapter 4), has not caused problems to operating personnel. It occurs only when the arc initiated by the fault has moved close to a spacer and remained stationary for sufficiently long time to melt the metal, causing burn through of the envelope. On the other hand, evaluation of the risk of burn through (Trinh, 1992) of gas-insulated cables has shown that these risks are one to two orders of magnitude lower than those associated with the failure of the cable, typically of the range of 10^{-6}–10^{-8}. Furthermore, the risk of burn through can be controlled during design of the equipment and protection system by the use of rupture discs, which control gas ejection and minimize the risk of injuring personnel.

11.4.3 Special Considerations for Operating Gas-Insulated Equipment

Although SF_6-insulated equipment operates in a contained environment, it is sensitive to ambient changes, especially when the GIS is located in open air. In the following, the main factors that can influence its operation are reviewed.

11.4.3.1 Temperature

In general, temperature has little effect on dielectric performance of gas insulation, which is rather determined by the gas density (as discussed in Chapter 4). However, there exist situations where a change in temperature does cause a change in the gas density and hence can affect the dielectric performances of the gas-insulated equipment.

Low temperatures: Operating gas-insulated equipment at very low temperatures can cause liquefaction of the gas, which, in turn, can considerably reduce the gas density and hence the withstand strength of gas insulation. Figure 11.30 presents the ranges of pressure and temperature for which SF_6 remains in the gaseous state. It can be seen that, for the range of pressures currently used (4–5 bars), the temperature limit for a safe operation of gas-insulated equipment is −40°C.

Mixtures of SF_6 and N_2: The use of SF_6–N_2 mixtures at a slightly higher pressure constitutes an elegant solution to avoid the liquefaction of pure SF_6 while maintaining an adequate dielectric performance of gas insulation. The partial pressure of SF_6 is selected so that the lowest operating temperature remains above its liquefaction threshold, while the added N_2 compensates for the reduced withstand value of SF_6 at reduced partial pressure (Cookson and Pedersen, 1978; Wooton and Chantry, 1980). However, it should be noted that the arc-quenching capability of the mixture is practically reduced proportionally to the partial pressure of SF_6.

Temperature difference: When a gas volume is subjected to a temperature difference, at equilibrium, this imposes a gradient of the gas density within the gas volume (Trinh, 1982) as discussed in Chapter 4. This results in a reduction of the dielectric withstand of the gas insulation, which is a function of the lowest gas density within the compartment. Properly compartmentalizing the gas-insulated bus with a gas-barrier spacer installed at the building wall will resolve this problem.

11.4.3.2 Humidity

In spite of the self-contained environments of GIS, it is observed that water can be absorbed in aluminum and, particularly, in epoxy spacers. Subjected to variations of ambient temperature, humidity continuously

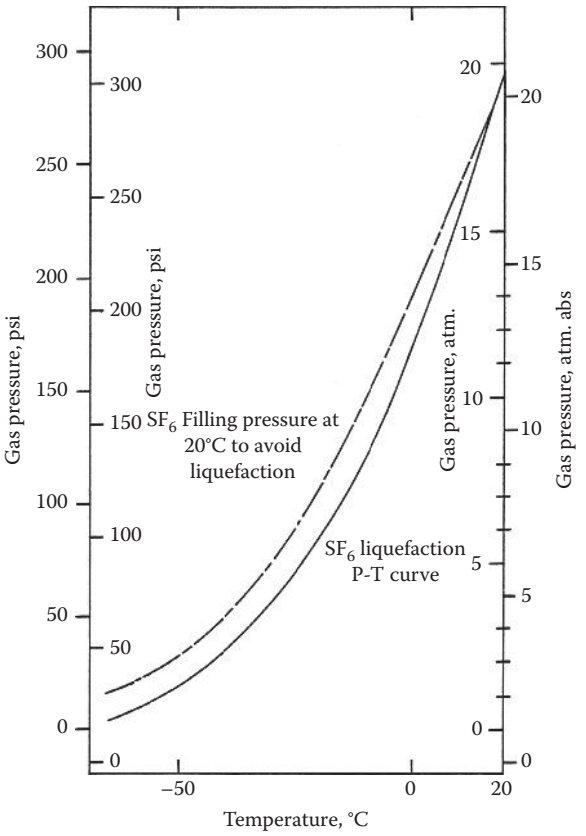


FIGURE 11.30 Characteristics of change in state of SF_6. (Trinh, N.G., Consideration of the effect of a temperature gradient on the dielectric performance of a CGI bus, *IEEE International Symposium on Electrical Insulation*, Philadelphia, 183, 1982.)

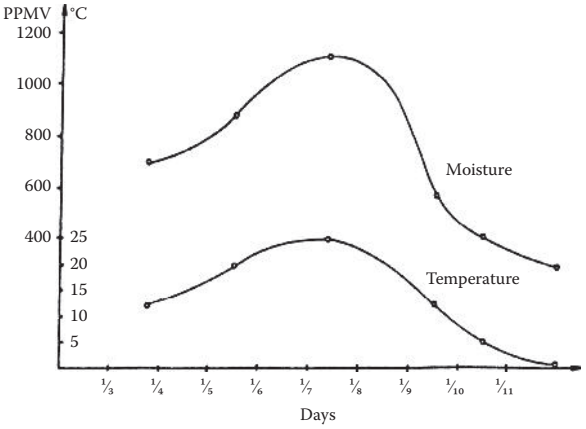


FIGURE 11.31 Seasonal variations of humidity in gas-insulated equipment carried out at the Norwegian Institute of Technology. (From Chu, F.Y. and J-M. Braun. *Assessment of Moisture in Gas-insulated Substations*. Canadian Electrical Association, report No. 217 T 424, October 1989.)

exchanges between the gas, spacers, and aluminum conductor and envelope, giving rise to a seasonal variation of humidity within the gas-insulated equipment as shown in Figure 11.31 (Chu and Braun, 1989).

These variations of humidity, combined with the wide range of temperatures to which gas-insulated equipment may be exposed, have resulted in the establishment of strict limits concerning the acceptable level of

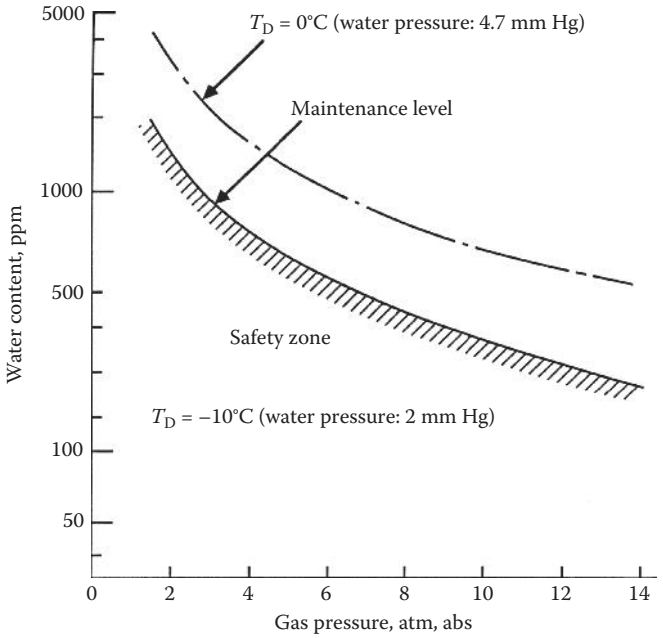


FIGURE 11.32 Recommended limits for the acceptable levels of humidity in gas-insulated equipment. (From Chu, F.Y. and J-M. Braun. *Assessment of Moisture in Gas-insulated Substations.* Canadian Electrical Association, report No. 217 T 424, October 1989.)

humidity. Schmidt recommends maintaining the relative humidity level in the gas-insulated equipment to keep the dew-point temperature below the lowest temperature encountered in service (typical dew-point temperature is −10°C) to avoid formation of liquid water at the gas/spacer interface (Schmidt and Szente, 1974). Figure 11.32 summarizes the recommendations regarding the admissible level of humidity for gas-insulated equipment. These are generally more strict for disconnecting equipment due to the presence of SF_6 decomposition by-products, which are more sensitive to humidity. Typically, a level of 65 ppm at 4 atm abs is recommended for equipment operating at temperatures as low as −40°C (Chu and Braun, 1989).

11.5 Accessories

High-voltage cables comprise relatively short sections, joined together to meet the required length. In addition, to connect the cable to either the overhead line or other equipment, terminations and bushing are also required. The distance between two joints, determined by the length of the cable in a reel, varies with the dimensions and type of cable. It can be in the range of hundreds of meters for impregnated paper–oil and polymer-insulated cables. It is only a few tens of meters for rigid gas-insulated cable imposed by the limits of transportation. Both joints and terminations are specific to the type of cable and must be built up on-site, which requires qualified technical personnel and particular working conditions regarding cleanliness and well sheltering from adverse weather conditions. Design principles for the basic accessories, straight joint and termination, are discussed in the following for the three insulation systems: paper–oil, polymer, and SF_6 insulation.

11.5.1 Impregnated Paper–Oil Accessories

11.5.1.1 Principal Types of Accessories

Impregnated paper–oil-insulated accessories are the most widely used, either as straight joints to extend a cable length, or terminations to connect the cable to overhead line conductor or other pieces of

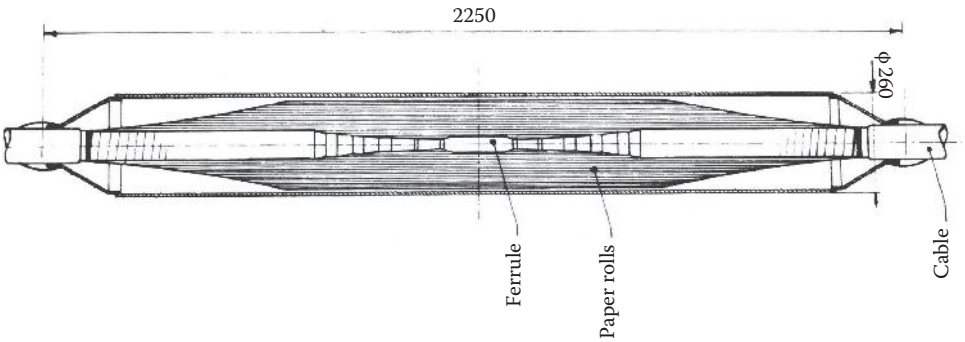


FIGURE 11.33 Illustration of cable straight joint. (From Luoni, G. et al., *IEEE Trans. Power Apparatus Syst*., PAS-100(1), 174, 1981.)

equipment, or wall bushing. Impregnated paper–oil-insulated accessories are sometimes used in conjunction with gas-insulated equipment or polymer-insulated cables.

Sectionalized straight joints: Are used to extend the length of a cable or to repair a failed cable. The design of a straight joint is necessarily symmetrical, connecting two identical cable sections. To build up a cable straight joint, it is necessary to complete the electrical and hydraulic circuits before building up the insulation of the joint, generally at the detriment to its physical dimensions, which can reach two to three times the diameter of the cable. Figure 11.33 shows a typical arrangement of a cable straight joint. For oil-filled cables, the central oil channel can be blocked by the conductor joint, the oil being diverted in the joint envelope. Furthermore, the cable being filled with oil, oil leakages are unavoidable during the work and must be replaced from another entry point to the cable. One can also locally freeze the oil at both sides of the joint with liquid nitrogen. The conductor joint is covered with a metal tube large enough to cover the whole insulation of the cables. The tube is electrically connected to the central conductor, thus providing an electrostatic screen to counter the effect of work imperfections on the local distribution of the electric field at the conductor joint.

The insulation of the joint is reconstituted from two stress cones to uniformly grade the longitudinal field over the distance that the cable sheath is expanded to the joint sheath. A set of metal screens provide uniform grading to the applied voltage within the joint insulation. Their dimensions are determined from the capacitive voltage distribution, a straightforward although tedious process. The insulation around the conductor joint is reconstituted with preimpregnated paper tape, sometimes with the help of a prefabricated insulation sleeve. In general, the insulation of the joint is thicker to reduce the electric field to about half of its nominal value. The electrostatic screen is made of metal tape or carbon and fixed to the insulation. The complete joint is placed in a metallic envelope hermetically welded to the cable sheath. Finally, a protecting envelope completes the cable joint and ensures its mechanical protection.

Terminations: Allow connection between a cable and the phase conductor of an overhead line. The insulation of a cable termination must ensure the transition of the compact cable insulation to that of air atmospheric insulation in overhead line, which requires much larger insulation clearance. The usual way to realize such a transition between the two insulation systems consists of terminating the cable insulation within an insulating housing, generally of porcelain, which provides the required insulation distances for the overhead line. Figure 11.34 illustrates a typical arrangement of an impregnated paper–oil-insulated termination. The cable conductor is joined to a connector, which also blocks the central oil channel. To maintain the dielectric integrity of the cable insulation, the cable sheath is sealed at the base of the porcelain housing, while the electrostatic screen is extended inside along a stress cone constituted from preimpregnated paper tape. A built-up insulation containing potential grading screens follows to ensure an adequate distribution of the applied potential over the exposed portion of the termination insulation.

Wall bushing: Is essentially a back-to-back assembly of two terminations to minimize the dimensions of the passage of a high-voltage conductor through the wall to join two sections of an overhead circuit. It is noticed, in this case, that the potential grading screens occupy the central part of the bushing insulation.

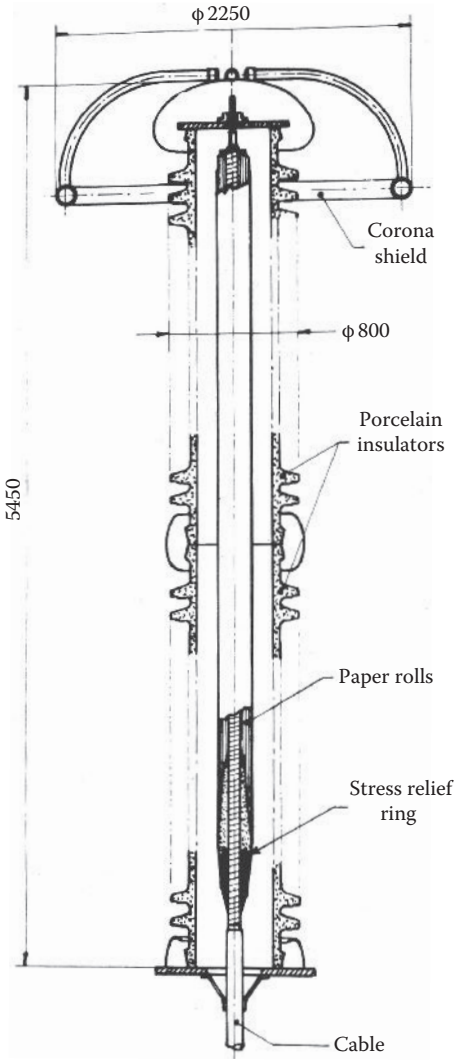
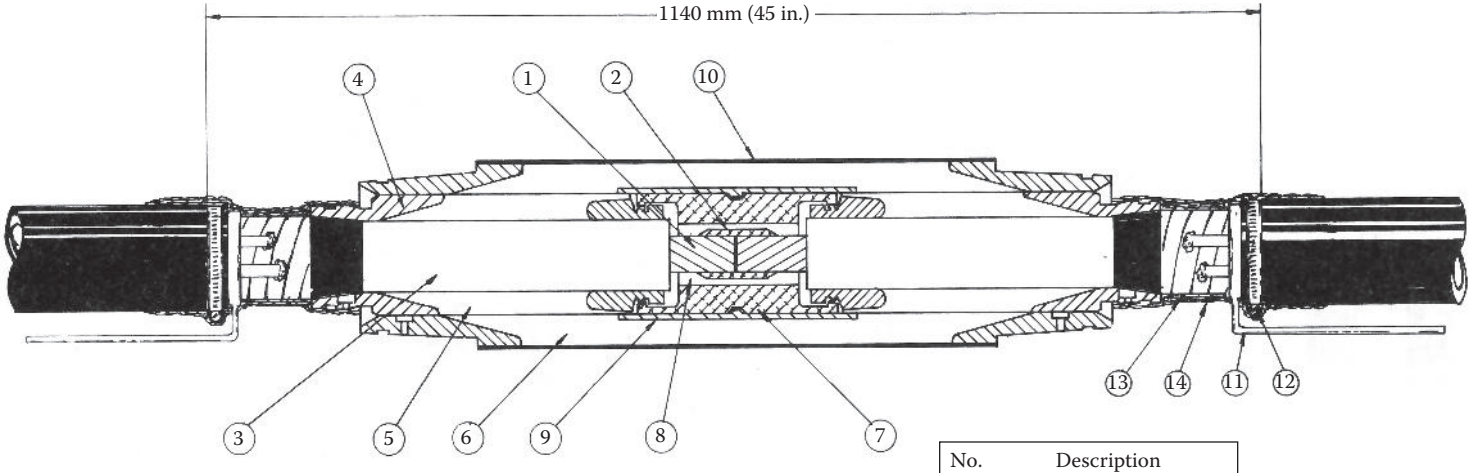


FIGURE 11.34 Illustration of paper–oil-insulated termination. (From Luoni, G. et al., *IEEE Trans. Power Apparatus Syst.*, PAS-100(1), 174, 1981.)

11.5.2 Extruded Insulation

The approach described earlier for impregnated paper–oil-insulated accessories applies also to accessories for solid cables with extruded insulation. Figure 11.35 illustrates the general arrangement of accessories. The building of a cable joint follows the same procedure:

- The cable conductors are joined together by compression or welding. Polymer insulation being more sensitive to heat, particular precautions must be taken to limit excessive heating of the cable conductor during the jointing process.
- A conductor shield covers the whole cable insulation to minimize the effect of discontinuity in the dielectric.
- The insulation at the joint is rebuilt, with the same precautions regarding the abrupt change in the insulation thickness at the joint. The insulation is built up along a stress cone to release the stress at the cable shield before it is opened and adequate control of the potential distribution within the joint insulation by means of a set of semiconducting screens.



138 kV Splice assembly

No.	Description
1	Cable conductor
2	Conductor connector
3	Cable insulation
4	Cable insulation shield
5	Cable adapter
6	Spice sleeve housing
7	Heat transfer sleeve
8	Heat transfer medium
9	Housing conductive insert
10	Semi conductive shield
11	Grounding ring
12	Clamp
13	Mastic sealing tape
14	Vinyl electrical tape

FIGURE 11.35 Illustration of polymer-insulated joints. (From Edgerton, N.W., A premolded splice for 138 kV extruded dielectric cable, *IEEE Trans*., PAS-97, 2178, 1978.)

- The profile of the stress cone is determined in the same way as for paper–oil-insulated joint. However, the polymer insulation does not favor the installation of multiple semiconducting screens for grading the potential within the insulation, and their number is kept to minimum.

To reconstitute the insulation around the conductor joint, several techniques exist, using copolymerized EPR tape, on-site molding, injection of PE, or using prefabricated insulation. The copolymerized rubber being less dielectrically performing than polymers, its use requires a thicker insulation. This, combined with a high loss factor of the rubber, tends to favor a thermal and electromechanical failure of the joint. However, practical experience shows that the joints with copolymerized rubber tape perform better than certain joints with PE insulation. Such a behavior may be attributed to the high flexibility of rubber to adapt itself to deformations of the conductor during thermal cycles.

The polymer insulation of the joint can be reconstituted by molding. Two techniques have been developed. The first uses PE tape to rebuild the joint insulation. The final insulation is obtained by thermal fusion under pressure to complete the curing of the polymer insulation. This technique provides the reconstituted insulation with a good dielectric withstand under impulse voltage. However, there are still some drawbacks in the long-term behavior of the joints, causing failures subsequent to thermal cycles at full load.

The second technique injects liquid PE in a mold covering the joint and kept under pressure and high temperature to assure the filling of the mold and the adhesion to the cable insulation. The insulation is completed with a semiconducting paint, recovered by semiconducting tape, and secured within a protecting metallic sleeve. The extrusion of polymers being a delicate operation, on-site use of this technique is made only on EHV accessories, 300 kV and higher. For low-voltage cables, prefabricated insulation sleeves of *slip-on* type exist, which simplify considerably their interconnections.

For connection of cables to conductors of an overhead line, impregnated paper–oil-insulated terminations are still used, lacked of fully developed terminations with dry insulation. Figure 11.36 illustrates the typical arrangement of a cable termination. The termination is prepared around a metallic tube replacing the cable conductor. During on-site installation, the cable conductor is pushed in place of the metal tube, and hermetic seals are installed prior to the filling of the termination with oil.

11.5.3 Gas (SF_6) Insulation

With their modular design, gas-insulated cables and equipment do not require specially designed joints. The numerous insulating spacers already required by the modular design are effectively factory-prefabricated joints, which simplify the assembly process while preserving the integrity of the SF_6 insulation.

The connection to an overhead line is provided by gas-insulated terminations of relatively simple design. The SF_6–air interface is ensured by an insulating housing of porcelain or composite resin to provide better protection against the possibility of shattering the porcelain housing subsequent to an internal failure. A gas-barrier spacer is normally used to compartmentalize the equipment from the insulating housing, facilitating its installation. Finally, the field distribution at the surface of insulating housing is controlled by a unique metallic grading screen at ground potential. The adjustment of the length of the grounded grading screen allows a control of the field distribution at the surface of the insulating housing. The arrangement is relatively less effective than grading screens in an impregnated paper–oil-insulated termination. It is often observed that users prefer a paper–oil-insulated termination for gas-insulated cables and equipment, even if this means additional complications related to a second insulation system within the same equipment.

SF_6-insulated terminations exist for use in oil/SF_6 and SF_6/air interfaces and are in service up to voltages of 800 kV ac. Pressurized porcelain housing may shatter following a puncture, with serious consequence to laboratory personnel. IREQ has developed for the needs of the high-voltage laboratory, an SF_6-insulated terminations of 1 MV ac with a BIL of 2100 kV, using a fiber-glass housing, an elegant solution to the problem of shattered porcelain (Figure 11.37). As for gas-insulated wall bushing, it is essentially a back-to-back assembly of two cable terminations to minimize the passage through the wall of a high-voltage connection of two sections of an overhead circuit.

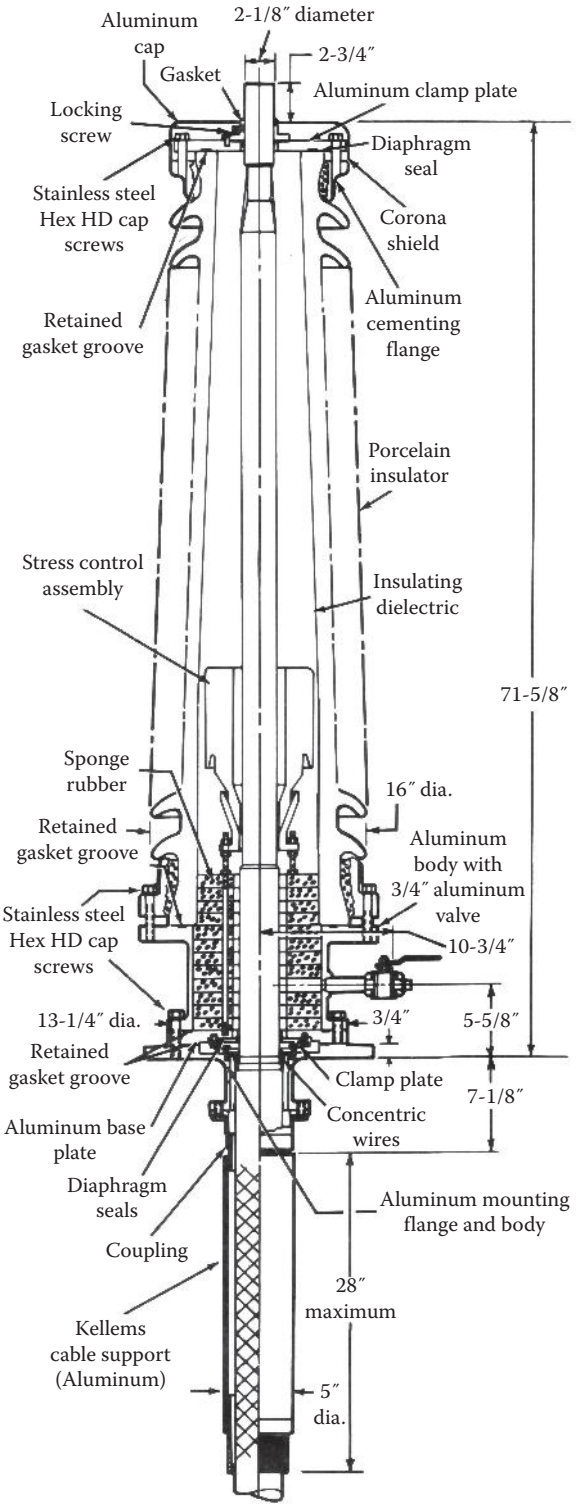


FIGURE 11.36 Illustration of polymer-insulated cable termination. (From Heppner, D.R. and Gear, R.B., New cable terminations for solid cable systems 15 kV and above, *IEEE Trans*., PAS-91, 975, May/June 1972.)



FIGURE 11.37 1 MV ac termination with fiber-glass housing at IREQ. (Photo courtesy of Hydro Québec.)

11.6 High-Voltage DC Cables and Accessories

In general, power transmission by HVDC is less problematic to high-voltage cables. A dc current does not induce circulating currents in the metallic sheath. It does not generate dielectric losses in cable insulation or hysteresis losses in magnetic material. HVDC is also less vulnerable to the development of PDs in voids within cable insulation, allowing a higher operating field as compared with those admissible in HVAC. Field experience has shown that high-voltage cable insulation is more tolerant to dc than ac stress. Furthermore, lower losses associated with dc current allow operating the cables at higher currents, increasing proportionally the power transmission capacity up to 30% higher. Finally, there is no reactive power with HVDC, and hence, the critical length is much longer, limited uniquely by dc voltage drop and resistive losses.

In spite of the numerous advantages associated with HVDC cables, there are only few operating installations, the majority of which concern long-distance submarine system unsuitable for HVAC cables: Kingsnorth, 88 km (53 miles) long, 640 MW at ±266 kV; Gotland, 60 miles long, 20 MW at ±100 kV (upgraded to 150 kV in 1970); and Sardinia, 125 km (75 miles) long. The ±280 kV level was reached in 1969 with the British Columbia to Vancouver Island link (Eyraud et al., 1970), and the level of ± 400 kV with the Finland–Scandinavia link realized in 1989. All use *solid* mass-impregnated cables.

The first application of HVDC-impregnated paper–oil-insulated cables was in 1977 with the British Columbia to Vancouver Island link at ±280 kV and reached the level of ±450 kV in the St. Lawrence River crossing in 1990 (Couderc et al. 1992; Chaaban et al., 1992; Trinh et al., 1992). The use of pipe-type (Allam and McKean, 1981), polymer-, and SF_6-insulated cables for HVDC power transmission is possible although there are still few practical installations to date.

Application of high-voltage cables to the dc power transmission does not require major modifications to the cable design, as long as the various specificities related to this mode of power transmission are taken into consideration. These aspects of the application of high-voltage cables to the HVDC power transmission will be discussed in the following.

11.6.1 Dimensioning of Conductors

The conductors for HVDC cables are simple in design: their structure is standard or of the Conci type (Figure 11.7), since only resistive losses contribute to energy losses. They are proportional to the resistance of the conductor according to (11.14)

The same procedure used for dimensioning of the ac cable conductor still applies for dc cable. The lower losses in dc cables result generally in conductors of smaller size for the same current rating, which often do not require forced cooling.

11.6.2 Dimensioning of the Insulation

For a dc cable, the insulation thickness must take into account the fact that the distribution of the electric field is dictated by volume resistivity of the insulation during the steady-state regime and by capacitive distribution during transient overvoltage.

11.6.2.1 Field Distribution in Steady-State Regime

The volume resistivity of the insulation is a function of both the local temperature and the applied electric field, according to (Fallou, 1965)

$$\rho = \rho_0 \exp(-\alpha\theta)\exp(-kE) \tag{11.37}$$

where

ρ_0 is the resistivity of the insulating material at 0°C
θ is the temperature of the insulating material
ρ is the corresponding value at temperature θ
E is the applied electric field,
α and k are the empirical coefficients of temperature and electric field

Since the dc resistivity of an insulation is a function of both the temperature and field intensity, the exact solution for the dc field distribution is complex. However, an approximate solution for the field distribution in a coaxial cable, taking into account of the variable resistivity of the insulation, Equation 11.38, has been obtained by Eoll (1975) as follows:

$$E(r) = \frac{\delta U_0 (r/r_i)^{\delta-1}}{r_i \left[1-(r_c/r_i)^{\delta}\right]} \tag{11.38}$$

with

$$\gamma = \frac{kU_0}{r_i - r_c}; \quad \beta = \frac{\alpha W \rho_t}{2\pi}; \quad \text{and} \quad \delta = \frac{\beta+1}{\gamma+1}$$

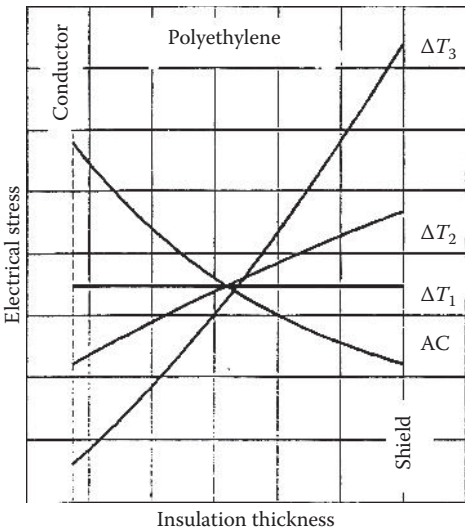


FIGURE 11.38 Distribution of electric field in cable insulation under ac and dc voltages at different loading conditions. (From Khalil, S. *Electr. Insul. Mag*., 13(6), 35–47, 1997.)

where

$E(r)$ is the field at r in MV/m
r_i is the maximum radius of the insulation in m
r_c is the radius of the conductor in m
W is the resistive losses generated by the conductor calculated according to Equation 11.12 in W/m
U_0 is the applied dc voltage between the conductor and sheath in MV
ρ_t is the thermal resistivity of the insulation in C m/W,
α (C^{-1}) and k (m/MV) are the temperature and field coefficients in Equation 11.38

The distribution of the electric field E between the conductor and the cable sheath varies with the load condition of the cable as illustrated in Figure 11.38, which shows the field distributions in a XLPE cable insulation for different loading conditions (Khalil, 1997). At no load, the field is maximum at the conductor and minimum at the cable shield and is identical to ac field. As the load current increases, the electric field at the conductor is reduced as its temperature rises. At full-load condition, the field may be minimum at the conductor and maximum at the cable sheath.

To take account of this "stress inversion," cable manufacturers sometimes use thin paper tapes not only close to the conductor but also near the cable sheath to reduce the local electric field. However, the peripheral layers of the insulation are more vulnerable than the inner layers in certain conditions (namely, during the bending tests on the cable). It is prudent to limit the design gradient at the cable sheath to a value lower than that at the conductor under conditions of full load, to take account of the inversion of the field within the insulation. The normal practice resides in specifying a maximum temperature difference ΔT between the temperature at the conductor and cable sheath that would result in an acceptable field inversion across the cable insulation.

11.6.2.2 Field Distribution in Transient Conditions

Because of the rapid variations of transient voltages, lightning or switching impulses, the field and potential distribution in cable insulation is controlled by cable capacitance. An important aspect of field distribution in a dc cable is related to its reversal of polarity subsequent to a transient voltage or following a change in the direction of energy transmission. In the latter case, the polarization phenomena being slow, the new charge distribution (of opposite polarity) within the insulation will slowly establish itself after

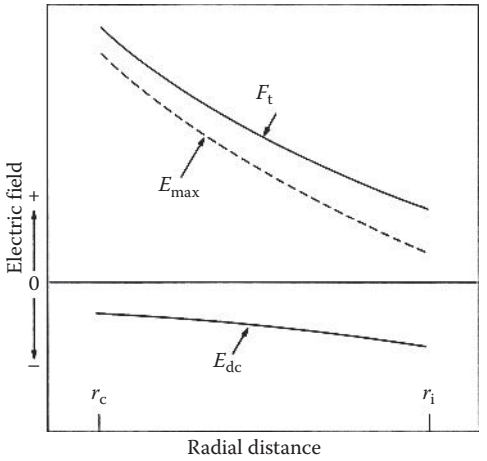


FIGURE 11.39 Distribution of the field under dc voltage superimposed by an impulse voltage of opposite polarity.

polarity reversal of the applied voltage. In transient conditions, the redistribution of charges remains unaffected. As a result, polarity reversal tends to locally overstress the insulation.

Referring to Figure 11.39, it shows the distributions of various stress components within cable insulation when a transient voltage occurs. It can be seen that cable insulation is subjected to a double stress corresponding to the superposition of the transient voltage $v_t(t)$ of amplitude V_t on the applied dc voltage U_{dc}:

$$u(t) = U_{dc} - V_t(t) \tag{11.39}$$

The corresponding electric field $e(t)$ is

$$e(t) = E_{dc} - f_t(t) \tag{11.40}$$

where

E_{dc} is the dc applied field

$f_t(t)$ is the transient field of amplitude F_t

To have a polarity reversal, the amplitude of the transient voltage V_t must exceed the absolute value $|U_0|$ of the applied voltage. The maximum field intensity occurs at the central conductor and has a value of

$$E_{max} = \frac{V_t}{r \ln(r_i/r_c)} - \frac{\delta U_0 (r/r_i)^{\delta-1}}{r_i \left[1 - (r_c/r_i)^{\delta}\right]} \tag{11.41}$$

with δ as defined earlier in (11.38).

11.6.2.3 Field Enhancement in Butt Gap

For ac cables, butt gaps, the free space between two consecutive tapes to facilitate the bending of the cable, are the weak points of the tape insulation. The situation is, however, different for dc cables where the field enhancement is dictated by the resistivities of paper and oil according to

$$\frac{E_h}{E} = \frac{n+1}{1 + n\frac{\rho_p}{\rho_h}} \tag{11.42}$$

where ρ_h and ρ_p are the resistivities of the oil and impregnated paper.

For a typical overlay of 70/30, $n = 3$, and the volume resistivities of $\rho_h = 2 \times 10^{13}$ and $\rho_p = 10^{14}$–10^{15}, the field enhancement in the butt gap amounts to less than one, which means that the field in the butt gap is effectively lower than the value for a homogeneous insulation. Thus, in dc, the greater part of the electric field is on the impregnated paper, which has better dielectric strength. This explains also why the impregnated paper–oil cables have better dielectric performance under dc voltage. The breakdown field is 100–120 kV/mm (as compared with approximately 50 kV/mm in ac), which is the same as under impulse voltages, and is practically independent of the rate of rise of the applied voltage (Miranda et al., 1976).

PDs do not significantly affect paper–oil insulation of dc cables as a result of the deposit of charges produced on the wall of the butt gap. The local field within the butt gap is reduced below the onset level of PDs, which are suppressed, and can resume their activities only when the deposit charges are sufficiently neutralized. Aging is much slower under dc voltage. The acceptable maximum gradient within the insulation of paper–oil insulation is 30 kV/mm for nonpressurized mass-impregnated cables and 40 kV/mm for the pressurized cables.

The less severe constraints of dc voltage have allowed the introduction of a new cable design for submarine cable (TOPIST), the structure of which differs considerably from the conventional design (Balog et al., 1987). The lapped insulation is made of bioriented polypropylene tape of 0.025 mm thick, similar to that used in the all-film insulation for condenser. No impregnating fluid is used. The tapes are pressed one upon the other with no possibility for the tape layers to slide during bending of the cable. It is the elasticity of the polypropylene tape that allows the flexion of the cable. The TOPIST cable went through the experimental stage in 1987, having successfully passed the CIGRE bending test (100 m with a radius of curvature of 5 m), the polarity inversion test ($U_0 = 250$ kV), and impulse test (between 1000 and 1100 kV). Aging test was conducted on three lengths of cable to characterize the reliability of the insulating material with encouraging results. The main drawback of this type of cable resides in the very large number of layers required to build up the insulation; the cable must pass three or four times through the taping machine.

Finally, since the electrical conductivity of dc cables is essentially controlled by temperature, the temperature difference across the cable insulation has a pronounced effect on the electric field within the insulation. Forced cooling of the dc cables when applied externally to the cable tends to increase this temperature difference by cooling its external surface and hence to increase the maximum electric field at the cable shield. SCOF cable lends itself easily to forced cooling with the oil channel located within the cable conductor. In practice, one aims at keeping the temperature difference across the insulation in the range of 20°C–25°C.

11.6.3 SF_6-Insulated Cable

In spite of the wide application of gas insulation in ac substation and short links up to the EHV level of 800 kV ac and important research work realized in the field of SF_6 insulation under dc voltage, the feasibility of which has been demonstrated up to the level of ±500 kV, no practical application has yet been made (Cooke et al., 1982; Cookson, 1985). Generally speaking, gas insulation and, by extension, gas-insulated cables and GIS do not have problems with accumulated charges and polarity reversal when operating under dc voltage. However, these problems do exist for the solid insulating spacers. They are of less significant due to the relatively small proportion between solid and gas insulation and to the rather low operating field intensity within the solid dielectric. Charge deposition on the surface of the insulating spacers may occur under conditions of prolonged PDs or repeated flashover at the gas–spacer interface, not expected under normal operating conditions.

Solid particle contamination: Is a specific aspect of gas-insulated equipment. Under dc voltage, the particles, once lift off, cross the whole gas gap and are neutralized at contact with the central conductor and fall back on the envelope, and the process can be repeated again. When the central conductor is at negative polarity, PDs developing at the particles can maintain them in a stationary mode close to the conductor (Cooke et al., 1977; Dale, 1983; Rizk et al., 1979). Such a behavior of particles in a dc electric field tends to indicate that their influence on the dielectric withstand of the gas gap is more critical than under ac.

Figure 11.40 compares breakdown voltage of a coaxial gap under dc and ac voltages under conditions of particle contamination by aluminum wire particles. It can be seen that particle contamination

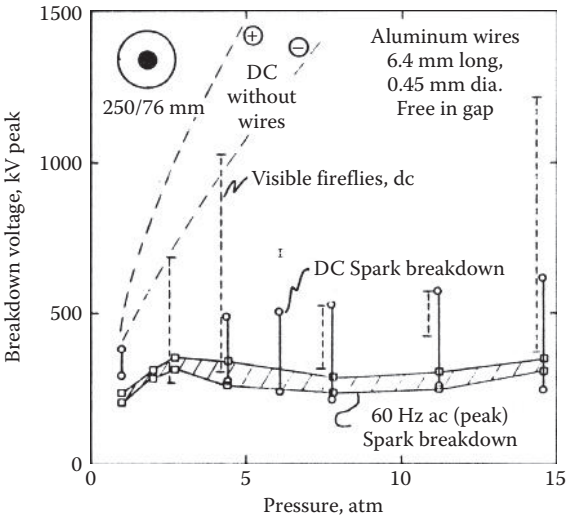


FIGURE 11.40 Effect of particle contamination on breakdown voltage of SF_6-insulated coaxial cable. (From Cooke, C.M. et al., Influence of particles on AC and DC electrical performance of gas-insulated system at extra high voltage, *IEEE Trans., PAS*-96, 768, 1977.)

can significantly reduce the dielectric withstand of the gap, although breakdown voltage with particle contamination does not differ under dc and ac (peak) voltages. Also, the fact that the particles cross the whole gas interval favors their deposit at locations critical to the spacers, that is, close to the central conductor. It is observed that more particles are deposed on the spacers under dc voltage than with ac voltage (Dale, 1983). These considerations on particle contamination may indicate that more precautions may be needed during the installation of gas-insulated cables to minimize the particle contamination.

11.6.4 Accessories

11.6.4.1 Impregnated Paper–Oil Insulation

The design of joint and terminations is similar for dc and ac cables, taking into account the fact that dimensioning of the grading screens is determined by the ratio of the conductivity of the insulating materials. A dc cable joint may be longer (up to ≈40%) than an equivalent ac joint, a direct result of a lower dc design limit field, which is a function of the resistivity of the insulation.

11.6.4.2 Polymer and SF_6 Insulation

No particular change is necessary for the design of accessories for dc voltage application. This is mainly due to the few dc applications of polymer- and SF_6-insulated cables so far. The explanation may simply be the range of dc voltage involved in today's project, between 400 and 600 kV dc, which is too high for polymer-insulated and too low for SF_6-insulated cables.

11.6.4.3 DC Pollution

This problem is dealt with in Chapter 10 on Insulators. As a demonstration of the severity of dc stress and outdoor pollution conditions, we have observed several flashovers on the 500 kV dc cable termination subjected to pollution test at IREQ. The porcelain has a leakage path of 22 m and a height of 6 m. The flashovers take place at voltages of 400 kV dc, with a light contamination (0.02 mg/cm^2) in clean fog. The operating experience of the Itaipu converter station (Brazil) at 600 kV dc shows several in-service failures of the wall bushings, under rain and in presence of a light pollution of the porcelain housing (Rizk and Kamel, 1991). Similar problems occur also in Radisson converter station (Manitoba) at voltages of 450 kV dc. The use of silicon rubber housing or booster sheds appears to offer viable solution to this problem.

11.7 Maintenance Practices Consideration

Being a self-contained system, high-voltage cables do not require any special precaution to operate other than those recommended by the manufacturer to maintain the insulation system at its optimal conditions. However, because of insulation aging, utilities are interested to know the actual state of the insulation and an idea concerning its remaining life.

11.7.1 Actual State of Insulation

Utilities can carry out verifications of the state of cable insulation in view of making decision on the adequacy of the equipment to remain in service via noninvasive measurements of

- The bulk electrical parameters at the terminal points of the equipment, which can be performed on-site
- The aging decomposition by-products, principally dissolved gases in oil, which can be related to the aging state of the individual constituents of the insulation system

Measurement of bulk parameters: Measurement of the PD level and the power-loss factor tanδ remains the principal means to assess the aging state of insulation. The subject is covered in Chapter 14. Monitoring the variations in PD and tanδ with time can give a good appreciation of the aging state of the insulation.

Measurement of the decomposition by-products: Since aging of the insulation produces decomposition by-products of its constituents, the reverse logic implies that the actual state of the insulation system may be assessed from appropriate measurements of their decomposition by-products. This is particularly true for paper–oil insulation where the decomposition by-products are known and well correlated with the aging state of the oil and paper.

Polymers also form decomposition by-products. The small amount of by-products produced and the difficulty to collect them have so far prevented their application in the evaluation of the aging state of polymer, which is evaluated in terms of the density and length of the water and electric trees present in the insulation.

11.7.2 End of Life

End of life represents the final stage of the insulation system, which is then considered as unsuitable for continuing service. However, in practice, the end of life has different meaning for the individual constituent components, paper, oil, etc., and the whole insulation system, which allows the utilities to take appropriate actions in response to specific aging conditions.

Bulk parameters: Measurement of PD and power-loss factor tanδ, although feasible on-site, suffers from a clear definition of end-of-life criteria.

Decomposition by-products: Are currently used to determine end of life of the insulating materials, principally for paper–oil insulation. Their application is, however, limited to criteria for maintenance purposes; the degree of depolymerization gives a good indication of the residual mechanical property of paper. They still suffer from no clear correspondence between the aging state of the materials and the dielectric performance of the insulation as a whole.

Tree length in polymers: The end of life for polymer insulation is more related to the density of water and/or electric trees per unit of length of cable insulation and their dimensions since each one has a probability to develop into breakdown of the insulation. An evaluation of the tree density in the cable insulation near the fault location can be used to determine the length of cable to be replaced. A clear assessment of the end of life remains to be defined in terms of treeing density and length.

REFERENCES

ABB Ltd. SF6 gas-insulated switchgear—Type ELK, 1990.

Allam, E.M. et al. Development and long term testing of a low-loss 765 kV high pressure oil-filled pipe cable. Rapport CIGRE 21-06, Paris, France, 1986.

Allam, E.M. and E.L. McKean. Laboratory development of ±600 kV DC pipe cable system. *IEEE Transactions on Power Apparatus and Systems* PAS-100: 1219–1225, 1981.

Bahder, G., Garrity, T., Sosnowski, M., Eaton, R., and C. Katz. Physical model of electric aging and breakdown of extruded polymeric insulated power cables. *IEEE Transactions on Power Apparatus and Systems* PAS-101: 1379–1390, June 1982.

Balog, G. et al. TOPIST une nouvelle technique de câble sous-marin pour haute tension continue. In: *Conference CIGRE*, pp.122–124, October 1987.

Bellport, B.P. 525 kV cable picked for Grande Coulée. *Electrical World*, pp. 29–31, April 1970.

Boggs, S. and J. Xu. Water treeing—Filled versus unfilled cable insulation. *Electrical Insulation Magazine* 17(1): 23–29, January/February 2001.

Boggs, S.A., Chu, F.Y., Fujimoto, N., Krenicky, A., Plessl, A., and D. Schlicht. Disconnect switch induced transient and trapped charge in gas-insulated substations. *IEEE Transactions on Power Apparatus and Systems* PAS-101: 3593–3602, 1982.

Chaaban, M. et al. Evaluation of HVDC cables for the St-Lawrence river crossing of hydro-Québec 500-kV DC line—Part III: Thermal behavior. *IEEE Transactions of Power Delivery* PWRD-7(2): 609–613, April 1992.

Chu, F.Y. and J.-M. Braun. *Assessment of Moisture in Gas-insulated Substations*. Canadian Electrical Association, report No. 217 T 424, October 1989.

Cooke, C.M., Wootton, R.E., and A. Cookson. Influence of particles on AC and DC electrical performance of gas-insulated system at extra high voltage. *IEEE Trans*. PAS-96, 768–777, 1977.

Cookson A.H. Gas-insulated cables. *IEEE Transactions on Electrical Insulation* EI-20: 859–890, 1985.

Couderc, D. Revue de l'État des Technologies des Câbles de Transport a Très Haute tension en Courant Alternatif et Continu. IREQ Report, November 1987.

Couderc, D. et al. Evaluation of HVDC cables for the St-Lawrence river crossing of hydro-Québec 500-kV DC line—Part I: Dielectric and accelerated aging tests on prototypes. *IEEE Transactions of Power Delivery* PWRD-7(2): 1034–1042, April 1992.

Crine, J.P. Rate theory and polyethylene relaxation. *IEEE Transactions on Electrical Insulation* EI-22(2): 169–174, April 1987.

Cygan, P. and J.R. Laghari. Models for insulation aging under electrical and thermal multistress. *IEEE Transactions on Electrical Insulation* EI-25(5): 923–934, October 1990.

Dakin, T.W. Electrical insulation deterioration treated as a chemical rate phenomena. *Transactions of the American Institute of Electrical Engineers* 67(Part I): 113–122, 1948.

Dakin, T.W. and S.A. Studniarz. The voltage endurance of cast epoxy resins. In: *IEEE International Symposium of Electrical Insulation*, 1978.

Dang, C., Lamarre, L., Landreville, L., Blais, R., and N.G. Trinh. Dielectric Performance of Distribution XLPE-Cable Accessories at High Temperatures. CEA report 139-D-505A, 1990.

Dang, C., Parpal, J.-L., and J.P. Crine. Electrical aging of extruded dielectric cables. Review of existing theories and data. *IEEE Transactions of Dielectrics and Electrical Insulation* DEI-3(2): 237–247, April 1996.

De Maris, S. 500 kV CGI System is installed in the Cascades. *Transmission and Distribution Magazine*, pp. 51, April 1975.

Densley, J. Ageing mechanisms and diagnostics for power cables—An overview. *Electrical Insulation Magazine* 17(1): 14–22, January/February 2001.

Dick, E.P., Fujimoto, N., Ford, G.L., and S. Harvey. Transient ground potential rise in a gas-insulated substation—Problems identification and mitigations. *IEEE Transactions on Power Apparatus and Systems* PAS-101: 3610–3619, 1982.

Edgerton, N.W. A premolded splice for 138 kV extruded dielectric cable. *IEEE Transactions on Power Apparatus and Systems*, PAS-97(6): 2178–2186, November/December 1978.

Eoll, C.K. Theory of stress distribution in insulation of high voltage DC cables—Part I. *IEEE Transactions on Electrical Insulation* EI-10(1): 27–35, 1975.

Eyraud, I. et al. Transport par câbles sous-marins à courant continu à 300 kV entre la Colombie-Britanique et l'Ile de Vancouver. Rapport CIGRE No. 21-07, Paris, France, 1970.

Fallou, M. Nouvelles expériences sur les câbles à courant continu isolés au papier imprégné. *Revue Générale de l'Electricité* 24: 177–190, 1965.

Farnetti, F. et al. Power transmission of a self-contained oil-filled 1100 kV cable system full-scale tests and design criteria. Rapport CIGRE No. 21-09, Paris, France, 1984a.

Farnetti, F. et al. Testing of a 1100 kV, 3 to 9 GVA underground transmission system. *IEEE Transactions on Power Apparatus and Systems* PAS-103: 2034–2042, 1984b.

Fujimoto, N., Dick, E.P., Boggs, S.A., and G.L. Ford. Transient ground potential rise in a gas-insulated substation—Experimental studies. *IEEE Transactions on Power Apparatus and Systems* PAS-101: 3603–3609, 1982.

Fukuda, T. Technological progress in high-voltage XLPE power cables in Japan—Part I. *Electrical Insulation Magazine* 4(5): 9–16, September/October 1988.

Fukuda, T. Technological progress in high-voltage XLPE power cables in Japan—Part II. *Electrical Insulation Magazine* 4(6): 15–20, November/December 1988.

Gazzana Priaroggia, P., Piscioneri, J., and S. Margolin. The long island sound submarine cable interconnection, *IEEE Trans.,* PAS-90(4): 1863–1873, July/August 1971.

Gotoh, H., Okamoto, T., Suzuki, S., and T. Tanaka. Method for estimation of the remaining lifetime of 6.6 kV XLPE cables after their first failure in service. IEEE *Transactions on Power Apparatus and Systems* PAS-103(9): 2428–2434, September 1984.

Graneau, P. *Underground Power Transmission—The Science, Technology and Economics of High Voltage Cables*, Science Publication, John Wiley & Sons, 1976.

Heppner, D.R. and R.B. Gear. New cable terminations for solid cable systems 15 kV and above. *IEEE Transactions on Power Apparatus and Systems*, PAS-91: 975–978, May/June 1972.

Honda, M., Aoyagi, H., Koya, M., Kobayashi, N., and M. Tamura. V-t characteristics of epoxy molded insulation for sustained AC voltage. *IEEE Transactions on Power Apparatus and Systems* PAS-103(5): 1017–1023, May 1984.

Hydro-Québec. Reseau de Transport. April 1978.

Jocteur, R. et al. Développement de liaisons 400 kV isolées au polyéthylène basse densité, Rapport CIGRE No. 21-09, Paris, France, 1986.

Kalkner, W., Miller, U., Peschke, E., Henkel, H.J., and R. vonOlhausen. Water treeing in PE and XLPE insulated High Voltage Cables. *International Conference on Large High Voltage Systems*, CIGRE, paper no. 21-07, 1982.

Khalil, S. International research and development trends and problems of HVDC cables with polymeric insulation. *Electrical Insulation Magazine* 13(6): 35–47, November/December 1997.

King, S.F. and N.A. Halfter. *Underground Power Cables*. London, U.K.: Longman, 1982.

Kobayashi, T. et al. Development of 275-kV internally cooled XLPE cable. *IEEE Transactions on Power Apparatus and Systems* PAS-104(4): 775–784, April 1985.

Kothe, R., Bamji, S., Bulinski, A., and J. Densley. Impulse life tests on field aged XLPE cables containing water trees. In: *IEEE International Symposium on Electrical Insulation*, Washington, DC, June 1986, pp. 37–40.

Kubo, H., Noda, N., Nishino, J., Hata, R., and T. Miyazaki. Development of 275 kV oil-filled cable insulated with polypropylene laminated paper (PPLP). *IEEE Transactions on Power Apparatus and Systems*, PAS-101(12): 4472–4483, December 1982.

Luoni, G., Occhini, C., and B. Parmigiani. Long term tests on a ±600 kV DC cable systems. *IEEE Transactions on Power Apparatus and Systems* PAS-100(1): 174–183, January 1981.

McKean, A.L., Merrell, E.J., and J.A. Moran Jr. EEI manufacturers 500/550 kV cable research project cable C—High pressure oil paper pipe type. *IEEE Transactions on Power Apparatus and Systems*, PAS-90(1): 224–239, January 1971.

Miranda, F.J. et al. Self-contained oil-filled cables—A review of progress. In: *Proceedings of the Institution of Electrical Engineers* 123(3): 229–238, March 1976.

Montanari, G.C., Pattini, P., and L. Simoni. Voltage endurance of XLPE insulated cable modes. In: *IEEE International Symposium on Electrical Insulation*, Montreal, Québec, Canada, 1984, pp. 54–57.

Montsinger, V.M. Loading transformers by temperature. *Transactions of the American Institute of Electrical Engineers* 49: 776–792, 1930.

Moreau, E., Mayoux, C., Laurent, C., and A. Boudet. The structure characteristics of water trees in power cables and laboratory specimens. *IEEE Transactions on Electrical Insulation* EI-28(1): 54–64, January/February 1993.

Nitta, T. and H. Kuwahara. Time dependence of breakdown voltage and endurance testing of compressed gas insulation. *IEEE Transactions on Power Apparatus and Systems* PAS-100(6): 3055–3065, June 1981.

Occhini, E. et al. High voltage transmission systems at 750 and 1100 kV with oil-filled cables—construction and tests, CIGRE 21-08; 1978.

Ogawa, K., Kurata, M., Suzuki, H., Kawasaki, K., and N. Imai. Field test of 275-kV internally water cooled XLPE cable system. *IEEE Transactions of Power Delivery* PWRD-4(1): 8–18, January 1989.

Parpal, J.L., Crine, J.P., and C. Dang. Electrical aging of extruded dielectric cables. A physical model. *IEEE Transactions of Dielectrics and Electrical Insulation* DEI-4(2): 197–209, April 1997.

Rizk, F.A.M., Masetti, C., and R.P. Comsa. Particle-initiated breakdown in SF6 insulated systems under high direct voltage. *IEEE Trans*. 98(3):825–836, May 1979.

Rizk, F.A.M. and Kamel, S.I. Modelling of HVDC wall bushing flashover in nonuniform rain. *IEEE Transactions of Power Delivery* PWRD-6(4): 1650–1662, October 1991.

Sakamoto, Y., Fukagawa, H., Ninomiya, K., Yoshida, S., and N. Ando. Investigation of test method on DC XLPE cable. *IEEE Transactions on Power Apparatus and Systems* PAS-101(6): 1352–1362, June 1982.

Schmidt, W. and V. Szente. Effect of humidity on the electrical strength of SF6 gas-insulated H.V. equipment. In: *IEEE Canadian Conference on Power & Communication*, Montreal, Québec, Canada, 1974, pp. 241–242.

Studniarz, S.A. and T.W. Dakin. The voltage endurance of cast epoxy resins II. In: *IEEE International Symposium of Electrical Insulation*, 1982, pp. 19–26.

Tareev, B.M. *Physics of Dielectric Materials*, Moscow, Russia: MIR Publications, 1975.

Trinh, N.G. Consideration of the effect of a temperature gradient on the dielectric performance of a CGI bus. In: *IEEE International Symposium on Electrical Insulation*, Philadelphia, PA, 1982, pp. 183–186.

Trinh, N.G. et al. Evaluation of HVDC cables for the St-Lawrence river crossing of hydro-Québec 500-kV DC line—Part II: Cable testing facility for dielectric and accelerated aging. *IEEE Transactions of Power Delivery* PWRD-7(2): 1043–1049, April 1992.

12

Power Transformers

12.1 Introduction

Power transformers have been introduced since the early days of power transmission. Its development combined with the development of circuit interrupting devices, interrupters, and circuit breakers has contributed to the establishment of ac power transmission as the principal mode of transmitting electric power over long distances as well as distributing it to the consumer. However, while the demand for higher interrupting capacity and the high risk of fire hazards have favored the diversification of circuit interrupting devices from bulk oil breakers into new technologies using nonflammable air and SF_6 as the arc quenching medium, the basic design of power transformers did not change significantly during the last hundred years while progressing to meet the ever-increasing needs of modern power transmission system. It reached the voltage level of 735 kV in the 1960s and then crossed the 1000 kV level in the 1990s. Its power rating has progressed from an initial few kVA to reach several hundreds of MVA in today's transformer units. Such a performance of power transformers is the result of the continuous improvement in material application and technology.

Power transformers are built around a magnetic core, which confines the magnetic flux and provides an effective means of transferring the electric energy from one winding to the other. The windings operating at different voltages are built closely around the magnetic circuit, on an insulating structure, usually pressboard cylinders, to minimize straying magnetic field and assure maximum efficiency in energy transfer. The whole assembly is located within a metallic tank, which provides a contained insulating environment to the transformer assembly with accesses to the external circuit via bushings connecting the winding ends to appropriate nodes of the external circuit.

Core: The vast majority of power transformers is of core-type design. A transformer core is assembled from laminations, 0.025–0.05 cm thick, containing approximately 3% silicon and 97% steel. One of the greatest contributions to transformer efficiency and low cost was the introduction of grain-oriented iron in the 1940s. Its higher permittivity and lower cost increased the working flux density by approximately 30%. The silicon content reduces the viscous resistance to magnetization or hysteresis and prevents increased loss with age. Most lamination materials are cold rolled and specially annealed to orient the grains, or iron crystals, to obtain very high permeability and low hysteresis to flux in the direction of rolling. Most lamination materials are treated in one or several ways to develop a chemical coating to insulate the laminations from each other. The core construction may be built up from separated laminations, with layers of lamination placed so that the gap between lamination ends of one layer is overlapped by the lamination in the next layer. It may also be wound from a long continuous strip so that the flux will always flow along the grain of the strip. The resulting cylindrical core does not lend itself to the winding of the coils on the transformer core, especially for large HV coils, which are easier to wound separately from the core (Bean et al., 1959).

Windings: Are the other elements of power transformers. They allow the transfer of energy from one winding to the other according to their turn ratio, which regulates the output voltage and current:

$$\frac{U_s}{U_p} = \frac{N_s}{N_p} = \frac{I_p}{I_s}$$

where N_s and N_p are the number of turns in the secondary and primary windings, respectively.

Windings are wound from insulated conductors to form either cylindrical or layer coils or continuous-wound or interleaved disc-type coils. The selection of a specific coil arrangement is a matter of finding the optimal arrangement with respect to

- Adequate dielectric strength against the various types of stresses subjected to power transformers: operating ac voltage, switching and lightning impulses, and fault and test conditions
- Adequate coil ventilation
- Adequate mechanical strength
- Minimum cost

The construction of the windings must permit bringing out properly insulated leads and taps. It must further allow multiwinding arrangements and practical schemes to minimize eddy current losses, for example, transposition of subdivided conductors (Bean et al., 1959). Figure 12.1 illustrates the arrangement of windings of an HV transformer: the low-voltage winding is next to the core, inside the HV winding. Insulating barriers are located in the interwinding space to improve the field distribution and hence the dielectric performance of the insulation in the region around the HV end of the coils. Figure 12.1 also shows a typical potential distribution around the insulation of a power transformer (Okubo et al., 1987).

Transformer insulation: Is the single factor, which accounts for the development of power transformers into higher voltages, up to the 1000 kV level at present. This is attributed to the excellent ability of oil–paper insulation to meet the specific requirements of power transformers: to have an excellent dielectric performance and heat transfer properties. In the oil–paper insulation system, the main component is the mineral oil, which serves as the insulating material and at the same time as a cooling fluid. The cellulose paper, principally in the form of pressboard, made of paper, upgraded Kraft papers and polymer-based paper (Nomex), is required to provide a mechanical support to the windings and to allow adequate oil circulation for removal of the heat generated from the windings to low-temperature regions within the transformer.

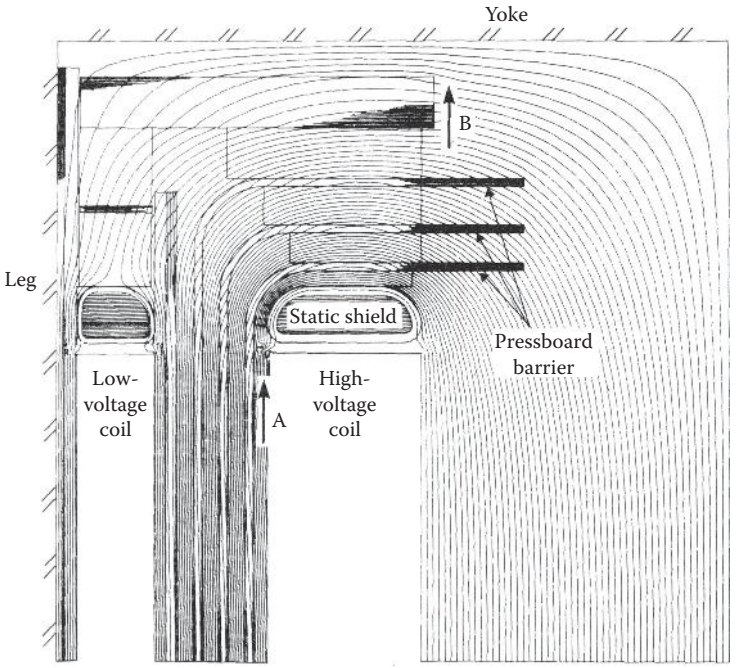


FIGURE 12.1 Field distribution in a typical transformer insulation. (From Okubo, H. et al., *IEEE Trans. Power Deliv.*, PWRD-2(1), 126, January 1987.)

For large power apparatus, the risk of fire hazards inherent to mineral oil is of most concern. The efforts to improve the insulation performances aim primarily at insulating fluids with low flammability: aliphatic hydrocarbons, silicon oils, the perfluorocarbons, and esters (Bartnikas and Srivastava, 1980). Upgraded Kraft papers and polymer-based paper (Nomex), with better thermal properties, are introduced in the insulation of power transformer to allow a higher operating temperature. Their utilization prevents solid particle contamination from bridging the oil gap. The dielectric stresses of power transformers remain relatively low, 2–5 kV/mm (Wilson, 1980; Rouse, 1987). This is explained by the fact that the ac dielectric performance of the oil–paper insulation is determined principally by the insulating fluid, and the different fluids have dielectric strength comparable to that of mineral oil. The presence of large volumes of oil combined with the distribution of the electric field (nonuniform and variable from one place to the other within the apparatus) and the unavoidable presence of particle contamination in the oil require an adequate operating margin and, hence, relatively low operating stresses. To improve the withstand characteristics and counter the effect of protrusions at the conductor surface, the winding conductors are varnished (for low-voltage windings) or taped with paper. The HV connections are also wrapped with paper tape; the thickness of the paper tape layer varies with the local stress.

Impregnation and preservation: Following the assembly of the transformer core and windings within the containing tank, the latter is cleaned and the paper vacuum dried before being filled with insulating oil for impregnation of the dry paper. Vacuum filling of the oil ensures that no gas pockets remain within the transformer tank. Drying the paper to remove the moisture is a delicate process, since water is also produced by the decomposition of paper and overdrying the paper will decompose it. In transformer, however, it is not necessary to carry the drying process near to the danger limit of 0.1% apparent moisture (Norris, 1963). The impregnation process is basically simple: it occurs naturally in time by simple immersion. However, to accelerate the process, heat, vacuum, and pressure are employed in industrial impregnation processes (Norris, 1963). To account for the expansion of the oil during load cycles, a conservator is added to the tank, usually located above the latter, and the oil is topped up within the conservator, thus keeping the whole insulation immersed within the insulating oil.

The dominant weakness of oil-impregnated paper insulation is its being easily contaminated, by solid particles, fibers, carbons, sand, etc., and, particularly, moisture. This emphasizes the need for preservation of the original state of the insulation throughout its service life if its initial strength is to be maintained. Since solid particles are most likely introduced during the manufacturing of the transformer, the preservation of the insulation simplifies to that of preventing moisture from entering the oil-impregnated paper via the oil. The current method using a conservator vessel with dehydrating breather plus an oil seal between the breather and the atmosphere has proved its efficiency and has been the standard practice for large HV transformers.

Hermetic sealing of the transformer tank with flexible metallic bellow or plastic diaphragm to take care of the oil expansion offers the possibility of preventing moisture from entering the impregnated paper insulation and further improving the dielectric performance of the oil-impregnated paper insulation by using degassed oil. Various methods of semisealing, often with nitrogen to eliminate possible oxidation effect as well as moisture, have been suggested. However, the question is far from settled since such an effective seal will also trap gas and moisture coming from the aging of impregnated paper insulation within the transformer and further accelerates the aging process.

SF_6 insulation: The introduction of SF_6 insulation in power apparatus also triggered the development of SF_6-insulated transformers as a solution to the fire hazard. However, while the gas insulation can handle the relatively moderate insulating stresses of power transformers, the problem remains regarding an efficient and economical solution to the removal of their heat losses. At present, their development is limited to units of moderate power ratings, 275 kV and 300 MVA, for use in urban areas where the land cost is high and severe control regarding the environmental impact of substations (Tokoro et al., 1982; Mukaiyama et al., 1991).

Design considerations: Design of power transformers obviously remains the property of manufacturers; we review in the following the main design aspects of interest to utility engineers, in particular the basic parameters that determine the size of power transformers.

The basic relationship between the flux in the core and the winding voltage is

$$u(t) = N\frac{\mathrm{d}\phi}{\mathrm{d}t} \tag{12.1}$$

where
$u(t)$ is the voltage developing across the winding
N is the number of turns
S is the core section
ϕ is the magnetic flux within the core

Under ac voltage, the earlier relation becomes

$$u(t) = U\sin\omega t = N\frac{\mathrm{d}\phi}{\mathrm{d}t} \tag{12.2}$$

where

U is the magnitude of the ac voltage
$\omega = 2\pi f$ the angular frequency

Integrating Equation 12.2 yields

$$\phi(t) = \frac{U}{\omega N}\cos\omega t = \phi_{\max}\cos\omega t \tag{12.3}$$

Equation 12.3 determines the maximum flux in the core for a given maximum voltage U across the winding. On the other hand, the maximum flux density in low-loss iron core is selected to provide a margin below the saturation density of the iron to limit the exciting current under event of TOVs. This allows the determination of the core cross section as a function of N, the number of turns. The kVA rating of the transformer fixes the nominal current I that, together with the number of turns N, determines the cost of copper for the winding. Some optimization is then possible to reach a design value for the core cross section and its cost, the number of turns N, and the copper cross section and its cost.

The voltage at the HV winding is the main parameter for the dimensioning of the transformer insulation: turn-to-turn and layer-to-layer insulation, insulation between windings, and between winding and the transformer tank. These aspects will be discussed further in the chapter.

In addition to the earlier two fundamental aspects, transformer design must take into account the following:

- The removal of heat generated in the windings. This is a two-stage process, where the generated heat is first transferred to the oil volume and, subsequently, to the heat exchanger to evacuate the generated heat into an ambient environment. In cylindrical wound coils, vertical spacers are placed around the insulating cylinder, over which the winding is wound, to form ducts for oil circulation between the cylinder and the inside of the coil. Spacers and washers are used in disc-type coils to separate the sections. Insulating spacers are also placed at the ends of the coil for mechanical support.

  In natural oil natural air (ONAN) transformers, the generated heat is transferred to the oil via the thermosiphon effect: the expansion of the oil volume in the region of high temperature initiates the oil circulation, which is sustained by the temperature difference between the hot winding and the cooler surrounding oil. When the heat removal efficiency exceeds 0.14 W/cm^2 (0.9 W/in.^{2}) (Bean et al., 1959), the surface temperature drop through the insulation may exceed 20°C, reducing the heat transfer efficiency due to the usual 55°C allowance for temperature rise in power transformers. Forced oil flow may be necessary. The heat transfer from the oil to the surrounding ambient is made via the transformer tank. For small transformers, this is sufficient; in large transformer units, the oil is circulated through radiators that are adequately dimensioned.

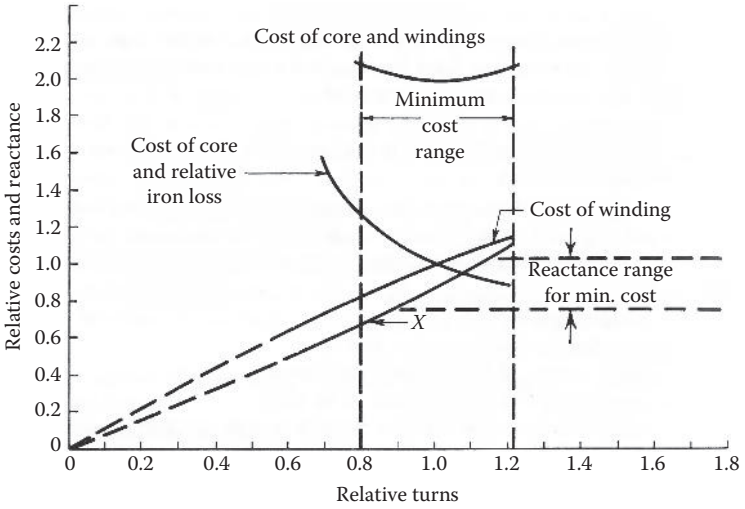


FIGURE 12.2 Cost-effective approach to power transformer design. (From Bean, R.L. et al., *Transformers for the Electric Power Industry*, McGraw-Hill Book Co., New York, 1959.)

- The mechanical stresses are related to load and short-circuit currents. Cylindrical coils are subjected mainly to radial forces. Axial forces can, however, develop as a result of imperfect coil alignment or by the presence of taps. Disc-type coils are subjected to axial forces. To counter these mechanical forces, collars are used to support the end turns, and the end of the windings is rigidly held in place by properly anchoring the leads.

Both these aspects, which involve specific manufacturer's experiences, are out of the scope for the present book. The readers can find a comprehensive discussion on the subject in the reference (Bean et al., 1959). Because of the large number of parameters involved, manufacturers usually take a cost-effective approach to design power transformers, where their in-house experience plays a significant role. Figure 12.2 illustrates such a cost-effective design approach, where the variations of the relative cost associated with various design parameters are presented in terms of the relative number of turns in the winding. It is shown that the winding cost goes up with the number of turns while the cost of the core decreases. A range of minimum cost of core and windings can be defined, from which the final design parameters are optimized.

This chapter reviews the main insulating properties of transformer insulation, practical approaches to its dimensioning, improvements to the insulating materials, the control of humidity and particle contamination, and the environmental impact, mainly generation of AN, of power transformers.

12.2 Transformer Insulation

12.2.1 Operating Stresses

Evolution of operating stresses in electric equipment follows closely improvements in the insulation system. A better dielectric performance improves the characteristics of related equipment, in voltage and power ratings, while enhancing their reliability and reducing the physical dimensions and sometimes their cost. Considerable improvements have been achieved since the introduction at the beginning of the twentieth century of oil–paper insulation, namely, with the development in material technology, which provides better basic components, polymer film and paper base, and impregnating fluid.

However, because of the specific needs and different operating conditions, the operating stresses vary considerably with each type of equipment. Generally speaking, the less severe stresses are found in large power apparatus, transformers, and shunt reactors. The most severe stresses are found in the small components,

TABLE 12.1

Typical Operating Stresses for Oil–Paper Insulation in Power Transformers

	Symbol	Notes	Units	Values
Dielectric stresses				
Nominal stress[a]	En	AC	kV_{rms}/mm	1–3
Maximal stress[b]	Em			2–5
Test stress[c]		AC		3–6
Lightning impulse			kV/mm	
Switching impulse				
Breakdown field[d]		AC	kV_{rms}/mm	30–40
Lightning impulse			kV/mm	80
Thermal constraints				
Operating temperature			C	85
Overloading temperature			C	95
Temperature rise			C	65
Hot spot temperature			C	100
Environmental stresses				
Minimal ambient temperature			C	–50
Maximal ambient temperature			C	40

[a] Stresses under normal operating conditions.
[b] Stresses under maximal operating conditions, typically 1.5–2 times the in-service stresses.
[c] Stresses defined by test conditions, typically 2 times the maximal stresses.
[d] Limit withstand of the insulation, established from laboratory tests on samples, models, or prototype.

condensers, where the need of storing large amounts of energy in the smallest volume possible contributes to favor a uniform field configuration operating at high stresses. Table 12.1 summarizes the typical operating stresses for power transformers. Withstand levels for lightning impulse, switching impulse and power frequency as a function of highest operating voltage are given in IEC Standard (IEC 600-71-1, 1993).

12.2.2 Oil–Paper Insulation in Power Transformers

The oil-impregnated paper insulation used in power transformers has a dielectric strength much higher than that of the oil and paper taken separately. However, it is sensitive to absorption of moisture and gases. As a result, adequate operation of power transformers depends on both its design and on the preservation of the initial state of the insulation. These aspects will be discussed in the following.

12.2.2.1 Winding Arrangement

As already mentioned, power transformers use one of the two types of winding: the cylindrical coil and the interleaved disc-type coil.

The cylindrical wound coil consists of one or more concentric layers of insulated conductors, wound on insulating cylinders. Each layer has several turns adjacent to each other. Generally, the coils have an even number of layers, so that both start and finish lead can be brought out at the same end of the coil. Figure 12.3 illustrates such an arrangement of a four-layer HV winding, with one end solidly grounded. The insulation to ground gradually increases from the layer next to the low-voltage coil out to the last layer connected to the HV line in step of approximately U/m, where U is the ac winding voltage and m the number of layers in the coil, and can be graded accordingly. The cylindrical wound coil suffers from the poor impulse voltage distribution between turns in the last layer connected to the HV line, due to the high ground capacitance and the low series capacitance between turns.

In the continuous-wound disc coil illustrated in Figure 12.4, the turns are wound in sections or discs, with the first (start) turn on the insulating cylinder and the subsequent turns wound over it to form a disc

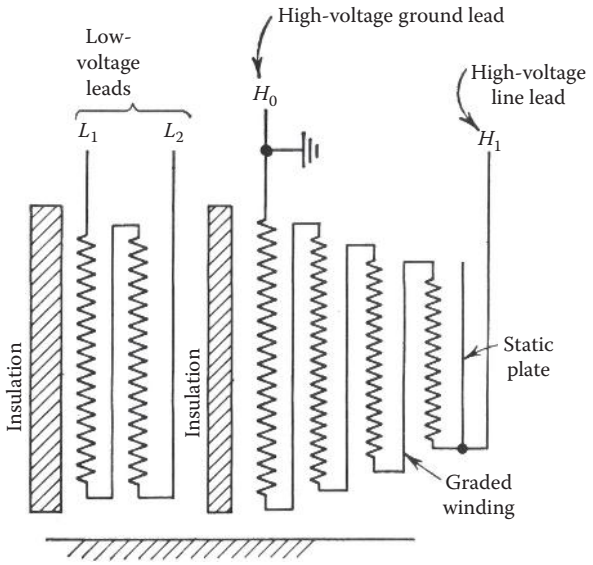


FIGURE 12.3 Arrangement of a four-layer winding. (From Bean, R.L. et al., *Transformers for the Electric Power Industry*, McGraw-Hill Book Co., New York, 1959.)

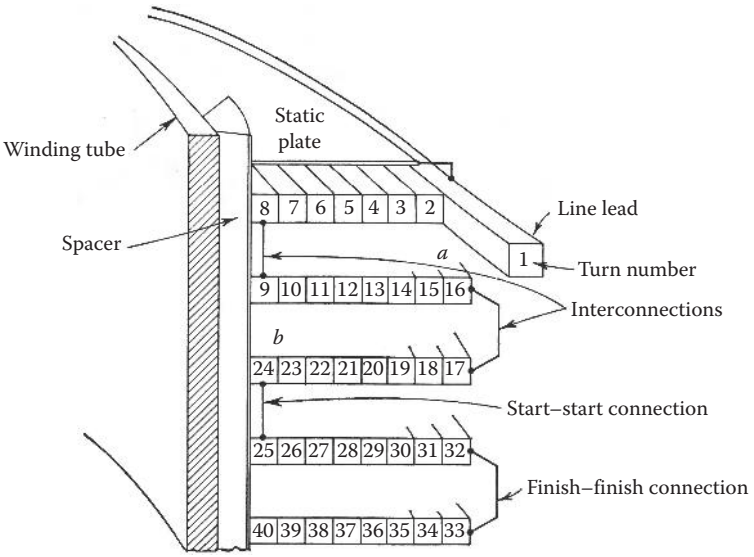


FIGURE 12.4 Illustration of a disc-type coil. (From Bean, R.L. et al., *Transformers for the Electric Power Industry*, McGraw-Hill Book Co., New York, 1959.)

section, whose thickness is equal to the turn width. The connection between adjacent discs is illustrated in Figure 12.4. The ac voltage distribution is graded among the series-connected disc sections, which are subjected to a stress of 2 U/m, where m is the number of disc sections. Figure 12.5 illustrates a winding arrangement of disc sections with the ends at ground potential and the center at the line potential.

12.2.2.2 Transformer Insulation Characteristics

It is obvious from the earlier discussion that transformer insulation is complex and cannot be described as a single uniform system. At best, one can subdivide the transformer insulation into a few subsystems,

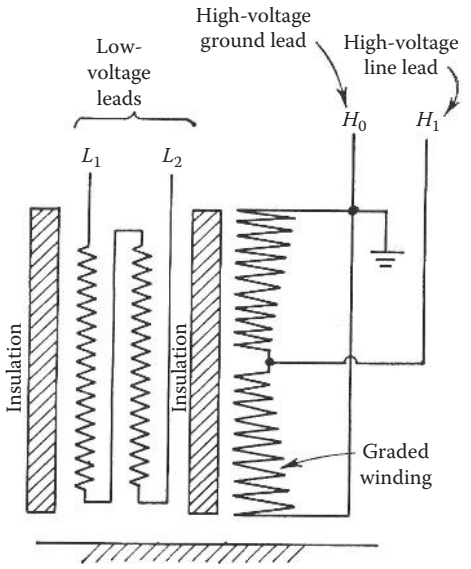


FIGURE 12.5 Arrangement of a disc–type coil winding. (From Bean, R.L. et al., *Transformers for the Electric Power Industry*, McGraw-Hill Book Co., New York, 1959.)

related to the individual windings, the interwinding insulation, the winding-to-ground insulation, and the insulation of the bushing and HV leads.

Insulation of the individual winding: Is essentially assured by the insulation of the conductor, filling most of the space between two adjacent conductors. Since the voltage is distributed over the whole length of the winding, the ac stress seen by the turn-to-turn gap is approximately U/N, where U is the voltage across the winding and N the number of turns. When the winding is made up of several layers or separate sections, the adjacent layers or sections are subjected to an ac stress of U/m or $2U/m$, where m is the number of layers or sections, depending on how the layers or sections are connected. Usually, there is no difficulty to design appropriate insulation for the ac stresses.

The problem is different under impulse voltage stresses, due to the unequal voltage distribution along the winding. Figure 12.6 illustrates the circuit representation of a winding, taking into account the capacitances to ground and series capacitances between turns. During impulse voltage, the voltage distribution is dictated mainly by the capacitances, resulting in a generally nonuniform distribution, with a large proportion of the impulse stress applied to the line end turns of the winding, as shown in Figure 12.6b. This has been identified as a cause for failure of power transformers under switching and lightning impulse conditions (Freyhult and Carlson, 1991).

Several possibilities exist to improve the transient voltage distribution along the winding. They generally aim at increasing the ratio of distributed series capacitance to ground capacitance, namely, by the use of disc windings, which have a naturally high ratio of series-to-ground capacitances. This practice is usually followed in EHV power transformers (Freyhult and Carlson, 1991).

The series capacitances between turns can be increased by the addition of an electrostatic shield to the line end winding, as illustrated in Figure 12.7. It can be further improved by the Hisercap design illustrated in Figure 12.8 (Grimmer and Teague, 1951): the disc-type coil is wound as a double conductor, with the second set of turns connected back in series with the first. The capacitance between the two sets of turns is increased many times the normal turn–turn capacitance. However, this design subjects the insulation of the coil conductor to half of the coil voltage.

Interwinding insulation: The space between the low- and HV windings is basically an oil space. The presence of large sheets of pressboard, subjected to the full potential difference across the windings, tends to favor the development of creep discharge over its surface, a recognized mode of failure of power transformer insulation. The phenomenon may also be enhanced by the gradual accumulation of carbon

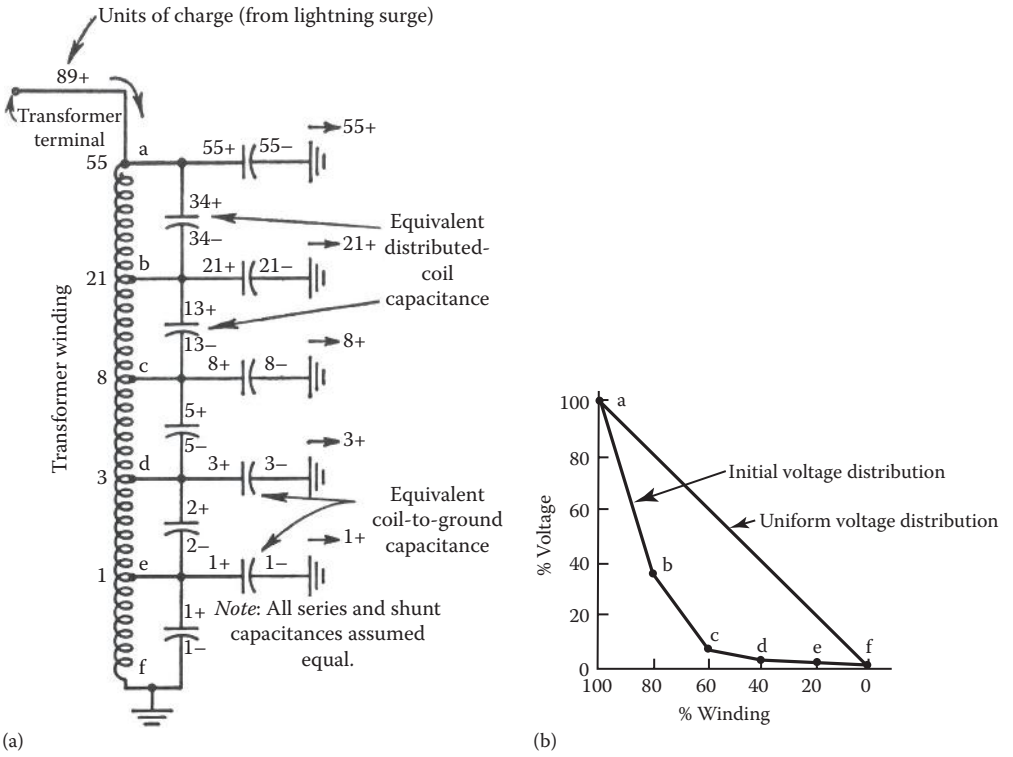


FIGURE 12.6 Circuit representation of a winding and its initial voltage distribution under impulse voltage. (a) Equivalent winding capacitance distribution. (b) Initial and steady state voltage distributions. (From Bean, R.L. et al., *Transformers for the Electric Power Industry*, McGraw-Hill Book Co., New York, 1959.)

particles at the pressboard interface. The problem is dealt with by installing several pressboard barriers, which extend above the winding end and are shaped to improve the field distribution and prevent bridging of the oil space by solid particles and, hence, the dielectric performance of the interwinding gap.

Winding to earth: The space between winding and the ground tank is essentially oil-filled. This oil gap usually has a considerable stress volume, and their design aims at minimizing the stress volume and the actual stresses as much as possible. Large oil volume breakdown is affected by particle contamination, discussed in more detail in Chapter 6, which, however, is unavoidable, but can be minimized by adequate filtering of the oil during the commissioning of power transformers (Palmer and Sharpley, 1969) and follow-up in service.

Bushing: Is necessary to connect the transformer winding to the overhead lines. Generally, bushing forms a separate component of the transformer, with its own insulation system, typically of the same type as the equipment it is connected to. Detailed discussions of bushing are presented in Chapter 11. Connections of the HV leads to the bushing terminal often produce local field enhancement, which can be countered by the use of bushing shield electrode. The bushing shield to ground forms a simple oil gap, subjected to volume effect that is treated in the following.

12.2.2.3 Physical–Chemical Properties of Oil-Impregnated Paper

Oils: Have a petroleum base and are complex mixtures of aromatic, alkane, and cycloalkane hydrocarbons, containing hundreds and possibly thousands of individual compounds, although the exact number has never been reported. The typical Voltesso 35 oil contains 12.9% of aromatic, 42.9% of naphthalene, and 44.2% of paraffin. Oil shows a variety of molecular sizes and structures. Its molecular weight is an average value of the molecular weight distribution. Aromatics tend to increase the dielectric losses of the oils, but their presence is necessary to inhibit gas evolution in the oil under electrical stress.

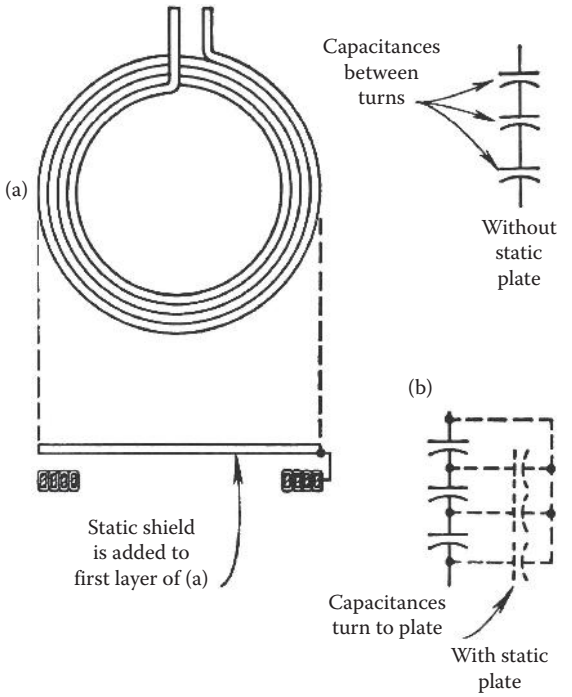


FIGURE 12.7 Improvement of the series capacitance between turns by an electrostatic shield. (a) Schematic diagram of added static shield. (b) Equivalent capacitive circuit. (From Bean, R.L. et al., *Transformers for the Electric Power Industry*, McGraw-Hill Book Co., New York, 1959.)

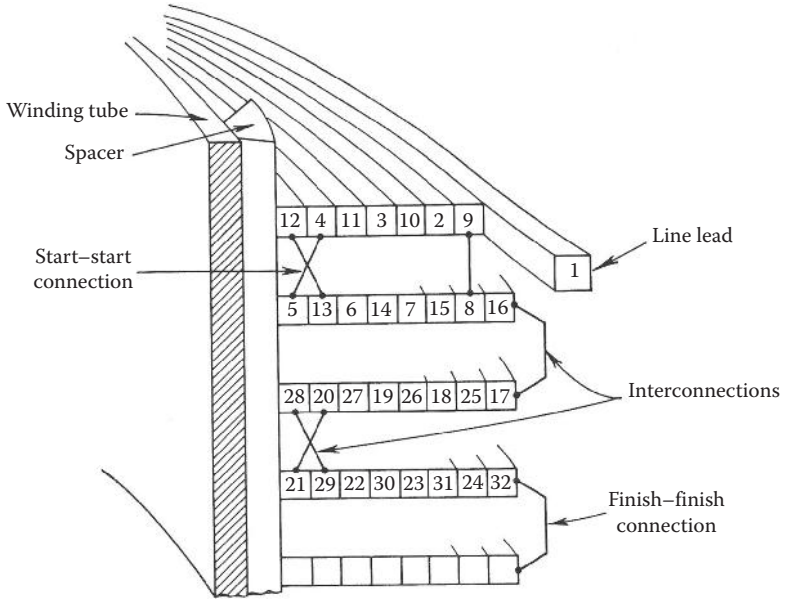


FIGURE 12.8 Illustration of Hisercap coil. (From Bean, R.L. et al., *Transformers for the Electric Power Industry*, McGraw-Hill Book Co., New York, 1959.)

Other additives are also used to delay oxidation. The dielectric losses in new purified oils are very low and attributed to the small permanent dipole moment or the polarity of the aromatic molecules.

Table 12.2 summarizes some of the properties of new transformer oils (Shroff and Stannett, 1985). Their viscosity can vary from 10 to 2500 cSt over the temperature range from 40°C to −40°C. The adequacy of the oil for service is determined by the extent to which it forms sludge and corrosive acidity compounds in the presence of oxygen. To reduce corrosiveness, oils should be free from sulfur, inorganic chlorides, and sulfates, usually introduced by direct contamination or inadequate refining.

Paper: Kraft papers consist of cellulose fibers felted together to form mechanically strong sheets. When properly dried and impregnated with dielectric liquids, they have good dielectric strength, have acceptable loss characteristics, and are suitable for use in the electrical insulation of power equipment. Table 12.3 summarizes some of the properties of Kraft paper. The porosity determines the ease

TABLE 12.2

Properties of Oil Used in Power Transformers

Parameters	Symbol	Unity	Value	Condition
Aromatic content		%	12.8	
AC dielectric strength		kV/mm	30	
Impulse dielectric strength		kV/mm	166–192	
Dielectric constant	ε_r		2.2–2.3	100°C
Dissipation factor	tanδ	%	0.05	25°C
			0.5	100°C
Density		g/mL	0.906	15°C
AC design electric field		kV/mm	3–5	
Interfacial tension		N-m	40.8×10^{-3}	
Neutralization number			0.01	
Design temperature		C	95–100	
Water content in oil		ppm	10	
Cloud point		C	−36	
Pour point		C	−46	
Flash point		C	150–160	
Fire point		C	177–180	
Viscosity		mm^2/s	10	40°C
			85	0°C
			6000–2500	−40°C
Coefficient of thermal expansion		$cm^3/cm^3/C$	$7–8 \times 10^{-4}$	
Gassing		μL/min	13	
Acidity index		mg KOH/g	0.03	
Thermal conductivity		cal./cm·s·C	$3–4 \times 10^{-4}$	

TABLE 12.3

Properties of Kraft Paper

Parameters	Symbol	Unit	Values
Dielectric constant	ε_r		2.4
Dissipation factor	tanδ	%	0.3
Density		g/ml	0.8
Electrical strength		kV/mm	18
Design temperature		C	95–100
Moisture in paper		%	1–5
Tensile strength of paper		kg/m^2	1300

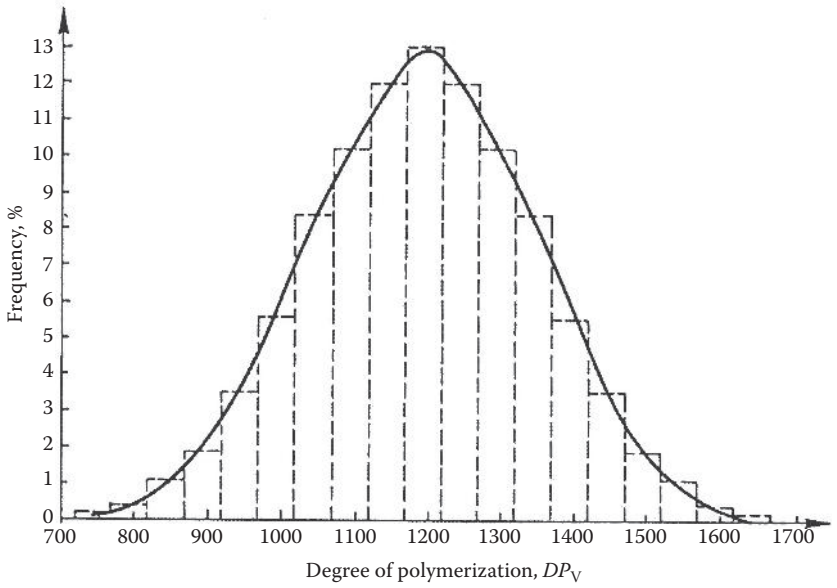


FIGURE 12.9 Typical distribution of the *DP* of Kraft paper. (From Bouvier, B., *Papier et papier imprégné*, Techniques de l'ingénieur, D-280, 1, 1977.)

with which the paper may be dried and impregnated. The density varies with the arrangement of the individual fibers but is usually around 0.8 g/cm^3. Higher-density papers are less porous and, therefore, possess higher tensile strength so that when impregnated with oil, they exhibit higher dielectric breakdown strength.

The cellulose paper is defined by the general chemical formula $C_{12}H_{20}O_{10}$. The paper fibers consist of a chain of *glucose repeating* units arranged in cellobiose pairs (Bartnikas and Srivastava, 1980). The number of glucose units in the chain is referred to as the *degree of polymerization* (*DP*) of the paper. Figure 12.9 illustrates a typical distribution of *DP* in Kraft paper, which varies from 700 to 1600, with an average value around 1200 (Bouvier, 1977). The polymolecular nature of the paper fibers prevents the determination of the exact molecular mass and the total length of the molecular chain. One estimates that the paper fibers can have a molecular mass of 10^5 and a length of 10^3 A.

Exposed to ambient air, the paper absorbs humidity in the air via capillary action of the fibers. Under normal conditions, the paper can contain up to 12% by weight of water (Bartnikas and Srivastava, 1980; Oommen et al., 1982). Most of this water can be removed by heating under vacuum. In regions where the cellulose molecules exhibit an orderly arrangement (crystallites), water is retained by absorption forces. This colloidal or bound water is believed to be held by hydrogen bonds that exist between the H_2O dipoles and the hydroxyl groups of the cellulose molecules. The strength of these dipole bonds prevents the removal under vacuum of the colloidal water that will contribute to the overall ionic conduction losses if dissociated.

12.2.2.4 Control of Humidity

Moisture can be absorbed readily by paper exposed to ambient air. The amounts vary with the relative humidity, as illustrated in Figure 12.10 (Fabre and Pichon, 1960; Bouvier, 1977), which shows the variations in the water content of Kraft paper as a function of the partial water vapor pressure in the ambient air, at different temperatures. It can be seen that the water absorption by the paper increases with the partial vapor pressure and decreases with the temperature.

Water is also absorbed by the oil in power transformers. Furthermore, in the presence of cellulose, paper, pressboard, etc., which have a higher affinity for water, a continuous exchange of humidity occurs

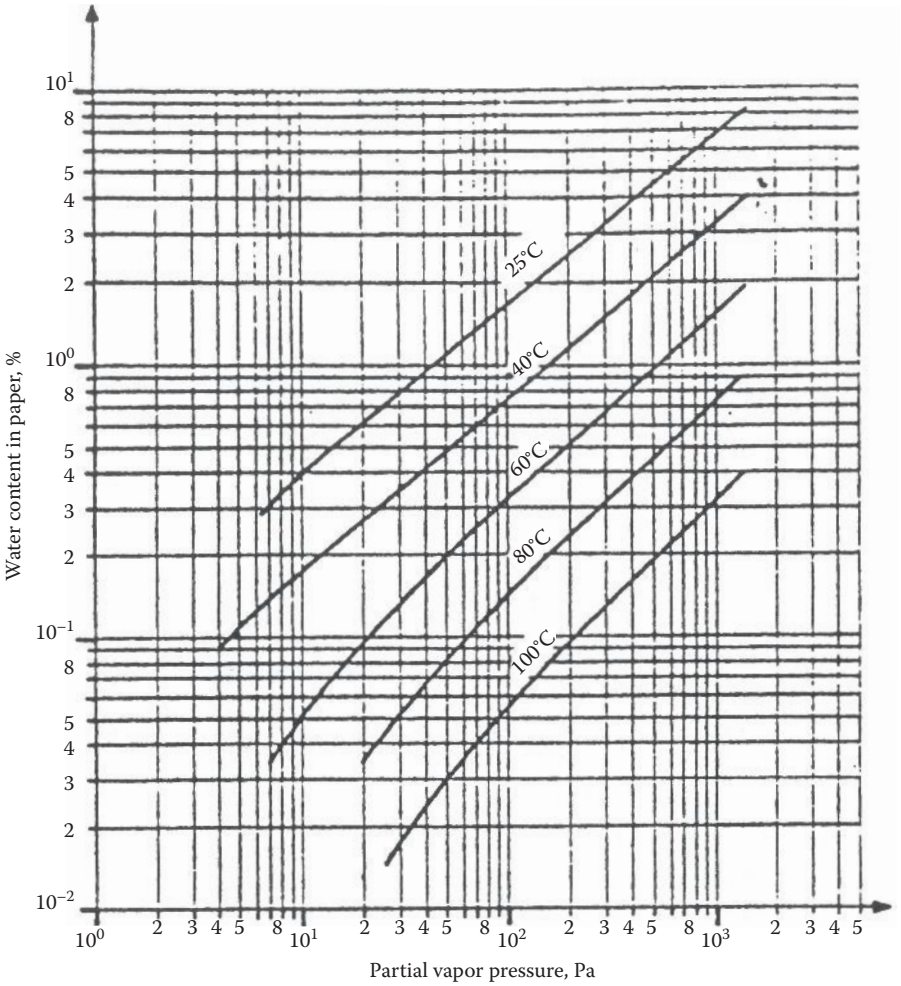


FIGURE 12.10 Variations of the water content in nonimpregnated Kraft paper with the partial pressure of water vapor and for different temperatures. (From Bouvier, B., *Papier et papier imprégné*, Techniques de l'ingénieur, D-280, 1, 1977.)

between the oil and the cellulose to maintain an equilibrium state. Figure 12.11 shows the variations of the water content in the oil and Kraft paper at equilibrium (Oommen et al., 1982). It can be seen that even with a relatively dry oil, containing 10–20 ppm of water, moisture in the paper can be several orders of magnitude higher, reaching 5%–8%. However, over the normal operating temperature range in power transformers, typically 70°C–90°C, water content in the paper is less than 1% for humidity in the oil of 10 ppm or lower.

The effect of humidity on oil and oil–paper insulation is a reduction of the breakdown voltage and increases electrical conductivity and dissipation factor tan δ (Fallou, 1970). The dielectric strength of mineral oil measured with *VDE* electrodes shows a slight reduction, about 15%, at a water content of 10 ppm. It passes by a plateau at 70% at a water content of 20 ppm before it reduces notably at water contents higher than 20 ppm (Miners, 1982). However, its estimation in a practical system is more difficult, and its effect on dielectric performance consequently less predictable than in laboratory tests.

With today's proper control of humidity in power transformers, its influence on the insulation performance does not present a problem. Typical water content in power transformers is of the order of 10 ppm (Norris, 1963). Two approaches are currently used to control the humidity:

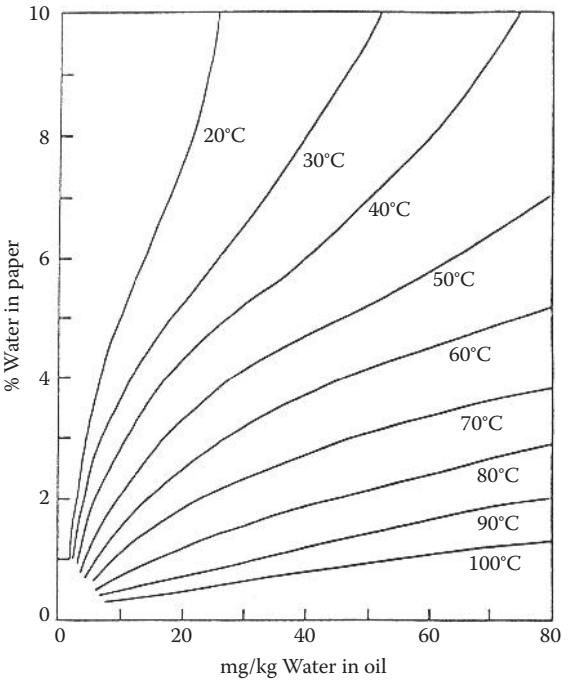


FIGURE 12.11 Variations of the water content in paper (in %) as a function of the water content (in ppm) on oil at equilibrium. (From Oommen, T.V. et al., *IEEE Trans. Power Appar. Syst*., PAS-101, 1048, May 1982.)

In one approach, a hermetic tank is used to completely separate the oil–paper insulation from the ambient environment. A cushion filled with neutral gas, usually nitrogen, compensates for the fluctuations in the oil volume during load cycles. In this approach, the gaseous decomposition by-product of the oil and cellulose by PDs or in the presence of hot spots is contained in the tank, and tends to increase with time, with the risk of forming gas bubbles when the dissolved gases in the oil exceed the equilibrium level.

In North America, the tendency is to allow open contact between the oil and ambient air, with humidity removed by silica gel, within the conservator. In this approach, the gaseous decomposition by-products of oil and cellulose are dispersed to the ambient air and do not accumulate. The oil is in constant equilibrium with the ambient air, and the risks of forming gas bubbles are minimized. Noting that dissolved gases in oil constitute one of the practical methods to monitor the insulating state of the oil–paper insulation, its analysis should take into account the method used by the manufacturer to control humidity ingress to oil discussed earlier.

12.2.2.5 Control of Particle Contamination

Particle contamination is another factor affecting the dielectric performances of oil–paper insulation. It is now recognized that solid particle contamination is unavoidable in power transformers and reactors under practical conditions.

Nature of particles: The nature of particles found in power transformers can be evaluated by *ferrography*. It varies significantly, but the most common are cellulose fibers, sand, carbon, copper, aluminum, and ion particles. Obviously, the particles found are related to materials used in the manufacture of the transformer, namely, cellulose fibers, sand, carbon, copper, aluminum, and iron. Figure 12.12 shows the result obtained from ferrographic analysis of oil samples taken from operating transformers. The ferromagnetic particles are aligned, while nonmagnetic particles are deposed in disorder on the glass plate.

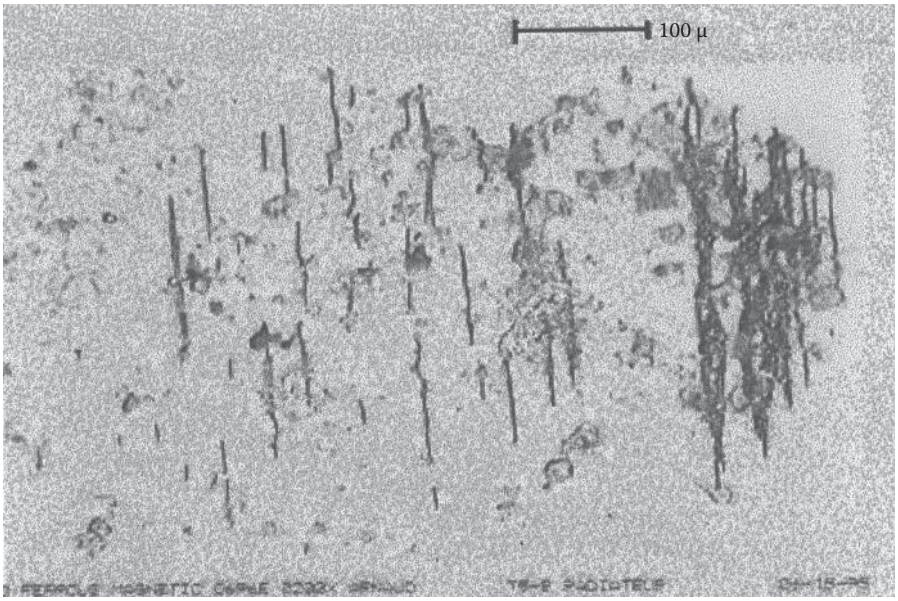


FIGURE 12.12 Result of a ferrographic analysis of an oil sample of an in-service power transformer.

It is generally accepted that particle contamination of power transformers is introduced during manufacturing, commissioning, and during major repairs, when the oil must be removed and the transformer refilled after repair work. Cellulose fibers come from paper and pressboard used in the insulation. They can have considerable dimensions and are sensitive to humidity: humid fibers become more conducting, with detrimental effects on dielectric performances of the insulation. Sand particles are probably introduced during the manufacturing process. Metallic particles from transformer core, conductors, windings, and metallic connections are also introduced during manufacturing.

In transformers equipped with automatic tap changers, carbon particles are produced due to arcing during operations of the tap changers and must be prevented from contaminating the bulk oil volume. This is done by separating the tap changers compartment, including its oil, from the main transformer tank. Monitoring the particle content in oil constitutes one of the practical methods to monitor the actual state of the insulation system for adequate use in power transformers. Any sudden change in the particle content in the oil is indicative of contamination and its source should be identified.

The particle content in power transformers may, therefore, vary significantly. Following the commissioning of power transformers, the particle content shows an initial sharp increase and gradually stabilizes afterwards and may even slightly improve with time (Palmer and Sharpley, 1969). The initial increase of particle content is attributed to the mechanical vibrations during operation, which liberates the particles from the core and insulation, while improvement in the particle content with time may be explained by the settling of the particles in natural particle traps within the transformer tank where the oil flow is minimal.

It may be expected that deterioration in the oil insulation strength occurs with increase in particle contamination, especially when the particles are conducting; carbon; metallic particles; and/or moisture-saturated cellulose fibers. In power transformers, the breakdown process of an oil gap can be divided into two stages: initiation and development of the breakdown. In uniform and quasi-uniform field gaps, breakdown initiation is greatly affected by the electrode surface condition and by the oil quality, which results in the well-known electrode area and stressed oil volume effects (Wilson, 1953; Weber and Endicott, 1956). The phenomenon is directly related to the statistical nature of discharge initiation and can be evaluated from the experimental distribution of the probability to initiate the breakdown from an elementary surface or volume (Trinh et al., 1982a,b) discussed in Chapter 6 and in Section 12.3.2.

Particle content: Measuring particle content is, at present, a useful and nonintrusive means to control and monitor the quality of the oil in operating power transformers. Oil samples are taken from operating transformers for laboratory analysis for their gas and particle content and dielectric strength. It should be borne in mind that oil sampling does require due precautions regarding cleanliness of the sampling bottles but also in the measurement of the particle contents and hence the dielectric strength. The last two parameters are affected by the time the oil remains in the sampling bottles due to the sedimentation of the particles. Figure 12.13 shows the variations in time of the particle contents in oil, represented by the number of particles having a diameter greater than the values in the x-axis (Trinh et al., 1980). One can see that the particle count varies with the size of the particles following approximately a power law.

However, particle content also changes in time due to sedimentation of the particles, as shown by the distributions obtained for different times at rest before the particle count. The particle content improves and with it, the dielectric strength of the oil sample being analyzed. This is the main cause of the significant differences observed in the early investigation of particle contamination, between the laboratory and measurements made on-site. The problem is settled by the introduction of the ultrasonic homogenization of the oil sample prior to analysis (Crine and Vincent 1988; Samat and Lacase, 1988).

Figure 12.14 illustrates the improvement in the particle count obtained with the ultrasonic homogenization: a stable particle content after a minimal homogenization time. On the other hand, Figure 12.15

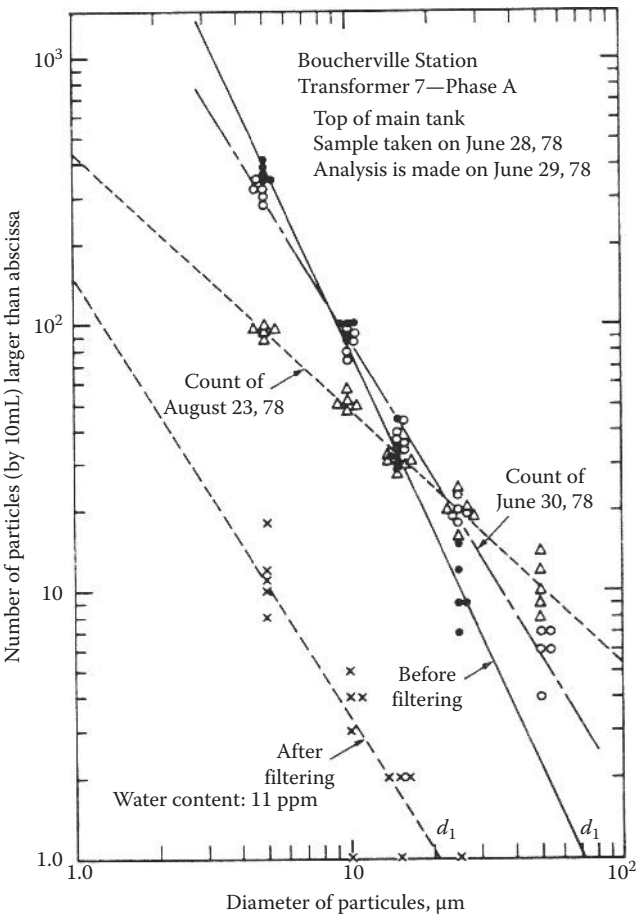


FIGURE 12.13 Variations in the distribution of particle content with time. (From Trinh et al., 1980.)

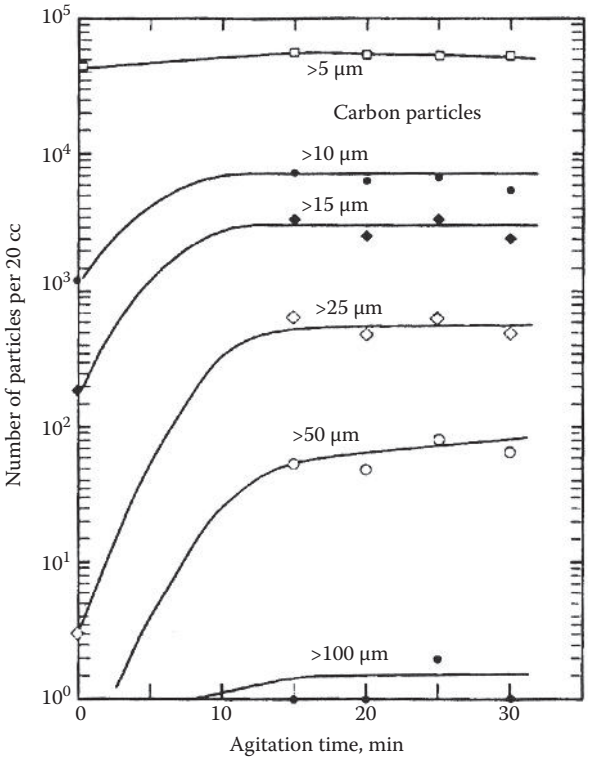


FIGURE 12.14 Influence of the ultrasonic homogenization on the measured particle content. (From Crine, J.P. and Vincent, C., *IEEE Trans. Electr. Insul*., EI-23(4), 751, August 1988.)

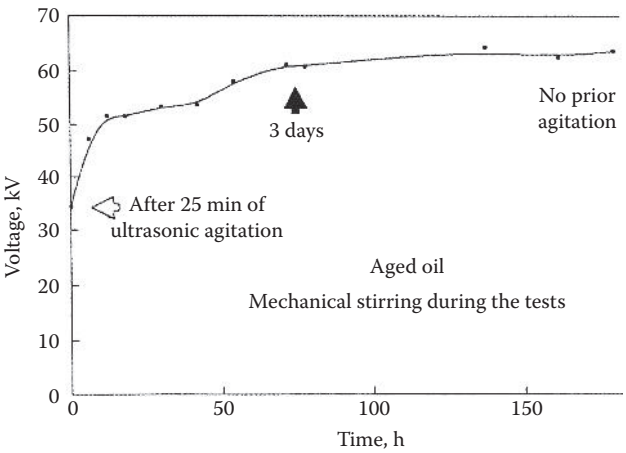


FIGURE 12.15 Influence of the sedimentation of particles on the measured dielectric strength of the oil sample. (From From Crine, J.P. and Vincent, C., *IEEE Trans. Electr. Insul*., EI-23(4), 751, August 1988.)

shows the effect of sedimentation of solid particles on the measured dielectric strength of the oil sample: a steady improvement during the first 100 h of rest time for the oil sample.

Adequacy of oil quality: Filtering the oil to remove solid particles is the logical answer to particle contamination, as illustrated by the results in Figure 12.13 comparing the particle content before and after filtering of the oil sample. However, super-clean oil is not necessarily the ultimate solution,

since it is sensitive to electrostatic charge accumulation resulting in flashover of the oil gap. As a result, utilities tend to establish criteria for an acceptable oil quality based on the measured particle content. The best way to present particle contamination in the oil is by a distribution of the measured particle content. A graphic paper with limit distributions defining the range of acceptable particle contents can be used to present the measurement (Figure 12.16): region A corresponds to severe particle contamination, region B to acceptable level of particle contamination, and region C to clean oil with little particle contamination. It allows a rapid evaluation of the adequacy of the oil sample regarding its particle content.

Index of particle content: An index of particle content δp (Trinh et al., 1982b) may also be defined as

$$\delta_p = \ln (n_0 * d_1) \tag{12.4}$$

where

n_0 is the number of particles larger than 1 μm per unit volume (100 mL)

d_1 the maximal diameter in μm of the particles in the sample

Typical distribution of particle content has $n_0 = 1 \times 10^4$ and $d_1 = 100$ μm, corresponding to an index of $\delta_p = 13.8$. Practical transformer oils have a particle content index between 13 and 15, a contaminated oil has an index higher than 15, while a well-filtered oil has an index below 13.

12.2.3 SF_6 Insulation

This constitutes an adequate answer to the fire hazard problem related to the presence of mineral oil in power transformers. The relatively low dielectric stresses in power transformers, between 3 and

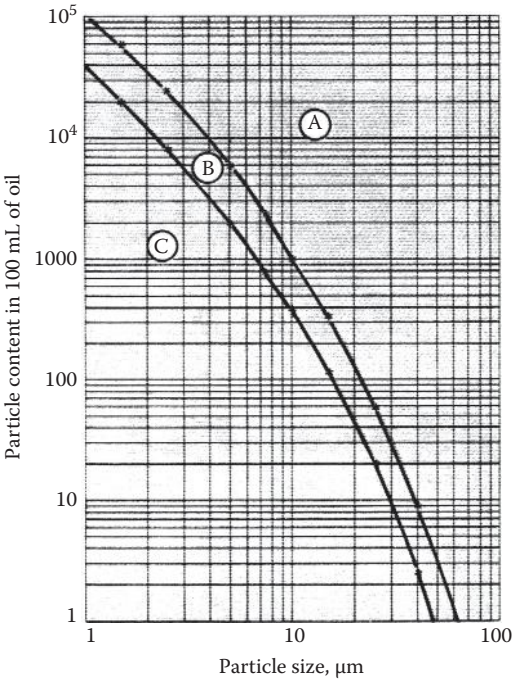


FIGURE 12.16 Representation of acceptable particle contents in transformer oil. A: Region of severe particle contamination. B: Region of acceptable particle contamination. C: Region of clean oil. (From Samat, J. and Lacasse, D., *Revue Alsthom*, (11), 47, 1988.)

5 kV_{rms}/mm, allow the use of SF_6 at relatively low pressure and do not present a particular difficulty. However, the relatively poor heat transfer characteristics of SF_6 present a serious problem to evacuate the heat generated by the power transformers. Two approaches are considered; both use perfluorocarbons as the cooling medium.

In the first approach illustrated in Figure 12.17, the perfluorocarbon liquid is dripping on the hot windings. The cooling by vaporization of the liquid is efficient; the vaporized liquid eventually condenses and is collected to recirculate. The main drawbacks of this solution reside in the difficulty to assure a uniform cooling over the whole winding, with the risk of forming hot spots in the winding insulation (Narbut et al., 1959; Tokoro et al., 1982).

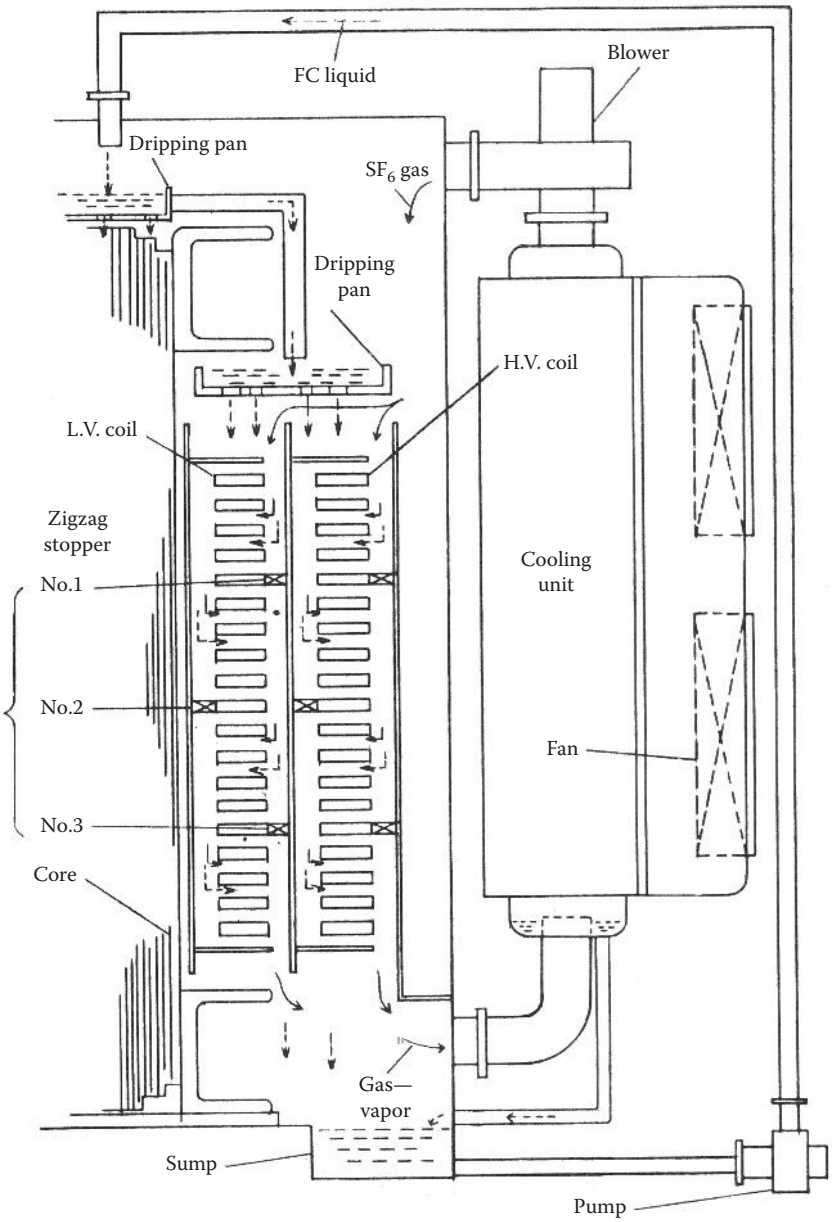


FIGURE 12.17 Perfluorocarbon vapor cooled gas-insulated power transformer. (From Tokoro, K. et al., *IEEE Trans. Power Appar. Syst*., PAS-101(11), 4341, 4349, November 1982.)

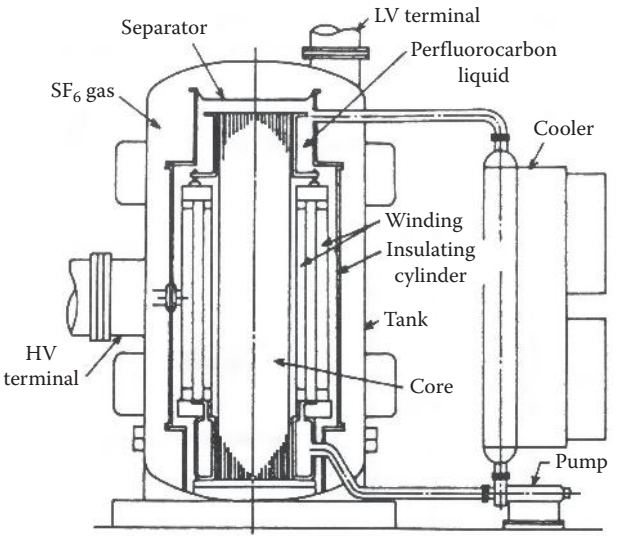


FIGURE 12.18 Liquid perfluorocarbon cooled gas-insulated transformer. (From Mukaiyama, Y. et al., *IEEE Trans. Power Deliv.*, PWRD-6(3), 1108, 1991.)

In the second approach shown in Figure 12.18, the windings are immersed in liquid perfluorocarbons, which literally replace the mineral oil. The principal drawback of this approach is the high cost of perfluorocarbons (Mukaiyama et al., 1991). Up to present, the development of SF_6-insulated power transformers has been modest; units of 275 kV, 300 MVA have been in operation in Japan since 1990s (Mori, 1990).

12.3 Considerations on the Dimensioning of Oil–Paper Insulation

Adequate dimensioning of the insulation is a principal aim in the design of power equipment. In power transformers, several causes have been identified for their failures (Freyhult and Carlson, 1991): failure of the bushing shield electrode, tracking of insulating surfaces, and turn-to-turn and interdisc insulation failures close to the line entrance. However, partial failures between turns or winding layers and sections do not always result in immediate failure of the insulation, which occur either across the oil space or along an insulating surface, between the windings to ground. The adequacy of the clearance distance in oil or along an insulating surface becomes essential to insulation of power transformer and can be evaluated in two different ways, namely:

- Evaluation of the cumulative stress
- Evaluation of the breakdown probability of the oil gap, using the stressed area or volume effect

12.3.1 Cumulative Stress

Evaluation of the cumulative stress provides a straightforward means to verify the adequacy of the clearance distances by making sure that the cumulative stress remains below a critical level, usually obtained from experimental data. It is defined as the average field E_b evaluated along a hypothetical breakdown path in the oil insulation, starting from an initial point located in the highly stressed region (Moser, 1979; Nelson, 1989), according to

TABLE 12.4

Moser Criterion, with $d_0 = 1$ cm

Parameters	Breakdown in Oil	Along Oil–Paper Interface
Exponent α	–0.38423	–0.46015
Maximal field, E_0 (kV/mm)	4.3468	4.0644

$$E_b = \frac{U_{max} - U}{\Delta l} \tag{12.5}$$

where

U_{max} is the potential at the initial point

U is the potential at a point P on the evaluation path

Δl the distance measured along the evaluation path from the initial point to P

In this manner, the cumulative stress is maximal at the initial point and is effectively equal to the local field; it decreases gradually along the evaluation path.

Moser criterion: Is essentially empirical, as established from the experimental data gathered on the cumulative breakdown field, E_b (kV/mm). Moser has shown that E_b varies with the distance d (mm) covered by the breakdown, according to the empirical relation (Nelson, 1989)

$$E_b = E_0 \left(\frac{d}{d_0}\right)^{-a} \tag{12.6}$$

where E_0 and α are experimental parameters obtained in the reference gap of length d_0.

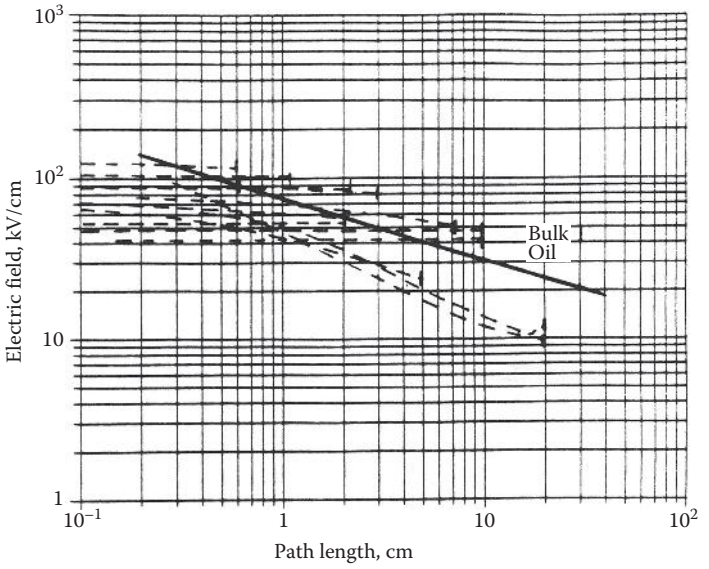
Taking the logarithm of both sides of Equation 12.6, one gets

$$\ln(E_b) = a * \ln d + A_0 \quad \text{with } A_0 = \ln E_0 - a \ln d_0 \tag{12.7}$$

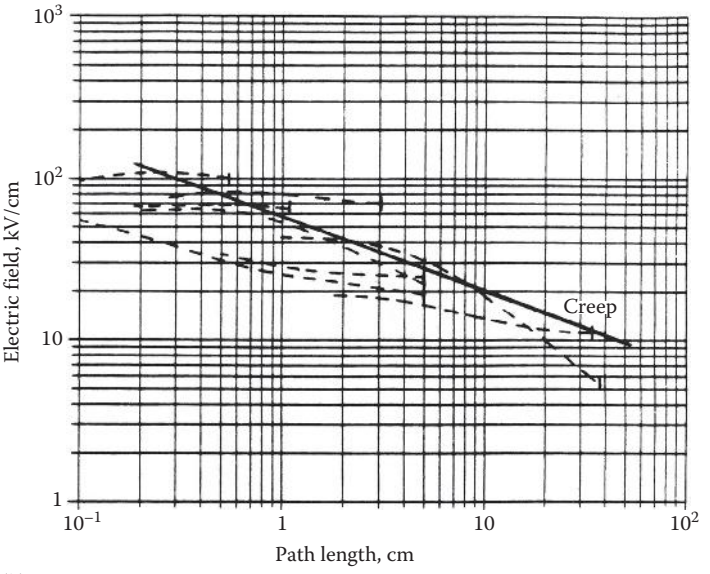
The experimental values of α and E_0 are given in Table 12.4 for the cases of breakdown in the bulk oil and along an oil–paper interface. Equation 12.7 implies that the Moser criterion can be represented by a straight line, when one presents the variations of cumulative stress in a *log–log* graphic paper, which should not be crossed by the design stress curves. Examples of the application of the Moser criterion in the dimensioning of transformer insulation are shown in Figure 12.19, which compare different cumulative stress curves in oil and along an oil–paper interface with the Moser straight line (Nelson, 1989). The cumulative stress curves, which intercept the Moser straight line, are considered as having insufficient clearance.

12.3.2 Breakdown Probability

Another approach to assess the adequacy of clearance distances in oil insulation comprises subdividing the oil gap in elementary surfaces and volumes, as illustrated in Figure 12.20, and evaluating the breakdown probability associated with a path, a surface, or a volume around an HV electrode. Proper design limits this breakdown probability below a threshold value generally defined from field experiences. Noting that the evaluation of the breakdown probability along a specific path is similar to the notion of cumulative stress of Moser, a comparative evaluation of the two approaches allows definition of the threshold probability to be respected in the dimensioning of oil–paper insulation. The evaluation of the breakdown probability consists, in general, in subdividing the oil insulation gap in N_s elementary



(a)



(b)

FIGURE 12.19 Illustration of the application of Moser criterion in the dimensioning of oil–paper insulation. (a) Cumulative stress in bulk oil. (b) Cumulative stress along an oil-paper interface. (From Nelson, J.K., *IEEE Trans. Electr. Insul*., EI-24, 835, October 1989.)

surfaces and N_v elementary volumes, of which the probability to initiate a breakdown is known, and then evaluating the breakdown probability, according to the general expression

$$P_n(u) = 1 - \left[1 - p_s(u)\right]^{N_s} \left[1 - p_v(u)\right]^{N_v} \tag{12.8}$$

where $p_s(u)$ and $p_v(u)$ are, respectively, the probabilities to initiate the breakdown of the oil gap from an elementary surface or volume at the voltage u.

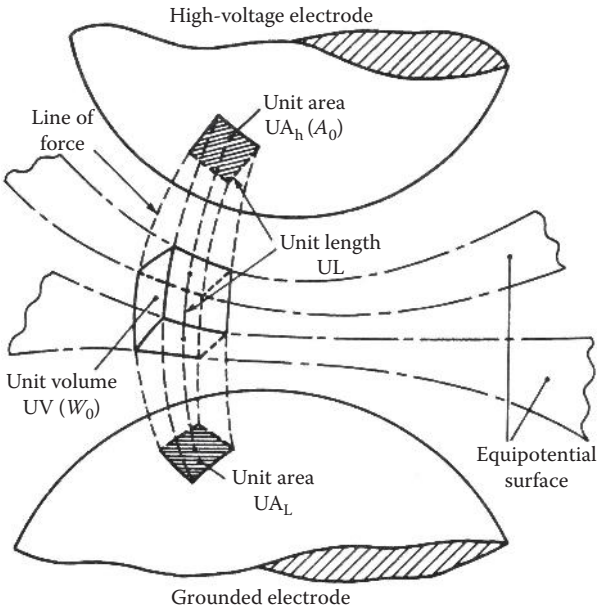


FIGURE 12.20 Illustration of elementary surfaces and volumes in an oil gap. (From Trinh, N.G. et al., Electrode area, stressed-volume: Two apparent effects of large-volume oil-insulation, in *IEEE International Symposium on Electrical Insulation*, Philadelphia, PA, June 6–9, 1982a, pp. 115–118; Trinh, N.G. et al., *IEEE Trans. Power Appar. Syst*., PAS-101(10), 3712, October 1982b.)

Distribution probability to initiate breakdown from an elementary surface or volume: As discussed in Chapter 6, the breakdown of an oil gap can be evaluated in terms of an effect of the surface and/or volume, from the distribution function of the probability to initiate breakdown from an elementary surface or volume. Their predominance is related to surface condition of the electrode and cleanliness of the oil. For a well-filtered oil, the effect of the electrode surface predominates over the volume effect, while the reverse is true for a solid particle-contaminated oil.

Tables 12.5 and 12.6 give the defining parameters for the probability distribution function to initiate breakdown from an elementary surface A_0 and volume W_0, taken arbitrarily as $A_0 = 0.1$ cm^2 and volume $W_0 = 2 \times 10^{-2}$ cm^3 for a typical transformer oil. The distribution function can be assumed to be of the *normal*, *extreme value*, *or* Weibull type (Trinh et al., 1982).

TABLE 12.5

Probability Distribution Parameters for Initiating Breakdown from an Elementary Surface, $A_0 = 0.1$ cm^2

Parameters	Units	Normal	Extreme Values	Weibull CIGRE Procedure
Impulse voltage				
Mean E_m, position parameter E_0	kV/mm	108.7	86.48	46.38
Sigma σ, scale parameter α	kV/mm	20.54	5.69	67.78
Form factor β				3.4
AC voltage				
Mean E_m, position parameter E_0	kV/mm	36.31	30.36	16.21
Sigma σ, scale parameter α	kV/mm	6.7	2.01	22.11
Form factor β				3.4

Source: Trinh, N.G. et al., *IEEE Trans. Power Appar. Syst*., PAS-101(10), 3712, October 1982b.

TABLE 12.6

Probability Distribution Parameters for Initiating Breakdown from an Elementary Volume, $W_0 = 2 \times 10^{-2}$ cm^3

Parameters	Units	Normal	Extreme Values	Weibull CIGRE Procedure
Impulse voltage				
Mean E_m, position parameter E_0	kV/mm	94.25	76.83	47.57
Sigma σ, scale parameter α	kV/mm	15.56	4.1	51.35
Form factor β				3.4
AC voltage				
Mean E_m, position parameter E_0	kV/mm	31.48	26.67	16.15
Sigma σ, scale parameter α	kV/mm	5.11	1.44	16.86
Form factor β				3.4

Source: Trinh, N.G. et al., *IEEE Trans. Power Appar. Syst.*, PAS-101(10), 3712, October 1982b.

TABLE 12.7

Dimensions of the Test Cell

Parameters	Dimensions (cm)	Remarks and Values
Main tank		
Radius	100	
Height	250	
Turret		
Radius	50	
Length	250	275 cm to the base of the bushing
HV electrode		
Bushing shield electrode	40	
Length of connector	205	
Test electrode, length	40	Baril type Electrode r_e = 20 cm
Height above ground	100	

12.3.3 Example of Assessment for Adequacy of a Test Cell

As an application of the earlier approaches to dimensioning of oil insulation, they will be used to assess the adequacy of a test cell to evaluate the dielectric performances of a bushing shield in turret assembly. Figure 12.20 shows the general arrangement of the test cell: a main cylindrical tank of 100 cm radius, surmounted by a cylindrical turret of 50 cm radius, which provides access to the HV source, via the bushing. Detailed dimensions are given in Table 12.7. Two standard bushing shield electrodes are used, one at the bushing end as part of the test bushing shield–turret assembly and the other bushing shield terminated with a hemispherical cap, at the end conductor connection, which completes the test assembly.

12.3.3.1 Field Calculation

Field calculations are made using the method of charge simulation (Singer et al., 1974; Trinh, 1980) discussed in Chapter 2. The results are summarized in Table 12.8 for different locations where the field is high, identified in Figure 12.21. The calculation of the normalized field is made with an applied voltage of 1 kV. To obtain the actual field at the test voltage, it suffices to multiply the normalized gradient (kV/cm) by the test voltage. Specific values of the electric field corresponding to the three voltage levels of 425, 700, and 960 kV are also given in Table 12.8 for different points of calculation: 1–9.

TABLE 12.8

Normalized and Actual Gradients at Calculation Points

Gradient (kV/cm) at	1 kV—Normalized	425 kV	700 kV	960 kV
Bushing shield				
Point of calculation 1	7.1737×10^{-3}	3.0488	5.0215	6.8867
Point of calculation 2	6.4914×10^{-3}	2.7588	4.5439	6.2317
At the turret	1.1906×10^{-3}	0.7570	1.2469	1.7101
Point of calculation 3	7.4111×10^{-3}	3.1497	5.1877	7.1146
HV connection				
Point of calculation 4	5.7432×10^{-3}	1.8175	2.9936	4.1055
Point of calculation 9	6.6771×10^{-3}	0.2795	4.6039	6.3140
Termination electrode				
Point of calculation 5	4.9529×10^{-3}	2.1049	3.4670	4.7547
Point of calculation 6	5.1586×10^{-3}	2.1924	3.6110	4.9522
At the surface of the tank	0.4084×10^{-3}	0.1791	0.2950	0.4046
Point of calculation 7	5.9747×10^{-3}	2.5392	4.1822	5.7357
At the bottom of the tank	0.2268×10^{-3}	0.0964	0.1587	0.2177
Point of calculation 8	2.5695×10^{-3}	1.0920	1.7986	2.4667

Note: The normalized gradient is calculated with a radius of curvature of 5 cm.

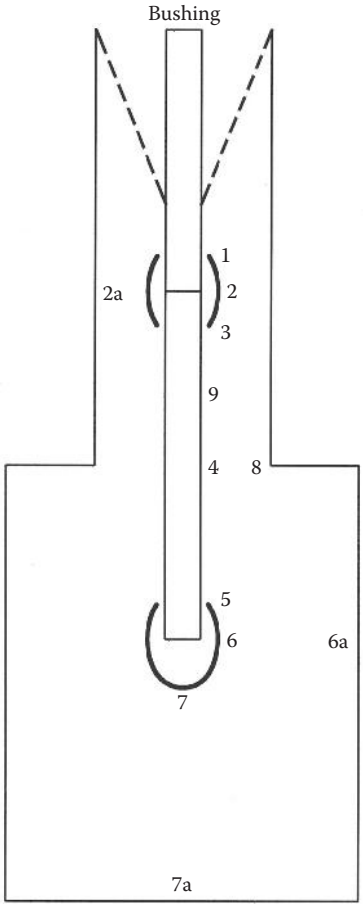


FIGURE 12.21 Arrangement of the test cell. Numbers refer to field calculation sites, with results provided in Table 12.8.

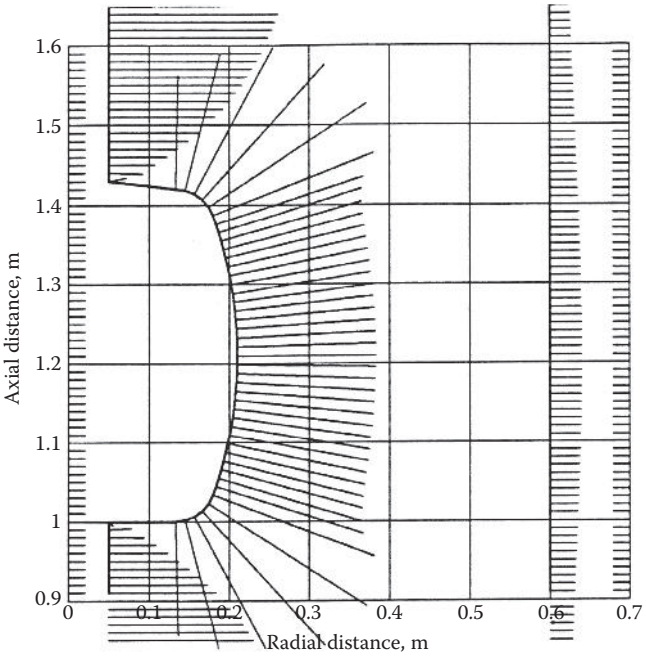


FIGURE 12.22 Calculated field distribution around the bushing shield.

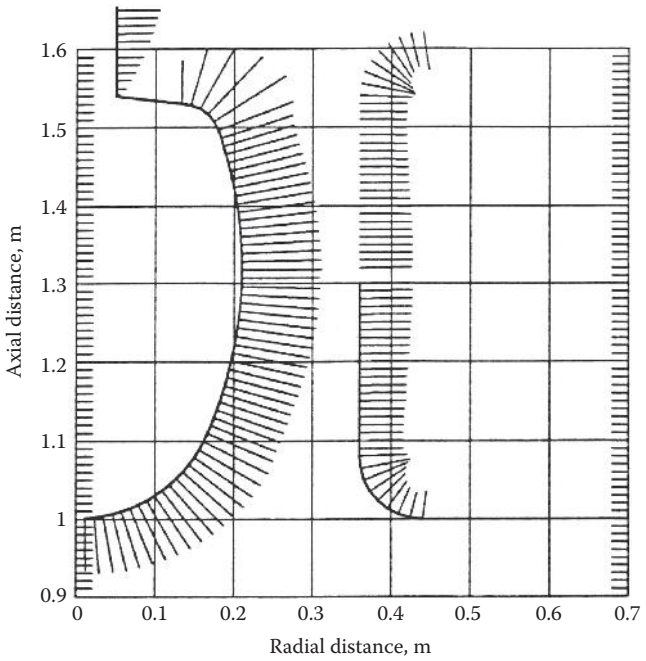


FIGURE 12.23 Calculated field distribution at the termination electrode.

Figures 12.22 and 12.23 show the field distribution at the bushing shield and termination electrode, represented by the local field vectors at the electrode surface. One notices that the maximum field occurs at the edges of the bushing shield, while a local maximum occurs at its central portion (points of calculation 1–3). This would ensure that breakdown would occur at the bushing shield electrode under test.

On the other hand, the termination electrode effectively controls the field distribution to relatively low values over its whole surface (points of calculation 5–7) to avoid undesirable breakdown initiated from the termination electrode.

The adequacy of the test cell for evaluating bushing shield electrodes will be evaluated using the approaches of cumulative stress and breakdown probability in the following.

12.3.3.2 Cumulative Stress

The cumulative stress is calculated along a probable breakdown path, typically along the radial path originating from a highly stressed point to the ground tank (or turret), and for the three voltage levels. The results are presented in Figures 12.24 through 12.26, for the voltages 425, 700, and 960 kV,

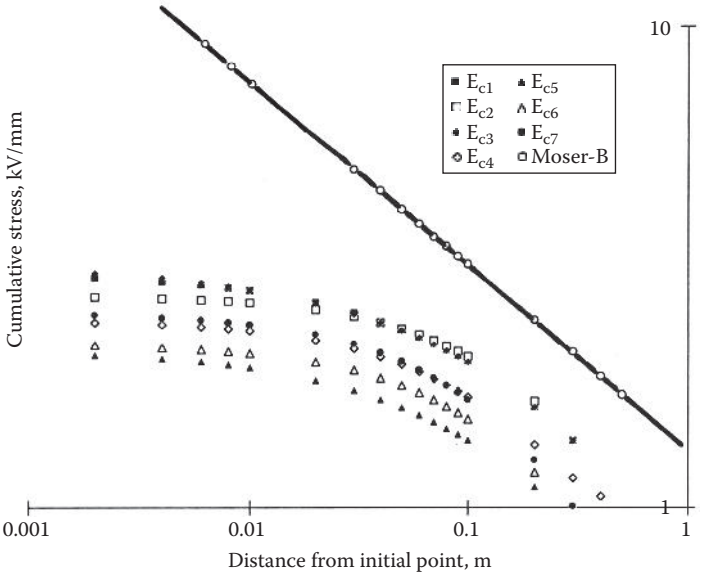


FIGURE 12.24 Curves of cumulative stress at 425 kV—Moser criterion. E_{c1}–E_{c8} refer to cumulative stress curves from field calculation sites 1–7, shown in Figure 12.21. The straight line represents the Moser criterion for Bulk oil.

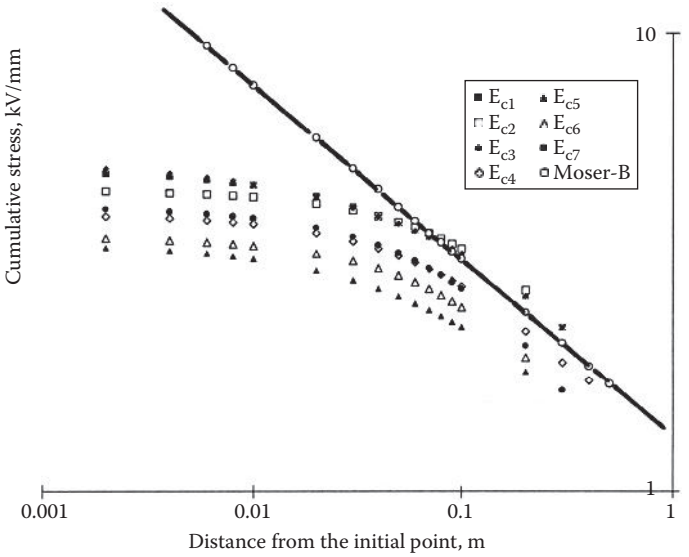


FIGURE 12.25 Curves of cumulative stress at 700 kV—Moser criterion. E_{c1}–E_{c8} refer to cumulative stress curves from field calculation sites 1–7, shown in Figure 12.21. The straight line represents the Moser criterion for Bulk oil.

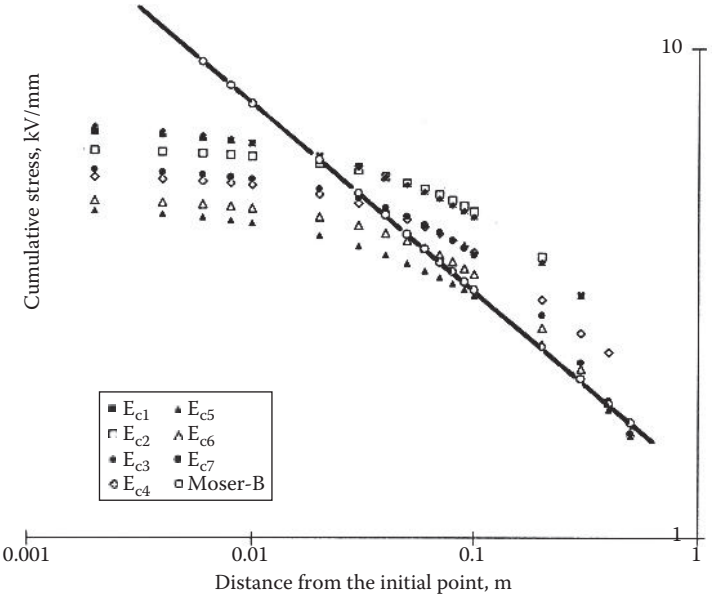


FIGURE 12.26 Curves of cumulative stress at 960 kV—Moser criterion. E_{c1}–E_{c8} refer to cumulative stress curves from field calculation sites 1–7, shown in Figure 12.21. The straight line represents the Moser criterion for Bulk oil.

respectively. The cumulative stress curves are compared with the straight line corresponding to the Moser criterion (Moser, 1979; Nelson, 1989): a cumulative stress curve remaining below the Moser criterion straight line is a good indication that no breakdown is likely to occur along the corresponding path. The following observations can be made:

- At the voltage level of 425 kV (Figure 12.24), all the cumulative stress curves remain below the Moser criterion line. The bushing shield should withstand this voltage level.
- At the voltage level of 700 kV (Figure 12.25), only the curves of cumulative stress originating from the bushing shield electrode intercept the Moser criterion line. Breakdown may occur from the bushing shield electrode.
- At the voltage level of 960 kV (Figure 12.26), all cumulative stress curves intercept the Moser criterion line. Breakdown may occur along any of the paths analyzed, although the probability is higher at the bushing shield electrode.

It is obvious from the earlier results that the cumulative stress can only provide a qualitative assessment of the likelihood that a specific path would result in breakdown of the oil gap at a given voltage level.

12.3.3.3 Probability of Breakdown

With the distribution function of the probability to initiate the breakdown of the oil gap from an elementary volume discussed previously, the probability that the breakdown will be initiated from a particular region within the oil gap can be readily evaluated by the following:

- Subdivide the region of interest into N_p hypothetical paths, initiated from the highly stressed electrode and crossing the oil gap.
- Subdivide the path into N_v elementary volumes of 2×10^{-2} cm^3, initiating from an elementary surface of 0.1 cm^2, at the highly stressed electrode.

Probability of initiating breakdown from a specific path: It is equivalent to the Moser criterion of cumulative stress, with the N_v elementary oil volumes aligning along the hypothetical breakdown path. The resultant probability of initiating the breakdown from the N_v elementary volumes is

$$P_p(u) = 1 - \prod_{N_v} \left[1 - p_i(u)\right] \tag{12.9}$$

where

$P_p(u)$ is the probability to initiate breakdown from the oil volume containing N_v elementary oil volumes
$p_i(u)$ is the probability to initiate breakdown from the ith elementary volume in the assumed breakdown path

Figure 12.27 presents the probabilities of initiating breakdown from the same paths used in the evaluation of the cumulative stress and for values of the applied voltages varying between 400 and 1000 kV. These probabilities are generally low, varying between 10^{-5} and 10^{-6}, and do not allow a direct conclusion on the dielectric performance of the oil interval. However, like the Moser cumulative stress, one can determine which breakdown path is critical to the dielectric performance of the oil gap. In the present case, the paths originating from the points of calculation 1–3 are more critical than all the other paths evaluated.

Probability of initiating breakdown from an equigradient contour: In the particular case where the HV test setup has an axial symmetry, the points located on the contour obtained by rotating the electrode around its axis, have the same gradient, forming an equigradient contour at the electrode surface. The probability to initiate the breakdown is the same for all the paths originating from the same equigradient contour at the electrode. Their combined effect is a higher probability to initiate the breakdown from the equigradient contour. Noting that the breakdown path is originated from an elementary surface of 0.1 cm^2 on the equigradient contour of 0.1 cm wide at the electrode, one gets

$$P_c(u) = 1 - \prod_{N_s} \left[1 - P_{pi}(u)\right] \tag{12.10}$$

where N_s is the number of paths initiating from the equigradient contour.

Figure 12.28 presents the probability to initiate breakdown from an equigradient contour passing by the same points of calculation 1–9 in Figure 12.12. One can see that these probabilities are in the order of 10^{-4} to 3×10^{-3} for the range of applied voltage between 400 and 1000 kV. The large number of

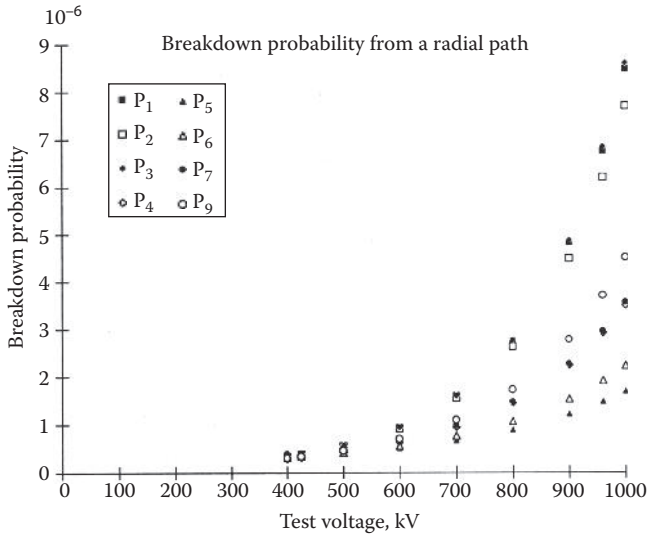


FIGURE 12.27 Variation of the probability of initiating breakdown from a specific path with the test voltage. P_1–P_9 refer to the breakdown paths initiating from field calculation sites 1–8, shown in Figure 12.21.

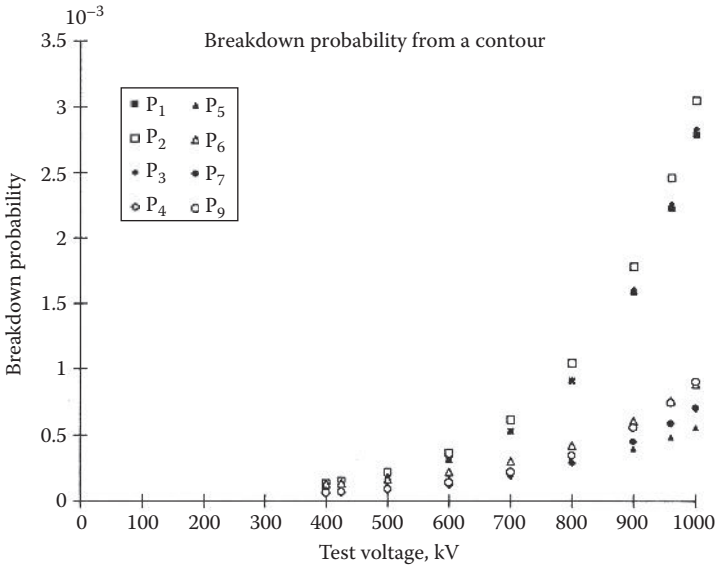


FIGURE 12.28 Variation of the probability of initiating breakdown from an equigradient contour with the test voltage. P_1-P_9 refer to the breakdown paths initiating from field calculation sites 1–8, shown in Figure 12.21.

breakdown paths originating from an equigradient contour at the electrode surface effectively increases and accentuates the probability to initiate the breakdown from the bushing shield–turret assembly, as compared with the other equigradient contours within the test cell. However, as in the case of breakdown probability from a specific path, the relatively low probabilities do not provide a clear indication regarding the dielectric performances of the test gap.

Probability of initiating the breakdown from a component: Noting that an electrode component (bushing shield electrode, HV connection, termination electrode) is composed of a number N_c of equigradient contours, one can evaluate the probability to initiate the breakdown from a specific component according to

$$P_s(u) = 1 - \prod_{N_c} \left[1 - P_{ci}(u)\right] \tag{12.11}$$

where N_c is the number of equigradient contours contained in a component.

Figure 12.29 presents the probabilities of initiating breakdown from the bushing shield electrode, assuming the same probability for the contours forming a given component.

The following observations can be made:

- At the voltage of 425 kV, all components of the HV circuit present relatively low probabilities to initiate breakdown, below 2%. No breakdown is expected at this voltage level.
- At the voltage of 700 kV, the probability to initiate the breakdown from the bushing shield electrode is 7% compared to probabilities less than 2% from the other components. The breakdown is unlikely at this voltage. However, if breakdown occurs, it should be initiated from the bushing shield electrode.
- At 960 kV, all components of the HV circuit have a finite probability to initiate the breakdown, although the probability of initiating breakdown from the bushing shield electrode reaches 25% compared with a probability less 10% from any other component.
- The probabilities to initiate breakdown from a component fall in the range of values with more practical meaning, which allows a direct assessment of the adequacy of the dielectric performance of the related component.

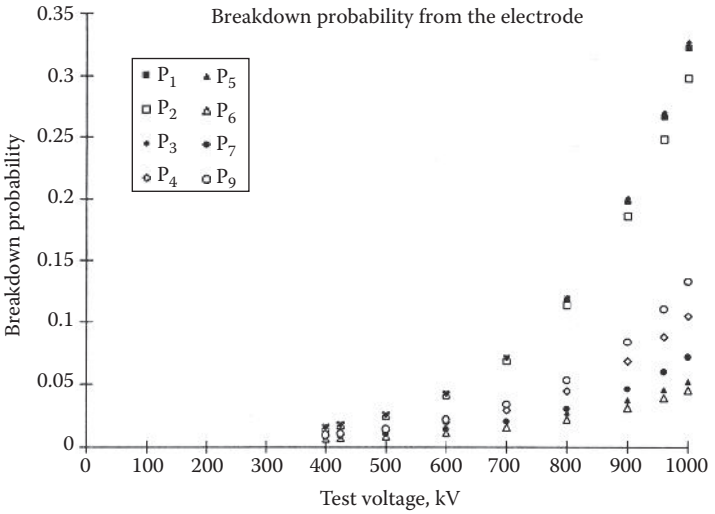


FIGURE 12.29 Variation of the probability of initiating breakdown from a component with the test voltage. P_1–P_3 Breakdown from the bushing shield electrode assuming constant field equal to that of point 1–3, P_4, P_9 Breakdown from the connecting conductor assuming constant field equal to that at point 4 and 9. P_5–P_7: Breakdown from the termination electrode assuming constant field equal to that at points 5–7.

12.4 Audible Noise from Power Transformers

The energization of power transformers generates acoustic noise due to vibration in the transformer core and in the cooling system. The noise generated may be sufficiently high to affect the local environment and have an impact on the choice of the location of the substation. Two mechanisms are responsible for the noise produced by the transformer core: the elongation of the core under magnetostriction effect and the transverse vibration of the core due to magnetic attraction. Both effects are independent of the polarity of the magnetic flux, and therefore, the transformer core vibrates essentially at twice the power supply frequency.

Figure 12.30 shows the octave-band frequency spectra of the AN generated by a 325/25 kV–275 MVA transformer in different modes of operation. One can see that the core vibration (curve *a*), measured

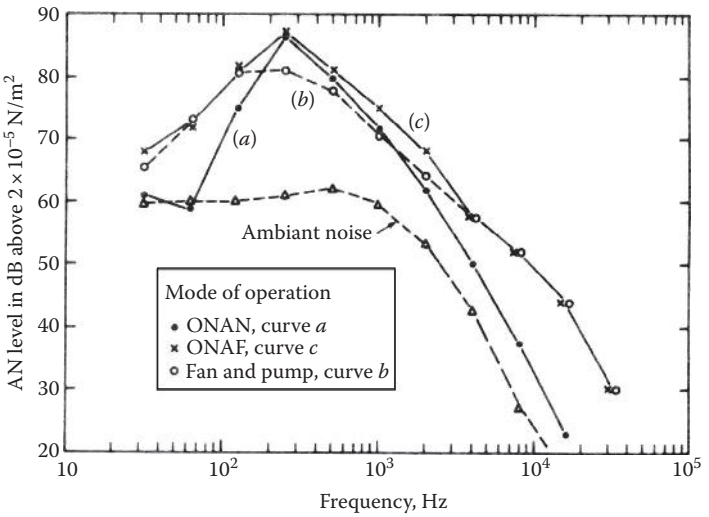
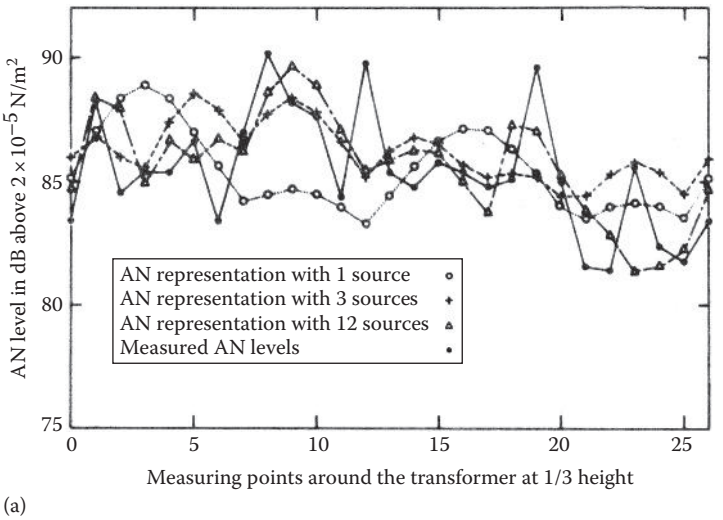


FIGURE 12.30 AN spectra from power transformer. (a) Noise from core vibration. (b) Noise from cooling system. (c) Resultant noise spectrum. (From Trinh, N.G. and Ménard, Y., Audible noise generated by power transformers of a substation—Its influence on the urban noise, Paper A76 473-9, presented at the *IEEE PES Summer Meeting*, Portland, OR, 1976.)

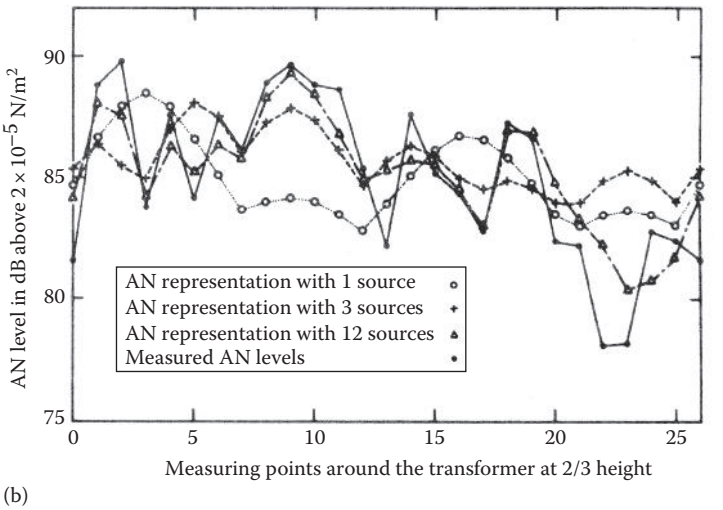
during the ONAN operation, has a frequency spectrum composed essentially of power frequency and its harmonics, with a maximal noise level at 240 Hz. The noise from the cooling system, pumps and fans, has a broader spectrum (curve *b*).

12.4.1 Transformer Audible Noise Characteristics

The AN characteristics of power transformers are determined by the average noise level obtained from a number of A-weighted measurements taken at regular intervals, 0.9 m around the major sound-producing surfaces of the transformer, and should comply with the limits set by national and international standards. The position of the microphone should be at 0.3 m from the major sound-producing surface and at least 1.8 m from any portion of the cooling system. The height of the microphone should be at midheight for small transformers and at 1/3 and 2/3 of the height of large power transformers (NEMA, 1973). Figure 12.31 shows the typical measurements of the AN made around a transformer of 425/25 kV–275 MVA. The noise level varies between 80 and 90 dBA.



(a)



(b)

FIGURE 12.31 Acoustic characteristics of a power transformer of 325/25 kV–275 MVA. (a) measured at 1/3 height (b) measured at 2/3 height. (From Trinh, N.G. and Ménard, Y., Audible noise generated by power transformers of a substation—Its influence on the urban noise, Paper A76 473-9, presented at the *IEEE PES Summer Meeting*, Portland, OR, 1976.)

12.4.2 Representation of the Audible Noise from Power Transformers

The earlier AN characteristics of power transformer do not lend themselves to a more detailed analysis. There is an incentive to define an acoustic representation of the power transformer that would reproduce the same AN characteristics and facilitate the analysis of a transformer noise. A logical approach consists of representing the power transformer by a number of point sources located within the transformer. The number of the noise sources and their position are arbitrary, with the highest number of noise sources not exceeding the number of measurements made. Their acoustic power is determined from the measurements as described in the following.

Referring to Figure 12.32, the sound pressure $P(x, y, z)$ at any point M is given by

$$P = \sqrt{\rho_0 c \sum_{1}^{N} \left(\frac{W_i}{4\pi r_i^2} + K \frac{W_i}{4\pi r_{im}^2} \right)} \tag{12.12}$$

where

r_i and r_{im} are distances from the measuring point M to the point source S_i and its image S_{im} with respect to the ground
W_i is the associated generated acoustic power
K is the coefficient of reflection of the ground
ρ_0 is the air density $\rho_0 = 1.293$ kg/m^3
c is the sound velocity in air, $c = 344.2$ m/s

Noting that the sound pressure at the measuring point is related to the measured noise level AN according to

$$P_i = 2 \times 10^{-5} \exp\left(\frac{AN_i}{20} \ln 10 \right) \tag{12.13}$$

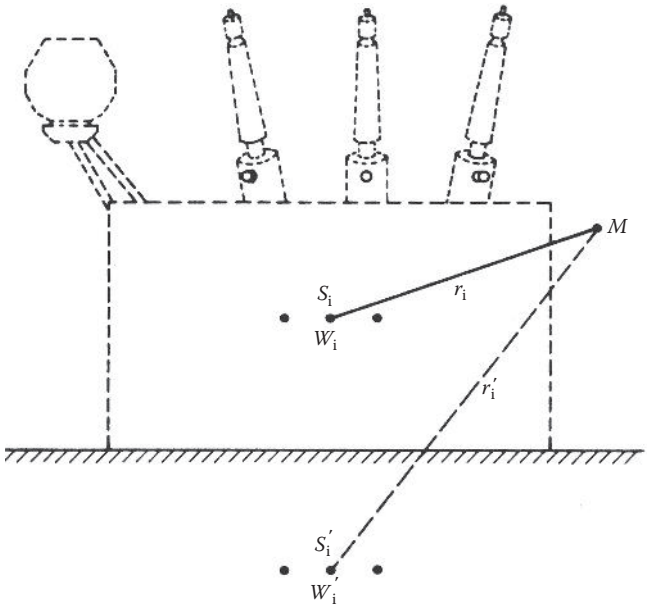


FIGURE 12.32 Acoustic representation of a power transformer. (From Trinh, N.G. and Ménard, Y., Audible noise generated by power transformers of a substation—Its influence on the urban noise, Paper A76 473-9, presented at the *IEEE PES Summer Meeting*, Portland, OR, 1976.)

a system of N equations can be obtained for the N_s unknown point sources as

$$\sqrt{r_0 c \sum_{1}^{N} \left(\frac{W_i}{4\pi r_i^2} + K \frac{W_i}{4\pi r_{im}^2} \right)} = 2 \times 10^{-5} \exp\left(\frac{AN_i}{20} \ln 10 \right) \tag{12.14}$$

The solution of the preceding system of N linear equations for W_i exists only if $N \geq N_s$, that is, if the number of point source N_s is less than or equal to the number of test points.

Acoustic power of transformer: With the proposed acoustic representation of power transformers, the total acoustic power W generated by a transformer can be readily evaluated according to

$$W = \sum_{1}^{N_s} W_i \tag{12.15}$$

where

W_i is the acoustic power of the ith point source

N_s the number of point sources representing the power transformer

In the earlier expression, the generated acoustic power is expressed in watts. It can also be expressed in terms of dB above a reference acoustic power $W_0 = 10^{-6}$ W as

$$W\,(\text{dB}) = 10 \log \frac{W}{W_0} \tag{12.16}$$

Figure 12.33 presents the typical variations of the generated acoustic power W as a function of the VA rating of the transformer obtained from conventional AN test results. The following observations can be made:

- The generated acoustic power W varies with the mode of operation. It approximately doubles when the transformer changes from the ONAN to ONAF mode. This implies that the contribution from the cooling system to the overall noise is comparable to the noise coming from the transformer core. In Figure 12.33, OFAF refers to forced oil, forced air cooling mode.

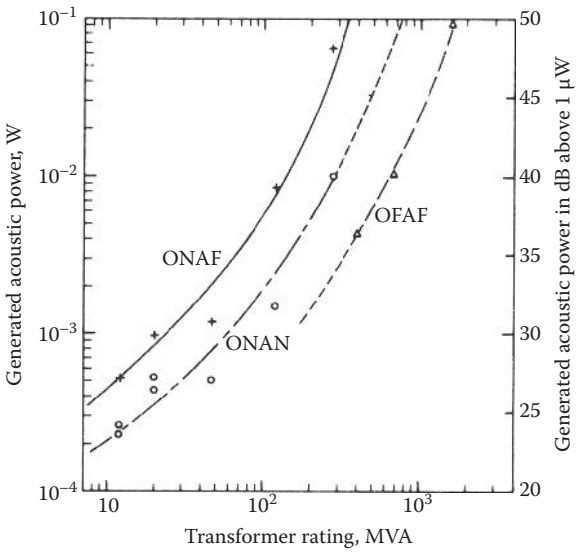


FIGURE 12.33 Variation of the acoustic power with the transformer rating for different modes of operation. (From Trinh, N.G. and Ménard, Y., Audible noise generated by power transformers of a substation—Its influence on the urban noise, Paper A76 473-9, presented at the *IEEE PES Summer Meeting*, Portland, OR, 1976.)

- The acoustic power increases with the VA rating of the transformer at a rate of about 4 dB per doubling of the VA rating. In terms of its absolute value, the generated acoustic power W can be approximately related to the VA rating according to

$$W = A_0 (\text{VA})^{1.3} \tag{12.17}$$

  where A_0 is a constant, depending on the mode of operation of the transformer.
- Transformers equipped with OFAF (forced oil, forced air) or OFWF (forced oil, forced water) cooling systems have a significantly lower acoustic power, due to their relatively small physical dimensions.

AN level: Once the acoustic power of the N_s sources is determined, the sound pressure P at any point around the transformer can readily be evaluated according to Equation 12.12 and the corresponding AN level according to

$$\text{AN} = 20 \ln \frac{P}{P_{\text{re}}} \ln 10 \quad \text{with } P_{\text{re}} = 2 \times 10^{-5} \text{ N/m}^2 \tag{12.18}$$

Figure 12.31 compares the calculated noise levels with the measurements made around the 325/25 kV–275 MVA transformer. As expected, the agreement improves with increased number of point sources used to represent the acoustic characteristics of the transformer.

12.4.3 Audible Noise in Far Field

It has been shown previously that a large number of point sources may be required to adequately represent the acoustic characteristics of a power transformer. The situation is different when one is interested only in the noise level at large distance from the transformer. With the representation of noise generation by point sources located within the transformer, a distance of several times the main transformer dimension could be considered as far field. Figure 12.34 compares the noise variations in the far field along the main axis of the transformer calculated with different acoustic representations of the transformer. No significant difference is observed among the calculated results beyond a few tens of meters from the transformer. This simplifies considerably the evaluation of acoustic impact of power transformers in a substation on the urban noise environment.

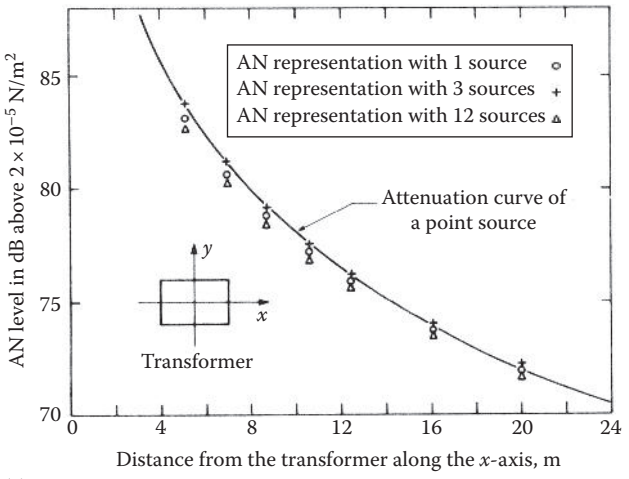
12.5 Standard HV Testing of Power Transformers

A number of tests are prescribed by international standards, ANSI and IEC, to verify the adequacy of power transformers and, in particular, their insulation with respect to the various stresses. For ac voltage, this implies *applied potential* and *induced voltage* tests, and for impulse voltage, it includes *standard impulse, chopped wave,* and *switching impulse* tests. Detailed test prescription and procedures are given in national and international standards (ANSI C57) (IEC 60076-3). These are briefly outlined in the following.

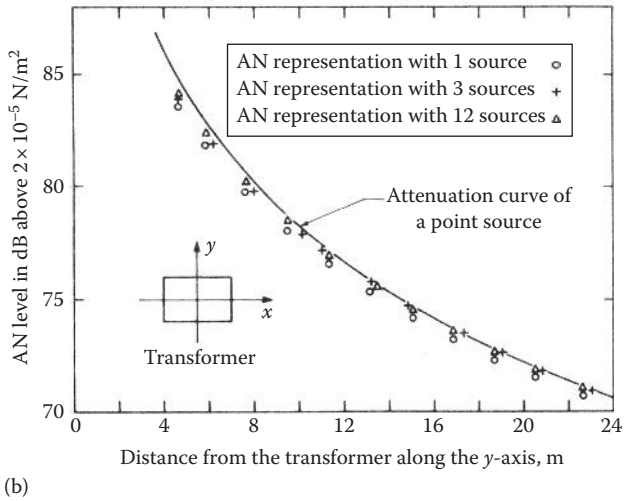
12.5.1 Test with AC Voltage

12.5.1.1 Applied Potential Test

It is carried out on transformers with full (ungraded) insulation. The power frequency test voltage is applied to the terminals of one winding at the time, with the other winding terminals maintained at ground potential.



(a)



(b)

FIGURE 12.34 Far-field behavior of AN from power transformer. (a) Variation along the transformer x-axis. (b) Variation along the transformer y-axis. (From Trinh, N.G. and Ménard, Y., Audible noise generated by power transformers of a substation—Its influence on the urban noise, Paper A76 473-9, presented at the *IEEE PES Summer Meeting*, Portland, OR, 1976.)

12.5.1.2 Induced Voltage Test

It is carried out under ac voltage at a multiple of power frequency, to avoid core saturation. The applied voltage is 1.73 p.u. for 7200 cycles, followed by a period of 1 h at 1.5 p.u., during which a PD is monitored and constitutes the base for acceptance.

Measurement of PDs: Figure 12.35 shows the typical circuit for measuring PDs during induced voltage test. It is noticed that in this case, the test voltage is generated by the power transformer itself, its low-voltage winding being energized from the high-frequency ac voltage source. The PD measuring equipment is connected across the HV winding via a series-connected coupling capacitor C_k, which isolates it from the low-frequency HV. It is particularly interesting to note that PDs in voids are sensitive to voltage changes. As a result, a test carried out at a frequency n times the power frequency is equivalent to a test at power frequency n times longer. Two methods for evaluation of PDs are currently followed: measurement of the apparent charge and measurement of the radio influence voltage (RIV), with the former method gaining wider acceptance in recent years. A detailed discussion of the two PD measurement methods is presented in Chapter 14.

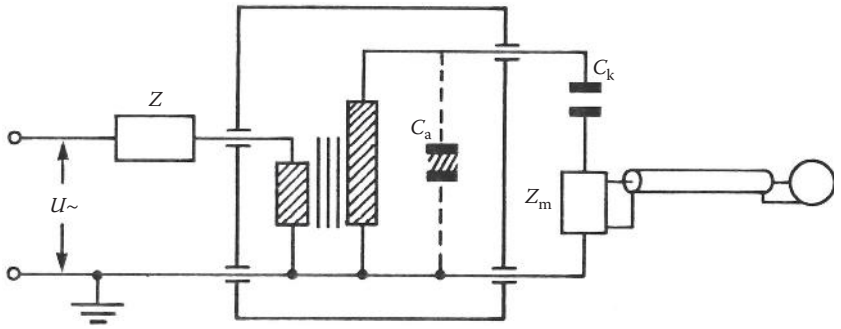


FIGURE 12.35 Circuit for PD measurement during induced voltage test on power transformers.

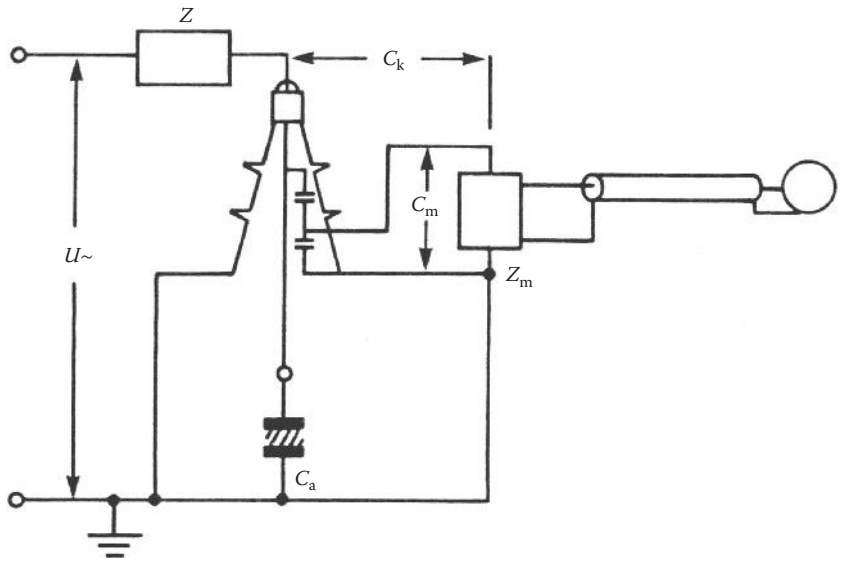


FIGURE 12.36 Circuit for PD measurement using a bushing capacitive tap. (From IEC Publication 60060-2, *High Voltage Testing Techniques, Part 2: Measuring Systems*, 2nd edn., IEC, Geneva, Switzerland, 1994a.)

In testing power transformers, advantage may also be taken of the availability on the bushing of a capacitive tap, which can serve as a coupling capacitor to the PD measuring instrument, as illustrated in the circuit shown in Figure 12.36. This is particularly useful in on-site PD measurement of power transformers.

Location of PD sites: The development of PDs may be accompanied by the generation of acoustic noise, in the form of acoustic pulses, whose frequency spectrum extends up to the ultrasonic range of several kHz. Acoustic pulses propagate across the insulation to impinge on the transformer tank, where they can be detected by means of ultrasonic detectors. The acoustic signals are delayed with respect to the electrical pulse by the traveling time of the acoustic wave from the PD site to the detectors, usually in the range of milliseconds. With several detectors fixed at different locations on the transformer tank and using the electrical PD signal to trigger the measurement of acoustic pulses, it is possible to locate the site of the PDs by means of triangulation.

12.5.2 Impulse Tests

HV impulse generators are used to generate lightning and switching impulses for testing of power transformers. The inductive nature of the transformer and shunt reactors requires particular considerations, principally to obtain the appropriate impulse wave shape, as discussed in the following.

12.5.2.1 Standard Impulse

Reference is made to the circuit of Figure 12.37, which shows the standard circuit for generating a double exponential impulse voltage, to which an inductive load L is connected. The curve of Figure 12.37 shows the variations of the required capacitance of the impulse generator to produce a time to half value of t_{50} of 50 μs (Train, 1981).

It is noticed that the smaller is the load inductance L, the larger will be the capacitance C_g of the impulse generator. Furthermore, for an inductive load of about 7 mH, it will not be possible to obtain an impulse with a time t_{50} of 50 μs. Such a limitation is due to the series-connected front resistor R_f with the inductive load L, which has a unit-step response according to

$$u_L(t) = u_o \exp\left(-\frac{R_f}{L}t\right) \tag{12.19}$$

It is obvious that the time to half value is determined by the circuit time constant $\tau = L/R_f$, independent of the capacitance of the generator. Reducing the resistance R_f will increase the time to half value of the impulse. However, a small value of R_f will make the circuit oscillate due to the stray inductance of the circuit and sets a lower limit for R_f.

For very low-impedance transformers, some standards allow the addition of a small resistance, 400 Ω or less, in series with the ground terminal, to increase the effective time to half value of the impulse. However, the voltage across the inductive load is considerably reduced and its wave shape significantly modified.

Another circuit that can be used in testing of low-impedance transformers is shown in Figure 12.38, where an inductance L_d is connected in parallel with the front resistor to bypass it after the peak voltage

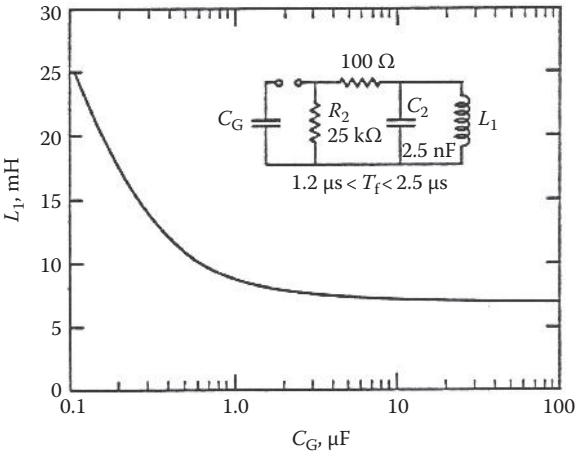


FIGURE 12.37 Variations of the required capacitance of the impulse generator to produce a double exponential impulse with a time to half value of 50 μs for different inductive loads.

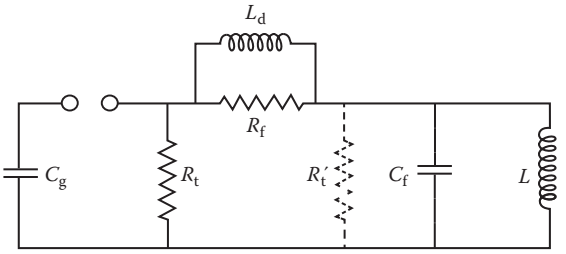


FIGURE 12.38 Circuit for testing low-impedance transformers.

is reached. The time to half value of the test impulse voltage is controlled by the natural oscillating frequency of the circuit:

$$w = \frac{1}{\sqrt{(L + L_d)C_g}} \tag{12.20}$$

and damped by the tail resistor R_t (Figure 12.38). The main drawback of this approach is the high energy required by the impulse generator, which may reach several hundreds of kJ.

12.5.2.2 Switching Impulse

The performance of an impulse generator can be conveniently analyzed by means of the single-stage equivalent circuit shown in Figure 12.39a, where C_g is the total capacitance of the generator; R_f and R_t are the wave front and tail resistances, respectively. C_f is the total wave front capacitance and L is the inductance of the test object, which, in the case of a transformer, is equal to the magnetizing inductance, since switching surge tests are normally produced on transformers, which have their nonimpulsed terminals open-circuited.

Figure 12.39b shows the required characteristics of the switching impulse for testing power transformer (IEC Standard 60071-1, 1993): the time-to-peak, $T_p \geq 100$ μs. The time T_{90} is defined as the time during which the voltage transient exceeds 90% of the peak value, which should be greater than 200 μs to ensure that the insulation is adequately stressed. T_0 is the time to the first voltage zero on the tail of the wave and shall not be less than 1000 μs.

An analysis of the circuit in Figure 12.38 by Train (Train, 1981) has shown that the Laplace transform of the voltage across the inductance is given by

$$u_s = \frac{U_c}{R_f C_f} \frac{s}{s^3 + s^2 K_1 + s K_2 + K_3} \tag{12.21}$$

where U_c is the charging voltage of the impulse generator, and

$$K_1 = \frac{(R_t + R_f) + (R_t C_g / C_f)}{C_g R_t R_f} \quad K_2 = \frac{1 + (C_g R_t R_f / L)}{C_g C_f R_t R_f} \quad \text{and} \quad K_3 = \frac{R_t + R_f}{L C_f C_g R_t R_f}$$

Appropriate charts are also produced for the selection of various circuit parameters so that the switching impulse will meet the specified characteristics. Figure 12.40 permits the test engineer to rapidly evaluate the value of the wave front capacitance required for any value of the inductance L of the test object and the impulse generator capacitance C_g. The figure also shows the circuit efficiency. The values selected must lie to the right of line a–b; otherwise, the time T_{90} will be less than 200 μs. Also, the

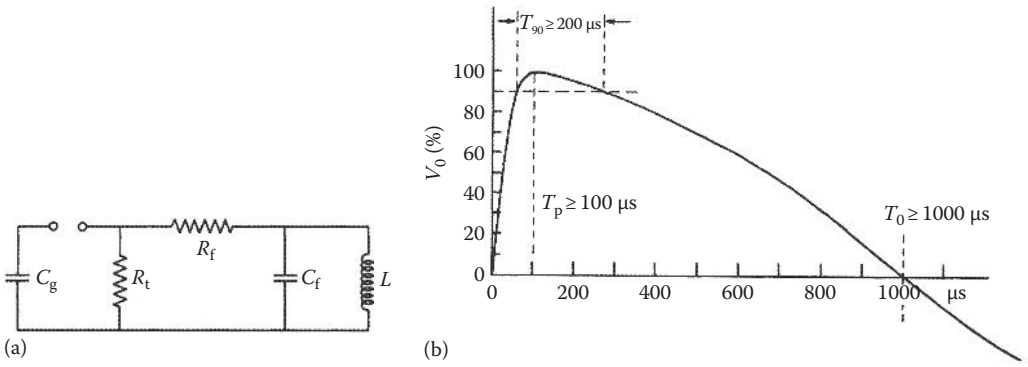


FIGURE 12.39 Equivalent circuit and required wave shape for switching impulse test on shunt reactors and power transformers. (a) Equivalent test circuit. (b) Standard switching impulse requirements. (From Train, D., *IEEE Trans. Power Appar. Syst.*, PAS-100(6), 3125, 1981.)

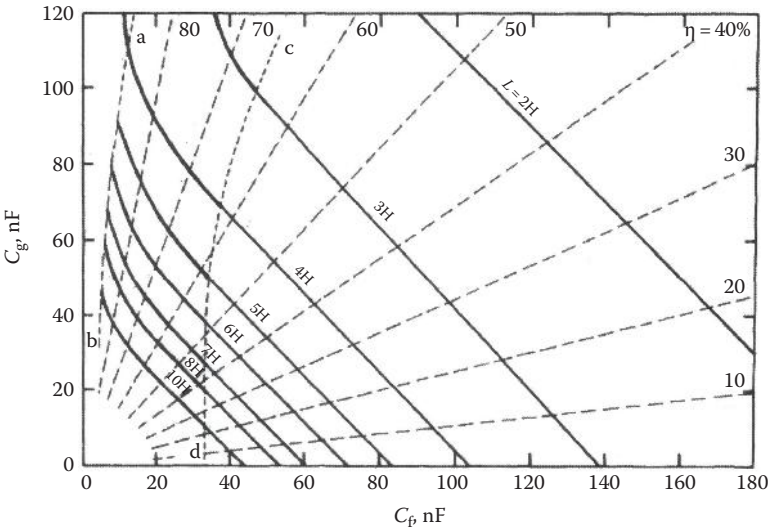


FIGURE 12.40 Test circuit characteristics for the selection of the wave front capacitance C_f. (From Train, D., *IEEE Trans. Power Appar. Syst*., PAS-100(6), 3125, 1981.)

values selected must lie to the left of line c–d; otherwise, the overshoot will exceed the 90% level. Thus, the effective working zone lies between the lines a–b and c–d.

Having found the value of the wave front capacitance, the wave front resistance R_f can be selected from Figure 12.41, which shows the variations of T_p with the time constant T_{rf} defined as

$$T_{rf} = R_f C_{eq} = R_f \frac{C_g C_f}{C_g + C_f} \tag{12.22}$$

where C_{eq} is the equivalent capacitance:

$$C_{eq} = \frac{C_g C_f}{C_g + C_f}.$$

For a given value of T_p, one can obtain the corresponding value of the time constant T_{rf} and calculate the appropriate value of R_f; for example, for T_p = 100 μs, the time constant T_{rf} is 20 μs.

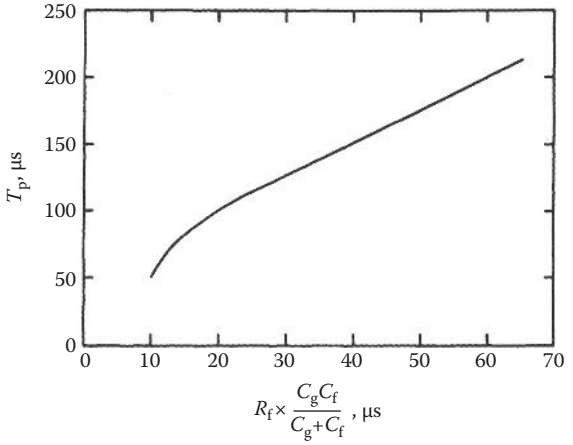


FIGURE 12.41 Influence of the wave front time constant, T_{rf}, on the time-to-peak, T_p. (From Train, D., *IEEE Trans. Power Appar. Syst*., PAS-100(6), 3125, 1981.)

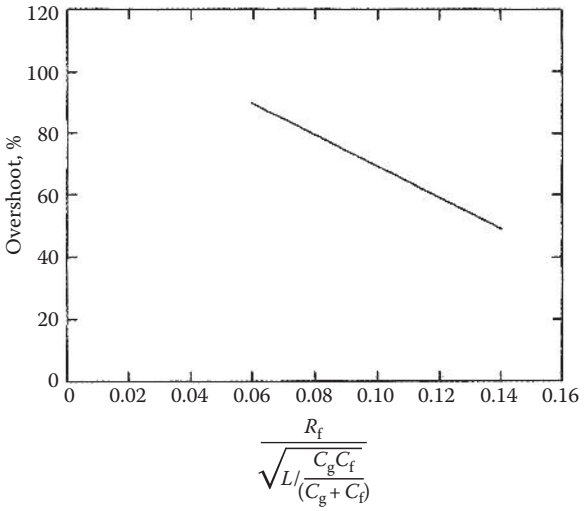


FIGURE 12.42 Influence of the damping factor on the overswing of the generated switching impulse. (From Train, D., *IEEE Trans. Power Appar. Syst*., PAS-100(6), 3125, 1981.)

Figure 12.42 shows the effect of the circuit damping factor, $\mathsf{a} = R_f \Big/ \sqrt{L/C_{eq}} = R_f \Big/ \sqrt{L\,(C_g + C_f)/C_g C_f}$, on the overswing of the generated switching impulse, expressed as a percentage of the maximum test voltage at T_p. The overswing should be less than 90%. A too high value of the overswing may require increasing the wave front resistance R_f and, hence, a longer time-to-peak T_p.

Finally, Figure 12.43 shows the influence of the ratio $C_g \big/ (C_g + C_f)$ on the time T_{90} during which the voltage transient remains above the 90% level. It should be pointed out that using the results of Figure 12.40 and Figure 12.43, values of T_{90} in the range of 200–256 μs are obtained.

As described earlier, the switching impulse test is made by discharging the impulse generator into the HV winding of an open-circuited transformer. The load inductance seen by the impulse generator is equal to the magnetizing inductance of the transformer and may be very high, usually above 100 H.

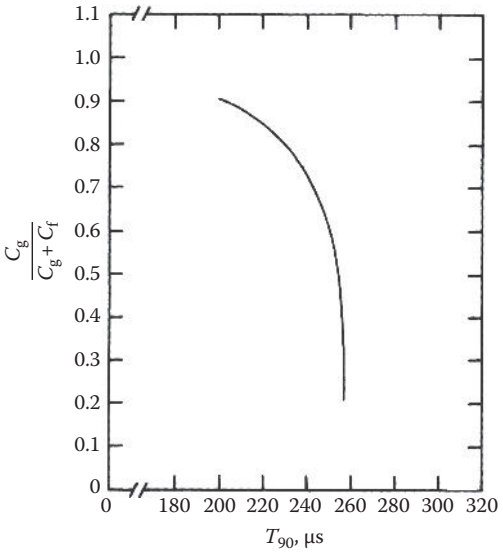


FIGURE 12.43 Influence of the ratio $C_g \big/ (C_g + C_f)$ on the time T_{90}. (From Train, D., *IEEE Trans. Power Appar. Syst*., PAS-100(6), 3125, 1981.)

The equivalent circuit shown in Figure 12.39 can still be used to evaluate the performance of the test circuit, however, with appropriate change in the values of

- The front capacitance: $C_f = C_f' + C_t$, with C_f' as the external load capacitance and C_t as the surge capacitance of the transformer winding
- The inductance of the test object: $L = L_m >> L_1 + L_2$, with L_1 and L_2 as the leakage inductances of the primary and secondary windings, respectively

Typical waveforms obtained during switching impulse tests on transformers are illustrated in Figure 12.44 and summarized in Figure 12.44d. In this figure, curve 1 indicates the waveform normally obtained. T_0 is very long in the absence of core saturation, typically 4000–5000 μs. In addition, the time T_{90} is also very long compared to the minimum required value of 200 μs. This results in prolonged overstressing of the insulation.

Magnetic saturation of the core frequently occurs, and the voltage will drop very rapidly as shown by the curve 1a of Figure 12.44c and d. When higher voltages are applied, core saturation will occur earlier as shown in curve 2 of Figure 12.44d. It is therefore impossible to have identical oscillograms at reduced and full test values. The core saturation can be minimized by magnetically biasing the core in the reverse

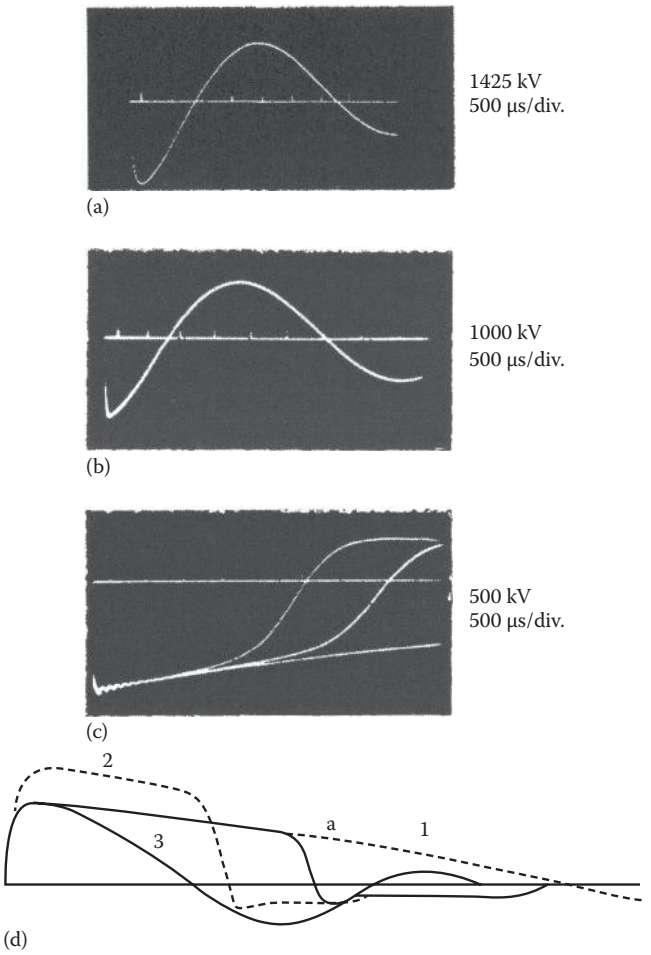


FIGURE 12.44 Typical waveforms obtained during switching impulse tests on power transformers. (a), (b) and (c) Switching impulse wave forms at different voltage levels. (d) Schematic description of the effect of voltage level on impulse waveform. (From Train, D., *IEEE Trans. Power Appar. Syst*., PAS-100(6), 3125, 1981.)

direction before applying the test voltages. This is usually obtained by either circulating a dc current through the winding or applying an impulse voltage of opposite polarity.

The duration of the test voltage on the transformer can be reduced if a low-inductance reactor is connected in parallel with the HV winding of the transformer. Curve 3 of Figure 12.44d shows the waveform that can be obtained with such an arrangement. A practical application of this approach may take advantage of the fact that

- Voltages are transferred according to the turn ratio under switching impulse conditions
- Most power transformers are provided with tertiary winding, having voltage ratings in the range of less than 20 kV

A compact air core, low-inductance coil can be used for this purpose, for example, a 735 kV transformer having a 9.6 kV tertiary winding has a turn ratio of 44.2; an inductance of 5 mH, connected to the tertiary winding, will have an effective value of 9.8 H when transferred to the HV winding.

Finally, the effective surge capacitance as seen by the impulse generator is not necessarily the capacitance of one phase only, since the other two phases may have voltage induced in them, depending on the arrangement of the tertiary windings. The surge capacitance can be determined from energy considerations by assuming that an equivalent capacitance stores the same amount of energy at the full test voltage. Figure 12.45 gives the equivalent capacitances for various arrangements of the tertiary windings.

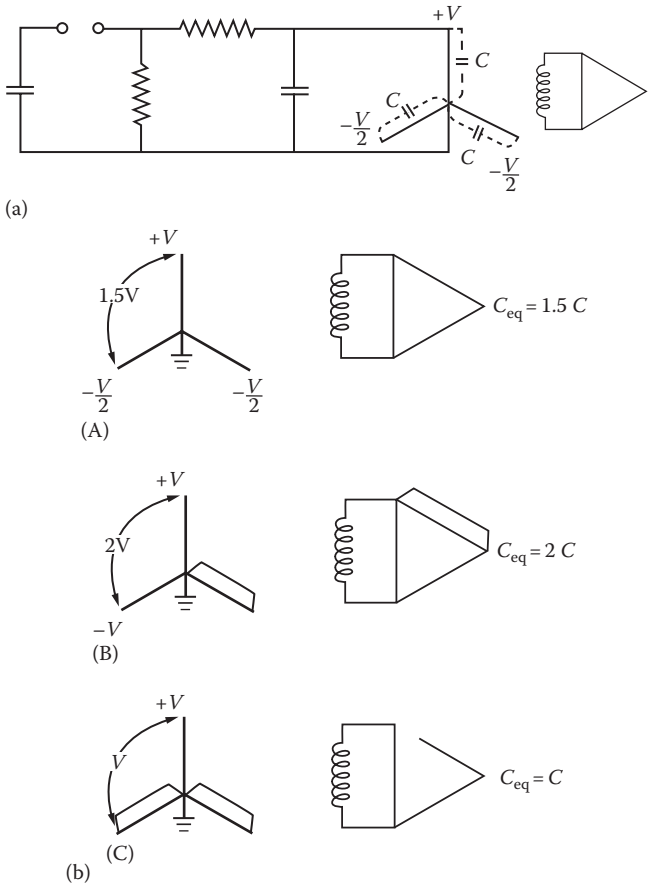


FIGURE 12.45 Equivalent surge capacitances for various arrangements of the tertiary windings. (a) Equivalent circuit. (b) Typical arrangements of the tertiary windings. (From Train, D., *IEEE Trans. Power Appar. Syst*., PAS-100(6), 3125, 1981.)

12.5.2.3 Chopped Wave

It is produced by connecting a spark gap, usually sphere gap, across the winding tested. By adjusting the distance between the sphere electrodes, the gap will flashover, producing an impulse wave chopped at the appropriate time. Natural flashover voltage of spark gaps may have a dispersion in the flashover voltage and, hence, results in variations of the time to chop in the order of microseconds. This is unacceptable for testing of power transformers, which requires a variation of less than 0.1 μs in the time to chop, to obtain reproducible oscillograms for fault detection. A solution to this problem is in the use of triggered spark gaps, which may be connected in series to meet the required test voltage. Details of this solution are given in Chapter 14.

12.5.3 Detection of Failure during Impulse Tests

Dielectric tests on power transformers sometimes result in failure of the transformer insulation. However, due to the relatively small energy of the test source, these failures do not always result in a complete collapse of the test voltage, but are limited to local breakdown of the winding insulation: turn-to-turn or layer-to-layer failures, with partial collapse in the test voltage. Partial failure of the winding also changes its impedance and, hence, affects the impulse current as measured in the ground circuit. Detection of failures occurring in dielectric tests is currently done by comparing oscillograms of the test voltages and currents made at reduced and full voltage and looking for minute changes in the recorded waveforms. Figure 12.46 compares such oscillograms of voltage and current for the case of a partial failure of the test winding and illustrates this approach.

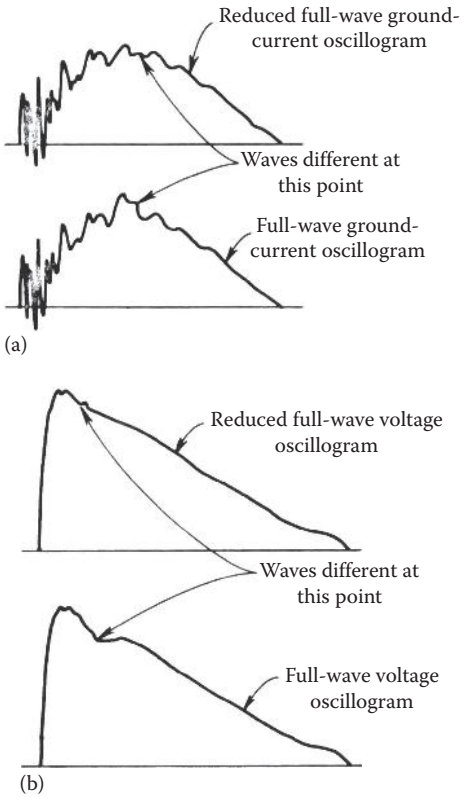


FIGURE 12.46 Comparison of impulse voltage oscillograms and ground currents to identify partial failure of transformer winding in dielectric tests. (a) Current signals. (b) Voltage signals. (From Bean, R.L. et al., *Transformers for the Electric Power Industry*, McGraw-Hill Book Co., New York, 1959.)

Practical experience shows that voltage oscillograms are sensitive to detect most of the disturbances, while oscillograms of ground current are sensitive to certain types of failure. Disturbances occurring during tests with chopped wave are more difficult to detect from the oscillograms. For these reasons, the procedure in all standard impulse tests is

- To apply a reduced full wave test, between 50% and 70% of the test level, at the start of the impulse tests
- To perform the full wave test at the end

Any partial failure occurs during the tests; it will usually appear as a difference in the oscillograms at reduced and full wave voltages.

Digital transient recorder: Important progress has been made in recent years by the introduction of digital transient recorders sufficiently performing for the measurement of fast transient signals. The recorded digital data offer the advantage that they can be processed to provide information otherwise impossible with analog signal:

- Reconstruction of the impulse signal deformed by the HV measuring system (Malewski, 1982)
- Determination of the transfer function of the test specimen, which can then be used to detect any change in the transfer function, resulting from partial failure during dielectric test (Malewski and Poulin, 1988; Freyhult and Carlson, 1991)

12.6 Aging and Incipient Faults

Operating power transformers subject their insulation to aging and development of incipient faults, which eventually can cause failure.

12.6.1 Aging Mechanism

Several aging processes are present in power transformers, namely, thermal, electrical, and environmental aging. They will be discussed in the following.

12.6.1.1 Thermal Aging

When oil–paper insulation is subjected to thermal stress, irreversible damage may be produced in both the oil and paper components of the insulation. The overall effect is a reduction of the mechanical and dielectric performance of the insulation with time.

Arrhenius relation: The life of varnish cloth subjected to a constant thermal stress, investigated by Montsinger in 1930 (Montsinger, 1930), was among the first studies of thermal aging. In this study, the aging state of the insulation was characterized by the residual tensile strength of the paper. The time required for the insulation to reach a given aging state follows an empirical equation

$$T = A\exp\left(-m\theta\right) \tag{12.23}$$

where
T is the life time
A is the initial state of the insulation
m is a constant
θ is the temperature in °C

Montsinger found that while the initial tensile strength was characteristic of the insulation system, the parameter m was relatively constant and amounts to $m = 0.088$ for the various insulation systems evaluated.

This results in the now familiar *8 degrees* rule, which states that *the thermal life of an insulation system is reduced by half for each 8°C increase in the operating temperature* (values between 7°C and 10°C have been used in actual practice).

In 1948, Dakin proposed the Arrhenius's chemical rate theory to explain thermal degradation (Dakin, 1948), by noting that the physical changes observed during thermal aging are reflections of internal chemical changes. Thermal aging of paper breaks the chemical bonds of the cellulose molecules, which results in a lower *DP* and a loss of mechanical properties, for example, the paper becomes brittle as a result of the reduced tensile strength. A more descriptive expression of the insulation life was derived:

$$T = A\exp\frac{B}{\theta} \tag{12.24}$$

where

T is the life time

θ is the temperature in K

A and B are constants determined by the activation energy of the particular chemical reaction responsible for thermal aging

Taking the logarithm of both sides yields

$$\ln T = \ln A + \frac{B}{\theta} \tag{12.25}$$

Thus, if one plots the logarithm of the insulation life against the reciprocal of the absolute temperature, the resulting graph is a straight line, often known as the Arrhenius life curve as illustrated in Figure 12.47, which compares the experimental results obtained by Dakin, Clark, and Montsinger (Dakin, 1948).

12.6.1.2 Electrical Aging

Oil–paper insulation subjected to a relatively uniform field has a well-defined dielectric strength, typically 30 kV/mm under ac voltage and 110 kV/mm under lightning impulses. When exposed to a constant electric field over a long period of time, the insulation will age and gradually loses its dielectric strength. The electrical life T of the insulation system varies according to the empirical *inverse power* law (Nelson, 1972; Kiersztyn, 1981):

$$T = A\frac{1}{U^n} \tag{12.26}$$

where

U is the applied voltage in p.u.

A is the nominal life expectation of the insulation system at 1 p.u.

the exponent n has a value between 6 and 12

Taking the logarithm of both sides in the earlier Equation 12.26 yields

$$\ln T = \ln A - n\ln U \tag{12.27}$$

which indicates a linear relationship between the logarithms of the life expectation T and the applied voltage U.

Attempts to formulate a theory for electrical aging (Kiersztyn, 1981) have not been conclusive. The reason appears to be that failure of the insulation system at HVs may not follow the same mechanism

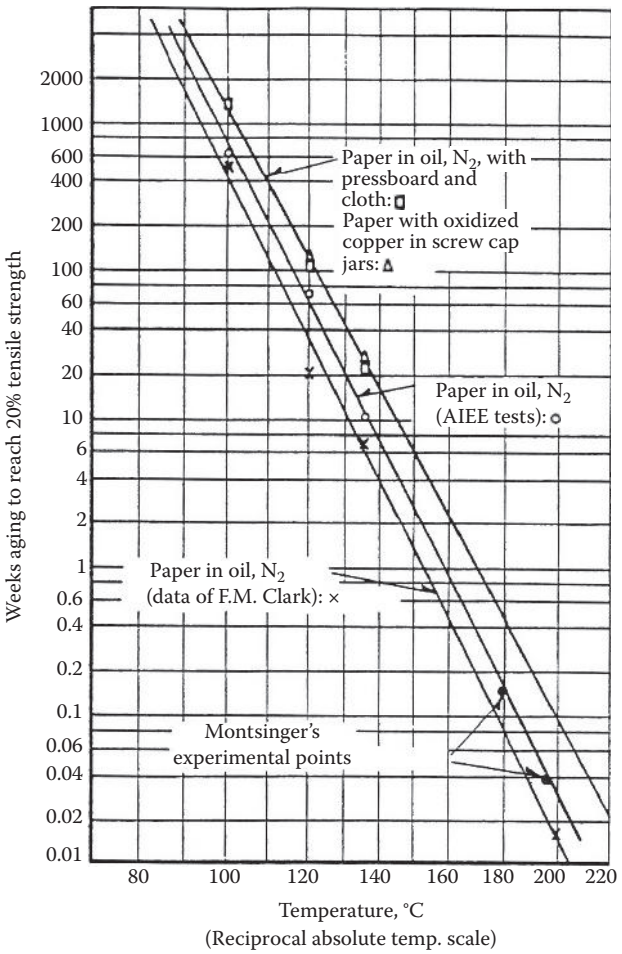


FIGURE 12.47 Thermal aging—Arrhenius curves. (From Dakin, T.W., *AIEE Trans*., 67(Part I), 113, 1948.)

active at lower voltages. Different breakdown mechanisms have effectively been identified in oil–paper insulation and discussed in Chapter 6:

- The direct breakdown by streamers burst at relatively short time under high field.
- Breakdown initiated by particle contamination at lower field intensities.
- Incipient faults developing at operating field intensities and involving intense PDs developing either in the bulk oil volume or at the oil–paper interface. One of the mechanisms for PD development in oil is via the formation of gas bubbles (Kao and McMath, 1970). Due to the difference in the dielectric constants of gas and oil, gas bubbles are subjected to higher field intensity than the surrounding oil, by a factor equal to their relative dielectric constants, typically 2.2. This local field enhancement, combined with the lower ionizing potential of gases, makes the bubbles the weak link in oil and oil–paper insulation, particularly favorable to PD development. The phenomenon is strongly affected by the gas content in the oil, since higher gas content favors the formation of gas bubbles.

12.6.1.3 Environmental Aging

During normal operation, the insulation of power transformers may experience environmental changes, which affect their dielectric performance. The most common of these changes is due to ingress of

moisture and air. Particles may also be generated or accidentally introduced. Both aspects are well recognized today by utilities and manufacturers (Boisdon et al., 1994).

Moisture increases the rate of degradation (Fournié, 1990). The effect may be partly attributed to the fact that water is released from paper during thermal aging and helps to further enhance the process (Fabre and Pichon, 1960).

Carbon particles result from oil and paper decomposition by PDs or carbonization at hot spots in the insulation system, for example, winding joints and core, and may be generated over the service life of the transformer.

Environmental aging is rarely the direct cause of failure of the insulation; it generally enhances other active aging processes such as thermal and electrical aging. It also triggers a number of changes in quality control, manufacturing processes, and maintenance practices; all contribute to minimize its impact and improve the dielectric performance of the equipment. These aspects will be discussed in the following.

Oxygen and air: The presence of oxygen (or air) causes oxidation of the transformer oil and accelerates the degradation of oil–paper insulation in power transformers. The process may be attributed to the oxidation by-products of the oil (Shroff and Stannett, 1985). The paper degradation rate may be tenfold higher in the presence of oil when compared to chlorine-impregnating liquids. The process also consumes oxygen so that, unless there is a constant supply of oxygen, the effect will eventually die out. Laboratory tests on reduced-scale transformer models (Fournié, 1990) show that the area of the air–oil interface has a definite effect on the aging rate. Replacing air by nitrogen also reduces the aging process by as much as 30% over the temperature range of 110°C–140°C. These results tend to indicate that the influence of oxygen is more pronounced in free-breathing transformers than in sealed units, due to the continuous diffusion of oxygen from ambient air into the oil–paper insulation. However, the diffusion process is complex and difficult to evaluate. Aging is estimated to be 1.6–2.5 times faster in free-breathing transformers than in sealed units (Bouvier, 1977; Murray et al., 1982).

12.6.1.4 Decomposition By-Products

Hot spots, PDs, electric arc, etc., due to their higher temperatures, can degrade the insulating oil to a higher degree and produce decomposition by-products that are specific to the insulating fluid:

- Low-level PDs produce large amounts of hydrogen H_2 with a small amount of methane CH_4.
- Overheating of the oil produces ethylene C_2H_4, while arcing in oil generates acetylene C_2H_2.
- By-products associated with PDs and hot spots involving H_2O, CO_2, CO, and carbon, and recently furans (furfuraldehydes), are related to paper degradation.

12.6.2 Assessment of the Actual State of the Insulation

From the application point of view, the most straightforward way to determine the aging state of an insulation system is from its residual dielectric performance. However, this approach has two major drawbacks: the necessity of performing HV tests on-site and the risk of damaging the equipment in doing so, even at reduced test levels. For these reasons, assessment of the aging state of the oil–paper insulation is generally obtained by

- Physical–chemical tests on the oil and paper components
- Nondestructive dielectric tests on the equipment, for example, measurement of power loss, PDs, and more recently transfer function of the windings

12.6.2.1 Measurement of Bulk Parameters

Capacitance and insulation loss factor tan δ, sensitive to thermal aging, and PD level, that may lead to incipient faults, are currently used to evaluate the insulation state of HV transformers. Although feasible in terms of methods of measurement and test equipment, on-site measurement of insulation

loss factor tan δ and PDs requires temporary removal of the equipment from the system, a situation not always acceptable to utilities, which have to deal with the unavailability of the transformer under investigation.

Online monitoring of power losses and PDs is a viable alternative. It requires that measuring devices, such as capacitive coupling and current probe, be added to the equipment. It is a formidable task unless it has been foreseen from the moment the equipment is purchased, a condition not always met in practice. As a result, the most frequently used methods to assess the actual state of the insulation system rely on the measurement of the decomposition by-products that can be obtained from samples of the insulating oil used.

12.6.2.2 Measurement of Physical–Chemical Characteristics of the Insulation Components

Aging of the insulation changes the physical–chemical properties of the insulation and produces decomposition by-products that can be detected by measurements made on the components of the insulation: oil and paper.

Characterization of oil: Aging of transformer oil is caused mainly by oxidation, which gradually degrades the oil, eventually making it unsuitable for service (Lamarre et al., 1987). Its dielectric and physical properties, such as breakdown strength, conductivity, dissipation factor, and interfacial tension, are affected by the oxygen-containing compounds with functional groups such as aldehydes, ketones, alcohols, phenols, peroxides, and carboxylic acids, which are more polar than the parent hydrocarbons (Lamarre et al., 1987). The degree of oxidation of transformer oil is usually determined by its soluble acidity, peroxide contents, and interfacial tension.

Oxidation of transformer oil is an autocatalytic phenomenon involving hydroperoxides that can be prevented by adding inhibitors, typically DBPC or DBP, to decompose the peroxide (Lamarre et al., 1987). However, in this process, the inhibitors are gradually destroyed, and their effect will therefore cease as soon as all the added inhibitors are destroyed. Sharp increases in the soluble acidity and polar compounds accompanied by a sharp drop in the interfacial tension occur when the DBPC is depleted. Sludge formation begins shortly after, accompanied by a reduction in the dissolved copper and followed by saturation of the oil with oxidation by-products.

Current practices aiming at keeping the oil free of soluble acidity would require reclaiming before complete depletion of the inhibitors (Lamarre et al., 1987) to avoid irreversible degradation of the oil due to the nonacid compounds, which are not eliminated by the reclaiming process. Removal of sludge by filtration (Lamarre et al., 1988) temporarily restores the oil that, however, takes less time to become oxidized.

Characterization of paper: As dry Kraft paper is heated above 100°C, its chemical bonds are readily broken, reducing the *DP*, which corresponds to the average number of glucose rings in the cellulose molecule. This is a direct measure of the aging state of the paper since it corresponds to the mechanical strength of the paper. This direct approach has a drawback in that it requires access to critical locations in the paper insulation inside the transformer. As a result, alternate means have been developed to measure *DP* indirectly by evaluating the changes in physical–chemical and dielectric properties of the oil–paper insulation.

CO and CO_2 dissolved in oil are most often measured since a direct correlation exists between their contents and the *DP* of the paper insulation. Figure 12.48 shows the variations in the residual tensile strength and *DP* as a function of the content of CO and CO_2 dissolved in the oil (Yoshida et al., 1987). One notices the strong correlation between the gas content and the *DP* of the paper, as the two curves almost coincide with one another. However, CO and CO_2 are not exclusive to paper; as a result, there has been an increasing interest to find new tracers, uniquely related to the degradation of paper.

Furans, being such candidates, are gaining importance in evaluating paper insulation aging. Figure 12.49 shows variations in the furfuraldehyde content of paper as a function of *DP* (Burton et al., 1984; Shroff and Stannett, 1985). It can be seen that a monotonic relationship exists, which allows the degree of aging of the paper to be estimated by measuring the furan content in the oil.

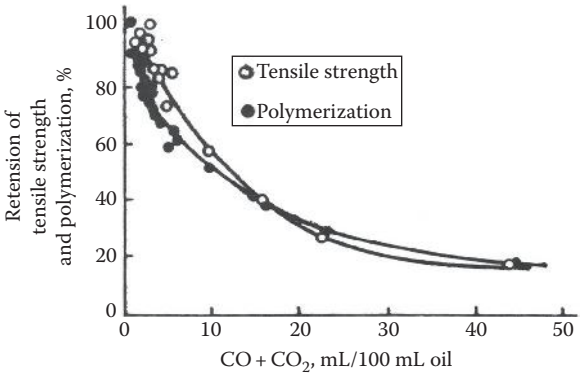


FIGURE 12.48 Correlation between the content of dissolved CO and CO_2 in oil and the *DP* of Kraft paper. (From Yoshida, H. et al., *IEEE Trans. Electr. Insul*., EI-22(6), 795, December 1987.)

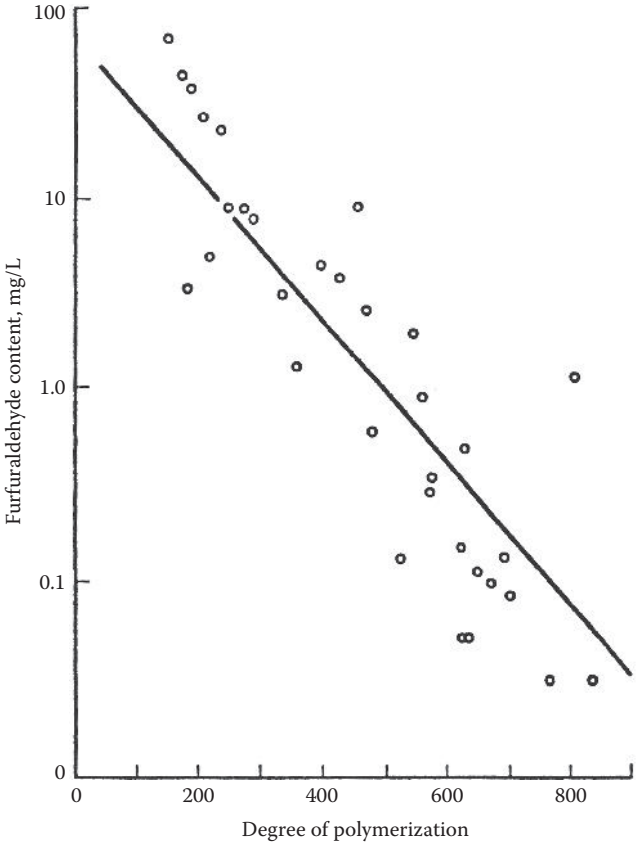


FIGURE 12.49 Correlation between the furan content dissolved in oil and the *DP* of the Kraft paper. (From Shroff, D.H. and Stannett, A.W., *IEE Proc*., 132(Part C, 6), 312, November 1985.)

Correlation of the dielectric parameters to aging of the paper insulation has not been as successful. This is illustrated by the results in Figure 12.50, which shows variations in the dissipation factor tan δ of the oil with *DP*. Although a general increase in tan δ was observed with a lower *DP*, the dispersion of the results does not allow a clear correlation between the two parameters (Shroff and Stannett, 1985).

Characterization of oil–paper insulation: The tacit assumption here is that there is a correspondence between the aging state of the insulation system as a whole and that of its two constituent components.

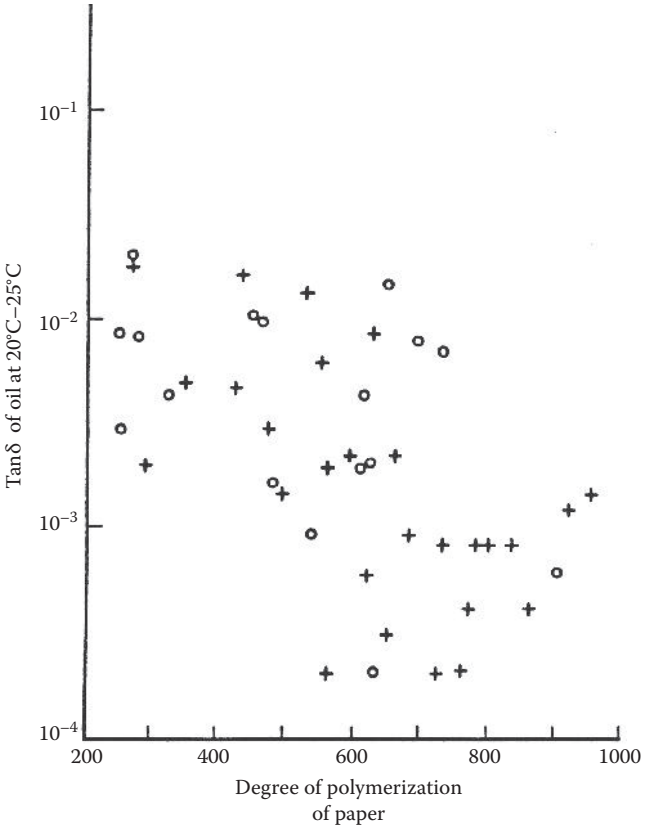


FIGURE 12.50 Correlation between power loss factor tanδ of oil–paper insulation and the *DP* of the Kraft paper. (From Shroff, D.H. and Stannett, A.W., *IEE Proc*., 132(Part C, 6), 312, November 1985.)

While this assumption seems reasonable, the actual relationship between the various aging states is still to be determined for each individual insulation system. This is illustrated by the results in Figure 12.51, which compares the variations in the residual tensile strength, *DP*, and the dielectric breakdown strength of insulating paper retrieved from power transformers as a function of their time in service (Yoshida et al., 1987). It can be seen that while significant changes occurred in both the tensile strength and *DP* of the paper, only a marginal reduction in its breakdown strength was observed over the 30 years of time period.

12.6.2.3 Nondestructive Tests

PD detection and tan δ measurements provide alternative means of directly evaluating the aging state of the transformer insulation. However, the correlation with the dielectric insulation state and, hence, the remaining life of the paper insulation remains difficult and so far has not been established.

12.6.2.4 End of Life

Because of the presence of different aging processes active simultaneously during the service life of power transformers, there is not a unique definition for end of life of the insulation, but each aging process may define an end of life for a component of the insulation system.

Oil: Complete oxidation of the oil is usually assumed when the soluble acidity reaches saturation, corresponding to an acidity index of 0.2 mg KOH/g oil. However, it is of current practice to delay the oxidation of the oil by the addition of inhibiting additives such as DBPC. The useful life of the oil corresponds to the depletion time of the inhibitors (DBPC). The oil is then due for reclaiming, although oxidation is still below saturation.

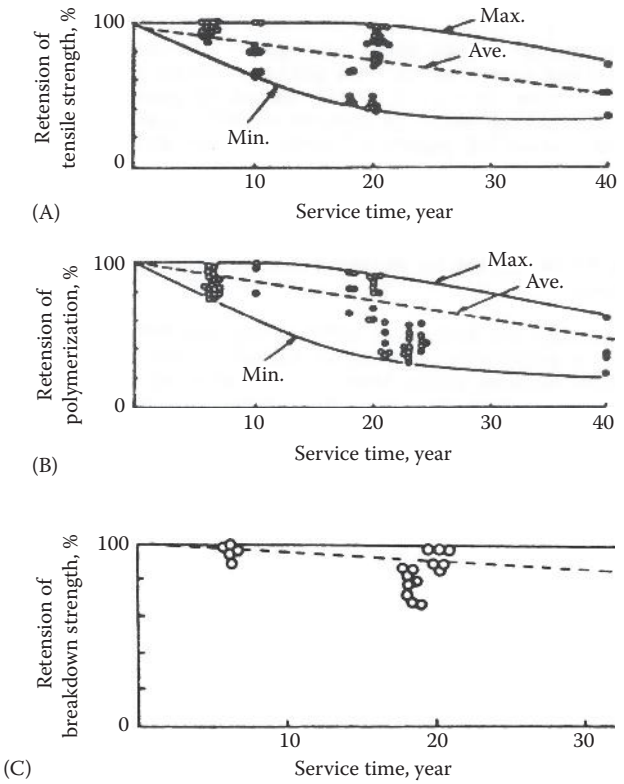


FIGURE 12.51 Variations of the residual performance with time in service. (A) Residual tensile strength to traction. (B) Residual degree of polymerization *DP* and (C) Residual dielectric performance of the oil-paper insulation of a transformer. (From Yoshida, H. et al., *IEEE Trans. Electr. Insul.*, EI-22(6), 795, December 1987.)

This is illustrated by the results of an accelerated oxidation test in Figures 12.52 and 12.53, showing variations in soluble acidity and peroxide contents of naphthenic and paraffinic oils as a function of oxidation time (Lamarre et al., 1987). Abrupt changes in the soluble acidity and peroxide contents were observed at the end of the induction period when the DBPC inhibitor was used up, followed shortly afterwards by the formation of sludge before oxidation reaches saturation.

Paper: For paper insulation, end of life is generally defined as the degradation stage when the paper has lost half of its mechanical strength, often measured by the tensile strength. Alternately, the end of life of paper insulation can also be related to its limit *DP*, typically 100–250. Figure 12.54 shows variations in tensile strength as a function of the *DP* of Kraft paper in free-breathing and nitrogen-blanketed transformers (Dakin, 1948). It can be seen that a linear relationship exists between these two parameters, and as the paper ages, the tensile strength is reduced proportionally with *DP* to a critical value of DP_l = 100–250 (Shroff and Stannett, 1985), where abrupt changes in the tensile strength are observed. The limit value DP_l corresponds to a fully aged paper, which has lost all its mechanical properties. Although there is no equivalent reclaiming process available for the paper, utilities can still extend the useful life of aged power transformers by moving them to locations with less operating stresses in the system.

Insulation system: The service life of power transformers is not a well-defined parameter, in part due to the lack of correspondence between the molecular structure of cellulose and its mechanical properties, on one hand, and the electrical properties of the oil–paper insulation on the other. Very few data actually are available on the dielectric performance of power transformers with aged insulation (Trinh et al., 1984; Campbell, 1991). Operating experiences have provided examples of transformers that are kept in operation even if their paper insulation has become brittle, normally an indication of aging beyond all reasonable limits. In practical terms, utilities would rather continue to operate the equipment until the

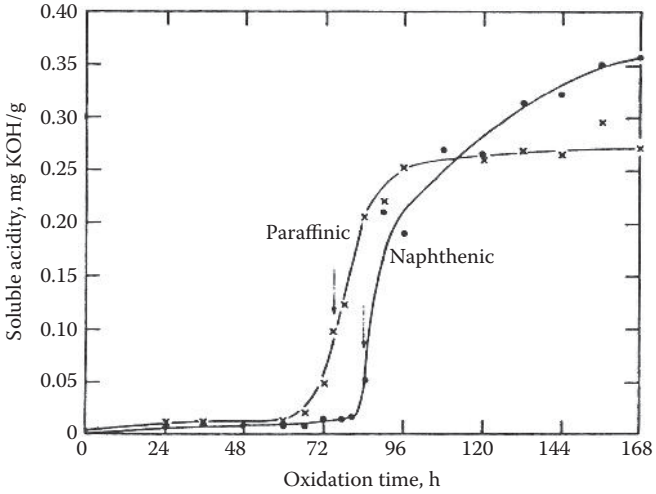


FIGURE 12.52 Variations of soluble acidity in naphthenic and paraffinic oils as a function of oxidation time. (From Lamarre, C. et al., *IEEE Trans. Electr. Insul*., EI-22(1), 57, February 1987a; Lamarre, C. et al., Antioxidant functionality in liquid and solid materials, in *CIGRE Symposium*, Report No. 900-05, Vienna, Austria, May 1987b.)

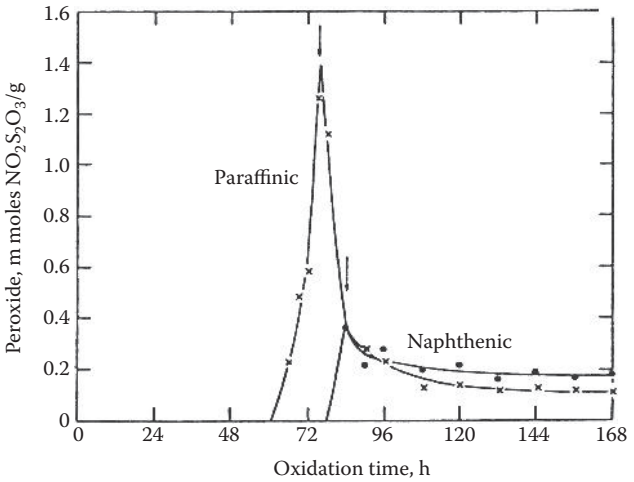


FIGURE 12.53 Variations of peroxide content in naphthenic and paraffinic oils as a function of oxidation time. (From Lamarre, C. et al., *IEEE Trans. Electr. Insul*., EI-22(1), 57, February 1987a; Lamarre, C. et al., Antioxidant functionality in liquid and solid materials, in *CIGRE Symposium*, Report No. 900-05, Vienna, Austria, May 1987b.)

costs of maintenance, energy losses, and forced outages become excessive. Canadian utilities usually consider a normal service life somewhere between 35 and 50 years. The difference may be related to the operating conditions of the equipment. In Europe, transformers are operated closer to their maximum rating when compared to Canadian practice.

12.7 Considerations for Operating and Maintenance

Operating and maintenance of oil–paper-insulated transformers consist essentially of attempting to keep the insulation in conditions as close as possible to those prevailing at its commissioning and to detect or prevent the development of PDs and incipient faults. Detailed procedures are generally developed by utilities from recommendations of manufacturers and their own operating experience. We are presenting in the following a few aspects that may need particular consideration.

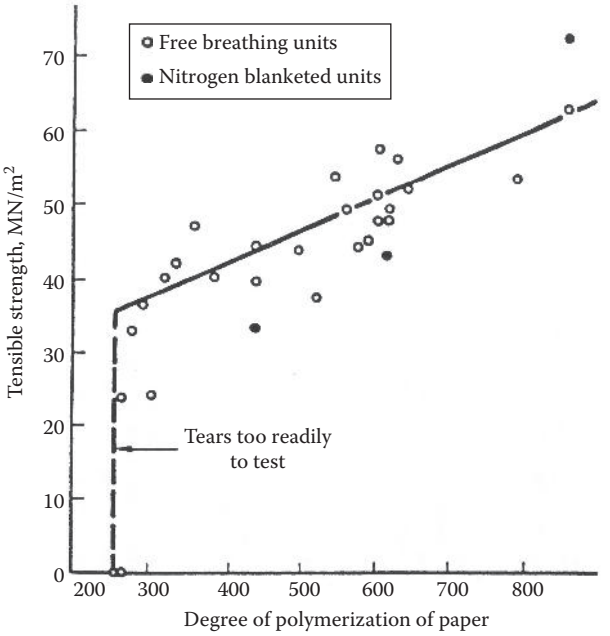


FIGURE 12.54 Variations of withstand to traction of Kraft paper as a function of the *DP* of the paper. (From Shroff, D.H. and Stannett, A.W., *IEE Proc*., 132(Part C, 6), 312, November 1985.)

12.7.1 Operating

Commissioning: Large power transformers are delivered to the site, emptied of its oils, and, sometimes, with its bushings removed for transportation. Particular care must be taken to minimize the risk of disturbing the dielectric integrity of the transformer insulation by on-site works. Among these, oil filling of the transformer can be improved by continuous monitoring of oil quality and, in particular, its particle content during the filling process. After filling of the transformer, a closed loop circulation of the oil is maintained, accompanied by filtering and monitoring the particle content in order to remove the residual particle contamination in the oil.

Figure 12.55 from Palmer and Sharpley (1969) shows the improvement in particle contamination obtained by such a procedure for oil filling of a transformer. Notice the marked increase in the particle content following oil filling, associated with the detachment of particles from the insulation, which is gradually filtered out during the 168 h of continuous filtering.

Cumulative aging: The well-defined mechanism of thermal aging in oil–paper insulation allows the establishment of the loading conditions for power transformers, based on the evaluation of life loss in tensile strength of the paper. Detailed recommendations for loading of power transformers are given in national and international standards (ANSI Standard C57.92). Table 12.9 summarizes typical operating conditions for power transformers, and their life expectation under constant temperature, assuming a loss of 80% of the tensile strength of paper.

Elaborate methods for the determination of the dynamic loading condition for power transformers are given in standards (ANSI C.57-92). They are elaborated by calculating the time that a transformer can operate under a given loading condition to limit the life loss to less than 1% of its life expectation. It assumes that

- The temperature at the beginning of the overload immediately rises to the value it will eventually have at the end of the overload
- The temperature will immediately drop back to the original value at the end of the overload

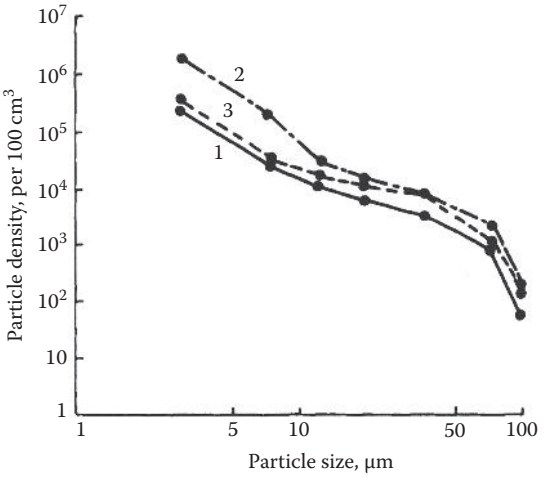


FIGURE 12.55 Variation of the particle content in transformer oil at initial oil filling: 1—before entering the transformer; 2—after filling; 3—after 168 h filtration. (From Palmer, S. and Sharpley, W.A., *Proc. IEE*, 116(12), 2029, December 1969.)

TABLE 12.9

Typical Operating Conditions and Life Expectation of Power Transformers

Parameters	Values
Average daily ambient temperature	30°C
Average winding temperature rise at full load	55
Average daily winding temperature	85
Differential between average winding and hottest spot	10
Hottest spot daily average temperature at full load	95
Maximum ambient temperature	40
Maximum hot spot temperature	105
Life expectation at constant temperature of 95°C	32,000 h
Life expectation at constant temperature of 115°C	2,900

Source: ANSI C57.92, *Guide for Loading Mineral Oil Immersed Power Transformers*.

The general procedure for determining the loss of life at any given overload is as follows:

1. From the test data on the transformer, the oil and copper-to-oil temperatures at the initial normal load and also the final temperature if the overload continues indefinitely.
2. Calculate the time constant τ from the physical data: weight of copper and oil, volume of oil, etc.
3. Calculate the actual oil rise at the end of the overload period, taking into account the time constant determined in step 2.
4. Calculate the hottest spot temperature.

The standard provides appropriate graphs and tables to determine the time that the transformer can operate under overload condition, without using up more than 1% of the life of the transformer.

Low temperature: Power transformers operate over a wide range of ambient temperatures, from −40°C to 50°C. Under conditions of very low temperatures, paraffin in the oil can form wax and disturb the operation of power transformers at start-up. In addition, the increased viscosity of the oil at low temperatures favors the development of hot spots within the insulation, which can occur under steady state and

transient loading conditions (Aubin and Langhame, 1992). At low ambient temperatures, hot spots developing under steady-state loading conditions remain below the limit temperature of 110°C. However, those developing under transient overload conditions can exceed the limit temperature after 4 h under overload.

Operating transformers and shunt reactors in extremely cold climate regions may require particular considerations (Lampe, 1985), including the following:

- Use of naphthenic oils with low viscosity to avoid formation of wax.
- Avoid start-up at low temperatures. When this is not possible, start-up can be made at reduced load, to allow the oil getting heated sufficiently before subjecting to full load conditions.
- Leave shunt reactors that must be switched on and off on the system as long as possible.
- Avoid tap changer operation below –25°C unless the tap changers are designed for low-temperature operations.

12.7.2 Maintenance

Maintenance practices comprise a set of measures adopted by the utility, in accordance with the recommended practices from national and international standards and equipment manufacturers, to ensure appropriate follow-up of the state of the insulation system in order to take a decision regarding the suitability of its continuing in service. The essential item in all maintenance practices is a logbook or computer file to keep record of all major works and changes in the recorded parameters, starting from the day the equipment is commissioned, serving as reference levels. The actual practices vary with each utility. We discuss in the following considerations regarding maintenance of power transformers.

12.7.2.1 Routine Maintenance

This consists of verifying the operating conditions of the equipment in accordance with the recommendations from the manufacturers. It corresponds generally to visual inspection and keeping record of the operating parameters: oil level, temperature, humidity, gas relays, and apparent state of insulators.

12.7.2.2 Diagnostic Maintenance

The diagnostic maintenance comprises a number of data sampling: oil sampling for gas in oil, various physical–chemical analyses, and on-site measurements on the equipment temporarily removed from service to detect changes in tan δ, winding capacitances, hipot tests, etc. Most of these tests, however, are at relatively low voltages, less than 50 kV, so that their value is more in detecting trends of variations in the parameters monitored based on adequate record keeping rather than in evaluating the current state of the insulation system.

Measurements in oil: Assessment of oil quality is the most common diagnostic used in practice, probably because oil is the most accessible component. Oil samples taken from operating transformers can be analyzed for dissolved gases, water content, DBPC content, interfacial tension, soluble acidity (neutralization number), conductivity, dissipation factor tan δ, dielectric strength, particle content, furan content, and polarization. Most of these measurements are related to the state of the oil; a few also provide information on the state of the paper and the insulation system as a whole.

Measurements of the *DBPC* content, the interfacial tension, and the neutralization number can provide information on the degree of oil oxidation (Yoshida et al., 1987). The dielectric degradation of the oil can be evaluated by measuring the conductivity, the dissipation factor, and the dielectric strength of oil samples.

Humidity: In a sealed insulation system, the ingress of humidity is well controlled, and any increase in the humidity level would require investigation regarding the source of humidity ingress. In a free-breathing insulation system having contact with the ambient air in the conservator, humidity is removed from the ambient air by silica gel, which needs to be regularly changed to keep its efficiency. The ingression of humidity in the oil–paper insulation is followed by a redistribution of water content between the

insulation components and, often, leads to a higher concentration of humidity in the paper than in the oil, which complicates the drying process.

Particles: Regular control of particle content in oil allows detecting anomalies within the insulation, which generate particle contamination. Particle contamination can be measured and the nature of the particles determined. Carbon particles are indicative of PD activities or the presence of hot spots. Efficiency of the control depends on the sampling point and good record-keeping procedure.

Gas-in-oil analysis: It is the most common method used to evaluate the insulation aging state. It provides information on the oil degradation from the presence of specific by-products, methane (CH_4), acetylene (C_2H_2), ethylene (C_2H_4), etc. (IEC Standard 60599, 1978; IEEE Standard C57.104-1991), and, to some extent, on the paper degradation in relation to the concentrations of CO, CO_2, and *furan or furfuraldehyde*. Although the decomposition by-products are common to these high-energy processes, the rate amounts of the by-products formed are specific to the individual process. This property of decomposition by-products provides a convenient means to detect, identify, and, to a certain degree, assess the severity of the aging process (Duval and De Pablo, 2001; Duval, 2002) and is included in the IEC standard for analysis of dissolved gas in transformer oil. It suffices to evaluate the relative gas ratios defined according to

$$\%CH_4 = \frac{\%CH_4}{\%CH_4 + \%C_2H_2 + \%C_2H_4} \quad \text{(Methane)}$$

$$\%C_2H_4 = \frac{\%C_2H_4}{\%CH_4 + \%C_2H_2 + \%C_2H_4} \quad \text{(Ethylene)}$$

and

$$\%C_2H_2 = \frac{\%C_2H_2}{\%CH_4 + \%C_2H_2 + \%C_2H_4} \quad \text{(Acetylene)}$$

The results are reported on a triangular chart shown in Figure 12.56 to identify the nature of the fault and its relative severity. Examples of diagnostics obtained with dissolved gases are illustrated in Figure 12.57.

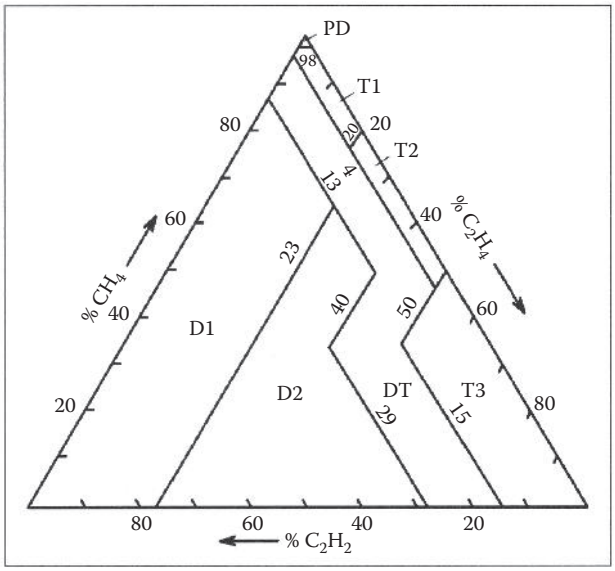


FIGURE 12.56 Triangular chart for diagnostics of incipient faults in power transformers: T—thermal faults, D—discharges, and DT—mixtures of thermal and electrical failures. (From Duval, M., *IEEE Electr. Insul. Mag.*, 18(3), 8, May/June 2002.)

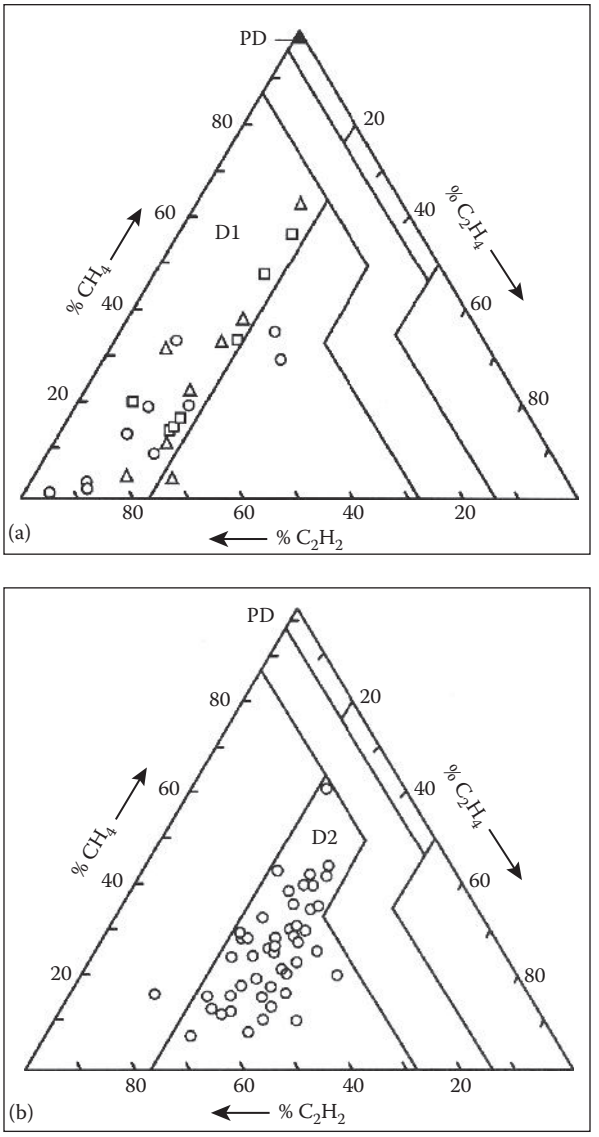


FIGURE 12.57 Examples of a dissolved gas analysis for diagnostics of incipient faults in power transformers. (a) Discharges of low energy - zone D_1. (b) Discharges of high energy - zone D_2. (From Duval, M., *IEEE Electr. Insul. Mag.*, 18(3), 8, May/June 2002.)

Additional diagnostics, comprising the measurement of moisture, particle content, and dielectric strength of the oil, are generally made to complete the analysis of the actual state of insulating oil.

The relative amounts of the dissolved gases generated can help identify the aging processes involved, thermal degradation, PDs, or arcing (Fallou, 1970; Duval, 1974). Variations of the gas content with time can be indicative of progression of the aging process. Finally, environmental aging can be estimated from water, air, nitrogen, and oxygen contents. It should be noted, however, that the interpretation of the results must take account of whether the oil–paper insulated is hermetically sealed or in constant contact with ambient air (Kant and Miyamoto, 1995; Duval and de Pablo, 2001).

Assessment of the paper: Assessment of the aging state of paper, when accessible, can be made by direct measurement of the *DP* and the mechanical strength: tensile, tear, burst, or double-fold. The latter parameters can all be correlated to *DP* and provide useful data on the aging state of the paper. Moisture

content in the paper is known to enhance its aging. Its measurement in transformer insulation has been difficult, although significant development is being achieved in this field.

12.7.2.3 Monitoring

A number of parameters have been identified and used to continuously monitor transformer insulation. Hydrogen generation is currently monitored, while potential for a multigas monitoring system exists; its use on operating transformer has not been widespread. Temperature and hot spot monitoring has been investigated by the Canadian Electrical Association (CEA), and a thermal life integrator has been developed but their use in power transformers has been limited, partly due to the reliability problem of the fiber optic system installed for temperature monitoring. PD detection, by both electrical and acoustic signals, has been explored.

12.7.2.4 On-Site Evaluation

Nondestructive on-site tests are not always possible, mainly because of the necessity to temporarily remove an important piece of equipment from the power system and the needs for special test equipment, which can be brought on-site. However, they can be planned ahead, taking advantage of scheduled revision work or subsequent repair or major overhaul work on the equipment. Different nondestructive tests can be made on-site: PD and power loss measurements, evaluation of the impedance transfer function, etc., which provide an insight to the insulation state of the equipment.

Measurements of PD and power loss: Nondestructive evaluation of the state of the oil–paper insulation system (equipment) can be done by measuring the PD level and dissipation factor tan δ. *PD* measurements are sensitive to local discharge activity, an early indication of local deterioration, and are part of the quality control of power transformers during acceptance tests. Monitoring or repeating the *PD* measurements at regular intervals may allow early detection of incipient faults prior to failure of the equipment. Location of the discharge site is also possible. The difficulty with this approach is the rapid transition of incipient faults to failure, leaving little time for advance notice of the runaway situation. Measurement of the dissipation factor tan δ can be a good indication of the aging condition, but its correlation with the paper degradation and oil oxidation has not been reliable due to the sensitivity of tan δ to other parameters, such as excessive moisture and contamination of the oil.

REFERENCES

ANSI C57.92. *Guide for Loading Mineral Oil Immersed Power Transformers*, 1981.

Aubin, J. and Y. Langhame. Effect of oil viscosity on transformer loading capability in low ambient temperatures. *IEEE Transactions on Power Delivery* PWRD-7(2): 516, 1992.

Bartnikas, R. and K.D. Srivastava. *Elements of Cable Engineering*. Waterloo, Ontario, Canada: Stanford Educational Press, June 1980.

Bean, R.L., Chackan Jr, N., Moore, H.R., and E.C. Wentz. *Transformers for the Electric Power Industry*. New York: McGraw-Hill Book Co., 1959.

Boisdon, C., Carballeira, M., Guinic, PH., and J. Pottevin. On-site conditioning of power transformers—Its control and impact on the dielectric withstand. CIGRE, Report No. 12-101, Paris, France, August 1994.

Bouvier, B. Papier et papier imprégné, *Techniques de l'ingénieur* D-280 : 1–26, 1977.

Burton, P.J., Graham, J., Hall, A.C., Laver, J.A., and A.J. Olivier. Développements récents au CEGB pour l'amélioration de la prévision et de la surveillance des performances des transformateurs. CIGRE, Report No. 12-09, Paris, France, 1984.

Campbell, M. Factory testing of thermally aged HVDC converter transformers. Montréal, Québec, Canada: Canadian Electrical Association, Report No. ST-270, December 1991.

Crine, J.P. and C. Vincent. Influence of ultrasonic homogenization on particle counts and dielectric strength measurements of transformer oil. *IEEE Transactions on Electrical Insulation* EI-23(4): 751–755, August 1988.

Dakin, T.W. Electrical insulation deterioration treated as a chemical rate phenomena. *AIEE Transactions* 67(Part I): 113–122, 1948.

Duval, M. Fault gases formed in oil-filled breathing EHV power transformers—The interpretation of gas analysis data. IEEE Paper No. C 74 476-8, 1974; In: *IEEE Summer Meeting*, Anaheim, CA, July 14–19, 1974.

Duval, M. A review of faults detectable by gas-in-oil analysis in transformers. *IEEE Electrical Insulation Magazine* 18(3): 8–17, May/June 2002.

Duval, M. and A. de Pablo. Interpretation of gas-in-oil analysis using new IEC publication 60599 and IEC TC 10 databases. *IEEE Electrical Insulation Magazine* 17(2): 31–41, March/April 2001.

Fabre, J. and A. Pichon. Deterioration process and products of paper in oil, application to transformers. CIGRE, Report No. 137, Paris, France, 1960.

Fallou, B. Synthèse des travaux effectués au LCIE sur le complexe papier-huile. *Revue Générale d'Électricité* 79(8): 645–661, September 1970.

Fournié, R. *Les isolants en électrotechnique—Essais, Mécanismes de dégradation, Application industrielles*. Paris, France: Edition Eyrolles, 1990.

Freyhult, T. and A. Carlson. Improved reliability of 800 kV transformers. In: *CIGRE Symposium*, Montréal, Québec, Canada, 1991.

Grimmer, E.J. and W.L. Teague. An improved core form transformer winding. *AIEE Transactions* 70: 962, 1951.

IEC Standard 60060-2. *High Voltage Testing Techniques, Part 2: Measuring Systems*, 2nd edn. Geneva, Switzerland: IEC, 1994.

IEC Standard 60071-1. Insulation Coordination, Part 1: Definitions, Principle and Rules. Geneva, Switzerland: IEC, 1993.

IEC Standard 60076-3. *Power Transformer, Part 3: Insulation Levels and Dielectric Tests*. Geneva, Switzerland: IEC, 1994.

IEC Standard 60599. *Interpretation of the Analysis of Gases in Transformers and Other Oil-filled Electrical Equipment in Service*, 1978.

IEEE Transformer Committee. *IEEE Guide for Transformer Loading*, IEEE Transformer Committee.

IEEE Standard C57.104. *IEEE Guide for the Detection and Determination of Generated Gases in Oil-Immersed Transformers and their Relation to the Serviceability of the Equipment*. IEEE Transformer Committee, 1991.

Kan, H. and T. Miyamoto. Proposals for an improvement in transformer diagnosis using dissolved gas analysis (DGA). *IEEE Electrical Insulation Magazine* 11(6): 15–26, November/December 1995.

Kao, K.C. and J.P. McMath. Time-dependent pressure effect in liquid dielectrics. *IEEE Transactions on Electrical Insulation* EI-5(3): 64–68, September 1970.

Kiersztyn, S.E. Formal theoretical foundation of electrical aging of dielectrics. *IEEE Transactions on Power Apparatus and Systems* PAS-100(11): 4333–4338, November 1981.

Lamarre, C., Crine, J.P., and M. Duval. Influence of oxidation on the electrical properties of inhibited naphthenic and paraffinic transformer oils. *IEEE Transactions on Electrical Insulation* EI-22(1): 57–62, February 1987a.

Lamarre, C., Crine, J.P., and H. St-Onge. Antioxidant functionality in liquid and solid materials. In: *CIGRE Symposium*, Report No. 900-05, Vienna, Austria, May 1987b.

Lamarre, C., Duval, M., and J.P. Crine. Optimum reclamation time for insulating oils. In: *55th Annual DOBLE Conference*, April 11–15, 1988, pp. 10-6.1/10-6.15.

Lampe, W. power transformers and shunt reactors for arctic regions. IEEE Transactions, Paper 85-SM 374-4, Vancouver, British Columbia, Canada, 1985.

Malewski, R. Digital techniques in high voltage measurements. *IEEE Trans*. PAS-101: 4508–4517, December 1982.

Malewski, R. and B. Poulin. Impulse testing of power transformers using the transfer function method. *IEEE Transactions on Power Delivery* PWRD-3(2): 476–489, 1988.

Miners, K. Particles and Moisture Effect on Dielectric Strength of Transformer Oil using VDE electrodes. *IEEE Trans*. PAS-101: 751–756, March 1982.

Montsinger, V.M. Loading transformers by temperature. *AIEE Transactions* 49: 776–792, 1930.

Mori, S. Development of gas-insulated transformer in Japan. In: *IERE Workshop on Gas-Insulated Substations*, Toronto, Ontario, Canada, October 1990, pp. 8–20.

Moser, H.P. *Transformerboard*. Rapperswil, Switzerland: Scientia Electrica, 1979.

Mukaiyama, Y., Nonaka, F., Tagaki, I., Higaki, M., Endo, K., Sakamoto, T., Hiraishi, K., and K. Kawashima. Development of a perfluorocarbon liquid immersed prototype large power transformer with compressed SF_6 gas insulation. *IEEE Transactions on Power Delivery* PWRD-6(3): 1108–1116, 1991.

Murray, D.W., McDonald, J.M., White, A.M., and P.G. Wright. The Effect of Basestock Composition on Lubricant Oxidation Performance. Petroleum Review, Paper IP 82-002, pp. 36–40, February 1982.

Narbut, P., Maslin, A.J., and C. Wasserman. Vaporization cooling for power transformer. *AIEE Transactions on Power Apparatus and Systems, Part III B*, 1319–1327, December 1959.

Nelson, J.K. An assessment of the physical basis for the application of design criteria for dielectric structures. *IEEE Transactions on Electrical Insulation* EI-24: 835–847, October 1989.

Nelson, W. Graphical analysis of accelerated life test data with the inverse power law model. *IEEE Trans*., EI-21(1): 2–11, February 1972.

NEMA Standard Publication TR-1. Transformers, regulators and reactors. National Electrical Manufacturer Association, 1973.

Norris, E.T. High voltage power transformer insulation. *Proceedings of IEE* 110(2): 428, February 1963.

Okubo, H., Okamura, K., Ikeda, M., and S. Yanabu. Creepage flashover characteristics of oil-pressboard interfaces and their scale effects. *IEEE Transactions on Power Delivery* PWRD-2(1): 126–132, January 1987.

Oommen, T.V., Moore, H.R., and L.E. Luke. Experience with gas-in-oil analysis made during factory tests on large power transformers. *IEEE Transactions on Power Apparatus and System* PAS-101: 1048–1052, May 1982.

Palmer, S. and W.A. Sharpley. Electric strength of transformer insulation. *Proceedings of IEE* 116(12): 2029, December 1969.

Rouse, T.O. Technical requirements dielectric liquids. In: *Proceedings of the Workshop on Substitute Insulation for Polychlorinated Biphenyls*, EPRI, Palo Alto, CA, April 1987.

Samat, J. and Lacasse, D. Micro-particules dans l'huile de transformateur: conséquence sur la tenue diélectrique. *Revue Alsthom*, (11): 47–58, 1988.

Shroff, D.H. and Stannett, A.W. A review of paper aging in power transformers. *IEE Proceedings* 132(Part C, 6): 312–319, November 1985.

Singer, H., Steinbigler, H., and Weiss, P. A charge simulation method for the calculation of high voltage fields. *IEEE Transactions on Power Apparatus and System* PAS-93: 1660–1668, September/October 1974.

Tokoro, K., Harumoto, Y., Kabayama, Y., Yamauchi, A., Sato, T., and T. Ina. Development of 72 kV 40 MVA gas-vapor cooled transformer. *IEEE Transactions on Power Apparatus and System* PAS-101(11): 4341–4349, November 1982.

Train, D. Switching surge test circuits for high voltage shunt reactors and power transformers. *IEEE Transactions on Power Apparatus and System* PAS-100(6): 3125, 1981.

Trinh, N.G. Electrode design for testing in uniform field gaps. *IEEE Transactions on Power Apparatus and System* PAS-99(3): 1235–1242, May/June 1980.

Trinh, N.G., Olivier, R., Vincent, C., and J. Régis. Effect of impurity particles on transformer oil under normal operating conditions. *IEEE International Symposium on Electrical Insulation*, Boston, pp. 225–228, June 1980.

Trinh, N.G., Aubin, J., and L. Bolduc. Evaluation of the dielectric and short-circuit capabilities of naturally aged power transformers. *IEEE Transactions on Power Apparatus and System* PAS-103(1): 109–120, January 1984.

Trinh, N.G. and Y. Ménard. Audible noise generated by power transformers of a substation—Its influence on the urban noise. Paper A76 473-9, presented at the *IEEE PES Summer Meeting*, Portland, OR, 1976.

Trinh, N.G., Vincent, C., and J. Régis. Electrode area, stressed-volume: Two apparent effects of large-volume oil-insulation. In: *IEEE International Symposium on Electrical Insulation*, Philadelphia, PA, June 6–9, 1982a, pp. 115–118.

Trinh, N.G., Vincent, C., and J. Régis. Statistical dielectric degradation of large-volume oil–insulation. *IEEE Transactions on Power Apparatus and System* PAS-101(10): 3712–3721, October 1982b.

Weber, K.H. and H.S. Endicott. Area effect and its extreme basis for the electric breakdown of transformer oil. *AIEE Transactions* 75: 371–381, June 1956.

Wilson, A.C.M. *Insulating Liquids: Their Use, Manufacture and Properties*. IEE Electrical and Electronic Materials and Devices Series 1. Stevenage, England: Peter Peregrinus Ltd, 1980.

Wilson, W.R. A fundamental factor controlling the unit dielectric strength of oil. *AIEE Transactions* 72(Part III): 68–73, February 1953.

Yoshida, H., Ishioka, Y., Yanari, T., Teranishi, T., and T. Suzuki. Degradation of insulating materials of transformers. *IEEE Transactions on Electrical Insulation* EI-22(6): 795–800, December 1987.

13

Insulation Coordination

13.1 Introduction

According to the IEC technical vocabulary (IEC 60050-604), *insulation coordination* is defined as "the selection of dielectric strength of equipment in relation to voltages which can appear on the system for which the equipment is intended, taking into account the service environment and the characteristics of the available protective devices." In less formal terms, coordination is performed between insulation strength and the different stresses to which such insulation is exposed.

Distinction is made between external and internal insulation. Besides dielectric stresses, external insulation is exposed to atmospheric conditions, including air density variations (altitude effects), rain, and pollution. The term internal insulation, on the other hand, refers to gaseous, liquid, and solid insulation that are protected from the effects of atmospheric and other external conditions.

Distinction is also made between self-restoring and non-self-restoring insulation. The former, normally referring to air clearances and outdoor insulators, completely recovers its insulating properties following a disruptive discharge. A condition that may violate this definition is that of an insulator that loses its dielectric strength due to permanent damage caused by a power arc. On the other hand, non-self-restoring insulation, as a rule, loses its insulating properties in part or in full following a disruptive discharge. This is typically the case for internal solid, liquid, or composite insulating systems within electrical equipment. The earlier classification has obvious consequences on laboratory testing techniques applied to assess insulation systems. For example, the statistical characteristics of self-restoring insulation can and are often determined by a large number of stress applications. Obviously, such approach cannot be used to test non-self-restoring insulation in HV equipment. For such equipment, a withstand test with a limited number of voltage applications becomes the norm (IEC 60060-1).

An insulation configuration can be defined as the geometric arrangement in service comprising the insulation and all electrical terminals. These can be classified as phase terminals to which voltage is applied; neutral, which is connected to the neutral of a three-phase system; and ground terminals, which are permanently grounded. The insulation configuration itself can be classified as three-phase, phase-to-earth, phase-to-phase, and longitudinal, which relates to open switching devices.

13.2 Classification of Voltages and Overvoltages

A fundamental quantity in insulation coordination is the highest voltage for equipment, U_m, defined as the highest r.m.s. value of phase-to-phase voltage for which the equipment is designed with regard to its insulation. IEC Standard 60071-1 (IEC 60071-1, 1993) refers to two U_m ranges:

- Range I for which $3.6 \leq U_m \leq 245$ kV
- Range II for which $300 \leq U_m \leq 765$ kV

The classes and shapes of overvoltages are given in the following (IEC 60071-1, 1993):

- Temporary overvoltages (TOVs) are characterized by a frequency in the range $10 < f < 500$ Hz and a duration $0.03 \leq T_1 \leq 3600$ s.

In the laboratory, TOVs are simulated by a short duration 1 min power frequency test with a frequency in the range $48 < f \leq 62$ Hz.

- *Transient overvoltages* comprise unidirectional impulses classified into slow front, fast front, and very fast front characterized by the following shapes:
  - *Slow front*: These are characterized by a time-to-crest t_p in the range $20 < T_p < 5000$ μs and a time to half value $T_2 \leq 20$ ms.

In the laboratory, slow-front overvoltages are simulated by a standard switching impulse with $T_p = 250$ μs and $T_2 = 2500$ μs.

- *Fast front*: These are characterized by a front time t_f in the range $0.1 < T_f < 20$ μs.

In the laboratory, fast-front overvoltages are simulated with a standard lightning impulse of 1.2/50 μs.

- *Very fast front*: These are characterized by a front time T_f in the range $3 < T_f < 10$ ns. This transient has a complex double frequency content. The higher frequency f_1 is in the range $0.3 < f_1 < 100$ MHz, while the lower frequency f_2 is in the range $30 < f_2 < 300$ kHz.

The total overvoltage duration $T_t \leq 3$ ms.

So far, no test has been standardized for laboratory simulation of very-fast-front transients.

- *Combined overvoltage* consists of two voltage components simultaneously applied between the two-phase terminals of a phase-to-phase or longitudinal configuration and earth. The standard combined switching impulse comprises two components of equal peak and opposite polarity. The positive component is a 250/2500 μs standard switching impulse. The time-to-peak of the negative component should not be less than that of the positive impulse.

13.3 Origin of Overvoltages

TOVs originate from faults, load rejection, etc., as already explained in Chapter 1. Slow-front overvoltages due to switching operations were also introduced in that chapter. Fast-front overvoltages mostly originate from lightning strikes and were introduced in Chapter 9.

Very-fast-front overvoltages originate mostly from switching operations of disconnecting switches in GISs as explained in Povh et al. (1996).

Combined overvoltages may have any origin mentioned earlier. They occur between the phases of a system (phase–phase) or on the same phase between separated parts of a system (longitudinal).

13.4 Representative Overvoltages

Representative overvoltages (U_{rp}) are assumed to produce the same dielectric effect on the insulation as overvoltages of a given class occurring in service due to various origins. They consist of voltages with the *standard shape* of the class and may be defined by one value, or a set of values, or a frequency distribution of values that characterize service conditions. This definition also applies to the continuous power frequency voltage representing the effect of service voltage on the insulation.

Determination of representative overvoltages is described in the section dealing with the procedure of insulation coordination.

13.5 Performance Criterion

This refers to the basis on which insulation is selected so as to reduce the probability of failure due to voltage stresses to an economically and operationally acceptable level. This criterion is usually expressed in terms of an acceptable failure rate of the insulation configuration. It usually takes the form of number of failures per year, years between failure, risk of failure, etc. (IEC 600 71-1, 1996).

For apparatus, acceptable failure rates R_a, due to overvoltages, have been quoted in the range $0.001/a < R_a < 0.004/a$ depending on repair times. These rates may appear totally unrealistic since the lifetime of a piece of equipment is normally expected to be in the range of 50 years. It should be noted, however, that the following applies:

- The earlier rates refer to a single piece of equipment, while in reality, many such pieces may be stressed simultaneously.
- The earlier rates refer to failures due to overvoltages. In practice, this is only one cause of failure, while other causes of failure may be attributed to thermal and mechanical stresses.

For overhead lines, failure rates due to lightning may vary in the range

$$\frac{0.1}{100}\,\text{km}\lozenge\text{year} < R_a < \frac{20}{100}\,\text{km}\lozenge\text{year}$$

with the higher failure rates tolerated only for distribution lines.

13.6 Withstand Voltage

This refers to the value of the test voltage applied under specified conditions in a withstand test, during which a specified number of disruptive discharges may be tolerated (IEC 600 71-1, 1996). The withstand voltage is designated as follows:

a. Conventional assumed withstand voltage, when no disruptive discharges are tolerated. It is deemed to correspond to a withstand probability P_w of 100%.
b. Statistical withstand voltage, when the number of disruptive discharges tolerated is related to a certain withstand probability. In IEC 60071-1, $P_w = 90\%$.

In general, for self-restoring insulation, statistical withstand voltages are specified, while for non-self-restoring insulation, conventional assumed withstand voltages are specified.

For each class of voltage, the value of the withstand voltage of an insulation configuration in actual service conditions, which meets the performance criterion, is designated as *coordination withstand voltage* (U_{cw}) (IEC 600 71-1, 1996).

13.7 Insulation Coordination Procedure

Figure 13.1 presents a flowchart for the insulation coordination procedure with special reference to IEC Standard 60071-1. The first fundamental step is the determination of the representative overvoltages U_{rp} for the different classes mentioned earlier. The final result of this exercise is the establishment of a set of standard insulation levels U_w characterizing the system insulation. The standard insulation levels are to be selected from Table 2 of IEC 60071-1 for range I ($1\text{ kV} < U_m \leq 245\text{ kV}$) and from Table 3 of the same standard for range II ($U_m > 245\text{ kV}$).

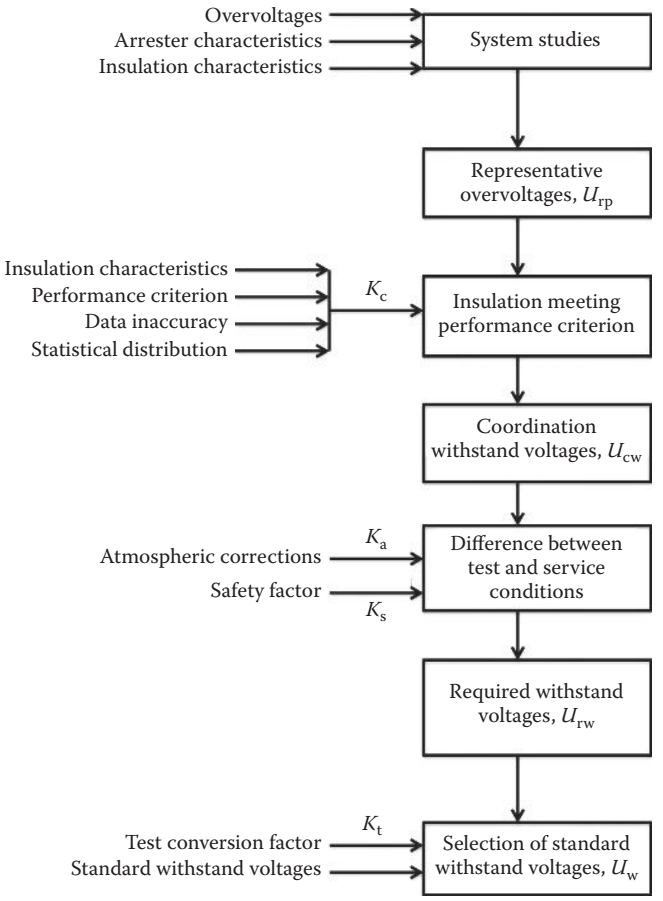


FIGURE 13.1 Flowchart for the insulation coordination procedure with special reference to IEC Standard 60071-1.

13.7.1 Determination of Representative Voltages and Overvoltages

13.7.1.1 Continuous Power Frequency Voltage

The representative continuous power frequency voltage is considered constant and equal to the highest system voltage U_s.

13.7.1.2 Temporary Overvoltages

The representative overvoltage is a power frequency voltage with a duration of 1 min, whose amplitude has to take into account the following:

- The amplitude and duration of the actual TOVs in service
- The amplitude–duration power frequency withstand characteristics of the insulation considered

13.7.1.3 Slow-Front Overvoltages

13.7.1.3.1 Phase-to-Earth Overvoltages (U_{re})

The representative phase-to-earth overvoltage has the shape of a standard switching impulse (250/2500 μs).

The representative amplitude can be either an assumed maximum or a probability distribution of the overvoltage amplitudes.

The assumed maximum is equal to either the truncation value of the overvoltages or the switching impulse protective level of the surge arrester.

The probability distribution of overvoltages, without surge arrester, is normally characterized by its 2% value U_{e2}, where 2% refers to the probability of being exceeded, standard deviation σ, and truncation value U_{et}. It can be approximated by a Gaussian or a modified Weibull distribution. If the overvoltages are severely limited by the surge arrester, however, the resulting distribution will be considerably skewed in the vicinity of the arrester protective level (IEC 600 71-2, 1996).

Normally, the amplitudes of the overvoltages are processed independently of their real time-to-peak. However, for EHV and UHV systems, it may be necessary to derive the amplitude of the representative overvoltage considering the amplitude-time-to-peak withstand characteristics of the insulation.

As an example, consider slow-front overvoltages associated with open line energization, already treated in Chapter 1 for EHV and UHV lines; this overvoltage origin results in U_{e2} values that are determining for insulation coordination. Comprehensive system analysis using the EMTP shows that the following applies:

- More severe energizing transients are encountered for transmission lines with three-phase re-energization. This is due to the effect of trapped charge and randomness of the circuit breaker closing angle.
- Energization transients can be effectively controlled by circuit breaker preinsertion resistors. These, however, introduce a complicating element in circuit breaker design.
- In general, an inductive feeding network results in more severe energization transients, compared with a complex network.
- Shunt reactor compensation, exceeding 50% of the line capacitive power, has a significant effect on suppression of energization transients.

Preliminary estimation of the maximum energizing transient overvoltage can be guided by the schematic diagram of Figure 13.2, adapted from (IEC 600 71-2, 1996). It is shown that, depending on the earlier factors, U_{e2} can vary from 1.2 to 3.7 p.u. For EHV lines, however, experience has shown that limiting U_{e2} to 2 p.u. will have economic advantage. This can be achieved by proper shunt reactor compensation, breaker preinsertion resistor, or surge arrester installation at the line input and output terminals. Obviously, for important transmission line projects, a detailed EMTP study is undertaken in order to assess the level of switching transients.

In Chapter 1, an example of EMTP study on energization of an open 300 km, 735 kV transmission line was undertaken. The line section in question had no shunt reactor compensation nor preinsertion resistors in the circuit breakers. The resulting energization transient amounted to 2.5 p.u., Figure 1.18,

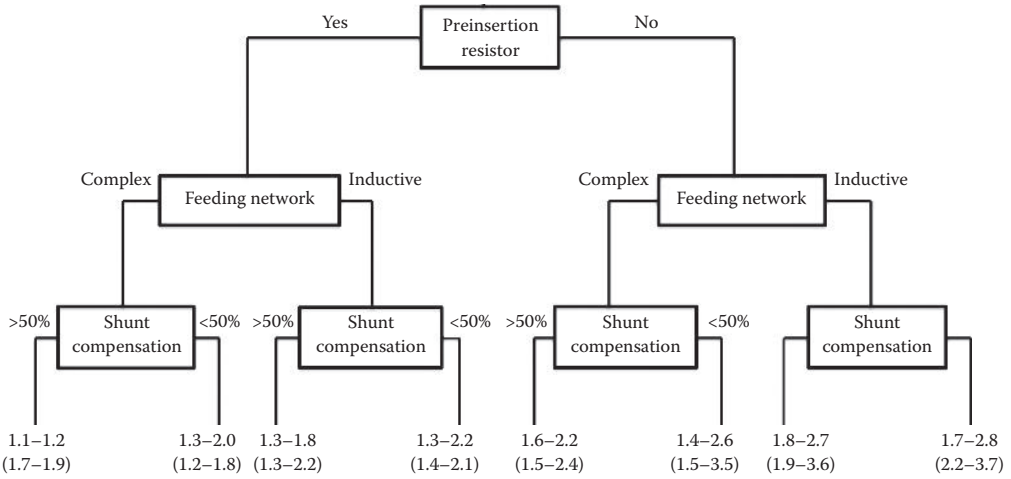


FIGURE 13.2 Schematic diagram for estimation of receiving end slow-front overvoltages (U_{e2}) due to line energization and re-energization. Values in brackets refer to lines with three-phase re-energization.

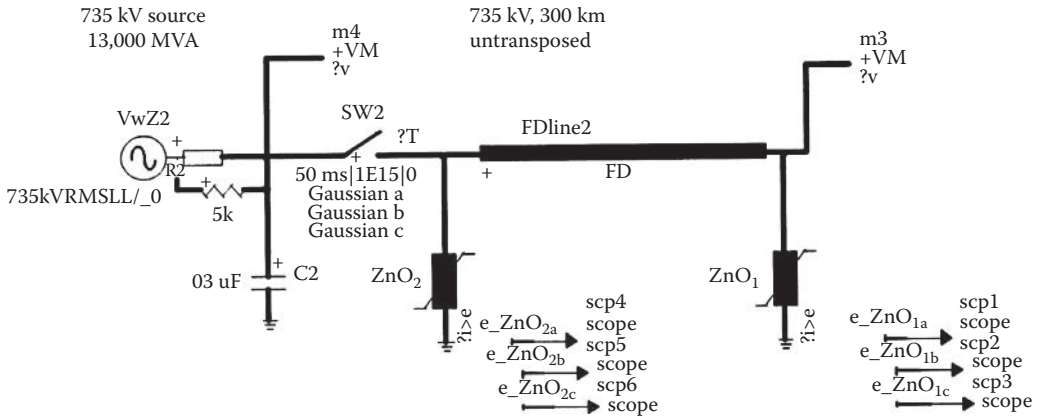


FIGURE 13.3 Single line diagram of a 300 km 735 kV line.

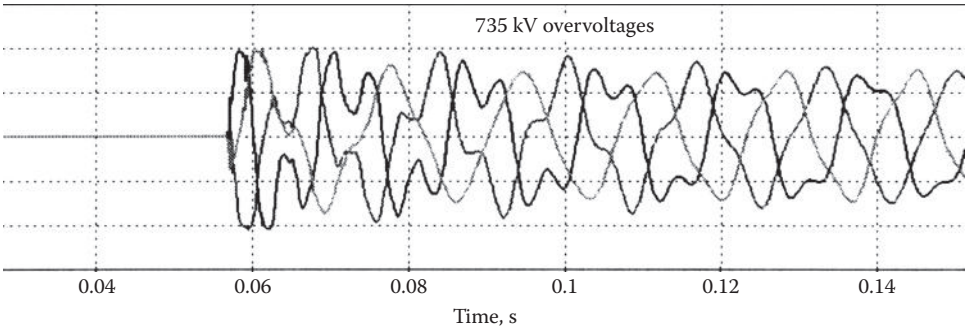


FIGURE 13.4 Transient voltage at open end.

which is too severe for such EHV level. Figure 13.3 shows a schematic diagram with arresters installed at the line terminals. Figure 13.4 shows an example where such overvoltage factor was suppressed to approximately 1.7 by installation of arresters (Khodabakhchian, 2013).

The maximum energy discharged into the surge arrester amounted to approximately 800 kJ. Considering a metal oxide arrester (MOA) with an MCOV of 448 kV, this discharge energy level corresponds to 1.79 kJ/kV MCOV. At the earlier voltage level, arresters are available for up to 10 kJ/kV MCOV so that this energy level is rather mild.

13.7.1.3.2 Phase-to-Phase Representative Overvoltage (U_{pre})

Determination of the phase-to-phase slow-front representative overvoltage U_{pre} requires analysis of the phase-to-phase insulation characteristics (Cortina et al., 1970; Kachler et al., 1971; Boyd et al., 1974; Menemenlis et al., 1976; Gallet et al., 1978; Paulson and Grant, 1981; Miyaka et al., 1987). A brief review of the most relevant factors (Rizk, 1993) is presented in the following:

- Phase-to-phase insulation strength depends not only on the shape and peak values of the phase-to-ground overvoltages but also on the time shift Δt between the instant of negative peak and the subsequent occurrence of the positive peak.
- Phase-to-phase insulation characteristics not only depend on the gap spacing d but can also be influenced by the conductor height h above ground plane.

- A fundamental parameter in the determination of the phase-to-phase insulation strength is the relative value k of the amplitudes of negative and positive impulse peaks, that is, U_n/U_p, also designated as U^-/U^+. Another measure of this quantity is the ratio α defined as $U_n/(U_p + U_n)$. The most interesting ranges of these parameters are $0 \leq k \leq 1$ or $0 \leq \alpha \leq 0.5$.
- A sufficiently high negative impulse occurring several milliseconds before the positive peak is applied to the other phase and leads to negative space charge generation and displacement, which can result in gap strength below that obtained with synchronized peaks.
- In spite of what has just been mentioned, the condition of synchronized positive and negative peaks is generally considered as the base case, since in situations of practical interest, the strength obtained is often not significantly different from the minimum and is moreover uniquely defined, contrary to the cases where $\Delta t \neq 0$.
- For situations of practical interest, the breakdown processes appear to be fundamentally governed by the inception and propagation of the positive leader with little evidence of significant negative leader formation before the final jump.
- For negative impulse fronts equal or longer than the positive, the critical front for phase-to-phase insulation strength is different from and often significantly shorter than the critical front for phase-to-ground insulation. As a consequence, some earlier reported test results may not have yielded minimum phase-to-phase strength as they were not always conducted with relevant critical fronts.
- Tests are obviously carried out under diverse atmospheric conditions, particularly air density, and the absence of reliable correction factors for phase-to-phase insulation introduced an additional uncertainty in the analysis of test results.

In Rizk (1993), the Rizk model for switching impulse breakdown of phase-to-ground air gaps was extended to account for phase-to-phase insulation exposed to critical switching impulses with synchronized peaks and opposite polarity. Some of the model findings are summarized in the following.

Figure 13.5a shows variation of the critical switching impulse 50% breakdown voltage with interphase spacing for a conductor–conductor configuration. The conductor height is maintained as $h = 9$ m, the conductor radius $a = 5$ cm, and the parameter $\alpha = 0.33$ characterizing the negative impulse content ($k = 0.5$). Model findings are compared with experimental results (Gallet et al., 1978) and the agreement is satisfactory.

Figure 13.5b shows similar results for $\alpha = 0.5$ ($k = 1$, i.e., equal amplitudes of positive and negative impulses).

Figure 13.6 shows dependence of the critical switching impulse 50% breakdown voltage on α, for the same conductor–conductor configuration. In the range investigated, it is shown that critical breakdown voltage $(U_p + U_n)_{50}$ increases significantly with α. Again, the agreement with the experimental results (Gallet et al., 1978) is satisfactory.

For the same 4 m phase-to-phase spacing as mentioned earlier, Figure 13.7 demonstrates the effect of the conductor height h on the 50% breakdown voltage for α values of 0, 0.33, and 0.5. Comparison with experiments (Gallet et al., 1978) is also shown. It is demonstrated that, as the negative impulse content increases, higher values of α, the effect of conductor height above ground, diminish. In other words, initiation and propagation of the leader from the positive conductor become more determined by the presence of the negative conductor. The same arguments apply to explain the reduction of the phase-to-phase 50% breakdown voltage with the increase of the conductor radius as shown in Figure 13.8.

Similar results were obtained when the model was applied to a horizontal rod–rod configuration (Rizk, 1993). As an example, for rod–rod spacings in the range 4–12 m and h/d ratio of 1.5 with $\alpha = 0.5$, the discrepancy in the 50% breakdown voltage between the model and experiments by a CIGRE task force (CIGRE 33.03.03, 1973) was determined to be in the range −2.3% to +1.5%, which is quite satisfactory.

Table 13.1 shows a further comparison between critical 50% switching impulse breakdown voltage of a 4 m rod–rod gap with $h = 8$ m for $\alpha = 0.33$ and 0.5 and experiments (Gargabnati et al., 1991). Also indicated is the corresponding gap factor.

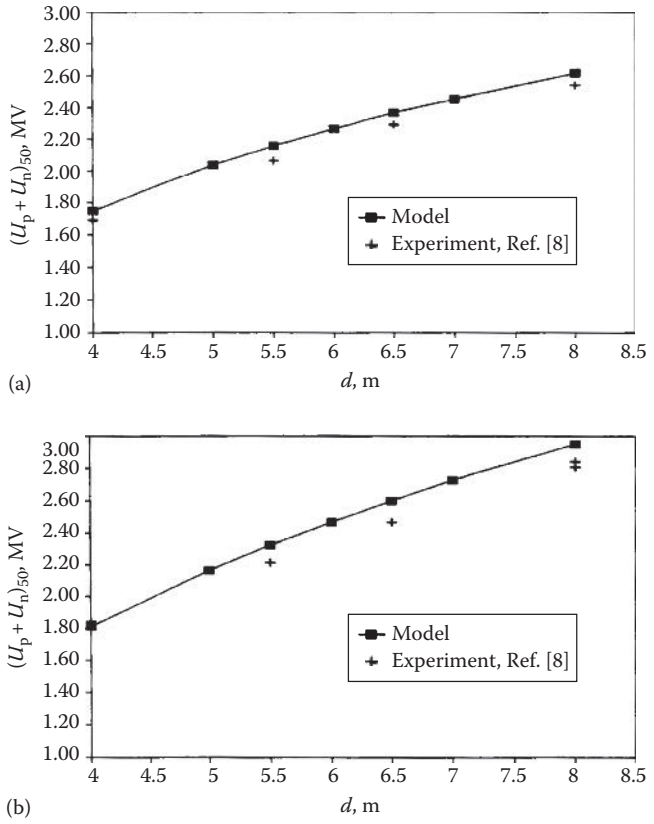


FIGURE 13.5 (a) Variation of the critical switching impulse 50% breakdown voltage with interphase spacing for conductor–conductor configuration. $h = 9$ m, $a = 5$ cm, $\alpha = 0.33$. (b) Variation of critical switching impulse 50% breakdown voltage with interphase spacing for conductor–conductor configuration. $h = 9$ m, $a = 5$ cm, $\alpha = 0.5$. (From Rizk, F.A.M. *IEEE Trans. on Power Delivery*, 8(3), 1492, 1993.) Reference [8] in the figure: (Gallet et al., 1978).

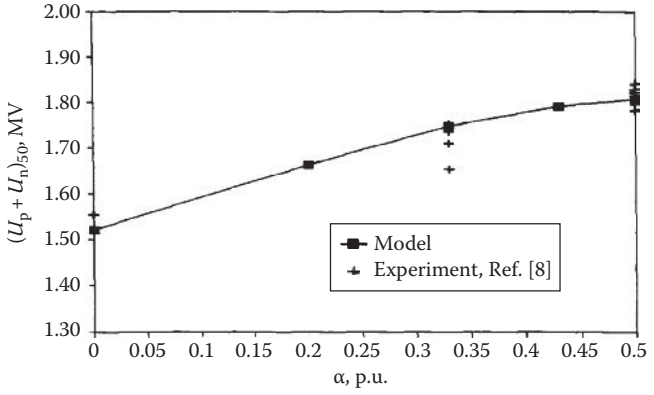


FIGURE 13.6 Dependence of the critical switching impulse 50% breakdown voltage on α for a conductor–conductor configuration. $d = 4$ m, $h = 9$ m, $a = 5$ cm. (From Rizk, F.A.M. *IEEE Trans. on Power Delivery*, 8(3), 1492, 1993.) Reference [8] in the figure: (Gallet et al., 1978).

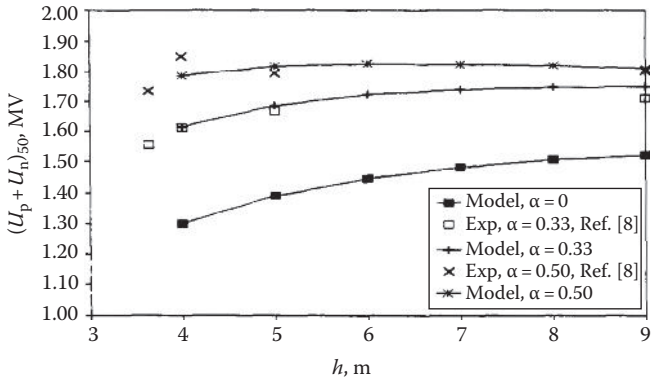


FIGURE 13.7 Effect of conductor height on critical switching impulse 50% breakdown voltage for conductor–conductor configuration at different values of α. $d = 4$ m, $a = 5$ cm. (From Rizk, F.A.M. *IEEE Trans. on Power Delivery*, 8(3), 1492, 1993.) Reference [8] in the figure: (Gallet et al., 1978).

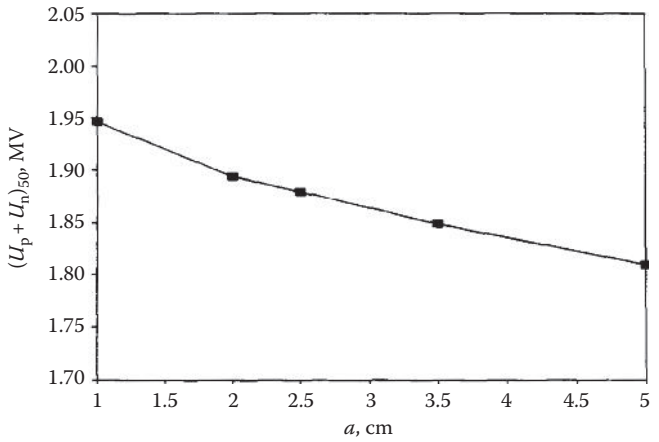


FIGURE 13.8 Effect of conductor radius on critical switching impulse 50% breakdown voltage of conductor–conductor configuration. $d = 4$ m, $h = 9$ m, α = 0.5. (From Rizk, F.A.M. *IEEE Trans. on Power Delivery*, 8(3), 1492, 1993.)

TABLE 13.1

Comparison of Model with Experiment Rod–Rod
Configuration: $d = 4$ m, $h = 8$ m

	$(U_p + U_n)_{50}$, kV		
α, p.u.	**Rizk Model [12]**	**Experiment [14]**	**Gap Factor, kg, p.u.**
0.33	1836	1845	1.63
0.50	2010	2003	1.78

Figure 13.9 shows model results of the dependence of the switching impulse breakdown voltage $(U_p + U_n)_{50}$ of a horizontal rod–rod as function of α, for different values of d in the range 4–12 m. Here, h/d is maintained at 2.5 with rod radius $a = 2.5$ cm.

Figure 13.10 shows the effect of height h on $(U_p + U_n)_{50}$ for a 4 m rod–rod gap, with α = 0.33 and 0.5. In comparison with Figure 13.5, it may be concluded that the rod–rod phase-to-phase insulation is more sensitive to height than the conductor–conductor configuration.

In general, the phase-to-phase insulation strength can be expressed in terms of $(U_p + U_n)$, or $U^+ + U^-$, for a given value of α as given earlier, or in terms of U_p, or U^+, as function of U_n or U^-.

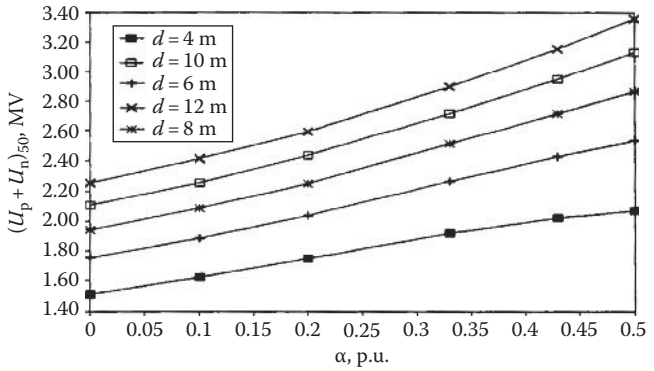


FIGURE 13.9 Dependence of critical switching impulse 50% breakdown voltage on α of rod–rod configurations with different spacings. $h/d = 2.5$, $a = 2.5$ cm. (From Rizk, F.A.M. *IEEE Trans. on Power Delivery*, 8(3), 1492, 1993.)

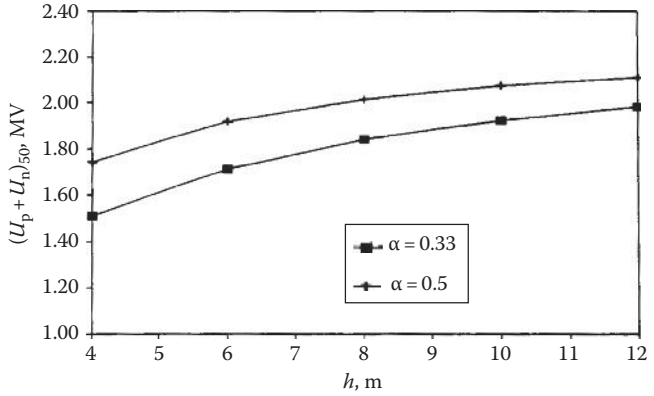


FIGURE 13.10 Effect of height on critical switching impulse breakdown voltage of a rod–rod configuration for different values of α. $d = 4$ m. (From Rizk, F.A.M. *IEEE Trans. on Power Delivery*, 8(3), 1492, 1993.)

The review of experimental results led to the conclusion that the relationship between U_p and U_n can be approximated as (IEC 60071-2, 1996)

$$U_p = U_{po} - BU_n \tag{13.1a}$$

where

U_{po} is the breakdown voltage of the phase-to-phase insulation when $U_n = 0$

$B = f(h/d)$ with $0 < B < 1$

It should be noted that only for a streamer breakdown mechanism with no significant role played by a leader discharge phase $B = 1$ so that

$$U_p + U_n = U_{po} \tag{13.1b}$$

Another formulation of (13.1) in terms of $U_p + U_n$ could be done as follows:

$$U_p + U_n = U_{po} + (1 - B)U_n$$

or

$$U_p + U_n = U_{po} + a(1 - B)(U_p + U_n)$$

TABLE 13.2

B Values for Conductor–Conductor Gap from Model (Rizk, 1993) and Experiment (Cortina et al., 1970)

***h/d*, p.u.**	**1.5**	**1.8**	**2.25**
Rizk model [12]	0.47	0.56	0.64
Experiments [5]	0.50	0.56	0.62

from which

$$U_p + U_n = \frac{U_{po}}{1 - a(1 - B)} \tag{13.2}$$

Table 13.2 shows values of B for a conductor–conductor configuration, as obtained from the earlier model (Rizk, 1993) and from experiments (Cortina et al., 1970), as function of h/d. The empirical relationship (Cortina et al., 1970) reads

$$B = 0.86 - 0.54\left(\frac{d}{h}\right) \tag{13.3}$$

Again, the agreement between the model and experiment is excellent.

It should be noted that (13.1) represents the characteristics of *pure* phase-to-phase insulation. In practice, such characteristic will be truncated at very high and very low values of U_p/U_n, as positive and negative flashovers to ground take place. Typical limiting values are $U_p/U_n = 3$ and $U_p/U_n = 0.4$ (IEC 60071-2, 1996).

There is a tendency, without much experimental justification, to assume that B is the same for conductor–conductor and rod–rod configurations (IEC 60071-2, 1996). The model shows, however, that for the same h/d, B assumes lower values for a rod–rod than for a conductor–conductor gap. For example, with $d = 4$ m, $h = 10$ m, that is, $h/d = 2.5$, a rod–rod gap has $U_{po} = 1530$ kV and at $\alpha = 0.5$, $(U_p + U_n)_{50} = 2080$ kV, yielding $B = 0.47$. For a conductor–conductor gap of the same dimensions, however, B is found to be as high as 0.64. This result is explained by the physical argument that leader initiation from a positive rod is less influenced by the presence of the negative rod than in the corresponding situation of a conductor–conductor gap. This renders the U_p versus U_n characteristic more flat, that is, lower B.

13.7.1.3.3 Phase-to-Phase Overvoltage Distributions

In the analysis of phase-to-phase overvoltages in a three-phase system, usually the effect of the third phase is neglected. Observation of overvoltages in any system study can be made at three instants (IEC 60071-2, 1996):

- Instant of the positive peak of the phase-to-earth overvoltage
- Instant of the negative peak of the phase-to-earth overvoltage
- Instant of the peak of the phase-to-phase overvoltage

For each set of observations, it may be assumed that the joint statistical distribution is defined by a bivariate normal distribution (Tule and Kendall, 1950; Hald, 1952; Freund and Walpole, 1987). The bivariate density function $f(U_p, U_n)$ can in general be expressed as

$$f(U_p, U_n) = \frac{1}{2\pi s_p s_n \sqrt{1 - r^2}} \exp\left\{\frac{-1}{2(1 - r^2)}\left[\left(\frac{U_p - U_{p50}}{s_p}\right)^2 - 2r\left(\frac{U_p - U_{p50}}{s_p}\right)\left(\frac{U_n - U_{n50}}{s_n}\right) + \left(\frac{U_n - U_{n50}}{s_n}\right)^2\right]\right\} \tag{13.4}$$

where the marginal cumulative distribution for the positive component U_p is normal Φ (U_{p50}, σ_p) and that for the negative component is Φ (U_{n50}, σ_n) and ρ is the correlation coefficient. The bivariate normal surface defined by

$$z = f(U_p, U_n) \tag{13.5}$$

has a maximum value at (U_{p50}, U_{n50}) expressed by

$$f(U_{p50}, U_{n50}) = \frac{1}{2\pi s_p s_n \sqrt{1-r^2}} \tag{13.6}$$

Any plane parallel to the U_pU_n plane expressing a constant density, $z = f(U_p, U_n)$ = const., intersects the bivariate normal surface expressed by (13.4) in an ellipse. This is called a contour of constant probability density. For any such value, three ellipses could be traced on the U_pU_n plane, each of which refers to one of the observation instants defined earlier (CIGRE 33.03.03, 1979).

It should be noted that for the phase-to-phase overvoltage, U_{pp} will have a cumulative normal distribution Φ (U_{pp50}, σ_{pp}) with

$$\begin{aligned} U_{pp50} &= U_{p50} + U_{n50} \\ s_{pp} &= \sqrt{s_p^2 + s_n^2 + 2r s_p s_n} \end{aligned} \tag{13.7}$$

As a further simplification, IEC (IEC 60071-2, 1996) defined a circle that envelopes the three ellipses mentioned earlier. The circle has a radius R_u and a center (U_{cp}, U_{cn}) so that its equation will be

$$(U_p - U_{cp})^2 + (U_n - U_{cn})^2 = R_u^2 \tag{13.8}$$

The circle parameters are determined from the following conditions:

$$\begin{aligned} &\text{A horizontal tangent to the circle results in } U_p = U_e \\ &\text{A vertical tangent to the circle results in } U_n = U_e \\ &\text{A tangent to the circle at } U_p = U_n \text{ result in the maximum} \\ &\text{phase-to-phase overvoltage } U_{pp} \end{aligned} \tag{13.9}$$

The circle is schematically shown in Figure 13.11. It should be noted, however, that the + and − signs characterizing the positive and negative overvoltages to ground correspond to the subscripts *p*, *n* in the present text.

The first two conditions in (13.9) can be expressed as

$$\begin{aligned} \frac{dU_p}{dU_n} &= 0, U_p = U_e \\ \frac{dU_n}{dU_p} &= 0, U_n = U_e \end{aligned} \tag{13.10}$$

From (13.8), this leads to

$$U_{cp} = U_{cn} = U_c = U_e - R_u \tag{13.11}$$

The third condition in (13.9) can be expressed as

$$\frac{dU_p}{dU_n} = -1, \quad U_p = U_n = \frac{U_{pp}}{2} \tag{13.12}$$

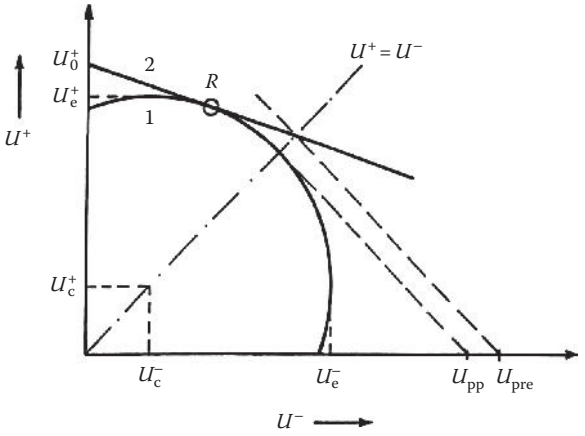


FIGURE 13.11 Principle of determination of the representative phase-to-phase overvoltage U_{pre}. 1: Simplified overvoltage circle for constant probability density level, with $U_e^+ = U_e^-$ and phase- to-phase overvoltage for the considered probability; 2: Simplified insulation flashover characteristic; *R*: Most critical overvoltage stress.

which yields

$$R_u = \frac{2U_e - U_{pp}}{2 - \sqrt{2}} \tag{13.13}$$

which, when substituted in (13.11), yields

$$U_{cp} = U_{cn}\frac{U_{pp} - \sqrt{2}\,U_e}{2 - \sqrt{2}} \tag{13.14}$$

so that the circuit parameters (U_{cp}, U_{cn}) are now determined by the maximum overvoltages to ground U_e and the maximum phase-to-phase overvoltage U_{pp}.

Coordination of the overvoltages and phase-to-phase insulation will be performed by ensuring that the insulation characteristic line expressed by (13.1) will be a tangent to the overvoltage circle. This sets the condition

$$R_u = \frac{U_{po} - (1+B)U_c}{\sqrt{1+B^2}} \tag{13.15}$$

Since phase-to-phase tests, according to IEC (IEC 60060-1, 1996; IEC 60071-1, 1996), are performed with $U_p = U_n$, that is, $\alpha = 0.5$, the representative phase-to-phase overvoltage U_{pre} is obtained from the intersection of the insulation characteristic straight line (13.1) and the line $U_p = U_n$, as shown graphically in Figure 13.11. Analytically, it could be shown from the earlier equations that the representative phase-to-phase overvoltage U_{pre} can be expressed as (IEC 60071-2, 1996):

$$U_{pre} = 2\left(F_1 \langle U_{pp} + F_2 \langle U_e\right) \tag{13.16}$$

where

U_{pp} is the maximum phase-to-phase overvoltage
U_e is the maximum overvoltage to ground

$$F_1 = \frac{1}{2-\sqrt{2}}\left(1 - \frac{\sqrt{1+B^2}}{1+B}\right)$$
$$F_1 = \frac{1}{2-\sqrt{2}}\left(\frac{2\sqrt{1+B^2}}{1+B} - \sqrt{2}\right) \tag{13.17}$$

This means that the slope B of the phase-to-phase insulation characteristics determines the relative effect on U_{pre} of the maximum phase-to-ground overvoltage U_e and the maximum phase-to-phase overvoltage U_{pp}.

As an example, with $B = 0.55$, (13.17) yields $F_1 = 0.450$ and $F_2 = 0.100$, showing that the representative phase-to-phase overvoltages are more sensitive to the maximum phase-to-phase than to the maximum phase-to-ground overvoltage. In this example, if we refer to overvoltages exceeded in 2% of the cases, with $U_e = 1250$ kV and $U_{pp} = 2100$ kV, substitution in (13.16) yields $U_{pre} = 2140$ kV.

If from system studies the standard deviations of the phase-to-ground and phase-to-phase overvoltages are known, or assumed (IEC 60071-2, 1996), the coordination could be performed at a different probability level or at the truncation level.

System studies show that in general, the ratio of phase-to-phase to phases-to-earth overvoltages U_{pp}/U_e goes down as U_e increases. Typical values are $U_{pp}/U_e = 1.6–1.7$ at $U_e = 2$ p.u., but U_{pp}/U_e goes down to approximately 1.5 at $U_e = 2.5$ p.u.

13.7.1.4 Fast-Front Overvoltages

13.7.1.4.1 General

For transmission voltages in IEC range II ($U_m > 300$ kV), line insulation requirements are hardly affected by lightning overvoltages. As previously mentioned, insulators are often determined by power frequency voltage stresses under pollution conditions, while tower clearances are selected with reference to switching overvoltages. In range I ($U_m \leq 245$ kV), however, as mentioned in the insulator chapter (Chapter 10), it may sometimes be economical to reinforce line insulators in order to reduce the frequency of backflashovers and meet the requirements of the performance criterion. It is therefore understandable that rarely is transmission line insulation characterized by a basic insulation level, that is, a standard lightning impulse withstand voltage.

For a substation, the representative fast-front overvoltage U_{re} can be expressed by (Baatz, 1956; Hileman, 1999)

$$U_{re} = U_{pl} + 2S\Delta T \tag{13.18}$$

where

U_{pl} is the protective level of the lightning arrester, usually for a lightning current amplitude of 10 kA
S is a representative steepness of the impinging surge, expressed in kV/μs
T is the traveling time associated with the maximum separation distance L between the arrester and protected equipment

$$T = \frac{L}{v} \tag{13.19}$$

Note that L includes the length of the HV and ground leads of the arrester (Baastz, 1956; IEC 60071-2, 1996), v: the speed of light, 300 m/μs. The steepness S is determined by damping of the impinging surge front due to corona on the power conductor (Baatz, 1956; IEC 60071-2, 1996):

$$S = \frac{S_o}{1 + \left(S_o d / K_c\right)} \tag{13.20}$$

where

S_o is the initial steepness where the line was struck
d is the distance of the strike location from the substation
K_c is a corona damping factor that depends primarily on the conductor bundle design (Table 13.3)

Usually, $S_o d/K_c \gg 1$ so that (13.20) simplifies to

$$S = \frac{K_c}{d} \tag{13.21}$$

For example, with $d = 1000$ m and two subconductors, (13.21) yields $S = 1000$ kV/μs.

TABLE 13.3

Dependence of Corona Lightning Surge Damping Factor K_c on Conductor Bundle

Number of Subconductors	K_c, kV·m/μs
1	0.7×10^6
2	1.0×10^6
3 or 4	1.7×10^6
6 or 8	2.5×10^6

Sources: Hileman, A.R., *Insulation Coordination*, Marcel Dekker Inc., New York, 1999; Eriksson, A.J. and Weck, K.H., Simplified procedure for determining representative substation impinging lightning overvoltages, CIGRE, Paper No. 33-16, 1988.

Furthermore, from the traveling wave theory, the steepness of the impinging surge is reduced by the number of transmission lines n connected to the substation so that (13.21) becomes

$$S = \frac{K_c}{nd} \tag{13.21a}$$

where normally n refers to the minimum number of lines connected at any time, so that n becomes 1 or 2.

There are several options for determination of S and, accordingly, the representative fast-front overvoltage U_{re}. A simple and probably too conservative approach is to determine an assumed maximum U_{re} based on $d = L_{sp}$, where L_{sp} is the span length of the incoming transmission line, in the vicinity of the substation, so that

$$U_{re} = U_{pl} + \frac{2K_c}{nL_{sp}} \lozenge T$$

or

$$U_{re} = U_{pl} + \frac{2K_c}{nv} \frac{L}{L_{sp}} \tag{13.22}$$

which can be expressed as (IEC 60071-2, 1996)

$$U_{re} = U_{pl} + \frac{A}{n} \lozenge \frac{L}{L_{sp}} \tag{13.22a}$$

where

$$A = \frac{2K_c}{v} \quad \text{(kV)}$$

The assumed maximum representative lightning overvoltage can also be obtained from corresponding values from an existing substation of known satisfactory service performance (IEC 60071-2, 1996). Consider an existing station with

$$U_{rp1} = U_{pl1} + 2S_1T_1 \tag{13.23}$$

where

S_1 corresponds to n_1 connected lines

T_1 corresponds to a maximum separation distance L_1

Consider that the new substation to be designed is characterized by n_2 connected lines and a maximum separation distance L_2. The representative steepness S_2 of the new substation can be related to S_1 of the existing station by

$$S_2 = \frac{n_1}{n_2} S_1 \tag{13.24}$$

so that

$$U_{rp2} = U_{pl2} + \frac{n_1}{n_2} 2 S_1 T_2$$

Substituting for S_1 from (13.23),

$$U_{rp2} = U_{pl2} + \frac{n_1}{n_2} \frac{T_2}{T_1} \left(U_{rp1} - U_{pl1} \right)$$

or

$$U_{rp2} = U_{pl2} + \frac{n_1}{n_2} \frac{L_2}{L_1} \left(U_{rp1} - U_{pl1} \right) \tag{13.25}$$

which establishes a relationship between the insulation coordination parameters of the existing and new substations.

13.7.1.4.2 Impinging Surge

A more comprehensive approach, although still approximate and simplified, for the determination of the representative impinging surge was described in Eriksson and Weck (1988). It recognizes transmission line backflashovers and shielding failures as the source of impinging surges. It is based on a design failure rate N_d, the reciprocal of which is the mean time between failures (MTBF).

With the earlier expression for the dependence of the front steepness S on the distance d to the strike point (13.21), the relationship between the coordination withstand voltage U_{wc} (obtained from station BIL through a safety factor) and the arrester protective level U_{pl}, assuming a steepness corresponding to the midpoint of the limit distance, becomes

$$U_{cw} = U_{pl} + \frac{4K_c}{nd} \Diamond T \tag{13.26}$$

with the symbols as defined earlier.

This gives the following expression for the limiting distance *d:*

$$d = \frac{4K_c T}{n \left(U_{cw} - U_{pl} \right)} \tag{13.27}$$

This means that under otherwise the same conditions, higher values of U_{cw}/U_{pl} result in lower values of d. This in turn means that the system can tolerate the resulting higher front steepness of the impinging surge.

Starting with backflashovers, assume that the number of strikes to the ground wire per unit length is N_s.

The number of strikes to the ground wire within the limiting distance N_{sd} will be

$$N_{sd} = d \cdot N_s \tag{13.28}$$

For a transmission line with proper tower grounding and insulator string design, most of these strikes will not cause backflashover. Only if the stroke current exceeds a minimum level I_b will the condition for a backflash be satisfied. The impulse voltage to which the insulator string is exposed is obviously

nonstandard, the criterion for flashover rather complex, and to obtain analytical expressions, certain simplifying assumptions will be necessary.

First, it will be assumed that the impulse voltage has a very short front and exponentially decaying due to reflections from adjacent towers, characterized by a time constant τ:

$$\tau = \frac{Z_g \, L_{sp}}{R \, v} \tag{13.29}$$

where

Z_g is the surge impedance of the ground wire
L_{sp} is the span length
R is the tower footing resistance
v is the speed of light

Again, for simplicity, it is assumed that the nonstandard flashover voltage U_{bns} is related to the critical positive standard impulse flashover voltage U_{50} by Eriksson (Eriksson and Weck, 1988):

$$U_{bns} = U_{50}\left(1 + \frac{2}{\tau}\right) \tag{13.30}$$

with τ in μs.

If U_o is the peak power frequency voltage to ground and C_f is the coupling factor between the ground wire (under corona) and the phase conductor, the minimum backflashover current I_b can then be determined from

$$I_b R\left(1 - C_f\right) + U_o = U_{50}\left(1 + \frac{2}{\tau}\right) \tag{13.31}$$

The probability that this current is reached or exceeded can be determined from the relevant cumulative distribution function, for example, CIGRE log-normal distribution.

Normally, the design failure rate is so small or the MTBF is so long that the corresponding current I is much higher than the minimum backflashover current I_b. Such current can be determined from the probability function $P(I)$ such that

$$P\left(I\right) = \frac{N_{dr}}{N_{sd}} \tag{13.32}$$

where

N_{dr} is the design failure rate
N_{sd} is the number of flashes to the limit distance d, as in (13.28) earlier

At such extremely high current, it is assumed that the insulator flashover takes place at the peak rather than on the tail as for the minimum backflash current I_b.

At the strike point, the initial peak U_s of the impinging surge can be approximated by

$$U_s = IR\left(1 - C_f\right) + U_o \tag{13.33}$$

As previously indicated, the steepness S_1 of the impinging surge will be taken as an average value corresponding to half the limit distance, that is, a distance of $d/2$ so that

$$S_i = \frac{2K_c}{d} \tag{13.34}$$

for $n = 1$.

Figure 13.12 shows a schematic diagram for simplified and approximate determination of the amplitude U_{im} of the impinging surge on arrival at the substation. For simplicity, it is assumed that the corona onset voltage of the conductor coincides with the power frequency voltage U_o to ground. The peak V_{im} of

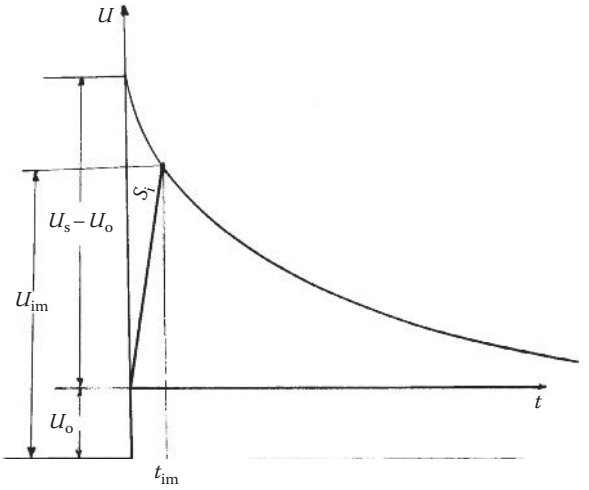


FIGURE 13.12 Simplified determination of the impinging lightning surge into the substation with consideration of damping due to corona; U_{im}: peak of impinging surge; t_{im}: impinging surge time-to-crest.

the impinging surge is determined by the intersection of the straight line $U = S_i t$ with the exponentially decaying impulse voltage so that the time t_{im} to peak can be determined from

$$S_i t_{im} = (U_s - U_o)\exp\left(-\frac{t_{im}}{\tau}\right) \tag{13.35}$$

which can be solved numerically. An approximate analytical solution can be obtained if it is recognized that in general, $t_{im} \ll \tau$, so that

$$S_i t_{im} \approx (U_s - U_o)\left(1 - \frac{t_{im}}{\tau}\right)$$

from which approximately

$$t_{im} = \frac{1}{(1/t_s) + (1/\tau)} \tag{13.36}$$

with

$$t_s = \frac{U_s - U_o}{S_i}$$

It follows that the peak U_{im} of the impinging surge can be approximated as

$$U_{im} = U_o + \frac{U_s - U_o}{1 + (t_s/\tau)} \tag{13.37}$$

A more detailed analysis of the impinging surge is given by Hileman (1999).

For illustration, we will consider a numerical example adapted from Eriksson and Weck (1988) for a 550 kV system with U_{cw} taken as 1348 kV. We will take an MOA with a maximum continuous voltage MCOV of 317 kV with a protective level U_{pl} = 861 kV; see in the following text. K_c is taken as 1.7×10^6 kV · m/μs, $n = 1$, and $L = 43$ m; substituting in (13.27), the limit distance d is obtained at 2001 m. From (13.34), S_i is obtained at 1699 kV/μs.

U_{50} for the 550 kV insulator string is taken as 2100 kV, $Z_g = 350\ \Omega$, $L_{sp} = 300$ m, and $R = 20\ \Omega$. From (13.29), τ is calculated as 17.5 μs. Substituting in (13.31), the minimum backflash current is determined at 135 kA. For this length of the limit distance, the number of strikes to the ground wire was taken as six flashes/year. Also in Eriksson and Weck (1988), an MTBF of 400 years was adopted corresponding to $N_{dr} = 2.5 \times 10^{-3}$ flashes/year that, when substituted in (13.32), results in $P(I) = 4.2 \times 10^{-4}$. From CIGRE

log-normal distribution, this corresponds to a current $I = 250$ kA. This current substituted in (13.33) to determine the peak of the impinging surge at the strike point, with $U_o = \left(550/\sqrt{3}\right)\sqrt{2} = 449$ kV and $C_f = 0.3$. U_s, is therefore obtained as 3949 kV. $U_s - U_0 = 3500$ kV yielding $t_s = \left(U_s - U_o\right)/S_i = 2.0\,\mu s$. From (13.36), the front time t_{im} of the impinging impulse is determined at 1.8 μs and the amplitude $U_{im} = 3590$ kV.

This surge is used for determining the traveling wave response of the substation. It should be noted, however, that at the above extremely low design failure rate and the resulting probability of 4.2×10^{-4}, determination of the design current level I will be quite uncertain. There are very few credible records of stroke currents as high as 250 kA.

For shielding failure, the amplitude of the impinging surge U_{isf} is taken as

$$U_{isf} = \frac{1}{2} I_m Z_c \tag{13.38}$$

where

I_m is the maximum shielding failure current

Z_c the surge impedance of the phase conductor

The initial shape of this impulse corresponds to that of the lightning current. As it propagates toward the substation, it will be exposed to damping by corona as explained earlier.

13.7.2 Determination of Coordination Withstand Voltage (U_{cw})

As indicated in the insulation coordination procedure chart of Figure 13.1, the coordination withstand voltage of the insulation system is obtained by multiplying the representative overvoltage U_{rp} by a coordination withstand factor K_{cw}. In principle, a coordination withstand voltage can be applied to the representative overvoltage of any class. The elements influencing the coordination withstand factor are also indicated in Figure 13.1. A distinction should be made between the deterministic approach of insulation coordination and the associated deterministic coordination withstand factor K_{cd} and the statistical approach with the statistical factor K_{cs}.

13.7.2.1 Deterministic Approach

In the deterministic method, the representative overvoltage is an assumed maximum stress, and the minimum dielectric strength is determined using a factor K_{cd} to ensure an adequate margin between these two levels.

For slow-front overvoltages and equipment not protected by surge arresters, the maximum stress is selected as the overvoltage truncation value, for phase-to-ground and phase-to-phase configurations. In such case, there is no need for an additional margin and the deterministic coordination factor $K_{cd} = 1$. However, for equipment protected by surge arrester, a coordination factor K_{cd} between 1.0 and 1.10 is recommended in IEC 60071-2 (IEC 60071-2, 1996) to account for possible skewing of the overvoltage distribution, depending on the ratio U_{pl}/U_{e2}. Here, U_{pl} is the arrester protective level, and U_{e2} is the 2% overvoltage to ground.

For fast-front overvoltages, the deterministic coordination factor is taken as $K_{cd} = 1$, since it is considered that the assumed maximum overvoltage due to lightning already includes probabilistic effects.

13.7.2.2 Statistical Approach: Risk of Failure

In the statistical approach, the system insulation is designed for an acceptable risk of failure R, which can in general be expressed by

$$R = \int_0^{\infty} f(U) \lozenge P_{ins}(U)\,dU \tag{13.39}$$

where

$f(U)$ is the probability density function of system overvoltages

$P_{ins}(U)$ is the cumulative statistical flashover distribution of the system insulation when exposed to an impulse peak U

In IEC Standard 60071-2 (1996), the overvoltage probability function is assumed Gaussian, while the insulation strength is taken as a Weibull distribution.

More realistically, the limits of the integral in (13.39) should be modified to read

$$R = \int_{U_{oins}}^{U_t} f(U) \lozenge P_{ins}(U) \, dU \tag{13.40}$$

where

U_{oins} is the lower truncation level of the insulation system strength, below which no flashover could take place

U_t is the upper truncation level of overvoltages, that is, the overvoltage level that cannot be exceeded

It is clear from (13.40) that the risk of failure U exists only if the overvoltage upper truncation level U_t exceeds the insulation lower truncation level U_{oins}. Otherwise, R would vanish for $U_{oins} \geq U_t$.

The risk function R can be normalized by referring all voltages in (13.40) to a base value. Normalizing w.r.t., U_t (13.40) would take the form

$$R = \int_{U^*_{oins}}^{1} f(U^*) \lozenge P_{ins}(U^*) \, dU^* \tag{13.41}$$

where

$U^* = U/U_t$

$U^*_{oins} = U_{oins}/U_t$

Equation (13.41) could then be expressed as

$$R = R\left(\frac{U_{oins}}{U_t}, U_t^*\right) \tag{13.42}$$

where U_t^* is the truncation voltage in per unit of the peak operating voltage to ground $\left(\sqrt{2}\,U_s/\sqrt{3}\right)$.

It is clear from (13.41) and (13.42) that the risk of failure R can be reduced to meet a performance criterion, for any value of U_t^*, by increasing the ratio U_{oins}/U_t.

In IEC Standard 60071-2, normalization of the risk function is taken with respect to U_{e2}, with a 2% probability of being exceeded, instead of U_t earlier, and U_{oins} is replaced by the coordination withstand voltage U_{cw}. It follows in this case that (13.42) could be replaced by

$$R = R\left(\frac{U_{cw}}{U_{e2}}, U_{e2}\right) \tag{13.43}$$

Note that $U_{cw}/U_{e2} = K_{cs}$, the statistical coordination factor.

Numerical examples of this function are given, for slow-front overvoltages, in IEC Standard 60071-2 (IEC 60071-2, 1996), where it is shown that R is quite sensitive to the ratio U_{cw}/U_{e2}. On the other hand, in the range of practical interest, R is insensitive to the overvoltage factor U_{e2}, in the range 1.5–3.5.

For lightning overvoltages, the statistical approach was explained, by a simplified method, in Section 13.7.1.4.2, dealing with impinging surge on a substation.

13.7.3 Determination of Required Withstand Voltage (U_{rw})

According to the insulation coordination procedure of Figure 13.1, the required withstand voltage U_{rw} is determined from the coordination withstand voltage U_{cw} by multiplying the latter with an altitude correction factor K_a, if any, and a safety factor K_s. These are described in the following sections.

13.7.3.1 Altitude Correction Factor

According to IEC Standards 60071-1, an altitude correction factor K_a is applied to the coordination withstand voltage, for installations at an altitude $H > 1000$ m. As explained in Chapter 5, this is to account for the effect of reduced air density at high altitude on the withstand voltage of external insulation. The question is sometimes asked, however, what exactly happens at $H = 1000$ m, which makes altitude correction required at $H = 1001$ m and not at $H = 1000$ m? The relative air density δ varies with altitude H, m by the relationship

$$\delta = \exp\left(-\frac{H}{8150}\right) \tag{13.44}$$

so that it is obvious that δ is a continuous function of H, and nothing particular takes place at $H = 1000$ m. It is just an implicit assumption on the part of IEC that for insulation coordination purposes, it can be considered that the air density effects within the first 1000 m of altitude are already accounted for, within the safety margins involved. However, if we are comparing the results of scientific investigations of breakdown voltage in two laboratories, one at sea level and the other at 900 m, introducing air density corrections is certainly recommended and will hopefully reduce discrepancy between the two sets of results.

As explained in Chapter 5, the altitude correction factor K_a can be expressed as (IEC 600711-2, 1996)

$$K_a = \exp\left(-m\frac{H}{8150}\right) \tag{13.45}$$

with H in meter, and where $m = 1$ for lightning impulses and short-duration power frequency withstand of air clearances and clean insulators and $m = 0.5$ for polluted insulators.

With regard to altitude corrections for polluted insulators, an extensive physically based investigation of the subject has been undertaken by Rizk and Rezazada (Rizk and Rezazada, 1997). The exponent $m = 0.5$ introduced earlier by IEC has been confirmed for simple-shaped insulators, with high utilization factor of the leakage path (Rizk and Rezazada, 1997). For complex-shaped insulators, like antifog types with deep ribs, however, it was shown that higher values of m will be necessary (Rizk and Rezazada, 1997). This practically means that at high altitudes, antifog insulators should be derated to a higher degree than simple-shaped insulators.

As explained in Chapter 5, air density correction is more complex for switching impulse withstand as it depends on the role played by the leader phase in the breakdown process (Garbagnati et al., 1991; Rizk, 1993). IEC 60071-2 (IEC 600711-2, 1996) expresses the exposed m as function of the coordination withstand voltage U_{cw}. In general, m decreases at higher U_{cw}, and separate curves are given for phase-to-earth, longitudinal, and phase-to-phase configurations (IEC 600711-2, 1996). This is clearly an oversimplification, since within each configuration, m will not be uniquely defined by the gap withstand voltage, but will also be influenced by the electrode geometry (Rizk, 1992, 1993).

13.7.3.2 Safety Factor (K_s)

The safety factor takes into consideration the effects of insulation aging in service, production and assembly dispersion, and inaccuracy of the withstand voltage tests. It is evident that some of those factors cannot be precisely evaluated, and, therefore, K_s will be mostly based on experience, taking into consideration the consequences of insulation system failure.

In IEC 600711-2 (1996), the following values of K_s are recommended:

$K_s = 1.15$ for internal insulation
$K_s = 1.05$ for external insulation

It should be noted within IEC that the final say over safety factors belongs to the apparatus committees and not to the insulation coordination technical committee.

13.7.4 Selection of Standard Withstand Voltage (U_w)

The final step in the insulation coordination procedure described in Figure 13.1 is the selection of standard withstand voltages. Here, reference must be made to standard insulation levels given in international standards, for example, IEC 60071-1 (IEC 60071-1, 1996).

For range I with $3.6 \leq U_m \leq 245$ kV, these tables provide, for each standard level of U_m, two sets of insulation levels: the first includes standard short-duration power frequency withstand voltages, while the second provides standard lightning impulse withstand voltages. For some values of U_m, more than one power frequency withstand levels are provided to choose from. Furthermore, for each power frequency withstand voltage, a corresponding lightning impulse withstand level is provided. It is noted that, in this range, no switching impulse withstand levels are provided and no switching impulse tests are carried out. Any required switching impulse withstand voltage in range I can be converted to an equivalent power frequency or lightning impulse test voltage by a recommended conversion factor K_t (IEC 600711-2, 1996).

As an example, consider a 245 kV system where, for phase-to-earth external insulation, a required switching impulse level is $U_{rw} = 550$ kV and, for phase-to-phase insulation, $U_{rw} = 825$ kV. It is required to convert these values to either short-duration power frequency or lightning impulse withstand.

For phase-to-earth insulation (IEC 600711-2, 1996):

$$\begin{aligned} &\text{Power frequency:} \quad K_t = 0.6 + \frac{U_{rw}}{8500} \\ &\text{Lightning:} \quad\quad\quad\ K_t = 1.05 + \frac{U_{rw}}{6000} \end{aligned} \tag{13.46}$$

Substituting $U_{rw} = 550$ kV, for power frequency, $K_t = 0.665$, resulting in a power frequency converted value $U_{rwc} = 0.665 \times 550 = 366$ kV.

If converted to a lightning impulse test instead, K_t is found as $K_t = 1.14$, yielding a lightning impulse withstand voltage of 628 kV. This level is too low and will not be retained.

For phase-to-phase insulation (IEC 600711-2, 1996):

$$\begin{aligned} &\text{Power frequency:} \quad K_t = 0.6 + \frac{U_{rw}}{12700} \\ &\text{Lightning:} \quad\quad\quad\ K_t = 1.05 + \frac{U_{rw}}{9000} \end{aligned} \tag{13.47}$$

Substituting $U_{rw} = 825$ kV, for conversion to power frequency, $K_t = 0.665$, yielding a power frequency converted value of 549 kV. This is excessive and will not be retained.

Converting to a lightning impulse test instead, it is found that $K_t = 1.14$, yielding a converted lightning impulse withstand $U_{rwc} = 825 \times 1.14 = 942$ kV.

The converted values retained will therefore be 366 kV for power frequency and 942 kV for lightning impulse.

For the system under consideration, system studies showed that the required power frequency withstand voltage was 240 kV for phase-to-earth and 368 kV for phase-to-phase. Furthermore, for fast-front overvoltages, it was found that the required withstand voltage was 900 kV for both phase-to-earth and phase-to-phase.

Consulting Table 2 of IEC 60071-1 (1996), it is found that a power frequency $U_w = 395$ kV and a lightning impulse $U_w = 950$ kV will satisfactorily cover all the earlier requirements.

13.8 Surge Arresters

13.8.1 General

In the previous section, a reference was made to the essential role played by surge arresters in insulation coordination. In substations, the coordination withstand voltage is basically determined by the arrester protective level. Also, switching surge voltages on EHV transmission lines were shown, through an

EMTP example, to be effectively controlled by surge arresters installed at the line terminals. However, so far, details of surge arrester characteristics have not been discussed. It is therefore overdue to describe surge arrester characteristics and protective performance in this section. The presentation is not intended as an extensive review and will furthermore be restricted to metal oxide surge arresters without gaps for ac systems, as defined by IEC Standard 60099-4 (IEC 60099-4, 1991). According to IEC standard, this is "an arrester having nonlinear metal oxide resistors connected in series and/or in parallel without any integrated series or parallel spark gaps" (IEC 60099-4, 1991). Such arresters are also covered in IEEE Std. C 62.11 (2012). Elimination of the series current limiting gap that was an essential element of the silicon carbide arrester was made possible by the exceptional nonlinearity of the voltage–current characteristics of zinc oxide blocks made available in the 1970s (Matsuoka, 1971; Sakshaug et al., 1977).

Figure 13.13 (Sakshaug et al., 1977) shows a comparison between normalized volt–ampere characteristics of zinc oxide and silicon carbide arrester elements. It is shown that the zinc oxide curve is so nonlinear that the voltage varies slightly with a very wide range of current variation. Specifically for a current density change from 10^{-3} to 10^{2} A/cm^2 (a factor of 10^5), the voltage gradient varies by only 56% (Sakshaug et al., 1977). It is noted that the nonlinearity of the silicon carbide element is much weaker in comparison. A result, and of particular interest, is the comparison of the two materials at relatively low voltage stress. For a stress of 150 V/mm, the current density of the zinc oxide element is approximately 1 mA/cm^2, while the silicon carbide material draws several tens of A/cm^2. It is this property that makes it possible to expose a proper height of the zinc oxide valve element to system operating voltage, while the corresponding silicon carbide elements would need the series gap to avoid destruction. While zinc oxide is the major element, other metal oxides are included so that reference to a MOA becomes more appropriate (IEC 60099-4, 1991; IEEE C 62.11-2012).

It is also noted that the normalized *V–i* characteristics of the metal oxide element in Figure 13.13 (Sakshaug et al., 1977) show a temperature sensitivity below a current density of 1 mA/cm^2 such that the block resistivity decreases as temperature increases, a negative temperature coefficient. This is an important factor with respect to TOV performance of an MOA. At each TOV level, the permissible duration must be such as to prevent thermal runaway. In the upper range above 10 A/cm^2, the normalized *V–i* characteristic turns upward showing reduced nonlinearity. This is the range of lightning protection.

Under operating voltage, a complete MOA normally draws a current of approximately 1 mA, which is substantially capacitive. The intermediate discharge current of up to 2 kA covers the switching surge and TOV protective function.

The highest currents in the tens of kA range are associated with lightning protection.

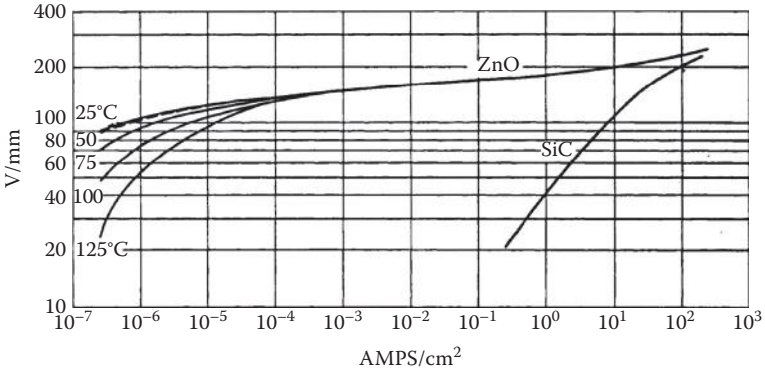


FIGURE 13.13 Normalized volt–ampere characteristic of zinc oxide element and comparison with silicon carbide.

13.8.2 Rated Voltage

MOAs are characterized by the following:

- The maximum continuous operating voltage (MCOV) of IEEE Std. C 62.11, which corresponds to U_c of IEC 60099-4.
- The duty cycle voltage of IEEE Std. C 62.11, which corresponds to the rated voltage of U_r in IEC 60099-4. IEC standard includes a note that presents U_r as a 10 s power frequency voltage (TOV) used in the operating duty test.

Table 1 of IEEE Std. C 62.11 provides a list of MCOV in the range 2.55–485 kV_{rms} and duty cycle voltages in the range 3–612 kV_{rms}. The ratio of duty cycle voltage to MCOV varies accordingly from 1.18 to 1.26. Similarly, IEC Standard 60099-4 specifies rated voltages in the range 3–756 kV_{rms}.

13.8.3 Discharge Current

The discharge current of an arrester is defined as the impulse current that flows through the arrester. The nominal discharge current of an arrester is designated as the peak value of the lightning impulse current used to classify an arrester. The standard nominal discharge currents are 8/20 μs of 1.5, 2.5, 5.0, 10, and 20 kA (IEC 60099-4, 1991). Arresters are classified by their standard nominal discharge currents, for example, for station type 10 and 20 kA arresters.

13.8.4 Impulse Current Tests

These tests include (IEC 60099-4, 1991) the following:

- A steep current impulse with a 1 μs virtual front.
- Lightning current impulse of 8/20 μs shape.
- Long-duration rectangular impulse. For 10 and 20 kA arresters, the long-duration withstand is demonstrated by an artificial line discharge test with different parameters defining a line discharge class.

13.8.5 Residual Voltages

The purpose is to obtain the maximum residual voltages of an arrester design for all specified currents and wave shapes (IEC 60099-4, 1991). This is obviously a fundamental quantity referred to earlier in this chapter as the protective level. Tests for determining residual voltages include the following:

- Steep current impulse (FOW) residual voltage test with 1 μs virtual front and a peak value equal to the nominal discharge current of the arrester.
- Lightning impulse residual voltage test with a 8/20 μs impulse.
- Switching impulse residual voltage test with a current impulse having a virtual front $30 < t_f < 100$ μs and a virtual time to half value of roughly double the virtual front. For a 10 kA arrester peak, switching impulse currents of 250 and 1000 A are specified, while for a 20 kA arrester, switching impulse currents of 500 and 2000 A are specified (IEC 60099-4, 1991).

IEEE Guide C 62.22 [29] gives a range of protective characteristics for the previous tests in per unit of MCOV crest. Here, values relevant to 10 and 20 kA arresters are quoted:

- FOW or 0.5 μs, 2.01–2.48 p.u.
- 8/20 μs lightning impulse, 1.97–2.25 p.u.
- Switching impulse current, 1.64–1.85

TABLE 13.4

Residual Voltage, kV_{peak}, of 10 and 20 kA MOA in per Unit of Rated Voltage (kV_{rms})

	20 kA			10 kA		
Rated Voltage, kV_{rms}	**Steep**	**Lightning**	**Switching**	**Steep**	**Lightning**	**Switching**
144–342	2.6–3.1	2.3–2.8	2.0–2.3	2.6–3.7	2.3–3.3	2.0–2.6
360–756	2.6–3.1	2.3–2.8	2.0–2.3	2.6–3.1	2.3–2.8	2.0–2.3

Source: IEC Standard 60099-4, *Metal-Oxide Surge Arresters without Gaps for AC Systems*, 1991.

IEC Standard 60099-4 (IEC 60099-4, 1991), on the other hand, provides typical maximum residual voltages for 10 and 20 kA arresters in per unit of rated voltage. The values also vary with the voltage range. An extract is given in Table 13.4 (IEC 60099-4, 1991).

13.8.6 Arrester Durability Requirements

International standards (IEC 60099-4, 1991; IEEE C 62.11-2012) include several categories of requirements to demonstrate the capacity of the arrester to function properly under diverse operational conditions, for an acceptable lifetime. Tests have been established to prove that the arrester meets such requirements. For brevity, we are going to list the most important requirements, without going into great detail (IEC 60099-4, 1991; C 62.11- 2012).

13.8.6.1 Insulation Withstand

The first obvious requirement is the ability of the arrester housing to pass a number of insulation withstand tests. These include the ability to withstand lightning and switching impulses exceeding, with an appropriate margin, the corresponding protection levels. This also includes power frequency withstand under wet and contamination conditions.

13.8.6.2 Thermal Stability

Thermal stability test in which the resistive component of the current or power losses of the arrester are monitored during a power frequency test to prove thermal stability.

13.8.6.3 Leakage Test

Arresters with sealed housing shall exhibit no measurable leakage.

13.8.6.4 Line Discharge Energy

For 10 and 20 kA station type, it is the ability of the arrester to handle the energy associated with line discharge.

Depending on the line discharge class as shown in Table 13.5 (IEC 60099-4, 1991), it is noted that both the surge impedance, Ω, and the line charging voltage, kV_{dc}, are given as multiple of the arrester rated voltage U_r, kV_{rms}.

TABLE 13.5

Parameters of Line Discharge Tests for 10 and 20 kA Station Arresters

Arrester Current, kA	**Line Discharge Class**	**Line Surge Impedance, Z_0, Ω**	**Peak Duration T, μs**	**Line Charge Voltage U_L, kV_{dc}**
10	1	$4.9U_r$	2000	$3.2U_r$
10	2	$2.4U_r$	2000	$3.2U_r$
10	3	$1.3U_r$	2400	$2.8U_r$
20	4	$0.8U_r$	2800	$2.6U_r$
20	5	$0.5U_r$	3200	$2.4U_r$

Source: IEC Standard 60099-4, *Metal-Oxide Surge Arresters without Gaps for AC Systems*, 1991.

As an example, consider a 20 kA arrester, rated 612 kV_{rms}, intended for a 765 kV system. For a line discharge class 5 test, the line surge impedance $Z_o = 0.5 \times 612 = 306\ \Omega$ and the line charging voltage should be $U_L = 2.4 \times 612 = 1469$ kV. It can be shown that, in a line with a surge travel time $T/2$, if it is assumed that the energy discharge duration is double the surge travel time, the energy W can be approximately expressed as (IEC 60094-4, 1991; Hileman, 1999)

$$W = U_{res} \left(U_L - U_{res}\right) \frac{T}{Z_o} \tag{13.48}$$

where U_{res} is the lowest arrester residual voltage in a switching impulse test.

In the present example, U_{res} is taken as 1200 kV_{peak}. Substituting in (13.48) for the different parameters, W is obtained as 3.376 MJ. This arrester has an MCOV of 485 kV so that this corresponds to 6.96 kJ/kV (MCOV). Commercial arresters of this class are available for 10 kJ/kV (MCOV).

13.8.6.5 Operating Duty Test

Here, service conditions are simulated by the application to the arrester of a number of specified impulses in combination with energization with power frequency voltage. The test sequence includes (IEC 60099-4, 1991) the following:

- Initial measurements
- Conditioning
- Impulse applications
- Examination and measurements

Through power loss measurements, it is demonstrated that no thermal runaway occurs. Measurements of the residual voltage before and after the test should not change by more than 5% to demonstrate that thermal stability is achieved.

13.8.6.6 Temporary Overvoltages

A relationship between the value U_t and duration T_t of allowable power frequency voltage to which the arrester can be exposed shall be established.

For an arrester of rated voltage U_r, the relation between the peak value of the TOV U_t and allowable duration T_t can be expressed by an empirical relationship such as (ABB, 1999)

$$U_t = \sqrt{2} U_r \left(\frac{10}{T_t}\right)^m \tag{13.49}$$

where m is an arrester-specific exponent with an average value of 0.02.

More detailed accounts of this relationship are included in the guide IEEE Std. C 62.22 (IEEE C 62.22 – 1991).

Here, a TOV capability TOV_c is related to the allowable duration T by a relationship of the form

$$\frac{TOV_c}{MCOV} = AT^{-B} \tag{13.50}$$

Tables for the constants A and B are included in two time ranges.

As an example, using the approximate relationship (13.49), for the arrester used in Section 8.6.4 with $U_r = 612\ kV_{rms}$, the U_t peak level permissible for 1 s duration will be 906 kV_{peak}.

13.8.6.7 Pressure Relief Test

This test shall demonstrate, for safety purposes within the substation, that the failure of the arrester under system short-circuit current shall not cause shattering of the housing.

REFERENCES

ABB Switchgear Manual, 10th edn., Cornelsen Verlag, Berlin, 1999.

Baatz, H. *Overvoltages in Power Supply Networks*. Springer-Verlag, Berlin, 1956. [In German.]

Boyd, H.A., Rohlfs, A.F., and L.E. Zaffanella. Phase-to-ground and phase-to-phase switching-surge flashover of external insulation of UHV stations. *IEEE Transactions on Power Apparatus and System* PAS-93(2): 518–528, 1974.

CIGRE Task Force 33.03.03. Switching impulse test procedure for phase-to-phase air insulation. *Electra* 30: 55–69, 1973.

CIGRE Task Force 33.03.03. The influence of non-standard conditions on the switching impulse strength of phase-to-phase insulation. *Electra* 64: 211–236, 1979.

Cortina, R., Sforzini, M., and A. Taschini. Strength characteristics of air gaps subjected to inter-phase switching surges. *IEEE Transactions on Power Apparatus and System* PAS-89(3): 448–452, 1970.

Creed, F. and M.M.C. Collins. Transient impedance of high voltage impulse generating systems. *IEEE Trans*. PAS-89, 1387, 1970.

Eriksson, A.J. and K.H. Weck. Simplified procedure for determining representative substation impinging lightning overvoltages. CIGRE, Paper No. 33-16, CIGRE, Paris, France, 1988.

Freund, J.E. and R.E. Walpole. *Mathematical Statistics*. Englewood Cliffs, NJ: Prentice Hall Inc., Englewood Cliffs, New Jersey, 1987.

Gallet, G., Hutzler, B., and J.-P. Riu. Analysis of the switching impulse strength of phase-to-phase air gaps. *IEEE Transactions on Power Apparatus and System* PAS-97(2): 485–494, 1978.

Garbagnati, E., Fonseca, J.A., Britten, A.C., Pigini, A., Sartorio, G., and B.C. LeRoux. The influence of atmospheric conditions on the dielectric strength of phase-to-phase insulation when subjected to switching impulses. In: *Seventh ISH*, Paper No. 42.14, TU Dresden, Dresden, Germany, August 26–30, 1991.

Hald, A. *Statistical Theory with Engineering Applications*. New York: Wiley, 1952.

Hileman, A.R. *Insulation Coordination*. New York: Marcel Dekker Inc., 1999.

IEC 60050-604. *International Electrotechnical Vocabulary,* IEC, Geneva, Switzerland, 1987.

IEC 60071-1. *Insulation Coordination*, IEC, Geneva, Switzerland, 1996.

IEC 60071-2. *Insulation Coordination*. *Application Guide*, IEC, Geneva, Switzerland, 1996.

IEC 60099-4. *Metal-Oxide Surge Arresters without Gaps for AC Systems*, IEC, Geneva, Switzerland, 1991.

IEC 60060-1. *High-Voltage Test Techniques—Part 1: General Definitions and Test Requirements,* IEC, Geneva, Switzerland, 1996.

IEC Standard 61325. Insulators for Overhead Lines with a Nominal Voltage above 1000 kV. IEC, Geneva, Switzerland, 1995.

IEEE Std. C 62.11. *IEEE Standard for Metal-Oxide Surge Arrester for Alternating Current Power Circuits*, 2012.

IEEE Std. C 62.22. *Guide for the Application of Metal-Oxide Surge Arrester for Alternating Current Power Systems*, 1991.

Kachler, A.J., LaForest, J.J., and L.E. Zaffanella. Switching surge flashover of UHV transmission line insulation. *IEEE Transactions on Power Apparatus and System* PAS-90: 1604–1611, 1971.

Kaden, H. *Wirbelstrome und Schirmung in der Nachrichtentechnik*, Spring Verlag, Berlin, 1959.

Khodabakhchian, B. A study case of opening a 735 kV line. Private communication, 2013.

Matsuoka, M. Nonohmic properties of zinc oxide ceramics. *Japanese Journal of Applied Physics* 10: 46, 1971.

Menemenlis, C., Anis, H., and G. Harbec. Phase-to-phase insulation—Part I, II. *IEEE Transactions on Power Apparatus and System* PAS-95: 643–659, 1976.

Miyake, K., Watanabe, Y., and E. Ohsaki. Effects of parameters on the phase-to-phase flashover characteristics of UHV transmission lines. *IEEE Transactions on Power Delivery* PWRD-2(4): 1285–1291, 1987.

Paulson, A.S. and I.S. Grant. Phase-to-phase switching surge flashovers: Design data. *IEEE Transactions on Power Apparatus and System* PAS-100(7): 3666–3672, 1981.

Povh, D., Schmitt, H., Volker, O., and R. Witzmann. Modelling and analysis guidelines for very fast transients. *IEEE Transactions on Power Delivery* 11(4): 2028–2035, 1996.

Rizk, F.A.M. Critical switching impulse strength of long air gaps: Modelling of air density effects. *IEEE Transactions on Power Delivery* 7(3): 1507–1515, 1992.

Rizk, F.A.M. Critical switching impulse strength of phase-to-phase air insulation. *IEEE Transactions on Power Delivery* PWRD-8(3): 1492–1506, 1993.

Rizk, F.A.M. and A.Q. Rezazada. Modelling of altitude effects on AC flashover of polluted high-voltage insulators. *IEEE Transactions on Power Delivery* 12(2): 810–822, 1997.

Sakshaug, E.C., Kresge, J.D., and S.A. Miske. A new concept in station arrester design. *IEEE Transactions on Power Apparatus and System* PAS-96(2): 647–656, 1977.

Tule, G.U. and M.G. Kendall. *An Introduction to the Theory of Statistics*, 14th edn. New York: Hafner Publishing Co., 1950.

14

High-Voltage Testing and Measuring Techniques

14.1 Introduction

HV testing and measurements are essential to evaluate the adequacy of power equipment to meet their design specifications and hence their performance requirements on the transmission and distribution system of the utility. This, in turn, implies that adequate means are available to produce the specified dielectric stresses, which can far exceed the operating level of the power system, and perform accurate measurements to assess the performances of the equipment tested.

Technical specifications of equipment correspond to conditions exceeding the normal system operating voltage, for example, test voltages for 735 kV equipment may be selected as 1550 kV for switching impulse and 1950 kV for lightning impulse (see Chapter 13). Special equipments are therefore necessary to produce in laboratory the required voltage and current during the test on power equipment. This is possible by decomposing the test parameters so that the test equipment can produce one test parameter such as ac or dc voltage, current, and impulse voltage at a time, thus keeping the overall required power to acceptable levels while allowing adequate control of the test parameters. By properly designing the test circuit, the required test conditions can be produced and applied to the test object. We will review in the following the basic design of different test equipment used to produce the necessary test parameters and the measuring techniques to assess the performance of the test object: voltage, current, power losses, PD level, etc.

14.2 Test Categories

Test methods are designed to assess the dielectric properties of the test object under conditions typical for its operation in service. Typical test procedures are usually prescribed in national and international standards, which specify the test procedures, test circuit and its parameters, and test condition to ensure reproducible results from different laboratories. They usually specify a range of test voltages so that the utility can select a specific value, appropriate to the constraints prevailing on the system. The detailed test procedure can be agreed upon by the manufacturer, the customer utility, and the laboratory personnel, in accordance with international standards such as IEC or ANSI. In general, the various tests can be classified in routine, type, special tests, demonstration, on-site, and commissioning test categories.

Routine tests: Are tests to which subjected each piece of a group of identical equipment (IEC Standard 61395, 1995).

Type test: Is a test made on one or several similar pieces of equipment intended to show that all equipment complies with the same specifications and the same essential details would pass an identical test. It is usually not repeated on different deliveries (IEC Standard 61395, 1995).

Special tests: Special tests are required to assess one specific aspect of the required insulation performances. Aging, corona, and pollution tests are examples of special tests. They are necessary when new designs are introduced to the system and need be properly assessed: lines, cables, or power equipment. They often require specific test setup—test cages (Figure 14.1), test lines (Figure 14.2) for corona test on conductors, and test area for HV cables (Figure 14.3)—and usually extend in time.



FIGURE 14.1 Test cage for corona test on line conductors at IREQ. (Photo Courtesy of Hydro-Québec.)



FIGURE 14.2 Test line for corona test on line conductors at IREQ. (Photo Courtesy of Hydro-Québec.)



FIGURE 14.3 Test station for HV cables at IREQ. (Photo Courtesy of Hydro-Québec.)

Demonstration tests: Introduction of a new technology usually requires a series of tests forming what are generally referred to as demonstration tests. They aim at demonstrating the main advantages associated with the new technology and comprise dielectric and, sometimes, some form of accelerating aging test.

On-site tests: Refer to the case when different tests are made on the equipment already installed in the system, usually after repairs or overhauling work (Figure 14.4). There is no basic difference between on-site and tests carried out in laboratories, except that site tests may be performed at reduced stress levels. However, they are furthermore limited by the availability of the test equipment and by the restrictions, both in space and facilities, at the test site, which are not designed for conducting HV tests.

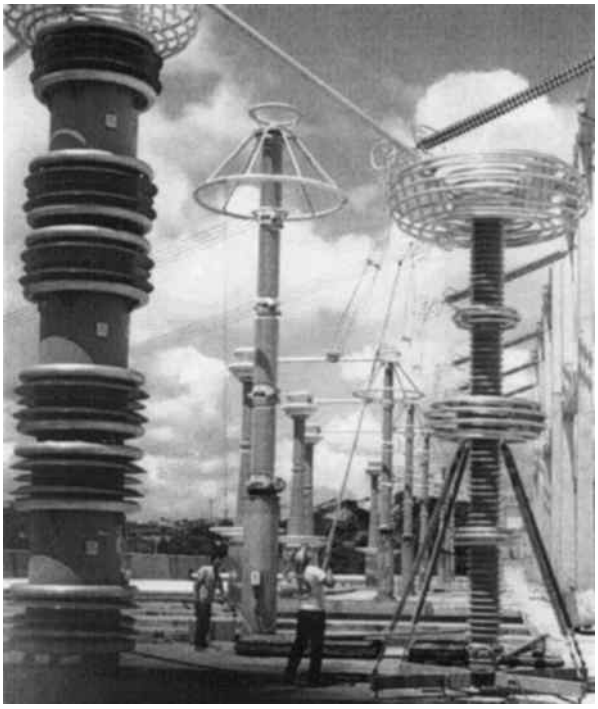


FIGURE 14.4 Preparation for a test on a gas-insulated bus in a generating station.

Commissioning tests: Refer to the set of preparatory work on a piece of equipment prior to its insertion in the power system. It officially denotes the transfer of the equipment from the manufacturer to the utility. The main purpose of commissioning tests is to prepare the equipment, especially its insulation system, so that it will withstand the system voltage when inserted into the power system.

14.3 Generation of the Test Voltage

14.3.1 AC Voltage

Because of its widespread use, the ac voltage is required in many tests to assess the adequacy of the equipment. The generation of an ac voltage at the power frequency can be made using a transformer with a high transformation ratio, typically 1:100. As a result, a test voltage of a few hundred kV can be obtained from a supply voltage of a few kV. Test voltages and currents higher than the nominal values of a single transformer may be produced by cascading several single-phase units in a series–parallel arrangement. Alternatively, for mainly capacitive test objects, as is often the case, an arrangement using an adjustable inductance in series with the test object can be used to produce an ac voltage at the resonant frequency of the circuit, which is also equal to the power frequency. Finally, rotating machines are necessary in specific tests, particularly on power transformers, requiring high power ac voltages at frequency higher than the system frequency. These different ac voltage sources will be reviewed in the following.

14.3.1.1 Cascaded Transformers

Connecting several transformers in cascade has been an elegant way to produce ac test voltage several times the nominal output of a single unit. For transformers with metal tank, the units at higher potential must be properly insulated from ground. This rapidly brings out the problem related to the insulation required for the primary winding at these units, which is a function of the position of the unit in cascade. The problem was solved with the use of three-winding transformers, with the tertiary winding connected to the HV end of the HV winding, as illustrated in Figure 14.5. No added insulation is necessary for the primary winding, and the test transformers are interchangeable in their cascade arrangement, which, nonetheless, remains quite cumbersome. The introduction of insulating tank transformers in the 1970s offers an interesting solution to this problem: the transformer units can be stacked one on top of the other, with the cascade ensemble rested on air-cushioned platform for easy displacement in the laboratory. Figure 14.6 shows an arrangement of several test transformers in cascade at IREQ.

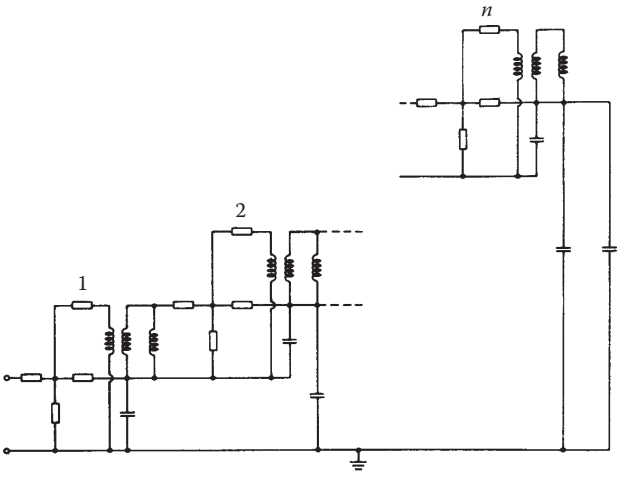


FIGURE 14.5 Equivalent circuit of cascaded transformers. (From Train, D. and Vohl, P.E., Determination of ratio characteristics of cascade connected transformers, *IEEE Trans*, PAS-95, 1911, 1976.)

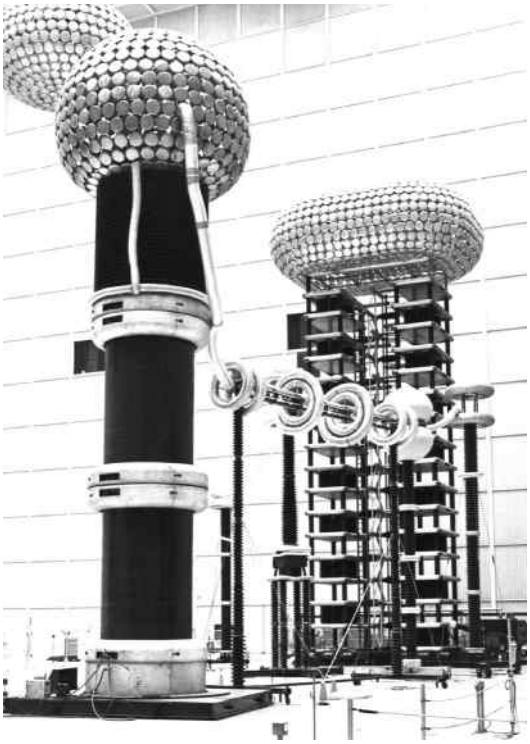


FIGURE 14.6 Cascade arrangement of three test transformers with insulating tank at IREQ. (Photo Courtesy of Hydro-Québec.)

Capacitive load: One particular aspect of testing using ac voltage is related to the capacitive nature of the test object, which causes the actual transformation ratio of the output to input voltages, to increase with the capacitive load (see Chapter 1). The problem can be illustrated by analyzing the simple case of a test transformer energizing a capacitive load C. The equivalent circuit may be simplified to a series RLC circuit. The voltage U_c across the capacitive load is related to the source voltage by

$$U_c = U_s \frac{jX_c}{R + j\left(X_l + X_c\right)} = \frac{U_s}{R\omega C + j\left(\omega^2 LC - 1\right)} = \frac{U_s}{1 - \omega^2 LC + j\omega CR} \tag{14.1a}$$

The ratio R_t between the output and no-load voltages is

$$R_t = \frac{U_c}{U_s} = \frac{1}{\sqrt{\left(1 - \omega^2 LC\right)^2 + \left(\omega CR\right)^2}} \tag{14.1b}$$

The variations of the overvoltage factor R_t with the capacitive load are shown in Figure 14.7. It can be seen that as the capacitive load increases, the ratio R_t increases to a maximum Q when the circuit is in resonance, corresponding to

$$Q = \frac{\omega L}{R} = \frac{1}{R\omega C}, \quad \text{with } \omega = 2\pi f$$

where f is the system frequency of normally 50 or 60 Hz, before it decreases.

The critical value of the capacitive load is

$$C_0 = \frac{1}{\omega^2 L}$$

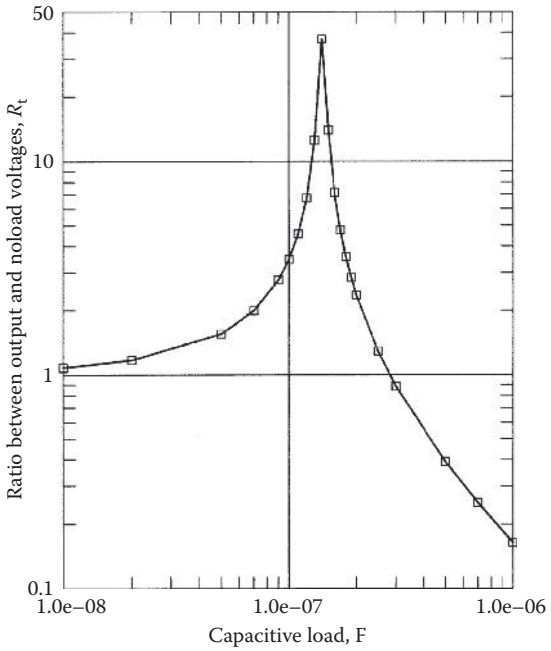


FIGURE 14.7 Variation of the ratio R_t with capacitive load.

With the leakage reactance L of the order of a few tens of H, the critical capacitive load C_0 at power frequency reaches several μF, a value rarely encountered in practice. It follows that for values currently observed in capacitive load, the operating conditions of the circuit are on the left-hand side of the curve for R_t in Figure 14.7, where the ratio R_t increases linearly with the capacitance of the test object if losses are neglected:

$$R_t = 1 + w^2 LC \tag{14.1c}$$

Such a behavior of the ratio R_t raises some concerns with respect to the possibility of overstressing the test transformer, especially when several units are connected in cascade. It was first investigated by Jayaram and Bahdas (Jayaram and Bahdas, 1963) who found that the output voltage can be related to the input admittance of the cascaded transformers by a predetermined linear relationship. The subject was further investigated by Train and Vohl (Train and Vohl, 1976), with respect to the inductive compensation at intermediate units and the unequal voltage distribution among the cascaded units. We summarize in the following their main findings.

Equivalent circuit

Single transformer unit: The equivalent circuit for a three-winding transformer is presented in Figure 14.8a. The impedances for the transformer comprise the winding resistances and leakage reactances. All reactances are referred to the HV winding and the same base kVA. The transformer ratio is then 1:1. The reactances can be measured by short-circuiting one winding and energizing a second winding, while the third winding is left open. The values of the various impedances are given in Table 14.1 for the 550 kV, 1.25 A transformer unit.

Figure 14.8b is a simplified equivalent circuit where the winding resistance is ignored as well as the magnetizing impedance Z_m. Furthermore, the negative secondary reactance of the HV winding is represented by a capacitance of the same value. This representation is valid for calculation performed at the power frequency of 60 Hz.

Cascaded transformers: Figure 14.9 illustrates the physical arrangement of a set of six transformer units in cascade, their self-capacitance C_w, together with the various stray capacitances. The equivalent circuit

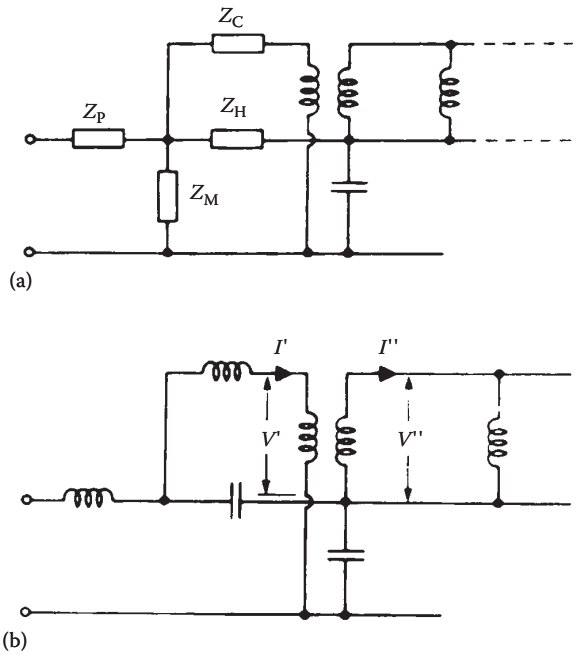


FIGURE 14.8 Equivalent circuit for a three-winding test transformer. (a) General circuit. (b) Lossless circuit. (From Train, D. and Vohl, P.E., *IEEE Trans*., PAS-95, 1911, 1976.)

TABLE 14.1

Characteristics of a 550 kV, 1.25 A Test Transformer

Winding	Reactance (H)	Resistance (Ω)
Primary	42.48	480.5
Coupling	61.86	1223.6
Secondary	−12.25	461.2

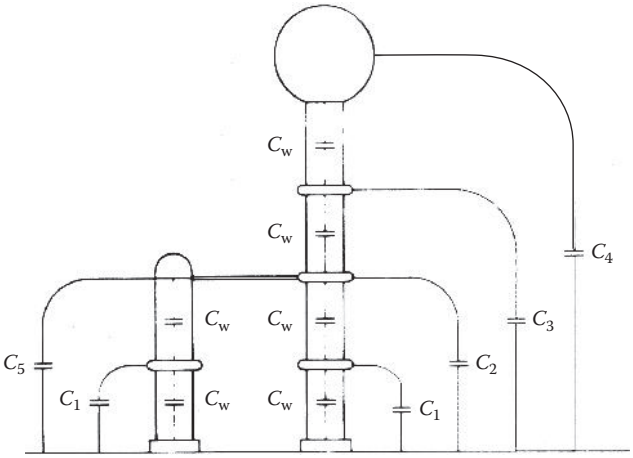


FIGURE 14.9 Six transformers in a cascade arrangement. (From Train, D. and Vohl, P.E., *IEEE Trans*., PAS-95, 1911, 1976.)

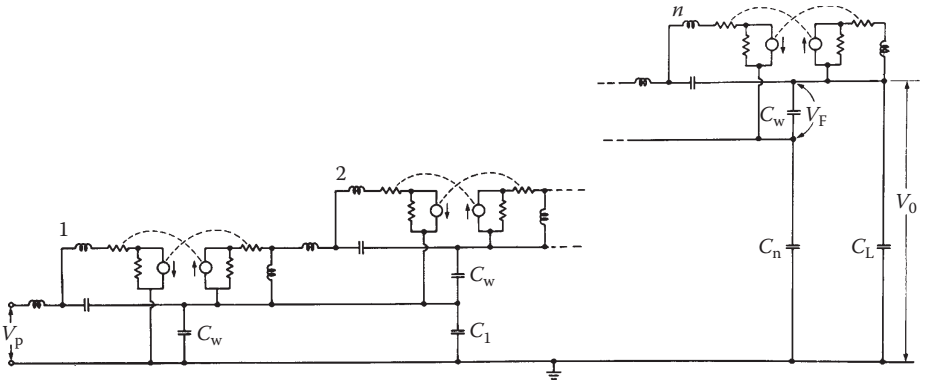


FIGURE 14.10 Equivalent circuit for a cascaded arrangement of test transformers. (From Train, D. and Vohl, P.E., *IEEE Trans*., PAS-95, 1911, 1976.)

is shown in Figure 14.10 for the computer model used by Train and Vohl (Train and Vohl, 1976), working with the ECAP (now MicroCap) program.

Voltage distribution: Extensive calculations made by Train and Vohl have confirmed the linear relationship between the ratio R_T of the output to input voltages with the input admittance of the cascaded arrangement of test transformers for various combinations of the transformer units used at IREQ. Figures 14.11, 14.12, and 14.14 show the variations of the total transformation ratio R_T:

$$R_t = \frac{\text{Output voltage}}{\text{Primary voltage}} = \frac{V_0}{V_p}$$

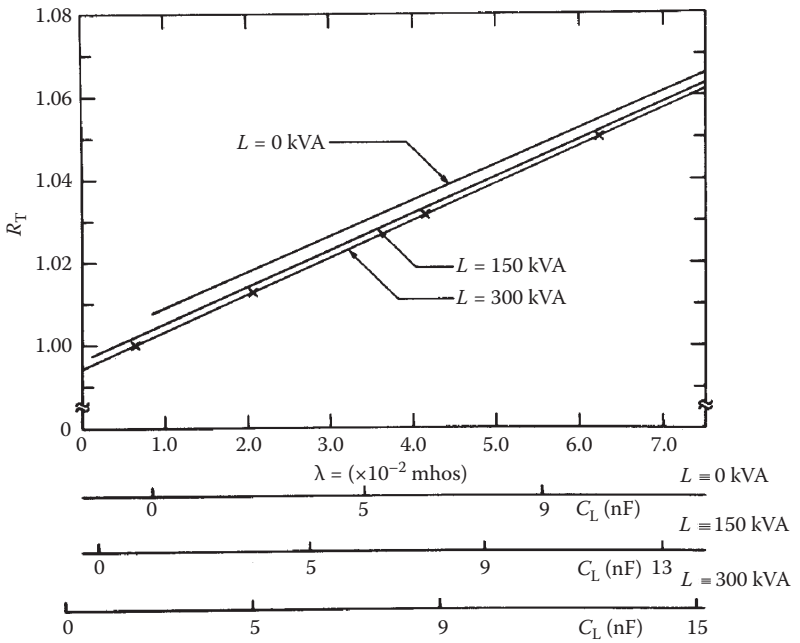


FIGURE 14.11 Output voltage ratio R_T as a function of the input admittance λ for a single transformer and for different levels of reactive compensation L. (From Train, D. and Vohl, P.E., *IEEE Trans*., PAS-95, 1911, 1976.)

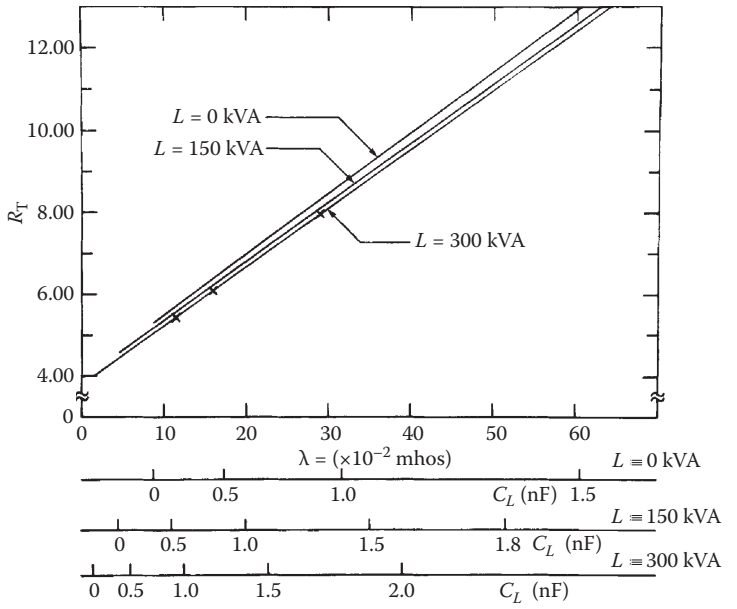


FIGURE 14.12 Output voltage ratio R_T as a function of the input admittance λ for a four-transformer arrangement in cascade and for different levels of reactive compensation L. (From Train, D. and Vohl, P.E., *IEEE Trans.*, PAS-95, 1911, 1976.)

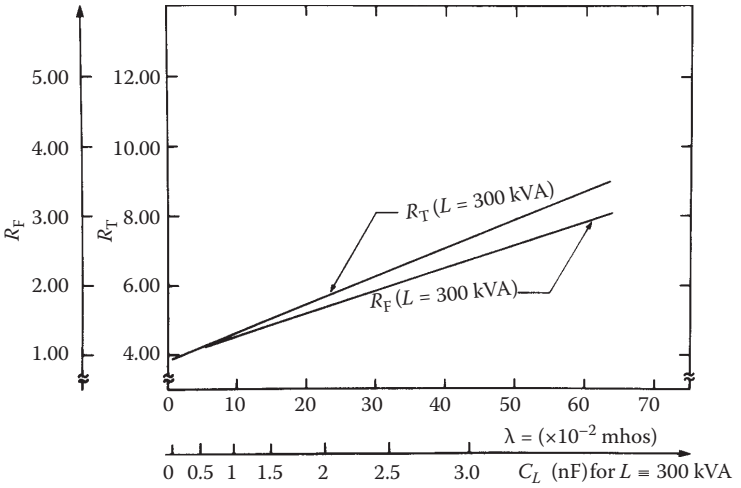


FIGURE 14.13 Output voltage ratio R_F as a function of the input admittance λ for a four plus two-transformer arrangement in cascade and for reactive compensation L. (From Train, D. and Vohl, P.E., *IEEE Trans.*, PAS-95, 1911, 1976.)

as a function of the input admittance λ for the case of a single, four- and six-transformer arrangements in cascade. In all figures, a scale of load capacitance C_L is provided for each value of compensating reactor L. The following observations can be made:

- Although the inductive compensation can have a significant effect on the actual value of the input admittance λ, they have little effect on the relationship between R_F and λ.
- While the ratio R_F remains close to unity for the single transformer unit, it increases considerably in the four- and six-transformer arrangement in cascade. The problem is related to the fact that the lower units have to supply the necessary power to the higher unit within the cascade arrangement. As a result, less energy is available to the secondary windings of the lower units and hence a reduced output voltage and a higher nonuniformity in the voltage distribution.

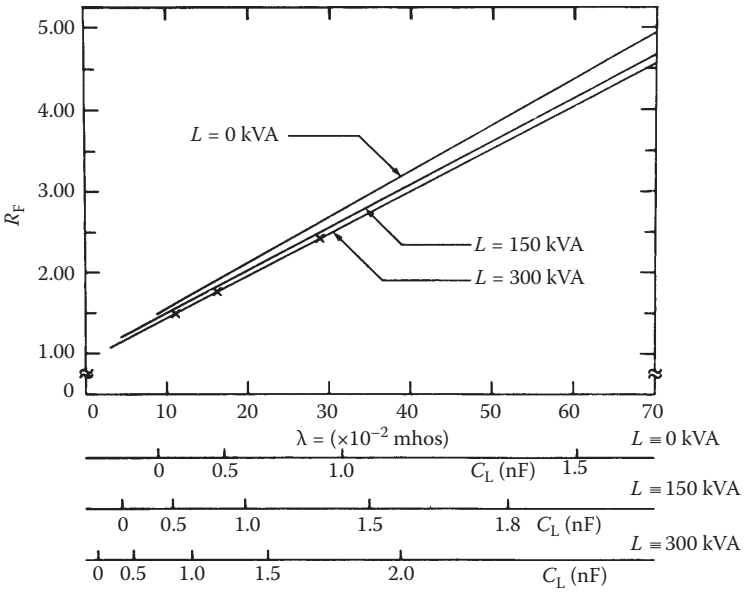


FIGURE 14.14 Variations of the voltage ratio at the top unit R_F as a function of the input admittance λ in a four-transformer arrangement in cascade and for different levels of reactive compensation L. (From Train, D. and Vohl, P.E., *IEEE Trans*., PAS-95, 1911, 1976.)

- Highest overvoltages occur at the top transformer unit, exposing it to high risk of failure. Figures 14.13 and 14.14 show variations of the ratio R_F of the voltage across the last unit in the cascade to the input voltage:

$$R_f = \frac{\text{Voltage on top unit}}{\text{Primary voltage}} = \frac{V_f}{V_p}$$

as a function of the input admittance λ for the four- and six-transformer arrangements.

Recovery overvoltage protection: HV testing sometimes results in breakdown of the test object. In ac voltage test, such a flashover would automatically trigger the opening of the main breaker on the primary winding of the test transformer (Parnell, 1961). However, since the main breaker takes several cycles to effectively open the circuit, transient recovery overvoltages result from the transformer remaining energized during this time and can produce repeated breakdown of the test object and/or subject the test transformers to considerable stresses as shown in Figure 14.15.

Noting that the flashover occurs at the peak of the ac voltage, when the supply current passes by zero, the only sources of energy available for sustaining the electric arc are

- The capacitance C_0 of the test object
- The capacitance C_w of the transformer
- The capacitance C_d of the voltage divider

Since the discharging of the stored energy lasts only a few μs, the arc is then extinguished afterward. The circuit will then attempt to restore the voltage at the test object. The transient voltage that follows, normalized to the source voltage, is

$$\frac{u_c(t)}{U_s} = \cos\omega t - \left(\cos\beta t + \frac{\alpha}{\beta}\sin\beta t\right)\cdot\exp(-\alpha t) \tag{14.2}$$

where $\alpha = \frac{R}{2L}$, $\beta = \sqrt{\frac{1}{LC} - \frac{R^2}{4L^2}}$, and U_s the amplitude of the test voltage.

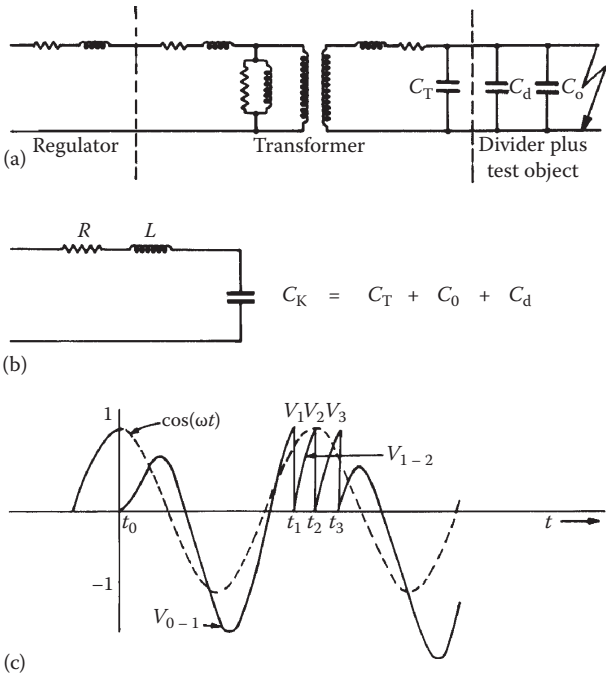


FIGURE 14.15 Recovery voltage following a flashover at the test object. (a) Circuit diagram. (b) Equivalent circuit. (c) Schematic representation of restrikes. (From Train and Trinh, 1973.)

Figure 14.15c illustrates the transient behavior of the circuit, following a flashover at the peak of the positive half cycle of the test voltage ($t = 0$). The transient recovery voltage is composed of two components: the test voltage and the transient response of the circuit to the sudden change in the test voltage at flashover. The latter component is an oscillating voltage at the natural frequency of the circuit and damped by the circuit resistance. One can see that the transient recovery voltage can exceed the peak ac voltage and may cause additional flashovers, as illustrated in Figure 14.15c. Furthermore, because of the polarity effect associated with breakdown in nonuniform field, which results in a higher breakdown voltage under negative polarity, the test object may withstand the first negative peak of the recovery voltage (Figure 14.5c). The test equipment is then subjected to higher stresses during the transient recovery, with possible detrimental effect to its insulation.

When multiple flashovers occur during the same half cycle, the transient recovery voltage is the sum of the test voltage and all the transient voltages associated the cancellation voltage at each flashover, according to

$$\frac{u_c(t)}{U_s} = \cos\omega t - \left[\cos\beta t + \frac{\alpha}{\beta}\sin\beta t\right]\cdot\exp(-\alpha t) - \sum_{j=1}^{i}\frac{U_j}{U_s}\left[\cos\beta t_j + \frac{\alpha}{\beta}\sin\beta t_j\right]\cdot\exp(-\alpha t_j) \qquad (14.3)$$

where

U_j is the voltage at the $(j + 1)$th flashover

t_j is the time evaluated from the $(j + 1)$th flashover

Transient recovery voltage under multiple flashovers can easily produce considerable overvoltages, reaching a factor of two during the negative half cycle. For cascade test transformers, the equivalent circuit is more complex but can be analyzed with transient analysis computer programs. Figure 14.16 compares the calculated transient recovery voltages (Figure 14.16a) with the actual recording of the recovery voltage at the test transformer shown in Figure 14.16b). The problem is further aggravated by the nonuniform distribution of the voltage among the units in cascade and, in particular, the top unit as discussed in the preceding

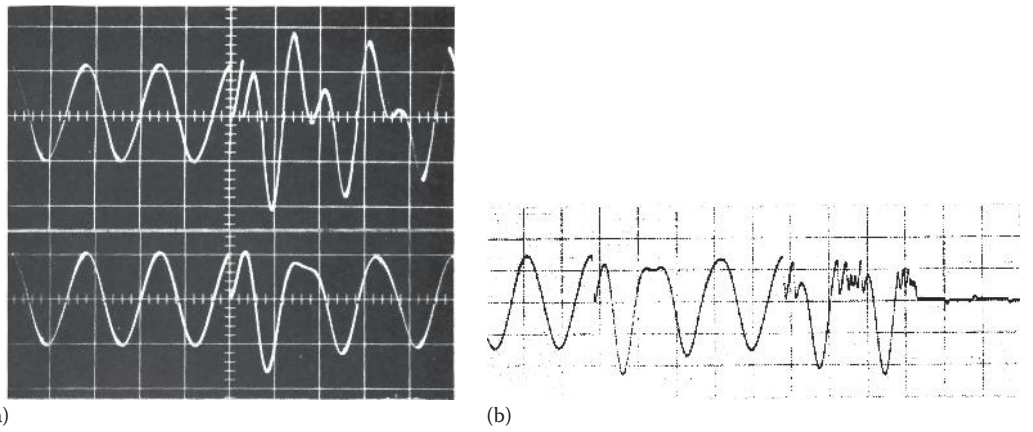


FIGURE 14.16 Recovery overvoltage following a flashover across the test object (From Train and Trinh, 1973): (a) oscillograms from computer simulation study, (b) recording of flashover voltage across the test transformer.

section (Figure 14.14). It is therefore crucial that some protection means be provided to the test transformers against the recovery overvoltages. Different approaches to eliminate the transient recovery overvoltage at test transformers have been evaluated by Train and Trinh (Train and Trinh, 1973). They are briefly summarized in the following, with their operating circuit presented in Figure 14.17.

Flashover voltage limitation: Is achieved by the use of a sphere gap connected across the test object as shown in Figure 14.17a. By adjusting the gap spacing to flashover at voltage slightly higher than the test voltage, adequate protection can be obtained for any voltage and test circuit parameters. Sphere gaps are, however, subjected to spurious flashovers by dust, flies, etc.; their dimensions and cost increase rapidly with the protection voltage level. Therefore, this technique is recommended only for indoor test at relatively low voltages.

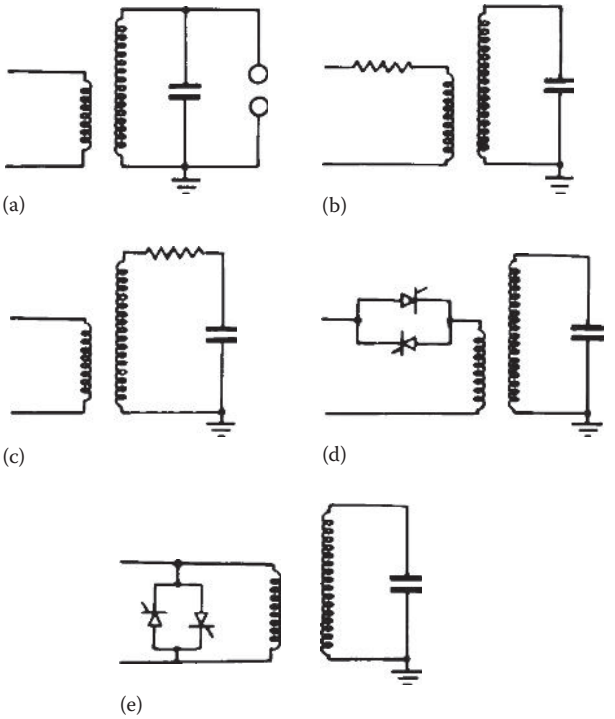


FIGURE 14.17 Protection schemes for recovery overvoltages. (a) Sphere gap. (b) Series primary damping. (c) Series secondary damping. (d) Series theyristor primary protection. (e) Paralleled thyristor primary protection. (From Train and Trinh, 1973.)

Limitation of the transformer short-circuit energy: May be achieved by insertion of a resistor in series with the transformer primary winding (Figure 14.17b) (Train, 1967). This protection technique is very reliable and inexpensive. However, the optimal value of the damping resistance is a function of the test circuit parameters: load capacitance, number of units in cascade, etc. Also, the resistance being permanently connected in the circuit may have to dissipate several tens of kilowatts.

Insertion of the damping resistor in the discharge circuit (Figure 14.17c) is possible (Parnell, 1961). The discharge is prolonged by the transformer self-capacitance until the power-frequency current from the supply can build up to a sufficiently high level to maintain the arc in a conducting state. The circuit is relatively inexpensive and protects the transformer against the voltage collapse produced by the flashover at the test object. However, it will not protect the transformer if the flashover occurs directly across its terminals. In addition, the protective resistor may have to dissipate several tens of kilowatts if the test object capacitance is high, and it must be very long for test at EHV levels, for example, some 20 m at voltage of 2 MV_{rms}.

Energy limitation can be made by means of a high-speed switch (Figure 14.17d), which rapidly disconnects the transformer primary winding from the supply following a flashover. The switch may be a pair of inverse-parallel-connected thyristors, ignitrons, or thyratrons. Opening the switch immediately after a flashover across the test object would disconnect the transformer from its supply, and no overvoltage would occur. However, the switch has to withstand the full supply voltage and continuously rate for the full primary current of the transformer.

Energy diversion technique: Figure 14.17e shows the protection scheme to divert the supply energy from the transformer circuit. The short-circuit current will flow through the switch until the primary protection of the transformer effectively opens the supply circuit. Since the primary winding is shorted immediately after the flashover occurs across the test object, no overvoltage would follow as illustrated by the result of a simulation study for two cascade transformers and a load capacitance of 3000 pF shown in Figure 14.18. The only drawback of this protection technique is the high short-circuit current experienced by the switching device and the regulator:

$$I_{sc} = U_{oc}/Z$$

where

U_{oc} is the open-circuit voltage across the transformer primary
Z is the short-circuit impedance of the regulator

To minimize the short-circuit current through the switch, an inductance of 5 mH, made of 30 turns of no. 2/0 conductor wound around the transformer base, is added in series with the regulator. This increases the regulator impedance by 2.5 Ω; however, considering the relatively high impedance, of some 50 Ω, of the

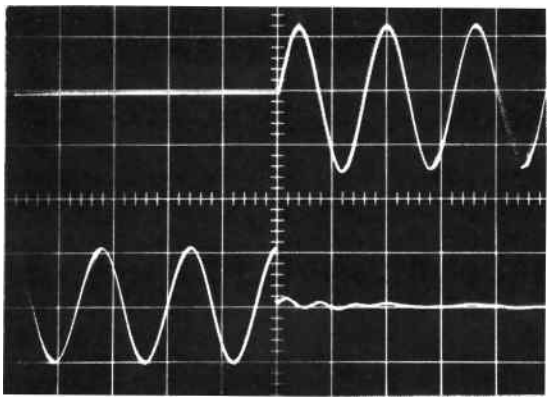


FIGURE 14.18 Simulation of the energy diversion technique for two cascade transformers and a capacitive load of 3000 pF. (From Train and Trinh, 1973.)

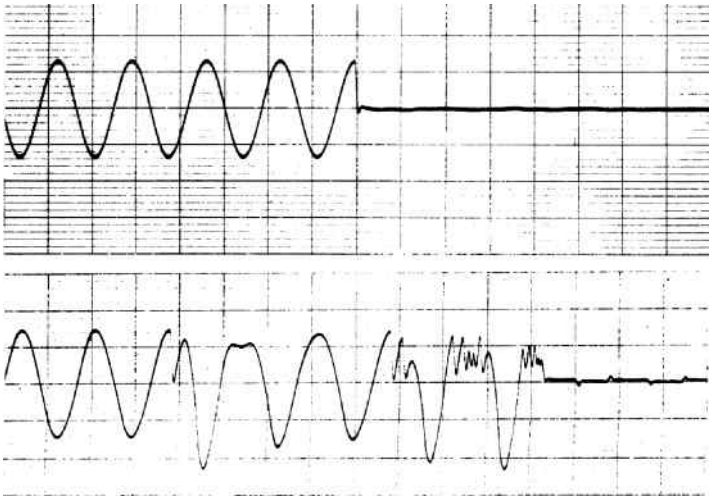


FIGURE 14.19 Recordings of the flashover voltages in a test with two cascade transformers on a capacitive load of 3000 pF with and without protection circuit. (From Train and Trinh, 1973.)

test transformer, the effect on its testing capability is less than 5%, which is quite acceptable. Figure 14.19 compares the voltages across a test object of 3000 pF, during a flashover with and without protection, and illustrates the performance of the protection circuit. Finally, a rugged switch is obtained with a triggered uniform field gap with tungsten-coated electrodes, which turns out to be a better fit for protection of the test transformer than the thyristor switch, which is somewhat sensitive to the short- circuit current.

14.3.1.2 Resonant Circuit

Resonant circuit is an alternative to generate an ac voltage. It is particularly adapted to high capacitive loads. Referring to the series-resonant circuit shown in Figure 14.20, which comprises an adjustable inductance L in series with an excitation transformer and the test capacitance C, the test voltage across the test object is

$$U_c = -\frac{jX_c}{R + j\left(X_l - X_c\right)}U_s$$

At resonance, $X_c = X_l$, the voltage U_c becomes

$$U_c = -j\frac{X_c}{R}U_s = \frac{-jX_l}{R}U_s = -jQU_s \tag{14.4}$$

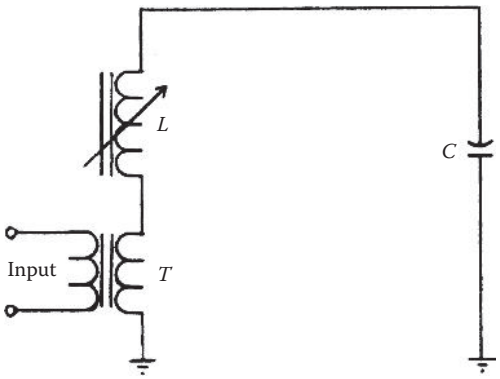


FIGURE 14.20 Series-resonant circuit. (From Booker, J.R. et al., *IEEE Trans*., PAS-102, 2501, 1983.)

where Q is the quality factor of the resonant circuit:

$$Q = \frac{X_l}{R} \tag{14.5}$$

The current in the test object is in phase with the source voltage. The power required from the supply source is

$$P_{in} = U_s I$$

Compared to the reactive power supplied to the capacitive load,

$$P_{re} = U_c I = Q U_s I = Q P_{in}$$

It follows that one can produce an HV from an exciting source of much lower voltage, which requires also lower power, depending on the quality factor Q. Normal operating condition of the series-resonant source requires therefore a relatively high quality factor, Q, typically higher than 50. Another advantage of the series-resonant circuit is the fact that the test object forms half of the circuit. This reduces considerably the size of the test equipment, comprising only the coil and the exciting source.

Circuit components: The preceding analysis, based on the equivalent circuit of Figure 14.20, has shown the importance to maintain a high quality factor Q for an adequate operation of the resonant circuit. The quality factor is largely dependent on the circuit components, namely, the adjustable reactances L and the capacitive load C. The influence of these two parameters on the operation of the resonant circuit will be examined in the following.

Adjustable reactance: Is the main element of the series-resonant circuit. It allows the tuning of the circuit to the frequency of the exciting source over the range of practical values of the capacitive load. The *Hipotronics* design uses a magnetic core made in two sections, one fixed and the other movable. The nominal inductance is formed of two series-connected windings around the two air gaps to minimize the losses associated with the leakage flux at the air gaps. By adjusting the position of the mobile half of the magnetic core, the air gaps are varied and hence, the inductance of the circuit, bringing it to resonance with the capacitive load at the frequency of the exciting source. Typical characteristics of the adjustable reactances used in the series-resonant circuit are given in Table 14.2. Each can cover a range of inductances between 470 and 9500 H (an adjustable ratio of 20:1).

The equivalent circuit for an adjustable reactance is shown in Figure 14.21a, where R_s is the winding resistance and R_p, in parallel with the leakage inductance, represents the leakage and hysteresis losses (Reid, 1974). The quality factor of the series-resonant circuit becomes

$$Q = \frac{1}{\frac{R_s}{X_L} + \frac{X_L}{R_p}}$$

TABLE 14.2

Typical Characteristics of an Adjustable Reactance for Series-Resonant Circuit

Reactance	**Values**	
Rated voltage	500 kV	
Current	5 A	
	Inductance (H)	**Capacitive Load (pF)**
One unit	470–9,500	1,000–60,000
Two units in series	940–19,000	500–30,000
Three units in series	1,410–28,500	330–20,000
Four units in series	1,880–38,000	250–15,000

Source: Reid, R. AC high voltage resonant testing. IEEE Paper No. C 74 038-6, *Winter Meeting*, New York, 1974.

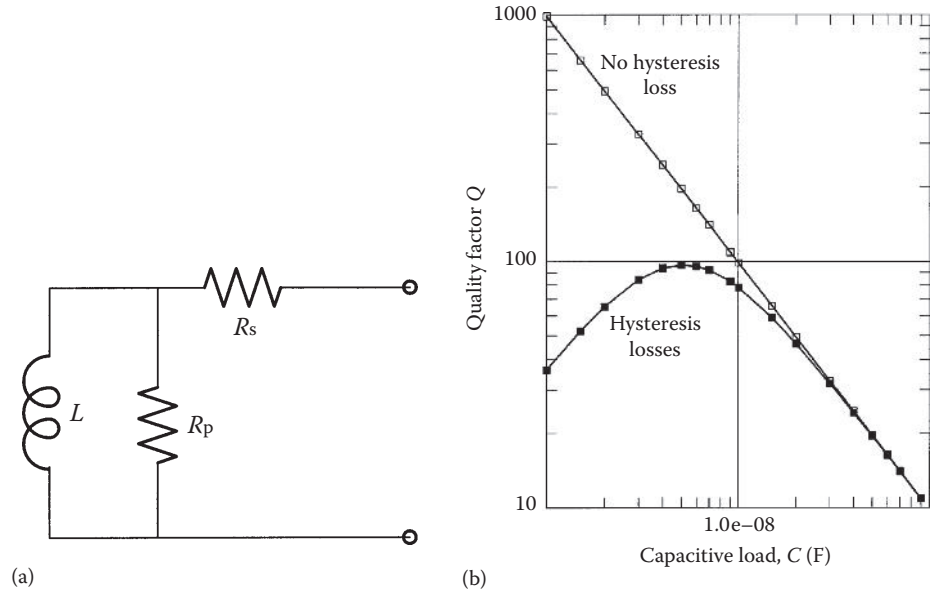


FIGURE 14.21 (a) Equivalent circuit of the coil with constant value for the leakage and hysteresis losses: L = 500 H, R_s = 2963 Ω and R_p = 10 MΩ. (b) Variations of the quality factor Q of the series-resonant circuit with the capacitive load. (Reid, R. AC high voltage resonant testing. IEEE Paper No. C 74 038-6, *Winter Meeting*, New York, 1974.)

that one can rewrite in terms of the capacitive load as

$$Q = \frac{1}{\omega R_s C + \dfrac{1}{\omega R_p C}} \tag{14.6}$$

Figure 14.21b illustrates the variations of the quality factor Q of a series-resonant circuit as a function of the capacitive load and a constant value of R_p. One can see that the effect of the hysteresis and leakage losses is considerable for low capacitive loads. It confirms the adequacy of the series-resonant circuit to high capacitive loads.

Capacitive load with losses: The influence of a capacitive load with losses on the quality factor of the circuit can be evaluated by representing these losses by a series resistance R_c (Reid, 1974). The circuit resistance R becomes

$$R = R_s + R_c$$

where

R_s is the resistance of the coil
R_c is the losses of the capacitive load

The quality factor becomes

$$Q = \frac{\omega L}{R} = \frac{\omega L}{R_s \left(1 + \dfrac{R_c}{R_s}\right)}$$

that one can express in terms of the quality factor Q_L and Q_c of the reactance and capacitive load, respectively:

$$Q = \frac{Q_L}{1 + \dfrac{Q_L}{Q_C}} \tag{14.7}$$

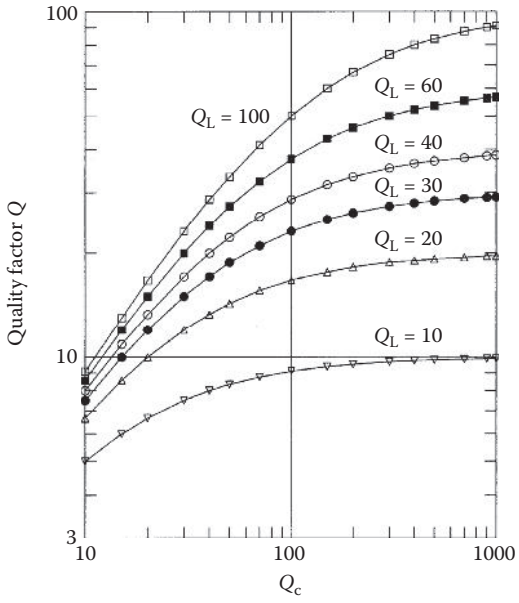


FIGURE 14.22 Variations of the quality factor Q of the series-resonant circuit with the quality factor Q_C of the capacitive load for different value of Q_L, the quality factor of the inductance.

Figure 14.22 shows the variations of the quality factor of the circuit Q as a function of the quality factor of the capacitive load Q_C for different values of the quality factor of the coil Q_L. It can be seen that a capacitive load with losses can considerably reduce the performance of the series-resonant circuit.

Cascade connection and distribution of the voltage: As with test transformers, several adjustable reactances can be connected in series/parallel to provide a higher output voltage than with a single unit. Figures 14.23 and 14.24 illustrate a few configurations for series/parallel resonant circuits. They allow the adaptation of the

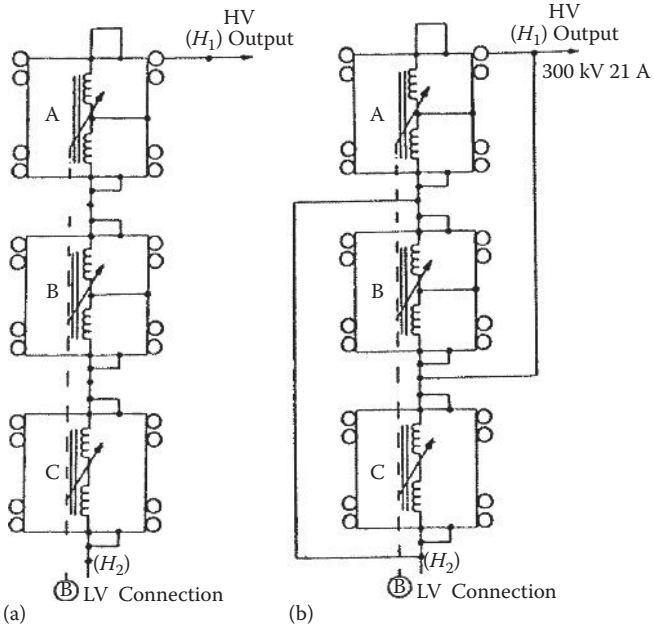


FIGURE 14.23 Typical (a) series/(b) parallel arrangements of reactances for generation of high ac voltage. (From Booker, J.R. et al., *IEEE Trans.*, PAS-102, 2501, 1983.)

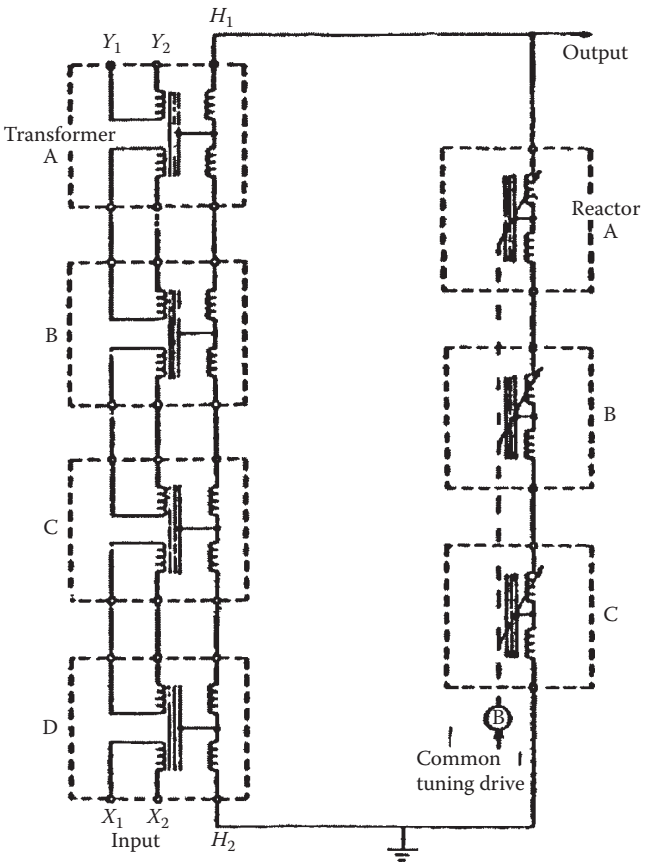


FIGURE 14.24 Series/parallel arrangement of reactances for generation of ac voltage. (From Booker, J.R. et al., *IEEE Trans*., PAS-102, 2501, 1983.)

circuit to a wide variety of capacitive loads—between 250 and 60,000 pF—and at voltages up to 900–1200 kV. Figure 14.25 shows an 800 kV cascaded series-resonant circuit at IREQ. The connection in cascade of the reactances also subjects these units to a nonuniform distribution of the voltage produced. The problem is, however, less severe since the generated voltage comes from the magnetic energy, stored in the individual reactances in cascade, and is affected only by the stray capacitances at these units.

Transient recovery voltage: The series-resonant circuit presents a great advantage associated with the complete absence of transient recovery overvoltage. In effect, the series-resonant circuit operates close to the resonance of the circuit, with a high quality factor Q. During flashover, the resistance of the electric arc detunes the circuit and discharges the stored energy. It takes several tens of cycles following the flashover for the circuit to build up the required energy for the test voltage. The analysis of the transient response of the circuit can be made using the series RLC circuit. The transient recovery voltage normalized to the source voltage U_s is given by

$$\frac{u_c(t)}{U_s} = \cos\omega t - \left(\cos\beta t + \frac{\alpha}{\beta}\sin\beta t\right)\cdot\exp(-\alpha t) \tag{14.2}$$

with the following conditions specific to the series-resonant circuit:

$$\beta = \omega\sqrt{1-\frac{1}{4Q^2}} \approx \omega, \quad \alpha = \frac{R}{2L} = \frac{\omega}{2Q}, \quad \text{and} \frac{\alpha}{\beta} = \frac{1}{2Q}$$

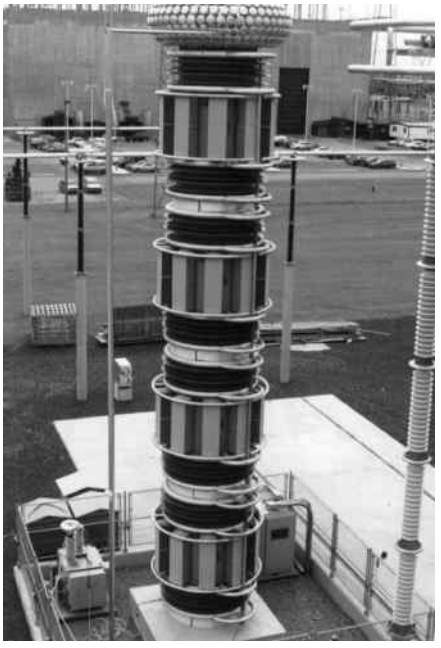


FIGURE 14.25 Cascaded series-resonant circuit at IREQ. (Photo Courtesy of Hydro-Québec.).

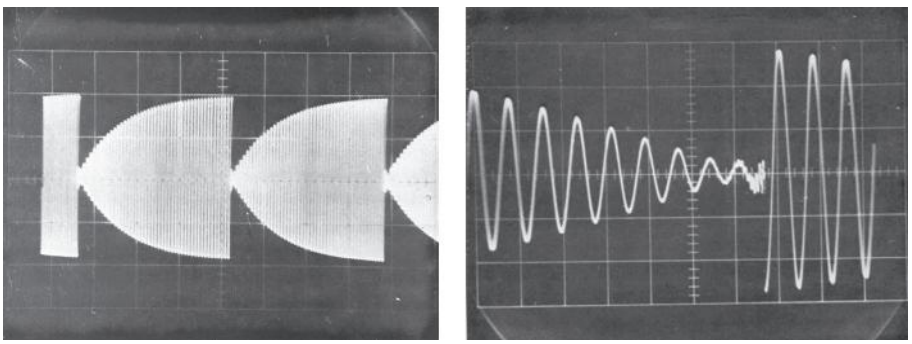
which simplify the earlier expression for the recovery voltage:

$$\frac{u_c(t)}{U_s} = \left[1 - \exp\left(-\frac{\omega t}{2Q}\right)\right]\cdot\cos\omega t \tag{14.8}$$

Equation 14.8 shows that the recovery voltage in a series-resonant circuit is essentially a sine wave with an exponentially increasing amplitude of $1 - \exp(-\alpha t)$. No overvoltage can occur during the recovery period of the test voltage, as shown in Figure 14.26, which shows the transient recovery voltage subsequent to a flashover in a series-resonant circuit. The time constant of the voltage recovery is

$$\tau = \frac{1}{\alpha} = \frac{2Q}{\omega} = \frac{2Q}{2\pi f} = \frac{Q}{\pi}T,$$

with T representing one cycle of the test voltage.



(a) (b)

FIGURE 14.26 Recovery voltage of a series-resonant circuit after a flashover across the test object. (a) Time scale: 0.2 s/div. (b) Time scale: 20 ms/div. (From Train, D. and Trinh, G.N., Prevention of recovery overvoltages on high voltage testing transformers, *IEEE Trans*,. PAS-92, 1631, 1973; Booker, J.R., Nichols, D.R., and Lazelere, W., Design of a modular UHV AC outdoor test system, *IEEE Trans*., PAS-102, 2501, 1983.)

It follows that the test voltage will get back to its test value after Q cycles of the applied voltage (three times the time constant τ), which gives enough time for the protection circuit to operate.

Frequency: Series-resonant circuit is particularly suitable for the generation of ac voltage of a different frequency than the power frequency. It suffices to vary the resonant frequency of the circuit to the selected value. However, it requires an exciting source that can operate over the appropriate range of frequencies. Series-resonant circuit operating up to frequencies in the kHz range is possible in this way.

14.3.1.3 Rotating Machines

Induced voltage tests on power transformers to verify its dielectric performance at voltages higher than its nominal value create a particular problem due to the saturation of the transformer core at the test voltage. To avoid saturation of the transformer core, the test is made at a frequency higher than the power frequency, typically 180 Hz. To provide the high power level required in the test, thyristor-controlled motor-generator are usually the appropriate solution. The frequency of the generated voltage can be varied over a range of frequencies of practical interest.

14.3.2 DC Voltage

Because of its ability to maintain a constant dielectric stress, HVDC testing has been performed in HV laboratories since the early days of insulation studies. Considerable works were devoted to the development of appropriate sources for HVDC test. We review in the following the most widely used today.

14.3.2.1 Basic Rectifier Circuit

Figure 14.27 shows the basic single-phase half-wave rectifier circuit currently used to produce a dc voltage, while its operating characteristics are illustrated in Figure 14.28. The ac voltage supplied by the HV transformer is rectified by the diode D and charges the source capacitor C. If no load current is drawn and the source capacitor is without loss, the output dc voltage is constant and equal to the peak value of the ac voltage.

When a resistive load is connected at the output, a current is circulating through the resistance R and discharging the capacitance C. If the time constant $T = RC$ is large, the dc voltage will remain higher than the instantaneous ac voltage $v_{ac}(t)$, and the diode remains open over most of the ac cycle. The dc voltage across the source capacitor $u_{dc}(t)$ will decrease according to

$$u_{dc}(t) = U_{max} \exp\left(-\frac{t}{RC}\right)$$

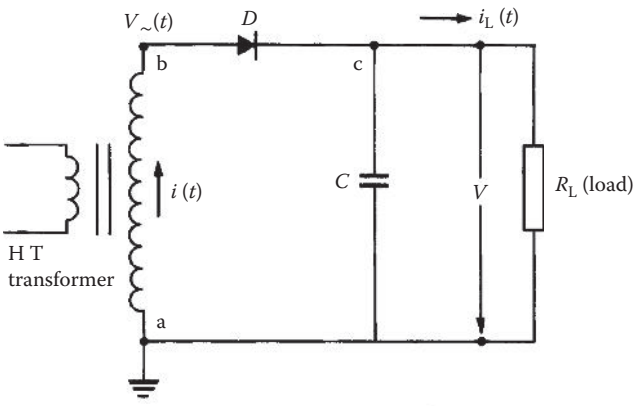


FIGURE 14.27 Single-phase half-wave rectifier circuit.

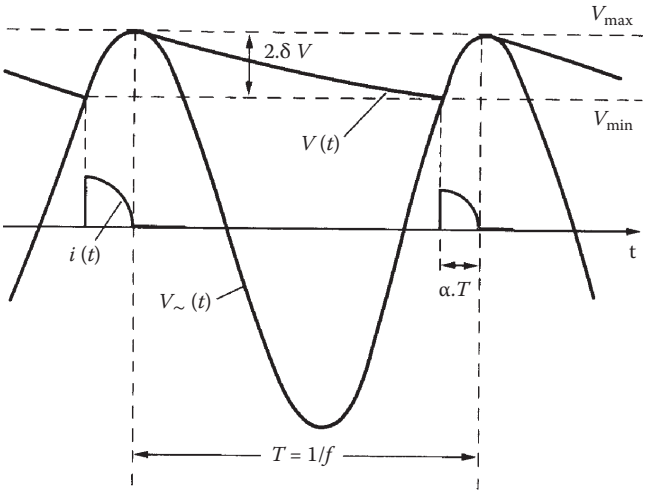


FIGURE 14.28 Voltage and current during one cycle of the ac voltage.

with the time origin taken at the peak of the ac voltage. As the dc voltage decreases, the ac voltage passes its negative peak value and increases to its positive peak voltage. Eventually, the ac voltage will exceed the dc voltage, initiating the charging of the source capacitor through the diode. This will last until the ac voltage reaches its peak value and the process repeats itself. The resulting dc voltage fluctuates in time, producing a ripple of amplitude $2\delta V$, with V the average value of the dc voltage. It effectively defines the quality of the dc voltage produced. The parameter δ is referred to as the *ripple factor* and should be less than 5%.

A simple relation can be derived for the ripple factor as

$$Q = 2\mathrm{d}VC = IT \quad \text{and} \quad \mathrm{d}V = \frac{IT}{2C} = \frac{I}{2fC} \tag{14.9}$$

where

Q is the charge transferred to the load in each cycle
I is the mean dc output current

Full-wave circuit: The preceding relation (14.9) shows that the ripple factor δ is inversely proportional to the charging frequency of source capacitor. One way to improve the ripple factor is with the full-wave rectifier circuit shown in Figure 14.29. One can verify that in this circuit, the source capacitor is charged up in every half cycle of the ac voltage, alternatively through the diodes D_1 and D_2, which doubles the charging frequency of the source capacitor C, and, accordingly, reduces the ripple factor.

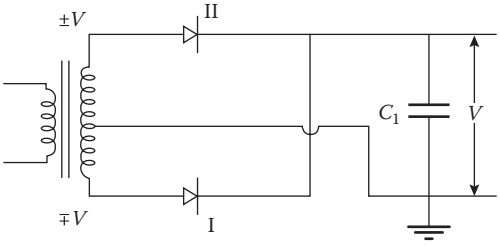


FIGURE 14.29 Full-wave rectifier circuit.

14.3.2.2 Voltage Doubling Circuit

Voltage doubling circuit is a convenient way to obtain a high dc voltage. Figure 14.30 shows a typical voltage doubling circuit. With the HV winding grounded at one end, the diode D_1 will conduct when the voltage at A decreases below zero during the negative half cycle of the ac voltage and charges the capacitor C_1 up to the peak voltage V_{max} at the peak of the negative half cycle. The voltage at point B is maintained at zero during the charging period of the capacitor C_1. Figure 14.31 illustrates the variations of the voltage at different points in the circuit.

As the ac voltage at point A starts to increase, pushing the voltage at B above zero, this blocks the diode D_1, while bringing the diode D_2 to conduction to charge the capacitor C_2. The capacitor C_2 is charged up to a voltage of $2V_{max}$, which is attained at the peak of the positive half cycle of the ac voltage.

As the ac voltage starts to decrease, the voltage at point A follows the ac voltage and brings with it the voltage at point B, which is, however, higher than the voltage at point A by V_{max}, the charged voltage across the capacitor C_1. The output voltage at point D remains at $2V_{max}$, the charged voltage of the capacitor C_2, since the diode D_2 is now blocked. As a result, after the first cycle of the ac voltage, the output voltage is $2V_{max}$, the charged voltage across the capacitor C_2; the voltage at point A varies with the applied voltage between $-V_{max}$ and V_{max}; and the voltage at point B fluctuates between 0 and $2V_{max}$, while the charged voltage across the capacitor C_1 remains at V_{max}.

When a resistive load is connected at the output, a current will circulate, discharging the capacitor C_2. The dc voltage across the source capacitor $u_{dc}(t)$ will decrease according to

$$u_{dc}(t) = U_{max} \exp\left(-\frac{t}{RC_2}\right)$$

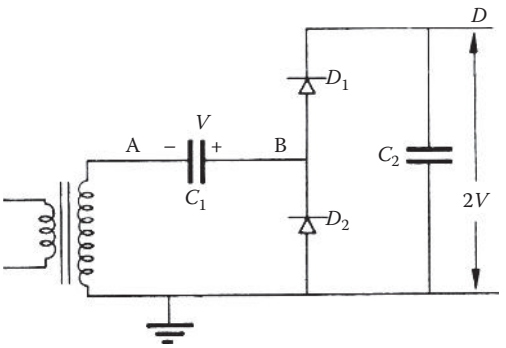


FIGURE 14.30 Voltage doubling circuit.

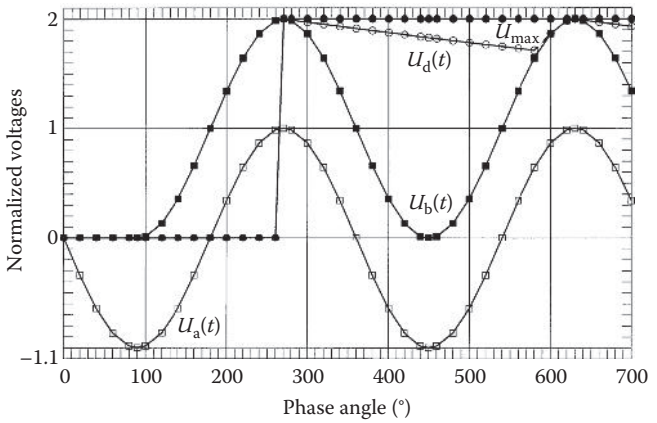


FIGURE 14.31 Variation of voltages at different points in the voltage doubling circuit.

with the time origin taken at the peak of the positive half cycle of the ac voltage. As the dc voltage decreases, the voltage at point B passes its minimum peak value and increases to its maximum peak voltage. Eventually, the voltage at point B will exceed the dc voltage, initiating the charging of the capacitor C_2 through the diode D_2. This will last until the voltage at point B reaches its peak value and the process repeats itself.

It follows from the preceding operation of the voltage doubling circuit that the source capacitor is C_2, which effectively keeps the charge and supplies the current to the load. The capacitor C_1 is actually the feeding capacitor to compensate for the loss of charge in the source capacitor C_2 due to a resistive load. The discharging of the source capacitor by the resistive load will result in a ripple in the output voltage, which defines the quality of the dc voltage source in terms of the ripple factor δ, according to

$$Q = 2\,\mathrm{d}V_{\max}C_2 = IT \quad \text{and} \quad \mathrm{d}V_{\max} = \frac{IT}{2C_2} = \frac{I}{2fC_2} \tag{14.10}$$

where

Q is the charge transferred to the load in each cycle
I is the mean dc output current

As discussed earlier, the efficiency of the voltage doubling circuit is also improved by the use of a double-phase rectifier circuit, which effectively doubles the charging frequency of the source capacitor C_2 and, correspondingly, reduces the ripple factor δ.

14.3.2.3 Cascade Rectifier

The voltage doubling circuit is the basic circuit for today's cascade rectifier, which was first introduced by Greinacher and improved by Cockcroft and Walton (Cockcroft and Walton, 1932). Figure 14.32 shows



FIGURE 14.32 1200 kV cascaded rectifier at IREQ cable test area. (Photo Courtesy of Hydro-Québec.)

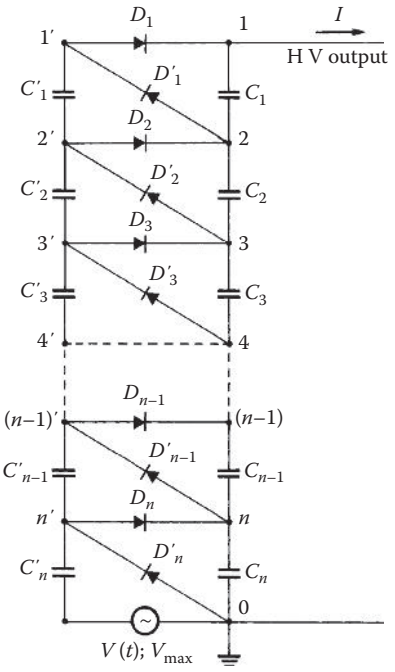


FIGURE 14.33 Cascade rectifier circuit.

the cascaded rectifier at IREQ cable test area. Figure 14.33 illustrates the circuit of a cascade rectifier, as currently used to produce HVDC test. One recognizes the voltage doubling circuit at the ground stage of the cascade arrangement, which is simply an assembly of n identical voltage doubling stages without the ac source. The source capacitance is formed of n series-connected capacitors $C_1 \ldots C_n$, while the feeding capacitance is formed of n series-connected capacitors C_1', $C_2' \ldots C_n'$ with the last capacitor connected to the HV end of the ac source.

The operation of the n-stage cascade rectifier is the same as in the voltage doubling circuit. Assuming all capacitors are identical, the output dc voltage is $2nV_{max}$, distributed equally among the n capacitors; each withholds a voltage of $2V_{max}$; and the effective source capacitance is C/n. The voltage at the feeding capacitors fluctuates between $2nV_{max}$ and $(2n - 1)V_{max}$ as the ac voltage varies between $-V_{max}$ and V_{max}, as illustrated in Figure 14.34.

When a resistive load is connected to the output, a current circulates and discharges the source capacitors C_k, which reduces the voltage at the nodes until the voltage on the feeding capacitors increases past the respective node voltages, causing the diodes D_k to conduct and charges the corresponding source capacitors. A ripple will result in the output voltage and define the quality of the cascaded rectifier in terms of a ripple factor δV. Furthermore, the output voltage will not reach the maximum value of $2nV_{max}$, short of a voltage drop ΔV_0. When all the capacitances have the same value, the following expressions can be derived for ΔV_0 and δV (Kuffel et al., 2000):

$$\delta V = \frac{I}{fC}\frac{n(n+1)}{4} \tag{14.11}$$

where δV is the ripple factor and

$$\Delta V_0 = \frac{I}{fC}\left(\frac{2n^3}{3} + \frac{n^2}{2} - \frac{n}{6}\right) \tag{14.12}$$

where ΔV_0 is the voltage drop in the output.

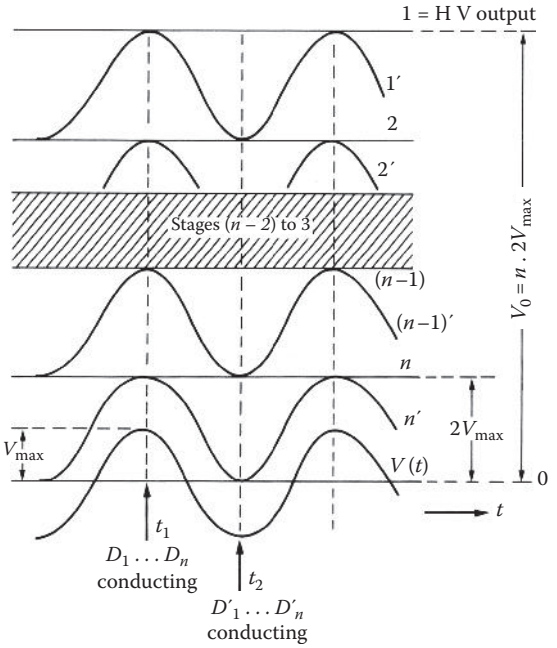


FIGURE 14.34 Variations of the potential at different nodes in the cascaded rectifier circuit. (From Kuffel and Zaengl, 1984.)

The maximum output voltage from a cascade rectifier is then

$$V_{0\max} = 2nV_{\max} - \Delta V_0 = 2nV_{\max} - \frac{I}{fC}\left(\frac{2n^3}{3} + \frac{n^2}{2} - \frac{n}{6}\right) \tag{14.13}$$

It follows from Equations 14.11 through 14.13 that the voltage drop and ripple factor are inversely proportional to $f\,C$. The best way to improve the performance of a cascade rectifier is by the use of a high-frequency ac supply source, a solution currently used with the ac frequency of a few kHz up to 10 kHz.

Rectifier using cascade transformers: Cascade rectifier can also be obtained from cascade transformers. Every HV winding feeds two half-wave rectifiers, and the output voltage is simply the sum of all the cascade stages. This circuit provides an economical dc power supply for HVDC testing, with low ripple factor and high power capability. However, as for cascade transformers, the number of cascade stages is limited since the lower units have to supply the required power for the upper units.

14.3.3 Impulse Voltage

Power systems are subjected to transient overvoltages from lightning incidences and switching operations (see Chapter 1). Since their actual wave shape varies as a result of reflections of the transient wave, it becomes necessary to simplify and standardize the representation of these overvoltages by a double exponential impulse having specific front time and time-to-half value: 1.2 μs/50 μs for lightning impulses and 250 μs/2500 μs for switching impulses (IEC Standard 60060-1, 1989).

Figure 14.35 shows the two basic impulse voltages representing, respectively, standard lightning and switching impulses. Because of the undefined origin of the impulse wave, the front time T_f is defined in IEC Standard 60060 (IEC Standard 60060-1, 1989) as

$$T_f = 1.67\left(T_{90\%} - T_{30\%}\right) \tag{14.14}$$

where $T_{30\%}$ and $T_{90\%}$ are, respectively, the times the impulse voltage reaches 30% and 90% of its peak value.

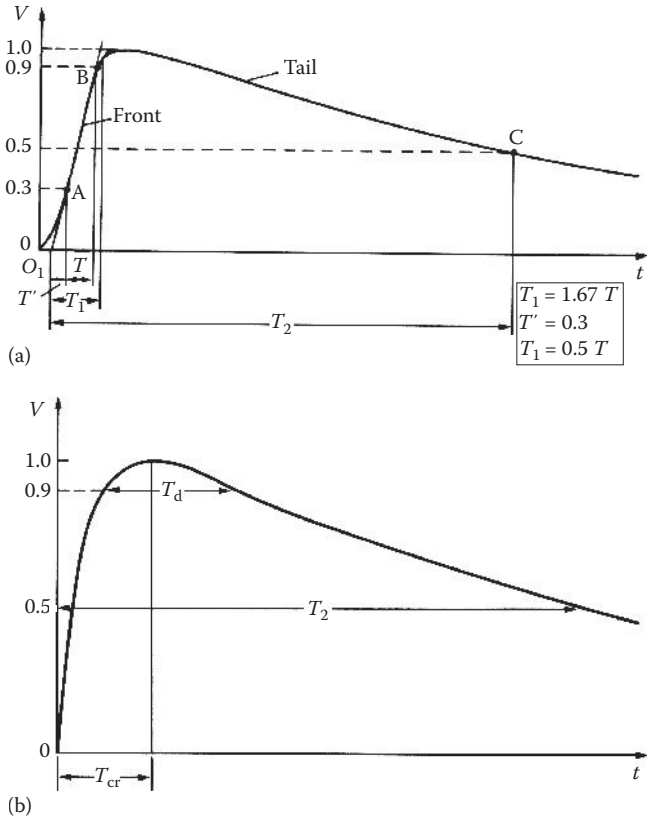


FIGURE 14.35 Wave shapes for standard impulse voltages. (a) Standard lightning impulse: 1.2 μs by 50 μs. (b) Standard switching impulse: 250 μs by 2500 μs. (From IEC Standard 60060–1, *High Voltage Test Techniques—Part 1: General Definitions and Test Requirements*, IEC, Geneva, Switzerland, 1989.)

14.3.3.1 Impulse Generators

The generation of an impulse voltage is basically achieved by charging a capacitor and discharging it through the test object in a controlled manner so as to produce the appropriate impulse shape.

Basic circuit: Two basic circuits of an impulse generator that produce a double exponential impulse voltage are presented in Figure 14.36, respectively, for the cases of high- and low-efficiency circuits. The generator has a capacitance C_0, charged to a voltage U_c and separated from the rest of the test circuit by a triggered spark gap G. The test object has a capacitance C, which includes also the capacitance of the divider connected across its terminals. The resistances R_1 and R_2 control the impulse front time and time to half value, respectively.

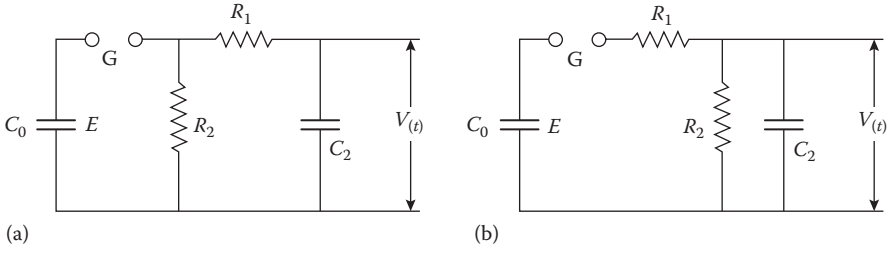


FIGURE 14.36 Basic circuit of a double exponential impulse generator. (a) High-efficiency circuit. (b) Low-efficiency circuit.

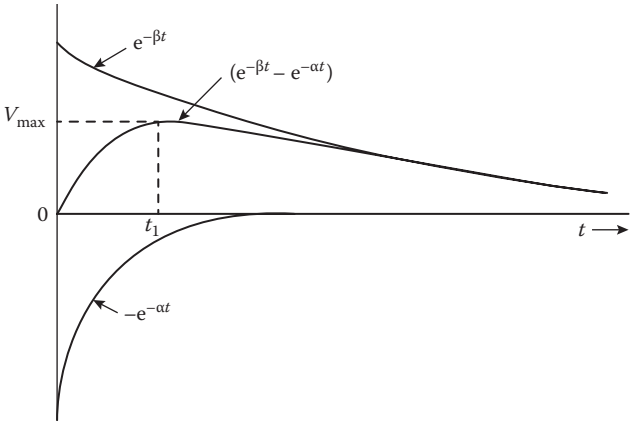


FIGURE 14.37 Double exponential wave shape of the impulse voltage.

Triggering the spark gap G discharges the generator capacitor C_0 through the test object. In this process, the capacitor C_2 is first charged up to its peak value before discharging again to zero. The resulting voltage $V(t)$, shown in Figure 14.37, is the sum of two exponential voltages:

$$v(t) = U_c K \left[\exp(-bt) - \exp(-at)\right] \tag{14.15}$$

where

α and β are, respectively, the inverse of time constants of the two exponential functions
K is a constant dependent of the circuit topology and parameters

Combining the circuits of Figure 14.36 gives the general circuit for producing a double exponential impulse voltage, shown in Figure 14.38. Applying the Kirchhoff law to the voltages in the loop R_2–R_1–C_2 and R_3–R_2–C_0,

$$R_1 i_2 + \frac{1}{C}\int_0^t i_2\,dt - R_2(i_1 - i_2) = 0$$

and

$$R_3 i_1 + R_2(i_1 - i_2) + \frac{1}{C_0}\int_0^t i_1\,dt = U_c$$

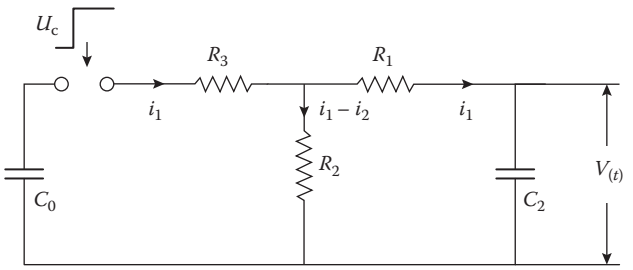


FIGURE 14.38 General circuit for double exponential impulse generator.

The solution of which is

$$V(t) = \frac{U_c A}{a - b}\left[\exp(-bt) - \exp(-at)\right] = U_c K\left[\exp(-bt) - \exp(-at)\right]$$

with

$$a, b = \frac{X \pm \sqrt{X^2 - 4Y}}{2} \quad \text{and} \quad K = \frac{A}{a - b}$$

$$A = \frac{R_2 C_0}{C_2\left(R_1 R_2 C_0 + R_2 R_3 C_0 + R_1 R_3 C_0\right)}$$

$$X = \frac{R_1 C_2 + R_2 C_0 + R_2 C_2 + R_3 C_0}{C_2\left(R_1 R_2 C_0 + R_2 R_3 C_0 + R_1 R_3 C_0\right)}$$

$$Y = \frac{1}{C_2\left(R_1 R_2 C_0 + R_2 R_3 C_0 + R_1 R_3 C_0\right)}$$

The solutions for the circuits of Figure 14.36a and b correspond to the cases where R_3 and R_1 are equal to zero, respectively.

Circuit efficiency: The efficiency η of the impulse generator circuit is defined as the ratio of the peak voltage U_p to the charging voltage U_c:

$$\eta = \frac{U_p}{U_c}$$

The peak value of the double exponential impulse occurs when

$$\frac{dV(t)}{dt} = 0$$

Taking the derivative of Equation 14.15 gives

$$\frac{dv(t)}{dt} = U_c K\left[-b\exp(-bt) + a\exp(-at)\right] = 0$$

or

$$b\exp(-bt) = a\exp(-at)$$

Taking the logarithm yields

$$(-bt) + \ln b = (-at) + \ln a$$

and

$$t_{max} = \frac{\ln a - \ln b}{a - b} = \frac{\ln\left(\frac{a}{b}\right)}{a - b}$$

The expression for the peak voltage U_p becomes

$$U_p = U_c K\left[\exp(-bt_{max}) - \exp(-at_{max})\right] \tag{14.16}$$

and the efficiency of the circuit η is

$$\eta = \frac{U_p}{U_c} = K\left[\exp\left(-bt_{max}\right) - \exp\left(-at_{max}\right)\right] = \eta_c\eta_w \tag{14.17}$$

Therefore, the circuit efficiency comprises two components:

- $\eta_c = K$ is the contribution of the circuit.
- $\eta_w = \exp\left(-bt_{max}\right) - \exp\left(-at_{max}\right)$ is the contribution from the shape of the impulse voltage.

The impulse shape efficiency η_w is a function of the ratio of the time-to-half value to front time, T_t/T_f, as illustrated in Figure 14.39:

- For a standard lightning impulse of 1.2/50 μs, $\alpha = 2.469\ \mu s^{-1}$, $\beta = 1.46 \times 10^{-2}\ \mu s^{-1}$, the wave shape efficiency η_w is 96%.
- For a standard switching impulse of 250/2500 μs, $\alpha = 9.756 \times 10^{-3}\ \mu s^{-1}$, $\beta = 3.413 \times 10^{-4}\ \mu s^{-1}$, the wave shape efficiency η_w is 85%.

The relative position of the resistances R_2 with respect to R_1 in the circuits of Figure 14.36 has a considerable influence on the efficiency of the circuit. In the circuit of Figure 14.36b, the two resistances form a voltage divider across the capacitance C_0, which results in a reduction of the voltage applied to C_2 and hence a lower efficiency. Figure 14.40 shows how the efficiency of the two circuits varies with the ratio C_2/C_0 for different impulse wave shapes.

Simplified method for estimation of circuit parameters: The preceding analysis of the double exponential impulse shows that the exact evaluation of the circuit parameters to meet a given impulse wave shape could be tedious. A practical approach is to obtain a first estimation of the circuit parameters from simplified circuit and finalize the choice subsequently according to the actual circuit components.

The final selection of the circuit parameters can also be achieved using an available program, for example, Microcap.

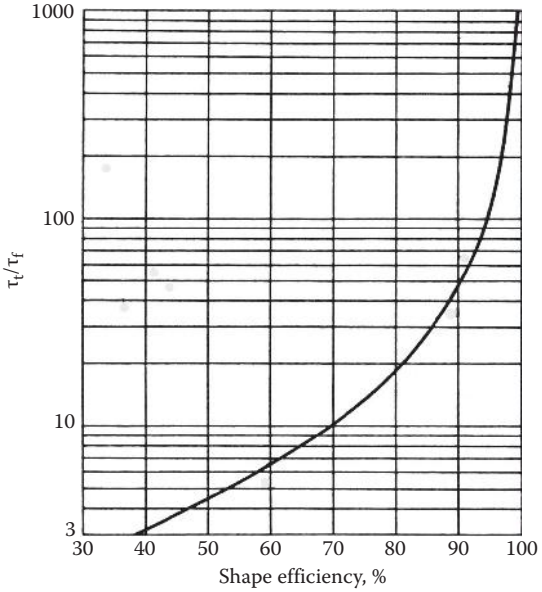
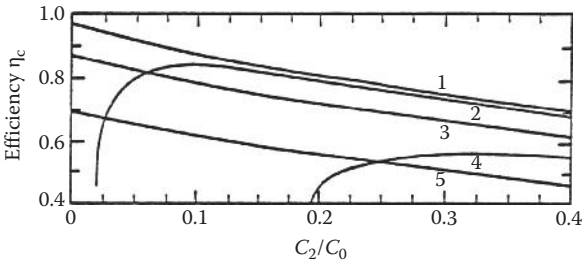


FIGURE 14.39 Variation of the shape efficiency η_w in % with the ratio of the wave tail to front time T_t/T_f. (From Creed, F. and Collins, T., The shaping circuit for high voltage impulses, *IEEE Trans*, PAS-90, 2239, 1971.)



Curve #	1	2	3	4	5
Ratio T_f/T_t	1/50	1/50	1/10	1/10	1/5
Circuit efficiency	High	Low	High	Low	High

FIGURE 14.40 (a) Variation of the circuit efficiency as a function of C_2/C_0 for high- and low-efficiency circuits. (b) Legend to Figure 14.40a.

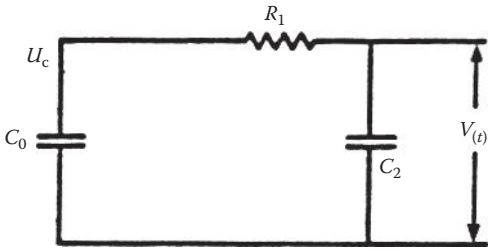


FIGURE 14.41 Charging circuit for evaluation of the front time.

A simplification of the general circuit for generation of the double exponential impulse can be obtained by breaking it down in two simplified circuits: one for the charging of capacitance C_2 (figure 14.41) and the second for the discharging of the two capacitances C_0 and C_2 (Figure 14.42).

From Figure 14.41,

$$\frac{1}{a} = R_1 C_{eq} = R_1 \frac{C_0 C_2}{C_0 + C_2}$$

The charging voltage $V(t)$ is

$$V(t) = U_c \left(1 - \exp\left(-\frac{t}{R_1 C_{eq}}\right)\right) \tag{14.18}$$

which allows the evaluation of the IEC front time as

$$T_f = 1.67\,(T_{90\%} - T_{30\%}) = 3.25\,R_1 C_{eq}$$

For a standard lightning impulse, T_f = 1.2 μs, and the circuit time constant is $R_1 C_{eq}$ = 0.37 μs, which allows a quick estimation of the resistance R_1.

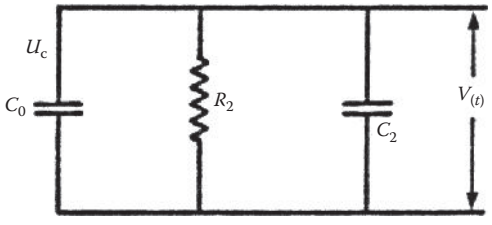


FIGURE 14.42 Discharging circuit for evaluation of the decaying time.

From Figure 14.42,

$$\frac{1}{\beta} = R_2 \left(C_0 + C_2\right) = R_2 C_p$$

The discharging voltage is

$$V(t) = U_c \exp\left(-\frac{t}{R_2 C_p}\right) \tag{14.19}$$

The approximate expression for the time to half value becomes

$$T_t = 0.7 R_2 C_p$$

For a standard lightning impulse, T_t = 50 μs, and the circuit time constant is R_2C_p = 70 μs, which allows a quick estimation of the resistance R_2.

It should be noted here that the simplified approach assumes that the peak value of the impulse voltage is 1, which is higher than the actual value of U_p. The error is higher with smaller ratio of T_t/T_f, being 4% for a standard lightning impulse and 15% for a switching impulse.

Influence of the circuit inductance on the wave front of the impulse voltage: A practical circuit comprises always some parasitic inductances in the generator, the test object, and the connection leads in the circuit. These are distributed inductances, but one can evaluate their influence on the wave front of the generated impulse voltage using the simplified circuit of Figure 14.43a, where the discharging resistance R_2 has been omitted.

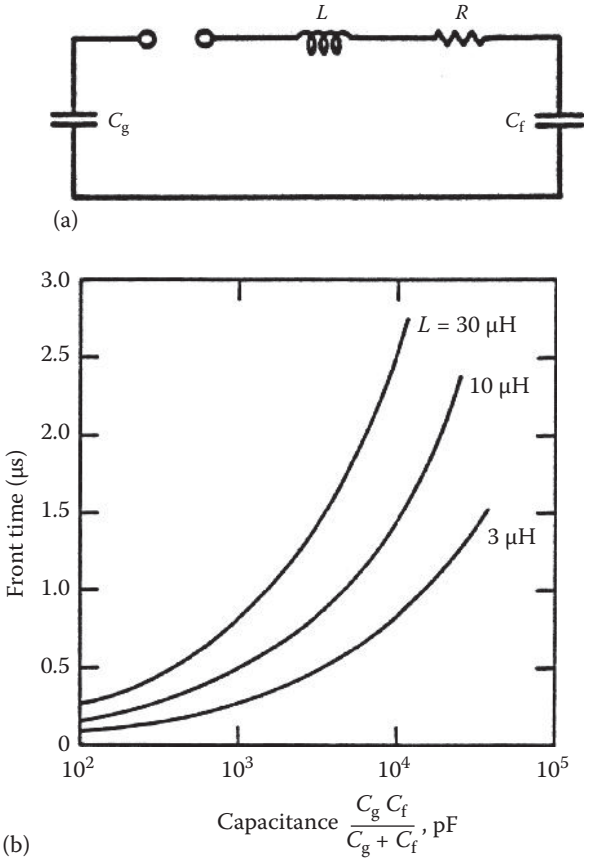


FIGURE 14.43 Influence of the circuit parasitic inductance on the front time T_f. (a) Equivalent circuit. (b) Variation of the front time with equivalent capacitance for different values of circuit inductance.

The transient voltage $V(t)$ will be a damped oscillation at the natural frequency of the circuit. It can be shown that, for any value of L, the shortest nonoscillatory front time corresponds to the conditions of a critically damped circuit, that is, when the resistance R is equal to

$$R = R_c = 2\sqrt{\frac{L}{C_s}} \quad \text{with} \quad C_s = \frac{C_g C_f}{C_g + C_f}$$

$$V(t) = U_c \frac{C_s}{C_f}\left[1 - \left(1 + \frac{2}{R_c t}\right)\exp\left(-\frac{2}{R_c}t\right)\right] \tag{14.20}$$

Figure 14.43b shows the variation of the front time T_f defined according to the IEC 60060-1 definition of the virtual front time $T_f = 1.67(T_{90\%} - T_{30\%})$, using Equation 14.20 for the critically damped oscillating impulse.

Multistage impulse generator: A single-stage impulse generator is limited in size and maximum charging voltage U_c and hence the generating impulse voltage U_p is typically a few hundreds of kV. To generate impulse voltage in the MV range, it is necessary to connect several stages in series. One obtains the multistage Marx impulse generator circuit, currently used in HV laboratories. Figure 14.44 shows a 3.2 MV, 200 kJ, multistage impulse generator at IREQ.

Referring to Figure 14.45 that shows an N-stage impulse generator circuit, each stage has a capacitor C' and a charging resistor R_c' of high values. The N stages are connected in series through N spark gaps S. Operating the generator consists of charging at first the N-stage capacitors C' in parallel to the voltage U_c, through the resistances R_c'. Triggering the N spark gaps connects the N-stage capacitors in series, discharging them through the test object through the resistors R_s' and R_t' of produce the appropriate wave shape to the generated impulse voltage.



FIGURE 14.44 A 3.2 MV, 200 kJ, 8-stage impulse generator at IREQ. (Photo Courtesy of Hydro-Québec.)

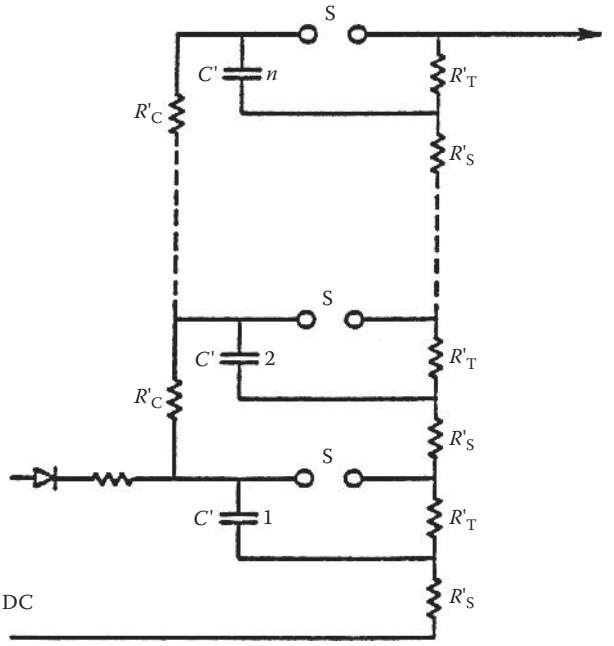


FIGURE 14.45 Multistage impulse generator circuit.

The series discharging of the *N*-stage capacitors means that the effective charging voltage is

$$U_c = NU_c$$

and the effective capacitance of the generator is

$$C_1 = C_s / N$$

The energy associated with the generated impulse voltage is

$$E = \frac{1}{2} C_g U_c^2 \tag{14.21}$$

It follows the expression for the capacitance of the impulse generator:

$$C_g = \frac{2E}{U_c^2} \tag{14.22}$$

For the 3.2 MV, 200 kJ impulse generator, the capacitance C_g amounts to C_g = 39.1 nF.

14.3.3.2 Chopped Impulse

Some standard tests (IEC Standard 60060-1, 1989) require the use of a chopped impulse voltage: the applied voltage is rapidly removed after a predetermined time. This can be achieved by adding a spark gap, typically a sphere gap, across the test object. By adjusting the gap spacing, the gap will flashover after an appropriate time. The voltage across the test object is short-circuited, producing the chopped impulse voltage. Nontriggered spark gaps may have wide dispersion in the flashover voltage and hence unacceptable variations in the time to chop.

Better control of the time to chop is obtained with multistage triggered sphere gaps (trigatron) at the preselected time. The reliability of triggered spark gaps is, however, the function of their physical

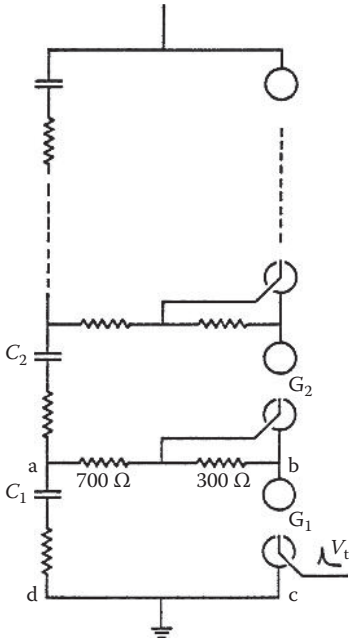


FIGURE 14.46 Triggered multistage sphere gaps for voltage chopping at 3.6 MV.

dimensions, which may require the series connection of several spark gaps to attain the required chopping voltage. Figure 14.46 illustrates such an arrangement of spark gaps for voltage chopping up to 3.6 MV, with a delay time dispersion of less than 50 ns. A total of 18 spark gaps are connected in series, and the set is connected in parallel with a voltage divider to grade the voltage among the spark gaps.

At a preselected time, a triggering impulse V_t of about 8 kV is applied to the triggering electrode, causes the breakdown of the gap G_1, and discharges the capacitance C_1 through the circuit a–b–c–d. In the process, a transient voltage develops across the resistive branch a–b and adds to the voltage across the gap G_2, while part of this transient voltage, across the 300 Ω resistance, is applied to its triggering electrode. This causes the breakdown of G_2, and the process rapidly continues until all the sphere gaps break down.

14.3.4 Long Front Switching Impulse

For different reasons, there has been a great interest to find alternative means to produce switching impulses: to have an additional switching impulse generator and to produce switching impulse with wave front longer than normal, in the order of 2–5 ms. This can be done, using a test transformer or transformer cascade, either by switching a precharged capacitor into the primary or simply by short time energization from the ac supply. This is explained in the following.

14.3.4.1 Capacitor Discharge

The usual approach consists in discharging a capacitor, initially charged to a voltage U_c, into a wave shaping circuit through an inductance (Bellaschi and Rademacher, 1946). The generated impulse voltage is essentially a damped oscillatory transient at the natural frequency of the RLC circuit. The wave front is essentially half the oscillation period of the transient voltage. Different circuits have been considered and used. The main advantage of the capacitor discharging method is its relative simplicity, and it can produce switching impulse of relatively short front time, below 3000 μs. It suffers, however, a number of disadvantages associated with the considerable amount of high-frequency distortion in the output wave shape. Furthermore, the capacitor bank, required to produce a reasonable output voltage, can be of considerable size. Variation of the front of the generated impulse is achieved by varying the inductance in series with the capacitor bank, which proves tedious and, in most cases, uneconomical.

14.3.4.2 Short Time Energization

A more effective method of producing long front switching impulse voltages is by energizing the transformer during a short time period, typically less than one half cycle of the power frequency (Rizk, 1960; Kind and Salge, 1965). Several advantages are inherent to this method: the low amounts of high-frequency distortion in the output voltage, the elimination of the energy storage capacitors, and the relative simplicity of the control unit. We briefly summarize the findings by Anis et al. regarding this method of producing switching impulses from test transformers, single and in cascade (Anis et al., 1975).

Single transformer: The equivalent circuit of a single transformer is given in Figure 14.47a. The main power supply is represented by a voltage source U_s, with an internal resistance R_s and inductance L_s. The test transformer is represented by its winding impedances (R_1, L_1, R_2, and L_2) and its magnetizing impedances R_0 and L_0. The capacitances C_0 and C_L are the transformer and load capacitances. All parameters are referred to the primary side of the transformer. The energization of the transformer is initiated via

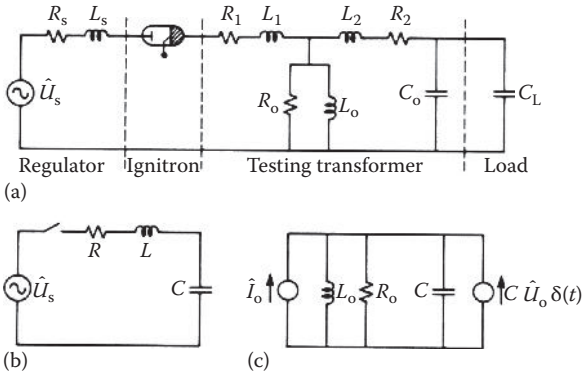


FIGURE 14.47 Equivalent circuit with a single transformer. (a) Single transformer equivalent circuit. (b) Equivalent circuit during charging of load capacitor. (c) Equivalent circuit during discharging period. (From Anis, H. et al., *IEEE Trans*., PAS-94, 187, 1975.)

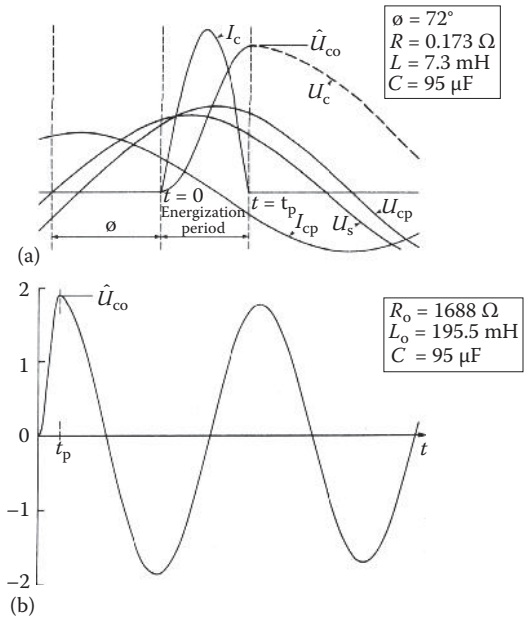


FIGURE 14.48 Response of a single transformer during (a) the energization period and (b) the discharge period. (From Anis, H. et al., *IEEE Trans*., PAS-94, 187, 1975.)

an ignitron, which can be triggered at different phase angles ϕ. The transformer then remains energized until the supply current passes through zero. Accordingly, in seeking the transient response, two distinct time periods must be distinguished (Figure 14.48): the first (energization period) is during the conduction of the ignitron, while the second (discharging period) begins immediately after the ignitron ceases to conduct, when the energy stored in the transformer is discharged through the load.

During the energization period, both the magnetizing inductance L_0 and the core losses equivalent resistance R_0 can be ignored due to their generally large values. The equivalent circuit is simplified to an *RLC* series circuit shown in Figure 14.47b. Considering the response of such a circuit to a sinusoidal supply voltage,

$$u_s(t) = U_s \sin(\omega t + \phi)$$

where ϕ is the switching angle, yields an output voltage across the load $C = C_0 + C_L$:

$$u_c(t) = U_{cp} \sin(\omega t + \phi - \theta) + A \exp(-\alpha t) \sin(\omega_1 t + \beta) \tag{14.23}$$

where

$\alpha = \dfrac{R}{2L}$ is the damping constant

$\omega_0 = \dfrac{1}{\sqrt{LC}}$ the natural angular frequency of the lossless circuit and $\omega_1 = \sqrt{\omega_0^2 - \alpha^2}$

$$U_{cp} = \frac{U_s}{\omega C \sqrt{R^2 + \left(\omega L - \dfrac{1}{\omega C}\right)^2}}$$

and

$$\theta = \tan^{-1}\left[\frac{R}{\omega L - \dfrac{1}{\omega C}}\right]$$

$$A = -U_{cp} \frac{\sin(\phi - \theta)}{\sin\beta}$$

and

$$\beta = \tan^{-1}\left[\frac{\omega_1 \sin(\phi - \theta)}{\omega \cos(\phi - \theta) + \alpha \sin(\phi - \theta)}\right]$$

Typical response of the circuit during the energization period is presented in Figure 14.48a where both the output voltage $u_c(t)$ and the supplied current $i_c(t)$ were calculated and compared with their steady-state values $u_{cp}(t)$ and $i_{cp}(t)$ and the supply voltage $u_s(t)$. It can be seen that because of the transient conditions following the triggering of the ignitron, the supply current actually lasts longer than expected from the steady-state values. During this time, the output voltage increases steadily from zero to a maximum value U_{c0}, which can be significantly larger than the supply voltage when the current $i_c(t)$ passes by zero. The time to peak of the switching impulse generated is approximately equal to the energization period of the transformer.

At the end of the energization period ($t = t_p$), the output capacitor is charged to the maximum voltage U_{c0}, and the magnetizing current reaches the value of I_0 given approximately by

$$I_0 = \frac{U_s}{\omega L_0} \cos(\omega t_p + \phi) \tag{14.24}$$

Since the ignitron does not conduct in the reverse direction, the transformer is isolated from the supply for time $t > t_p$. The energy stored in the transformer magnetizing inductance L_0 and in the output capacitance C is now discharging through the load capacitance in a series of damped oscillations. The equivalent circuit of the test setup is now simplified to an *RLC* parallel circuit shown in Figure 14.47c, both the winding resistance and the leakage inductance being neglected.

The output voltage during the discharge period is given by

$$u_c(t') = \frac{\exp(-\alpha' t')}{C\omega'} \left[(I_0 - \alpha' C U_{c0}) \sin \omega' t' + C U_{c0} \omega' \cos \omega' t' \right] \tag{14.25}$$

where $t' = t - t_p$ the new time base, $\alpha' = 1/2R_0C$ the damping constant, $\omega_0' = 1/\sqrt{L_0C}$ the natural angular frequency, and $\omega' = \sqrt{\omega_0'^2 - \alpha'^2}$.

A typical response of the test circuit during the discharge period is shown in Figure 14.48b. Since the damping coefficient α' is generally small, the output voltage oscillates at the natural frequency of the circuit ω_1' for several cycles before the stored energy is completely discharged.

Cascaded transformers: To meet test requirements at EHV levels, several transformer units are arranged in cascade to provide a higher output voltage. The complete equivalent circuit of a typical cascade arrangement of three transformers is shown in Figure 14.49, where Z_{1i}, Z_{2i}, and Z_{3i} are the winding impedances; Z_{0i} the transformer magnetizing impedance; and C_{ii} and C_{0i} the resultant stray capacitances at primary and secondary windings, respectively. By separating the response of the circuit during the energization and the discharge periods, the circuit of Figure 14.49 can be simplified to the simple circuits of Figure 14.47b and c, respectively, for the energization and discharge periods. The circuit components can be determined from the conventional short-circuit test and from the wave shape of the output voltage under natural oscillation conditions. Typical values of the circuit components, measured for different cascade arrangement of the test transformer at IREQ, each rated at 4.8/550 kV–690 kVA, are given in Table 14.3.

The addition of several transformers in a cascade arrangement effectively increases both the overall resistance R and inductance L of the circuit. As a result, the natural frequency ω_0 of the circuit is reduced,

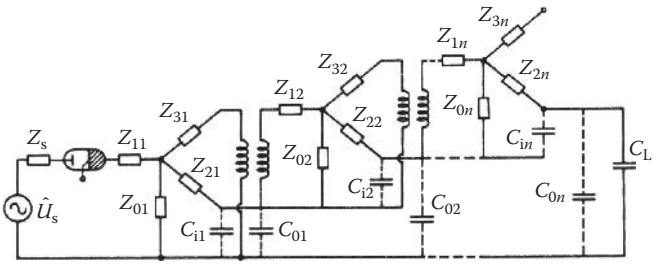


FIGURE 14.49 Equivalent circuit of *n* transformers in cascade. (From Anis, H. et al., *IEEE Trans*., PAS-94, 187, 1975.)

TABLE 14.3

Characteristics of the Cascade Arrangements of Test Transformers

Number of Transformers	Winding Resistance, R(Ω)	Winding Leakage Inductance L (mH)	Core Loss Resistance R_0 (Ω)	Magnetizing Inductance L_0 (mH)
1	0.100	2.27		
2	0.125	4.75	681	162
3	0.173	7.30	1688	195
4	0.270	12.00		

Source: Anis, H. et al., *IEEE Trans*., PAS-94, 187, 1975.

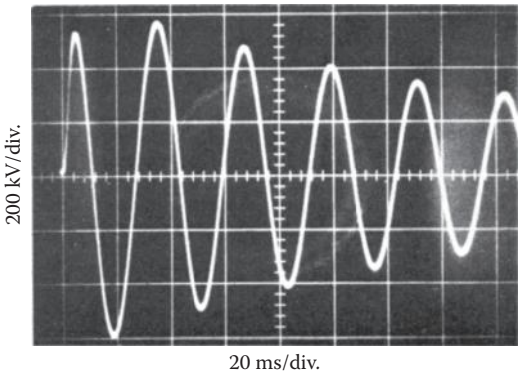


FIGURE 14.50 Oscillating impulse from a cascade arrangement of two transformers. (From Anis, H. et al., *IEEE Trans*., PAS-94, 187, 1975.)

increasing thus the time to peak of the generated impulse. Likewise, during the discharge period, the circuit of Figure 14.49 is simplified to that shown in Figure 14.47c. Figure 14.50 illustrates a typical wave shape of the switching impulse generated from two transformers in cascade. The load in this case is a capacitor of 3000 pF. One can easily recognize the steep wave front corresponding to the voltage rise during the energization period of the transformer, followed by a slowly decaying series of oscillations at the natural frequency of the test circuit.

Generalized characteristics: One of the advantages of the short time energization method to produce switching impulse is its flexible control via the firing angle of the ignitron. Effectively, both the time to crest and the peak value of the impulse voltage vary with the firing phase angle, as illustrated by the results shown in Figure 14.51, which compare the calculated values with actual measurements made on three transformers in cascade and illustrate the adequacy of the approach. The load in this case is simply the capacitance of the voltage divider, which gives a primary-referred value of 95 μF used in the calculation.

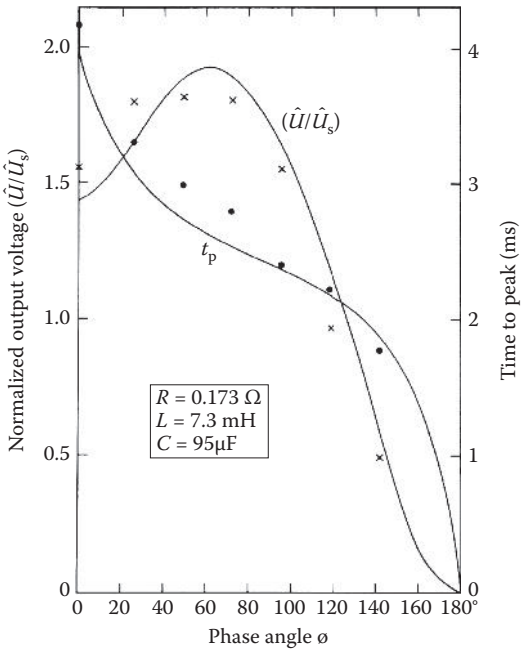


FIGURE 14.51 Comparison of the test results with calculated switching impulse characteristics at 60 Hz energization. (From Anis, H. et al., *IEEE Trans*., PAS-94, 187, 1975.)

Time to peak: Since the output voltage reaches its maximum value at the end of the energization period of the transformer, the time to peak of the switching impulse can be evaluated by solving the equation

$$i_c(t) = 0$$

The results shown in Figure 14.51, evaluated with a damping constant of $\alpha = 10\ s^{-1}$, show that the time to peak t_p of the generated impulses covers a remarkably wide range, from 1000 to 10 000 μs.

Impulse magnitude: The amplitude of the generated impulse is a function of the natural frequency and varies with the firing angle ϕ. It passes by a maximum at a phase angle ϕ_0 between 0° and 90°, which is related to the natural frequency of the circuit, according to

$$f_0 = \frac{p}{2}\left(1 - \frac{w}{w_0}\right) \quad \text{for } w_0 > w$$

A limiting value of the load capacitance can then be defined as that beyond which the system's efficiency rapidly decreases and is given by

$$C_{max} = \frac{1}{N^2 w^2 L} \tag{14.26}$$

where

N is the overall turns ratio of the transformer
L is the transformer leakage inductance, and ω the supply frequency

The circuit damping constant, $\alpha = R/2L$, reduces the magnitude of the generated switching impulse, the effect being more pronounced, the larger is the damping constant. The limiting case corresponds to

$$a = w_0 = \frac{1}{\sqrt{LC}}$$

when the circuit is no longer oscillatory.

Practical limitations: Referring to Figure 14.48, two characteristics of the transient response of the circuit may constitute the main restriction to the short time energization method of producing switching impulses: the excessive in-rush current, which stresses the ignitron during the energization period and the unacceptable high output voltage during the discharge period. A third point of concern is related to the unequal voltage distribution among the cascaded transformer units. These aspects will be discussed in the following.

In-rush current: The maximum energization current I_c, normalized to its steady-state value I_s, varies with the phase angle ϕ for different loading conditions. The overcurrent can be reduced by either reducing the natural frequency ω_0 or increasing the damping constant α of the circuit. This is, however, accompanied by some reduction of the output voltage, and a compromise must then be sought.

Overvoltage during discharge period: The deenergization of the transformer consists generally of a series of damped oscillations at the natural frequency of the discharge circuit, as illustrated by the results of Figure 14.48b. Because of the low damping constant α′ of most test circuits and also because of the magnetizing current at the turnoff of the ignitron, the output voltage during the first cycle of the discharge oscillations may remain comparable to or even higher than the initial peak value of the impulse voltage as shown in Figure 14.50. Unwanted flashover may take place during the discharge period of the transformer rather than during the switching impulse.

Since the equivalent discharge circuit of the transformer is considerably different from its energizing circuit, it is possible to damp out the discharge oscillations without seriously affecting the switching impulse front. Such additional damping can be obtained by adding a parallel resistance R_d to the primary winding of the transformer. It can be shown that increasing the circuit damping attenuates significantly the output voltage during the discharge of the transformer without affecting the time to peak of the

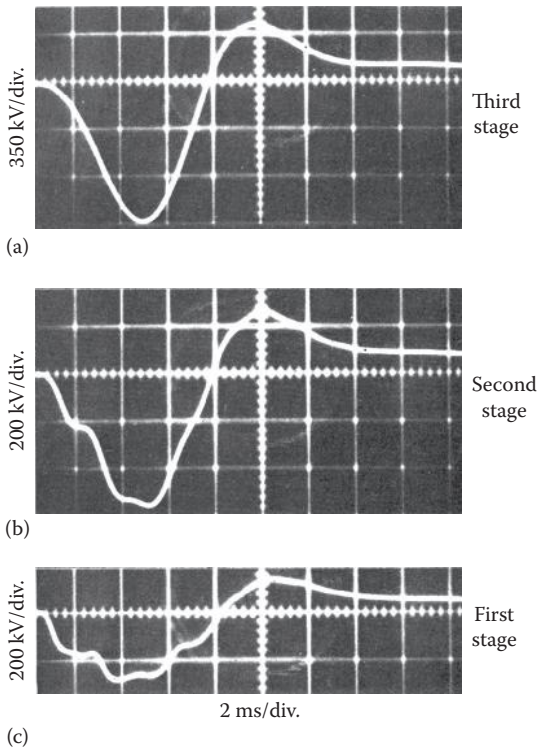


FIGURE 14.52 Actual test voltage at the output and at intermediate stages of a three-transformers cascade. (a) Output voltage. (b) Voltage of second stage. (c) Voltage of first stage. (From Anis, H. et al., *IEEE Trans*., PAS-94, 187, 1975.)

generated switching impulse (Rizk, 1960). The duration of the switching impulse, that is, its tail, is reduced with increasing damping of the circuit. Finally, it should be noted that a well-damped discharge circuit has the additional advantage of avoiding the creation of a residual flux in the transformer core.

Voltage distribution: The voltage distribution among the cascaded transformers was investigated by Anis et al. (Anis et al., 1975), using computer simulation, and the results are validated by actual measurements on a cascade arrangement of three single-phase transformers, rated at 4.8/550 kV–690 kVA. Figure 14.52 shows the actual output voltage of a damped circuit and, at intermediate stages of the cascade and illustrates well the unequal distribution of the output voltage among the units in cascade. The load in this case consists uniquely of the capacitance of the voltage divider, which gives a transferred value of 65 μF, used in the calculation. A damping resistance between 7 and 20 Ω was used to effectively damp the discharge oscillations. Figure 14.53 shows the voltage distributions measured during the test under different operating conditions defined by the firing angle of the ignitron, as compared with the ideal linear distribution. One can see that the voltage distribution among the units in cascade varies with the operating condition of the circuit. The largest voltage occurs at the last unit in the cascade. The problem is attributed to the unloaded tertiary winding of the last transformer unit. By properly loading the tertiary winding of the last transformer unit, the voltage distribution was improved to acceptable limits.

Response of the cascaded transformers to flashovers: The effect on the cascade transformer of a sharp drop in the output voltage associated with a flashover at the test object is minor, with no dangerous overvoltage observed. Since flashovers occur, in general, at the crest of the switching impulse at which instant the cascade is separated from the supply, no particular protection arrangement is needed.

Overstress on the primary winding: At the instant of firing the ignitron, the input capacitance of the primary winding of the first transformer unit may oscillate with the lead impedance to produce dangerous overstress to the winding. The problem was solved by inserting a 5 mH between the supply and the cascade primary winding and shunting the input to the cascade by a 23 nF capacitance.

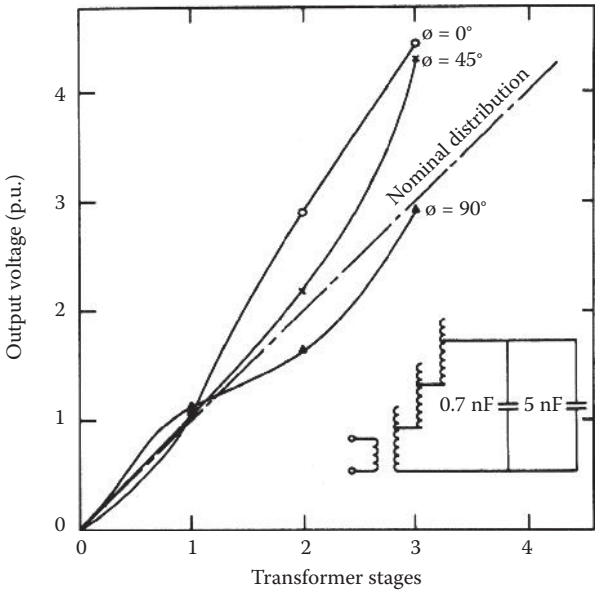


FIGURE 14.53 Voltage distribution along the cascaded transformers during tests. (From Anis, H. et al., *IEEE Trans.*, PAS-94, 187, 1975.)

14.4 HV Measuring Techniques

As a general rule, measuring devices should not affect the test parameters in any significant way, and their signals should not be modified by noise generated in the test circuit. In addition, since it is the test object being evaluated, the measuring devices must be placed as close as possible to the test object, without affecting its performances.

14.4.1 Grounding and Shielding of Control and Measuring Cables

14.4.1.1 Grounding of HV Test Area

Because of the large dimensions of the HV test circuit, the circulation of the ground return current during impulse testing can produce significant voltage differences along the ground return path, unless appropriate measures be taken to minimize its effect. Figure 14.54 illustrates the basic problem related to the ground return current: the open-loop-induced voltage on a conductor grounded at one end and the closed-loop current circulating in the conductor when it is grounded at both ends. Let us consider a ground plane made of a metal plated of thickness t, width w, with a ground return current i_p.

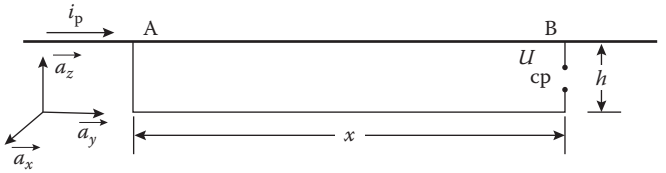
Open-loop voltage U_{cp}: Occurs when the shield of the cable is grounded at one end only. At the open end of a conductor of length x, parallel with the ground plane at a distance h, is

$$U_{cp} = \left(Z_p + Z_{mp}\right) i_p$$

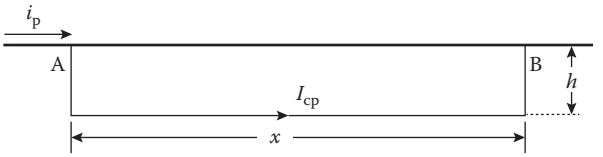
where Z_p is the impedance of the ground plane between two grounding points, usually one in the test area and the other in the control room, separated by the distance x.

$$Z_p \frac{\hat{E}}{\hat{E}} \frac{r}{2d} + j\omega \frac{\mu d}{4} \tilde{} \frac{x}{w} = \frac{x}{w} \sqrt{\frac{r\mu\omega}{8}} \left(1 + j\right) \ll j\omega L_p \tag{14.27}$$

with $L_p = \dfrac{\mu d}{4} \dfrac{x}{w}$ the self-inductance along the ground plane and $\delta = \sqrt{\dfrac{2r}{\mu\omega}}$ the penetration depth of the ground current due to skin effect.



(a) Voltage developing at the open end of conductor close to ground plate.



(b) Current circulating in conductor close to ground plate.

FIGURE 14.54 Illustration of (a) open-loop-induced voltage and (b) closed-loop-induced current. (From Hyltén-Cavallius, N.R. and Trinh, N.G., *IEEE Trans*., PAS-88, 996, 1969.)

Z_{mp} is the mutual impedance between the ground plane and the conductor 1.0 m long:

$$Z_{mp} = j\omega M_p = j\omega \frac{\mu_0 h}{2} \frac{x}{w} \tag{14.28}$$

with $M_p = \mu_0 h/2$ the mutual inductance per unit length of the conductor above the ground plane. Usually, this term is much higher than the inductive impedance of the ground plane, thus the importance of keeping the distance h as small as practicable to minimize the open-loop voltage and avoid breakdown of the air gap subjected to the open-loop voltage.

Closed-loop current I_{cp}: Occurs when the cable shield is grounded at both ends. The current circulating in the conductor is, according to the Thevenin's theorem,

$$I_{cp} = \frac{U_{cp}}{Z_{th}} \tag{14.29}$$

where Z_{th} is the Thevenin's impedance of the circuit, which may be approximated by

$$Z_{th} \approx Z_{lc} \approx j\omega \frac{\mu_0}{\pi} \ln\left(\frac{4h}{d_c}\right) \tag{14.30}$$

where Z_{lc} is the impedance of the conductor of diameter d_c and located at a height h above the metal ground plane.

The circulation of the closed-loop current produces a voltage drop along the shield conductor of a measuring cable, which adds on the measured signal and constitutes a measuring error to be minimized.

Best solution to this problem is obtained with the use of a metal plane as ground return. However, such a ground plane is rather cumbersome in a test area, and a meshed metal grid embedded into the concrete floor of the laboratory has been shown to be a good alternative (Hyltén-Cavallius and Trinh, 1969). Figure 14.55 illustrates an expanded metal grid and its model using rectangular meshes of dimension a, the distance between two conductors. The expanded grid has the same thickness as the metallic ground plane t, which is also equal to the diameter d of the conductor in the model rectangular meshes.

Figure 14.56 compares the distributions of the magnetic field near the ground when it is made of a metal plate with a metal grid of conductors of diameter d and separating distance a. One can see that beyond a distance of $a/2$ from the ground, there is practically no difference between the two distributions of the magnetic field.

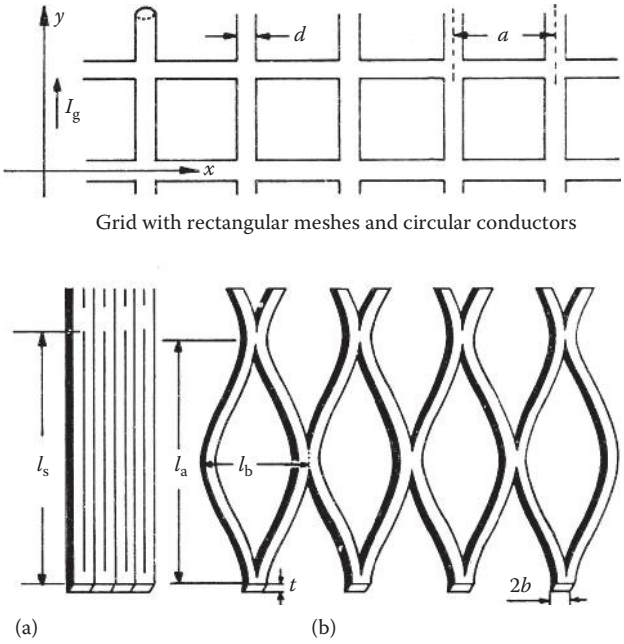


FIGURE 14.55 Illustration of an expanded metal grid and its rectangular mesh model. (a) Grid with rectangular meshes. (b) Grid with expanded meshes. (From Hyltén-Cavallius, N.R. and Trinh, N.G., *IEEE Trans*., PAS-88, 996, 1969.)

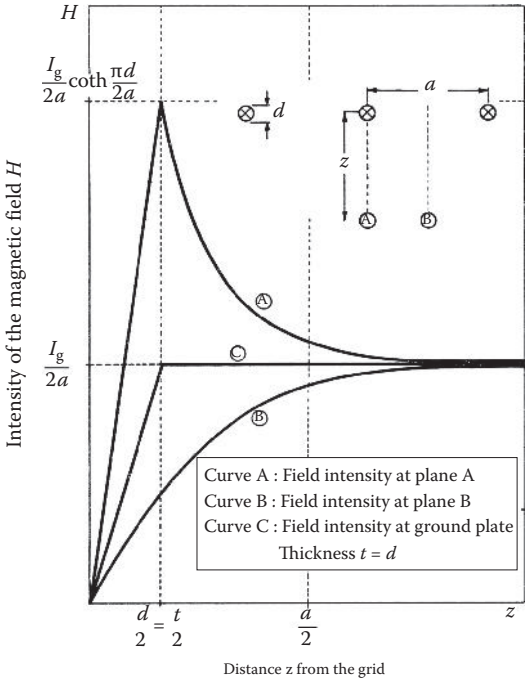


FIGURE 14.56 Comparison of the magnetic field distributions near a metal plane and metal grid. (From Hyltén-Cavallius, N.R. and Trinh, N.G., *IEEE Trans*., PAS-88, 996, 1969.)

The use of a metal grid increases effectively both impedance along the ground grid and the mutual impedance to a parallel conductor, which can be expressed in terms of the grid expansion factor defined as $\kappa = a/2d$ and the normalized conductor height from ground $\eta = 2h/d$ according to

$$L_g = -\frac{\mu}{2\pi} \ln \left(\sin \frac{\pi d}{2a} \right) = -\frac{\mu}{2\pi} \ln \left(\sin \frac{\pi}{4\kappa} \right) \tag{14.31}$$

$$M_g = \frac{\mu}{2\pi} \ln \left(\cosh \frac{\pi h}{a} \right) = \frac{\mu}{2\pi} \ln \left(\cosh \frac{h}{4h} \right) \tag{14.32}$$

The corresponding self- and mutual impedances in the case of a ground grid become

$$Z_g = j\omega L_g \quad \text{and} \quad Z_{mg} = j\omega M_g$$

As a result, higher open-loop voltages and closed-loop currents are produced with meshed metal grid. Figure 14.57 shows the variations of the ratios aL_g/L_p and aM_g/M_p with the expansion factor k of the grid and illustrates the effect of the expanded grid on the self- and mutual inductances. Furthermore, since both the self- and mutual impedances along the ground plane (or grid) contribute to the open-loop-induced voltage, an enhancement ratio to the induced open-loop voltage and closed-loop current, U_{cg}/U_{cp} and I_{cg}/I_{cp}, as a function of the expansion factor of the metal grid is also presented in Figure 14.57. The parallel conductor is located at 40 cm from the ground plane. One can see that by properly choosing the grid expansion factor, the enhancement ratio can be limited to 1.5–3.5. When this solution cannot be implemented, the ground return path should be made of relatively large metal sheets, to which all ground connections will be made, and serves as shielding to the control and measuring cables laid underneath.

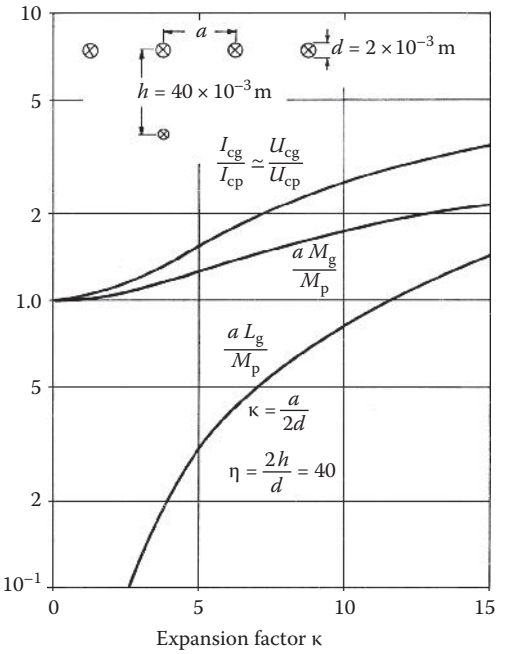


FIGURE 14.57 Variation of the enhancement ratio U_{cg}/U_{cp} and I_{cg}/I_{cp} with the expansion factor $\kappa = a/2d$ of the grid. (From Hyltén-Cavallius, N.R. and Trinh, N.G., *IEEE Trans*., PAS-88, 996, 1969.)

14.4.1.2 Shielding of Control and Measuring Cables

It is obvious from the preceding section that the ground return current can have a significant impact on the performances of measuring cables:

- An excessive induced open-loop voltage, which can cause breakdown at the open end of a shield conductor grounded at one end only
- An induced closed-loop current, which can cause error to the measured signal

In a more specific way, the question becomes how should measuring cables be grounded to provide adequate protection and minimize error to the measured signal.

Coaxial cables: Are currently used for transmitting control and measuring signals. In an HV test area, proper grounding of the cable shield is crucial to their adequate functioning. Grounding of the cable shield can be made at either end or at both ends of the cable.

Grounding the cable shield at one end subjects it to an open-loop-induced voltage, $u_{cg}(t)$:

$$u_{cg}(t) = (L_g + M_g)\frac{di_g(t)}{dt} \tag{14.33}$$

where

$i_g(t)$ is the injected ground current

L_g and M_g are the self- and mutual inductances of the ground grid and the parallel conductor according to Equations 14.31 and 14.32

Figure 14.58 shows the variation of the maximum normalized open-loop voltage to an injected ground current of 1 kA with the distance separating the conductor from the ground grid and with different rise times. One can see that the open-loop voltage can reach several kV particularly for short rise time of the injected current, sufficient to cause damage to the measuring equipment connected to it.

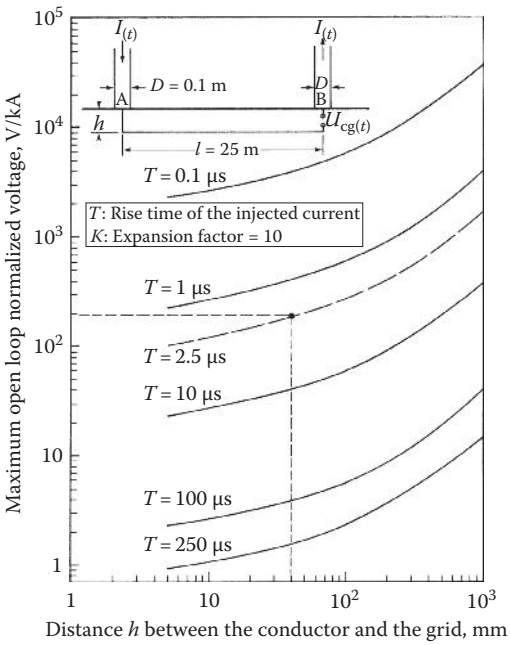


FIGURE 14.58 Variation of the normalized open-loop voltage to an injected ground current of 1 kA with the distance separating the conductor from the ground grid and with different rise times.

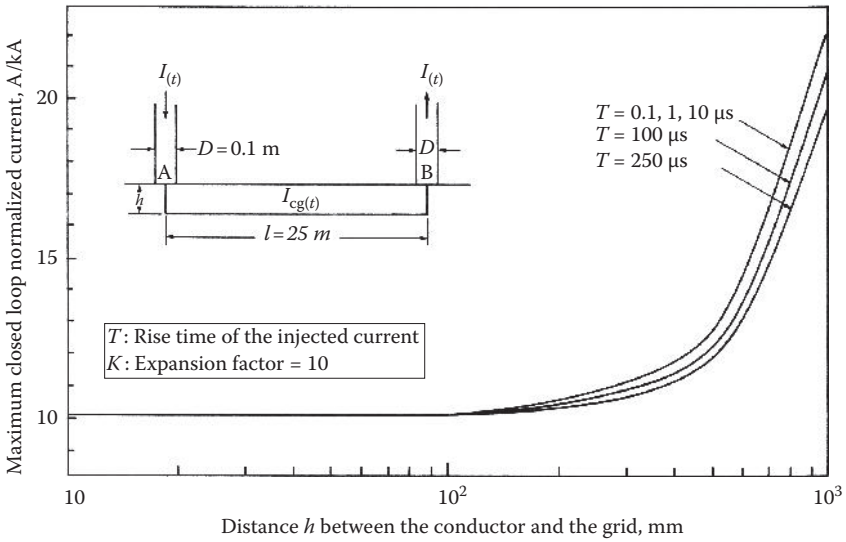


FIGURE 14.59 Variations of the maximum normalized closed-loop current to an injected ground current of 1 kA as a function of the distance h separating the conductor from the ground grid.

Grounding the cable shield at both ends diverts part of the ground return current through the cable shield and introduces a measuring error, which may be expressed as

$$i_{cg}(t) = \frac{u_{cg}(t)}{Z_{th}} \tag{14.34}$$

Figure 14.59 shows the variations of the maximum normalized closed-loop current to an injected ground current of 1 kA, as a function of the distance h separating the conductor from the ground grid. One can see that significant current can circulate in the conductor grounded at both ends due to the injection of a ground current. As a result, coaxial cables are not adequate for use in HV test areas.

Double-shield cables: The use of double-shield cables provides an adequate answer to the severe requirements of HV test areas. By grounding the outer shield at both ends, the problem of open-loop-induced voltage is solved. What remains is a common mode voltage equal to the voltage drop associated with the circulation of the portion of the ground return current diverted through the outer shield and seen at both the inner shield and the central conductor. This common mode voltage is essentially an electrostatic induced voltage and may be eliminated by grounding the inner shield at the test site end only.

Practical arrangement of control and measuring cables in HV test areas: Uses a copper conduit grounded at both ends to the meshed metal ground grid—one end in the test area and the other in the control room—through which several cables can be laid with their shield grounded at the test site only. The copper conduit serves then as a common outer shield for the cables, which can be of conventional coaxial type. Typical shielding efficiency, defined as the ratio in dB between the induced voltages at the central conductor of the measuring cable to that of an unshielded conductor, is in the order of 60 dB.

14.4.1.3 Electromagnetic Shielding of HV Laboratory

Electromagnetic shielding of HV laboratory is necessary to permit sensitive PD detection in HV insulation. The problem is particularly important in UHV laboratories due to the physical dimensions of the PD detection circuit and of the laboratory, which become comparable to the wavelength of the disturbing field. In a study of the shielding efficiency of IREQ HV laboratory (Rizk et al., 1975), Rizk has shown that the shielding efficiency of the HV laboratory is very much dependent on the frequency of the disturbing signal.

For low-frequency interference signal, when the dimensions of the laboratory are much smaller than the wavelength of the disturbing signal, the ratio between the outer (disturbing) field H_0 and the inner field H_i can be evaluated using a circuit approach according to

$$S = \left|\frac{H_0}{H_1}\right| = Q\left|\frac{\sqrt{2\delta}}{2d}\right| \quad \text{with} \quad Q = j\frac{\omega L_s}{R_s} \tag{14.35}$$

where

L_s and R_s are the inductance and resistance of an equivalent coil
$\delta = \sqrt{2\rho/\omega\mu}$ is the skin depth at the frequency of the signal
d the thickness of the shield

Applying to the case of IREQ's double-shield HV laboratory, Rizk obtains

$$S = S_1 + S_2 + 20\log\left|1 - \frac{a^2}{b^2}\right| \tag{14.36}$$

where

S_1 and S_2 are the shielding efficiency of the two shields, according to (14.35)
a and b are the inner radii of the shields

For high-frequency signal, above 1 MHz, where the dimensions of the shield approach the wavelength, the low-frequency shielding efficiency must be supplemented by a high-frequency term, according to (Kaden, 1959)

$$\Delta S_m = 20\log\left|\pi J_1(k_0,a)H_1(k_0,a)\right| = 20\log\left|\pi J_1(k_0,a)\sqrt{J_1^2(k_0,a) + H_1^2(k_0,a)}\right| \tag{14.37}$$

where

$J_1(k_0, a)$ is the Bessel function of the first kind
$H_1(k_0, a)$ is the Hanckel function of the first kind

It follows that in the vicinity of the zeros of the function $J_1(k_0, a)$, the shielding efficiency will suffer serious deterioration. Figure 14.60 compares the variation of the measured shielding effectiveness in the center of the UHV hall with the calculated values for the range of frequencies up to 20 MHz. The results are satisfactory and illustrate well the adequacy of this approach.

Finally, it should be mentioned that the highly conductive metal enclosure of the UHV hall also acts as a huge cavity resonator when excited from inside by the fast discharge with very high steepness of an impulse generator. Oscillations occur simultaneously at several frequencies determined by the resonator geometry, typically in the range of 5–7 MHz (Malewski et al., 1977).

14.4.2 Sphere Gaps as a Voltage Measuring and Protection Device

A sphere gap comprises two metal spheres of equal dimension, located along the same axis, horizontal or vertical, and separated by an adjustable distance d. Sphere gap is among the earliest measuring instrument for HV, due to its relatively simple design and reproducible breakdown voltage. For a long time, sphere gap provided the standard voltage measurement in HV test. Its use must respect specific requirements specified in international and national standards (IEC-60052, 1960), especially regarding the clearance distances with respect to nearby objects. Table 14.4 gives the typical clearance distances for most commonly used sphere gaps.

Sphere gap responds to the peak value of ac and impulse voltages, although not at the same levels, and is sensitive to temperature and RAD. The corrections for RAD are given in Table 14.5. We reproduce in Tables 14.6 and 14.7 the breakdown voltage of sphere gaps as recommended in the IEC standard on the application of sphere gaps in HV measurement.

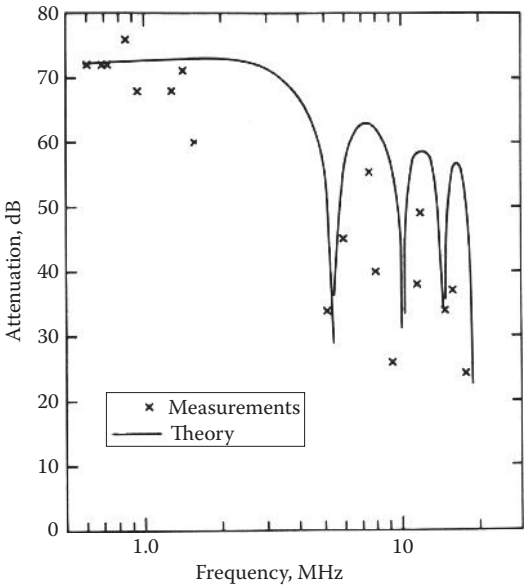


FIGURE 14.60 Variation of the shielding effectiveness with the frequency in the center of the UHV hall. (From Rizk, F.A.M. et al., *IEEE Trans*., PAS-94, 2077, 1975.)

TABLE 14.4

Recommended Clearance Distances around the Sphere Gap

Sphere Diameter *D* (mm)	Min. Value of *A*	Max. Value of *A*	Min. Distance *B*
62.5	7 D	9 D	14 D
125	6	8	12
250	5	7	10
500	4	6	8
750	4	6	8
1000	3.5	5	7
1500	3	4	6
2000	3	4	6

Source: IEC-60052, 1960.

Notes: *A*, the height of the spark point above ground; *B*, the radius of a sphere that covers most of the sphere gap.

TABLE 14.5

Correction Factor for RAD

RAD	Correction Factor, k_d
0.70	0.72
0.75	0.77
0.80	0.82
0.85	0.86
0.90	0.91
0.95	0.95
1.00	1.00
1.05	1.05
1.10	1.09
1.15	1.13

TABLE 14.6

Breakdown Voltages of Sphere Gaps

Gap Spacing (mm)	Sphere Diameter (cm)							
	6.25	**12.5**	**25**	**50**	**75**	**100**	**150**	**200**
5	17.2	16.8						
10	31.9	31.7						
15	45.5	45.5						
20	58.5	59						
25	69.5	72.5	72.5					
30	79.5	85	86					
35	(87.5)	97	99					
40	(95)	108	112					
45	(101)	119	125					
50	(107)	129	137	138	138	138	138	
55	(112)	138	149					
60	(116)	146	161					
65		154	173					
70		(161)	184					
75				202	203	203	203	203
80		(174)	206					
90		(185)	226					
100		(195)	244	263	265	266	266	266
110		(203)	261					
120		(212)	275					
125		(214)	282	320	327	330	330	330
150			(314)	373	387	390	390	390
175			(342)	420	443	443	450	450
200			(366)	460	492	510	510	510
225			(385)					
250			(400)	530	585	615	630	630
300				(585)	665	710	745	750
350				(630)	735	800	850	855
400				(670)	(800)	875	955	975
450				(700)	(850)	945	1050	1080
500				(730)	(895)	1010	1130	1180
600					(970)	(1110)	1280	1340
700					(1025)	(1200)	1390	1480
750					(1040)	(1230)	1440	1540
800						(1260)	(1490)	1600
900						(1320)	(1580)	1720
1000						(1360)	(1660)	1840
1100							(1730)	(1940)
1200							(1800)	(2020)
1300							(1870)	(2100)

Note: One sphere is grounded, under ac, dc, and negative impulse voltages at 20°C and 101.3 kPa. Values in brackets are accurate within ±5%.

TABLE 14.7

Breakdown Voltages of Sphere Gaps

Gap Spacing (mm)	Sphere Diameter (cm)							
	6.25	**12.5**	**25**	**50**	**75**	**100**	**150**	**200**
5	17.2	16.8						
10	31.9	31.7	31.7					
15	45.9	45.5	45.5					
20	59	59	59					
25	71.0	72.5	72.7					
30	82	85.5	86					
35	91.5	98	99					
40	(101)	110	112					
45	(108)	122	125					
50	(115)	134	138	138	138	138	138	138
55	(122)	142	151					
60	(127)	155	163					
65		(164)	175					
70		(173)	187					
75				203	202	203	203	203
80		(189)	211					
90		(203)	233					
100		(215)	254	263	265	266	266	266
110		(229)	273					
120		(234)	291					
125		(239)	299	323	327	330	330	330
150			(337)	380	387	390	390	390
175			(368)	432	447	450	450	450
200			(395)	480	505	510	510	510
225			(416)					
250			(433)	555	605	620	630	630
300				(620)	695	725	745	750
350				(670)	770	815	858	860
400				(715)	(855)	900	965	980
450				(745)	(890)	980	1060	1090
500				(775)	(940)	1040	1150	1190
600					(1020)	(1150)	1310	1380
700					(1070)	(1240)	(1430)	1550
750					(1090)	(1280)	(1480)	1620
800						(1310)	(1530)	1690
900						(1370)	(1630)	1830
1000						(1410)	(1720)	1930
1100							(1790)	(2030)
1200							(1860)	(2120)
1300							(1930)	(2200)

Note: One sphere is grounded under positive impulse voltages at 20°C and 101.3 kPa. Values in brackets are accurate within ±5%.

The reproducibility of the breakdown voltage depends largely on the uniformity of the field distribution along the gap axis, which is essentially a function of the ratio *d*/*D* of gap distance to the sphere diameter *D* (discussed in Chapter 2). As the field distribution becomes less uniform at large values of the ratio *d*/*D*, the dispersion of the breakdown voltage of the sphere gap increases, making it unsuitable for accurate measurement of the breakdown voltage. As a result, sphere gaps are reliable over a defined range of gap lengths only, usually equal to the sphere radius.

With the development of sophisticated voltage measuring equipment, the use of sphere gaps has gradually been left aside, although it still serves as an independent measurement of the test voltage. It is mostly used as a simple and reliable protective device against overvoltage at the test object. Triggered sphere gaps are currently used to produce chopped impulse voltages required in some specific test procedures, as explained in Section 3.3.2.

14.4.3 Voltage Measurement

Voltage measurement has to accommodate the presence of high test voltages and the required accuracy in the measured parameters. The measuring system comprises the connecting lead between the test object and the HV end of the divider, the voltage divider, its low voltage arm, and the connecting cable to the voltage recording instrumentation represented by its input impedance. It can be considered as one or several series-connected four-terminal (or two-port) networks to better identify their relative contribution. A transfer function $H(t)$ relates the measured signal $u_m(t)$ to the input signal $u_s(t)$ according to

$$u_m(t) = H(t)u_s(t)$$

Ideally, $H(t)$ should be a real number, N, equal to the transfer ratio of the voltage divider. The measured voltage $u_m(t)$ would then be proportional to the input voltage $u_s(t)$. However, the actual test conditions as stray capacitances to ground, nonideal grounding, and connecting leads, etc., affect the transfer function and distort the measured signal.

For a transient signal $V(t)$, its continuous frequency spectrum is given by the Fourier transform, according to

$$V(j\omega) = \int_{-\infty}^{\infty} V(t)\exp(-j\omega t)\,dt \tag{14.38}$$

The measured output signal $V_0(t)$ is obtained by making the inverse Fourier transform:

$$V_0(t) = \frac{1}{2\pi}\int_{-\infty}^{\infty} V_i(j\omega)H(j\omega)\exp(j\omega)\,d\omega \tag{14.39}$$

From the preceding expression, one can see that for $V_0(t)$ to properly reflect the input signal, the transfer function $H(j\omega)$ must have a constant amplitude over the whole range of the frequency spectrum of the input signal. Figure 14.61 shows the normalized frequency spectra of a standard impulse voltage of 1.2/50 μs, as well as chopped at different times T_c: 4, 0.5, and 0.1 μs. The most widespread frequency spectrum is associated with the shortest impulse duration. The desirable bandwidth of the measuring circuit would be about 100 MHz for a chopped impulse of 0.5–0.1 μs, which, however, is not met by measuring systems for very HV.

For actual HV measuring system, the transfer characteristic is evaluated experimentally by measuring its unit step response (USR). This is possible since the frequency spectrum of the unit step function contains all frequencies. Figure 14.62 illustrates the normalized USR $g(t)$, related to the actual output voltage by a scale factor 1/N that corresponds to the steady-state output voltage. The circuit response time T^0, illustrated in Figure 14.62 (Hyltén-Cavallius, 1957), is given by

$$T^0 = \int_0^{\infty} [1 - G(t)]\,dt \tag{14.40}$$

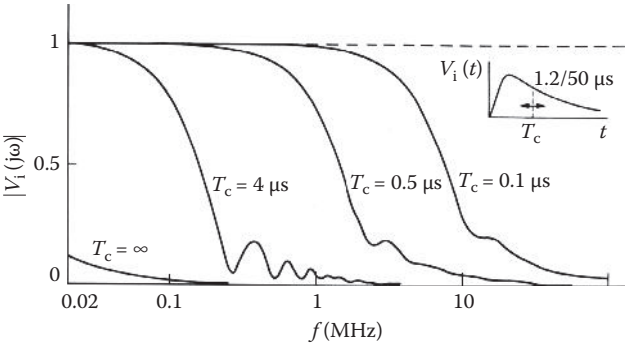


FIGURE 14.61 Normalized frequency spectra. (From Kuffel, E. et al., *High Voltage Engineering—Fundamentals*, 2nd edn., Pergamon Press, Oxford, 2000.)

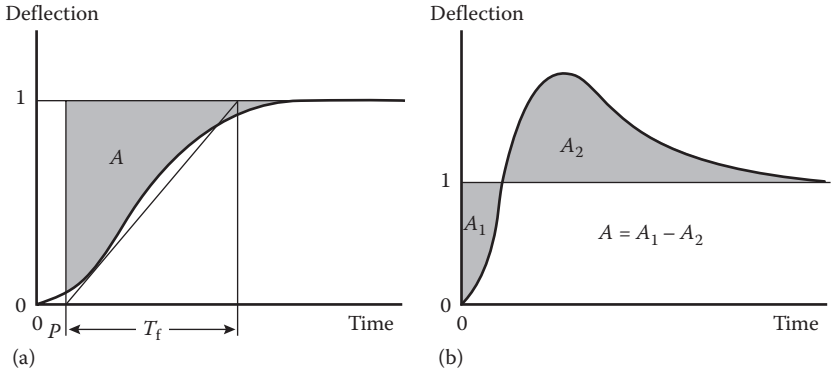


FIGURE 14.62 Normalized unit response of a voltage measuring system. (a) Critically damped response. (b) Under-damped response. (From Hyltén-Cavallius, N.R., Impulse tests and measuring errors, ASEA Publications, 7551 E/ASEA Reg. 0977, 1957.)

A delay time t_{dc} is mostly associated with wave propagation along the measuring cable (IEC Standard 60060-2, 1994). As a result, the effective unit response T corresponds to the algebraic sum of the shaded areas in unit response curves in Figure 14.62b:

$$T = \sum A_i$$

In a general way, the response time T is given by

$$T = T^0 - t_{dc} = \int_{t_{dc}}^{\infty} \left[1 - g(t)\right] dt$$

Figure 14.63 illustrates the influence of the measuring circuit, characterized by its response time T^0, on the wave shape of the recorded signal: a 500 ns rise time front-chopped standard 1.2 μs/50 μs impulse. One can note a roundoff effect at the peak of the recorded impulse and a decaying time the longer the response time of the measuring circuit is.

As shown by Zaengl et al. (Kuffel et al., 2000), the unit response of a measuring system can be calculated from its equivalent circuit. The output voltage response to any arbitrary input voltage can be obtained from the superposition theorem (Duhamel's integral), according to

$$V_0(t) = V_i(t)G(0) + \int_0^t V_i(\tau)G'(t-\tau)d\tau = G(t)V_i(0) + \int_0^t V_i'(t-\tau)G(\tau)d\tau \tag{14.41}$$

where $G'(t-\tau)$ and $V_i'(t-\tau)$ are the derivatives of $G(t)$ and $V_i(\tau)$ with respect to τ.

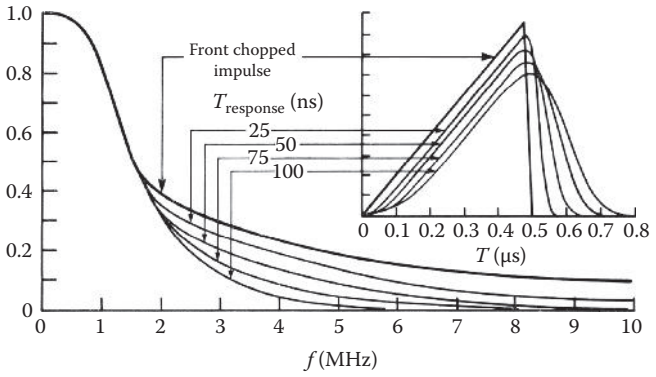


FIGURE 14.63 Frequency spectrum of the response time of the measuring circuit and its influence on the recorded voltage wave shape of standard 1.2/50 μs impulse chopped at 0.5 μs. (From Malewski, R., *IEEE Trans*., PAS-101, 4508, 1982.)

Figure 14.64 compares the output voltage with an input impulse voltage chopped on the front and illustrates the measuring error in this case. The error in the measured amplitude ΔV is

$$\Delta V = ST = S\left(T^0 - t_{dc}\right) \tag{14.42}$$

where S is the slope of the impulse front.

The relative amplitude error for a chopped linearly rising voltage is

$$\delta = \frac{\Delta V}{ST_c} = \frac{T}{T_c} \tag{14.43}$$

For an effective response time of 50 ns and a chopping time $T_c = 0.5$ μs, the relative error is therefore 10%.

With the four-terminal network model, the following matrix relation can be established between the Laplace transform input voltage and current parameters V_i and I_i and the corresponding output parameters V_o and I_o:

$$\begin{bmatrix} V_i(s) \\ I_i(s) \end{bmatrix} = \begin{bmatrix} A_{11}(s) & A_{12}(s) \\ A_{21}(s) & A_{22}(s) \end{bmatrix} \cdot \begin{bmatrix} V_0(s) \\ I_0(s) \end{bmatrix}$$

For $I_0 = 0$, the transfer function $H(s)$ is then

$$H(s) = \frac{V_0(s)}{V_i(s)} = \frac{1}{A_{11}(s)}$$

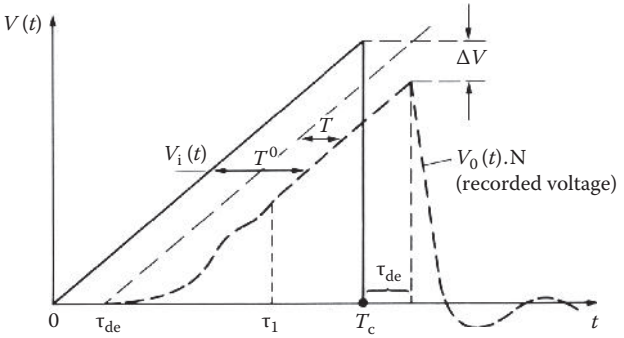


FIGURE 14.64 Measuring error ΔV for a linearly rising voltage chopped at T_c. Definition of the measured response time T^0 and the effective response time T. (From IEC Standard 60060-2, *High Voltage Test Techniques. Part 2: Measuring Systems*, 2nd edn., IEC, Geneva, Switzerland, 1994.)

The transfer ratio n is

$$n = \lim_{s \to 0} \left(\frac{V_i(s)}{V_0(s)} \right) = \lim_{s \to 0} \left(A_{11}(s) \right) = A_{11}(0)$$

and the normalized transfer function with respect to n is

$$h(s) = nH(s) = \frac{A_{11}(0)}{A_{11}(s)}$$

The USR $G(t)$ is obtained by applying the Laplace inverse integral to the product of the transfer function by $(1/s)$, the Laplace transform of a unit step:

$$G(t) = \mathcal{L}^{-1}\left[\frac{1}{s} H(s) \right] = \mathcal{L}^{-1}\left[\frac{1}{s A_{11}(s)} \right]$$

and its normalized expression is

$$g(t) = nG(t)$$

We will review in the following the major factors that can affect the measurement of the voltage at the test object.

14.4.3.1 Voltage Divider

Voltage divider is the main element in the HV measurement circuit. It converts the applied HV into a low-voltage signal compatible with the electronic measuring equipment. Its operating principle is quite simple: by putting n identical elements in series and using the last element on the ground side as the low-voltage arm, one obtains a voltage divider with a transfer ratio of

$$n = \frac{\hat{\mathbf{A}} Z_i}{Z_1} = \frac{nZ}{Z}$$

However, in practice, stray capacitances can affect the actual impedance of the individual elements, making the impedance Z_i different from one element to the next. The transfer ratio n is no longer a real number but a complex function of the stray capacitance, residual inductance, the large value of the transfer ratio, the HV electrode, and the considerable voltage developing across the low-voltage arm, etc. Voltage dividers have been the subject of numerous investigations over the years (Elsner, 1939; Zinke, 1939; Asner, 1961; Zaengl, 1965; Schwab and Pagel, 1972). The following summary of the subject is based on such investigations.

Figure 14.65 shows the equivalent circuit of a voltage divider, taking into account the stray distributed capacitance to ground associated with the individual impedance elements. The total impedances are

$$Z_1 = \hat{\mathbf{A}} Z_i = nZ_i \quad \text{and} \quad Z_q = \left[\hat{\mathbf{A}} \frac{1}{Z_q} \right]^{-1} = \frac{Z_q}{n} \tag{14.44}$$

and the following expressions are for the transfer function $h(s)$ and normalized unit response $g(t)$, for $n >> 1$:

$$h(s) = \frac{nV_2}{V} = \frac{n \sinh \frac{1}{n} \sqrt{Z_1(s)/Z_q(s)}}{\sinh \sqrt{Z_l(s)/Z_q(s)}} \quad \text{and} \quad g(t) = \mathcal{L}^{-1}\left[\frac{1}{s} h(s) \right] \tag{14.45}$$

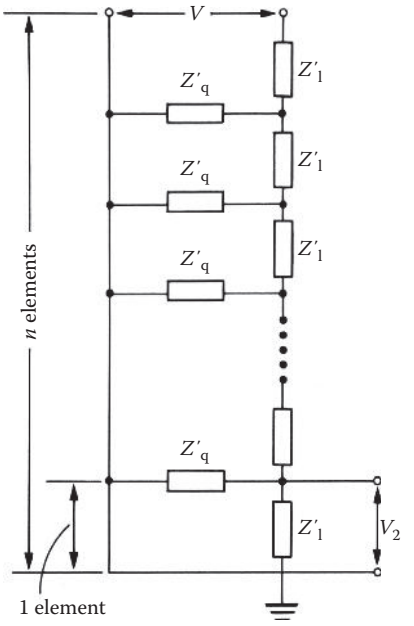


FIGURE 14.65 Voltage divider circuit.

Resistive divider: High ohmic dividers in the range of hundreds of megaohms are used in measurement of direct voltage. For fast impulse voltages treated in this section, resistive dividers in the 10 kΩ range are utilized. It is formed of n wire wound resistors connected in series. The resistance of the HV arm of the divider can vary from 2 to 20 kΩ depending on the nominal voltage. In spite of the fact that the winding is bifilar wound to allow mutual cancellation of the inductance, there remains a small residual inductance with each resistor element. Combined with the self- and stray capacitance to ground of the individual elements, the resulting equivalent is complex, as shown in Figure 14.66. Note that despite its complexity, it is assumed that both the distribution of stray and ground capacitances are uniform, which is certainly a simplification, particularly with respect to ground capacitances. Moreover, these capacitances are not necessarily known and cannot be easily measured. The transfer function $h(s)$ and response time $g(t)$ are (Kuffel et al., 2000)

$$h(s) = n\frac{\sinh\frac{1}{n}\sqrt{\frac{(R+sL)sC_e}{1+(R+sL)sC_p}}}{\sinh\sqrt{\frac{(R+sL)sC_e}{1+(R+sL)sC_p}}}$$

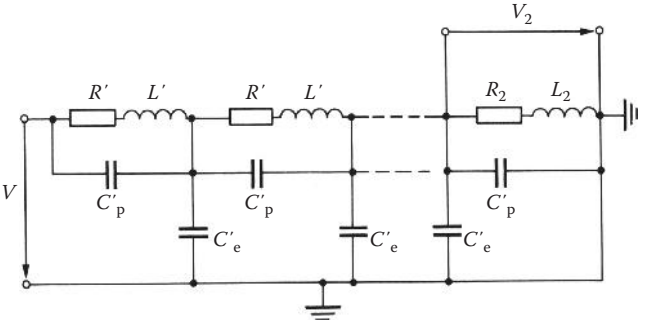


FIGURE 14.66 Equivalent circuit of a resistive divider. $R = nR'$, $L = nL'$, $C_e = nC_e'$, $C_p = C_p'/n$, $R_2 = R'$, $L_2 = L'$, and $R_1 = (n-1)R'$.

and

$$g(t) = 1 + 2\exp(-at)\sum_{1}^{\infty}(-1)^k \frac{\cosh(b_k t) + \frac{a}{b_k}\sinh(b_k t)}{1 + \frac{C_p}{C_e}k^2\pi^2} \tag{14.46}$$

where

$$a = R/2L$$

$$b_k = \sqrt{a^2 - \frac{k^2\pi^2}{LC_e\left(1 + \frac{C_p}{C_e}k^2\pi^2\right)}}$$

If L and C_p are small, the preceding expressions simplify to (Kuffel et al., 2000)

$$h(s) = n\frac{\sinh\frac{1}{n}\sqrt{sRC_e}}{\sinh\sqrt{sRC_e}}$$

and

$$g(t) = 1 + 2\sum_{1}^{\infty}(-1)^k \exp\left(-\frac{k^2\pi^2}{RC_e}t\right) \tag{14.47}$$

The bandwidth of the divider can be approximated by

$$f_B = \frac{1.46}{RC_e}$$

and the response time T^0 is approximately

$$T^0 = \frac{RC_e}{6} \approx T \tag{14.48}$$

Figure 14.67 compares the USRs evaluated for equivalent circuits with the distributed parameters and lumped parameters. The effect of the distributed stray capacitances is in the initial slope of the USR, which is zero rather than having a positive value.

Capacitive divider—measurement of ac voltage: As with resistive divider, a capacitive divider can be obtained by using a capacitor as the impedance element. Here also, the inherent inductance and resistance, combined with the stray capacitance to ground, will produce a complex equivalent circuit, shown in Figure 14.68. Here again, the following expressions apply for the transfer function $h(s)$ and the USR $g(t)$:

$$h(s) = n\frac{\sinh\frac{1}{n}\sqrt{\frac{(R+sL)sC_e}{1+(R+sL)sC_p}}}{\sinh\frac{1}{n}\sqrt{\frac{(R+sL)sC_e}{1+(R+sL)sC_p}}}$$

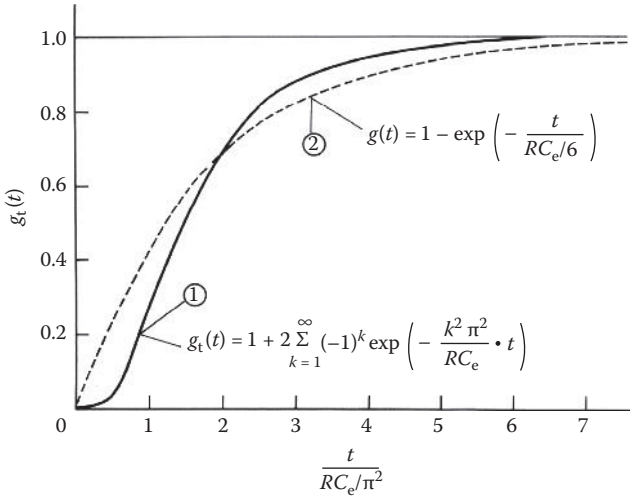


FIGURE 14.67 Unit step response evaluated for equivalent circuits with distributed and lumped parameters. (From Kuffel, E. et al., *High Voltage Engineering—Fundamentals*, 2nd edn., Pergamon Press, Oxford, 2000.)

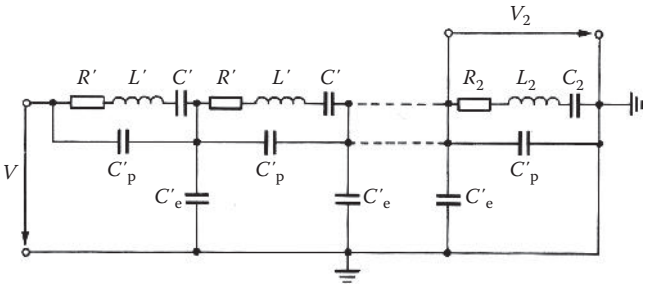


FIGURE 14.68 Equivalent circuit of a capacitive voltage divider. $R = nR'$, $C_e = nC_e'$, $C_p = C_p'/n$, $R_2 = R'$, and $C_2 = C'$.

and

$$g(t) = 1 - \frac{C_e}{6(C + C_p)} + 2\exp(-at)\sum_{0}^{\infty}(-1)^k \frac{\cosh(b_k t) + \frac{a}{b_k}\sinh(b_k t)}{AB} \tag{14.49}$$

with

$$A = 1 + \frac{C_p}{C} + \frac{C_e}{Ck^2\mathrm{p}^2}$$

and

$$a = \frac{R}{2L}$$

$$B = 1 + \frac{C_p k^2 \mathrm{p}^2}{C_e}$$

and

$$b_k = \sqrt{\frac{k^2 \mathrm{p}^2 A}{LC_e B}}$$

Capacitive divider is usually adequate for measurement of ac voltage and low-frequency content transients, for example, switching impulses, but has a tendency to oscillate when measuring fast transient events.

Compensated R–C voltage divider—measurement of transient voltages: To improve the transient response of capacitive divider, Zaengl has come up with the solution by inserting real resistor units in series with the capacitors. By properly selecting the value of the series resistor, the oscillatory response of the capacitive divider can be adequately damped out (Zaengl, 1965). Figure 14.69 compares the USRs of a series-compensated capacitive divider with different values of the series resistor. Finally, by adding a parallel branch of high ohmic resistors to the capacitors, the dc voltage can also be measured. The resulting series-compensated capacitive divider has since become the universal voltage divider (Feser, 1974). Figure 14.70 shows such a universal series-compensated voltage divider at IREQ, rated at 6.4 MV.

14.4.3.2 Low-Voltage Arm

In the preceding analysis of the voltage divider, the low-voltage arm is one impedance element of the divider, connected to ground. In practice, the low-voltage arm actually comprises also the coaxial cable connection, assumed lossless, to the measuring instrumentation, which usually has high input impedance and wide bandwidth. Such a complex arrangement of the low-voltage arm can introduce additional distortion, reflections, etc., to the measure signal at the output of the voltage divider. Particular care must be taken to design the low-voltage arm to meet its objectives and transmit the measured signal to the measuring device with minimal distortion. Figure 14.71 shows different arrangements of the low-voltage arm for the various types of voltage divider used.

Resistive divider: In a resistive divider shown in Figure 14.71a, the reflections in the measuring cable can be damped out by placing a resistance $R = Z_k$, the surge impedance of the measuring cable, in parallel with the input of the measuring scope.

Capacitive divider: For the capacitive divider shown in Figure 14.71b, to avoid overloading the low-voltage arm, the damping resistor $R = Z_k$ must be placed at the input end of the measuring cable. At input, the

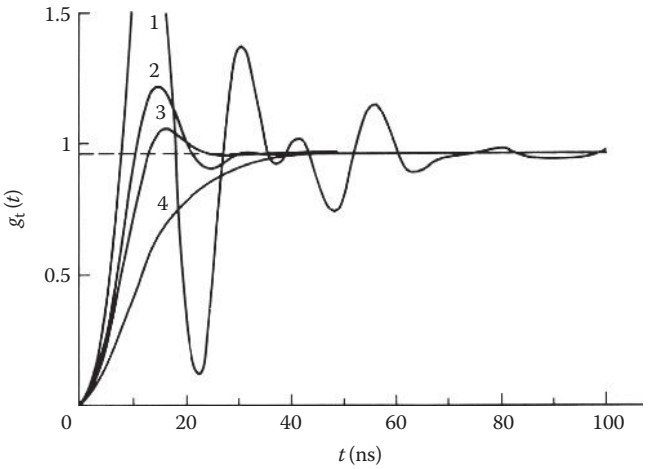


FIGURE 14.69 Computed USR $G_t(t)$ for damped capacitive dividers according to equivalent circuits with C = 150 pF, L = 2.5 μH, C_e = 40 pF, and C_p = 1 pF. Damping resistances R: (1) 250 Ω, (2) 750 Ω, (3) 1000 Ω, and (4) 2000 Ω. (From Kuffel, E. et al., *High Voltage Engineering—Fundamentals*, 2nd edn., Pergamon Press, Oxford, 2000.)



FIGURE 14.70 A 6.4 MV compensated *R–C* voltage divider at IREQ. (Photo Courtesy of Hydro-Québec.)

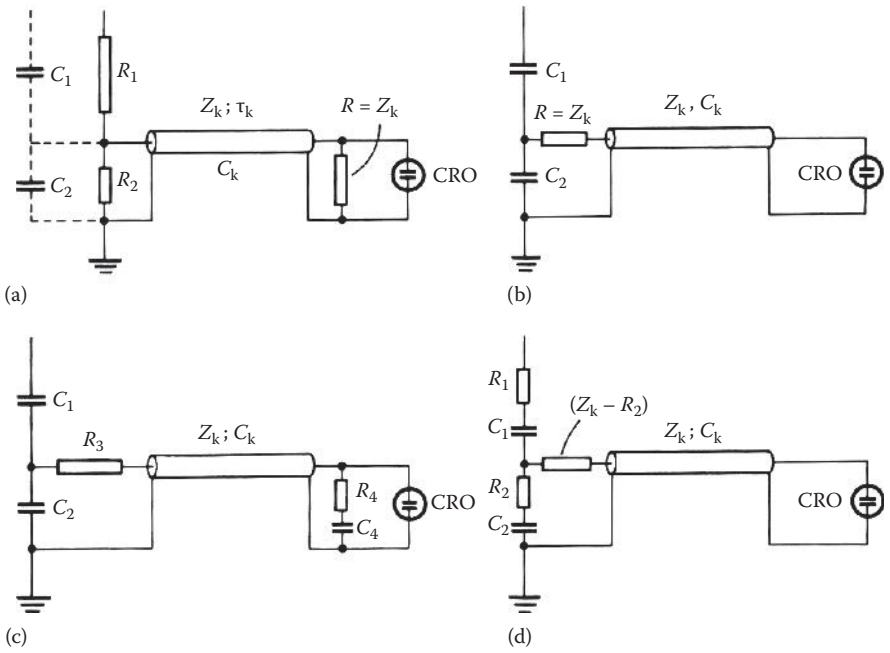


FIGURE 14.71 Arrangement for the low-voltage arm of voltage dividers: (a) resistive divider, (b) capacitive divider, (c) capacitive divider, and (d) series-damped capacitive divider.

measured signal is reduced by half. However, as it reaches the open end of the cable due to the high input impedance of the scope, it will be reflected and doubled, thus restoring the initial measured signal at the input of the recording instrument. The reflected wave charges the cable to its final voltage and is absorbed by the resistance R, which also discharges the capacitance C_2 during this transient period, close to twice the travel time T_r of the transient wave. It follows that the voltage divider ratio has two slightly different values:

$$n_0 = \frac{C_1 + C_2}{C_1} \quad \text{for } t = 0$$

and

$$n_e = \frac{C_1 + C_2 + C_k}{C_1} \quad \text{for } t > 2T_r$$

The signal cable therefore introduces an initial overshoot of the voltage, which is usually neglected.

The response of the capacitive divider can be improved by transferring part of the low-voltage arm capacitor C_2 to the cable end and connecting it in series with a resistor as shown in Figure 14.71c. The method introduced by Burch (Burch, 1932) proposed to make both matching resistances equal: $C_1 + C_2 = C_4 + C_k$ and $R_3 = R_4 = Z_k$. The original overshoot of $C_k/(C_1 + C_2)$ is reduced to 1/6.

Series-damped capacitive divider: For damped capacitor dividers shown in Figure 14.71d, the reflected wave will see the matching resistor R_3 in series with the parallel resistors R_1 and R_2. The value of the matching resistor is therefore

$$R_3 = Z_k - \frac{R_1 R_2}{R_1 + R_2} \triangleq Z_k - R_2$$

since, in practice, R_1 is usually much larger than R_2.

Physical layout of the low-voltage arm: Finally, it should be noted that whereas the matching resistors for coaxial cables, that is, the resistors between the central and outer conductors, are commercially available, the series resistors for all capacitor dividers are an integral part of the low-voltage arm. In addition, the capacitor C_2 is usually large to keep the measured signal at reasonable level. A coaxial arrangement of the circuit elements forming the low-voltage arm of an R–C-compensated divider is highly recommended to minimize its inductance, as illustrated in Figure 14.72 (Malewski and Hyltén-Cavallius, 1974).

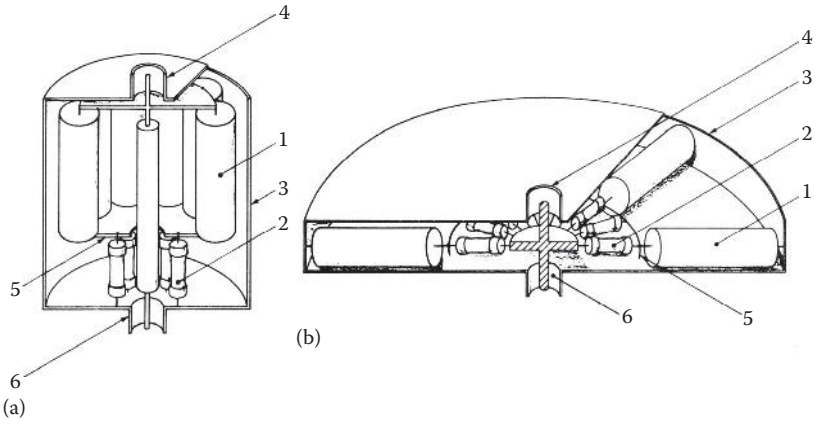


FIGURE 14.72 (a) Cylindrical and (b) radial constructions of low-voltage arm for EHV voltage dividers: (1) capacitor, (2) resistor, (3) metal box, (4) output coaxial terminal, (5) intermediate electrode, (6) input coaxial terminal. (From Malewski, R. and Hyltén-Cavallius, N.R., *IEEE Trans.*, PAS-93, 1797, 1974—Luhrmann's discussion.)

14.4.3.3 Connecting Lead

To minimize the effect of stray capacitance on the voltage divider, the latter must be located away from large objects: voltage generator, laboratory wall, and even the test object. The connecting lead, located above ground, constitutes a short transmission line for the high-frequency signal and *should not be made of thin wire*, which tends to introduce unwanted inductance into the circuit. Furthermore, since the connecting lead can have some length, the connection to the impulse generator should be made at the test object rather than at the voltage divider.

In measurement of fast transients, the connecting lead can and should be treated as a lossless transmission line, which causes reflections to occur at its ends if not properly taken into account (Creed and Collins, 1970). The time between two reflections is equal to the traveling time of the reflecting wave across the connecting lead, typically a few tens of nanoseconds. Proper evaluation of the influence of the connecting lead can be made using computer transient analysis program. However, in practice, the problem is dealt with by introducing a damping resistor at the test object side such that $R_d = Z_l$, the surge impedance of the transmission line formed by the connecting lead.

14.4.3.4 High Voltage Electrode

Because of the HV applied to the voltage divider, it is necessary to provide the latter with an adequate electrode to prevent the development of corona discharges at the HV end of the divider. However, the presence of such an HV electrode introduces a capacitance to ground higher than the stray capacitance, normally associated with the HV end of the divider, and affects its nominal voltage distribution. The design of the HV electrode, usually a toroid, is a compromise between the following:

- A time-invariant voltage distribution along the resistive column subject to a step voltage, that is, the initial potential distribution dictated by the field distribution along the divider, should be as close as possible to its final distribution dictated by its resistive voltage distribution.
- The input capacitance of the divider, largely dictated by the capacitance of the HV electrode, should be as small as possible to minimize the roundoff effect caused by the time constant R_dC on the measured impulse voltage. R_d is the damping resistance added to the connecting lead.
- The diameter of the HV electrode should be sufficiently large to prevent the development of corona discharge during high voltage application.

These considerations have led to a new approach to design resistive voltage divider based on field optimization (Malewski and Maruvada, 1976). Referring to Figure 14.73, which illustrates the voltage and current flowing in a resistive voltage divider, the following relations can be derived:

$$u(l,t) = u(0,t) - \int_0^l i(x,t)\frac{dR(x)}{dx}dx$$

$$i(x,t) = i(l,t) + \int_x^l \frac{di(z,t)}{dz}dz \quad \text{with} \quad \frac{di(z,t)}{dz} = \frac{d^2Q(z,t)}{dt\,dz}$$

where $Q(\zeta, t)$ is the amount of charge that passes by the resistance $R(\zeta)$ to charge the stray capacitance $C(\zeta)$. It follows

$$u(l,t) = u(0,t) - i(l,t)\int_0^l \frac{dR(x)}{dx}dx - \int_0^l \frac{dR(x)}{dx}\left[\int_x^l \frac{di(z,t)}{dz}dz\right]dx = 0$$

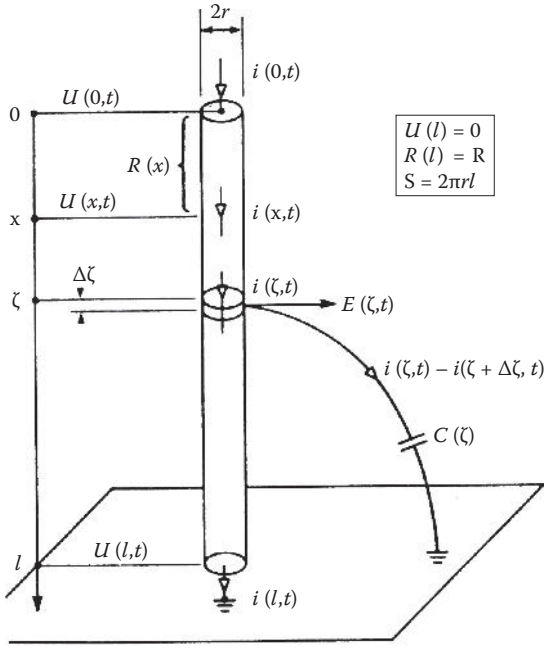


FIGURE 14.73 Illustration of the current flowing in a resistive divider. (From Malewski, R. and Maruvada, P.S., *IEEE Trans*., PAS-95, 1267, 1976.)

So that

$$1-\frac{R\,i(l,t)}{u(0,t)}=\frac{1}{u(0,t)}\int_0^l \frac{dR(x)}{dx}\left[\int_x^l \frac{d^2Q(z,t)}{dt\,dz}dz\right]dx$$

since the output voltage of the divider is

$$u_o(t)=\frac{R}{n}i(l,t)$$

where
n is the division ratio
R/n is the resistance of the low-voltage arm

The transfer function $f(t)$ is given by

$$f(t)=\frac{R}{n}\frac{i(l,t)}{u(0,t)} \tag{14.50}$$

The USR of the divider is then

$$G(t)=n\,f(t) \tag{14.51}$$

and the response time T, according to IEC definition, is

$$T=\int_0^{\infty}\left[1-G(t)\right]dt=\frac{1}{U}\int_0^{\infty}\left[\int_0^l \frac{dR(x)}{dx}\left[\int_0^l \frac{d^2Q(z,t)}{dt\,dz}dz\right]dx\right]dt$$

From Gauss's law, the charge $Q(z, t)$ is related to the normal field component at the surface of the divider column according to

$$Q(z,t) = \varepsilon_0 2\pi r E(z,t)$$

The response time T is

$$T = \frac{2\pi\varepsilon_0 r}{U}\int_0^{\ell}\frac{dR(x)}{dx}\left[\int_0^{z}E(z,\bullet) - E(z,0)\right]dz\,dx \tag{14.52}$$

where $E(z,\bullet)$ and $E(z, 0)$ are the final and initial distributions of the normal field component at the surface of the divider column. These field distributions can be calculated using a computer program. The numerical calculation was made by subdividing the divider column into n elements; the preceding expression for the response time becomes

$$T = S\varepsilon_0\frac{\ell}{n^2}\left[\sum_1^n K_i\sum_1^n\left(E_{j,\bullet} - E_{j,0}\right)\right] \tag{14.53}$$

where $S = 2\pi r\ell$ is the surface of the divider column, $K_i = dR(x)/dx$, and $E_j = E(z)/U$.

For a linear distribution of the resistance along the divider column, one has

$$R(x) = \frac{R}{\ell}x \quad \text{and} \quad K_i = \frac{R}{l}$$

One gets

$$T = S\varepsilon_0\frac{R}{n^2}\left[\sum_1^n\sum_1^n\left(E_{j,\bullet} - E_{j,0}\right)\right] \tag{14.54}$$

For the 2.7 MV divider designed by Malewski and Maruvada, according to the field optimization approach, the response time is 55 ns (Malewski and Maruvada, 1976).

14.4.3.5 Measuring Instrument

The recording of impulse voltage is characterized by the following:

- The short duration of the signal and the required high accuracy, expressed in percent, of the voltage.
- The signal is not repetitive, and its exact time of appearance cannot be foreseen.
- The generation of impulse voltage is always accompanied by intense electromagnetic interferences from the impulse generator operating in the MV range.

14.4.4 Measurement of Current

Measurement of current in a test circuit can be made in many ways using ampere meter, current transformer, and resistive shunt, which is most widely used due to its simplicity: the measured current is proportional to the voltage drop across the shunt. Two situations merit some discussion, namely, the measurement of fast transient current in corona and gap discharges and the measurement of standard impulse currents. A special problem is measurement of short circuits in circuit breaker testing with associated post-arc current.

14.4.4.1 Measurement of Fast Transient Corona Pulses

The measurement of fast transient corona pulses is made by inserting a resistive shunt between the plane electrode and ground. The actual measuring circuit is a parallel *R–C*, the response time of which, in this case, is characterized by the time constant $\tau = RC$, where R is the measuring resistance and C is the stray capacitance to ground. Noting that the resistive shunt is normally adapted to the surge impedance of coaxial measuring cable, typically in the range of 50 to a few hundred ohms, and a stray capacitance of a few tens of picofarads, the typical time constant is 5 ns, which is adequate most of the time.

Such a circuit time constant is, however, insufficient to measure gap discharge current developing between the line conductor and a floating object like rain drops leaving the conductor, loose connecting wires, etc. The only way to reduce the circuit time constant is to reduce the stray capacitance, a parameter largely dependent on the experimental setup. Janischewskyj and Arainy achieved this by using an inverted test setup, with the highly stressed electrode at ground potential, and minimizing the actual size of the discharge electrode, thus reducing significantly the stray capacitance of the measuring circuit (Janischewskyj and Arainy, 1981).

14.4.4.2 Measurement of Impulse Current

The design of high-current shunt usually adopts a tubular configuration for the resistive element. To take advantage of the absence of a magnetic field within the current-carrying tube, the measuring circuit is located inside the tube, connecting to both ends of the resistive element. The output signal is thus free of magnetic coupling and corresponds to the voltage drop across the resistive element. However, due to the magnetic flux inside the wall of the resistive tube, there is some coupling between the current-carrying tube and the measuring circuit.

The transient response of a resistive cylindrical shunt has been examined in (Hannakam, 1970; Zaengl, 1986). It has been shown that the response time can be approximated by

$$T_r = \frac{\mu d^2}{6\rho} \tag{14.55}$$

where
- μ is the permeability
- ρ resistivity of the shunt material
- d is the wall thickness

For a tube with thick wall, the response time becomes prohibitive, and some compensating means are necessary. One effective compensation method consists of placing the measuring conductor in a groove located within the wall of the resistive element. By controlling the profile of the groove and hence of the measuring cable, its magnetic coupling can be minimized if not eliminated (Malewski et al., 1981).

The current density distribution within the wall of the resistive element is described by the diffusion equation (Malewski et al., 1981):

$$\frac{d^2 i(r,t)}{dr^2} + \frac{1}{r}\cdot\frac{di(r,t)}{dr} - \frac{\mu}{\rho}\frac{di(r,t)}{dt} = 0 \tag{14.56}$$

which, after a change of variables,

$$x = \frac{r}{a} \quad \text{and} \quad t = \frac{\tau}{\mu a^2/\rho}$$

where a is the outer radius of the tube, can be rewritten as

$$\frac{\mathrm{d}^2 i(x,t)}{\mathrm{d}x^2} + \frac{1}{x}\cdot\frac{\mathrm{d}i(x,t)}{\mathrm{d}x} - \frac{\mathrm{d}i(x,t)}{\mathrm{d}t} = 0 \tag{14.57}$$

Since the cross section of the conductor is finite, the total current $I(t)$ must be equal to the integral of the current density over the whole cross section, with an inner tube radius b and $k = b/a$

$$I(t) = 2\pi a^2 \int_k^1 i(x,t)\, x\, \mathrm{d}x \tag{14.58}$$

The radial derivative of the current density, on the other hand, must vanished at the inner surface of the tube, since there is no magnetic field inside the tube:

$$\left.\frac{\mathrm{d}i(x,t)}{\mathrm{d}x}\right|_{x=k} = 0 \tag{14.59}$$

Subjected to a unit step current $I(t)$, a transfer function $T(x, y)$, normalized by the cross-sectional area of the tube $\pi a^2 (1 - k^2)$, was determined for the shunt as (Malewski et al., 1981)

$$T(x,t) = \frac{I(x,t)}{I(t)} = 1 + \frac{1-k^2}{2} \sum_1^\infty \frac{N(xs_\mathrm{i})\exp(-s_\mathrm{i}^2 t)}{s_\mathrm{i} D'(ks_\mathrm{i})} \tag{14.60}$$

with

$$N(x, s_\mathrm{i}) = K_1(xs_\mathrm{i})\,I_0(xs_\mathrm{i}) + I_1(xs_\mathrm{i})\,K_0(xs_\mathrm{i})$$

and

$$D(k, s_\mathrm{i}) = I_1(s_\mathrm{i})\,K_1(ks_\mathrm{i}) - I_1(ks_\mathrm{i})\,K_1(s_\mathrm{i})$$

where

$I(x, t)$ is the solution of the diffusion equation obtained with the earlier boundary condition
I and K are modified Bessel functions of the first and second order, and
s_i are obtained from solving $s_\mathrm{i}\, D(ks_\mathrm{i}^{1/2}) = 0$

By properly choosing the profile of the measuring circuit, it is possible to make the transfer function equal to 1.0, ensuring a delay-free measurement of the current $I(t)$.

Referring to Figure 14.74a, let $f(x)$ be the length of the measuring circuit at a radius x, normalized to the length of the resistive element, the actual path of the measured circuit within the tube wall (Figure 14.74b) is given by

$$g(x) = \int_k^x f(u)\,\mathrm{d}u \tag{14.61}$$

with

$$g(1) = \int_k^1 f(u)\,\mathrm{d}u = 1$$

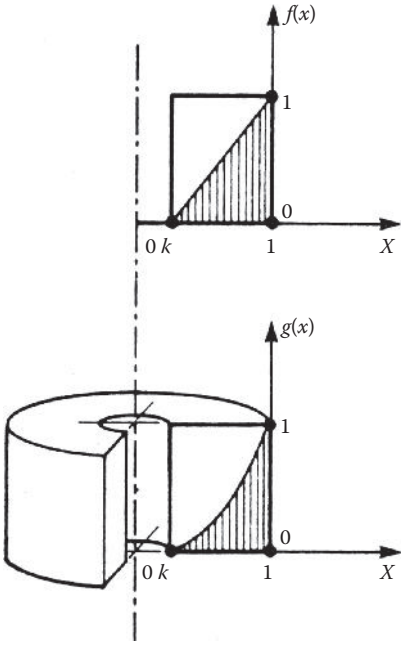


FIGURE 14.74 Illustrations of the length of the measuring circuit and of its integral $g(x)$, representing the actual path of the measured circuit within the tube wall. (From Malewski, R. et al., *IEEE Trans.*, PAS-100(3), 1333.1981.)

Malewski et al. have shown that a simple function $f(x) = Ax$ would bring the transfer function equal to 1.0, in addition, by making

$$A = \frac{2}{1 - k^2}$$

The condition $g(1) = \int_k^1 f(u)\,du = 1$ is also fulfilled.

The actual profile of the measuring circuit $g(x)$ inside the tube wall is obtained by (Malewski et al., 1981)

$$g(x) = \int_k^x f(u)\,du = \frac{2}{1 - k^2} \int_k^x u\,du = \frac{x^2 - k^2}{1 - k^2} \tag{14.62}$$

For the particular case of a solid conductor, $k = 0$, the profile $g(x)$ simplifies to

$$g(x) = x^2 \tag{14.63}$$

For a hollow conductor, $k > 0$, the ideal profile of the measuring conductor follows a parabola, illustrated in Figure 14.75 for different values of k.

For a flat conductor shunt, it can be shown that the ideal profile is linear as given by

$$g(x) = \int_0^x 1\,du = x \tag{14.64}$$

Figure 14.76 shows two model shunts of tubular and flat conductors, showing the groove in the conductor wall with the measuring conductors connected at both ends of the groove. It was shown (Malewski et al., 1981) that such compensated shunt design is particularly suited to high short circuit current measurements.

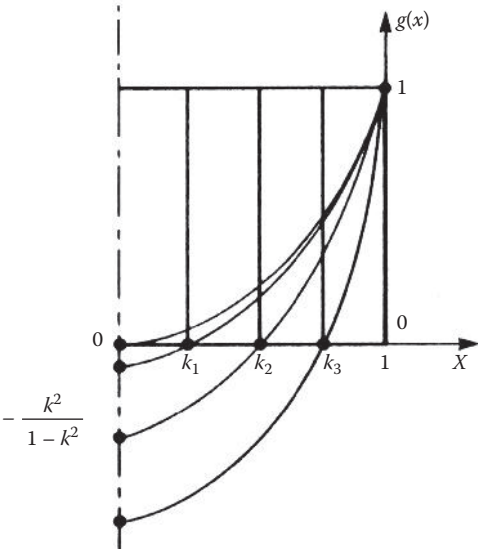


FIGURE 14.75 Ideal profile for the measuring circuit, located in a groove within the wall of the resistive element. (From Malewski, R. et al., *IEEE Trans*., PAS-100(3), 1333.1981.)

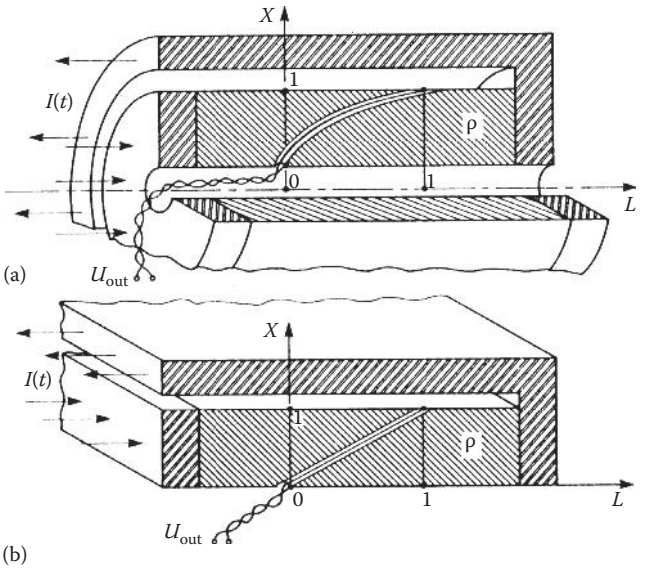


FIGURE 14.76 Design principle of the compensated shunt with (a) cylindrical and (b) flat geometry. (From Malewski, R. et al., *IEEE Trans*., PAS-100(3), 1333.1981.)

Figure 14.77 compares the responses of the model shunts with and without elimination of the measuring error caused by skin effect and well illustrates the performance of the compensated shunt.

14.4.5 Measurement of Power Losses

HV equipment requires adequate dielectric performances for its insulation system. This implies low dielectric losses, and the insulation of an HV equipment can be represented by a series or parallel *R*–*C* circuit, the series *R*–*C* representation being the default option. Different methods exist for the measurement of the capacitance and the power loss tan δ, defining the dielectric properties of an insulation system. We will review the two common methods currently in use: the Schering and the current comparator bridge methods.

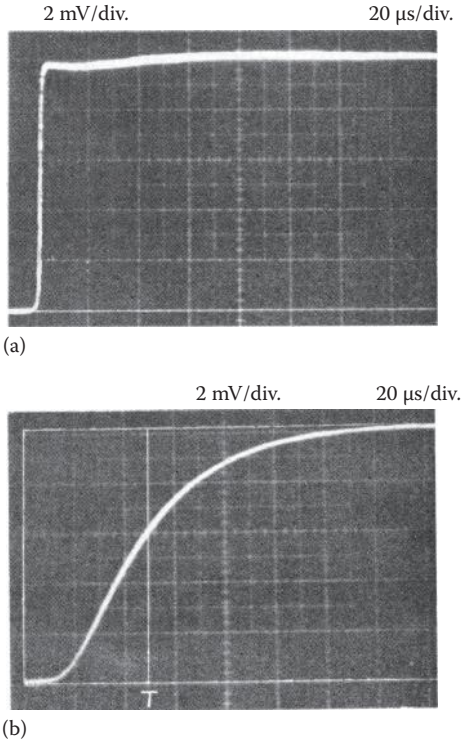


FIGURE 14.77 Step response of the model shunt: (a) with and (b) without elimination of the measuring error caused by skin effect. (From Malewski, R. et al., *IEEE Trans*., PAS-100(3), 1333.1981.)

14.4.5.1 Schering Bridge

Figure 14.78 shows the basic circuit of a Schering bridge (Palm, 1932; Keller, 1950). The test object, in the first arm of the bridge, is represented by a capacitance C_x in series with a resistance R_x, representing its power losses; both parameters are to be determined. The second arm of the bridge contains a standard capacitor C_s with negligible loss, the values of which are known and stable over the whole range of voltage. The third arm of the bridge contains an adjustable resistor R_3, while the fourth arm of the bridge contains an adjustable capacitor C_4 in parallel with a resistor R_4 to balance the bridge.

A null detector—a sensitive galvanometer—is connected between the two midpoints of the bridge, which are the ground terminals of the test object and the low-voltage terminal of the standard capacitor C_s. The bridge configuration offers the advantage of using the dielectric insulation performances of the test object and standard capacitor to provide adequate protection to the sensitive measuring instrumentation from the test voltage. The measurement of both the capacitance and the power losses can be made at full voltage applied to the test object, while the sensitive measuring instrumentation sees only a few volts. However, some protective means—paralleled protecting gaps—must be provided to protect the measuring instrumentation in case of failure of the test object.

When the bridge is not balanced, the current flowing through the null detector represents the unbalanced current resulting from the potential difference between the midpoints of the bridge and can circulate in any direction. Varying the impedances Z_3 and Z_4 changes the potentials at the midpoints of the bridge. One can thus bring the bridge to the balanced condition when these potentials are equal: no current circulates then through the null detector. The following conditions exist when the bridge is balanced:

- The potentials at the midpoint of the bridge are equal; one has $\dfrac{Z_x}{Z_3} = \dfrac{Z_s}{Z_4}$.
- The current flowing through the test object is the same through the impedance Z_3.
- The current flowing through the standard capacitor C_s is the same through the impedance Z_4.

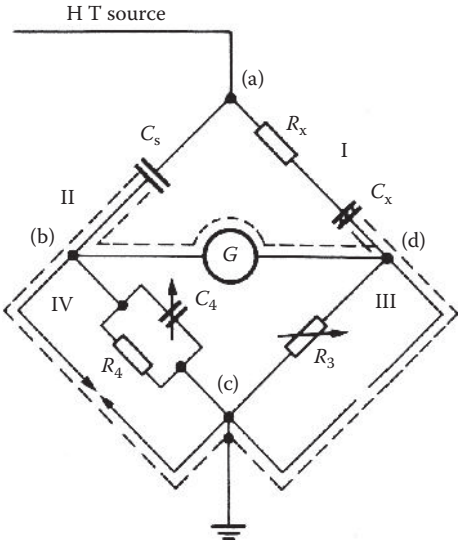


FIGURE 14.78 Schering bridge. (From Palm, A., *Archiv fur Tech. Messen*, 921, 1932; Keller, A., *ETZ*, 71, 232, 1950.)

These specific conditions at bridge balance allow the determination of both the capacitance C_x and the power loss tan δ of the test object. One can express the balance conditions as

$$R_x + \frac{1}{j\omega C_x} = \frac{R_3}{j\omega C_s}\left(\frac{1}{R_4} + j\omega C_4\right)$$

By separating the real and imaginary components in the preceding expression, one obtains

$$R_x = R_3\frac{C_4}{C_s} \quad \text{and} \quad C_x = C_s\frac{R_4}{R_3} \tag{14.65}$$

and the power loss factor tan δ is

$$\tan\delta = \omega R_x C_x = \omega R_4 C_4 \tag{14.66}$$

Modern Schering bridge can measure capacitances over a wide range of values, from a few pF to several μF, and the power loss factor tan δ from 10^{-4} to 10.

Operating notes: In the bridge configuration shown in Figure 14.78, the bridge is grounded at the low-voltage end of the transformer, which supplies the high voltage, and hence, the bridge is also grounded at point (*c*). Under balance condition, both sides of the null detector are at the same potential, with the shield grounded. Partial stray capacitances appear at the branches I and II of the bridge and can affect the measured value of tan δ. If C_I and C_{II} are, respectively, the partial stray capacitances at branches I and II, then it can be shown that

$$\tan\delta = R\omega\left(C_4 + C_{II}\right) - R\omega C_I$$

This problem can be solved by an appropriate grounding arrangement as proposed by Wagner, which allows separate balancing of the bridge and the stray capacitances (Wagner, 1911). This procedure is, however, rarely used today, thanks to operational amplifiers, which allow automatic balancing of the Wagner earth. Although the bridge may be grounded at point (*c*), the potential at the shields is shifted to the potential of the detector branch by an operational amplifier with unit voltage gain. The shields of the leads to C_x and C_s are not grounded but connected to the output of the operational amplifier.

14.4.5.2 Current Comparator Bridge (Peterson, 1964)

The basic circuit of a current comparator bridge is shown in Figure 14.79. The two windings N_x and N_s with adjustable number of turns are mounted on the same toroidal core to form the low-voltage arms of the bridge. In addition, a parallel adjustable capacitance C_2 and an adjustable series-connected resistance R_2 complete the low-voltage arm of the bridge below the standard capacitor C_s. A third winding feeds the null detector for balancing the bridge. Because of the very small resistances of the windings, the currents flowing in the measured capacitor C_x and the standard capacitor C_s are

$$I_x = U\omega C_x \quad \text{and} \quad I_s = U\omega C_s$$

and the ampere-turns are $N_x I_x$ and $N_s I_s$.

Varying the inductances N_x, N_s, the capacitance C_2, and the resistance R_2 brings the bridge to the balance condition and yields the following conditions:

$N_x I_x = N_s I_s$, which gives

$$N_x U\omega C_x = N_s U\omega C_s$$

One can deduce

$$C_x = \frac{N_s}{N_x} C_s \tag{14.67}$$

and

$$\tan\delta = R_2\omega C_2 \tag{14.68}$$

Operating notes: Comparing to the Schering bridge, the current comparator bridge is relatively insensitive to the stray capacitances. It has a higher accuracy in the measurement of the capacitance, but its resolution is lower for the measurement of tan δ.

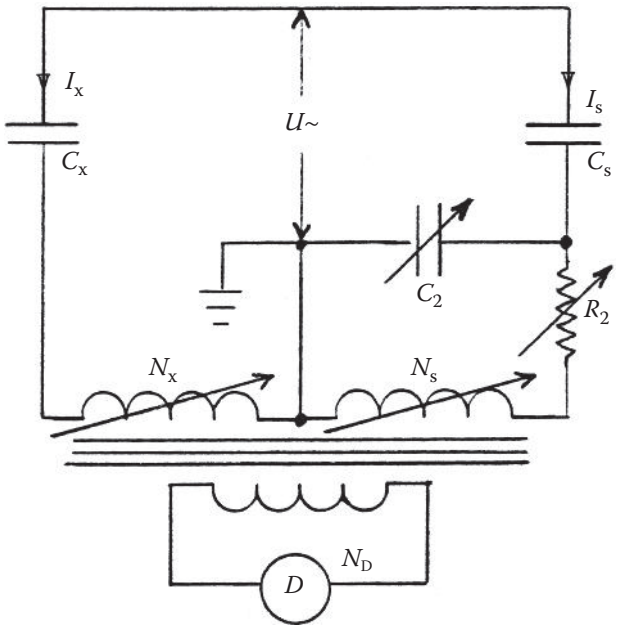


FIGURE 14.79 Basic circuit of a current comparator bridge.

14.4.5.3 Parallel R–C Representation

In both the Schering and current comparator bridges, the *R–C* series representation of the test object is systematically used. To convert the results into the *R–C* parallel representation of the test object, it suffices to compare the expressions of the respective impedances. One gets for the *R–C* parallel representation

$$Y_{xs} = \frac{1}{R_{xs} + \dfrac{1}{j\omega C_{xs}}} = \frac{R_{xs} - \dfrac{1}{j\omega C_{xs}}}{R_{xs}^{\,2} + \dfrac{1}{\omega^2 C_{xs}^{\,2}}} = \frac{(\omega C_{xs})^2}{1 + (\omega R_{xs} C_{xs})^2} R_{xs} - \frac{1}{j\omega C_{xs}} = \frac{1}{R_{xp}} + j\omega C_{xp}$$

It follows

$$R_{xp} = \frac{1 + (\omega R_{xs} C_{xs})^2}{(\omega R_{xs} C_{xs})^2} R_{xs} \quad \text{and} \quad C_{xp} = C_{xs} \frac{1}{1 + (\omega R_{xs} C_{xs})^2} \tag{14.69}$$

The power loss factor tan δ is

$$\tan\delta = \frac{1}{\omega R_{xp} C_{xp}} \tag{14.70}$$

14.4.6 Gas-Insulated Capacitor

Several HV measurements—capacitance, power loss factor tan δ, etc.—require a close to ideal capacitor with stable capacitance, negligible loss over the range of test voltages. Gas insulation offers the advantages of stable permittivity and low power loss. However, it has relatively low dielectric strength and requires operating at pressures of several atmospheres. Different designs of compressed-gas-insulated capacitor have been introduced over the years, using air, CO_2, and recently SF_6, which can operate at lower gas pressure than the other options. Figure 14.80 shows the cross section of a 900 kV, 60 pF,

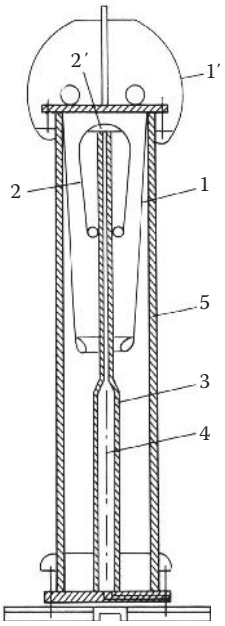


FIGURE 14.80 Compressed-gas-insulated capacitor: HV electrode (1) and corona shield 1′, low-voltage electrode (2) and guard shield 2′, (3) supporting tube, (4) coaxial connection, and (5) insulating housing. (From Keller, A., *ETZ*, 71, 232, 1950.)

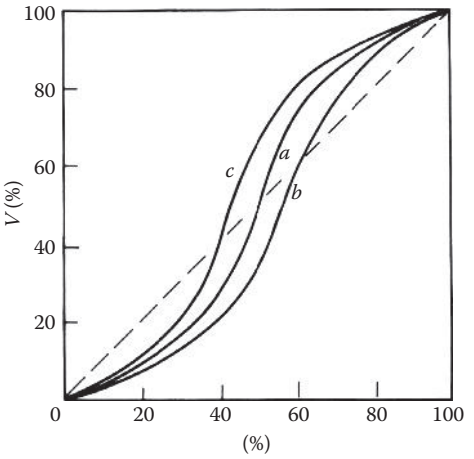


FIGURE 14.81 Influence of the length of the high voltage electrode: (a) 50%, (b) 60% and (c) 40% of the insulating column, on the voltage distribution along the surface of the insulating housing. (From Keller, A., *ETZ*, 71, 232, 1950.)

compressed-gas-insulated capacitor adapted by Keller, from the original design proposed by Schering and Wieweg in 1928. The capacitance is formed of two coaxial cone electrodes, an arrangement simple to produce and tolerant to minor eccentricity of the electrodes. The whole assembly is contained within an insulating housing, which provides a controlled environment to the capacitor insulation.

The insulating housing has to withstand the gas pressure and the rated voltage; the potential distribution along the insulating column is very much dependent on the length of the HV electrode, as illustrated by Figure 14.81, which shows the potential distributions along the insulating column for different lengths of the HV electrode. One observes a maximum gradient at the position corresponding to the tip of the HV electrode, which is difficultly controllable (Keller, 1955). The influence of the pressure-dependent relative permittivity of the gas upon the capacitance value may be taken into account by

$$\varepsilon_r = 1 + \alpha \frac{273P}{100T} \tag{14.71}$$

where

P is the gas pressure in kPa

T is the gas temperature in K

α is a constant characteristic of the gas: $\alpha = 0.00232$ for SF_6; $\alpha = 0.00055$ for N_2 and $\alpha = 0.00076$ for CO_2

Measurement of peak ac voltage: A good-quality standard capacitor offers also other applications, namely, in measurement of the ac voltage. This can be simply made by adding a capacitive low-voltage arm to the standard capacitor to form a capacitive voltage divider with good accuracy. Another application is in the measurement of the peak value of the ac voltage, using the Chubb–Fortescue method (Chubb and Fortescue, 1913). Figure 14.82 shows the circuit proposed by Chubb and Fortescue: the current through the standard capacitor is separated in its positive and negative components by means of two parallel back-to-back diodes. By inserting a current integrating ammeter in series with one of the diodes, the mean value of the rectified current can be measured. In effect, referring to Figure 14.83, which shows the ac current flowing through the standard capacitor C, the average current measured by the ammeter is given by

$$I = \frac{1}{T}\int_{t_1}^{t_2} i(t)\,dt = \frac{C}{T}\int_{t_1}^{t_2} dV = \frac{C}{T}\left(V_{+\max} + |V_{-\max}|\right)$$

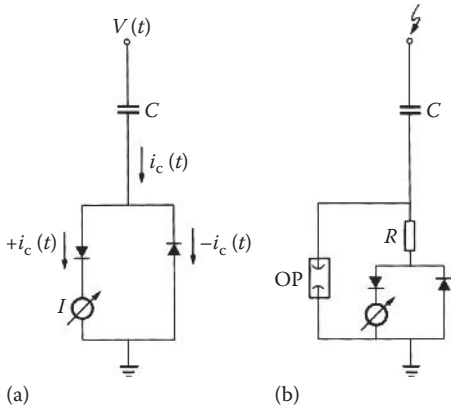


FIGURE 14.82 Chubb–Fortescue circuit for measurement of the peak value of an ac voltage. (a) Basic circuit and (b) recommended circuit with overvoltage protection.

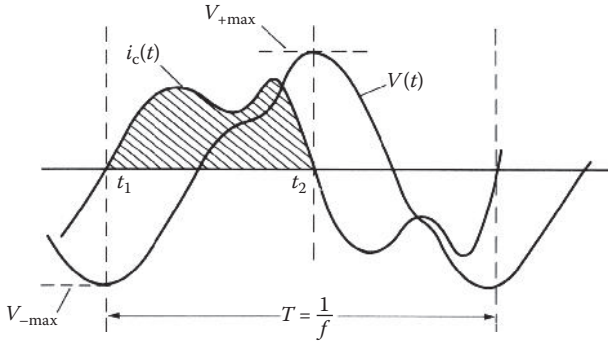


FIGURE 14.83 Illustration of the current flowing through the standard capacitor and the measuring instrument.

which yields

$$V_{max} = \frac{1}{2}V_{p\text{-}p} = \frac{I}{2Cf} \tag{14.72}$$

where $V_{p\text{-}p}$ is the peak-to-peak voltage of the ac voltage in a single cycle.

14.4.7 Partial Discharges Measurement

Partial discharge (PD) measurement is required in the evaluation of the dielectric performances of major equipment—power transformers and reactors. Two PD measurement methods are currently used, corresponding to the wide bandwidth and narrow bandwidth detector circuits. Their requirements, test procedures, etc., are detailed in international standards (IEC Standard 270, 1981) (NEMA Publication 107, 1970). We will review in the following, the basic principles for PD measurement.

The development of PD within a void in the insulation of HV equipment occurs when the gradient within the void reaches a critical level to produce a gas discharge. The avalanche process produces electrons and ions of both polarities, which are deposed on the wall of the void, forming a dipole of charge q. This PD process is perceived in the external circuit as a current PD pulse. In both wide and narrow bandwidth methods, the PD current from the test object is measured; the evaluation addresses either the apparent charge Q_a or the radio interference voltage (RIV). Figure 14.84 shows a typical circuit for measuring PD in a test object. The PD current is diverted to the measuring impedance Z_m by means of a coupling capacitor C_k of typical capacitance 1 nF, connected in parallel with the test object, which also isolates the measuring equipment from the applied test voltage. Although it is possible to place the measuring impedance Z_m in series with

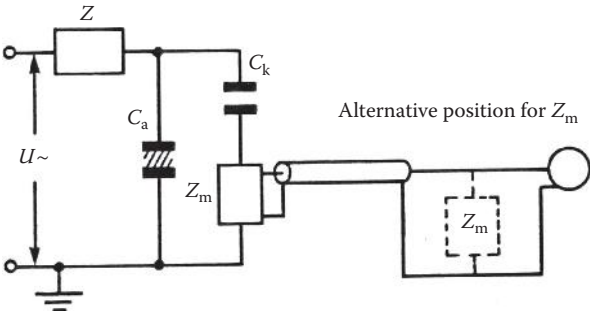


FIGURE 14.84 Typical arrangement for measuring PD in a test object. (From IEC Standard 60270, *Partial Discharge Measurement*, 3rd edn., IEC, Geneva, Switzerland, 2000.)

the test object, this arrangement is not favored due to the risk of damaging the measuring equipment in case of failure of the test object. The filter Z blocks any high frequency interference from the voltage source.

14.4.7.1 PD Measurement Using Large Bandwidth Detector Circuit

The PD measurement using large bandwidth detector circuit is recommended by the IEC Publication 60270 (IEC-60270, 2000). It is based on the evaluation of the apparent charge associated with the current pulses generated by PDs within the insulation of the test object.

Apparent charge: The definition of the apparent charge Qa of PD pulse given in IEC 60270 is "that unipolar charge which, if injected within a very short time between the terminals of a test object in a specified test circuit, would give the same reading on the measuring instrument as the PD current pulse itself. The apparent charge is usually expressed in picocoulombs." With the note: "the apparent charge is not equal to the amount of charge locally involved at the site of the discharge and which cannot be measured directly."

Referring to Figure 14.85, which shows the PD model used by the IEC—the a–b–c model—the void is represented by a capacitance C_c, the dielectric portion of the gap is represented by two capacitances C_a

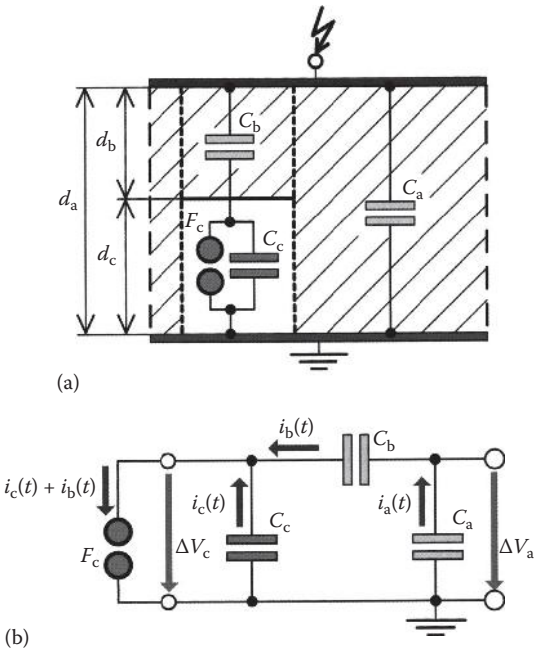


FIGURE 14.85 Circuit representation of PD current. (a) Schematic diagram. (b) Equivalent circuit. (From Lemke, E., *IEEE Electr. Insul. Mag.*, 28(6), 11, 2012.)

and C_b, where the latter corresponds to the dielectric portion of the gap in series with the void. The occurrence of a PD is described by a sudden short-circuiting of the capacitance C_c through a discharging resistance R_c, corresponding to a voltage drop δV_c, across the void. One can see that although both the voltage within the void and the discharge current generated by the PD are not known, its effect is felt as a PD current circulating in the external circuit and as a voltage drop δV_a related to the voltage drop across the void δV_c according to

$$dV_a = \frac{C_b}{C_a + C_b} dV_c \tag{14.73}$$

In the actual PD test circuit, the test equipment is energized by the test voltage source, and the PD current is measured via an impedance in series with the coupling capacitance C_k, as shown in Figure 14.84. The sudden voltage drop δV_a across the test object will produce a measured PD current $i(t)$ in the external circuit, the charge of which is given by

$$q = \int i(t)\,dt = (C_a + C_b)\,dV_a \tag{14.74}$$

assuming that $C_k >> (C_a + C_b)$. Replacing the expression for δV_a in Equation 14.73, one gets

$$q = (C_a + C_b)\,dV_a = (C_a + C_b)\frac{C_b}{C_a + C_b} dV_c = C_b dV_c \tag{14.75}$$

which is directly related to the voltage drop δV_c across the void caused by the development of a PD. Since the charge q is readily measurable while the voltage drop δV_c is not, this charge q is referred to as the *apparent charge* Q_a, which can be measured at any location in the test circuit shown in Figure 14.84. In practice, due to the presence of stray capacitances and the differences within the various circuit elements, the PD current and hence the measured apparent charge Q_a will vary slightly from one location to another. For example, the PD current circulating through the coupling capacitor and the measuring impedance Z_m is slightly lower than the PD current circulating through the capacitance of test object; this current in turn is smaller than the PD current within the void.

Furthermore, the presence of the coupling capacitance C_k also affects the measured charge Q_m according to

$$Q_a = dV_c C_b = dV_a (C_a + C_b) = dV_m (C_a + C_b + C_k) \tag{14.76}$$

On the other hand, the measured Q_m is given by

$$Q_m = C_k\, dV_m \approx \frac{C_k}{C_a + C_k} Q_a$$

or

$$\frac{Q_m}{Q_a} \approx \frac{C_k}{C_a + C_k} \approx \frac{C_k}{C_t + C_k} \tag{14.77}$$

The preceding relation (14.77) indicates the difficulties of PD measurements for test objects of large capacitance values C_t. Although both C_k and C_t may be known, the ability of detecting small values of Q_a will decrease with large values of C_t, fixing a limit on the recording of small pC in large test objects.

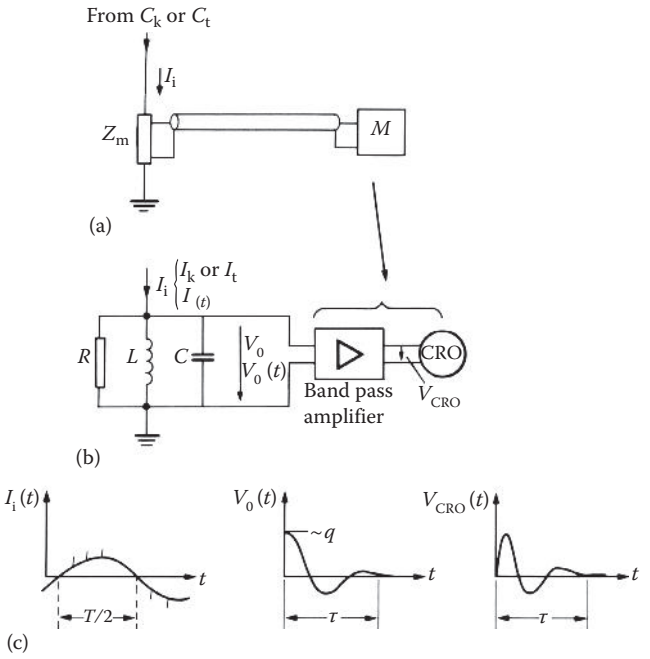


FIGURE 14.86 Wide bandwidth detector circuit. (a) Circuit diagram. (b) Equivalent circuit. (c) Schematic display of different variables. (From Kuffel, E. et al., *High Voltage Engineering—Fundamentals*, 2nd edn., Pergamon Press, Oxford, 2000.)

Evaluation of the apparent charge: From the preceding discussion, it is obvious that the apparent charge is the main characteristic parameter of PD current pulse. It is relatively insensitive to the circuit parameter and readily quantified from the measured PD current, namely, by integrating it to obtain the measured apparent charge. Integration of the PD current can be made either in the time domain or in the frequency domain:

$$Q_a = \int_0^{\infty} i_p(t)\,dt = \int_{-\infty}^{\infty} I_p(\omega)\,d\omega$$

The latter approach is used in the integration of the PD current. Figure 14.86 shows the measuring impedance used for the evaluation of the apparent charge of the PD pulse. It is a parallel RLC circuit, which represents a wideband filter with the characteristic parameters as follows:

Lower cutoff frequency:

$$30\ \text{kHz} \le f_1 \le 100\ \text{kHz}$$

Upper cutoff frequency:

$$f_2 = 500\ \text{kHz}$$

Effective bandwidth:

$$\Delta f = 400\text{kHz}$$

The characteristics of the band-pass filter must be adjusted with respect to the frequency spectrum of the PD pulse to make sure that its upper cutoff frequency is well within the PD frequency spectrum (IEC Standard 60270, 2000).

The voltage developing across the measuring impedance due to a Dirac function current pulse is

$$V_0(t) = \frac{q}{C}\exp(-\alpha t)\left(\cos\beta t - \frac{\alpha}{\beta}\sin\beta t\right) \tag{14.78}$$

with

$$\alpha = \frac{1}{2RC}$$

and

$$\beta = \sqrt{\frac{1}{LC} - \alpha^2} = \omega_0 \sqrt{1 - \alpha^2 LC}$$

The voltage $V_0(t)$ at the output of the detector circuit is a damped oscillatory voltage, the amplitude of which is directly proportional to q. The integration of the PD current is thus performed instantaneously ($t = 0$) by the capacitance C. The oscillatory response of the detector must be damped to avoid superposition error, which occurs when the time intervals between the PD pulses are shorter than the oscillatory period of the measured PD signal. A very efficient damping is obtained with a quality factor of $Q = 1$, which implies $R = \sqrt{L/C}$.

The damping constant becomes

$$\alpha = \frac{\omega_0}{2} = \pi f_0$$

The resolution time is then approximately

$$T_r \approx \frac{3}{\alpha}$$

For a typical resonance frequency of $f_0 = 100$ kHz, the resolution time amounts to approximately 10 μs. Finally, it should be noted that the resonant frequency is also affected by the main circuit elements, C_k and C_a. Therefore, the RLC input impedance must be adjusted in reference with the test object to keep the resonant frequency f_0 within acceptable limits.

Merits of the apparent charge PD evaluation method: The principal merit of the apparent charge method is that the evaluation is made with respect to the defining characteristics of the PD current pulse: its apparent charge Q_a. It represents an objective measurement of the PD performance of the equipment, easily reproduced in different laboratories. The wide bandwidth of the detector circuit also gives a high sensibility to the PD detection and, sometimes, its localization in the test equipment. Its use is increasingly adopted worldwide.

Apparent charge or induced charge: In spite of the widespread use of the apparent charge method for measurement of the PD level of an equipment, there has been serious criticism raised by Pedersen et al. (1991, 1995) concerning the validity to represent the void by a capacitance. The latter is intrinsically related to conducting electrodes between which a space-charge-free electrostatic field can be established. A meaningful application of the relation

$$Q = CU$$

to the case of a void is not possible since the void wall is not an equipotential surface, and once the space charges are present, the field is no longer Laplacian. Consequently, the electromagnetic transients detectable at the electrodes are not caused by discharging the imaginary capacitance of the void but by the dipole moment established in the void subsequent to a gas discharge.

Figure 14.87 illustrates the field lines associated to the buildup of the dipole within the void (Lemke, 2012). To satisfy the continuity equation, the current $i_c(t)$ due to the moving charge carriers across the void must be equal to the displacement current $i_b(t)$ within the solid dielectric and to the current $i_a(t)$ through the test object. As a result, the capacitance C_a is partially discharged, manifested by a sudden voltage drop δV_a. Integrating the currents over the transition time required for the establishment of the dipole, one gets

$$\int_0^{t_c} i_c \, dt = \int_0^{t_c} i_b \, dt = \int_0^{t_c} i_a \, dt$$

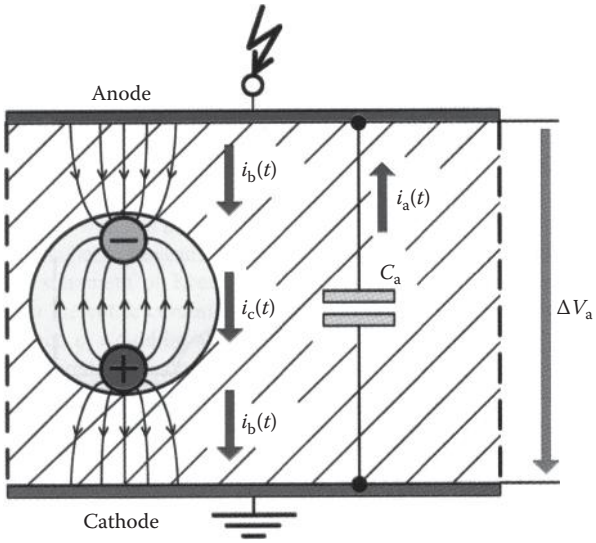


FIGURE 14.87 Induced charge. (From Lemke, E., *IEEE Electr. Insul. Mag.*, 28(6), 11, 2012.)

and

$$q_c = q_b = q_a = \mathrm{d}V_a C_a \tag{14.79}$$

Pedersen et al. showed that these charges are the charges induced on the electrodes of the test object and can be expressed as (Pedersen, 1987)

$$q_c = q_b = q_a = \mathrm{m}\,\mathrm{grad}\,\mathrm{l} \tag{14.80}$$

where

λ is a dimensionless function depending on the position of the space charges within the dielectric volume
μ is the dipole moment established in the cavity as a consequence of gas discharges

Since the induced charges at the electrodes of the test object corresponds to the apparent charge used in the IEC standard. No modification is required other than the correct definition of the measured quantity.

14.4.7.2 PD Measurement with Narrow Bandwidth Detector Circuit

The PD measurement with narrow band detector circuit, recommended in the NEMA publication 107, has been used for evaluation of the PD current for a long time, especially in North America. It is the voltage across the measuring impedance that is evaluated with the same equipment used for measuring radio interference (discussed in Chapter 8). The PD measuring impedance is a resistance R in series with the coupling capacitance C_k. The voltage measured across the measuring impedance is proportional to the PD current. It is read by a measuring circuit, essentially a superheterodyne radio receiver, illustrated in Figure 14.88, which, to each PD pulse at input, yields an output impulse voltage according to

$$V_m(t) = \frac{S_0 G_0 \mathrm{D}\omega}{\mathrm{p}} S_a \frac{\mathrm{E}\mathrm{D}\omega}{\mathrm{f}\ 2}(t - t_0)\cos\omega_m(t - t_0) \tag{14.81}$$

where

S_0 is the input signal
G_0 is the amplifier gain
$\Delta\omega$ is the bandwidth of the tuning circuit
ω_m is the measuring frequency

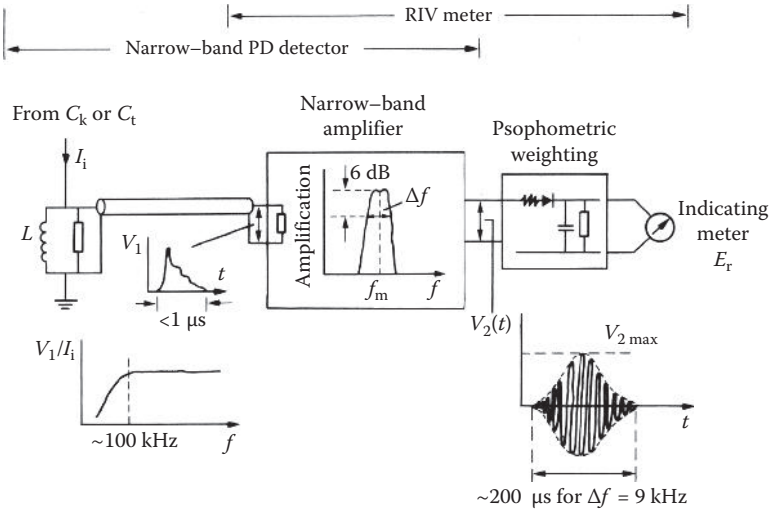


FIGURE 14.88 Narrow bandwidth detection circuit for evaluation of the RIV.

S_a is the sampling function, $S_a(x) = (\sin x/x) \Diamond V_m(t)$, that has a maximum value V_{max} of

$$V_{max} = \frac{S_0 G_0 \Delta\omega}{\pi} = 2 S_0 G_0 \Delta f \tag{14.82}$$

This output voltage is passed through a weighting circuit to give a final reading proportional to the quasi-peak (QP) value, which correlates best with the human appreciation of the annoyance level to the AM radio reception.

Merit of the RIV PD evaluation method: The PD measurement method using narrow bandwidth detection circuit is based on the acceptable level of interference to the AM radio reception of the noise produced by HV equipment. It suffers from using a somewhat subjective evaluation of the PD performance of the equipment. With the development of new radio transmission method and the digitalization of the signal, the interference level to the reception of AM radio has lost its basic justification, and the RIV evaluation method is nowadays less used for evaluation of the PD performance of HV equipment. Furthermore, since the two methods of PD evaluation follow different approaches, there is no direct correlation between the results obtained with these methods.

14.4.7.3 Calibration

Because of the finite bandwidth of the measuring impedance used in the PD measurements, both wide and narrow bandwidth circuits, the apparent charge Q_a, and RIV do not take account of the complete frequency spectrum of the PD pulse. Their evaluation in practice must be carried out with a calibrated signal, which provides the reference response to a unit apparent charge or RIV signal.

Calibration for measurement of apparent charge: Is made by injecting short-duration repetitive current pulses of known charge magnitude q_0, across the test objects, whatever the test circuit used. The calibrator consists, in general, of a generator producing repetitive square wave voltage pulses with a rise time shorter than 60 ns to ensure a sufficiently large frequency spectrum. The injected charge is then $q_0 = C_0 V_0$, which serves as the reference level for the measured PD. Referring to Figure 14.89, the capacitance C_0 of the calibrator is effectively in series with the load capacitance C_a; the injected charge is therefore

$$q_0 = \frac{C_0 C_a}{C_0 + C_a} V_0 = \frac{1}{1 + \dfrac{C_0}{C_a}} C_0 V_0 \tag{14.83}$$

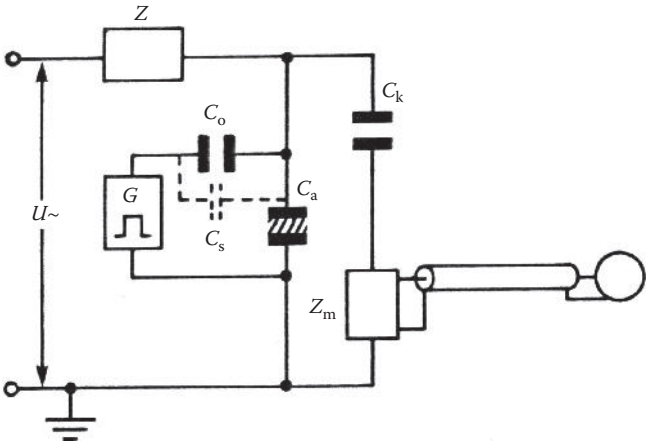


FIGURE 14.89 Calibration circuit for measurement of the apparent charge Q_a. (From IEC Standard 60270, 1981.)

It is essential to keep the capacitance C_0 as small as possible.

Calibration for measurement of RIV: The calibration circuit for measurement of RIV is the same as shown in Figure 14.84. However, since the RIV is a voltage, the calibration is made by measuring the RIV level generated at the output of the generator and at the measuring circuit to define the reference RIV level. Calibration for RIV can be made with a sine wave generator adjusted to the measuring frequency, 1 MHz in North America and 500 kHz in Europe, or using a square wave voltage generator. In the latter case, the calibration signal corresponds to a line in the frequency spectrum produced by the square wave voltage of the generator.

14.4.7.4 Capacitive Tap

HV equipment is equipped with bushings for their connection to the overhead lines, which often include capacitive taps. The use of the capacitive tap is particularly efficient during on-site testing, where it can serve as

- The coupling capacitor to a current probe for measurement of transient currents
- The HV arm of a capacitive divider for measurement of the ac voltage and transient voltage (Malewski et al., 1988)

14.4.8 Digital Techniques in HV Measurements

With the advent of digital measurement methods, powerful analytical tools have been introduced to the field of HV engineering. In most of the cases, the measured data in digital form can be rapidly analyzed and the results presented in user-friendly graphics, allowing real-time interactive actions during the test. Elaborated calculations can also be made on the digital data as illustrated in Figure 14.90, which shows the time-domain deconvolution method to reconstruct the actual voltage applied at the test object from the recorded digital signal of the breakdown voltage in a compressed-gas-insulated test cell (Malewski, 1982). The measured voltage is smoothed out of its high-frequency distortion, introduced by the measuring circuit, before its reconstruction to obtain the actual voltage seen at the test object.

However, although the digital approach is becoming unavoidable in almost every field, its application to HV testing and measurement of fast transient phenomena merits some considerations regarding drawbacks inherent to the digitization process. The reader can refer to a comprehensive review in Kuffel et al. (2000). We summarize in the following the main errors, which can be classified as static errors inherent in digitization process and dynamic errors associated with the operation of the digitalizing devices.

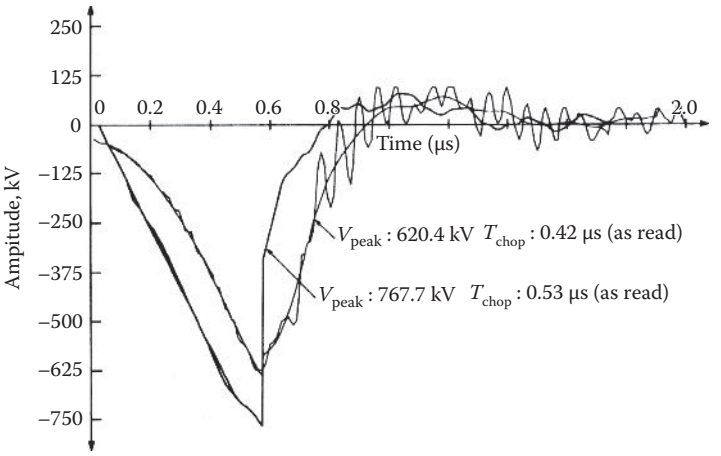


FIGURE 14.90 Time-domain reconstruction of the actual voltage applied at the test object from the recorded digital signal of the breakdown voltage in a compressed-gas-insulated test cell: (a) reconstructed signal, (b) smoothed signal, and (c) recorded digital signal. (From Malewski, R., *IEEE Trans*., PAS-99, 4508, 1982.)

14.4.8.1 Inherent Errors in Digital Recorders

In contrast to analog recorder, which writes a continuous trace of the measured signal, the digital recorder only records and stores the instantaneous values of the signal rounded off to the integer number and sampled at a certain rate over a finite period. The measured signal is reconstructed subsequently from the stored data by positioning them in chronological order. Two inherent errors are recognized and referred to as quantization and discrete-time sampling errors.

Quantization error: Is present because the analog value of a data sample is converted into a digital word, which is expressed in one of the 2^N possible representations made with N bits; each can take a value of 0 or 1. Here, the number of bits N represents the resolution of the A/D converter, and the quantization error corresponds to the minimum amount of information contained in one bit, referred to as the least significant bit (LSB). In practical terms, N-bit A/D converter defines 2^N code bins: the bands or ranges of voltage that can be subdivided on the full-scale screen of the display panel of the digital recorder, as illustrated in Figure 14.91. The LSB corresponds thus to $1/2^N$ of the full-scale deflection. This corresponds to 0.10% of its full-scale deflection for a 10-bit recorder.

Discrete-time sampling error: Describes the adequacy of representing an analog signal by a number of discrete points. The problem is best illustrated by considering a sine wave signal represented by the digital data sampled at four times the frequency of the signal. By taking the highest signal as the peak value of the measured signal and compare it with the real amplitude of the sine wave, one can see that the accuracy of the digital reading is a function of the phase shift ϕ between the sampling time and the measured signal, according to

$$\Delta = A\left(1 - \cos\phi\right) \tag{14.84}$$

Δ is zero when ϕ = 0, that is, the sampling time is in phase with the measured signal. It reaches a maximum at ϕ = π/4. The maximum per unit value of the discrete-time sampling error is

$$\Delta_{max} = 1 - \cos\left(\pi f t_s\right) \tag{14.85}$$

where

t_s is the time between two samplings

f is the frequency of the measured sine wave signal

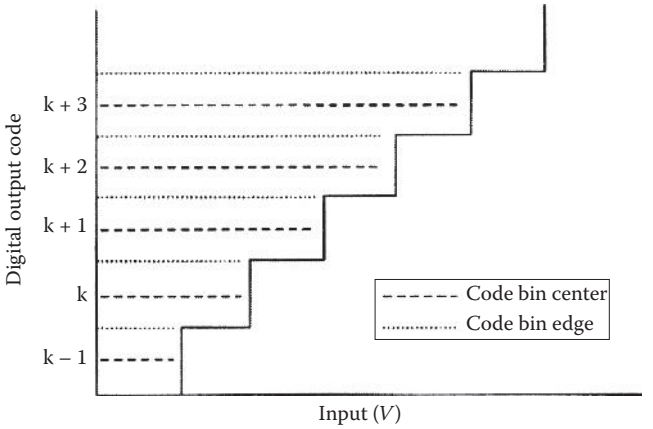


FIGURE 14.91 Quantization characteristics of an ideal digital recorder. (From Kuffel, E. et al., *High Voltage Engineering—Fundamentals*, 2nd edn., Pergamon Press, 2000.)

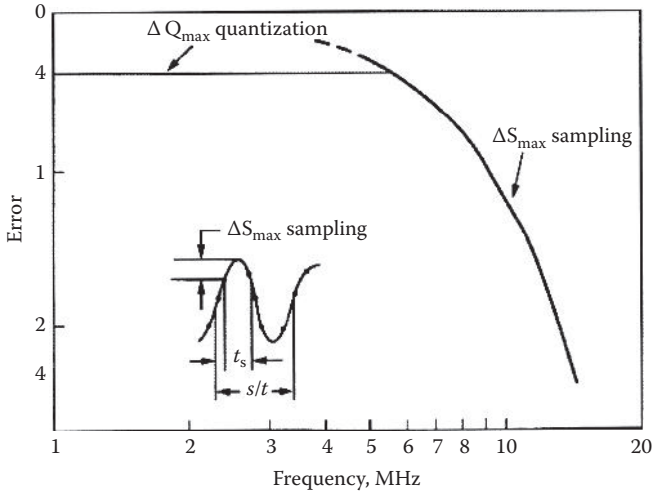


FIGURE 14.92 Sampling and quantization errors of an ideal recorder. (From Kuffel, E. et al., *High Voltage Engineering—Fundamentals*, 2nd edn., Pergamon Press, 2000.)

Figure 14.92 presents the maximum quantization and time sampling errors when recording a sine wave voltage. The results are evaluated for an 8-bit 200 MHz recorder. It can be seen that for an 8-bit A/D converter, the maximum quantization error is:

$$\Delta Q_{max} = 1/2^N = 1/256 = 0.39\%$$

The maximum sampling error ΔS_{max} for measuring a sine wave of 5.7 MHz with a sampling rate of 200 × 106, according to Equation 14.85 is:

$$\Delta S_{max} = 1 - \cos(8.95 \times 10^{-2}) = 4 \times 10^{-3} = 0.4\%$$

The error due to sampling will be less than 0.4 % when measuring a sine wave of frequency lower than 5.7 MHz. It will increase when measuring a sine wave of frequency higher than 5.7 MHz as illustrated in Figure 14.92.

The magnitude of the maximum possible discrete-time sampling error depends on the shape of the impulse rather than its magnitude. Therefore, the sampling rate requirement must be examined with respect to the specific signal measured. Table 14.8 gives the required sampling rate for adequate

TABLE 14.8

Requirements for Sampling Rated for Adequate Recording of Short-Duration Impulses

Sampling Rate (MHz)	Standard Lightning Impulse	Sawtooth—500 ns Rise Time
2	0.195 in% of FSD	
2.8	0.097	
4	0.048	
5.7	0.024	
8.6	0.012	
12.0	0.006	
50		4 in% of peak value
100		2
200		1

Source: Kuffel, E. et al., *High Voltage Engineering—Fundamentals*, 2nd edn., Pergamon Press, 2000.

recording of the peak value of a full-wave standard lightning impulse and a 500 ns rise time sawtooth waveform (Kuffel et al., 2000). It can be seen that while a sampling rate of a few MHz is sufficient to properly record the peak value of a standard lightning impulse, it must be increased to a few hundred MHz to properly record a front-chopped lightning impulse, represented by a 500 ns rise time sawtooth wave shape.

14.4.8.2 Dynamic Errors

Dynamic errors refer to those observed in actual digital recorder and associated to statistical variations in their operating parameters. They are of four generic types, namely, differential nonlinearity (DNL), integral nonlinearity, aperture uncertainty, and internal noise.

DNL: Refers to the variation in the widths of the recorder code bins. The result is a not well-defined quantization, as illustrated in Figure 14.93.

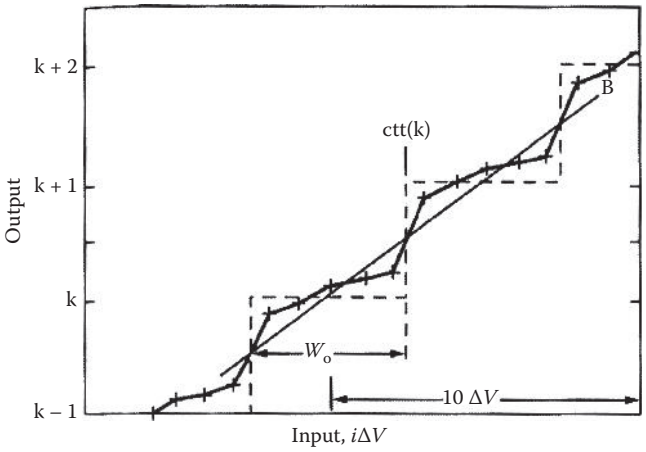


FIGURE 14.93 Illustration of DNL. (From Kuffel, E. et al., *High Voltage Engineering—Fundamentals*, 2nd edn., Pergamon Press, 2000.)

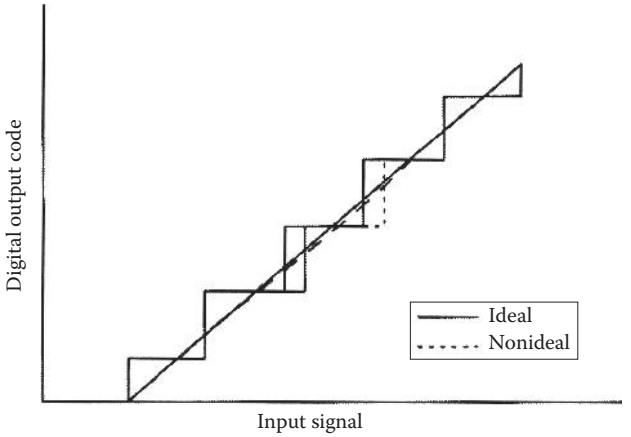


FIGURE 14.94 Illustration of the integral nonlinearity, as shown by a deviation between the real and ideal quantization characteristics. (From Kuffel, E. et al., *High Voltage Engineering—Fundamentals*, 2nd edn., Pergamon Press, 2000.)

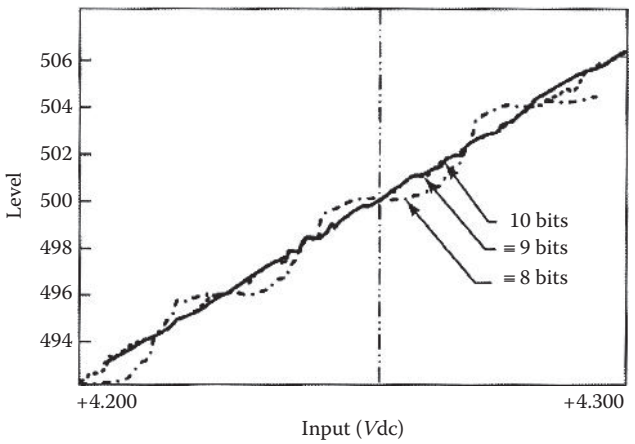


FIGURE 14.95 Illustration of the effect of internal noise on the quantization characteristics. (From Kuffel, E. et al., *High Voltage Engineering—Fundamentals*, 2nd edn., Pergamon Press, 2000.)

Integral nonlinearity: Represents the integrated effect of the variations in the widths of the code bins on the overall quantization, as illustrated in Figure 14.94. Some code bin may correspond to a wider range of the input signal.

Aperture uncertainty: Refers to the variation in the delay time between the reception of the sampling instruction and the actual initiation of the sampling process.

Internal noises of the electronic components cause a variation in the quantization step size. Its effect is particularly pronounced when the noise level is comparable to the quantization step size and is equivalent to a reduction in the resolution of the recorder as illustrated in Figure 14.95.

REFERENCES

Anis, H., Trinh, N.G., and D. Train. Generation of switching impulse using high voltage testing transformers. *IEEE Transactions* PAS-94: 187, 1975.

Asner, A. Equivalent circuit of the leads in high voltage measuring technique, particularly for measuring fast impulse voltages. *Bulletin SEV* 52: 192–203, 1961.

Bellaschi, P.L. and L.B. Rademacher. Dielectric strength of station and line insulation to switching surges. *AIEE Transactions* 65: 1047, 1946.

Booker, J.R., Nichols, D.R., and W. Lazelere. Design of a modular UHV AC outdoor test system. *IEEE Transactions*, PAS-102: 2501, 1983.

Burch, F.G. On potential dividers for cathode ray oscillographs. *Philosophical Magazine*, *Series 7* 13: 760, 1932.

Chubb, L.W. and C. Fortescue. Calibration of the sphere gap voltmeter. *AIEE Transactions* 32: 739, 1913.

Creed, F. and T. Collins. The shaping circuit for high voltage impulses. *IEEE Transactions*, PAS-90: 2239, 1971.

Creed, F. and M.M.C. Collins. Transient impedance of high voltage impulse generating systems. *IEEE Transactions* PAS-89: 1387, 1970.

Crockcroft, J.D. and Walton, E.T.S. Experiments with high velocity ions. *Proceedings of the Royal Society of London, Series A* 136: 619, 1932.

Elsner, R. The measurement of fast high voltage impulse using voltage dividers. *Archives fur Elektrotechnik* 33: 23–40, 1939.

Feser, K. Transient behavior of damped capacitive voltage divider of some millions volts. *IEEE Transactions* PAS-93: 116, 1974.

Hannakam, L. Calculation of the transient current distribution in cylindrical massive conductor. *ETZ-A* 91: 50–54, 1970 (in German).

Hyltén-Cavallius, N.R. Impulse tests and measuring errors. ASEA Publications, 7551 E/ASEA Reg. 0977, 1957.

Hyltén-Cavallius, N.R. and N.G. Trinh. Floor net used as ground return in high voltage test areas. *IEEE Transactions* PAS-88: 996, 1969.

Hyltén-Cavallius, N.R. et al. A new approach to minimize response errors in the measurement of high voltages. *IEEE Transactions* PAS-102: 2077, 1983.

IEC Standard 60052. *Recommendations for Voltage Measurements by means of Sphere Gaps (One Sphere Earthed)*. IEC, Geneva, Switzerland, 1960.

IEC Standard 60060-2. *High Voltage Test Techniques. Part 2: Measuring Systems*, 2nd edn. IEC, Geneva, Switzerland, 1994.

IEC Standard 60060-4. *High Voltage Test Techniques. Part 4: Application Guide for Measuring Devices*. IEC, Geneva, Switzerland, 1977.

IEC Standard 60270. *Partial Discharge Measurement*, 3rd edn. IEC, Geneva, Switzerland, 2000.

IEC Standard 60060–1. High Voltage test techniques—Part 1: General Definitions and Test Requirements, IEC, Geneva, Switzerland, 1989.

IEC Standard 61325. Insulators for Overhead Lines with a Nominal Voltage above 1000 kV, IEC, Geneva, Switzerland, 1995.

Janischewskyj, W. and A. Arainy. Corona characteristics of simulated rain. *IEEE Transactions* PAS-98: 539–551, 1981.

Jayaram, B.N. and D.J. Badkas. Determination of output voltage in cascade connected transformers. *AIEE Transactions, Part III* 936, 1963.

Kaden, H. Wirbelstrome und Schirmung in der Nachrichtentechnik. Spring Verlag, Berlin, 1959.

Keller, A. The measuring range and sensitivity of high voltage bridge according to Schering. *ETZ* 71: 232–235, 1950.

Kind, D. and J. Salge. Uber die Erzeugung von Schaltspannungen mit Hochspannungs-Pruftransformatoren. *ETZ-A* 86: 648, 1965.

Kuffel, E., Zaengl, W.S., and J. Kuffel. *High Voltage Engineering—Fundamentals*, 2nd Edition. Pergamon Press, Oxford, 2000.

Lemke, E. A critical review of partial discharge models. *IEEE Electrical Insulation Magazine* 28(6): 11, 2012.

Malewski, R. Digital techniques in high voltage measurements. *IEEE Transactions* PAS-99: 4508, 1982.

Malewski, R., Douville, J., and L. Lavallée. Measurement of switching transients in 735-kV substations and assessment of their severity for transformer insulation. *IEEE Transactions* PWRD-3: 1380–1390, 1988.

Malewski, R. and N.R. Hyltén-Cavallius. A low voltage arm for EHV impulse divider. *IEEE Transactions* PAS-93: 1797, 1974.

Malewski, R. and P.S. Maruvada. Computer assisted design of impulse voltage dividers. *IEEE Transactions* PAS-95: 1267, 1976.

Malewski, R., Nguyen, T,C., Feser, K., and N. Hyltén-Cavallius. Elimination of the skin effect error in heavy current shunts. *IEEE Transactions* PAS-100(3): 1333–1340, 1981.

Malewski, R., Train, D., and A. de Champlain. Cavity resonance effect in large HV laboratories equipped with electromagnetic shield. *IEEE Transactions* PAS-96: 1863, 1977.

NEMA Standard 107. *Method of Measuring Radio Noise*, 1940.

Palm, A. The Schering measuring bridge. *Archiv fur Tech. Messen*, 921, 1932.

Parnell, T.M. The influence of circuit parameters on power frequency flashover tests. *Australian Electrical and Mechanical Engineering Transactions*, 1961.

Pedersen, A. Partial discharge in voids in solid dielectrics, an alternative approach. In *Conference on Electrical Insulation and Dielectric Phenomena*, IEEE Publication 87CH2462-0, 58, 1987.

Pedersen, A., Critchton, G.C., and I.W. McAllister. The theory and measurement of partial discharge transients. *IEEE Transactions on Electrical Insulation* 26(3): 487, 1991.

Pedersen, A., Critchton, G.C., and I.W. McAllister. The functional relation between partial discharge and induced charge. *IEEE Transactions on Dielectrics and Electrical Insulation* 2(4): 487, 1995.

Peterson, O. A self balancing high-voltage capacitance bridge. *IEEE Transactions* IM-13: 216–224, 1964.

Reid, R. AC high voltage resonant testing. IEEE Paper No. C 74 038-6, *Winter Meeting,* New York, 1974.

Rizk, F.A.M. Flashover characteristics of insulators and spark-gaps with a power frequency half-cycle pulse. Thesis, Royal Institute of Technology, Stockholm, Sweden, 1960.

Rizk, F.A.M., Gervais, Y., and H. Luhrmann. Performance of electromagnetic shields in high voltage laboratories. *IEEE Transactions* PAS-94: 2077, 1975.

Schwab, A. and J. Pagel. Precision capacitive voltage divider for impulse voltage measurements. *IEEE Transactions* PAS-91: 2376–2382, 1972.

Train, D. Transient overvoltages on testing transformers. *Electrical Times*, 1967.

Train, D. and G.N. Trinh. Prevention of recovery overvoltages on high voltage testing transformers. *IEEE Transactions* PAS-92: 1631, 1973.

Train, D. and P.E. Vohl. Determination of ratio characteristics of cascade connected transformers. *IEEE Transactions* PAS-95: 1911, 1976.

Wagner, K.W. Zur Messung Dielektrischer Verluste mit der Wechselstrombrucke. *Elektrotechnische Zeitschrift* 32: 1001, 1911.

Zaengl, W.S. A new voltage divider for fast impulse voltages. *Bulletin SEV* 56: 232–240, 1965.

Zaengl, W.S. High voltage measuring techniques. In *High Voltage Engineering*, Book, Springer-Verlag, 1986, Chapter 10 (in German).

Zinke, O. Frequency independent capacitive-resistive voltage divider for measuring purposes. *ETZ* 60: 927–938, 1939.

Index

A

Ac breakdown voltage
  mechanism, 241
  test data, 243–244
  test procedures, 241–243
Acoustic impedance, 400
Acoustic intensity, 400
Ac power transmission lines, 351–352
ANSI rated withstand voltage test, 121
Arrhenius life curve, 551, 632–633
Audible noise, 401
  acoustic impedance, 400
  acoustic intensity, 400
  acoustic wave propagation, 394–397
  corona discharges, acoustical characteristics
    high-voltage line, 403, 406
    single corona source, 401–405
  measurement, 406
  methods of calculation
    empirical formulae, 408–409
    single-phase line, 409–410
    three-phase line, 410–412
  power transformers, 617
    characteristics, 618
    in far field, 621
    representation, 619–621
  sound meter, 406–408
  static and acoustic pressures, 394
  wave equation solution, 397–400

B

Biphenyl polychlorides (BPCs), 263–264
Bohr's atomic model, 145
  centrifuge force, 147
  first hypothesis, 147–149
  orbital movement of electron, 146
  radial force of attraction, 146
  second hypothesis, 148–150
Breakdown characteristics, long air gaps
  ac breakdown
    mechanism, 241
    test data, 243–244
    test procedures, 241–243
  altitude effect
    air density correction factor, 245–246
    conductor-type configuration, 245
    gap configurations and altitudes, 245–246
    relative air density, 244
    relative length variation, 245
    streamer mechanism, 244
  composite stress
    composite voltages, 238–241
    4-conductor bundle–lattice structure gap, 237–238
    negative space charge, 237–238
    rod-plane gap, 236
    rod–rod gap, 237
  dc breakdown, 228–230
  fast front impulses
    breakdown mechanism, 224–228
    standard lightning impulse breakdown voltage, 228
  humidity effects, 246
    comparison of correction factors, 255–256
    generalized correction approach, 256–257
    humidity correction procedure, 250–252
    streamer breakdown, 247
    switching impulse breakdown, 248–250, 252–254
  instantaneous leader gradient, 223
  negative breakdown, 224–225
  positive switching impulse, 224
  positive switching surge strength
    air gap strength data, 231–232
    impulse breakdown, 233–235
    system overvoltages, 230
  streamer, 223
Breakdown mechanisms, liquids electric breakdown
  anode processes, 268
  cathode processes, 268
  closed-cycle liquid purification system, 267
  collision processes, 268
  commercial liquids, 269–270
  current–field characteristics, 267–268
  liquid-solid dielectrics, 270–271
  long oil gaps (*see* Long oil gaps, breakdown)
  oil-impregnated paper, 270
  pure liquids, 267
  short gaps (*see* Short gaps, breakdown)
Bruce profile electrodes, 32–35
Bundle conductors
  corona loss characteristics, 366
  electrostatic field optimization, 354–356
  excitation function, 414–415
  natural transmission capability, 352–354
Butyl rubber, 308–309

C

Cables, 66–69; *See also Specific types*
Capacitive current, 20–21
Capacitive load
  ac voltage, 681–682
  critical value, 681
  with losses, 692–693

Capacitor discharge, 710
Cascaded transformers, 680, 713–714
  capacitive load, 681–682
  effect, 716
  equivalent circuit, 682–684
  recovery overvoltage protection, 686–690
  rectifier using, 701
  voltage distribution, 684–686
Coaxial cables, 37–38, 721–722
Commercial liquids, breakdown
  gaseous inclusion, 269
  liquid globules, 269
  solid particles, 270
Composite voltages
  breakdown voltage characteristics, 240
  corona current, 239
  dc bias voltage, 241
  linear leader charge, 239
  positive streamer gradient, 238
  rod–plane gap, 238
  space charge field, 240
Constant voltage test, 119–120
Corona discharges
  acoustical characteristics
    high-voltage line, 403, 406
    single corona source, 401–405
  active ionization processes, 188–189
  alternating voltage, 208–209
  components of dc current, 426–427
  corona onset conditions, 362–363
  energy losses, 363–364
  frequency spectra, 391–392
  generation mechanism of interference
    harmonic content, 368–370
    time *vs.* frequency domains, 367–368
  high-voltage testing, 209
  negative polarity
    electron avalanche and space charges, 189–192
    negative pulseless glow, 194, 196–197
    negative streamer, 194, 196, 198
    onset conditions, cathode, 193
    Trichel streamers, 194–196
  overhead lines
    audible noise, 212–213
    electromagnetic interferences, 211–212
    emission of polluting effluents, 212–213
    energy losses, 210–211
  positive polarity
    breakdown streamer, 206–208
    burst corona, 201–203
    electron avalanche and ion space charge, 199–200
    onset streamer, 201–204
    positive glow, 202–206
  practical gap configuration, 188
Cross-linked polyethylene (XLPE), 310, 311
Cumulative ionization, 157
Current
  interruption
    capacitive current, 20–21
    inductive currents, 19–20
  measurement, 739
    fast transient corona pulses, 740
    high-magnitude power frequency current, 740–743

D

Dc breakdown voltage, 228–230
Dielectric interfaces, oil insulation factors
  electrostatic discharges, 295
  incipient fault, 294–295
Double-phase half-wave rectifier circuit, 697

E

Electrical breakdown, gases
  atomic structure
    Bohr's atomic model, 145–150
    emission spectra, 145–146
    energy states of electron, 150
    interpretation of periodic table of elements, 150–151
    Pauli's exclusion principle, 150
  classical theory, gaseous discharges
    influence of secondary processes, 176–178
    self-sustained discharges (*see* Self-sustained discharges)
  corona discharges in atmospheric air
    active ionization processes, 188–189
    alternating voltage, 208–209
    high-voltage testing, 209
    negative polarity, 189–198
    overhead lines, 209–213
    positive polarity, 199–208
    practical gap configuration, 188
  deionization and deexcitation, 164–165
    attachment, 166
    by diffusion, 166–167
    recombination, 165–166
  development of electron avalanches
    electronegative gases, 175–177
    mechanism of discharge, 171–173
    Townsend discharge, 170–171
    Townsend ionization coefficient, 173–175
  diffusion
    accidental spill of SF_6, 144–145
    air, 142
    gas molecules traversing per second, 139–140
    general equation, 140–141
    mixture of SF_6-N_2, 143
    nitrogen column, 141
  energy conservation, 130
  equal partition of energy, 136–137
  excitation and ionization of atoms
    absorbed energy, 151
    cumulative ionization, 157
    electronic collisions, 152–154
    ionic collisions, 154–155
    metastable state, 152
    photoionization, 155–156
    reactions, 152
    rules of transfer, 152
    thermal ionization, 156

Gay-Lussac law, 132–133
hypothesis of Avogadro, 132
inelastic collisions, 131–132
ion movement, electric field
electric current, charged molecule movement, 163–164
electron mobility, 161–162
ion mobility, 157–160
ions of charge, 162–163
mean free path
evaluation, 138–139
statistical distribution, 137
momentum conservation, 130–131
sources of free electrons
electron detachment from negative ions, 167
electron emission by collisions and radiations, 168
electron emission from solids, 167–168
field emission, 168–170
natural and artificial, 167
thermionic emission, 168
sulfur hexafluoride, 129
breakdown, 218–220
electrolysis, 213
ionization processes and source of free electrons, 214–215
neutral gases, 215–217
principal characteristics, 213–214
uniform and quasiuniform fields, 217–218
velocity distribution
air and SF_6, 135–136
gas-insulated bus, 133
Maxwell distribution function, 134
temperature difference, 134
Electric arc
characteristics, 186–187
low *vs.* high-pressure arcs, 185
physical mechanism, 186
Electric breakdown, liquids
mechanisms
anode processes, 268
cathode processes, 268
closed-cycle liquid purification system, 267
collision processes, 268
commercial liquids, 269–270
current-field characteristics, 267–268
liquid-solid dielectrics, 270–271
long oil gaps (*see* Long oil gaps, breakdown)
pure liquids, 267
short gaps (*see* Short gaps, breakdown)
mineral oil, chemical composition, 261–262, 264
oil insulation factors
dielectric interfaces, 294–295
dissolved gases, 284
dissolved metals, 285
humidity, 285
hydrostatic pressure, 284
impurities, 284
oil molecules decomposition, 295
oxidation, 295
solid particle contamination (*see* Solid particle, contamination)
oil-paper insulation, 261
synthetic oils
principal, 263–266
properties, 263–265
Electric breakdown, solid and composite materials
aging and incipient fault, 301–302
chemical deterioration, 305
combined stress, 304–305
electrical discharges breakdown, 303
electrochemical deterioration, 305–306
mechanical aging, 304
thermal breakdown, 302–303
decomposition by-products, 306
initial breakdown and strength, 301
intrinsic breakdowns
description, 299
McKeown method, 300–301
recessed specimen method, 300
stress-enhanced conductivity, 299
theory of intrinsic strength, 299–300
paper–oil composite insulation (*see* Paper–oil composite insulation)
polymeric insulation (*see* Polymeric insulation)
SF_6–epoxy insulation factors
accumulation of electrostatic charges, 348–349
characteristics, 328–329
corona onset field, 329–330
electrode surface conditions, 345–346
gas pressure, 345
humidity, 348
limit withstand field, 331
particle contamination, 346–348
voltage-time breakdown characteristics, 331–335
solid (epoxy) insulation
composite profile spacers, 340
cone-profile spacers, 339–340
dielectric performances, 341–343
disc-profile spacers, 338, 339
gas-dielectric interface, 338
initial breakdown strength, 341–342
nonpolymerized form, 336, 338
spacer, 337–338
triple junction, 340–341
voltage–time breakdown characteristics, 341–344
Electrogeometric model, lightning, 452–453
Electromagnetic interference, 211–212, 366
empirical formulae, 379–380
generation mechanism, corona discharges
harmonic content, 368–370
time *vs.* frequency domains, 367–368
measurement
factors affecting, 379
magnetic and electric interference field, 378
measurement apparatus, radio interference, 376–378
noise meter characteristics, 375–376
quality of radio reception, 378
radio interference, power lines, 378
quantification
Percival theorem, 373
spectral power density, 373–375
stationary random signal, 373

radio reception
AM radio receiver, 370–371
background noise, 373
frequency spectrum, 370
short-duration pulse, 372
tuning circuit, 371–372
single-phase line
excitation function, 383
interference propagation, 381
power spectral density, 381–383
radio interference, 383–385
streamer discharge, 380
television interference
amplitude and frequency modulation, 390
frequency spectra, 391–392
gap discharges, 392, 393
image quality, 392, 394
measurement of, 392–393
video reception, 391
three-phase line
coefficients of modal attenuation, 388–390
modal analysis, 386
modal transformation matrix, 387–388
phase conductors, 385, 386
propagation, 386
RI current, 386
Electromagnetic shielding of high-voltage laboratory, 722–723
Electromagnetic transient program (EMTP), 21–23
Electron avalanches
electronegative gases, 175–177
mechanism of discharge, 171–173
space charges, 189–192, 199–200
Townsend discharge, 170–171
Townsend ionization coefficient, 173–175
Electronic ionization process, 273
Electron mobility, 161–162
Electrostatic discharges, breakdown mechanism, 295
Electrostatic field calculation
Laplace equation (*see* Laplace equation)
Maxwell equations, 26–27
methods of images
cylindrical conductor, 55–56
ground plane, 53–55
sphere gap, 56–60
Equivalent circuit
adjustable reactance, 691
cascaded transformers, 680, 682–684
single transformer, 682, 711
Equivalent salt deposit density (ESDD), 491, 494–498
Eriksson and Dellera–Garbagnati models, lightning, 453–454
Ethylene–propylene rubber, 307–308

F

Fast-front overvoltages, 650
general, 662–664
impinging surge, 664–667
Ferranti effect
electrical length of line, 5
open end temporary overvoltage factor, 6–7
short-circuit power, 6–7
shunt-compensated line, 5
shunt reactors, 7
sinusoidal voltage, 4
surge impedance loading, 6
Ferrography, 600
Floating electrode, 72–74
Fryxell test procedure, 126

G

Gas-insulated cables
accessories, 575–577
burn through risk, 569
electrical aging, 560–562
environmental aging, 562
thermal and mechanical aging, 560
Gas-insulated lines (GIL), 535
Gas-insulated stations (GISs)
burn through risk, 568–569
components, 565–566
development, 536
equipment, 569–571
fast transients, 565–568
Gas (SF_6) insulation, 575–577
characteristics, 328–329
corona onset field, 329–330
limit withstand field, 331
SF_6–epoxy insulation factors
accumulation of electrostatic charges, 348–349
electrode surface conditions, 345–346
gas pressure, 345
humidity, 348
particle contamination, 346–348
voltage–time breakdown characteristics, 331–332
formative time lag, 334
joint time lag probability distribution, 334–336
statistical time lag, 332–334
Gay-Lussac law, 132–133
Glass insulators, 482
Glow discharges
electrical characteristics, 184–185
electric arc, 185–187
physical mechanism, 183

H

Half-wave rectifier circuit, 696–697
Hancox test procedure, 125
High pressure oil-filled (HPOF) cable, 533–534
High-temperature vulcanized (HTV) silicone rubber, 483
High-voltage ac (HVAC) cables
Conci conductor design, 540–542
conductor, 540
energy losses, 540–545
thermal dissipation, 545–547
electric field distribution, 536–539
with forced cooling, 537

insulation based on limit field, 547
design field, determination, 548–549
insulation thickness, determination, 549–550
selection of withstand voltage level, 547–548
Milliken conductor design, 540, 542
parameters, 539–540
High-voltage dc (HVDC) cables, 577
accessories, 582–583
audible noise, 434–436
conductors, 578
corona performance, 436–437
electrical conductivity, 581
field distribution
in steady-state regime, 578–579
transient conditions, 579–580
field enhancement in butt gap, 580–581
line dimensioning
average conductor height, 424–425
radio interference, 431–434
selection of conductors
corona losses, 425–431
corona onset, 425
generating functions, 425
SF_6-insulated cable, 581–582
High-voltage insulators
design approach
flowchart, 520–522
statistical approach to insulator selection, 522–526
electrical performance
lightning impulse flashover, 484–487
pollution flashover (*see* Pollution flashover, high-voltage insulators)
switching impulse flashover, 487–489
materials, 481–484, 519–520
electrical porcelain, 481–482
glass, 482
polymers, 482–484
mechanical requirements, 517–519
parameters, 520
roles, 479
surface wetting
ceramic insulator, 498–500
nonceramic insulator, 500–501
suspension insulators, 479
transmission line insulators, 479
types, 479–481, 519–520
High-voltage (HV) measuring techniques, 717
current measurement, 739
fast transient corona pulses, 740
high-magnitude power frequency current, 740–743
digital techniques, 756
discrete-time sampling error, 757–759
dynamic errors, 759–760
quantization error, 757
electromagnetic shielding, 722–723
gas-insulated capacitor, 747–749
high-voltage test area grounding, 717–720
PD measurement, 749
calibration, 755–756
capacitive tap, 756
with narrow band detector circuit, 754–755
using large bandwidth detector circuit, 750–754
power losses measurement, 743
current comparator bridge, 746
R–C parallel representation, 747
Schering bridge, 744–745
shielding of control and measuring cables, 721–722
sphere gap, 723–727
voltage measurement, 727–730
connecting lead, 737
high-voltage electrode, 737–739
instrument, 739
low-voltage arm, 734–736
voltage divider, 730–734
High-voltage (HV) testing techniques, 209, 677
ac voltage
cascaded transformers (*see* Cascaded transformers)
generation, 680, 694, 696
resonant circuit (*see* Resonant circuit, ac voltage)
categories, 677–680
dc voltage, 696
cascaded rectifier, 699–701
half-wave rectifier circuit, 696–697
voltage doubling circuit, 698–699
impulse voltage, 701
chopped, 709–710
circuit inductance on wave front, 707–708
generation, 702
impulse generators (*see* Impulse generators)
power transformers
applied potential test, 621–622
impulse tests (*see* Impulse tests, power transformers)
induced voltage test, 622–623
switching impulse
capacitor discharge, 710
short time energization method, 711–717
HPOF cable, *see* High pressure oil-filled (HPOF) cable
HTV silicone rubber, *see* High-temperature vulcanized (HTV) silicone rubber
Humidity effects, breakdown characteristics, 246
comparison of correction factors, 255–256
generalized correction approach, 256–257
humidity correction procedure, 250–252
streamer breakdown, 247
switching impulse breakdown
conductor-plane gap, 253
continuous leader inception voltage variation, 253–254
continuous positive leader inception voltage, 252
discharge parameters, 249
flashover characteristics, 248
leader charge per unit length variation, 249–250
leader propagation speed variation, 249
voltage variation, 249–250, 253–254

I

IEC rated withstand voltage test, 120–121
Impulse generators
  circuits, 702–704
    efficiency, 704–705
    parameters, 705–707
  multistage, 708–709
Impulse tests, power transformers, 623
  chopped wave, 630
  detection of failure during, 630–631
  standard impulse, 624–625
  switching impulse, 625–629
Inductive currents, 19–20
Insulation
  configuration, 649
    withstand voltage, 651
  external *vs.* internal, 649
  self-restoring *vs.* non-self-restoring, 649
Insulation coordination, 649
  overvoltages (*see* Overvoltages)
  performance criterion, 651
  procedure, 651
    continuous power frequency voltage, 652
    coordination withstand voltage, 667–668
    fast-front overvoltages (*see* Fast-front overvoltages)
    flowchart, 652
    required withstand voltage, 668–669
    slow-front overvoltages (*see* Slow-front overvoltages)
    standard withstand voltage, 670
    temporary overvoltages, 652
  surge arresters (*see* Surge arresters)
  voltages, 649–650
Insulators
  high-voltage (*see* High-voltage insulators)
  polymeric, 482–484, 517, 519
  porcelain, 480–482
Intrinsic breakdowns
  description, 299
  McKeown method, 300–301
  recessed specimen method, 300
  stress-enhanced conductivity, 299
  theory of intrinsic strength, 299–300
Ion mobility
  electrostatic force, 157
  free path, 158
  ion of charge, 157
  kinetic energies, 159
  SF_6, 160
  singly charged gaseous ions, 159
  velocities, 158

L

Laplace equation
  Cartesian coordinates
    Bruce profile electrode, 32–35
    plane electrode, 30–31
    Rogowski profile electrode, 30–33
    uniform field, 29–30, 35–36
  charge simulation method
    dielectric, 70
    floating electrode, 72–74
    three-dimensional field, 70–72
    two-dimensional field, 69–70
  cylindrical coordinates, 36
    coaxial cable, 37–38
    dielectrics, 38–40
  field and potential, elementary charges
    circular charge, 61–62
    infinite linear charge, 61
    linear charge element, 61
    point charge, 60
  global solution method
    finite differences, 74–75
    finite elements, 75–79
  hyperboloidal field, 49–50
  oblate spheroidal protrusion, 50–52
  Poisson equation, 28
  prolate spheroidal coordinates
    cavity of low permittivity, 49
    charged metal spheroid, 43–45
    dielectric spheroid, 45–47
    equipotential surfaces, 42
    high permittivity spheroid, 47–49
    Legendre-associated functions, 43
  separation of variables, 28–29
  spherical coordinates, 40–42
  successive images method, 62–63
    high-voltage cable, 66–69
    overhead line, 63–66
Lightning
  backflashover, 459
    conductor coupling, 465–466
    rate estimation, 467
    reflections from adjacent towers, 466
    tower grounding, 466–467
    tower surge impedance, 463–465
    tower top potential, 461–463
  cloud charging, 439–440
  detection and location
    direction finders, 442–443
    flash counters, 442
    time-of-arrival (TOA) method, 443
  electrogeometric model, 452–453
  Eriksson and Dellera–Garbagnati models, 453–454
  flash parameters
    classification, 444
    current waveform, 444–447
    statistical distribution, 444
    statistical parameters, 447–449
  impulse flashover
    insulator strings, 484–486
    transmission line insulator, 486–487
  meteorological data, 440–442
  negative downward flash, 449–450
  protective measures
    ground wires, 470–471
    improving grounding, 471–472
    lightning rods and masts, 469–470

line arresters, 472–473
streamer inhibition, 473–474
return stroke
general, 450
models, 450–452
Rizk model
conductor lateral attractive distance, 457
electrical shadow, 458
illustrative examples, 455
negative downward strike, 455
prospective return stroke current, 456–458
regression formula, 456
space potential, 454
shielding failure, 459–461
upward flash, 467–469
Long oil gaps, breakdown
direct breakdown, 276
discharge length measuring, 281
extension of gaseous channel, 279
gas discharge of leader channel, 279
gaseous channel, formation, 277
leader channel evolution, 280
polarity effect, 279–280
reillumination of leader channel, 279
switching impulse, 280
visual aspect of, 277–278
streamer burst discharge, 281–284
Lumped circuits
angular natural frequency, 2
parallel damping, 2–3
series damping, 2
temporary overvoltage factor, 3–4
transient overvoltage, 3

M

Mass-impregnated cables, 534
Maxwell equations, 26–27
McKeown method, intrinsic breakdowns, 300–301

N

Natural rubber, 307
Negative polarity
electron avalanche and space charges, 189–192
negative pulseless glow, 194, 196–197
negative streamer, 194, 196, 198
onset conditions, cathode, 193
Trichel streamers, 194–196
Neoprene, 309
Non-self-restoring insulation, 649

O

Oil insulation factors, liquids electric breakdown
dielectric interfaces, 294–295
dissolved gases, 284
dissolved metals, 285
humidity, 285
hydrostatic pressure, 284
impurities, 284
oil molecules decomposition, 295
oxidation, 295
solid particle contamination (*see* Solid particle, contamination)
Oil–paper insulation, power transformers, 588–589
aging state, 634
breakdown probability, evaluation of, 607–610
characteristics, 593–595, 636–637
cumulative stress, evaluation of, 606–607
dimensioning, 606
humidity control, 598–600
Kraft paper, 597–598, 635–636
maintenance, 639, 642–645
operation, 639–642
stresses, 592
particle contamination control, 600–604
physical–chemical properties, 595–598
properties, 595–597
winding arrangement, 592–593
ONAN transformers, 590
Overhead lines, 63–66
average height, 356
electric field, ground, 357–360
magnetic field, ground, 360–362
corona discharges, 209–213
audible noise, 212–213
electromagnetic interferences, 211–212
emission of polluting effluents, 212–213
energy losses, 210–211
development, 351
ac power transmission lines, 351–352
bundle conductor, 352–354
electrostatic field optimization, 354–356
emission of effluents, 422, 423
selection
audible noise (*see* Audible noise)
corona onset conditions, 362–363
corona performances of bundle conductors, 418–421
corona performances of single conductors, 416–418
electromagnetic interference (*see* Electromagnetic interference)
energy losses, 363–366
excitation function, 414–416
fair-weather corona onset field, 413
field intensity, 413
generated acoustic power density, 416
generated losses, 414
HVDC (*see* High-voltage dc (HVDC) cables)
long-term corona performance, 421–423
Peek experimental law, 412
Overvoltages; *see also Specific types*
classification, 649–650
during discharge period, 715–716
recovery protection, 686–690
representative, 650
temporary, 652

P

Paper–oil composite insulation
  dielectric performances
    butt gaps dimensions, 327
    conductor surface roughness, 328
    failure mode, 325–326
    impurities and humidity, 328
    initial strength, 326–327
    oil-filled butt gaps, 326
    paper tape puncture, 325
  lapped insulation
    impregnated paper–oil cables design, 316–317
    ionic impurities, 324–325
    oil with reduced flammability, 325
    physical–chemical properties, impregnated paper–oil, 318–323
    polypropylene–paper–laminate, 324
    synthetic paper, 324
    taping process control, 317–318
Paper–oil-insulated cables, 531–534
Parallel conductors, 364
Pauli's exclusion principle, 150
PD measurement, 749
  apparent charge evaluation, 750–754
  calibration, 755–756
  capacitive tap, 756
  induced voltage test, 622–623
  with narrow band detector circuit, 754–755
  on-site evaluation, 645
  radio interference voltage and, 755–756
Pentaerythritol esters, 266
Percival theorem, 373
Photoionization, 155–156
Plane electrodes, 30–31
Pollution flashover, high-voltage insulators, 490
  distance from pollution source effect, 495–496
  exposure time effect, 492–493
  insulator surface wetting, 498–501
  mechanism, 490
    description, 501–502
    experimental flashover characteristics, 515–517
    fast arc growth, 504–505
    modeling of flashover characteristics, 508–514
    pollution layer resistance, 502–503
    pollution resistance during arc growth, 505–508
    slow arc growth, 503
  operating voltage effect, 495
  pollution layer
    buildup, 490–491
    pattern, 494
  site severity, 491–492
  test techniques, 515
  wind speed effect, 496–498
Polychloroprene, 309–310
Polydimethylsiloxane (PDMS), 265
Polyethylene (PE), 310–311
Polymeric insulation
  dielectric performance
    initial breakdown, 312–313
    limit withstand fields, 312
    synthetic polymer insulation, 313–316
  physical–chemical properties, 307
    butyl rubber, 308–309
    cross-linked polyethylene, 310
    ethylene–propylene rubber, 307–308
    natural rubber, 307
    neoprene and polychloroprene, 309
    polyethylene, 310–311
    polyvinyl chloride, 310
    silicone rubber, 309
Polymeric insulators, 482–484, 517, 519
Polymer-insulated cables, 304
  decomposition by-products, 560
  electrical aging, 553–558
  environmental aging, 558–560
  joints, 574
  termination, 575–576
  thermal aging, 553
Polyvinyl chloride, 310
Porcelain insulator, 480–482
Positive polarity
  breakdown streamer, 206–208
  burst corona, 201–203
  electron avalanche and ion space charge, 199–200
  onset streamer, 201–204
  positive glow, 202–206
Positive switching surge strength
  air gap strength data, 231–232
  impulse breakdown, 233–235
  system overvoltages, 230
Power system overvoltages
  distributed parameter circuits
    current interruption, 19–21
    temporary overvoltages (*see* Temporary overvoltages)
    transient overvoltages (*see* Transient overvoltages)
  electromagnetic transient program, 21–23
  lumped circuits, 2–4
Power transformers, 587
  aging mechanism
    decomposition by-products, 634
    electrical aging, 632–633
    environmental aging, 633–634
    thermal aging, 631–632
  applied potential test, 621–622
  audible noise, 617
    characteristics, 618
    in far field, 621
    representation, 619–621
  core construction, 587
  design, 589–591
  gas-insulated, 604–606
  impregnation and preservation, 589
  impulse tests, 623
    chopped wave, 630
    detection of failure during, 630–631
    standard impulse, 624–625
    switching impulse, 625–629
  induced voltage test, 622–623, 696

insulation, 588–589
bulk parameters measurement, 634–635
nondestructive tests, 637
operating stresses, 591–592
physical–chemical characteristics, 635–637
service life, 637–639
maintenance, 639
diagnostic, 642–645
monitoring, 645
on-site evaluation, 645
routine, 642
oil–paper insulation (*see* Oil–paper insulation, power transformers)
operation, 639–642
SF_6 insulation, 589, 604–606
test cell adequacy, assessment for
breakdown probability, 614–617
cumulative stress, 613–614
field calculation, 610–613
windings construction, 587–588
Pressurized oil-filled paper-impregnated cables, 532–534, 541

R

Recessed specimen method, intrinsic breakdowns, 300
Rectifier
cascaded, 699–701
circuit, 696–697
Resonant circuit, ac voltage, 690
adjustable reactance, 691–692
capacitive load with losses, 692–693
cascade connection, 693–694
quality factor, 691
transient recovery voltage, 694–696
voltage distribution, 693–694
Rigid gas-insulated cables, 535–536
Rizk model, lightning
conductor lateral attractive distance, 457
electrical shadow, 458
illustrative examples, 455
negative downward strike, 455
prospective return stroke current, 456–458
regression formula, 456
space potential, 454
Rogowski profile electrode, 30–33

S

Salt fog test, 515–516
Self-contained oil-filled (SCOF) cable, 532–533
conductor, 540
electrical aging, 551–553
environmental aging, 553
thermal aging, 551
Self-restoring insulation, 649, 651
Self-sustained discharges
glow discharge
electrical characteristics, 184–185
electric arc, 185–187
physical mechanism, 183
onset conditions of
Paschen's law, 179–181
Streamer criterion, 180–181
regimes of sustained, 178–179
Short gaps, breakdown
gaseous cavity formation, 273–276
streamer discharges in oil, 271–273
Silicone rubber, 309
insulators, 482
HTV, 483
pollution buildup on, 494
pollution flashover, 501–502
properties, 483
salt deposit density, 517
Single-phase half-wave rectifier circuit, 696–697
Slow-front overvoltages, 650
phase-to-earth overvoltages, 652–654
phase-to-phase overvoltage
distributions, 659–662
representative, 654–659
Solid (epoxy) insulation
composite profile spacers, 340
cone-profile spacers, 339–340
dielectric performances, 341–342
disc-profile spacers, 338–339
gas-dielectric interface, 338
initial breakdown strength, 341–342
nonpolymerized form, 336, 338
SF_6–epoxy insulation factors
accumulation of electrostatic charges, 348–349
electrode surface conditions, 345–346
gas pressure, 345
humidity, 348
particle contamination, 346–348
spacer,337–338
triple junction, 340–341
voltage–time breakdown characteristics, 341–344
Solid particle, contamination
particle content, 286
short gap, 286
stressed area and volume effect
ac withstand voltage, 288, 291, 294
breakdown voltage of oil gap, 288, 292–293
latter parameters, 286–287
probability function of, 288–291
well-filtered oil, 286
Standard lightning impulse breakdown voltage, 228
Statistical analysis
characteristics/behavior verification
AC test with increasing voltages, 123
AC test with ramp voltages, 123
ANSI rated withstand voltage test, 121
constant voltage test, 119–120
Fryxell test procedure, 126
Hancox test procedure, 125
IEC rated withstand voltage test, 120–121
increasing step voltages test, 120
modified α-β test procedure, 126
optimization, 118

rated AC withstand voltage test, 122
Tezner test procedure, 121–122
withstand voltage of oil gap, 124
data characterization
ac breakdown field, 81–82
binomial distribution, 86–87
experimental distribution, 82–85
extreme value distribution, 91–92
global parameters, 82
Maxwell distribution, 89
normal distribution, 89–91
Poisson distribution, 87–88
uniform distribution, 86
Weibull distribution, 92–94
joint probability, 117
optimization, experimental data
component distributions, 113–114
improvement of experimental data, 114–117
population distribution estimation
ac breakdown field, 105–107
chi-square test, 98
confidence interval, 96–97
direct extrapolation, 110
extreme value distribution, 107–108
graphical test, 98–103
linear regression analysis, 103–104
optimal des distributions, 105
randomness test, 94
regression analysis, 104
sample statistic parameters, 94–96
verification of experimental law, 110–112
Weibull distribution, 108–110
weak link statistics, 112
Sulfur hexafluoride (SF_6), 129
breakdown criteria, 219–220
breakdown mechanism, 218–219
electrolysis, 213
insulation
features, 565
power transformers, 589, 604–606
ionization processes and source of free electrons, 214–215
neutral gases, 215–217
principal characteristics, 213–214
uniform and quasiuniform fields, 217–218
Sulfur hexafluoride (SF_6)-insulated cable
compressed, 538
electrical aging, 560–562
environmental aging, 562
HVDC, 581–582
thermal and mechanical aging, 560
Surge arresters, 670–671
discharge current, 672
durability requirements, 673–674
impulse current tests, 672
rated voltage, 672
residual voltages, 672–673
Switching impulse flashover, 487–489
Synthetic oils, electric breakdown
principal of, 263–266
aliphatic hydrocarbons, 265
BPC, 263–264
perfluorocarbons, 266
silicone oil, 265–266
synthetic esters, 266
properties, 263–265
Synthetic polymer insulation factors
cavities and solid contaminants, 314–315
humidity, 315–316
migration of solid contaminants, 315
protrusions at conductor surface, 313–314
separation of insulation layers, 315

T

Temporary overvoltages
Ferranti effect
electrical length of line, 5
open end temporary overvoltage factor, 6–7
short-circuit power, 6–7
shunt-compensated line, 5
shunt reactors, 7
sinusoidal voltage, 4
surge impedance loading, 6
sound phases, 8–10
Tezner test procedure, 121–122
Thermal ionization, 156
Three-phase lines, 17–18
Time-of-arrival (TOA) method, lightning, 443
TOPIST cable, 581
Toughened glass, properties of, 482
Townsend discharge, 170–171
Transient overvoltages
energization of open line, 17
lattice diagram, 16–17
points of discontinuity
Bergeron method, 14
current limiting reactor, 13
forward voltage wave, 11
series capacitor compensation, 14
shunt reactor, 11–12
transmission coefficient, 12–13
wave impedance, 11–12
three-phase lines, 17–18
traveling waves, 14–16
wave equations, 10–11
Transient recovery voltage, 687, 694–696
Trichel pulses, 275

U

Underground cables
accelerated aging tests, 562–563
accessories
extruded insulation, 573–575
gas (SF_6) insulation, 575–577
impregnated paper–oil-insulated, 571–573
aging and incipient fault
gas-insulated cables, 560–562
polymeric PE/XLPE cables, 553–560
SCOF, 551–553
analysis of data, 563–564
characteristics, 540

compressed SF_6-insulated cable, 538
design electric fields, 549
drawbacks, 531
extruded insulation cables, 534–535
forced cooling, 536–537
gas insulation, 535–536
HVAC cables (*see* High-voltage ac cables)
HVDC cables (*see* High-voltage dc cables)
maintenance practices consideration, 583
mass-impregnated cables, 534
paper–oil insulation, 531–534
pressure, 538
pressurized oil-filled paper-impregnated cable, 531–534
synthetic paper and tape, 537–538
test parameters optimization, 564

V

Very-fast-front overvoltages, 650
Voltage divider, 730–734
low-voltage arm, 734–736
Voltages
classification, 649–650
constant test, 119–120
doubling circuit, 698–699
measurement, 727–730
connecting lead, 737
high-voltage electrode, 737–739
instrument, 739
low-voltage arm, 734–736
voltage divider, 730–734

W

Withstand voltage
altitude correction factor, 669
coordination, 651, 667–668, 670
of insulation configuration, 651
safety factor, 669
standard, selection of, 670

X

XLPE-insulated cables, 555

HIGH VOLTAGE ENGINEERING

Inspired by a new revival of worldwide interest in extra-high-voltage (EHV) and ultra-high-voltage (UHV) transmission, **High Voltage Engineering** merges the latest research with the extensive experience of the best in the field to deliver a comprehensive treatment of electrical insulation systems for the next generation of utility engineers and electric power professionals. The book offers extensive coverage of the physical basis of high-voltage engineering, from insulation stress and strength to lightning attachment and protection and beyond.

Presenting information critical to the design, selection, testing, maintenance, and operation of myriad high-voltage power equipment, this must-have text:

- Discusses power system overvoltages, electric field calculation, and statistical analysis of ionization and breakdown phenomena essential for proper planning and interpretation of high-voltage tests
- Considers the breakdown of gases (SF6), liquids (insulating oil), solids, and composite materials, as well as the breakdown characteristics of long air gaps
- Describes insulation systems currently used in high-voltage engineering, including air insulation and insulators in overhead power transmission lines, gas-insulated substation (GIS) and cables, oil-paper insulation in power transformers, paper-oil insulation in high-voltage cables, and polymer insulation in cables
- Examines contemporary practices in insulation coordination in association with the International Electrotechnical Commission (IEC) definition and the latest standards
- Explores high-voltage testing and measuring techniques, from generation of test voltages to digital measuring methods

With an emphasis on handling practical situations encountered in the operation of high-voltage power equipment, **High Voltage Engineering** provides readers with a detailed, real-world understanding of electrical insulation systems, including the various factors affecting—and the actual means of evaluating-insulation performance and their application in the establishment of technical specifications.

CRC Press
Taylor & Francis Group
an informa business
www.crcpress.com

6000 Broken Sound Parkway, NW
Suite 300, Boca Raton, FL 33487
711 Third Avenue
New York, NY 10017
2 Park Square, Milton Park
Abingdon, Oxon OX14 4RN, UK

K14968

ISBN: 978-1-4665-1376-1
90000
9 781466 513761